Conference Proceedings of the Society for Experimental Mechanics Series

Matt Allen · Randall L. Mayes · Daniel Rixen *Editors*

Dynamics of Coupled Structures, Volume 4

Proceedings of the 34th IMAC, A Conference and Exposition on Structural Dynamics 2016

Springer

Conference Proceedings of the Society for Experimental Mechanics Series

Series Editor
Kristin B. Zimmerman, Ph.D.
Society for Experimental Mechanics, Inc.,
Bethel, CT, USA

More information about this series at http://www.springer.com/series/8922

Matt Allen • Randall L. Mayes • Daniel Rixen
Editors

Dynamics of Coupled Structures, Volume 4

Proceedings of the 34th IMAC, A Conference and Exposition on Structural Dynamics 2016

Springer

Editors
Matt Allen
Engineering Physics Department
University of Wisconsin Madison
Madison, WI, USA

Daniel Rixen
Lehrstuhl für Angewandte Mechanik
Technische Universitat München
Garching, Bayern, Germany

Randall L. Mayes
Sandia National Laboratories
Albuquerque, NM, USA

ISSN 2191-5644 ISSN 2191-5652 (electronic)
Conference Proceedings of the Society for Experimental Mechanics Series
ISBN 978-3-319-29762-0 ISBN 978-3-319-29763-7 (eBook)
DOI 10.1007/978-3-319-29763-7

Library of Congress Control Number: 2014932412

© The Society for Experimental Mechanics, Inc. 2016
This work is subject to copyright. All rights are reserved by the Publisher, whether the whole or part of the material is concerned, specifically the rights of translation, reprinting, reuse of illustrations, recitation, broadcasting, reproduction on microfilms or in any other physical way, and transmission or information storage and retrieval, electronic adaptation, computer software, or by similar or dissimilar methodology now known or hereafter developed.
The use of general descriptive names, registered names, trademarks, service marks, etc. in this publication does not imply, even in the absence of a specific statement, that such names are exempt from the relevant protective laws and regulations and therefore free for general use.
The publisher, the authors and the editors are safe to assume that the advice and information in this book are believed to be true and accurate at the date of publication. Neither the publisher nor the authors or the editors give a warranty, express or implied, with respect to the material contained herein or for any errors or omissions that may have been made.

Printed on acid-free paper

This Springer imprint is published by Springer Nature
The registered company is Springer International Publishing AG Switzerland

Preface

Dynamics of Coupled Structures represents one of ten volumes of technical papers presented at the 34th IMAC, A Conference and Exposition on Structural Dynamics, organized by the Society for Experimental Mechanics and held in Orlando, Florida, January 25–28, 2016. The full proceedings also include volumes on nonlinear dynamics; dynamics of civil structures; model validation and uncertainty quantification; sensors and instrumentation; special topics in structural dynamics; structural health monitoring, damage detection, and mechatronics; rotating machinery, hybrid test methods, vibro-acoustics, and laser vibrometry; and shock and vibration, aircraft/aerospace, energy harvesting, acoustics and optics, and topics in modal analysis and testing.

Each collection presents early findings from experimental and computational investigations on an important area within structural dynamics. Coupled structures or substructuring is one of these areas.

Substructuring is a general paradigm in engineering dynamics where a complicated system is analyzed by considering the dynamic interactions between subcomponents. In numerical simulations, substructuring allows one to reduce the complexity of parts of the system in order to construct a computationally efficient model of the assembled system. A subcomponent model can also be derived experimentally, allowing one to predict the dynamic behavior of an assembly by combining experimentally and/or analytically derived models. This can be advantageous for subcomponents that are expensive or difficult to model analytically. Substructuring can also be used to couple numerical simulation with real-time testing of components. Such approaches are known as hardware-in-the-loop or hybrid testing.

Whether experimental or numerical, all substructuring approaches have a common basis, namely, the equilibrium of the substructures under the action of the applied and interface forces and the compatibility of displacements at the interfaces of the subcomponents. Experimental substructuring requires special care in the way the measurements are obtained and processed in order to assure that measurement inaccuracies and noise do not invalidate the results. In numerical approaches, the fundamental quest is the efficient computation of reduced order models describing the substructure's dynamic motion. For hardware-in-the-loop applications, difficulties include the fast computation of the numerical components and the proper sensing and actuation of the hardware component. Recent advances in experimental techniques, sensor/actuator technologies, novel numerical methods, and parallel computing have rekindled interest in substructuring in recent years leading to new insights and improved experimental and analytical techniques.

The organizers would like to thank the authors, presenters, session organizers, and session chairs for their participation in this track.

Madison, WI, USA — Matt Allen
Albuquerque, NM, USA — Randall L. Mayes
Garching, Bayern, Germany — Daniel Rixen

Contents

Chapter 1
Verification of Experimental Component Mode Synthesis in the Sierra Analysis Framework

Brian C. Owens and Randall L. Mayes

Abstract Experimental component mode synthesis (CMS) seeks to measure the fundamental modes of vibration of a substructure and develop a structural dynamics model of an as-built structural component through modal testing. Experimental CMS has the potential to circumvent laborious and costly substructure model development and calibration in lieu of a structural dynamics model obtained directly from experimental measurements. Previous efforts of interfacing an experimental CMS model with a production finite element code proved cumbersome. Recently an improved "Craig-Mayes" approach casts an experimental CMS model in the familiar Craig-Bampton form. This form is easily understood by analysts and more readily interfaced with non-trivial, discrete finite element models. The approach/work-flow for interfacing an experimental Craig-Mayes CMS model with the Sierra analysis framework is discussed and the procedure is demonstrated on a verification problem.

Keywords Component mode synthesis • Craig-Bampton • Substructure • Sierra • Finite elements

Nomenclature

CMS	Component mode synthesis
FE	Finite element(s)
M	Mass matrix
TS	Transmission simulator

1.1 Introduction

The concept of experimental component mode synthesis (CMS) seeks to measure the fundamental modes of vibration of a substructure and develop a structural dynamics model of a component or subsystem which may be inserted into an analytical model of a higher-level system. Strengths of experimental CMS allow for one to circumvent laborious and costly substructure model development and calibration in lieu of a structural dynamics model obtained directly from experimental measurements. Furthermore, experimental CMS allows for a better modelling capability of as-built structural components.

This work will interface an experimentally derived "Craig-Bampton" like substructure with a discrete finite element model within Sandia National Laboratories Sierra analysis framework [1, 2]. A previously developed transmission simulation approach is employed to match interface locations with a discrete system level finite element model. Previous efforts will be discussed and strengths of the current approach in streamlining the use of experimentally derived substructures will be highlighted. This approach will be discussed and verification exercises will be presented.

Sandia National Laboratories is a multi-program laboratory managed and operated by Sandia Corporation, a wholly owned subsidiary of Lockheed Martin Corporation, for the U.S. Department of Energy National Nuclear Security Administration under Contract DE-AC04-94AL85000.

B.C. Owens (✉) • R.L. Mayes
Sandia National Laboratories, P.O. Box 5800 – MS0346, Albuquerque, NM 87185, USA
e-mail: bcowens@sandia.gov; rlmayes@sandia.gov

© The Society for Experimental Mechanics, Inc. 2016

M. Allen et al. (eds.), *Dynamics of Coupled Structures, Volume 4*, Conference Proceedings of the Society for Experimental Mechanics Series, DOI 10.1007/978-3-319-29763-7_1

1.2 Craig-Mayes Experimental Sub-Structuring Method

The Craig-Mayes experimental dynamic sub-structuring method improves upon previous experimental sub-structuring methods by representing the substructure system matrices (mass, stiffness, and damping) in a Craig-Bampton [3] like form. This form contains structural matrices with generalized/modal and interface degrees of freedom. This approach uses a transmission simulator to model the interface of the sub-structure to the remainder of the system. The transmission simulator approach requires an accurate discrete finite element model of the transmission simulator/fixture to accurately recover the interface degrees of freedom in an experimental substructure. The Craig-Mayes experimental sub-structuring method and transmission simulator approach are discussed in references [4, 5].

1.3 Interface of Experimental CMS Model to Sierra

Previous efforts of coupling experimental CMS models within the Sierra framework employed multi-point constraints and a non-Craig-Mayes CMS representation. This approach proved overly cumbersome for all but the simplest model configurations, and was prone to numerical conditioning issues. The Craig-Mayes format provides a readily realizable interface to a high fidelity structural dynamics model with an interface similar to CMS or "super element" model derived purely from analytical methods. The experimental CMS model is typically provided by experimentalists as a collection of Craig-Bampton like mass, stiffness, and damping matrices [4]. Note that the damping matrix is not required to define a baseline experimental CMS model, but is readily available from experimental measurements.

The Craig-Bampton like matrices are $p \times p$ in dimension, such that $p = m + n$. Here, m is the number of modes retained in the CMS reduction, and n is the number of interface degrees of freedom in the CMS model. The required form of these equations is shown in Eq. (1.1). Note that the form of the mass matrix is shown, but identical forms are required for the stiffness and damping matrices. These matrices are symmetrical in nature. $\hat{M}$ defines couplings between the generalized (modal) degrees of freedom in the CMS model (this matrix should be diagonal in nature), $\overline{M}$ defines couplings between the interface degrees of freedom, and $\widetilde{M}$ defines the couplings between generalized and interface degrees of freedom.

$$M_{CMS} = \begin{bmatrix} \hat{M}_{m\times m} & \widetilde{M}_{m\times n} \\ \widetilde{M}^{T}_{m\times n} & \overline{M}_{n\times n} \end{bmatrix} \tag{1.1}$$

An $r \times 3$ coordinate array is also required that defines the coordinates of the r interface points. In addition to interface point coordinates an $n \times 1$ map array is required that specifies the "local" degrees of freedom of the interface degrees of freedom. The order of this array should be consistent with the ordering of the coordinate array.

In summary, the following data is required to accompany an experimentally derived CMS model:

- Number of modes retained in the CMS reduction (m)
- Number of interface degrees of freedom (n)
- Interface point coordinate array
- CMS mass matrix
- CMS stiffness matrix
- Interface degree of freedom map array
- CMS damping matrix (optional)

This information can be provided to the MATLAB based "CMS Toolkit" to create a Sierra super element of the experimental CMS model. The CMS toolkit creates two files. First, an Exodus finite element mesh is created defining the geometry of the super element. This includes the coordinates of the interface nodes for the n-node super element. Next, the formulation of this super element (mass, stiffness, and damping) are characterized in a NetCDF binary file. The super element Exodus file is inserted into a discrete finite element model using GJOIN [6] or a similar mesh joining utility. From here, the super element NetCDF file is referenced in a Sierra input deck and subsequent modal, vibration, or transient analysis accounts for the coupling between the discrete finite element model and the experimentally derived Craig-Mayes substructure. This workflow is depicted in Fig. 1.1.

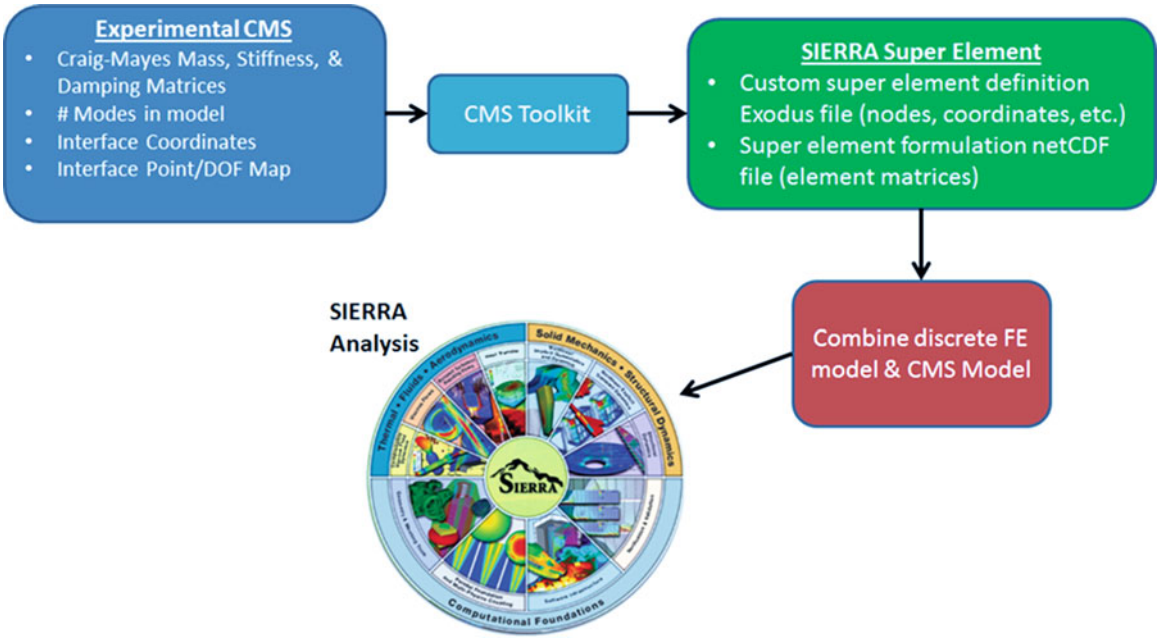

Fig. 1.1 Workflow for interfacing an experimentally derived CMS model in Sierra analysis

1.4 Demonstration

This section presents a demonstration of the aforementioned process for interfacing an experimentally derived Craig-Mayes substructure to a discrete finite element modal for Sierra-SD analysis. First the model/test configuration is described followed by results of the exercise.

1.4.1 Configuration

A 2-D simple beam configuration documented in reference [4] was considered for a proof of concept analysis for interfacing an experimentally derived CMS substructure model with Sierra-SD analysis. The configuration is shown in Fig. 1.2. Two beams are connected together over a specified region of overlap. The left beam is to be modeled by finite elements, whereas the dynamics of the right beam are measured experimentally and an experimental CMS model is derived. This is done using a "transmission simulator" shown as "TS Beam" in Fig. 1.2. Details of the transmission simulator are elaborated on in references [4, 5]. The transmission simulator essentially allows one to generate interface degree of freedom responses at discrete locations from those measured from a modal test. This is a very convenient means for interfacing an experimentally derived CMS model to discrete points of a finite element model.

Note that there are five nodes in the overlap between the left finite element beam and the right experimental CMS beam. Thus, the transmission simulator approach was used to derive an experimental CMS model with five interface points (coincident with the finite element nodes). Each interface point had 3 degrees of freedom (axial translation, bending translation, and rotation). Therefore, a total of 15 interface degrees of freedom exist in the model. Three modes were retained in the CMS reduction. This resulted in CMS mass, stiffness, and damping matrices that had dimension of 18×18.

1.4.2 Results

The Craig-Mayes substructure model of the beam was interfaced to the discrete "FE Beam" model in Sierra-SD described in Sect. 1.2. Results show good agreement between the "truth model" described in reference [4] and the Sierra-SD implementation. Table 1.1 presents a comparison of modal frequencies. The first five modes have 1 % error or less and

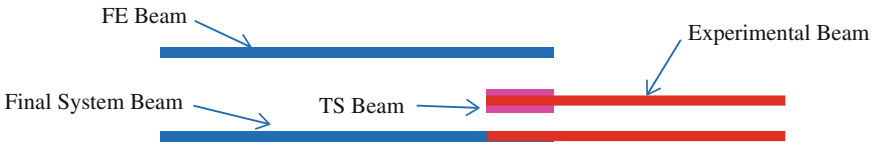

Fig. 1.2 2D beam configuration [4]

Table 1.1 Comparison of Sierra-SD sub-structured modal frequency vs. truth frequency

Truth frequency (Hz) [4]	Sierra-SD sub-structured frequency (Hz)	Error (%)
212.0	210.4	−0.7
574.6	568.6	−1.0
1121.0	1132.0	1.0
1867.3	1863.9	−0.2
2750.2	2767.6	0.6
3341.7	3383.9	1.3
3949.6	4003.2	1.4
5115.9	5105.0	−0.2
5965.5	5945.8	−0.3

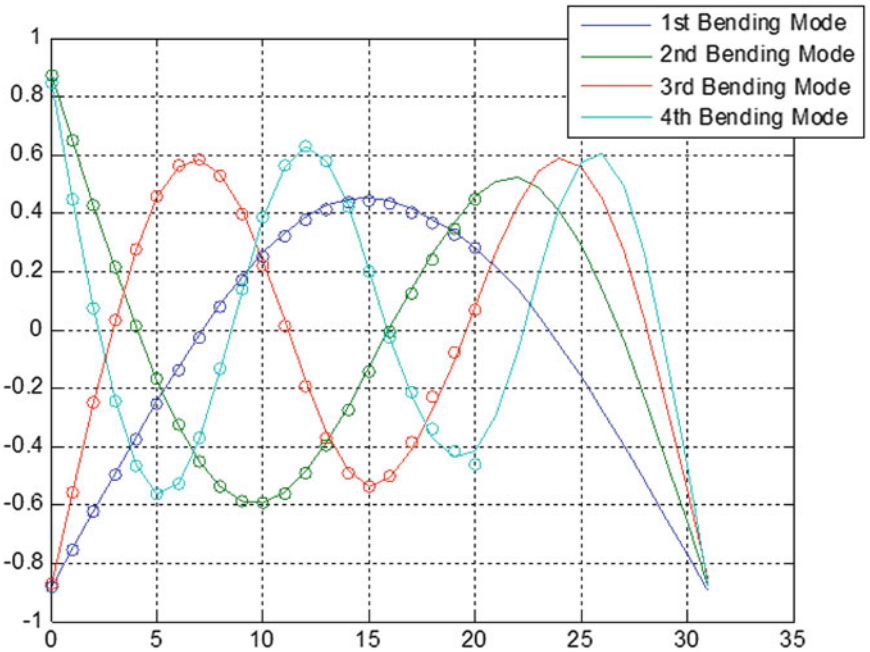

Fig. 1.3 Comparison of "truth" and Sierra-SD sub-structured lower bending mode shapes (*solid line* = truth model, *circle* = sub-structured model)

the 6th–9th modes have at most 1.4 % error. Bending mode shape comparisons of a discrete finite element model of the entire system and those of the discrete "FE beam" coupled with the Craig-Mayes experimental beam are shown in Figs. 1.3 and 1.4. Solid lines represent the finite element results of the complete system while markers represent the mode shape of the discrete left beam coupled with the Craig-Mayes right beam. Overall, good agreement is seen between the "truth" FEM mode shapes and those of the discrete finite element model of the left beam coupled to the Craig-Mayes substructure of the right beam. Some differences are apparent for the 4th–7th bending mode shapes in the vicinity of the interface to the Craig-Mayes substructure. This may be due to some artifacts of the transmission simulator approach providing an increased stiffening effect at this location.

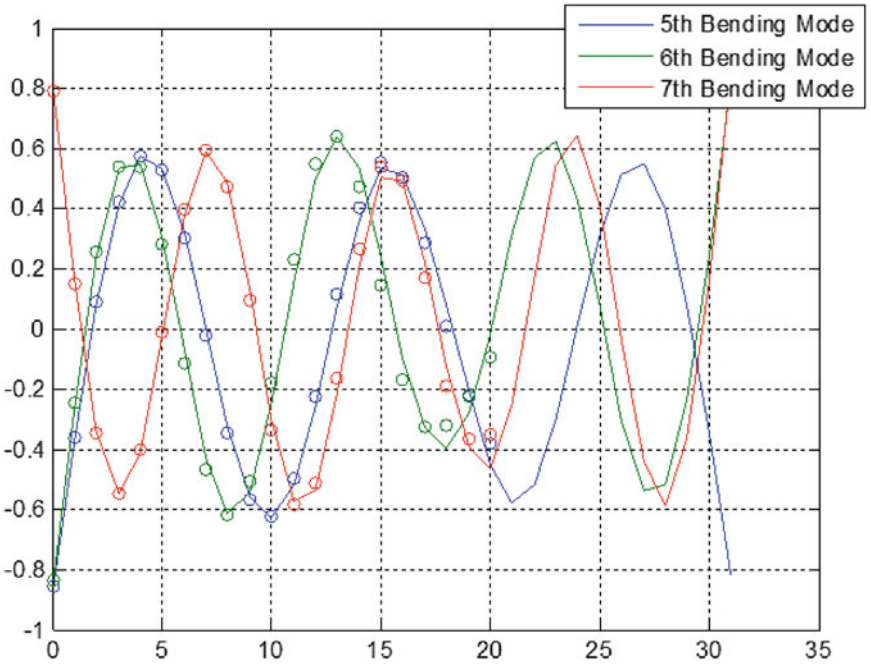

Fig. 1.4 Comparison of "truth" and Sierra-SD sub-structured higher bending mode shapes (*solid line* = truth model, *circle* = sub-structured model)

1.5 Conclusions

This paper has presented the motivation for using experimentally derived substructures within the Sierra analysis framework. The Craig-Mayes sub-structuring approach allows for a straightforward interface of an experimental CMS model with a discrete finite element model by using a representation similar to the Craig-Bampton CMS approach. This allows for the experimental CMS model to be treated virtually the same way as a numerically derived Craig-Bampton "super element", although the experimental model may be prone to some numerical conditioning issues as a result of flaws in measurement data and mathematical operations being performed on that data. The work-flow of interfacing a Craig-Mayes model with the Sierra analysis framework was discussed and the process was demonstrated successfully on a proof-of-concept application.

Future work will consider more complicated substructures. This may include sub-structures generated from actual experimental data or substructures derived from "virtual" modal testing with the Sierra-SD analysis software. The concept of virtual modal testing allows for more idealized accelerometer data to be considered within the general process of an experimental sub-structuring method while allowing control of the imperfections in the test data through the introduction of measurement noise or other flaws.

References

1. Reese, G., Bhardwaj, M., Walsh, T.: Sierra Structural Dynamics-Theory Manual. Sandia National Laboratories, Albuquerque (2014)
2. Sierra Structural Dynamics Development Team: Sierra Structural Dynamics-User's Notes. Sandia National Laboratories, Albuquerque (2014)
3. Craig, R.R., Bampton, M.C.: Coupling of substructures for dynamic analysis. AIAA J. **6**(7), 1313–1319 (1968)
4. Mayes, R.L.: A Craig-Bampton experimental dynamic substructure using the transmission simulator method. In: Proceedings of the 32nd International Modal Analysis Conference, Orlando, February 2015
5. Allen, M.S., Kammer, D.C., Mayes, R.L.: Experimental based substructuring using a Craig-Bampton transmission simulator model. In: Proceedings of the 32nd International Modal Analysis Conference, Orlando, February 2014
6. Sjaardema, G.D.: GJOIN: a program for merging two or more GENESIS databases, SAND92-2290 (1992)

Chapter 2
Multi-DoF Interface Synchronization of Real-Time-Hybrid-Tests Using a Recursive-Least-Squares Adaption Law: A Numerical Evaluation

Andreas Bartl, Johannes Mayet, Morteza Karamooz Mahdiabadi, and Daniel J. Rixen

Abstract Cyber Physical Testing or Real Time Hybrid Testing is a Hardware-In-The-Loop approach allowing for tests of structural components of complex machines with realistic boundary conditions by coupling virtual components. The need to actuate the physical interface makes the tests on structural systems challenging. In order to deal with stability and accuracy issues, we propose the use of an Adaptive Feed-Forward Cancellation approach with a Recursive Least Squares (RLS) adaption law for interface synchronization of harmonically excited systems. The interface forces are generated from multiple harmonic components of the excitation force. A RLS adaption law sets the amplitudes and phases of the harmonic interface force components and minimizes the interface gap. One major practical advantage of using a RLS adaption law is that only one forgetting factor has to be chosen compared to other adaption algorithms with various tuning parameters. As a consequence, it is possible to test systems with multiple interface DoF. In order to illustrate the performance and robustness of the proposed testing algorithm, the contribution includes a numerical investigation on a lumped mass system.

Keywords Hybrid testing • Hardware-in-the-loop • Real-time substructuring • Interface synchronization • Recursive least squares

2.1 Introduction

Real Time Hybrid Testing, Cyber Physical Testing or Hardware-in-the-Loop for structural systems is a testing approach connecting experimental test rigs (experimental component) with simulation models (virtual component) in a real time test (see Figs. 2.1 and 2.2). In contrast of testing the experimental component by applying fictitious load cases, realistic boundary conditions are provided in these test procedures. The approach is always valuable were neither full experimental tests nor full simulations are applicable. Real Time Hybrid Testing was applied in engineering of earthquake save civil structures in [3, 12, 17]. A testing example on a full wind turbine nacelle is presented in [6] and an automotive application is given in [18].

The objective of the interface synchronization control in Real Time Hybrid Testing (RTHT) is to satisfy equilibrium and compatibility constraints within the desired frequency range. Consider for example structural applications with commonly low damping of the overall system. Controlling a system with poles close to the imaginary axis can cause instability of the real time test due to small control errors and inaccuracies in measurement or actuation. The problem of interface synchronization is closely linked to actual compensation methods. The performance of actuator compensation methods is compared in [5]. The authors of [15, 21] present frameworks for the development of RTHT controllers. A Linear-Quadratic-Regulator controller framework is presented in [22]. In the contribution [7] the Real Time Hybrid Testing problem is analyzed with conventional control theory. As in many applications the dynamics of the experimental substructures are unknown, Model Reference Adaptive Control (MRAC) is proposed as a control strategy in [19, 23]. A widely used approach is based on polynomial forward prediction used in [8, 12] for compensation of the actuator dynamics. The authors of [24] extend this approach by gain and phase estimation. More recently neuronal network feedforward compensation for the use in Real Time Hybrid Testing were proposed in [16]. Model Predictive Control is proposed as a control strategy for RTHT in [20].

In [1] we presented a adaptive feedforward algorithm with a harmonic regressor (see e.g. [2, 4, 10]) applied to RTHT. The adaption is based on a gradient algorithm. This approach is closely linked to fxLMS Algorithm as presented in [14]. However, in case of multiple DoF interfaces the choice of the adaption gain matrix, which defines the stability of the algorithm, is getting impractical. The entries of the adaption gain matrix can vary within several orders of magnitude and wrong choices may cause instability of the test. Therefore, we propose in this contribution an adaptive feedforward filter with harmonic

A. Bartl (✉) • J. Mayet • M.K. Mahdiabadi • D.J. Rixen
Technical University of Munich, Boltzmannstraße 15, D-85748 Garching, Germany
e-mail: andreas.bartl@tum.de

© The Society for Experimental Mechanics, Inc. 2016

M. Allen et al. (eds.), *Dynamics of Coupled Structures, Volume 4*, Conference Proceedings of the Society for Experimental Mechanics Series, DOI 10.1007/978-3-319-29763-7_2

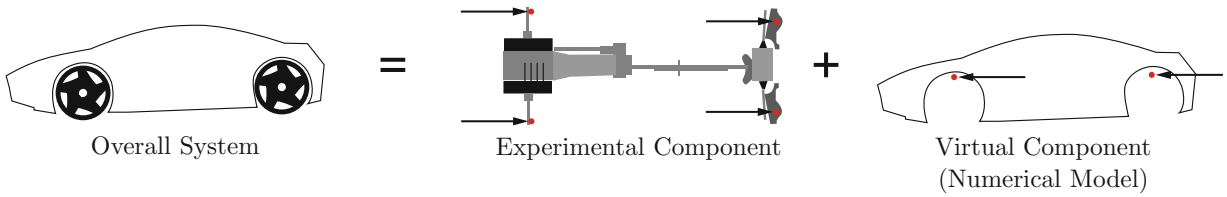

Fig. 2.1 The overall system is split into a virtual and an experimental component

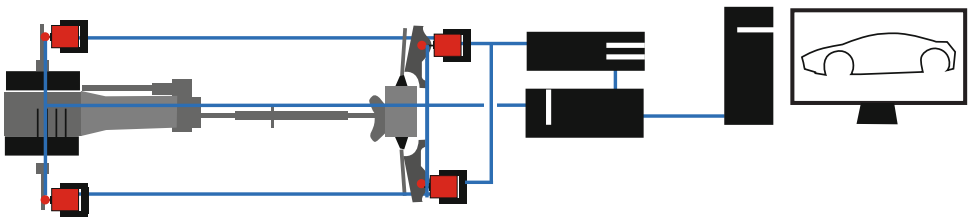

Fig. 2.2 The test rig is coupled with sensors and actuators to the virtual component running on a real time computer

regressor based on a Recursive Least Squares (RLS) adaption law with only a single tuning parameter. The fact that the user has only to choose one tuning parameter makes the suggested approach applicable to carry out various tests on systems with a multi DoF interface.

2.2 Hybrid Testing Problem Formulation

The objective of the RTHT control is to satisfy compatibility (Eq. (2.1)) and equilibrium (Eq. (2.2)) constraints between virtual and experimental components. The Boolean matrices $\boldsymbol{G}_V$ and $\boldsymbol{G}_E$ are selecting the interface forces and displacements (see [9] for details). $\boldsymbol{y}_{b,V}$ and $\boldsymbol{y}_{b,E}$ are the interface displacement vectors. The interface gap is denoted as $\boldsymbol{e}$. $\boldsymbol{f}_{b,V}$ and $\boldsymbol{f}_{b,E}$ are the interface force vectors

$$\boldsymbol{G}_V\boldsymbol{u} - \boldsymbol{G}_E\boldsymbol{u}_{=}\boldsymbol{y}_{b,V} - \boldsymbol{y}_{b,E} = \boldsymbol{e} = \boldsymbol{0} \tag{2.1}$$

$$\boldsymbol{G}_V\boldsymbol{f}_{b,V} + \boldsymbol{G}_E\boldsymbol{f}_{b,E} = \boldsymbol{0} \tag{2.2}$$

In principal two distinctive ways for setting up an control scheme do exist. One possibility is to define the interface displacements as compatible and controlling the interface forces in order to achieve equilibrium. In contrast one can define the interface forces as forces with equal magnitude and opposite sign, controlling the interface gap. In this contribution, we use the latter one, which is comparable to the to the dual formulation in substructuring (see [9] for details). In practice, this foregoing is absolutely meaningful since one will end up with forces as controller setpoint rather than gaps which would necessarily require inner-loop actuator control algorithms. The applied forces $\boldsymbol{\lambda}$ are subsequently measured and applied to the virtual subcomponent with opposite sign. The dynamics of both components are given by Eq. (2.3).

$$\begin{bmatrix} \boldsymbol{M}_V & \boldsymbol{0} \\ \boldsymbol{0} & \boldsymbol{M}_E \end{bmatrix} \begin{bmatrix} \ddot{\boldsymbol{u}}_V \\ \ddot{\boldsymbol{u}}_E \end{bmatrix} + \begin{bmatrix} \boldsymbol{D}_V & \boldsymbol{0} \\ \boldsymbol{0} & \boldsymbol{D}_E \end{bmatrix} \begin{bmatrix} \dot{\boldsymbol{u}}_V \\ \dot{\boldsymbol{u}}_E \end{bmatrix} + \begin{bmatrix} \boldsymbol{K}_V & \boldsymbol{0} \\ \boldsymbol{0} & \boldsymbol{K}_E \end{bmatrix} \begin{bmatrix} \boldsymbol{u}_V \\ \boldsymbol{u}_E \end{bmatrix} + \begin{bmatrix} \boldsymbol{G}_V^T \\ -\boldsymbol{G}_E^T \end{bmatrix} \boldsymbol{\lambda} = \begin{bmatrix} \boldsymbol{f}_V \\ \boldsymbol{f}_E \end{bmatrix} \tag{2.3}$$

The objective of an interface synchronization controller will be to apply $\boldsymbol{\lambda}$ such that the interface gap $\boldsymbol{e}$ is closed. The assumptions of the control strategy are an harmonic excitation and steady-state system behaviour. The block diagram of the overall control system is given in Fig. 2.3. Before deriving the algorithm the hybrid testing problem is reformulated such that it can be used for an adaptive feedforward compensator in this section. The corresponding state space formulations are given in Eqs. (2.4) and (2.5).

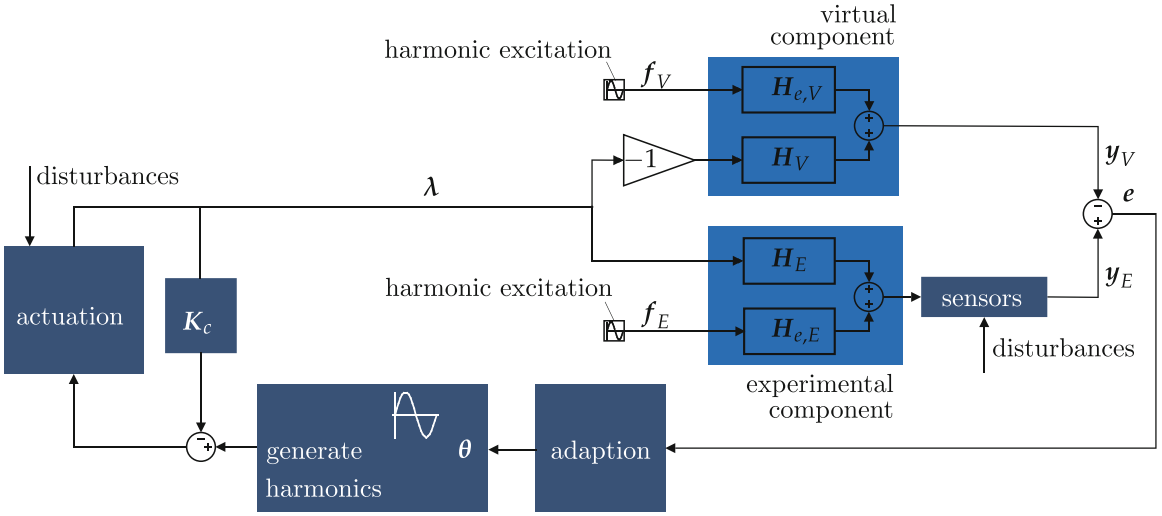

Fig. 2.3 The block diagram shows the hybrid test with adaptive feedforward compensation. Harmonic excitation on both the experimental and virtual component are possible. The actuator is exciting the experimental and contrariwise the virtual component in the present of real and virtual harmonic excitations. The controller adapts phase and gain of the harmonic inputs to the actuator such that the interface gap $\boldsymbol{e}$ is closed. (adapted from [1])

$$\begin{aligned}
\dot{\boldsymbol{x}}_V &= \underbrace{\begin{bmatrix} \boldsymbol{0} & \boldsymbol{I} \\ -\boldsymbol{M}_V^{-1}\boldsymbol{K}_V & -\boldsymbol{M}_V^{-1}\boldsymbol{D}_V \end{bmatrix}}_{\boldsymbol{A}_V} \boldsymbol{x}_V + \underbrace{\begin{bmatrix} \boldsymbol{0} \\ \boldsymbol{M}_V^{-1}\boldsymbol{G}_V^T \end{bmatrix}}_{\boldsymbol{B}_V} \boldsymbol{\lambda} + \underbrace{\begin{bmatrix} \boldsymbol{0} \\ \boldsymbol{M}_V^{-1} \end{bmatrix}}_{\boldsymbol{E}_V} \boldsymbol{f}_V \\
\boldsymbol{y}_V &= \boldsymbol{G}_V \boldsymbol{u}_V = \underbrace{\begin{bmatrix} \boldsymbol{G}_V & \boldsymbol{0} \end{bmatrix}}_{\boldsymbol{C}_V} \boldsymbol{x}_V
\end{aligned} \tag{2.4}$$

$$\begin{aligned}
\dot{\boldsymbol{x}}_E &= \underbrace{\begin{bmatrix} \boldsymbol{0} & \boldsymbol{I} \\ -\boldsymbol{M}_E^{-1}\boldsymbol{K}_E & -\boldsymbol{M}_E^{-1}\boldsymbol{D}_E \end{bmatrix}}_{\boldsymbol{A}_E} \boldsymbol{x}_E - \underbrace{\begin{bmatrix} \boldsymbol{0} \\ \boldsymbol{M}_E^{-1}\boldsymbol{G}_E^T \end{bmatrix}}_{\boldsymbol{B}_E} \boldsymbol{\lambda} + \underbrace{\begin{bmatrix} \boldsymbol{0} \\ \boldsymbol{M}_E^{-1} \end{bmatrix}}_{\boldsymbol{E}_E} \boldsymbol{f}_E \\
\boldsymbol{y}_E &= \boldsymbol{G}_E \boldsymbol{u}_E = \underbrace{\begin{bmatrix} \boldsymbol{G}_E & \boldsymbol{0} \end{bmatrix}}_{\boldsymbol{C}_E} \boldsymbol{x}_E
\end{aligned} \tag{2.5}$$

The interface responses can be written as

$$\boldsymbol{y}_V = \underbrace{\int_{t_0}^{t} \boldsymbol{C}_V e^{\boldsymbol{A}_V(t-\tau)} \boldsymbol{B}_V \boldsymbol{\lambda} \, \mathrm{d}\tau}_{\substack{\text{contribution of interface excitation} \\ \text{with transfer function } \boldsymbol{H}_V(j\omega)}} + \underbrace{\int_{t_0}^{t} \boldsymbol{C}_V e^{\boldsymbol{A}_V(t-\tau)} \boldsymbol{E}_V \boldsymbol{f}_V \, \mathrm{d}\tau}_{\text{contribution of external excitation}} + \underbrace{\boldsymbol{C}_V e^{\boldsymbol{A}_V(t-\tau)} \boldsymbol{x}_V(t_0)}_{\text{contribution of initial conditions}} \tag{2.6}$$

$$\boldsymbol{y}_E = \underbrace{\int_{t_0}^{t} \boldsymbol{C}_E e^{\boldsymbol{A}_E(t-\tau)} \boldsymbol{B}_E \boldsymbol{\lambda} \, \mathrm{d}\tau}_{\substack{\text{contribution of interface excitation} \\ \text{with transfer function } \boldsymbol{H}_E(j\omega)}} + \underbrace{\int_{t_0}^{t} \boldsymbol{C}_E e^{\boldsymbol{A}_E(t-\tau)} \boldsymbol{E}_E \boldsymbol{f}_E \, \mathrm{d}\tau}_{\text{contribution of excitation}} + \underbrace{\boldsymbol{C}_E e^{\boldsymbol{A}_E(t-\tau)} \boldsymbol{x}_E(t_0)}_{\text{contribution of initial conditions}} \tag{2.7}$$

Assuming harmonic excitations and steady state behavior, the contribution of initial conditions are neglected. The interface forces can be expressed as a combination of harmonic functions:

$$\begin{aligned}
\boldsymbol{\lambda} &= \sum_{i=1}^{m} \boldsymbol{W}_i(t) \boldsymbol{\theta}_i \\
\boldsymbol{W}_i(t) &= \begin{bmatrix} \boldsymbol{I}_{nn} \cos(\alpha_i) & \boldsymbol{I}_{nn} \sin(\alpha_i) \end{bmatrix} \quad \text{with} \quad \boldsymbol{W}_i \in \mathbb{R}^{n \times 2n}
\end{aligned} \tag{2.8}$$

In Eq. (2.8) the regressor matrix $\boldsymbol{W}_i(t)$ contains the amplitudes for the cosine and sine part of the interface forces and thus the phase angle $\alpha_i = \int_0^t \omega_i(t)\mathrm{d}t$ and frequency $\omega_i(t)$, which are allowed to vary slowly. The important parameter vector $\boldsymbol{\theta}_i$ defines the phases and amplitudes of the interface forces. Since we assume steady state behavior $\boldsymbol{y}_V$ and $\boldsymbol{y}_E$ can now be rewritten as

$$\boldsymbol{y}_V = \sum_{i=1}^{m} \underbrace{\boldsymbol{W}_i(t)\boldsymbol{P}_{V,i}\boldsymbol{\theta}_i}_{\substack{\text{influence}\\ \text{interfaceforces}}} + \underbrace{\boldsymbol{W}_i(t)\boldsymbol{\pi}_{V,i}}_{\substack{\text{influence external}\\ \text{excitation (disturbance)}}} = \boldsymbol{W}(t)\boldsymbol{P}_V\boldsymbol{\theta} + \sum_{i=1}^{m} \boldsymbol{W}_i(t)\boldsymbol{\pi}_{V,i} \tag{2.9}$$

$$\boldsymbol{y}_E = \sum_{i=1}^{m} \underbrace{\boldsymbol{W}_i(t)\boldsymbol{P}_{E,i}\boldsymbol{\theta}_i}_{\substack{\text{influence}\\ \text{interface forces}}} + \underbrace{\boldsymbol{W}_i(t)\boldsymbol{\pi}_{E,i}}_{\substack{\text{influence external}\\ \text{excitation (disturbance)}}} = \boldsymbol{W}(t)\boldsymbol{P}_E\boldsymbol{\theta} + \sum_{i=1}^{m} \boldsymbol{W}_i(t)\boldsymbol{\pi}_{E,i}, \tag{2.10}$$

where the matrices $\boldsymbol{P}_{V,i}$ and $\boldsymbol{P}_{E,i}$ are created using transfer function $\boldsymbol{H}_V(j\omega_1)$ and $\boldsymbol{H}_E(j\omega_1)$ respectively (see Fig. 2.3 and Eqs. (2.11) and (2.12)). These matrices basically apply a phase shift and gain to the parameter vector $\boldsymbol{\theta}$. The vectors $\boldsymbol{\pi}_{V,i}$ and $\boldsymbol{\pi}_{E,i}$ define phase and amplitude of the contributions of the external forces to the interface displacements.

$$\boldsymbol{P}_{V,i} = \begin{bmatrix} Re(\boldsymbol{H}_V(j\omega_i)) & Im(\boldsymbol{H}_V(j\omega_i)) \\ -Im(\boldsymbol{H}_V(j\omega_i)) & Re(\boldsymbol{H}_V(j\omega_i)) \end{bmatrix} = \begin{bmatrix} \boldsymbol{P}_{R,V,i} & \boldsymbol{P}_{I,V,i} \\ -\boldsymbol{P}_{I,V,i} & \boldsymbol{P}_{R,V,i} \end{bmatrix} \quad \text{with} \quad \boldsymbol{P}_{V,i} \in \mathbb{R}^{2n\times 2n} \tag{2.11}$$

$$\boldsymbol{P}_{E,i} = \begin{bmatrix} Re(\boldsymbol{H}_E(j\omega_i)) & Im(\boldsymbol{H}_E(j\omega_i)) \\ -Im(\boldsymbol{H}_E(j\omega_i)) & Re(\boldsymbol{H}_E(j\omega_i)) \end{bmatrix} = \begin{bmatrix} \boldsymbol{P}_{R,E,i} & \boldsymbol{P}_{I,E,i} \\ -\boldsymbol{P}_{I,E,i} & \boldsymbol{P}_{R,E,i} \end{bmatrix} \quad \text{with} \quad \boldsymbol{P}_{E,i} \in \mathbb{R}^{2n\times 2n} \tag{2.12}$$

2.3 Adaptive Feedforward Algorithm

In order to couple virtual and experimental components, the parameter vector $\boldsymbol{\theta}$ has to be chosen such that the interface gap $\boldsymbol{e}$ is closed. In order to adapt $\boldsymbol{\theta}$ online, the use of a recursive least squares algorithm (see e.g. [11, 13]) is proposed, which minimizes the integral cost functional J defined in Eq. (2.13). Note that for the derivation of the adaption law, the above mentioned functions are used in their time discretized form. Here we use brackets to indicate a specific time instance. The cost functional includes a forgetting factor $\mu \in [0,1]$, which enables a decreasing weighting of old values of $\boldsymbol{e}^T[i]\boldsymbol{e}[i]$ at ith time instances. The phase and gain matrices $\boldsymbol{P}_E$ and $\boldsymbol{P}_V$ as well as $\boldsymbol{P}_A$, which characterizes the actuator dynamics, are combined to $\boldsymbol{P}$.

$$\begin{aligned} J[k] &= \sum_{i=0}^{k} \mu^{k-i}\boldsymbol{e}^T[i]\boldsymbol{e}[i] \\ \text{with} \quad \boldsymbol{e}[i] &= \boldsymbol{y}_E[i] - \boldsymbol{y}_V[i] = \boldsymbol{W}[i]\underbrace{(\boldsymbol{P}_E - \boldsymbol{P}_V)\boldsymbol{P}_A}_{\boldsymbol{P}}\boldsymbol{\theta}[i] + \boldsymbol{W}[i]\underbrace{(\boldsymbol{\pi}_E[i] - \boldsymbol{\pi}_V[i])}_{\boldsymbol{\pi}[i]} \end{aligned} \tag{2.13}$$

Starting point for deriving the adaption law for the hybrid testing problem is the solution of the least squares problem, which is then rearranged as recursive algorithm:

$$\boldsymbol{0} = \frac{\partial J[k]}{\partial \boldsymbol{\theta}[k]} = \sum_{i=0}^{k} 2\mu^{k-i}\left(\boldsymbol{P}^T\boldsymbol{W}[i]^T\boldsymbol{W}[i]\boldsymbol{P}\boldsymbol{\theta}[k] + \boldsymbol{P}^T\boldsymbol{W}[i]^T\boldsymbol{W}[i]\boldsymbol{\pi}[i]\right) \tag{2.14}$$

$$\boldsymbol{\theta}[k] = \underbrace{\left(\sum_{i=0}^{k} \mu^{k-i}\boldsymbol{P}^T\boldsymbol{W}[i]^T\boldsymbol{W}[i]\boldsymbol{P}\right)^{-1}}_{\boldsymbol{R}[k]} \left(\sum_{i=0}^{k} -\mu^{k-i}\boldsymbol{P}^T\boldsymbol{W}[i]^T\boldsymbol{W}[i]\boldsymbol{\pi}[i]\right) \tag{2.15}$$

The solution of the least squares problem for the next time step $k+1$ is arranged as follows:

$$\boldsymbol{\theta}[k+1] = \overbrace{\left(\sum_{i=0}^{k} \mu^{k+1-i} \boldsymbol{P}^T \boldsymbol{W}[i]^T \boldsymbol{W}[i] \boldsymbol{P} + \boldsymbol{P}^T \boldsymbol{W}[k+1]^T \boldsymbol{W}[k+1] \boldsymbol{P}\right)^{-1}}^{\boldsymbol{R}[k+1]} \cdot \left(\sum_{i=0}^{k} -\mu^{k+1-i} \boldsymbol{P}^T \boldsymbol{W}[i]^T \boldsymbol{W}[i] \boldsymbol{\pi}[i] - \boldsymbol{P}^T \boldsymbol{W}[k+1]^T \boldsymbol{W}[k+1] \boldsymbol{\pi}[k+1]\right)$$

Applying the Woodbury matrix identity allows to replace the inverse of the regressor matrix:

$$\boldsymbol{\theta}[k+1] = \overbrace{\left(\frac{1}{\mu}\boldsymbol{R}[k] - \frac{1}{\mu}\boldsymbol{R}[k]\boldsymbol{P}^T \boldsymbol{W}[k+1]^T \left(\boldsymbol{I} + \frac{1}{\mu}\boldsymbol{W}[k+1]\boldsymbol{P}\boldsymbol{R}[k]\boldsymbol{P}^T \boldsymbol{W}[k+1]^T\right)^{-1} \boldsymbol{W}[k+1]\boldsymbol{P}\boldsymbol{R}[k]\right)}^{\boldsymbol{R}[k+1]} \cdot \left(\sum_{i=0}^{k} -\mu\mu^{k-i} \boldsymbol{P}^T \boldsymbol{W}[i]^T \boldsymbol{W}[i] \boldsymbol{\pi}[i] - \boldsymbol{P}^T \boldsymbol{W}[k+1]^T \boldsymbol{W}[k+1] \boldsymbol{\pi}[k+1]\right)$$

Further simplification of the equations finally yields the recursive least squares adaption law:

$$\boldsymbol{\gamma}[k+1] = \frac{1}{\mu}(\boldsymbol{R}[k]\boldsymbol{P}^T \boldsymbol{W}[k+1]^T)(\boldsymbol{I} + \frac{1}{\mu}\boldsymbol{W}[k+1]\boldsymbol{P}\boldsymbol{R}[k]\boldsymbol{P}^T \boldsymbol{W}^T[k+1])^{-1} \tag{2.16}$$

$$\boldsymbol{\theta}[k+1] = \boldsymbol{\theta}[k] + \boldsymbol{\gamma}[k+1] \underbrace{(\boldsymbol{W}[k+1]\boldsymbol{P}\boldsymbol{\theta}[k] + \boldsymbol{W}[k+1]\boldsymbol{\pi}[k+1])}_{\boldsymbol{e}'[k+1]} \tag{2.17}$$

$$\boldsymbol{R}[k+1] = \frac{1}{\mu}(\boldsymbol{R}[k] - \boldsymbol{\gamma}[k+1]\boldsymbol{W}[k+1]\boldsymbol{P}\boldsymbol{R}[k]) \tag{2.18}$$

Note that $\boldsymbol{e}'$ is the a-priori gap, which can be measured, whereas $\boldsymbol{e}$ is the a-posteriori interface gap, which is used in the cost functional J. The RLS algorithm allows the practical application of adaptive feedforward compensation in Real Time Hybrid Testing with multiple DoF interfaces as a single forgetting factor μ has to be chosen. Note that the phase and gain matrix $\boldsymbol{P}$ characterizing plant dynamics are used in the adaption law. $\boldsymbol{P}$ can be identified prior to the adaption process by exciting each actuation DoF separately or with uncorrelated noise.

2.4 Numerical Case Study

The algorithm is applied to a simple lumped mass problem with a two DoF interface. The arrangement of the masses is illustrated in Fig. 2.4. The mass and stiffness parameters are given in Table 2.1. Proportional damping with a stiffness proportional coefficient $\alpha = 0.01$ and a mass proportional coefficient $\beta = 0.001$ is used, which confers a modal damping of 0.5 % to the submodels. The models and the interface synchronization control were implemented in Matlab® Simulink®. The excitation force $f_{V,ext} = \sum_{i=1}^{4} = A_i \sin \omega_i t$ was applied on mass 1. The excitation frequencies were $\omega_1 = 20\frac{1}{\text{rad}}$, $\omega_2 = 30\frac{1}{\text{rad}}$, $\omega_3 = 50\frac{1}{\text{rad}}$ and $\omega_4 = 60\frac{1}{\text{rad}}$. The amplitudes $A_1 = 4\,\text{N}$, $A_2 = 10\,\text{N}$, $A_3 = 10\,\text{N}$ and $A_4 = 20\,\text{N}$. The forgetting factor for the RLS algorithm was chosen as $\mu = 0.99$ The identification was running for 10 s with an excitation of 5 s on each actuation DoF. The adaption with the RLS algorithm starts at $t = 10\,\text{s}$.

Figures 2.5 and 2.6 show the interface synchronization for both interface DoF. In the investigated case the algorithm adapts within 2 s and is then accurately ensuring compatibility. The adaption time is depending on the properties of the coupled components. Figure 2.7 shows the comparison of the displacement of mass 4 with the reference overall system. After the adaption process the reference system is simulated accurately. In all of our numerical studies the algorithm was found to be very robust. As indicated by Fig. 2.8 noisy force and displacement signals have little impact on adaption time and stability issues in this numerical case study which indicates a good feasibility for practical implementation.

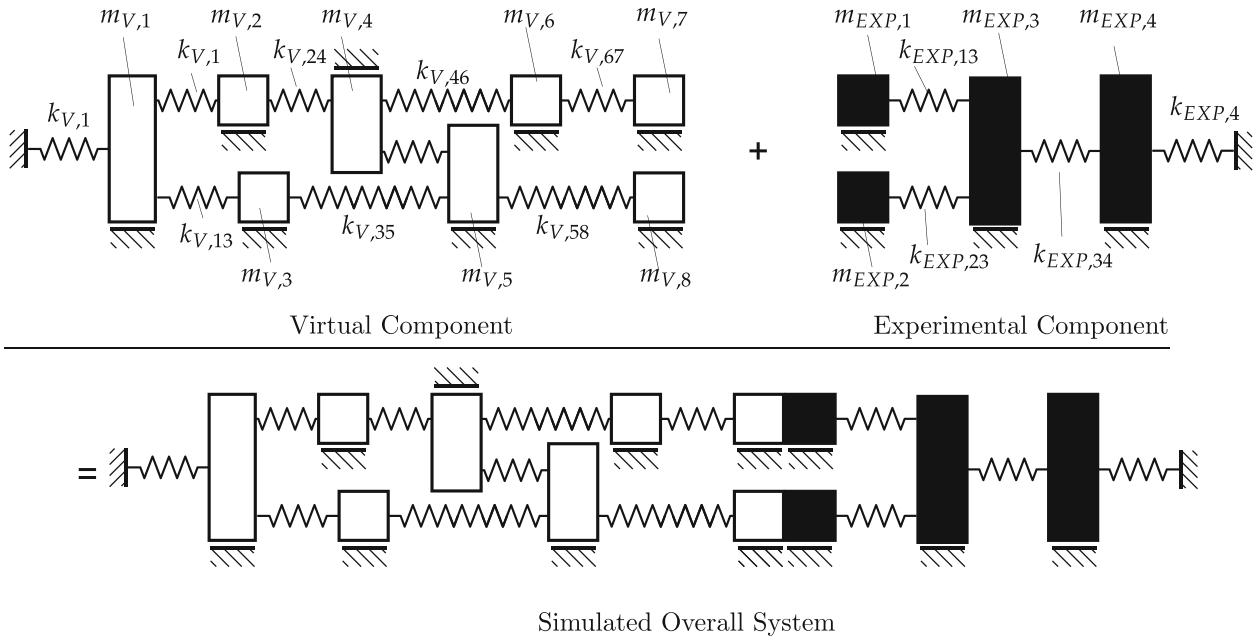

Fig. 2.4 Arrangement of the lumped mass system used for numerical studies

Table 2.1 System parameters used in the numerical case study

Virtual component (V)			
Stiffness (N/m)		Mass (kg)	
$k_{V,1}$	25,000,000	$m_{V,1}$	10
$k_{V,12}$	10,000,000	$m_{V,2}$	3
$k_{V,13}$	10,000,000	$m_{V,3}$	3
$k_{V,24}$	10,000,000	$m_{V,4}$	3
$k_{V,35}$	10,000,000	$m_{V,5}$	3
$k_{V,45}$	10,000,000	$m_{V,6}$	2
$k_{V,58}$	500,000	$m_{V,7}$	2
$k_{V,46}$	20,000,000	$m_{V,8}$	4
$k_{V,67}$	20,000,000		
Test specimen (EXP)			
Stiffness (N/m)		Mass (kg)	
$k_{EXP,13}$	2,500,000	$m_{EXP,1}$	2
$k_{EXP,23}$	2,000,000	$m_{EXP,2}$	4
$k_{EXP,34}$	10,000,000	$m_{EXP,3}$	8
$k_{EXP,4}$	10,000,000	$m_{EXP,4}$	5

2.5 Conclusion

In this paper we propose an adaptive feedforward technique with harmonic regressor for interface synchronization in Real Time Hybrid Testing. The approach makes use of the assumption of harmonic excitation and steady state. It addresses stability and accuracy issues in cases where the simulated overall system is a structural system with low damping. Multiple DoF interfaces are necessary in many applications. As the choice of adaption gain parameters is getting a complex task for tests with multiple DoF interfaces, we propose the use of a recursive least square algorithm for the adaption of the harmonic parameters with only a single parameter for the controller design. Future work will include the experimental validation on a test rig with a multiple DoF interface as well as the comparison with other interface synchronization techniques for Real Time Hybrid Testing.

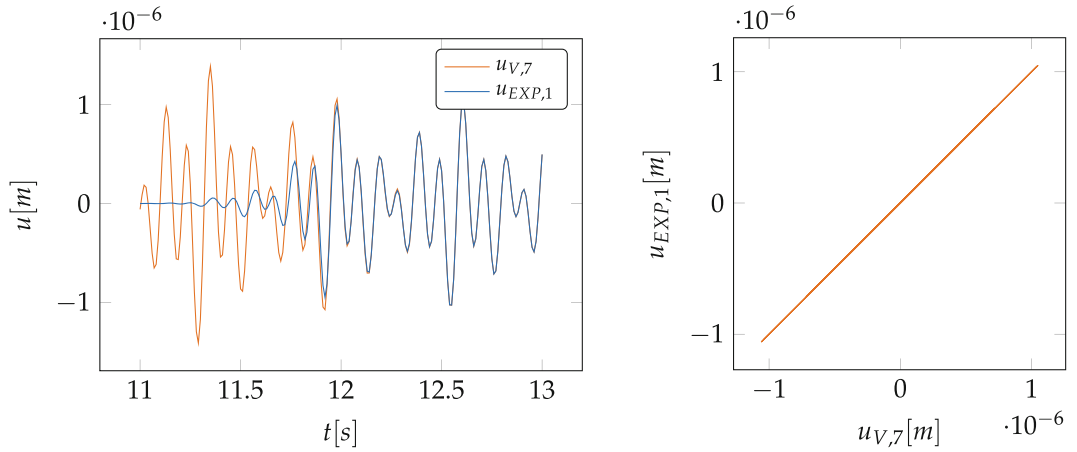

Fig. 2.5 Interface synchronization for the first interface DoF: the *left hand figure* shows the adaption process, the *right hand figure* shows the synchronization in the adapted state

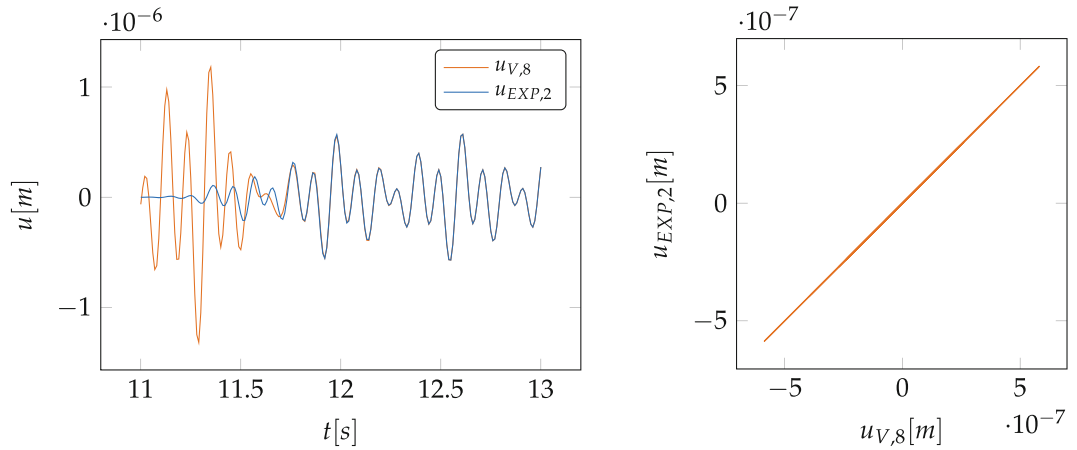

Fig. 2.6 Interface synchronization for the second interface DoF: the *left hand figure* shows the adaption process, the *right hand figure* shows the synchronization in the adapted state

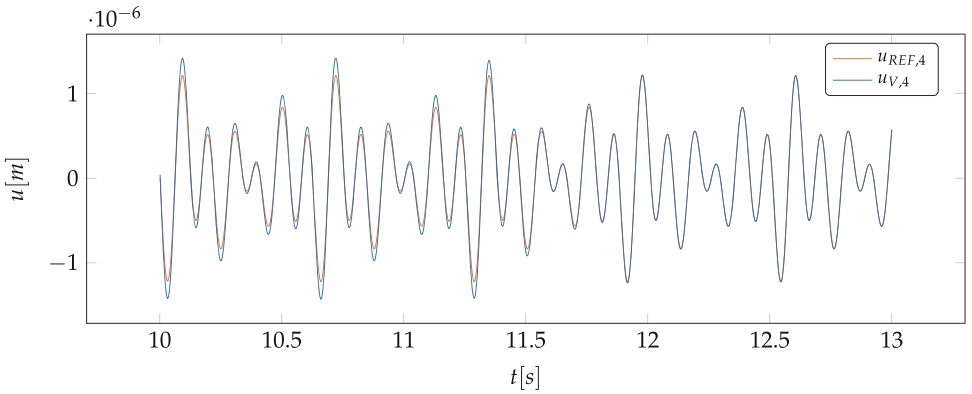

Fig. 2.7 Displacement of mass 4 during the adaption process compared with the reference overall system

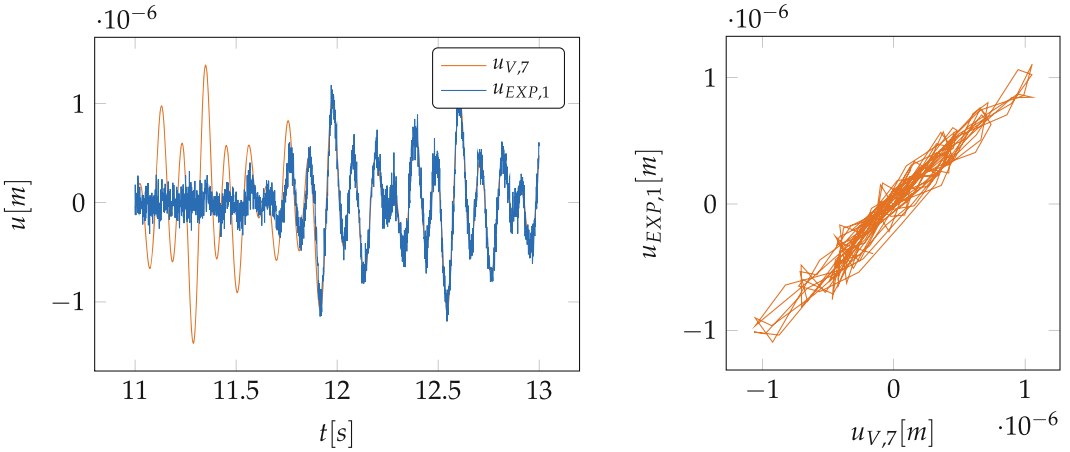

Fig. 2.8 Interface synchronization for the first interface DoF with added noise on force and displacement signals: the *left hand figure* shows the adaption process, the *right hand figure* the synchronization in the adapted state

References

1. Bartl, A., Mayet, J., Rixen, D.J.: Adaptive feedforward compensation for real time hybrid testing with harmonic exciation. In: Proceedings of the 11th International Conference on Engineering Vibration, Sept 2015
2. Bayard, D.S.: A general theory of linear time-invariant adaptive feedforward systems with harmonic regressors. IEEE Trans. Autom. Control **45**(11), 1983–1996 (2000)
3. Blakeborough, A., Darby, A., Williams, M.: The development substructure of real-time testing. Philos. Trans. Math. Phys. Eng. Sci. **359**(1786), 1869–1891 (2001)
4. Bodson, M., Sacks, A., Khosla, P.: Harmonic generation in adaptive feedforward cancellation schemes. IEEE Trans. Autom. Control **39**(9), 1939–1944 (1994)
5. Bonnet, P.A.: The development of multi-axis real-time substructure testing. Ph.D. thesis (2006)
6. Bosse, D., Radner, D., Schelenz, R., Jacobs, G.: Analysis and application of hardware in the loop wind loads for full scale Nacelle ground testing. DEWI Mag. **43**, 65–70 (2013)
7. Botelho, R.M., Christenson, R.E.: Mathematical equivalence between dynamic substructuring and feedback control theory. In: Proceedings of the 33rd IMAC (2015)
8. Darby, A.P., Williams, M.S., Blakeborough, A.: Stability and delay compensation for real-time substructure testing. J. Eng. Mech. **128**, 1276–1284 (2002)
9. De Klerk, D., Rixen, D.J., Voormeeren, S.N.: General framework for dynamic substructuring: history, review and classification of techniques. AIAA J. **46**(5), 1169–1181 (2008)
10. Glover, J.: Adaptive noise canceling applied to sinusoidal interferences. IEEE Trans. Acoust. Speech Signal Process. **25**, 484–491 (1977)
11. Haykin, S.: Adaptive Filter Theory. Upper Saddle River, Prentice Hall (2010)
12. Horiuchi, T., Inoue, M., Konno, T., Namita, Y.: Real-time hybrid experimental system with actuator delay compensation and its application to a piping system with energy absorber. Earthq. Eng. Struct. Dyn. **28**(10), 1121–1141 (1999)
13. Ioannou, P., Sun, J.: Robust Adaptive Control. Dover Publications, New York (2013)
14. Jungblut, T., Wolter, S., Matthias, M., Hanselka, H.: Using numerical models to complement experimental setups by means of active control of mobility. Appl. Mech. Mater. **70**, 357–362 (2011)
15. Li, G.: A generic dynamically substructured system framework and its dual counterparts, pp. 10101–10106 (2014)
16. Li, G., Na, J., Stoten, D.P., Ren, X.: Adaptive neural network feedforward control for dynamically substructured systems. IEEE Trans. Control Syst. Technol. **22**(3), 944–954 (2014)
17. Nakashima, M., Kato, H., Takaoka, E.: Development of real-time pseudo dynamic testing. Earthq. Eng. Struct. Dyn. **21**, 79–92 (1992)
18. Plummer, A.: Model-in-the-loop testing. Proc. Inst. Mech. Eng. I: J. Syst. Control Eng. **220**, 183–199 (2006)
19. Stoten, D., Hyde, R.: Adaptive control of dynamically substructured systems: the single-input single-output case. Proc. Inst. Mech. Eng. I: J. Syst. Control Eng. **220**(2), 63–79 (2006)
20. Stoten, D., Li, G., Tu, J.: Model predictive control of dynamically substructured systems with application to a servohydraulically actuated mechanical plant. IET Control Theory Appl. **4**(2), 253–264 (2010)
21. Stoten, D., Tu, J., Li, G.: Synthesis and control of generalized dynamically substructured systems. Syst. Control Eng. **223**, 371–392 (2010)
22. Tu, J.: Development of numerical-substructure-based and output-based substructuring controllers. In: Structural Control and Health Monitoring, June 2012, pp. 918–936. Wiley, New York (2013)
23. Wagg, D.J., Stoten, D.P.: Substructuring of dynamical systems via the adaptive minimal control synthesis algorithm. Earthq. Eng. Struct. Dyn. **30**(6), 865–877 (2001)
24. Wallace, M.I., Wagg, D.J., Neild, S.a.: An adaptive polynomial based forward prediction algorithm for multi-actuator real-time dynamic substructuring. Proc. R. Soc. A Math. Phys. Eng. Sci. **461**(2064), 3807–3826 (2005)

Chapter 3
Controls Based Hybrid Sub-Structuring Approach to Transfer Path Analysis

Joseph A. Franco, Rui M. Botelho, and Richard E. Christenson

Abstract In the design of mechanical systems, there are constraints imposed on the vibration of mechanical equipment to limit the vibration transmission into its support structure. To accurately predict the coupled system response, it is important to capture the coupled interaction of the two portions, i.e., the mechanical equipment and the support structure, of the mechanical system. Typically during a design, the analysis of the full mechanical system is not possible because a large part of the system may be non-existent. Existing methods known as Transfer Path Analysis and Frequency Based Substructuring are techniques for predicting the coupled response of vibrating mechanical systems. In this paper, a control based hybrid substructuring approach to Transfer Path Analysis is proposed. By recognizing the similarities between feedback control and dynamic substructuring, this paper demonstrates that this approach can accurately predict the coupled dynamic system response of multiple substructured systems including operating mechanical equipment with a complex vibration source. The main advantage of this method is that it uses blocked force measurements in the form of a power spectral density matrix measured uncoupled from the rest of the system. This substructuring method is demonstrated using a simplified case study comprised of a two-stage vibration isolation system and excited by operating mechanical equipment.

Keywords Transfer path analysis • Frequency based substructuring • Hybrid substructuring • Feedback control • System level vibration analysis

3.1 Introduction

Vibration of mechanical equipment can result in fatigue, detection, and/or environmental concerns for a structural system. A critical aspect of the design of systems that include mechanical equipment is quantifying the level of transmitted vibration energy through the supporting structure. The system design typically consists of strict constraints imposed on the vibration transmission of the mechanical equipment through the support structure. During the design phase of a system, the mechanical equipment is pre-existing either from previous designs or they are commercially available components purchased from a vendor. The support structure is typically non-existent and is designed and optimized using Computer Aided Design (CAD) software. This makes testing of the full mechanical system, impossible. For these reasons, the analysis of the mechanical system normally requires the combination of multiple quantifications of dynamics of various substructures of the mechanical system.

Existing methods known as Transfer Path Analysis (TPA) are frequency response functions (FRF) based techniques that describe the dynamics of the mechanical system by the multiplication of the FRFs of the system substructures. This method can also be used to combine theoretical (FEM) models and experimental measurements of system substructures. Some of these methods were developed by Plunt [1, 2] for the automotive industry and Darby [3] for the marine industry. However, the disadvantage of these TPA methods is that they do not always consider the dynamic coupling between the receiving and exciting substructures. This limitation becomes critical at low frequencies due to the interaction between the modes of the individual substructures.

Variations of TPA methods are known as Frequency Based Substructuring (FBS) methods which allow for the calculation of the entire mechanical system dynamic response based on the FRFs of the system substructures using various methods. Primary developments of FBS methods are Crowley et al. [4], Jetmundsen et al. [5], Imregun and Robb [6] and later on Gordis [7] and de Klerk [8]. Generally, this work demonstrated a wide variety of methods to couple substructures based on

J.A. Franco (✉) • R.M. Botelho • R.E. Christenson
Department of Civil and Environmental Engineering, University of Connecticut, 261 Glenbrook Road Unit 3037, Storrs, CT 06269-3037, USA
e-mail: joseph.franco@uconn.edu

© The Society for Experimental Mechanics, Inc. 2016

M. Allen et al. (eds.), *Dynamics of Coupled Structures, Volume 4*, Conference Proceedings of the Society for Experimental Mechanics Series, DOI 10.1007/978-3-319-29763-7_3

either numerically computed or experimentally measured FRFs. However, a large drawback of these methods is that they generally require that the vibratory excitation be known and be able to be quantified; de Klerk [9] did significant work to develop methods to identify and quantify these excitation sources. However, this can be fairly difficult and labor intensive in a real life experimental environment.

Real-time hybrid substructuring (RTHS) is a relatively new test method, recently made more practical because of advances in computer power, digital signal processing hardware/software, and hydraulic control hardware that is used for vibration testing for calculating the dynamic performance of a mechanical system by partitioning a mechanical system into physical and numerical substructures and then interfacing them together in real-time similar to hardware-in-the-loop testing. Early developments of RTHS include Horiuchi et al. [10], Nakashima and Masaoka [11], and Darby et al. [12]. As in FBS methods, RTHS is also a hybrid method, which takes advantage of both experimental methods along with numerical computational methods of system substructures. This method allows the dynamic excitation of the system to be unknown since it is represented in the physical substructure. However, this system is highly dependent on the performance of the actuator system that is used to transmit the displacement feedback from the numerical substructure to the physical substructure. For low frequencies, this is typically a hydraulic system which can be difficult to get accurate reference tracking performance.

In this paper, a practical control based hybrid experimental-numerical approach referred to Transfer Path Hybrid Substructuring (TPHS) is proposed. This approach was developed out of recognition of the similarities of techniques in both the feedback control and the dynamic substructuring fields. Botelho [13] provides an excellent comparison of the mathematically similar formulations for both feedback control theory and dynamic substructuring. By identifying these similarities, it allows the leveraging of elementary feedback control theory, to the Transfer Path Analysis and Frequency Based Substructuring fields. This paper, leverages these similarities in order demonstrates that this new TPHS method can be used to accurately predict the coupled dynamics of multiple substructures of a mechanical system. This method is also a hybrid approach which allows for each of the system substructures to be represented by either experimentally obtained or numerically computed FRFs. This paper will demonstrate in a simplified case study how a power spectral density (PSD) matrix can be used as input to the substructuring procedure.

3.2 Real Time Hybrid Substructuring

Real Time Hybrid Substructuring (RTHS) is a test method that provides the capability to isolate and physically test the more advanced critical mechanical equipment of a mechanical system at the design phase of the system while including the dynamic interaction with a numerical representation of the remainder of the support structure. This is advantageous over more traditional substructuring techniques because the portion of the system that makes up the physical substructure is not required to be dynamically quantified. A typical RTHS test is made up of the numerical substructure, the physical substructure as well as the actuator system required to command calculated displacements from the numeric substructure to the physical substructure. Figure 3.1 shows this typical RTHS test layout displayed as a control based block diagram.

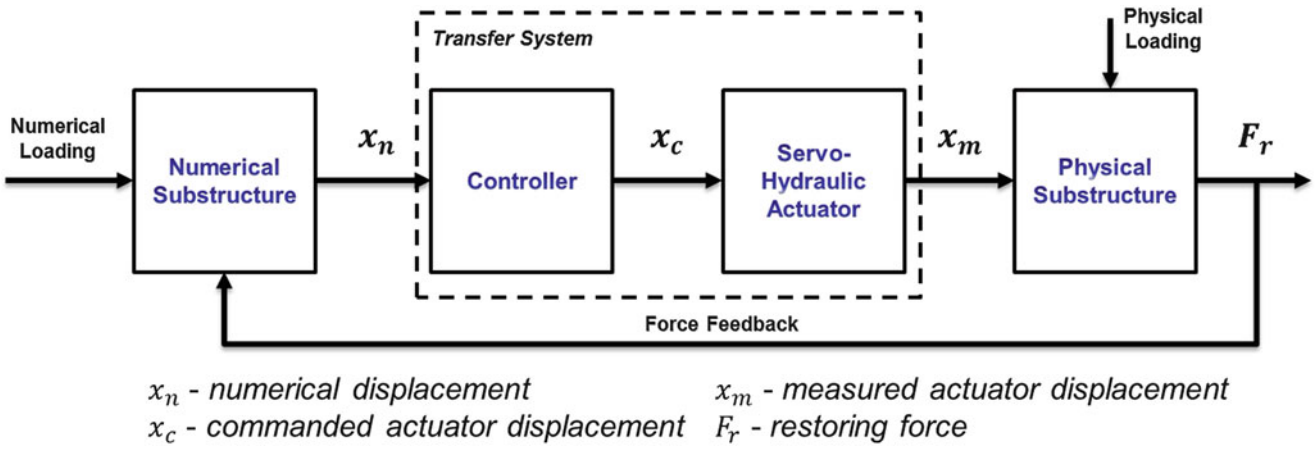

Fig. 3.1 Control block diagram of a typical RTHS test

The main disadvantage of RTHS is the dependence on this transfer system's dynamics. At low frequencies, where dynamic coupling of system substructures is necessary, this transfer system is typically a servo-hydraulic actuator system. Servo-hydraulic actuator systems tend to have significant frequency dependent magnitude attenuation and time delay. A large portion of the research done concerning RTHS is compensating and controlling these frequency dependent dynamics.

The mechanical system of interest in this paper is that which consists of mechanical equipment, which is the vibration source, and its support structure. The mechanical portion of the system lends itself well to the physical substructure of the RTHS layout. This mechanical equipment typically have complex dynamics and acoustic excitations which are difficult to model with classic numerical methods also possibility because of non-linarites and time-variant properties of the mechanical equipment. The support structure, on the other hand, lends itself well to the numerical substructure of the RTHS layout shown in Fig. 3.1. This paper's interest is the system excitation source's that come from the mechanical component, i.e., the physical substructure and is not interested in vibratory excitations that come from the support structure, i.e., the numerical substructure. Therefore, the numerical loading shown in Fig. 3.1 will be ignored for this paper.

The physical loading shown in Fig. 3.1 is analogous to what is known in the controls field as a system disturbance. In this case, the disturbance is the excitation of the physical substructure and it is the interest of this paper to quantify how that excitation affects the system dynamics as well as how the excitation is transmitted through the system. Spite the difference in the desired outcome of the analysis, controls based analysis methods and tools can be leveraged to analyze the system.

3.3 Controls Approach to Transfer Path Hybrid Substructuring

This paper attempts to use the RTHS control diagram shown in Fig. 3.1 and simple control diagram analysis to develop a new approach to substructuring referred to Transfer Path Hybrid Substructuring (TPHS). From the block diagram shown in Fig 3.1 (not including the numerical loading), the equation for the closed loop control diagram is given by

$$F_r = -PANF_r + P_i \tag{3.1}$$

Where P is the physical substructure, N is the numeric substructure, A is the transfer system, and P_i is the excitation load on the system, referred to here as the physical loading. Rearranging Equation (3.1) in terms of the reactant force, F_r gives the fundamental equation of TPHS shown below

$$F_r = \left[\frac{1}{1 + PAN}\right] P_i \tag{3.2}$$

This simple equation gives the formula for solving for the coupled reactant force of the numerical and physical substructures at the interaction points between the two substructures.

One portion of the control diagram shown in Fig 3.1 that is not necessary with this method is the actuator dynamics transfer function. Specifically, when the physical substructure is tested, the input signals to the FRF calculations either could be x_c, or the measured displacements, x_m. If x_c is used as the physical substructure input signals, then the measured transfer function will include the actuator transfer function which is the quantification of the transmission of the x_c, to the actual x_m, of the actuators. With servo-hydraulic actuators this can be a significant level of frequency dependent magnitude attenuation in addition to frequency dependent time delay. However, if x_m is used as the physical substructure input signal, then the measured transfer function does not include these additional actuator dynamics and the measured performance of the physical substructure is calculated in terms of a normalized input. If it is assumed that we have perfect actuator tracking, i.e., x_m is equal to x_c, then the numerical and physical substructures have like terms and can be multiplied together and the A transfer function can be removed from Eq. (3.2). This is a significant advantage of this method over RTHS. A large portion of the complication of RTHS is compensating for the frequency dependent actuator dynamics which can be substantial. TPHS bypasses this complication by assuming ideal actuator reference tracking. This simplifies the governing equation of TPHS even further to

$$F_r = [I + PN]^{-1} P_i \tag{3.3}$$

Equation (3.3) calculates the coupled reactant forces at the interaction points between the two substructures; however, this is not the metric of interest. To calculate the force at the base of the full system, the reactant force is then multiplied by a force

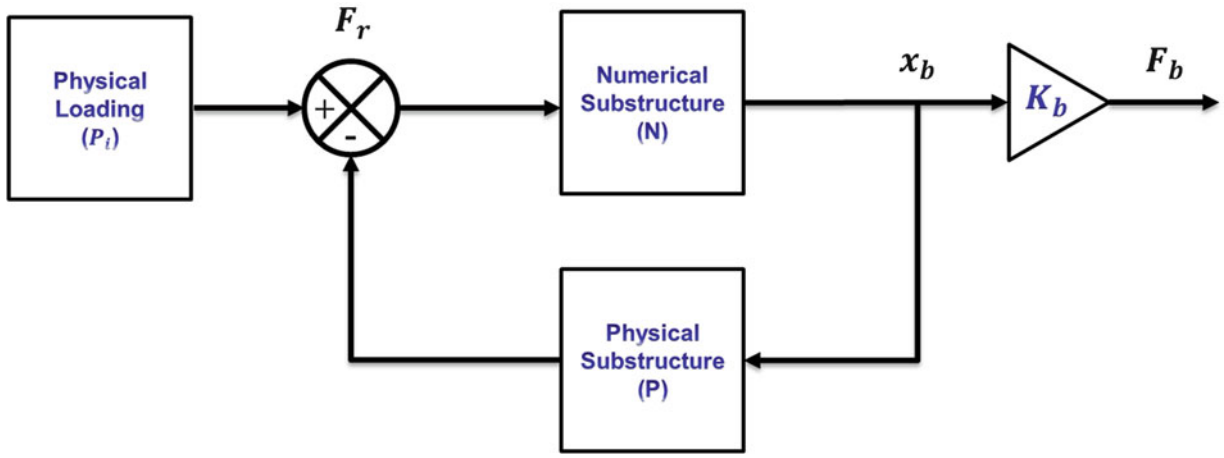

Fig. 3.2 Control diagram representing the TPHS method

transmissibility transfer function which is equal to the numeric substructure multiplied by the base isolator stiffness, K_bN. The TPHS equation for the base forces of the full system is

$$F_b = K_bN[I + PN]^{-1}P_i \tag{3.4}$$

where F_b is the force at the base of the full system. Figure 3.2 shows Eq. (3.4) as a simple feedback control diagram.

Figure 3.2 shows that the critical part of this analysis method is the feedback loop. Without it, the open-loop solutions is given by

$$F_b = K_bNP_i \tag{3.5}$$

and by comparing this to Eq. (3.4), it is shown that this critical feedback loop is represented by the $[I + PN]^{-1}$ term. The difference between the closed-loop and open-loop analysis will be investigated further later on.

3.3.1 Physical Loading Using Auto Power Spectral Densities

In most cases, mechanical systems have many complex excitations and it may be very difficult to quantify them. Therefore, mechanical equipment vibration is typically quantified in power spectral densities (PSD). This is a main disadvantage of most transfer path and frequency base substructuring methods; the source of the dynamics is needed in order to experimentally measure transfer functions of the physical substructure used in these hybrid methods.

This is the main advantage of Transfer Path Hybrid Substructuring. The controls based approach allows the physical excitation of the system to be in the form of a PSD (or a PSD matrix for the MDOF case). In the case of MDOF, the power spectral density matrix consists of auto power spectral densities along the diagonal of the matrix and cross power spectral densities in the off-diagonal terms between the two respective signals. The form of this PSD matrix is given below

$$\boldsymbol{G}_{p_ip_i} = \begin{bmatrix} G_{11} & G_{12} & \cdots & G_{1n} \\ G_{21} & G_{22} & \cdots & G_{2n} \\ \vdots & \vdots & \ddots & \vdots \\ G_{n1} & G_{n2} & \cdots & G_{nn} \end{bmatrix} \tag{3.6}$$

Where $\boldsymbol{G}_{p_ip_i}$ is the PSD matrix of the physical loading and n is the number of signal locations. The diagonal terms, G_{11}, G_{22}, ... G_{nn} are the auto power spectral densities while all other off diagonal terms, G_{12}, G_{21}, ... terms are the cross power spectral densities.

3.4 Numeric Example

In order to demonstrate this method numerically, each of the substructures, as well as the physical loading, must be quantified. One complication of quantifying each of these quantities is that they are frequency dependent. The simplest solution to this issue is to use Laplace domain or s-domain transfer functions to represent the frequency dependent response of the substructures. The following is a simplified example of this approach.

The numeric substructure, as shown in Fig. 3.2, has a force input and a displacement output. In dynamics, this is known as flexibility. The equation for the system flexibility is derived starting with the equation of motion

$$\left[Ms^2 + Cs + K\right] x = F \tag{3.7}$$

where M, C and K are the substructures' mass, damping and stiffness properties, F is the excitation force, x is the system displacement and s is the Laplace constant. The flexibility equation of the numerical substructure, in the s-domain, is then derived by rearranging Equation (3.7) into

$$\frac{x}{F} = \frac{1}{Ms^2 + Cs + K} \tag{3.8}$$

The physical substructure, as shown in Fig. 3.2 has an input base displacement and a resultant base force. This transfer function is derived using the following rigid body diagram shown in Fig. 3.3.

where F_b is the reactant force at the base due to the input base displacement, x_b. The characteristic equation of motion of this system is Eq. (3.7) where the input force is calculated by

$$[Cs + K]\, x_b = F \tag{3.9}$$

Therefore, the equation of motion becomes

$$[Cs + K]\, x_b = \left[Ms^2 + Cs + K\right] x \tag{3.10}$$

Rearranging this equation to solve for the system displacement due to base input displacement gives

$$\frac{x}{x_b} = \frac{Cs + K}{Ms^2 + Cs + K} \tag{3.11}$$

Using Eq. (3.11) in the equation for the reactant force of the spring-damper shown below

$$F_b = [Cs + K]\,(x_b - x) \tag{3.12}$$

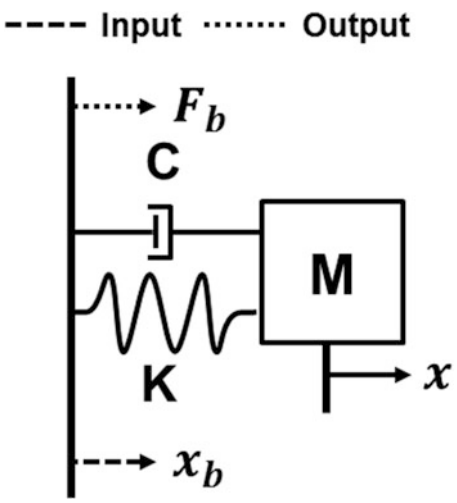

Fig. 3.3 Rigid body diagram of a single DOF system with a base displacement input

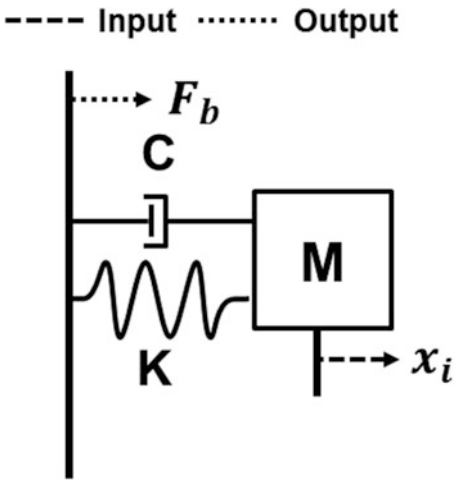

Fig. 3.4 Rigid body diagram of a single DOF system with a displacement input

gives the s-domain transfer function for the physical substructure

$$\frac{F_b}{x_b} = [Cs + K]\left(1 - \frac{Cs + K}{Ms^2 + Cs + K}\right) \tag{3.13}$$

This is the equation for the reactant base force due to a base displacement excitation, also sometimes known as dynamics stiffness.

Lastly, the physical loading needs to be realized using s-domain transfer functions. For this simple example it is assumed that the physical loading is a commanded displacement excitation. The transfer function of the physical loading is reactant force due to an input displacement excitation. This transfer function is derived using a rigid body diagram shown in Fig. 3.4.

where x_i is the input displacement. The characteristic equation of motion of this system is Eq. (3.7) where the input force is calculated by

$$Ms^2 x_i = F \tag{3.14}$$

Therefore, the equation of motion becomes

$$\left[Ms^2 + Cs + K\right]\{x\} = Ms^2 x_i \tag{3.15}$$

Rearranging this equation to solve for the system displacement due to base input displacement gives

$$\frac{x}{x_i} = \frac{Ms^2}{Ms^2 + Cs + K} \tag{3.16}$$

From this equation, to get the reactant forces, we multiply by the characteristic equation of the system's spring/damper shown in

$$\frac{F_b}{x_i} = (Cs + K)\frac{Ms^2}{Ms^2 + Cs + K} \tag{3.17}$$

In order to verify that TPHS is an accurate method, it was compared to the traditional dynamic substructuring approach to solve a simple uni-axial two DOF system. Figure 3.5 shows a diagram of this example two DOF uni-axial system.

For this example the displacement excitation is applied to M_1 and both the TPHS and traditional dynamic substructuring is used to solve for the reactant force at the connection between the two substructures similar to what is shown in Fig. 3.2. The equations of motion of this system are given by the following system of equations.

$$\begin{Bmatrix} F_1 \\ F_2 \end{Bmatrix} = \left[\boldsymbol{M}s^2 + \boldsymbol{C}s + \boldsymbol{K}\right]\begin{Bmatrix} x_1 \\ x_2 \end{Bmatrix} \tag{3.18}$$

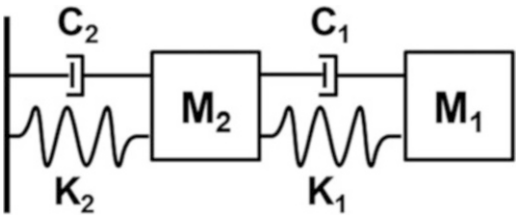

Fig. 3.5 Diagram of example two DOF uni-axial system

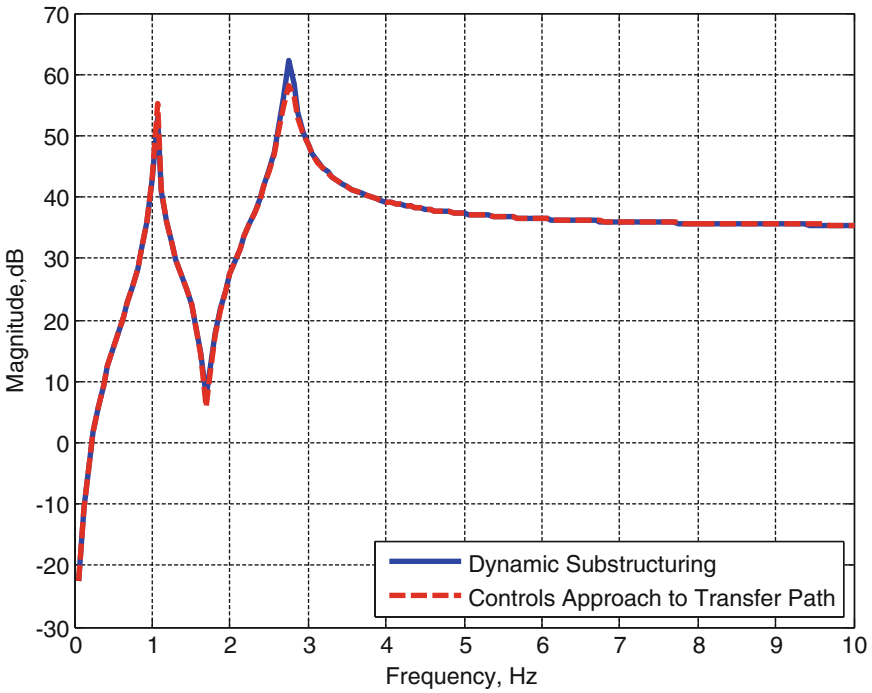

Fig. 3.6 Comparison of dynamic substructuring vs. transfer path hybrid substructuring

where

$$\boldsymbol{M} = \begin{bmatrix} M_1 & 0 \\ 0 & M_2 \end{bmatrix} \tag{3.19}$$

$$\boldsymbol{C} = \begin{bmatrix} C_1 & -C_1 \\ -C_1 & C_1 + C_2 \end{bmatrix} \tag{3.20}$$

$$\boldsymbol{K} = \begin{bmatrix} K_1 & -K_1 \\ -K_1 & K_1 + K_2 \end{bmatrix} \tag{3.21}$$

The same equation for reactant force due to displacement excitation shown in Eq. (3.17) can be applied here but replacing the SDOF scalars with MDOF matrices.

$$\frac{\{F_r\}}{\{x_i\}} = (\boldsymbol{C}s + \boldsymbol{K}) \cdot \boldsymbol{M}s^2\left[\boldsymbol{M}s^2 + \boldsymbol{C}s + \boldsymbol{K}\right]^{-1} \tag{3.22}$$

The results from Eq. (3.22) and the results from the TPHS using Eq. (3.2) are compared in Fig 3.6.

These results show that the TPHS method can accurately substructure two substructures together in the same manner as dynamic substructuring. This example shows that the fundamental theory of TPHS is equivalent to the more traditional method of dynamic substructuring.

3.5 Experimental Example

Because of the realization that the controls based closed loop equation, shown in Eq. (3.4), can be solved discretely in the frequency domain, it is observed that TPHS leads itself well to similar Frequency Based Substructuring (FBS) methods. These methods allow the calculation of the entire mechanical system dynamic response based on the FRFs of the system substructures. FBS methods are usually a hybrid method, which means that they incorporate both experimentally measured system dynamics as well as numerically computed system dynamics. Using FBS techniques, experimental results can be used interchangeably with respective numerical results. Therefore, FBS methods allow the substructuring of numerical substructures with other numerical substructures, the substructuring of experimental substructures with numerical substructures, as well the substructuring of experimental substructures with other experimental substructures. The same multi degree of freedom (MDOF) test case used in Franco et al. [14] was used to verify the TPHS method using a combination of both numerical and experiment substructures to accurately predict the dynamics of a mechanical system. This system is shown in Fig. 3.7.

As in previous work, this mechanical system was separated into a physical substructure which consisted of the Quanser Shake Table, its bedplate and its four spring isolators, and a numerical substructure which consisted of the support structure and its four spring isolators. Figure 3.8 shows both these physical and numerical substructures.

The same numerical lumped parameter model of the numerical substructure as used in previous work and the physical substructure were tested. The full system, shown in Fig 3.7, was also tested as experimental verification of the TPHS method. The full system experiment was excited in the horizontal direction with the Quanser Shake Table which was commanded a random white noise displacement signal. The output of the experiment was the tri-axial force sensors below the isolators at the base of the system for a total of 12 forces.

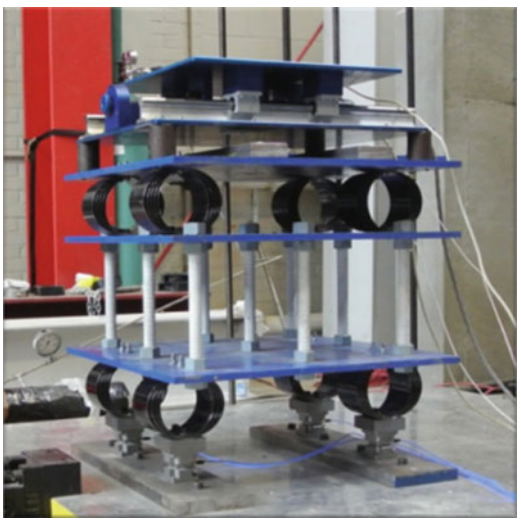

Fig. 3.7 MDOF test case mechanical system

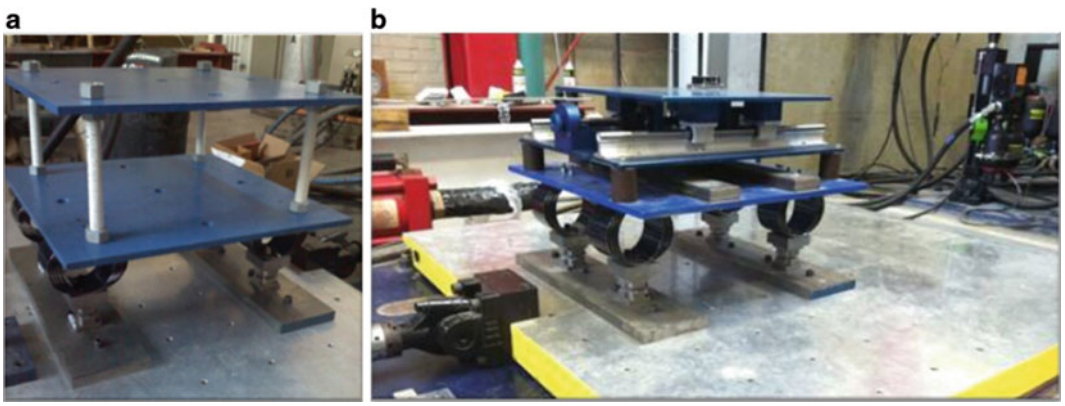

Fig. 3.8 (**a**) Numerical substructure (**b**) Physical substructure

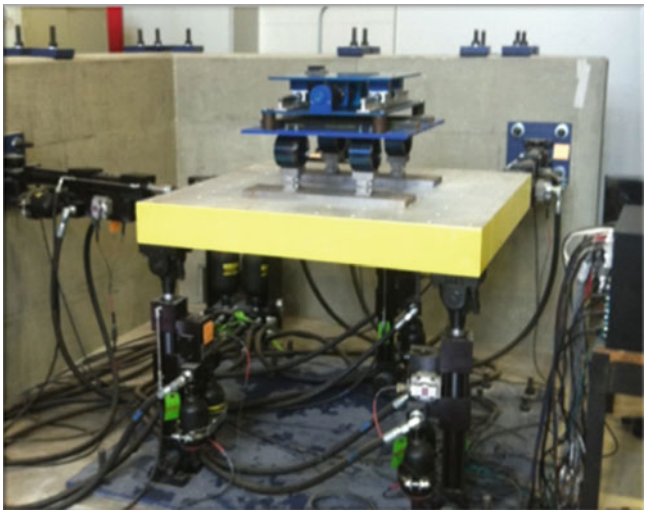

Fig. 3.9 Six degree of freedom Shore Western shake table

For the TPHS method to work, the physical loading of the full system needs to be quantified so that it is the force due to the physical loading at the interaction point between the physical and numerical substructures. In this test case the physical loading is the displacement excitation of the Quanser Shake Table. This was measured by testing the physical substructure with the Quanser Shake Table excitation with the output being tri-axial force sensors below the physical substructure's isolators at the base, which is the interaction point between the numerical and physical substructures.

Lastly, the physical substructure was experimentally tested. In the TPHS arrangement, this is a reactant force due to a base displacement excitation. To experimentally measure this relationship, a six degree of freedom (6DOF) Shore Western Shake Table, shown in Fig 3.9, was used.

The physical substructure was excited with a band-limited white noise (BLWN) displacement from 0 to 20 Hz in all six Cartesian directions. Similar to when the physical loading was recorded, the physical substructure had tri-axial force sensors below its isolators at the base to record the reactant force. This arrangement allowed for the direct measurement of the desired physical substructure transfer function.

To experimentally verify the TPHS calculation using a PSD matrix as the physical loading, the numerical substructure model and the physical substructure experimental test were coupled together using Eq. (3.4) and then compared to the experimental full system which was constructed and tested. Figure 3.10 shows the comparison of the TPHS method vs. the experimental measurement of the mechanical systems base force PSDs. Being able to calculate the PSDs of the coupled systems response is typically more advantageous because it is measure of the actual levels of response instead of transfer function calculations which are normalized measurements of the mechanical systems response.

This comparison shows that TPHS is a viable substructuring method that can use PSDs of mechanical system excitation to calculate the coupled dynamics of the mechanical system. This is the major advantage of this method.

3.6 Conclusion

This paper demonstrated a new frequency based substructuring method referred to as Transfer Path Hybrid Substructuring. It was demonstrated that this method is mathematically equivalent to traditional dynamic substructuring. In addition, it was shown that this method can be used to accurately couple physical loading with unknown vibration excitation, with the dynamics of a numerically modeled support structure. This is the main advantage of this method over other substructuring methods since typically it is very difficult to quantify the exact source of the system excitation.

This method does have required conditions. The physical loading should be measured with the physical substructure having a perfectly rigid interface to the test base in the frequency range of interest. This method also requires that the physical substructure transfer function (reactant force due to an applied base motion excitation) can be measured using linear signal processing techniques. This obviously assumes that this substructure is a stationary, ergodic system. In the case study

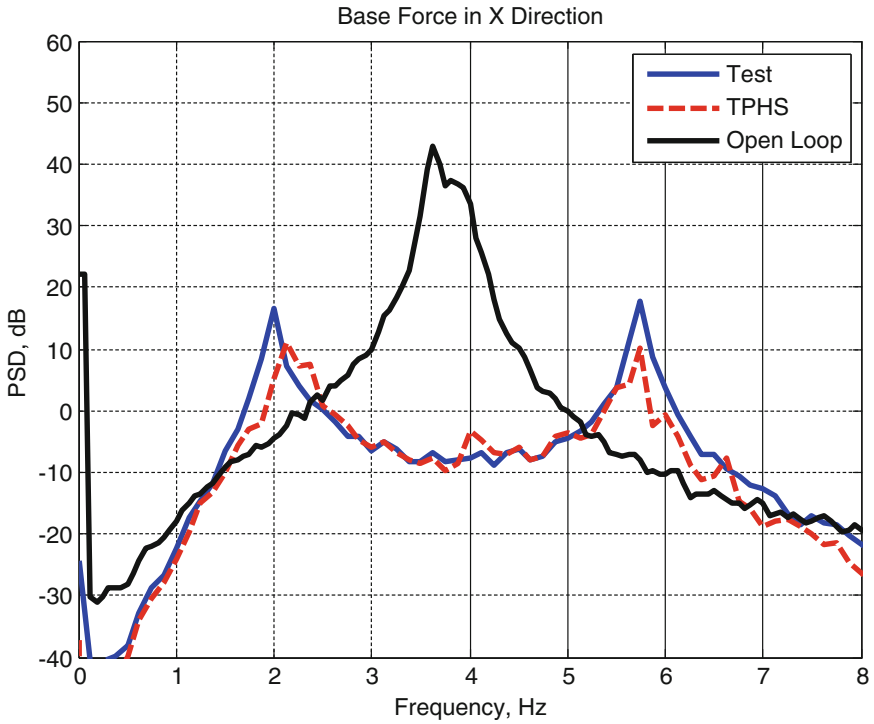

Fig. 3.10 Comparison of TPHS vs. full system test PSDs

presented in this paper, this was true and the physical substructure transfer function was able to be measured because of the availability of a 6DOF shake table which could be used to apply a base motion and record the reactant forces of the physical substructure. This will typically be cost and time prohibitive so other methods to achieve this transfer function could be a subject of further research.

References

1. Plunt, J.: Strategy for transfer path analysis applied to vibro-acoustic systems at medium and high frequencies. In: Proceedings of the Twenty-third International Conference on Noise & Vibration Engineering, Leuven, 1998
2. Plunt, J.: Examples of using transfer path analysis together with CAE-models to diagnose and find solutions for NVH problems late in the vehicle development process. *SAE*, 2005-01-2508 (2004)
3. Darby, R.A.: A practical method for predicting acoustic radiation or shock excursions of Navy machinery. Shock Vib. Bull. **3** (1964)
4. Crowley, J., Klosterman, A., Rocklin, G., Vold, H.: Direct structural modification using frequency response functions. In: Proceedings of the Second International Modal Analysis Conference, Orlando, 1984
5. Jetmundsen, B., Bielawa, R., Flannelly, W.: Generalized frequency domain substructure synthesis. J. Am. Helicopter Soc. **33**(1), 55–65 (1998)
6. Imregun, M., Robb, D., Ewins, D.: Structural modifications and coupling dynamic analysis using measured FRF data. In: Proceedings of the Fifth International Modal Analysis Conference, London, 1987
7. Gordis, J., Bielawa, R., Flannelly, W.: A generalized theory for frequency domain structural synthesis. J. Sound Vib. **150**, 139–158 (1991)
8. de Klerk, D., Rixen, D., de Jong, J.: The frequency based substructuring method reformulation according to the Dual Domain Decomposition method. In: Proceedings of the Fifteenth International Modal Analysis Conference, St. Louis, 2006
9. de Klerk, D., Rixen, D., Coomeeren, S.: General framework for dynamic substructuring history, review and classification of techniques. AIAA J. **46**(5), 1169–1181 (2008)
10. Horiuchi, T., Inoue, M., Konno, T., Namita, Y.: Real time hybrid experimental system with actuator delay compensation and it's applications to a piping system with energy absorber. Earthq. Eng. Struct. Dyn. **28**(10), 1121–1141 (1999)
11. Nakashima, M., Masaoka, N.: Real time on-line test for MDOF systems. Earthq. Eng. Struct. Dyn. **28**, 393–420 (1999)
12. Darby, A.P., Blakeborough, A., Williams, M.S.: Real time substructure test using hydraulic actuator. J. Eng Mech **125**(10), 1133–1139 (1999)
13. Botelho, R., Christenson, R.: Mathematical equivalence between dynamic substructuring and feedback control theory. In Dynamics Of Coupled Structures, vol. 4, pp. 31–40. Springer International Publishing (2015)
14. Franco, J., Christenson, R., Botelho, R.: System-level vibration testing of marine equipment using real time hybrid simulation. In: Proceedings of the 2013 Conference of the ASCE Engineering Mechanics Institute, Evanston, 2013

Chapter 4
Force Identification Based on Subspace Identification Algorithms and Homotopy Method

Zhenguo Zhang, Xiuchang Huang, Zhiyi Zhang, and Hongxing Hua

Abstract This paper addresses an inverse problem to determine dynamic forces acting on a structure from response data. Data-driven subspace algorithms and the linear regression are used to facilitate the estimation of the state sequences and system parameters. The force identification model is then reasonably established on the basis of the estimated system model. A weighted algorithm based on the homotopy analysis method is employed to discretize the well-known ill-posed problems. Moreover, a criterion based on L-curves is adopted for choosing the level of regularization. Finally, laboratory experiments are presented to demonstrate robustness and effectiveness of the proposed solution technique.

Keywords Force identification • Inverse problem • The homotopy method • Subspace algorithm • Regularization

4.1 Introduction

Accurate knowledge of dynamic force characteristics acting on structures is essential for the reliable prediction of structural vibrations, which generally provides a crucial premise of mechanical design, optimization and control. However, it may not always be possible to perform direct measurements or calculations of external forces in realistic situations (such as propeller forces of ships or wind loads acting on buildings) due to number of practical difficulties. An applicatory, and in some cases, the only feasible approach may be to indirectly determine loads from response data by force identification technique.

Several different methods, which are either frequency domain based or time domain based, have been currently utilized for force identification [1, 2]. Frequency domain techniques commonly have severe ill-conditioning at frequencies with regard to natural frequencies of the system, and might not be feasible for nonstationary or transient phenomena [3]. Therefore, time domain based techniques are recently receiving more and more attention. Liu [4] applied Kalman filter with a recursive estimator for input force estimation of a mechanical grey-box model. By degenerating the force identification problem to a parameter identification problem, Lu et al. [5] presented a method based on sensitivities of dynamic response in the time domain to identify input forces. Hwang et al. [6] developed an analytical procedure based on the Kalman filtering for modal wind load identification from across-wind load responses, where the Kalman filter gain in modal space was derived for different types of measured data solving the Riccati equation. Mao et al. [7] identified the input force of non-linear structural systems based on the combination of the extended Kalman filter and a recursive least-squares estimator.

The force identification problem is generally ill-conditioning due to inversion process as well as the white noise in measured data, which may result in the instability of solutions. Truncated singular value decomposition was primely used to deal with ill-conditioning problem, but discarding of the smallest singular values may reduce the identification accuracy [8]. Jacquelin et al. [9] utilized the regularization methods to solve the force identification problem and different regularization methods were discussed. Choi et al. [10] employed Tikhonov regularization to improve the conditioning of the matrix inversion, and some available methods for selection of the optimal regularization parameter were compared. Recently, the homotopy method has been widely employed in heat conduction problems [11] and shown to be an efficient matrix regularization technique. However, the application of the homotopy method in the force identification problem is limited [12]. In this work, an extended inverse method comprising the subspace algorithm and the homotopy method is developed to estimate input forces acting on structural systems from measured dynamic responses. The robustness and accuracy of the proposed method are verified with laboratory tests on a scale model of a civil ship.

Z. Zhang, Ph.D. (✉) • X. Huang, Ph.D. • Z. Zhang • H. Hua
B219, Institute of Vibration, Shock & Noise, Shanghai Jiao Tong University, 800 Dongchuan Road, Shanghai 200240, P.R. China
e-mail: zzgjtx@sjtu.edu.cn

© The Society for Experimental Mechanics, Inc. 2016

M. Allen et al. (eds.), *Dynamics of Coupled Structures, Volume 4*, Conference Proceedings of the Society for Experimental Mechanics Series, DOI 10.1007/978-3-319-29763-7_4

4.2 System Identification Based on Subspace Identification Algorithm

For a linear system, a combined deterministic-stochastic discrete-time state-space model can be written as [13]:

$$\begin{cases} \boldsymbol{X}_{k+1} = \boldsymbol{A}\boldsymbol{X}_k + \boldsymbol{B}\boldsymbol{F}_k + \boldsymbol{w}_k \\ \boldsymbol{Y}_k = \boldsymbol{C}\boldsymbol{X}_k + \boldsymbol{D}\boldsymbol{F}_k + \boldsymbol{v}_k \end{cases} \tag{4.1}$$

where $\boldsymbol{X}_k \in \mathbb{R}^n$ and $\boldsymbol{F}_k \in \mathbb{R}^m$ are the state vector and the force vector in the state space. $\boldsymbol{A} \in \mathbb{R}^{n\times n}$, $\boldsymbol{B} \in \mathbb{R}^{n\times m}$, $\boldsymbol{C} \in \mathbb{R}^{l\times n}$ and $\boldsymbol{D} \in \mathbb{R}^{l\times m}$ denote the system matrix, input influence matrix, output influence matrix and direct transmission matrix, respectively. $\boldsymbol{w}_k$ and $\boldsymbol{v}_k$ refer to the process noise and the measurement errors.

Subspace identification algorithms [13] based on input–output measurements is employed to obtain the unknown matrices ($\boldsymbol{A}$, $\boldsymbol{B}$, $\boldsymbol{C}$ and $\boldsymbol{D}$). The measured input data can be grouped into the block Hankel matrix as follows:

$$\boldsymbol{U}_{0|2i-1} = \left(\begin{array}{cccc} \boldsymbol{F}_0 & \boldsymbol{F}_1 & \cdots & \boldsymbol{F}_{j-1} \\ \boldsymbol{F}_1 & \boldsymbol{F}_2 & \cdots & \boldsymbol{F}_j \\ \vdots & \vdots & \ddots & \vdots \\ \boldsymbol{F}_{i-1} & \boldsymbol{F}_i & \cdots & \boldsymbol{F}_{i+j-2} \\ \hline \boldsymbol{F}_i & \boldsymbol{F}_{i+1} & \cdots & \boldsymbol{F}_{i+j-1} \\ \boldsymbol{F}_{i+1} & \boldsymbol{F}_{i+2} & \cdots & \boldsymbol{F}_{i+j} \\ \vdots & \vdots & \ddots & \vdots \\ \boldsymbol{F}_{2i-1} & \boldsymbol{F}_{2i} & \cdots & \boldsymbol{F}_{2i+j-2} \end{array}\right) = \left(\begin{array}{c} \boldsymbol{U}_p \\ \hline \boldsymbol{U}_f \end{array}\right) = \left(\begin{array}{cccc} \boldsymbol{F}_0 & \boldsymbol{F}_1 & \cdots & \boldsymbol{F}_{j-1} \\ \boldsymbol{F}_1 & \boldsymbol{F}_2 & \cdots & \boldsymbol{F}_j \\ \vdots & \vdots & \ddots & \vdots \\ \boldsymbol{F}_i & \boldsymbol{F}_{i+1} & \cdots & \boldsymbol{F}_{i+j-1} \\ \hline \boldsymbol{F}_{i+1} & \boldsymbol{F}_{i+2} & \cdots & \boldsymbol{F}_{i+j} \\ \boldsymbol{F}_{i+2} & \boldsymbol{F}_{i+3} & \cdots & \boldsymbol{F}_{i+j+1} \\ \vdots & \vdots & \ddots & \vdots \\ \boldsymbol{F}_{2i-1} & \boldsymbol{F}_{2i} & \cdots & \boldsymbol{F}_{2i+j-2} \end{array}\right) = \left(\begin{array}{c} \boldsymbol{U}_p^+ \\ \hline \boldsymbol{U}_f^- \end{array}\right) \tag{4.2}$$

where "i" is a user defined index with respect to the maximum order of the system to be identified, and $j \gg i$. The output block Hankel matrices $\boldsymbol{Y}_p$, $\boldsymbol{Y}_f$, $\boldsymbol{Y}_p^+$ and $\boldsymbol{Y}_p^-$ can be constructed similarly. The block Hankel matrices collected by inputs and outputs are defined as:

$$\boldsymbol{W}_p^{\mathrm{T}} = \boldsymbol{W}_{0|i-1}^T = \left[\boldsymbol{Y}_p^{\mathrm{T}} \;\; \boldsymbol{F}_p^{\mathrm{T}}\right]^{\mathrm{T}},\; \boldsymbol{W}_p^{+\mathrm{T}} = \left[\boldsymbol{Y}_p^{+\mathrm{T}} \;\; \boldsymbol{F}_p^{+\mathrm{T}}\right]^{\mathrm{T}} \tag{4.3}$$

Secondly, defining $\boldsymbol{O}_i$ the oblique projection of the row space of $\boldsymbol{Y}_f$ along the row space of $\boldsymbol{U}_f$ on the row space of $\boldsymbol{W}_p$, the singular value decomposition (SVD) of the weighted oblique projection can be expressed as:

$$\boldsymbol{W}_1\boldsymbol{O}_i\boldsymbol{W}_2 = \boldsymbol{W}_1\left(\boldsymbol{Y}_f/_{\boldsymbol{U}_f}\boldsymbol{W}_p\right)\boldsymbol{W}_2 = \begin{pmatrix}\boldsymbol{U}_1 & \boldsymbol{U}_2\end{pmatrix}\begin{bmatrix}\boldsymbol{S}_1 & \boldsymbol{0} \\ \boldsymbol{0} & \boldsymbol{0}\end{bmatrix}\begin{pmatrix}\boldsymbol{V}_1^{\mathrm{T}} \\ \boldsymbol{V}_2^{\mathrm{T}}\end{pmatrix} = \boldsymbol{U}_1\boldsymbol{S}_1\boldsymbol{V}_1^{\mathrm{T}} \tag{4.4}$$

where $\boldsymbol{W}_1$ and $\boldsymbol{W}_2$ are user defined weighting matrices and $\mathrm{rank}(\boldsymbol{W}_p) = \mathrm{rank}(\boldsymbol{W}_p\boldsymbol{W}_2)$ and $\boldsymbol{W}_1$ has full rank. The extended observability matrix can be accordingly given as:

$$\boldsymbol{\Gamma}_i = \boldsymbol{W}_1^{-1}\boldsymbol{U}_1\boldsymbol{S}_1^{1/2} \tag{4.5}$$

The sequence of reference-based Kalman filter can then be determined as [13]:

$$\widehat{\boldsymbol{X}}_i = \boldsymbol{\Gamma}_i^{\dagger}\boldsymbol{O}_i, \quad \boldsymbol{Z}_i = \boldsymbol{\Gamma}_i\widehat{\boldsymbol{X}}_i + \boldsymbol{H}_i^d\boldsymbol{U}_f \tag{4.6}$$

where $\boldsymbol{H}_i^d$ is the block triangular Toeplitz matrix. The substitution of Eq. (4.6) into the reference-based forward innovation model and manipulation, leads to the following relation:

$$\begin{pmatrix}\boldsymbol{A} & \begin{pmatrix}\boldsymbol{B} & \boldsymbol{\Gamma}_{i-1}^{\dagger}\boldsymbol{H}_{i-1}^d\end{pmatrix} - \boldsymbol{A}\boldsymbol{\Gamma}_i^{\dagger}\boldsymbol{H}_i^d \\ \boldsymbol{C} & \begin{pmatrix}\boldsymbol{D} & \boldsymbol{0}\end{pmatrix} - \boldsymbol{C}\boldsymbol{\Gamma}_i^{\dagger}\boldsymbol{H}_i^d\end{pmatrix} = \begin{pmatrix}\boldsymbol{\Gamma}_i^{\dagger}\boldsymbol{Z}_i \\ \boldsymbol{U}_f\end{pmatrix}\begin{pmatrix}\boldsymbol{\Gamma}_{i-1}^{\dagger}\boldsymbol{Z}_{i+1} \\ \boldsymbol{Y}_{i\big|i}\end{pmatrix}^{-1} \tag{4.7}$$

After the estimate of $\boldsymbol{A}$, $\mathbf{C}$ with least-squares solution of Eq. (4.7) and the recalculation of the observability matrix with obtained $\boldsymbol{A}$, $\mathbf{C}$, one may determine $\boldsymbol{B}, \boldsymbol{D}$ with the linear regression by solving a set of linear equations:

$$\boldsymbol{B}, \boldsymbol{D} = \arg \min_{\boldsymbol{B},\boldsymbol{D}} \left\| \begin{pmatrix} \boldsymbol{\Gamma}_{i-1}^{\dagger} \boldsymbol{Z}_{i+1} \\ \boldsymbol{Y}_{i|i} \end{pmatrix} - \begin{pmatrix} \boldsymbol{A} \\ \boldsymbol{C} \end{pmatrix} \boldsymbol{\Gamma}_i^{\dagger} \boldsymbol{Z}_i - \boldsymbol{K}(\boldsymbol{B}, \boldsymbol{D}) \boldsymbol{U}_f \right\|_F^2 \tag{4.8}$$

4.3 The Force Identification Model

Resorting to Eq. (4.1) and stacking the input and output data for various discrete-time instants, the force identification model can be readily given as follows:

$$\boldsymbol{Y} = \begin{Bmatrix} \boldsymbol{Y}_0 \\ \boldsymbol{Y}_1 \\ \vdots \\ \boldsymbol{Y}_k \end{Bmatrix} - \begin{Bmatrix} \boldsymbol{C} \\ \boldsymbol{CA} \\ \vdots \\ \boldsymbol{CA}^k \end{Bmatrix} \boldsymbol{X}_0 = \begin{bmatrix} \boldsymbol{D} & \boldsymbol{0} & \cdots & \boldsymbol{0} \\ \boldsymbol{CB} & \boldsymbol{D} & \cdots & \boldsymbol{0} \\ \vdots & \vdots & \ddots & \vdots \\ \boldsymbol{CA}^{k-1}\boldsymbol{B} & \boldsymbol{CA}^{k-2}\boldsymbol{B} & \cdots & \boldsymbol{D} \end{bmatrix} \begin{Bmatrix} \boldsymbol{F}_0 \\ \boldsymbol{F}_1 \\ \vdots \\ \boldsymbol{F}_k \end{Bmatrix} = \boldsymbol{HF} \tag{4.9}$$

Once the system matrices ($\boldsymbol{A}, \boldsymbol{B}, \mathbf{C}$ and $\boldsymbol{D}$) have been determined, the system transfer matrix $\boldsymbol{H}$ is correspondingly determined, and then the input forces can be reasonably calculated with Eq. (4.9). However, the measurement noise and the process errors cannot generally be neglected, thus the force identification problem can be viewed as an optimization problem with the following optimal object function:

$$\min_{\boldsymbol{F}} J = \|\boldsymbol{\varepsilon}\|_2^2 = \|\boldsymbol{Y} - \boldsymbol{HF}\|_2^2 \tag{4.10}$$

A weighted algorithm based on the homotopy method is employed to discretize the ill-posed problems and the homotopy function is defined as follows [13]:

$$\min_{\boldsymbol{F}} T(x, \lambda) = \lambda K(x) + (1 - \lambda) G(x) \tag{4.11}$$

where $G(x)$ and $K(x)$ correspond to the equation set of difficult and simple solutions, respectively. λ is the homotopy parameter with $0 < \lambda < 1$. In the category of the force identification problem, letting $G(x) = \|\boldsymbol{\varepsilon}\|_2^2 = \|\boldsymbol{Y} - \boldsymbol{HF}\|_2^2$ and $K(x) = \|\boldsymbol{F}\|_2^2$, Eq. (4.10) can be rewritten as a cost function:

$$\min_{\boldsymbol{F}} J = \lambda \boldsymbol{F}^H \boldsymbol{F} + (1 - \lambda) (\boldsymbol{Y} - \boldsymbol{HF})^{\mathrm{H}} (\boldsymbol{Y} - \boldsymbol{HF}) \tag{4.12}$$

where the superscript "H" indicates Hermitian transpose. To minimize Eq. (4.12), the first derivative of J with respect to $\boldsymbol{F}$ must be zero:

$$\frac{\partial J}{\partial \boldsymbol{F}} = 2(1 - \lambda) \boldsymbol{H}^H (\boldsymbol{HF} - \boldsymbol{Y}) + 2\lambda \boldsymbol{F} = 0 \tag{4.13}$$

The optimal solution to minimize the error amplification in force reconstruction is then found to be:

$$\boldsymbol{F} = \left[(1 - \lambda) \boldsymbol{H}^H \boldsymbol{H} + \lambda \boldsymbol{I} \right]^{-1} (1 - \lambda) \boldsymbol{H}^H \boldsymbol{Y} \tag{4.14}$$

Moving and merging the terms of Eq. (4.12), the following relationship can be obtained:

$$\boldsymbol{F} = \|\boldsymbol{Y} - \boldsymbol{HF}\|_2^2 + \lambda \left[\|\boldsymbol{F}\|_2^2 - \|\boldsymbol{Y} - \boldsymbol{HF}\|_2^2 \right] \tag{4.15}$$

Finally, the L-curve criterion is employed to select an appropriate homotopy parameter in order to obtain the optimal force, where the norm of $\|\boldsymbol{Y} - \boldsymbol{HF}\|$ is plotted against $\|\boldsymbol{F}\|_2^2 - \|\boldsymbol{Y} - \boldsymbol{HF}\|_2^2$ as λ is varied. The point at the "corner" of L-curve that has maximum curvature should be chosen as the optimal homotopy parameter value.

4.4 Practical Application

As an application of the present algorithm, laboratory experiments for the propeller force identification of a scale model of a civil ship shown in Fig. 4.1 have been considered to demonstrate robustness and effectiveness of the method. The test structure mainly consists of a hull structure and a propeller-shaft system, which are connected through two journal bearings and one thrust bearing. The whole system is supported by three sets of isolation air springs to prevent transmission of vibrations from the supporting structure to the hull. The test structure was instrumented with an array of accelerometers, power amplifier, and linear variable accelerometers, while all sampling data were simultaneously collected through a 16-channel LMS data acquisition system.

In this study, the measured response data from one longitudinal acceleration channel at the pedestal of the thrust bearing and the input force measured at the propeller hub were used. The force transducer (B&K 8200) was connected to a shaker (HEV-200) with a stinger. The scene drawing of the exciting device and the location of the accelerometer (HD-YD-216) are shown in Figs. 4.2 and 4.3, respectively. The entire verification process to be performed is organized as follows:

(1) **Construction of the state-space model**: To determine the matrices $\boldsymbol{A}$, $\boldsymbol{B}$, $\boldsymbol{C}$ and $\boldsymbol{D}$, the system is firstly excited by a zero-mean Gaussian random input with the sampling frequency 2048 Hz. The measured acceleration signal is transformed to a displacement signal (Fig. 4.4) by frequency-domain integral equation solvers to allow the direct application of the

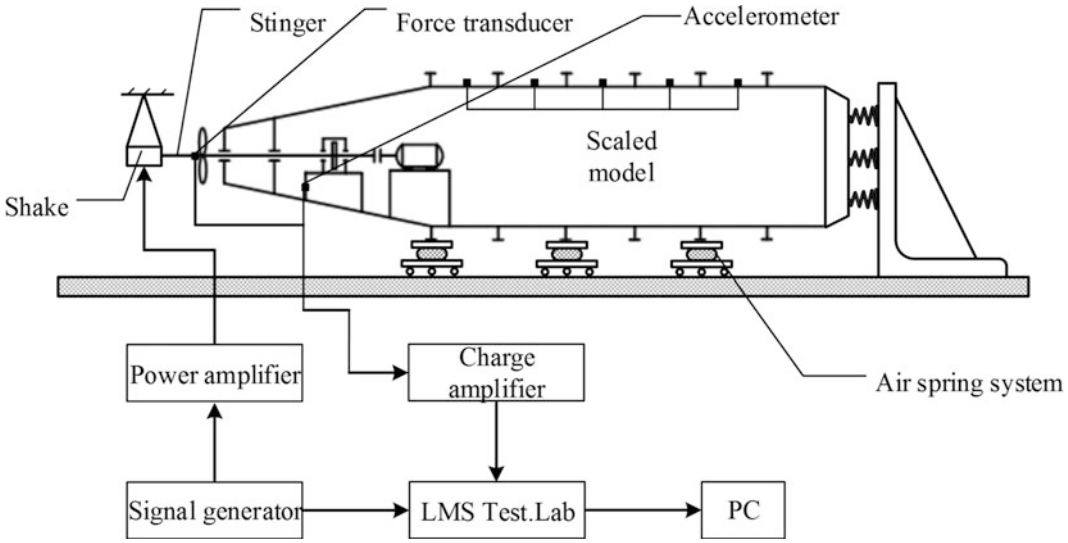

Fig. 4.1 Schematic diagram of the experimental apparatus

Fig. 4.2 Scene drawing of the exciting system

Fig. 4.3 The mounting of the accelerometer

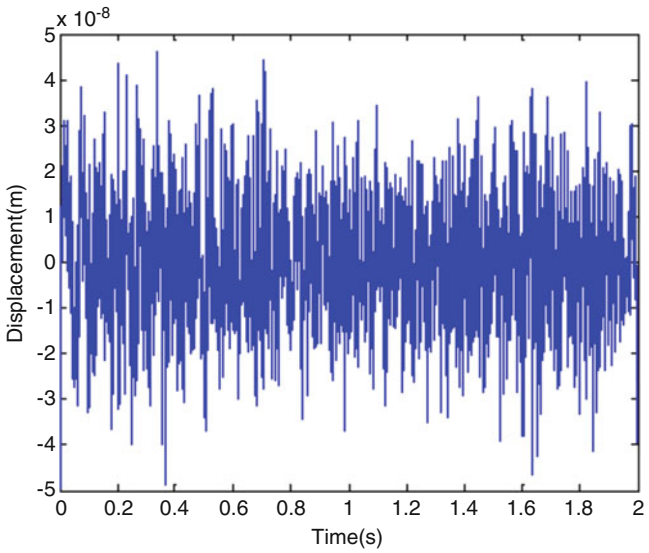

Fig. 4.4 The displacement response at the pedestal

subspace identification algorithms. In the current study, a Hankel matrix is formed using the input–output data with 50 block-rows when the window length of 2 s is used. From the singular value plot, the model order is specified as $n = 8$ due to a big jump between model order 8 and 9, as shown in Fig. 4.5. Thereafter the state matrices can be identified according to Sect. 4.2.

(2) **Identification of sinusoidal excitation forces**: Considering cases of sinusoidal excitation forces at 60 Hz and 80 Hz applied on the structure, the forces can be identified with Eq. (4.15) from the measured responses. Figure 4.6 shows the comparison of the identified results and the real forces. The curve of identified force is found to be slightly overlap the true force curve, which checks the validity and good robustness of the proposed method.

(3) **Identification of random excitation forces**: Considering the case of Gaussian random excitation force applied on the structure, the identified result is shown in Fig. 4.7. Although some fluctuation can be found from the curve of identified force, it is consistent well with the real curve overall at a reasonable accuracy. The result illustrates the good performance of anti-interference with respect to the proposed method.

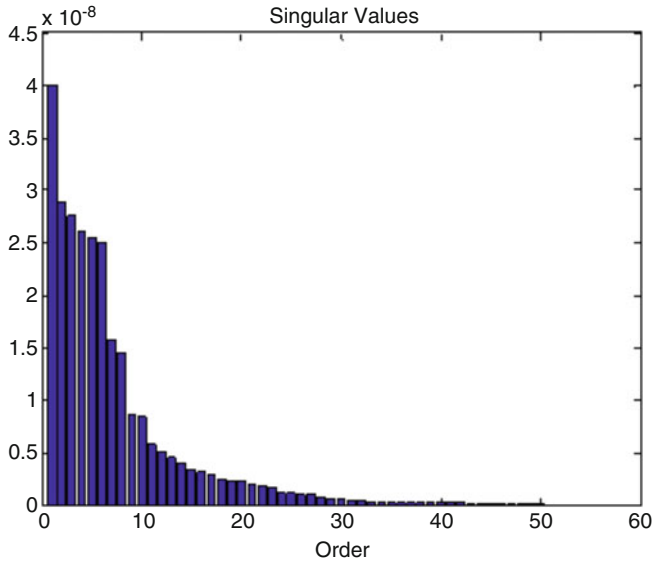

Fig. 4.5 The singular value plot

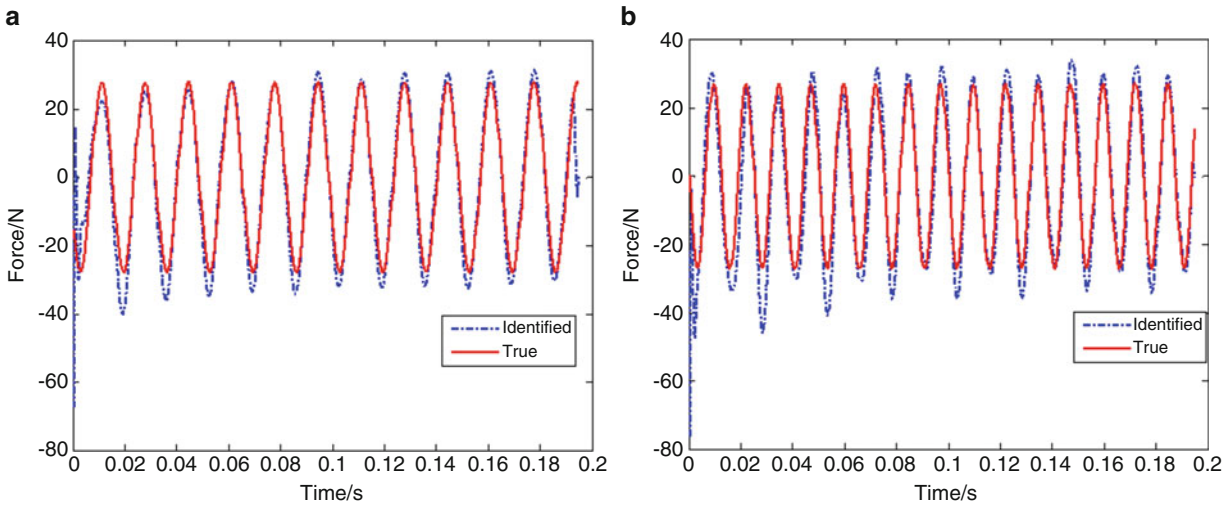

Fig. 4.6 Time histories of the estimated and measured sinusoidal force: (**a**) 60 Hz and (**b**) 80 Hz

4.5 Conclusions

An efficient inverse method combining the subspace identification algorithm and the homotopy method has been successfully used to estimate dynamic forces acting on structures from measured dynamic responses. The data-driven subspace algorithm is utilized to facilitate the estimation of state space model of the system. Meanwhile, the homotopy method based on the L-curve criterion is employed to discretize the ill-posed problems due to the inversion process. The feasibility of the present method is verified with laboratory experiments on a scale model of a civil ship. The comparisons of the measured and estimated results have demonstrated the effectiveness of the proposed technique for the identification of excitation forces. The present approach is expected to be extended to force identification problems of the nonlinear systems in the future work.

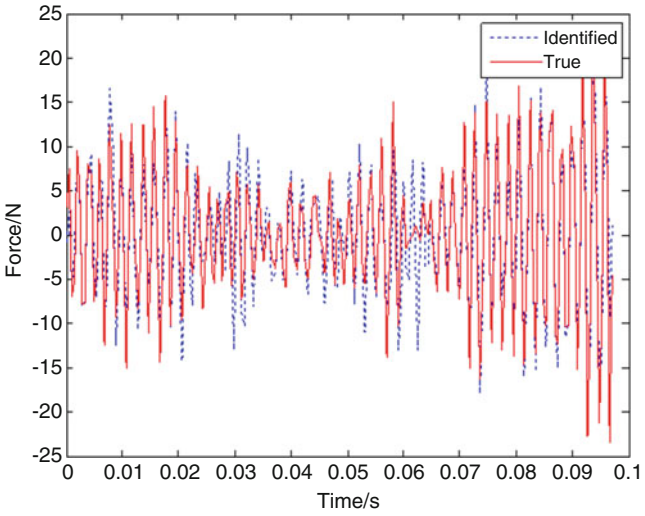

Fig. 4.7 Time histories of the estimated and measured random force

Acknowledgments This research is sponsored by the National Natural Science Foundation of China (NSFC), Grant No. 51505281. The authors greatly appreciate the support provided by NSFC during this research.

References

1. Innoue, H., Harrigan, J.J., Reid, S.R.: Review of inverse analysis for indirect measurement of impact force. Appl. Mech. Rev. **54**(6), 503–525 (2001)
2. Dobson, B.J., Rider, E.: A review of the indirect calculations of excitation forces from measured structural response data. Proc. Inst. Mech. Eng. Sci. **204**, 69–75 (1990)
3. Shiozaki, H., Geluk, T., et al.: Time-domain transfer path analysis for transient phenomena applied to tip-in/tip-out (Shock &Jerk), SAE Technical Paper, 2012-01-1545, 2012
4. Liu, J.J., Ma, C.K., Kung, I.C.: Input force estimation of a cantilever plate by using a system identification technique. Comput. Methods Appl. Mech. Eng. **190**(11–12), 1309–1322 (2000)
5. Lu, Z., Law, S.: Force identification based on sensitivity in time domain. J. Eng. Mech. **132**(10), 1050–1056 (2006)
6. Hwang, J.S., Kareem, A., Kim, H.: Wind load identification using wind tunnel test by inverse analysis. J. Wind Eng. Ind. Aerodyn. **99**(1), 18–26 (2011)
7. Mao, Y.M., Guo, X.L., Zhao, Y.: A state space force identification method based on Markov parameters precise computation and regularization technique. J. Sound Vib. **329**(15), 3008–3019 (2010)
8. Liu, Y., Steve, S.J.W.: Dynamic force identification based on enhanced least squares and total least-squares schemes in the frequency domain. J. Sound Vib. **282**(1–2), 37–60 (2005)
9. Jacquelin, E., Bennani, A., Hamelin, P.: Force reconstruction: analysis and regularization of a deconvolution problem. J. Sound Vib. **265**(1), 81–107 (2003)
10. Choi, H.G., Thite, A.N., Thompson, D.J.: A threshold for the use of Tikhonov regularization in inverse force determination. Appl. Acoust. **67**(7), 700–719 (2006)
11. Shidfar, A., Molabahrami, A.: A weighted algorithm based on the homotopy analysis method: application to inverse heat conduction problems. Commun. Nonlinear Sci. Numer. Simul. **15**(10), 2908–2915 (2010)
12. Ma, C., Hua, H.X.: Force identification technique by the homotopy method. J. Mech. Sci. Tech. **29**(10), 4083–4091 (2015)
13. Reynders, E., De Roeck, G.: Reference-based combined deterministic–stochastic subspaceidentification for experimental and operational modal analysis. Mech. Syst. Signal Process. **22**(3), 617–637 (2008)

Chapter 5
Response DOF Selection for Mapping Experimental Normal Modes-2016 Update

Robert N. Coppolino

Abstract A modified Guyan reduction strategy for response degree-of-freedom (DOF) selection to map experimental normal modes is described and demonstrated. The method employs static load patches, rather than point loads, in regions defined by 3-D elastic elements and other problematic zones on a highly detailed finite element model (FEM). Three key benefits are realized by the methodology, namely (1) definition of a well-posed test-analysis mass (TAM) matrix, (2) application of a previously published residual kinetic energy matrix for definition of appropriate measurement DOFs, and (3) elimination of irrelevant modes from the measured mode set. Improved qualities of the modified Guyan reduction strategy are demonstrated with a problematic spacecraft-type FEM, which cannot be readily treated using classical Guyan reduction methodology.

5.1 Introduction

The United States Air Force Space Command [1] and NASA [2] maintain standards for the proper execution of spacecraft and launch vehicle modal tests, which require measured mode shapes satisfying strict orthogonality criteria. Modal vector orthogonality, based on the fundamental energy principles owing to Ritz [3], require a test-analysis mass (TAM) matrix that is most often developed by employment of the Guyan reduction method [4]. The TAM matrix, generally developed as part of the modal test planning process, is defined on the basis of proposed instrumented (accelerometer) degrees of freedom (DOF), which are a subset of a corresponding (often highly detailed) finite element model (FEM).

Advances in computers and software resources and ever increasingly detailed FEMs rendered selection of an adequate instrumentation array and TAM matrix quite challenging. Development of a residual kinetic energy (RKE) method [5] provided a path for automated completion of an initially deficient instrumentation array and TAM matrix (employing Guyan reduction as the underlying principle). However, additional difficulties owing to (a) displacement pattern (Boussinesq) singularities for models based on 3-D finite elements [6] and (b) breathing modes of shells [7] rendered the popular Guyan reduction method to be deficient in such situations. In response to these challenges, a "modified" Guyan reduction strategy employing load patches [8], rather than concentrated point loads (implicitly) used in "classical" Guyan reduction, appears to remedy this situation.

The present paper revisits the "modified" Guyan reduction method and introduces a generalized RKE procedure for reliable definition of an instrumentation array and TAM matrix. In addition, the generalized RKE procedure appears to be useful for other model order reduction strategies such as SEREP [9], modal sensitivity vector augmentation [10], and others. The generalized Guyan-RKE methodology is demonstrated on an aerospace-type branched shell configuration, which was previously studied [8]. Results of the demonstration indicate that (1) "classical" Guyan reduction produces a TAM matrix that fails to satisfy strict orthogonality criteria, (2) "modified" Guyan reduction produces TAM matrices satisfying strict orthogonality criteria (without the need for additional instrumentation degrees of freedom), and (3) RKE is a useful metric for discrimination of "body" and shell "breathing" modes as well as a means for improvement of the instrumentation array.

R.N. Coppolino (✉)
Measurement Analysis Corporation, 23850 Madison Street, Torrance, CA 90505, USA
e-mail: bobcoppolino@gmail.com

© The Society for Experimental Mechanics, Inc. 2016

M. Allen et al. (eds.), *Dynamics of Coupled Structures, Volume 4*, Conference Proceedings of the Society for Experimental Mechanics Series, DOI 10.1007/978-3-319-29763-7_5

5.2 Nomenclature

Symbol	Matrix or Array
{F}	Force
[I]	Identity
[K]	Stiffness
{KE}	Modal Kinetic Energy
[M]	Mass
$[M_{aa}]$	TAM Mass
$[M_{eff}]$	Modal Effective Mass
[OR]	Orthogonality
[P]	Modal Participation Factor
[R]	Residual Displacement
[RKE]	Residual Kinetic Energy
{SE}	Modal Strain Energy
[Φ]	Modes
[Γ]	Force Allocation
[Ψ]	Displacement Shapes
{q}	Generalized Displacements
{u}	Physical Displacements

Symbol	Variable
i	Imaginary Number
η	Structural Damping
λ	Eigenvalue
ω	Circular Frequency
h	Frequency Response

Symbol	Subscript
a	analysis or "instrumented" dof
b	base dof
c	"Classical" Guyan
f	free dof
g	"General"
m	"Modified" Guyan
n	Mode "n"
o	"Omitted" or "Other" dof
q	"Generalized" dof

5.3 Understanding Normal Modes

A vital step in the modal test planning process involves development of a thorough, quantitative understanding of predicted dynamic characteristics of the subject structural system. Detailed characteristics of the subject system's normal modes are revealed, not only from modal frequencies and "geometric" mode shapes, but from modal kinetic and strain energy distributions (which are sorted in terms of overall direction and substructure groups). When the subject test article is a component of a larger, complete system, the relative significance of a subset of modes within a predetermined frequency band is evaluated on the basis of modal effective mass. This section of the paper presents mathematical details of important modal kinetic and strain energies and modal effective mass.

The fundamental set of matrix equations describing forced response of a linear structural dynamic FEM (in the frequency domain with uniform structural damping) are

$$[\mathrm{M}]\{\ddot{\mathrm{u}}(\omega)\} + (1 + \mathrm{i}\eta)[\mathrm{K}]\{\mathrm{u}(\omega)\} = \{\mathrm{F}(\omega)\}. \tag{5.1}$$

For the case of undamped free vibration, the orthonormal mode transformation and properties with respect to system mass and stiffness are

$$\{\mathrm{u}\} = [\Phi]\{\mathrm{q}\}, \quad [\Phi]^{\mathrm{T}}[\mathrm{M}][\Phi] = [\mathrm{I}], \quad [\Phi]^{\mathrm{T}}[\mathrm{K}][\Phi] = [\lambda]. \tag{5.2}$$

The distributions of kinetic and strain energies in one particular mode are the following respective term-by-term products:

$$\{\mathrm{KE}\}_{\mathrm{n}} = \{[\mathrm{M}]\{\Phi\}_{\mathrm{n}}\} \otimes \{\Phi\}_{\mathrm{n}}, \quad \mathrm{KE}_{\mathrm{TOT,n}} = \sum_{\mathrm{i}=1}^{\mathrm{DOF}} \mathrm{KE}_{\mathrm{in}} = 1 \tag{5.3}$$

$$\{\mathrm{SE}\}_{\mathrm{n}} = \{[\mathrm{K}]\{\Phi\}_{\mathrm{n}}\} \otimes \{\Phi\}_{\mathrm{n}}, \quad \mathrm{SE}_{\mathrm{TOT,n}} = \sum_{\mathrm{i}=1}^{\mathrm{DOF}} \mathrm{SE}_{\mathrm{in}} = \lambda_{\mathrm{n}}. \tag{5.4}$$

The individual terms in each of these "energy" vectors are directly associated with the dynamic system degrees of freedom. As such, they provide appropriately weighted metrics for kinetic and strain energy distributions that are not indicated by the

geometric modes shape (e.g., "heavier" degrees of freedom have greater kinetic energy than "lighter" degrees of freedom with equivalent modal displacements). Further insight into the character of individual modes is gained by summations of subgroups according to (a) subcomponents and/or (b) activity directions.

In the case of a supported (e.g., base-fixed) system, the displacement degrees of freedom are partitioned into interior (or free) and boundary (or fixed) degree of freedom subsets, as shown below.

$$\begin{bmatrix} M_{ii} & M_{ib} \\ M_{bi} & M_{bb} \end{bmatrix} \begin{Bmatrix} \ddot{u}_i \\ \ddot{u}_b \end{Bmatrix} + (1 + i\eta) \begin{bmatrix} K_{ii} & K_{ib} \\ K_{bi} & K_{bb} \end{bmatrix} \begin{Bmatrix} u_i \\ u_b \end{Bmatrix} = \begin{Bmatrix} F_i(t) \\ F_b(t) \end{Bmatrix} \tag{5.5}$$

The Craig-Bampton [11] modal transformation describes the interior degrees of freedom in terms of boundary fixed modes and "constraint modes" associated with unit boundary displacements.

$$\begin{Bmatrix} u_i \\ u_b \end{Bmatrix} = \begin{bmatrix} \Phi_{iq} & -K_{ii}^{-1} K_{ib} \\ 0_{bq} & I_{bb} \end{bmatrix} \begin{Bmatrix} q \\ u_b \end{Bmatrix} = \begin{bmatrix} \Phi_{iq} & \Psi_{ib} \\ 0_{bq} & I_{bb} \end{bmatrix} \begin{Bmatrix} q \\ u_b \end{Bmatrix} \tag{5.6}$$

It should be noted that when the boundary is statically determinate, the "constraint modes" are rigid body vectors, referenced at the boundary. When the above transformation is applied, the resulting Craig-Bampton component dynamic equations are

$$\begin{bmatrix} \mathrm{I_{qq}} & \mathrm{P_{qb}} \\ \mathrm{P_{bq}} & \overline{\mathrm{M}}_{\mathrm{bb}} \end{bmatrix} \begin{Bmatrix} \ddot{\mathrm{q}} \\ \ddot{\mathrm{u}}_{\mathrm{b}} \end{Bmatrix} + (1 + \mathrm{i}\eta) \begin{bmatrix} \omega_{\mathrm{q}}^2 & 0_{\mathrm{ib}} \\ 0_{\mathrm{bi}} & \overline{\mathrm{K}}_{\mathrm{bb}} \end{bmatrix} \begin{Bmatrix} \mathrm{q} \\ \mathrm{u_b} \end{Bmatrix} = \begin{bmatrix} \Phi_{\mathrm{iq}}^{\mathrm{T}} & 0_{\mathrm{qb}} \\ \Psi_{\mathrm{ib}}^{\mathrm{T}} & \mathrm{I_{bb}} \end{bmatrix} \begin{Bmatrix} \mathrm{F_i} \\ \mathrm{F_b} \end{Bmatrix}, \tag{5.7}$$

The boundary mass and stiffness matrix partitions reduce to (a) the 6×6 rigid body mass matrix and (b) a null 6×6 boundary stiffness matrix, respectively, if the boundary is statically determinate. It is of interest to consider the response of such a system to simple harmonic boundary accelerations. The modal accelerations in this situation are:

$$\ddot{\mathrm{q}}_{\mathrm{n}}(\omega) = -\mathrm{h_n}(\omega)\left[\mathrm{P_{nb}}\right]\left\{\ddot{\mathrm{u}}_{\mathrm{b}}(\omega)\right\}, \quad \mathrm{h_n}(\omega) = \frac{-(\omega/\omega_{\mathrm{n}})^2}{1 + \mathrm{i}\eta_{\mathrm{n}} - (\omega/\omega_{\mathrm{n}})^2}. \tag{5.8}$$

And the boundary reaction loads, for a statically determinate boundary, are:

$$\left\{\mathrm{F_b}(\omega)\right\} = \left[\overline{\mathrm{M}}_{\mathrm{bb}} - \sum_{\mathrm{n}=1}^{\mathrm{N}} \left[\mathrm{P_{bn}P_{nb}}\right] \mathrm{h_n}(\omega)\right] \left\{\ddot{\mathrm{u}}_{\mathrm{b}}(\omega)\right\}. \tag{5.9}$$

The modal participation products are called modal effective mass matrices (one per mode), which when summed are approximately the total system rigid body mass (equal only if the boundary is massless). Modal effective mass is a modal metric that indicates direction of modal activity as well as degree with which the boundary reacts to modal response:

$$\left[\mathrm{Meff}\right]_{\mathrm{n}} = \left[\mathrm{P_{bn}}\right]\left[\mathrm{P_{nb}}\right], \quad \sum_{\mathrm{n}=1}^{\mathrm{N}} \left[\mathrm{Meff}\right]_{\mathrm{n}} \approx \left[\overline{\mathrm{M}}_{\mathrm{bb}}\right]. \tag{5.10}$$

5.4 Model Order Reduction Strategies

While many authors have developed and refined dynamic finite element model reduction procedures since the late 1960s, Guyan reduction [4] endures as the industry preferred strategy. In 2011, a modified Guyan reduction strategy [5] was introduced in order to alleviate difficulties encountered with large-order, problematic finite-element models.

5.4.1 Classic Guyan Reduction

The underlying idea that defines Guyan reduction is static condensation . . . and Guyan's monumental formulation was published as a one-half page technical note! The "free" degrees of freedom describing a structural dynamic system are first separated into "analysis" and "omitted" subsets, which lead to the partitioned matrix equations (ignoring damping):

$$[\mathrm{M_{ff}}]\{\ddot{\mathrm{u}}_\mathrm{f}\} + [\mathrm{K_{ff}}]\{\mathrm{u_f}\} = \{\mathrm{F_f}\} \rightarrow \begin{bmatrix} \overline{\mathrm{M}}_{\mathrm{aa}} & \mathrm{M_{ao}} \\ \mathrm{M_{oa}} & \mathrm{M_{oo}} \end{bmatrix} \begin{Bmatrix} \ddot{\mathrm{u}}_\mathrm{a} \\ \ddot{\mathrm{u}}_\mathrm{o} \end{Bmatrix} + \begin{bmatrix} \overline{\mathrm{K}}_{\mathrm{aa}} & \mathrm{K_{ao}} \\ \mathrm{K_{oa}} & \mathrm{K_{oo}} \end{bmatrix} \begin{Bmatrix} \mathrm{u_a} \\ \mathrm{u_o} \end{Bmatrix} = \begin{Bmatrix} \mathrm{F_a} \\ \mathrm{F_o} \end{Bmatrix}. \tag{5.11}$$

If only the "analysis" partition of the mass matrix were non-zero, and external forces were only applied to "analysis" degrees of freedom, the relationship between "analysis" and "omitted" degrees of freedom would be

$$\{\mathrm{u_f}\} = \begin{Bmatrix} \mathrm{u_a} \\ \mathrm{u_o} \end{Bmatrix} = \begin{bmatrix} \mathrm{I_{aa}} \\ -\mathrm{K_{oo}^{-1}K_{oa}} \end{bmatrix} \{\mathrm{u_a}\} = [\Psi_{\mathrm{fa}}]_\mathrm{c}\{\mathrm{u_a}\}. \tag{5.12}$$

In that situation, the reduction transformation in Eq. (5.12) would be exact. When the "omit" partitions of the mass matrix are non-zero, the reduction transformation is approximate (its columns are Ritz [3] shape functions). Application of the reduction transformation, in a symmetric manner following the Ritz method, yields the "classical" Guyan reduction TAM mass matrix,

$$[\mathrm{M_{aa}}]_\mathrm{c} = [\Psi_{\mathrm{fa}}]_\mathrm{c}^\mathrm{T}[\mathrm{M_{ff}}][\Psi_{\mathrm{fa}}]_\mathrm{c}. \tag{5.13}$$

It should be noted that the reduction transformation matrix columns (in Eq. 5.12) are physically consistent with deflection shapes associated with application of individual unit "analysis" set loads.

5.4.2 *Modified Guyan Reduction*

When the Guyan reduction method was introduced in 1965, the majority of matrix structural dynamic models were assembled using finite elements based on technical theories (e.g., beams, plates and shells). Deformation shapes for technical theory based structural models, subjected to point loads, are generally smooth resulting in "well-behaved" Ritz shape functions. As finite element technology continued to evolve, elements based on 3-D elasticity theory matured to the point that many of today's highly refined finite element models incorporate 3-D elastic elements. Dynamic models using 3-D elastic elements are generally quite accurate and effective, except for situations in which reduced models are required (e.g., preparation of test-analysis models or TAMs). Since highly refined 3-D elastic models closely follow exact mathematical behavior, deformations associated with point loads are extreme (infinite in the limit, as in the case of the Boussinesq problem [6]), producing Ritz shape functions that do not resemble normal modes. Thus application of Guyan Reduction on dynamic models composed of 3-D elements, as well as several types of one and two dimensional elements (especially shells), is inappropriate.

Consider the general distribution of static loads described by the matrix equation,

$$\{\mathrm{F_f}\} = [\Gamma_{\mathrm{fa}}]\{\mathrm{F_a}\}, \tag{5.14}$$

where $[\Gamma_{\mathrm{fa}}]$, represents the collection of unit load patterns (or load patches). The static displacement shapes due to unit load patches are

$$[\Psi_{\mathrm{fa}}] = [\mathrm{K_{ff}}]^{-1}[\Gamma_{\mathrm{fa}}], \text{ which implies that, } \{\mathrm{u_f}\} = [\Psi_{\mathrm{fa}}]\{\mathrm{F_a}\}. \tag{5.15}$$

Pre-multiplication of this result by the transpose of unit loadings yields,

$$\{\mathrm{q}\} = [\Psi_{\mathrm{fa}}]^\mathrm{T}[\mathrm{K_{ff}}]^{-1}[\Psi_{\mathrm{fa}}]\{\mathrm{F_a}\}. \tag{5.16}$$

Substitution of this result into Eq. (5.15) yields the modified Guyan reduction transformation,

$$\{\mathrm{u_f}\} = [\Psi_{\mathrm{fa}}]\left[{\Psi_{\mathrm{fa}}}^\mathrm{T}{\mathrm{K_{ff}}}^{-1}\Psi_{\mathrm{fa}}\right]^{-1}\{\mathrm{q}\} = \left[\Psi_{\mathrm{fq}}\right]\{\mathrm{q}\}. \tag{5.17}$$

Unlike the reduction transformation defined by classic Guyan reduction, which provides a direct relationship between "free" and "instrumented" DOFs, the above transformation requires further development. This is accomplished by first focusing on a partition that relates "instrumented" and generalized DOFs, i.e.,

$$\{\mathrm{u_a}\} = \left[\Psi_{\mathrm{aq}}\right]\{\mathrm{q}\}, \tag{5.18}$$

where $[\Psi_{aq}]$ is the rectangular partition of $[\Psi_{fq}]$ corresponding to measured DOFs. The least-squares inverse transformation (assuming there are more $\{u_a\}$ DOFs than $\{q\}$ DOFs) is finally

$$\{q\} = \left[\Psi_{aq}^{T}\Psi_{aq}\right]^{-1}\left[\Psi_{aq}^{T}\right]\{u_a\} = \left[\Psi_{qa}\right]\{u_a\}. \tag{5.19}$$

Thus the modified Guyan reduction transformation relating "free" and "instrumented" DOFs is

$$\{u_f\} = \left[\Psi_{fq}\right]\left[\Psi_{qa}\right]\{u_a\} = [\Psi_{fa}]_m\{u_a\}. \tag{5.20}$$

Application of the reduction transformation, in a symmetric manner, yields the "modified" Guyan reduction TAM mass matrix

$$[M_{aa}]_m = [\Psi_{fa}]_m^{T}[M_{ff}][\Psi_{fa}]_m. \tag{5.21}$$

5.4.3 General Model Order Reduction

The general model order reduction transformations for any assumed set of Ritz vectors (e.g. SEREP and others [9, 10]) are:

$$\{u_f\} = \left[\Psi_{fq}\right]_g\{q\} \rightarrow \{u_a\} = \left[\Psi_{aq}\right]_g\{q\} \rightarrow \{q\} = \left[\Psi_{aq}^{T}\Psi_{aq}\right]_g^{-1}\left[\Psi_{aq}^{T}\right]_g\{u_a\} = \left[\Psi_{qa}\right]_g\{u_a\} \rightarrow \{u_f\} = \left[\Psi_{fq}\right]_g\left[\Psi_{qa}\right]_g$$
$$\{u_a\} = [\Psi_{fa}]_g\{u_a\}. \tag{5.22}$$

Application of the reduction transformation, in a symmetric manner yields the "general" reduction TAM mass matrix

$$[M_{aa}]_g = \left[\Psi_{fa}\right]_g^{T}\left[M_{ff}\right]\left[\Psi_{fa}\right]_g \tag{5.23}$$

5.5 Reduced Order Model Orthogonality and Residual Kinetic Energy

The three above types of model order reduction serve as alternatives for development of a TAM mass matrix to be employed in experimental mode evaluations conforming to U.S. Air Force and NASA standards [1, 2]. For the purposes of modal test planning, the adequacy of a selected instrumentation (accelerometer) array may be evaluated by taking the "instrumented" subset partition, $[\Phi_a]$, of the predicted "free" modal set, $[\Phi_f]$, and estimating test mode orthogonality,

$$[OR] = [\Phi_a]^{T}[M_{aa}][\Phi_a]. \tag{5.24}$$

The simulated "expanded" modes, calculated as,

$$[\Phi_{fa}] = [\Psi_{fa}][\Phi_a], \tag{5.25}$$

are then employed to form a residual error matrix,

$$[R] = [\Phi_f] - [\Phi_{fa}] = [\Phi_f] - [\Psi_{fa}][\Phi_a]. \tag{5.26}$$

The residual modal kinetic energy matrix [5] is therefore,

$$[RKE] = [M_{ff}R] \otimes [R]. \tag{5.27}$$

The summed residual kinetic energy for a particular mode ([RKE] column) ideally has an upper bound of 1.0 (or 100 %). This is the case for "classical" Guyan reduction, which has a direct (non-least squares) relationship between "free" and

"instrumented" DOFs (see Eq. 5.12). For "modified" Guyan reduction and "general" reduction, an indirect, least-squares approximation is utilized (see Eqs. 5.17 and 5.22), and an inherent singularity causes residual kinetic energy to have an upper bound that may exceed 1.0. Nevertheless, when "instrumented" DOFs are adequate to map modes of interest, the [RKE] column sums will be substantially below 1.0 (or 100 %). When the "instrumented" DOFs do not adequately map a mode of interest, the non-negligible terms of the particular [RKE] column indicate DOF locations required to complete the mapping.

5.6 Branched Shell Illustrative Example

5.6.1 Model Description and Dynamic Characteristics

The shell structure, shown in Fig. 5.1, serves as the illustrative example in this paper. It consists of five substructures, namely (1) a lower cylindrical skirt (fully fixed at its base), (2) a lower hemispherical bulkhead, (3) lower cylindrical section, (4) upper cylindrical section, and (5) upper hemispherical bulkhead. The overall dimensions of the aluminum structure are length, L = 100 inches, radius, R = 20 inches, and wall thickness, h = 0.4 inches.

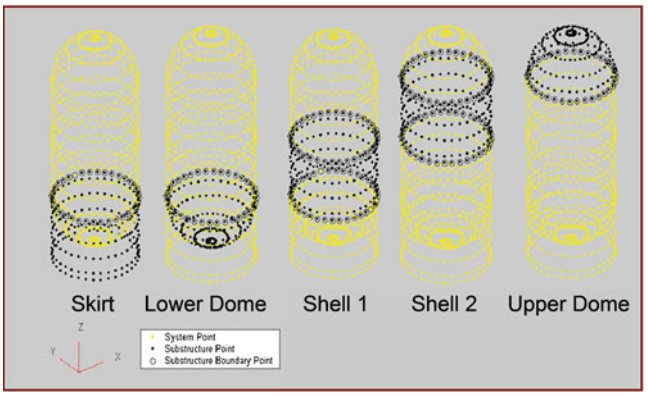

Fig. 5.1 Multi-segmented shell structure

The shell's finite element model, fixed at the lowest skirt station, is described in terms of 5616 "free" degrees of freedom (936 grid points). The lowest 146 normal modes of the model includes 22 modes characterized by "body" and "n = 0, 1 breathing" modes, whose characteristics are summarized below in Tables 5.1 and 5.2.

Table 5.1 Shell "body" and "n = 0, 1 breathing" mode substructure energy characteristics

Body Mode	System Mode	Description	FREQ (Hz)	Kinetic Energy (%)					Strain Energy (%)				
				SKIRT	DOME1	SHELL1	SHELL2	DOME2	SKIRT	DOME1	SHELL1	SHELL2	DOME2
1	1	Y-Bending	122.2	1	1	11	36	51	65	0	27	8	1
2	2	X-Bending	122.2	1	1	11	36	51	65	0	27	8	1
3	11	RZ-Torsion	316.9	4	6	22	43	26	59	0	31	9	0
4	14	Y-Bending	377.6	12	36	28	9	16	67	5	15	11	2
5	15	X-Bending	377.6	12	36	28	9	16	67	5	15	11	2
6	24	Z-Axial	469.4	3	7	18	35	37	56	1	29	11	3
7	49	Y-Bending	708.9	3	37	14	27	19	10	21	37	23	9
8	50	X-Bending	709.3	3	37	15	27	19	10	21	37	23	9
9	63	RZ-Torsion	851.9	19	5	35	38	3	11	12	37	34	6
10	76	Y-Bending	1005.7	17	19	27	25	13	20	14	29	35	1
11	77	X-Bending	1011.5	18	18	27	25	11	20	14	30	35	1
12	86	N=0 Domes	1036.2	8	52	10	4	27	24	28	11	20	17
13	103	N=1	1228.2	19	4	36	36	6	20	4	35	35	7
14	104	N=1	1228.3	19	4	36	36	6	20	4	35	34	7
15	111	N=1	1244.3	0	0	46	53	0	0	0	46	53	0
16	112	N=1	1244.3	0	0	46	53	0	0	0	46	53	0
17	121	N=0 Skirt	1302.3	96	0	2	1	0	95	1	2	1	0
18	128	N=1	1378.2	2	1	46	49	1	3	2	45	48	2
19	129	N=1	1378.4	2	1	46	49	1	3	2	45	48	2
20	140	N=1	1475.4	14	23	19	21	23	15	22	19	22	23
21	141	N=1	1476.0	13	20	22	22	23	14	19	23	23	22
22	146	N=0 Shells	1507.2	8	2	44	43	2	8	4	43	43	3

Table 5.2 Shell "body" and "n = 0, 1 breathing" mode directional kinetic energy and modal effective mass

Body Mode	System Mode	Description	FREQ (Hz)	Kinetic Energy (%)			Modal Effective Mass (%)					
				X	Y	Z	X	Y	Z	RX	RY	RZ
1	1	Y-Bending	122.2		96	4		62		98		
2	2	X-Bending	122.2	96		4	62				98	
3	11	RZ-Torsion	316.9	50	50							82
4	14	Y-Bending	377.6		91	9		30				
5	15	X-Bending	377.6	91		9	30					
6	24	Z-Axial	469.4			99			81			
7	49	Y-Bending	708.9	1	90	10		1				
8	50	X-Bending	709.3	90	1	9	1					
9	63	RZ-Torsion	851.9	50	50	1						
10	76	Y-Bending	1005.7	2	61	37						
11	77	X-Bending	1011.5	63	2	35						
12	86	N=0 Domes	1036.2	8	8	85			8			
13	103	N=1	1228.2	46	53							
14	104	N=1	1228.3	50	50							
15	111	N=1	1244.3	50	50							
16	112	N=1	1244.3	50	50							
17	121	N=0 Skirt	1302.3	50	50							
18	128	N=1	1378.2	50	50							
19	129	N=1	1378.4	50	50							
20	140	N=1	1475.4	35	35	30			1			
21	141	N=1	1476.0	14	68	18						
22	146	N=0 Shells	1507.2	50	50							

The first 12 "body" modes (especially "body" modes 1–6) possess significant modal effective mass, which indicates that they may be easily excited by base acceleration motions. The low modal effective mass associated with "body" modes 13–22 suggests that they are "self-equilibrated" and not excitable by base acceleration motions. All 124 remaining modes are characterized by higher harmonic, $n \geq 2$, "breathing" deformations; in general such modes are of secondary interest for estimation of overall structural dynamic loads, unless vibro-acoustic responses and loads are sought.

It is well-known that higher harmonic breathing modes of thin cylindrical shells generally occur in a frequency band below that associated with doubly curved shells (such as domes) [7]. Therefore, stimulation of the 22 "body" modes (without significant excitation of higher harmonic "breathing" modes) is effected by applied forces on the upper dome, as illustrated below in Fig. 5.2.

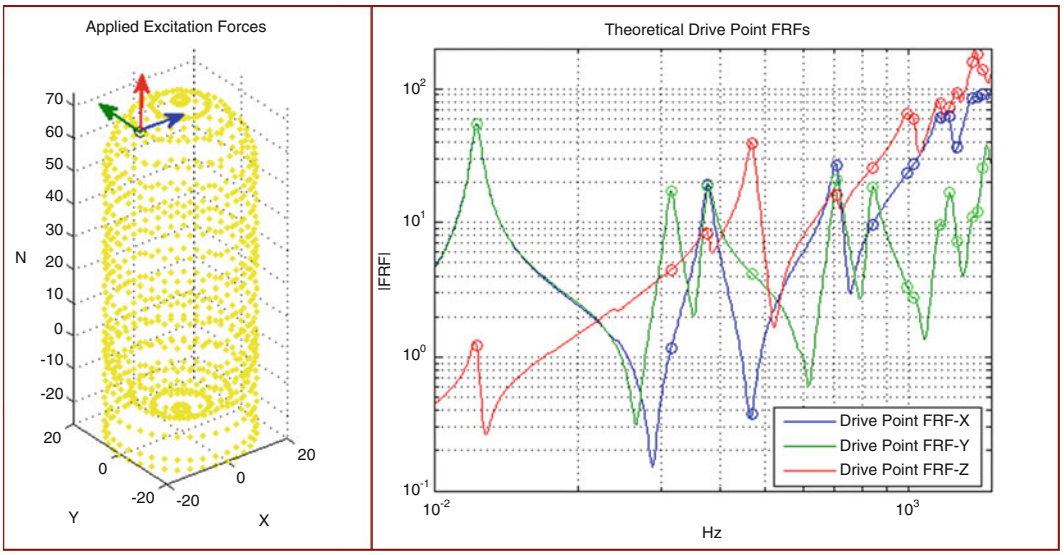

Fig. 5.2 Drive point frequency responses associated with applied upper dome forces

5.6.2 Allocation of instrumented DOFS (Accelerometers)

An array consisting of 103 instrumented grid points (separated by 90° at each shell station), each having a triaxial (X, Y, Z directed) accelerometer (total of 309 DOF) is selected for evaluation, as illustrated below in Fig. 5.3.

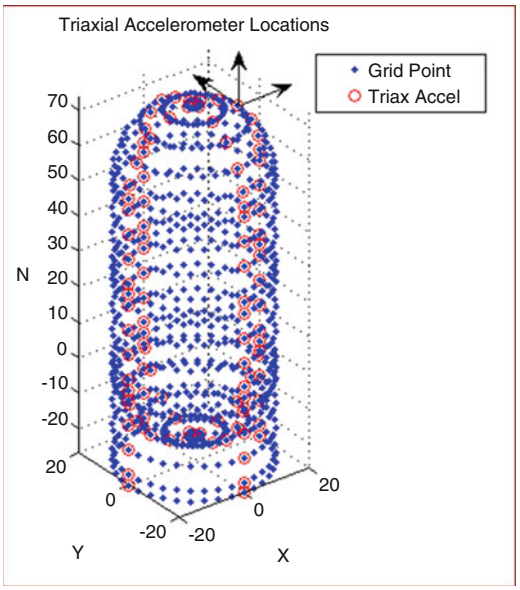

Fig. 5.3 Triaxial accelerometer array

It should be noted that for situations in which n = 0 shell bulge modes are not of interest, accelerations normal to the shell surface are often not allocated in order to suppress mapping of such modes. In the present example, however, the normal accelerations are included [Note that in fluid-filled shell situations (not the present example), the n = 0 shell "bulge" modes are generally of primary importance].

5.6.3 *TAM Definition Using "Classical" Guyan Reduction*

Application of "classical" Guyan reduction, employing the above described instrumentation array results in a TAM mass matrix, produces predicted test mode orthogonality (for the 22 "body" modes) and residual kinetic energy (summed for each mode) as summarized below in Table 5.3.

Table 5.3 Predicted test mode orthogonality and summed residual kinetic energy for a "classical" Guyan reduction TAM

Body Mode	System Mode	Freq (Hz)	Description	Sum(RKE)	Orthogonality Check																					
1	1	122.2	Y-Bending	0	100			-9			24			-2			16		-14			-10		-26		
2	2	122.2	X-Bending	0		100			-9			-24			-2			16		14			10		26	
3	11	315.2	RZ-Torsion	0			100																			
4	14	377.2	Y-Bending	1	-9			100			-4			19			-16		6			1		1		
5	15	377.2	X-Bending	1		-9			100			4			19			-16		-6			-1		-1	
6	24	467.8	Z-Axial	0						100											-8					-6
7	49	706.7	Y-Bending	16	24			-4			100			17			28		-2			-11		-45		
8	50	706.7	X-Bending	16		-24			4			100			-17			-28		-2			-12		-45	
9	63	841.3	RZ-Torsion	5									100													
10	76	997.5	Y-Bending	24	-2			19			17			100			-11		26			-7		-18		
11	77	997.5	X-Bending	24		-2			19			-17			100			-11		-26			7		18	
12	86	1029.9	N=0 Domes	2												100					-3					20
13	103	1169.6	N=1	38	16			-16			28			-11			100					2		-33		
14	104	1169.6	N=1	38		16			-16			-28			-11			100					-1		33	
15	111	1223.5	N=1	64	-14			6			-2			26					100			-7		-8		
16	112	1223.5	N=1	64		14			-6			-2			-26					100			-6		-8	
17	121	1273.4	N=0 Skirt	8						-8						-3					100					1
18	128	1368.3	N=1	61	-10			1			-11			-7			2		-7			100		-10		-1
19	129	1368.4	N=1	61		10			-1			-12			7			-1		-6			100		-10	
20	140	1402.8	N=1	29	-26			1			-45			-18			-33		-8			-10		100		
21	141	1402.8	N=1	29		26			-1			-45			18			33		-8			-10		100	
22	146	1440.4	N=0 Shells	40						-6						20					1	-1				100

The predicted test mode orthogonality associated with the "classical" Guyan reduction TAM mass matrix is unacceptable with respect to U.S. Air Force and NASA standards (off-diagonal terms greater than 10 %). This is attributed to the fact that many of the shape functions, $[\Psi_{af}]_c$, are the result of concentrated normal point loads that cause cross-sectional distortions

(not purely n = 0, 1 shapes). It is also noted that non-negligible summed RKE corresponds to unsatisfactory predicted modal orthogonality (off-diagonal terms greater than 10 %).

5.6.4 TAM Definition Using "Modified" Guyan Reduction

The load patch distribution selected for the present sample consists of a set of six (6) or seven (7) unit load patterns per axial (Z) station, which are illustrated below in Fig. 5.4.

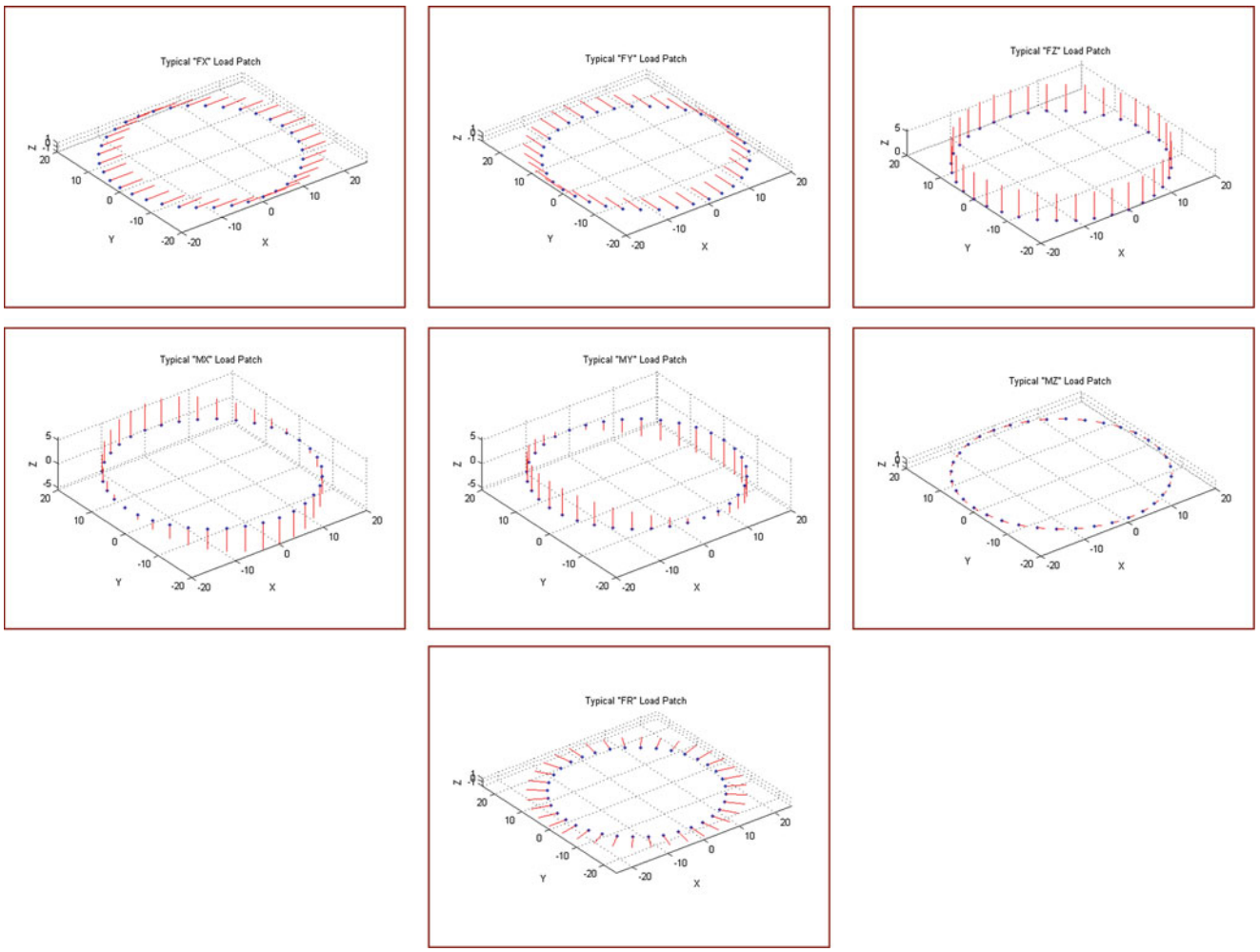

Fig. 5.4 "Modified" Guyan reduction selected load patches

Two separate reduction schemes and TAM mass matrices are evaluated herein, namely:

(1) Six load patches per axial station (excluding the seventh "bulge, FR" patch)
(2) Seven load patches per axial station.

Application of "modified" Guyan reduction (scheme 1), employing the same instrumentation array used for "classical" Guyan reduction results in a TAM mass matrix, produces predicted test mode orthogonality (for the 22 "body" modes) and residual kinetic energy (summed for each mode) as summarized below in Table 5.4.

Table 5.4 Test mode orthogonality and summed residual kinetic energy for "modified" Guyan reduction TAM (scheme 1)

Body Mode	System Mode	Description	Sum(RKE)	Orthogonality Check																				
1	1	Y-Bending	0	100																		-1		2
2	2	X-Bending	0		100																			
3	11	RZ-Torsion	0			100																		
4	14	Y-Bending	0				100																	2
5	15	X-Bending	0					100																
6	24	Z-Axial	0						100											2				2
7	49	Y-Bending	0							100											-1	1		-3
8	50	X-Bending	0								100													
9	63	RZ-Torsion	0									100												
10	76	Y-Bending	0										100											2
11	77	X-Bending	0											100										
12	86	N=0 Domes	1												100									
13	103	N=1	0													100						1		-1
14	104	N=1	0														100							
15	111	N=1	0															100						-1
16	112	N=1	0																100					
17	121	N=0 Skirt	5						2											100				3
18	128	N=1	1							-1											100	1		-5
19	129	N=1	1																			100	0	
20	140	N=1	1	-1						1						1					1		100	3
21	141	N=1	1																					100
22	146	N=0 Shells	40	2			2		2	-3			2			-1		-1		3	-5		3		100

The predicted test mode orthogonality associated with the "modified" Guyan reduction TAM mass matrix is acceptable with respect to U.S. Air Force and NASA standards (off-diagonal terms less than 10 %). This is attributed to the fact that many of the shape functions, $[\Psi_{af}]_m$, accentuate cross-sectional nearly rigid body displacement patterns. The non-negligible summed RKE in the 22nd "body" mode, while 40 %, is not associated with unsatisfactory predicted modal orthogonality. However, study of this mode's deformation, kinetic energy distribution, and RKE distribution provides some indication of regions of the structure requiring further TAM definition, as illustrated below in Fig. 5.5.

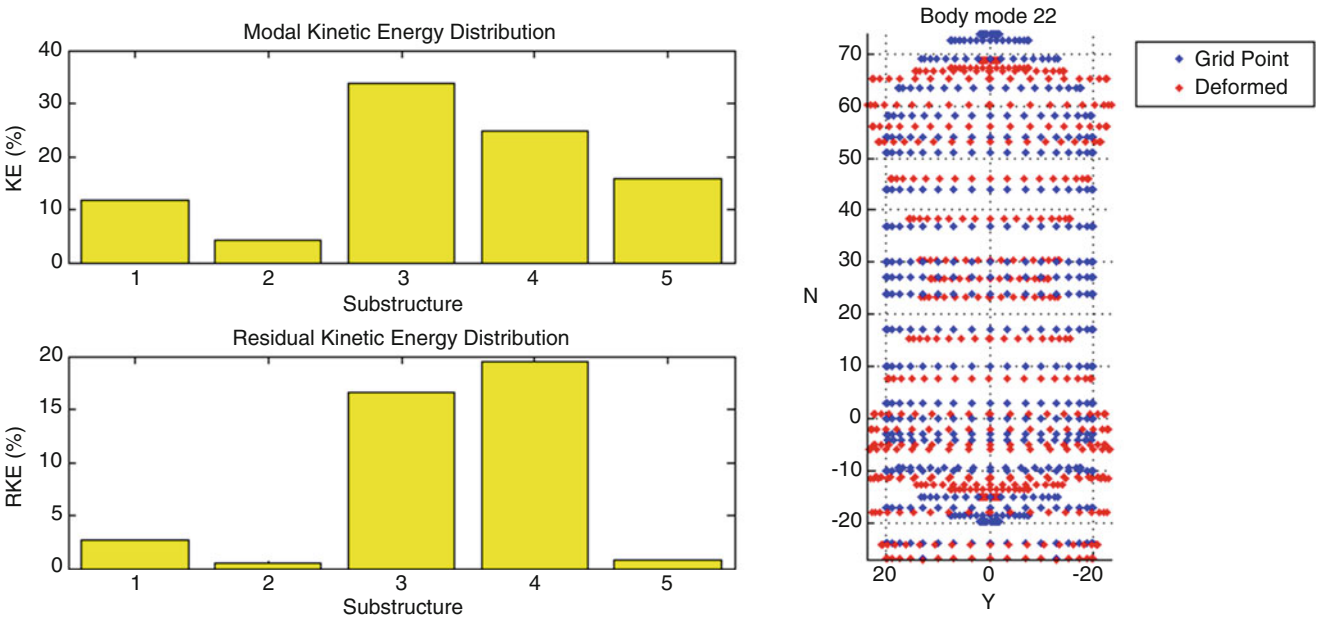

Fig. 5.5 Evaluation of "modified" Guyan reduction adequacy for body mode 22 (scheme 1)

The above results indicate RKE deficiency focusing on the two cylindrical shell regions (substructures 3 and 4), which have significant n = 0 breathing activity that is not represented in the "scheme 1" load patches.

Application of "modified" Guyan reduction (scheme 2), employing the same instrumentation array used for "classical" Guyan reduction results in a TAM mass matrix, produces predicted test mode orthogonality (for the 22 "body" modes) and residual kinetic energy (summed for each mode) as summarized below in Table 5.5.

Table 5.5 Test mode orthogonality and summed residual kinetic energy for "modified" Guyan reduction TAM (scheme 2)

Body Mode	System Mode	Description	Sum(RKE)	Orthogonality Check																						
1	1	Y-Bending	0	100																			-1			
2	2	X-Bending	0		100																					
3	11	RZ-Torsion	0			100																				
4	14	Y-Bending	0				100																			
5	15	X-Bending	0					100																		
6	24	Z-Axial	0						100																	
7	49	Y-Bending	0							100													-1		1	
8	50	X-Bending	0								100															
9	63	RZ-Torsion	0									100														
10	76	Y-Bending	0										100													
11	77	X-Bending	0											100												
12	86	N=0 Domes	0												100											
13	103	N=1	0													100							-1		1	
14	104	N=1	0														100									
15	111	N=1	0															100								
16	112	N=1	0																100							
17	121	N=0 Skirt	0																	100						
18	128	N=1	1							-1						-1					100		1		-1	
19	129	N=1	1																			100				
20	140	N=1	1	-1						1						1					1		100		1	
21	141	N=1	1																					100		
22	146	N=0 Shells	0																		-1		1		100	

Addition of "bulge" load patches in scheme 2 removes the RKE deficiency in body mode 22 as indicated below in Table 5.6.

Table 5.6 Evaluation of "modified" Guyan reduction adequacy for body mode 22 (schemes 1 and 2)

			RKE (%)	
Substructure	Description	KE (%)	Scheme 1	Scheme 2
1	Skirt	11.85	2.69	0.01
2	Lower dome	4.13	0.49	0.00
3	Shell 1	33.88	16.64	0.01
4	Shell 2	24.69	19.53	0.01
5	Upper dome	15.70	0.76	0.00

5.6.5 Further Reflections on "Modified" Guyan Reduction Results

Employment of the particular family of load patches (see Fig. 5.4) yields particularly informative modal vectors described in terms of generalized cross-sectional centerline displacements and "radial" bulge degrees of freedom. Moreover, exploitation of the generalized modal vectors and a corresponding generalized TAM mass matrix produces orthogonality and residual kinetic energy matrices that do not suffer from singularities noted in Sect. 5.5 of this paper. These matters are discussed in Appendix.

5.7 Concluding Remarks

Quantitative understanding of a system's modal characteristics is gained by review of the detailed finite element model's modal kinetic and strain energy distributions, and modal effective mass (in addition to modal frequencies and geometric mode shapes that are commonly referenced). Utilization of these metrics facilitates selection of the significant subset of "target" modes (e.g., "body" modes) to be identified in a modal test, while ignoring or suppressing the many "insignificant" breathing modes that commonly occur in shell-type structures. The modal kinetic and strain energy, and modal effective mass metrics address the NASA criterion [2], which specifically notes that, "The goal of the modal survey test shall be to measure and correlate all significant modes . . . ". It should be noted that the Air Force modal test criterion [1] calling for measurement of all modes in the 0–70 Hz band is often relaxed through negotiation based on system complexities.

Alternatives to "classical" Guyan reduction may improve quality of the analytically derived TAM mass matrix. Specifically, the "modified" Guyan reduction process, employing load patches, produces a TAM mass matrix that satisfies the generally accepted mode orthogonality criterion (less than 10 % off-diagonal coupling) for a selected "instrumentation" DOF array. Other more general reduction strategies [9, 10], possibly the subject of a future paper, may also produce TAM mass matrix improvements that are relatively insensitive to parametric uncertainties.

The concept of residual kinetic energy (RKE), introduced in an earlier paper [4], has been expanded for application to the "modified" Guyan reduction and more general reduction strategies. RKE applied to the branched shell illustrative example in this paper (a) appropriately separates significant "body" and shell breathing mode subsets, and (b) identifies "instrumentation" and TAM mass matrix deficiencies and remedies.

A.1 Appendix: Exploitation of Generalized Modal Data

The modified Guyan reduction transformation relating "free" and "instrumented" DOFs, presented in Eq. (5.20), combines two levels of coordinate transformation, namely,

$$\{u_f\} = \left[\Psi_{fq}\right]\{q\} = \left[\Psi_{fq}\right]\left[\Psi_{qa}\right]\{u_a\} = \left[\Psi_{fa}\right]_m\{u_a\}. \tag{5.28}$$

And it is recalled that the explicit relationship between "instrumented" DOFs and "generalized" DOFs (see Eq. 5.19) is

$$\{q\} = \left[\Psi_{aq}^T\Psi_{aq}\right]^{-1}\left[\Psi_{aq}^T\right]\{u_a\} = \left[\Psi_{qa}\right]\{u_a\}. \tag{5.29}$$

Employing the above transformation, the relationship between "instrumented" and "generalized" DOF structural modes is

$$\left[\Phi_q\right] = \left[\Psi_{qa}\right][\Phi_a]. \tag{5.30}$$

The "generalized" TAM mass matrix (based on Eq. 5.28),

$$\left[M_{qq}\right] = \left[\Psi_{fq}\right]^T[M_{ff}]\left[\Psi_{fq}\right], \tag{5.31}$$

does not have singularities that are present in $[M_{aa}]_m$ (see Eq. 5.21).

Therefore, the orthogonality check matrix, which is mathematically equivalent to the result in Eq. (5.24), is

$$[OR] = \left[\Phi_q\right]^T\left[M_{qq}\right]\left[\Phi_q\right]. \tag{5.32}$$

In order to define modal kinetic energy and RKE relationships in terms of the "generalized" DOFs, the "free" DOF modes, $[\Phi_f]$, must be expressed in terms of "generalized" DOFs. This is accomplished by noting from Eq. (5.28) that,

$$\left[\Phi_f\right] = \left[\Psi_{fq}\right]\left[\Phi_q\right] \tag{5.33}$$

Solution for $[\Phi_q]$ by weighted least squares is accomplished by the following manipulation

$$\left[\Phi_q\right]_f = \left[M_{qq}\right]^{-1}\left[\Psi_{fq}\right]^T[M_{ff}][\Phi_f], \tag{5.34}$$

which is a more accurate representation than Eq. (5.30). The "generalized" residual error matrix is therefore,

$$\left[R_q\right] = \left[\Phi_q\right]_f - \left[\Phi_q\right], \tag{5.35}$$

and the modal kinetic energy and RKE in terms of "generalized" DOF are,

$$\left[KE_q\right] = \left[M_{qq}\Phi_q\right] \otimes \left[\Phi_q\right], \quad \left[RKE_q\right] = \left[M_{qq}R_q\right] \otimes \left[R_q\right] \tag{5.36}$$

The columns of $[KE_q]$ and $[RKE_q]$ are bounded by 1.0 (100 %) due to the fact that $[M_{qq}]$ is not singular.

The generalized DOFs associated with the seven load patches per axial station for the branched shell structure represent the following physically equivalent displacements: Centerline "X", "Y", "Z", "Θ_X", "Θ_Y", "Θ_Z" (Torsion), Radial "Bulge". Tabular displays for six representative branched shell modes, expressed in terms of modal kinetic energy components are presented below in Tables 5.7, 5.8 and 5.9.

Table 5.7 Branched shell kinetic energies for modes 1 (Y) and 2 (X)

Location				Mode 1 (Lateral Y)					Mode 2 (Lateral X)				
Component	Station	R	Z	Lateral X	Lateral Y	Axial Z	Torsion	Bulge	Lateral X	Lateral Y	Axial Z	Torsion	Bulge
Skirt	1	20.00	0.00		0.68				0.68				
	2	20.00	-3.00		0.49				0.49				
	3	20.00	-10.00		0.34				0.34				
	4	20.00	-17.00		0.12				0.12				
	5	20.00	-24.00		0.01				0.01				
	6	20.00	-27.00		0.00				0.00				
Lower Dome	7	19.60	-4.00		0.46				0.46				
	8	17.60	-9.50		0.38				0.38				
	9	13.20	-15.00		0.19				0.19				
	10	7.60	-18.50		0.06				0.06				
	11	2.00	-19.90		0.01				0.01				
Shell 1	12	20.00	3.00		0.92				0.92				
	13	20.00	10.00		2.06				2.06				
	14	20.00	17.00		3.17				3.17				
	15	20.00	24.00		3.18				3.18				
	16	20.00	27.00		2.30				2.30				
Shell 2	17	20.00	30.00		4.42				4.42				
	18	20.00	37.00		8.04				8.04				
	19	20.00	44.00		10.34				10.34				
	20	20.00	51.00		9.07				9.07				
	21	20.00	54.00		7.10				7.10				
Upper Dome	22	19.60	58.00		10.72				10.73				
	23	17.60	63.50		14.10				14.10				
	24	13.20	69.00		12.73				12.74				
	25	7.60	72.50		7.30				7.30				
	26	2.00	73.90		1.81				1.80				
			Sum KE	0.00	100.00	0.00	0.00	0.00	100.00	0.00	0.00	0.00	0.00

Table 5.8 Branched shell kinetic energies for modes 11 (Torsion) and 24 (Z)

Location				Mode 11 (Torsion)					Mode 24 (Axial Z)				
Component	Station	R	Z	Lateral X	Lateral Y	Axial Z	Torsion	Bulge	Lateral X	Lateral Y	Axial Z	Torsion	Bulge
Skirt	1	20.00	0.00				2.09				2.28		
	2	20.00	-3.00				1.60				1.40		
	3	20.00	-10.00				1.21				1.03		
	4	20.00	-17.00				0.43				0.27		
	5	20.00	-24.00				0.04				0.02		
	6	20.00	-27.00				0.00				0.00		
Lower Dome	7	19.60	-4.00				1.92				1.02		
	8	17.60	-9.50				1.83				1.89		
	9	13.20	-15.00				0.88				1.80		
	10	7.60	-18.50				0.17				1.00		
	11	2.00	-19.90				0.01				0.23		
Shell 1	12	20.00	3.00				2.58				1.89		
	13	20.00	10.00				4.93				3.86		
	14	20.00	17.00				6.46				5.19		
	15	20.00	24.00				5.63				4.58		
	16	20.00	27.00				3.72				2.96		
Shell 2	17	20.00	30.00				6.75				5.45		
	18	20.00	37.00				10.69				8.75		
	19	20.00	44.00				11.87				9.80		
	20	20.00	51.00				9.10				7.66		
	21	20.00	54.00				6.53				5.02		
Upper Dome	22	19.60	58.00				8.63				7.84		
	23	17.60	63.50				8.20				10.38		
	24	13.20	69.00				3.94				9.31		
	25	7.60	72.50				0.77				5.14		
	26	2.00	73.90				0.03				1.19		
			Sum KE	0.00	0.00	0.00	100.00	0.00	0.00	0.00	99.96	0.00	0.00

Table 5.9 Branched shell kinetic energies for modes 86 (bulge) and 146 (bulge)

Location				Mode 86 (Axial+Bulge)					Mode 146 (Axial+Bulge)				
Component	Station	R	Z	Lateral X	Lateral Y	Axial Z	Torsion	Bulge	Lateral X	Lateral Y	Axial Z	Torsion	Bulge
Skirt	1	20.00	0.00			0.84		0.35			3.81		1.68
	2	20.00	-3.00			4.17		0.01			1.21		1.08
	3	20.00	-10.00			3.02		0.20			0.88		2.11
	4	20.00	-17.00			0.64		0.32			-0.01		1.51
	5	20.00	-24.00			-0.10		0.06			-0.10		0.15
	6	20.00	-27.00			0.00		0.00			0.00		0.00
Lower Dome	7	19.60	-4.00			2.09		0.53			0.90		1.38
	8	17.60	-9.50			10.23		0.26			0.40		1.15
	9	13.20	-15.00			20.58		0.02			2.26		0.16
	10	7.60	-18.50			13.87		0.00			4.50		0.00
	11	2.00	-19.90			3.15		0.00			1.02		0.00
Shell 1	12	20.00	3.00			2.85		0.18			2.01		0.81
	13	20.00	10.00			2.71		0.11			4.18		0.00
	14	20.00	17.00			1.81		0.14			2.74		5.55
	15	20.00	24.00			0.61		0.15			0.33		9.77
	16	20.00	27.00			0.17		0.15			0.00		9.74
Shell 2	17	20.00	30.00			0.12		0.19			0.16		9.33
	18	20.00	37.00			0.01		0.24			2.04		5.94
	19	20.00	44.00			0.30		0.24			3.61		0.31
	20	20.00	51.00			0.85		0.32			2.22		0.35
	21	20.00	54.00			-0.32		0.44			1.38		0.90
Upper Dome	22	19.60	58.00			1.73		0.41			1.91		1.56
	23	17.60	63.50			6.06		0.16			0.61		1.35
	24	13.20	69.00			11.13		0.01			2.56		0.18
	25	7.60	72.50			7.36		0.00			5.19		0.00
	26	2.00	73.90			1.66		0.00			1.18		0.00
			Sum KE	0.00	0.00	95.53	0.00	4.47	0.00	0.00	44.98	0.00	55.02

References

1. Independent structural loads analysis, Air Force Space Command, SMC-S-004, 2008
2. Load analyses of spacecraft and payloads, NASA-STD-5002, 1996
3. Ritz, W.: Über eine neue Methode zur Lösung gewisser Variationsprobleme der mathematischen Physik (1908)
4. Guyan, R.: Reduction of stiffness and mass matrices. AIAA J. **3**, 380 (1965)
5. Coppolino, R.: Automated response DOF selection for mapping of experimental normal Modes, IMAC XVI, 1998
6. Timoshenko, S.: History of Strength of Materials. Dover Publications, New York (1983)
7. Leissa A.: Vibration of shells, NASA SP-288, 1973
8. Coppolino, R.: DOF reduction strategy for large order finite element models, IMAC XXIX, 2011
9. O'Callahan, J., Avitabile, P., Reimer, R.: System equivalent reduction expansion process, IMAC VII, 1989
10. Coppolino, R.: FEM sensitivity vector basis for measured mode expansion, IMAC XXXI, 2013
11. Craig, R., Bampton, M.: Coupling of substructures for dynamic analysis. AIAA J. **6**, 1313–1319 (1968)

Chapter 6
Experimental Modal Substructuring with Nonlinear Modal Iwan Models to Capture Nonlinear Subcomponent Damping

Matthew S. Allen, Daniel Roettgen, Daniel Kammer, and Randy Mayes

Abstract This work proposes a means whereby weak nonlinearity in a substructure, as typically arises due to friction in bolted interfaces, can be captured experimentally on a mode-by-mode basis and then used to predict the nonlinear response of an assembly. The method relies on the fact that the modes of a weakly nonlinear structure tend to remain uncoupled so long as their natural frequencies are distinct and higher harmonics generated by the nonlinearity do not produce significant response in other modes. Recent experiments on industrial hardware with bolted joints has shown that this type of model can be quite effective, and that a single degree-of-freedom (DOF) system with an Iwan joint, which is known as a modal Iwan model, effectively captures the way in which the stiffness and damping depend on amplitude. Once the modal Iwan models have been identified for each mode of the subcomponent(s) of interest, they can be assembled using standard techniques and used with a numerical integration routine to compute the nonlinear transient response of the assembled structure. The proposed methods are demonstrated by coupling a modal model of a 3DOF system with three discrete Iwan joints to a linear model for a 2DOF system.

Keywords Reduced order modeling • Friction • Interface • Nonlinear modes • Complexification and averaging

6.1 Introduction

Experimental-analytical substructuring allows one to couple an experimentally derived model for a structure that is difficult to model, with a finite element model for the rest of the assembly in order to predict the system's response. While there are countless compelling industrial applications, many of the systems that are most difficult to model, and hence where experimental-analytical substructuring would be most beneficial, contain many interfaces with bolted joints. Interfaces in built up structures are responsible for much of the damping in the assembly, and are the most common source of nonlinearity. This work presents an extension of modal substructuring for this class of structure.

Recent works have shown that bolted interfaces can cause the damping in a system to increase by a factor of two or more (see, e.g. [1–3]), while the effective natural frequency tends to change relatively little. Furthermore, under the conditions outlined in [4] (simplistically that the joint forces and their harmonics are distinct from each modal frequency), the modes of the structure tend to remain uncoupled, so that the structure can be modeled accurately using a collection of uncoupled, weakly-nonlinear oscillators [5, 6]. This was thoroughly confirmed in [1] for an assembly of automotive exhaust components, by exciting the structure at multiple locations and various force levels (in the micro-slip regime). A second investigation on a cylindrical structure with bolted joints and nonlinear contact between foam and an internal structure also highlighted the usefulness of this approach [7].

In this work we propose to use this class of model (e.g. uncoupled SDOF oscillators) to represent a subcomponent and then to assemble that subcomponent to the rest of the structure of interest. Specifically, the set of nonlinear oscillators are assembled using standard finite element assembly techniques. The assembled equation of motion and its Jacobian are then used in a Newmark integration routine to predict the transient response of the assembled structure. The methods are tested through simulations on a simple spring mass system. While the method is applicable for a wide range of nonlinear SDOF oscillator models, this work uses a modal Iwan model for each subcomponent. This type of model accurately captures the

M.S. Allen • D. Roettgen (✉) • D. Kammer
Department of Engineering Physics, University of Wisconsin – Madison, Madison, WI 53706, USA
e-mail: msallen@engr.wisc.edu; droettgen@wisc.edu; kammer@engr.wisc.edu

R. Mayes
Sandia National Laboratories, Albuquerque, NM, USA
e-mail: rlmayes@sandia.gov

© The Society for Experimental Mechanics, Inc. 2016

M. Allen et al. (eds.), *Dynamics of Coupled Structures, Volume 4*, Conference Proceedings of the Society for Experimental Mechanics Series, DOI 10.1007/978-3-319-29763-7_6

power-law dependence of damping on amplitude that is frequently observed in experiments [1, 5, 8, 9]. Other SDOF models, some of which may be simpler or less expensive to use, were evaluated in a recent study by the authors [7].

The paper is organized as follows. Section 6.2 outlines the approach used. In Sect. 6.3 the proposed techniques are validated by deriving modal Iwan models for the three modes of a 3DOF system, which is then assembled to a linear 2DOF system. The conclusions are then presented in Sect. 6.4.

6.2 Theoretical Development

In the most general case, the equation of motion for substructure A can be written as follows,

$$\mathbf{M}^A\ddot{\mathbf{x}}^A + \mathbf{C}^A\dot{\mathbf{x}}^A + \mathbf{K}^A\mathbf{x}^A + \sum_{k=1}^{N_J} \mathbf{f}_{J,k}^A f_{J,k}^A \left(\mathbf{x}^A, \phi_{k,1}^A \ldots \phi_{k,N_j}^A\right) = \mathbf{f}^A(t) \tag{6.1}$$

where $\mathbf{M}^A$, $\mathbf{C}^A$ and $\mathbf{K}^A$ are the $N \times N$ linear mass, damping and stiffness matrices and the kth scalar joint force, $f_{J,k}^A\left(\mathbf{x}^A, \phi_{k,1}^A \ldots \phi_{k,N_j}^A\right)$ depends on the displacement vector $\mathbf{x}^A$ and on its internal slider states $\phi_{k,1}^A \ldots \phi_{k,N_j}^A$. The constant vector $\mathbf{f}_{J,k}^A$ maps each scalar joint force $f_{J,k}^A$ to the points to which the joint is attached. For example, in the example that will be discussed later, shown in Fig. 6.1 the first Iwan joint is between DOF 1 and ground so $\mathbf{f}_{J,1}^A = \begin{bmatrix} 1 & 0 & 0 \end{bmatrix}^{\mathrm{T}}$ and the third Iwan joint is connected between DOF 2 and 3, so $\mathbf{f}_{J,3}^A = \begin{bmatrix} 0 & 1 & -1 \end{bmatrix}^{\mathrm{T}}$. Similar equations could be written for substructures B, C, etc ....

When each mode of the substructure is represented as a modal Iwan model, the matrices $\mathbf{M}$, $\mathbf{C}$ and $\mathbf{K}$ would be diagonal and the kth joint force would depend on only one modal displacement.

We shall employ a primal formulation [10] to couple the substructures. Without loss of generality, consider the case where substructure A will be joined to substructure B. The substructures can be coupled by writing constraint equations of the following form,

$$\mathbf{B}\begin{bmatrix} \mathbf{x}^A \\ \mathbf{x}^B \end{bmatrix} = 0 \tag{6.2}$$

and then eliminating the redundant degrees of freedom using

$$\begin{bmatrix} \mathbf{x}^A \\ \mathbf{x}^B \end{bmatrix} = \mathbf{L}\mathbf{q} \tag{6.3}$$

$$\mathbf{L} = null\,(\mathbf{B}) \tag{6.4}$$

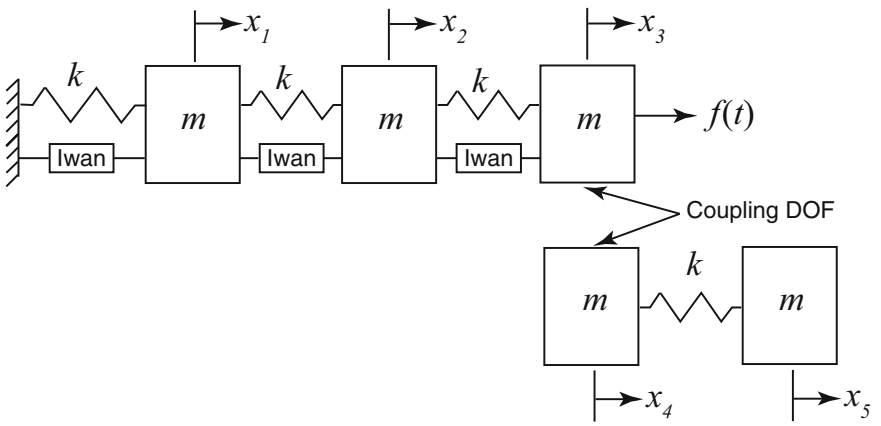

Fig. 6.1 Schematic of the discrete system used to validate the proposed substructuring procedure. (*top-left*) Substructure A, (*bottom-right*) Substructure B. Mass and stiffness proportional damping was added to simulate material damping (dashpots not shown)

to obtain a set of independent (or unconstrained [11]) coordinates, $\mathbf{q}$. The equations of motion for the coupled system then become the following in terms of the coordinates $\mathbf{q}$,

$$\widehat{\mathbf{M}}\ddot{\mathbf{q}} + \widehat{\mathbf{C}}\dot{\mathbf{q}} + \widehat{\mathbf{K}}\mathbf{q} + \mathbf{L}^{\mathrm{T}} \begin{bmatrix} \sum_{k=1}^{N_J} \mathbf{f}_{J,k}^{A} f_{J,k}^{A}\left(\mathbf{x}^{A}, \phi_{k,1}^{A} \ldots \phi_{k,N_j}^{A}\right) \\ \sum_{k=1}^{N_J} \mathbf{f}_{J,k}^{B} f_{J,k}^{B}\left(\mathbf{x}^{B}, \phi_{k,1}^{B} \ldots \phi_{k,N_j}^{B}\right) \end{bmatrix} = \mathbf{L}^{\mathrm{T}} \begin{bmatrix} \mathbf{f}^{A}(t) \\ \mathbf{f}^{B}(t) \end{bmatrix} \tag{6.5}$$

where

$$\widehat{\mathbf{M}} = \mathbf{L}^{\mathrm{T}} \begin{bmatrix} \mathbf{M}^{A} & 0 \\ 0 & \mathbf{M}^{B} \end{bmatrix} \mathbf{L} \tag{6.6}$$

and similarly for $\widehat{\mathbf{C}}$ and $\widehat{\mathbf{K}}$. Further details can be found in [10] or ([11], Chapter 9).

In order to simulate the response of the assembly, the unconditionally stable Newmark algorithm [12] is used (e.g. with $\beta_{\mathrm{N}} = 0.25$ and $\gamma = 0.5$). This procedure was first developed by Simmermacher as reported in [8]. A Newton iteration loop is used to adjust the displacement of the joint (and the internal slider states) so that the joint force is in dynamic equilibrium at each time step. Specifically, if the displacement at the jth time step is denoted $\mathbf{q}_j$, then the residual is defined as.

$$\mathbf{r}_j = \widehat{\mathbf{M}}\ddot{\mathbf{q}}_j + \widehat{\mathbf{C}}\dot{\mathbf{q}}_j + \widehat{\mathbf{K}}\mathbf{q}_j + \mathbf{L}^{\mathrm{T}} \begin{bmatrix} \sum_{k=1}^{N_J} \mathbf{f}_{J,k}^{A} f_{J,k}^{A}\left(\mathbf{L}\mathbf{q}_j, \phi_{k,1}^{A} \ldots \phi_{k,N_j}^{A}\right) \\ \sum_{k=1}^{N_J} \mathbf{f}_{J,k}^{B} f_{J,k}^{B}\left(\mathbf{L}\mathbf{q}_j, \phi_{k,1}^{B} \ldots \phi_{k,N_j}^{B}\right) \end{bmatrix} - \mathbf{L}^{\mathrm{T}} \begin{bmatrix} \mathbf{f}^{A}(t) \\ \mathbf{f}^{B}(t) \end{bmatrix} \tag{6.7}$$

Then, the Jacobian is

$$\mathbf{J}_j = \widehat{\mathbf{M}} + \gamma\Delta t\widehat{\mathbf{C}} + \beta(\Delta t)^2 \left(\widehat{\mathbf{K}} + \mathbf{L}^{\mathrm{T}} \begin{bmatrix} \sum_{k=1}^{N_J} \mathbf{f}_{J,k}^{A} K_{J,k}^{A} \\ \sum_{k=1}^{N_J} \mathbf{f}_{J,k}^{B} K_{J,k}^{B} \end{bmatrix} \begin{bmatrix} \sum_{k=1}^{N_J} \mathbf{f}_{J,k}^{A} K_{J,k}^{A} \\ \sum_{k=1}^{N_J} \mathbf{f}_{J,k}^{B} K_{J,k}^{B} \end{bmatrix}^{\mathrm{T}} \mathbf{L} \right) \tag{6.8}$$

where $K_{J,k}^{A}$ is the instantaneous stiffness of the kth Iwan joint and depends on the corresponding slider states, $\phi_{k,1}^{A} \ldots \phi_{k,N_j}^{A}$. The estimate of the acceleration, displacement and velocity at this time step are updated as follows. For the first iteration the same procedure is used, only with $\mathbf{r}_j = 0$.

$$\begin{aligned} \ddot{\mathbf{q}}_{j,new} &= \ddot{\mathbf{q}}_j - \mathbf{J}_j\mathbf{r}_j \\ \dot{\mathbf{q}}_{j,new} &= \dot{\mathbf{q}}_j + \Delta t\,(1-\gamma)\,\ddot{\mathbf{q}}_{j-1} + \gamma\ddot{\mathbf{q}}_{j,new} \\ \mathbf{q}_{j,new} &= \mathbf{q}_j + \Delta t\dot{\mathbf{q}}_{j-1} + \tfrac{1}{2}(\Delta t)^2\,(1-2\beta_N)\,\ddot{\mathbf{q}}_{j-1} + 2\beta_N\ddot{\mathbf{q}}_{j,new} \end{aligned} \tag{6.9}$$

Note that $\mathbf{L}^{\mathrm{T}} \begin{bmatrix} \mathbf{f}_{J,k}^{A} \\ \mathbf{0} \end{bmatrix}$ and $\mathbf{L}^{\mathrm{T}} \begin{bmatrix} \mathbf{f}_{J,k}^{A}\left(\mathbf{f}_{J,k}^{A}\right)^{\mathrm{T}} & \mathbf{0} \\ \mathbf{0} & \mathbf{0} \end{bmatrix} \mathbf{L}$, and similarly for substructure B, are simply constant matrices that map each joint force onto the appropriate degrees of freedom in the assembled system. These matrices, and the assembled system matrices $\widehat{\mathbf{M}}$, $\widehat{\mathbf{C}}$ and $\widehat{\mathbf{K}}$ are calculated in advance and only the joint forces and stiffnesses need to be updated in each iteration.

6.2.1 Iwan Joint

The preceding discussion is valid for a variety of joint models. In this work the Iwan model is used, so each joint can be characterized by four parameters $\mathrm{F_s}$, $\mathrm{K_T}$, χ and β [13]. The first two parameters describe, respectively, the force at which

the joint slips completely (macro-slip) and the stiffness of the joint when all sliders are stuck. The model exhibits energy dissipation per cycle, D, that depends on magnitude of the displacement $|x|$ in a power-law fashion as

$$D = R|x|^{3+\chi} \tag{6.10}$$

where R is a constant. By analogy with a linear system, the effective damping ratio ζ of an SDOF system with mass m and with an Iwan joint in parallel with a spring of stiffness K_0 is the following,

$$\zeta = D/\left(m2\pi\omega_d\omega_n|x|^2\right) \tag{6.11}$$

where ${\omega_n}^2 = (K_0 + K_T)/m$ and $\omega_d = \omega_n\sqrt{1-\zeta^2}$. These relationships together with a Hilbert transform were used to fit an Iwan model to simulated measurements of each substructure. For further details, see [1, 5].

6.3 Simulated Application

The proposed approach was applied to the system depicted in Fig. 6.1.

Substructure A consists of three masses connected by linear springs of stiffness k in parallel with Iwan elements with the parameters shown in Table 6.1. The other system parameters are $m = 10$ kg, $k = 5$ N/m, $\boldsymbol{C}^A = 0.002(\mathbf{M}^A + \mathbf{K}^A)$, $\boldsymbol{C}^B = 0.002\mathbf{K}^B$. The goal is to simulate a test on Substructure A to determine modal Iwan models for each mode of that substructure, and then to utilize modal substructuring to predict the response of the assembly when the masses are joined as indicated with $x_3 = x_4$.

6.3.1 Estimating Modal Iwan Models for Substructure A

The linear mode shapes $[\varphi_1\ \varphi_2\ \varphi_3]$ of Substructure A were assumed to be known (e.g. having been measured from a low-amplitude linear test). Note that in such a test each Iwan joint acts as linear spring with stiffness K_T. Then, to identify a nonlinear model for Substructure A, an experiment was simulated in which a half-sine impulse with a 0.1 s long period and amplitude of 100 N was applied to mass 3. The Newmark routine was used to determine the transient response and then the response of each mode was estimated using $\mathbf{q} = \boldsymbol{\varphi}^{-1}\mathbf{x}$. Note that the mode matrix used in this calculation corresponds to the linear, low amplitude modes that include the stiffness of the joints. The FFT $Q_r(\omega) = \mathrm{FFT}(q_r(\mathrm{t}))$ of each modal response is shown in Fig. 6.2. A weak nonlinearity, as is typical of a structure with bolted joints, is visible near each peak.

The simulated measurements were then post processed using the procedure outlined in [1] to identify modal Iwan parameters for each mode. Briefly, each mode's response was band-pass filtered and a smoothed Hilbert transform was used to estimate the instantaneous phase and amplitude as a function of time. The derivative of the phase gives the damped natural frequency, $\omega_\mathrm{d} \approx \omega_\mathrm{n}$, as a function of time, and the derivative of the amplitude gives $\zeta(t)\omega_\mathrm{n}(t)$, from which the damping can be determined. Then the frequency and damping were plotted versus amplitude to determine the modal Iwan parameters. To assure that the power-law behavior was accurately captured, the low-level material damping ζ_0 was subtracted from the estimated damping by visually inspecting the damping versus amplitude curve. Then, a line of the following form

$$\zeta\left(|Q_r|\right) = R|Q_r|^{\chi+1} \tag{6.12}$$

where R and χ are constants, was fit to the log damping versus log amplitude using least squares. Note that macro-slip was not observed in any of these simulations (and must be avoided for the modal Iwan model to retain its validity). Hence, the joint stiffness cannot be measured and so it was simply assumed to be such that the frequency of each mode shifts by 0.05 Hz

Table 6.1 Parameters of Iwan Joints in Substructure A

Iwan joint	F_S	K_T	χ	β
x_1—ground	10 N	5 N/m	−0.5	0.1
x_1—x_2	1 N	4 N/m	−0.2	0.01
x_2—x_3	100 N	3 N/m	−0.8	1

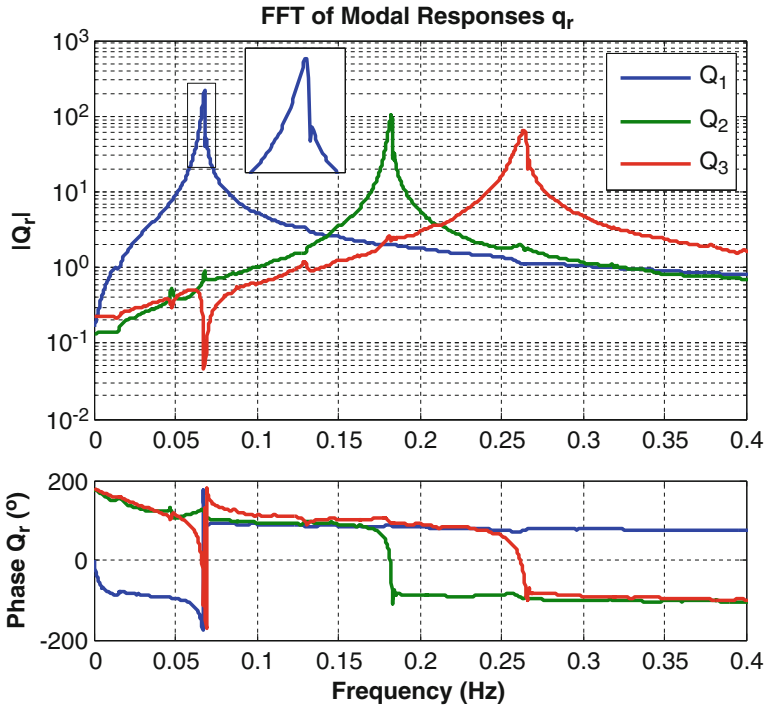

Fig. 6.2 Fast Fourier transform of the modal response of substructure A

Table 6.2 Parameters of modal Iwan models of substructure *A*, estimated from simulated measurements

Modal Iwan models (substructure *A*)	(F_S)	(K_T)	χ	β	f_{n0}	ζ_0
Mode 1	0.886	0.171	−0.023	0.0519	0.0683	0.0032
Mode 2	17.7	0.629	−0.641	0.132	0.184	0.00161
Mode 3	0.508	0.959	−0.564	0.000833	0.268	0.00172

The parameters in parenthesis are not fully relevant since the modal Iwan model is only valid if the response is low enough to avoid macro-slip

in macro-slip. This and the linear natural frequency were then used to find K_T, and then these values were used to solve for a value of F_S and β such that the power law strength, *R*, in the Iwan model was equal to that obtained from the curve fit. In essence, the model used is equivalent to a Palmov model [14], since macro-slip is never activated. In all cases the modal Iwan model was found to fit the measured modal response very well, as illustrated for Mode 1 in Fig. 6.3. The modal Iwan parameters obtained for each mode are shown in Table 6.2.

The modal Iwan model is a SDOF model that could be integrated in response to an applied load (mapped onto the mode of interest) to compute the transient response. For example, the 100 N half-sine pulse used to derive the parameters for Mode 1 was applied to its modal Iwan model and the transient response was computed using the Newmark integrator. The transient response thus computed is compared to the "measured" modal response $q_1(t)$ in Fig. 6.4. While the computed and "measured" responses do eventually go out of phase due to small frequency errors, the simulation captures the amplitude and frequency of the "measured" response very well over the entire range of response amplitude. Thus, we can proceed to use this modal Iwan model with confidence.

The same procedure was repeated for Modes 2 and 3 and the resulting modal Iwan parameters are shown in Table 6.2. For reference, the true natural frequencies and damping ratios of the linearized system are $f_{n0,true} = [0.0686, 0.185, 0.269]$ Hz and $\zeta_{0,true} = [0.00255, 0.001532, 0.001548]$. The identification procedure has estimated the frequencies quite accurately, but there are errors of up to 25 % in some of the damping ratios. While these errors could have been reduced by integrating longer time histories and using a finer time step to improve the accuracy of the Newmark integrator, this level of error is probably to be expected in a real experiment.

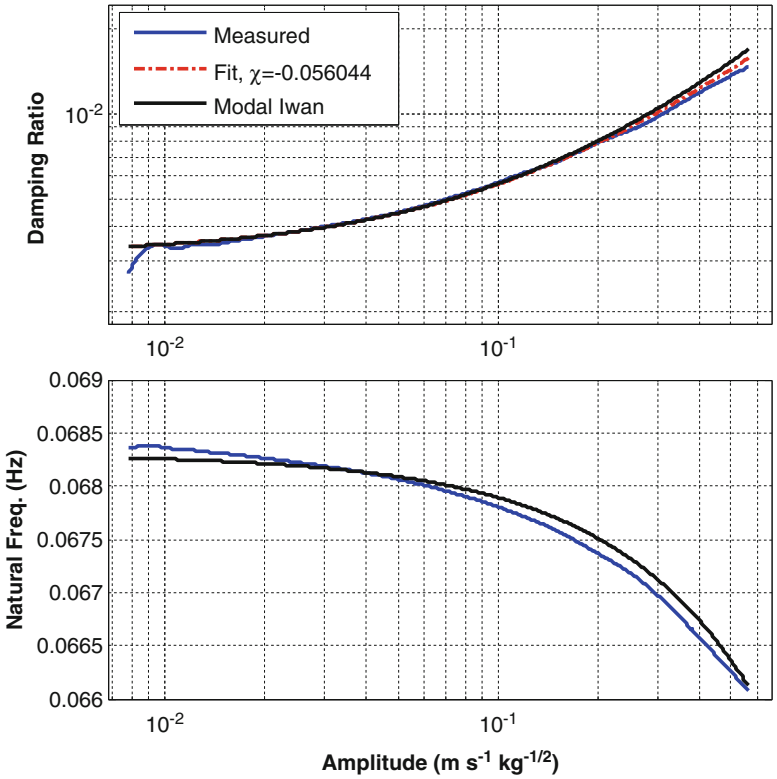

Fig. 6.3 (*blue*) Damping ratio and natural frequency estimated using the Hilbert transform, and (*black*) those of a modal Iwan model fit to the measurements. (*red dash-dot*) Curve fit $\zeta\left(|Q_r|\right) = R|Q_r|^{\chi+1}$ to the damping ratio vs. amplitude, which was used to estimate the modal Iwan parameters

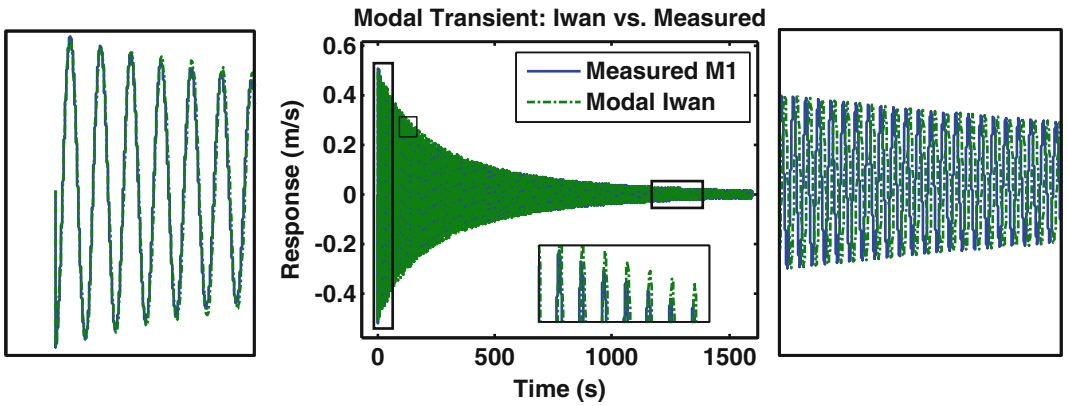

Fig. 6.4 (*blue*) True transient response of Mode 1, $q_1(t)$, due to the half-sine impulse $\mathbf{f}(t)$. (*green dash-dot*) Estimated modal response $\hat{q}_1(t)$ computed using the modal Iwan model and the modal force ${\varphi_1}^{\mathrm{T}}\mathbf{f}(t)$

6.3.2 Substructuring Predictions

The substructures were assembled and the low-amplitude, linearized modal properties were calculated by solving an eigenvalue problem with the assembled mass and stiffness matrices including the linearized joint stiffnesses. The damping ratios were then calculated using the light damping approximation [11] (preserving the classical real modes) and are compared with the true values in Table 6.3. Because these modal properties were computed with the joints linearized, they include only the linear viscous damping that was used to represent the material damping and thus there is no effect from friction in the joints. The results show that the frequencies were accurately estimated, but the damping ratios show errors that are of a similar level as the errors in the estimates of the modal damping ratios of Substructure *A*.

Table 6.3 Linear natural frequencies and damping ratios predicted by substructuring

Mode	True Freq. f_0 (Hz)	Estimated Freq. f_0 (Hz)	% Error	True ζ_0	Estimated ζ_0	% Error
1	0.04502	0.044842	**-0.40**	0.00156	0.001948	**24.92**
2	0.1287	0.12852	**-0.14**	0.001185	0.001307	**10.31**
3	0.17712	0.17629	**-0.47**	0.001402	0.001465	**4.49**
4	0.26524	0.26423	**-0.38**	0.001524	0.00171	**12.19**

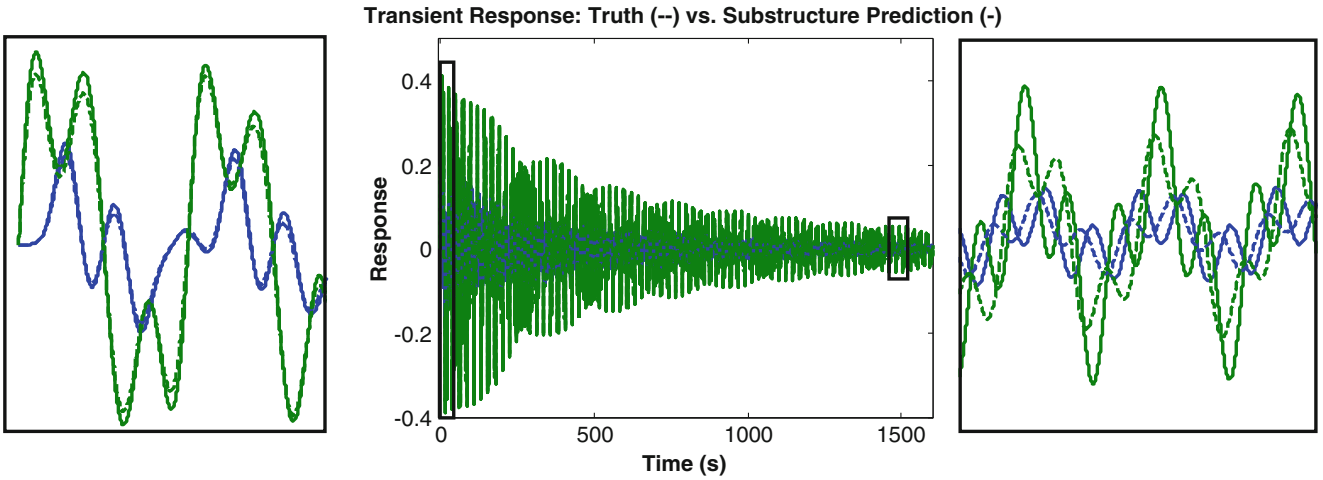

Fig. 6.5 Transient response of the 4DOF assembly to a 100 N impulse. (*solid lines*) True response, (*dashed lines*) Substructuring prediction, using the modal Iwan model for Substructure A, (*blue*) $x_1(t)$, (*green*) $x_5(t)$. The panes on the *left* and *right* show a magnified view near the beginning and end of the response

The response of the assembly to a 100 N input was then computed, and the responses $x_1(t)$ and $x_5(t)$ are shown in Fig. 6.5. The substructuring predictions agree very well with the true transient response, both in frequency and damping. Perhaps further insight can be gained by considering the FFT of the response, projected onto each linearized mode of the assembly, as shown in Fig. 6.6. This shows that the substructuring predictions contain the correct frequency content for each mode, including small distortions which cause the modal responses to show slight coupling. (The modal responses shown were estimated my multiplying the responses with the inverse of the linear, low-amplitude mode shape matrix.)

Most previous research, and industry practice is based on a linear approximation. Hence, it is also informative to consider whether the predictions shown above improve upon a linear approximation. An example of such a comparison is shown in Fig. 6.7, for an impulsive input with a 500 N amplitude. The linear approximation greatly overestimates the amplitude of the vibration, producing a response whose RMS is a factor of two larger (+99 % error) than the true RMS response. Of course, the level of error incurred by using a linear model depends on the strength of the forcing. For the 100 N impulsive input mentioned previously the linear model is in error by only 38 %. At higher load levels the errors would be larger.

6.4 Conclusions

This work has proposed to model a nonlinear substructure with strong damping nonlinearities (and weak stiffness nonlinearity) due to friction at bolted interfaces using a modal approach. The linear modes are assumed to be preserved and to diagonalize the system, so that each mode's response depends only on its displacement, velocity, and on the slider states used to capture its nonlinearity. These nonlinear modal models can then be assembled using standard techniques and the equations of motion of the assembly can then be integrated using the Newmark algorithm or some other suitable integrator.

The methods were demonstrated by estimating a modal Iwan model for each mode of a 3DOF system from simulated transient response measurements due to an impulsive load. Then these modal Iwan models were used to create a nonlinear

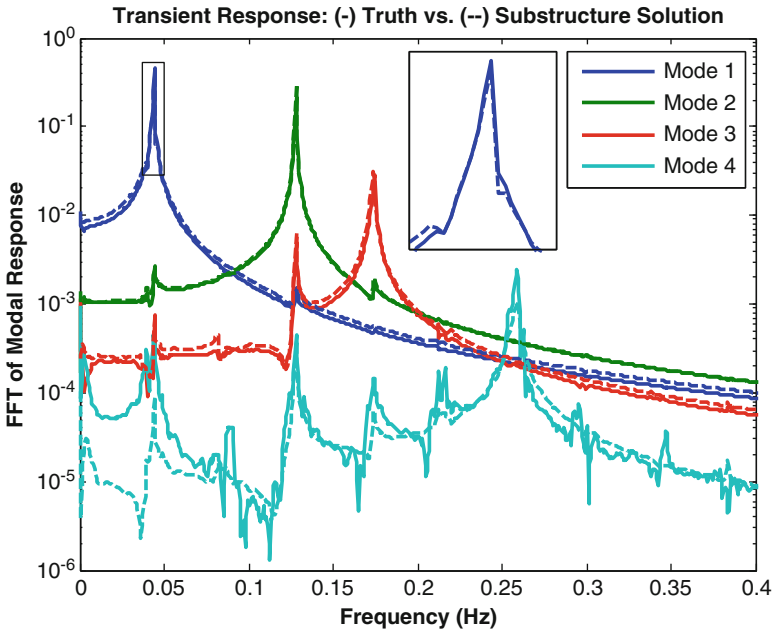

Fig. 6.6 FFT of the transient response of the 4DOF assembly to a 100 N impulse. (*solid lines*) True response of each mode, estimated from the true response using $\mathbf{q} = {\boldsymbol{\varphi}_0}^{-1}\mathbf{x}$ with the linear (low amplitude) modes, (*dashed lines*) Substructuring prediction, using the modal Iwan model for Substructure A

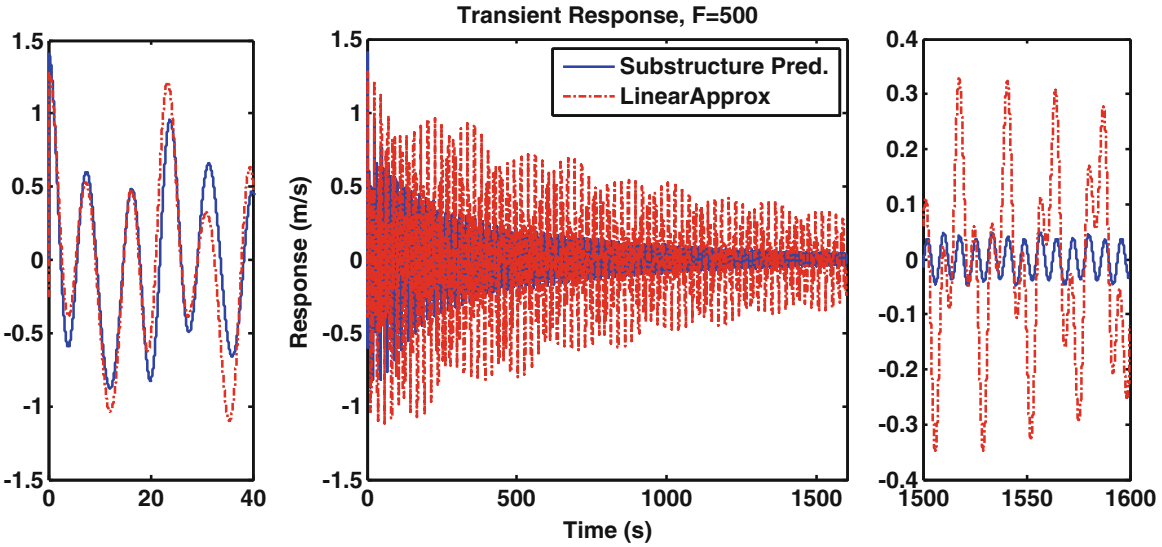

Fig. 6.7 Transient response, $x_5(t)$, of the 4DOF assembly to a 500 N impulse. (*solid blue*) Nonlinear substructuring prediction, (*dashed red*) Response predicted by linear substructuring

model for the substructure that was then assembled to a linear 2DOF system. The proposed approach was then used to integrate the assembled equations subject to various impulsive loadings, producing estimates of the response that were found to be quite accurate. The accuracy seemed to be primarily limited by the accuracy with which the modal Iwan model could be fit to the simulated measurements. Of course, if the forcing amplitude became so large that one of the joints exhibited significant macro-slip then the modal approximation breaks down and errors were observed (although, for brevity, no such cases were reported here).

Acknowledgements This work was partially supported by Sandia National Laboratories. Sandia is a multi-program laboratory operated under Sandia Corporation, a Lockheed Martin Company, for the United States Department of Energy under Contract DE-AC04-94-AL85000.

References

1. Roettgen, D.R., Allen M.S.: Nonlinear characterization of a bolted, industrial structure using a modal framework. Mech. Syst. Signal Process (2015)
2. Bograd, S., Reuss, P., Schmidt, A., Gaul, L., Mayer, M.: Modeling the dynamics of mechanical joints. Mech. Syst. Signal Process. **25**, 2801–2826 (2011)
3. Schwingshackl, C.W., Maio, D.D., Sever, I., Green, J.S.: Modeling and validation of the nonlinear dynamic behavior of bolted flange joints. J Eng Gas Turbines Power **135**, 122504 (2013)
4. Eriten, M., Kurt, M., Luo, G., Michael McFarland, D., Bergman, L.A., Vakakis, A.F.: Nonlinear system identification of frictional effects in a beam with a bolted joint connection. Mech. Syst. Signal Process. **39**, 245–264 (2013)
5. Deaner, B., Allen, M.S., Starr, M.J., Segalman, D.J., Sumali, H.: Application of viscous and Iwan modal damping models to experimental measurements from bolted structures. ASME J. Vib. Acoust. **137**, 12 (2015)
6. Segalman, D.J.: A modal approach to modeling spatially distributed vibration energy dissipation. Sandia National Laboratories, Albuquerque (2010)
7. Mayes, R.L., Pacini, B.R., Roettgen, D.R.: A modal model to simulate typical structural dynamic nonlinearity. Presented at the 34th International Modal Analysis Conference (IMAC XXXIV), Orlando 2016
8. Segalman, D.J., Gregory, D.L., Starr, M.J., Resor, B.R., Jew, M.D., Lauffer, J.P., Ames, N.M.: Handbook on Dynamics of Jointed Structures. Sandia National Laboratories, Albuquerque (2009)
9. Segalman, D.J., Allen, M.S., Eriten, M., Hoppman, K. Experimental assessment of joint-like modal models for structures. Presented at the ASME 2015 International Design Engineering Technical Conferences & Computers and Information in Engineering Conference IDETC/CIE 2015, Boston, 2015
10. de Klerk, D., Rixen, D.J., Voormeeren, S.N.: General framework for dynamic substructuring: history, review, and classification of techniques. AIAA J. **46**, 1169–1181 (2008)
11. Ginsberg, J.H.: Mechanical and Structural Vibrations, 1st edn. John Wiley and Sons, New York (2001)
12. Cook, R.D., Malkus, D.S., Plesha, M.E., Witt, R.J.: Concepts and Applications of Finite Element Analysis, 4th edn. Wiley, New York (2002)
13. Segalman, D.J.: A four-parameter Iwan model for lap-type joints. J. Appl. Mech. **72**, 752–760 (2005)
14. Palmov, V.: Vibrations of Elasto-Plastic Bodies. Springer, Berlin (1998)

Chapter 7
A Modal Model to Simulate Typical Structural Dynamic Nonlinearity

Randall L. Mayes, Benjamin R. Pacini, and Daniel R. Roettgen

Abstract Some initial investigations have been published which simulate nonlinear response with almost traditional modal models: instead of connecting the modal mass to ground through the traditional spring and damper, a nonlinear Iwan element was added. This assumes that the mode shapes do not change with amplitude and there are no interactions between modal degrees of freedom. This work expands on these previous studies. An impact experiment is performed on a structure which exhibits typical structural dynamic nonlinear response, i.e. weak frequency dependence and strong damping dependence on the amplitude of vibration. Use of low level modal test results in combination with high level impacts are processed using various combinations of modal filtering, the Hilbert Transform and band-pass filtering to develop response data that are then fit with various nonlinear elements to create a nonlinear pseudo-modal model. Simulations of forced response are compared with high level experimental data for various nonlinear element assumptions.

Keywords Nonlinear system identification • Nonlinear simulation • Structural dynamics • Modal model

Nomenclature

$d(t)$	Decay function for damping as function of time
ζ	Modal damping ratio
ω	Frequency in radians per second
$\mathscr{H}$	Hilbert transform
$\theta(t)$	Phase as a function of time
$\underline{\chi}$	Iwan parameter related to power law damping
$\underline{\boldsymbol{\Psi}}$	Modal filter vector
$\mathcal{F}$	Subscript for Fourier transform
$+$	Superscript indicating the Moore-Penrose pseudo-inverse of a matrix
A	Amplitude
c	Damping coefficient
d	Subscript for damped
dof	Degree of freedom
f	Frequency in cycles/sec
F	Force
FRF	Frequency response function
$\mathbf{H}$	Frequency response function matrix
k	Stiffness coefficient

Sandia National Laboratories is a multi-program laboratory managed and operated by Sandia Corporation, a wholly owned subsidiary of Lockheed Martin Corporation, for the U.S. Department of Energy National Nuclear Security Administration under Contract DE-AC04-94AL85000.

R.L. Mayes (✉) • B.R. Pacini
Structural Dynamics X-Ray/NDE Department, Sandia National Laboratories, P.O. Box 5800 – MS0557, Albuquerque, NM 87185, USA
e-mail: rlmayes@sandia.gov; brpacin@sandia.gov

D.R. Roettgen
Engineering Mechanics Department, University of Wisconsin – Madison, Madison, WI, USA
e-mail: droettgen@wisc.edu

© The Society for Experimental Mechanics, Inc. 2016

M. Allen et al. (eds.), *Dynamics of Coupled Structures, Volume 4*, Conference Proceedings of the Society for Experimental Mechanics Series, DOI 10.1007/978-3-319-29763-7_7

K_∞ Linear stiffness for Iwan model
lin Subscript for linear
n Subscript for natural
nl Subscript for nonlinear
P Modal response matrix
Q Analytic signal created with use of Hilbert transform
q Modal dof
sdof Single degree of freedom
t Time
U Known force vector
W Weighting matrix
x Physical displacement dof
Φ Mode shape matrix

7.1 Introduction and Motivation

A large class of structural dynamic system responses are mildly nonlinear in stiffness (a few percent modal frequency change) and significantly nonlinear in damping (hundreds of percent damping ratio change) as a function of amplitude of vibration. We desire to experimentally test in a way to identify such a system and then simulate the nonlinear response analytically. Such systems will typically be linear at low level excitation. At higher levels of excitation the resonant frequencies typically decrease slightly and the apparent damping can increase up to 300 %. Structures with joints typically have this softening behavior. Low level linear models used to simulate the response may over-predict the nonlinear response by tens to hundreds of percent. Consider a frequency response function (FRF) from the hardware used in this work due to a high level and a low level impact as shown in Fig. 7.1. The low level FRF peak is almost a factor of 2 greater than the high level FRF peak. Occasionally the resonant frequency will go up slightly and the apparent damping will go down with an increase in the amplitude. We desire to be able to simulate both softening and stiffening behavior. Segalman [1] explored the possibility of utilizing a modal Iwan approach to capture spatially distributed nonlinear energy dissipation with a two degree-of-freedom (dof) analytical model. Deaner [2] fleshed out the concept with a nonlinear beam model, and with jointed beam hardware. He used a modal approach with a four parameter Iwan element in parallel with a linear spring and damper to achieve a satisfactory simulation. We expand on his approach.

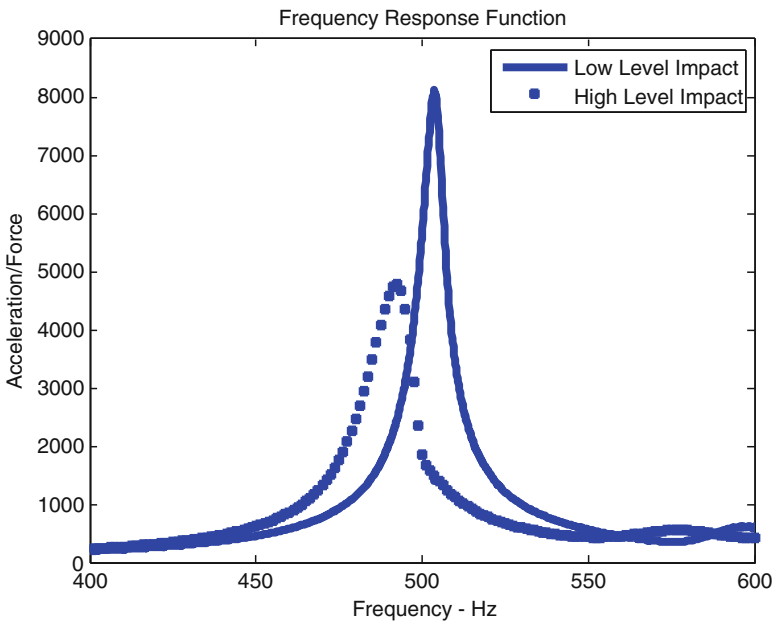

Fig. 7.1 Drive point FRF magnitude—low level vs. high level impact force

The approach utilizes a pseudo-modal model. We assume that a superposition of the modal responses can be multiplied by the mode shape matrix to estimate the response at physical dof. Inherent in this approach is the assumption that the mode shapes do not change with response amplitude, and that the modal dof do not interact. Our approach begins with the standard modal model using a linear spring and damper for each modal mass. The spring and damper are identified in a standard low-level modal impact test. Then we assume that nonlinear elements can be connected in parallel with the standard linear elements. A high level impact test on the nonlinear structure provides data for fitting the nonlinear parameters. Three different nonlinear elements were examined in this work: (1) a four parameter Iwan in parallel with a linear stiffness and damper; (2) Feldman's FREEVIB stiffness and damping; and (3) cubic polynomials of stiffness and damping as a function of response amplitude. We set these models on approximately the same footing by identifying six parameters in each model for each mode of vibration. After the elements were identified, we simulated a high level structural response and propagated the modal responses to all the measured dof and compared simulations to measured responses. A key portion of the success of this approach comes from a modal filter that can filter out all the modal responses of the structure except the single mode of interest. The single dof modal filtered response is used to identify the nonlinear parameters. The Iwan and Feldman models also require that the Hilbert Transform of the modal response be computed as a step in the identification process. The cubic stiffness/damping model does not have this requirement.

In Sect. 7.2 the test hardware and instrumentation is described along with the test approach. Signal preprocessing of modal filters, band-pass filters and the Hilbert Transform is presented in Sect. 7.3. Section 7.4 describes the three nonlinear modeling options and their parameter identification processes. In Sect. 7.5 the simulation results are compared against measured high level data, and observations associated with each model are given. Section 7.6 provides conclusions.

7.2 Experiment

7.2.1 Hardware Description

A solid model cross-section of the test hardware chosen for this analysis is shown in Fig. 7.2 and some of the physical hardware is shown in Fig. 7.3. The foam, mass, and compression plate are placed in the cylinder and a hydraulic press is used to compress these internals to a specified pre-load as measured by three load cells mounted on the mass. The threaded ring is then screwed in to hold the assembly together. The plate-beam is then mounted on the forward face of the cylinder using eight bolts. The cylinder and plate-beam are 6061 T6 aluminum, the rigid urethane foam is Coastal Enterprises PBLT-20 nominal 20 pound/ft^3, and the mass is steel.

7.2.2 Test Set-Up

The test hardware shown in Fig. 7.4 was softly suspended using two bungee cords to approximate a free–free boundary condition and instrumented with 100 mV/g accelerometers. External triaxial accelerometers were mounted at 15 locations shown in Fig. 7.5. The internal mass was instrumented with ten accelerometer channels to capture its rigid body motion.

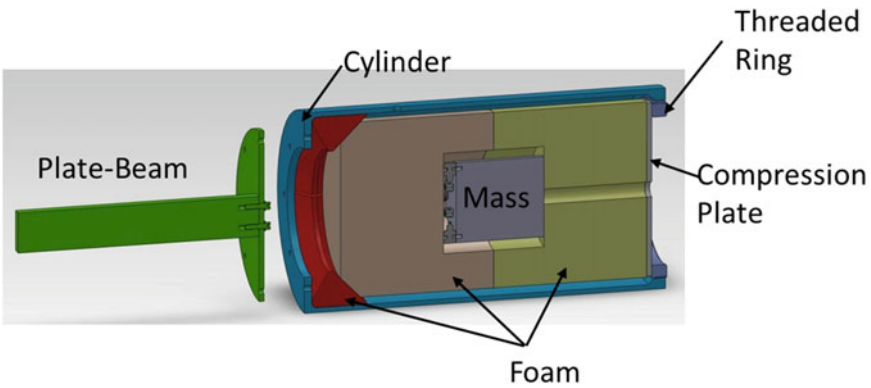

Fig. 7.2 Full system solid model

Fig. 7.3 Physical test hardware

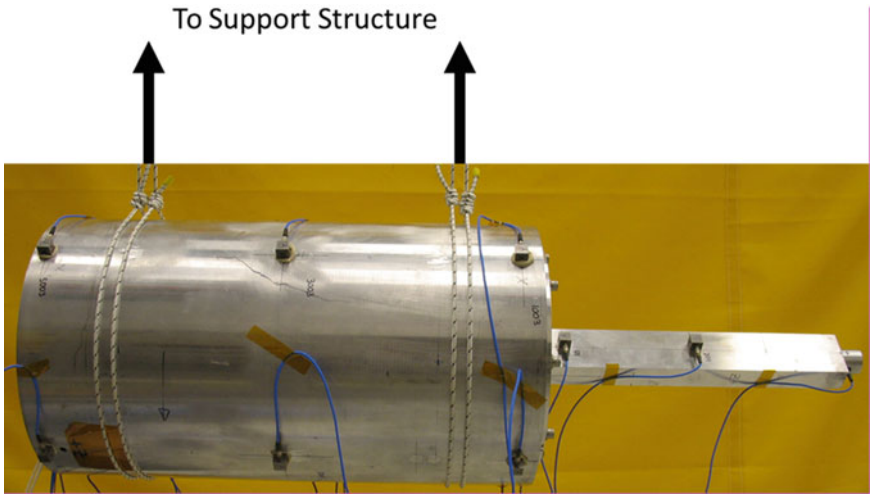

Fig. 7.4 Test hardware suspension

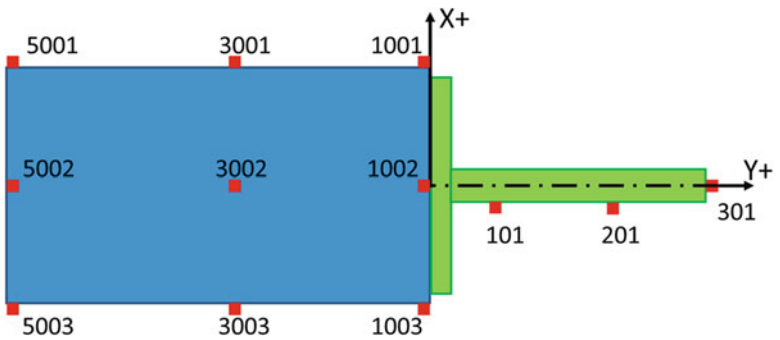

Fig. 7.5 External geometry, side view

Two series of hammer impact tests were conducted on the hardware described above. The first minimized the nonlinear response by applying low level inputs with peak forces of approximately 23 N at the three locations shown in Table 7.1. These data were used to extract parameters for the linear modal model of the hardware. The second set of tests excited nonlinearities with inputs at these same locations but with much higher peak forces: 180 and 400 N for the radial and axial

Table 7.1 Excitation information

Input DOF	Description	Low level peak force (N)	High level peak force (N)
301Y-	Axial input at tip of beam	23	400
5002R-	Radial input at aft end of can in the stiff direction of the beam	23	180
5003R-	Radial input at aft end of can in the soft direction of the beam	23	180

Table 7.2 Linear modal parameters[a, b]

Mode	Low Level		High Level		Δf_n (%)	$\Delta\zeta$ (%)	Reference	Shape Description
	f_n (Hz)	ζ (%cr)	f_n (Hz)	ζ (%cr)				
7	119	0.36	116	0.95	-3	167	5003R-	1st beam bend in X
8	160	0.21	158	0.60	-1	190	5002R-	1st beam bend in Z
9	276	2.46	273	3.60	-1	46	5002R-	Torsion of internal mass
10	282	2.10	280	1.92	-1	-9	5003R-	Translation in X of internal mass
11	302	2.34	298	2.40	-1	3	5002R-	Internal mass off-axis twist
12	503	0.67	491	1.23	-3	84	301Y-	Axial mode of beam Y
13	592	2.02	570	2.91	-4	44	301Y-	Rotation of internal mass about Z
14	635	2.00	630	2.27	-1	14	5002R-	Rotation of internal mass about X
15	699	1.26	692	1.44	-1	14	301Y-	Axial mode of internal mass Y
16	734	1.27	732	1.38	0	9	5003R-	Foam mode X
17	759	1.13	758	1.16	0	3	5002R-	Foam mode Z

[a]Modes highlighted in green were considered nonlinear
[b]Rigid body modes not shown

hits, respectively. 400 N was not used for the radial inputs because this force level over-ranged the drive point accelerometers. The high level data was used to first identify which modes were nonlinear (see Sect. 7.2.3) and secondly to extract parameters for the nonlinear models discussed in Sect. 7.4.

7.2.3 Preliminary Modal Results

The Synthesize Modes And Correlate (SMAC) program by Mayes and Hensley [3] was used to extract two sets of modal parameters from the low and high level impact data using a real modes approximation in Table 7.2. Rigid body mode shapes were calculated from solid model mass properties.

The low level modal parameters were used to create the linear modal model used in the later sections of this report.

The high level modal parameters were used to determine which modes should be modeled as nonlinear. Since damping values extracted from measured data can have 10 % uncertainty, the heuristic used in this work was that any mode with a damping shift of greater than 30 % was declared nonlinear. Modes 7–9, 12, and 13 were thus selected to be modeled as nonlinear.

7.3 Signal Processing

To develop a nonlinear modal model, our approach requires the structural response be separated into the individual modal responses. This requires some type of filter that can transform multiple sensor measurements into modal coordinates. Once these modal responses are calculated, further processing is required to aid nonlinear parameter identification. The following sections detail this two-step procedure. Section 7.3.1 describes three different types of modal filters, discusses the advantages and disadvantages of each, and concludes by selecting the modal filter used for this work. Section 7.3.2 discusses band-pass filtering and the Hilbert Transform which are then used to extract frequency and damping information from the modally filtered data that will be later used to calculate parameters for two nonlinear models.

7.3.1 Modal Filtering

This section describes three modal filters that can be used to transform measurements in physical coordinates to modal responses. We desire a modal filter such that

$$\overline{\boldsymbol{\Psi}}^T \overline{\mathbf{x}} = q_i \tag{7.1}$$

where q_i is the i^{th} modal dof, column vector $\overline{\mathrm{x}}$ contains measured responses, and $\overline{\boldsymbol{\Psi}}$ is the vector of weights transforming the measured responses to the modal response. Three modal filters are investigated.

7.3.1.1 SMAC Modal Filter

The SMAC modal filter [4] operates directly on the FRFs. If one operates on (7.1) in the frequency domain and divides by the input force, then

$$\overline{\boldsymbol{\Psi}}^T \overline{\mathbf{H}}_x = H_{qi} \tag{7.2}$$

where $\mathbf{H}_x$ is now a vector of measured FRFs and H_{qi} is an analytically calculated single dof (sdof) FRF with frequency and damping as extracted from the high level impact data. Columns for every frequency line are added to $\mathbf{H}_x$ and H_{qi} creating a matrix of $\mathbf{H}_x$ and a vector of the analytical FRF $\mathbf{H}_{qi}$. Transposing and isolating the modal filter on the left side yields

$$\overline{\boldsymbol{\Psi}} = \mathbf{H}_x^{T+} \overline{\mathbf{H}}_{qi}^T \tag{7.3}$$

where the superscript $^+$ represents the pseudo-inverse. Hence, the SMAC modal filter is obtained with the measured FRFs and an analytical sdof FRF constructed using the extracted frequency and damping from the high level linear modal parameter extraction.

7.3.1.2 Full Modal Filter

We denote the Full Modal Filter (FMF) as one derived from extracted mode shapes. The modal substitution can be written as

$$\overline{\mathbf{x}} = \boldsymbol{\Phi} \overline{\mathbf{q}} \tag{7.4}$$

where $\boldsymbol{\Phi}$ is a matrix of all rigid body and elastic extracted mode shapes in the frequency band. By pre-multiplying by the pseudo-inverse of the mode shape matrix one obtains

$$\boldsymbol{\Phi}^+ \overline{\mathbf{x}} = \overline{\mathbf{q}} \tag{7.5}$$

so one can recognize the set of all modal filters in the $\boldsymbol{\Psi}$ matrix as

$$\boldsymbol{\Psi}^T = \boldsymbol{\Phi}^+ \tag{7.6}$$

Thus the full modal filter is derived from extracted mode shapes and rigid body mode shapes. In this work, the elastic mode shapes were extracted from the low level impact data.

7.3.1.3 Single Modal Filter

The single modal filter (SMF) was derived using only one mode shape in (7.5) as

$$\overline{\boldsymbol{\Phi}}_i^+ \overline{\mathbf{x}} = q_i \tag{7.7}$$

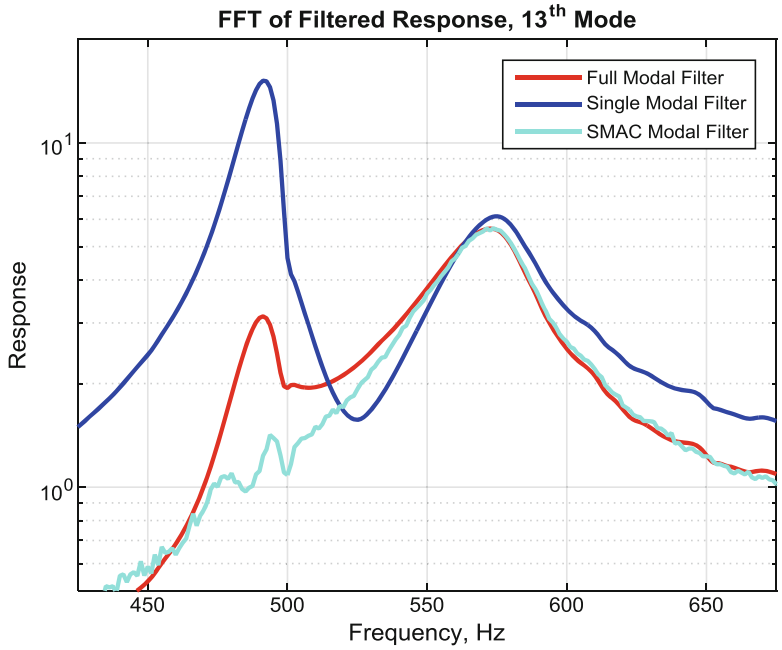

Fig. 7.6 Modal filter results for mode 13 at 592 Hz

so that

$$\overline{\boldsymbol{\Psi}}_i^T = \overline{\boldsymbol{\Phi}}_i^+ \tag{7.8}$$

The FMF and SMAC modal filters inherently suppress the response of all modes but one. However, the SMF does not, so it relies on the frequency being isolated and band-pass filtering to suppress other modes.

7.3.1.4 Modal Filter Results and Comparison

All three modal filters were evaluated for each mode extracted from the experimental system. Consider the results for mode 13 at about 590 Hz shown in Fig. 7.6. Neither the SMF or FMF can remove the effects of the 491 Hz axial mode like the SMAC modal filter.

However, the SMAC modal filter does not always perform better. Consider the modal filter results for mode 9 at 273 Hz in Fig. 7.7. Notice the small shoulder in the SMAC modal filter result (cyan) at 282 Hz. The 282 Hz mode was not removed as well with the SMAC modal filter as with the other two. Note that all three modal filters failed to get rid of the mode at 302 Hz. The effects of these contaminating peaks will be discussed in later sections of this work.

Although it did not perform better for every single mode, the SMAC modal filter generally suppressed all other modes besides the one desired better than the FMF and SMF, so it was chosen for this work.

7.3.2 Hilbert Transform and Band-Pass Sensitivity

Once we have obtained a single degree of freedom response from a combination of modal and band-pass filtering, two of the nonlinear methods require quantifying the damping and frequency as a function of response amplitude. The procedure for accomplishing this closely follows the work from [5, 6]. In this work, the Hilbert Transform is computed and a cubic polynomial is fit to the time varying amplitude and phase. This approach fits the modal impulse response, $\ddot{q}(t)$, to the following functional form,

$$\ddot{q}(t) = e^{d(t)} \cos\left[\theta(t)\right] \tag{7.9}$$

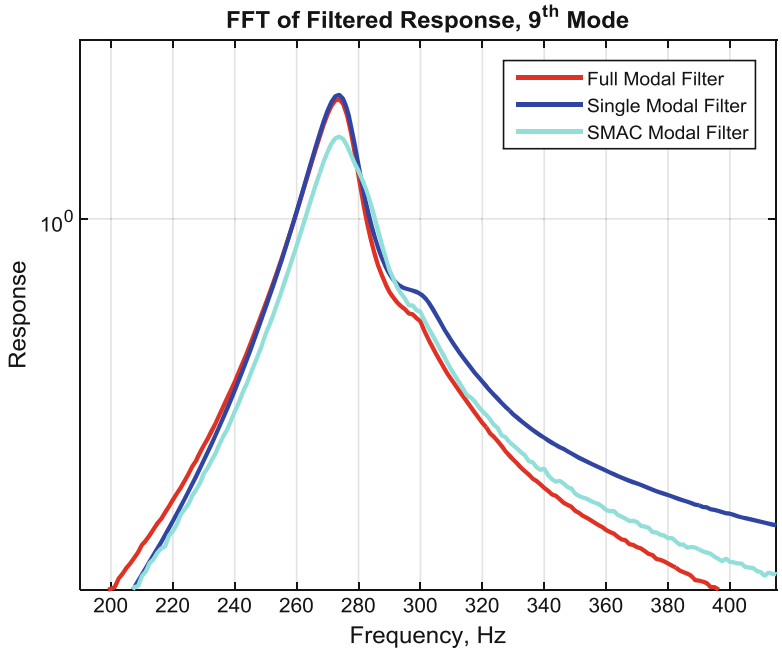

Fig. 7.7 Modal filter comparison mode 9

where $d(t)$ and $\theta(t)$ are each cubic polynomials in time and are, respectively, the decay and phase of the time varying response model. In order to calculate the time-varying natural frequency and damping, the analytic signal, $\ddot{Q}(t)$, is used:

$$\ddot{Q}(t) = \ddot{q}(t) + i\,\mathcal{H}\left(\ddot{q}(t)\right) \tag{7.10}$$

where $\mathscr{H}$ represents a Hilbert Transform. The decay, $d(t)$, is fit to the natural log of the amplitude of the analytic signal, $d(t) = \ln\left|\ddot{Q}(t)\right|$, and the phase, $\theta(t)$, is fit to the unwrapped angle, $\theta(t) = \arg\left[\ddot{Q}(t)\right]$.

The phase of the analytic signal gives the oscillation frequency, so the damped natural frequency was defined as its derivative in [5],

$$\omega_d(t) \triangleq \dot{\theta}(t) \tag{7.11}$$

which one can readily show gives the desired result for a linear time invariant system. Similar expressions can be found for ω_n and ζ.

$$\omega_n(t) \triangleq \left(\omega_d(t)^2 + \dot{d}^2(t)\right)^{\frac{1}{2}} \tag{7.12}$$

$$\zeta(t) \triangleq \frac{\dot{d}(t)}{\omega_n(t)} \tag{7.13}$$

The nonlinear stiffness and damping of each mode can now be evaluated based on changes in damping ratio and frequency with respect to time. The instantaneous damping and frequency can be plotted against velocity and displacement amplitude to bring these parameters into a response based form rather than time based.

It is essential to reduce the signal to a single degree of freedom before completing the above process else the envelope and instantaneous phase will be distorted by interference of other modes. In order to assist the modal filter in eliminating unwanted frequency content, a band-pass filter is applied to the modal response. A forward-backward filter was utilized for this supplemental filter which maintained the timing of the original response signal. A brief sensitivity study was completed to investigate the influences of various passbands on each mode. In this study, passbands were varied from ± 10 % of the natural frequency to as high as ± 50 %. For each passband and modal response, the time-varying damping and natural frequency (Eqs. (7.12) and (7.13)) were plotted versus time to determine the consequences of narrower/wider passbands. The objective was

to find a passband for each mode that successfully eliminated unwanted frequency content without distorting the damping. For this structure the authors have selected to use a 50 % passband for all modes which was robust for every mode when using the SMAC modal filter. Note that the passband used here is not universal and might need modification for a different system.

7.4 Nonlinear Models

This work compared the capabilities of three different models/methods to capture the nonlinear dynamics of the test object: Iwan, FREEVIB (FV), and Restoring Force Surface (RFS). A brief description of each model is provided in the sub sections below. As mentioned in Sect. 7.2.3, only those modes that had a damping change greater than 30 % between the low and high-level input tests were modeled as nonlinear.

In order to have a fair comparison of their capabilities, each of the three aforementioned models were parameterized with six parameters to capture the dynamics. This quantity was selected as it matches the number of parameters used in the Iwan model.

7.4.1 Modal Iwan Model

As discussed in [5, 7] each mode can be modeled with a single degree of freedom system as a modal coordinate. Each modal degree of freedom will be linked to ground with a linear spring and damper. In order to capture the nonlinearity in each mode we then add a four parameter Iwan element in parallel with the linear spring and damper. This element can be described as a joint force as shown in Fig. 7.8.

The system is very similar to a standard modal coordinate set-up but with the nonlinear joint force adding complexity due to the nonlinearity of each mode. The equation of motion for the system now takes the form of

$$\ddot{q}(t) + C\dot{q}(t) + K_{\infty}q(t) = \mathbf{\Phi}^T F_{ext} + F_j \tag{7.14}$$

where the nonlinear force in the joint, F_j, is a function of four parameters, [F_S, K_T, χ, β]. F_S is the slip force or the force required to begin macro-slip. K_T is the stiffness in the joint related to the nonlinear frequency shift from linear conditions to macro-slip. χ is related to the exponent in a power-law relationship between damping and amplitude in the macro-slip regime. Finally, β defines the shape of the dissipation curve near the transition from micro to macro-slip. These four parameters can be obtained from experimental measurements as outlined in [5].

In this work data were obtained solely in the linear and micro-slip regimes of response. Thus some of the parameters became more difficult to estimate. The stiffness in the joint, K_T, is defined as the change in stiffness as shown in (7.15)

$$K_T = \omega_n^2 - (\omega_n - \Delta\omega_n)^2 \tag{7.15}$$

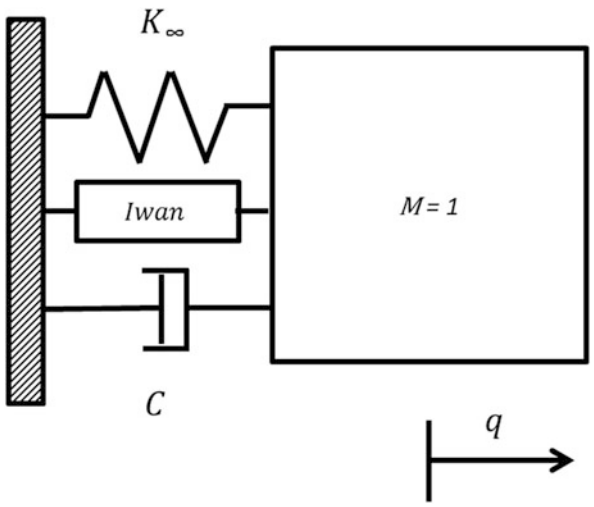

Fig. 7.8 Schematic of SDOF for Iwan model modal coordinate

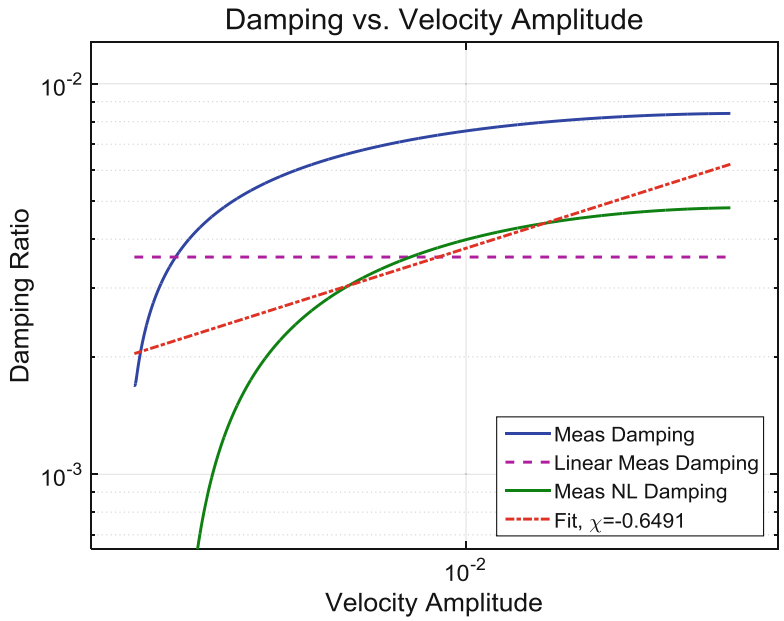

Fig. 7.9 Damping ratio versus velocity amplitude—mode 7

where ω_n is the natural frequency when the joint is completely stuck and $\Delta\omega_n$ is the shift in natural frequency when the joint is in macro-slip. Our experiment did not reach macro-slip so this can be used as a bound knowing that $\Delta\omega_n$ must be larger than that seen in the experiment or the results will prove dissatisfactory.

The parameter χ can be determined directly from the damping ratio versus velocity amplitude curve. χ defines the power law exponent on the dissipation versus velocity amplitude curve. In Fig. 7.9 the blue curve shows the measured damping ratio calculated using (7.13) from the Hilbert Transform. Using this curve one must then subtract off the linear damping ratio (depicted in magenta) from the measured curve. This removes the linear damping portion from the damping ratio and leaves just the nonlinear contribution. This curve can then be fit on a log-log scale in order to determine the slope which is equal to $\chi + 1$.

As discussed in [8] the damping ratio is fit to the form of (7.16). C_{zt} is calculated as the intercept of the power law fit from Fig. 7.9.

$$\zeta\left(\dot{q}\right) = C_{zt}\left|\dot{q}\right|^{\chi+1} \tag{7.16}$$

In [7], Segalman defines dissipation in a similar form as shown in (7.17).

$$Dissipation = R|q|^{\chi+3} \tag{7.17}$$

In Ginsberg's text [9], the relationship between damping ratio and dissipation can be used to solve for the coefficient R.

$$\zeta = \frac{Dissipation}{m2\pi\omega_d\omega_n|q|^{\chi+3}} \tag{7.18}$$

$$R = C_{zt}2\pi\omega_d^{\chi+2}\omega_n \tag{7.19}$$

Based on additional 4-parameter Iwan model definition from [7] one can solve for the remaining unknown parameters β and F_S using an assumed K_T along with extracted values for χ and R. Using these 4-parameters the joint force can now be calculated and integrated. The identification procedure described above was performed on the nonlinear modes specified in Sect. 7.2.3 and the results are provided in Table 7.3.

Table 7.3 Modal Iwan model parameters

Mode	χ	β	F_S	K_T	$f_{n,lin}$	ζ_{lin}
7	−0.65	0	245	2.10E + 05	119	0.0036
8	−0.31	0	39	2.91E + 05	160	0.0021
9	−0.22	0	51	9.92E + 05	276	0.0246
12	−0.77	0	52	9.69E + 05	503	0.0067
13	−0.79	0	108	2.24E + 06	592	0.0202

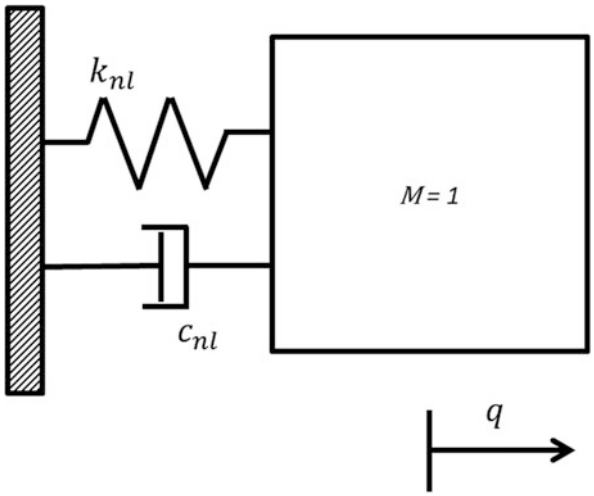

Fig. 7.10 Schematic of SDOF for FV modal coordinate

7.4.2 FREEVIB

This nonlinear model was developed by Feldman in [10] and bases its theory on the free vibration of a nonlinear system. Unlike the Iwan model, FREEVIB combines the linear and nonlinear restoring elements as seen in Fig. 7.10.

The governing equation of motion is in the following form:

$$\ddot{q}(t) + 2c\left(A_q\right)\dot{q}(t) + k\left(A_q\right)q(t) = 0 \tag{7.20}$$

where c and k are the instantaneous damping and stiffness coefficients as a function of amplitude, A_q, which is the Hilbert envelope of the displacement. Note that, using the nomenclature from Sect. 7.3.2, $A_q = e^{d(t)}$. With the assumption that $c(A_q)$ and $k(A_q)$ vary slowly, the Hilbert Transform is utilized to create (7.20) in terms of the analytic signal of $q(t)$, i.e.,

$$\ddot{Q}(t) + 2c\left(A_q\right)\dot{Q}(t) + k\left(A_q\right)Q(t) = 0 \tag{7.21}$$

where $\ddot{Q}(t)$ comes from (7.10). Given that the 1st and 2nd derivatives of the analytic signal can be written in terms of $Q(t)$, the envelope, and instantaneous phase, a closed-form, nonparametric function can be derived for c and k. Using the definitions for the envelope and instantaneous phase from Sect. 7.3.2 and ignoring negligibly small terms, the instantaneous damping and stiffness terms are determined to be:

$$c(t) = -\dot{d}(t) - \frac{\dot{\omega}_d(t)}{2\omega_d(t)} \tag{7.22}$$

$$k(t) = {\omega_d}^2(t) \tag{7.23}$$

where $\omega_d(t)$ is the instantaneous damped natural frequency defined in (7.11).

Typically, damping is associated with velocity and therefore it is desired to derive an expression for c in terms of velocity. If small terms are neglected, the velocity envelope, $A_{\dot{q}}$, can be written as

$$A_{\dot{q}} = \omega_d A_q. \tag{7.24}$$

Now $c(t)$ and $k(t)$ can be plotted against $A_{\dot{q}}(t)$ and $A_q(t)$, respectively, to get amplitude-dependent instantaneous damping and stiffness coefficients. For the work described herein, it was desired to have all nonlinear models utilize the same number of parameters. Therefore, instead of conducting the nonlinearity identification step described in [10], the stiffness and damping were estimated using quadratic polynomials (resulting in linear, quadratic, and cubic terms in the equation of motion).

$$c\left(A_{\dot{q}}\right) = c_0 + c_1 A_{\dot{q}} + c_2 A_{\dot{q}}^2 \tag{7.25}$$

$$k\left(A_q\right) = k_0 + k_1 A_q + k_2 A_q^2 \tag{7.26}$$

When implementing FREEVIB in simulation, we calculated the instantaneous damping and stiffness as:

$$c\left(\dot{q}_i\right) = c_0 + c_1 \left|\dot{q}_i\right| + c_2 \dot{q}_i^{\,2} \tag{7.27}$$

$$k\left(q_i\right) = k_0 + k_1 \left|q_i\right| + k_2 q_i^{\,2} \tag{7.28}$$

where q_i and $\dot{q}_i$ are the displacement and velocity at time step i. The absolute values are used to preserve the sign of the signal.

FREEVIB requires that the data used in the nonlinear parameter identification can only include the response after the excitation is removed. Since the measured force was filtered and never reached a value of identically zero, this was approximated as when the filtered force had dropped below 0.5 % of its maximum value. Depending on the post-processing and degree of nonlinearity of the measurements, a significant amount of time may have elapsed prior to this event occurring. This could result in the exclusion of a significant portion of the nonlinear response from the analysis, reducing the accuracy of the extracted parameters. This effect can be seen in the results for mode 9.

The identification procedure described above was performed on the nonlinear modes specified in Sect. 7.2.3 and the results are provided in Table 7.4.

7.4.3 *Restoring Force Surface*

This method has been extensively researched and refined with several permutations. Reference [11] contains an extensive synopsis of the past variances and applications of the Restoring Force Surface (RFS) method. Similar to the Iwan model, the version of the RFS model structure adopted for this work is shown in Fig. 7.11 where the linear elements are in parallel with the nonlinear ones.

The foundation of RFS is in the Newtonian equation of motion:

$$\ddot{q}(t) + F_r\left(q(t), \dot{q}(t)\right) = F(t) \tag{7.29}$$

where $F_r\left(q, \dot{q}\right)$ represents the damping and stiffness forces (called the restoring forces) and $F(t)$ is the excitation force. Assuming the acceleration and excitation force are measured, then at every time instant, the restoring force is also known. We write F_r as in the following:

$$F_r\left(q(t), \dot{q}(t)\right) = c_0 \dot{q}(t) + c_1 \left|\dot{q}(t)\right| \dot{q}(t) + c_2 \dot{q}^3(t) + k_0 q(t) + k_1 \left|q(t)\right| q(t) + k_2 q^3(t) \tag{7.30}$$

Table 7.4 FREEVIB damping and stiffness coefficients

Mode	c_2	c_1	c_0	k_2	k_1	k_0
7	−6.12E + 03	301	2	2.08E + 13	−1.77E + 09	5.60E + 05
8	−1.01E + 04	454	0.43	2.63E + 13	−1.98E + 09	1.01E + 06
9	−1.49E + 06	1.15E + 04	39	−2.29E + 16	1.49E + 11	2.79E + 06
12	−144	30	24	6.91E + 13	−1.04E + 10	9.80E + 06
13	4.57E + 04	−1.96E + 03	95	−1.87E + 15	−1.53E + 10	1.31E + 07

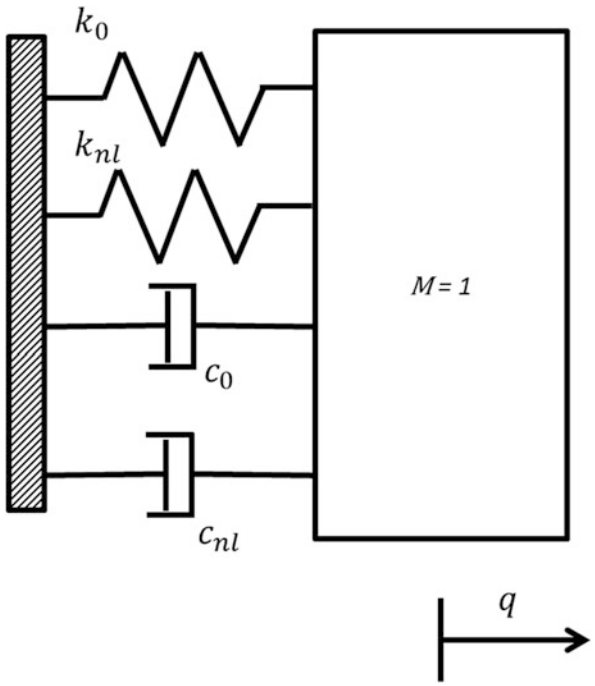

Fig. 7.11 Schematic of SDOF for RFS modal coordinate

where c_1, c_2, k_1, and k_2 are constants. Since c_0 and k_0 are already known from the low level modal tests, (7.29) is rearranged to

$$\begin{bmatrix} |\dot{q}|\,\dot{q} & \dot{q}^3 & |q|\,q & q^3 \end{bmatrix} \begin{bmatrix} c_1 \\ c_2 \\ k_1 \\ k_2 \end{bmatrix} = F - \ddot{q} - c_0\dot{q} - k_0 q \tag{7.31}$$

Or

$$[P] \begin{bmatrix} c_1 \\ c_2 \\ k_1 \\ k_2 \end{bmatrix} = [U] \tag{7.32}$$

where the time-dependency associated with each row has been omitted for clarity. Recall that $[P]$ and $[U]$ are processed measurements and that there is a row for each time sample. Thus (7.32) should be written as

$$\mathbf{P} \begin{bmatrix} c_1 \\ c_2 \\ k_1 \\ k_2 \end{bmatrix} = \overline{\mathbf{U}}. \tag{7.33}$$

We obtained the best results by taking the Fourier transform of each column of $\mathbf{P}$ and $\bar{\mathbf{U}}$ giving

$$\mathbf{P}_{\mathcal{F}} \begin{bmatrix} c_1 \\ c_2 \\ k_1 \\ k_2 \end{bmatrix} = \overline{\mathbf{U}}_{\mathcal{F}} \tag{7.34}$$

Table 7.5 Restoring force surface damping and stiffness coefficients

Mode	c_2	c_1	c_0	k_2	k_1	k_0
7	−1.36E + 03	367	5	1.69E + 13	−1.5E + 09	5.56E + 05
8	−3.77E + 03	579	4	1.52E + 13	−1.8E + 09	1.01E + 06
9	−1.94E + 05	6.63E + 03	85	6.14E + 14	−1.5E + 10	3.01E + 06
12	−5.35E + 02	299	42	1.49E + 14	−1.9E + 10	1.00E + 07
13	−3.24E + 04	3.33E + 03	150	4.42E + 15	−1.6E + 11	1.38E + 07

Note that in order to yield real coefficients, $\mathbf{P}_f$ must be reconfigured to

$$\mathbf{P}_{\mathcal{F}} = \begin{bmatrix} real\,(\mathbf{P}_{\mathcal{F}}) \\ imaginary\,(\mathbf{P}_{\mathcal{F}}) \end{bmatrix}. \tag{7.35}$$

$\mathbf{U}_f$ must be similarly restructured. Pre-multiplying $\bar{\mathbf{U}}_f$ by the pseudo-inverse of $\mathbf{P}_f$ results in the least-squares estimate for c_1, c_2, k_1, and k_2.

We obtained good results by applying a weighting matrix to (7.34) near resonances. If the weighted bandwidth is taken to be ±5 % of the frequency of the resonance, this method gave better parameters than the time domain results from (7.33).

$$\mathbf{W}\mathbf{P}_{\mathcal{F}} \begin{bmatrix} c_1 \\ c_2 \\ k_1 \\ k_2 \end{bmatrix} = \mathbf{W}\overline{\mathbf{U}}_{\mathcal{F}} \tag{7.36}$$

where $\mathbf{W}$ is the block diagonal weighting matrix. For the Restoring Force Surface results in Sect. 7.5.1, this weighted frequency domain approach was utilized with a weight of 100 applied to the narrow resonance bands and 1 elsewhere.

Note that acceleration, velocity, and displacement must all be known (estimated or measured). For this work, acceleration was obtained from the modal filtered measured accelerations and the other two states were estimated by integrating in the frequency domain. The first step was to band-pass filter the modal acceleration as prescribed in Sect. 7.3.2. The velocity and displacement in the frequency domain were then calculated by dividing this acceleration by $i\omega$ and $-\omega^2$, respectively, followed by band-pass filtering using the same filter that was applied to the modal acceleration.

The identification procedure described above was performed on the five nonlinear modes, and the results are provided in Table 7.5.

7.5 Results and Observations

This section compares the results of each of the three nonlinear modal models to the actual nonlinear measured data. First, a discussion of the simulations used to create the analytical modal responses for linear and nonlinear modes is presented followed by a comparison to measured data in physical coordinates. Discussions of features of each method will conclude this section.

7.5.1 Simulation Results and Observations

The three pseudo-modal models with 17 modes were excited with simulated modal forces corresponding to the measured high level impacts from the three different locations. The modal responses were extended to the physical dof using the linear mode shape matrix extracted from low level modal tests using (7.4). These responses were compared against the measured high level data in the plots below. Note that the line labeled “Linear” is the response of a linear model that used the low-level linear parameters from Table 7.2 for all 17 modes.

A representative sample of results are presented. Figure 7.12 compares the linear model response with the measured data by considering the primary singular value of the complex mode indicator function (CMIF). The CMIF compresses all the

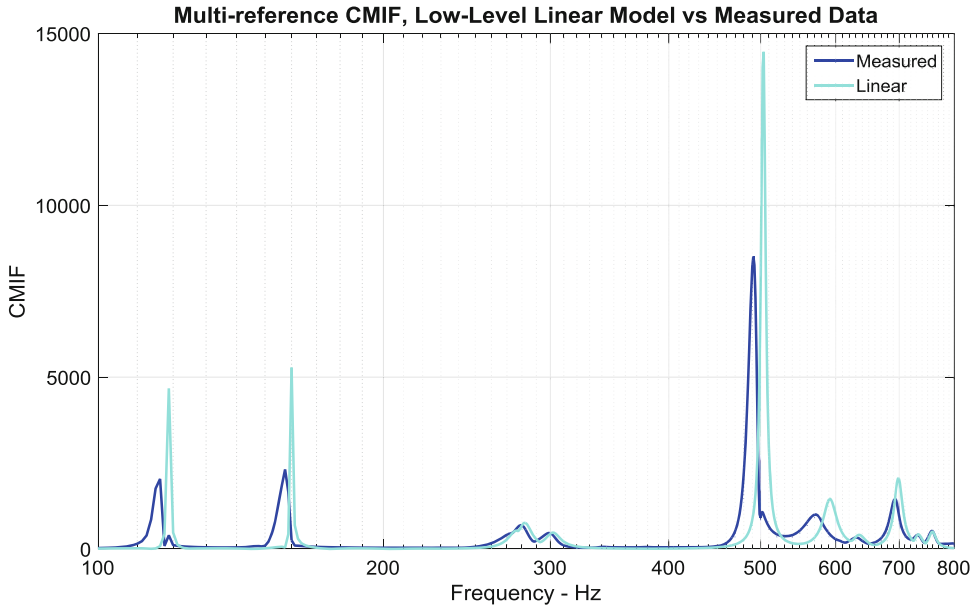

Fig. 7.12 Multi-reference CMIF, linear model versus measured data, max singular value only

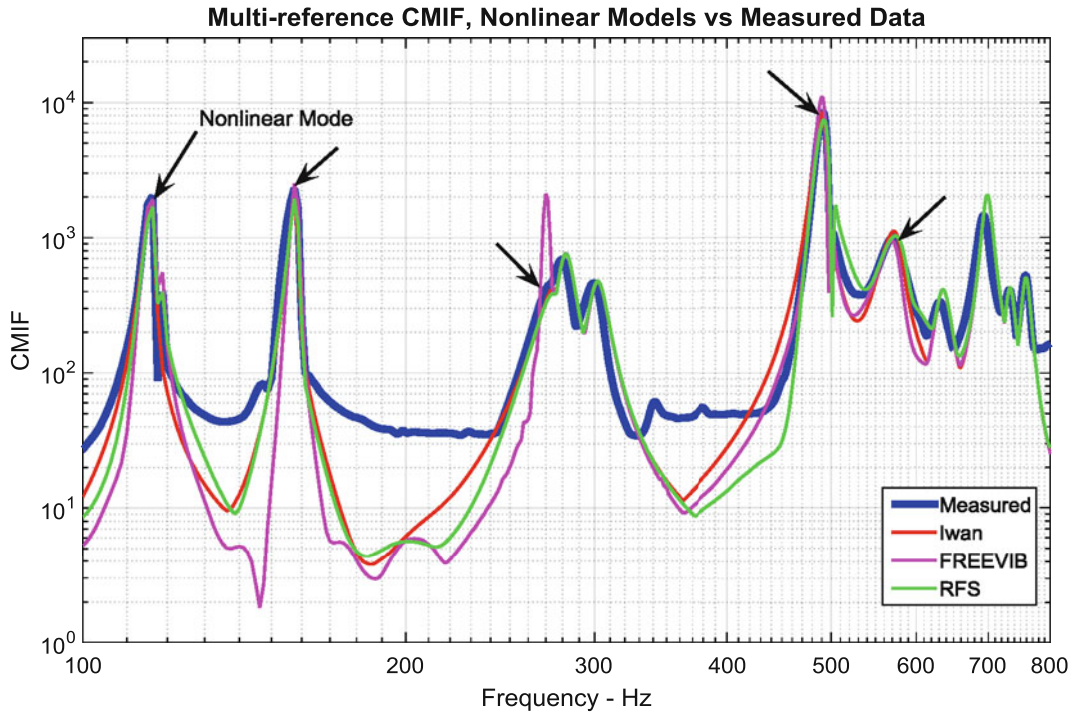

Fig. 7.13 Multi-reference CMIF, nonlinear models versus measured data, max singular value only

responses from all three force impacts into one plot. This plot illustrates that the linear model over-predicts the response from a high level impact; the three main modes of the system (7, 8, and 12) are over-predicted by almost 100 %. Additionally, the linear model is slightly too stiff.

Figure 7.13 shows the primary singular value of the multi-reference CMIF of the high-level measured data and the corresponding predictions of the three nonlinear models. All models are able to predict the high-level test data better than the linear model, with the exception of FV's 273 Hz response. Only the Iwan and RFS models will be addressed further, since the FV model over-predicts two modes. Note that for declared linear modes, the three model results overlay, an expected result since all three pseudo-modal models were the same for the linear modes.

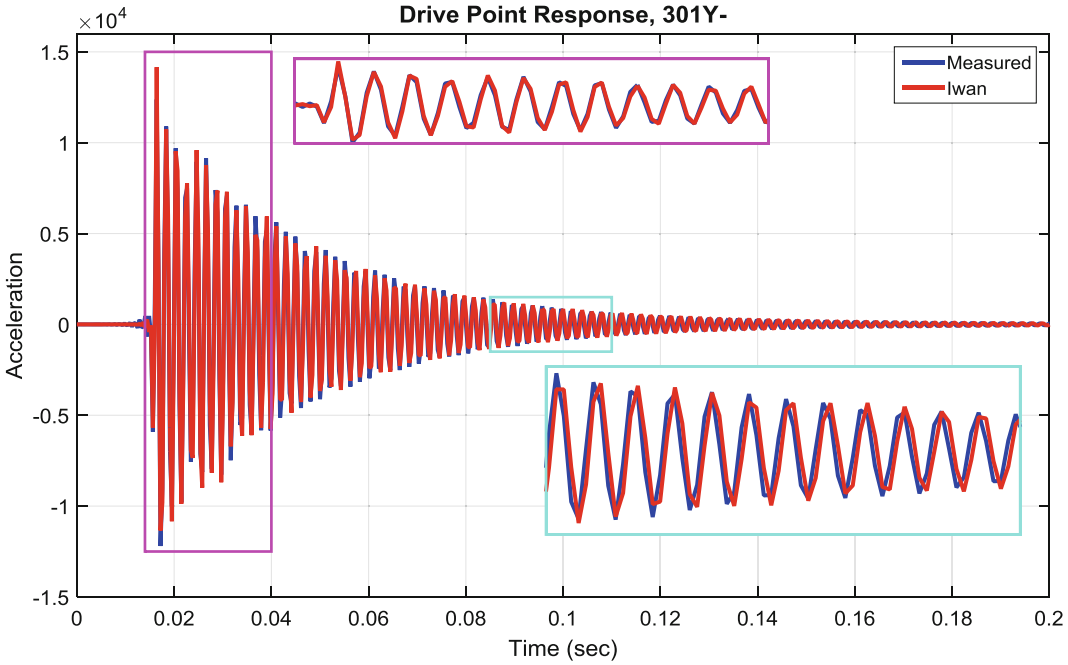

Fig. 7.14 Axial drive point response, Iwan versus measured

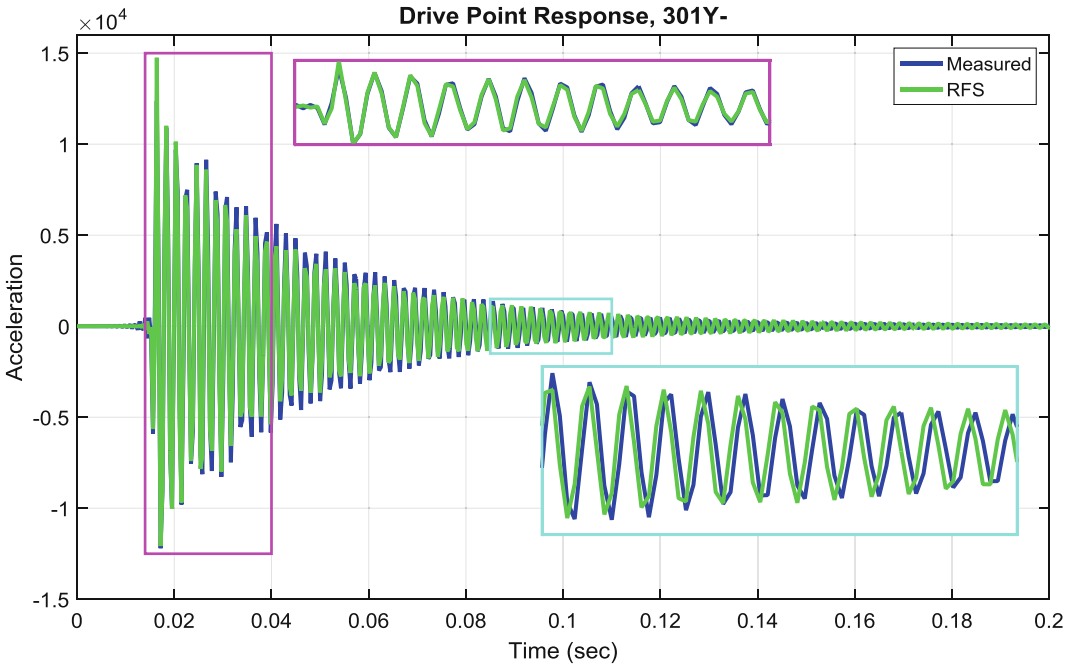

Fig. 7.15 Axial drive point response, RFS versus measured

The time history plots of Figs. 7.14, 7.15, 7.16 and 7.17 reinforce the results from Fig. 7.13. The drive point response to the axial input (Figs. 7.14 and 7.15) is dominated by mode 12. The Iwan model was able to accurately replicate the measured data in Fig. 7.13, and there is a good agreement in the time response shown in Fig. 7.14. Results are similar for the RFS approach with cubic springs and dampers in Fig. 7.15.

The Iwan and RFS models comparably predicted the drive point response from the radial input in Figs. 7.16 and 7.17. Neither achieved the proper amplitude of the initial acceleration spike, but they simulate the rest of the time history well.

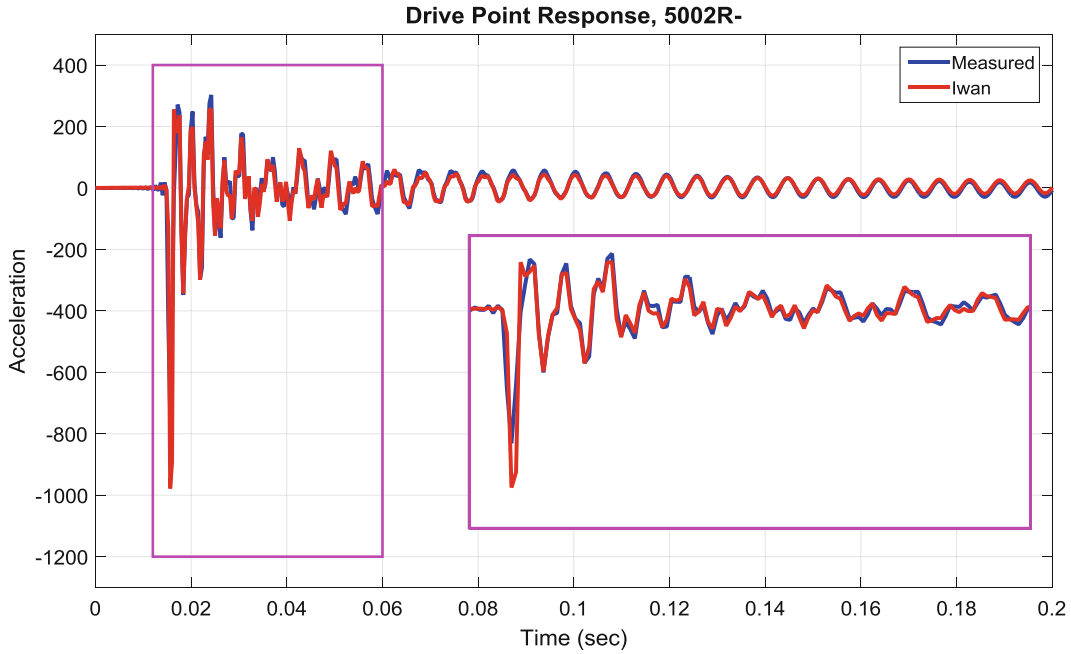

Fig. 7.16 Radial drive point response, Iwan versus measured

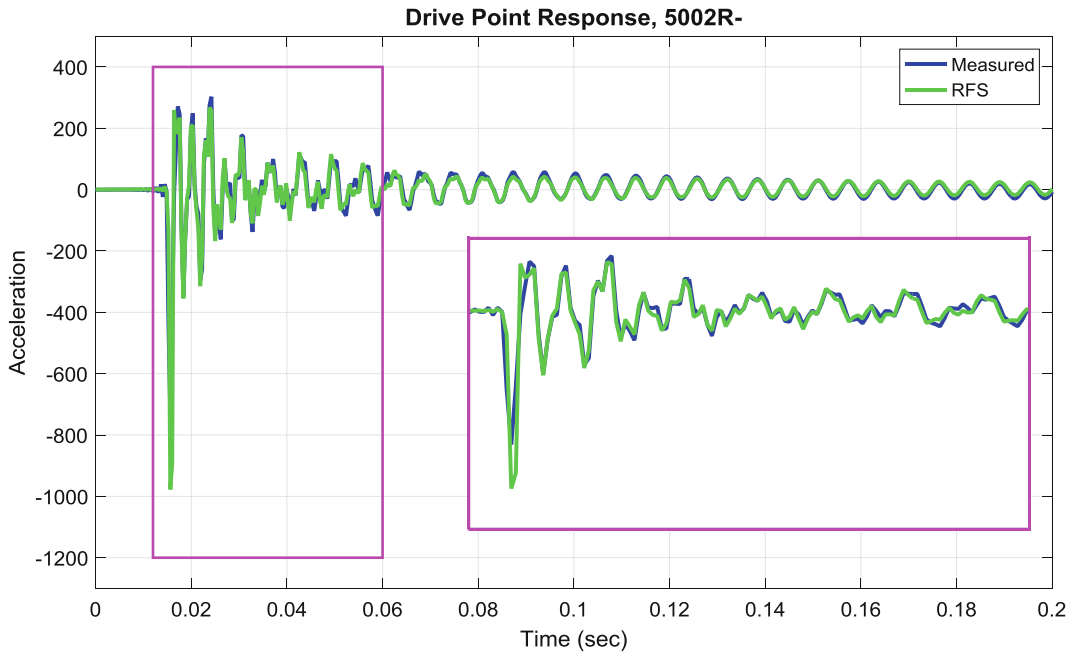

Fig. 7.17 Radial drive point response, RFS versus measured

7.5.2 Discussion

Although not readily apparent from the figures, it is important to note the significant role of the Hilbert Transform in the Iwan and FV models. While an extremely valuable and versatile tool that provides great qualitative insight into the frequency and damping variation, it can also have adverse effects depending on the characteristics of the data. In the presence of step changes in signal amplitude or frequency, the envelope and instantaneous phase produced by the Hilbert Transform will have some overshoot and settling time characteristics [12]. Given that this work utilized impact data which has a large step-like change in amplitude, the envelopes and instantaneous phases extracted from the Hilbert Transform of the measured data were

distorted during the initial portion of the response. These errors consequently influenced the polynomial fits for the envelope and instantaneous phase upon which the Iwan and FV models depend.

Another aspect worth mentioning is the interplay of the Hilbert Transform and the quality of the modal filter. In addition to the transient effects mentioned above, any non-targeted modal peaks that are not adequately attenuated in the modally-filtered response can produce ripples throughout the entire envelope. These ripples influence the polynomial fits to the Hilbert Transform and hence the nonlinear parameters of the Iwan and FV models. In extreme cases when the modal filter cannot eliminate a nearby mode (e.g. mode 9), the envelope and instantaneous frequency (and hence the nonlinear parameters) are distorted by the non-suppressed mode. This phenomenon contributed to the inaccurate response of mode 9 predicted by FV, see Fig. 7.13. Note that FV results could be improved with user interaction, see Sect. 7.6.4. The Iwan model avoids these struggles with mode 9 because the Iwan element is placed in parallel with a known linear spring and damper. Rather than letting the Hilbert transform fit these linear terms the Iwan element is constrained to be in a reasonable range when the parameters are being determined. The RFS method can also suffer from non-targeted poorly attenuated modal peaks in the modally-filtered response, but does not rely on the Hilbert Transform, which eliminates effects from the Hilbert distortions as well as the extra steps of calculating and fitting the Hilbert Transform.

As one can see from Fig. 7.9, the process for subtracting the linear damping and fitting a line to the log plot of damping vs. amplitude are not completely straight-forward. Significant trial-and-error was required to iterate to the final high quality solutions that were achieved.

7.6 Conclusions

The conclusions here will address the model assumptions, test approach, signal pre-processing and the three nonlinear models.

7.6.1 Nonlinear Pseudo-Modal Model Assumptions

The assumptions that the mode shapes do not change and that the modal degrees of freedom do not interact appear valid to a reasonable approximation for this hardware testing. The hardware showed the typical structural dynamic nonlinearity of softening spring and increasing damping with amplitude for at least five modes. Other modes were considered linear enough that they were approximated as linear. No modes exhibited the hardening spring effect that is occasionally seen in some hardware.

7.6.2 Nonlinear Pseudo-Modal Model Testing Approach

The testing approach included a low level impact modal test to obtain the normal linear modal parameters from three input locations. The key effort here was to provide as perfect as possible co-linear force input with the driving point accelerometer so that the linear experimental modal model is extracted with accurate modal mass and accurate mode shapes scaling. The low level modal test is a very standard test in the industry and quite tractable for most laboratories. The high level impact is just a repeat of the low level test at higher levels, and does not require much extra effort once the test is set up. Some care is required to make sure the sensors do not overload and corrupt the data. The maximum response capability of the drive point accelerometer was a limiting factor in this test.

7.6.3 Signal Pre-Processing with Modal Filter, Band Pass Filter and Hilbert Transform

The quality of the modal filtering has a direct impact on the quality of the nonlinear parameter identification for all three nonlinear model forms. When one observes the modal filtered signal in the frequency domain, one can usually discern with the eye whether modes at other frequencies have been removed. Nonlinear parameter results tend to be very good with a sdof modal filtered response and worse as more modes are observed in the supposedly filtered response.

The Full Modal Filter and the SMAC modal filter each had certain modes on which they excelled. The SMAC modal filter was better at removing extra modes than the Full Modal Filter in general. The Single Modal Filter was much worse than the other two.

Band-pass filtering was very helpful for improving the Hilbert Transform results. Without band-pass filtering the Hilbert Transform results were much more oscillatory and nebulous, usually due to other modes that were not completely filtered. Band-pass filtering was not helpful if the pass band was too narrow (e.g. 5 % of the resonant frequency). It could be tailored to each mode for optimum results, but generally a band-pass of 30–50 % of the resonant frequency was robust.

The Hilbert Transform is required for the FREEVIB and Iwan approaches to obtain frequency and damping variation as a function of amplitude. If the modal filtered response was not uni-modal, these functions of frequency and damping were oscillatory, hampering the fitting. The Hilbert Transform tends to have some early-time oscillations of frequency and damping at the very high amplitudes. The spurious oscillations at the high amplitude can be problematic, since that is the region most important to the nonlinear model.

7.6.4 Nonlinear Pseudo-Modal Model Forms

We contend that all three methods would give satisfactory nonlinear simulations with enough user interaction. For these studies, the Iwan model and the RFS frequency fit model gave satisfying simulation results. The FV model was not quite as good, but with some user interaction these results could be improved. We did not iterate on the FV fits near as much as the Iwan fits. Six parameters were chosen for each mode for each method to put them on equal footing. This was initially based on the Iwan approach, which uses a linear spring and damper and a four parameter Iwan. With this many parameters, any of the model forms could be used for this nonlinear hardware.

The Iwan model is the most utilized in simulating structural dynamic joint nonlinearities in the recent past. Its form appeared to be a very good representation for the nonlinearities where damping increased and frequency decreased with amplitude, which seems to be typical of many joints. We considered the simulations with the Iwan models very good. The disadvantages we noted with the Iwan were: (1) a great deal of user interaction (and iteration) was required to get good Iwan parameters; (2) the understanding of those parameters is complex compared to FREEVIB stiffness and damping or cubic springs and damping; (3) the inability to simulate constant damping with softening or decreased damping with stiffening; (4) a strong dependence on the quality of the Hilbert Transform results.

The Feldman FREEVIB model is relatively easy to understand. We modified the nonparametric approach by fitting cubic polynomials to the functions of frequency and damping vs. amplitude to keep it on the same six parameter footing as the other two model forms. FREEVIB requires free response ringdown data, which works well with impact testing as was performed on this hardware. Simulation results are very dependent on the results of the Hilbert Transform and the modal filter. We found that parameters for mode 9 were not well quantified using FV, causing significant over-prediction for this mode. However, if we removed the band-pass filtering which allowed us to include earlier time data while still maintaining the free-vibration requirement, we could get better results. Additionally, using the FMF (which performed better for mode 9, see Fig. 7.7) instead of the SMAC modal filter for this particular mode also resulted in a better prediction of the measured data. We surmise that capturing the most nonlinear response early in time and eliminating non-target modes is critically important to FV. We did not include the improved results since the data processing (different modal filter and/or exclusion of band pass filtering) was inconsistent with the other two nonlinear models.

The cubic springs and dampers as a function of amplitude are easy for an engineer to understand. The RFS approach in the frequency domain focused on the frequency lines around each resonance gave results on par with the best results from iterative Iwan fits. The RFS frequency approach also has other significant advantages over the other models because it does not require the Hilbert Transform or extensive user interaction. Because of the ease of understanding the polynomial type nonlinearity, elimination of Hilbert Transform step, low user interaction and the final quality of the nonlinear simulation, RFS with cubic nonlinearities emerged as our favored approach.

Notice This manuscript has been authored by Sandia Corporation under Contract No. DE-AC04-94AL85000 with the U.S. Department of Energy. The United States Government retains and the publisher, by accepting the article for publication, acknowledges that the United States Government retains a non-exclusive, paid-up, irrevocable, world-wide license to publish or reproduce the published form of this manuscript, or allow others to do so, for United States Government purposes.

References

1. Segalman, D.J.: A modal approach to modeling spatially distributed vibration energy dissipation, Sandia National Laboratories, Albuquerque, NM and Livermore, CA, SAND2010-4763, 2010
2. Deaner, B.J.: Modeling the nonlinear damping of jointed structures using modal models. Master of Science Thesis, University of Wisconsin-Madison (2013)
3. Hensley, D.P., Mayes, R.L.: Extending SMAC to multiple references. In: Proceedings of the 24th International Modal Analysis Conference, pp 220–230, (2006)
4. Mayes, R.L., Johansen, D.D.: A modal parameter extraction algorithm using best-fit reciprocal vectors. In: Proceedings of the 16th International Modal Analysis Conference, pp 517–521 (1998)
5. Deaner, B., Allen, M.S., Starr, M.J., Segalman, D.J., Sumali, H.: Application of viscous and Iwan modal damping models to experimental measurements from bolted structures. ASME J. Vib. Acoust. **137**, 021012 (2015)
6. Sracic, M. W. et al.: Identifying the modal properties of nonlinear structures using measured free response time histories from a scanning laser Doppler vibrometer. Presented at the 30th International Modal Analysis Conference Jacksonville, Florida, 2012
7. Segalman, D.J.: A four-parameter Iwan model for lap-type joints. J. Appl. Mech. **72**, 752–760 (2005)
8. Roettgen, D.R., Allen, M.S.: Nonlinear characterization of a bolted, industrial structure using a modal framework. Mech. Syst. Signal Process. (2015, Submitted)
9. Ginsberg, J.H.: Mechanical and Structural Vibrations, 1st edn. John Wiley and Sons, New York (2001)
10. Feldman, M.: Non-linear system vibration analysis using Hilbert transform—I. Free vibration analysis method 'FREEVIB'. Mech. Syst. Signal Process. **8**, 119–127 (1994)
11. Gaëtan, K., Worden, K., Vakakisc, F.A., Golinval, J.C.: Past present, and future of nonlinear system identification in structural dynamics. Mech. Syst. Signal Process. **20**, 505–592 (2006)
12. Feldman, M.: Hilbert Transform Applications in Mechanical Vibration, p. 29. John Wiley & Sons Ltd, Chichester (2011)

Chapter 8
Optimal Replacement of Coupling DoFs in Substructure Decoupling

Walter D'Ambrogio and Annalisa Fregolent

Abstract Substructure decoupling consists in the identification of a dynamic model of a structural subsystem, starting from an experimental dynamic model (e.g. FRFs) of the assembled system and from a dynamic model of a known portion of it (the so-called residual subsystem). The degrees of freedom (DoFs) of the assembled system are partitioned into internal DoFs (not belonging to the couplings) and coupling DoFs. To achieve decoupling, a negative structure opposite to the residual subsystem is added to the assembled system, and compatibility and equilibrium conditions are enforced at interface DoFs. Interface DoFs can include coupling DoFs only (standard interface), additional internal DoFs of the residual subsystem (extended interface), subsets of coupling DoFs and internal DoFs (mixed interface), or a subset of internal DoFs only (pseudo interface). As shown in previous papers, the use of a mixed interface allows to replace some coupling DoFs (e.g. rotational DoFs) with a subset of internal DoFs. Furthermore, qualitative criteria for an appropriate selection of the internal DoFs used to replace unwanted coupling DoFs are stated. In this paper, a procedure to optimally replace coupling DoFs with internal DoFs is developed, using either the Frequency Response Function (FRF) or the transmissibility between internal and coupling DoFs. The procedure is tested on an assembled structure made by a cantilever column with two staggered short arms (residual substructure) coupled to a horizontal beam (unknown substructure).

Keywords Optimal DoF selection • Substructure decoupling • Rotational DoFs • Mixed interface • Experimental dynamic substructuring

8.1 Introduction

Substructure decoupling represents a special case of experimental dynamic substructuring. Specifically, it consists in the identification of the dynamic behaviour of a structural subsystem, starting from the dynamic behaviour of both the assembled system and the residual subsystem (the known portion of the assembled system). Decoupling is a need for subsystems that cannot be measured separately, but only when coupled to their neighboring substructure(s), such as fixtures needed for testing. In Frequency Based Substructuring, Frequency Response Functions (FRFs) are used instead of modal parameters to avoid modal truncation problems. A general framework for dynamic substructuring is provided in [1].

A well known issue in experimental dynamic substructuring is related to rotational DoFs: rotational FRFs are quite difficult to be obtained experimentally, both from translational FRFs [2] and by measuring directly the rotational responses [3, 4]. However, whilst rotational FRFs are needed when coupling together different subsystems, they are not essential in substructure decoupling as shown in [5, 6].

To achieve decoupling, a fictitious subsystem that is the negative of the residual subsystem is added to the coupled system, and appropriate compatibility and equilibrium conditions are enforced at interface DoFs. Interface DoFs may include coupling DoFs only (standard interface), additional internal DoFs of the residual subsystem (extended interface), subsets of coupling DoFs and internal DoFs of the residual subsystem (mixed interface), or a subset of internal DoFs of the residual subsystem only (pseudo interface).

As shown in previous papers [5, 6], the use of a mixed interface allows to replace some coupling DoFs (e.g. rotational DoFs) with a subset of internal DoFs. In fact, the actions exchanged through the connecting DoFs, and specifically through

W. D'Ambrogio (✉)
Dipartimento di Ingegneria Industriale e dell'Informazione e di Economia, Università dell'Aquila Via G. Gronchi, 18, 67100 L'Aquila, Italy
e-mail: walter.dambrogio@univaq.it

A. Fregolent
Dipartimento di Ingegneria Meccanica e Aerospaziale, Università di Roma La Sapienza Via Eudossiana, 18, 00184 Rome, Italy
e-mail: annalisa.fregolent@uniroma1.it

© The Society for Experimental Mechanics, Inc. 2016

M. Allen et al. (eds.), *Dynamics of Coupled Structures, Volume 4*, Conference Proceedings of the Society for Experimental Mechanics Series, DOI 10.1007/978-3-319-29763-7_8

rotational DoFs, are already embedded in each FRF of the assembled system. Furthermore [7], qualitative criteria for an appropriate selection of the internal DoFs used to replace unwanted coupling DoFs are stated.

In this paper, a procedure to optimally replace coupling DoFs with internal DoFs is developed, using indicators based either on the Frequency Response Function (FRF) or on the transmissibility between internal and coupling DoFs. Such indicators are tested with satisfactory results on an assembled structure made by a cantilever column with two staggered short arms (residual substructure) coupled to a horizontal beam (unknown substructure).

8.2 Direct Decoupling Using Dual Assembly

The unknown substructure U (N_U DoFs) is a portion of a larger structure RU (N_{RU} DoFs). The known portion of the assembled structure RU, defined as residual substructure R (N_R DoFs), is joined to the unknown substructure through a number of couplings (see Fig. 8.1). The degrees of freedom (DoFs) can be partitioned into internal DoFs (not belonging to the couplings) of substructure U (u), internal DoFs of substructure R (r), and coupling DoFs (c).

The goal is to find the FRF of the unknown substructure U starting from the FRFs of the assembled structure RU and of the residual substructure R. The dynamic behaviour of the unknown substructure U can be extracted from that of the assembled structure RU by taking out the dynamic effect of the residual subsystem R. This can be accomplished by considering a negative structure, i.e. by adding to the assembled structure RU a fictitious substructure with a dynamic stiffness opposite to that of the residual substructure R and satisfying compatibility and equilibrium conditions. The dynamic equilibrium of the assembled structure RU and of the negative substructure is expressed in block diagonal format as:

$$\begin{bmatrix} \mathbf{Z}^{\mathbf{RU}} & \mathbf{0} \\ \mathbf{0} & -\mathbf{Z}^{\mathbf{R}} \end{bmatrix} \begin{Bmatrix} \mathbf{u}^{\mathbf{RU}} \\ \mathbf{u}^{\mathbf{R}} \end{Bmatrix} = \begin{Bmatrix} \mathbf{f}^{\mathbf{RU}} \\ \mathbf{f}^{\mathbf{R}} \end{Bmatrix} + \begin{Bmatrix} \mathbf{g}^{\mathbf{RU}} \\ \mathbf{g}^{\mathbf{R}} \end{Bmatrix} \tag{8.1}$$

where:

- $\mathbf{Z}^{\mathbf{RU}}$, $-\mathbf{Z}^{\mathbf{R}}$ are the dynamic stiffness matrices of the assembled structure RU and of the negative structure, respectively;
- $\mathbf{u}^{\mathbf{RU}}$, $\mathbf{u}^{\mathbf{R}}$ are the vectors of degrees of freedom of the assembled structure RU and of the negative structure, respectively;
- $\mathbf{f}^{\mathbf{RU}}$, $\mathbf{f}^{\mathbf{R}}$ are the external force vectors on the assembled structure RU and on the negative structure, respectively;
- $\mathbf{g}^{\mathbf{RU}}$, $\mathbf{g}^{\mathbf{R}}$ are the vectors of disconnection forces between the assembled structure and the negative structure (constraint forces associated with compatibility conditions).

Equilibrium of disconnection forces and compatibility must be considered at the interface between the assembled structure RU and the negative structure: such interface includes not only the coupling DoFs between substructures U and R, but includes as well the internal DoFs of substructure R (the blue part of the structure in Fig. 8.1). However, it is not required to consider the full set of these interface DoFs, because it is sufficient that the number of interface DoFs be not less than the number of coupling DoFs n_c. Therefore, several options for interface DoFs can be considered:

- standard interface, including only the coupling DoFs (c) between substructures U and R;
- extended interface, including also a subset of internal DoFs ($i \subseteq r$) of substructure R;

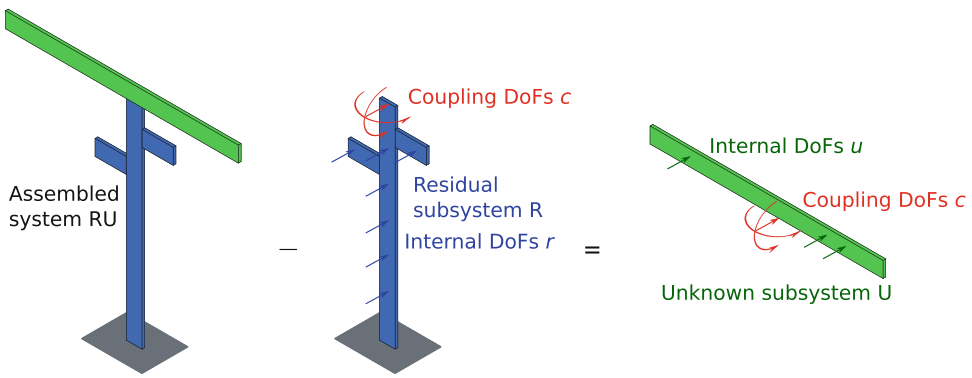

Fig. 8.1 Scheme of the direct decoupling problem

- mixed interface, including subsets of coupling DoFs ($d \subset c$) and internal DoFs ($i \subseteq r$);
- pseudo interface, including only internal DoFs ($i \subseteq r$) of substructure R.

The use of a mixed or pseudo interface may allow to ignore rotational coupling DoFs by substituting them with translational internal DoFs.

The compatibility condition at the (standard, extended, mixed, pseudo) interface DoFs implies that any pair of matching DoFs u_l^{RU} and u_m^R, i.e. DoF l on the coupled system RU and DoF m on subsystem R must have the same displacement, that is $u_l^{RU} - u_m^R = 0$. Let the number of interface DoFs on which compatibility is enforced be denoted as N_C.

The compatibility condition can be generally expressed as:

$$\begin{bmatrix} \mathbf{B_C^{RU}} & \mathbf{B_C^R} \end{bmatrix} \begin{Bmatrix} \mathbf{u^{RU}} \\ \mathbf{u^R} \end{Bmatrix} = \mathbf{0} \tag{8.2}$$

where each row of $\mathbf{B_C} = \begin{bmatrix} \mathbf{B_C^{RU}} & \mathbf{B_C^R} \end{bmatrix}$ corresponds to a pair of matching DoFs. Note that $\mathbf{B_C}$ has size $N_C \times (N_{RU} + N_R)$ and is, in most cases, a signed Boolean matrix.

It should be noted that the interface DoFs used to enforce the compatibility condition need not to be the same where equilibrium of disconnection forces is required, provided that compatibility is ensured by disconnection forces applied at such DoFs. If the compatibility and the equilibrium DoFs are not the same, the approach is called non-collocated [8]. The traditional approach, in which compatibility and equilibrium DoFs are the same, is called collocated.

Let N_E denote the number of interface DoFs on which equilibrium is enforced. The equilibrium of disconnection forces implies that their sum must be zero for any pair of matching DoFs belonging to the equilibrium interface, i.e. $g_r^{RU} + g_s^R = 0$. Furthermore, for any DoF k on the coupled system RU (or on the residual subsystem R) not belonging to the equilibrium interface, it must be $g_k^{RU} = 0$ ($g_k^R = 0$). Overall, the previous conditions can be expressed as:

$$\begin{bmatrix} \mathbf{L_E^{RU}} \\ \mathbf{L_E^R} \end{bmatrix}^T \begin{Bmatrix} \mathbf{g^{RU}} \\ \mathbf{g^R} \end{Bmatrix} = \mathbf{0} \tag{8.3}$$

where the matrix $\mathbf{L_E} = \begin{bmatrix} \mathbf{L_E^{RU}} & \mathbf{L_E^R} \end{bmatrix}$ is a Boolean localisation matrix. Note that the number of columns of $\mathbf{L_E}$ is equal to the number N_E of equilibrium interface DoFs plus the number N_{NE} of DoFs not belonging to the equilibrium interface. Note that $N_{NE} = N_{RU} + N_R - 2N_E$: in fact, the number of DoFs belonging to the equilibrium interface must be subtracted once from N_{RU} and once from N_R. Therefore, the size of $\mathbf{L_E}$ is $(N_{RU} + N_R) \times (N_{RU} + N_R - N_E)$.

By gathering Eqs. (8.1)–(8.3), one obtains the so-called 3-field formulation, from which several assembly techniques can be devised, such as: dual assembly [1, 9] where equilibrium is satisfied exactly by defining a unique set of disconnection force intensities; primal assembly [1, 10] where compatibility is satisfied exactly by defining a unique set of interface DoFs; hybrid assembly [11] where both compatibility and equilibrium are satisfied exactly. It can be shown [11] that whenever $N_C = N_E$, i.e. the number of compatibility and equilibrium DoFs is the same, all assembly techniques provide the same result. In the sequel, only the dual assembly is recalled.

8.2.1 Disconnection Force Intensities Provided by Dual Assembly

In the dual assembly, the equilibrium condition $g_r^{RU} + g_s^R = 0$ at a pair of equilibrium interface DoFs is ensured by choosing $g_r^{RU} = -\lambda_r$ and $g_s^R = \lambda_r$. If a Boolean matrix $\mathbf{B_E}$ related to interface equilibrium DoFs is defined similarly to $\mathbf{B_C}$, the overall interface equilibrium can be ensured by writing the disconnection forces in the form:

$$\begin{Bmatrix} \mathbf{g^{RU}} \\ \mathbf{g^R} \end{Bmatrix} = -\begin{bmatrix} \mathbf{B_E^{RU}}^T \\ \mathbf{B_E^R}^T \end{bmatrix} \boldsymbol{\lambda} \tag{8.4}$$

where $\boldsymbol{\lambda}$ are Lagrange multipliers corresponding to disconnection force intensities and $\mathbf{B_E}$ is a $N_E \times (N_{RU} + N_R)$ matrix. Since there is a unique disconnection force intensity λ_r for any pair of equilibrium DoFs, the interface equilibrium is satisfied automatically for any $\boldsymbol{\lambda}$, i.e.

$$\begin{bmatrix} \mathbf{L_E^{RU}} \\ \mathbf{L_E^R} \end{bmatrix}^T \begin{Bmatrix} \mathbf{g^{RU}} \\ \mathbf{g^R} \end{Bmatrix} = -\begin{bmatrix} \mathbf{L_E^{RU}} \\ \mathbf{L_E^R} \end{bmatrix}^T \begin{bmatrix} \mathbf{B_E^{RU}}^T \\ \mathbf{B_E^R}^T \end{bmatrix} \boldsymbol{\lambda} = \mathbf{0} \tag{8.5}$$

In the dual assembly, the total set of DoFs is retained, i.e. each interface DoF appears twice. Since Eq. (8.5) is always satisfied, the 3-field formulation reduces to:

$$\begin{cases} \begin{bmatrix} \mathbf{Z}^{\mathbf{RU}} & \mathbf{0} \\ \mathbf{0} & -\mathbf{Z}^{\mathbf{R}} \end{bmatrix} \begin{Bmatrix} \mathbf{u}^{\mathbf{RU}} \\ \mathbf{u}^{\mathbf{R}} \end{Bmatrix} + \begin{bmatrix} \mathbf{B}_{\mathbf{E}}^{\mathbf{RU}\,T} \\ \mathbf{B}_{\mathbf{E}}^{\mathbf{R}\,T} \end{bmatrix} \boldsymbol{\lambda} = \begin{Bmatrix} \mathbf{f}^{\mathbf{RU}} \\ \mathbf{f}^{\mathbf{R}} \end{Bmatrix} & (8.1^*) \\ \begin{bmatrix} \mathbf{B}_{\mathbf{C}}^{\mathbf{RU}} & \mathbf{B}_{\mathbf{C}}^{\mathbf{R}} \end{bmatrix} \begin{Bmatrix} \mathbf{u}^{\mathbf{RU}} \\ \mathbf{u}^{\mathbf{R}} \end{Bmatrix} = \mathbf{0} & (8.2) \end{cases}$$

or in more compact form:

$$\begin{cases} \mathbf{Z}\mathbf{u} + \mathbf{B}_{\mathbf{E}}{}^{T}\boldsymbol{\lambda} = \mathbf{f} & (8.1^*) \\ \mathbf{B}_{\mathbf{C}}\mathbf{u} = \mathbf{0} & (8.2) \end{cases}$$

To obtain $\boldsymbol{\lambda}$, Eq. (8.1*) can be written:

$$\mathbf{u} = -\mathbf{Z}^{-1}\mathbf{B}_{\mathbf{E}}{}^{T}\boldsymbol{\lambda} + \mathbf{Z}^{-1}\mathbf{f} \tag{8.6}$$

i.e., by noting that the inverse of the block diagonal dynamic stiffness matrix $\mathbf{Z}$ is:

$$\begin{bmatrix} \mathbf{Z}^{\mathbf{RU}} & \mathbf{0} \\ \mathbf{0} & -\mathbf{Z}^{\mathbf{R}} \end{bmatrix}^{-1} = \mathbf{Z}^{-1} = \mathbf{H} = \begin{bmatrix} \mathbf{H}^{\mathbf{RU}} & \mathbf{0} \\ \mathbf{0} & -\mathbf{H}^{\mathbf{R}} \end{bmatrix} \tag{8.7}$$

where $\mathbf{H}^{\mathbf{RU}}$ and $\mathbf{H}^{\mathbf{R}}$ are the FRFs of the assembled structure and of the residual substructure, Eq. (8.6) becomes:

$$\mathbf{u} = -\mathbf{H}\mathbf{B}_{\mathbf{E}}{}^{T}\boldsymbol{\lambda} + \mathbf{H}\mathbf{f} \tag{8.8}$$

which substituted in Eq. (8.2) gives:

$$\mathbf{B}_{\mathbf{C}}\mathbf{H}\mathbf{B}_{\mathbf{E}}{}^{T}\boldsymbol{\lambda} = \mathbf{B}_{\mathbf{C}}\mathbf{H}\mathbf{f} \tag{8.9}$$

from which the vector of disconnection force intensities $\boldsymbol{\lambda}$ is found as:

$$\boldsymbol{\lambda} = \left(\mathbf{B}_{\mathbf{C}}\mathbf{H}\mathbf{B}_{\mathbf{E}}{}^{T}\right)^{+}\mathbf{B}_{\mathbf{C}}\mathbf{H}\mathbf{f} \tag{8.10}$$

To obtain a determined or overdetermined matrix for the generalized inversion operation, the number of rows of $\mathbf{B}_{\mathbf{C}}$ must be greater or equal than the number of rows of $\mathbf{B}_{\mathbf{E}}$, i.e.

$$N_C \geq N_E \geq n_c \tag{8.11}$$

8.2.2 FRF and Transmissibility Indicators

The set of disconnection forces is not unique since it depends on the choice of equilibrium and compatibility DoFs. However, disconnection forces must be able to cancel constraint forces at the coupling DoFs. If coupling DoFs include rotational DoFs, constraint forces include moments about some given axes. Several sets of disconnection forces can be devised:

- the trivial set, consisting of disconnection forces acting at the coupling DoFs and opposite to the constraint forces;
- non trivial sets of disconnection forces acting at different DoFs but able to cancel the constraint forces at the coupling DoFs.

In the former case, disconnection forces may include disconnection moments opposite to the constraint moments. In the latter case, disconnection moments can be substituted by disconnection forces applied to internal DoFs, but able to provide a moment about the rotation axes. Therefore, a qualitative criterion for the selection of internal DoFs to replace coupling DoFs that are difficult to observe, such as rotational DoFs, was proposed as [7]:

Internal DoFs must be such that disconnection forces that are applied to them are able to control coupling DoFs, e.g., if one of the coupling DoFs is a rotation about a given axis, the line of action of the substituted force must not intersect such axis.

To devise a quantitative indicator for the optimal selection of a set of disconnection forces, a theoretical model of either the coupled structure or the residual substructure must be available: in fact, unmeasured DoFs (e.g. rotational DoFs) are required to set up any such indicator. A model of the residual substructure can be built more easily than a model of the coupled structure, and it is therefore preferred.

With reference to the case when unmeasured coupling DoFs are rotations, the rotation ϑ_c at a coupling DoF c due to a force f_i acting at any given internal DoF i and to a moment M_c acting at the coupling DoF, can be written as:

$$\vartheta_c = H_{ci} f_i + H_{cc} M_c \tag{8.12}$$

Possible indicators are:

- the rotation ϑ_c at an unloaded coupling DoF c ($M_c = 0$) for a force f_i at any given internal DoF i, leading to the frequency response function H_{ci}, which can be denoted as FRF indicator:

$$\left.\frac{\vartheta_c(\omega)}{f_i(\omega)}\right|_{M_c=0} = H_{ci}(\omega) \tag{8.13}$$

- the moment M_c at a blocked coupling DoF c ($\vartheta_c = 0$) determined by a force f_i at any given internal DoF i, leading to a sort of force transmissibility T_{ci}, which can be denoted as Transmissibility indicator:

$$\left.\frac{M_c(\omega)}{f_i(\omega)}\right|_{\vartheta_c=0} = -\frac{H_{ci}(\omega)}{H_{cc}(\omega)} = T_{ci}(\omega) \tag{8.14}$$

The FRF indicator can be also evaluated by using a truncated modal expansion, whilst the use of a truncated modal expansion for the Transmissibility indicator produces bad results around the zeros of H_{cc}.

The proposed indicators are frequency dependent. However, it is believed that the low frequency range is the most significant since it accounts for the static behaviour which is at the origin of qualitative criterion stated previously. The estimation of the static FRF indicator can be performed using a truncated modal expansion:

$$H_{ci}(\omega = 0) = \sum_{r=1}^{N_m} \frac{\psi_c^{(r)} \psi_i^{(r)}}{m_r \omega_r^2} \tag{8.15}$$

where N_m is the number of used modes, $\psi_c^{(r)}$ is the amplitude of mode r at DoF c, m_r is r-th modal mass and ω_r is the r-th eigenfrequency.

The estimation of the static Transmissibility indicator can also be performed using a truncated modal expansion:

$$T_{ci}(\omega = 0) = -\frac{\displaystyle\sum_{r=1}^{N_m} \frac{\psi_c^{(r)} \psi_i^{(r)}}{m_r \omega_r^2}}{\displaystyle\sum_{r=1}^{N_m} \frac{\psi_c^{(r)} \psi_c^{(r)}}{m_r \omega_r^2}} \tag{8.16}$$

8.2.3 Prediction of the FRF of the Unknown Subsystem

The FRF of the unknown subsystem U can be obtained by back-substituting $\boldsymbol{\lambda}$ in Eq. (8.1*), and by isolating $\mathbf{u}$ at the left hand side:

$$\mathbf{u} = \left(\mathbf{H} - \mathbf{H}\mathbf{B}_{\mathbf{E}}{}^{T}\left(\mathbf{B}_{\mathbf{C}}\mathbf{H}\mathbf{B}_{\mathbf{E}}{}^{T}\right)^{+}\mathbf{B}_{\mathbf{C}}\mathbf{H}\right)\mathbf{f} \tag{8.17}$$

which is in the form $\mathbf{u} = \mathbf{H}\mathbf{f}$, so that the FRF of the unknown subsystem U is:

$$\mathbf{H}^{\mathbf{U}} = \mathbf{H} - \mathbf{H}\mathbf{B}_{\mathbf{E}}{}^{T}\left(\mathbf{B}_{\mathbf{C}}\mathbf{H}\mathbf{B}_{\mathbf{E}}{}^{T}\right)^{+}\mathbf{B}_{\mathbf{C}}\mathbf{H} \tag{8.18}$$

With the dual assembly, the rows and the columns of $\mathbf{H}^{\mathbf{U}}$ corresponding to compatibility and equilibrium DoFs appear twice. Furthermore, when using an extended or mixed interface, $\mathbf{H}^{\mathbf{U}}$ contains some meaningless rows and columns: those corresponding to the internal DoFs of the residual substructure R. Obviously, only meaningful and independent entries are retained.

8.3 Test Bed

The assembled system is an aluminium tree structure (Fig. 8.2). The residual substructure R is a cantilever column with two staggered short arms and the unknown substructure U is a horizontal beam. The horizontal beam is bolted to the top of the column, involving both translational and rotational DoFs. The geometrical dimensions are shown in Table 8.1. The cross section is 40 mm×8 mm for all beams, with the short side along the z-direction.

The experimental FRFs of the assembled system RU up to 2000 Hz are obtained by applying impact excitation and measuring the resulting accelerations along z-direction at seven locations (3, 6, 9, 10, 11, 13, 20), as shown in Fig. 8.3. For

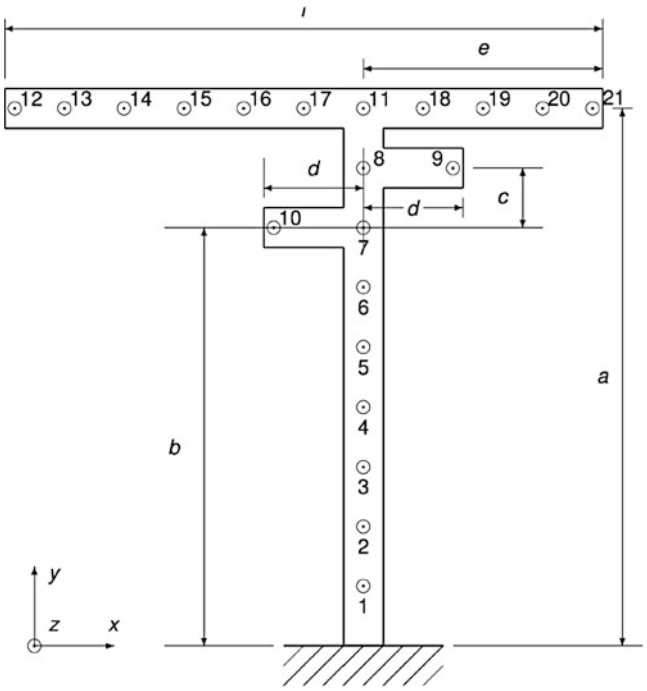

Fig. 8.2 Sketch of the test structure

Table 8.1 Geometrical dimensions (mm)

a	b	c	d	e	l
540	420	60	100	240	600

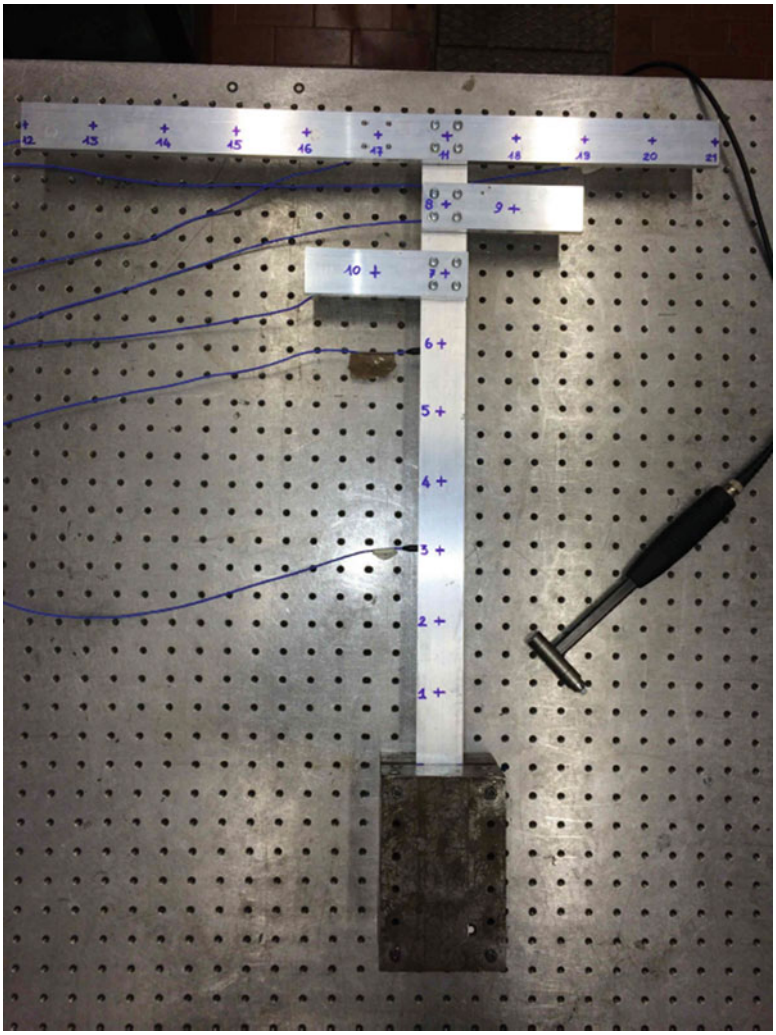

Fig. 8.3 Assembled system

the residual subsystem R (column) the experimental FRFs are similarly measured at five locations (3, 6, 9, 10, 11), as shown in Fig. 8.4. Coupling DoFs are: $11z$, $11\vartheta_x$ and $11\vartheta_y$, that is one translational DoF and two rotational DoFs.

A detail of the bolted junction between the beam and the column is shown in Fig. 8.5. Finally, to check decoupling results, FRFs are measured also at three locations (11, 13, 20) of the unknown subsystem U (beam), supported by an inflated rubber tube, shown in Fig. 8.6, giving rigid body eigenfrequencies well separated from the first flexible mode of the beam.

Measurements are performed by placing the accelerometers at the underside of each (sub)-structure. In order to obtain a complete FRF matrix, as required by the decoupling technique, impact excitation is sequentially provided on all DoFs at the topside of each (sub)-structure.

To compute the indicators that are required for the optimal selection of the location of disconnection forces, an FE model of the residual substructure is built using beam elements. The mechanical properties of the structure are: $E = 7.0 \cdot 10^{10}$ N/m^2, $\rho = 2700$ kg/m^3, modal damping $\zeta = 0.005$. Inertance FRFs are obtained from the FE model at DoFs $1z$–$11z$, $11\vartheta_x$ and $11\vartheta_y$ shown in Fig. 8.2: among them, DoFs $11z$, $11\vartheta_x$ and $11\vartheta_y$ are the coupling DoFs, DoFs $1z$–$10z$ are the internal DoFs of the residual substructure R. Table 8.2 shows the natural frequencies of the residual substructure, obtained from the initial FE model and identified from the measured FRFs. In order to improve the correlation between experimental and FE natural frequencies, a simple model updating is performed by tuning the stiffness of two rotational springs acting on DoFs ϑ_x and ϑ_y of the fixed joint. The natural frequencies obtained using the updated model are also shown in Table 8.2: the three lowest natural frequencies are in perfect agreement, and the agreement between higher natural frequencies is anyway improved.

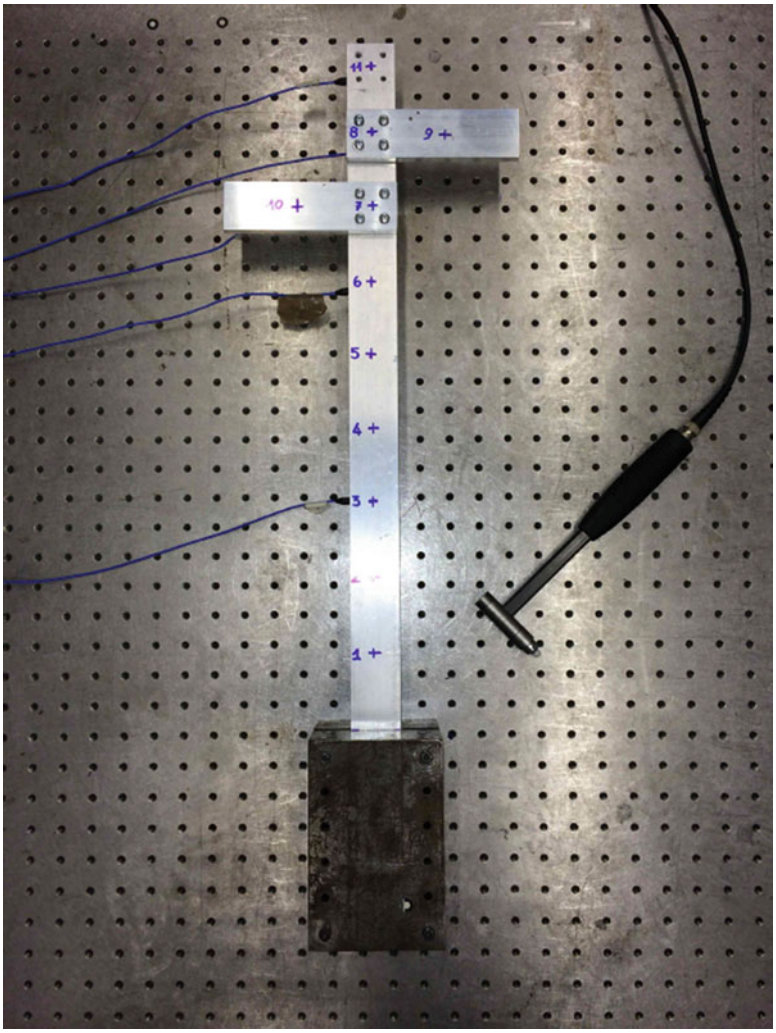

Fig. 8.4 Residual subsystem

8.3.1 Analysis of FRF and Transmissibility Indicators

Since rotational DoFs at the junction between the residual subsystem and the unknown subsystem are not measured, an analysis of FRF and Transmissibility indicators is performed to select the optimal DoFs that should be used to substitute DoFs $11\vartheta_x$ and $11\vartheta_y$.

Figures 8.7 and 8.8 show the FRF indicators $H_{11\vartheta_x,i}$ and $H_{11\vartheta_y,i}$ computed by Eq. (8.13), showing the propensity of a force applied to DoF i to excite a rotation on Dofs $11\vartheta_x$ and $11\vartheta_y$ respectively. From Fig. 8.8 it can be noticed that a force should be applied either to DoF $9z$ or to DoF $10z$ in order to excite Dof $11\vartheta_y$: the effect of a force applied to a different DoF is several order of magnitude lower especially in the low frequency range. By applying a force either to DoF $9z$ or to DoF $10z$, DoF $11\vartheta_x$ is sufficiently excited, as confirmed by the observation of Fig. 8.7. The same conclusions can be drawn by observing Table 8.3 which shows the static FRF indicators: in order to excite DoF $11\vartheta_y$ it is essential to apply a force either to DoF $9z$ or to DoF $10z$.

Figures 8.9 and 8.10 show the Transmissibility indicators $T_{11\vartheta_x,i}$ and $T_{11\vartheta_y,i}$, computed by Eq. (8.14), showing the propensity of a force applied to DoF i to produce a moment about Dofs $11\vartheta_x$ and $11\vartheta_y$ respectively. From Fig. 8.10 it can be noticed that a force should be applied either to DoF $9z$ or to DoF $10z$ in order to produce a moment about DoF $11\vartheta_y$: the effect of a force applied to a different DoF is several order of magnitude lower. By applying a force either to DoF $9z$ or to DoF $10z$, a significant moment about DoF $11\vartheta_x$ is produced, as confirmed by the observation of Fig. 8.9. The same conclusions can be drawn by observing Table 8.4 which shows the static Transmissibility indicators: in order to produce a moment about DoF $11\vartheta_y$ it is essential to apply a force either to DoF $9z$ or to DoF $10z$.

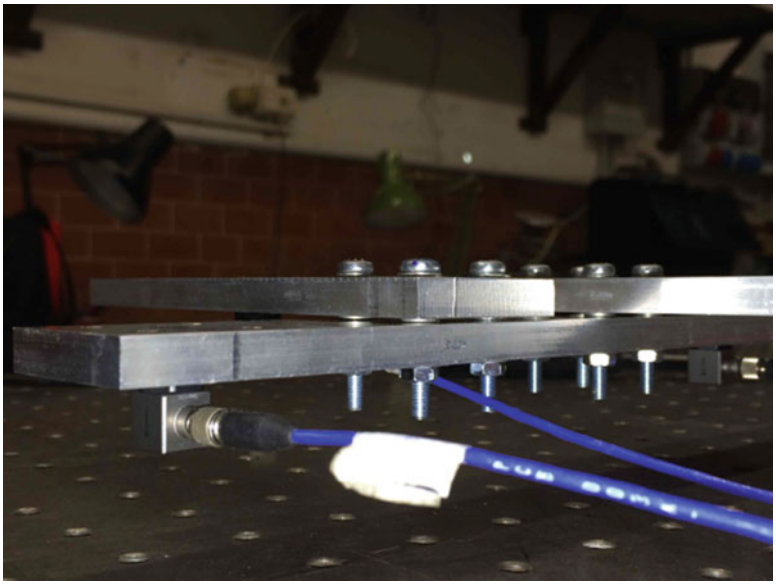

Fig. 8.5 Detail of the bolted junction

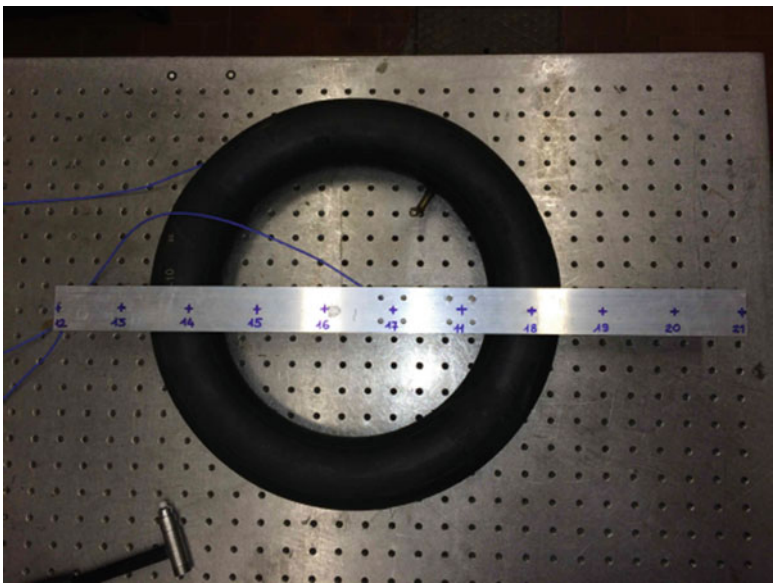

Fig. 8.6 Unknown subsystem

Table 8.2 Natural frequencies of the residual substructure

Mode	1	2	3	4	5	6	7	8	9
Initial model	16.40	109.63	144.01	376.67	549.15	763.61	1219.28	1256.53	1764.07
Experimental	13.51	89.04	124.56	314.65	450.22	658.82	989.98	1053.01	1507.24
Updated model	13.51	89.03	125.65	340.22	533.96	680.65	904.98	1129.27	1637.79

8.3.2 Decoupling

The FRFs of subsystem U can be determined by the procedure described previously and summarized in Eq. (8.18), where compatibility and equilibrium DoFs are defined case by case. A collocated approach is adopted in which compatibility and equilibrium DoFs are the same. Only mixed interfaces are considered. FRFs to be used in decoupling can be either the raw FRFs or can be obtained by a curve fitting procedure. Raw FRFs are used.

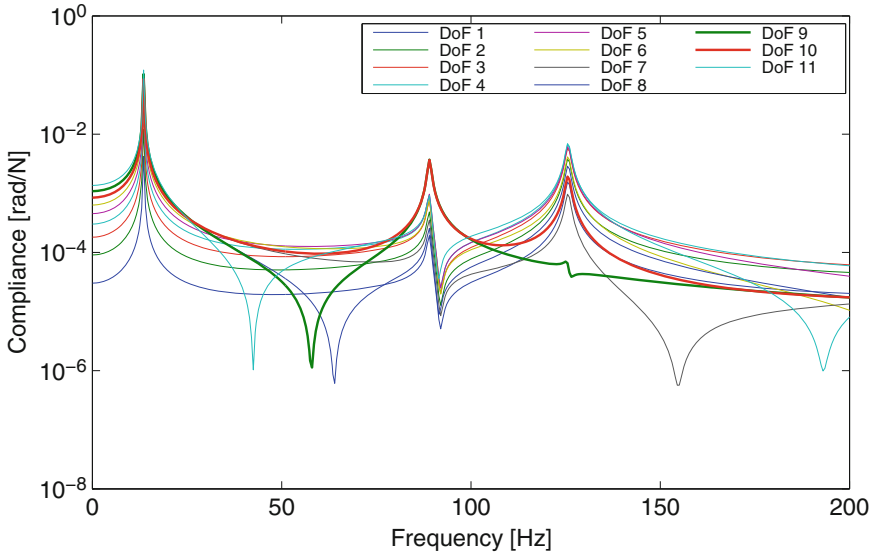

Fig. 8.7 FRF indicator $H^R_{11\vartheta_x,i}$ for $i = 1z \dots 11z$

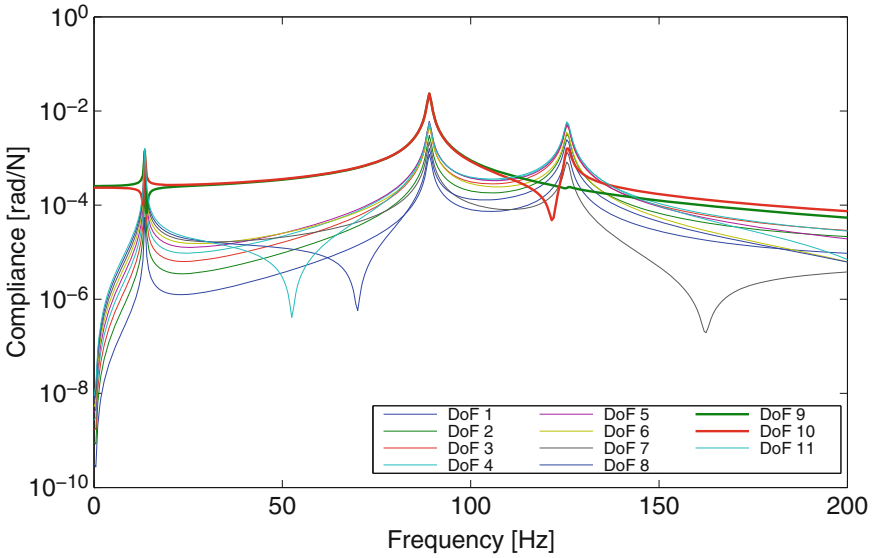

Fig. 8.8 FRF indicator $H^R_{11\vartheta_y,i}$ for $i = 1z \dots 11z$

The number n_c of coupling DoFs is 3 so that it must be $N_E \geq n_c = 3$. Some tests using mixed interfaces with $N_C = N_E = 4$ are performed.

First, a mixed interface including the coupling DoF $11z$ and the internal DoFs $3z$, $6z$ and $9z$ is used. As shown previously, a force applied to DoF $9z$ is able to excite the coupling DoF $11\vartheta_y$, whilst forces applied to DoFs $3z$, $6z$ and $9z$ are all able to excite the coupling DoF $11\vartheta_x$. Therefore

$$\mathbf{B_C} = \mathbf{B_E} = \begin{array}{c} \begin{matrix} u^{RU}_{3z} & u^{RU}_{6z} & u^{RU}_{9y} & u^{RU}_{11z} & u^{R}_{3z} & u^{R}_{6z} & u^{R}_{9z} & u^{R}_{11z} \end{matrix} \\ \left[\begin{array}{cccc|cccc} 1 & 0 & 0 & 0 & -1 & 0 & 0 & 0 \\ 0 & 1 & 0 & 0 & 0 & -1 & 0 & 0 \\ 0 & 0 & 1 & 0 & 0 & 0 & -1 & 0 \\ 0 & 0 & 0 & 1 & 0 & 0 & 0 & -1 \end{array}\right] \\ \mathbf{B^{RU}_C} \qquad\qquad\qquad \mathbf{B^{R}_C} \end{array} \tag{8.19}$$

Table 8.3 Static FRF indicators (values indicating which DoFs should be selected are highlighted in bold)

DoF i	$H_{11\vartheta_x,i}(\omega = 0)$	$H_{11\vartheta_y,i}(\omega = 0)$
$1z$	2.9e-05	6.8e-08
$2z$	9.1e-05	4.9e-08
$3z$	1.8e-04	2.4e-08
$4z$	3.0e-04	1.0e-07
$5z$	4.5e-04	7.4e-08
$6z$	6.3e-04	8.6e-08
$7z$	8.4e-04	1.2e-07
$8z$	1.1e-03	3.8e-07
$9z$	1.1e-03	**2.5e-04**
$10z$	8.4e-04	**2.3e-04**
$11z$	1.3e-03	5.9e-07

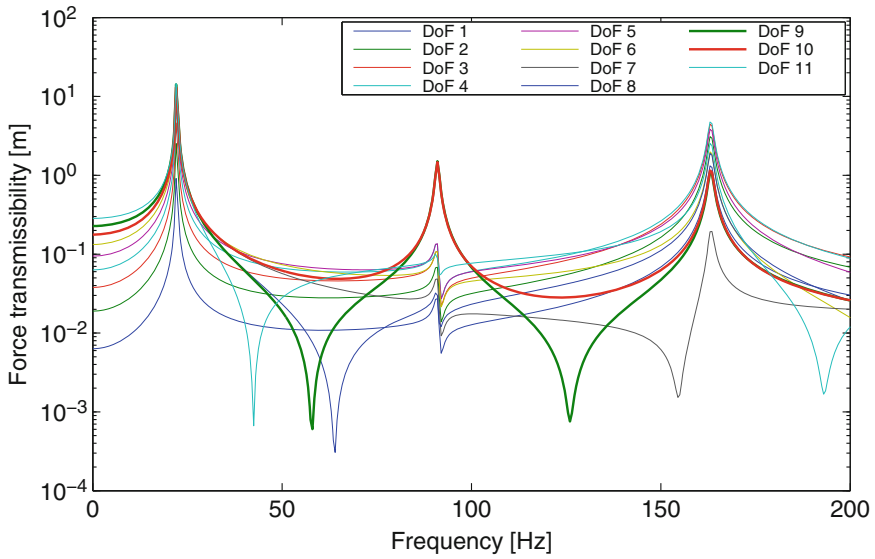

Fig. 8.9 Transmissibility indicator $T_{11\vartheta_x,i}$ for $i = 1z \ldots 11z$

Table 8.4 Static transmissibility indicators (values indicating which DoFs should be selected are highlighted in bold)

DoF i	$T_{11\vartheta_x,i}(\omega = 0)$	$T_{11\vartheta_y,i}(\omega = 0)$
$1z$	6.6e-03	1.3e-05
$2z$	2.0e-02	9.8e-06
$3z$	4.0e-02	4.8e-06
$4z$	6.7e-02	2.0e-05
$5z$	1.0e-01	1.5e-05
$6z$	1.4e-01	1.7e-05
$7z$	1.8e-01	2.4e-05
$8z$	2.4e-01	7.6e-05
$9z$	2.4e-01	**5.1e-02**
$10z$	1.8e-01	**4.7e-02**
$11z$	3.0e-01	1.1e-04

The FRF of the unknown substructure U is shown in Fig. 8.11: the peak around 1000 Hz is not well described and some other peaks are shifted towards higher frequencies.

Another mixed interface including the coupling DoF $11z$ and the internal DoFs $3z$, $9z$ and $10z$ is used. Forces applied to DoFs $9z$ and $10z$ are able to excite the coupling DoF $11\vartheta_y$, whilst forces applied to DoFs $3z$, $9z$ and $10z$ are all able to excite the coupling DoF $11\vartheta_x$. $\mathbf{B_C}$ and $\mathbf{B_E}$ are built similarly to the first case. The FRF of the unknown substructure U is shown in Fig. 8.12: the peak around 600 Hz is shifted forward and the FRF around it is scattered. However, the peak around 1000 Hz is very well described.

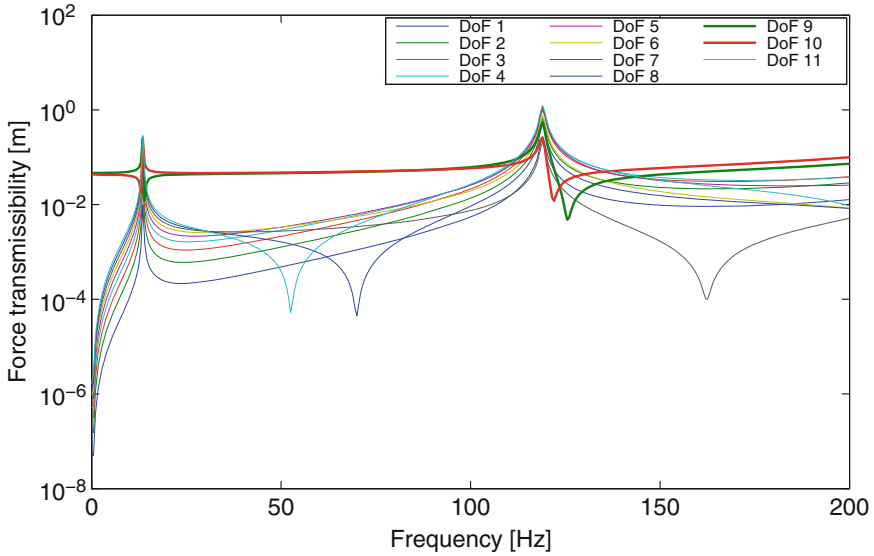

Fig. 8.10 Transmissibility indicator $T_{11\vartheta_y,i}$ for $i = 1z \dots 11z$

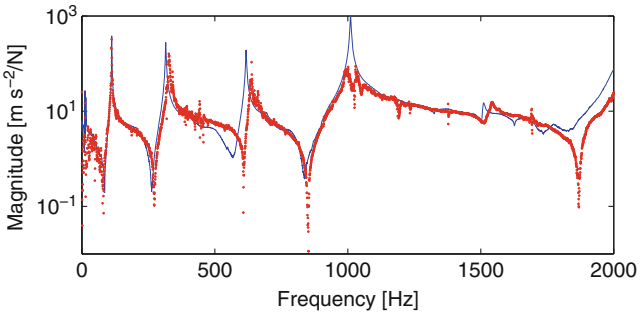

Fig. 8.11 $H^U_{11z,11z}$: measured (*blue solid line*), computed using coupling DoF $11z$ and internal DoFs $3z$, $6z$, $9z$ (*red astrerisks*)

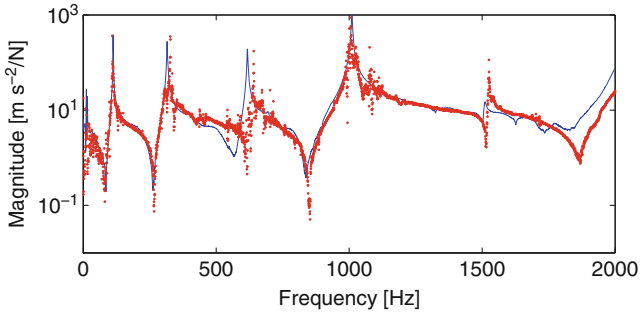

Fig. 8.12 $H^U_{11z,11z}$: measured (*blue solid line*), computed using coupling DoF $11z$ and internal DoFs $3z$, $9z$, $10z$ (*red astrerisks*)

A new set of attempts is performed using mixed interfaces including only 3 DoFs. A mixed interface that includes the coupling DoF $11z$ and the internal DoFs $3z$ and $9z$ is used. A force applied to DoF $9z$ is able to excite the coupling DoF $11\vartheta_y$, whilst forces applied to DoFs $3z$ and $9z$ are all able to excite the coupling DoF $11\vartheta_x$. The FRF of the unknown substructure U is shown in Fig. 8.13: the result is quite clean with no significant drawbacks.

It can be noticed that, although in all previous cases the selected internal DoFs comply with the directions provided by FRF and Transmissibility indicators, the quality of results is not always the same. This can be ascribed to systematic errors that affect measured FRFs, and can not be easily estimated.

However, if the selected internal DoFs do not comply with the FRF and a transmissibility indications, results are much worse. For instance, a mixed interface that includes the coupling DoF $11z$ and the internal DoFs $3z$ and $6z$ is used: in this

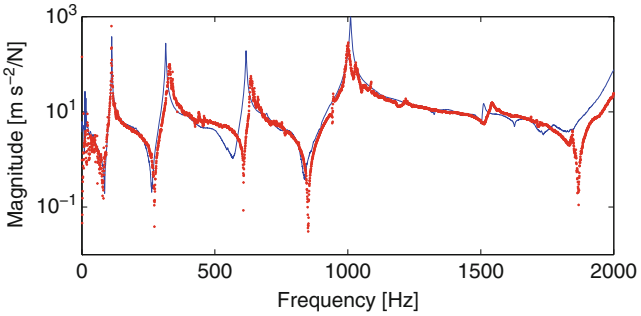

Fig. 8.13 $H^U_{11z,11z}$: measured (*blue solid line*), computed using coupling DoF $11z$ and internal DoFs $3z$, $9z$ (*red astrerisks*)

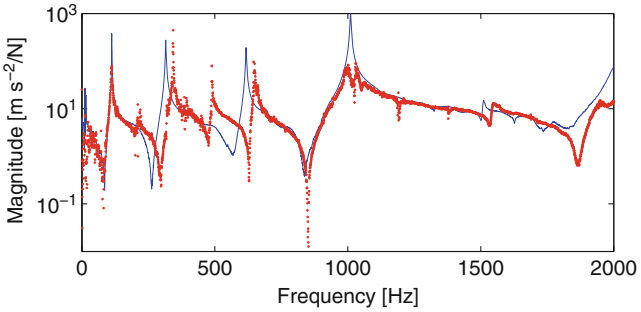

Fig. 8.14 $H^U_{11z,11z}$: measured (*blue solid line*), computed using coupling DoF $11z$ and internal DoFs $3z$, $6z$ (*red astrerisks*)

case, the coupling DoF $11\vartheta_y$ is not sufficiently excited. The FRF of the unknown substructure U is shown in Fig. 8.14. The result is quite bad as expected: the two peaks around 315 Hz and 615 Hz are shifted forward, a spurious peak appears around 500 Hz, and the peak around 1000 Hz is not well described.

8.4 Concluding Remarks

In this paper, a procedure for an optimal selection of translational internal DoFs used to replace rotational coupling DoFs is developed. Two families of indicators are proposed, based either on the Frequency Response Function (FRF) or on the transmissibility between internal and coupling DoFs.

Such indicators are tested with satisfactory results on an assembled structure made by a cantilever column with two staggered short arms (residual substructure) coupled to a horizontal beam (unknown substructure). This type of coupling involves both flexural and torsional DoFs, on which rotational FRFs can not be measured. It is found that bad results are obtained whenever forces applied to the selected internal DoFs are either unable to excite rotational coupling DoFs or unable to produce a moment about such DoFs. However, even when internal DoFs are optimally selected, the quality of the results may be affected by systematic errors that are difficult to detect a priori.

Acknowledgements This research is supported by grants from University of Rome La Sapienza and University of L'Aquila.

References

1. de Klerk, D., Rixen, D.J., Voormeeren, S.: General framework for dynamic substructuring: history, review, and classification of techniques. AIAA J. **46**(5), 1169–1181 (2008)
2. Sestieri, A., Salvini, P., D'Ambrogio, W.: Reducing scatter from derived rotational data to determine the frequency response function of connected structures. Mech. Syst. Signal Process. **5**(1), 25–44 (1991)
3. Stanbridge, A., Ewins, D.: Measurement of translational and angular vibration using a scanning laser Doppler vibrometer. Shock. Vib. **3**, 141–152 (1996)

4. Bello, M., Sestieri, A., D'Ambrogio, W., La Gala, F.: Development of a rotation transducer based on bimorph PZT's. Mech. Syst. Signal Process. **17**(5), 1069–1081 (2003)
5. D'Ambrogio, W., Fregolent, A.: Are rotational DoFs essential in substructure decoupling? In: Allen, M., Mayes, R., Rixen, D. (eds.) Dynamics of Coupled Structures, vol. 1. Conference Proceedings of the Society for Experimental Mechanics Series, pp. 27–36. Springer International Publishing, Cham (2014)
6. D'Ambrogio, W., Fregolent, A.: Ignoring rotational DoFs in decoupling structures connected through flexotorsional joints. In: Allen, M., Mayes, R.L., Rixen, D.J. (eds.) Dynamics of Coupled Structures, vol. 4. Conference Proceedings of the Society for Experimental Mechanics Series, pp. 57–69. Springer International Publishing, Cham (2015)
7. D'Ambrogio, W., Fregolent, A.: Selection of internal DoFs to replace hard to measure coupling dofs in substructure decoupling. Proceedings of ICoEV 2015, International Conference on Engineering Vibration, pp. 1225–1234. Faculty for Mechanical Engineering, University of Ljubljana, 7–10 September 2015
8. Voormeeren, S.N., Rixen, D.J.: A family of substructure decoupling techniques based on a dual assembly approach. Mech. Syst. Signal Process. **27**, 379–396 (2012). doi:10.1016/j.ymssp.2011.07.028
9. D'Ambrogio, W., Fregolent, A.: The role of interface DoFs in decoupling of substructures based on the dual domain decomposition. Mech. Syst. Signal Process. **24**(7), 2035–2048 (2010). Also in Proceedings of ISMA 2010, pp. 1863–1880, Leuven. doi:10.1016/j.ymssp.2010.05.007
10. D'Ambrogio, W., Fregolent, A.: Direct decoupling of substructures using primal and dual formulation. In: Linking Models and Experiments, vol. 2. Conference Proceedings of the Society of Experimental Mechanics Series, vol. 4, pp. 47–76. Springer, Jacksonville, FL (January 31–February 3, 2011)
11. D'Ambrogio, W., Fregolent, A.: Inverse dynamic substructuring using direct hybrid assembly in the frequency domain. Mech. Syst. Signal Process. **45**(2), 360–377 (2014)

Chapter 9
State-Space Substructuring with Transmission Simulator

Maren Scheel and Anders T. Johansson

Abstract The dynamic substructuring focus group of SEM organizes sessions on experimental substructuring each IMAC conference and has been doing so for a number of years. Over the last decade, the use of so-called transmission simulators has trended within the community. Transmission simulators are well-modeled parts that fit to the interface of the substructures to be coupled to allow distributed interfaces and relaxation of the coupling conditions by the transmission simulator's analytical modes at the cost of adding a decoupling step to the substructuring problem. In this paper, the transmission simulator concept is adapted to state-space substructuring. Experimental-analytical substructuring of the focus group benchmark structure, the Ampair A600 wind turbine, is used to verify the methodology.

Keywords Dynamic substructuring • Transmission simulator • State-space coupling • Ampair wind turbine • Experimental dynamics

9.1 Introduction

Dynamic substructuring is the idea of dividing complex structures into simpler components which can be analyzed in more detail. Then, the dynamics of the substructures are combined to obtain an assembled model. If the substructures are moreover developed by separate project groups, dynamic substructuring is highly beneficial and widely used for Finite Element (FE) simulations [1].

While substructuring has been performed with great success in FE applications, comparatively few applications of experimental substructuring can be found, although recent years have seen an increased interest in the latter. The most commonly used experimental substructuring techniques are Component Mode Synthesis (CMS) and Frequency Based Substructuring (FBS). Su and Juang [2] introduced a different approach using first-order state-space systems, which was further developed by Sjövall [3]. This method was extensively used by Liljerehn (e.g. [4]) who also contributed to the system identification procedure. Liljerehn concluded that great care has to be taken in deriving physical models from the measurement data. Particularly, non-passive state-space systems or systems that do not fulfill Newton's second law may cause unphysical coupling results [5].

Experimental-analytical coupling causes difficulties connected to the interface. In general, not all degrees of freedom at the coupling interface can be measured as would be needed to enforce strict compatibility. For some structures, the actual connection points are not accessible at all.

Another crucial obstacle for experimental-analytical substructuring is the possibly inadequate mode shape basis. Generally, the experimental model is obtained by measurements with free-free boundary conditions. However, stress at the interface is not included in free-free mode shapes. Thus, a large number of mode shapes is typically necessary in order to replicate the interface motion in a coupled configuration. An enlargement of the mode shape basis, e.g. using also constraint modes, as done in the Craig-Bampton Method [6], is on the other hand infeasible for experimental models since this would require the application of displacements on distinct degrees of freedom.

To overcome these drawbacks, the transmission simulator was introduced for CMS by Allen et al. [7] and for FBS by Mayes et al. [8]. The transmission simulator also allows for the inclusion of joint properties in the model if the joints of

M. Scheel (✉)
Applied Mechanics, Chalmers University of Technology, Hörsalsvägen 7A, S-41296 Göteborg, Sweden

Institute for Nonlinear Mechanics, University of Stuttgart, Pfaffenwaldring 9, D-70569 Stuttgart, Germany

A.T. Johansson
Applied Mechanics, Chalmers University of Technology, Hörsalsvägen 7A, S-41296 Göteborg, Sweden

© The Society for Experimental Mechanics, Inc. 2016

M. Allen et al. (eds.), *Dynamics of Coupled Structures, Volume 4*, Conference Proceedings of the Society for Experimental Mechanics Series, DOI 10.1007/978-3-319-29763-7_9

the transmission simulator resemble the actual joints of the coupled system. The method works as follows: A well-modeled additional structure dubbed transmission simulator is joined with the structure of interest, and the compound system is then measured. This has the effect of exciting and mass-loading the interface to extract a more suitable mode shape basis. To obtain a model of the structure of interest, an analytical model of the transmission simulator is used to remove its effect from the measured system. This is done with dynamic substructuring, but instead of equating the motion of the coupling degrees of freedom at the interface between transmission simulator and structure of interest, the measurement points on the transmission simulator are coupled to the exact same points of the negative, analytical transmission simulator model. Thus, measuring the actual connection points is avoided. The compatibility conditions are fulfilled in a least-squares sense by the use of the Modal Constraints for Fixture and Subsystem (MCFS) method suggested by Allen et al. [7], and hence, MCFS is further also capable to compensate for measurement errors.

Dynamic substructuring with the transmission simulator approach has been repeatedly applied to the SEM subtructuring focus group benchmark structure Ampair A600 wind turbine, as has been presented over the last few IMAC conferences. Rohe and Mayes [9] used the hub as transmission simulator to couple the rotor to the tower of the wind turbine, whereas Roettgen and Mayes [10] coupled one blade to the hub three times to obtain a full rotor model, again using the hub as transmission simulator. The hub is a convenient transmission simulator since it is stiff compared to the blades and can be modelled fairly easily. Furthermore, the actual joints are used for connecting the interfaces yielding a realistic interface excitation.

In this paper, the transmission simulator approach is applied to state-space substructuring. To the best of the authors' knowledge, relaxed compatibility constraints and the inclusion of the transmission simulator in state-space coupling theory is novel. The methodology is verified on the Ampair A600 wind turbine. In this work, the substructuring task of Roettgen and Mayes [10] is repeated. However, three different blades are measured in order to account for the spread found in the blades [11]. Figure 9.1 sketches the coupling scheme. First, the blades labeled with the numbers 790, 828, and 852 are individually attached to the hub, and these one-bladed hub configurations are measured. Then, a FE model of the hub used as transmission simulator is subtracted twice. Finally, the three-bladed hub dubbed assembled structure is obtained. To compare the coupled model, the assembled three-bladed hub is also measured.

The present paper is based on the Master's thesis of Maren Scheel [12] and is structured as follows: First, MCFS in the modal domain is briefly reiterated from the paper of Allen et al. [7] followed by the derivation of the transmission simulator method in state-space in the ensuing theory section. Then, the experimental setup is elaborated on, and the results of the substructuring are presented. The paper is rounded off by a discussion and final remarks.

9.2 Theory

Removing the influence of one structure from another is equal to adding a negative representation of the first one to the latter [7]. In the subsequent, this procedure will be dubbed subtraction of a system. Further, the system to remove is denoted transmission simulator *ts* and is supposed to be subtracted from the so-called total structure *tot*. The result is a model for the structure of interest, which is typically one of the components to make up the assembled structure; see also Fig. 9.1. A negative system has a negative mass, damping, and stiffness [7]. The still uncoupled system of negative transmission simulator and total structure can be written in compact form using block diagonal matrices [1]. In the modal domain, this is

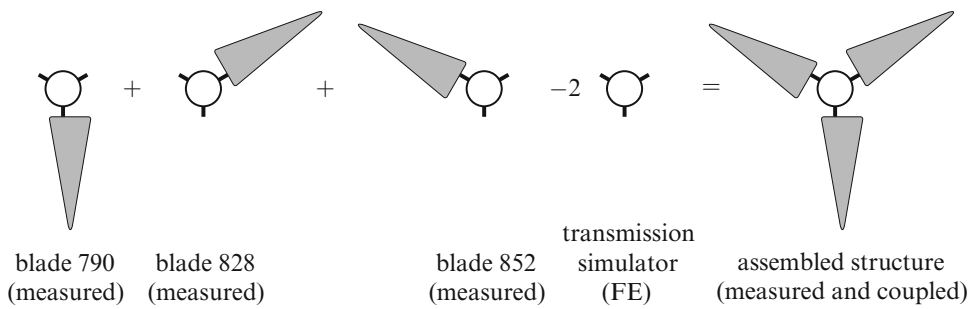

Fig. 9.1 The substructuring task in this paper. Three one-bladed hubs are measured and coupled with two negative FE transmission simulators. The obtained coupled model of the assembled structure is compared with measurements

$$\begin{bmatrix} \boldsymbol{M}_{mod}^{(tot)} & \boldsymbol{0} \\ \boldsymbol{0} & -\boldsymbol{M}_{mod}^{(ts)} \end{bmatrix} \begin{Bmatrix} \ddot{\eta}^{(tot)} \\ \ddot{\eta}^{(ts)} \end{Bmatrix} + \begin{bmatrix} \boldsymbol{V}_{mod}^{(tot)} & \boldsymbol{0} \\ \boldsymbol{0} & -\boldsymbol{V}_{mod}^{(ts)} \end{bmatrix} \begin{Bmatrix} \dot{\eta}^{(tot)} \\ \dot{\eta}^{(ts)} \end{Bmatrix} + \begin{bmatrix} \boldsymbol{K}_{mod}^{(tot)} & \boldsymbol{0} \\ \boldsymbol{0} & -\boldsymbol{K}_{mod}^{(ts)} \end{bmatrix} \begin{Bmatrix} \eta^{(tot)} \\ \eta^{(ts)} \end{Bmatrix} = \begin{Bmatrix} f_{mod}^{(tot)} \\ f_{mod}^{(ts)} \end{Bmatrix}. \tag{9.1}$$

Here, $\boldsymbol{M}_{mod}$, $\boldsymbol{V}_{mod}$, and $\boldsymbol{K}_{mod}$ are the modal mass, damping, and stiffness matrices, respectively. If the mode shapes are mass normalized, $\boldsymbol{M}_{mod} = diag(1)$, $\boldsymbol{V}_{mod} = diag(2\xi_i\omega_i)$, and $\boldsymbol{K}_{mod} = diag(\omega_i^2)$ holds. η are the modal coordinates and f_{mod} the modal forces. The superscripts distinguish the models.

The compatibility condition for MCFS is a modal relaxation of the constraint $q_{meas}^{(ts)} = q_{meas}^{(tot)}$, that is

$$\eta^{(ts)} = \boldsymbol{\Phi}_{meas}^{(ts)\,+} q_{meas}^{(ts)} = \boldsymbol{\Phi}_{meas}^{(ts)\,+} q_{meas}^{(tot)} = \boldsymbol{\Phi}_{meas}^{(ts)\,+} \boldsymbol{\Phi}_{meas}^{(tot)} \eta^{(tot)}. \tag{9.2}$$

Here, q_{meas} is the displacement at the measurement points, $\boldsymbol{\Phi}_{meas}$ the associated partition of the mode shape matrix, and $^+$ indicates the pseudo-inverse. There are as many equations as there are modes in the representation of the transmission simulator. If fewer modes than measurement points are considered, the constraints do not enforce strict equality of the displacements but the compatibility condition will be fulfilled in a least-squares sense [7].

Coupling is achieved by enforcing compatibility and equilibrium at the interface, relaxed by the mode shape matrix $\boldsymbol{\Phi}_{meas}^{(ts)\,+}$ as above. In matrix notation, the coupling condition is

$$\boldsymbol{\Phi}_{meas}^{(ts)\,+} \begin{bmatrix} \boldsymbol{I}_{meas} & -\boldsymbol{I}_{meas} \end{bmatrix} \begin{Bmatrix} q_{meas}^{(tot)} \\ q_{meas}^{(ts)} \end{Bmatrix} = \begin{bmatrix} \boldsymbol{\Phi}_{meas}^{(ts)\,+} \boldsymbol{\Phi}_{meas}^{(tot)} & -\boldsymbol{I}_{mod} \end{bmatrix} \begin{Bmatrix} \eta^{(tot)} \\ \eta^{(ts)} \end{Bmatrix} = 0. \tag{9.3}$$

Here, the identity matrix $\boldsymbol{I}_{meas}$ has as many rows and columns as there are measurement points, whereas $\boldsymbol{I}_{mod}$ has as many rows and columns as there are modes in the representation of the transmission simulator.

Next, the influence of one state-space model will be removed from another. To achieve this, a positive and a negative state-space model will be coupled applying MCFS. A model described by n second order differential equations can be transformed to a state-space system consisting of $2n$ first order differential equations. One possible representation of a system with negative mass, stiffness, and damping is expressed with the state vector $x = \begin{Bmatrix} q & \dot{q} \end{Bmatrix}^T$ and the state-space equations

$$\begin{cases} \dot{x} = \boldsymbol{A}x + \boldsymbol{B}u \\ y = \boldsymbol{C}x \end{cases} \tag{9.4}$$

with

$$\begin{cases} \boldsymbol{A} = \begin{bmatrix} \boldsymbol{0} & \boldsymbol{I} \\ -(-\boldsymbol{M})^{-1}\left(-\boldsymbol{K}^{-1}\right) & -(-\boldsymbol{M})^{-1}\left(-\boldsymbol{V}^{-1}\right) \end{bmatrix} = \begin{bmatrix} \boldsymbol{0} & \boldsymbol{I} \\ -\boldsymbol{M}^{-1}\boldsymbol{K}^{-1} & -\boldsymbol{M}^{-1}\boldsymbol{V}^{-1} \end{bmatrix} \\ \boldsymbol{B} = \begin{bmatrix} \boldsymbol{0} \\ -\boldsymbol{M}^{-1}\boldsymbol{P}_u \end{bmatrix} = -\begin{bmatrix} \boldsymbol{0} \\ \boldsymbol{M}^{-1}\boldsymbol{P}_u \end{bmatrix} \\ \boldsymbol{C} = \begin{bmatrix} \boldsymbol{P}_y & \boldsymbol{0} \end{bmatrix}. \end{cases} \tag{9.5}$$

The inputs are forces connected by the relation $f = \boldsymbol{P}_u u$, where the Boolean matrix $\boldsymbol{P}_u$ localizes the input locations among all physical degrees of freedom. The output of a system will be a set of displacements unless stated otherwise, defined by $y = \boldsymbol{P}_y q$ where $\boldsymbol{P}_y$ is again a Boolean selection matrix. In short, a negative system differs from a positive system only by a negative input matrix $\boldsymbol{B}$. Note that for displacement outputs, the relation $\boldsymbol{D} = \boldsymbol{0}$ for the direct feedthrough matrix holds since forces have a direct influence on acceleration only according to Newton's second law.

The MCFS can be implemented in the state-space domain similar to FBS. The latter was explained in brief by Mayes and Arviso [13]. In the following, the procedure to obtain a valid model for the structure of interest will be sketched. Starting with the measurement data of the total structure, a state-space model can be extracted by system identification. In this work, subspace identification was performed using the command n4sid of Matlab's system identification toolbox [14]. Next, a state-space representation of the FE model of the transmission simulator is subtracted from the identified total model.

In an identified state-space system, the states are no longer directly related to physical coordinates but rather arbitrarily chosen. However, the inputs and outputs are known and can be split. The forces and displacements at the measurement points on the transmission simulator are denoted u_{meas} and y_{meas}. All other inputs and outputs are dubbed body degrees of freedom

indicated by the subscript b. The corresponding partitions of the input and output matrices $\boldsymbol{B}$ and $\boldsymbol{C}$ are distinguished by the same subscripts. The state-space representation of the identified total system is then

$$\begin{cases} \dot{x}^{(tot)} = \boldsymbol{A}^{(tot)} x^{(tot)} + \begin{bmatrix} \boldsymbol{B}_{meas}^{(tot)} & \boldsymbol{B}_{b}^{(tot)} \end{bmatrix} \begin{Bmatrix} u_{meas}^{(tot)} \\ u_{b}^{(tot)} \end{Bmatrix} \\ \begin{Bmatrix} y_{meas}^{(tot)} \\ y_{b}^{(tot)} \end{Bmatrix} = \begin{bmatrix} \boldsymbol{C}_{meas}^{(tot)} \\ \boldsymbol{C}_{b}^{(tot)} \end{bmatrix} x^{(tot)}. \end{cases} \tag{9.6}$$

In order to relax the coupling constraints, the measured inputs and outputs are expressed in terms of modal coordinates marked by the subscript *mod*. This is done by means of the modal matrix $\boldsymbol{\Phi}_{meas}^{(ts)\,+}$. The body inputs and outputs remain unchanged. Thus, the new inputs and outputs are given by

$$\begin{Bmatrix} u_{meas}^{(tot)} \\ u_{b}^{(tot)} \end{Bmatrix} = \begin{bmatrix} \left(\boldsymbol{\Phi}_{meas}^{(ts)\,+}\right)^{T} & \boldsymbol{0} \\ \boldsymbol{0} & \boldsymbol{I} \end{bmatrix} \begin{Bmatrix} u_{mod}^{(tot)} \\ u_{b}^{(tot)} \end{Bmatrix}, \qquad \begin{Bmatrix} u_{meas}^{(ts)} \\ u_{b}^{(ts)} \end{Bmatrix} = \begin{bmatrix} \left(\boldsymbol{\Phi}_{meas}^{(ts)\,+}\right)^{T} & \boldsymbol{0} \\ \boldsymbol{0} & \boldsymbol{I} \end{bmatrix} \begin{Bmatrix} u_{mod}^{(ts)} \\ u_{b}^{(ts)} \end{Bmatrix} \tag{9.7}$$

and

$$\begin{Bmatrix} y_{mod}^{(tot)} \\ y_{b}^{(tot)} \end{Bmatrix} = \begin{bmatrix} \boldsymbol{\Phi}_{meas}^{(ts)\,+} & \boldsymbol{0} \\ \boldsymbol{0} & \boldsymbol{I} \end{bmatrix} \begin{Bmatrix} y_{meas}^{(tot)} \\ y_{b}^{(tot)} \end{Bmatrix}, \qquad \begin{Bmatrix} y_{mod}^{(ts)} \\ y_{b}^{(ts)} \end{Bmatrix} = \begin{bmatrix} \boldsymbol{\Phi}_{meas}^{(ts)\,+} & \boldsymbol{0} \\ \boldsymbol{0} & \boldsymbol{I} \end{bmatrix} \begin{Bmatrix} y_{meas}^{(ts)} \\ y_{b}^{(ts)} \end{Bmatrix}, \tag{9.8}$$

respectively, while the new state-space models are defined as

$$\begin{cases} \dot{x}^{(tot)} = \boldsymbol{A}^{(tot)} x^{(tot)} + \begin{bmatrix} \boldsymbol{B}_{meas}^{(tot)} & \boldsymbol{B}_{b}^{(tot)} \end{bmatrix} \begin{bmatrix} \left(\boldsymbol{\Phi}_{meas}^{(ts)\,+}\right)^{T} & \boldsymbol{0} \\ \boldsymbol{0} & \boldsymbol{I} \end{bmatrix} \begin{Bmatrix} u_{mod}^{(ts)} \\ u_{b}^{(tot)} \end{Bmatrix} \\ \qquad\qquad = \boldsymbol{A}^{(tot)} x^{(tot)} + \begin{bmatrix} \boldsymbol{B}_{mod}^{(tot)} & \boldsymbol{B}_{b}^{(tot)} \end{bmatrix} \begin{Bmatrix} u_{mod}^{(ts)} \\ u_{b}^{(tot)} \end{Bmatrix} \\ \begin{Bmatrix} y_{mod}^{(ts)} \\ y_{b}^{(tot)} \end{Bmatrix} = \begin{bmatrix} \boldsymbol{\Phi}_{meas}^{(ts)\,+} & \boldsymbol{0} \\ \boldsymbol{0} & \boldsymbol{I} \end{bmatrix} \begin{bmatrix} \boldsymbol{C}_{meas}^{(tot)} \\ \boldsymbol{C}_{b}^{(tot)} \end{bmatrix} x^{(tot)} = \begin{bmatrix} \boldsymbol{C}_{mod}^{(tot)} \\ \boldsymbol{C}_{b}^{(tot)} \end{bmatrix} x^{(tot)} \end{cases} \tag{9.9}$$

and

$$\begin{cases} \dot{x}^{(ts)} = \boldsymbol{A}^{(ts)} x^{(ts)} - \begin{bmatrix} \boldsymbol{B}_{meas}^{(ts)} & \boldsymbol{B}_{b}^{(ts)} \end{bmatrix} \begin{bmatrix} \left(\boldsymbol{\Phi}_{meas}^{(ts)\,+}\right)^{T} & \boldsymbol{0} \\ \boldsymbol{0} & \boldsymbol{I} \end{bmatrix} \begin{Bmatrix} u_{mod}^{(ts)} \\ u_{b}^{(ts)} \end{Bmatrix} \\ \qquad\qquad = \boldsymbol{A}^{(ts)} x^{(ts)} - \begin{bmatrix} \boldsymbol{B}_{mod}^{(ts)} & \boldsymbol{B}_{b}^{(ts)} \end{bmatrix} \begin{Bmatrix} u_{mod}^{(ts)} \\ u_{b}^{(ts)} \end{Bmatrix} \\ \begin{Bmatrix} y_{mod}^{(ts)} \\ y_{b}^{(ts)} \end{Bmatrix} = \begin{bmatrix} \boldsymbol{\Phi}_{meas}^{(ts)\,+} & \boldsymbol{0} \\ \boldsymbol{0} & \boldsymbol{I} \end{bmatrix} \begin{bmatrix} \boldsymbol{C}_{meas}^{(ts)} \\ \boldsymbol{C}_{b}^{(ts)} \end{bmatrix} x^{(ts)} = \begin{bmatrix} \boldsymbol{C}_{mod}^{(ts)} \\ \boldsymbol{C}_{b}^{(ts)} \end{bmatrix} x^{(ts)}. \end{cases} \tag{9.10}$$

Note the minus in front of the transmission simulator input matrix to indicate a negative system. Coupling these models, the influence of the transmission simulator is removed from the total structure and the system of interest is deduced. The subsequent steps are the same as for state-space coupling and can be found in [3].

If multiple copies of a system are coupled in one step, the matrix $\boldsymbol{B}_{vv}$ of this substructure in coupling form must be divided by the number of copies (see [4] for further explanations of the coupling form). In this case, the term $\bar{\boldsymbol{B}}_{vv}$ for the coupled system also changes. The complete derivation can be found in [12].

9.3 Experiments and System Identification

This section depicts first the used experimental setup, and then, the system identification procedure is sketched, including a description of the FE models. Finally, the identified models are analyzed.

9.3.1 Experimental Setup

Four measurements were performed (see Fig. 9.1). Each blade was assembled to a specific bracket to replicate the configuration used in the three-bladed hub. The measurements were executed simulating free-free boundary conditions. Thus, the structure was hung with fishing lines attached to the hub via a metal wire. Moreover, the fishing lines were connected to the suspending structure with springs. The blades were assembled to the bracket applying a bolt tightening torque of 16 lbf-ft according to the specifications [15]. Figure 9.2 shows the experimental setup.

The three-bladed hub was equipped with 9 triaxial and 24 uniaxial sensors and the one-bladed hub with 10 triaxial and 25 uniaxial sensors (see Figs. 9.3 and 9.4). From these configurations, the total mass loading was 21 g and 22.5 g, respectively, which was considered negligible. Great care was taken to align the triaxial sensors with the FE coordinate systems, and all sensors were glued to the structure. The sensors of the three-bladed hub were distributed over the whole structure such that the symmetry of the structure was not disturbed. The sensor locations on the blades were chosen among the positions used by Harvie and Avitabile [16].

The conditioning of the mode shape matrix is greatly influenced by the sensor placement on the transmission simulator [13]. Therefore, the placement was tested beforehand using numerical models, considering sensor configurations on either bracket, hub, or both. It was found that the sensor placement in Fig. 9.4 is best with respect to the condition number and the simulated results considering the number of available sensors. Three triaxial sensors were placed on the front side of each bracket close to the bolts, and three uniaxial were mounted at the same locations on the opposite side of the bracket.

The structure was excited with a shaker hung in strings. Its threaded nylon stinger was attached via a fastener glued to the bracket. Great care was taken to align the stinger. The driving-point locations were decided based on preliminary impact hammer testing results. All tested locations were chosen to be on or close to the bracket. The best input locations were found to be at the positions 3, 6, and 9 for the three-bladed hub and 1, 4, and 7 for the one-bladed hubs 790, 828, and 852,

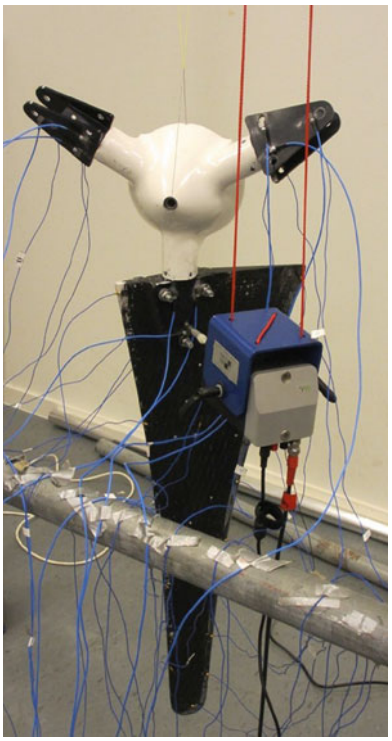

Fig. 9.2 Experimental setup for the one-bladed hub. Both the structure and the shaker are hung. The blade and the hub as transmission simulator are equipped with sensors. The shaker is attached to the bracket as described in Sect. 9.3.1. Note that the clamp connecting blade 828 with the hub is slightly deformed

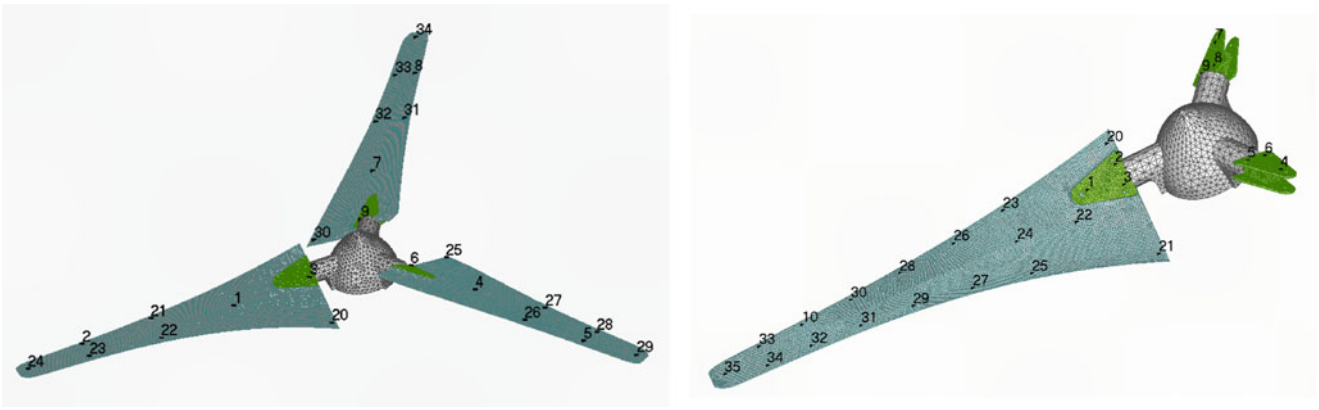

Fig. 9.3 FE models of the three-bladed and one-bladed hubs with sensor locations as used in the measurements. Sensors 11–19 are mounted on the back side of the brackets

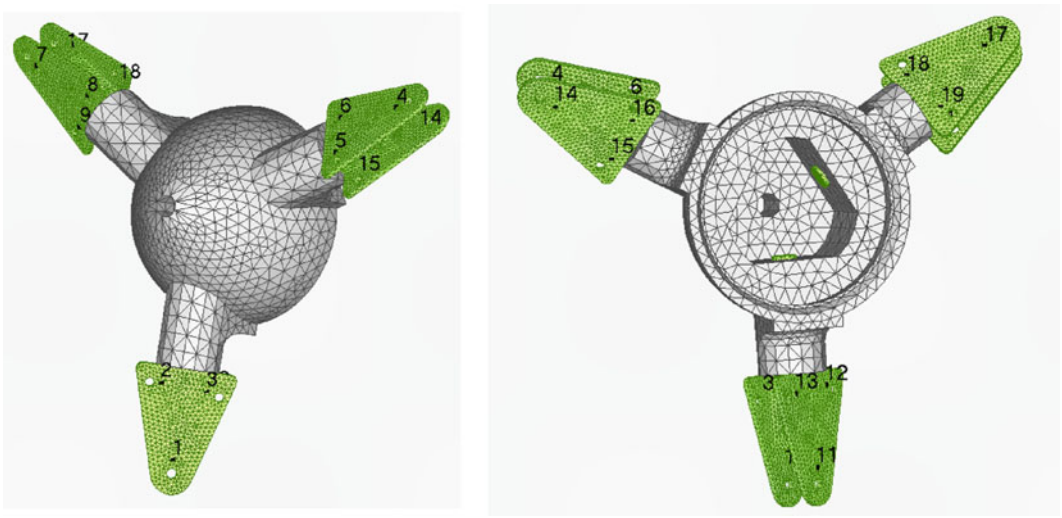

Fig. 9.4 FE model of the hub with sensor locations as used in the measurements. One the front side of the hub, three triaxial sensors are mounted on each bracket. Nine uniaxial sensors are placed at the same locations on the opposite side

respectively. Since the measurements were performed using a force cell and a set of accelerometers only, the fastener was mounted next to the sensor position closer to the hub (see Fig. 9.2). Only out-of-plane excitation was applied.

First, the reciprocity feature of the models was checked with impact hammering. Next, chirps with different amplitudes were generated to find the linear range of the system and ensure repeatability of tests. Low level multisine excitation was then performed to obtain the lowest noise level possible. The measurements revealed minor deviations around 250 Hz and pronounced effects between 400 and 600 Hz, as illustrated in Fig. 9.5. The measurements shown in Fig. 9.5 were taken directly after each other, altering nothing but the level of excitation. Because of this and since the frequency range of interest of the three-bladed hub is below 400 Hz, only measurement data up to 400 Hz was used for the system identification.

9.3.2 System Identification and FE Models

At the beginning of the system identification procedure, the measurement data was investigated thoroughly to distinguish between physical and spurious modes. Following the system identification, Betti's reciprocity principle was used to obtain the unmeasured FRFs, and passivity of the system was enforced [4]. To fulfill Newton's second law, $\boldsymbol{CB} = \boldsymbol{0}$ for displacement outputs must hold. For the identified model, the absolute value of the maximum entry of $\boldsymbol{CB}$ is of order 10^{-4} which was found to be small enough to obtain physical results after coupling. After analyzing the identified mode shapes, defective sensors on

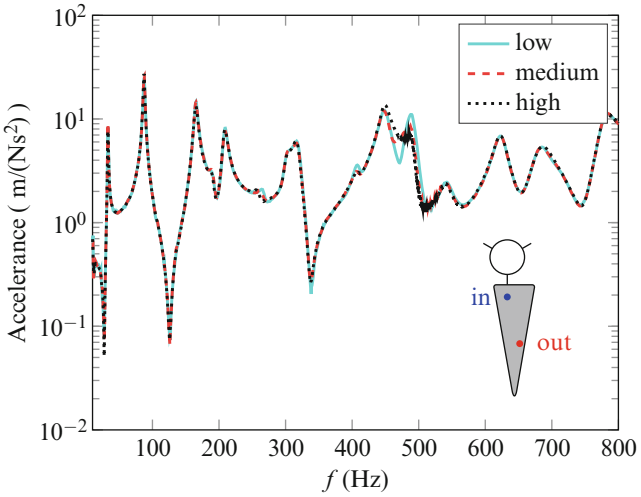

Fig. 9.5 Chirp measurements of the one-bladed hub 790 for different amplitude levels. Input at location 1 in z-direction (out-of-plane), output location 29. Note that the measurements differ between 400 and 600 Hz

Table 9.1 Measured masses and density properties of the FE model

Component	Mass in kg	FE density in kg/m^3
Hub, brackets	3.707	–
Hub, brackets, bolts	3.980	–
Three bolts, nuts, washers, averaged	0.03	–
Bracket, bolts, shaft, averaged [19]	0.432	–
Hub	–	2095
Bracket, shaft	–	4050
Bracket, shaft, bolts	–	5000

The measurements were performed, using a scale with a precision of 0.1 g, and the densities are calculated such that the FE models match the measured weights

the blade were discarded (sensors 24, 27, and 31 on blade 790 and 24, 26, 28, and 31 on blade 828 and 852), and the whole procedure was redone, which substantially improved the results. Finally, the rigid body modes of the FE models were added to the models.

In order to add the rigid body modes, the eigenvalue problems for the FE models of all measured structures were solved in FEMAP v11.1.0 with NX Nastran. The FE blade model, built from a combination of solid and layered composite shell elements, is calibrated to another available blades [17], while the hub, shafts, and brackets are modeled using isotropic solid elements. The density of these components is chosen to match measured weights, as listed in Table 9.1. Depending on the configuration, the density of the bracket changes to account for the mass of the bolts. The interfaces, bracket–blade, shaft–bracket, and shaft–hub, are modeled as flexible connections using the CWELD element of NASTRAN [18] which tend to overestimate the stiffness of the actual connection between blade and hub. After solving the eigenvalue problem, the resonance frequencies and mode shape vectors corresponding to the six rigid body modes were extracted. Since damping is not included in the FE models, it was chosen to be $\xi = 0.1\,\%$ for all rigid body modes.

9.3.3 Identified Models

Figure 9.6 compares the identified model with the measurements for the blade 790 by means of one representative channel. Further, a MAC value comparison for the first eight flexible modes of the FE model can be found in the same figure. Table 9.2 states the identified resonance frequencies $f_i = \omega_i/(2\pi)$ and the modal damping ξ_i for all one-bladed hubs including errors between the FE model and the identified models. The first four flexible modes are captured well, yet the first resonance frequency of the measured blades is higher than in the FE model. This stems from the fact that the FE blade model was

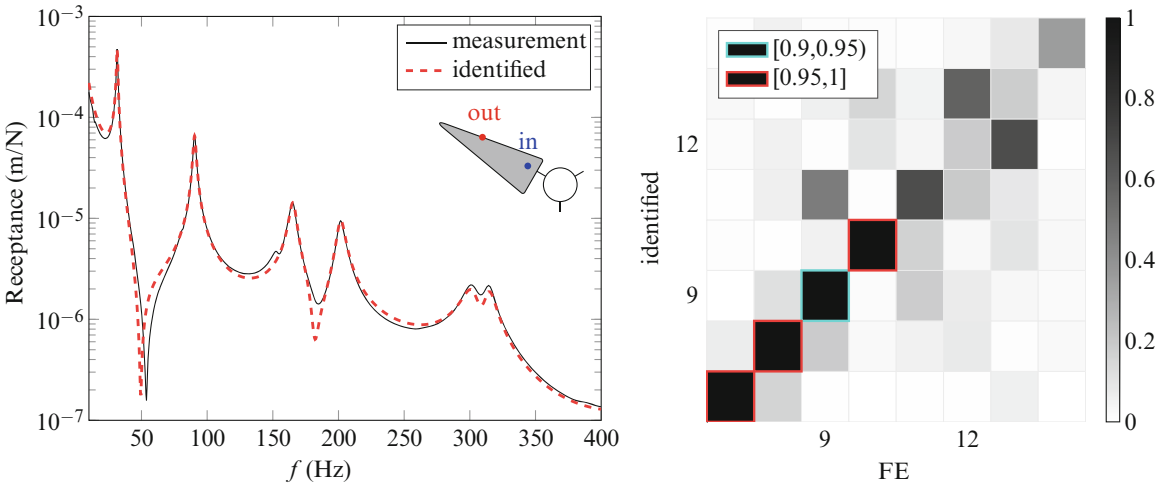

Fig. 9.6 FRF from the measurements and the identified model of the one-bladed hub 852; input at location 7 and output at location 10, both in z-direction (out-of-plane) as visualized in the sketch. The MAC plot compares the identified experimental flexible mode shapes with the FE mode shapes

Table 9.2 Identified modal parameters for the one-bladed hubs used in substructuring compared to the parameters of the FE model

	FE	One-blade hub 790			One-blade hub 828			One-blade hub 852		
	f_i	f_i	Error f_i	ξ_i	f_i	Error f_i	ξ_i	f_i	Error f_i	ξ_i
	(Hz)	(Hz)	(%)	(%)	(Hz)	(%)	(%)	(Hz)	(%)	(%)
7	30.32	33.11	9.2	1.34	31.38	3.6	1.33	31.51	4.0	1.50
8	89.72	87.57	−2.4	1.24	89.75	0.3	1.32	90.42	1.0	1.22
9	180.90	165.27	−8.6	1.71	164.89	−8.0	1.69	165.40	−7.8	1.59
10	191.46	190.72	−0.4	2.30	176.01	−8.0	4.84	178.87	−6.4	3.24
11	234.06	208.83	−10.8	1.68	199.36	−11.2	1.52	201.68	−10.2	1.48
12	330.78	300.84	−9.1	1.79	301.15	−8.1	2.35	302.01	−7.8	2.21
13	341.88	316.97	−7.3	1.89	318.16	−6.4	1.77	314.53	−7.4	1.48
14	475.64	450.42	−5.3	12.90	410.54	−12.1	14.65	448.2	−3.3	12.47

Further, the errors between the identified and the FE resonance frequencies are calculated

calibrated to another blade; the spread between the blades is known to be considerable [11]. The third flexible mode is the third bending mode whereas the fifth flexible mode combines the bending with in-plane motion, explaining the lower MAC value of mode eleven. The fourth flexible mode is highly damped in the identified system. The sixth and seventh flexible modes (number 12 and 13) are closely spaced. For blade 852, this yields a mix-up between the modes compared to the FE model. For the other two blades, these modes were identified as a linear combination of the FE modes. The last mode is an unphysical mode added to account for high frequency residuals.

Figure 9.7 shows one identified receptance FRF for the three-bladed hub compared to the measurement. Further, the MAC values for the flexible modes of the identified model are compared to the FE mode shapes. The first nine modes of the FE and the identified model are either mixed up or have a low MAC value. However, this can be explained by the symmetry of the structure. Due to the symmetry, the flexible modes can be sorted in groups of three with at least two of them close in frequency (see Table 9.3). If modes are close in frequency, the calculated eigenvectors of the identified system span the subspace associated with these modes, yet they can be arbitrarily rotated. Thus, the identified mode shapes are most likely a linear combination of the associated FE mode shape vectors yielding low MAC values. To account for that, the angle between the subspaces spanned by the identified eigenvectors and the FE mode shapes is calculated for modes close in frequency [20]. If the angle is close to zero, the subspaces align well, and the corresponding mode shapes replicate the same motion. In the subsequent MAC plots, the squared cosine of the angle between the subspaces is illustrated by a colored frame. Note that the squared cosine of the angle between subspaces spanned by only one vector each is equal to the MAC value. Applying this metric, it can be seen that the first nine flexible modes correlate well with the FE model. The identified parameters can

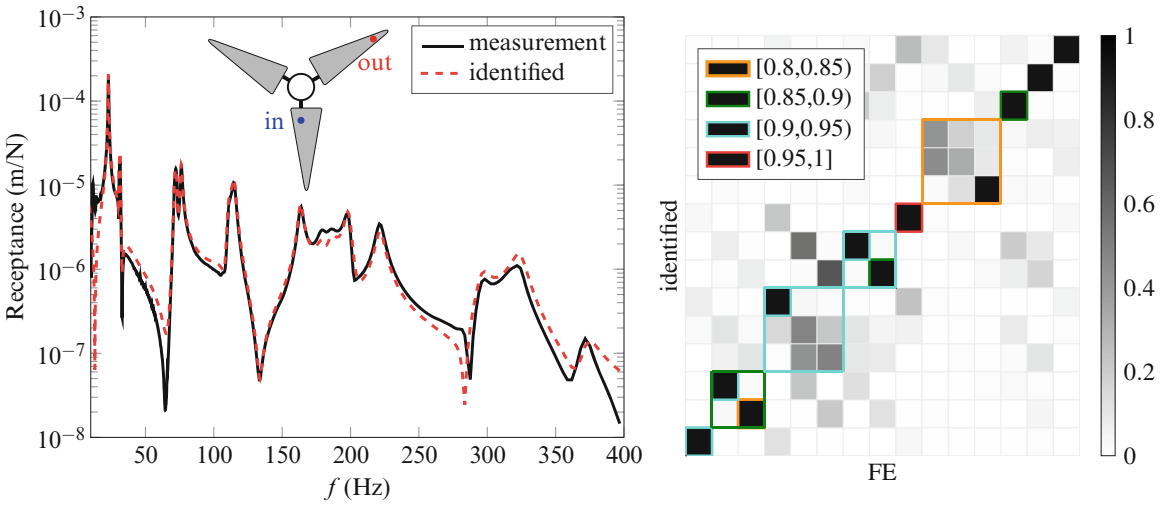

Fig. 9.7 FRF from the measurements and the identified model of the three-bladed hub; input at location 3 in z-direction (out of plane) and output location 28 as visualized in the sketch. The MAC plot compares the identified flexible mode shapes with the FE mode shapes. The colored frames are connected to the angles between the subspaces spanned by mode shape groups

Table 9.3 Modal parameters of the identified and the coupled system of the first five flexible mode groups for the three-bladed hub compared to the FE model

FE	Identified		Substructured		Errors f_i		Errors ξ_i
f_i	f_i	ξ_i	f_i	ξ_i	FE-ident	Ident-substr	Ident-substr
(Hz)	(Hz)	(%)	(Hz)	(%)	(%)	(%)	(%)
22.91	22.91	0.80	24.57	1.05	0.0	7.24	31.02
30.34	30.69	0.85	30.96	1.37	1.2	0.89	62.21
30.34	31.57	0.89	31.94	1.35	4.1	1.17	50.78
83.01	71.34	1.23	75.62	1.05	−14.1	6.01	−14.36
83.02	72.71	1.10	78.04	1.14	−12.4	7.32	3.50
79.12	76.19	0.86	82.40	1.09	−3.7	8.15	26.70
134.52	110.62	1.39	118.57	1.43	−17.8	7.18	2.90
134.49	114.93	1.27	120.44	1.29	−14.5	4.80	1.32
176.45	163.46	1.03	168.23	1.52	−7.4	2.92	47.30
189.63	179.78	1.90	174.01	4.26	−5.2	−3.21	124.34
188.85	181.36	1.89	176.18	2.93	−4.0	−2.86	55.17
189.63	185.50	2.43	185.33	2.00	−2.2	−0.09	−17.59
205.45	198.12	1.24	195.41	1.80	−3.6	−1.36	44.93
205.45	200.24	1.42	199.40	1.75	−2.5	−0.42	23.11
246.91	221.58	1.37	212.91	2.33	−10.3	−3.91	69.69

The errors for the resonance frequencies and modal damping ratios between the systems are also shown. The substructured results are obtained with state-space coupling, and the FE modes are sorted to obtain the highest MAC correlation with the identified modes

be found in Table 9.3. Note also that the order of the FE modes in the table are sorted, taking into account the mode mix-up. Interestingly enough, the first resonance frequency of the identified model match the first FE resonance perfectly even though the first resonance frequency of all one-bladed hubs is higher than in the FE model.

9.4 Substructuring Results

The first flexible mode of the FE model hub is above 1700 Hz, which is far above the frequency range of interest. Therefore, the transmission simulator is treated as rigid, which yields the condition number 1.9 of the used mode shape matrix. An attempt was made using also flexible modes of the transmission simulator but that resulted in higher errors in the modal

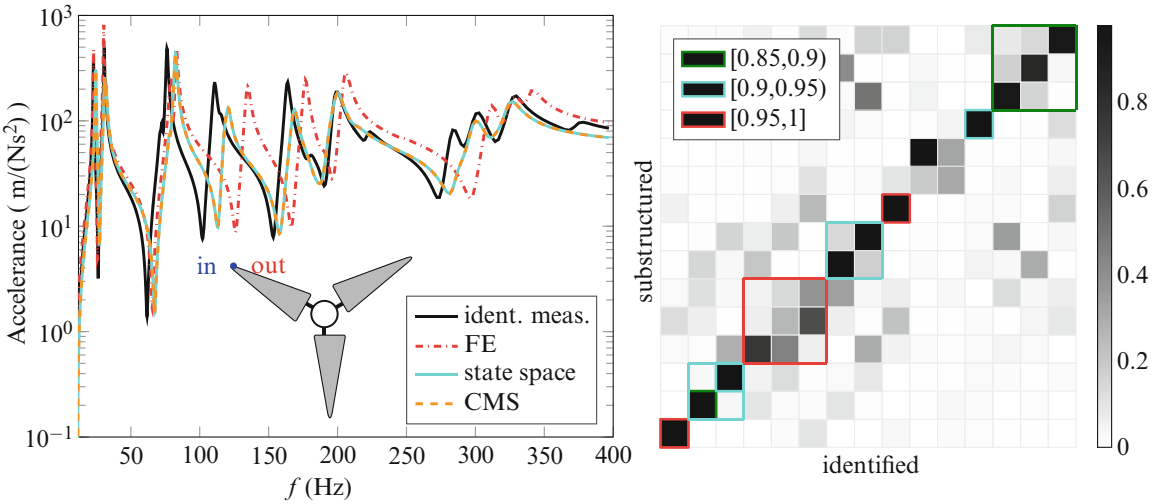

Fig. 9.8 FRF of the three-bladed hub; input/output location at 34 as visualized in the sketch. The FRFs obtained from the identified measured structure are compared with the coupled model obtained with state-space and CMS coupling. The chosen channel is representative for the substructuring results. Further, the FRF from the FE model is plotted. Note that the identified modal damping ratios are chosen for the FE damping in this figure. The MAC plot shows a comparison between the first flexible mode shapes of the identified system and the state-space substructuring results, and the colored frames are connected to the angles between the subspaces spanned by mode shape groups

parameters. Adding more modes to the transmission simulator representation increased the condition number, which is believed to be a possible metric for the applicability of the transmission simulator technique [13]. However, other effects may also have influenced the results, since the increase is not substantial (i.e. a condition number of 2.8 for seven mode shapes).

Figure 9.8 shows the substructuring results compared to those of the identified model of the measured three-bladed hub for one representative channel. Further, the FRF of the FE model is plotted. Note that state-space coupling yields the same results as CMS. According to the angle between the subspaces in the MAC plot, the first nine flexible modes are well captured. The same modes are visualized in Fig. 9.9 together with a description of the motion. Table 9.3 lists the resonance frequencies and damping values. The overall behavior of the system is captured well. Most resonance frequencies of the substructured system are higher than in the identified one, and the damping is clearly overestimated (up to 124 %). The coupled model represents the identified three-bladed hub better than the nominal FE model. Apart from two modes, the substructured resonance frequencies are closer to the true values than the FE model. The same conclusion can be drawn from investigating the FRFs. Thus, using experimental models to build up the model of the assembled structure is superior to the used nominal FE model for this application.

9.5 Discussion

In order to judge the satisfaction of the constraint equations, the motions of the hub of the three substructures and the transmission simulator are plotted, similar to [9]. If the constraints are fulfilled perfectly, there should be no difference in the motion. However, for low frequency flexible modes, the motion of some sensors differs which can stem either from the modal relaxation of the constraints or from measurement errors.

So far, this check cannot be performed with state-space synthesis. The physical coordinates describing the measurement points' motion are transformed to modal coordinates using the matrix $\boldsymbol{\Phi}_{meas}^{(ts)\,+}$. Then, a reduced set of modal coordinates is chosen to represent the coupled system. In CMS, the choice allows for a transformation back to physical coordinates using the mode shape matrices of the substructures. In state-space coupling, the modal coordinates of only the transmission simulator are chosen as the reduced set assuming that all modal coordinates are exactly equal. After this choice, the physical motion can no longer be deduced in a direct way.

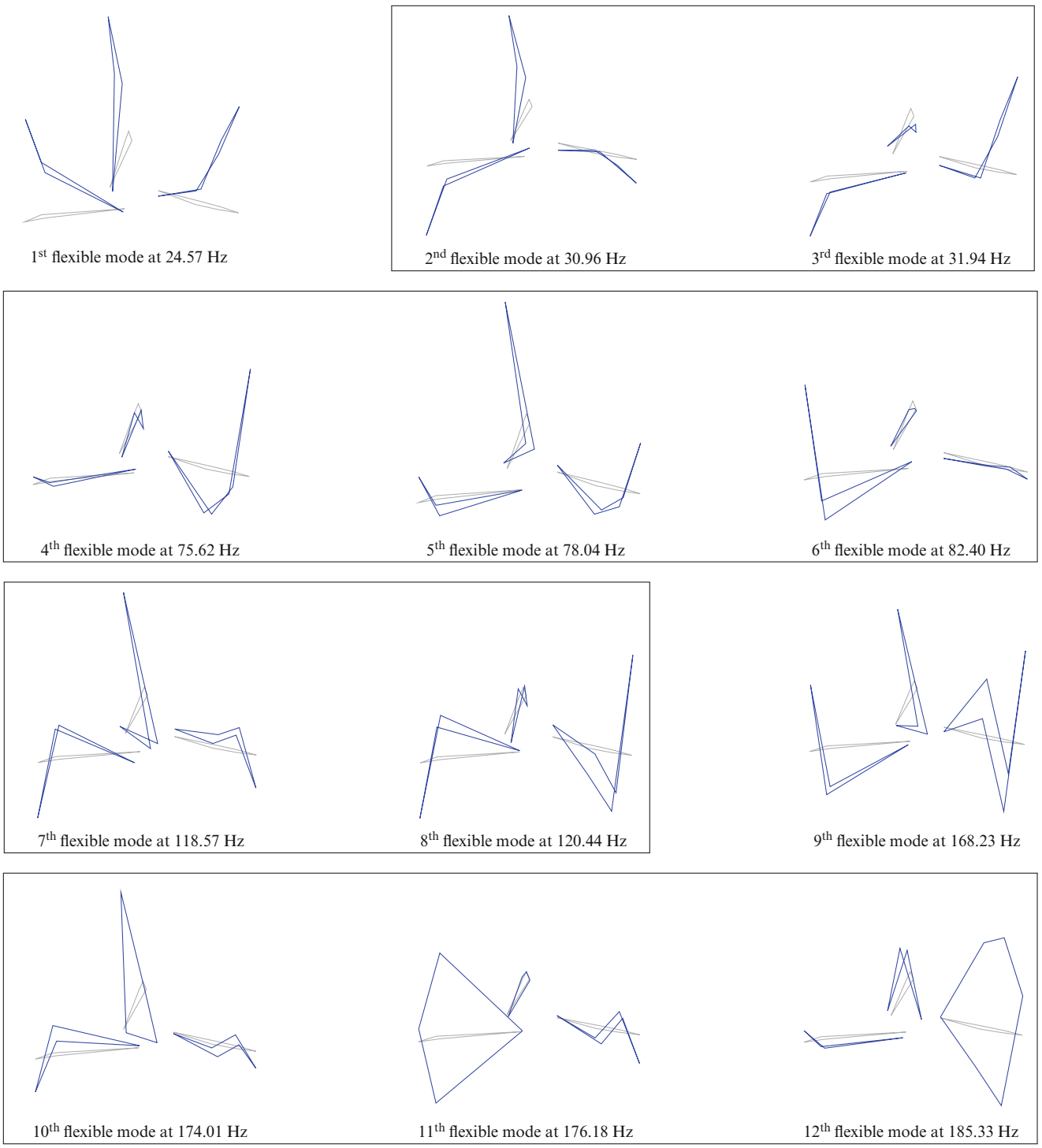

Fig. 9.9 The first 12 flexible mode shapes of the coupled system are shown here. Symmetric mode shapes that are close in frequency are framed. The first flexible mode is a bending mode with all blades in phase followed by two symmetric first bending modes where one blade is out of phase. The modes in the second row are second bending modes whereas the third row shows the third bending motion. Here, the seventh and eighth modes are symmetric, and in the ninth mode all blades are in phase. The next three modes combine bending with torsional motion where one blade is dominated by the latter. Not all nodes measured are plotted here and only out-of-plane displacements of the triaxial sensors are considered for the sake of visualization. The gray lines indicate the undeformed structure

To improve the constraints, more modes could be added to the transmission simulator mode shape matrix. For experimental coupling, the condition number of this matrix is believed to be crucial. In order to lower the condition number, more sensors have to be included along with more modes. However, this approach is limited by the number of sensors available.

It is known that the bolts introduce nonlinearities to the interface [21]. These might become more apparent by measuring close to the joints. On the other hand, mounting the sensors on the brackets enables excitation and measurement in the same direction due to the plain surface.

Other possible sources of errors include the measurement setup. It was found that stinger resonance has no impact on the frequency range of interest. The pronounced differences in the measurements above 400 Hz could be due to resonances in the suspension. However, the modes in this frequency range are dominated by an in-plane motion which may be particularly sensitive to the input direction. A slight misalignment of the stinger could then cause large deviations. Similar issues were reported in the work of Gibanica et al. [11]. In total eleven sensors, listed in Sect. 9.3.2, turned out to be defective and where removed from the system identification procedure. Repeating the measurement to achieve a full set of measured points could possibly improve the substructuring results.

Liljerehn and Abrahamsson [4] found that the peak height of the identified FRF has a large influence on the substructuring results. The identified models in this work are believed to replicate the measurements well enough, as indicated by the results. However, the absolute value of the error for the first mode in the receptance FRF (used for coupling) is larger than for the other modes due to larger displacements. This might be an explanation for the rather high error in the substructuring results for the first mode. The high damping errors could be a sign of an inappropriate damping model. The main source of dissipation is likely to be in the joints, which is probably unsatisfactorily represented by modal damping [10].

9.6 Concluding Remarks

In this paper, the transmission simulator technique is transferred to state-space synthesis of substructures. The interface is coupled with MCFS similar to FBS, and the method is then verified with measurements of the Ampair A600 wind turbine. Three blades attached to the hub were measured, and coupled with two negative FE models of the hub to arrive at a system with one hub and three blades. Physical properties of the identified models like passivity and adherence to Netwon's second law were checked and enforced if necessary. The substructuring results correlate well with the measured three-bladed hub. The overall behavior is captured but the damping is overestimated. Moreover, substructuring predicted the system's behavior better than the nominal FE model.

The transmission simulator was successfully applied to state-space substructuring, and it was shown that CMS and state-space coupling yield the same results. The results may improve with better measurements since they are believed to be a great source of errors, yet the transmission simulator with least squares constraints can level out such kinds of measurement errors. More work should be done to find a way to judge the constraint equations with state-space models.

References

1. de Klerk, D., Rixen, D.J., Voormeeren, S.N.: General Framework for dynamic substructuring: history, review and classification of techniques. AIAA J. **46**(5), 1169–1181 (2008)
2. Su, T.-J., Juang, J.-N.: Substructure system identification and synthesis. J. Guid. Control. Dyn. **17**(5), 1087–1095 (1994)
3. Sjövall, P., Abrahamsson, T.: Component system identification and state-space model synthesis. Mech. Syst. Signal Process. **21**(7), 2697–2714 (2007)
4. Liljerehn, A., Abrahamsson, T.: Experimental-analytical substructure model sensitivity analysis for cutting machine chatter prediction. In: Proceedings of the 30th International Modal Analysis Conference, Jacksonville, FL (2012)
5. Liljerehn, A., Abrahamsson, T.: Dynamic sub-structuring with passive state-space components. In: 26th International Conference on Noise and Vibration Engineering, ISMA, Leuven (2014)
6. Craig, R.R., Kurdila, A.J.: Fundamentals of Structural Dynamics. Wiley, Hoboken, NJ (2006)
7. Allen, M.S., Mayes, R.L., Bergman, E.J.: Experimental modal substructuring to couple and uncouple substructures with flexible fixtures and multi-point connections. J. Sound Vib. **329**(23), 4891–4906 (2010)
8. Mayes, R., Hunter, P.S., Simmermacher, T.W.: Combining lightly damped experimental substructures with analytical substructures. In: Proceedings of the 25th International Modal Analysis Conference, Orlando, FL (2008)
9. Rohe, D.P., Mayes, R.L.: Coupling of a bladed hub to the tower of the ampair 600 wind turbine using the transmission simulator method. In: Proceedings of the 31st International Modal Analysis Conference, Garden Grove, CA, pp. 193–206 (2013)

10. Roettgen, D.R., Mayes, R.L.: Ampair 600 wind turbine three-bladed assembly substructuring using the transmission simulator method. In: Proceedings of the 33rd International Modal Analysis Conference, Orlando, FL, pp. 253–266 (2015)
11. Gibanica, M., et al.: Spread in modal data obtained from wind turbine blade testing. In: Proceedings of the 31st International Modal Analysis Conference, Garden Grove, CA, pp. 207–216 (2013)
12. Scheel, M.: State-space experimental-analytical dynamic substructuring using the transmission simulator. M.Sc. thesis, University of Stuttgart (2015)
13. Mayes, R.L., Arviso, M.: Design studies for the transmission simulator method to generate experimental dynamic substructures. In: International Seminar on Modal Analysis (ISMA), Leuven (2010)
14. Mckelvey, T., Akcay, H., Ljung, L.: Subspace-based multivariable system identification from frequency response data. IEEE Trans. Autom. Control **41**(7), 960–979 (1996)
15. Sandia National Laboratories: Substructuring testbed assembly instructions (2012)
16. Harvie, J., Avitabile, P.: Comparison of some wind turbine blade tests in various configurations. In: Proceedings of the 30th International Modal Analysis Conference, Jacksonville, FL, pp. 73–80 (2012)
17. Johansson, A.T., et al.: Modeling and calibration of small-scale wind turbine blade. In: Proceedings of the 31st International Modal Analysis Conference, Garden Grove, CA, pp. 51–58 (2013)
18. SIEMENS: NX Nastran 10 - Quick reference guide (2014)
19. Gibanica, M.: Experimental-analytical dynamic substructuring. M.Sc. thesis, Chalmers University of Technology (2013)
20. Brincker, R., Ventura, C.: Introduction to Operational Modal Analysis. Wiley, Chichester (2015)
21. Reuss, P., et al.: Identification of nonlinear joint characteristic in dynamic substructuring. In: Proceedings of the 31st International Modal Analysis Conference, Garden Grove, CA, pp. 27–36 (2013)

Chapter 10
Applying the Transmission Simulator Techniques to the Ampair 600 Wind Turbine Testbed

Johann Gross, Benjamin Seeger, Simon Peter, and Pascal Reuss

Abstract Predicting dynamic properties of modern industrial systems in their fully assembled state can be a challenging task. Numerical analysis or physical testing of the entire system is often not possible due to its sheer size or computational effort. Various substructuring and model reduction techniques make it possible to analyze the subcomponents separately and reunite their reduced representations to build the entire system later. However, models of all subcomponents are not always available or certain dynamic properties cannot be captured by FEM. Experimentally derived substructures become more and more important to overcome this problem. In this work the Transmission Simulator techniques are applied to a realistic FE model of the Ampair600 wind turbine to explore the chances and limitations of the method. The procedure to obtain the dynamic representation of the entire rotor derived from a hub-one-blade assembly is presented. Starting from an experimental free-free representation of the hub-one-blade assembly the hub is considered as flexible fixture and its FE representation is removed from the assembly. The obtained experimental Craig-Bampton-representation of one blade is then duplicated and circumferentially rotated to build the complete blading of the wind turbine. These three blades are finally coupled to the hub to complete the rotor.

Keywords Experimental substructures • Substructuring • Craig-Bampton

10.1 Introduction

Engineering of dynamic structures intends to design a system, which can be operated safely and predictably. To successfully accomplish this task reliable information about the structural properties of the system must be known. To simplify the problem it is common practice to divide complex assemblies in their components, so-called substructures, and analyze them separately. Some of the components can be easily modeled using commercial finite element (FE) software packages. However, other substructures exhibit complex geometries or material properties, which can hardly be described using common tools. In these cases, the dynamics of the substructure of interest often are obtained by an experimental modal analysis, yielding an experimentally derived substructure model. The arising challenge, however, is the reassembly of the entire system now consisting of partly numerically and partly experimentally described components.

The recently developed Transmission Simulator (TS) method was introduced by Allen and Mayes [1, 2] to overcome this problem. The TS can be a simply shaped hardware component, which can be modeled easily using FEs and can be tested with little effort. Used as a fixture attached to the substructure of interest in exactly the same way as the complement of the real system will be attached. The TS allows not only to capture the interface characteristics, i.e. joint damping and stiffness, of the combined structure but also brings a larger number of modes into the testable frequency range. When mass is used to load an interface experimentally, as done by the TS, its effect on the measured responses must be removed to get the dynamics of the isolated substructure of interest. This is achieved by using a finite element (FE) model of the TS, producing the desired experimental based representation of the substructure of interest. The process of removing one substructure from another is called substructure de-coupling and is a known dynamic substructuring tool [6]. Two different approaches to de-couple the combined system and the TS were presented by Mayes et al. [1, 2], the FRF coupling admittance approach and the CMS approach. The latter provides the basis for this work.

Present paper is organized in four sections. First section gives a short review on the theoretical background of the MCFS and CB-IP [1, 4] TS techniques used in this work. The investigated FE model of the rotor of the Ampair 600 Wind Turbine is introduced in the second section. The third section presents the numerical results obtained by subtracting the dynamic

J. Gross (✉) • B. Seeger • S. Peter • P. Reuss
Institute for Nonlinear Mechanics, University of Stuttgart, Pfaffenwaldring 9, 70569 Stuttgart, Germany
e-mail: gross@inm.uni-stuttgart.de

© The Society for Experimental Mechanics, Inc. 2016

M. Allen et al. (eds.), *Dynamics of Coupled Structures, Volume 4*, Conference Proceedings of the Society for Experimental Mechanics Series, DOI 10.1007/978-3-319-29763-7_10

influence of the TS from the hub-one-blade assembly. In the forth section the TS method is applied in an extended way deriving the dynamics of the entire rotor, just by knowing the dynamic properties of one blade and the hub. The paper closes with a short conclusion.

10.2 Theoretical Development of the Transmission Simulator

The theoretical background of the method is reviewed based on the notation of [1]. More detailed derivations can be found in [1–4].

10.2.1 Uncoupled Equation of Motion

Given that the eigenfrequencies $\omega_r^2, r = 1 \ldots n_C$ and the respective eigenvectors $\boldsymbol{\Phi}^C$ of the combined structure C are available from experimental analysis, its equation of motion can be written as

$$\boldsymbol{I}^C \ddot{\boldsymbol{q}}^C + \left[\diagdown\, \omega_r^2 \,\diagdown\right]^C \boldsymbol{q}^C = \bar{\boldsymbol{f}}^C + \bar{\boldsymbol{g}}^C. \tag{10.1}$$

The vector of physical coordinates $\boldsymbol{u}^C$ can be recovered from modal coordinates $\boldsymbol{q}^C$ using the transformation matrix $\boldsymbol{T}^C$.

$$\boldsymbol{u}^C = \boldsymbol{T}^C \boldsymbol{q}^C = \boldsymbol{\Phi}^C \boldsymbol{q}^C \tag{10.2}$$

The vectors $\bar{\boldsymbol{f}}^C$ and $\bar{\boldsymbol{g}}^C$ on the right hand side of Eq. (10.1) are the generalized external and coupling forces, respectively.

The equation of motion of the FE model of the TS^{FE} can be described analogously.

$$\bar{\boldsymbol{M}}^{FE} \ddot{\boldsymbol{p}}^{FE} + \bar{\boldsymbol{K}}^{FE} \boldsymbol{p}^{FE} = \bar{\boldsymbol{f}}^{FE} + \bar{\boldsymbol{g}}^{FE} \tag{10.3}$$

Please note, that the TS model is explicitly described in generalized coordinates $\boldsymbol{p}^{FE}$ for the sake of generality. The known transformation,

$$\boldsymbol{u}^{FE} = \boldsymbol{T}^{FE} \boldsymbol{p}^{FE}, \tag{10.4}$$

can be used to recover physical coordinates $\boldsymbol{u}^{FE}$. However, the content of the transformation matrix $\boldsymbol{T}^{FE}$ can vary depending on the modeling method used, as will be discussed in Sect. 10.2.2.

Concatenating the equations of motion of C and $(-FE)$ in block-diagonal form yields

$$\begin{bmatrix} \boldsymbol{I}^C & \boldsymbol{0} \\ \boldsymbol{0} & -\bar{\boldsymbol{M}}^{FE} \end{bmatrix} \begin{bmatrix} \ddot{\boldsymbol{q}}^C \\ \ddot{\boldsymbol{p}}^{FE} \end{bmatrix} + \begin{bmatrix} \left[\diagdown\, \omega_r^2 \,\diagdown\right]^C & \boldsymbol{0} \\ \boldsymbol{0} & -\bar{\boldsymbol{K}}^{FE} \end{bmatrix} \begin{bmatrix} \boldsymbol{q}^C \\ \boldsymbol{p}^{FE} \end{bmatrix} = \begin{bmatrix} \left(\boldsymbol{\Phi}^C\right)^T \boldsymbol{f}^C \\ \left(\boldsymbol{T}^{FE}\right)^T \boldsymbol{f}^{FE} \end{bmatrix} + \begin{bmatrix} \left(\boldsymbol{\Phi}^C\right)^T \boldsymbol{g}^C \\ \left(\boldsymbol{T}^{FE}\right)^T \boldsymbol{g}^{FE} \end{bmatrix}. \tag{10.5}$$

Since the effect of the TS^{FE} on the combined structure C has to be removed, the sign of the mass and stiffness matrices of the FE model of the TS is changed to minus.

The equations of motion in Eq. (10.5) are still uncoupled. The coupling procedure depends on the reduced order model chosen as representation of the FE model of the TS. The representation in turn depends on the component modes used to assemble the coordinate transformation matrix $\boldsymbol{T}^{FE}$. Section 10.2.2 discusses the two different reduced order models (ROMs) of the TS used in this work, Sect. 10.2.3 gives a short review of the coupling procedures.

10.2.2 Transmission Simulator Models

Two kinds of ROMs of the TS and the resulting uncoupled equations of motion are considered.

10.2.2.1 Free-Free Modal Transmission Simulator Model

The free-free modal TS model is obtained by choosing the modal matrix of the free normal modes $\boldsymbol{\Phi}^{FE}$ as transformation matrix $\boldsymbol{T}^{FE}$. The motion of the TS^{FE} is described by a linear combination of rigid body modes and elastic free normal modes, i.e. the interface of the TS is free [2]. Projecting the modal matrix of the TS on the equation of motion yields

$$\boldsymbol{I}^{FE}\ddot{\boldsymbol{q}}^{FE} + \left[\begin{array}{c} \\ \omega_r^2 \\ \\ \end{array}\right]^{FE} \boldsymbol{q}^{FE} = \left(\boldsymbol{\Phi}^{FE}\right)^T \boldsymbol{f}^{FE} + \left(\boldsymbol{\Phi}^{FE}\right)^T \boldsymbol{g}^{FE}, \tag{10.6}$$

with $\boldsymbol{\Phi}^{FE} \in \mathbb{R}^{N_u \times N_k}$. N_u is the number of physical DoFs and N_k corresponds to the number of kept normal modes of the TS. See [5] for more detail.

Inserting Eq. (10.6) into Eq. (10.5) yields

$$\begin{bmatrix} \boldsymbol{I}^C & \boldsymbol{0} \\ \boldsymbol{0} & -\boldsymbol{I}^{FE} \end{bmatrix} \begin{bmatrix} \ddot{\boldsymbol{q}}^C \\ \ddot{\boldsymbol{q}}^{FE} \end{bmatrix} + \begin{bmatrix} \left[\begin{array}{c} \\ \omega_r^2 \\ \\ \end{array}\right]^C & \boldsymbol{0} \\ \boldsymbol{0} & -\left[\begin{array}{c} \\ \omega_r^2 \\ \\ \end{array}\right]^{FE} \end{bmatrix} \begin{bmatrix} \boldsymbol{q}^C \\ \boldsymbol{q}^{FE} \end{bmatrix} = \begin{bmatrix} \left(\boldsymbol{\Phi}^C\right)^T \boldsymbol{f}^C \\ \left(\boldsymbol{\Phi}^{FE}\right)^T \boldsymbol{f}^{FE} \end{bmatrix} + \begin{bmatrix} \left(\boldsymbol{\Phi}^C\right)^T \boldsymbol{g}^C \\ \left(\boldsymbol{\Phi}^{FE}\right)^T \boldsymbol{g}^{FE} \end{bmatrix} \tag{10.7}$$

with

$$\begin{bmatrix} \boldsymbol{u}^C \\ \boldsymbol{u}^{FE} \end{bmatrix} = \begin{bmatrix} \left(\boldsymbol{\Phi}^C\right)^T & \boldsymbol{0} \\ \boldsymbol{0} & \left(\boldsymbol{\Phi}^{FE}\right)^T \end{bmatrix} \begin{bmatrix} \boldsymbol{q}^C \\ \boldsymbol{q}^{FE} \end{bmatrix}. \tag{10.8}$$

10.2.2.2 Craig-Bampton Transmission Simulator Model

Using a Craig-Bampton TS model, the motion of the TS^{FE} is described by its fixed-interface normal modes and its constraint modes. For more detail on Craig-Bampton reduction the reader is referred to [5]. Choosing the Craig-Bampton transformation matrix $\boldsymbol{T}_{CB}$ to reduce the FE model of the TS^{FE} yields the equation of motion of the Craig-Bampton TS model,

$$\bar{\boldsymbol{M}}_{CB}^{FE}\ddot{\boldsymbol{p}}_{CB}^{FE} + \bar{\boldsymbol{K}}_{CB}^{FE}\boldsymbol{p}_{CB}^{FE} = \left(\boldsymbol{T}_{CB}^{FE}\right)^T \boldsymbol{f}^{FE} + \left(\boldsymbol{T}_{CB}^{FE}\right)^T \boldsymbol{g}^{FE}, \tag{10.9}$$

with $\boldsymbol{T}_{CB}^{FE} \in \mathbb{R}^{N_u \times (N_k + N_c)}$. N_c is the number of constraint DoFs [5]. Inserting Eq. (10.9) into Eq. (10.5) gives

$$\begin{bmatrix} \boldsymbol{I}^C & \boldsymbol{0} \\ \boldsymbol{0} & -\bar{\boldsymbol{M}}_{CB}^{FE} \end{bmatrix} \begin{bmatrix} \ddot{\boldsymbol{q}}^C \\ \ddot{\boldsymbol{u}}_{CB}^{FE} \end{bmatrix} + \begin{bmatrix} \left[\begin{array}{c} \\ \omega_r^2 \\ \\ \end{array}\right]^C & \boldsymbol{0} \\ \boldsymbol{0} & -\bar{\boldsymbol{K}}_{CB}^{FE} \end{bmatrix} \begin{bmatrix} \boldsymbol{q}^C \\ \boldsymbol{u}_{CB}^{FE} \end{bmatrix} = \begin{bmatrix} \left(\boldsymbol{\Phi}^C\right)^T \boldsymbol{f}^C \\ \left(\boldsymbol{T}_{CB}^{FE}\right)^T \boldsymbol{f}^{FE} \end{bmatrix} + \begin{bmatrix} \left(\boldsymbol{\Phi}^C\right)^T \boldsymbol{g}^C \\ \left(\boldsymbol{T}_{CB}^{FE}\right)^T \boldsymbol{g}^{FE} \end{bmatrix}. \tag{10.10}$$

with

$$\begin{bmatrix} \boldsymbol{u}^C \\ \boldsymbol{u}^{FE} \end{bmatrix} = \begin{bmatrix} \left(\boldsymbol{\Phi}^C\right)^T & \boldsymbol{0} \\ \boldsymbol{0} & \left(\boldsymbol{T}_{CB}^{FE}\right)^T \end{bmatrix} \begin{bmatrix} \boldsymbol{q}^C \\ \boldsymbol{u}_{CB}^{FE} \end{bmatrix}. \tag{10.11}$$

10.2.3 Coupling Procedures

In CMS the substructures are usually coupled at the points where they physically connect, the connection degrees of freedom in the interface [6]. In practice the connection point motion of the combined structure C normally is not measured. Instead, the measurements are taken at discrete points distributed on the surface of C. This requires a coupling procedure using the motion at the measured DoF rather than the motion at the connection DoF. Two different approaches are the subject of this section.

In the following the subset of physical DoF in the interface of a (sub)structure is denoted with the subscript c. The subset of measurable DoF of the TS is denoted with the subscript m. It is pointed out that if the TS is part of the combined structure C, only the measurable DoF of the physical representation of the TS, TS^A, are in this subset (i.e. not those of the structure of

interest B), denoted as $\boldsymbol{u}_m^C$. The measurement points on the TS^A are generally modeled as a set of nodes on the surface of the FE model of the TS^{FE}. These nodes on TS^{FE} ideally are at the exact same location as the sensors on the physical TS^A. The mode shapes calculated analytically for this set of nodes describe the motion of the "measurement" DoF of the FE model of the TS.

10.2.3.1 Modal Constraints (MCFS)

In 2007, Allen, Mayes and Bergman introduced the so-called Modal Constraint for Fixture and Subsystem (MCFS) method [1]. The MCFS method constrains two spatially distributed sets of points to assure that the TS^A, being part of C, and its FE model TS^{FE} undergo the same motion. The two sets to be constrained are the subsets of measurable DoF of the TS and its FE model,

$$\boldsymbol{u}_m^C = \boldsymbol{u}_m^{FE}. \tag{10.12}$$

Equation (10.12) forces the physical displacement of the measurable DoF to be precisely equal. If there are more measurable DoF than modes, some of the constraints are redundant. Furthermore, if either the experimental results or the FE model of the TS are not accurate grave errors can occur. The basic idea behind the MCFS method is to overcome these difficulties by using an over-determined set of measurement DoFs enforcing the constraints in Eq. (10.12) in a least squares sense.

10.2.3.2 MCFS for Free-Free Transmission Simulator (MCFS-FF)

Choosing the generalized inverse of the modal matrix of the TS's FE model $\left(\boldsymbol{\Phi}_m^{FE}\right)^\dagger$ as a weighting factor, the constraints from Eq. (10.12) now can be described by

$$\left(\boldsymbol{\Phi}_m^{FE}\right)^\dagger \boldsymbol{u}_m^C = \left(\boldsymbol{\Phi}_m^{FE}\right)^\dagger \boldsymbol{u}_m^{FE}. \tag{10.13}$$

The right-hand side is equal to the modal coordinates of the TS's FE model, since $\boldsymbol{\Phi}_m^{FE}\boldsymbol{q}^{FE} = \boldsymbol{u}_m^{FE}$. Transforming $\boldsymbol{u}_m^C$ to modal coordinates yields the modal constraints

$$\left(\boldsymbol{\Phi}_m^{FE}\right)^\dagger \boldsymbol{\Phi}_m^C \boldsymbol{q}^C = \boldsymbol{q}^{FE}, \tag{10.14}$$

or in matrix notation

$$\left[\left(\boldsymbol{\Phi}_m^{FE}\right)^\dagger \boldsymbol{\Phi}_m^C \; -\boldsymbol{I}\right] \begin{bmatrix} \boldsymbol{q}^C \\ \boldsymbol{q}^{FE} \end{bmatrix} = \boldsymbol{B}_{MCFS}^{FF} \begin{bmatrix} \boldsymbol{q}^C \\ \boldsymbol{q}^{FE} \end{bmatrix} = \boldsymbol{0}, \tag{10.15}$$

with the subscript m denoting row partitions corresponding to the measurable DoF. Equation (10.14) constrains the modal coordinates of the FE model of the TS FE to their orthogonal projection onto the motion of the combined structure C. Equation (10.14) states that the modal coordinates $\boldsymbol{q}^C$ and $\boldsymbol{q}^{FE}$, i.e. not the physical coordinates, have to be equal. There is one constraint equation for each mode that is included in $\boldsymbol{\Phi}_m^{FE}$. Usually there are more measurable DoFs than modes and thus fewer constraints than measurable DoF, so Eq. (10.14) satisfies Eq. (10.12) in a weak sense [2].

Calculating the nullspace of the constraint matrix $\boldsymbol{B}_{MCFS}^{FF}$ [6] gives the coordinate transformation matrix $\boldsymbol{L}_{MCFS}^{FF}$, which is necessary to assemble the concatenated equations of motion of the free-free modal TS model from Sect. 10.2.2.1. The assembled system matrices approximating the substructure of interest B are

$$\begin{aligned}
\tilde{\boldsymbol{M}}_{FF}^B &= \left(\boldsymbol{L}_{MCFS}^{FF}\right)^T \begin{bmatrix} \boldsymbol{I}^C & \boldsymbol{0} \\ \boldsymbol{0} & -\boldsymbol{I}^{FE} \end{bmatrix} \boldsymbol{L}_{MCFS}^{FF} \\
\tilde{\boldsymbol{K}}_{FF}^B &= \left(\boldsymbol{L}_{MCFS}^{FF}\right)^T \begin{bmatrix} \left[\diagdown\, \omega_r^2 \,\diagdown\right]^C & \boldsymbol{0} \\ \boldsymbol{0} & -\left[\diagdown\, \omega_r^2 \,\diagdown\right]^{FE} \end{bmatrix} \boldsymbol{L}_{MCFS}^{FF} \\
\tilde{\boldsymbol{q}}_{FF}^B &= \left(\boldsymbol{L}_{MCFS}^{FF}\right)^T \begin{bmatrix} \boldsymbol{q}^C \\ \boldsymbol{q}^{FE} \end{bmatrix}
\end{aligned} \tag{10.16}$$

and the approximation's free normal modes can be found by solving the eigenvalue problem (EVP) for $\tilde{\boldsymbol{M}}_{FF}^B$ and $\tilde{\boldsymbol{K}}_{FF}^B$.

10.2.3.3 Motion Relative to the Interface (CB-IP)

The Craig-Bampton Interface Preserving (CB-IP) method takes into account the special structure of the generalized coordinates of a Craig-Bampton TS model. As it is known, the generalized coordinates of a CB model represent a mixed formulation of physical and fixed-interface modal coordinates, i.e. the interface DoF are being let in the physical domain and are not projected into modal space [5]. Allen et al. introduced the CB-IP method in order to retain the structure of the CB model and especially the partition of the interface DoF as a unique set of coordinates [4].

As in the MCFS method, the physical displacement of the transmission simulator being part of C and the FE model of the TS is forced to be equal at the measurable DoF, stated by

$$\boldsymbol{u}_m^C = \boldsymbol{u}_m^{FE}. \tag{10.17}$$

Here it is assumed that none of the connection DoF are in the set of measurable DoF. Transforming to Craig-Bampton coordinates for the FE model of the TS and transforming to modal coordinates for the combined structure C yields

$$\boldsymbol{\Phi}_m^C \boldsymbol{q}^C = \hat{\boldsymbol{\Phi}}_m^{FE} \hat{\boldsymbol{q}}^{FE} + \boldsymbol{\Psi}_m^{FE} \boldsymbol{u}_c^{FE} \tag{10.18}$$

with the subscript m denoting row partitions corresponding to the measurable DoF. Solving Eq. (10.18) for the fixed-interface modal response of the TS gives the modal constraints

$$\hat{\boldsymbol{q}}^{FE} = \left(\hat{\boldsymbol{\Phi}}_m^{FE}\right)^{\dagger} \left[\boldsymbol{\Phi}_m^C \boldsymbol{q}^C - \boldsymbol{\Psi}_m^{FE} \boldsymbol{u}_c^{FE}\right]. \tag{10.19}$$

The term within the brackets is the difference between the response of the TS A being part of C during the modal analysis, $\boldsymbol{\Phi}_m^C \boldsymbol{q}^C$, and the static response of the FE model of the TS FE to a unit displacement of the interface DoF, $\boldsymbol{\Psi}_m^{FE} \boldsymbol{u}_c^{FE}$, at the same measurable DoF. This term can be considered as an estimate for the response of the measurable DoF with respect to the interface DoF. Therefore Eq. (10.19) constrains the fixed-interface modal response of the FE model of the TS to its projection onto the motion of the combined structure C relative to the interface (in contrast to Sect. 10.2.3.1, where the total responses are constrained). In analogy to the MCFS method, the constraint in Eq. (10.17) is not strictly enforced but satisfied in a weak sense by Eq. (10.19). By defining the coordinate transformation

$$\begin{bmatrix} \boldsymbol{q}^C \\ \hat{\boldsymbol{q}}^{FE} \\ \boldsymbol{u}_c^{FE} \end{bmatrix} = \begin{bmatrix} \boldsymbol{I} & \boldsymbol{0} \\ \left(\hat{\boldsymbol{\Phi}}_m^{FE}\right)^{\dagger} \boldsymbol{\Phi}_m^C & -\left(\hat{\boldsymbol{\Phi}}_m^{FE}\right)^{\dagger} \boldsymbol{\Psi}_m^{FE} \\ \boldsymbol{0} & \boldsymbol{I} \end{bmatrix} \begin{bmatrix} \boldsymbol{q}^C \\ \boldsymbol{u}_c^{FE} \end{bmatrix} = \boldsymbol{L}_{IP} \begin{bmatrix} \boldsymbol{q}^C \\ \boldsymbol{u}_c^{FE} \end{bmatrix} \tag{10.20}$$

the modal constraint in Eq. (10.19) can be applied to the concatenated equations of motion for the Craig-Bampton TS model from Sect. 10.2.2.2. The assembled system matrices approximating the substructure of interest B can be written as

$$\tilde{\boldsymbol{M}}_{CBIP}^B = (\boldsymbol{L}_{IP})^T \begin{bmatrix} \boldsymbol{I}^C & \boldsymbol{0} \\ \boldsymbol{0} & -\bar{\boldsymbol{M}}_{CB}^{FE} \end{bmatrix} \boldsymbol{L}_{IP} = \begin{bmatrix} \tilde{\boldsymbol{M}}_{qq}^B & \tilde{\boldsymbol{M}}_{qc}^B \\ \tilde{\boldsymbol{M}}_{cq}^B & \tilde{\boldsymbol{M}}_{cc}^B \end{bmatrix} \tag{10.21}$$

$$\tilde{\boldsymbol{K}}_{CBIP}^B = (\boldsymbol{L}_{IP})^T \begin{bmatrix} \left[\begin{smallmatrix} \ddots & \\ & \omega_r^2 \\ & & \ddots \end{smallmatrix}\right]^C & \boldsymbol{0} \\ \boldsymbol{0} & -\bar{\boldsymbol{K}}_{CB}^{FE} \end{bmatrix} \boldsymbol{L}_{IP} = \begin{bmatrix} \tilde{\boldsymbol{K}}_{qq}^B & \tilde{\boldsymbol{K}}_{qc}^B \\ \tilde{\boldsymbol{K}}_{cq}^B & \tilde{\boldsymbol{K}}_{cc}^B \end{bmatrix} \tag{10.22}$$

and

$$\tilde{\boldsymbol{f}}_{CBIP}^B = (\boldsymbol{L}_{IP})^T \begin{bmatrix} \left(\boldsymbol{\Phi}^C\right)^T & \boldsymbol{0} \\ \boldsymbol{0} & \left(\boldsymbol{T}_{CB}^{FE}\right)^T \end{bmatrix} \begin{bmatrix} \boldsymbol{f}^C \\ \boldsymbol{f}^{FE} \end{bmatrix}$$

$$\tilde{\boldsymbol{q}}_{CBIP}^B = (\boldsymbol{L}_{IP})^T \begin{bmatrix} \boldsymbol{q}^C \\ \boldsymbol{p}_{CB}^{FE} \end{bmatrix}. \tag{10.23}$$

Since the generalized coordinates $\tilde{\boldsymbol{q}}^B_{CBIP}$ are a mix of physical DoF related to the interface and modal DoF related to the free part of the substructure, this representation of B is similar to a Craig-Bampton representation, i.e. it can be easily connected to other FE models. It is not precisely a CB representation of B because the stiffness matrix given in Eq. (10.22) is not block diagonal. Unlike the CB representation, the modal degrees of freedom can not be truncated due to the stiffness coupling resulting from $\tilde{\boldsymbol{K}}^B_{qc}$ and $\tilde{\boldsymbol{K}}^B_{cq}$.

A disadvantage of the CB-IP method is that due to the retention of the interface DoF indefinite mass and stiffness matrices can be obtained. Indefinite mass and stiffness matrices result in nonphysical eigenvalues. The matrices in Eqs. (10.21) and (10.22) can be written as

$$\begin{bmatrix} \tilde{\boldsymbol{M}}^B_{qq} & \tilde{\boldsymbol{M}}^B_{qc} \\ \tilde{\boldsymbol{M}}^B_{cq} & \tilde{\boldsymbol{M}}^B_{cc} \end{bmatrix} = \begin{bmatrix} \boldsymbol{I}^C - \boldsymbol{\tau}^T\boldsymbol{\tau} & \boldsymbol{\tau}^T\boldsymbol{\theta} - \boldsymbol{\tau}^T\boldsymbol{M}^{FE}_{qc} \\ \boldsymbol{\theta}^T\boldsymbol{\tau} - \boldsymbol{M}^{FE}_{cq}\boldsymbol{\tau} & \boldsymbol{M}^{FE}_{cq}\boldsymbol{\theta} + \boldsymbol{\theta}^T\boldsymbol{M}^{FE}_{qc} - \boldsymbol{\theta}^T\boldsymbol{\theta} - \boldsymbol{M}^{FE}_{stat} \end{bmatrix} \tag{10.24}$$

$$\begin{bmatrix} \tilde{\boldsymbol{K}}^B_{qq} & \tilde{\boldsymbol{K}}^B_{qc} \\ \tilde{\boldsymbol{K}}^B_{cq} & \tilde{\boldsymbol{K}}^B_{cc} \end{bmatrix} = \begin{bmatrix} \left[\diagdown\, \omega_r^2 \,\diagdown\right]^C - \boldsymbol{\tau}^T \left[\diagdown\, \hat{\omega}_r^2 \,\diagdown\right]^{FE} \boldsymbol{\tau} & \boldsymbol{\tau}^T \left[\diagdown\, \hat{\omega}_r^2 \,\diagdown\right]^{FE} \boldsymbol{\theta} \\ \boldsymbol{\theta}^T \left[\diagdown\, \hat{\omega}_r^2 \,\diagdown\right]^{FE} \boldsymbol{\tau} & -\boldsymbol{\theta}^T \left[\diagdown\, \hat{\omega}_r^2 \,\diagdown\right]^{FE} \boldsymbol{\theta} - \boldsymbol{K}^{FE}_{stat} \end{bmatrix} \tag{10.25}$$

with $\boldsymbol{\tau} = \left(\hat{\boldsymbol{\Phi}}^{FE}_m\right)^\dagger \boldsymbol{\Phi}^C_m$ and $\boldsymbol{\theta} = \left(\hat{\boldsymbol{\Phi}}^{FE}_m\right)^\dagger \boldsymbol{\Psi}^{FE}_m$. The partitions corresponding to the physical interface DoFs, $\tilde{\boldsymbol{M}}^B_{cc}$ and $\tilde{\boldsymbol{K}}^B_{cc}$, are negative by design of the CB-IP method. The negative mass and stiffness associated with the interface of the TS FE has no equivalent in the modal space of C to cancel out with while being subtracted. These partitions make the matrices of the substructure B indefinite.

One possible way to overcome this problem is to project the connection DoFs onto the modal space of the combined structure C, using $\boldsymbol{u}^{FE}_c = \boldsymbol{\Phi}^C_c \boldsymbol{q}^C$. In fact, this way was used to calculate the free normal modes in Sect. 10.4.2. When the experimental based representation of the substructure of interest B is coupled to another substructure of comparable or larger size than the transmission simulator, the excess mass and stiffness due to the TS at the interface properly cancel out because of the coupling terms in $\tilde{\boldsymbol{M}}^B_{CBIP}$ and $\tilde{\boldsymbol{K}}^B_{CBIP}$.

An advantage of the representation obtained with the CB-IP method is that the fixed-interface normal modes and frequencies of the substructure of interest B can be determined directly from Eqs. (10.24) and (10.25) by crossing out the block row and column corresponding to the interface DoF. Thus the fixed-interface normal modes and frequencies for the substructure of interest B can be obtained by performing a free-free modal analysis of the combined substructure C and subsequently solving the EVP for $\tilde{\boldsymbol{M}}^B_{qq}$ and $\tilde{\boldsymbol{K}}^B_{qq}$. In the partitions corresponding to the modal DoF, $\tilde{\boldsymbol{M}}^B_{qq}$ and $\tilde{\boldsymbol{K}}^B_{qq}$, the mass and stiffness associated with the TS fixed-interface normal modes is subtracted. The positive mass and stiffness associated with the modes describing the motion of the interface DoF of the combined structure C still remains.

10.3 Modeling of the Wind Turbine Rotor Assembly

The application of the TS method to structures that are composed of both numerically and experimentally derived substructures requires very accurate models. The Ampair 600 wind turbine blade was investigated by Johansson et al. [7] in great detail. Material tests performed by the authors revealed the structural layup of the composite material as well as material properties which are crucial information for analysts. On this basis the FE modeling and subsequent model updating with respect to experimental modal analysis results of the wind turbine blade can be performed using the HyperWorks suite from Altair Engineering.

The FE model of the blade is designed as a composite material structure consisting of both, 2-D shell to model the skin and 3-D solid elements for the core. The hub is considered as a homogeneous structure for the sake of simplicity and is modeled with 3D-solid elements. An overview of FE model parameters is given in Table 10.1.

Table 10.1 FE model parameters of the blade

	Eltype	No. elts	No. nodes
Skin	Six nodes quadr. trias	4577	9302
Core	Eight nodes quadr. tetras	7998	15,888
Hub	Eight nodes quadr. tetras	47,227	81,934

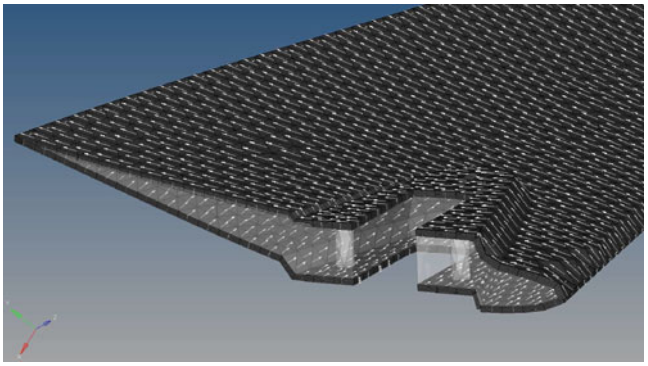

Fig. 10.1 Cross-section of the composite layup of the blade

Table 10.2 Avaraged material parameters of the blades

Hub	Young's modulus $\left(\frac{\mathrm{N}}{\mathrm{mm}^2}\right)$	Poisson's ratio $(-)$	Density $\left(\frac{\mathrm{t}}{\mathrm{mm}^3}\right)$
Nominal FE	210,000	0.3	$7.9e-9$
Updated FE	210,000	0.3	$7.9e-90$

Core	Young's modulus $\left(\frac{\mathrm{N}}{\mathrm{mm}^2}\right)$	Poisson's ratio $(-)$	Density $\left(\frac{\mathrm{t}}{\mathrm{mm}^3}\right)$
Nominal FE	1500	0.4	$9e-10$
Updated FE	1900	0.4	$8.9e-10$

Skin	Young's modulus in fiber E_1 $\left(\frac{\mathrm{N}}{\mathrm{mm}^2}\right)$	Young's modulus $\perp$ to fiber E_1 $\left(\frac{\mathrm{N}}{\mathrm{mm}^2}\right)$	Shear modulus $\left(\frac{\mathrm{N}}{\mathrm{mm}^2}\right)$	Poisson's ratio $(-)$	Density $\left(\frac{\mathrm{t}}{\mathrm{mm}^3}\right)$
Nominal FE	25,475	3328	1229	0.3	$2.09e-9$
Updated FE	32,656	5212	2006	0.3	$1.9e-9$

Fig. 10.2 Tetraeder mesh of the hub

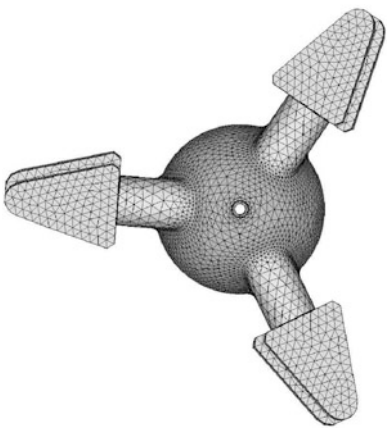

Johansson et al. found that the skin of the blade consists of two layers of glas fiber fabric, which is woven with a 90° braid angle, respectively. The woven pattern cannot be realized with the software used. Instead the skin is modelled by two plies using orthotropic material properties and individual stack orientations, which can be seen in Fig. 10.1 (Table 10.2).

This realistic high fidelity model of a structure consisting of one blade attached to the rotor hub is used for further investigations of the TS methods. Note that the areal interface between the two substructures includes 166 nodes on the blade side and 188 nodes of the hub. Areal linear multi-point-constraints (MPCs) are used to connect the two separated meshes (Fig. 10.2).

10.4 Numerical Study of the Hub-one-Blade System

The TS procedures from Sect. 10.2 are examined here using the FE model introduced in the previous section. One of the goals of this work is to investigate the performance of the TS methods on high fidelity models with areal interfaces. The authors focused on a numerical study to eliminate uncertainties present in experimental analysis, which would contaminate the results.

Figure 10.3 gives an illustration of the TS method applied to the Ampair600 Wind Turbine components. An exemplary combined structure C with the blade of a small wind turbine being the substructure of interest B and the hub of the wind turbine being the TS, TS^{FE}. Written as an equation, the TS example can be summarized as

$$C - FE = (B + A) - FE = \tilde{B}.$$

The illustration of the substructuring problem contains both physical and numerical representations of components. The physically represented substructures, hub-one-blade assembly C and the blade $\tilde{B}$ simulate the experimentally derived components, while the TS^{FE} is represented as a FE model. Additionally, it is differentiated between the TS-derived substructure of interest $\tilde{B}$ and its reference representation B. The combined structure C is the physical TS^{A} attached to the reference substructure of interest B. For the sake of simplicity the hub substructure is used also as TS, because it provides perfect coupling conditions at the interface, also for future experimental analysis.

In this section the FE model of the TS^{FE} is subtracted from the combined structure C, blade and hub assembly, yielding the TS-derived representation of the substructure of interest $\tilde{B}$. The subtraction is achieved by using the coupling procedures outlined in Sect. 10.2.3. Goal of the subtraction process(es) is to determine the dynamic behavior of the substructure $\tilde{B}$ by its reference representation B. Thus the normal modes of the reference representation of B are calculated and compared to the normal modes directly computed from the FE model of substructure B.

Two different component modes of the structure of interest are derived in this section using respectively the suitable TS techniques.

10.4.1 Free-Free Modes of the Blade $\tilde{B}$

To obtain the free-free normal modes of the blade the MCFS approach is used, as is suggested in Sect. 10.2.2.1. The FE model of the TS^{FE}, here hub, is subtracted from the combined structure C, again, as illustrated in Fig. 10.3. The analysis shows that the quality of results strongly depends on the parameter set chosen for particular calculations, when the MCFS method is used. Not only the number of considered modes plays an important role, but also the frequency ranges covered and modal spaces spanned by the modal substructure representations influence the results. In particular no certain strategy could be found to a priori predict a set of parameters for good results. Additionally, numerous spurious modes arise using this substructuring method. It could be observed that in contrast to real solutions the spurious modes changed their frequencies much stronger or vanished completely when the number of considered modes of the TS^{FE} and C component was varied. This property could be used to localize real solutions and compare them to reference results. The results for a one certain set of substructuring modes are shown in Table 10.3. The reference free-free normal modes are computed directly from the FE model of the substructure of interest B.

The table shows the first five free-free blade modes. It can be observed, that for this set of parameters the TS MCFS method seems to work very well. The maximum frequency deviation of the derived from the reference component amounts to 3.8 %, indicating a small stiffening effect, and all the modal assurance criterium (MAC) values for the respective mode shapes are close to one.

Fig. 10.3 Schematic of the one blade substructuring problem

Table 10.3 Free normal modes $\tilde{B}$, CB-IP, 13 modes C and 16 modes TS

Modes C:	26
Modes TS^{FE}:	17
Coupling procedure:	MCFS

B from FEA		$\tilde{B}$ from TS		
Mode No.	Frequency (Hz)	Frequency (Hz)	Error (%)	MAC (-)
7	46.3	48.06	3.8	0.9910
8	130.9	135.62	3.6	0.9890
9	201.3	201.95	0.32	0.9968
10	253.3	254.14	−0.33	0.9885
11	339.4	334.05	−1.58	0.9963

Table 10.4 Free normal modes $\tilde{B}$, CB-IP, 13 modes C and 16 modes TS

Modes C:	15
Modes TS^{FE}:	10
Coupling procedure:	CB-IP

B from FEA		$\tilde{B}$ from TS		
Mode No. (-)	Frequency (Hz)	Frequency (Hz)	Error (%)	MAC (-)
1	19.6	19.60	1.69	0.9997
2	69.6	73.71	5.91	0.9872
3	139.1	162.02	16.49	0.9561
4	176.8	180.42	2.02	0.9814
5	182.9	187.26	2.38	0.8196

10.4.2 Fixed-Free Modes of the Blade $\tilde{B}$

Similarly to the free-free modes from the above section the fixed-free (fixed-interface) normal modes of the blade can be derived using the CB-IP TS method. However, on the contrary to the MCFS method, only the partitions of the system matrices that correspond to the modal coordinates are used to calculate the eigenfrequencies and modeshapes of the constraint system B. It can be observed, that the CB-IP method gives much more robust results for fixed-free modes, than the MCFS method for free-free modes. Furthermore, less spurious modes occurred during the study.

The first five fixed-interface normal modes of the blade are shown in Table 10.4. From this table one reads that the frequency error with 16.49 % is higher compared to the MCFS method. The MAC values, however, are also very close to unity.

10.4.3 Assembly of the Rotor System

When performing this numerical study the CB-IP method was found to be the most versatile TS coupling method due to the retention of the physical TS interface. To complete the study the CB-IP method is used to derive a full rotor system starting with only one blade attached to a TS like illustrated in Fig. 10.4. The FE representation of the hub is used as TS in this case.

The model of the hub was subtracted from the combined structure, yielding the derived representation of the blade, $\tilde{B}$, illustrated in Fig. 10.5.

The obtained model of the blade $\tilde{B}$ was duplicated and rotated by 120° and 240°, respectively, yielding three blades basing on $\tilde{B}$ as illustrated in Fig. 10.6a.

The three TS derived blades were coupled to a Craig-Bampton model of the hub (see Fig. 10.6b) using primal assembly, yielding a derived full model of the rotor. The free normal modes of the derived rotor were calculated and compared to the free normal modes directly computed from the full FE model of the rotor.

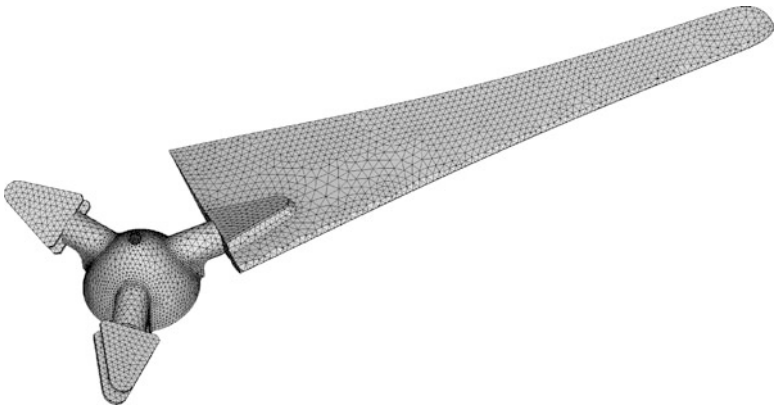

Fig. 10.4 Hub with one blade C

Fig. 10.5 TS-derived representation of one blade $\tilde{B}$

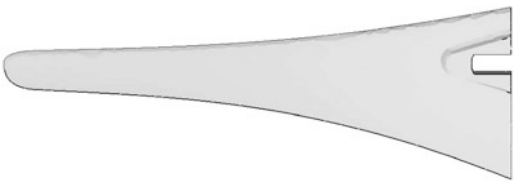

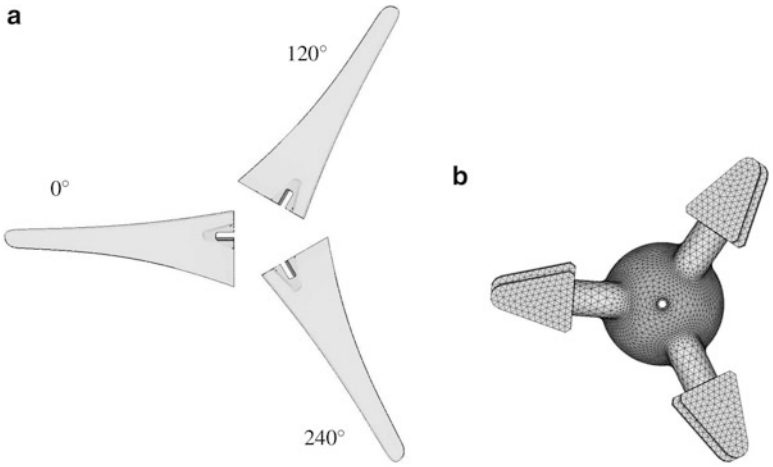

Fig. 10.6 (**a**) Expanded representation of $\tilde{B}$; (**b**) Single hub

Table 10.5 Free-free normal modes of the rotor

Modes C:	15
Modes A:	10
Coupling procedure:	CB-IP

Rotor from FEA		Rotor from expansion		
Mode No. (-)	Frequency (Hz)	Frequency (Hz)	Error (%)	MAC (-)
7	20.8	20.8	0.00	1.0
8	30.7	30.7	0.02	0.9999
9	31.0	31.0	0.03	0.9999
10	75.8	75.79	−0.01	0.999
11	84.1	84.19	0.11	0.9999

The results are shown in Table 10.5. The first five elastic free normal modes are estimated very well, with relative errors between 0.11 % and −0.01 % and the lowest MAC value being 0.9999.

10.5 Conclusion

Two different TS techniques have been applied to a high fidelity FE model of a small-scale wind turbine. Both of the techniques have been proven applicable in deriving respective component modes of the structure of interest. Both frequency and modeshape predictions gave high quality results for the numerical study. Especially, the CB-IP method has been found to be more versatile in possible applications due to the resulting structure of the system matrices. It has been used to reproduce the dynamic properties of an a priori unknown assembly.

In conclusion, it has been shown that the TS techniques are applicable to large scale FE structures with areal interfaces. Only the arising spurious modes remain a problem and will be investigated in future analysis.

References

1. Allen, M.S., Mayes, R.L.: Experimental modal substructuring to couple and uncouple substructures with flexible fixtures and multi-point connections. In: Proceedings of the 25th International Modal Analysis Conference, Orlando, FL (2007)
2. Allen, M.S., Mayes, R.L., Bergmann, E.J.: Comparison of FRF and modal methods for combining experimental and analytical substructures. J. Sound Vib. **329**, 4891–4906 (2010)
3. Allen, M.S., Kammer, D.C., Mayes, R.L.: Formulation of a Craig-Bampton experimental substructure using a transmission simulator. In: Proceedings of the 31st International Modal Analysis Conference, Orlando, FL (2013)
4. Allen, M.S., Kammer, D.C., Mayes, R.L.: Experimental based substructuring using a Craig-Bampton transmission simulator model. In: Proceedings of the 32nd International Modal Analysis Conference, Orlando, FL (2014)
5. Géradin M, Rixen D: Mechanical Vibrations, 3rd edn., Wiley, Chichester (2015)
6. de Klerk, D., Rixen, D.J., Voormeeren, S.N.: General framework for dynamic substructuring: History, review, and classification of techniques. AIAA J. **46**, 1169–1181 (2008)
7. Johansson, A.T., Lindholm, C.-J., Khorsand, M., Abrahamsson, T.: Modelling and calibration of small-scale wind turbine blade. In: Proceedings of the 31st International Modal Analysis Conference, Orlando, FL (2013)

Chapter 11
Effect of Interface Substitute When Applying Frequency Based Substructuring to the Ampair 600 Wind Turbine Rotor Assembly

Morteza Karamooz Mahdiabadi, Andreas Bartl, and Daniel J. Rixen

Abstract This study is an experimental validation of dual assembly frequency based substructuring method for coupling the rotor components of the Ampair 600 wind turbine (the Substructuring Focus Group's test bed). The method is applied for the assembly of the hub and three blades using a substitute (also called transmission simulator in modal based substructuring methods) in order to induce the effect of constrained interface of the blades. A method of virtual point transformation is used to tackle the problem of rotational degrees of freedom for interfaces. The hub is chosen to be the substitute and the frequency based substructuring approach is used for development of the full model. Finally, the results of substructuring with different substitutes are compared with the truth model of the rotor assembly.

Keywords Substructuring • FBS • Experiment • Virtual point transformation • Transmission simulator • Ampair 600 W wind turbine

11.1 Introduction

Substructuring methodology is a useful tool in structural dynamics for analysis of large and complex structures, by dividing the structures into subparts (called substructures) to simplify the analysis and assemble the analyzed substructures with a proper modeling of the interfaces to achieve the dynamics of the whole structures. It can also be used when one component of a multi-component structure is to be optimized, so that a redundant analysis of the whole structure could be reduced to only the analysis of the component which is under study.

Substructuring can be studied in various domains including modal [1, 2], frequency [3, 4], and time [5] domains, each method having its own properties and advantages. Among the substructuring methodologies, frequency based substructuring is especially good when the modes in a structure are not easy to be extracted, the damping in the system is relatively high, and the effect of unmeasured eigenfrequencies in the desired frequency range are considerable [6].

Although frequency based substructuring is well defined in theory, there are still challenges in experimental implementation of it, including the measurement of rotational degrees of freedoms (RDOFs) at the interface of substructures and modeling of the interface dynamics of substructures when they are coupled. The virtual point transformation (VPT) method was proposed [7] in order to solve the problem of coupling of rotational degrees of freedom at rigid interfaces which cannot be measured. Also, the transmission simulator (TS) method was presented to capture the dynamic properties at the interface and affect the compliance of the substructures near the interface [8].

This paper is an experimental example for the implementation of the recently proposed methods in experimental frequency based substructuring on the Ampair 600 W wind turbine rotor assembly which is the Substructuring Focus Group's Benchmark [9]. The hub is considered to be both one of the substructures and at the same time the substitute (transmission simulator), and three blades are to be coupled to it, using the Lagrange Multiplier frequency based substructuring method (LM FBS). The VPT method is employed for the assembly of RDOFs at the interface of the hub and blades. Finally, the substructuring results are compared to the truth frequency response data measured from the whole rotor assembly.

M.K. Mahdiabadi (✉) • A. Bartl • D.J. Rixen
Technical University of Munich, Institute of Applied Mechanics, Boltzmannstr. 15, 85748 Garching, Germany
e-mail: m.karamooz@tum.de

© The Society for Experimental Mechanics, Inc. 2016

M. Allen et al. (eds.), *Dynamics of Coupled Structures, Volume 4*, Conference Proceedings of the Society for Experimental Mechanics Series, DOI 10.1007/978-3-319-29763-7_11

11.2 Test Setup

In this work, the rotor assembly of the Ampair 600 W wind turbine is considered as an example for implementation of the coupling and decoupling Lagrange multiplier frequency based substructuring methods [6, 10]. In order to add the mass loading and compliance effects of the assembled blades, the hub is coupled to the blade as the substitute. The desired frequency range for substructuring is considered to be 300 Hz, however, the measured frequency range is set to be twice the desired range in order to observe how the methods behave at higher frequencies. Since the first eigenfrequency of the hub is almost twice the desired frequency range, it is approximated as a rigid body in the calculations. The blades are considered to have the same shape and material and therefore, only one blade is measured.

In the first stage, the full FRF matrix of the hub-blade assembly is measured for the internal points of the blade and interface DOFs (Fig. 11.1). In order to capture the FRFs at the interface (the bracket) in three translational directions, three 3D accelerometers are mounted on the bolts as shown in Fig 11.1. Then, for the sake of comparison of the substructuring results with the truth model, the same points of the blade and the bracket are measured when all three blades are assembled to the hub (see Fig. 11.2)

As mentioned, the hub is considered as a rigid body. Therefore, a proper CAD model [13] of the hub is used to construct the FRF matrix of that, which is defined as following:

$$Y^H = \begin{bmatrix} Y^H_{I_1I_1} & Y^H_{I_1I_2} & Y^H_{I_1I_3} \\ Y^H_{I_2I_1} & Y^H_{I_2I_2} & Y^H_{I_2I_3} \\ Y^H_{I_3I_1} & Y^H_{I_3I_2} & Y^H_{I_3I_3} \end{bmatrix} \tag{11.1}$$

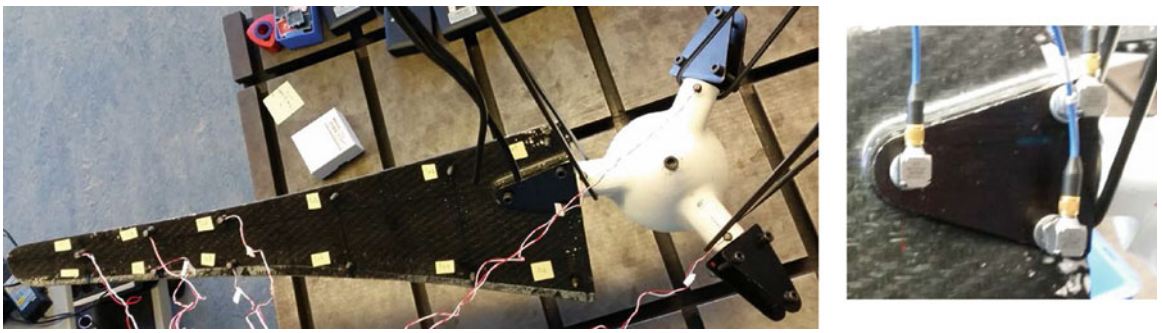

Fig. 11.1 Hub-blade measurement and position of the sensors on the interface

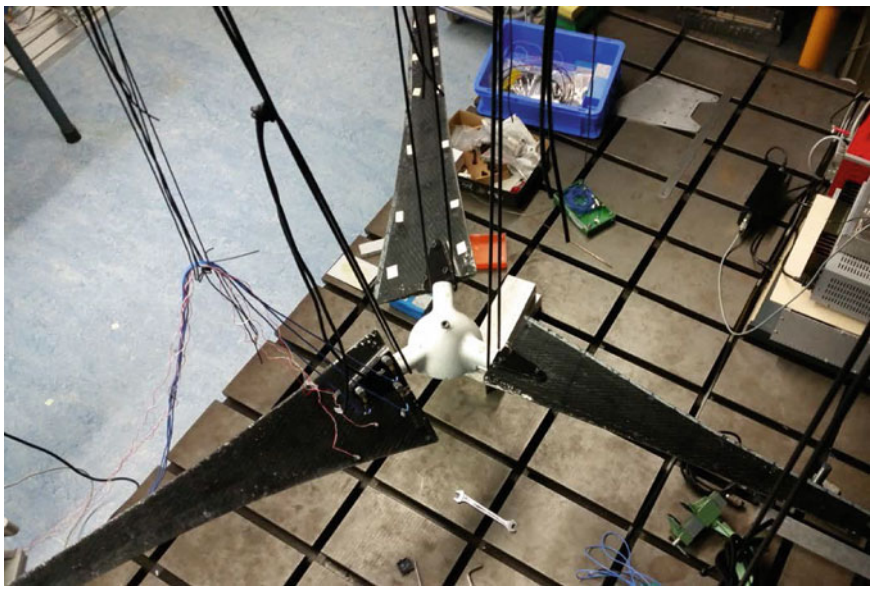

Fig. 11.2 Ampair 600 W rotor assembly measurement (truth model)

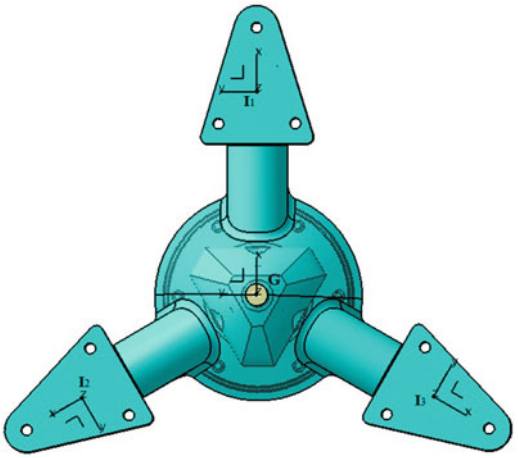

Fig. 11.3 Schematic of the hub model with global (G) and local (I_1, I_2, I_3) coordinates

Indexes I_1, I_2 and I_3 denote three virtual points at the hub interfaces and are shown in Fig. 11.3. Since the hub structure is a cyclic symmetric structure [4, 11], and due to the reciprocity property in linear structures, it can be concluded that all the driving point FRFs and all the cross point FRFs are equal, when considering local axis as indicated in Fig. 11.3. In other words, by calculating one driving point FRF and one cross point FRF for the hub the full FRF matrix of the hub (Eq. 11.1) can be constructed. The Inertia properties with respect to the global coordinate, G, is obtained using CATIA v5. Then, these properties are transformed to the virtual point coordinates using proper translation and rotation matrices [4].

To obtain the rotational FRFs at the interfaces of the hub-blade assembly, the VPT method [4, 7] was employed to transform the measured 3D translational FRFs at each interface to a 6D FRF matrix at a virtual point. This 6D FRF matrix at the virtual point includes the rotational FRFs. The virtual points for three interfaces are chosen to be at the centroid of the triangles having the same vertices as the position of the three interface bolts (see Fig. 11.3).

11.3 Substructuring Methodology

The Lagrange multiplier frequency based coupling and decoupling methods are properly explained in [6, 10]. These methods can especially be used as an experimental substructuring approach when the modes cannot be properly extracted and the FRFs not synthesized by a pole-residue model; for the current application, a mode identification could be applied although the presence of relatively high structural damping and the existence of several modes outside of the frequency range of interest make modal synthesis challenging.

In this case, first the substitute (hub) has to be subtracted from the hub-blade to obtain the FRFs of the blade alone. Knowing Y^{HB} and Y^{H} the FRF matrices of the hub-blade and hub, respectively, the FRF matrix of the blade can be obtained using the following dual decoupling formula:

$$Y_{decoupled} = Y^{HB} - Y^{HB}B^{HB^T}\left(B^{HB}Y^{HB}B^{HB^T} - B^{H}Y^{H}B^{H^T}\right)^{-1}B^{HB}Y^{HB} \tag{11.2}$$

Where B is a signed Boolean matrix and specifies the compatibility conditions in the system, namely, it specifies the DOFs at each substructure interface, which should be connected to the corresponding DOFs at other substructures' interfaces.

Now, having the FRF matrices of the hub and the blades, the LM FBS method can be applied to obtain the FRF matrix of the whole assembly:

$$Y_{Rotor\_Assembly} = Y_{Total}\left(I - B^{T}\left(BY_{Total}B^{T}\right)^{-1}BY_{Total}\right) \tag{11.3}$$

Table 11.1 Inertia properties around the global coordinate of the hub and its local coordinates

Parameter	Global (G)
$Mass$	$3.853\,kg$
I_{xx}	$0.03\,kg.m^2$
I_{yy}	$0.03\,kg.m^2$
I_{zz}	$0.03\,kg.m^2$
x_{cg}	$0.000\,m$
y_{cg}	$0.000\,m$
z_{cg}	$-0.59445\,m$

Where B is the Boolean matrix specifying the corresponding DOFs at the interfaces and I is the identity matrix. The matrix Y_{Total} is a block diagonal matrix including the FRF matrices of all substructures as follows:

$$Y_{Total} = \begin{bmatrix} \left[Y^{H}\right] & 0 & 0 & 0 \\ 0 & \left[Y^{Blade1}\right] & 0 & 0 \\ 0 & 0 & \left[Y^{Blade2}\right] & 0 \\ 0 & 0 & 0 & \left[Y^{Blade3}\right] \end{bmatrix} \tag{11.4}$$

And the FRF matrices of the blades are:

$$Y^{Blade1} = \begin{bmatrix} Y_{BB}^{Blade1} & Y_{BI_1}^{Blade1} \\ Y_{I_1B}^{Blade1} & Y_{I_1I_1}^{Blade1} \end{bmatrix},\ Y^{Blade2} = \begin{bmatrix} Y_{BB}^{Blade2} & Y_{BI_2}^{Blade2} \\ Y_{I_2B}^{Blade2} & Y_{I_2I_2}^{Blade2} \end{bmatrix},\ Y^{Blade3} = \begin{bmatrix} Y_{BB}^{Blade1} & Y_{BI_3}^{Blade1} \\ Y_{I_3B}^{Blade1} & Y_{I_3I_3}^{Blade1} \end{bmatrix} \tag{11.5}$$

where index B denotes the internal points on each blade. The substructuring results are discussed in the next section.

11.4 Results

By measuring the full FRF matrix of the hub-blade assembly and calculating the full inertial matrix of the hub (Eq. 11.1), the LM FBS method can be applied to find the full FRF matrix of the whole rotor assembly. The calculated inertia properties of the hub around the global coordinate (G) is shown in Table 11.1. These inertia properties are transformed to the local coordinates I_1, I_2 and I_3 to find the full FRF matrix for the hub.

Figure 11.4 shows the substructuring results obtained from the driving and cross point measurements on blade2. As it can be seen in the figure, the substructuring FRF result for this driving point, can reasonably well capture many of the resonances and anti-resonances up to 300 Hz compared to the FRF of the truth model, however, at some frequency ranges (e.g. around 100 Hz) the deviation of the substructuring FRF with respect to the corresponding truth one is relatively high (15.5 % Max error).

The extracted eigenfrequencies from the substructuring results are compared which the truth model in Table 11.2. The errors of the substructuring eigenfrequencies in all eight extracted modes are less than 10 %, except the second mode in which the error is 15.5 %.

The drive point FRF at the hub-blade2 interface is shown Fig. 11.5 for both substructuring and truth models. The substructuring result again seems to be affected by the presence of two close eigenfrequencies in the range of 100–150 Hz, however, for the rest of the frequency range, it could properly follow the truth model.

The aim of this work was to improve the valid substructuring frequency range for this assembly which was first investigated by [4] and was about 200 Hz. Looking at the drive and cross point measurement results obtained from substructuring approach, it was shown that the substructuring data could follow most of the corresponding ones in the truth model.

The error sources of the substructuring result can be caused by several reasons [1, 6] including inaccuracy in the direction of the hammer excitation and different material properties in the blades which leads to different eigenfrequencies for each of them [12].

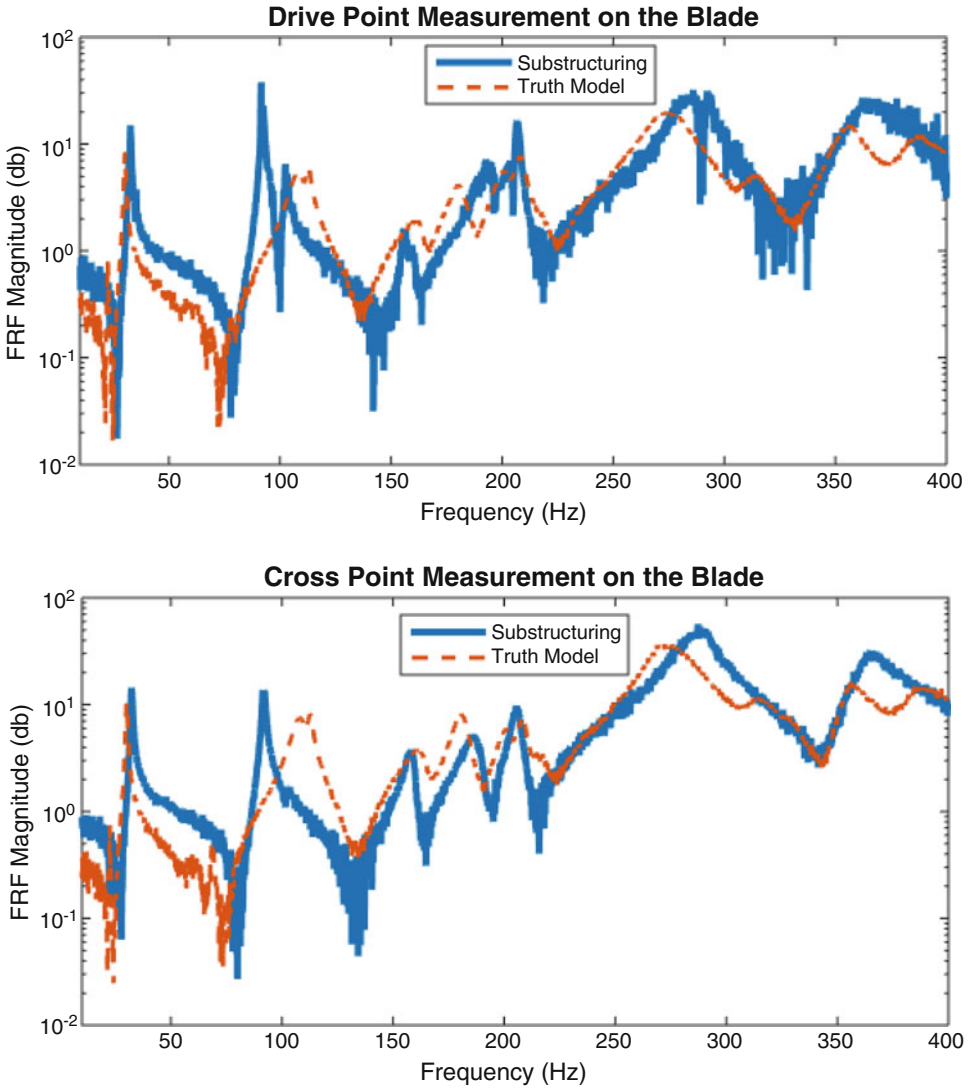

Fig. 11.4 Comparing the drive point and cross point substructuring FRFs for blade2 with the truth model

Table 11.2 Comparing the eigenfrequencies for a drive point on the blade

Flexible mode	Truth model (Hz)	Substructuring (Hz)	Error (%)
1	30.16	32.66	8.3
2	108.3	91.56	15.5
3	113	102.3	9.5
4	161.3	155.5	3.6
5	180	192.7	7.1
6	200.8	203.4	1.3
7	208.1	206.7	0.7
8	274.2	285.9	4.3

11.5 Conclusion

This work is an experimental example in implementation of the Lagrange multiplier frequency based substructuring method alongside the recent developments for experimental substructuring techniques to improve the substructuring result. The hub and three blades of the Ampair 600 W are considered as substructures to be assembled. In order to find the rotational

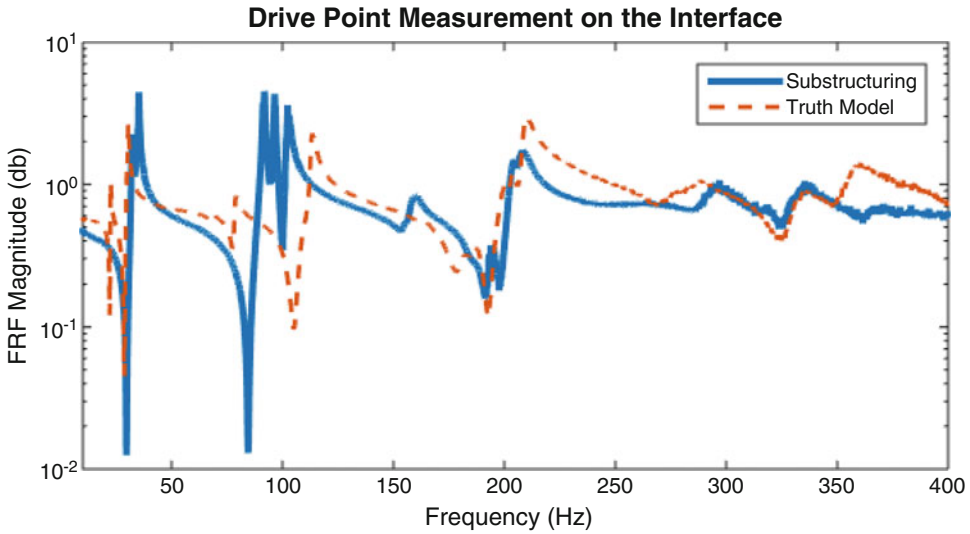

Fig. 11.5 Comparing the drive point substructuring FRFs at the interface I2 with the truth model

DOFs at interfaces, the virtual point transformation is used to transform the 3D translational FRFs to a 6D full FRF at the corresponding virtual point which includes rotational DOFs. The effect of mass loading and compliance of the assembled interfaces are taken into account using a proper substitute to couple to the blades to the hub.

The Substructuring results showed a reasonable correlation with the truth model for a relatively wide frequency range (up to 300 Hz), namely, the maximum error of the substructuring eigenfrequencies was 15.5 % with respect to the truth data. Future investigation of this work could be on further improvement of the substructuring results by considering the hub as a flexible substructure, taking the flexible modes of the interfaces into account and trying to reduce the noise errors using more accurate data acquisition system.

References

1. Roettgen, D.R., Mayes, R.L.: Ampair 600 wind turbine 3-bladed assembly substructuring using the transmission simulator method. In: IMAC-XXXIII: International Modal Analysis Conference, 2015
2. Rohe, D., Mayes, R.: Coupling of a bladed hub to the tower of the Ampair 600 wind turbine using the transmission simulator method. In: Proceedings of the XXXI: International Modal Analysis Conference, February 2013
3. de Klerk, D., Rixen, D.J., de Jong, J.: The frequency based substructuring (FBS) method reformulated according to the dual domain decomposition method. In: IMAC-XXIV: International Modal Analysis Conference, 2006
4. Rahimi, S., de Klerk, D., Rixen, D.J.: The Ampair 600 wind turbine benchmark: results from the frequency based substructuring applied to the rotor assembly. In: IMAC-XXXI: International Modal Analysis Conference, Garden Grove, 2013
5. Rixen, D.J., van der Valk, P.L.C.: An impulse based substructuring approach for impact analysis and load case simulations. J. Sound Vib. **332**(26), 7174–7190 (2013)
6. de Klerk, D., Rixen, D.J., Voormeeren, S.N.: General framework for dynamic substructuring: history, review and classification of techniques. AIAA J. **46**(5), 1169–1181 (2008). doi:10.2514/1.33274
7. de Klerk, D., Voormeeren, S.N., Petzsche, T.: Solving the Rdof problem in experimental dynamic substructuring. In: IMAC-XXVI: International Modal Analysis Conference, 2008
8. Matthew, S.A., Randall, L.M., Bergman, E.J.: Experimental modal substructuring to couple and uncouple substructures with flexible fixtures and multi-point connections. J. Sound Vib. **329**(23), 4891–4906 (2010). doi:10.1016/j.jsv.2010.06.007. ISSN 0022-460X
9. Mayes, R.: An introduction to the SEM substructures focus group test bed – the Ampair 600 wind turbine. In: Proceedings of the 30th International Modal Analysis Conference, Orlando, Florida, February 2012
10. Voormeeren, S.N., Rixen, D.J.: A family of substructure decoupling techniques based on a dual assembly approach. J. Mech. Syst. Signal Process. **27**, 379–396 (2012). doi:10.1016/j.ymssp.2011.07.028
11. Rixen, D., Lohman, R.: Efficient computation of eigenmodes of quasi-cyclic structures. In: IMAC-XXIII: International Modal Analysis Conference, 2005
12. Rixen, D.J.: How measurement inaccuracies induce spurious peaks in frequency based substructuring. In: IMACXXVII: International Modal Analysis Conference, 2008
13. http://substructure.engr.wisc.edu/substwiki/index.php/University_of_Stuttgart

Chapter 12
Improving Floor Vibration Performance Using Interstitial Columns

Michael J. Wesolowsky, J. Shayne Love, Todd A. Busch, Fernando J. Tallavo, and John C. Swallow

Abstract Lightweight, long-span steel office floors of both new and old construction are commonly susceptible to objectionable footfall-induced vibrations. Frequently, older buildings are renovated for newer purposes that require the removal of partitions that had previously provided some vibration control through added structural damping and stiffness. It can be prohibitive, both economically and operationally, to either retrofit the original structure with more beams, or to add external damping devices such as Tuned Mass Dampers (TMDs). This paper provides three case studies of lightweight, long-span steel buildings, and demonstrates the effectiveness of using interstitial columns to vertically link two or more floors together. In doing so, the mass and/or stiffness of the floor will be increased, which serves to reduce footfall vibration levels.

Keywords Human-induced vibration • Vibration measurements • Vibration mitigation • Model validation • Dynamic loading

12.1 Introduction

The primary sources of vibration in most buildings are mechanical equipment and human activity, especially footfalls. For mechanical equipment, it is critical to provide sufficient vibration isolation to limit the transmission of vibration from the source to nearby sensitive areas. In the case of footfalls, as people walk, the impact from each footfall induces floor motions that may also easily transmit to nearby spaces. This paper presents three case studies in which existing long-span steel floors have experienced objectionable, disruptive or destructive motions due to footfall-induced vibrations. In all three cases, Tuned Mass Dampers (TMDs) and/or additional beams were not possible due to the structural capacity of the floors. Interstitial columns were implemented as an alternative mitigation strategy due to their low cost, and relative ease of installation.

The first case involves a new long-span four-storey structure intended to house a fitness center directly below lawyers' offices. The second case involves the conversion of a three-storey office building into a vivarium, in which pre-retrofit vibrations were eight times greater than post-retrofit allowable limits. The final case involves a high-rise office building that had all of the partitions on two floors removed, and was thereafter experiencing vibrations that were objectionable to office staff.

12.2 Vibration Criteria

Widely used in North America, the American Institute of Steel Construction Design Guide 11 (Floor Vibration Due to Human Activity) [1] has recommended acceleration criteria for various occupancies of residential and commercial buildings. These criteria are specified as peak acceleration values, and are dependent on the fundamental frequency of response of the floor. These curves have been defined as a series of multiples of the original ISO 2631-2 (1989) [2] base curve for human response to whole body vibration, which is the threshold of human perception. As an example, the recommended acceleration levels for rhythmic activities are ten times greater than those for residential and office occupancies, as people engaged in those

M.J. Wesolowsky (✉) • T.A. Busch • F.J. Tallavo • J.C. Swallow
Swallow Acoustic Consultants Ltd., 23-366 Revus Avenue, Mississauga, ON, Canada L5G 4S5
e-mail: mwesolowsky@swallowacoustic.ca

J.S. Love
Rowan Williams Davies & Irwin Inc., 650 Woodlawn Road West, Guelph, ON, Canada N1K 1B8

© The Society for Experimental Mechanics, Inc. 2016

M. Allen et al. (eds.), *Dynamics of Coupled Structures, Volume 4*, Conference Proceedings of the Society for Experimental Mechanics Series, DOI 10.1007/978-3-319-29763-7_12

activities are more likely to accept greater vibrations due to the nature of their activities. A greater allowance is also made for indoor footbridges, shopping malls and spaces used for dining and dancing.

Another method for defining vibration criteria for human comfort expresses uses the root mean square (RMS) velocity response of each one-third octave band from 1 Hz to 80 Hz [3]. For sensitive equipment, this criterion may be expressed in one-third octave bands, or other formats, including power spectral densities, peak-to-peak levels, etc. Over the past 25 years, generic vibration limits have been developed which provide frequency-dependent sensitivities for wide classes of equipment, and are used extensively in design of healthcare and research facilities [3]. These vibration criterion (VC) curves are internationally accepted as a basis for designing and evaluating the performance of vibration sensitive equipment and the structures that support them. The VC curves range between Workshop (least stringent) through VC-G (most stringent). Most laboratories target at least VC-A as a maximum baseline for the majority of the facility, with certain areas requiring more stringent criteria, depending on the expected use of the space.

These curves were also originally based on the ISO 2631-2 (1989) [2] base curve for human response to whole body vibration, which is considered the threshold of human perception, but have since evolved. The ISO base curve is often referred to as the ISO-Operating Room criteria. The above noted criteria are also specified as RMS velocities in one-third octave bands. The VC curves should not be used to replace manufacturers' specifications for vibration requirements, but are beneficial where manufacturers' specifications are non-existent, incomplete, or where specific equipment has not yet been selected.

The AISC criteria and VC curves will be used as a basis of evaluating the performance of the case studies in this paper.

12.3 Case Study #1: Long Span Steel Fitness Floor

The building used for Case Study #1 was constructed from 2009 to 2011, and is located in Las Vegas, NV. It is part of a large mixed use commercial/residential development, comprised of approximately 20 low- and mid-rise structures. Several of the buildings were constructed using castellated beams, which are manufactured by cutting a WF beam in a zigzag pattern along the web with an automated computer-controlled plasma torch, separating the two halves, then welding the web post back together at the high points, as shown in Fig. 12.1. This process increases the depth of the beam by approximately 50 %, therefore increasing the strength and stiffness by approximately 40 %. The final openings are usually either circular or hexagonal.

Typical bays were approximately 9 m by 18 m, with only 80 mm of lightweight concrete toping over steel deck. The second floor of this building was intended to be used as a fitness centre, with insurance and law offices located on the floors directly above. During construction it was observed that the footfall-induced vibrations caused by the construction staff was causing motion so great, that the concrete topping was cracking. Further, walkers on the second floor were inducing considerably noticeable vibrations on the third and fourth floors. It should be noted that all three floors had nearly identical structural layouts.

Vibration measurements were conducted to identify the fundamental frequencies and the inherent damping of the monitored floor, as well as to assess the level of vertical accelerations due to human activities taking place on the floor. Vibration data was collected which was caused by construction activities at the site, random/synchronized walking excitation and rhythmic excitation. Walking and rhythmic excitations were made possible through the assistance of several site workers performing different walking and jumping scenarios.

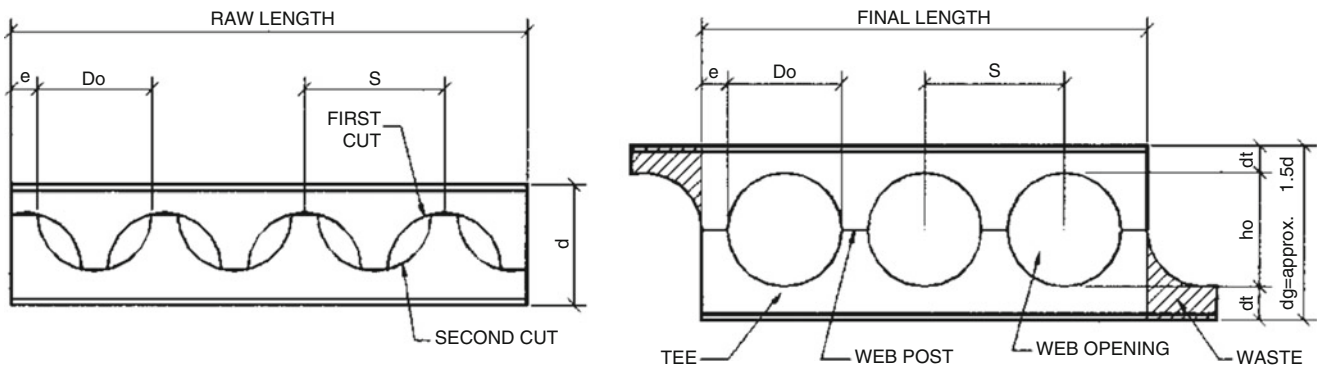

Fig. 12.1 Manufacturing process for castellated beams [4]

Table 12.1 Comparison of pre-retrofit measured peak accelerations at the center of the slab with the AISC criteria

	Random walking[a]	Synchronized walking[b]	Rhythmic activities[c]
Measured peak acceleration (%g)	2.7	5.4	7.8
AISC recommended criteria (%g)	0.5	0.5	5.0

[a]Groups of 3–4 individuals walking randomly together
[b]Groups of 3–4 individuals walking together under controlled synchronization
[c]Groups of 4–6 individuals engaged in simple aerobic activities

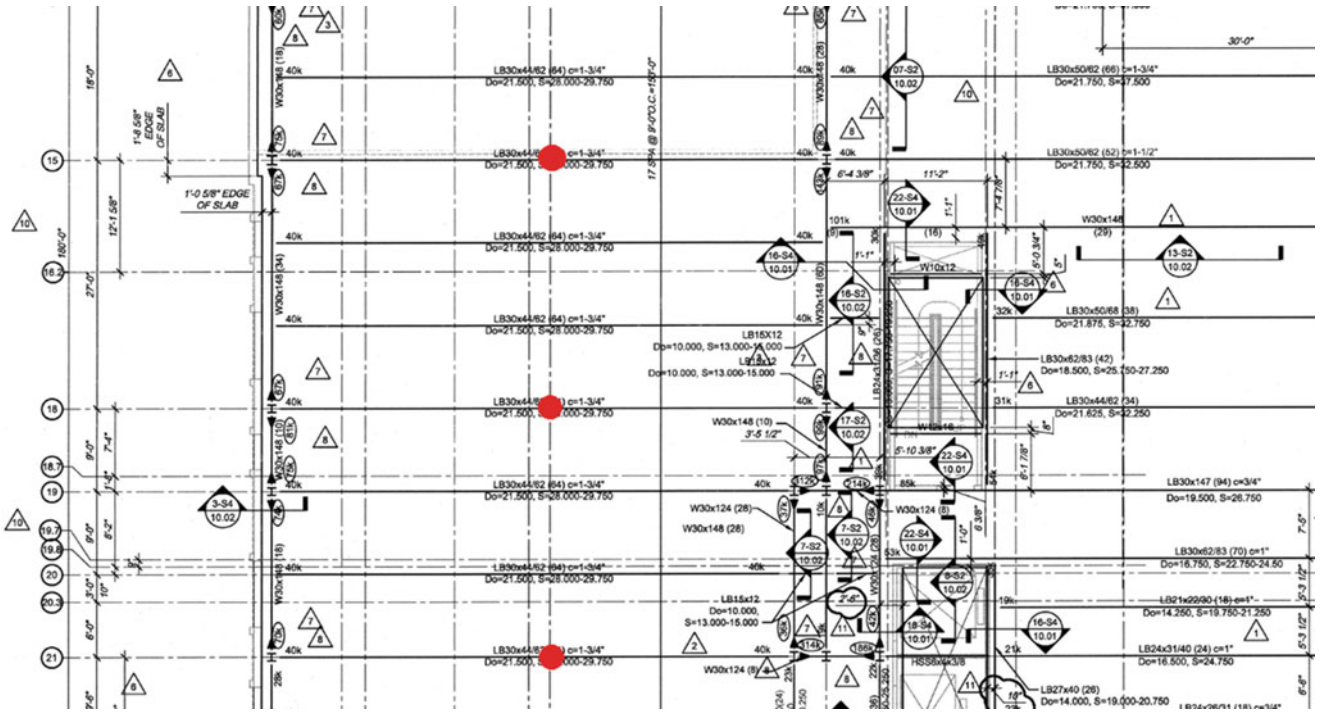

Fig. 12.2 Mitigated structure (*red dots* denote interstitial columns)

The fundamental frequency of the typical bays was determined to be approximately 4.5 Hz, and the damping ratio was estimated to be between 0.9 and 1.2 %. This combination of dynamic properties lends itself poorly to controlling footfall-induced vibrations, which was evident from the tests conducted, as shown in Table 12.1. The AISC criteria are also included in Table 12.1 for comparison. It is evident from these measurements that the floor was exceeding criteria by a significant margin for all activity types.

Several mitigation schemes were considered analytically, including Tuned Mass Dampers (TMDs), infill beams, and infill columns. The first two options were discounted due to cost, and the design capacity of the existing structural system being unable to carry significant further dead load. Further, due to clear-space clauses in the leasing agreements with the commercial tenants who were going to occupy the first floor, ownership was unwilling to consider columns directly below the fitness floor to control the vibrations.

It was decided by the structural team to try installing interstitial columns at the mid-points of the 18 m girders that would structurally link the second, third and fourth floors together (see Fig. 12.2). This would increase the overall stiffness of the floor, as well as engage more modal mass when occupants were either walking across the floor or performing fitness activities. Both of these factors were expected to reduce the footfall-induced vibrations.

Initial tests were conducted with temporary jack posts that were compression fit between the floors over two bays of the building. As the results from these tests were favorable, permanent columns were then installed across all long span floors in the building. Final testing was then conducted, which showed that all tested areas now met the AISC criteria (See Table 12.2).

Table 12.2 Comparison of post-retrofit measured peak accelerations at the center of the slab with the AISC criteria

	1 Walker	3 Synchronized walkers	Rhythmic activities
Measured peak acceleration (%g)	0.21–0.48	0.26–0.49	0.48–0.99
AISC recommended criteria (%g)	0.5	0.5	5.0

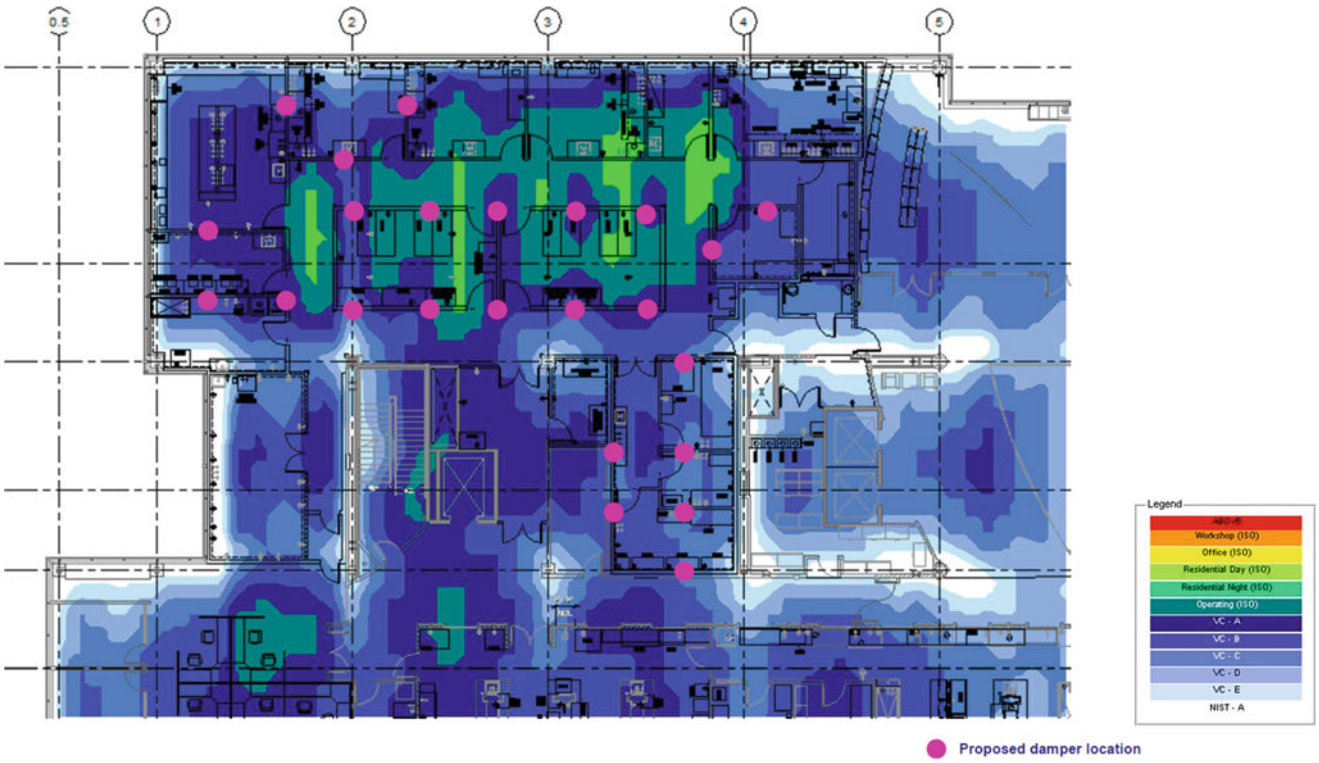

Fig. 12.3 Predicted floor vibrations due to originally proposed viscous damper layout

12.4 Case Study #2: Office to Laboratory Conversion

The building used for Case Study #2 was constructed in the mid-1980s. It is a typical office building of its era, with approximately 9 m bays, W-section steel beams and girders, and 75 mm lightweight concrete topping on a steel deck. The second floor of the building was being converted from conventional office use to a research laboratory, complete with a vivarium. The commonly used criterion for vivaria applications is VC-A (50 μm/s), which is described in Sect. 12.2. Initial vibration measurements in the space indicated that velocities up to criterion ISO Office (400 μm/s) were being experienced over large portions of the floor.

The user of the space had indicated that their preferred method of mitigation was the installation of 20 vertical viscous dampers, to be hidden in the proposed partitions of the laboratory layout. A structural finite element method (FEM) model representing the second and third floors of the facility was developed using SAP2000 Nonlinear analysis software. Predictions of footfall vibration levels for the proposed layout were computed according to the methodologies outlined by the Steel Construction Institute (SCI P354) [5]. Walkers were considered on Floors 2 and 3, due to the proposed mitigation scheme closely coupling those floors. Responses were estimated at all locations on the second floor, and can be seen in Fig. 12.3. Figure 12.3 also shows the originally proposed layout of the damping columns. This Figure indicates that although many areas were expected to show an improvement in vibration levels, several other areas were expected to result in an increase in vibration (above the criterion). Further analysis indicated that this was due to the regular spacing of the proposed columns, which forced all modal maxima to the same location on the floor, thus amplifying the predicted motions.

Further analysis also indicated that the maximum expected levels of peak-to-peak displacement were in the range of 14 μm (0.014 mm). The minimum displacement usually considered for viscous dampers to be effective is approximately 1000 times greater than this value. Should dampers be installed at the proposed locations, they would only act as stiffening

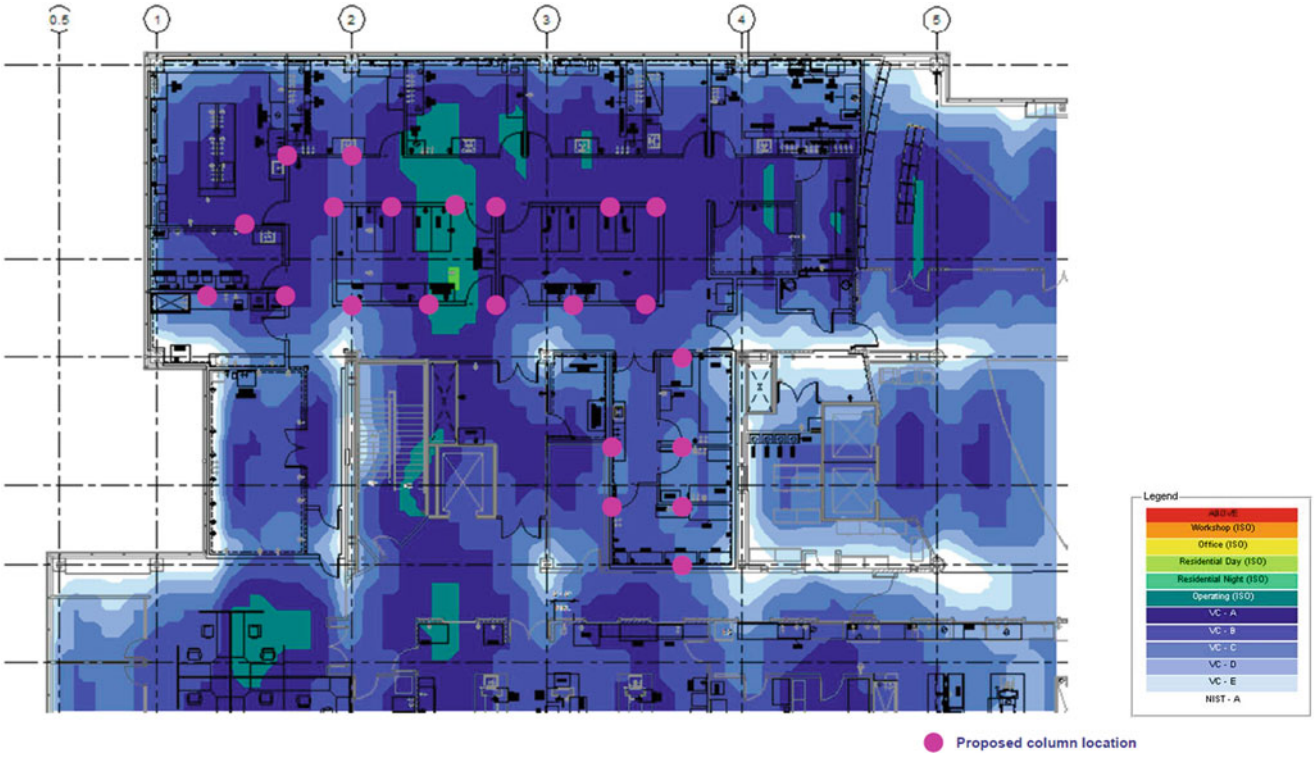

Fig. 12.4 Predicted floor vibrations due to modified steel column layout

members (i.e. conventional columns), as the applied force from the vibrating floor would not be able to overcome the force of friction required to engage the dampers. As a result of these low expected displacement levels, and the increased predicted floor response shown in Fig. 12.3, it was decided to use conventional steel columns installed in an irregular pattern, in order to modify the mode shapes of the floor. Figure 12.4 shows the modified column layout, and the resulting floor vibration predictions. From this figure it can be seen that there are only three very small areas that exceed the criterion, two of which are not in sensitive areas. The other area that exceeds the criterion is insignificant, due to its small size and location in a doorway. It should also be noted that the level of assumed inherent damping of 3 % was expected to be conservative, as the installation of the columns will tie down and engage the partition walls, thereby increasing damping. It should be noted that post-retrofit tests were not conducted, but anecdotal evidence indicated that there have been no concerns by the tenant.

12.5 Case Study #3: Disappearing Partitions

The building considered for Case Study #3 was an office tower built in 1980, and had exceptionally large 18 m by 30 m bays. The normal-weight concrete topping was 80 mm. A new tenant had recently moved into the 15th and 16th floors, and had retrofit the space by removing almost all the floor to ceiling partitions in favour of a large open office arrangement. This arrangement is unique to the building, as all other floors had considerable floor to ceiling partition layouts. Since the tenant moved in, numerous complaints had been recorded by users of the space regarding footfall-induced vibrations, including items on desks falling on the floor while people walked in the nearby aisles. Initial vibration testing indicated that the natural frequency of the main bays was approximately 4.3 Hz, and the inherent damping was only 1.4 %. The testing also indicated that although the vibration levels measured in most areas satisfied ISO Office, the measured levels were near 800 μm/s (which in the authors' experience could be considered as excessive by some occupants).

Several mitigation options were considered, with TMDs and additional beams immediately dismissed due to the structural system being unable to carry the additional load. A remedial approach was proposed to the client, which included three interstitial columns per bay. A structural finite element method (FEM) model representing the 15th and 16th floors of the tower was developed using SAP2000 Nonlinear analysis software. Predictions of footfall vibration levels for the proposed layout were computed according to the methodologies outlined by the Steel Construction Institute (SCI P354) [5]. Walkers

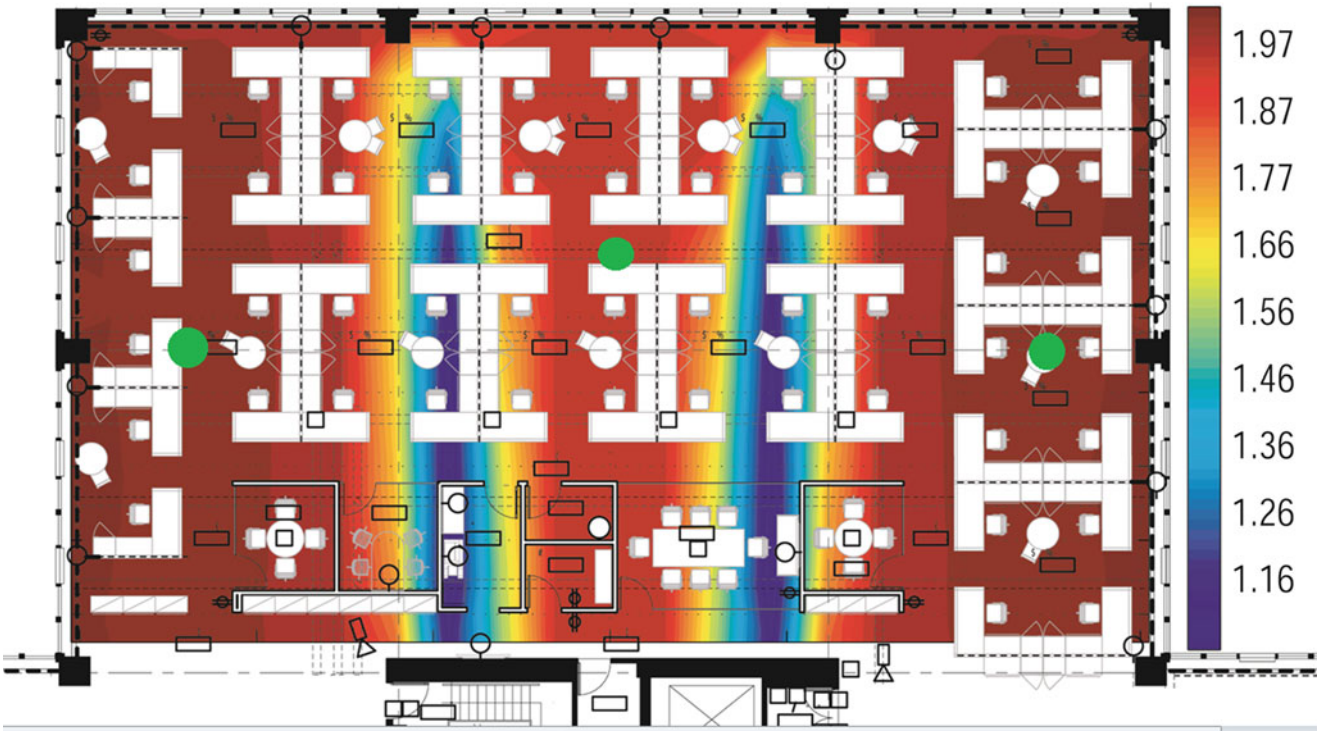

Fig. 12.5 Expected vibration attenuation factors in the North Bay (interstitial columns indicated by *green circles*)

were considered on the 15th and 16th floors, due to the proposed mitigation scheme closely coupling those floors. Responses were estimated at all locations on the 16th floor. Figure 12.5 shows the expected attenuation factor across the North bay of the building. From this figure it is seen that most areas of the floor are expected to experience an attenuation factor of close to two, with limited areas having an expected attenuation factor closer to unity. Similar reductions were predicted for the other bays of the floors. The columns are currently being installed, and post-retrofit measurements have not been completed at the time of writing this paper.

12.6 Conclusions

Three case studies have been presented in which existing long-span steel floor have experienced objectionable, disruptive or destructive motions due to footfall-induced vibrations. In all three cases, Tuned Mass Dampers (TMDs) and/or additional beams were not possible due to the structural capacity of the floors. Interstitial columns were implemented as an alternative mitigation strategy due to their low cost, and relative ease of installation. The following conclusions have been made:

1. Interstitial columns are often a cost-effective and low-intrusive mitigation strategy for long-span floors that require vibration mitigation.
2. Using interstitial columns has been shown analytically and practically to reduce floor vibrations by factors between 2 and 8 over large areas of steel floors.
3. Care should be taken to install these interstitial columns at the proper locations so as to not cause an *increase* in floor motion, due to aligned modal maxima causing constructive interference.
4. If floors are to be coupled for vibration control, it is important to consider walkers on multiple floors in order to more accurately assess the vibrations on each level.

References

1. Murray, T.M., Allen, D.E., Ungar, E.E.: Floor Vibration Due to Human Activity, AISC Design Guide, Series No. 11, American Institute of Steel Construction, Chicago (1997)
2. ISO 2631-2, Evaluation of human exposure to whole-body vibration-part 2: human exposure to continuous and shock-induced vibrations in buildings (1 to 80 Hz), International Standard, ISO 2631-2, 1989
3. Amick, H., Gendreau, M., Busch, T., Gordon, C.: Evolving criteria for research facilities: vibration. In: Proceeding of SPIE Conference 5933: Buildings for Nanoscale Research and Beyond, San Diego, CA, July 31 to August 1, 2005
4. Milligan, B.: The “smart” solution, modern steel construction. American Institute of Steel Construction, May, 2001
5. Smith, A.L., Hicks, S.J., Devine, P.J.: Design of Floors for Vibration: A New Approach – Revised Edition (SCI P354). Steel Construction Institute, Ascot (2009)

Chapter 13
Probabilistic Model Updating of Controller Models for Groups of People in a Standing Position

Albert R. Ortiz and Juan M. Caicedo

Abstract The effects of occupants over the dynamic properties of a structure have been traditionally modeled showing the human body as lumped masses connected with spring and dampers. A new approach for modeling the effects of a standing person was developed 2 years ago based on control theory. The new approach starts from the assumption that the human body can input energy into the system, changing the response of the structural system. The control theory based models have shown to work for a single occupant. This work presents the modeling of groups of standing people using a controller model. The parameters of the controller are obtained using a probabilistic approach based on Bayesian model updating.

Keywords Human-structure interaction • Closed loop control • Human loads • Feedback • Vibration induced by people

13.1 Introduction

Humans can affect considerably the dynamics of the structures that they occupy. For example [1–3] have shown that structures show highly different dynamics properties when occupied by crowds. Loading the structure with a crowd can produce conditions to which the structures have no been design independently if people are moving or not.

There are two main scenarios that are usually studied in human-structure interaction. The first one is when the crowd is moving and produce a dynamic interaction with the structure. The second scenarios studies the interaction of standing people. Pedersen [4, 5], Ortiz et al. [3] show evidence of how passive occupants of a structure can have a significant affect in the behavior of the human-structure system, and the effect of the human body goes beyond the addition of a mass, as often used for design.

In the last decades, many authors started to detail the importance of modeling the humans and their interaction with the structure. Originally additional lumped masses were adopted by some design codes. Later more complex models based on lumped masses, spring, and dampers (MDS) were developed to model the dynamics of a standing person. In the last 2 years, Ortiz and Caicedo [6, 7] have developed a different kind of models starting from the assumption that the human is a controller system. Their work demonstrated that a PD controller could represent the dynamics generated by a single human standing over a structure. Models are usually proposed for single humans and only a papers have proposed groups models. This paper focuses in comparing results of modeling standing groups of people using controller models. Controllers models are generated for three single humans independently. Then groups of two people occupied at the same time an instrumented structure. Models are used to see if they can track the dynamics of the human-structure system.

This paper is divided in four sections. The next section briefly describes the proposed methodology. The Experimental setup section discussed the properties of the structure and the experiments performed. Finally the results and conclusions sections show the performance of the PD model when modeling a crowd.

A.R. Ortiz (✉) • J.M. Caicedo
Department of Civil and Environmental Engineering, University of South Carolina, Columbia, SC 29208, USA
e-mail: aro@email.sc.edu; alrortiz@gmail.com; caicedo@cec.sc.edu

© The Society for Experimental Mechanics, Inc. 2016

M. Allen et al. (eds.), *Dynamics of Coupled Structures, Volume 4*, Conference Proceedings of the Society for Experimental Mechanics Series, DOI 10.1007/978-3-319-29763-7_13

13.2 Methodology

Ortiz and Caicedo [6, 7] developed models based on Closed loop control theory for modeling the human-structure interaction of standing people. A graphical representation of the model is presented in Fig. 13.1. The human, noted as $H(s)$, and the structure, noted as G(s), form a system where feedback relations alter the original dynamics of the empty system G(s) once it is occupied.

13.2.1 Structural Model (G(s))

The mathematical expression for modeling the structure was modified from what was used in [6]. Previous work used the parameters of stiffness, mass and damping to model the structure and then calculate its associated transfer function. Here, the Transfer Function, $G(s)$, is expressed using poles and zeros as shown in (13.1).

$$G(s) = K\frac{(s-z_1)(s-z_2)\dots(s-z_{m_1})(s-z_m)}{(s-p_1)(s-p_2)\dots(s-p_{m_1})(s-p_m)} \tag{13.1}$$

Each pole p of the system represent a natural frequency of the structure and its corresponding damping ratio. The zeros of the transfer function are expressed by z. The system is assumed to be stable [8]. Based on poles, zeros and the gain parameter (K), the dynamical model of the structure can be expressed in terms of natural frequencies ω, damping ratios ζ and the gain K. Experimental tests of the structure used in this paper shows two clear natural frequencies. Therefore, the transfer function of the empty structural system will be modeled using two poles and one zero and the parameters to model the empty structure are $\Theta_{empty} = \{\omega_1, \omega_2, \zeta_1, \zeta_2, \omega_{z1}, \zeta_{z1}, K\}$. These parameters are updated in a probabilistic sense as briefly described in Sect. 13.2.3

13.2.2 Human Model (H(s))

This paper proposes the use of many controllers, one modeling each person, to model a crowd over a structure. Figure 13.2 shows a block diagram of the whole human-structure interaction system with two people. The controllers $H_1(s)$ and $H_2(s)$ represent the two people over the structure $G(s)$. Each person acts as an independent controller, using acceleration from the structure as feedback, and commanding a control force on the structure.

The Transfer Function of the full HSI system occupied by two people can be presented as:

$$TF(s) = \frac{G(s)}{1 + G(s)[H_1(s) + H_2(s)]} \tag{13.2}$$

In (13.2) it is assumed that controllers are acting in parallel, indicating that the motion of one person has little effect on the motion of the next person. This assumption is reasonable for standing people but should be further tested for crowds in motion.

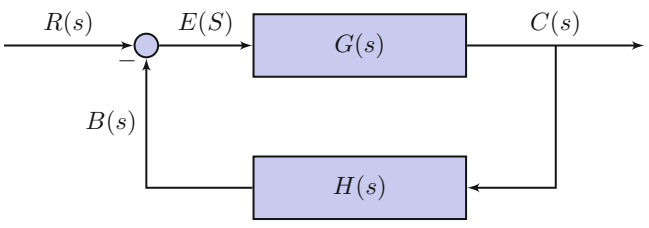

Fig. 13.1 Human structure interaction as a controller system

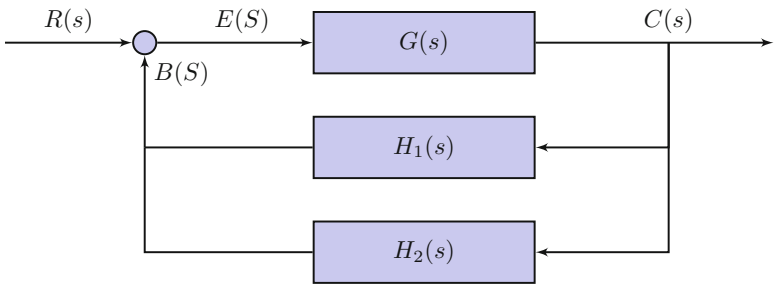

Fig. 13.2 Human-structure interaction controller model for a group of three people

Table 13.1 Properties of the individuals involved in tests

Person ID	Height [lbs]	Weight [ft, in]
P1	161	5'8"
P2	148	5'6"
P3	159	5'10"

13.2.3 Model Updating

The parameters of the structural and human models were updated in a probabilistic fashion using Bayesian inference [9]. This process estimates the probability density function of the model parameters given a set of experimental data and any prior knowledge that the analyst might have about the parameters. Bayes' theorem is usually expressed as:

$$P(\Theta|D) \propto P(D|\Theta)P(\Theta) \tag{13.3}$$

Where the prior knowledge of the parameters Θ is expressed in $P(\Theta)$, the term $P(\Theta|D)$ is the posterior PDF of the parameters, D denotes the experimental observations, and $P(D|\Theta)$ is the likelihood. A more detailed description of the model updating process within the context of HSI can be found in [6]. Interested readers are encouraged to read [9, 10] for a full discussion in Bayesian model updating.

13.3 Experimental Setup

A steel structure with additional concrete blocks to simulating dead loads was build in the structures' lab at the University of South Carolina [6, 7, 11]. For this specific paper, the supports of the structure and the mass were set to produce a vertical natural frequency of 3.9 Hz. Experimental tests involved impulse hammer testing to determine transfer function estimates. Three sets of tests were performed. The first set was for the empty structure. The second set involved three single occupants. Weight and height the people involved in tests are presented in Table 13.1. The last test involved three groups of two people. The last set of tests were used to validate the methodology proposed in this paper. The test names indicates who were on each test. For example P1P2 means that the person 1 (P1) and the person 2 (P2) are at standing on the structure.

The Impact Hammer used during testing was a PCB 096D50 with a maximum load of $\pm$ 22240 N peak. A PCB accelerometer with a sensitivity of 100 mV/g was placed in the middle of the structure, below the persons and close to the hammer hit location. Force (input) and accelerations (output) where read using a NI CompactDAQ data acquisition system with a NI9234 module. Data was acquired using a sampling frequency of 1652 Hz. Three records of 20 s where done for each single test.

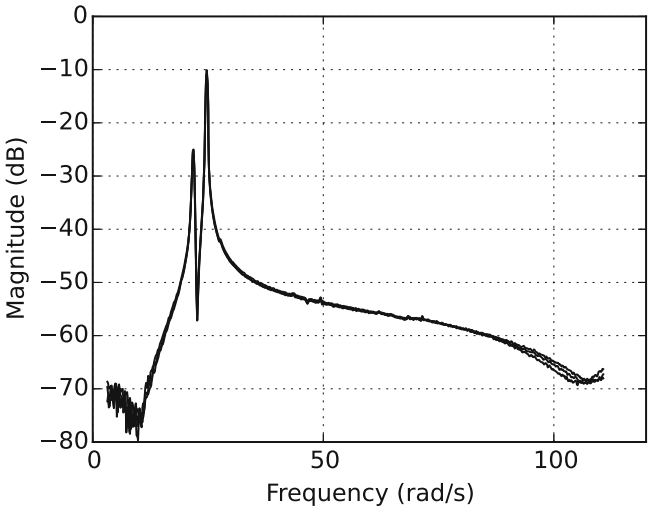

Fig. 13.3 Transfer functions of experimental tests of the empty structure

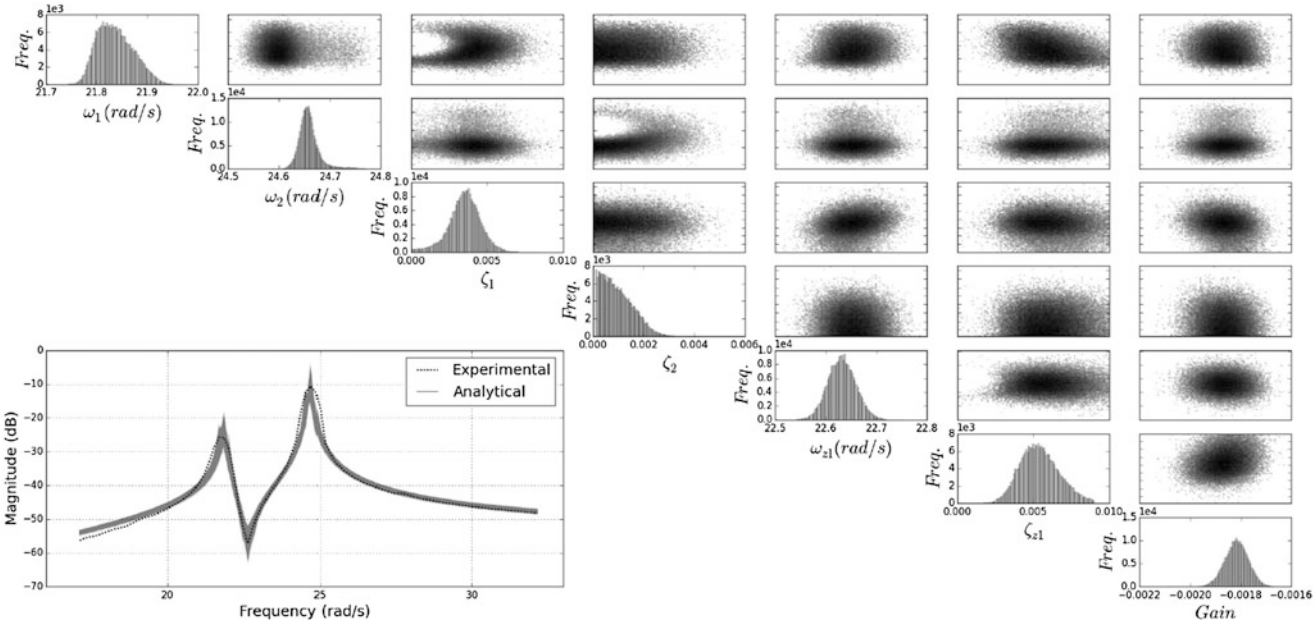

Fig. 13.4 Marginal histograms for structural parameters (diagonal), MCMC samples showing possible dependency between parameters (above diagonal) and comparison between experimental and numerical transfer functions (*bottom left*)

13.4 Results

13.4.1 Parameters of the Structure

The model of the structure described in Sect. 13.2.1 was updated using experimental transfer functions of the empty structure (Fig. 13.3). Here, two modes and one antiresonance frequency are clearly observed. Figure 13.4 shows the results of a MCMC chain of the posterior distribution. The plots in the represent the marginal histograms, while the plots in the upper right can be used to explore dependencies between parameters. The bottom left plot compares the experimental transfer function (dashed line) with the transfer function from all the MCMC chain. The results show no apparent dependency between parameters except between the natural frequencies and their corresponding damping ratios.

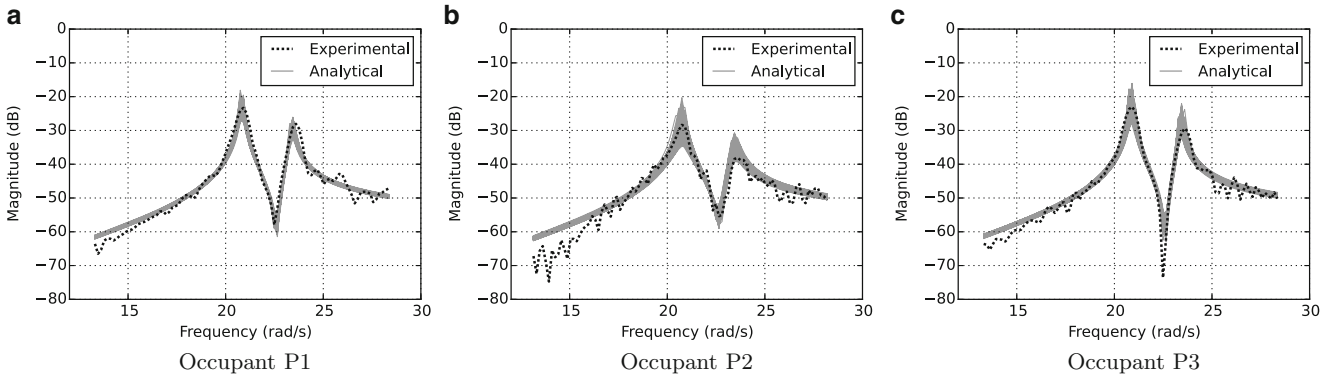

Fig. 13.5 Comparison between experimental and numerical transfer functions for single occupant. (**a**) Occupant P1. (**b**) Occupant P2. (**c**) Occupant P3

13.4.2 Human-Structure Interaction for a Single Human

A second model updating process is performed with the combined HSI model. The posterior PDF of the structural parameters discussed in the previous section are used as priors. The prior for the controller (human model) parameters are set as a uniform distributions with limits based on stability criteria. One model was updated for each individual using experimental transfer functions obtained when each person was standing on the structure.

Figure 13.5 shows the experimental transfer functions (dashed lines) and the numerical transfer functions obtained with each value of the MCMC chain (gray area). The experimental results shown in the figure corresponds to the average transfer function between three consecutive tests. As shown in [6, 7], the results indicate that the PD controller model is able to human in the HSI problem. An interesting observation is that the uncertainty on the estimated transfer functions each different for each person. For example, the shaded area for P2 is larger than the shaded area for P1. This indicates a larger range of possible values for the transfer function estimates of P2 at a particular frequency. The numerical transfer function also show a higher uncertainty close to the natural frequencies for all individuals tested.

13.4.3 Human-Structure Interaction for Groups of Two People

The samples of the PD controller found in the previous section are used to estimate the transfer function where two people are standing on the structure. The combinations studied are P1P2, P1P4 and P2P4. The estimated transfer functions are then compared with the corresponding experimental data. The results are shown in Fig. 13.6. Similar to previous plots the experimental transfer function (dashed line) is the average of three consecutive tests. The uncertainty in the estimation of the transfer functions is bigger when compared with results of a single person (Fig. 13.5). The model was able to capture the natural frequency and damping ratio for P1P3 and P2P3. Estimated transfer functions show some discrepancy with the experimental results for the P1P2 combination.

13.5 Conclusions

The main goal of this paper is to explore the use of closed loop control theory to model groups of people for human-structure interaction problems. Probabilistic controller models were developed for three individuals independently. These probabilistic models are estimated using Bayesian inference and experimental transfer functions. The individual models are then combined to estimate the behavior of the structure when two people are standing on the structure. Results show that the proposed methodology does a good job estimating the dynamic characteristics of the combined HSI system for two out of the three combinations tested. The estimation of the natural frequency for the third group (P1P2) could be improved. The uncertainty on the individual models appears to be different depending on the person. Uncertainty in the estimations is also larger when considering groups of people when compared with the transfer function estimation of a single occupant. Future work will concentrate in testing the proposed technique with larger groups of people.

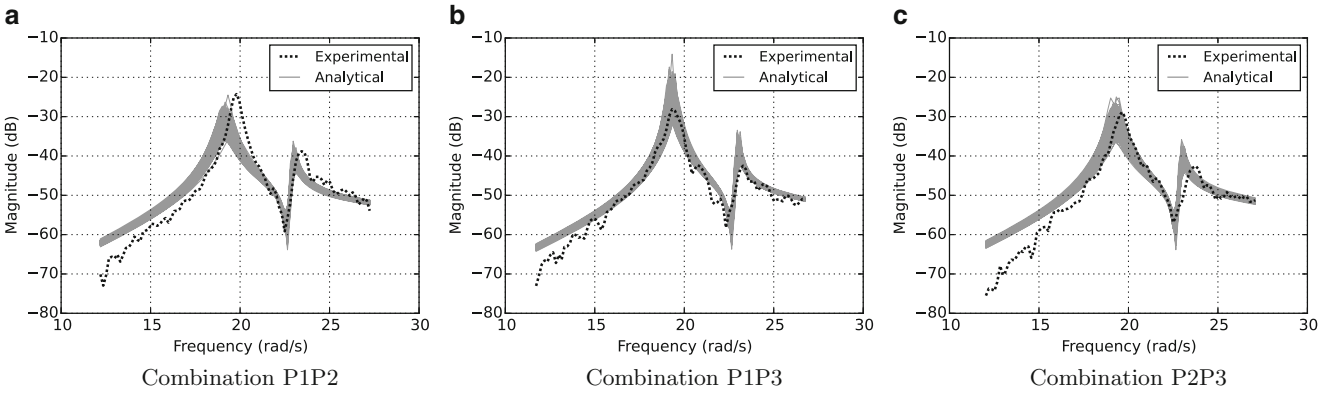

Fig. 13.6 Estimated transfer function and experimental transfer functions for group of people. (**a**) Combination P1P2. (**b**) Combination P1P3. (**c**) Combination P2P3

Acknowledgements This material is based upon work supported by the National Science Foundation under Grant No.CMMI-0846258

References

1. Živanović, S., Díaz, I., Pavić, A.: Influence of walking and standing crowds on structural dynamic properties. In: Proceedings of IMAC-XXVII, pp. 9–12, Orlando (2009)
2. Behnia, A., Hong, A.K.B., Shabazi, M.M., Ranjbar, N., Behnia, N., Vafaei, M.R.: Finite element analysis of high modal dynamic responses of a composite floor subjected to human motion under passive live load. Lat. Am. J. Solids Struct. **10**(3), 601–630 (2013)
3. Ortiz, A.R., Gómez, D., Thomson, P.: Efectos de la interacción humano estructura en las propiedades dinámicas de una tribuna. Revista Ingenieria y competitividad **12**(1), 601–630 (2013)
4. Pedersen, L.: Damping added to floors by seated crowds of people. In: Smart Structures and Materials, pp. 61690P–61690P. International Society for Optics and Photonics (2006). doi:http://dx.doi.org/10.1117/12.658579
5. Pedersen, L.: An aspect of dynamic human-structure interaction. In: The International Modal Analysis Conference (2007)
6. Ortiz-Lasprilla, A.R., Caicedo, J.M.: Comparing closed loop control models and mass-spring-damper models for human structure interaction problems. In: Dynamics of Civil Structures, vol. 2, pp. 67–74. Springer, Berlin (2015)
7. Ortiz-Lasprilla, A.R., Caicedo, J.M., Ospina, G.A.: Modeling human–structure interaction using a close loop control system. In: Dynamics of Civil Structures, vol. 4, pp. 101–108. Springer, Berlin (2014)
8. Ogata, K.: Modern Control Engineering. Prentice-Hall, New York (2002)
9. Beck, J., Katafygiotis, L.S.: Updating models and their uncertainties i: Bayesian statistical framework. J. Eng. Mech. **124**, 455–461 (2009)
10. Cheung, S.H., Beck, J.: Bayesian model updating using hybrid monte carlo simulation with application to structural dynamic models with uncertain parameters. J. Eng. Mech. **135**, 243–225 (2009)
11. Noss, N.C., Salyards, K.A.: Development of a laboratory test program to examine human-structure interaction. In: Topics on the Dynamics of Civil Structures, Volume 1, pp. 7–16. Springer, New York (2012)

Chapter 14
Fundamental Frequency of Lightweight Cold-Formed Steel Floor Systems

S. Zhang and L. Xu

Abstract As an alternative to traditional wood framing in residential building construction, cold-formed steel (CFS) framing inherits many advantages of steel construction. However, if not appropriately designed, CFS floors with longer spans and lighter weight are likely to be susceptible to annoying vibrations induced by human activity such as walking. The fundamental frequency is a critical parameter for floor vibration serviceability. In current practice, the floor frequency is evaluated based on the simplification of a floor system to a simply-supported beam, which results in a considerable disparity in frequencies obtained from field tests and evaluation. In this research, based on current construction practice, the CFS floor system is modelled as an orthotropic plate with edges of joist-ends being partially restrained and edges that are parallel to floor joists being either freely or simply supported. The deflection of the partially restrained CFS floor joist is adopted as the admissible function of the plate in the derivation of equations to evaluate the fundamental frequency of the equivalent orthotropic plate. Simplified equations and equivalent rigidity properties are proposed for CFS floor systems.

Keywords Human-induced vibration • Cold-formed steel floor systems • Fundamental frequency • Partially restrained • Rayleigh-Ritz method

14.1 Introduction

In characterizing the dynamic response of a floor system, the fundamental frequency plays a major role and needs to be calculated for the basic manual calculation check in design. Previous widely used design equations for lightweight floor systems [1, 2] were developed based on the beam theory. Although the beam theory is simple and practical for design engineers, the design equations cannot always provide reasonably accurate prediction for the fundamental frequency of a floor. Efforts made by Ohlsson [3] and Chui [4] to develop design equations using the plate theory have had some success. Ohlsson [3] calculated the frequencies by assuming a simply supported rectangular orthotropic plate for lightweight floor systems but the equivalent structural properties were not provided. Chui [4] presented a model for frequency analysis of ribbed plates (i.e., stiffened plates). This model, however, the model is limited to plates simply supported on all edges whereas the boundaries of joist ends in practical construction are commonly partially restrained.

CFS floor systems can be regarded as a thin plate reinforced by a series of equidistant stiffeners on one side with various transverse elements such as strapping and blocking. They can be simplified as an orthotropic plate. Although extensive investigation has been carried out on the analysis of free vibrations of orthotropic plates with general boundary conditions [5], it is too complex to be applied by structural engineers in their daily practice. A simple equation of the fundamental frequency with reasonable accuracy will be helpful in the design of vibration serviceability. In this paper, CFS floor systems are collectively considered as equivalent orthotropic plates with edges partially restrained against rotation. An analytical method based on the Rayleigh-Ritz method is presented to develop a design equation of the fundamental frequency of CFS floor systems considering partial restraints along the boundaries. Lastly, simplified equations and equivalent rigidity properties are proposed for CFS floor systems.

S. Zhang (✉) • L. Xu
Department of Civil and Environmental Engineering, University of Waterloo, 200 University Ave W, Waterloo, ON, Canada N2L 3G1
e-mail: zhangsigong@gmail.com

© The Society for Experimental Mechanics, Inc. 2016

M. Allen et al. (eds.), *Dynamics of Coupled Structures, Volume 4*, Conference Proceedings of the Society for Experimental Mechanics Series, DOI 10.1007/978-3-319-29763-7_14

14.2 Prediction of the Fundamental Frequency of Partially Restrained Orthotropic Plate by Rayleigh-Ritz Method

By making use of the Stokes's transformation, Wang and Lin [6] used Fourier sine series to investigate the vibration of beams with generally restrained boundaries. This approach was also studied by Li [7], and Kim and Kim [8]. Li [7] pointed out that the Fourier sine series approach is essentially feasible only for the simply supported beams with rotational end restraints. Kim and Kim [8] derived the frequency equations in matrix form by using the same Fourier series in [6] for beams with general restraints and investigated several boundary conditions in detail.

The applicability of Fourier series to the dynamic analysis of beams [6–8] can also be extended to analyze the vibration of plates with various boundary conditions. For a rectangular orthotropic plate simply supported with partial restraints against rotation in the pair of edges perpendicular as shown in Fig. 14.1, the determination of the fundamental frequency by using Rayleigh-Ritz method applying Fourier sine series as admission functions is presented as follows.

The boundary conditions of the orthotropic plate shown in Fig. 14.1 are

$$\begin{aligned} w_{x0} &= 0, \quad R_{x0}\frac{\partial w}{\partial x} = D_x\left[\frac{\partial^2 w}{\partial x^2} + v_y\frac{\partial^2 w}{\partial y^2}\right], \quad at\ x = 0 \\ w_{xa} &= 0, \quad R_{xa}\frac{\partial w}{\partial x} = -D_x\left[\frac{\partial^2 w}{\partial x^2} + v_y\frac{\partial^2 w}{\partial y^2}\right], \quad at\ x = a \\ w_{y0} &= 0, \quad D_y\left[\frac{\partial^2 w}{\partial y^2} + v_x\frac{\partial^2 w}{\partial x^2}\right] = 0, \quad at\ y = 0 \\ w_{yb} &= 0, \quad -D_y\left[\frac{\partial^2 w}{\partial y^2} + v_x\frac{\partial^2 w}{\partial x^2}\right] = 0, \quad at\ y = b \end{aligned} \tag{14.1}$$

where a is the floor span, b is the floor width, R_{x0} and R_{xa} are the rotational spring stiffness (per unit length) along the corresponding edges $x = 0$ and $x = a$, respectively, D_x and D_y are flexural rigidities, v_x and v_y are Poisson's ratios. The end restraints are assumed to be proportional to the end rotations and the restraint stiffness, R_{x0} and R_{xa}, may have any value in the range between simply supported (i.e., zero) and completely restrained (i.e., infinity). Using the Rayleigh-Ritz method, the fundamental frequency of the plate can be obtained by equating the maximum potential energy $U_{\max}$ and the maximum kinetic energy $T_{\max}$. For the free vibration of a plate vibrating harmonically with circular frequency ω, the deflection $w(x, y, t)$ can be expressed as

$$w(x, y, t) = W(x, y)\cos\omega t \tag{14.2}$$

The maximum strain energy (i.e. potential energy) of an orthotropic plate considering the partial restraints is given by

$$\begin{aligned} U_{\max} = \frac{1}{2}\int_0^a\int_0^b \left[D_x\left(\frac{\partial^2 W}{\partial x^2}\right)^2 + 2D_1\frac{\partial^2 W}{\partial x^2}\frac{\partial^2 W}{\partial y^2} + D_y\left(\frac{\partial^2 W}{\partial y^2}\right)^2 + 4D_{xy}\left(\frac{\partial^2 W}{\partial x\partial y}\right)^2\right]dx\,dy \\ - \frac{1}{2}D_x\int_0^b\left[\frac{\partial^2 W}{\partial x^2}\frac{\partial W}{\partial x} + v_y\frac{\partial^2 W}{\partial y^2}\frac{\partial W}{\partial x}\right]\Bigg|_{x=0}^{x=a} dy \end{aligned} \tag{14.3}$$

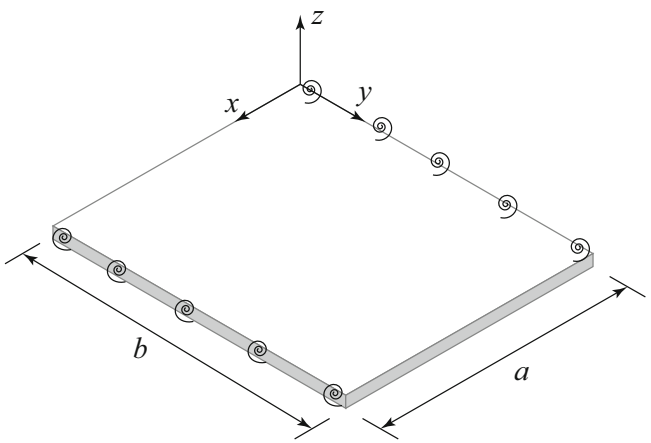

Fig. 14.1 Rectangular orthotropic plate with edges partially restrained against rotation

The maximum kinetic energy is calculated by

$$T_{\max} = \frac{1}{2}\rho\omega^2 h\int_0^a\int_0^b W^2 dydx \tag{14.4}$$

where ρ is the mass density of the plate and h is the thickness of the plate.

The Rayleigh quotient for the natural frequency ω is given as

$$\omega^2 = \frac{\int_0^a\int_0^b\left[D_x\left(\frac{\partial^2 W}{\partial x^2}\right)^2 + 2D_1\frac{\partial^2 W}{\partial x^2}\frac{\partial^2 W}{\partial y^2} + D_y\left(\frac{\partial^2 W}{\partial y^2}\right)^2 + 4D_{xy}\left(\frac{\partial^2 W}{\partial x\partial y}\right)^2\right]dx\,dy - D_x\int_0^b\left[\frac{\partial^2 W}{\partial x^2}\frac{\partial W}{\partial x} + v_y\frac{\partial^2 W}{\partial y^2}\frac{\partial W}{\partial x}\right]\Big|_{x=0}^{x=a}dy}{\rho h\int_0^a\int_0^b W^2 dydx} \tag{14.5}$$

In order to obtain the fundamental frequency, a series of sine function is assumed for the first mode shape as

$$W(x,\ y) = a_{11}\psi_1(x)\phi_1(y) = a_{11}\sum_{m=1}^{M} A_m \sin\frac{m\pi x}{a}\sin\frac{\pi y}{b} \tag{14.6}$$

In Eq. (14.6), a_{11} is a constant for the first mode, $\psi_1(x) = \sum_{m=1}^{M} A_m \sin\frac{m\pi x}{a}$ represents the characteristic beam function in the first mode for simply supported beam with rotational restraints, $\phi_1(y) = \sin\frac{\pi y}{b}$ is the characteristic function for first mode of the simply supported beam. Substituting Eq. (14.6) to Eq. (14.5), then

$$\omega^2 = \frac{ab\pi^4\left[\frac{D_x}{a^4}\sum_{m=1}^{M} m^4A_m^2\Big/\sum_{m=1}^{M}A_m^2 + \frac{2D_1}{a^2b^2}\sum_{m=1}^{M} m^2A_m^2\Big/\sum_{m=1}^{M}A_m^2 + \frac{D_y}{b^4} + \frac{4D_{xy}}{a^2b^2}\sum_{m=1}^{M} m^2A_m^2\Big/\sum_{m=1}^{M}A_m^2\right] + 2D_x\left[\psi_0''\frac{\pi b}{a}\sum_{m=1}^{M} mA_m - \psi_a''\frac{\pi b}{a}\sum_{m=1}^{M}(-1)^m mA_m\right]\Big/\sum_{m=1}^{M}A_m^2}{\rho hab} \tag{14.7}$$

From [8], it can be found that

$$A_m = \frac{2a^2\psi_0''}{\pi^3}\frac{m}{\lambda^4 - m^4}\left(1 - (-1)^m\frac{\psi_a''}{\psi_0''}\right) \tag{14.8}$$

where λ is a frequency coefficient which can be found in Eq. 14.20 of [8], ${\psi_0}''$ and ${\psi_a}''$ can be obtained by two homogeneous equations in which the coefficients are the functions of frequency. The coefficient matrix of equations about ${\psi_0}''$ and ${\psi_a}''$ for simply supported beam with partial restraints is expressed as [8]

$$\begin{bmatrix} 1 - \frac{2R_{x0}L}{\pi^2 EI}\sum_{m=1}^{\infty}\frac{m^2}{\lambda^4 - m^4} & \frac{2R_{x0}L}{\pi^2 EI}\sum_{m=1}^{\infty}\frac{(-1)^m m^2}{\lambda^4 - m^4} \\ \frac{2R_{xa}L}{\pi^2 EI}\sum_{m=1}^{\infty}\frac{(-1)^m m^2}{\lambda^4 - m^4} & 1 - \frac{2R_{xa}L}{\pi^2 EI}\sum_{m=1}^{\infty}\frac{m^2}{\lambda^4 - m^4} \end{bmatrix} \tag{14.9}$$

Natural frequencies (including in λ) are obtained numerically by requiring the determinant of Eq.(14.9) to vanish. Substituting Eq. (14.8) to Eq. (14.7) yields

$$\omega^2 = \frac{ab\pi^4\left[c_1\frac{D_x}{a^4} + 2c_2\frac{H}{a^2b^2} + \frac{D_y}{b^4}\right]}{\rho hab} \tag{14.10}$$

where $H = D_1 + 2D_{xy}$,

$$c_1 = \left\{ \begin{array}{l} \sum_{m=1}^{M} \frac{m^6}{(\lambda^4 - m^4)^2} \left(1 - (-1)^m \frac{\psi_a''}{\psi_0''}\right)^2 \\ + \sum_{m=1}^{M} \frac{m^2}{\lambda^4 - m^4} \left(1 - (-1)^m \frac{\psi_a''}{\psi_0''}\right) \\ + \sum_{m=1}^{M} \frac{m^2}{\lambda^4 - m^4} \left(\left(\frac{\psi_a''}{\psi_0''}\right)^2 - (-1)^m \frac{\psi_a''}{\psi_0''}\right) \end{array} \right\} \Big/ \sum_{m=1}^{M} \frac{m^2}{(\lambda^4 - m^4)^2} \left(1 - (-1)^m \frac{\psi_a''}{\psi_0''}\right)^2,$$
$$c_2 = \sum_{m=1}^{M} \frac{m^4}{(\lambda^4 - m^4)^2} \left(1 - (-1)^m \frac{\psi_a''}{\psi_0''}\right)^2 \Big/ \sum_{m=1}^{M} \frac{m^2}{(\lambda^4 - m^4)^2} \left(1 - (-1)^m \frac{\psi_a''}{\psi_0''}\right)^2. \tag{14.11}$$

Equation (14.10) is derived for the fundamental frequency of the orthotropic plate with two opposite edges (i.e., $x = 0$ and $x = a$) partially restrained and the other two edges (i.e., $y = 0$ and $y = b$) simply supported. If edges parallel to the span (i.e., $y = 0$ and $y = b$) are free, $\phi_1(y)$ in Eq. (14.6) can be defined as $\phi_1(y) = 1$. Following the same procedure above, the fundamental frequency is expressed as

$$\omega^2 = c_1 \frac{\pi^4}{\rho h} \frac{D_x}{a^4} \tag{14.12}$$

where c_1 is same as shown in Eq. (14.11).

14.3 Equivalent Orthotropic Plate for CFS Floor Systems

14.3.1 Equivalent Rigidity Properties of CFS Floor Systems

The success of simplifying CFS floor systems by equivalent orthotropic plate depends primarily on defining appropriate values of flexural and torsional rigidity constants. The equivalent orthotropic plate can represent the desired behaviour of the original floor systems as exactly as possible but cannot be equivalent in every respect. Thus, in the free vibration analysis one requires that the equivalent orthotropic plate should provide the natural frequencies and modal shapes of the original structure as accurately as possible. Iyengar and Iyengar [9] developed a method to obtain these equivalent rigidity constants through equating the expressions for the natural frequencies for both the stiffened plate and the orthotropic plate by Rayleigh-Ritz method. This method will be adopted to establish equivalent rigidity constants between orthotropic plates and CFS floor systems. Specifically, stiffness of transverse elements such as strapping, blocking will be considered.

The maximum potential energy of a CFS floor system as shown in Fig. 14.2 consists of three components.

$$U_{\max} = U_{s\max} + U_{j\max} + U_{t\max} \tag{14.13}$$

where $U_{s\max}$, $U_{j\max}$, $U_{t\max}$ are the maximum potential energy associated with the subfloor, joists and transverse elements, respectively. For the simplicity of presenting the analysis procedure, only one row of blocking at the mid-span with strapping is considered for transverse elements. They can be expressed as

$$U_{s\max} = \frac{1}{2} \int_0^a \int_0^b \left[D_{sx} \left(\frac{\partial^2 W}{\partial x^2}\right)^2 + 2D_{s1} \frac{\partial^2 W}{\partial x^2} \frac{\partial^2 W}{\partial y^2} + D_{sy} \left(\frac{\partial^2 W}{\partial y^2}\right)^2 + 4D_{sxy} \left(\frac{\partial^2 W}{\partial x \partial y}\right)^2 \right] dx\, dy \tag{14.14}$$

$$U_{j\max} = \frac{1}{2} EI_j \sum_{i=1}^{I} \int_0^a \left(\frac{\partial^2 W}{\partial x^2}\right)^2_{y=y_i} dx - \frac{1}{2} EI_j \sum_{i=1}^{I} \left(\frac{\partial^2 W}{\partial x^2} \frac{\partial W}{\partial x}\right)_{y=y_i} \Bigg|_{x=0}^{x=a} \tag{14.15}$$

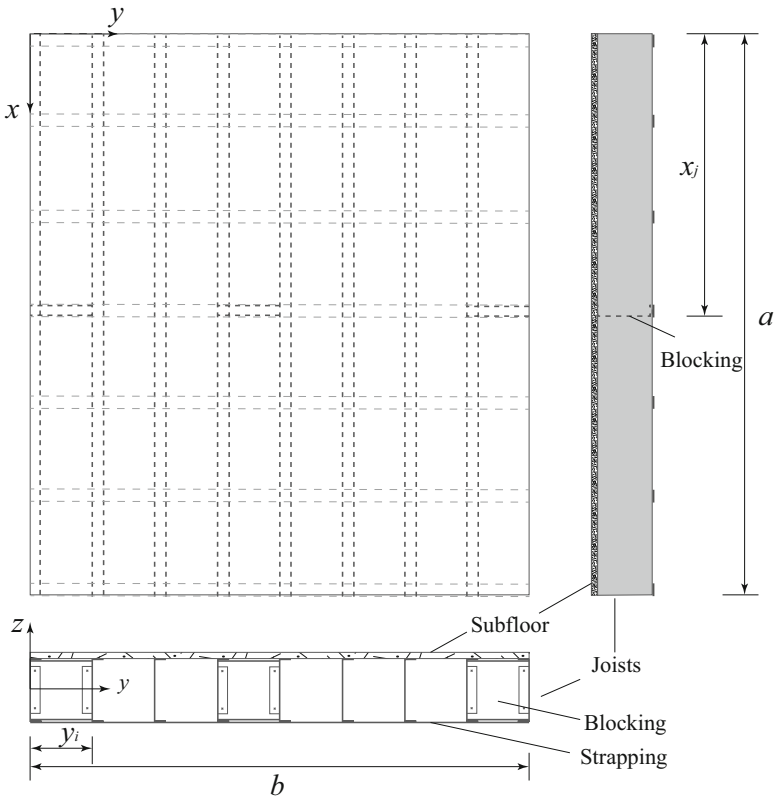

Fig. 14.2 CFS floor systems considered

$$U_{t\max} = \frac{1}{2}\sum_{j=1}^{J} EI_b \int_0^b \left(\frac{\partial^2 W}{\partial y^2}\right)^2_{x=x_j} dy \tag{14.16}$$

where D_{sx}, D_{sy}, D_{s1} and D_{sxy} are the flexural and torsional rigidities of the subfloor, EI_j and EI_b are flexural rigidities of joists and blocking, separately, y_i and x_j represents the location of joists and blocking, respectively.

The maximum kinetic energy of a CFS floor system is given by

$$T_{\max} = \frac{1}{2}\omega^2 \left[\rho_s h \int_0^a \int_0^b W^2 dy dx + \rho_j A_j \sum_{i=1}^{I} \int_0^a W^2_{y=y_i} dx + \rho_b A_b \sum_{j=1}^{J} \int_0^b W^2_{x=x_j} dy\right] \tag{14.17}$$

where ρ_s, ρ_j and ρ_b are the densities of the subfloor, steel joists and blocking, separately; A_j and A_b are the cross-sectional areas of the joists and the blocking, respectively.

Equating the maximum potential and kinetic energies, $U_{\max}$ and $T_{\max}$, and then substituting the Eq. (14.6), the natural circular frequency, ω, can be obtained as

$$\omega^2 = \frac{ab\pi^4 \left[\frac{c_1' D_{sx} + \left(c_1' + c_3' + c_4'\right)\frac{EI_j}{b/(I-1)}}{a^4} + 2c_2' \frac{\left(D_{s1} + 2D_{sxy}\right)}{a^2 b^2} + \frac{D_{sy} + 2c_5' EI_b/a}{b^4}\right]}{\rho_s hab + (I-1)\,\rho_j A_j a + 2c_5' \sum_{j=1}^{J} \rho_b A_b b} \tag{14.18}$$

where

$$
\begin{aligned}
c_1' &= \sum_{m=1}^{M} \frac{m^6}{\left(\lambda^4 - m^4\right)^2}\left(1-(-1)^m \frac{\psi_a''}{\psi_0''}\right)^2 \Bigg/ \sum_{m=1}^{M} \frac{m^2}{\left(\lambda^4 - m^4\right)^2}\left(1-(-1)^m \frac{\psi_a''}{\psi_0''}\right)^2 \\
c_2' &= \sum_{m=1}^{M} \frac{m^4}{\left(\lambda^4 - m^4\right)^2}\left(1-(-1)^m \frac{\psi_a''}{\psi_0''}\right)^2 \Bigg/ \sum_{m=1}^{M} \frac{m^2}{\left(\lambda^4 - m^4\right)^2}\left(1-(-1)^m \frac{\psi_a''}{\psi_0''}\right)^2 \\
c_3' &= \sum_{m=1}^{M} \frac{m^2}{\lambda^4 - m^4}\left(1-(-1)^m \frac{\psi_a''}{\psi_0''}\right) \Bigg/ \sum_{m=1}^{M} \frac{m^2}{\left(\lambda^4 - m^4\right)^2}\left(1-(-1)^m \frac{\psi_a''}{\psi_0''}\right)^2 \\
c_4' &= \sum_{m=1}^{M} \frac{m^2}{\lambda^4 - m^4}\left(\left(\frac{\psi_a''}{\psi_0''}\right)^2 - (-1)^m \frac{\psi_a''}{\psi_0''}\right) \Bigg/ \sum_{m=1}^{M} \frac{m^2}{\left(\lambda^4 - m^4\right)^2}\left(1-(-1)^m \frac{\psi_a''}{\psi_0''}\right)^2 \\
c_5' &= \left[\sum_{m=1}^{M} \frac{m}{\lambda^4 - m^4}\left(1-(-1)^m \frac{\psi_a''}{\psi_0''}\right) \sin\frac{m\pi x_j}{a}\right]^2 \Bigg/ \sum_{m=1}^{M} \frac{m^2}{\left(\lambda^4 - m^4\right)^2}\left(1-(-1)^m \frac{\psi_a''}{\psi_0''}\right)^2
\end{aligned}
\tag{14.19}
$$

As mentioned previously, if the equivalent orthotropic plate is used to predict the fundamental frequency of the actual stiffened plate, Eq. (14.10) and Eq. (14.18) should be equal. This equality is obtained by taking

$$
\begin{aligned}
D_x &= \frac{c_1'}{c_1} D_{sx} + \frac{c_1' + c_3' + c_4'}{c_1} \frac{EI_j}{b/(I-1)} \\
D_y &= D_{sy} + 2c_5' EI_b/a \\
H &= D_{s1} + 2D_{sxy} \\
\rho hab &= \rho_s hab + (I-1)\,\rho_j A_j a + 2c_5' \sum_{j=1}^{J} \rho_b A_b b
\end{aligned}
\tag{14.20}
$$

Comparing Eq. (14.11) and Eq. (14.19), it can also find that

$$
\begin{aligned}
c_1 &= c_1{}' + c_3' + c_4' \\
c_2 &= c_2'
\end{aligned}
\tag{14.21}
$$

Therefore, Eq. (14.20) will be used as the rigidity constants when the CFS floor system is represented by the equivalent orthotropic plate.

14.3.2 Simplified Equations for Equivalent Rigidity Properties

For the computational efficiency and design convenience, the "fixity factor" designated by Monforton and Wu [10] is introduced to replace the rotational stiffness in Eq. (14.1). This factor reflects the relative stiffness of the joists to the rotational end-spring connections and is expressed as

$$
r = \frac{1}{1 + \frac{3EI_j}{RL}} \tag{14.22}
$$

in which R is rotational stiffness representing the partial restraints at joist ends or floor edges, and EI_j/L is the flexural stiffness of the joists. This factor is commonly used for semi-rigid beam-column connections [11]. The advantage of using fixity factor r instead of R is that it allows dealing with rotational stiffness in terms of numbers ranging from 0 (i.e., rotation free) to 1 (i.e., rotation completely restrained) [12].

Numerical investigations have been performed to confirm the validity of the present equations for evaluating the fundamental frequency of rectangular orthotropic plates with rotational restraints and the results are shown in Table 14.1. When $r_{x0} = r_{xa} = 0$, all sides of the plate are simply supported (i.e. S-S-S-S). The coefficients, $c_1 = c_2 = 1$, can be calculated from literature [13]. Accordingly, for the plate with two sides simply supported and two other sides clamped (i.e. S-C-S-C), $c_1 = 5.138$, $c_2 = 1.246$. It can be observed that the coefficients c_1 and c_2 increase as fixity factors increase as expected and approach to the value of the S-C-S-C case.

Table 14.1 Frequency coefficients for different rotational restraints

	End-fixity factor $r_{x0} = r_{xa}$													
Coefficients	0	0.01	0.05	0.1	0.2	0.3	0.4	0.5	0.6	0.7	0.8	0.9	0.999	1
c_1'	1	1	1	1.004	1.019	1.051	1.109	1.211	1.386	1.686	2.217	3.200	4.882	5.138
c_1	1	1.012	1.063	1.131	1.284	1.464	1.680	1.945	2.274	2.695	3.254	4.023	5.133	5.138
c_2	1	1	1	1	1.001	1.003	1.006	1.012	1.022	1.040	1.071	1.130	1.246	1.246
c_5'	1	1	1.003	1.008	1.018	1.0291	1.043	1.060	1.080	1.107	1.143	1.192	1.261	/

Table 14.2 Constant values

Coefficients	a	b	c	d
c_1'	23.7	−5.4	−21.4	25.9
c_1	0	72.8	−41.6	59.2
c_2	0.28	−0.07	−4.22	5.06
c_5'	0	1.05	−9.5	13.5

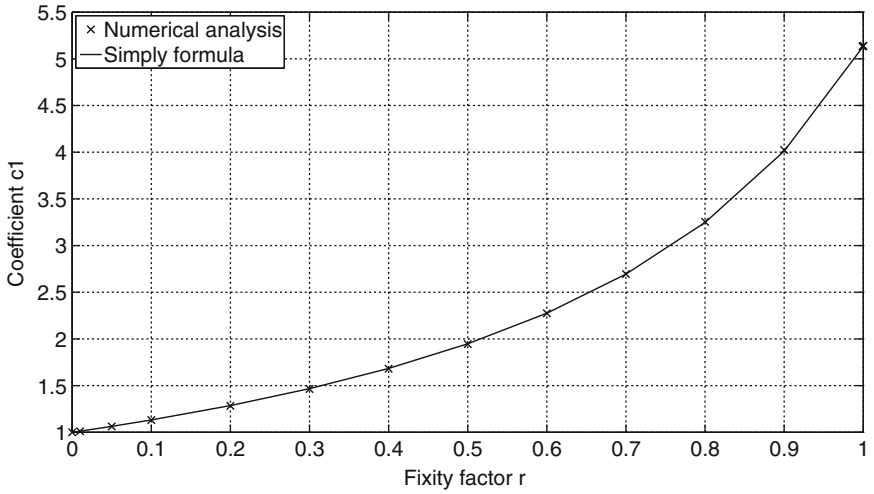

Fig. 14.3 Comparison of results of c_1 between numerical analysis and simplified equation c_1

In attempting to find a simple formula for computing these coefficients, they can be closely approximated by

$$c_i = 1 + \frac{ar^2 + br}{cr + d} \tag{14.23}$$

where $r = r_{x0} = r_{xa}$, a, b, c and d are constants as shown in Table 14.2.

A comparison of values by simplified equation Eq. (14.23) and values by numerical analysis of c_1 is presented in Fig. 14.3. As it can be seen, the simplified equation can provide close predictions. Comparisons of other coefficients also present same conclusion which are not reviewed here due to the page limitation.

Furthermore, as the stiffeners (floor joists) located on only one side of the plate, the location of the neutral plane is unknown. An approximate solution will be developed by assuming the neutral plane is located at the middle of the joists and Poisson's ratio equal to zero. In this case, the fundamental frequency of CFS floor systems considering partially restrained edges be expressed as

$$\omega^2 = \frac{ab\pi^4 \left[\frac{D_x}{a^4} + 2\frac{H}{a^2b^2} + \frac{D_y}{b^4}\right]}{m} \tag{14.24}$$

where

$$\begin{aligned} D_x &= c_1{}' D_{sx} + c_1 \tfrac{EI_j}{s} \\ D_y &= D_{sy} + 2c_5 \tfrac{EI_b}{a} \\ H &= c_2 \left[\tfrac{G_p t_s^3}{12} + \tfrac{J}{2s} \right] \\ D_{sx} &= \tfrac{E_{sx} t_s^3}{12} + E_{sx} t_s z_s^2 \\ D_{sy} &= \tfrac{E_{sy} t_s^3}{12} + E_{sy} t_s z_s^2 \end{aligned} \tag{14.25}$$

with s is the space of floor joists, E_{sx} and E_{sy} are Young's moduli of the subfloor, t_s is the uniform thickness of the subfloor, z_s is the distance to the center of the joist from the center of subfloor, G_p is shear modulus of the subfloor, J is the joist torsional constant which is provided by joist manufacturer, and c_1, $c_1^{'}$, c_2 and c_5 can be obtained from Eq. (14.23).

14.3.3 Discussion

Hu [14] concluded that the installation of a gypsum board ceiling significantly contributes to the stiffness of a floor and adds some damping and a significant mass to the floor. As a result, the floor's natural frequencies will reduce accordingly. This impact of the ceiling becomes more significant with the increase of the layers of the ceiling. Same conclusion can also be found by Liu [15]. The potential energy and the kinetic energy of the ceiling have same forms as that of the subfloor. They can be expressed as follows.

$$U_{c\max} = \frac{1}{2} \int_0^a \int_0^b \left[D_{cx} \left(\frac{\partial^2 W}{\partial x^2} \right)^2 + 2D_{c1} \frac{\partial^2 W}{\partial x^2} \frac{\partial^2 W}{\partial y^2} + D_{cy} \left(\frac{\partial^2 W}{\partial y^2} \right)^2 + 4D_{cxy} \left(\frac{\partial^2 W}{\partial x \partial y} \right)^2 \right] dx\, dy \tag{14.26}$$

$$T_{c\max} = \frac{1}{2} \omega^2 \rho_c h \int_0^a \int_0^b W^2 dy dx \tag{14.27}$$

in which D_{cx}, D_{cy}, D_{c1} and D_{cxy} are the flexural and torsional rigidities of the ceiling.

With consideration of the ceiling, D_{cx} and D_{cy} should be added into D_{sx} and D_{sy} of Eq. (14.25) and expressed as

$$\begin{aligned} D_{cx} &= \tfrac{E_{cx} t_c^3}{12} + E_{cx} t_c z_c^2 \\ D_{cy} &= \tfrac{E_{cy} t_c^3}{12} + E_{cy} t_c z_c^2 \end{aligned} \tag{14.28}$$

where E_{cx} and E_{cy} are Young's moduli of the ceiling, t_c is the uniform thickness of the ceiling, and z_c is the distance to the center of the joist from the center of ceiling.

Transverse elements such as blocking, strapping and cross-bridging provide transverse floor stiffness. However, these contributions depend on the relative stiffness of floor deck and joists [2]. Hu [14] claimed that the addition of resilient channels does not noticeably contribute to floor's transverse stiffness. Steel strappings are similar to resilient channels. Liu [15] observed that the number of bridging rows slightly affects the performance of floor system. Practically, at least one row of bridging with blocking is always discretely attached to the bottom of the blocking and floor joist as shown in Fig. 14.4. Therefore, the bridging and blocking can be approximately simulated as a continuous member across the joists in section.

14.4 Conclusion

An analytical approach based on the Rayleigh-Ritz method has been presented for calculating the fundamental frequency of a CFS floor system considering the effect of the partially restrained edges by using the Fourier sine series as the admission function. Furthermore, the rigidities properties of equivalent orthotropic plates for CFS floor systems were developed. This method was compared with the existing studies on simply supported or clamped plates with close agreement. At last, simplified equations were proposed for calculating the fundamental frequency of CFS floor system for design practice..

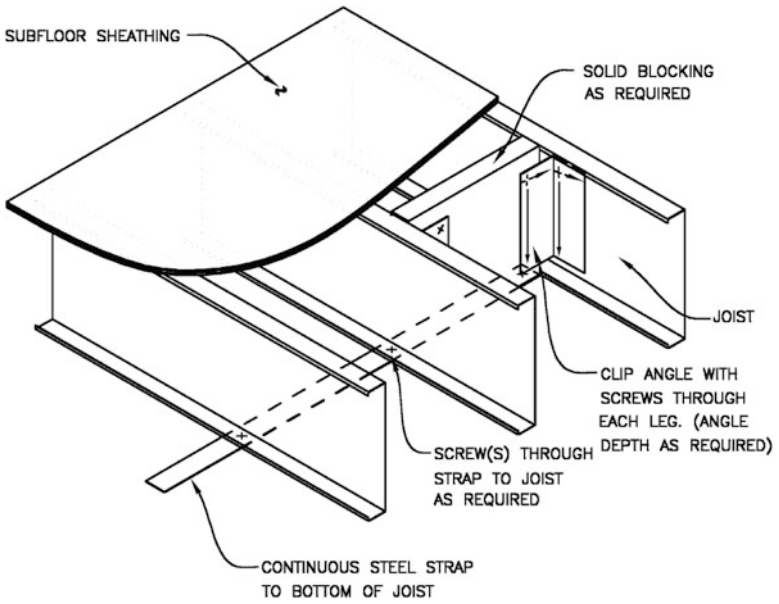

Fig. 14.4 Floor blocking and strapping [16]

References

1. Johnson, J. R.: Vibration acceptability in wood floor systems. Master thesis, Virginia Polytechnic Institute and State University, Blacksburg (1994)
2. Applied Technology Council: ATC Design Guide 1: Minimizing Floor Vibration. Redwood City (1999)
3. Ohlsson, S.: Springiness and human-induced floor vibrations: a design guide (B. Evert, L. Gruber Trans.), Swedish Council for Building Research, Stockholm (1988)
4. Chui, Y.H.: Application of ribbed-plate theory to predict vibrational serviceability of timber floor systems. In: Proceedings of the 7th World Conference on Timber Engineering, vol. 4, pp. 87–93. Shah Alam, Malaysia, 12–15 August 2002
5. Khov, H., Li, W.L., Gibson, R.F.: An accurate solution method for the static and dynamic deflections of orthotropic plates with general boundary conditions. Compos. Struct. **90**(4), 474–481 (2009)
6. Wang, J.T.-S., Lin, C.-C.: Dynamic analysis of generally supported beams using Fourier series. J. Sound Vib. **196**(3), 285–293 (1996)
7. Li, W.L.: Free vibrations of beams with general boundary conditions. J. Sound Vib. **237**(4), 709–725 (2000)
8. Kim, H.K., Kim, M.S.: Vibration of beams with generally restrained boundary conditions using Fourier series. J. Sound Vib. **245**(5), 771–784 (2001)
9. Iyengar, K.S.R., Iyengar, R.N.: Determination of the orthotropic plate parameters of stiffened plates and grillages in free vibration. Appl. Sci. Res. **17**(6), 422–438 (1967)
10. Monforton, G.R., Wu, T.H.: Matrix analysis of semi-rigid connected frames. J. Struct. Div. **89**(6), 13–24 (1963)
11. Xu, L.: Second-order analysis for semirigid steel frame design. Can. J. Civ. Eng. **28**(1), 59–76 (2001)
12. Tangorra, F.M.: A design procedure for floors supported by cold formed steel joists. Master thesis, University of Waterloo, ON, Canada (2001)
13. Hearmon, R.F.S.: The frequency of flexural vibration of rectangular orthotropic plates with clamped or supported edges. J. Appl. Mech. **26**, 537–540 (1959)
14. Hu, L.J.: Effects of solutions for sound isolation and fire resistance on serviceability performance of engineered wood floors. In: World Conference on Timber Engineering, Lausanne, 1998
15. Liu, W.: Vibration of Floors Supported by Cold-Formed Steel Joists. Master thesis, University of Waterloo, ON, Canada (2001)
16. North American Steel Framing Alliance: Low-Rise Residential Construction Details. North American Steel Framing Alliance, Washington (2000)

Chapter 15
Fundamental Studies of AVC with Actuator Dynamics

E.J. Hudson, P. Reynolds, and D.S. Nyawako

Abstract Active vibration control (AVC) of human-induced vibrations in structures with proof-mass actuators has been subject to much research in recent years. This has predominantly focussed on footbridges and floors and there is some evidence that this research is paving the way for commercial installations of AVC where traditional vibration control measures are not appropriate. However, the design of an AVC system is a complex task because of the influence of actuator dynamics, the contributions from higher frequency modes of vibration and the effect of low and high pass filters that are required to make the control algorithm implementable. This puts the AVC design process beyond the abilities of the vast majority of civil design engineers, even at a scheming stage to approximate what sort of reductions could be achieved by such a system. This paper considers a generalised system and investigates what sort of performance can be achieved in theory by a perfect AVC system, then considers the added complexity of actuator dynamics to demonstrate how this degrades the performance from optimal.

Keywords Active control • Human-induced vibrations • Direct velocity feedback • Actuator dynamics • Stability

15.1 Introduction

Much research has investigated the use of active vibration control (AVC) for human-induced vibrations in structures in recent years [1–5]. Many of these implementations have been based on direct velocity feedback (DVF) because this is a very simple and effective controller that can achieve significant reductions in structural response.

At its simplest, DVF provides a control force that is proportional to the structural velocity, thereby increasing damping over a broad range of frequencies. However, in practice in many civil engineering structures there is no fixed frame of reference against which an actuator could react; therefore inertial actuators are frequently used [4, 6]. These have their own dynamics that significantly change the closed loop system dynamics and introduce potential stability issues. In addition two key non-linearities are introduced, namely force and stroke saturation, the latter of which being particularly restrictive in the design of a robust AVC system.

Further to this, both low and high pass filters are required to avoid implementation issues due to high frequency noise and the integration of low frequencies to convert the measured acceleration to velocity. The net result of all these factors is that there are limits to the potential performance improvements that can be achieved through AVC with a DVF controller [7, 8]. However, quantifying these limits requires fairly complex control design and analysis which although is not a problem for a control specialist, is generally far beyond the scope of most civil engineers. Therefore it is very difficult for civil engineers to come up with even approximate response reductions or actuator sizing when they encounter a structure that doesn't meet vibration serviceability limits.

This paper investigates some of the issues surrounding implementing DVF on a real system and how this varies from an 'ideal' case. The ideal case of DVF is analysed for a single degree of freedom (SDOF) in Sect. 15.2. Then the effect that actuator dynamics and filters have is investigated in Sect. 15.3 and conclusions are drawn in Sect. 15.4.

E.J. Hudson (✉) • P. Reynolds
College of Engineering, Mathematics and Physical Sciences, Kay Building, North Park Road, University of Exeter, EX4 4QF, UK

Full Scale Dynamics Limited, 40 Leavygreave Road, Sheffield, South Yorkshire, S3 7RD, UK
e-mail: e.j.hudson@exeter.ac.uk; p.reynolds@exeter.ac.uk;

D.S. Nyawako
College of Engineering, Mathematics and Physical Sciences, Kay Building, North Park Road, University of Exeter, EX4 4QF, UK
e-mail: d.s.nyawako@exeter.ac.uk

© The Society for Experimental Mechanics, Inc. 2016

M. Allen et al. (eds.), *Dynamics of Coupled Structures, Volume 4*, Conference Proceedings of the Society for Experimental Mechanics Series, DOI 10.1007/978-3-319-29763-7_15

15.2 Ideal Direct Velocity Feedback

The simplest starting point for this work is to consider ideal velocity feedback on a single degree of freedom (SDOF) system. The following work describes some important relationships between the feedback gain and change in damping and the corresponding reductions in response.

A simple schematic showing the key components of an AVC system are shown in Fig. 15.1. This includes the open loop structure dynamics, G, the actuator dynamics, G_a, and the controller dynamics, C. Generally, accelerometers are used to measure the structural vibration response therefore the output from the structure dynamics, G, is acceleration. The accelerometers can be chosen so that they provide a relatively flat frequency response within the bandwidth of interest and therefore these dynamics can be safely ignored for the purposes of this study.

The equation of motion for an SDOF system is:

$$m\ddot{x} + c\dot{x} + kx = f_E + f_C \tag{15.1}$$

where m, c, k are the mass, damping and stiffness values, f_E and f_C are the excitation and control forces, and x, $\dot{x}$, $\ddot{x}$ are the displacement, velocity and acceleration of the SDOF system. Considering ideal DVF with negative feedback gain g:

$$f_C = -g\dot{x} \tag{15.2}$$

this can be substituted into Eq. (15.1) to give:

$$m\ddot{x} + (c+g)\dot{x} + kx = f_E \tag{15.3}$$

It is often easier to discuss the system parameters in terms of damping ratio, ζ, and natural frequency, ω. Therefore, taking the definition of $\zeta = \frac{c}{2m\omega}$, one can calculate the difference in damping ratio, $\Delta\zeta$, due to DVF:

$$\Delta\zeta = \zeta_{cont} - \zeta_{unc} = \frac{c+g}{2m\omega} - \frac{c}{2m\omega} = \frac{g}{2m\omega} \tag{15.4}$$

and rearrange for the required gain:

$$g = (\Delta\zeta)2m\omega = (\Delta\zeta)4\pi mf \tag{15.5}$$

This relationship therefore demonstrates what feedback gain is required to achieve a specific change in damping for a dynamic system with a given natural frequency and mass.

Following from this, the derived closed loop plant for this system is:

$$G_{CL} = \frac{G}{1 + G \cdot G_a \cdot C} \tag{15.6}$$

Similarly, the closed loop between the excitation force and the control force is given by:

$$\frac{f_C}{f_E} = G_a \cdot C \cdot G_{CL} \tag{15.7}$$

Equation (15.5) is demonstrated in Fig. 15.2 which shows three uncontrolled systems with damping ratios $\zeta = 1\%, 6\%, 11\,\%$. For this and subsequent plots, the mass and frequency of the first mode of vibration have been normalised and are

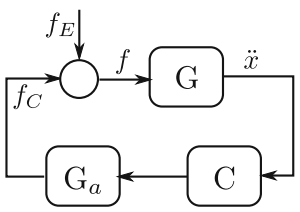

Fig. 15.1 Simplified schematic for active vibration control

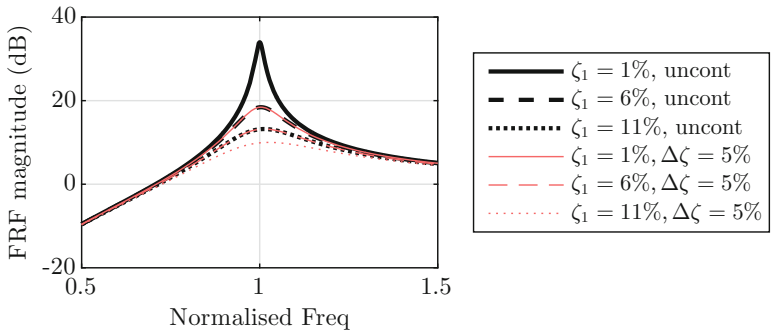

Fig. 15.2 Structure FRF for open and closed loop systems

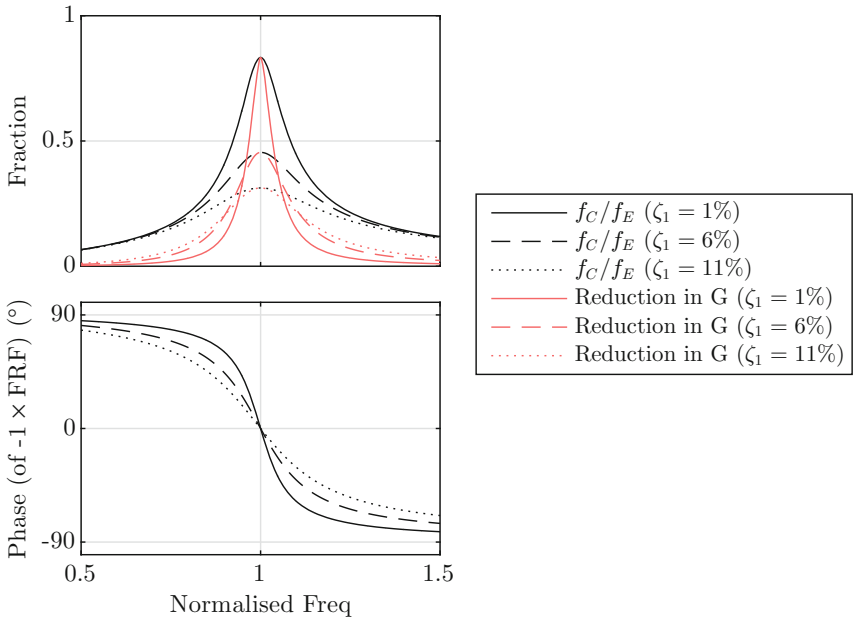

Fig. 15.3 Control force per excitation force and structural response reduction

set to 1 kg and 1 rad/s. There are also three controlled systems with ideal DVF and a feedback gain which corresponds to a change in damping, $\Delta\zeta = 5\,\%$—i.e. giving systems with damping ratios $\zeta = 6\,\%, 11\,\%, 16\,\%$, as calculated from Eq. (15.5). As expected, the gains chosen result in FRFs of the controlled systems with net damping ratio equal to the damping ratio of the uncontrolled systems.

The closed loop between the control force from DVF and the excitation force into the system is shown in Fig. 15.3 along with the reduction in FRF between open and closed loop cases. The control force per excitation force peaks at the frequency of the structural mode and rolls off to low values away from resonance. This is because, as seen in Eq. (15.7), for the case of ideal DVF with no actuator dynamics the magnitude of the control force per excitation force tracks the magnitude of the mobility FRF of the closed loop system.

The phase of the control force per excitation force FRF shown has been shifted by 180° to better show results around resonance; therefore a phase of 0° on this plot means that the control force and excitation force are perfectly *out of phase*. This is observed at $\omega = 1$, meaning that at structural resonance the DVF controller provides a control force that perfectly cancels the excitation force resulting in the maximum reduction in response; this reduction is equal to the ratio of control force to excitation force. Away from resonance the phase tracks the phase of the mobility FRF and shifts from 0°, resulting in reduced effectiveness. This, combined with the drop in magnitude, results in the very sharp roll off of reductions away from resonance.

15.3 Effect of Actuators and Filters

Up to this point, for the purposes of simplifying the analysis all actuator dynamics have been ignored and it has been assumed that any controller is perfectly implementable without the need for high or low pass filters. This is not the case in reality and the influence of these dynamics can significantly alter both performance and stability of the resultant controller. Their effect on the simple SDOF system is discussed below.

In order to make the ideal controller implementable, the actuator dynamics, G_a, must be accounted for as well as any high and low pass filters, C_{HP}, C_{LP}. It is considered that the actuator dynamics are sufficiently well known to allow a compensator to be designed to modify the physical actuator dynamics. This is generally possible through either pole-zero cancellation [9] or an inner feedback loop on the actuator displacement [8]. The inclusion of an actuator compensator, G_{aC}, allows any desired dynamics to be realised which is a very important design tool for AVC.

The net controller considered from this point is shown in Eq. (15.8):

$$C_{imp} = C_{ideal} \cdot (G_a \cdot G_{aC}) \cdot C_{HP} \cdot C_{LP} \tag{15.8}$$

It is well known that when inertial actuators are used, the actuator resonance must be at least half the natural frequency of the first mode to be controlled [8]. However, there are lower bounds on the feasible natural frequency because as the frequency decreases the displacement at that frequency increases for a given force demand (inversely proportional to frequency squared). In addition to this, the optimal damping ratio of the actuator is dependent on this ratio of actuator resonance to structural resonance: when the ratio is low a higher damping is preferable because this helps limit otherwise high displacements; when the ratio is high (close to 0.5) a lower damping ratio is preferable as this avoids phase distortion around the structural frequency to be controlled.

In this paper, the damping ratio is chosen to vary linearly between 70 % and 30 % for actuator frequency ratios of 0.25 and 0.5 with a maximum value of 70 % for very low frequency ratios. A high pass filter is required to avoid numerical issues associated with integration of acceleration signals to velocity. In this work, this is set as a second order Butterworth filter with a cut-off frequency of $0.7 \times \omega_A$. A low pass filter is also required to avoid spillover issues because the broadband controller would otherwise work to control all high frequency accelerations, even when these are noise on the signal line. In this work this is set as a second order Butterworth filter with a cut-off frequency of $3 \times \omega_1$.

The combined effect of introducing actuator dynamics and filters into the feedback loop modifies both the magnitude and phase of the controller at different frequencies. To allow for a more direct comparison between different systems the gain of the following systems have been modified so that they all result in the desired gain at $\omega = 1$, namely that required to achieve $\Delta\zeta_1 = 20\,\%$ for an open loop system with $\zeta_1 = 1\,\%$, as per Eq. (15.5).

The open and closed loop FRFs for three systems with varying actuator resonant frequencies are shown in Fig. 15.4 and compared with the ideal DVF case.

All systems have approximately the same closed loop structural response at $\omega = 1$; at this frequency the only difference between the feedback controllers is any phase change because they were gain normalised to match at this frequency. This shows that the phase change at this frequency is relatively small so as to result in insignificant changes. There is a general

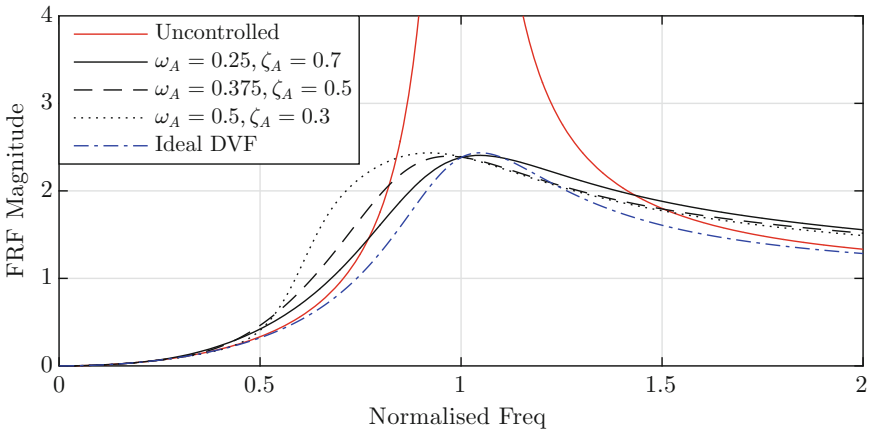

Fig. 15.4 Open and closed loop structure responses for DVF with $\Delta\zeta = 20\,\%$ and actuator dynamics of varying frequency and damping ratio

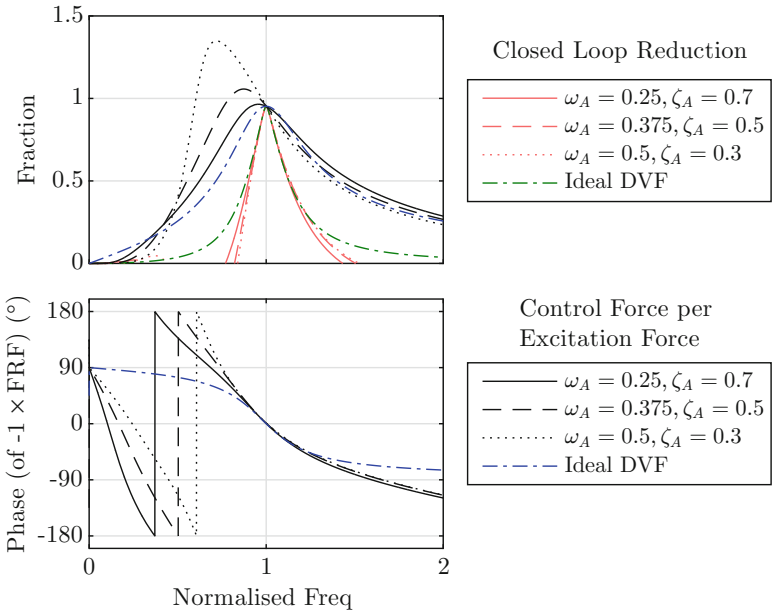

Fig. 15.5 Actuator control force per excitation force for DVF with $\Delta\zeta = 20\,\%$ and actuator dynamics of varying frequency and damping ratio

trend that as the natural frequency of the actuator increases, the peak of the closed loop system increases in magnitude slightly and lowers in frequency. However, more insights can be drawn when considering the closed loop system between control force and excitation force, as described by Eq. (15.7) and shown in Fig. 15.5. This plot clearly demonstrates the effect of varying actuator natural frequency on the frequency at which the phase crosses 180°, and how in the ideal DVF case this situation never arises. The magnitude of the control force per excitation force increases for frequencies just below 1, being exaggerated as the actuator frequency increases, but this does not equate with improved performance. In fact, the opposite is true because of the phase distortion away from 0°.

The effect that this has on the stability of the closed loop systems is shown in Fig. 15.6. Here the gain and phase margins are shown for the system with $\omega_A = 0.5$. The system becomes unstable when the phase crosses 180° and the magnitude is greater than 1; the gain and phase margins describe how much change in magnitude and phase of the controller can be tolerated before the system becomes unstable.

$$\mathrm{CL}_{\mathrm{stab}} = G_a \cdot C \cdot G_{OL} \tag{15.9}$$

The key difference between the systems shown here is the frequency at which the phase crosses 180° which in turn determines the gain margin. The magnitude plots for all systems are very similar and have a steep roll off around resonance. However this means that the gain margin is very sensitive to the changing frequency at which a 180° cross-over occurs.

Following from this, it is important to investigate the resultant actuator dynamics. The displacements are related to the actuator force by:

$$G_d = \frac{G_a}{m_A \cdot s^2} \tag{15.10}$$

where m_A is the actuator mass and $s = j\omega$.

At $\omega = 1, f_C \approx R \times f_E$, where R is the peak reduction in structural response. Therefore the displacement per excitation force at this frequency is given by:

$$\left| \frac{G_d}{f_E} (\omega = \omega_1) \right| = \frac{R}{m_A \cdot \omega_1^2} \tag{15.11}$$

Away from structural resonance the relationship is more complicated and this is presented in Fig. 15.7, defined by Eq. (15.12). A set of feedback gain choices are shown to demonstrate the evolution with increasing gain.

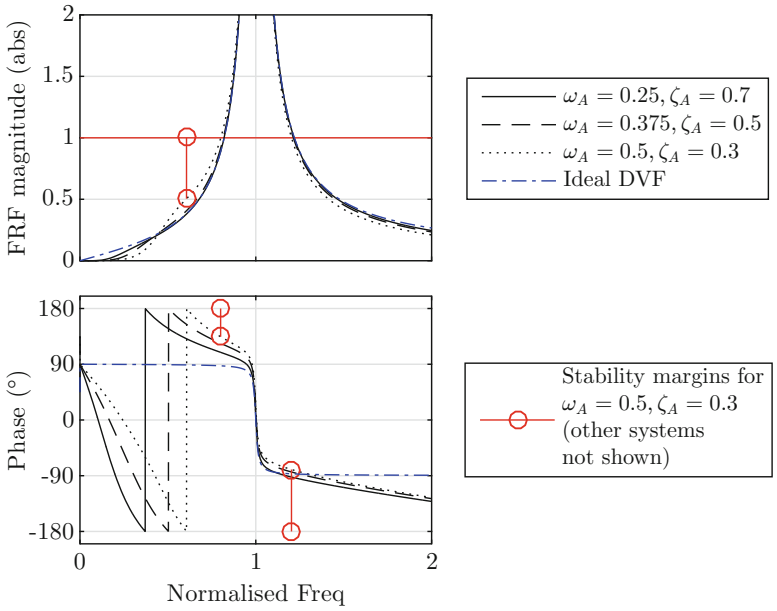

Fig. 15.6 Stability margins of DVF with $\Delta\zeta = 20\,\%$

$$\frac{d}{f_E} = G_d \cdot C \cdot G_{CL} \tag{15.12}$$

where G_d is the actuator voltage:displacement relationship $G_d = \frac{G_a}{m \cdot s^2}$.

In general there are higher displacements at lower frequencies than structural resonance (albeit a small difference in the case of low gain with $\omega_A = 0.25$). As the actuator frequency increases, so too does the displacement at frequencies less than $\omega = 1$, such that for $\omega_A = 0.5$ the peak displacement is 2.94 compared with 0.96 at $\omega = 1$ for $\Delta\zeta_1 = 20\,\%$. This has profound implications for sizing the required mass of any actuator that has to generate the required inertial forces. This is especially so when the natural frequency of the actuator is low. The previous plots have shown that the system with $\omega_A = 0.25$ has performed the best out of these three systems which makes sense because its gain and phase distortions around resonance are the smallest. However, Fig. 15.7 shows that this comes at a cost of increased displacement at low frequencies. To pick an extreme case, the displacements at $\omega = 0.25$ for systems with $\omega_A = 0.25$ and $\omega_A = 0.5$ are 1.15 and 0.19 respectively for $\Delta\zeta_1 = 20\,\%$. Given that in the control of human-induced vibrations in structures it is often (though not always) the second or third harmonics of the force that are close to structural frequencies and that these typically have much smaller magnitudes than the first harmonic, the fact that a controller has significant displacements at low frequencies can be a real issue.

The previous plots were generated for a nominal SDOF system with frequency 1 rad/s, mass 1 kg and damping 1 %. The mass and frequency of the SDOF system essentially provide scaling which can easily be accounted for. The level of damping inherent in the structure has a more complex interaction with the performance of DVF. The effect that differing open loop damping has on the stability and displacement of the actuators is shown in Fig. 15.8.

The range of ζ_1 shown in Fig. 15.8 varies from 0.2 % (possible very low damping associated with, for example, steel footbridges) to 5 % (higher level of damping found in fully-fitted out floors) to encompass a range of typical damping values found in scenarios involving human-induced vibrations that could require AVC. The peak displacements are not significantly affected by ζ_1, especially for higher values of $\Delta\zeta_1$ where the actuator resonance is crucial. The effect of increasing ζ_1 is beneficial for a given $\Delta\zeta_1$ as the actuator displacements due to structural resonance are decreased. Similarly, the stability of the systems are not significantly affected—the difference in gain margin is predominantly due to the slight change in crossover frequency because of the differing phase roll-offs with ζ_1. This change is relatively small, as shown in the example case of $\omega_A = 0.375$, $\zeta_A = 0.5$ of Fig. 15.8.

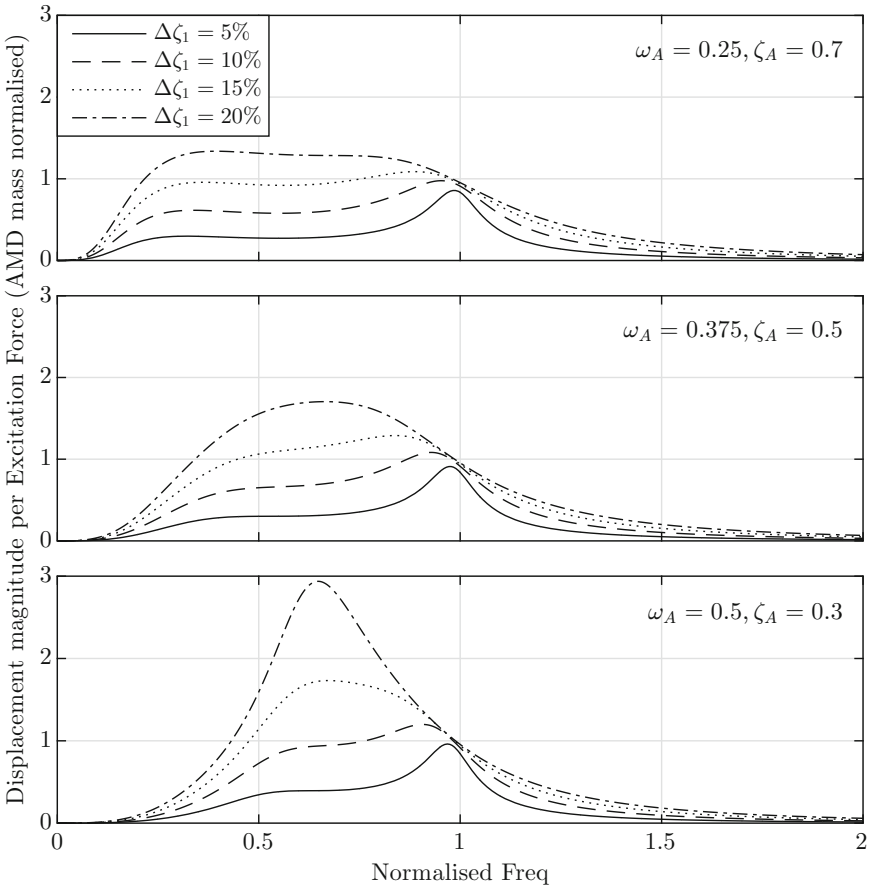

Fig. 15.7 Actuator displacement per excitation force for DVF with actuator dynamics of varying frequency and damping ratio

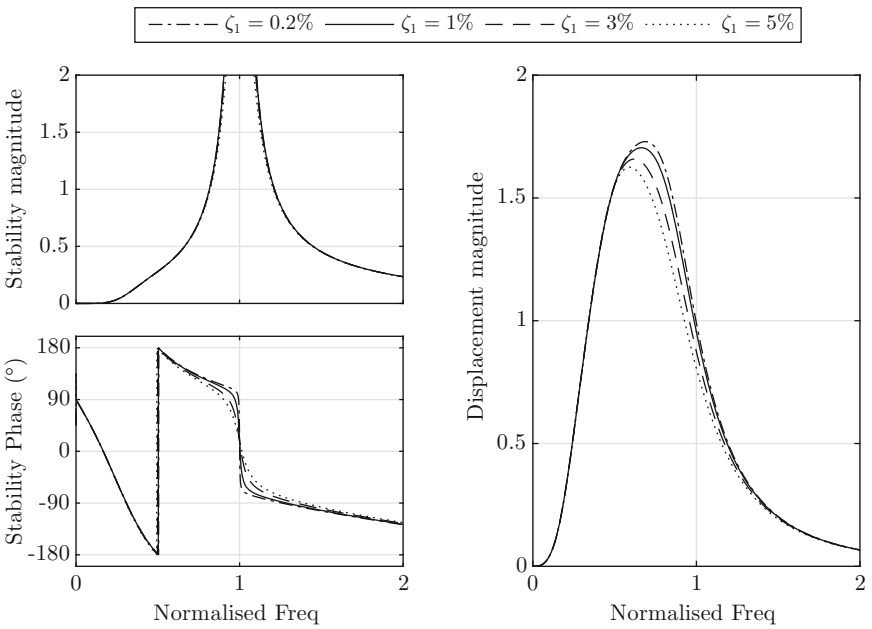

Fig. 15.8 Stability and actuator displacement for systems with varying ζ_1 with $\Delta\zeta = 20\,\%$ and $\omega_A = 0.375$, $\zeta_A = 0.5$

15.4 Conclusions

This paper has investigated an ideal implementation of DVF applied to an SDOF system. The magnitude and phase of the control force per excitation force was investigated for the 'ideal' case and shown to peak in magnitude and have perfectly cancelling phase at the structural resonant frequency. Either side of resonance the magnitude drops off and the phase shifts from 0°; the compound effect of these is that the reductions achieved drop off at a very fast rate, which is why DVF is very good for targeting structural resonances but performs poorly away from resonance.

The additional complexity of actuator dynamics and filters was shown to introduce a phase crossing at 180° and the phase distortions resulted in decreased performance, especially at lower frequencies. The actuator displacements for a series of DVF systems were presented and it was shown that for most systems the peak displacement per excitation force was at lower frequencies than resonance. This has significant implications for the sizing of actuators for a particular application based on a preliminary analysis of controller force demands.

Acknowledgements The authors would like to acknowledge the financial support given by the UK Engineering and Physical Sciences Research Council through a responsive mode grant entitled 'Active Control of Human-Induced Vibration' (Ref: EP/H009825/1) and Leadership Fellowship grant entitled 'Advanced Technologies for Mitigation of Human-Induced Vibration' (Ref: EP/J004081/1).

References

1. Hudson, E.J.: Incorporating active control of human-induced vibrations in floors into buildings. Ph.D. Thesis, The University of Sheffield (2013)
2. Pereira, E., Díaz, I.M., Hudson, E.J., Reynolds, P.: Optimal control-based methodology for active vibration control of pedestrian structures. Eng. Struct. **80**, 153–162 (2014)
3. Diáz, I.M., Pereira, E., Reynolds, P.: Integral resonant control scheme for cancelling human-induced vibrations in light-weight pedestrian structures. Struct. Control. Health Monit. **19**(November 2010), 55–69 (2012)
4. Moutinho, C., Cunha, A., Caetano, E.: Analysis and control of vibrations in a stress-ribbon footbridge. Struct. Control. Health Monit. **18**(6), 619–634 (2011)
5. Díaz, I.M., Reynolds, P.: Acceleration feedback control of human-induced floor vibrations. Eng. Struct. **32**(1), 163–173 (2010)
6. Hanagan, L.M.: Active control of floor vibrations. Ph.D. thesis, Polytechnic Institute and State University, Virginia (1994)
7. Brennan, M.J., Ananthaganeshan, K.A., Elliott, S.J.: Instabilities due to instrumentation phase-lead and phase-lag in the feedback control of a simple vibrating system. J. Sound Vib. **304**(3–5), 466–478 (2007)
8. Díaz, I.M., Pereira, E., Hudson, M.J., Reynolds, P.: Enhancing active vibration control of pedestrian structures using inertial actuators with local feedback control. Eng. Struct. **41**, 157–166 (2012)
9. Hudson, E.J., Reynolds, P.: Implications of structural design on the effectiveness of active vibration control of floor structures. Struct. Control. Health Monit. **21**(5), 685–704 (2014)

Chapter 16
Mitigating Existing Floor Vibration Issues in a School Renovation

Linda M. Hanagan

Abstract For over 40 years, students, faculty, and staff have been living with an often disturbing level of floor vibration caused by pedestrian traffic in an open plan library area of a suburban middle school. The library extends just beyond a 47×52 ft bay framed with a 3 in. slab on metal deck supported by 28 in deep steel joists spanning the short direction and W36 rolled girders in the long direction. As part of an upcoming major renovation, there is interest in exploring cost effective alternatives to reducing the impact of the current conditions. To quantify and understand the existing behavior and make suggestions to alter the behavior, a research study was undertaken. This paper describes the vibration measurements taken, assesses the behavior found including the surprising impact of higher order modes, and explores possible options to mitigate the impact of vibration on the occupants.

Keywords Floor vibration measurements • Floor vibration serviceability • Floor vibration mitigation • Floor vibration modes

16.1 Introduction

Complaints of annoying floor vibration prompted an investigation of a bay on the 2nd floor of a middle school building. The area of study, primarily used as an open library/media center area, is shown in Fig. 16.1. It is primarily an open thoroughfare with pedestrian traffic occurring primarily between classes as students move from one area to another. Figure 16.2 shows a partial framing plan of the problem area. The black lines represent the non-structural partition walls that define the media center area. The girders span 52 ft with 28DJ11 joists framing at 2 ft on center between them. The joists, spanning 47′–2″, are supported by 2 ½″ joist seats. A 3″, total thickness, normal weight concrete slab on metal form deck spans between the joists. The joist framing on the other side of each girder defining the bay switches direction to be parallel to the girder. The same joist and spacing continues above and below the bay as shown in the figure. An analytical and experimental investigation, described herein, was undertaken to characterize and assess the affected area for vibration serviceability due to pedestrian traffic and make recommendations to mitigate the problem.

16.2 Analytical Investigation

To discern its susceptibility to complaints due to walking induced vibration, the evaluation procedure described in Chapter 4 of the AISC Design Guide 11 [1] was implemented using a spreadsheet. It should be noted that this evaluation procedure was not available when this building was originally designed in the early 70s. The floor bay in question was evaluated without the full height partitions and a damping value that is recommended by Murray [2]. That is, 2.5 % modal damping was assumed. From this evaluation, the predicted acceleration amplitude is 0.0058 g. The Design Guide recommends a limit of 0.005 g for offices spaces and classrooms. This indicates a floor susceptible to objectionable levels of walking induced vibration in the absence of full height partitions. From these calculations, it is not surprising that objections are being raised in the large bay of the media center area. It should also be noted that the fundamental frequency is predicted to be 3.9 Hz.

L.M. Hanagan (✉)
Department of Architectural Engineering, Pennsylvania State University, 104 Engineering Unit A, University Park, PA 16802, USA
e-mail: hanagan@psu.edu

© The Society for Experimental Mechanics, Inc. 2016

M. Allen et al. (eds.), *Dynamics of Coupled Structures, Volume 4*, Conference Proceedings of the Society for Experimental Mechanics Series, DOI 10.1007/978-3-319-29763-7_16

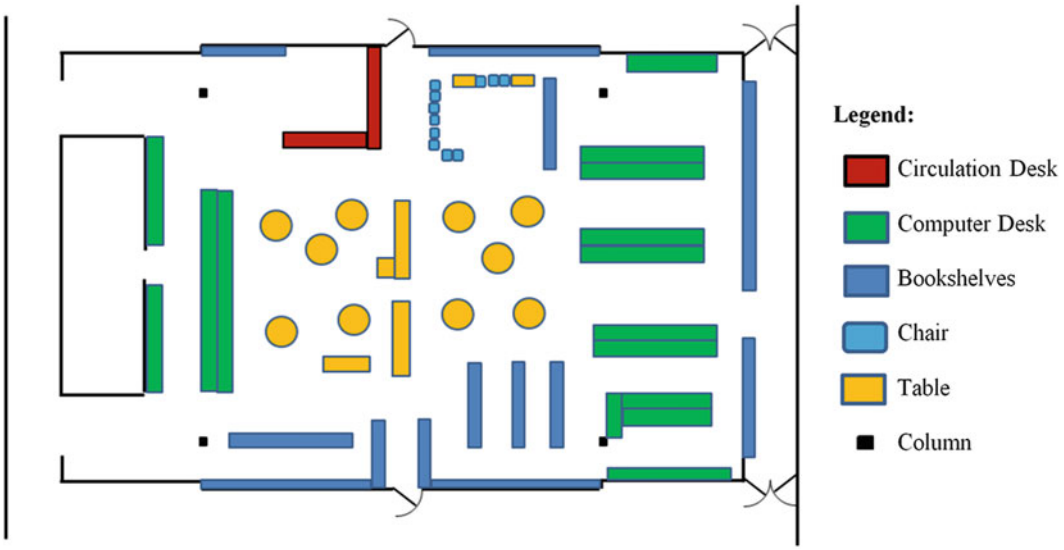

Fig. 16.1 Architectural layout of media center

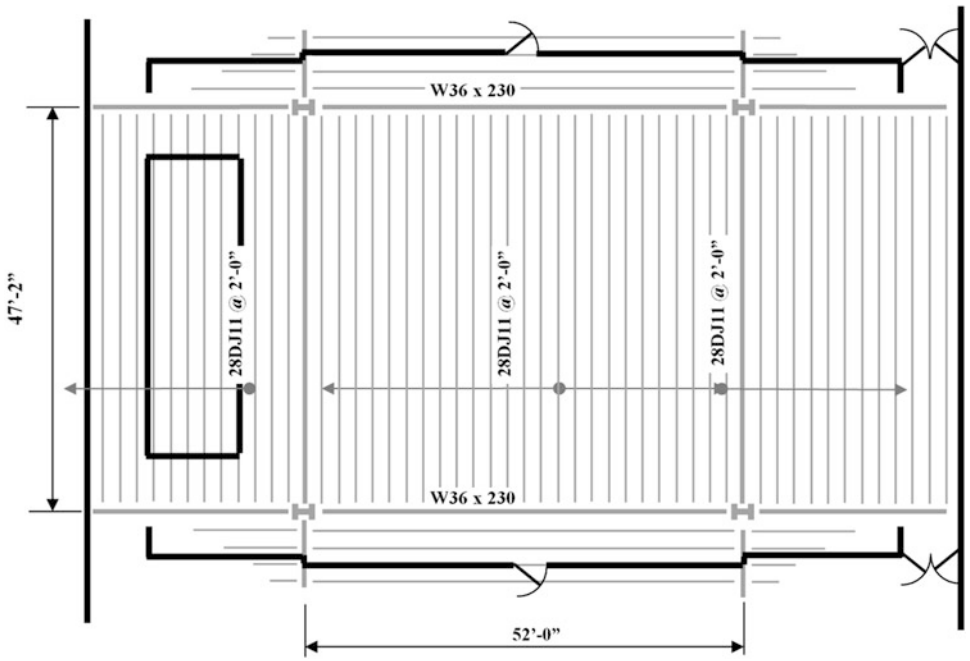

Fig. 16.2 Partial framing plan of the problem area

16.3 Experimental Testing

Three types of tests were conducted to assess the actual dynamic behavior of the floor. These can be broadly described as "Walking Tests", "Heel Drop Tests", and "In-Service Tests". These tests are described below. The measurements that shed the most insight on the floor behavior are presented in this paper.

Walking Tests Twenty-seven walking tests were conducted. In this type of test, a person walks at a pace that excites one of the floors natural modes of vibration while acceleration levels are measured. This test can be used to simulate the kind of disturbance that is being found objectionable and assess it in the context of human perception scales. The necessary vibration reduction required can also be estimated from this kind of test. Each of these tests consisted of 16 s acceleration

measurements as the walker passed the sensor locations. All of the walking tests were conducted using a pace set by a metronome with the intent of walking in resonance with one of the floor's natural frequencies. Resonant frequencies are determined from heel drop tests, described next.

Heel Drop Tests Fourteen heel-drop tests were conducted. Heel drop tests consist of measuring the force and response to an impact that is caused by a person impacting the floor by dropping from their toes to their heels. The measurements can be used to compute the frequency response function (FRF) for that location of heel drop and sensor. The FRF, when plotted as a magnitude, shows sharp peaks at floor system natural frequencies. Additionally, magnitude and phase information can give insight as to the shape of a particular vibration mode.

In-Service Tests Ten "In-Service" tests were conducted to capture vibration levels during normal operation. These tests were conducted to measure the actual behavior of the floor being found objectionable.

16.4 Interpretation of Results

A magnitude plot of frequency response measurements from the heel-drop testing at the center of the bay is shown in Fig. 16.3. In this measurement, both the heel-drop force and the accelerometer measurement are at the center of the 47 ft × 52 ft bay. This heel-drop test revealed a fundamental frequency of the bay at 4.25 Hz and another dominant natural frequency of 6.375 Hz as indicated by the sharp peaks in Fig. 16.3. It should be noted that the measured fundamental natural frequency of 4.25 Hz is close to the predicted fundamental frequency of 3.9 Hz presented in the previous section. A calculation utilizing the half-power bandwidth method indicates approximately 4.7 % damping in the fundamental mode. This is significantly higher than that estimated in the analytical section, thus one might expect lower than predicted levels of vibration due to walking. The fundamental frequency of 4.25 Hz would likely be excited by the second harmonic of a 2.125 Hz step frequency. This indicates a metronome setting of 127 beats per minute (2.125*60).

Measurements of the floor's acceleration response at locations indicated in Fig. 16.4 due to controlled walking along path 1 are shown in Fig. 16.5. The walking test data presented utilizes a walking pace of 127 steps per minute controlled by the beat of the metronome. The graphs on the left of Fig. 16.5 show a 16 s time history of the acceleration response caused by the walker at the five different locations. The largest amplitudes are at the center of the bay, as expected. The graphs on the right are the same measurement as the time history expressed in the frequency domain. This type of graph illustrates the different frequencies present in the measurement. The amplitudes are the spectral accelerations at discrete frequencies.

When walking excitation produces steady-state vibration amplitudes in excess of 0.005 g for several cycles, complaints of office workers being distracted or annoyed by the motion are much more likely. The function of the area being studied is, at times, similar to that of an office. During class times, there may be one or two people walking around while students are sitting quietly working, mostly at the computer desks. The time histories for location 1 indicate that the walking path shown in Fig. 16.4 causes disturbances well above those that would be considered acceptable by most occupants. This was true for other walking paths through the space. In fact, the measures acceleration levels are much larger than one would expect from the analytical predictions. Since the walker was "tuned" to the fundamental frequency, the largest spectral accelerations should be found at the fundamental frequency of 4.25 Hz. Inspection of the right hand graphs for location 1 show that the largest spectral content is at 6.375 Hz. The mode at 6.375 Hz is called a "higher order mode" and is being excited by the same step frequency as the fundamental mode. A quick calculation reveals that 6.375 Hz is at the third harmonic of the step frequency, thus two dominant modes are being excited by the same step frequency resulting in much larger than predicted

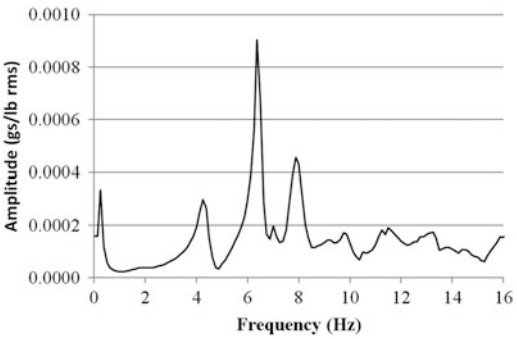

Fig. 16.3 Frequency response magnitude at the center of the floor

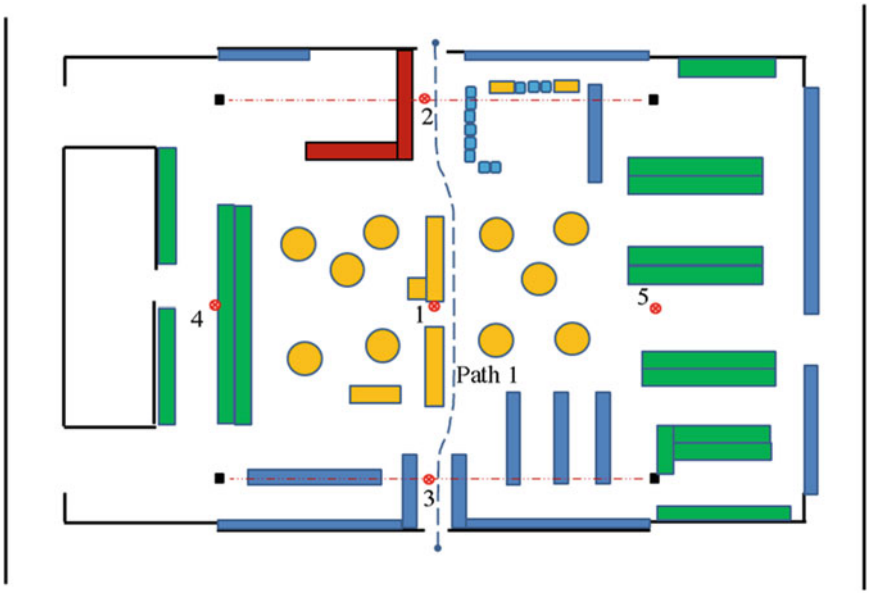

Fig. 16.4 Accelerometer layout and walking path

levels of vibration. This is a very unusual occurrence and not predictable from the usual analytical means. Although it will be discussed in more detail later in this paper, it should be noted here that a modification that alters one of these modes slightly so that they are not both harmonic multiples of the same step frequency would significantly improve the floor behavior.

The observations made from Fig. 16.5 reveals a need to better understand the mode shapes related to the 4.25 Hz and 6.375 Hz natural frequencies. Measurements from heel drop test locations can be utilized to estimate the mode shapes for the two frequencies noted. Specifically, the FRF magnitudes indicate a magnitude at discrete frequencies of each point measured as shown in Fig. 16.3 for location 1. Additionally, the phase of the FRF indicates the direction of a particular point relative to the excitation point. If the point has a similar phase angle to the excitation point (ie. Heel drop location), it is vibrating with the excitation point. If the point is approximately 180° out of phase, that point is up when the driving point is down. Table 16.1 shows the relative magnitudes of the center of the bay to the center of each girder (locations 2 and 3 in Fig. 16.4) and the center of the joists at the other two column lines (locations 4 and 5 in Fig. 16.4). These are noted as the top girder, bottom girder, bottom joist, and top joist in Table 16.1. The negative amplitudes indicate that the location is moving out of phase with the driving point at the center of the bay.

The amplitudes from the mode at 4.25 Hz show that the girders move at 30 % of the amplitude noted at the center for the 4.25 Hz mode and that the joists at the edge of the bay have only 4–5 % of the movement seen at the center. This is the type of shape characteristic that is expected for the fundamental mode and is very difficult to change structurally. At the 6.375 Hz mode, there is very little motion in the girder, 3–9 % of the motion at the center; however, the amplitude at the center of the joists at each edge of the bay have a motion that is approximately 34 % of the amplitude in the opposite vertical direction indicating a wave-like mode shape perpendicular to the joists. A structural modification to target a change in this mode shape may eliminate the additive nature of the two modes that currently exists. This will be discussed more as part of the Recommendations section of this paper.

While the heel-drop tests and the controlled walking studies are useful in understanding the vibration behavior of the floor and, thus, how to mitigate the levels, it is also of interest to understand the character of the in-service levels that are the primary cause of concern. Understanding vibration behavior from the perspective of identifying the largest levels was the objective of the in-service tests. After speaking with the library staff, it was determined that the media center area experiences the largest levels of vibration when used as a thoroughfare during the change of classes. During this time (lasting approximately 3 min/h), dozens of students criss-cross the library utilizing various paths. As noted in the previous section, in-service measurements were captured during some of the liveliest episodes that occurred. The liveliest recorded episode is shown in Fig. 16.6. Amplitudes similar to those found in Fig. 16.6 were observed throughout the 3 min class change intervals.

Interpreting the "between class" results may need to consider a different tolerance criteria than that used for an office environment noted previously. During the class change time, the only people possibly working quietly at a desk are the library personnel. For these personnel, the pedestrian activity in the library would likely be disturbing, even in the absence

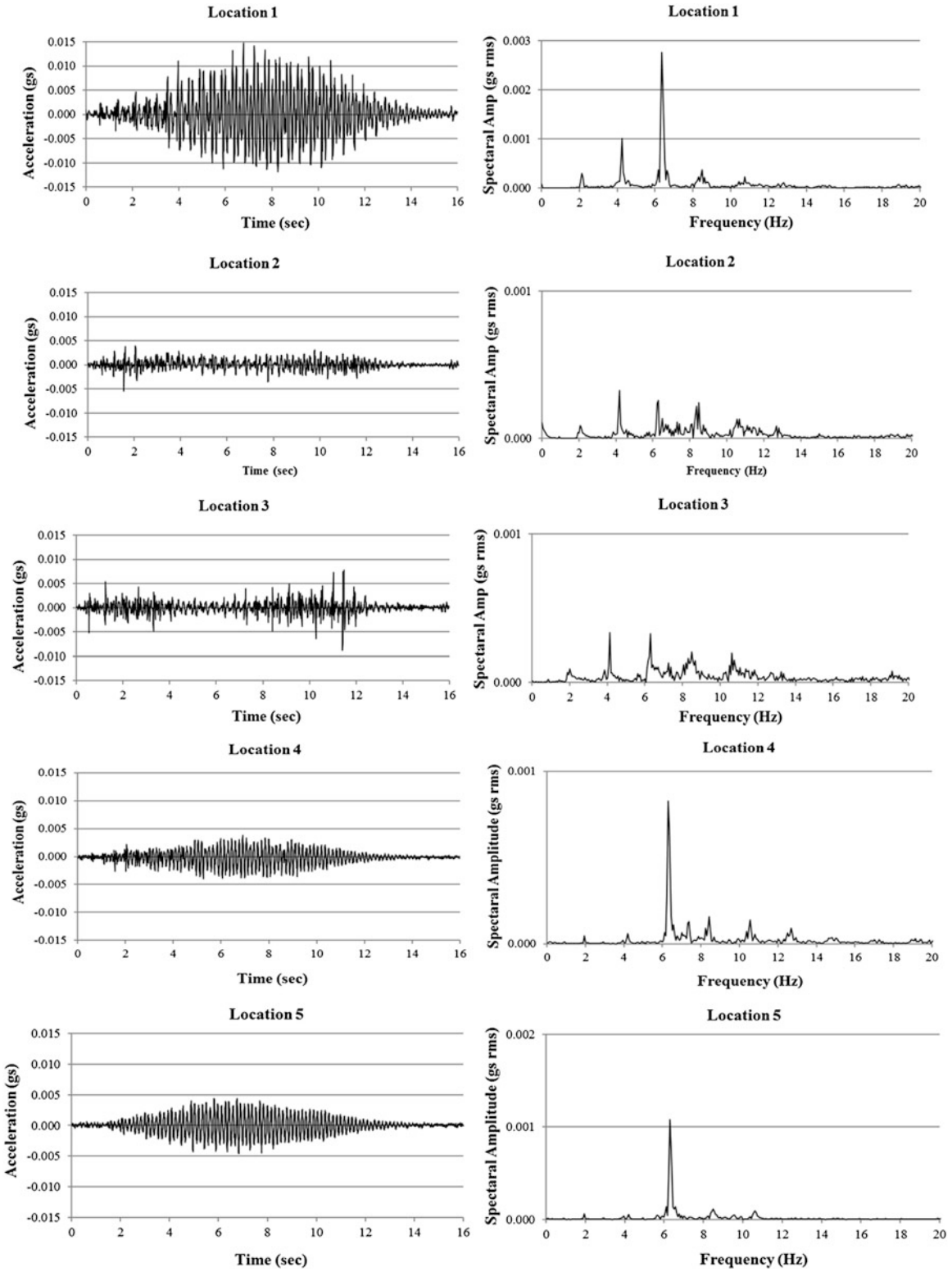

Fig. 16.5 Acceleration response at locations 1–5 due to walking along path 1

Table 16.1 FRF magnitudes for fundamental and higher order mode

Mode	Center of bay (1)	Top girder (2)	Bottom girder (3)	Left joist (4)	Right joist (5)
4.25 Hz	1	0.30	0.29	0.05	0.04
6.375 Hz	1	0.09	0.03	−0.33	−0.35

Note: Numbers in () are locations shown in Fig. 16.4

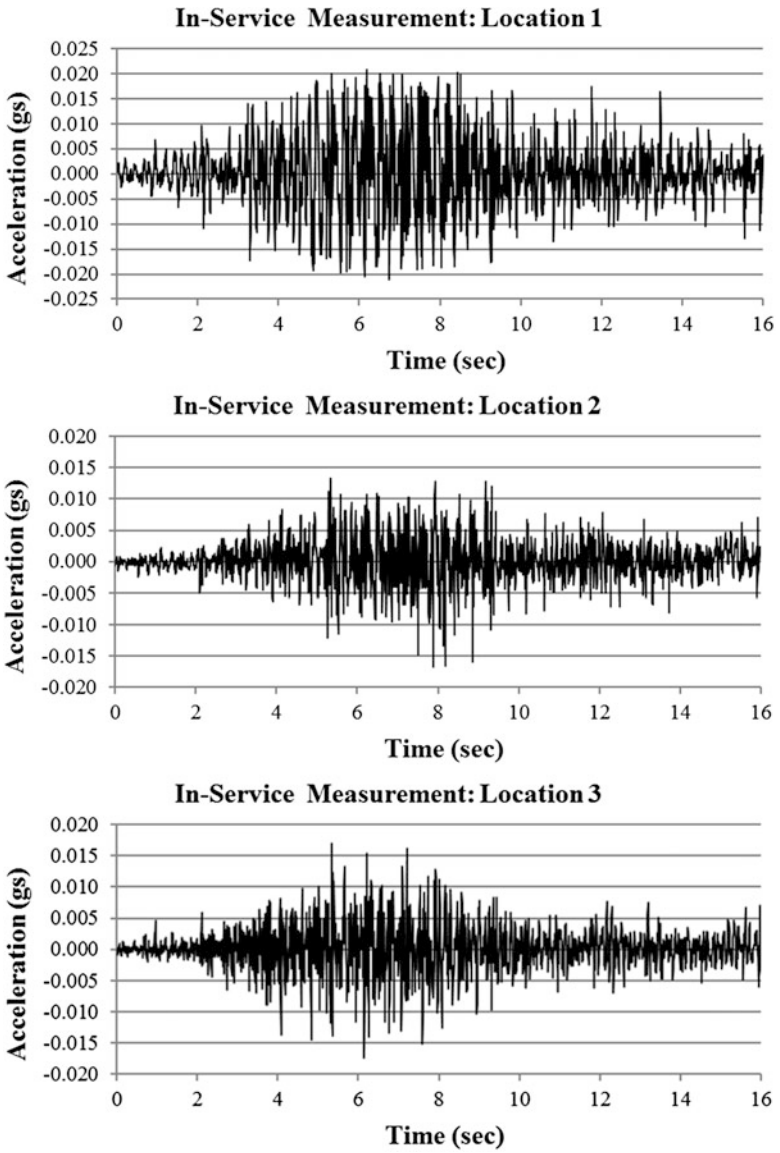

Fig. 16.6 Liveliest in-service measurement

of very perceptible vibration levels. If one were to consider the perception of objectionable vibration by the users to be more like that of a shopping mall, the level expected to disturb climbs to 0.02 g [1], four times greater than that of an office environment. With this criterion in mind, the in-service measurements indicate borderline behavior with respect to the human tolerance criteria.

Since this type of floor vibration problem is difficult and expensive to fix via structural modification, architectural solutions to mitigate the magnitude of the levels and their effect on occupants can be considered. It can be observed from several of the measurements presented that the largest amplitudes occur at the center of the floor when the walker is near the center of the floor. It can also be observed that Locations 4 and 5 experience their largest levels when the walker is near the center of the floor.

16.5 Recommendations to Mitigate Excessive Vibration Levels

Altering an existing floor structure to reduce vibration is expensive, disruptive and often results in minimal improvement. Although not typically recommended in renovations because of cost and disruption, increasing stiffness of the system without commensurate increases in mass is the most effective structural modification. It should be specifically noted that just increasing the mass can be shown to be ineffective relative to the Design Guide 11 criteria. The reason this is true is that while more mass increases the denominator of the amplitude prediction, it also increases the numerator by lowering the frequency of the system, thus resulting in little change to the predicted amplitudes. The best way to increase stiffness without commensurately increase mass is to add material to make the system deeper. This can be done by adding depth to the joists and/or girders. Increased slab thickness is also very effective because while it does increase mass, it also increases the width of the participating area and the effective moment of inertia of the members so there is more participating mass without a lowering of the fundamental frequency. Several cautions must be made about adding a concrete topping to an existing slab system. First, a structural engineer should carefully consider whether the system has sufficient strength to carry the additional concrete. Second, some effort may be needed to bond the new slab to the existing so that composite action is realized. It should be noted that composite action is not as difficult to achieve for walking induced vibration response as it would be for strength. For example, concrete on a non-composite form deck welded to a member behaves compositely when subjected to walking excitation. From this, it can be theorized that very smooth or painted slabs would only need to be roughened or scoured slightly to achieve composite action between the existing slab and the new topping.

In certain situations, the girder can be specifically targeted for structural stiffening, particularly when they support joists. It was noted in the Interpretation of Results that the measured fundamental system frequency was higher than the analytical results predicted, indicating either less mass or more stiffness than predicted. Upon inspection of the experimental results, it appears from the fundamental mode shape that the girder is stiffer than predicted. In typical joist/girder systems, the joist seats have been shown to reduce the composite action with the slab, thus reducing stiffness [3]. In this system, it appears that the details related to the change in deck direction may be having the effect of improving composite action between the girder and the slab. Since the results indicate that the largest levels of vibration have minimal contribution from the girders, structural modifications to the girders will likely have little effect on improving system behavior.

Perhaps the most important factor contributing to the largest level of vibration observed is there are two modes that can be excited by the same step frequency. A structural modification that targets removing the coupling of these modes may be the least onerous structural solution. Specific details of this type of solution will require more extensive analytical study and were therefore outside the scope of this project.

As noted previously, structural modifications are not the only way to improve floor system performance. Architectural features like full height partitions within the objectionable bay are often found very effective [1, 4]. Although the open plan of the library, with the high ceilings and clerestory windows, is architectural pleasing, the open plan is contributing significantly to the problem that exists. If the center third of the bay could be tied into the roof with full height partitions, it is expected that a significant reduction in vibration levels would be observed. A partitioned area in the center of the bay would also keep pedestrians away from the most objectionable walking paths. Because of the resonant nature of the most objectionable walking vibrations, any space planning which interrupts the flow of foot traffic through the center of the room would be beneficial. Along these same lines, anything that disrupts the pace of a walker would be beneficial.

Since it is the quiet users that are disrupted by the pedestrian traffic, not the pedestrians themselves, it is recommended that the middle half of the bay in each direction not be planned for quiet users. Specifically, the study tables, the circulation desk and the computer tables should not be located in this area. This avoids the possibility of users sitting quietly and being disturbed in the liveliest area of the media center. Positioning the low book shelves in the middle part of the bay may preserve the architectural impact of this area and also serve to disrupt free flowing traffic if placed strategically. Since the users of this would likely be standing and moving around, they will probably tolerate higher levels of vibration than those sitting quietly.

As noted previously, the primary users of this space are the media center staff. The students and teachers only use the space intermittently in quiet engagement. As such, it is very important to put the circulation desk in one of the quieter areas outside of the central portion of the large bay. Also noted previously, the largest levels are created during the class change times. As long as the users are aware that there should be no concerns about structural safety (the disruption of all the students scurrying about is probably as disruptive to the staff as the floor motion), the staff may be willing to tolerate only moderate improvements to the existing conditions that can be affected by space planning.

References

1. Murray, T.M., Allen, D.E., Ungar, E.E.: Floor Vibrations Due to Human Activity. Steel Design Guide Series 11, p. 69. American Institute of Steel Construction (1997)
2. Murray, T.M.: Tips for Avoiding Office Building Floor Vibrations. Modern Steel Construction (2001)
3. Band, B.S., Murray, T.M.: Vibration characteristics of joist and joist-girder members. Research Report CE/VPI-ST 96/07, Department of Civil Engineering, Virginia Polytechnic Institute and State University, Blacksburg (1996)
4. Hanagan, L.M.: Walking-induced floor vibration case studies. J. Archit. Eng. ASCE **11**(1), 14–18 (2005)

Chapter 17
Vibration Serviceability Assessment of an In-Service Pedestrian Bridge Under Human-Induced Excitations

Amir Gheitasi, Salman Usmani, Mohamad Alipour, Osman E. Ozbulut, and Devin K. Harris

Abstract Pedestrian bridges may experience significant vibrations under pedestrian traffic and wind loads. Design codes address the vibration limit state levels either by ensuring the frequency ranges associated with typical pedestrian passages are outside the lower fundamental frequencies of the structure or by restricting the maximum accelerations below the limits for pedestrian comfort. This paper discusses vibration serviceability assessment of a highly trafficked local pedestrian bridge based on the field dynamic tests. The selected bridge is a 60-m-long three-span steel structure with a continuous reinforced concrete slab supported on two longitudinal steel girders. First, a finite element model of the pedestrian bridge is developed to obtain the natural frequencies and mode shapes. Then, ambient vibration tests are conducted to validate the modal characteristics of the pedestrian bridge. Next, the dynamic response of the bridge in terms of peak accelerations is determined both experimentally and analytically under various pedestrian excitations. Finally, the implications of the results for the serviceability limit state assessment of the pedestrian bridge are discussed.

Keywords Modal analysis • Dynamic testing • Vibrations • Footbridges • Serviceability

17.1 Introduction

As opposed to highway or rail road bridges, pedestrian footbridges are not typically subjected to heavy traffic loads. In their design and construction process, several light and slender members are being used to not only take advantage of the low strength demand on the system, but also to fulfill the architectural demands which more often than not seek artistic designs with longer spans. These geometrical characteristics of the pedestrian footbridges make them susceptible to human induced vibrations, as they tend to have natural frequencies similar to those detected for the pedestrian walking. Although current design methodologies guarantee the safety and stability of the lightweight footbridge structures, it is their serviceability, in terms of level of comfortless and safety that pedestrians feel, that has been the major concern affiliated with this specific types of structures. Some well-known examples of serviceability issues associated with in-service pedestrian bridges include the London Millennium footbridge [1], the Pont du Solferino in Paris [2], and the T-Bridge in Japan [3].

In order to address these challenges, several code and design provisions have provided guidelines to control the vibration of footbridges to satisfy the corresponding serviceability limit states. Eurocode5 [4], British National Annex [5], French Guideline SETRA [6], and the European guideline HIVOSS [7] are the examples of existing guidelines which have characterized the pedestrian loading under crowd conditions and provided methodologies to predict the response of the bridge system using the SDOF approach or finite element analysis [8]. In the design codes, the serviceability of a given footbridge system is being evaluated through limiting the natural frequencies of the system to avoid pedestrian-vibration induced resonance. The corresponding limits for the structural modal frequency are called critical frequencies. If the given footbridge fails to satisfy the limits of the code, the serviceability of the structure shall then be evaluated by limiting the levels of vibration (in terms of maximum acceleration) under human induced excitations.

The values of modal frequencies for any given footbridge can be obtained through experimental testing (vibration testing) or computational simulations (finite element analysis). However, the accuracy of the numerical results highly depends on the modeling approach, details of the structural components included in the model, and the corresponding analysis approach. The experimental data can also be used to calibrate the numerical models, so that further details on the response of the structure can be collected from the structural analysis. As opposed to the natural frequencies and mode shapes that are intrinsic characteristics of any structural system, the acceleration response of a structure under human excitations is a function of

A. Gheitasi • S. Usmani • M. Alipour • O.E. Ozbulut (✉) • D.K. Harris
Department of Civil and Environmental Engineering, University of Virginia, Charlottesville, VA, USA
e-mail: ozbulute@yahoo.com

© The Society for Experimental Mechanics, Inc. 2016

M. Allen et al. (eds.), *Dynamics of Coupled Structures, Volume 4*, Conference Proceedings of the Society for Experimental Mechanics Series, DOI 10.1007/978-3-319-29763-7_17

the imposed loading scenarios. From the experimental testing perspective, the loading configuration can be defined and controlled over the course of the corresponding vibration test. In the numerical models, however, there is a need to define the loading function that can simulate the details of the walking-induced loading profile. These details include number of pedestrians passing over the structure, their walking speed, as well as the level of synchronization. Applying these predefined loading scenarios to the calibrated numerical models would provide more insights on the dynamic response of the structures. Nevertheless, the accuracy of the existing proposed models to predict the human walking behavior and its applicability to a wide range of existing inventory of footbridges are still under investigation.

In order to overcome this challenge, several design codes and provisions have proposed simplified equations to estimate the maximum dynamic response of footbridges, as a function of walking habits, but also dynamic characteristics of the system. These equations would provide the opportunity to evaluate the serviceability of the system during the design process, when there is no actual structure to test. In recent years, several research studies have been conducted to evaluate the accuracy and validity of the code-specified critical frequencies and proposed equations to predict the maximum dynamic response in pedestrian bridges [8–14]. In these studies, in-service footbridges were subjected to experimental testing to extract actual modal response and dynamic behavior. The collected responses in the field were then used to evaluate the accuracy of currently proposed limits for the serviceability check, through application of numerical and computational simulations. This paper aims to build on the foundation of exiting research and extend the knowledge in experimental testing and computational simulation to evaluate the vibrational serviceability of a highly-trafficked footbridge. First, a finite element model of the pedestrian bridge is developed and the fundamental natural frequencies and mode shapes of the footbridge is obtained. Then, ambient vibration tests are conducted to validate the modal characteristics of the pedestrian bridge. Next, the dynamic response of the bridge in terms of peak accelerations is determined both experimentally and analytically under various pedestrian excitations. Finally, the implications of the results for the serviceability limit state assessment of the pedestrian bridge are discussed.

17.2 Description of Footbridge

The footbridge in this study is one of two footbridges located south on Emmet Street on US 29 in the city of Charlottesville, Virginia. The footbridge links University of Virginia's Ruffner Hall at Curry School of Education with South Newcomb Road on the other side. Due to its location at the center of University of Virginia, it is frequently used by students, staff and faculty members. The bridge is essentially a multi-span steel girder with a concrete deck. The concrete deck is supported by side girders with cross bracings on the columns and diaphragms at regular lengths of the substructure. Other important features of the bridge include its cantilever on both ends and parapets with railings. Figure 17.1 shows pictures of the footbridge from different angles.

The total length of the bridge is 57.9 m with five spans of 4.6, 15.9, 21.3, 11.6 and 4.6 m. The total width of the bridge is 4.9 m including 0.3 m parapets on each side. The center span girders have a thin plate under the bottom flange for added stability.

17.3 Finite Element Simulation

A 3D finite element model of the pedestrian bridge was developed using SAP 2000 [15]. Due to the uncertainties in the material and structural properties, engineering judgment was used to make the modeling assumptions. A free vibration analysis was conducted to obtain natural frequencies and mode shapes of the footbridge. The six lowest transverse and vertical modes of vibration were computed and shown in Fig. 17.2. The information provided by the vibration modes was employed in planning the instrumentation of the bridge for human-induced vibration tests.

The current guidelines that incorporate the pedestrian effect on the serviceability of a pedestrian bridge employ a two-stage evaluation method. In the first stage, the fundamental frequencies of the bridge are compared with the critical frequency range. If the frequency limits suggested by the code is not fulfilled, a more detailed confirmation is required as a second stage evaluation. In this case, the vertical and horizontal accelerations obtained from a dynamic analysis should be in accordance with the maximum allowable values. Table 17.1 provides the critical frequency limits in the vertical and horizontal direction according to different design guidelines. Comparing the natural frequencies of the pedestrian bridge provided in Fig. 17.2

Fig. 17.1 Views of the bridge from each side and then from the deck

with the critical frequency limits, it can be concluded that the fundamental frequency in the vertical direction falls within the critical ranges of frequencies defined by all guidelines of Table 17.1. Therefore, a more detailed dynamic analysis is needed. In what follows, the dynamic tests that were conducted to obtain more accurate natural frequencies and to gather the dynamic response of the bridge are described.

17.4 Test Set-Up and Instrumentation

The test setup for the bridge included the installation of 10 Bridge Diagnostics Inc. (BDI) accelerometers with a range of ±2 g and a differential sensitivity of 1 V/g. These sensors were connected by cables to BDI STS-WiFi nodes which were then connected wirelessly to the BDI mobile base station which in turn was connected to the laptop through an IP address. The data acquisition software package used was BDI WinSTS. An acquisition sampling frequency of 100 Hz was used. The data obtained from the WinSTS was then processed in MATLAB. The test setup for the bridge can be seen in Fig 17.3.

Sensor locations were chosen based on the vibration modes obtained through the finite element model to capture maximum acceleration amplitude. The vertical sensors were attached on top of the deck next to the parapets, whereas transverse sensors were installed on the sides of the concrete deck and the longitudinal sensor was installed on top of the east end column. All sensors were attached onto the surface through mount studs using Loctite 410 adhesive and Loctite 7452 Accelerator. The locations of these sensors can be seen in Fig. 17.4.

17.5 Dynamic Tests Conducted on the Footbridge

17.5.1 Ambient Vibration Tests

Dynamic tests were conducted on the pedestrian bridge to obtain its dynamic characteristics and response. First, an ambient vibration test was conducted to determine the natural frequencies of the bridge. The ambient excitation consisted of wind pressure, vehicles passin underneath the bridge, and light pedestrian traffic on the bridge during the test. The accelerations from the transverse and vertical sensors were obtained for an extended time period of 900 s at a sampling frequency of 100 Hz.

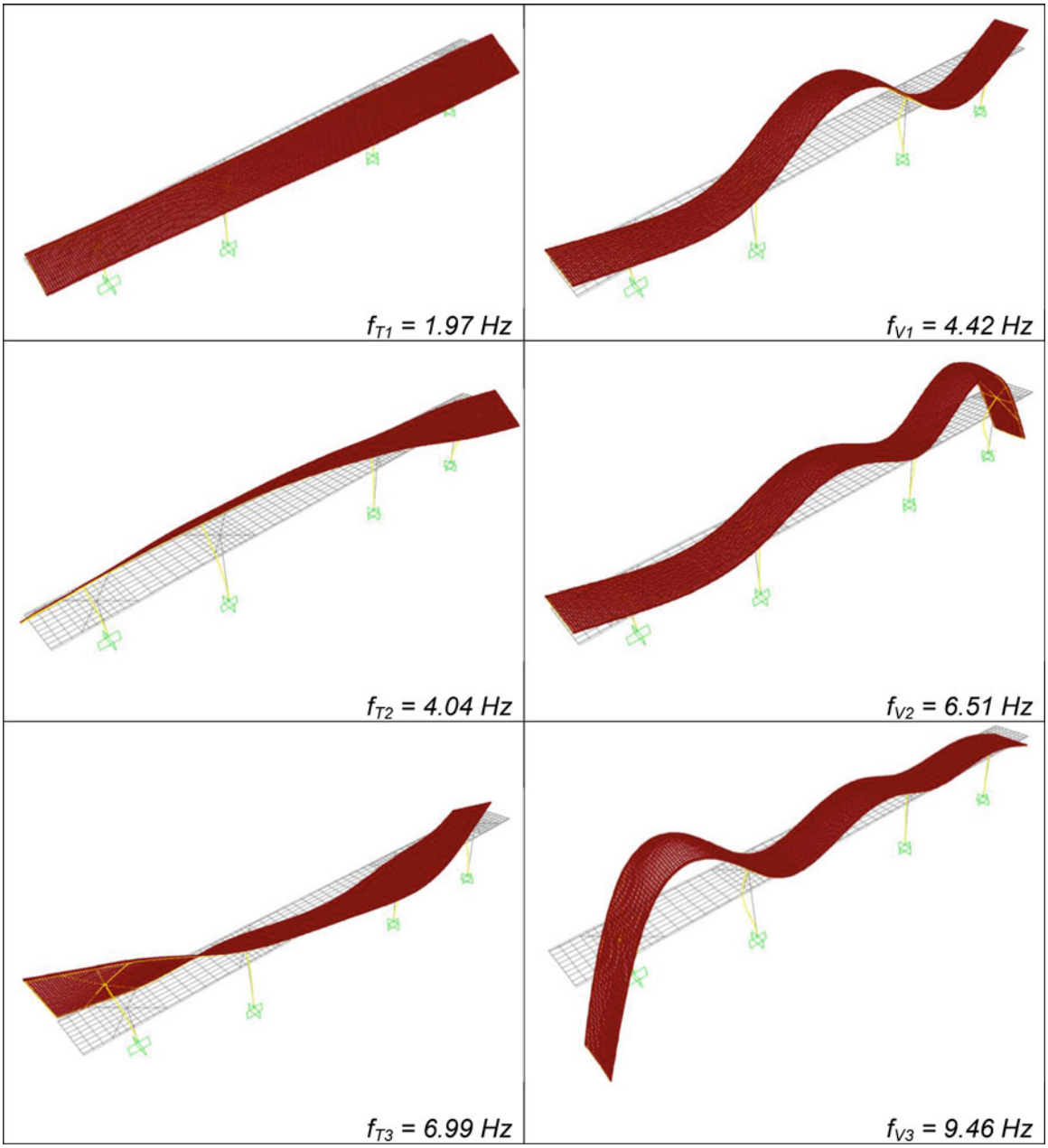

Fig. 17.2 Modes of vibrations calculated from the initial finite element model

Table 17.1 Critical frequency limits according to current guidelines (Hz) [12]

Reference	Vertical	Horizontal
British National Annex to Eurocode 1	<8	<1.5
Eurocode 5	<5	<2.5
SETRA	1–5	0.3–2.5
HIVOSS	1.25–4.6	0.5–1.2

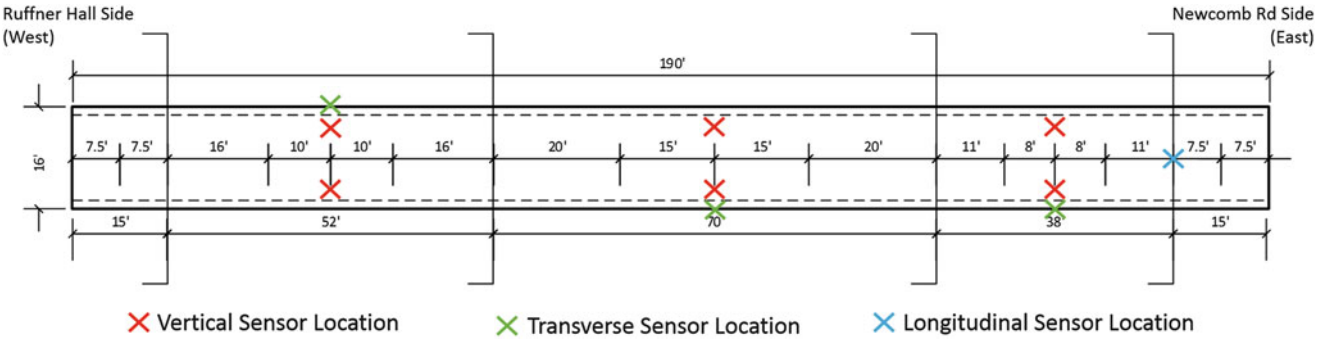

Fig. 17.3 Instrumentation plan

Fig. 17.4 (**a**) Transverse sensor installation, (**b**) vertical sensor installation

Table 17.2 Pedestrian interaction test plan

Test	Number of people	Frequency of steps (Hz)
1–3	9	1.0
4–6	9	1.5
7–9	9	2.0
10	1	1.0
11–13	1	1.5
14–16	1	2.0

17.5.2 Pedestrian Interaction Tests

To assess the serviceability performance of the pedestrian bridge under real service-loading conditions, the dynamic tests were performed under crowd excitation and the acceleration response of the bridge was collected from the sensors installed at different locations of the bridge as shown in Fig. 17.3. The approach is similar to the one discussed by Ivorra et al. [16]. Each test except one was repeated three times to reduce the effect of uncertainties and improve the accuracy of data. The first three tests were conducted with nine people walking in a 3×3 formation at three different frequencies and the next three tests were conducted with 1 person walking at three different frequencies. These frequencies were measured through a metronome (Table 17.2).

17.6 Modal Identification Using Frequency Domain Decomposition

Operational modal analysis enables the derivation of the modal parameters from the dynamic response of a structure under operational loads. A number of methods have been developed for output-only system identification of structures. In this study, Frequency Domain Decomposition (FDD) method is used to obtain the modal parameters. In FDD method [16], the unknown inputs $x(t)$ and the acquired outputs $y(t)$ can be related through their power spectral densities and frequency response functions as follows:

$$G_{yy}(j\omega) = \overline{H}(j\omega) G_{xx}(j\omega) H^{T}(j\omega) \tag{17.1}$$

where $G_{yy}(j\omega)$ is the (r x r) power spectral density (PSD) matrix of r inputs and $G_{xx}(j\omega)$ is the (m x m) power spectral density matrix of m outputs. $H(j\omega)$ is the (m x r) frequency response function (FRF) matrix with $^{-}$ and ^{T} denoting the complex conjugate and transpose respectively.

The first step in the process is to estimate the power spectral density matrix $G_{yy}(j\omega)$ for the outputs from the experimental data. The output PSD known at discrete frequencies $\omega = \omega_i$ is then decomposed by taking the Singular Value Decomposition (SVD) of the matrix;

$$G_{yy}(j\omega_i) = U_i S_i U_i^{H} \tag{17.2}$$

Where the matrix $U_i = [u_{i1}, u_{i2}, \ldots, u_{im}]$ is the unitary matrix holding singular vectors u_{ij} and S_i is a diagonal matrix holding the scalar singular values s_{ij}. At a peak corresponding to the k th mode in the spectrum this mode or a close mode will be dominating. If only the k th mode is dominating there will only be one term in Eq. (17.1). The first singular vector in this case u_{i1} would be an estimate of the mode shape:

$$\phi = U_{i1} \tag{17.3}$$

The corresponding singular value is the power spectral density function of the single degree of freedom system. This power spectral density function is identified by isolating the peak and comparing the mode shape estimate with the singular vectors obtained for frequency lines around the peak.

The recorded acceleration time history data was processed in MATLAB and frequency domain decomposition method was implemented to identify the first three natural frequencies for the transverse and vertical from the singular values. The measured data was digitally filtered using eight-order high pass and low pass infinite impulse response (IIR) filters with cut-off frequencies of 0.5 Hz and 30 Hz, respectively. Figures 17.5 and 17.6 show the vertical and transverse frequencies obtained through peak picking in the singular values plot:

The frequencies identified from the singular values plot of the vertical power spectral density matrix are as follows:

$$f_{V1} = 4.019 \text{ Hz}, \quad f_{V2} = 5.841 \text{ Hz}, \quad f_{V3} = 9.121 \text{ Hz}$$

The frequencies identified from the singular values plot of the vertical power spectral density matrix are as follows:

$$f_{T1} = 2.788 \text{ Hz}, \quad f_{T2} = 4.026 \text{ Hz}, \quad f_{T3} = 6.324 \text{ Hz}$$

The natural frequencies obtained from the experimental testing verify that further dynamic investigation is needed in the vertical direction, while the natural frequencies in the transverse direction are in accordance with the limit values specified by the guidelines. Although the computed natural frequencies have not indicated serviceability problems, the dynamic analysis of the bridge in both vertical and transverse directions are discussed in the next section for the completeness and for assessing the accuracy of the equations used for predicting the maximum acceleration response by design guidelines.

17.7 Evaluation of Pedestrian Interaction Test Results

In order to evaluate the vibration levels under human-induced excitations, acceleration time histories i6n vertical (V) and transverse (T) directions were collected from the performed pedestrian interaction tests. The collected data included acceleration records over the course of the tests for all of the six loading scenarios (one person and nine people at three

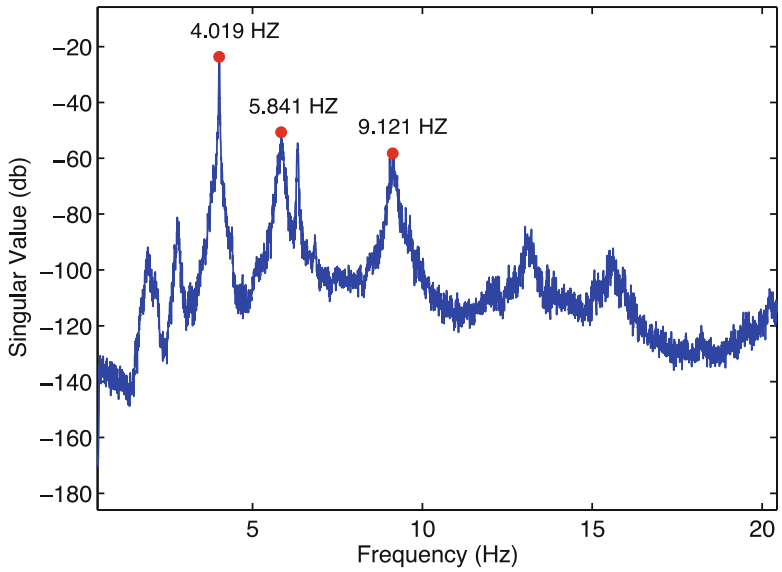

Fig. 17.5 Singular values for vertical power spectral density matrix

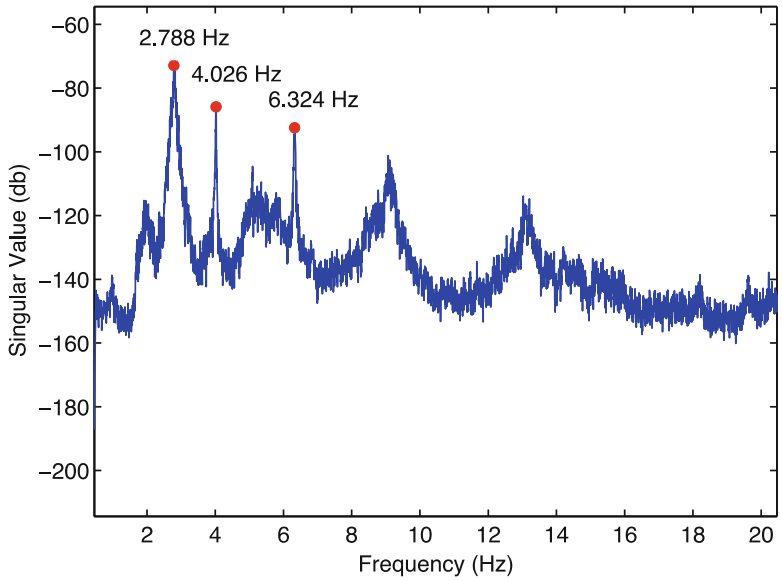

Fig. 17.6 Singular values for transverse power spectral density matrix

different walking frequencies) and their corresponding repetitive runs (3 runs for each scenario except for 1 person walking at 1 Hz). A representative set of raw data collected from the test is illustrated in Fig. 17.7, which highlights the sensitivity of the bridge dynamic response to the imposed loading scenarios (in terms of number of pedestrians and their walking frequencies). The raw data was then post-processed to define the peak acceleration values obtained from each test run. Table 17.3 summarized the average peak acceleration values according to the mounted instrumentations. As it is given, the peak acceleration values in both vertical and horizontal directions demonstrate significant variations. However, the maximum average acceleration responses for each direction were highlighted in the table, and used in this study for comparison to the allowable limits provided by current design guidelines. The bold values indicate the maximum average peak acceleration responses collected from vertical (V1 to V6) and transverse (T1 to T3) sensors.

In addition to the test results, a dynamic response analysis was also performed using existing models to estimate the maximum acceleration for the selected footbridge. A modeling approach for prediction of human-induced walking loads, proposed by Eurocode 5 [4], was used in this study. Accordingly, the maximum acceleration response, in both vertical and horizontal directions, for n persons crossing the bridge can be estimated using the following equations:

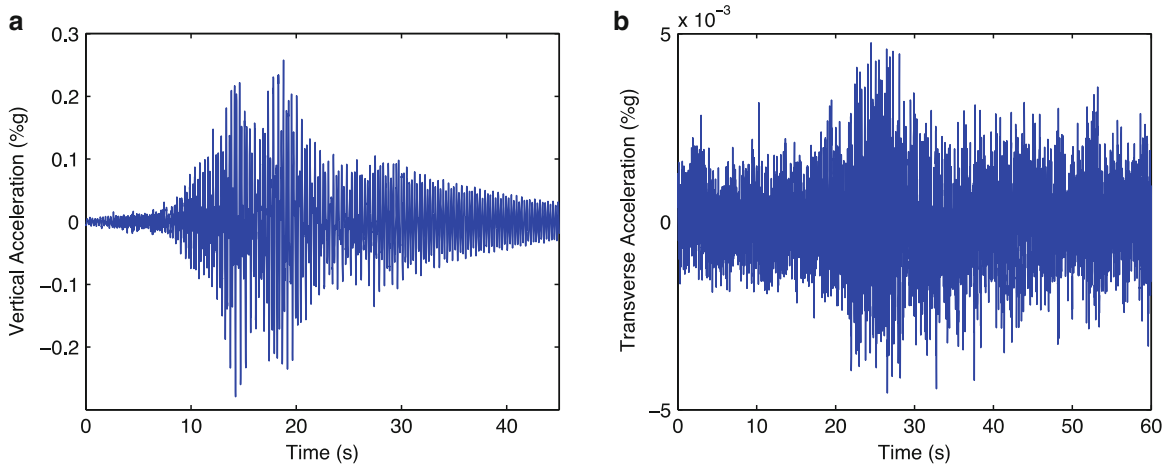

Fig. 17.7 Representative collected acceleration data (**a**) V5 in test 8 (**b**) T3 in test 10

Table 17.3 Average peak acceleration responses (%g)

Test	V_1	V_2	V_3	V_4	V_5	V_6	T_1	T_2	T_3
1–3	0.89	***1.38***	0.54	0.46	1.32	0.92	0.12	0.09	***0.18***
4–6	1.28	1.36	0.79	0.92	***1.45***	1.32	***0.29***	0.14	***0.29***
7–9	1.77	2.88	1.22	1.23	***3.00***	1.68	0.28	0.19	***0.31***
10	0.45	***0.70***	0.28	0.30	***0.70***	0.43	0.04	0.04	***0.05***
11–13	0.29	***0.38***	0.36	0.36	***0.38***	0.32	0.07	0.05	***0.08***
14–16	0.35	1.16	0.35	0.35	***1.21***	0.38	0.06	0.04	***0.08***

The bold values indicate the maximum average peak acceleration responses collected from vertical (V1 to V6) and transverse (T1 to T3) sensors

$$a_{ver,n} = 0.23 \times a_{ver,1} \times n \times k_{ver} \tag{17.4-1}$$

$$a_{hor,n} = 0.18 \times a_{hor,1} \times n \times k_{hor} \tag{17.4-2}$$

where $a_{ver,1}$ and $a_{hor,1}$ are the maximum vertical and horizontal response under one individual walking, respectively, which can be obtained as:

$$a_{ver,1} = \begin{cases} \frac{200}{M\xi} & 0 < f_v \leq 2.5 \\ \frac{100}{M\xi} & 2.5 < f_v \leq 5.0 \end{cases} \tag{17.5-1}$$

$$a_{hor,1} = \frac{50}{\mu\xi} \quad 0.5 < f_v \leq 2.5 \tag{17.5-2}$$

In these equations, M and ξ are the mass and damping ratio of the structure. The mass of the tested bridge was extracted from the calibrated FE model and assumed to be 18,370 kg, whereas the damping ratio was assumed to be 0.4 %, which is suggested by SETRA [6] for bridges with steel girders [13]. The parameters k_{ver} and k_{hor} are the constant factors which are functions of vertical and horizontal fundamental frequencies of the system, and were both set to 0.4 according to the Eurocode 5 recommendations. Once calculated, the obtained analytical dynamic response together with the critical maximum values of the recorded accelerations in both vertical and horizontal directions were compared to the limits provided in current guideline. Table 17.4 provides a summary of these limits according to Eurocode 1, Eurocode 5, SETRA, and HIVOSS [8, 12].

Figure 17.8 illustrates the comparison between critical acceleration values obtained from experimental and analytical approaches, to the limits provided in current guidelines. As demonstrated, the maximum critical acceleration responses obtained from the pedestrian interaction tests, satisfy the limits of the codes, which would ensure the vibration serviceability of the selected structure. However, the analytical values for critical dynamic responses of the system, obtained from Equations 17.4 and 17.5, exceed the allowable limits. This might be attributed to the fact that the equations proposed by Eurocode 5

Table 17.4 Critical acceleration limits according to current guidelines (%g) [12]

Reference	Vertical	Horizontal
Eurocode 1	7.0	1.5
Eurocode 5	7.0	2.0
SETRA	10.0	3.0
HIVOSS	10.0	3.0

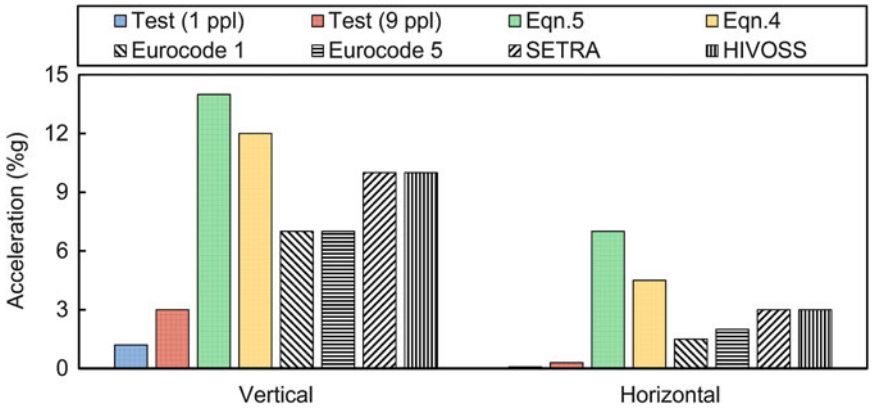

Fig. 17.8 Evaluation of pedestrian-induced dynamic response

are attributed to timber footbridges. Although these equations were defined to be material-independent [8], results from this experimental investigation clearly highlight the inapplicability of the proposed equations beyond the limits (e.g. timber structures) of the code.

17.8 Conclusions

This study examines the serviceability of an in-service pedestrian bridge through experimental tests. A preliminary finite element model of the bridge was developed to gain insight on the dynamic characteristics of the bridge before field-testing. Then, ambient vibration tests were conducted to determine the natural frequencies in the vertical and transverse directions. The data obtained from the ambient vibration tests were processed using frequency domain decomposition method. The fundamental frequency of the bridge in the vertical direction was found to be within the critical range described by various design guidelines. Dynamic tests were conducted to evaluate the maximum acceleration response of the pedestrian bridge when either single person or a group of nine people walked along the whole structure at three different frequencies. The induced accelerations were below the recommended limits for all loading conditions. The peak acceleration response was also calculated using the equations provided by a design guideline. Results suggests that the design code overestimates the response of the bridge and further research is needed to develop more reliable analysis methods to predict the dynamic response of pedestrian bridges.

References

1. Dallard, P., Fitzpatrick, T., Flint, A., Low, A., Smith, R.R., Willford, M., Roche, M.: London Millennium bridge: pedestrian-induced lateral vibration. J. Bridg. Eng. **6**(6), 412–417 (2001)
2. Danbon, F., Grillaud, F.: Dynamic behavior of a steel footbridge. Characterization and modeling of dyanamic loading induced by a moving crowd on the Solferino foorbridge in Paris. In: Proceedings of Footbridge, Venice, Italy, 2005
3. Fujino, Y., Pacheco, B.M., Nakamura, S.I., Warnitchai, P.: Synchronization of human walking observed during lateral vibration of a congested pedestrian bridge. Earthq. Eng. Struct. Dyn. **22**(9), 741–758 (1993)
4. Eurocode 5, design of timber structures - Part 2: bridges, in EN 1995–2, European Committee of Standardization, 2004
5. British Standards: UK National Annex to Eurocode 1: actions on structures - Part 2: Traffic loads on bridges, in BS NAEN 1991–2, 2003
6. SETRA: Assessment of virbational behavior of footbridges under pedestrian loading, in Technical Guide SETRA. Paris, France, 2006
7. HIVOSS: Design of Footbridges Guideline: Human Induced Vibrations of Steel Structures, in RFS2-CT-2007-00033, 2008

8. Dey, P., Walbridge, S., Narasimhan, S.: Vibration serviceability analysis of aluminum pedestrian bridges subjected to crowd loading. In: 6th International Conference on Advances in Experimental Structural Engineering. Urbana-Champaign, Illinois (2015)
9. Ivorra, S., Foti, D., Bru, D., Baeza, F.J.: Dynamic behavior of a pedestrian bridge in Alicante, Spain. J. Perform. Constr. Facil., 04014132 (2013)
10. Van Nimmen, K., Van den Broeck, P., Gezels, B., De Roeck, G.: Vibration serviceability of footbridges: a comparative study of 3 design methodologies. In: Proceedings of ISMA2010 International Conference on Noise and Vibration Engineering, 2010
11. Živanović, S.: Benchmark footbridge for vibration serviceability assessment under the vertical component of pedestrian load. J. Struct. Eng. **138**(10), 1193–1202 (2012)
12. Salgado, R., Branco, J.M., Cruz, P.J., Ayala, G.: Serviceability assessment of the Góis footbridge using vibration monitoring. Case Stud. Nondestruct. Test. Eval. **2**, 71–76 (2014)
13. Van Nimmen, K., Lombaert, G., De Roeck, G., Van den Broeck, P.: Vibration serviceability of footbridges: evaluation of the current codes of practice. Eng. Struct. **59**, 448–461 (2014)
14. Ingólfsson, E.T., Georgakis, C.T., Jönsson, J.: Pedestrian-induced lateral vibrations of footbridges: a literature review. Eng. Struct. **45**, 21–52 (2012)
15. SAP (Structural Analysis Program): Integrated finite element analysis and design of structures, CSI Inc., Berkley, 2000
16. Brincker, R., Zhang, L., Andersen, P: Modal identification from ambient responses using domain decomposition. In: IMAC 18: Proceedings of the International Modal Analysis Conference (IMAC), pp. 625–630. San Antonio, 7–10 February 2000

Chapter 18
Numerical and Experimental Studies on Scale Models of Lightweight Building Structures

Ola Flodén, Kent Persson, and Göran Sandberg

Abstract Lightweight buildings are sensitive to low-frequency vibrations, making it difficult to construct them in such a way that noise and disturbing vibrations are kept at an acceptable level. In the design of vibration reduction measures, it is desirable to have computational models for predicting the effects of structural modifications. Validations of the models to experimental data have to be performed to ensure reliable predictions. The experimental studies are simplified if full-scale models can be scaled down in size. In the paper, methods for designing scaled experimental models of building structures are discussed. An example, the scaling of a wooden building structure, is presented.

Keywords Lightweight buildings • Impact sound • Vibration transmission • Model validation • Scale models

18.1 Introduction

Noisy neighbours are a common cause of annoyance for residents in multi-family houses. Compared to heavier structures, lightweight buildings are more sensitive to vibrations, making it difficult to construct them in such a way that noise and disturbing vibrations are kept at an acceptable level. Despite newly constructed lightweight buildings complying with regulations for sound insulation, many of the residents perceive the impact sound as annoying [1]. Building regulations in most European countries take frequencies in the range 100–3150 Hz into account, whilst the lower limit in Sweden is 50 Hz. The measured sound insulation correlates much better to residents annoyance when extending the frequency range in the evaluations down to 20 Hz [1], pointing out the importance of improved sound insulation at lower frequencies. In wood buildings, for example, a common measure for reducing vibration transmission is to insert elastomers in-between building parts [2]. The design of such measures is based primarily on experience. To optimise the design, it is desirable to have computational models for predicting the effects of structural modifications. The models have to be calibrated, correlated and validated to measurement results for the predictions to be reliable. An alternative to employing full-scale experimental structures for performing the measurements is to design scaled experimental models that behave in a similar way.

In the paper, methods for designing scaled experimental models of building structures are discussed. The objective of the scaling procedure is to arrive at scaled experimental models that preserve the dynamic behaviour of the full structures. An example regarding the scaling of a wooden building structure is presented here.

18.2 Governing Theory

The equations of motion for a structure can be derived through its Lagrangian, which for an undamped system is given by

$$L(q_1, \ldots, q_n, t) = T(q_1, \ldots, q_n, t) - V(q_1, \ldots, q_n, t), \tag{18.1}$$

O. Flodén (✉) • K. Persson • G. Sandberg
Faculty of Engineering, Department of Construction Sciences, Lund University, John Ericssons väg 1, SE-223 63 Lund, Sweden
e-mail: ola.floden@construction.lth.se

© The Society for Experimental Mechanics, Inc. 2016

M. Allen et al. (eds.), *Dynamics of Coupled Structures, Volume 4*, Conference Proceedings of the Society for Experimental Mechanics Series, DOI 10.1007/978-3-319-29763-7_18

where T is kinetic energy, V is potential energy, $q_1, \ldots, q_n$ is a set of n generalised coordinates and t is time. The equations of motion of the system is given by the Lagrange's equations

$$\frac{d}{dt}\left(\frac{\partial L}{\partial \dot{q}_j}\right) = \frac{\partial L}{\partial q_j}. \tag{18.2}$$

Scaling the size of a model affects its Lagrangian. The Lagrangian of a scale model, can be expressed as

$$L_s = T_s - V_s = a\left(T_f - bV_f\right), \tag{18.3}$$

where subscripts s and f denote quantities belonging to the scale model and to the full model, respectively, and a and b are constants. The resulting equations of motion are not affected by a, whilst $b = 1$ is required in order to preserve the equations of motion. A scale model should, hence, be constructed in such a way that b is as close to unity as possible. This approach for determining parameters of scale models is possible when expressions for the energies can be derived. For more complex structures, numerical models of the full and the scaled experimental models have to be analysed and compared in order to ensure accurate scaling.

18.3 Scale Models of Building Structures

The Lagrangians used in scaling procedures are constructed based on the physical phenomena expected to occur. Residential buildings are normally constructed using different types of beam-, column- and plate-like structures which are exposed to different types of deformations. To illustrate the scaling procedure, the scaling of a beam is derived by considering its bending, an important type of deformation in the dynamics of building structures. In the derivations presented here, the coordinate system in Fig. 18.1 is used. The beam is assumed to have rectangular cross-section; the width b, the height h and the length l of the beam is defined in Fig. 18.1. The kinetic energy of an Euler-Bernoulli beam in bending is given by

$$T = \frac{1}{2}\int_0^l \rho A \dot{u}^2 dx, \tag{18.4}$$

where $A = bh$ is the cross-sectional area, ρ is the density and u is the deflection in the z-direction. The potential energy is given by

$$V = \frac{1}{2}\int_0^l EI\left(\frac{\partial^2 u}{\partial x^2}\right)^2 dx, \tag{18.5}$$

where E is the Young's modulus and I is the moment of inertia of the cross-section,

$$I = \frac{bh^3}{12}. \tag{18.6}$$

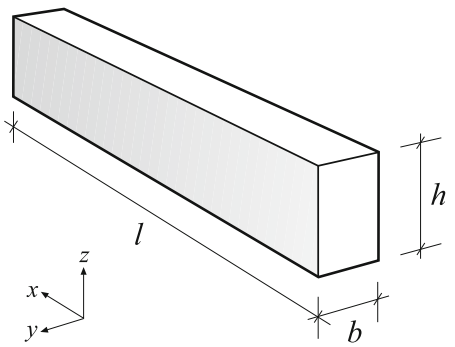

Fig. 18.1 Coordinate system and dimensions used in the derivations of the scaling of a beam

The scaling is introduced by defining the following dimensionless parameters:

$$\mu = \frac{A_s}{A_f}, \qquad \kappa = \frac{I_s}{I_f}, \qquad \chi = \frac{x_s}{x_f} = \frac{l_s}{l_f}. \tag{18.7}$$

By inserting the dimensionless parameters in the energy expressions for the scaled and the full models, it can be shown that

$$T_s = \mu\chi T_f \tag{18.8}$$

and

$$V_s = \frac{\kappa}{\chi^3} V_f. \tag{18.9}$$

Scaling parameters could be introduced also for the material properties (E and ρ) and the time. It is, however, assumed here that the same material is used for both models. Not scaling the time results in the eigenfrequencies being preserved. Inserting Eqs. (18.8) and (18.9) in the first equation in Eq. (18.3) results in

$$L_s = \mu\chi T_f - \frac{\kappa}{\chi^3} V_f = \mu\chi \left(T_f - \frac{\kappa}{\mu\chi^4} V_f \right). \tag{18.10}$$

By comparing the result to the second equation in Eq. (18.3), it is found that the scaling condition $b = 1$ results in

$$\frac{\kappa}{\mu\chi^4} = 1 \qquad \Leftrightarrow \qquad \left(\frac{l_s}{l_f} \right)^2 = \frac{h_s}{h_f}. \tag{18.11}$$

When using this condition for creating a scale model of a beam, the eigenfrequency of the bending modes are preserved. It can be seen that bending in the z-direction is unaffected by the width. Hence, if a length scaling is assumed, the scaled height can be determined or vice versa. A corresponding expression can be determined for the width by considering bending in the y-direction.

The procedure presented above can be employed for other types of deformations, such as the torsion of beams or the bending of plates. The type of deformation to consider in the scaling depends on the type that is expected to dominate the dynamics of the structure.

18.3.1 Example: Wooden Building Structure

The structure studied here was designed to represent the physics involved in low-frequency (below 100 Hz) vibration transmission in multi-storey wood buildings. Specifically, a type of construction called timber volume element (TVE) buildings was used as reference for designing the experimental model. A main feature of such buildings, from a dynamical point-of-view, is the use of elastomer layers for vibration isolation. The load-bearing structure in TVE buildings consists of wood frames covered by plasterboards and particleboards. The buildings are constructed by stacking box-like volume elements (the TVEs) with layers of elastomers in-between. The experimental model considered here, illustrated in Fig. 18.2, consists of parts of two TVEs, one comprising a floor with walls on top and the other comprising a ceiling with walls below. Only half the height of the walls, compared to complete TVEs, is included in the model. The floor and the ceiling consist of a number of primary beams (seven and ten, respectively) attached to edge beams and have surfaces of particleboard and plasterboard, respectively. The walls consist of seven primary beams each, attached to edge beams on one side, and have surfaces of plasterboard. Two sides of the model have one type of walls, apartment separating walls, and the other two sides have another type of walls, facade walls. In Table 18.1, the dimensions are shown for the floor, the ceiling and the two types of walls. Elastomer blocks of the material Sylodyn NB [3] are placed in-between the two TVE structures. A total of 28 elastomer blocks, each being $100 \times 95 \times 25\,\text{mm}^3$ large, are placed with a centre-to-centre distance (cc) of 600 mm along the walls. The outer dimensions of the full experimental model are $4000 \times 3600 \times 2800\,\text{mm}^3$.

The scaling of the beams was made using Eq. (18.11) for bending in the two directions, resulting in relations between the length and the height, and between the length and the width,

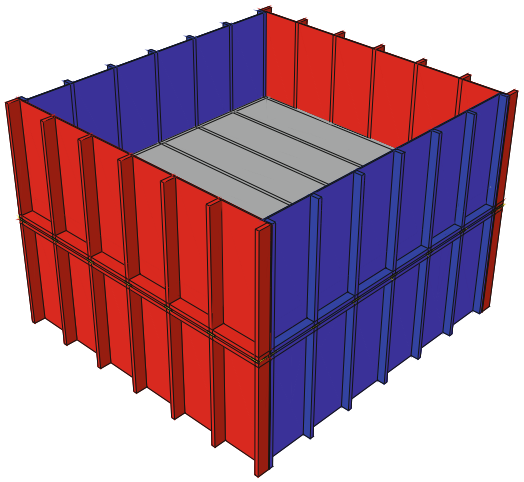

Fig. 18.2 The full-scale wooden building structure studied here. The floor is shown in *grey*, the apartment separating walls in *red*, the facade walls in *blue* and the elastomer blocks in *yellow*. The ceiling, placed under the floor, cannot be seen in the figure

Table 18.1 Length (l), centre-to-centre distance (cc) and cross-sectional dimensions ($b \times h$) of the primary beams, and thickness (t) of the plates in the full model and in the scale model. The unit is mm

	Full model					Scale model				
	l_f	cc_f	h_f	b_f	t_f	l_s	cc_s	h_s	b_s	t_s
Floor	3430	600	220	45	22	2330	408	95	21	10
Ceiling	3430	400	120	45	13	2330	272	55	21	6
Apartm sep wall	1390	600	95	45	13	950	408	45	21	6
Facade wall	1390	600	145	45	13	950	401	70	21	6

$$\left(\frac{l_s}{l_f}\right)^2 = \frac{h_s}{h_f}, \qquad \left(\frac{l_s}{l_f}\right)^2 = \frac{b_s}{b_f}. \tag{18.12}$$

The thickness of the plates (particleboards and plasterboards) were scaled by regarding them as beams spanning the cc between the primary beams, i.e. assuming one-dimensional deformations for the plates. By considering bending of the plates, Eq. (18.12) can be used to obtain the relation between cc and plate thickness t,

$$\left(\frac{cc_s}{cc_f}\right)^2 = \frac{t_s}{t_f}. \tag{18.13}$$

The scaling ratio for the cc is employed also for the length of the beams, i.e.

$$\frac{cc_s}{cc_f} = \frac{l_s}{l_f}. \tag{18.14}$$

Moreover, the floor, the ceiling and the walls have to be scaled so that their sizes match, i.e. using the same four scaling ratios (scaling of height, width, length and cc) for all structures. First, the scaling ratio for the thickness of the plates was chosen since particleboard and plasterboard are manufactured in only a few different thicknesses. Thereafter, Eqs. (18.12)–(18.14) were used to determine the remaining scaling ratios. The dimensions of the beams and of the plates in the scale model are shown in Table 18.1.

The final step in determining the dimensions of the scale model is to scale the elastomer blocks. The dimensions of the blocks were determined by regarding the two TVE structures as rigid masses and the elastomer layer as a spring. The eigenfrequency of a system with two masses, m_1 and m_2, connected by a spring with stiffness k is given by

$$f = \sqrt{k\frac{m_1 + m_2}{m_1 m_2}} = \sqrt{\frac{k}{m^{eff}}}, \qquad m^{eff} = \frac{m_1 m_2}{m_1 + m_2}, \tag{18.15}$$

where m^{eff} is the effective mass. The ratio between the eigenfrequencies of the full model and of the scale model is, consequently,

$$\frac{f_f}{f_s} = \sqrt{\frac{k_f}{k_s}\frac{m_s^{eff}}{m_f^{eff}}}. \tag{18.16}$$

The effective masses of the full and the scaled models, calculated using the densities found in [2], are 281 kg and 53 kg, respectively. It is assumed that the eigenfrequency of the two-mass-system is preserved, $f_s = f_f$. The ratio between the spring stiffness of the two models can then be calculated as

$$\frac{k_f}{k_s} = \left(\frac{f_f}{f_s}\right)^2 \frac{m_f^{eff}}{m_s^{eff}} = 5.30. \tag{18.17}$$

Assuming the elastomer blocks to be linear elastic, their combined stiffness is given by

$$k = \frac{EA}{d}, \tag{18.18}$$

where A is the total contact area of the blocks and d is the thickness of the blocks. The same type of elastomer was used for the scale model as for the full model, so that $E_s = E_f$. Consequently,

$$\frac{k_s}{k_f} = \frac{d_f}{d_s}\frac{A_s}{A_f}. \tag{18.19}$$

Combining Eqs. (18.17) and (18.19) results in

$$\frac{d_s}{d_f} = 5.30\frac{A_s}{A_f}. \tag{18.20}$$

Hence, if a thickness scaling is specified, an area scaling can be determined and vice versa. The thickness of the scaled elastomer blocks was chosen to be the same as for the full blocks, $d_s = d_f$. This results in the scaled area being $A_s = A_f/5.30 = 1800\,\text{mm}^2$. Assuming a squared shape for the blocks, their dimensions can be determined as $42 \times 42 \times 25\,\text{mm}^3$. In order to match the width of the beams in the apartment separating walls, the blocks were chosen to be $45 \times 45 \times 25\,\text{mm}^3$ large. The outer dimensions of the scale model are $2600 \times 2400 \times 1900\,\text{mm}^3$. The volume of the full model is, hence, reduced by 70 % in the scaling.

Finite element (FE) models of the full and the scaled experimental models were created to investigate how well the scaling procedure works when the scaled plates and beams are assembled to larger structures. The material properties found in [2] were used in the FE models. The element sizes were decided based on the accuracy in eigenfrequencies below 100 Hz, the highest frequency of interest. All connections in the FE models were modelled as fully tied. The comparison of the scale models to the full models was carried out in terms of free-free eigenfrequencies, i.e. eigenfrequencies calculated with no boundary conditions applied. The difference in eigenfrequencies was evaluated in terms of the normalised relative frequency difference (NRFD), defined as

$$\text{NRFD} = \frac{\left|f_i^s - f_i^f\right|}{f_i^f}, \tag{18.21}$$

where f_i^s and f_i^f are the ith eigenfrequencies of the scale model and of the full model, respectively. First, FE models of the floor, the ceiling and the walls were investigated. Eigenfrequencies below 100 Hz and the resulting NRFD values are shown in Figs. 18.3 and 18.4, respectively. The curves have different lengths along the horizontal axis since the structures have different numbers of eigenfrequencies below 100 Hz. The NRFD values are, with a few exceptions, below 10 %. The mean NRFD value is between 2 and 6 % for the different structures. The mode shapes were compared visually, most modes of the scale models being similar to those of the full models. Some of the higher frequency modes were found to be shifted in order. At higher frequencies, the mode shapes are more localised, for example due to resonances in each *cc*-section of the plates.

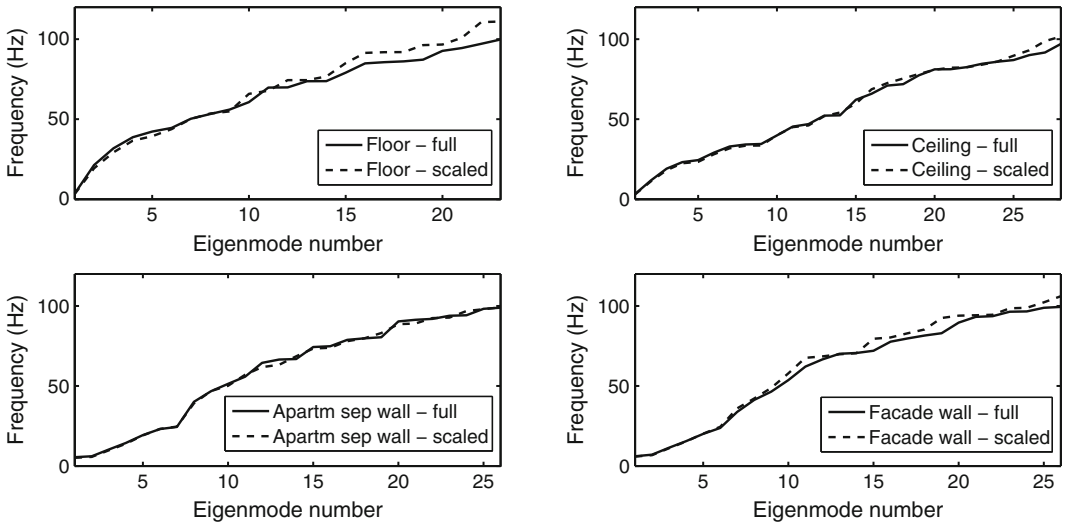

Fig. 18.3 Eigenfrequencies for the full and the scaled models of the floor, the ceiling and the walls

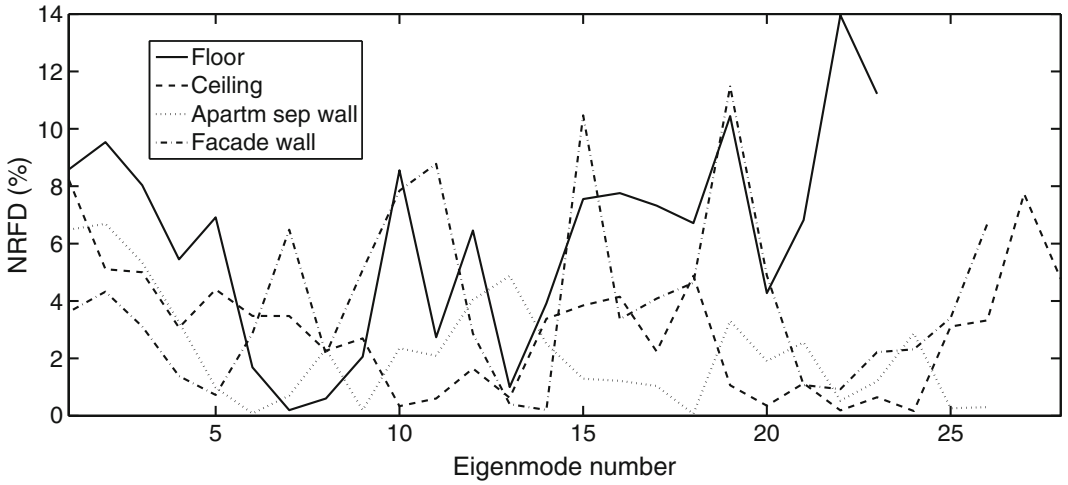

Fig. 18.4 NRFD values for the floor, the ceiling and the walls

Therefore, discrepancies between eigenfrequencies of the beams and of the plates can have larger impact on the resulting mode shapes. The global mode shapes at low frequencies are, however, well preserved in the scale models.

Second, FE models (full and scaled) of the complete structure were created. The elastomer blocks were modelled as linear viscoelastic with properties determined by employing the procedure developed in [4]. The free-free eigenfrequencies of the full and the scaled models are shown in Fig. 18.5, and the resulting NRFD values are shown in Fig. 18.6. The modal density is high, especially around 80 Hz, because of local resonances occurring primarily in the plates of the walls. It is therefore difficult to distinguish the mode shapes from each other. It can, however, be seen that similar trends in modal density are found for the full and the scaled models.

In addition to comparing eigenfrequencies, the vibration transmission from the floor to the TVE below was studied. A harmonic point load was applied in the vertical direction at the middle of the floor, free-free boundary conditions being used. A unit load was used for the scale model, whilst a load of 5.28 N was used for the full model since the ratio of total masses between the models is 5.28. The resulting complex acceleration amplitudes, $\hat{a}_i$ (i denoting node number), were evaluated at the surface of the ceiling and at the surface of one of the facade walls. Root-mean-square (RMS) values of the accelerations in all nodes of each surface were calculated as

$$a_{RMS}(f) = \sqrt{\frac{1}{n}\sum_{i=1}^{n} |\hat{a}_i(f)|^2}, \tag{18.22}$$

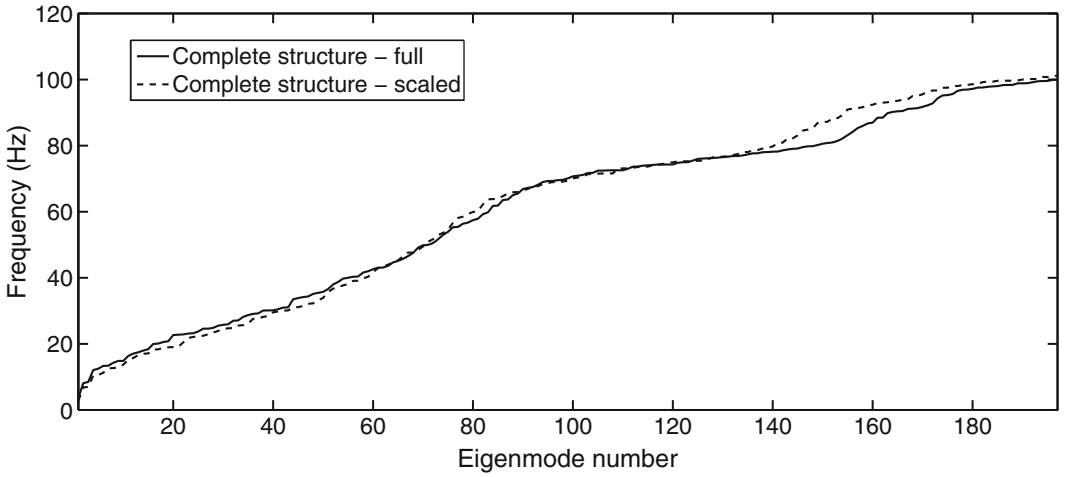

Fig. 18.5 Eigenfrequencies for the full and scaled models of the complete structure

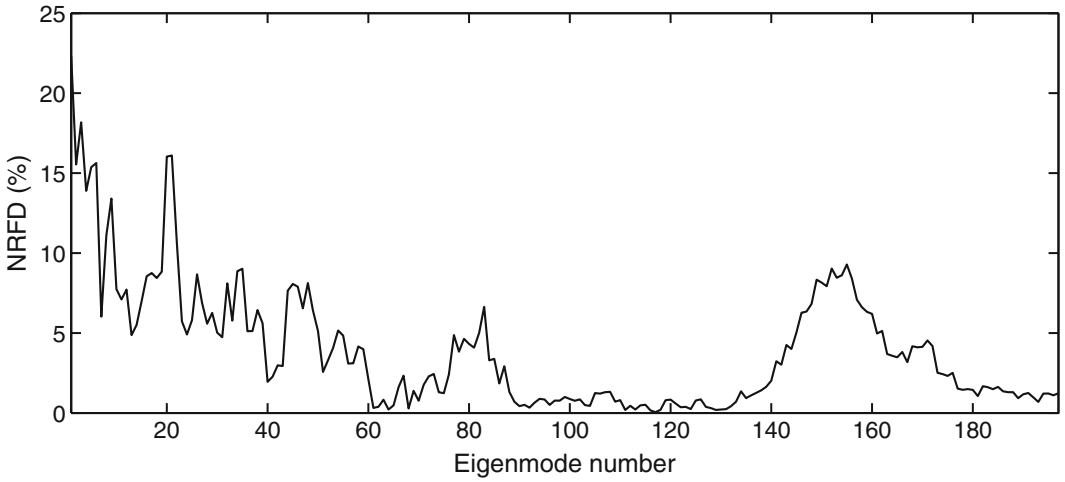

Fig. 18.6 NRFD values for the complete structure

where n is the number of FE nodes at the surface in question. The RMS values at the ceiling surface and at the wall surface are shown in Figs. 18.7 and 18.8, respectively. For frequencies below 50 Hz, the scaled and the full FE models produce similar results, the differences being larger at higher frequencies. Consequently, the scale model performs well below 50 Hz. Above that frequency, the effect of physical phenomena which were not considered in the scaling becomes larger.

18.4 Concluding Remarks

In the paper, the designing of scaled experimental models of building structures was discussed. The scaling is based on assumptions of basic physical phenomena, such as bending of beams, governing the dynamic behaviour. As an example, a wooden building structure representing parts of two storeys in a multi-storey building was considered. The vibration transmission from a floor to the storey below was studied, finding that the scale model produced results similar to the full model for frequencies below 50 Hz. The scale model needs to be developed if better correlation to the full model is desired for higher frequencies. The results may be improved by not using the same scaling ratios for the cc as for the length of the beams. Moreover, other phenomena such as shear deformations of the elastomer layers could be considered in order to improve the scaling.

The degree to which the full and the scaled models need to correlate depends on the aim of the experimental studies. If the scaled experimental structure is used for predicting absolute values of some sort, a high degree of correlation is required. The example structure studied here will be used for developing FE models by comparisons between simulations

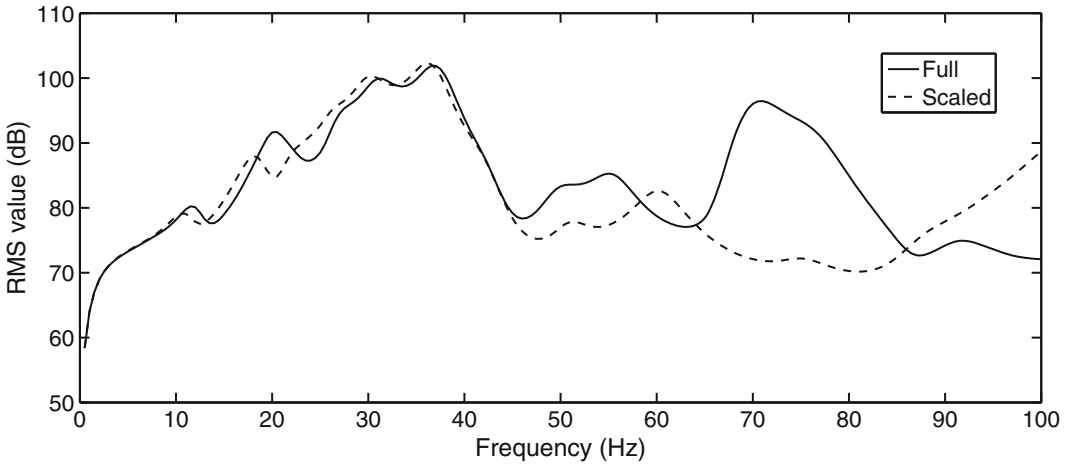

Fig. 18.7 RMS values of the acceleration amplitudes at the ceiling surface for the full and the scaled models of the complete structure

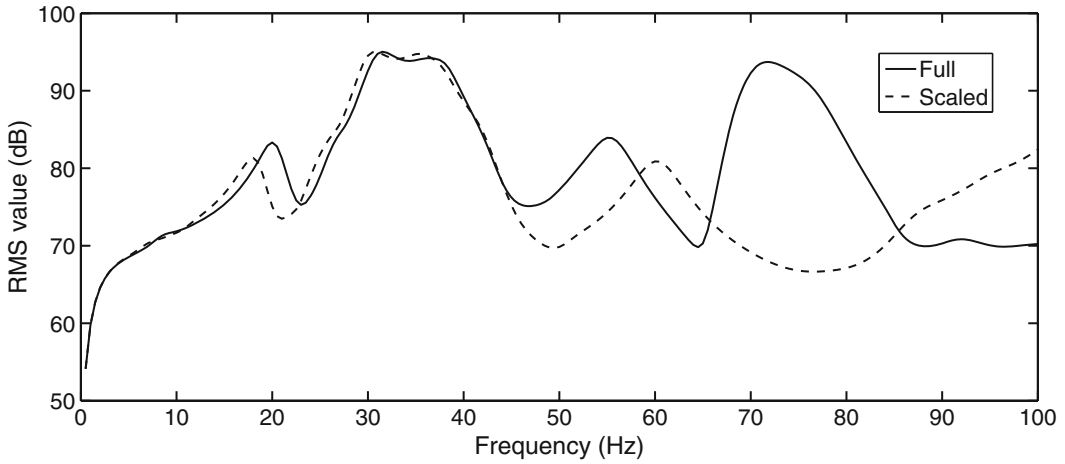

Fig. 18.8 RMS values of the acceleration amplitudes at the facade wall surface for the full and the scaled models of the complete structure

and measurements. In such situations, it is less important to have very good correlation between the full and the scaled models in terms of, for example, eigenfrequencies and amplitudes. It is instead sufficient to represent the physical phenomena governing the dynamic behaviour of the full experimental model, so that the FE models developed (with help of the scaled experimental model) are able to represent these phenomena.

A restriction in the methods discussed here for deriving scaled experimental models is that numerical modelling is employed for investigating their correlation to full-scale models. In the example, the joints were modelled in the same manner in the FE models of the full models and of the scale models. Hence, any difference in joint behaviour, which may be the case in reality, is neglected here.

References

1. Ljunggren F., Simmons S., Hagberg K. Correlation between sound insulation and occupants' perception – proposal of alternative single number rating of impact sound. Appl. Acoust. **85**, 57–68 (2014)
2. Flodén O., Persson K., Sandberg G. Numerical investigation of vibration reduction in multi-storey lightweight buildings. In: Dynamics of Civil Structures, vol. 2, pp. 443–453. Springer International Publishing, Berlin (2015)
3. Getzner W.: GmbH. Data sheet for Sylodyn NB, 2014
4. Negreira J., Austrell P.E., Flodén O., Bard, D.: Characterisation of an elastomer for noise and vibration insulation in lightweight timber buildings. Build Acoust. **21**(4), 251–276 (2014)

Chapter 19
A Wavelet-Based Approach for Generating Individual Jumping Loads

Guo Li and Jun Chen

Abstract This paper suggests an approach to generate human jumping loads using wavelet decomposition and a database of individual jumping force records. A total of 1201 individual jumping force records of various frequencies were first collected. For each record, every single jumping impulse was extracted and decomposed by DB10 Wavelet into seven levels, and all the related decomposition information was stored into a database. The period of each jumping impulse in the same record was found to follow a normal distribution, and so does the contact ratio. In order to generate a jumping load time history having *N* impulses, Wavelet coefficients are first randomly selected from the database for different levels. They are then used to reconstruct *N* impulses by inverse wavelet transform. The periods and contract ratios are then randomly generated according to their probabilistic function. These parameters are assigned to each of the *N* impulses. The final jumping force time history is obtained by linking all the *N* impulses end to end. Examples are presented to show the simulation procedure. Due to the application of the Wavelet decomposition, the non-stationary features of the jumping load force in time-frequency domain can be preserved by the suggested simulation approach.

Keywords Vibration serviceability • Jumping force • Stochastic model • DB10 wavelet • Wavelet transform

19.1 Introduction

Long-span civil engineering structures, such as floors, grandstands, fitness centers and pedestrian bridges, may experience severe vibrations when subjected to human-induced loads (walking, jumping, etc.) leading to the so-called vibration serviceability problem [1, 2]. Jumping action is generally considered as the most severe loading scenario. If the vibration serviceability problem was not well considered at the structural design state, large resonant structural vibrations may make people feel uncomfortable when jumping frequency is close to the natural frequency of the structure [3, 4]. In 1985, a concert held at Nya Ullevi Stadium in Sweden, excited audiences jumped along with the beats of music and caused damage to the foundation of that stadium [5]. In 1994, during a pop concert in London the temporary grandstand collapsed due to the audience's rhythmic motions including jumping and 50 people were injured [6]. More recently in July 2011, a group of people did excises at an aerobics center in a 39-story building in Seoul Korea, their jumping frequency was close to the building's natural frequency. As a result, that building swayed for 10 min which caused occupants in it fleeing in panic [7]. More similar events were also reported in Ref. [8–12].

In design practice, accurate dynamic time-domain analysis method has been developed as a predominant solution to the above-mentioned problems, a finite element model (FEM) needs to be established and jumping loads are introduced to the model to calculate the structural responses. In this procedure, a reliable jumping load model that can represent real jumping force becomes the key aspect of the problem. At present, deterministic jumping load models are widely used [13–15]. Assuming the jumping activity as a periodic process, these model represent jumping load time history by Fourier series function. However, there are significant differences between the resonant responses due to real jumping loads and the equivalent periodic simulation, the latter is often over-conservative resulting in bulky and uneconomic design.

Brownjohn et al. [16] noted that human-induced load was actually a near-periodic narrowband stochastic process, rather than 'perfectly' periodic force. In order to obtain a more realistic jumping load model, first attempts were attributed to studies by Bachmann and Ammann [17], Ellis and Ji [18]. Zivanovic suggested a stochastic load model for individual walking [19]. Racic proposed a stochastic jumping load model [20, 21]. He employed more than 100 Gaussian functions to fit the shape of each jumping impulse and some parameters were generated randomly, then a stochastic method to produce synthetic

G. Li • J. Chen (✉)
Department of Structural Engineering, College of Civil Engineering, Tongji University, Shanghai, People's Republic of China
e-mail: cejchen@tongji.edu.cn

© The Society for Experimental Mechanics, Inc. 2016

M. Allen et al. (eds.), *Dynamics of Coupled Structures, Volume 4*, Conference Proceedings of the Society for Experimental Mechanics Series, DOI 10.1007/978-3-319-29763-7_19

jumping force was developed based on an experimentally measured jumping load database. This paper also attempts to develop a stochastic jumping load model based on Wavelet analysis which claims to be the most powerful tool for processing non-stationary signals.

Wavelet analysis has been widely used in signal processing, numerical analysis, fault diagnosis and many other areas since it was developed in 1984 [22]. It is known as mathematical "microscope" since it can capture the local irregularities of signals [23]. Thus the Wavelet analysis may be a good tool to describe the time-frequency localization characteristics in jumping forces. In this paper, a vast experimentally measured jumping load database was built. Based on it, key parameters were extracted and their statistical properties were studied. Then a method was present to create new jumping impulses by wavelet analysis. Furthermore, a stochastic model was developed to generate force time history due to single people jumping. Finally, the model was verified by comparing a synthetic jumping force time history with a measured one. Results show that the proposed model can be used in structure vibration serviceability assessment.

19.2 Jumping Load Data Collection

A database comprising a large number of high-quality jumping load records is a prerequisite for developing a stochastic model of jumping load. Therefore, we conducted two experiments to measure individual jumping load forces. Experimental data from other source were also collected.

A total of 67 test subjects took part in the first experiment which performed in the movement functional laboratory in Shanghai Ruijin Hospital (see Fig. 19.1a). Each of the subject completed five test cases on a fixed force plate (AMTI OR6-7, USA), including four cases with fixed jumping frequencies (1.5, 2.0, 2.67, and 3.5 Hz) timed by a metronome and one free jumping case without sound instruction. A detailed description of the experimental setup and test procedure can be found in Ref. [24].

The second experiment was conducted on 25 test subjects in the laboratory of Tongji University as shown in Fig. 19.1b. In this experiment, each subject was asked to wear comfortable footwear with the Novel Pedar system (Novel Co., Germany) and jump on the rigid floor. Seven test cases were completed including six fixed jumping frequencies at 1.5, 1.9, 2.3, 2.7, 3.1, 3.5 Hz and one free-jumping case. A detailed description of this experiment is available in Ref. [25].

To further increase the jumping load signals in both number and frequency contents, data was collected from experiment which conducted by other investigators. The third experiment was carried out by Dr. Racic in the Light Structures laboratory in the University of Sheffield. The forces of one person jumping at a time were recorded by a single AMTI BP-400600 force plate rigidly fixed to the laboratory floor. fifty five volunteers participated in the experiment and each of them was asked to jump in 15 fixed frequencies in the 1.4–2.8 Hz having fine resolution of 0.1 Hz. A detailed description can be gotten from Ref. [21].

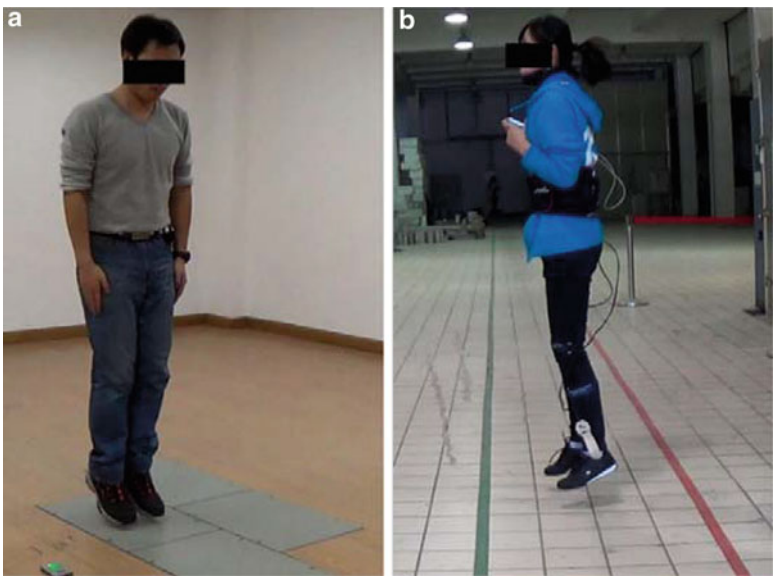

Fig. 19.1 Experimental setup in (**a**) Ruijin Hospital and (**b**) Tongji University

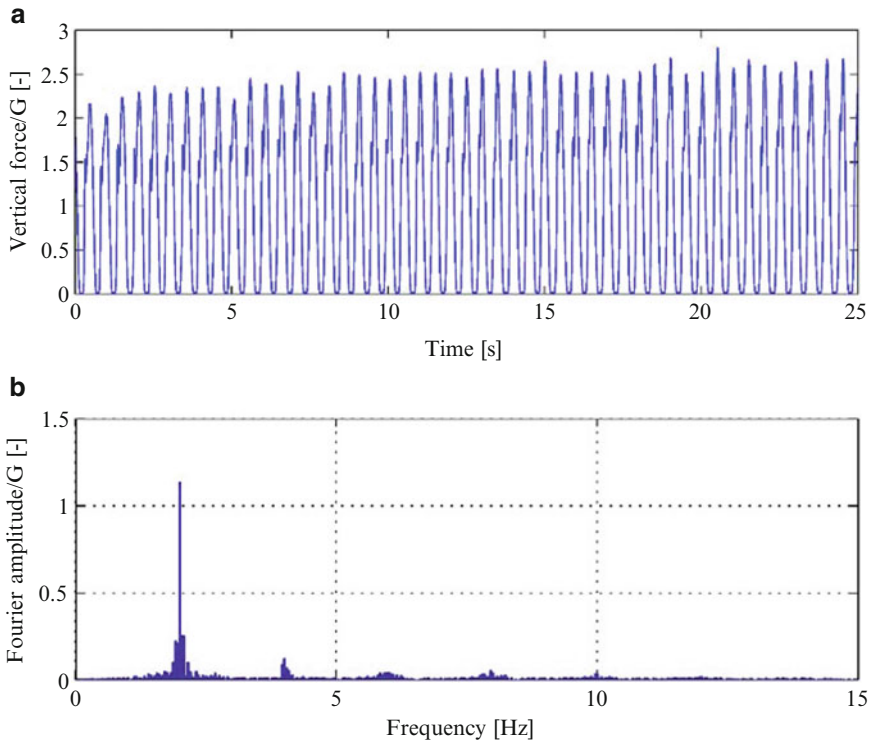

Fig. 19.2 A typical jumping force signal at 2.0 Hz and its Fourier amplitude spectrum (**a**) A measured jumping force signal (**b**) Fourier amplitude spectrum

All the volunteers in the three experiments were drawn from students, academics and technical staffs. Prior to the experiments, the test protocol required that each participant should complete a Physical Activity Readiness Questionnaire and/or pass a preliminary fitness test to confirm whether they were able to finish the kind of physical activity required during the measurements. In the first two experiments, the test procedure for each participant was as follows:

(1) Stood on the force plate or fixed the Novel Pedar system on the participant's body,
(2) A brief rehearsal under the metronome guide prior to the data collection,
(3) Jumped for more than 25 s following a metronome beat,
(4) Rest until felt no tired and then went on the next test case.

After the experiments, data quality was checked and some invalid jumping loads were cast aside. All together, we collected 1201 individual jumping force time histories. A typical measured jumping force signal which normalized by the body weight for 2.0 Hz jumping frequency takes the form illustrated in Fig. 19.2 corresponding to its Fourier amplitude spectrum.

19.3 Model Parameters

From the collected jumping data we can find that jumping force is characterized by a series of individual impulses separated by zero-force periods as illustrated in Fig. 19.3. So it is reasonable to cut the continuously measured jumping force signal into cycles and then develop model for each impulse.

Each jumping cycle is defined as: point A (Fig. 19.3) is the starting point which is the state of test subject toes touching the ground during declining, then the feet contact with the ground until departure (point B) is a jump impulse: A to B segment, and until the toes touch the ground again (point C). Considering there are still some relatively small values on the zero platform segment (B to C segment) due to the measurement errors, 0.15 times body weight of the participant is taken as a threshold value for determining point A, B and C in the original record. In next sections, a window comprising 49 successive jumping cycles in the Fig. 19.2 was selected as an example for further analysis.

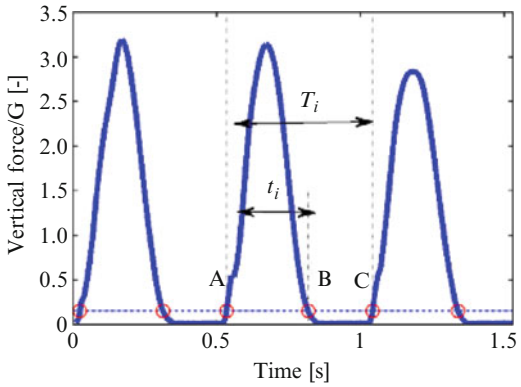

Fig. 19.3 Definition of a jumping cycle

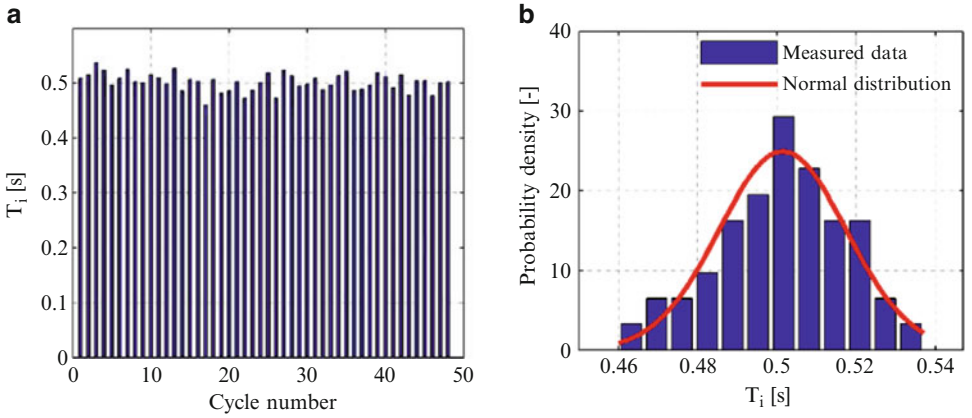

Fig. 19.4 In the 2.0 Hz jumping force signal (**a**) Time intervals T_i and (**b**) corresponding distribution property

19.3.1 Time Interval OF Jumping Cycle: T_i

According to above definition, the time interval T_i between the point A and the point C is a complete jumping period. Note that there are non-ignorable differences for each jumping time interval instead of 'perfect' period, for the intra-subject variability. Therefore, Sim et al. [26] proposed a first-order autoregression model for the variations $\Delta T_i = T_i - mean\ (T_i)$. But a low value of the autoregression coefficient indicated no significant correlation in the variation of the successive intervals. Racic [20] suggested quite recently that the time intervals can be regard as approximately normal distribution in a jumping force signal. Fig. 19.4a shows the jumping time of each cycle in the Fig. 19.2a and their distribution property is shown in Fig. 19.4b. Kolmogorov-Smirnov test shows that time intervals of jumping cycles follow normal distribution property in most jumping signals, and we can ignore the influence of the jumping cycle number on the distribution property.

19.3.2 Contact Ratio: α_i

In each jumping cycle, contact ratio α_i is defined as the ratio of the feet contact time with the ground t_i and the time interval of jumping cycle T_i:

$$\alpha_i = \frac{t_i}{T_i} \tag{19.1}$$

Analysis shows a normal distribution property for α_i in each jumping force signal and it passed the Kolmogorov-Smirnov test with a 95 % confidence level [27]. Figure 19.5a shows the contact ratio of each jumping and the distribution property is shown in Fig. 19.5b. The comparison of the measured and synthetic contact ratios, which is generated by the same parameters

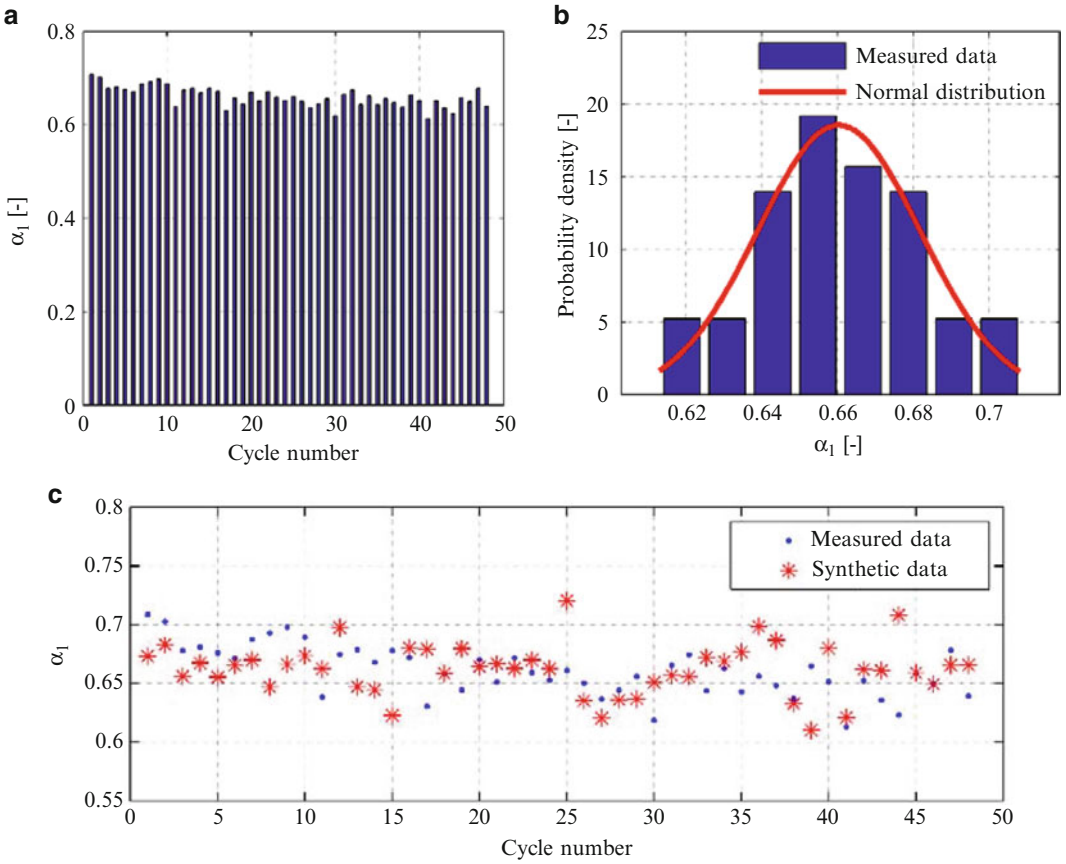

Fig. 19.5 In the 2.0 Hz jumping force signal (**a**) contact ratios α_i, (**b**) corresponding distribution property and (**c**) comparison of the measured and synthetic contact ratio

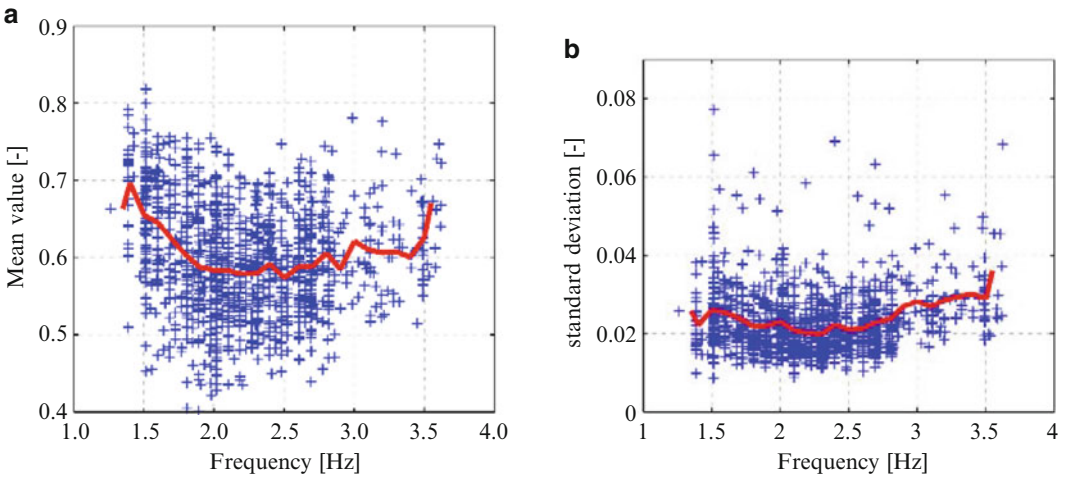

Fig. 19.6 Parameters of all measured jumping force signals (**a**) Mean value μ_α (**b**) Standard deviation σ_α

(mean value μ_α and standard deviation σ_α), are illustrated in Fig. 19.5c. Note that the synthetic contact ratios are similar to the measured one, so it can indicate that normal distribution assumption is reasonable for the contact ratio.

All the calculated μ_α and σ_α for each jumping force signals are shown in Fig. 19.6. It shows a strong discreteness even at the same frequency for both parameters. Note that all the parameters in Fig. 19.6 are reasonable for they come from the measured jumping force signals, so all of them were stored as model parameters which then used to be chosen.

19.4 Wavelet Analysis of Jumping Impulses

Some researchers noted that morphology (size and shape) of single jumping impulse is another important random factor for jumping load [21, 26]. Jumping force is considered as the most dramatic force in the human-induced load for its impulse shape changing rapidly with the time. So the traditional Fourier model can hardly to fit the local irregular characteristics of jumping load. Hence, Racic et al. [21] developed a model which using many Gaussian functions as the base function to fit the measured jumping impulses, but it was also difficult to reserve the high frequency components. Meanwhile, there is no efficient method to get initial parameters for the least square method which used in the model. But, Wavelet analysis provide a novel method to solve the problems in the above-mentioned models.

19.4.1 Basis of Wavelet Analysis [28, 29]

Supposing function $\psi(t) \in L^2(\mathbb{R})$, if it satisfies the compatible condition:

$$C_\psi = \int_R \frac{|\Psi(\omega)|^2}{|\omega|} d\omega < \infty \tag{19.2}$$

we call function $\psi(t)$ is the mother wavelet, where $\Psi(\omega)$ is the Fourier transform of $\psi(t)$. If the mother wavelet $\psi(t)$ is dilated and translated on the time base, a wavelet basis function can be given by equation:

$$\psi_{a,b}(t) = \frac{1}{\sqrt{a}} \psi\left(\frac{t-b}{a}\right) \tag{19.3}$$

where $a \in \mathbb{R} \backslash \{0\}$ and $b \in \mathbb{R}$ is dilation parameter and translation parameter respectively.

In order to reduce coefficients redundancy of continuous wavelet transform, critical sampling is introduced: $0a = 2^j$, $b = k2^j$. Then the wavelet basis function (19.3) can be transformed into a set of orthogonal basis functions:

$$\psi_{j,k}(t) = 2^{-j/2} \psi\left(2^{-j}t - k\right) \qquad j,k \in \mathbb{Z} \tag{19.4}$$

Where j indicates the jth scale, changing its size means stretching the wavelet function so that function (19.4) can capture the local irregular characteristics of signals.

It is provable that in every closed subspace V_0, function $x(t)$ can be approached by a set of orthogonal basis functions $\phi(t)$ (scaling function) accompanying with some approaching coefficients c^0. According to Mallat multi-resolution theory, the approaching coefficients c^0 can be decomposed into approximation complements c^1 on the subspace V_1 and detail complements d^1 on orthogonal complement space W_1 of V_1, using the wavelet function and scaling function, namely: $V_0 = V_1 \oplus W_1$. Then the approximation complements c^1 are decomposed into subspace V_2 and orthogonal complement space W_2 in the same way, and so on. The algorithm is shown in Fig. 19.7.

Following this algorithm, approximation complements and detail complements can be gotten on any j th scale:

$$c_k^j = \sum_l h_l c_{2k+l}^{j-1}, \quad d_k^j = \sum_l g_l c_{2k+l}^{j-1} \tag{19.5}$$

For a given decomposition level J, we can get the wavelet reconstruction algorithm by inversing the wavelet transform as follows:

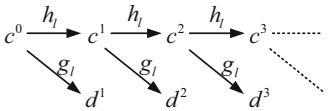

Fig. 19.7 Decomposition algorithm of wavelet transform

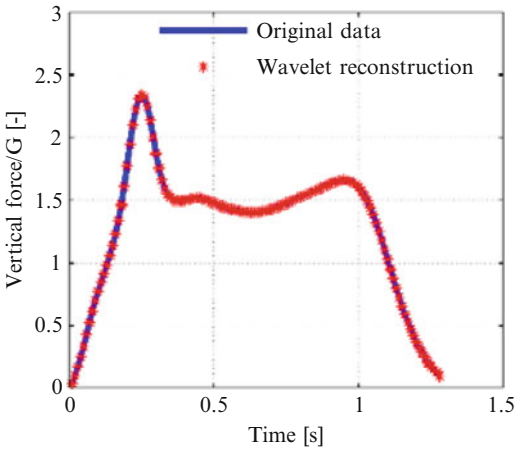

Fig. 19.8 Comparison and reconstruction of a jumping impulse

$$x(t) = \sum_{k=-\infty}^{\infty} c_k^J \phi_{J,k}(t) + \sum_{j=1}^{J} \sum_{k=-\infty}^{\infty} d_k^j \psi_{j,k}(t) \tag{19.6}$$

Where h_l and g_l is the constant filter corresponding to the wavelet $\psi_{j,k}(t)$.

Daubechies orthogonal compactly supported wavelets is widely used for its features such as good regularity, multiple vanishing moments and approximate symmetry. With the increase of vanishing moments, Daubechies wavelet become smooth gradually and oscillation enhancement, these properties make it possible to describe the local irregular characteristics of jumping impulses. Hence, this paper chooses ten vanishing moments Daubechies wavelet (DB10) as the basis function to fit jumping impulses.

19.4.2 Analysis OF Jumping Impulses

In order to deal with all the data conveniently, sampling frequency of the measured jumping loads was taken to 100 Hz. Using the method described in Sect. 19.3, jumping impulses were extracted from the measured jumping force signal, such as segment A to B in Fig. 19.3.

All jumping impulses were resampled to 2^7 data based on Shannon sampling theorem [22, 30] in order to use the dyadic wavelet analysis. After seven levels decomposition of the 2^7 data by DB10 wavelet for an impulse, wavelet coefficients on each level and scale coefficients can be gotten. Then we can reconstruct the impulse step by step using the calculated coefficients by inverse wavelet transform. Figure 19.8 shows the comparison of a measured impulse and the reconstruction jumping impulse. It is clear that the local irregular characteristics can be fitted well.

For impulses in the same jumping force signal are analogical due to the strong near-periodic nature of jumping loads, the wavelet coefficients at the same level have some similarities after the impulses are decomposed. Also there is stochastic between different impulses which reflects the intra-subject variability. However, the reconstruction in Fig. 19.8 just try to replicate the measured information of an impulse. In order to create new jumping impulses which have jumping morphology, inspired by the theory of DNA recombination, a method was developed by interchanging the wavelet coefficients at the same level between different jumping impulses which have been decomposed by DB10 wavelet. Then the new wavelet coefficients were used for inverse wavelet transform and new jumping impulses can be generated. By this method, it is possible to generate impulses of arbitrary number and have analogical morphology. Figure 19.9 shows the flow chart of the "decomposition-interchanging-reconstruction" procedures of the above method.

Following this flow chart, 49 jumping impulses were reconstructed by interchanging the wavelet coefficients randomly in a 2.0 Hz jumping force signal which equal to the number of the actual impulses. Figure 19.10a is the actual jumping impulses and Fig. 19.10b is the reconstructed impulses. It is clear that the reconstructed impulses reserve the morphology of jumping impulses of 2.0 Hz jumping load, meanwhile, have a certain of variability. Hence, the method can be used to generate any number of jumping impulse randomly.

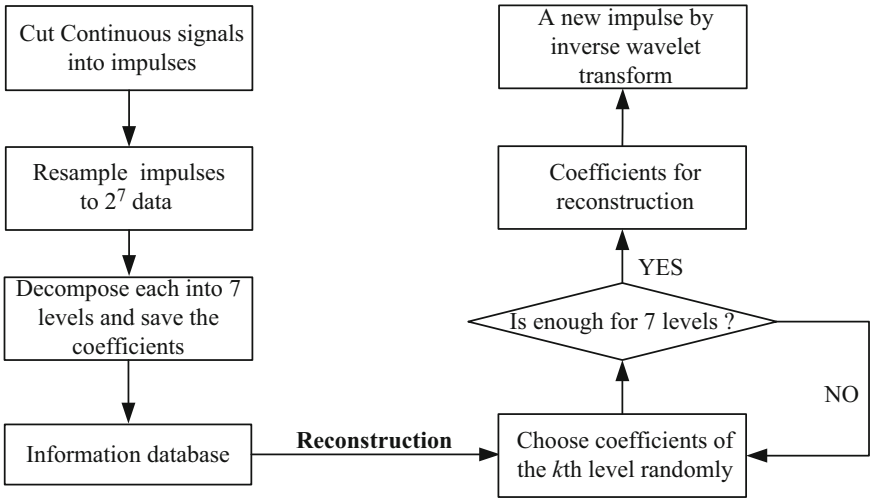

Fig. 19.9 Flow chart of decomposition-interchanging-reconstruction

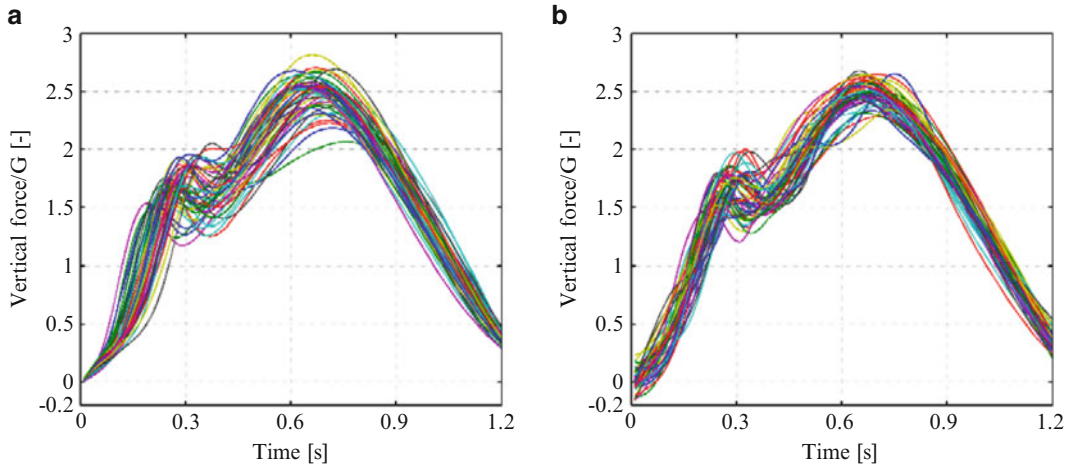

Fig. 19.10 49 jumping impulses of the 2.0 Hz jumping load (**a**) Actual impulses and (**b**) Synthetic impulses

19.5 Stochastic Jumping Load Model and Verification

Up to now, the models of three main random factors: Time interval of each cycle (Sect. 19.3.1), contact ratio (Sect. 19.3.2), morphology of jumping impulse (Sect. 19.4.2) have been developed. Together with the measured jumping force signals database, a stochastic model of continuous jumping force time history will be present in the next sections.

19.5.1 The Information Database of Wavelet Analysis

Some typical measured jumping impulses at different jumping rates are shown in Fig. 19.11 which illustrates that the morphology of impulse changing significantly with the jumping rate. Impulses are bimodal at low jumping rate and become unimodal with the increase of jumping rate, the peak also shifts from right to left gradually.

Racic et al. [20] noted that participants in the test may not jumped as the metronome beat accurately, sometimes far from that frequency. This is because not all individuals were able to synchronize their movements to the beats. In order to avoid destructing the impulse morphology when interchanging wavelet coefficients between different jumping rates, the measured 1201 jumping force signals were classified into 22 clusters with respect to the actual jumping rate (1.4–3.5 Hz with a step

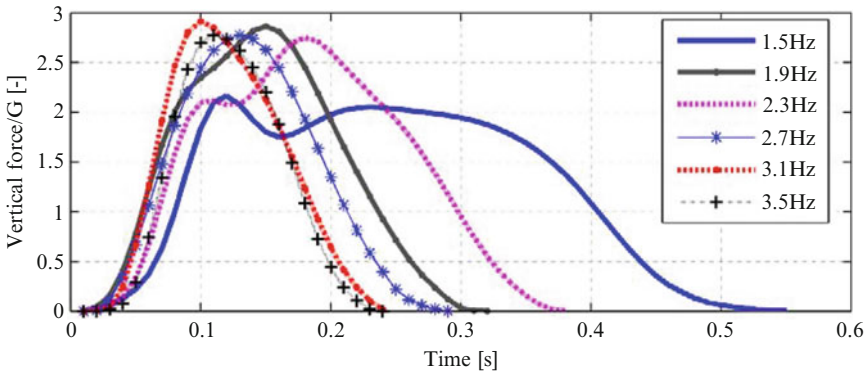

Fig. 19.11 Impulses at different jumping rates of a participant

of 0.1 Hz). It means that all jumping signals in $(f_j - 0.05\,,\, f_j + 0.05]$ were gathered into the same cluster and have similar morphology.

Calculating the key parameters of actual jumping loads in each cluster: mean value μ_T and standard deviation σ_T of jumping cycle, and mean value μ_α and standard deviation σ_α of contact ratio. At the same time, seven levels wavelet coefficients getting from the decomposed impulses by DB10 were calculated. All the information above-mentioned was stored within clusters with respect to the actual jumping rates which called information database, and will be used in the new jumping model.

19.5.2 Stochastic Jumping Load Model

At the design stage, engineers often need to assess the vibration serviceability of structures based on the assumption of resonance when structures subject to occupants' jumping loads. So a new model was developed to generate continuous jumping force time histories with specified jumping rate *f*. The flow chart of the proposed model is shown in Fig. 19.12 and the procedure is:

(1) Determine the number of impulses N which need in the synthetic jumping load by the specific jumping rate f and duration t.
(2) Choose time interval parameters (μ_T, σ_T) of jumping cycle randomly in the jth cluster where f in ($f_j - 0.05 < f \leq f_j + 0.05$), then N time intervals T_i ($i = 1 : N$) of jumping cycles can be generated artificially following normal distribution property.
(3) Choose contact ratio parameters (μ_α, σ_α) of jumping impulse randomly in the jth cluster, then generating N contact ratios as step (2).
(4) Use the time intervals and contact ratios generated in step (2) and step (3), durations of N jumping impulses can be calculated by $t_i = T_i \times \alpha_i$.
(5) Choose wavelet coefficients corresponding to seven jumping force signals in jth cluster of the information database randomly.
(6) Interchange the chosen coefficients at same level randomly and generate N impulses by inverse wavelet transform.
(7) Resample the N jumping impulses into N durations t_i ($i = 1 : N$) in the step (4).
(8) N jumping cycles can be gotten by combining the impulses with zero values according to the N time intervals.
(9) A forces time history due to continuous jumping can be recreated by adding a sequence of cycles on a jump-by-jump basis.

19.5.3 Model Verification

Figure 19.13a shows an example of the jumping force signal generated when the stochastic model was run once for the jumping rate 2 Hz and lasting 25 s. Figure 19.13b is a measured signal at the same jumping rate. A visual comparison of

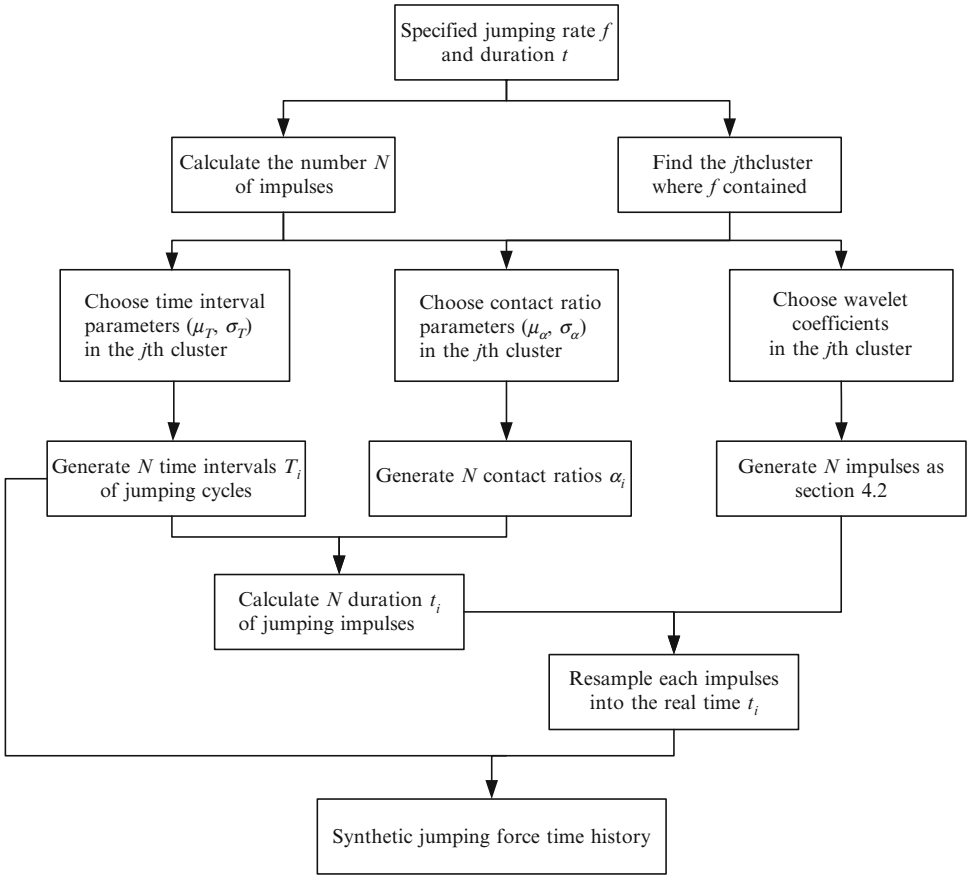

Fig. 19.12 Flow chart of the proposed model for generating synthetic jumping force time history

the two signals provides convincing evidence that the model not only can generate signal similar to the measured, but also account for the inter-subject variability. Then, the corresponding Fourier amplitude spectra are compared in Fig. 19.14. All this indicates good match at temporal and spectral features between the measured and the synthetic signal.

Furthermore, if resonance of a single degree of freedom system (SDOF) representing a mode of interest is assumed, the two signals were applied to a SDOF whose frequency was 2.0 Hz and damping ratio was 3.0 %, respectively. The acceleration responses were shown in Fig. 19.15 and they matched well with each other. Results illustrates that jumping force generated by the proposed model can be utilized in vibration serviceability assessment of civil engineering assembly structures.

19.6 Conclusions

This paper developed a stochastic model for generating continuous vertical jumping force time history. A vast database comprising 1201 high-quality jumping load records was developed. Based on this database, the morphology of jumping impulse was studied and a wavelet coefficients information database was built. Motivated by the theory of DNA recombination, a method was developed to generate jumping impulses by interchanging the wavelet coefficients at the same level between different jumping impulses within the same cluster. Then, adding the information of contact ratio and time interval, synthetic jumping cycles can be gotten. Finally, a forces time history due to continuous jumping will be recreated by adding a sequence of synthetic cycles on a jump-by-jump basis. The proposed model strategy has the following considerable advantages:

(1) Key parameters of time interval and contact ratio were introduced to consider the near-periodic nature of jumping force. The normal distribution property of them make it is easy to generate the synthetic parameters randomly by the measured mean value and standard deviation.

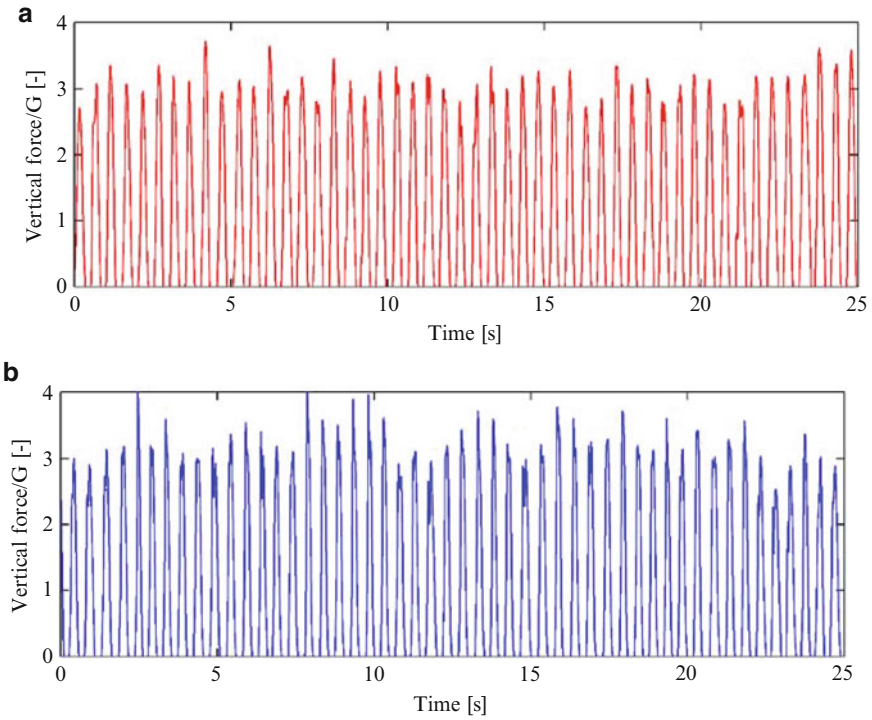

Fig. 19.13 (**a**) Synthetic and (**b**) measured jumping force signals at 2.0 Hz

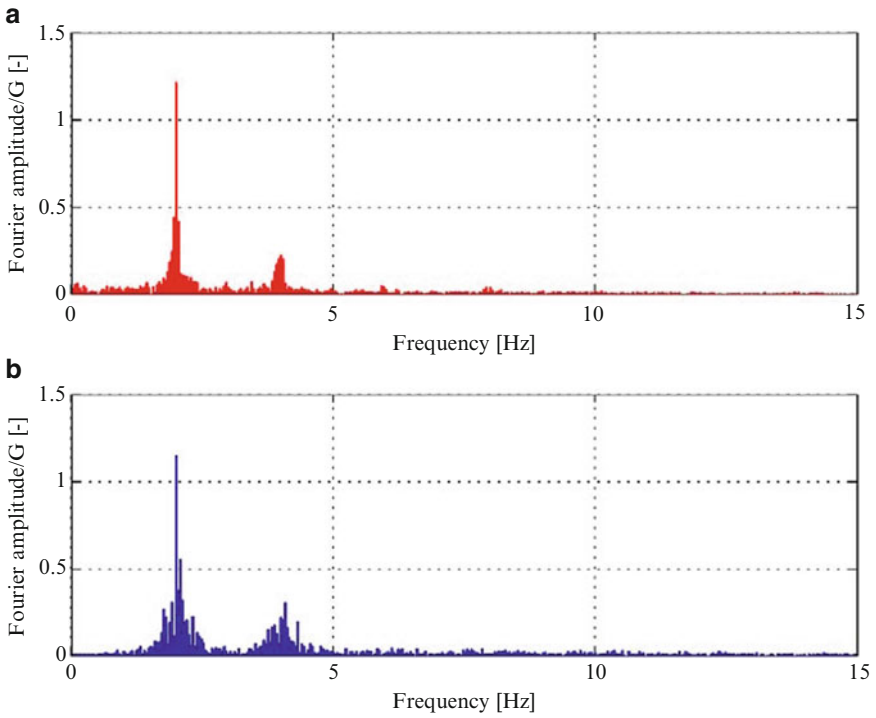

Fig. 19.14 Fourier amplitude spectrum of (**a**) synthetic and (**b**) measured force due to 2.0 Hz jumping rate

(2) Wavelet analysis can capture the irregular characteristics of jumping morphology both of the bimodal and unimodal impulses. It can reserve temporal and spectral features more effectively than the conventional Fourier series approach.
(3) Using the method of inverse wavelet transform after interchanging wavelet coefficients at same level can recreate new jumping impulses and generate a large number of them than the measured.

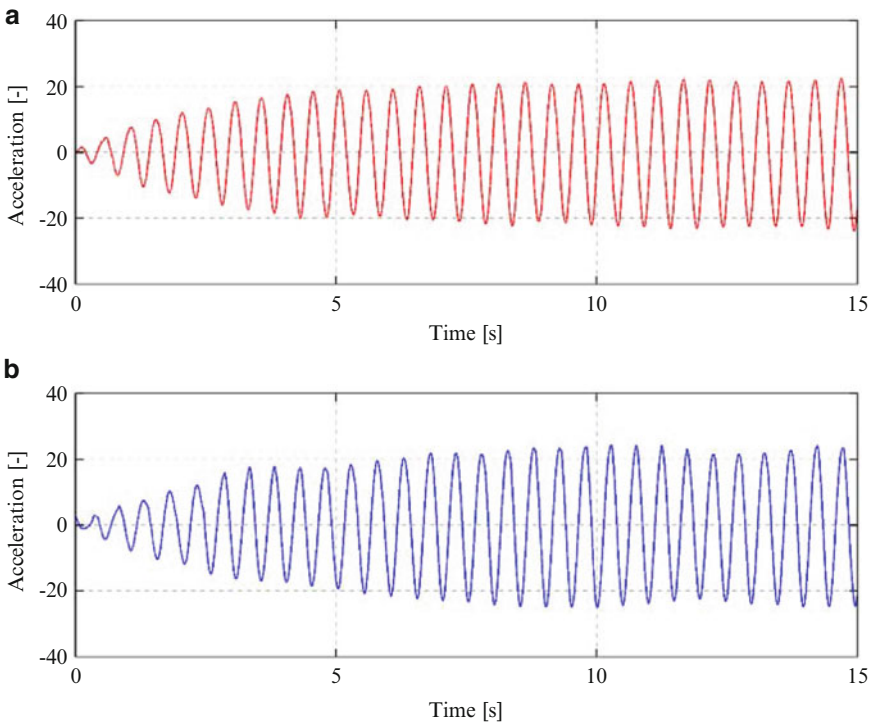

Fig. 19.15 Acceleration responses of SDOF due to (**a**) synthetic and (**b**) measured jumping force

Model verification shows that the synthetic jumping force signals can represent the real jumping forces both in time and frequency domain. Comparison of the SDOF responses due to synthetic jumping load and the measured force was conducted. Results illustrate that the synthetic forces generated by the model can be utilized in vibration serviceability assessment of civil engineering structures due to single people jumping.

References

1. Zivanovic, S., Pavic, A., Reynolds, P.: Vibration serviceability of footbridges under human-induced excitation: a literature review. J. Sound Vib. **279**(1), 1–74 (2005)
2. Jones, C.A., Reynolds, P., Pavic, A.: Vibration serviceability of stadia structures subjected to dynamic crowd loads: a literature review. J. Sound Vib. **330**(8), 1531–1566 (2011)
3. Rogers D.: Two more 'wobbly' stands. Construction news (2000)
4. Parker, D.: Rock fans uncover town hall floor faults. New Civ. Eng. **20**, 1531–1566 (2003)
5. Erlingsson, S., Bodare, A.: Live load induced vibrations in Ullevi Stadium—dynamic dynamic soil analysis. Soil Dyn. Earthq. Eng. **15**(3), 171–188 (1996)
6. de Brito, V.L., Pimentel, R.L.: Cases of collapse of demountable grandstands. J. Perform. Constr. Facil. **23**, 151–159 (2009)
7. News. Gym workout caused Seoul building tremor. Bingtimes, (2011). http://epaper.jinghua.cn/html/2011-07/21/content_682126.htm
8. Wolmuth, B., Surtees, J.: Crowd-related failure of bridges. In: Proceedings of the ICE-Civil Engineering. Thomas Telford, 2003
9. Marhsall, R.D., Pfrang, E.O., Leyendecker, E.V., et al.: Investigation of the kansas city hyatt regency walkways collapse. US National Bureau of Standards (1982)
10. Dallard, P., Fitzpatrick, A.J., Flint, A., et al.: The London millennium footbridge. Struct. Eng. **79**(22), 17–21 (2001)
11. Dallard, P., Fitzpatrick, T., Low, A., et al.: The Millennium Bridge, London: problems and solutions. Struct. Eng. **79**(8), 15–17 (2001)
12. Fujino, Y., Pacheco, B.M., Nakamura, S.I., et al.: Synchronization of human walking observed during lateral vibration of a congested pedestrian bridge. Earthq. Eng. Struct. Dyn. **22**(9), 741–758 (1993)
13. Murray, T.M., Allen, D.E., Ungar, E.E.: Floor vibrations due to human activity (1997)
14. Bachmann, H., Pretlove, A.J., Rainer, J.H.: Dynamic forces from rhythmical human body motions (1991)
15. Ji, T., Ellis, B.R.: Floor vibration induced by dance-type loads: theory. Struct. Eng. **72**(3/1), 37 (1994)
16. Brownjohn, J.M., Pavic, A., Omenzetter, P.: A spectral density approach for modelling continuous vertical forces on pedestrian structures due to walking. Can. J. Civ. Eng. **31**(1), 65–77 (2004)
17. Bachmann, H., Ammann, W.: Vibrations in structures: induced by man and machines. Iabse (1987)
18. Ellis, B.R., Ji, T.: Loads generated by jumping crowds: numerical modelling. Struct. Eng. **82**(17), 35–40 (2004)

19. Zivanovic, S., Pavić, A., Reynolds, P.: Probability-based prediction of multi-mode vibration response to walking excitation. Eng. Struct. **29**(6), 942–954 (2007)
20. Racic, V., Pavic, A.: Mathematical model to generate near-periodic human jumping force signals. Mech. Syst. Signal Process. **24**(1), 138–152 (2010)
21. Racic, V., Pavic, A.: Stochastic approach to modelling of near-periodic jumping loads. Mech. Syst. Signal Process. **24**(8), 3037–3059 (2010)
22. Vidakovic, B.: Statistical Modeling by Wavelets. A Wiley-Interscience Publication, Hoboken (1999)
23. Hu, C.H., Li, G.H., Zhou, T.: System Analysis and Design Based on 7.x MATLAB- Wavelet Analysis. Third edition. Xi'an Electronic Science & Technology University Press, Xi'an (2003)
24. Jun, C., Ling, W., Bo, C., et al.: Dynamic properties of human jumping load and its modeling: experimental study. J. Vib. Eng. **27**(1), 16–24 (2014)
25. Chen, J., Li, G., Lou, J., et al.: Acceleration response spectrum for predicting floor vibration subjected to occupants jumping. Eng. Struct. **43**(7), 972–979 (2015)
26. Sim, J., Blakeborough, A., Williams, M.S., et al.: Statistical model of crowd jumping loads. J. Struct. Eng. **134**(12), 1852–1861 (2008)
27. Massey Jr., F.J.: The Kolmogorov-Smirnov test for goodness of fit. J. Am. Stat. Assoc. **46**(253), 68–78 (1951)
28. Daubechies I.: Ten lectures on wavelets. SIAM (1992)
29. Cui, J.: An Introduction to Wavelets. Xi'an Jiaotong University Press, Xi'an (1995)
30. Walter, G.G.: A sampling theorem for wavelet subspaces. IEEE Trans. Inf. Theory **38**(2), 881–884 (1992)

Chapter 20
A Numerical Round Robin for the Prediction of the Dynamics of Jointed Structures

J. Gross, J. Armand, R. M. Lacayo, P. Reuss, L. Salles, C. W. Schwingshackl, M. R. W. Brake, and R. J. Kuether

Abstract Motivated by the current demands in high-performance structural analysis, and by a desire to better model systems with localized nonlinearities, analysts have developed a number of different approaches for modelling and simulating the dynamics of a bolted-joint structure. However, the types of conditions that make one approach more effective than the others remains poorly understood due to the fact that these approaches are developed from fundamentally and phenomenologically different concepts. To better grasp their similarities and differences, this research presents a numerical round robin that assesses how well three different approaches predict and simulate a mechanical joint. These approaches are applied to analyze a system comprised of two linear beam structures with a bolted joint interface, and their strengths and shortcomings are assessed in order to determine the optimal conditions for their use.

Keywords Nonlinear damping • Nonlinear vibration • Bolted joint • Finite element analysis • Harmonic balance

20.1 Introduction

A large number of systems that many structural dynamics engineers study are composed of two or more elastic components that are mechanically joined together, such as through a bolted lap joint. To predict the dynamics and vibration of such systems, analysts typically develop linear finite element models for each component separately, and then couple the components with nonlinear models that are localized to the region of the joint. With current methods, analysts are very good at creating predictive models for the individual components. However, a general process to account for the contribution of the joint in the dynamics of the system has yet to be established fully. Fortunately, researchers in recent years have developed a number of different approaches for modelling joints in specific systems. This research attempts to apply and compare the methods used in three different approaches on a recognized benchmark system in order to gain insight on the best practices for modelling joints.

This research is a product of the numerical round robin project from the 2015 Nonlinear Mechanics and Dynamics (NOMAD) Summer Research Institute hosted by Sandia National Laboratories, and is a continuation of the research done under the same project during the 2014 NOMAD Institute [1]. The objective for the 2015 numerical round robin is largely the same in that the authors seek a better understanding of the capabilities for different approaches to model the nonlinear dynamic behaviour of bolted joints. This round robin project examines three different nonlinear response prediction methods developed respectively at the Vibration University Technology Centre at Imperial College London (hereafter referred to as Imperial), the Component Science and Mechanics Center at Sandia National Laboratories (referred to as Sandia), and the Institute of Nonlinear Mechanics at the University of Stuttgart (referred to as Stuttgart). The three methods are applied to model a bolted lap joint in a straight beam (Brake-Reuss beam) benchmark structure, and their simulated nonlinear dynamic responses are used as the basis for comparison.

Sandia National Laboratories is a multi-program laboratory managed and operated by Sandia Corporation, a wholly owned subsidiary of Lockheed Martin Corporations, for the U.S. Department of Energy's National Nuclear Security Administration under Contract DE-AC04-94AL85000.

J. Gross • P. Reuss
Institute of Nonlinear Mechanics, University of Stuttgart, Stuttgart, Germany

J. Armand • L. Salles • C.W. Schwingshackl
Vibration University Technology Centre, Imperial College London, London, UK

R.M. Lacayo (✉) • M.R.W. Brake • R.J. Kuether
Component Science and Mechanics, Sandia National Laboratories, Albuquerque, NM, USA
e-mail: rmlacay@hotmail.com

© The Society for Experimental Mechanics, Inc. 2016

M. Allen et al. (eds.), *Dynamics of Coupled Structures, Volume 4*, Conference Proceedings of the Society for Experimental Mechanics Series, DOI 10.1007/978-3-319-29763-7_20

More so than in the 2014 project, the 2015 round robin project emphasized modelling the Brake-Reuss beam more realistically. For example, the 2015 beam includes a model for the bolts, and uses advanced modelling techniques for incorporating bolt pre-tension. In addition, boundary conditions are prescribed based on performed experiments. This work presents new insights into the differences between the methods, and new ways of comparing their predictions in terms of the changes in the modal natural frequency and damping with forcing/response amplitude. A single-degree of freedom system was studied to shed light onto the different model parameters (slip force, tangential stiffness, etc.) used in each method and on the physics that they capture. This research practices all these methods in preparation for a future validation study with experimental data.

20.2 The Benchmark Model

The model chosen for the round robin investigation is the Brake-Reuss beam [2], a structure consisting of two identical straight beams connected with a lap joint (see Fig. 20.1). The beams are made of stainless steel alloy 304, and have an assembled dimension of $28.38 \times 1 \times 1$ in. In the middle of the structure, the two component beams have half-width extensions, which overlap each other to form the lap joint while preserving the prismatic shape of the entire structure. The lap joint contains three through-holes along its length that allow bolts to clamp the two separate beams together.

20.2.1 The Finite Element Mesh

A linear finite element model of the Brake-Reuss beam, depicted in Fig. 20.2, is built in Abaqus and used in all three approaches. Each beam is composed of 8240 8-node hexahedral elements, along with 340 6-node wedge elements on account of the shape irregularities introduced by the circular lap-joint holes. A particular care has been taken to ensure a matching

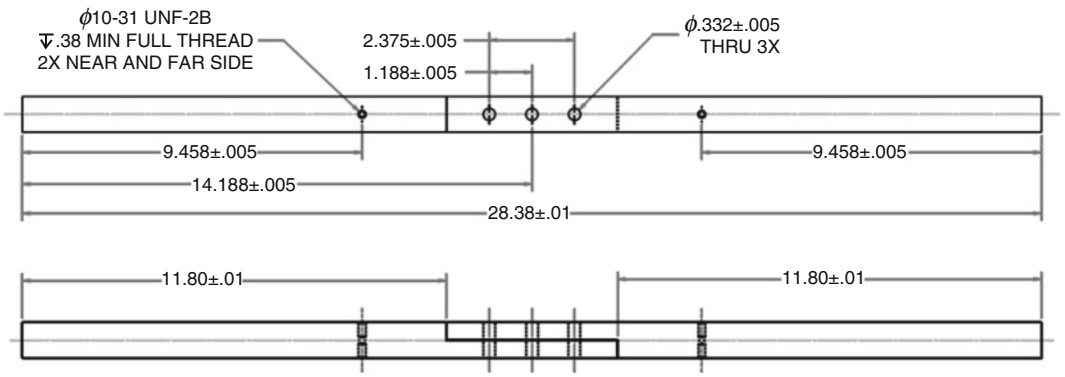

Fig. 20.1 Mechanical drawing of the Brake-Reuss beam and its dimensions (in inches)

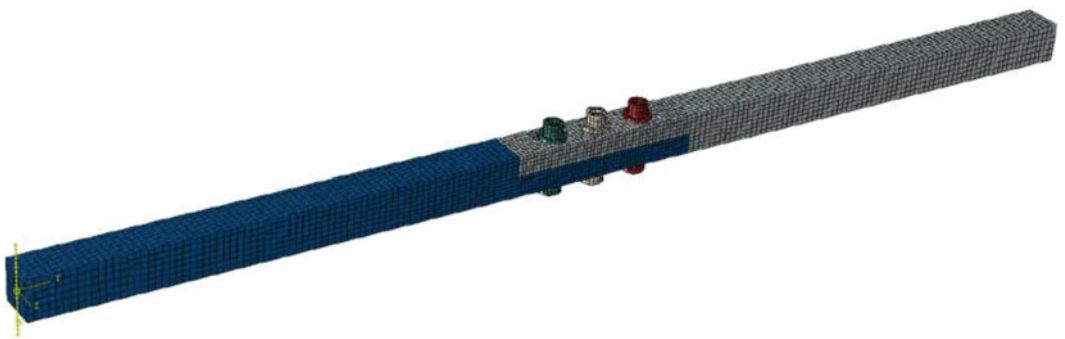

Fig. 20.2 Finite element model of the Brake-Reuss beam

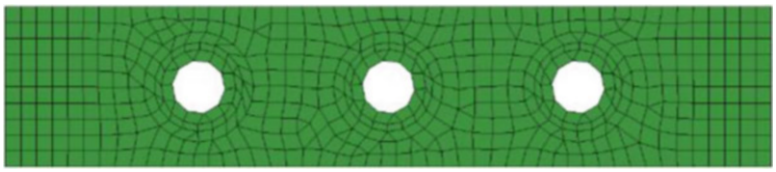

Fig. 20.3 Contact interface mesh

Fig. 20.4 Bolt pre-tensioning

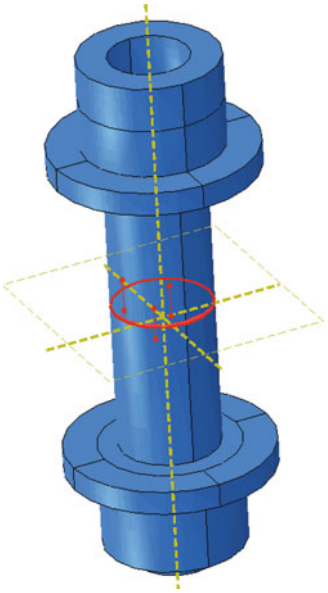

mesh at the contact interface between the two beams to allow the option to couple the coincident nodes between the two surfaces with a nonlinear contact element. The interface mesh, shown in Fig. 20.3, contains 592 nodes, so up to 592 nonlinear contact elements may be used for analysis.

The beam finite element model includes the three bolts at the lap-joint. Each bolt assembly contains a bolt, a nut, and two washers, which are all modelled as a single, solid mesh. The bolt meshes are uncoupled from the rest of the beam structure except at the interface between the washers and the top and bottom surfaces of the beams where fixed coupling is applied.

In all subsequent analyses, both the beams and bolts use an isotropic, linear elastic material model with Young's modulus $E = 189{,}768$ N/mm^2, Poisson's ratio $\nu = 0.32$, and mass density $\rho = 7.82 \times 10^{-6}$ kg/mm^3. The structure is given fixed-free boundary conditions, where the square surface on the left extremity of the beam in Fig. 20.2 is fixed.

20.3 Nonlinear Static Analysis

A non-linear static analysis is performed on the bolted structure to determine the pressure distribution at the contact interface between the two beams.

The pre-tensioning of the bolts is applied by using the 'bolt load' feature available in Abaqus. The shaft of the bolt is cut at mid-length through a pre-tension section, and the prescribed force is applied to this section along the axis of the bolt, as illustrated in Fig. 20.4. A surface-to-surface approach with a direct enforcement method (based on Lagrange multipliers) is used to solve the contact problem. A penalty method formulation with a friction coefficient $\mu = 0.6$ is used to describe the frictional behaviour.

Figure 20.5a shows the obtained pressure distribution for an applied pre-tension load of 4 kN. As expected, the pressure is maximum around the bolt holes and reduces concentrically leading to an area of lower compression between the holes. There is a nil pressure near both ends of the contact interface, which is due to a small gap opening that can be observed Fig. 20.5b. The pressure results of the nonlinear static analysis are used as a starting point to generate the nonlinear dynamic models, as will be explained subsequently.

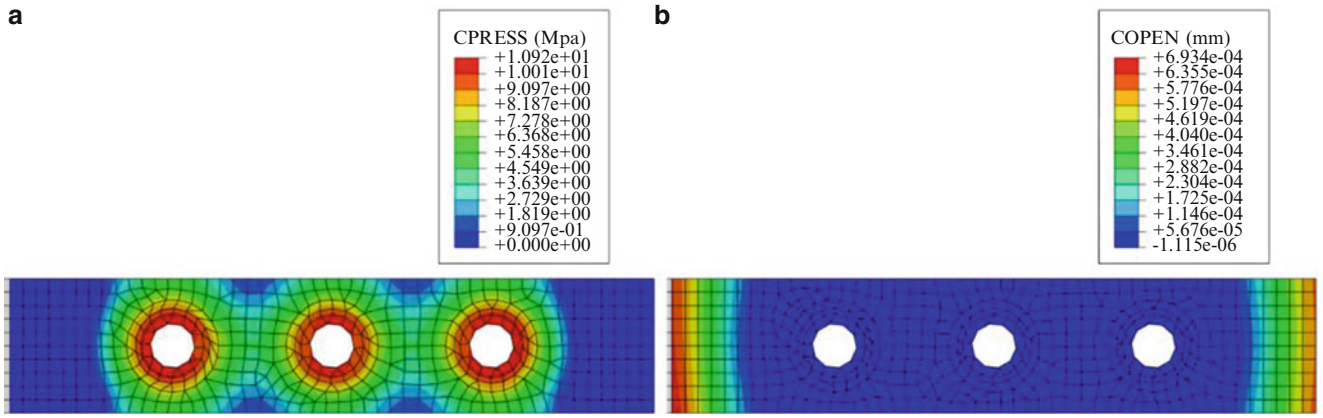

Fig. 20.5 (**a**) The calculated contact pressure and (**b**) gap spacing in the contact interface

Table 20.1 Summary of considered approaches for modelling joints

	Sandia approach	Stuttgart approach	Imperial approach
Finite element tool	SIERRA/SD	CalculiX	NASTRAN
Model fidelity	Craig-Bampton ROM or full FE Model	Craig-Bampton ROM	Hybrid ROM
Nonlinear element	Iwan element	Jenkins element	3D contact element
Solver type	Time integrator	Single-harmonic balance	Multi-harmonic balance

20.4 Considered Approaches to Modelling Friction Joints

The Brake-Reuss beam benchmark system defined in Sect. 20.2 is tested with three different joint-modelling approaches as developed respectively by the three contributing institutions: Sandia, Stuttgart, and Imperial. The major differences between the three approaches are summarized in Table 20.1.

Each approach is explained in more detail in the subsections that follow, but a general comment must be made about the response output that each nonlinear solver produces. The responses for the methods developed at Sandia are obtained in the time domain, whereas Stuttgart and Imperial both use harmonic balance methods (HBM) to obtain responses in the frequency domain. The Sandia transient methods are versatile in that they are developed for arbitrary excitations and nonlinear constitutive models, but they become very expensive if the steady state frequency response is desired (because one would have to integrate the response from some initial condition until steady state is reached). In contrast, the Stuttgart and Imperial HBM can compute the steady-state response in a computationally efficient manner, but are not currently capable of computing the transient response of the structure. The two HBM approaches differ mainly in the implementation of the nonlinear forces (linearization for Stuttgart versus alternating frequency-time procedure for Imperial). These differences will need to be kept in mind when evaluating the resulting responses of the beam. In general, transient response methods are not easily comparable to frequency response methods, but this work has exploited the similarity between the resonant response of a nonlinear structure and the response to a slowly decaying transient to make a meaningful comparison, as will be explained subsequently.

20.4.1 Sandia Approach

Over the past few decades, Sandia pioneered an approach in which a joint is replaced with a "whole joint element," such as Segalman's four-parameter Iwan element [3], which is able to capture the amplitude-dependent energy dissipation and stiffness of the joint. In general, an Iwan element, as seen in Fig. 20.6a, is a one-dimensional model consisting of an infinite number of friction sliders (Jenkins elements) in parallel whose slip force strengths follow a certain distribution [4]. The four-parameter formulation assumes a power-law distribution ending with a Dirac delta function at maximum slip strength (see Fig 20.6b). Such a distribution produces a joint whose energy dissipation per cycle follows a power-law relationship with the joint excitation force (shown in Fig. 20.6c), a phenomenon that has been observed experimentally in several structures [5,6]. The four parameters for this Iwan element formulation are the joint force at the inception of macro-slip (typically denoted

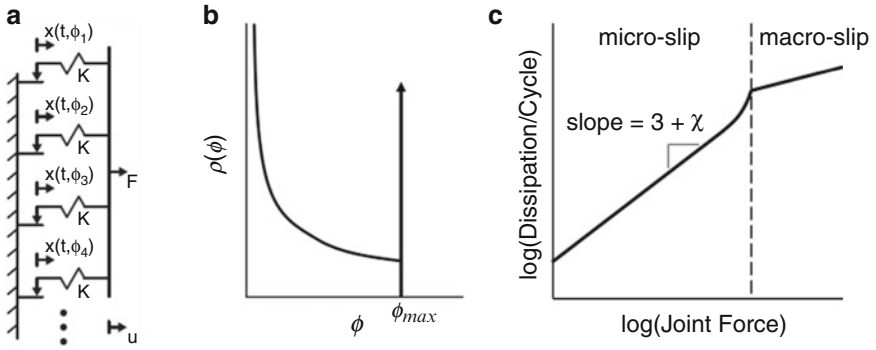

Fig. 20.6 (**a**) A parallel-series Iwan element, (**b**) the population density function ρ for sliders with slip strength in the four-parameter formulation of the Iwan element, and (**c**) the resulting power-law relationship between energy dissipation per cycle and joint force

as F_S), the tangent stiffness in microslip (K_T), the power-law slope of energy dissipation (χ), and the ratio (β) of the Dirac delta function (associated with macro-slip) to the power-law term (associated with micro-slip). The Iwan model has been well-validated at least within joint micro-slip regimes [3, 6–8].

It should be noted that the Iwan model was not developed to predict the response of a single joint, but to represent a joint with known properties in a larger structural model. In contrast, the approaches developed at Imperial and Stuttgart predict the response of a single joint, by assuming that a Coulomb friction model holds at the interface. The four-parameter Iwan model is designed to reproduce the power-law energy dissipation vs. joint force behaviour observed in experimental tests on the hardware of interest [6]. As such, the parameters for the Iwan element can only be tuned after measurements have been made or based on high fidelity simulations of the interface mechanics. Hence, the Iwan model is not perfectly comparable to the other two approaches. On the other hand, the Iwan model is known to exhibit the power-law behaviour that is observed in many jointed structures, whereas it is not yet clear whether the other formulations will predict power-law behaviour or how that behaviour will relate to their input parameters.

Since the intent of an Iwan element is to use a single element to represent the joint as a whole, only one Iwan element is typically used to represent an interface, which may in fact contain some microscopic regions that are stuck and others that are sliding. In the context of finite elements, an Iwan element should not be used to couple individually all coincident nodes between the two interfacing surfaces. Rather, the state of all nodes on a friction surface should contribute to the state of the Iwan element. This can be done in practice by creating a virtual node to represent the surface, and then tying all the physical nodes to the virtual node with rigid bar elements or with an averaging-type multi-point constraint. The two virtual nodes corresponding to the opposite surfaces respectively would then be coupled with the Iwan element.

As was done in previous works, Sandia's in-house finite element solver, SIERRA/SD [9], is used to build the mass and stiffness matrices from the finite element mesh. The matrices are reduced using the Craig-Bampton method [10], and then imported into a structural dynamics solver developed in MATLAB, where the Iwan elements are added to the system. The solver uses a numerical time integrator to solve the time-domain equations of motion,

$$\mathbf{M}\ddot{\mathbf{q}} + \mathbf{C}\dot{\mathbf{q}} + \mathbf{K}\mathbf{q} = \mathbf{f}_{ext} + \mathbf{f}_{NL}\left(\mathbf{q}, \dot{\mathbf{q}}, \boldsymbol{\theta}\right), \tag{20.1}$$

where $\mathbf{M}$ is the system mass matrix, $\mathbf{K}$ is the stiffness matrix, $\mathbf{C}$ is the matrix of linear material damping coefficients, and $\mathbf{q}$, $\dot{\mathbf{q}}$, and $\ddot{\mathbf{q}}$ are the coordinate displacement, velocity and acceleration response vectors, respectively, for which the integrator solves. The vector $\mathbf{f}_{ext}$ contains the time-dependent external loads applied on the coordinates, and $\mathbf{f}_{NL}$ is the vector of nonlinear forces from the Iwan elements. The vector $\boldsymbol{\theta}$ records a finite number of slider states for each Iwan element, and there are typically 25–100 sliders per element.

20.4.2 Stuttgart Approach

The Stuttgart approach [11] relies on a node-to-node contact model with friction in the tangential direction and a nonlinear contact law in the normal direction. The nonlinear contact law is used to compute the normal force at each node-to-node contact based on the applied loading of the bolts. This is established by the nonlinear static pressure distribution presented in Sect. 20.3, which is converted to nodal forces for the dynamic analyses. In subsequent analyses, however, the relative

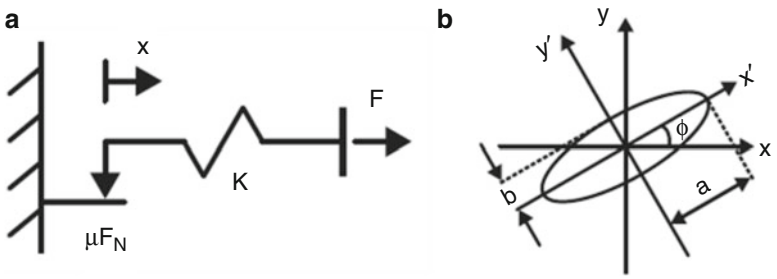

Fig. 20.7 (**a**) A 2D Jenkins element and (**b**) the elliptical motion it undergoes in the first harmonic

dynamics in the normal direction are suppressed, and the normal force at each node in contact is assumed constant for the HBM calculation. In the tangential direction the interface nodes can have relative displacements in two dimensions. Since in this approach only the fundamental response is considered, the resulting motion is an ellipse in the plane of the joint, as seen in Fig. 20.7b.

The friction forces are then computed for the major and minor axis a and b separately using the analytical equations for the Fourier coefficients [11] in terms of equivalent stiffness and damping of the one dimensional case. This is a further approximation which does not take into account the coupling of the friction force in two dimensions but has been found to produce reasonable results when the motion in one dimension is dominant. In the local coordinate system x' and y', the equivalent stiffness and damping matrix as well as the transformation matrix, including the angle ϕ between the local and the global coordinate system can be written as

$$\mathbf{K}^{l}_{hbm} = \begin{bmatrix} k^{x'}_{hbm} & 0 \\ 0 & k^{y'}_{hbm} \end{bmatrix}, \ \mathbf{D}^{l}_{hbm} = \begin{bmatrix} d^{x'}_{hbm} & 0 \\ 0 & d^{y'}_{hbm} \end{bmatrix}, \ \mathbf{T} = \begin{bmatrix} \cos\phi & \sin\phi \\ -\sin\phi & \cos\phi \end{bmatrix} \tag{20.2}$$

Transforming the matrices into the global coordinate system by

$$\mathbf{K}^{g}_{hbm} = \mathbf{T}\mathbf{K}^{l}_{hbm}\mathbf{T}^{T}, \ \mathbf{D}^{g}_{hbm} = \mathbf{T}\mathbf{D}^{l}_{hbm}\mathbf{T}^{T} \tag{20.3}$$

a pseudo-receptance matrix in the frequency domain can be established containing the sum of all node-to-node friction contacts by

$$\mathbf{H}_{hbm}\left(\widehat{\mathbf{x}}\right) = \left(\mathbf{K} + \mathbf{K}_{hbm}\left(\widehat{\mathbf{x}}\right)\right) + i\omega\left(\mathbf{D} + \mathbf{D}_{hbm}\left(\widehat{\mathbf{x}}\right)\right) - \omega^{2}\mathbf{M}. \tag{20.4}$$

The linear mass and stiffness matrices are established by the Craig-Bampton method [10] and hence retain the interface degrees of freedom where the friction forces act. The resulting equations of motion in the frequency domain can be arranged in an implicit form by

$$\mathbf{r} = \mathbf{H}_{hbm}\left(\widehat{\mathbf{x}}\right)\widehat{\mathbf{x}} - \mathbf{f}_{ext}. \tag{20.5}$$

The residual $\mathbf{r}$ is then minimised using a Nonlinear Successive Over-Relaxation Method [12] to obtain the nonlinear dynamic response. The advantage of this method is that it avoids having to establish a Jacobian matrix of the equations which is expensive for the large number of considered degrees-of-freedom when using a standard finite-difference method to compute the derivative numerically. On the other hand, this method requires two evaluations of the nonlinear friction forces to compute the Fourier coefficients per iteration step, such that the efficiency of this method in the present case is only guaranteed by fact that the coefficients are computed analytically.

20.4.3 Imperial Approach

The Imperial-developed code, FORSE, used for the analysis of the nonlinear response of flange joints is based on the multi-harmonic representation of the steady-state response and allows large scale realistic friction interface modelling. Major

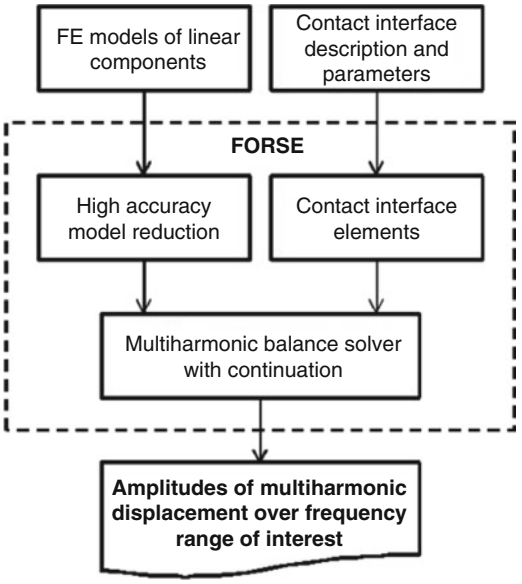

Fig. 20.8 The scheme of the forced response analysis

features of the methodology were described in [13] and only an overview of the analysis is presented in this paper. The equation of motion consists of a linear part, which is independent of the vibration amplitudes, and the nonlinear part due to the friction interfaces at the interface joint. The nonlinear equation of motion can be written as

$$\mathbf{Kq}\left(\mathrm{t}\right)+\mathbf{C}\dot{\mathbf{q}}\left(\mathrm{t}\right)+\mathbf{M}\ddot{\mathbf{q}}\left(\mathrm{t}\right)+\mathbf{f}\left(\mathbf{q}\left(\mathrm{t}\right),\dot{\mathbf{q}}\left(\mathrm{t}\right)\right)-\mathbf{p}\left(\mathrm{t}\right)=\mathbf{0}, \tag{20.6}$$

where $\mathbf{q}$ is a vector of displacements; $\mathbf{K}$, $\mathbf{C}$, and $\mathbf{M}$ are the stiffness, damping and mass matrices, respectively, of the linear model; $\mathbf{f}$ is a vector of nonlinear friction interface forces, which is dependent on displacements and velocities of the interacting nodes, and $\mathbf{p}$ is a vector of periodic exciting forces. The variation of the displacements in time is represented by a restricted Fourier series, which can contain as many harmonic components as it is necessary to approximate the solution, i.e.

$$\mathbf{q}(t)=\mathbf{Q}_0+\sum_{j=1}^{n}\mathbf{Q}_j^c\cos\left(m_j\omega t\right)+\mathbf{Q}_j^s\sin\left(m_j\omega t\right). \tag{20.7}$$

In Eq. 20.7, $\mathbf{Q}$ are vectors of harmonic coefficients for the system degrees of freedom (DOFs), n is the number of harmonics that is used in the multi-harmonic displacement representation, and ω is the principal vibration frequency. The flowchart of the calculations performed with the code is presented in Fig. 20.8. The contact interface elements developed in [13] (see Fig. 20.9) are used for modelling of nonlinear interactions at contact interfaces and analytical expressions for the multi-harmonic representation of the nonlinear contact forces and stiffnesses. The nonlinear algebraic system of the reduced model is obtained using a hybrid method of reduction developed by Petrov [14, 15]. The nonlinear system in the frequency domain is

$$\tilde{\mathbf{Q}}=A\left(\omega\right)\left(\tilde{\mathbf{F}}-\tilde{\mathbf{F}}_{\mathrm{nl}}\left(\tilde{\mathbf{Q}}\right)\right), \tag{20.8}$$

with $\tilde{\mathbf{Q}}$ defined as the vector of the Fourier coefficients of the displacements at the interface, $A(\omega)$ the frequency response, $\tilde{\mathbf{F}}$ is the vector of the Fourier coefficients of the excitation force and $\tilde{\mathbf{F}}_{nl}$ is the vector of the Fourier coefficients of the nonlinear contact forces.

20.5 SDOF Comparison Between Nonlinear Elements

An Iwan element is a collection of parallel Jenkins elements, so one would expect it to produce joint behaviour similar to the Jenkins and 3D contact elements. However, the latter elements assume a Coulomb friction formulation, where the energy dissipated can be predicted after deriving the slip force based on the normal contact pressure. In contrast, the four-parameter

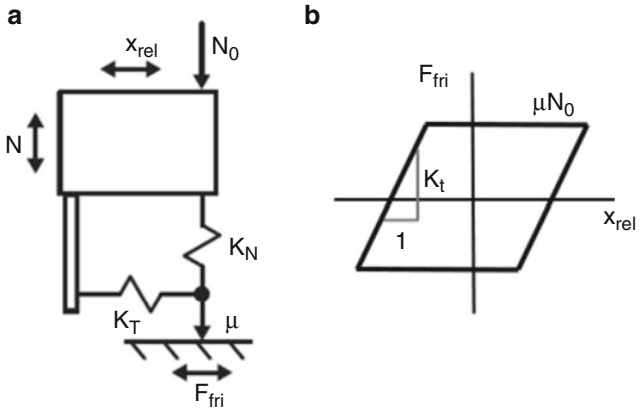

Fig. 20.9 (**a**) The 3D contact element and (**b**) its approximate hysteresis curve

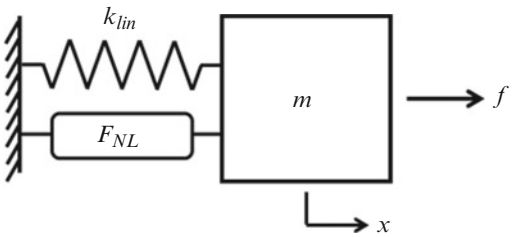

Fig. 20.10 A single-degree of freedom system used in the comparison study. The system contains a single mass, m, connected to ground with a linear spring of stiffness k_{lin} and a nonlinear element applying reaction force F_{NL} on the mass

Iwan element used in this work is formulated a priori to produce a power-law relationship between energy dissipation and the force, based on experiments that were reported in [6]. These different formulations make it difficult to gauge, relative to each other, how each element will dissipate energy within a structure. In order to clarify the similarities and differences between these elements, a study is conducted to compare how each element dampens the motion of the single-degree of freedom (SDOF) system in Fig. 20.10. This will also illustrate the extent to which the models can be tuned to give similar dynamic responses.

The two parameters for the Jenkins element are the slip force, which is set to a value of 100 N, and the tangent stiffness, which is set to a value of 3000 N/mm. The mass in the system is set to be unitary, and a value of 40,000 N/mm is chosen for the stiffness of the linear spring so that the natural frequency for the linear system matches that of the first bending mode for the fixed-free Brake-Reuss beam (approximately 31 Hz).

20.5.1 How Each Approach Calculates Damping

Each of the three considered approaches calculates the equivalent damping using different methods. Stuttgart's harmonic balance method calculates the amplitude-dependent nonlinear force from the Jenkins element at every frequency, and represents that force with equivalent damping and stiffness values. The phase plot of the frequency response was used to determine the frequency where the displacement phase lags that of the input force by 90° (resonance), then the damping coefficient was extracted at that same frequency.

Imperial's method solves for the frequency-domain tangential force and displacement at resonance. The inverse discrete Fourier transform is then applied to the solution to obtain the time histories for force and displacement over one cycle at resonance. The time histories are used to construct a hysteresis curve, the area of which is the energy dissipated in that cycle. The energy dissipation is converted to an equivalent damping using the following equation derived in [8],

$$\zeta_r = \frac{D_r}{2\pi |V_r|^2}, \tag{20.9}$$

where D_r is the energy dissipated per cycle at resonance and ζ_r is the equivalent critical damping ratio near the resonance mode of interest. In a single-degree of freedom system with unit mass, $|V_r|$ is the peak velocity of the mass at resonance.

Otherwise, $|V_r|$ is the peak velocity of the mass-normalized modal coordinate corresponding to the resonance mode of interest.

While the Jenkins and 3D contact elements rely on harmonic balance methods to compute the steady state response, Iwan elements are typically simulated in the time domain. One could reconcile the responses by using the transient method to simulate the forced response to a harmonic input until steady state is reached. In this case such an approach would be time consuming and challenging because the nonlinearities couple the modes, creating a steady-state response composed of many signals. Instead, the energy dissipation is calculated using the analytical formulas derived in [3], which develop distinct expressions for energy dissipation in micro-slip and macro-slip. The analytical energy dissipation values are converted to a damping values via Eq. (20.9).

20.5.2 SDOF Comparison Results

Using the values for the Jenkins element parameters defined previously, both the Stuttgart and Imperial approaches calculated damping values for their respective nonlinear elements at excitation force amplitudes of 20, 30, 50, and 70 N. The resulting damping values of both the Jenkins element and the 3D contact element are identical, as expected, because the 3D contact element reduces to a Jenkins element when applied to only one dimension. The parameters for the Iwan element were adjusted until the analytical damping curves aligned as closely as possible with those of the Jenkins element.

Figure 20.11 compares the final Iwan element analytical curves for effective critical damping ratio versus displacement amplitude with the calculated damping versus amplitude for the Jenkins element. The following parameters were used for the Iwan model: $F_S = 2.5$ N, $K_T = 20{,}000$ N/mm, $\chi = -0.5$, and $\beta = 0.5$. The comparison illustrates that a single Jenkins element exhibits power-law energy dissipation with a slope of -1 on a log-log damping versus amplitude plot, and to mimic this behaviour the Iwan element must be in the macro-slip regime. The micro-slip parameter of the Iwan element, χ, controls the shape of the left half of the curve and, hence, is irrelevant for this comparison.

Of course, this simple example does not really illustrate the intended regime that will likely be observed in the Brake-Reuss beam, micro-slip, where some of the Jenkins elements remain stuck while others slip. The net effect of all of those Jenkins elements is expected to produce power law energy dissipation with a slope greater than zero on a plot similar to that shown in Fig. 20.11. In the micro-slip regime, the parameters for the Iwan element can presumably be adjusted until its behaviour matches the observed behaviour.

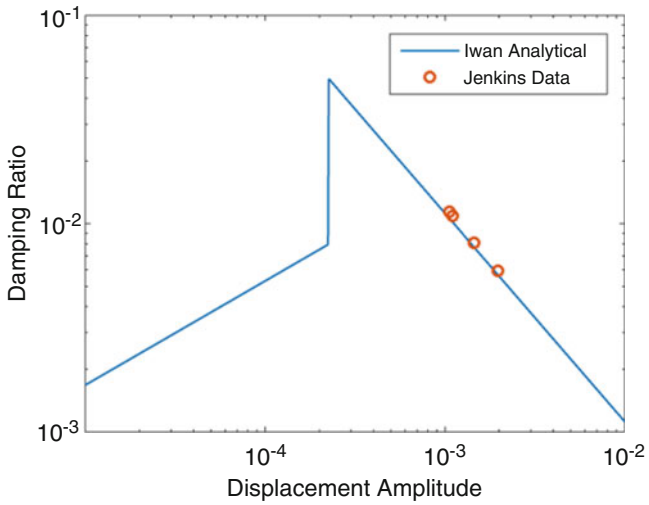

Fig. 20.11 Comparison of damping vs. amplitude behaviour of a single Jenkins element in the SDOF system shown in Fig. 20.10 with the analytical damping behaviour of an Iwan element

20.6 Brake-Reuss Beam Nonlinear Dynamic Anlaysis

20.6.1 Reduced Interface Frequency Response Analysis

The two harmonic balance approaches, those used at Stuttgart and Imperial, performed a preliminary nonlinear dynamic analysis on the Brake-Reuss beam by applying their nonlinear elements on a smaller portion of the full contact interface. The specific nodes that are activated for this "reduced interface" analysis are those highlighted in Fig. 20.12 with dots, which consist of the nodes inside the 0.688-inch diameter circular areas surrounding the holes. Each node is tied to its coincident node belonging to the opposite surface with a nonlinear element.

The finite element conditions of the beam are the same as described in Sect. 20.2.1. In addition, a force acting in the x-direction is applied on a corner node at the opposite end of the structure from the fixed end, as shown in Fig. 20.13. This same driving node is also chosen as the output node for the x-direction response. A static pre-tension load of 4 kN is applied for each of the bolts to model the bolt compression on the joint. The simulations were conducted for input force magnitudes of 1, 10, 20, 50, 100, and 200 N between a frequency range of 150 Hz and 180 Hz in order to capture the 2nd bending mode of the Brake-Reuss beam.

Figure 20.14 shows the nonlinear frequency response function (FRF) curves estimated by Stuttgart's approach (Jenkins element) for all six simulated excitation levels. The response curves are normalized by the input force magnitude to better illustrate how the resonance peaks change shape as the force magnitude is increased. These results show the expected behaviour for a joint in that, as the forcing magnitude increases, more elements change their contact states to slip and therefore decrease the resonance frequency. The shrinking and widening of the peaks implies an increase in the effective damping. Figure 20.14 also shows the linear FRFs for the elastic cases when all the Jenkins elements are stuck (effectively acting as linear springs), and when they are all slipping (zero spring behaviour), representing the two extremes of the dynamic behaviour of the two jointed beams. Note that for both models the linear response for elastic stick and the nonlinear response to a 1 N excitation do not differ.

Figure 20.15 shows the FRF obtained by the Imperial with the 3D contact nonlinear elements. For the smaller excitations the change in frequency and damping behaviour is quite similar to Stuttgart's responses, however several differences can be observed at higher excitation levels. Imperial's model allows a relative displacement in surface normal direction, and therefore allows variations in the contact normal forces as well as lift-off phenomena, which are increased by higher excitation amplitudes. These effects can reduce the magnitude of relative displacement in tangential directions and therefore result in less dissipation and sliding of contact elements.

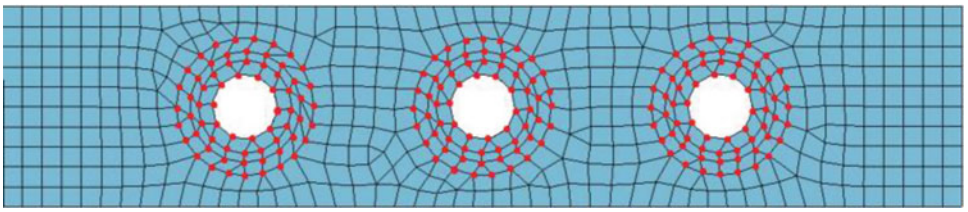

Fig. 20.12 The activated nonlinear nodes in the reduced interface dynamic simulations

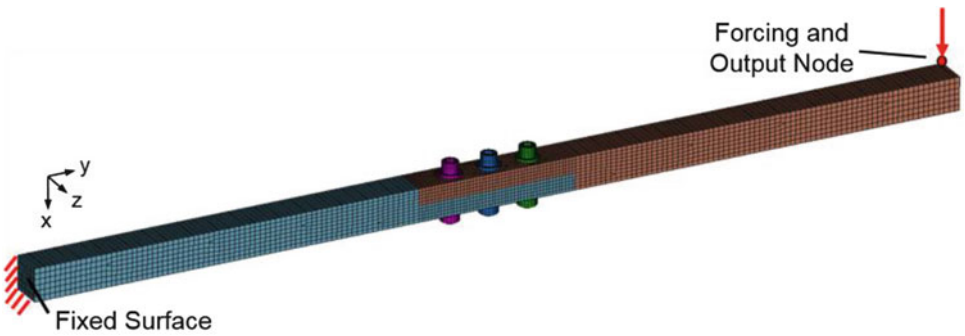

Fig. 20.13 Finite element nodal definitions for the reduced interface simulations

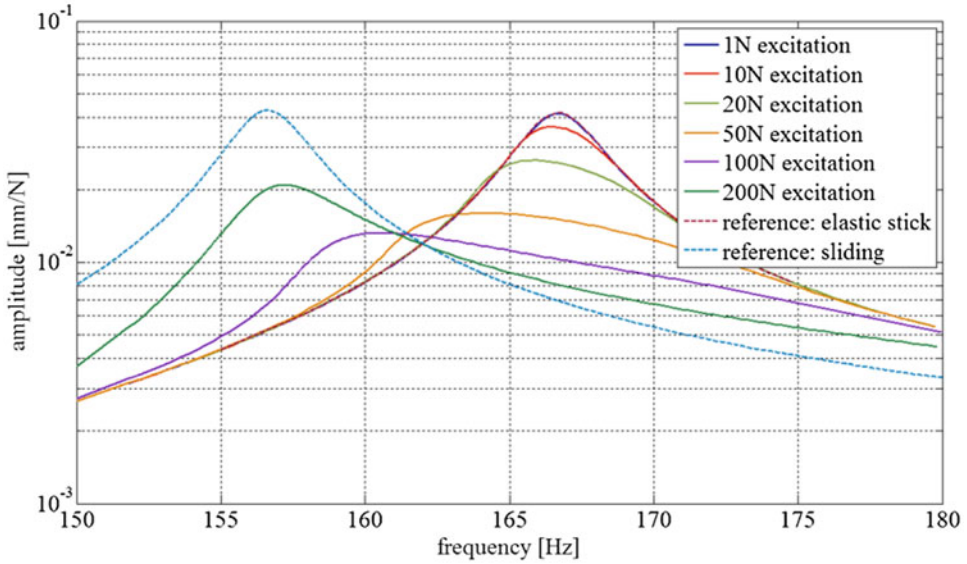

Fig. 20.14 Stuttgart's frequency response prediction for the reduced interface model

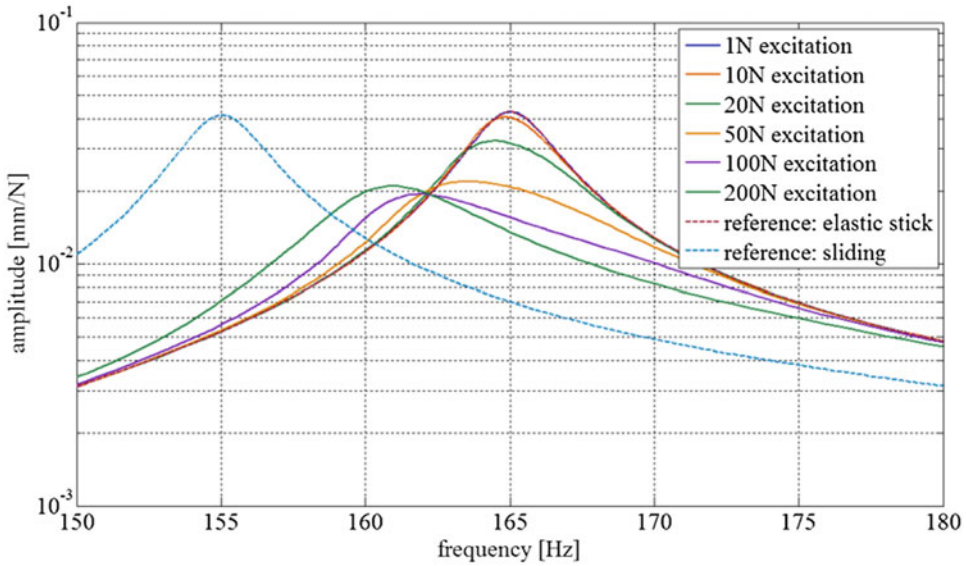

Fig. 20.15 Imperial's frequency response prediction for the reduced model

The observation that lift-off phenomena and contact normal force variation play a considerable role even for the reduced contact interface motivated the authors to investigate the dissipative behaviour of the beam structure considering the entire interface.

20.6.2 Full Interface Analysis

Following the reduced interface analysis, another analysis is conducted involving all three approaches in which all the nodes over the entire contact interface are considered for coupling with nonlinear elements. Stuttgart's model assigned the interpolated contact normal forces to individual nodes based on the previous nonlinear static analysis (Fig. 20.5). Only the 460 statically loaded nodes, seen in Fig. 20.16, are activated under the assumption that the contact state in normal direction would not change for the dynamic analysis. Imperial's model, on the other hand, activates all 592 nodes on the contact interface for coupling with 3D contact elements to their coincident counterparts.

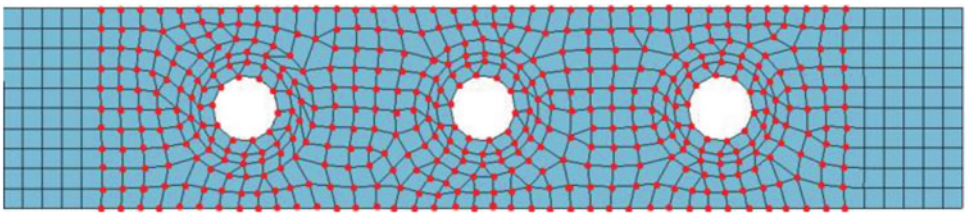

Fig. 20.16 The active nodes used in Stuttgart's full interface model

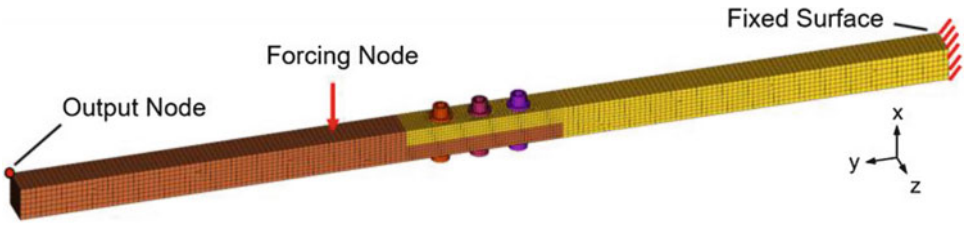

Fig. 20.17 Finite element nodal definitions for the harmonic balance full interface simulations

The nodal definitions for the Brake-Reuss beam finite element model are altered slightly from the reduced interface analysis in an attempt to reproduce the experimental testing being done on the beam in parallel with this analysis. As seen in Fig. 20.17, the input force location is moved to the opposite surface of the beam to act in the x-direction at a point 18.9 in. away from the fixed end of the beam (the location of a threaded hole in Fig. 20.1). The output node is moved to another corner at the free end of the beam, but the x-direction response is still measured. The same 4 kN static pre-load is applied on the bolts, and simulations are conducted for input force magnitudes of 1, 10, 50, and 100 N for a frequency range between 160 Hz and 190 Hz. For Imperial's multi-harmonic balance method, the 0th, 1st, 2nd, and 3rd harmonics are used for simulation.

Figures 20.18 and 20.19 show the nonlinear FRF results for the Stuttgart and Imperial models, respectively. Interesting to observe is that the shape of the 1 N excitation in Imperial's FRF differs strongly from Stuttgart's. It seems that in Imperial's model the 1 N excitation provides just enough energy in the vicinity of the resonance to generate a nonlinear stiffening effect due to contact closure during harmonic motion. The 10 N excitation, however, provides enough energy to additionally induce relative motion in the interface, and therefore softening and increased damping of the system. The effects of the 1 N excitation do not show in Stuttgart's FRF, so they may be realized by the additional harmonics used in Imperial's simulation and by the fact that Imperial's 3D contact elements account for changes in the normal contact state (like surface separation) whereas Stuttgart's Jenkins elements do not. Comparing the peak locations for these nonlinear FRFs with those from the reduced interface analysis (Sect. 20.6.1), the full interface models have about a 15 Hz resonance frequency increase from that of the reduced interface at small amplitude excitations. This is expected as extending nonlinear elements to more of the interface increases the joint stiffness due to an increased number of coupled nodes along the length of the interface.

20.6.3 Tuning the Iwan Element Joint Model Using Amplitude-Dependent Damping

When observing the effect that the presence of a joint has on a structure, the typical quantities of interest are how both the resonance frequency and the energy dissipation (or critical damping ratio) for a particular vibration mode changes as the structure is excited with larger excitation forces. This opens a route for comparison between transient and harmonic responses because there exist methods to extract these two quantities from either type of response. Other works have shown that one can obtain insight into the joint dynamics by plotting energy dissipation versus the amplitude of either the response or the force in the joint, and that dissipation tends to follow a power-law relationship [6]. If power-law relationships can be established for the energy dissipated by the Jenkins and 3D contact elements, then the four-parameter Iwan model may be tuned to match those relationships.

For both of the harmonic approaches, the energy dissipated is calculated as described in Sect. 20.5.1 for Imperial's approach. In effect, the hysteresis curves for each nonlinear element can be constructed at resonance, and the total energy dissipated is the sum of the areas of all the hysteresis curves. If the energy dissipation follows a power-law relationship with an exponent of $\chi + 3$, then damping ratio will also follow a power-law with an exponent $\chi + 1$ because the damping ratio

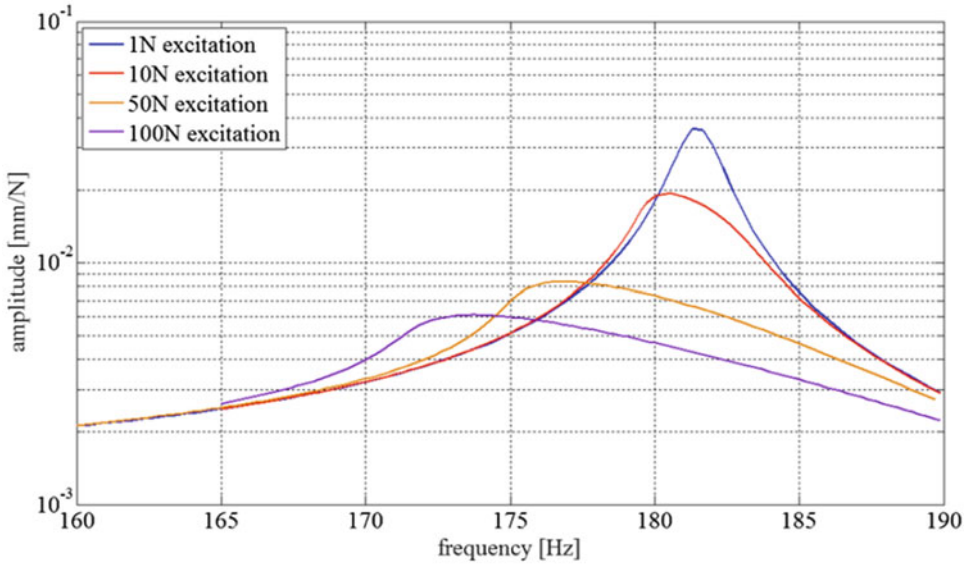

Fig. 20.18 Stuttgart's frequency response prediction for the full interface model

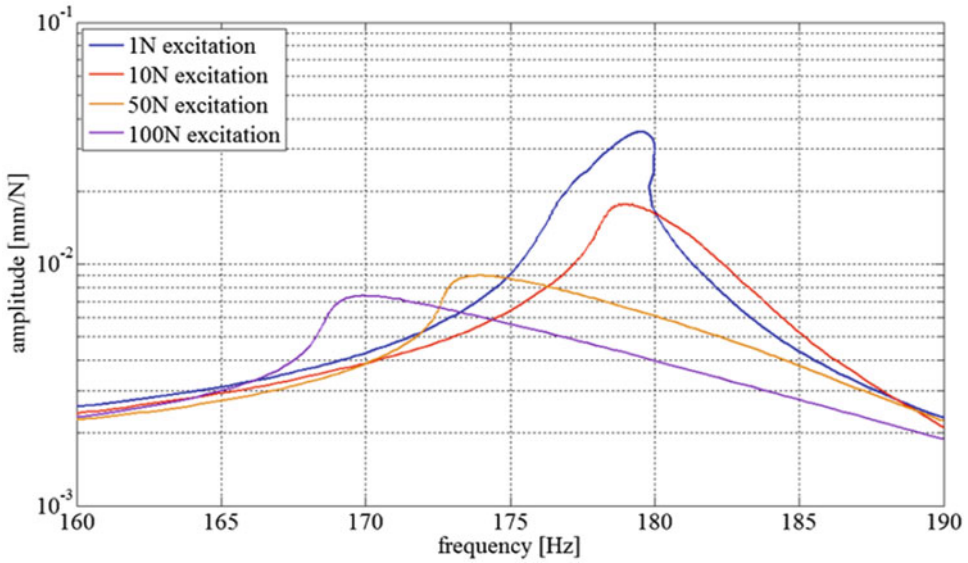

Fig. 20.19 Imperial's frequency response prediction for the full interface model

is related to dissipation via Eq. 20.9, in which dissipation is divided by a power 2 term in the denominator. A plot of the damping versus amplitude on a logarithmic scale for the two harmonic balance approaches is shown in Fig. 20.20. The data for each approach are from the four nonlinear frequency response simulations calculated under the conditions described in Sect. 20.6.2.

The results seem to show that both the Stuttgart and Imperial codes predict that this mode's damping will follow a power-law relationship at low amplitudes, but then at higher amplitudes the damping begins to level off, presumably as the system approaches macro-slip. The dashed lines correspond to a power-law fit to the damping versus amplitude of the following form,

$$\zeta_r = C_r |V_r|^{\chi+1}. \tag{20.10}$$

Imperial's model has a power law strength of $C_r = 2300$ while Stuttgart's is $C_r = 656$. Both have relatively similar power-law exponents, $\chi = 1.10$ for Imperial and $\chi = 0.95$ for Stuttgart. It is interesting to note that in previous works χ has typically

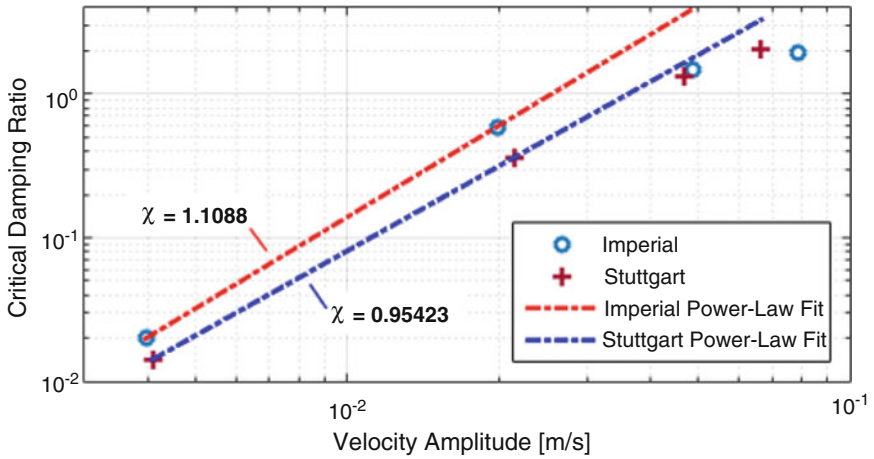

Fig. 20.20 Damping ratio versus beam tip velocity amplitude for the second mode (near 178 Hz) predicted by each method

been found to have values near −0.3 (see, [6] or [7]). Here χ is positive and near 1.0 so damping is growing with the second power of the velocity amplitude. As a result, the damping measured in a low amplitude test would quickly become erroneous as amplitude increases. On the other hand, it appears that the system only follows a power-law relationship over a relatively small range of amplitude, and then it seems to transition to macro-slip.

In principle, one could use the power law fit above to fit a modal Iwan model [16, 17] to this damping vs. amplitude behaviour. One could then predict the response of this mode in the micro-slip regime using the SDOF equation of motion for the modal Iwan model at a low computational cost. However, the power law coefficients, C_r, above are quite large. An Iwan model with $\chi = 1.10$ and $R = 1.591 \times 10^{17}$ would reproduce the power-law fit above, but since (from [3])

$$R = \frac{K_T^{\chi+2}\,(\chi+1)\left(\beta + \frac{\chi+1}{\chi+2}\right)^{\chi+1}}{F_S^{\chi+1}(1+\beta)^{\chi+2}}, \tag{20.11}$$

and hence $R \simeq K_T^{\chi+2}/F_S^{\chi+1}$, or $1.591 \times 10^{17} \simeq K_T^{3.1}/F_S^{2.1}$, the stiffness of the joint, K_T, will have to be much higher than the slip force, F_S, for this is to be realized. The joint stiffness governs the shift in the resonance frequency as the joint goes from micro to macro-slip, and the resonance frequency of this mode decreases only to 155 Hz (a reduction of 25 Hz) if the joint stiffness goes to zero. Hence, the large K_T value that this demands is physically unreasonable. This discussion pertains only to Segalman's four-parameter Iwan model [3]. An alternative model, such as Mignolet's 5-parameter model [18] might have the flexibility needed to describe this behaviour.

It is also interesting to ask whether a finite element model with discrete Iwan elements at the locations of the bolts, such as the models that were advocated in [6], might reproduce the response of this structure. In [6] it was presumed that experiments could be performed on each joint in isolation to deduce their Iwan parameters, but no such experiments are available for this analysis. One could, instead, postulate a set of Iwan parameters and adjust them until simulations of the structure's response reproduce the desired damping versus amplitude behaviour. This was pursued by creating a reduced-order model of the Brake-Reuss beam as follows.

Since the Iwan element is a whole-joint model, it is counter to its intended use to define several hundred node parings over the joint interface to be coupled with the elements, as is done for the other approaches. Instead, the nodes on the interface are divided into three regions, and all the nodes within each region are tied to a representative virtual node with element spiders, as illustrated in Fig. 20.21. The element spiders are defined as NASTRAN RBE3 elements [9], which are interpolation elements that force the motion of the virtual node to be a weighted average of the motion of the tied nodes on the surface. The same virtual node and RBE3 specification is defined for the opposite surface.

The three virtual node pairs, the output point shown in Fig. 20.17, and the fixed surface nodes are selected as boundary nodes for Craig-Bampton reduction [10]. The first 21 fixed-interface modes are kept to ensure that the model is accurate up to at least 4000 Hz, though such detail in the response may be unnecessary. Post-reduction, the out-of-plane rotational degrees of freedom between virtual node pairs are constrained to move with each other. In addition, each virtual node pair is coupled with two Iwan elements, one for each surface tangent direction. With three virtual node parings, there are six total Iwan elements in the Sandia joint model.

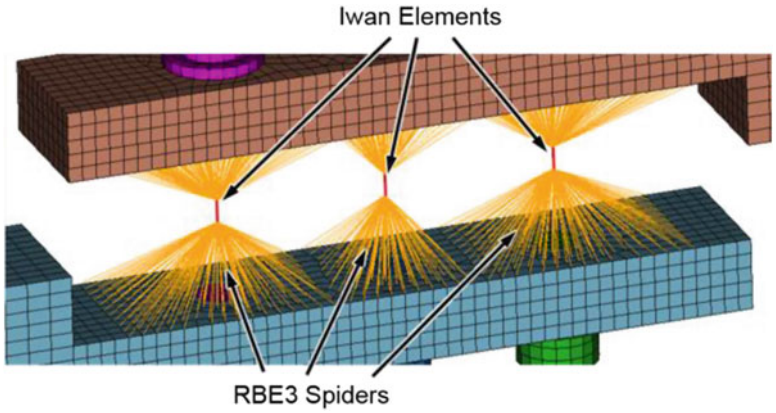

Fig. 20.21 The Sandia joint model for the full interface analysis. The interface shown in an exploded view

Since the parameterization for each Iwan element is unknown, they are all assumed to have the same parameter values. The slip force F_S is set to 2400 N, and the joint stiffness K_T is set to 10^7 N/mm, a minimum value that produces the same resonance frequency for the 2nd bending mode as the harmonic approaches when all the joints are completely stuck. The value for β is held constant at 0.05, and χ is left as a variable to observe how it affects the calculated damping.

Material damping is added to the structure by transforming a diagonal matrix of modal damping ratios ζ_m obtained from previous experiments into the damping coefficient matrix $\widehat{\mathbf{C}}$ in the Craig-Bampton space. This is done through

$$\widehat{\mathbf{C}} = \widehat{\mathbf{M}}\boldsymbol{\Phi} \cdot \mathrm{diag}\left(2\omega_r\zeta_r\right) \cdot \boldsymbol{\Phi}^T\widehat{\mathbf{M}}, \tag{20.12}$$

where $\boldsymbol{\Phi}$ is the matrix of mass-normalized mode shapes $\boldsymbol{\phi}_r$ produced from the Eigen analysis of

$$\left(\widehat{\mathbf{K}} - \lambda_r\widehat{\mathbf{M}}\right)\phi_r = \mathbf{0}. \tag{20.13}$$

$\widehat{\mathbf{M}}$ is the Craig-Bampton-reduced mass matrix, $\widehat{\mathbf{K}}$ is the reduced stiffness matrix that includes the full stick joint stiffness contribution, and $\omega_r = \sqrt{\lambda_r}$ are the circular resonance frequencies. The modal damping ratios for the 1st and 2nd bending modes are 0.008 and 0.0051, respectively.

In transient methods, the instantaneous nonlinear damping can be retrieved from the free-response signal using the Hilbert transform methods outlined in [8]. The 2nd bending mode of the beam is excited by applying a force in the shape of the mode as follows,

$$\mathbf{f}_{ext} = p\widehat{\mathbf{M}}\boldsymbol{\phi}_2 \tag{20.14}$$

Where $\boldsymbol{\phi}_2$ is the mode shape for the 2nd bending mode, and p is a scalar for the force magnitude. Several transient simulations were performed with an impulsive input in the shape of one cycle of a sine with period of 5.59 ms (2nd bending mode period) and amplitude $p = 5000$. The transient response was found by integrating the equations of motion, including the six Iwan joints, using the Newmark routine with a time step between 1 and 10 microseconds. The reduced model had 54 degrees of freedom and about 30 min were required to find the response at the approximately 2 million time steps that were needed for the transient signal to decay. These simulations were on a desktop computer with a 3-GHz quad-core processor; though only one of the cores was utilized by the Newmark routine. Relatively little effort was exerted to find the optimal time step or to minimize the size of the Craig Bampton model, so these simulation times could probably be improved.

Figure 20.22 shows how the frequency and damping of the mode in question varies as χ is adjusted. More negative values of χ produce higher dissipation (for fixed values of F_S and K_T), and a larger shift in the resonance frequency with amplitude. All of these simulations remained in the micro-slip regime. Note that, in contrast to the results shown in Fig. 20.20, the damping ratios in Fig. 20.22 includes contributions from both the material damping and the damping due to the joint. As a result, the curves do not seem to show power-law behaviour but instead converge to a low amplitude asymptote (the material damping, which is 0.0051).

It is also interesting to note that the χ value used for the discrete joints does not end up having the same χ value that best fits the modal damping versus displacement curves. For example, for the case where $\chi = -0.9$, a power-law model was fit

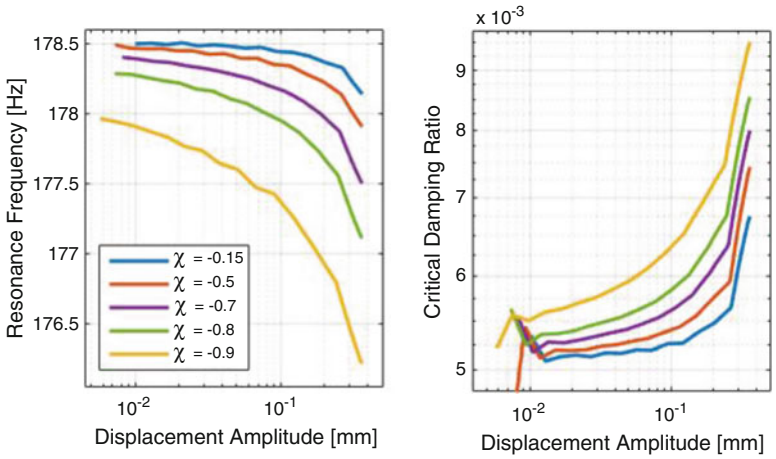

Fig. 20.22 Frequency and damping versus displacement amplitude at the tip for various models with discrete Iwan joints

and the parameters found were $\chi = -0.27$ and $C_r = 0.00472$. This power-law strength, C_r, is far lower than what is predicted by the Imperial and Stuttgart approaches, so the parameters of the discrete Iwan joints would have to be adjusted significantly to match that behaviour. Even so, it is probably not possible to obtain agreement for this mode using a 4-parameter Iwan model for the joints.

20.7 Conclusion

This project investigates three modelling approaches on their ability to model the dynamic behaviour exerted by a bolted joint in a structure. In the course of completing the analyses described in previous sections, a number of conclusions and lessons learned are gained regarding the optimal use of each approach and their nonlinear elements.

If using nonlinear elements similar to the Jenkins and 3D contact elements, which describe binary stick–slip behaviour in a very localized region of the friction interface, then effort must be made to model many such elements distributed over most, if not the entire, interface. As is shown in Sect. 20.5.2, using a single Jenkins or 3D contact element would capture macro-slip behaviour of a joint, but not the essential micro-slip behaviour that simulates the small-amplitude response produced in bolted lap joint structures. In addition, Sect. 20.6.2 shows that spreading nonlinear contact elements over the entire interface may capture the resonant frequencies in a structure more accurately than over reduced regions in the interface.

The downside to adding tens or hundreds of nonlinear elements in the interface is that they strain the convergence rate in implicit transient solvers. If convergence is possible, the time step required may be so small as to require weeks or months of computation to simulate a useful amount of response history. Such a time investment is not practical from a design standpoint, and the analyst would need to rely on more efficient methods for retrieving the response, like the harmonic balance method. In using the harmonic balance method, the analyst is restricted to periodic inputs. Of course, this is not a problem if the forced harmonic response is desired, and the harmonic balance method is recommended for its efficiency in these cases provided that the influence of the nonlinear element can be represented somehow in the frequency domain.

An alternative for many stick–slip elements is a single whole-joint formulation, such as the Iwan element, that in itself describes the local stick–slip distribution needed to model micro-slip. A finite element model would only require at most a few whole-joint models, which restores the practicality for numerical time integration schemes. In return, the whole-joint modelling methods used in this research require rigid element spiders or averaging MPCs to couple the joint interfaces, which potentially add artificial stiffness to the joint and may adversely alter the structure's resonance frequencies. In addition, whole-joint elements may not carry the same level of detailed contact states shown by many individual stick–slip elements. As such whole-joint models like the Iwan element are recommended if the influence that the joint has on the rest of the structure is of greater interest than the dynamics occurring within the joint itself.

This research shows that harmonic and transient responses can be linked for comparison by observing how a structure's resonant frequencies and nonlinear damping changes with response amplitude. In Sect. 20.6.3, the damping versus amplitude power-law relationships from the two harmonic balance models are used to try and parameterize the Iwan joint to reproduce their energy dissipation behaviours. This approach did not succeed as well as hoped. Nonetheless, the dynamic response

output from the harmonic balance approaches is recast in a way that shows that their power-law exponents apparently exceed those seen in experiments on some jointed structures, and that it is difficult for the four-parameter Iwan model to reproduce that behaviour. Further study would need to be conducted to determine the source of these anomalies and whether additional corrections are needed for a more fair tuning analysis.

Although much is gained from this research, it is still very much a work in progress. Further studies will improve on the modelling methods used in the three approaches, and may introduce new approaches into the round robin. In addition, the models will be compared with test data on the Brake-Reuss beam. Such a study will also facilitate a more meaningful comparison between the transient and harmonic balance methods, since all models will work to simulate the response from the same, real structure.

Acknowledgements This work was funded by Sandia National Laboratories. Sandia National Laboratories is a multi-program laboratory managed and operated by Sandia Corporation, a wholly owned subsidiary of Lockheed Martin Corporation, for the U.S. Department of Energy's National Nuclear Security Administration under contract DE-AC04-94AL85000.

Special thanks is given to Professor Matthew Allen at the University of Wisconsin-Madison for his insights on the use of Iwan models in numerical simulation, and for his guidance in the analysis of the dynamic response results to compare their modal damping behaviours. Thanks is given to Dr. Timothy Truster from the University of Tennessee for his suggestions on the directed course of this research during the latter half of the Institute.

References

1. Salles, L., Swacek, C., Lacayo, R.M., Reuss, P., Brake, M.R.W., Schwingshackl, C.W.: Numerical round robin for prediction of dissipation in lap joints. In: IMAC XXXIII A Conference and Exposition on Structural Dynamics, Orlando, 2015
2. Brake, M.R., Reuss, P., Segalman, D.J., Gaul, L.: Variability and repeatability of jointed structures with frictional interfaces. In: IMAC XXXII A Conference and Exposition on Structural Dynamics, Orlando, 2014
3. Segalman, D.J.: A four-parameter Iwan model for lap-type joints. ASME J. Appl. Mech. **72**, 752–760 (2005)
4. Iwan, W.D.: A distributed-element model for hysteresis and its steady-state dynamic response. ASME J. Appl. Mech. **33**(4), 893–900 (1966)
5. Smallwood, D.O., Gregory, D.L., Coleman, R.G.: Damping Investigations of a Simplified Frictional Shear Joint, SAND2000-1929C. Sandia National Laboratories, Albuquerque (2000)
6. Segalman, D.J., Gregory, D.L., Starr, M.J., Resor, B.R., Jew, M.D., Lauffer, J.P., Ames, N.M.: Handbook on the Dynamics of Jointed Structures. Sandia National Laboratories, Albuquerque (2009)
7. Deaner, B.J., Allen, M.S., Starr, M.J., Segalman, D.J., Sumali, H.: Application of viscous and Iwan modal damping models to experimental measurements from bolted structures. ASME J. Vib. Acoust. **137**(2), 021012 (2015)
8. Roettgen, D.R., Allen, M.S.: Nonlinear characterization of a bolted, industrial structure using a modal framework. Mech. Syst. Signal Process. (2016). http://dx.doi.org/10.1016/j.ymssp.2015.11.010.
9. Reese, G., Segalman, D., Bhardwaj, M.K., Alvin, K., Driessen, B., Pierson, K., Walsh, T., Dohrmann, C., Wilson, C.R.: Salinas-User's Notes. Sandia National Laboratories, Albuquerque (2012)
10. Bampton, M.C.C., Craig, R.R.: Coupling of substructures for dynamic analyses. AIAA J. **6**(7), 1313–1319 (1968)
11. Bograd, S., Reuss, P., Schmidt, A., Gaul, L., Mayer, M.: Modeling the dynamics of mechanical joints. Mech. Syst. Signal Process. **25**, 2801–2826 (2011)
12. Cigeroglu, E., Özgüven, H.N.: Nonlinear vibration analysis of bladed disks with dry friction dampers. J. Sound Vib. **295**, 1028–1043 (2006)
13. Petrov, E.P., Ewins, D.J.: Analytical formulation of friction interface elements for analysis of nonlinear multiharmonic vibrations of bladed discs. ASME J. Turbomach. **125**, 364–371 (2003)
14. Petrov, E.P., Ewins, D.J.: Generic friction models for time-domain vibration analysis of bladed disks. ASME J. Turbomach. **126**, 184–92 (2004)
15. Petrov, E.P.: A high-accuracy model reduction for analysis of nonlinear vibrations in structures with contact interfaces. Trans. ASME: J. Eng. Gas Turbines Power **133**, 102503 (2011)
16. Segalman, D.J.: A Modal Approach To Modeling Spatially Distributed Vibration Energy Dissipation, SAND2010-4763. Sandia National Laboratories, Albuquerque (2010)
17. Deaner, B.J.: Modeling the Nonlinear Damping of Jointed Structures using Modal Models. University of Wisconsin-Madison, Madison (2013)
18. Mignolet, M.P., Song, P., Wang, X.Q.: A stochastic Iwan-type model for joint behaviour variability modeling. J. Sound Vib. **349**, 289–298 (2015)

Chapter 21
A Method to Capture Macroslip at Bolted Interfaces

Ronald N. Hopkins and Lili A.A. Heitman

Abstract Relative motion at bolted connections can occur for large shock loads as the internal shear force in the bolted connection overcomes the frictional resistive force. This macroslip in a structure dissipates energy and reduces the response of the components above the bolted connection. There is a need to be able to capture macroslip behavior in a structural dynamics model. A linear model and many nonlinear models are not able to predict marcoslip effectively. The proposed method to capture macroslip is to use the multi-body dynamics code ADAMS to model joints with 3-D contact at the bolted interfaces. This model includes both static and dynamic friction. The joints are preloaded and the pinning effect when a bolt shank impacts a through hole inside diameter is captured. Substructure representations of the components are included to account for component flexibility and dynamics. This method was applied to a simplified model of an aerospace structure and validation experiments were performed to test the adequacy of the method.

Keywords Macroslip • ADAMS • Shock response spectrum • Substructure • Joint

Nomenclature

SRS	Shock response spectrum
dB	Decible
ms	Millisecond

21.1 Introduction

This paper presents a simple method to capture macroslip at bolted interfaces for mechanical assemblies which utilizes conventional linear finite element techniques including substructures which could be supplied by most any commercial finite element software as well as the commercial multibody dynamics software ADAMS from MSC/Software. Further, experimental testing was performed which produced macroslip at bolted interfaces, and this paper summarizes the experimental testing including demonstration of the varying degrees of macroslip. Next, the experiment was modeled within MSC/ADAMS including bolted and preloaded interfaces and was exercised with the same experimental base excited acceleration time history. Varying acceleration amplitudes, the same as the experiment, were used to excite the system and the response on either side of the bolted interface as well as the response a distance away from the bolted joint was computed. The measured response from the experiment and the predicted response from the MSC/ADAMS simulations were then compared. The comparisons were in the form of acceleration time histories and shock response spectrums (SRS) [1–6].

Mechanical assemblies are often a collection of components which are connected though a number of bolted joints or interfaces. When subjected to high acceleration, short duration shock events, these mechanical assemblies often experience macroslip at bolted interfaces. Macroslip is defined when the slip or lateral relative motion occurs over an entire contact

Sandia National Laboratories is a multi-program laboratory managed and operated by Sandia Corporation, a wholly owned subsidiary of Lockheed Martin Corporation, for the U.S. Department of Energy National Nuclear Security Administration under Contract DE-AC04-94AL85000.

R.N. Hopkins • L.A.A. Heitman (✉)
Analytical Structural Dynamics Department, Sandia National Laboratories, P.O. Box 5800 – MS0840, Albuquerque, NM 87185, USA
e-mail: rnhopki@sandia.gov; laakin@sandia.gov

© The Society for Experimental Mechanics, Inc. 2016

M. Allen et al. (eds.), *Dynamics of Coupled Structures, Volume 4*, Conference Proceedings of the Society for Experimental Mechanics Series, DOI 10.1007/978-3-319-29763-7_21

surface. For the case of Coulomb friction, the force which resists the slip is simply the normal force in the joint (tensile force in the bolt) multiplied by the coefficient of friction between the two bolted surfaces. While there is also microslip occurring at each bolted interface (small relative motion in regions away from the bolt where the normal load is reduced), the energy loss due to microslip is small compared to macroslip and can be accounted for in a gross sense with modal or structural damping. Macroslip, which can dissipate significant energy, cannot be accounted for with modal or structural damping.

The standard approach to analyze such an assembly which would include capturing the energy loss due to macroslip would be to perform a nonlinear explicit solution. A detailed finite element model (FEM) of the components including the bolts which connect the components would be generated. The detailed FEM would include contact including friction between the bolt head and adjacent component, between the two attached components, and the threads of the bolt may be connected to the component which they thread into using glued or tied contact. The solution would be performed in two parts; the first part would be to preload the bolt and solve for equilibrium, and the second part would be to maintain the preload and solve for the application of external loads. This type of analysis, while straight forward in the modeling of the physics involved, is computationally very intensive and depending on the complexity and number of bolted joints, may or may not result in accurate solutions.

A more typical approach when performing analytical simulations on these types of mechanical assemblies is to employ a linear implicit analysis. While much less complex from both a modeling and a computer resource perspective, this approach is not able to account for the energy dissipation due to macroslip, and therefore over-predicts the response of components which comprise the assembly.

The analysis approach presented in this paper utilizes linear FEMs in the form or substructures, but the equations of motion are solved with a nonlinear solution within MSC/ADAMS. The substructures can be provided by multiple commercial finite element codes such as MSC/NASTRAN, NX/NASTRAN, ANSYS or ABAQUS. Each of these software packages will output substructures in the required format for MSC/ADAMS. The equations of motion are nonlinear differential equations where the nonlinearity is due to the 3-D contact and frictional behavior at the bolted interfaces. A major advantage of this approach is that almost all of the mechanical assembly is modeled as linear with the a greatly reduced number of degrees of freedom as the mass and stiffness is decomposed to the substructure boundaries, in this case, the bolted connections. The nonlinear portion of the model only includes the bolted interfaces. This results in solution times on the order of minutes rather than hours and days. Additionally, ADAMS offers very robust numerical integration routines as well as the ability to model very complex physics such as sliding contact and impacts.

21.2 Test Setup

A series of experiments were developed and performed to induce and capture macroslip in a bolted joint connection of a structure. Two components were bolted together via three bolted joints with preload applied equally to each joint. The preload was varied in the experiments to investigate slip as a function of preload level. A 2 ms duration half sine pulse was applied to the components via a base acceleration using a hydrodynamic vibration shaker. The direction of loading focused the majority of the macroslip at a single joint within the structure. The load was applied in the lateral direction, with the magnitude of the shock and the amount of preload varied to investigate the initiation of macroslip.

A depiction of the general test setup is shown in Fig. 21.1. The test system consisted of two components, a stainless steel base, and a titanium top. Four triaxial accelerometers were used to control and measure the response of the system. In addition to the control accelerometer on the base of the structure where it was bolted to the shaker, an accelerometer was placed on each side of the bolted joint and at the top of the structure in line with the other accelerometers.

The test matrix is summarized in Table 21.1. Sixty-four half sine pulses were applied to the base of the structure. Torque levels of 43, 56, 70, and 100 in-lbs were applied to the three bolted joints for the different test series. The general strategy was to perform a single re-torque, and then to run through various dB levels of the 250 g 2 ms half sine pulse until clear evidence of macroslip was visible in the acceleration response data and computed SRSs. Once it was determined where macroslip was occurring, the test setup was re-torqued to the desired level, a calibration test was run at −27 dB, and then the test was run at the load level at which macroslip was expected to occur. The system was then re-torqued and the process repeated with the −27 dB calibration and a higher input to investigate macroslip and energy dissipation as a function of load level. This process was repeated at various torque levels, with the 43 in-lbs done three times to assess repeatability of the experiment.

A set of sample inputs from Test 1 is shown in Fig. 21.2a and b. The reference 250 g 2 ms half sine pulse is shown in both figures, and the dotted lines are the actual inputs that were applied to the base of the structure in tests 1.1–1.6.

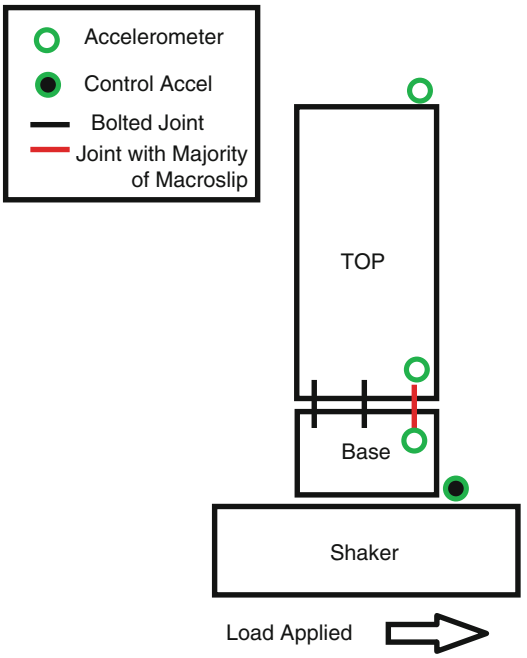

Fig. 21.1 Test setup

Table 21.1 Test matrix

Test/Torque	Load	Re-torque?	Test/Torque	Load	Re-torque?
1.1/43 in-lb	−27 dB	Yes	9.1/70 in-lb	−27 dB	Yes
1.2/43 in-lb	−21 dB	No	9.2/70 in-lb	−9 dB	No
1.3/43 in-lb	−18 dB	No	10.1/70 in-lb	−27 dB	Yes
1.4/43 in-lb	−15 dB	No	10.2/70 in-lb	−6 dB	No
1.5/43 in-lb	−12 dB	No	11.1/56 in-lb	−27 dB	Yes
1.6/43 in-lb	−9 dB	No	11.2/56 in-lb	−24 dB	No
2.1/43 in-lb	−27 dB	Yes	11.3/56 in-lb	−21 dB	No
2.2/43 in-lb	−24 dB	No	11.4/56 in-lb	−18 dB	No
2.3/43 in-lb	−18 dB	No	11.5/56 in-lb	−15 dB	No
2.4/43 in-lb	−15 dB	No	11.6/56 in-lb	−12 dB	No
3.1/43 in-lb	−27 dB	Yes	11.7/56 in-lb	−9 dB	No
3.2/43 in-lb	−15 dB	No	12.1/56 in-lb	−27 dB	Yes
4.1/100 in-lb	−27 dB	Yes	12.2/56 in-lb	−12 dB	No
4.2/100 in-lb	−24 dB	No	13.1/56 in-lb	−27 dB	Yes
4.3/100 in-lb	−21 dB	No	13.2/56 in-lb	−9 dB	No
4.4/100 in-lb	−18 dB	No	14.1/56 in-lb	−27 dB	Yes
4.5/100 in-lb	−15 dB	No	14.2/56 in-lb	−6 dB	No
4.6/100 in-lb	−12 dB	No	15.1/43 in-lb	−27 dB	Yes
4.7/100 in-lb	−9 dB	No	15.2/43 in-lb	−21 dB	No
4.8/100 in-lb	−6 dB	No	15.3/43 in-lb	−18 dB	No
5.1/100 in-lb	−27 dB	Yes	15.4/43 in-lb	−15 dB	No
5.2/100 in-lb	−6 dB	No	15.5/43 in-lb	−12 dB	No
6.1/100 in-lb	−27 dB	Yes	15.6/43 in-lb	−9 dB	No
6.2/100 in-lb	−3 dB	No	15.7/43 in-lb	−6 dB	No
7.1/70 in-lb	−27 dB	Yes	16.1/43 in-lb	−27 dB	No
7.2/70 in-lb	−24 dB	No	16.2/43 in-lb	−24 dB	No
7.3/70 in-lb	−21 dB	No	16.3/43 in-lb	−21 dB	No
7.4/70 in-lb	−18 dB	No	16.4/43 in-lb	−18 dB	No
7.5/70 in-lb	−15 dB	No	16.5/43 in-lb	−15 dB	No
7.6/70 in-lb	−12 dB	No	16.6/43 in-lb	−12 dB	No
8.1/70 in-lb	−27 dB	Yes	16.7/43 in-lb	−9 dB	No
8.2/70 in-lb	−12 dB	No	16.8/43 in-lb	−6 dB	No

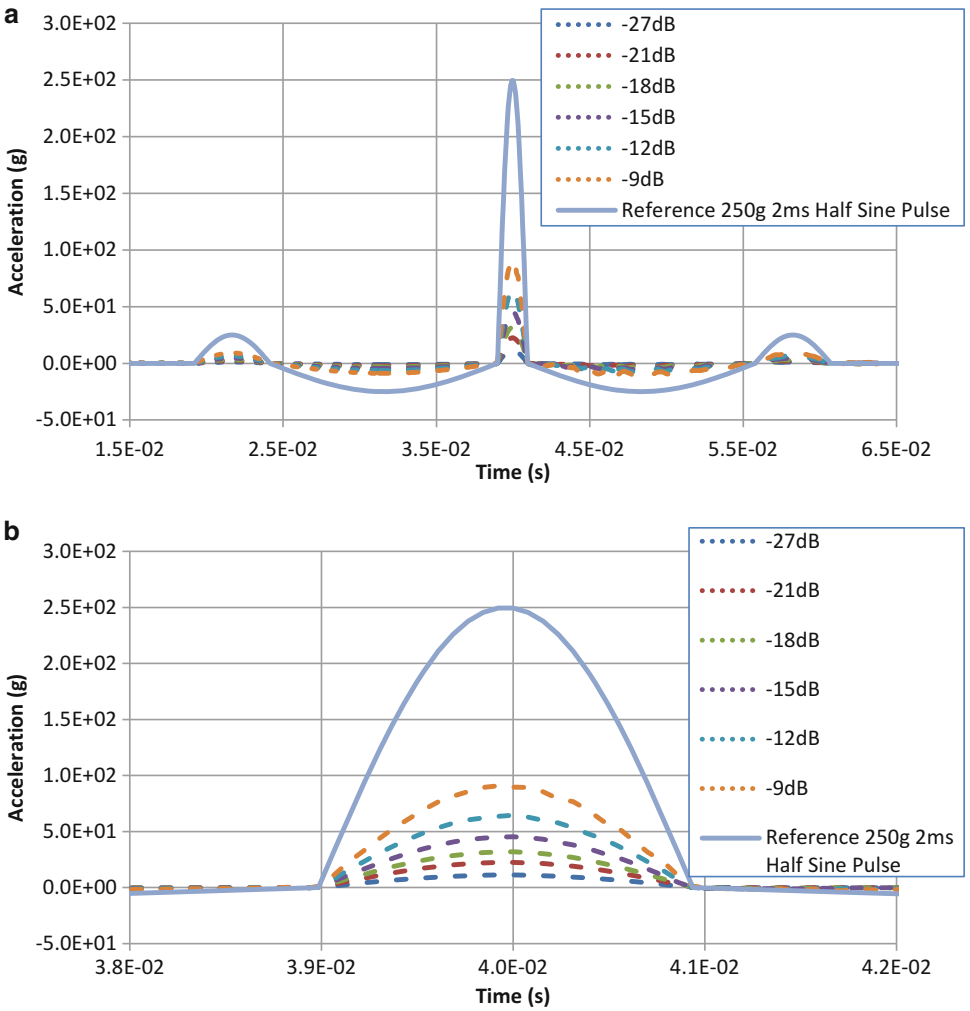

Fig. 21.2 (**a**) Sample input to base of structure (**b**) zoomed in

21.3 Test Results

A set of sample results from tests 7–10 is included below. First, a comparison of velocity response of the top of the joint and of the top of the structure for test 7.1 through 7.6 is provided in Figs. 21.3 and 21.4. The tests in the series which ramped up at regular dB levels were used to identify the first instance of definite macroslip. In these tests, macroslip was evident in the –12 dB test sequence, so this was the first level tested in the next round of tests. The slip tended to be easier to identify in the acceleration response at the top of the bolted joint, but the top of the test item was investigated extensively in the analyses, so is included here as well.

After the calibration series of tests were performed, the test to capture macroslip for use in FEM model validation was completed. These tests began at the level where macroslip was expected, and then was repeated at a higher load level to look at macroslip as a function of load level. A look at the acceleration and velocity response of the structure at all locations for tests 8.1, 8.2, 9.2, and 10.2 is provided in Figs. 21.5, 21.6, 21.7, 21.8, 21.9, 21.10, 21.11, 21.12, 21.13, 21.14, 21.15 and 21.16 respectively. The results from these tests were provided because these are the tests which were modeled analytically. The TopMock designation refers to the accelerometer at the top of the tested structures. The macroslip could be clearly seen in the velocity and acceleration response data, especially when comparing the response of the top of the structure and bolted joint to the base input.

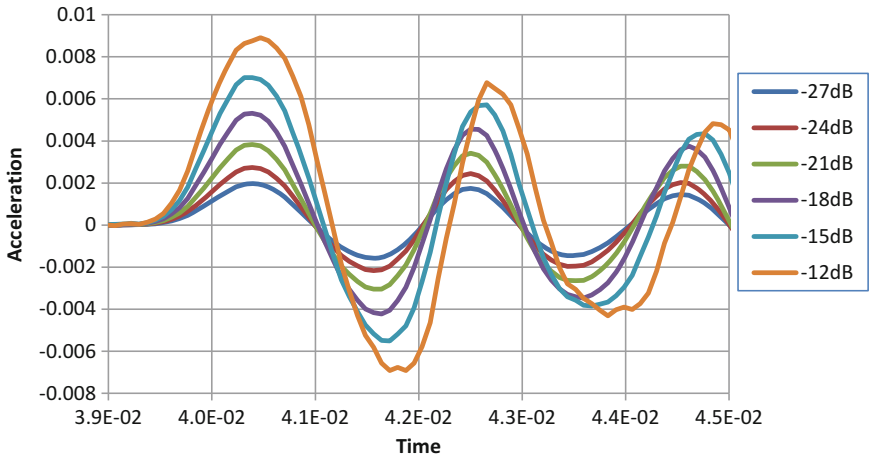

Fig. 21.3 Response of top of the test structure with 70 in-lb torque applied to bolted joints as a function of load in test series 7

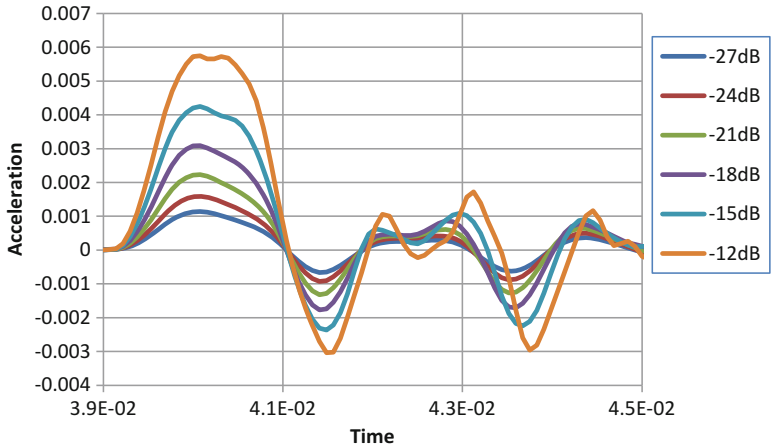

Fig. 21.4 Response of top of bolted joint with 70 in-lb torque applied to bolted joints as a function of load in test series 7

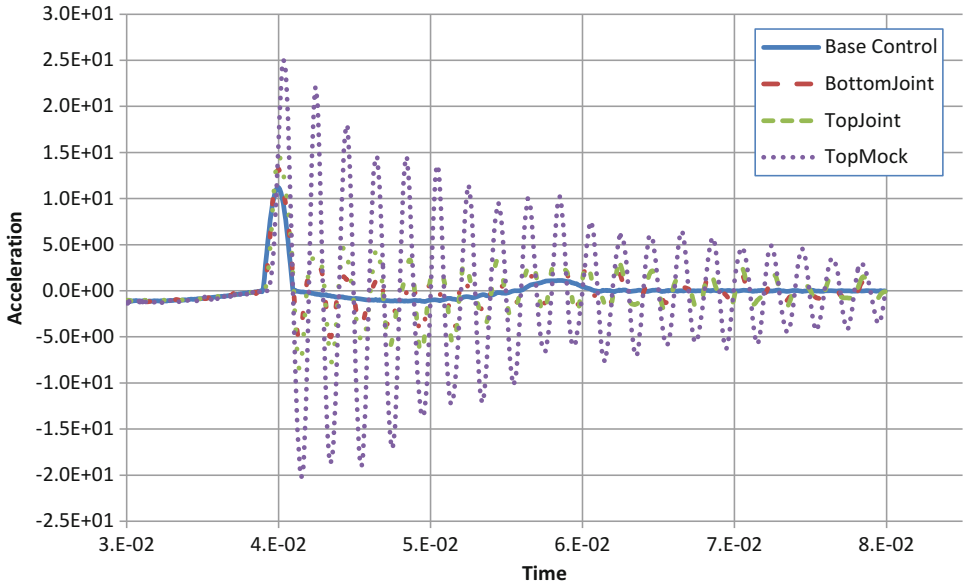

Fig. 21.5 Acceleration response of structure with 70 in-lb torque applied to bolted joints at −27 dB load as a function of location

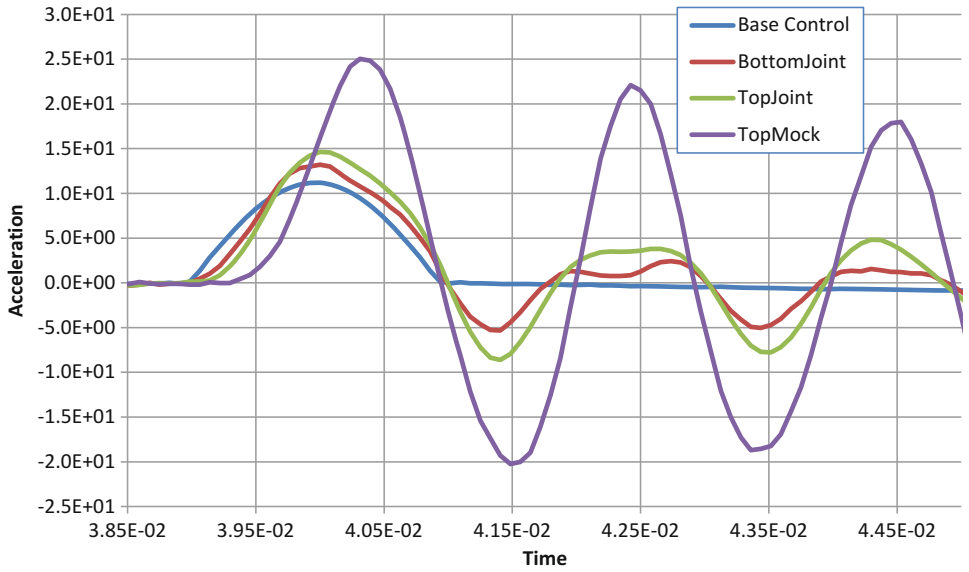

Fig. 21.6 Acceleration response of structure with 70 in-lb torque applied to bolted joints at −27 dB load as a function of location (zoomed in)

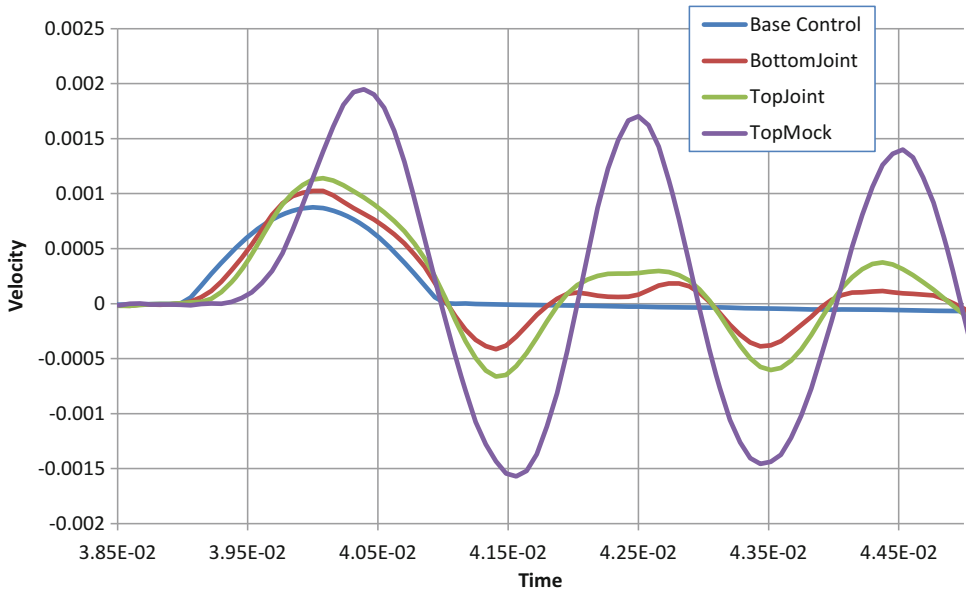

Fig. 21.7 Velocity response of structure with 70 in-lb torque applied to bolted joints at −27 dB load as a function of location (zoomed in)

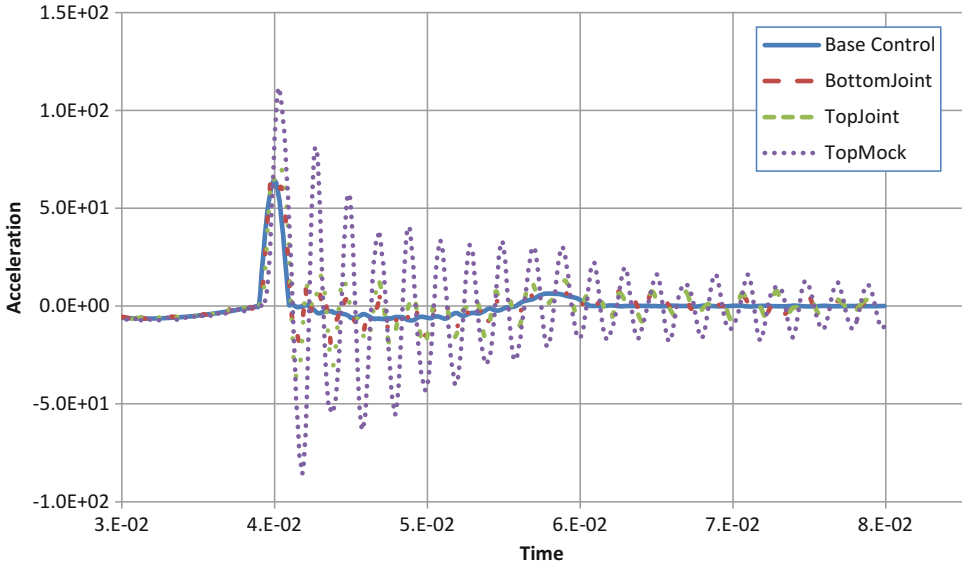

Fig. 21.8 Acceleration response of structure with 70 in-lb torque applied to bolted joints at −12 dB load as a function of location

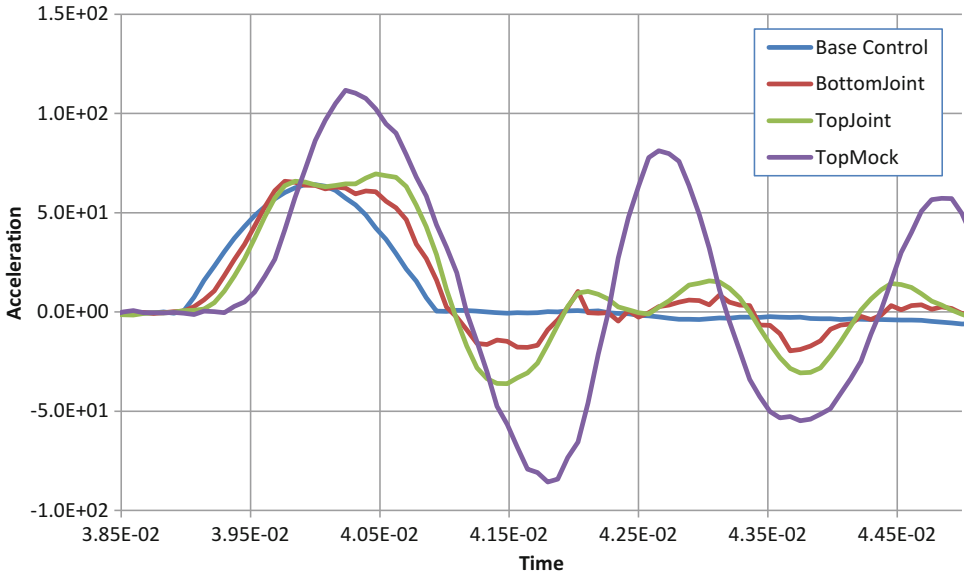

Fig. 21.9 Acceleration response of structure with 70 in-lb torque applied to bolted joints at −12 dB load as a function of location (zoomed in)

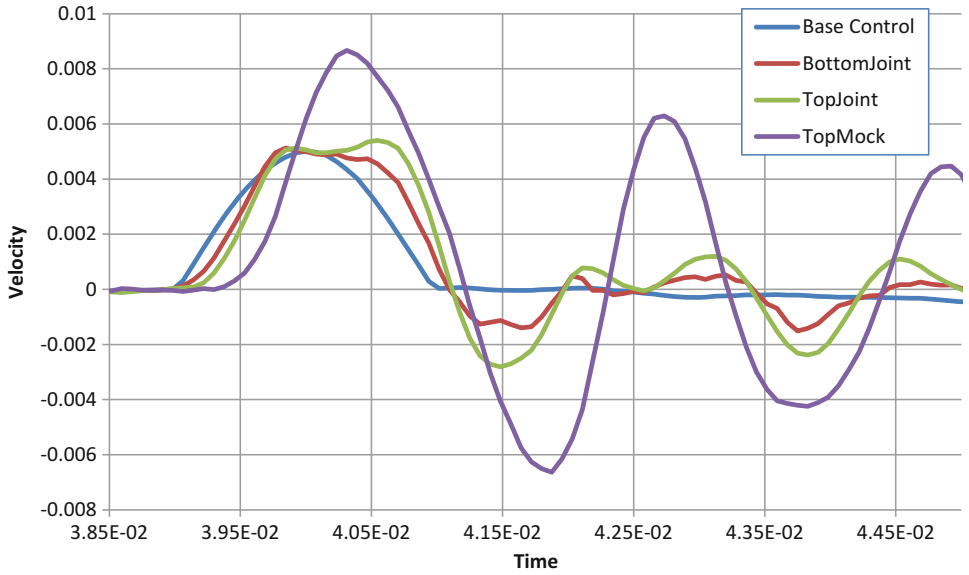

Fig. 21.10 Velocity response of structure with 70 in-lb torque applied to bolted joints at −12 dB load as a function of location (zoomed in)

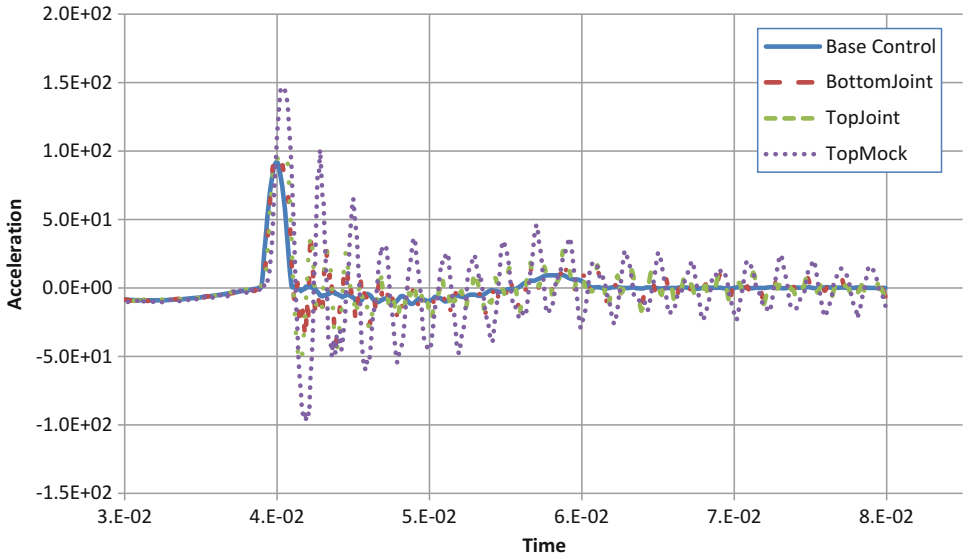

Fig. 21.11 Acceleration response of structure with 70 in-lb torque applied to bolted joints at −9 dB load as a function of location

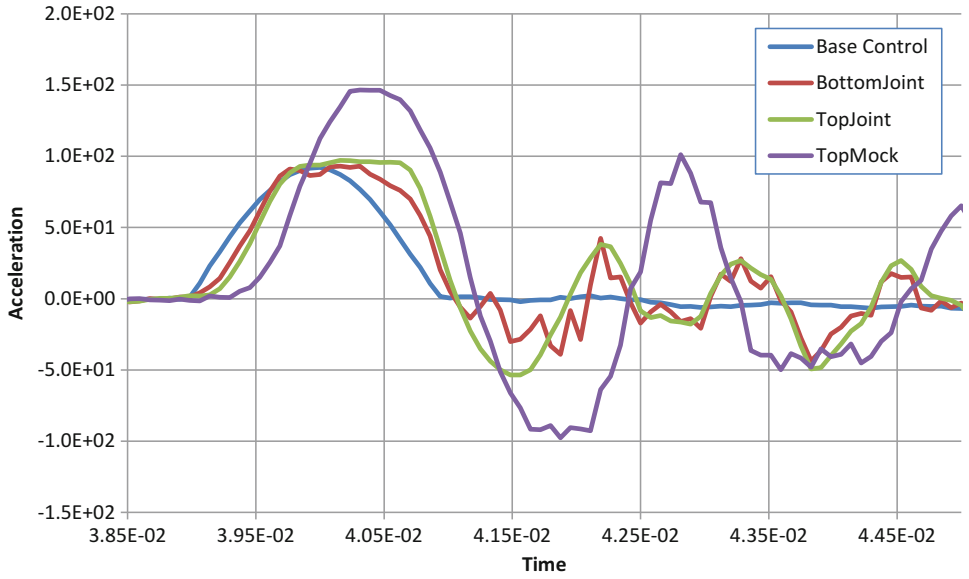

Fig. 21.12 Acceleration response of structure with 70 in-lb torque applied to bolted joints at −9 dB load as a function of location (zoomed in)

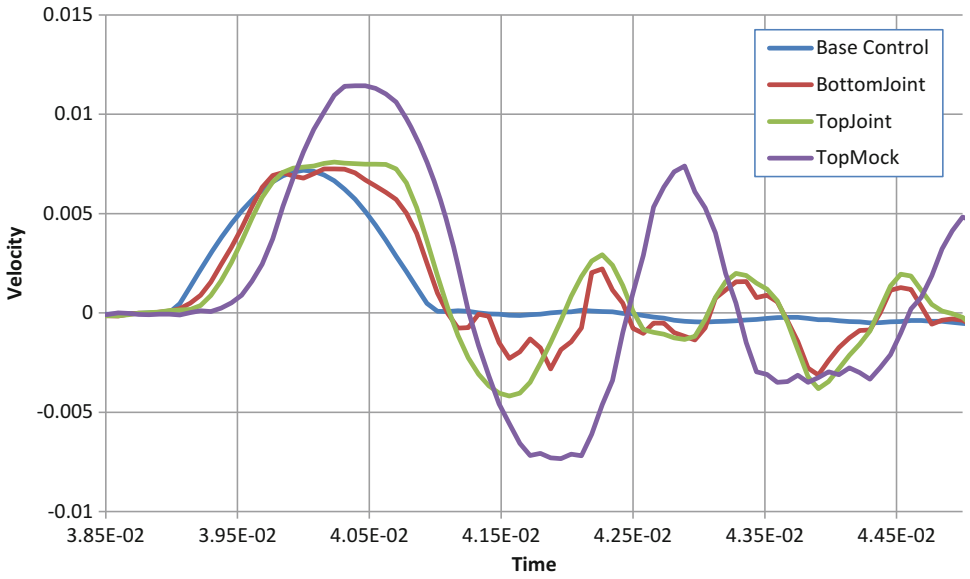

Fig. 21.13 Velocity response of structure with 70 in-lb torque applied to bolted joints at −9 dB load as a function of location (zoomed in)

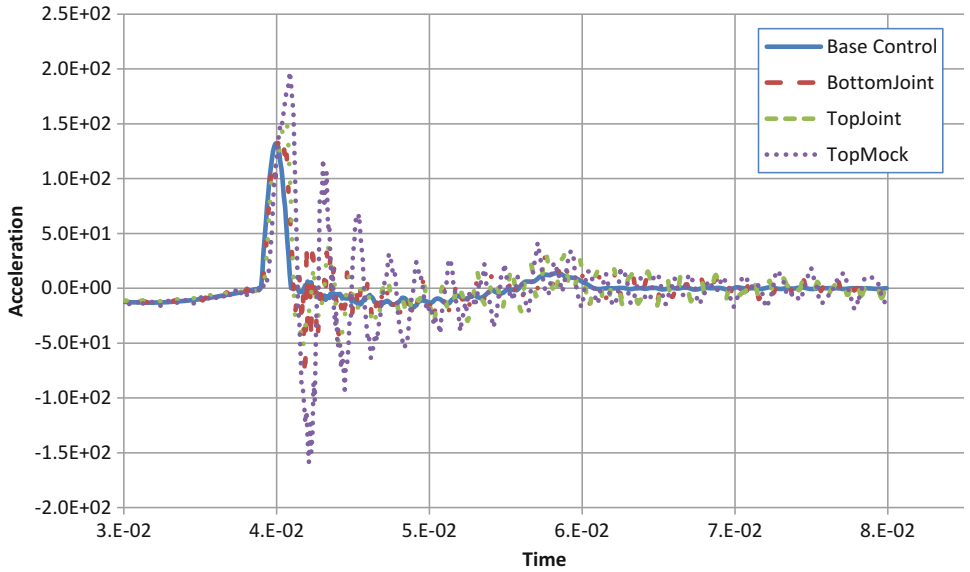

Fig. 21.14 Acceleration response of structure with 70 in-lb torque applied to bolted joints at −6 dB load as a function of location

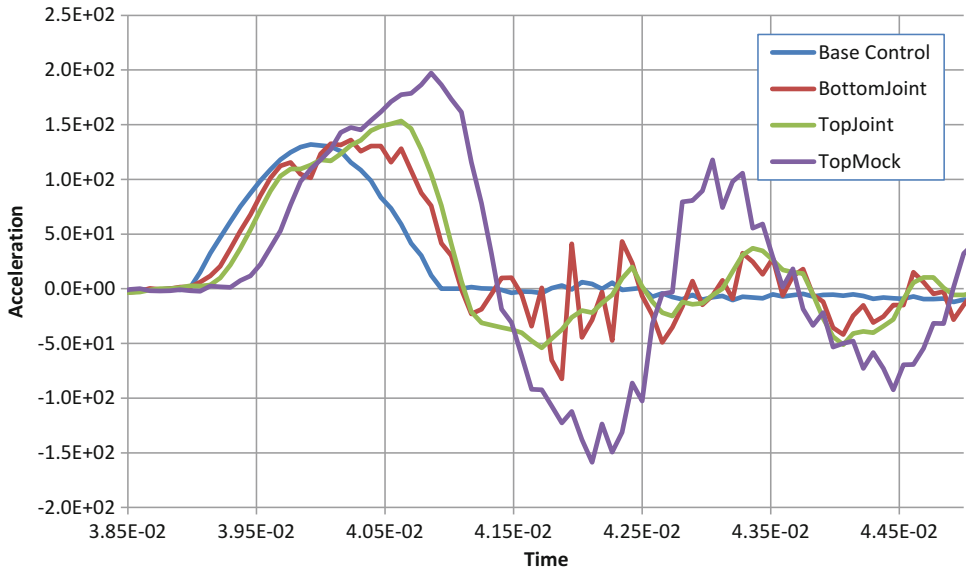

Fig. 21.15 Acceleration response of structure with 70 in-lb torque applied to bolted joints at −6 dB load as a function of location (zoomed in)

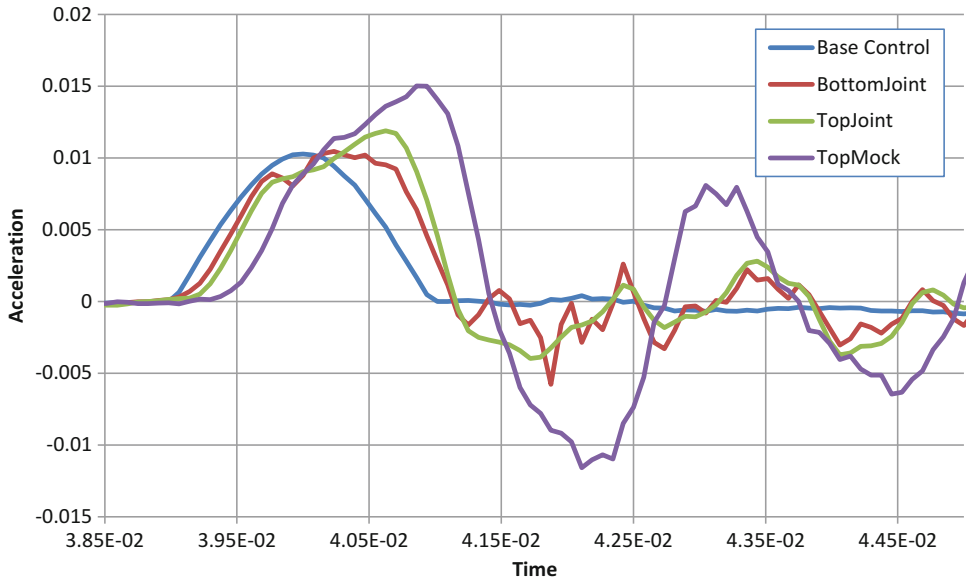

Fig. 21.16 Velocity response of structure with 70 in-lb torque applied to bolted joints at −6 dB load as a function of location (zoomed in)

21.4 Analysis Approach

The analysis approach uses a combination of linear FEMs in the form of substructures incorporated into a nonlinear multi-body dynamics solver (MSC/ADAMS). The nonlinear portion of the model is the complex behavior of the bolted interfaces. Contact between preloaded 3-D surfaces is included as well as friction, both static and dynamic, to model the relative motion at the bolted interfaces. The two contacting surfaces are preloaded using a spring element with a stiffness equivalent to the axial stiffness of the bolt. Once the preload portion of the solution is obtained, the solution is continued with the application of the external load. The entire system response to a complex loading is performed within MSC/ADAMS. If it is desired, it is also possible to calculate the response of individual substructures in terms of stress, strain, displacement, however this data recovery step must be performed in the same software pack used to generate the substructure.

The various components are modeled with linear finite element techniques and then reduced to their boundary mass and stiffness representation through substructures. The boundaries include the average stiffness at the bolted interfaces. If the bolted interface is the internal threads, a central node is created and connected to the thread region using a rigid or constraint type element (Fig. 21.17), if the bolted interface is the region where the head of the bolt bears up, a central node is created and connected to the diameter of the through hole (Fig. 21.18). These central nodes become fixed boundary nodes during the creation of the component substructure. There may also be specific nodes where external loads are applied or where the response is desired. These nodes are also boundary nodes for the substructure creation, but are free boundary nodes rather than fixed boundary nodes. The information included at the substructure boundaries includes the stiffness, mass and normal modes. The normal mode shapes reflect the condition of the boundary nodes, i.e., fixed or free. The frequency content of the normal modes should be on the order of two times the highest frequency content of the input load or the response resolution.

Each substructure is imported into ADAMS and the appropriate boundary nodes are connected with spring elements to establish the proper preload and 3-D contact between the substructures (called flexbodies within ADAMS) is defined. The 3-D contact is not computed in the same manner as in a finite element solution, however it does employ an interface (similar to penalty) stiffness that resists penetration in the presence of a compressive load between contacting parts. For the lateral interaction, Coulomb friction is specified for the static and dynamic interaction between the contacting parts. For a typical joint, the compressive stiffness is controlled by the stiffness of the mating parts, and the tensile stiffness is controlled by the mating parts until preload is overcome (then the tensile stiffness is that only of the bolt). The shear stiffness is a function of the preload and the coefficient of friction between the two mating parts. To account for joint pinning in the shear direction, which occurs when the bolt shank impacts the through hole inside diameter, a bistop element is used. This element allows lateral motion until a certain value of relative motion in the shear direction of the joint (plus and minus) is achieved.

To compare the nonlinear solution within ADAMS to a linear solution similar to that which would be computed in a linear implicit finite element analysis, bushing elements (6 DOF springs) were used instead of the nonlinear joint models to compare to the nonlinear results as well as the experimental results. It is expected that until macroslip occurs, the linear

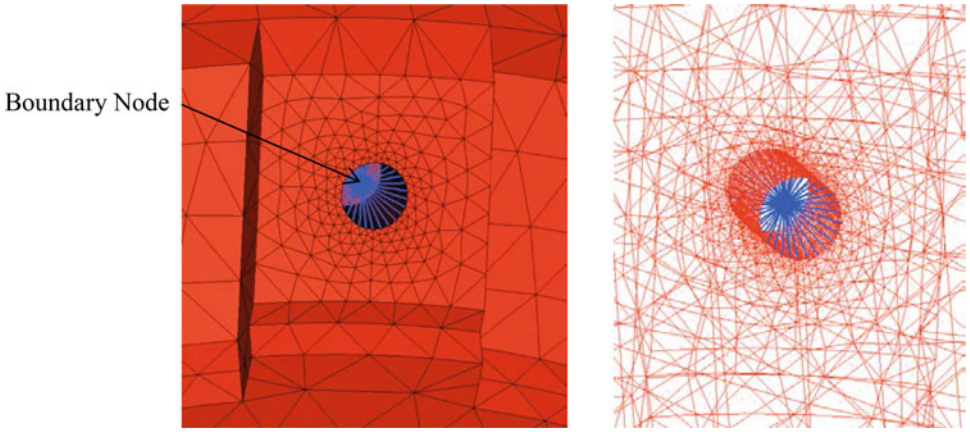

Fig. 21.17 Boundary node, internal thread region

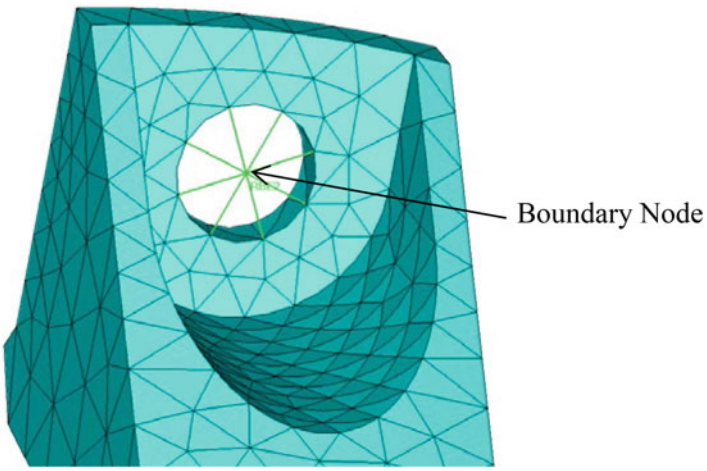

Fig. 21.18 Boundary node, bolt head region

model results, the nonlinear model results and the experimental data should all be similar. Once macroslip occurs, there should be a difference between the linear and nonlinear results, but the nonlinear results and the experimental results should be similar.

21.5 Analysis Results

Experiments 7–10 were used for comparison of experimental results to modeling results. In these experiments, the bolted joints were preloaded with 70 in-lbs of torque which is equivalent to roughly 1400 lbs of axial load in the bolts. The same configuration was modeled in ADAMS and the results are compared between the experimental data, the linear solution from ADAMS and the nonlinear solution from ADAMS. The comparisons which follow are for a 63 G peak acceleration, a 89 G peak acceleration and 125 G peak acceleration.

21.5.1 Analysis Results, 63 G Peak Acceleration

For a peak acceleration of 63 Gs, Fig. 21.19 shows the predicted velocity at each side of the critical joint, Fig. 21.20 shows the acceleration of the upper component (linear analysis, nonlinear analysis and experimental) well away from the joint and Fig. 21.21 shows the SRS for the same three quantities. Examination of the velocity at each side of the joint shows that

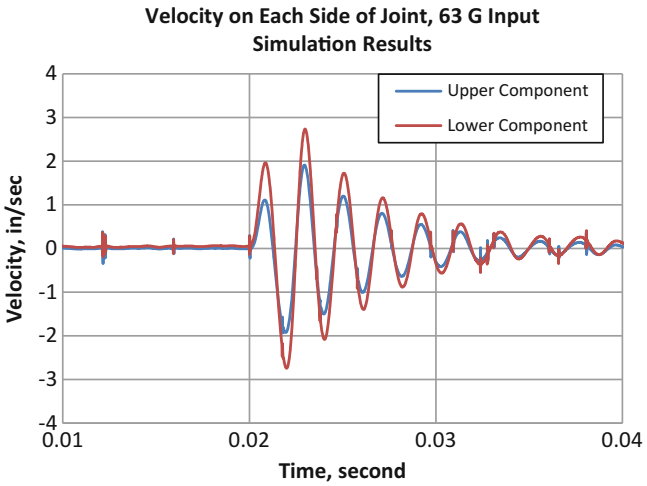

Fig. 21.19 Joint velocity, 63 G peak acceleration input

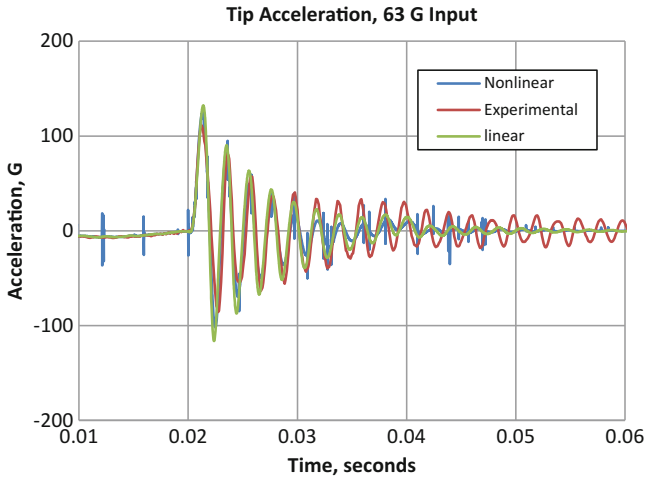

Fig. 21.20 Upper component acceleration, 63 G peak acceleration input

little or no slipping has occurred and the response is quite linear. Comparison of the accelerations in Fig. 21.20 and of the acceleration SRS in Fig. 21.21 also confirm that the response is linear. There is very good agreement between the linear model, the nonlinear model and the experimental data. The spikes in the simulated data are numerical noise as evidenced by the width of the spikes which is equivalent to the integration time step.

21.5.2 Analysis Results, 89 G Peak Acceleration

For a peak acceleration of 89 Gs, Fig. 21.22 shows the predicted velocity at each side of the critical joint, Fig. 21.23 shows the acceleration of the upper component well away from the joint and Fig. 21.24 shows the SRS for each of the same three quantities. The discrepancy in the velocity measured at each side of the joint shows that slipping has occurred in the first half cycle of the response. Comparison of the accelerations from Fig. 21.23 confirms a change in the period of the response for the linear solution vs. the nonlinear solution and the experimental data. The SRS from Fig. 21.12 also shows that reduction in acceleration amplitude which is due to the energy loss due to macroslip. The high frequency asymptote (peak Gs) is higher for the simulation than for the experiment as the peak acceleration is higher in the simulation than that measured in the test. This higher peak acceleration is only evident in the first cycle of response and this is reflected in the SRS shown in Fig. 21.24.

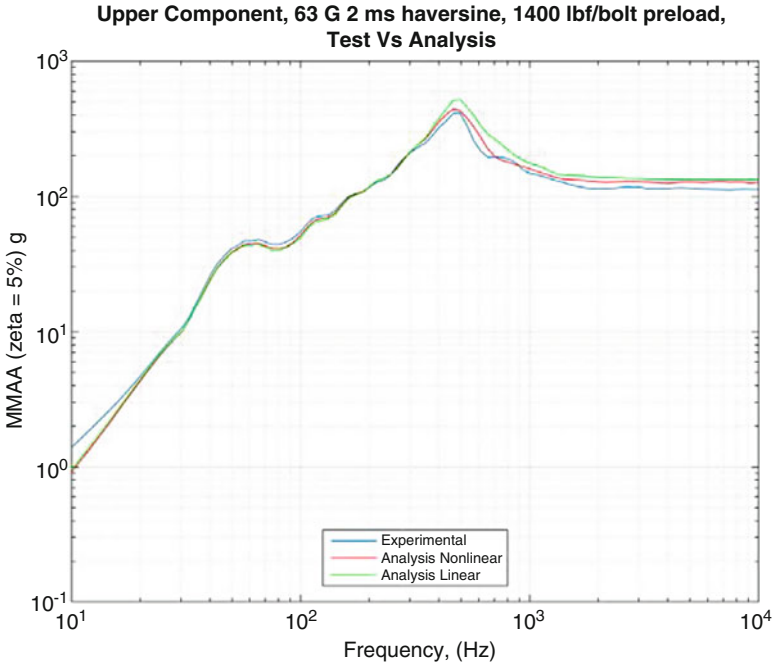

Fig. 21.21 Upper component acceleration SRS, 63 G peak acceleration input

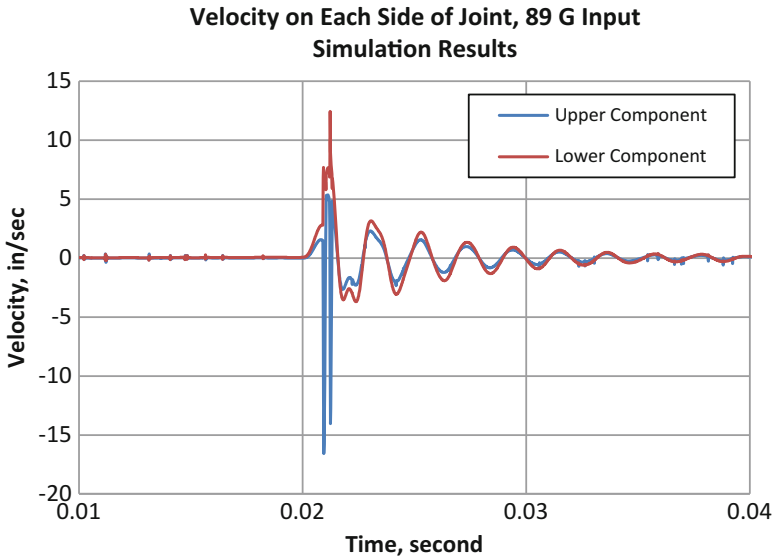

Fig. 21.22 Joint velocity, 89 G peak acceleration input

21.5.3 Analysis Results, 125 G Peak Acceleration

For a peak acceleration of 125 Gs, Fig. 21.25 shows the predicted velocity at each side of the critical joint, Fig. 21.26 shows the acceleration of the upper component well away from the joint and Fig. 21.27 shows the SRS for each of the same three quantities. The discrepancy in the velocity measured at each side of the joint shows that slipping has occurred in the first full cycle of the response. Comparison of the accelerations in Fig. 21.26 confirms a change in the period as well as the amplitude of the response for the linear solution vs. the nonlinear solution and the experimental data. The nonlinear solution acceleration

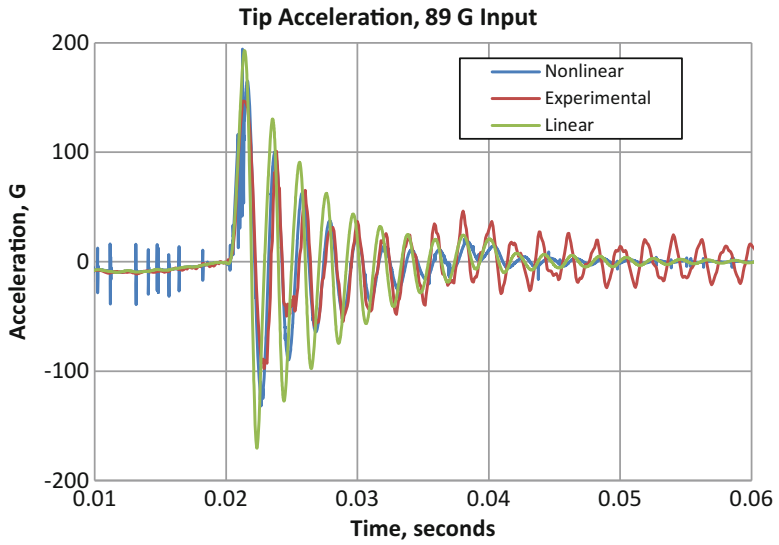

Fig. 21.23 Upper component acceleration, 89 G peak acceleration input

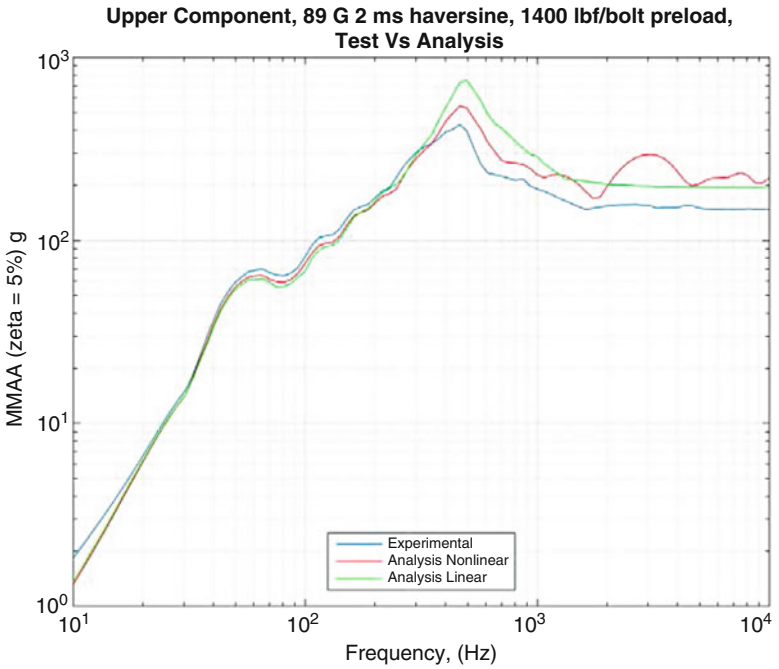

Fig. 21.24 Upper component acceleration SRS, 89 G peak acceleration input

peaks are higher than the experimental data for the first cycle and lower than the experimental data for subsequent cycles, but the period of the nonlinear solution very closely matches that of the experimental data. The SRS shown in Fig. 21.27 also shows a significant reduction in acceleration amplitude which is due to the energy loss due to macroslip. As was for the previous results, the high frequency asymptote (peak Gs) is higher for the simulation than for the experiment.

21.6 Summary

The experiments performed produced various levels of macroslip at a bolted interface depending on preload and peak acceleration of the input. Macroslip was induced at the bolted connections, and identified via accelerometers at various locations on the structure. A representative experiment was selected and modeled using a combination of linear finite

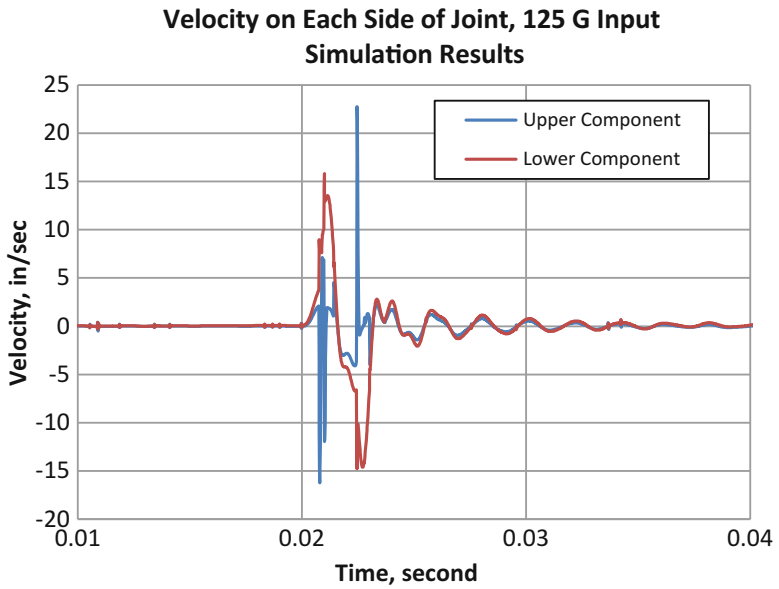

Fig. 21.25 Joint velocity, 125 G peak acceleration input

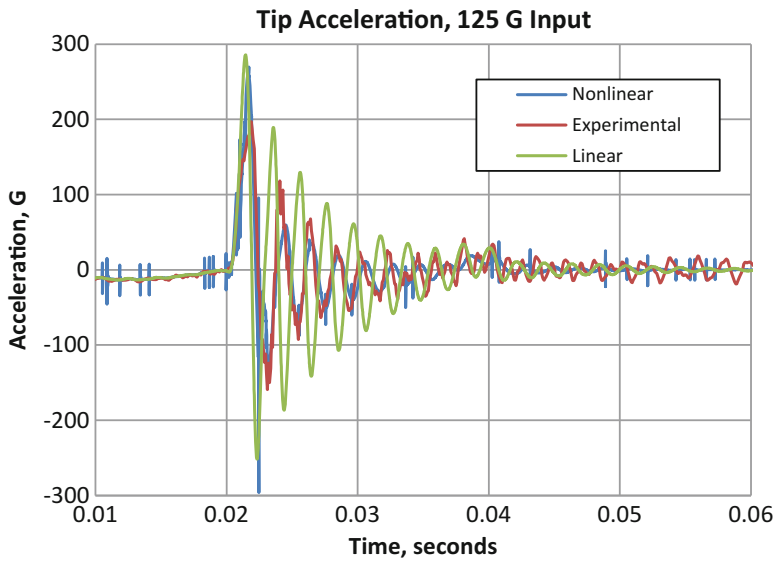

Fig. 21.26 Upper component acceleration, 125 G peak acceleration input

elements within a nonlinear multi-body dynamics solver with conventional numerical integration schemes. The modeling techniques described herein were able to improve the ability to capture macroslip in the finite element model representation of the structure, and to prevent massive over-prediction of the response of a structure to a large shock load in which macroslip is induced. This approach shows promise for improving analysis capabilities when dealing with mechanical assemblies which experience macroslip at bolted interfaces.

Acknowledgements The authors would like to thank Fernando Bitsie and Glen White for performing the testing. In addition thanks go to Todd Simmermacher and David Weigand for their support in completing this work.

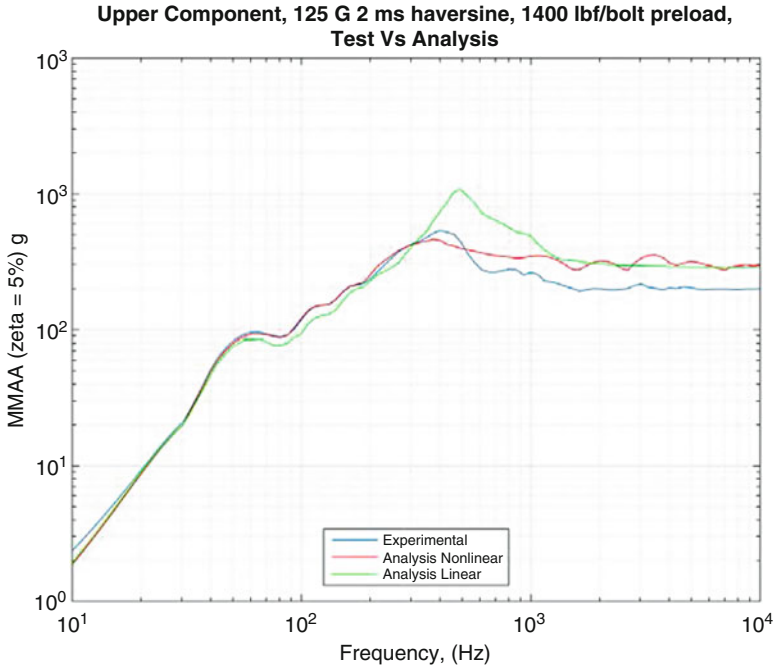

Fig. 21.27 Upper component acceleration SRS, 89 G peak acceleration input

References

1. Brake, M.R.W: A Reduced Iwan Model That Includes Pinning for Bolted Joint Mechanics. Technical Report SAND2015-8624C. Sandia National Laboratories, Albuquerque (2015)
2. Mayes, R.L.: A Feasibility Study for Experimentally Determining Dynamic Force Distribution in a Lap Joint. Technical Report SAND 2013–9582. Sandia National Laboratories (2013)
3. Segalman, D.J.: Observations on Simulation of Joint Friction. Technical Report SAND99-0599C. Sandia National Laboratories, Albuquerque (1999)
4. Segalman, D.J.: Modeling Joint Friction in Structural Dynamics. Technical Report SAND2005-2811J. Sandia National Laboratories, Albuquerque (2005)
5. Segalman, D.J., Starr, M.J.: Relationships Among Certain Joint Constitutuive Models. Technical Report SAND2004-4321. Sandia National Laboratories, Albuquerque (2004)
6. Segalman, D.J., et al.: Handbook on Dynamics of Jointed Structures. Technical Report SAND2009-4164. Sandia National Laboratories, Albuquerque (2009)

Chapter 22
A Reduced Iwan Model that Includes Pinning for Bolted Joint Mechanics

M.R.W. Brake

Abstract Bolted are joints are prevalent in most assembled structures; however, predictive models for the behavior of these joints do not yet exist. Many calibrated models have been proposed to represent the stiffness and energy dissipation characteristics of a bolted joint. In particular, the Iwan model put forth by Segalman and later extended by Mignolet has been shown to be able to predict the response of a jointed structure over a range of excitations once calibrated at a nominal load. The Iwan model, however, is not widely adopted due to the high computational expense of implementing it in a numerical simulation. To address this, an analytical, closed form representation of the Iwan model is derived under the hypothesis that upon a load reversal, the distribution of friction elements within the interface resembles a scaled version of the original distribution of friction elements. Additionally, the Iwan model is extended to include the pinning behavior inherent in a bolted joint.

Keywords Joint Mechanics • Iwan model • Pinning • Friction • Hysteresis

22.1 Introduction

One of the great remaining challenges in classical structural dynamics and solid mechanics is the prediction of the behavior of a jointed connection. Despite the prevalence of jointed connections in engineering structures, predictive models do not exist for several reasons: in most applications there is no penalty for over designing a joint to ensure that it survives most realistic loading scenarios, the physics to predict the behavior of a joint is reliant upon an improved understanding of friction (which is a nontrivial undertaking), and what joint models do exist are often computationally burdensome (which results in analysts favoring simplistic and hopefully conservative representations instead). However, in several industries (aerospace, defense, automotive, etc.) there is becoming a pressing need to better understand the behavior of a jointed connection. In many of the pertinent applications, the jointed connections are part of a system that will only be fabricated a small number of times and that has strict weight and space limits (increasing the penalty for over designing the joint). Conventional approaches to modeling the joint, due to harsh loading environments and nonlinearities, often are not as conservative as an analyst anticipates. In fact, the use of linear models, calibrated at low excitation levels, significantly over predict the energy dissipation and joint stiffness at high load levels. Consequently, a number of failures have been reported in recent years that are related to bolted joints (see, for instance, [3]).

The present research is motivated by one particular class of joint models that are used in finite element analysis as well as analytical mechanics and reduced order models: the Iwan model. The broad category of constitutive models referred to as Iwan models are used to model dissipative behavior with a single degree of freedom. These models originally were applied to elastic-plastic material responses [5, 6] and have more recently been adapted to joint mechanics [11, 12]. In particular, the four-parameter Iwan model [11] regularizes the joint interface to be represented by a single degree of freedom. The four-parameter Iwan model is, essentially, a constitutive model that describes the hysteretic behavior of micro- and macroslip across a jointed interface and replaces the kinematics of the adjacent interfacial surfaces with a nonlinear constitutive model.

Sandia National Laboratories is a multi-program laboratory managed and operated by Sandia Corporation, a wholly owned subsidiary of Lockheed Martin Corporations, for the U.S. Department of Energy's National Nuclear Security Administration under Contract DE-AC04-94AL85000.

M.R.W. Brake (✉)
Sandia National Laboratories†, P.O. Box 5800, MS 1070, Albuquerque, NM 87185-1070, USA
e-mail: mrbrake@sandia.gov

© The Society for Experimental Mechanics, Inc. 2016

M. Allen et al. (eds.), *Dynamics of Coupled Structures, Volume 4*, Conference Proceedings of the Society for Experimental Mechanics Series, DOI 10.1007/978-3-319-29763-7_22

The model's constitutive parameters can be populated either with representative experimental data or deduced from fine mesh finite element analysis. The constitutive formulation is fundamentally that of a Preisach model and has basis in [1, 4–6, 9, 10]. More recently, the Iwan model has been extended to be considered in modal space (as opposed to physical coordinates) [2].

One difficulty present in the implementation of the Iwan model is its high computational cost. The Iwan models used for the analysis of bolted joints are based on a discretized set of dry friction sliders [11]. This discretization leads to the need to store the individual state of each dry friction slider in the model, effectively increasing the degrees of freedom from one to an arbitrarily large number. In what follows, a reduced formulation of the Iwan model is derived based on the assumption that when a load reversal occurs, the state of each dry friction slider is reset (this assumption is discussed in Sect. 22.2.2.1. While this is a subtle change from the four-parameter Iwan model formulated in [11], both the new and old models are still approximations that can be calibrated to fit the data accurately, and the resulting model thus does not lose applicability from this new assumption.

22.2 Analytical Development

Conceptually, there are three distinct regimes for the model, as can be seen in Fig. 22.1: microslip ($0 \leq \delta < \phi_{MAX}$), macroslip ($\phi_{MAX} \leq \delta < \delta_P$), and pinning ($\delta_P \leq \delta$). In what follows, these three regimes will be calculated as part of two separate calculations: one calculation for the force due to the Iwan model, which includes micro- and macroslip, and one calculation for the pinning force.

22.2.1 Pinning Force

The pinning force occurs when the shank of the bolt engages the edge of the through hole (of diameter $2\delta_P$) in which it is located. This contact is thus between two cylindrical surfaces. If no plasticity is assumed to occur, this can be modeled using Hertz's [8] elastic contact formulation for two cylinders

$$F_{PIN} = \frac{\pi}{4} E^* L d. \tag{22.1}$$

For this formulation, E^* is the effective modulus of the two materials in contact (each having elastic modulus E_j and Poisson's ratio ν_j)

$$E = \left(\frac{1 - \nu_1^2}{E_1} + \frac{1 - \nu_2^2}{E_2} \right)^{-1}. \tag{22.2}$$

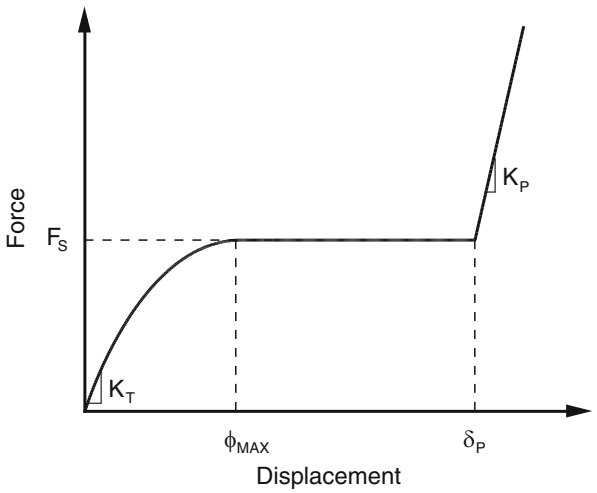

Fig. 22.1 Illustrative drawing of the constitutive force F for a bolted joint as a function of displacement δ

The engagement length of the bolt's shank with the through hole (i.e. the height of the hole) is L, and d is the interference/contact displacement of the two surfaces. As (22.1) is linear in d, F_{PIN} can be expressed as a spring force $F_{PIN} = K_P d$ with stiffness

$$K_P = \frac{\pi}{4} E^* L. \tag{22.3}$$

All parameters needed to define K_P are based on material and geometric properties, which can be easily determined.

22.2.1.1 Relation of Relative and Global Displacements for the Iwan and Pinning Forces

In what follows, the relative displacement u is defined to be positive in the slip direction. Additionally, δ_0 is defined to be the global displacement of the system at the start of a slip event (e.g. a load reversal), and F_0 is defined to be the force due to the Iwan element at the start of a slip event. In order to relate the force due to the Iwan model and the force due to pinning,

$$\delta = \delta_0 + u. \tag{22.4}$$

This relationship establishes the constraint that at $u \geq \delta_P - \delta_0$, the pinning force is engaged

$$F_{PIN} = \pm H|u + \delta_0 \mp \delta_P| K_P (u + \delta_0 \mp \delta_P). \tag{22.5}$$

22.2.2 Four-Parameter Iwan Model Overview

For both the micro- and macroslip regimes, the Iwan model is proposed. As a starting point, the four parameter Iwan model developed in [11] is used. In that research, the constitutive representation for the Iwan forces is

$$F_{IWAN} = \int_0^\infty \rho(\phi) \left(u(t) - x(t, \phi)\right) \mathrm{d}\phi, \tag{22.6}$$

which describes a distribution $\rho(\phi)$ of dry friction sliders (Jenkins elements) such as shown in Fig. 22.2. Note that in [11], the global displacement U is used in place of the relative displacement u; this substitution is made, though, without loss of generality in what follows due to the introduction of F_0 and δ_0, mentioned above. The jth slider has instantaneous displacement $x_j = x(t, \phi_j)$, and transitions from sticking to sliding at a displacement of $x_j = \phi_j$. The choice of distribution $\rho(\phi)$ is a nontrivial task, and several choices are discussed in what follows. For the model proposed in [11], the general form of the hysteresis loop is illustratively shown in Fig. 22.3.

The four-parameter Iwan model of Segalman [11] is subject to the two Masing conditions (which are both visible in Fig. 22.3): the forward and backward curves are reflections of one another and are scaled to fit between the initiation of the loading point and the force for macroslip, and that if a trajectory intersects the curve of a previous loading cycle, then it will change to follow the previous curve. In what follows, the first Masing condition is exploited: a displacement in the negative direction is the same as a displacement in the positive direction with a change of coordinates. The second Masing condition, though, due to possible transitions from microslip to macroslip to pinning, is neglected. By assuming that this condition can be neglected, the need for a burdensome approach that tracks the history of previous loading cycles, can be eliminated from this reduced formulation (a challenge that is evident in models such as [12, 14]).

The distinguishing feature of the Iwan model is the proposed distribution of Jenkins elements $\rho(\phi)$, each element of which slips once they have been stretched a distance ϕ. In [11], the proposed distribution (shown in Fig. 22.4a) is

$$\rho(\phi) = R\phi^\chi \left(H(\phi) - H(\phi - \phi_{MAX})\right) + S\delta(\phi - \phi_{MAX}) \tag{22.7}$$

$$R = \frac{F_S(\chi + 1)}{\phi_{MAX}^{\chi+2}\left(\beta + \frac{\chi+1}{\chi+2}\right)} \tag{22.8}$$

$$S = \frac{F_S}{\phi_{MAX}} \frac{\beta}{\beta + \frac{\chi+1}{\chi+2}} \tag{22.9}$$

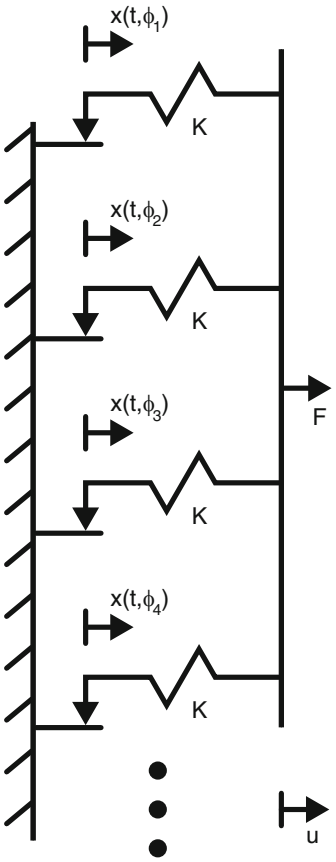

Fig. 22.2 Illustrative drawing of an Iwan model as a parallel arrangement of dry friction sliders

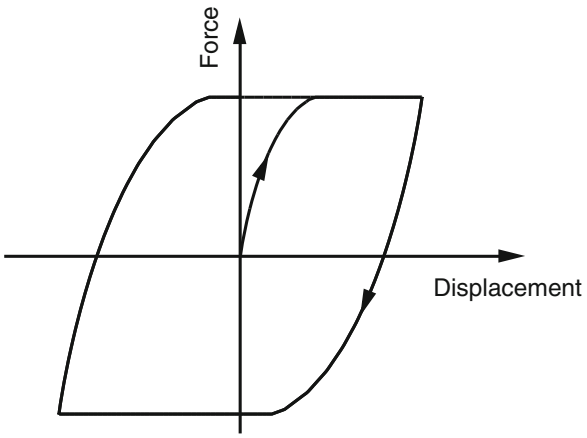

Fig. 22.3 Illustrative drawing of a typical hysteresis curve for a four-parameter Iwan model described by Segalman [11]

$$\phi_{MAX} = \frac{F_S(1+\beta)}{K_T\left(\beta + \frac{\chi+1}{\chi+2}\right)}, \tag{22.10}$$

with Heaviside step function $H(\cdot)$ and Delta function $\delta(\cdot)$. In this formulation, $3+\chi$ is the energy dissipated per cycle of small amplitude oscillation. Thus, $-1 < \chi \leq 0$ in this model. The distribution ρ is a power law relationship that is truncated at ϕ_{MAX} with a Delta function. The ratio of the stiffness of the Delta function portion of the distribution S to the power law portion of the distribution R is defined as β

$$\beta = \frac{S}{R\phi_{MAX}^{\chi+1}/(\chi+1)}. \tag{22.11}$$

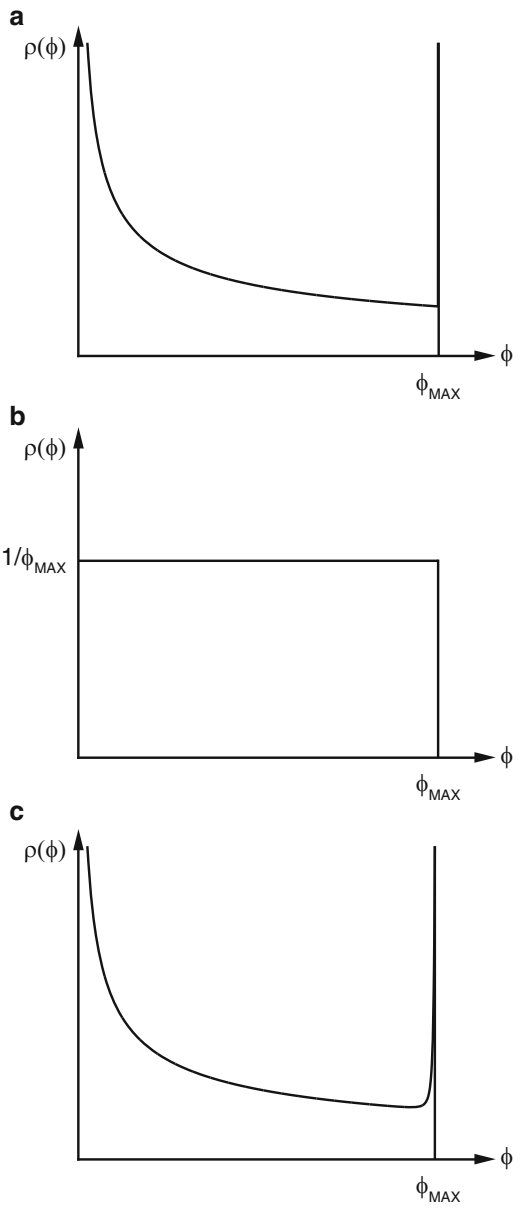

Fig. 22.4 Illustrations of (**a**) the distribution of Segalman [11], (**b**) the uniform distribution of [5], and (**c**) Segalman's proposed distribution

Note that with the definition of β, the model of Segalman [11] can be posed in terms of F_S, K_T, χ, and β, as opposed to a different set of parameters that are more difficult to directly measure (e.g. F_S, R, S, and ϕ_{MAX}). The relationships of Eqs. (22.8)–(22.10) are developed in [11] with this ease of model parameter determination in mind.

Observe that with the definition of u the quantity from Eq. 22.6

$$u - x(t,\phi) = \begin{cases} u & \text{if slider } \phi \text{ is stuck} \\ \phi & \text{if slider } \phi \text{ is sliding.} \end{cases} \tag{22.12}$$

Thus, define

$$\Gamma(u,\phi) = u - x(t,\phi) = \begin{cases} u & u < \phi \\ \phi & u \geq \phi. \end{cases} \tag{22.13}$$

Substituting Γ and ρ into Eq. 22.6 yields

$$F_{IWAN} = \int_0^{\phi_{MAX}} \Gamma(u,\phi) R \phi^{\chi} \mathrm{d}\phi + S\Gamma(u,\phi_{MAX}). \tag{22.14}$$

Based on Γ, this can be broken into two integrals

$$F_{IWAN} = \int_0^{u} R\phi^{\chi+1} \mathrm{d}\phi + \int_u^{\phi_{MAX}} uR\phi^{\chi} \mathrm{d}\phi + S\Gamma(u,\phi_{MAX}), \tag{22.15}$$

which has solution

$$F_{IWAN} = R\left(\left(\frac{1}{\chi+2} - \frac{1}{\chi+1}\right) u^{\chi+2} + \frac{\phi_{MAX}^{\chi+1}}{\chi+1} u\right) + S\Gamma(u,\phi_{MAX}). \tag{22.16}$$

Substituting Eqs. 22.8 and 22.9 gives the full expression for the Iwan forces

$$\begin{aligned} F_{IWAN} = {} & \frac{F_S(\chi+1)}{\phi_{MAX}^{\chi+2}\left(\beta + \frac{\chi+1}{\chi+2}\right)} \left(\left(\frac{1}{\chi+2} - \frac{1}{\chi+1}\right) u^{\chi+2} + \frac{\phi_{MAX}^{\chi+1}}{\chi+1} u\right) \\ & + \frac{F_S}{\phi_{MAX}} \frac{\beta}{\beta + \frac{\chi+1}{\chi+2}} \Gamma(u,\phi_{MAX}). \end{aligned} \tag{22.17}$$

In the limiting case of $u \geq \phi_{MAX}$, the Iwan force reduces to $F_{IWAN} = F_S$.

22.2.2.1 Considerations for Cyclic Loading

Two cases must be considered for the cyclic loading: loading to macroslip, and loading within the microslip regime. In loading to macroslip, all of the Jenkins sliders are, by definition, in slip. Thus the first Masing condition can be applied. For the first cycle of loading, it is assumed that $F_0 = 0$ and $\delta_0 = 0$. After the first cycle in which the joint is in macroslip, $F_0 = F_S$ (as F_0 doesn't include pinning forces), and each Jenkins element is fully stretched in the direction opposite from the new loading direction. For oscillations between two extremes (i.e. $-F_S$ and F_S), the first Masing condition [7, 11] yields

$$F_+(u) = -F_S + 2F_{IWAN}\left(\frac{\delta - \delta_0}{2}\right) \tag{22.18}$$

$$F_-(u) = -F_S - 2F_{IWAN}\left(\frac{\delta_0 - \delta}{2}\right). \tag{22.19}$$

The forces F_+ and F_- are for positive and negative loading cycles respectively. Essentially, Eqs. 22.18 and 22.19 have the form

$$F_\pm = \mp F_S \pm \gamma F_{IWAN}\left(\frac{\pm\delta \mp \delta_0}{\gamma}\right), \tag{22.20}$$

where γ scales the function appropriately.

In many vibratory environments, however, the limits of oscillation are not necessarily between the two extreme values. Thus, an incomplete case (e.g. never loading to the point of macroslip) must be considered. In the previously defined relative coordinate system for u, after a load reversal, $-F_0 > -F_S$, the Jenkins elements of strength ϕ are fully stretched in the direction opposite from the new loading direction for $\phi < u_0$, and are stretched a distance u_0 in the direction opposite from the new loading direction for $\phi > u_0$. As a result, Eq. 22.15 becomes

$$F_{IWAN} = \int_0^{u} R\left(\frac{\phi}{2}\right)^{\chi+1} \mathrm{d}\phi + \int_u^{\phi_{MAX}} uR\phi^{\chi} \mathrm{d}\phi + S\Gamma(u,\phi_{MAX}) - F_0, \tag{22.21}$$

for $u \leq 2u_0$, and, with $\psi = \phi - 2u_0$, for $u > 2u_0$

$$F_{IWAN} = \frac{1}{2^{\chi+1}} \int_0^{2u_0} R\phi^{\chi+1} \mathrm{d}\phi + \int_{2u_0}^{u} R\psi^{\chi+1} \mathrm{d}\psi + \int_u^{\phi_{MAX}} uR\phi^{\chi} \mathrm{d}\phi + S\Gamma(u, \phi_{MAX}) - F_0. \tag{22.22}$$

The form of Eq. 22.22 is a (nonlinearly) scaled version of Eq. 22.15. Thus, the hypothesis is proposed:

Hypothesis For an arbitrary load reversal, there is a new distribution of Jenkins elements that are now stuck that approximately resembles a scaled version of the original distribution of Jenkins elements.

As a first order approximation of the new distribution, a linear scaling function is used in which γ is bounded by $0 < \gamma \leq 2$. This leads to the functional form

$$F_{SLIDING} = \begin{cases} F_0 + \frac{F_S - F_0}{F_S} F_{IWAN}\left(u \frac{F_S}{F_S - F_0}\right) & \text{loading} \\ F_0 - \frac{-F_S - F_0}{-F_S} F_{IWAN}\left(-u \frac{-F_S}{-F_S - F_0}\right) & \text{reverse loading} \end{cases} \tag{22.23}$$

This is rewritten as

$$F_{SLIDING} = F_0 + \frac{F_S \mp F_0}{F_S} F_{IWAN}\left(\pm u \frac{F_S}{F_S \mp F_0}\right). \tag{22.24}$$

This relationship is predicate on F_0 being a global value such that $-F_S \leq F_0 \leq F_S$. The complete formulation for the RIPP joint model can now be expressed as

$$F_{RIPP} = F_{PIN} + F_{SLIDING}. \tag{22.25}$$

In the case of $\delta_0 \geq \delta_P - \phi_{MAX}$, this implies that macroslip is not necessary to achieve pinning. It should be noted, however, that the force F_0 should be determined solely from $F_{SLIDING}$ in order for the model to be consistent.

22.2.2.2 Comparison with the Discrete Four-Parameter Iwan Model

As a verification of the analytical RIPP joint formulation, the RIPP joint model (22.25) is compared to the discretized four-parameter Iwan model of Segalman [11] on which it is based in Fig. 22.5. The parameters for [11] are chosen based on a 304 Stainless Steel lap joint, such as found in [13], and are listed in Table 22.1. The range for the displacement to calculate the hysteresis curve is specified as ±2.25 mm. Outside of the pinning region, the two curves are coincident. Near the transition from microslip to macroslip, the discretization of Segalman [11] is evident under high magnification (as the curve appears faceted), but at the scale shown the two models are in complete agreement.

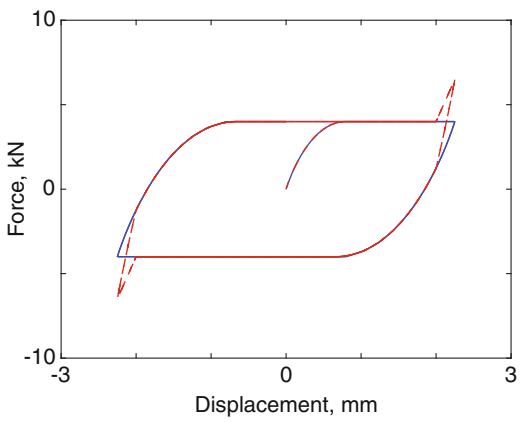

Fig. 22.5 Hysteresis curves for the discretized four-parameter Iwan model of Segalman [11] (*solid line*), and the RIPP joint model (*dashed line*)

Table 22.1 Joint parameters

Property	Value
Tangential stiffness, K_T	1.5×10^7 N/m
Macroslip force, F_S	4 kN
Dissipation exponent, χ	-0.5
Stiffness ratio, β	0.005
Pinning stiffness, K_P	10^7 N/m
Pinning clearance, δ_P	2 mm

22.2.3 Extension to the Five-Parameter Iwan Model

The five-parameter Iwan model, championed by Mignolet [15], belongs to a class of split Iwan models in which the response is split into two regimes. The fifth parameter is defined as the ratio between dynamic μ_D and static μ_S friction

$$\theta = \frac{\mu_D}{\mu_S}. \tag{22.26}$$

The conceptual split in this model is that once a Jenkins element begins to slide, it is governed by dynamic friction rather than the static friction that governed it in the stick state. The proposed distribution $\rho(\phi)$, though, remains the same. Consequently, the Iwan force becomes

$$F_{IWAN} = \theta \int_0^u R\phi^{\chi+1}\mathrm{d}\phi + \int_u^{\phi_{MAX}} uR\phi^{\chi}\mathrm{d}\phi + S\Gamma(u,\phi_{MAX}). \tag{22.27}$$

In the limiting case of $\theta = 1$, this reduces to Eq. 22.15. As before, the solution follows that

$$F_{IWAN} = R\left(\left(\frac{\theta}{\chi+2} - \frac{1}{\chi+1}\right)u^{\chi+2} + \frac{\phi_{MAX}^{\chi+1}}{\chi+1}u\right) + S\Gamma(u,\phi_{MAX}). \tag{22.28}$$

Substituting R and S yields the final form of the Iwan force equation for the five-parameter Iwan model

$$\begin{aligned} F_{IWAN} = {} & \frac{F_S(\chi+1)}{\phi_{MAX}^{\chi+2}\left(\beta+\frac{\chi+1}{\chi+2}\right)}\left(\left(\frac{\theta}{\chi+2} - \frac{1}{\chi+1}\right)u^{\chi+2} + \frac{\phi_{MAX}^{\chi+1}}{\chi+1}u\right) \\ & + \frac{F_S}{\phi_{MAX}}\frac{\beta}{\beta+\frac{\chi+1}{\chi+2}}\Gamma(u,\phi_{MAX}). \end{aligned} \tag{22.29}$$

In the limiting case of $u \geq \phi_{MAX}$,

$$F_{IWAN} = F_S\frac{\beta+\theta\frac{\chi+1}{\chi+2}}{\beta+\frac{\chi+1}{\chi+2}}, \tag{22.30}$$

which is less than F_S for $\theta < 1$.

In Fig. 22.6, the RIPP joint model of the four-parameter Iwan model is compared to the RIPP joint model of the five-parameter Iwan model with $\theta = 0.75$ and all other parameters the same as before. Both models exhibit the same tangent stiffness immediately after a load reversal; however the five-parameter model has a lower peak force due to $\theta < 1$. One unexpected consequence of this (coupled with the neglecting of the second Masing condition, as mentioned above) is that the maximum and minimum forces vary from one loading cycle to the next.

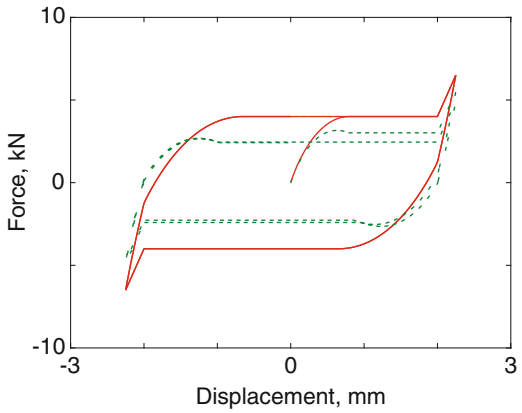

Fig. 22.6 Hysteresis curves for the RIPP joint model of the four-parameter Iwan model (*solid line*), and of the five-parameter Iwan model with $\theta = 0.75$ (*dashed line*)

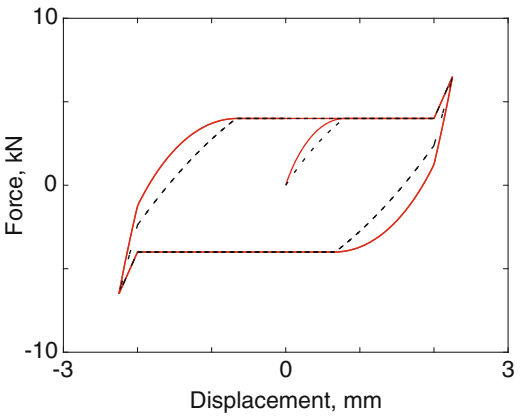

Fig. 22.7 Hysteresis curves for the RIPP joint model of the four-parameter Iwan model (—), and of the uniform distribution Iwan model (– –)

22.2.4 Extension to the Uniform Iwan Distribution

In [5], the Iwan element is formulated with a uniform distribution for ρ (Fig. 22.4b). The width of the distribution for the present work is taken to be ϕ_{MAX}, with a height of $1/\phi_{MAX}$. This distribution leads to the Iwan force

$$F_{IWAN} = \int_0^{\phi_{MAX}} \frac{c}{\phi_{MAX}} \Gamma(u, \phi) \mathrm{d}\phi. \tag{22.31}$$

The constant c is determined by setting the resulting solution equal to F_S, yielding

$$F_{IWAN} = \begin{cases} \frac{2F_S}{\phi_{MAX}} \left(u - \frac{u^2}{2\phi_{MAX}} \right) & u < \phi_{MAX} \\ F_S & u \geq \phi_{MAX}. \end{cases} \tag{22.32}$$

Using the same parameters as from Figs. 22.5 and 22.7 compares the hysteresis curves for the RIPP joint model of the four-parameter Iwan model to that of the uniform distribution Iwan model. Due to the uniform distribution for $\rho(\phi)$, the tangent stiffness appears much lower than for the four-parameter Iwan model. By definition, the macroslip forces and pinning behavior is the same for the two models though.

22.3 Summary

The analytical representation of the discretized Iwan model is formulated in this research for several different friction models: the four-parameter distribution of Segalman, the five-parameter distribution of Mignolet, and the uniform distribution originally used by Iwan. The advantage of an analytical representation of the Iwan model is a dramatic improvement in

computational time compared to the discretized Iwan model developed in [11]. The key hypothesis that enables the analytical formulation is that on a load reversal, there is a new distribution of sliders in sticking and slipping states that resembles a scaled version of the original distribution of sliders.

References

1. Bauschinger, J.: On the change of position of the elastic limit of iron and steel under cyclic variations of stress. In: Mitt. Mech. Tech. Lab, Munchen, vol. 13, pp. 1–115 (1886)
2. Deaner, B.J. et al.: Investigation of modal Iwan models for structures with bolted joints. In: 31st International Modal Analysis Conference (IMAC XXXI) Garden Grove, CA (2013)
3. Deckstein, D., Traufetter, G.: Weight loss for superjumbos: the A380 and the aviation engineering dilemma. In: Der Spiegel (2012)
4. Ishlinskii, A.Y.: Some applications of statistical methods to describing deformations of bodies. Izv. Akad. Nauk SSSR **9**, 580–590 (1944)
5. Iwan, W.D.: A distributed-element model for hysteresis and its steady state dynamic response. ASME J. Appl. Mech. **33**, 893–900 (1966)
6. Iwan, W.D.: On a class of models for the yielding behavior of continuous and composite systems. ASME J. Appl. Mech. **34**, 612–617 (1967)
7. Jayakumar, P.: Modeling and identification in structural dynamics Doctoral Dissertation. California Institute of Technology (1987)
8. Johnson, K.L.: Contact Mechanics. Cambridge University Press, Cambridge (1985)
9. Masing, G.: Self-stretching and hardening for brass. In: Proceedings of the Second Inter- National Congress for Applied Mechanics, pp. 332–335, 1926
10. Prandtl, L.: Ein Gedankenmodell zur kinetischen Theorie der festen Korper. Z. Angew. Math. Mech. **8**, 85–106 (1928)
11. Segalman, D.J.: A four-parameter Iwan model for lap-type joints. ASME J. Appl. Mech. **72**, 752–760 (2005)
12. Segalman, D.J., Starr, M.J.: Relationships among certain joint constitutive models Technical Report SAND2004-4321. Sandia National Laboratories, Albuquerque, NM (2004)
13. Segalman, D.J., et al.: Handbook on dynamics of jointed structures. Technical Report SAND2009-4164. Sandia National Laboratories, Albuquerque, NM (2009)
14. Smallwood, D.O., Gregory, D.L., Coleman, R.G.: A three parameter constitutive model for a joint which exhibits a power law relationship between energy loss and relative displacement. In: 72nd Shock and Vibration Symposium. Destin, FL (2001)
15. Wang, X.Q., Mignolet, M.P.: Stochastic Iwan-type model of a bolted joint: formulation and identification. In: 32nd International Modal Analysis Conference (IMAC XXXII) Orlando, FL (2014)

Chapter 23
Nonlinear Vibration Phenomena in Aero-Engine Measurements

Ibrahim A. Sever

Abstract Measured aero engine vibration responses vary in character and amplitude depending on the operating environment and prevailing loading conditions. When these responses are limited to linear dynamics range, existing analysis tools which are mostly targeted at such responses, can be used to analyse and characterise the underlying mechanisms. However when responses are nonlinear, use of the same tools may result in nontrivial errors or may not at all be applicable. Some methods have been put forward with the premise of dealing with nonlinearities in measured data. However, they are often very simplistic and cannot effectively deal with complexities an aero engine environment can produce. With designs getting more complex and non-traditional materials, such as composites, becoming more widely used; strong nonlinearities are becoming a more common occurrence. Therefore from industrial perspective, development of effective tools that can deal with identification, classification and eventually quantification of nonlinear features is a very real and present need.

In this paper, a number of scenarios, in which sufficiently strong nonlinear responses have been measured, will be presented. Approaches available to an industrial practitioner in such cases will be discussed. Areas that need development of new methods, as well as the degree of robustness with which such methods need to be deployed, will be outlined from an industrial perspective.

Keywords Nonlinear vibrations • Measurement • Identification • Characterisation • Quantification

23.1 Introduction

Aero engine vibration responses vary in character and amplitude depending on the operating environment and prevailing loading conditions. When these responses are limited to linear dynamics range, existing analysis tools that have been matured over the years [1], can be used to analyse and characterise the underlying mechanisms. However when responses are nonlinear, the use of the same tools may result in great errors and may lead to inefficient overdesigns. Therefore it is important to have appropriate tools in place to recognise the existence of nonlinearity in response to ensure that correct analysis is performed (Fig. 23.1).

Nonlinearities in aero engines are present at all levels from component to sub-system, all the way to whole engine level. Although challenges are present at all levels, they get progressively complex when moving from component to system level. As it stands, both experimental and simulation areas need significant capability development to effectively address these challenges. Given the complexities involved, nonlinear simulations are more demanding than linear ones and rely on accurate input parameters from adequate experiments. Test methods that can be used in fulfilling these requirements are not necessarily fit for purpose. Although recognising nonlinearity is rightly the first stage, understanding will have to go much further into assessing its strength, determining its location and identifying its character.

The end goal from industrial perspective is not only recognising the existence of nonlinearity qualitatively but also to be able to classify type of nonlinearity with appropriate means of providing quantitative assessment of underlying parameters. This is a formidable task, especially in the absence of precise knowledge of input force as is the case in engine environment, and cuts across various challenging branches of nonlinear research. Achieving all of these will require a combined effort from the research community. The purpose of this paper is to call for such unified action by presenting qualitative evidence for range of circumstances where significant nonlinearities are observed in operational responses.

I.A. Sever (✉)
Rolls-Royce plc., SinA-33, PO Box 31, Derby DE24 8BJ, UK
e-mail: Ibrahim.sever@rolls-royce.com

© The Society for Experimental Mechanics, Inc. 2016

M. Allen et al. (eds.), *Dynamics of Coupled Structures, Volume 4*, Conference Proceedings of the Society for Experimental Mechanics Series, DOI 10.1007/978-3-319-29763-7_23

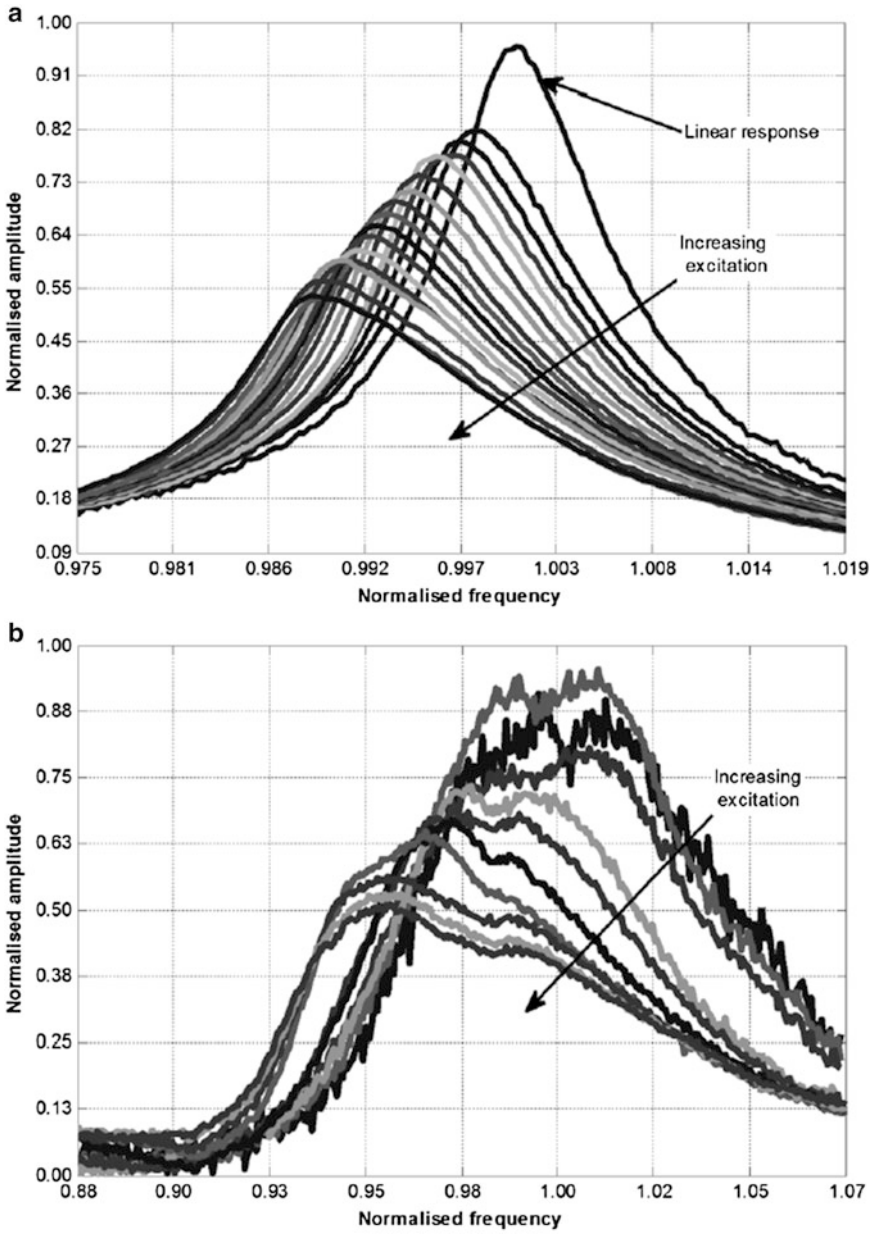

Fig. 23.1 (**a**) Effect of root damping on response amplitudes in a blade-in-root block experiment to increasing excitation force. (**b**) Effect of under-platform friction dampers on response amplitudes to increasing excitation force

23.2 Nonlinearity in Measured Data

There are two main mechanisms leading to presence of nonlinear responses in measurements: Nonlinearity as a consequence of undesirable behaviour (e.g. cracks, rubs etc.), and, nonlinearity as a consequence of normal behaviour of components in operating environment (e.g. bolted-joints, contact surfaces, friction damping devices, etc.). Although they may present themselves in similar ways, ability to separate them is critical to engine's health monitoring. Naturally, the former is of concern as resulting behaviour may threaten structural integrity. Therefore, uncovering early indicators to such behaviour is very valuable from engine manufacturer point of view. The latter on the other hand is often a desired, or even designed, behaviour where its presence may be welcome. Either way, tools and methods are needed to reliably identify existence of such behaviour from measured data. With that in place then follow up tasks involving their localisation, determining their type and quantify their defining parameters can be undertaken.

In following sections, a number of different scenarios in which nonlinearities in measured response are encountered will be presented. This will range from controlled laboratory testing undertaken on individual components to testing of sub-systems where a number of these components are assembled together, all the way to engine testing where the whole system is run in its actual operating conditions. In each case, evidence pointing to nonlinear behaviour will be presented. No effort will be made to identify the type of nonlinearity or quantify of its underlying parameters as main issue is precisely the lack of such suitable tools and methods to do so.

23.3 Component Level

Component level testing is often used in qualification of individual blades, vanes, blisks, pipes etc. to ensure they behave and perform to their design intent. Depending on the testing done and the phenomena pursued, the nonlinear responses measured may be readily explained if they are expected, or may be due to an unexpected phenomenon and will have to be evaluated.

Figure 23.1 shows results from a typical test setup put together for investigation of under-platform friction dampers where three adjacent blades are fixed in a representative blade-disk interface with possibility of inserting friction dampers between blades at platform level. These are metal inserts placed between adjacent blades in a turbine stage to provide friction damping and control otherwise excessive vibration amplitudes. In this case total friction damping is sum of that from under-platform dampers and blade-disk interface contact. In Fig. 23.1a, the effect of blade root contact alone is demonstrated in the absence of under-platform dampers, to increasing excitation force. Figure 23.1b, on the other hand shows results when the dampers are also present and actively contribute to total damping achieved.

In both cases the presence of nonlinearity due to friction interface is evident. As the excitation increases, total friction effect due to increased relative motion is also increased, leading to steady amplitude reduction. Reduction in natural frequency and steady build-up of asymmetry in raising and falling flanks of response curves, typical of nonlinear responses, is also present. In case of root damping alone (a), response curves present a more consistent and clearer trend, whereas, with the addition of under-platform dampers response curves are more complex. Nevertheless, in both cases, characterisation of the response curves for quantification of system properties is not readily available. Evaluation is often limited to correlation of these response curves with those from the predictions. Even this correlation is not straightforward or available in a robust manner. Typically, peak response amplitude will be compared for evaluation amplitude reduction rations. Attempts made at correlating response patterns are sensitive potential shifts in frequency axes and may not be true indications of actual correlation present.

Increased drive for optimised components is leading to more and more complex designs. Under such circumstances behaviours previously not encountered or infrequent are becoming commonplace, often in the form of nonlinear responses. Geometric nonlinearities are a good example to this. Figure 23.2, taken from [2], shows a results from a laboratory test carried out on an engine component at various excitation amplitudes, from low to high. Here a compressor rotor blade is fixed at the root and excited by a so-called Chopped Airjet excitation system where continuous air jets are “chopped” via a rotating perforated disk to create forcing at desired excitation frequencies. Linear, symmetrical response curves for the system (not shown here), are observed to get gradually nonlinear, with a clear softening spring nonlinearity emerging as excitation amplitudes are increased. Unlike previous under-platform damper example given above, root interface contact in this setup had very little nonlinear effect. This was confirmed experimentally by insignificant changes in response when clamping loads were changed through a wide range. The behaviour seen here is purely due to geometric nonlinearities where beyond a certain response amplitude significant deviations from expected linear response are observed. Naturally linear FE codes with embedded small-displacement assumption are not able to capture this behaviour. However the observed behaviour could be confirmed by a separate LS-Dyna simulations where this assumption is not imposed. In this case the root contact was modelled completely linear to demonstrate that it was not a driver for the observed nonlinearity.

23.3.1 Sub-System Level

Although significant nonlinearities can also be observed at component level as shown in the previous section, by far the biggest challenges are observed as two or more of these components are brought together to form sub-assemblies. The task is made complicated here due to increased number of interfaces, presence of joints; leading to complex interactions between the components involved.

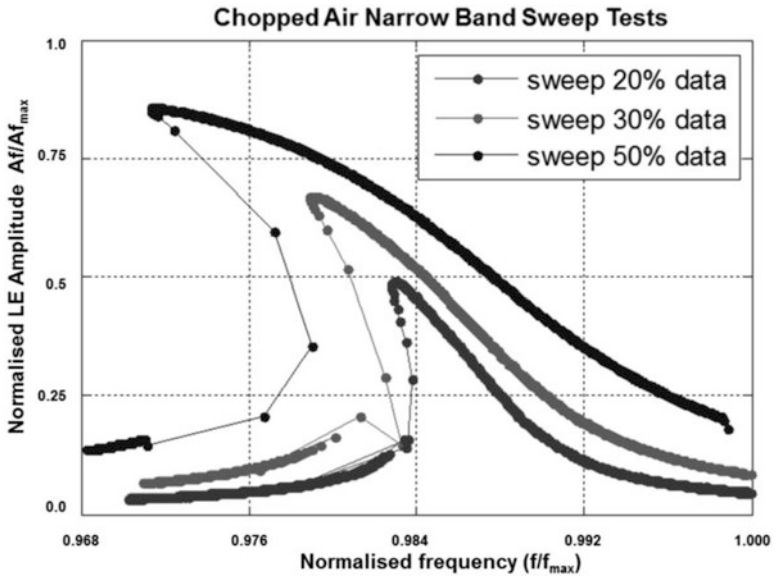

Fig. 23.2 Measured frequency response of an engine component with geometric nonlinearity [2]

Investigations into whole engine dynamics, particularly model validation activities targeting large structures such as casings and casing assemblies forming the engine carcass are a good example to this. In this activity, to ensure that a reliable, validated whole engine model is obtained, targeted tests are carried out to "correct" model properties so that such a model can be realised. Given the level of complexity one will have to deal with when engaging a whole assembly analysis, the common practice is to adopt a bottom-up approach where starting from a component-alone state, complexity is gradually increased by addressing uncertainties introduced at each stage along the way. Thus, for example, by the time two casings are assembled to analyse their combined behaviour, the main source of uncertainty is the interface between them since by that stage individual casing models would have been validated.

Figure 23.3 presents some results from modal analysis of an assembly formed of an engine casing with stator vanes. In Fig. 23.3a, results from casing alone prior fitting of vanes are shown. In this case the FRFs, as can be seen from the sample given, are clean, allowing successful extraction of system properties via conventional modal analysis tools. Correlation results, also given in Figure 23.3b, show that a good match is obtained in terms of mode shapes for all modes of interest (MAC > 80 %). However the picture is very different when the vanes are assembled in, as shown in Fig. 23.3c. Loose joints between the casing and the vanes, and, significant damping at these interfaces make it almost impossible to extract system properties successfully using the same modal analysis tools. Subsequent correlation with predictions is also very poor with most of the mode shapes not matching and natural frequencies significantly different.

Results presented in Fig. 23.3 expose two main problems. The first one is that the linear FE analysis carried out to predict the system normal modes when stator vanes are present is not adequate. However, even if the present nonlinearities could be modelled and more representative predictions could be produced, their counterparts from measured data could not be recovered as necessary characterisation techniques are not present. Significant advances, therefore, in both areas are needed to handle such cases. Bearing in mind that this behaviour is observed in a laboratory environment where excitation amplitudes applied were relatively small, the problem is likely to be exasperated in operating environment where forcing amplitudes are known to be much higher thereby exposing stronger interactions.

Following on from the example above, in its current state when a component alone is being investigated without any major interfaces or joints, the main challenges are in representing its mass and stiffness distributions correctly. In such cases refined enough models where these distributions are captured without any apologies can readily be created by available linear FE modelling tools. One can even argue that they can be predicted better than they can be measured in the absence of nonlinearities. This capability is currently exploited to evaluate design solutions in computer early on in the design phase before any manufacturing is done. It is important to note that this is only applicable to cases in which components are one integral piece without any interfaces, and, material properties are well-understood and can be modelled adequately. Although this could be argued to be true for metallic components, it is not so for composites which are now being more commonly used. A more pressing challenge with materials like composites is that nonlinearities do not only occur in high amplitudes

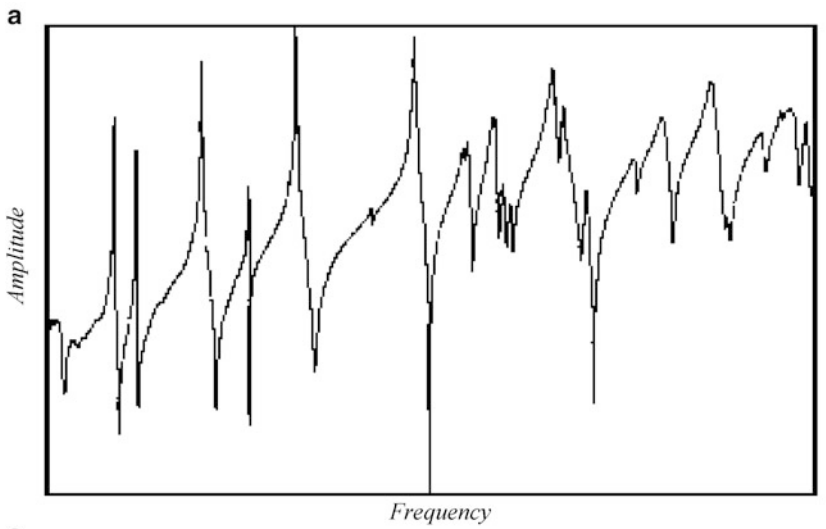

b

#	Diff.	MAC
1	-6.87	98.1
2	-7.06	96.4
3	-6.89	96
4	-6.82	94.4
5	-7.54	98.6
6	-7.27	98.3
7	-1.89	96.8
8	-1.81	96.5
9	-6.96	97.6
10	-7.55	97.3
11	0.75	95.3
12	0.66	93.1
13	-6.6	96.5
14	-6.86	95.6
15	-13.05	92.7
16	4.64	89.1
17	3.52	84.4
18	1.06	86.3
19	1.66	82

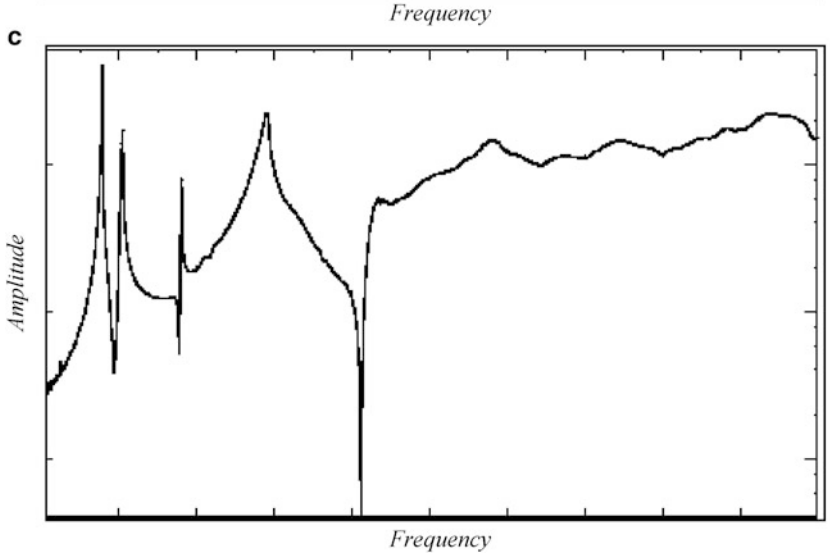

d

#	Diff.	MAC
1	-12.55	91.8
2	-12.05	89.8
3	-5.87	90.5
4	-6.53	90.1
5	-13.27	91.7
6	-13.39	89.8
7	5.96	76.7
8	4.96	51.6
9	-13.77	83.4
10	-13.62	65.9
11	-14.02	82.5
12	-13.63	37.7
13	-11.37	64.9
14	-11.37	54
15	-18.91	86.3
16	-34.65	12.2
17	-44.51	2.4
18	-18.56	84.7
19	-23.64	37.7

Fig. 23.3 (**a**) Sample FRF and (**b**) correlation results from a casing, (**c**) sample FRF and (**d**) correlation results for the same casing assembled with stator vanes

but are present throughout the dynamic response range. This, together with need to evaluate sub-system level dynamics when interface complexities are activated, highlights the urgent need for a structured and accessible approach to model validation that can work beyond its current linear reach.

23.3.2 System Level

The ultimate aim of Component and Sub-system level assessments presented in previous section is to help build confidence in individual constituents such that the task of whole system analysis is made manageable. The expectation, following on from the bottom-up approach mentioned earlier, is that by the time whole system dynamics is being looked at major uncertainties will have been addressed. However, system level testing is fundamentally different from that of component and sub-system cases where inputs and outputs are known. In the case of aero engines, system level testing refers to test bed runs where engine is operated through a set number of different cycles, often mimicing what it is ecpeted to do on wing. This means that forcing inputs are not precisely known even if they can be approximated in character and strength at some parts of the engine. As a result measurements are entirely of output-only in character. Not only that but since the real running environment is being operated, forces generated and subsequent responses measured are much higher and more complex in character than those of the component and sub-system level testing.

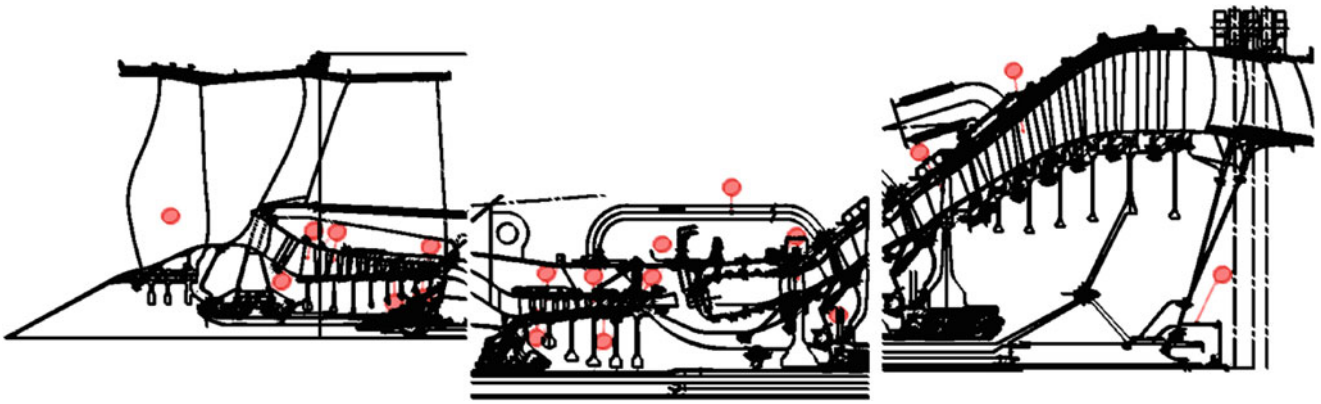

Fig. 23.4 A typical engine cross-section indicating (*red circles*) locations at which strong nonlinear vibration responses have been measured

It is not surprising that combined with a large number complex interfaces and different material combinations, such high amplitude responses should feature non-trivial nonlinearities. This beahviour is evident throughout the engine albeit to different degrees of severity. Figure 23.4 shows a schematic of an engine where strong nonlinearities were observed in measured dynamic responses. This is not a complete map but informative enough to indicate that it is not a local phenomenon to some parts of this complex machine. As can be seen from the distribution of red cricles, nonlinear responses are seen on blades, vanes, bolted casings, rotors, struts, pipes, brackets, external units, bearings, seals, as well as, parts that are made from complex novel materials such as composites.

Type of nonlinearity depends on underlying mechanism driving the response and depending on dominant mechanism at play, response characteristics vary. In the absence of a comprehensive identification strategy, main capability in recognising type of nonlinearity present is often achieved by examining the shape of forced response obtained. In an engine environment, forcing is predominantly a function of rotor speed, resulting in what is known as synchronous response (non-synchronous responses are also possible where observed behaviour is independent of rotor speed). Depending on the arrangement of blades and vanes in a given engine stage, forcing at the multiple of rotor speed, known as engine order excitation, can be generated. When vibration maps are plotted in the form of spectrograms, or zmods as they are more commonly known, with speed on x-axis, frequency on y-axis, and, vibration amplitudes plotted in the third dimension, the engine order lines appear as angled lines at the multiples of engine speed. A typical zmod is given in Fig. 23.5 complete with engine order lines and a typical mode indicated.

Figure 23.6 presents a selection of engine order tracks extracted from measured responses on a number of engine components, including blades and vanes. In these cases the engine is operated in such a way to sweep its operational speed range, from idle to maximum allowable speed, in a steady rate. Figure 23.6a–c show a number of responses with typical nonlinear characteristics. It is important to note that some of these responses, such as in Fig. 23.6b, are heavily nonlinear. Figure 23.6d shows that sweep direction dependent nature of nonlinear responses. Jump phenomenon seen in heavy nonlinearities can be clearly observed here in real engine measurements.

Nevertheless, in these cases, as mentioned before, only practical assessment criterion available to a measurement analyst tasked with recognition of nonlinearity is the degree of asymmetry in the response curves. This is a very limited, and sometimes even misleading, assessment means since the asymmetry in response curves is not always caused by a nonlinear mechanism. Depending on the engine operation in progress at the time (i.e. engine speed changes, abnormal scheduling etc.), it is perfectly possible to generate such curves that are not driven by an underlying nonlinear phenomenon. In addition, even if the response was driven by nonlinearity, there are many nonlinear mechanisms that result in the same or similar distortions in response curves that it may not be possible to tell what exactly is causing the observed behaviour.

Regardless of such complications, characterisation of these measured responses to the point of quantifying dominant parameters affecting the dynamics poses the greatest challenge yet. Given that the responses in question are not necessarily isolated and almost certainly due to combined effect of complicated interactions, this appears to be an optimistic prospect at this moment in time.

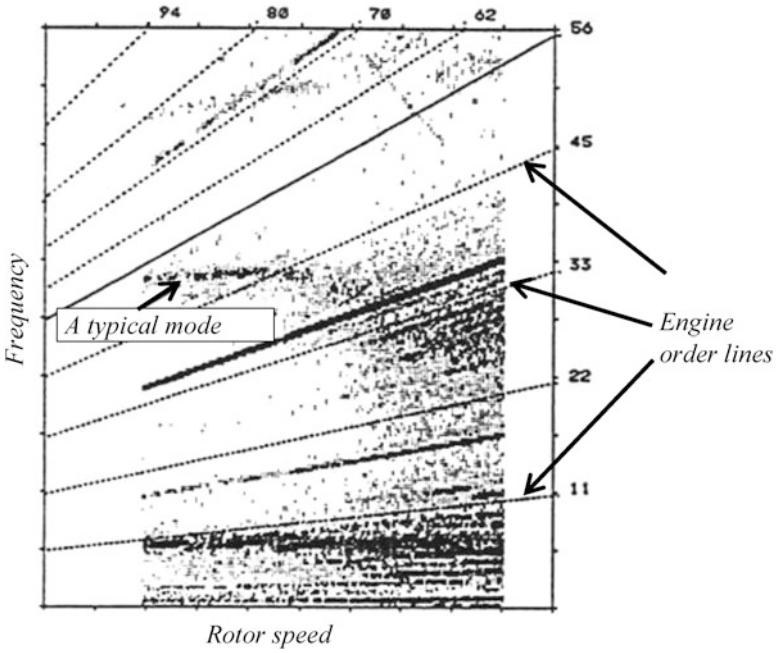

Fig. 23.5 A typical zmod showing engine order lines and dominant responses

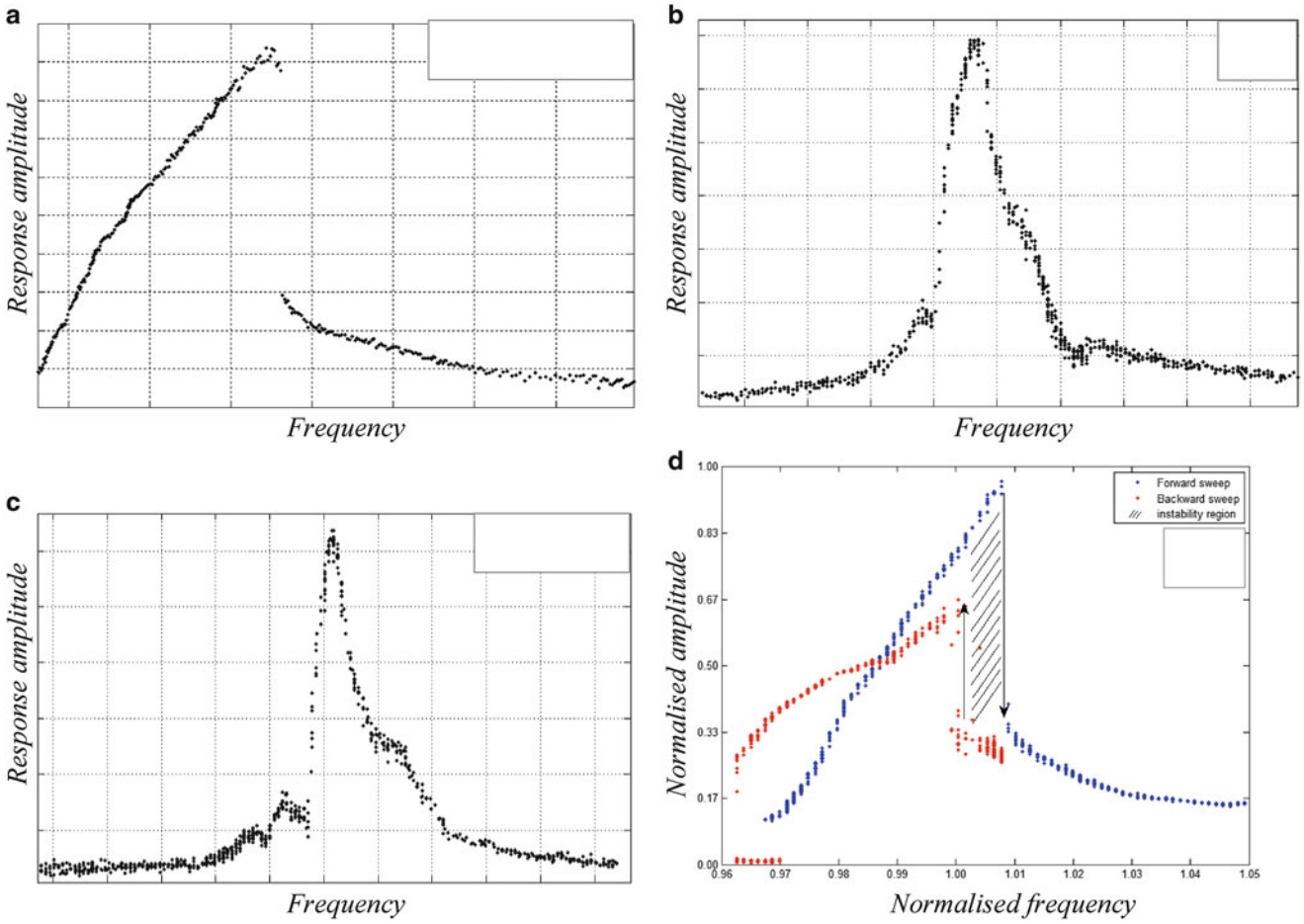

Fig. 23.6 Tracked order responses extracted from zmods showing nonlinear behaviour

23.4 Assessment of Nonlinear Responses

Given the diverse range of nonlinear responses presented in previous sections, spanning from component to whole system level, lack of capability to handle their characterisation in a robust manner is a major shortcoming. Nevertheless, depending on the environment (e.g. lab, rig, operation etc.) in which a given investigation is carried out; there are some tools and methods available that maybe used to assess nonlinearities. Although limited in scope, it is useful to document some of them here in order to establish the current capability.

Type and depth of assessment that can be applied depends on the nature of the way in which test data are acquired. What can be done greatly varies from a well-controlled lab test to an output only engine test where forcing is usually unknown or at best known only in character. With possibility of access to both excitation and response measurements, laboratory testing presents the best chance of truly evaluating some of the nonlinear behaviours. In this case characterisation is made possible via linearization of the nonlinear system via carefully executed amplitude-controlled measurements. Assuming that the system properties are the function of response amplitude, controlling the amplitude at the same level across a frequency range allows effectively the same system to be tested. Subsequent analysis is then straightforward as what is really exploited is the use of linear modal analysis tools. Figure 23.7a shows some of the linearized FRFs from such a test, and, Fig. 23.7b characterisation of damping from these curves as function of response amplitudes [3]. In this case for each level of response the same test is repeated to generate linear FRFs of Fig. 23.7a. Damping extracted from each FRF indeed reveals a steady variation, confirming the amplitude-dependent nature of this quantity.

Although this appears to be a neat solution to a complicated problem, the method presents some practical challenges. First of all, since the test is effectively repeated as many times as amplitudes at which controlling is done, it takes a long time. In a production environment time pressures associated with running costs and delivery deadlines almost certainly rule this out as a viable option. Even if this could be justified, depending on the range of frequencies over which the amplitudes are to be controlled, it may not be possible to achieve response levels away from resonance frequencies. This in return limits amplitude levels at which quantification can be carried out. As operational levels are of interest, often in the form of large amplitudes, it may not be possible to cater for the very dynamic range of interest.

In addition to output-controlled testing mentioned above, free decay response measurements are also used in characterising damping and natural frequency variations. In this case the, the component of interest is excited to sufficiently large amplitudes at one of its natural modes and then forcing is cut from the system suddenly. Assuming that that the free decay vibrations from that point on are in the mode of interest alone, cycle-to-cycle decay in amplitudes can be utilised to characterise both damping and frequency. However, in practice such tests are not suitable for all components often limited to blades and vanes. Having said that, impact-like responses from engine or rig environment, such as bird-strike, may be processed to similar effect. However, subsequent signal processing of the time domain data is not straightforward and extreme care should be taken.

Nonlinear characterisation tests are usually run to evaluate validity of a model put together with a claim to simulate such behaviour realistically. The objective is that once this is demonstrated via carefully gathered experimental evidence, the resultant model can be used in circumstances beyond what can be achieved in laboratory. A study of this kind at sub-system level was carried out in [3, 4]. Figure 23.8a shows the subsystem used, which is 2 casings assembled via a bolted flange

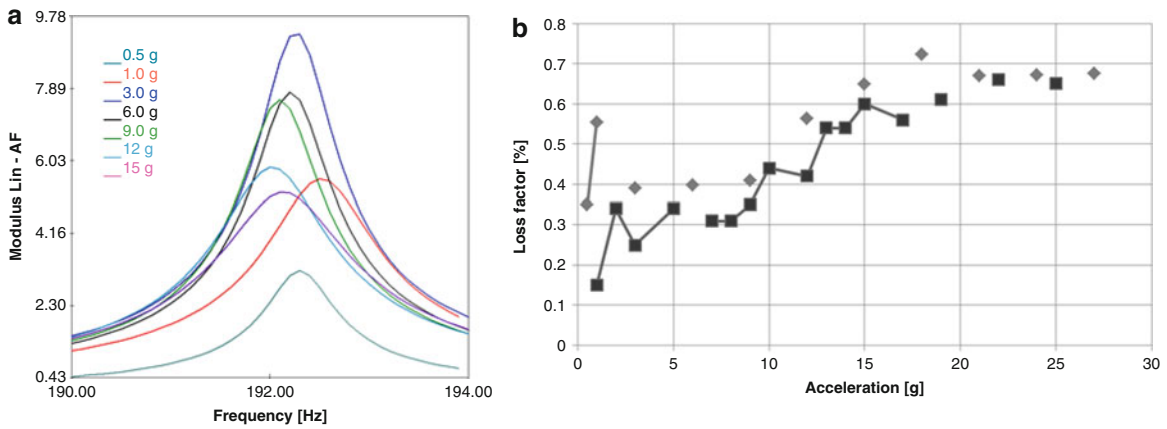

Fig. 23.7 (**a**) Linearized FRFs at different response levels, (**b**) Variation of damping as a function of response amplitude (*dark* and *light* sets are for different boundary conditions) [3]

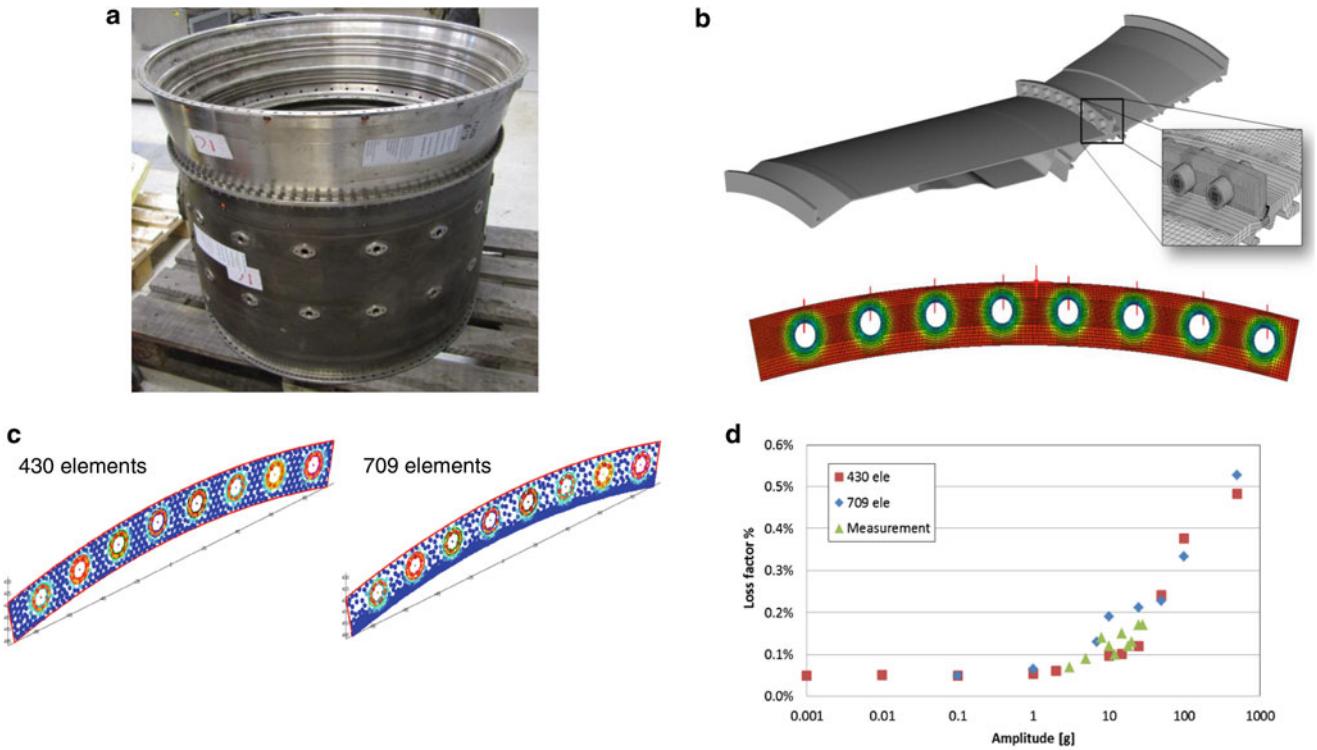

Fig. 23.8 (**a**) Sub assembly of two casings, (**b**) Sector model and static pressure distribution, (**c**) Different representations of nonlinear interface, (**d**) Damping comparison

joint in the middle. Also shown in Fig. 23.8d is the comparison of measurement results and the equivalent FE predictions, together with the details of FE model used in Fig. 23.8b, c. The measurements were carried out using amplitude-controlled testing described above. The linear elastic properties of the FE model and its individual parts were validated using linear model validation process described earlier in this paper. In order to capture the true nonlinear behaviour of bolted joints, a large number of nonlinear elements had to be used, as shown in Fig. 23.8c. The whole assembly problem got so complicated with such detailed description of each bolt that, only an 8-bolt section of whole sub-assembly could be modelled and tested.

Although the degree of correlation obtained in the context of complexity that could be modelled was a great success, it is clear this approach is far from being a capability that can be used in anger. Both testing and modelling requires long lead times as well as significant computational capabilities. Given that even a small sub-assembly had to be scaled down to make testing and modelling viable, extension of such an approach to larger assemblies or whole system are impractical.

If assessment capabilities in terms of nonlinearities for components and sub-assemblies were limited, then they are almost certainly in very short supply at whole system level. When it comes to output-only measurements there is very little room to manoeuvre. Current assessment tools and means for identification of presence of nonlinearities in measured responses from engine and rig tests, as well as from uncontrolled laboratory tests, are limited to observability of nonlinearity. No substantial effort, at this stage, is made to quantify nonlinear behaviour completely. Some limited capability is present for classification of nonlinearities. However this is not robust and fails to provide any clear insight when a combination of nonlinearities is present. Most of the assessment tools operate by exploiting the deviations from expected linear dynamic responses. For this purpose a number of measured and computed quantities are used, such as; time domain data, frequency domain data/zmods, tracked order responses/FRFs, Nyquist plots, damping carpets, etc. In most of these quantities, expected linear characteristics are well known. The deviations from these characteristics and the way in which these deviations manifest themselves are used as clues to presence of various common nonlinearities. Expected characteristics for given nonlinearities are derived through simulation of simple models. A sample map of such characteristics was given in [5] and are reproduced here for reference in Fig. 23.9. Guidelines are expressed mainly for SDOF behaviour which also holds for practical cases where modes of vibration are reasonably isolated. More complex cases, including nonlinearity in the vicinity of increased modal density, are not currently within reach and will no doubt require substantial research effort to advance.

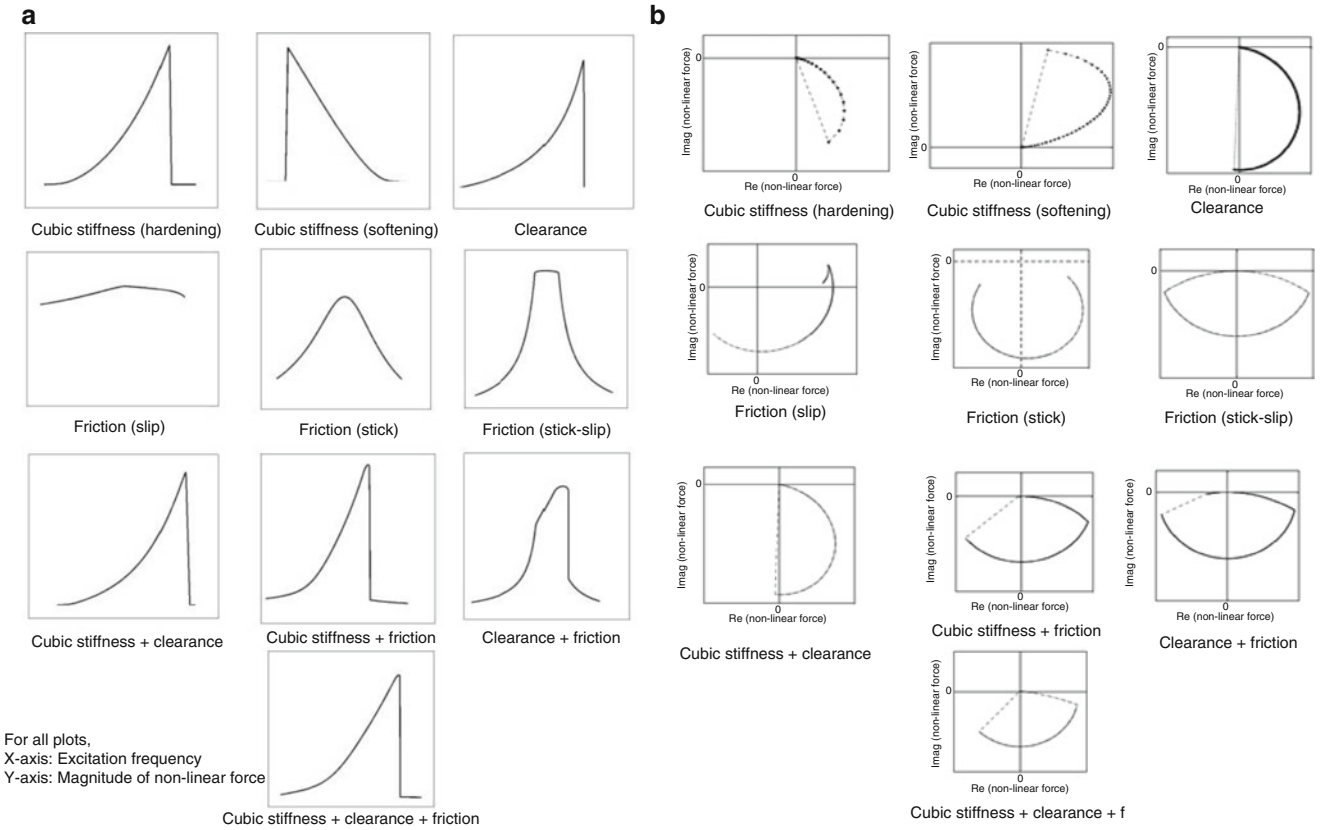

Fig. 23.9 Footprints for typical nonlinearities and their combinations: (**a**) Magnitude FRFs, and, (**b**) Nyquist plots (simulations on a 2-DOF system), taken from [5]

23.5 Capability Requirements

It is evident from the material presented so far that significant capability development is needed before true nature of nonlinear response can be understood and utilised in industrial applications. Following are key areas which will benefit from development of robust tools.

In its current state, performing nonlinear analyses, be it experimentally or via simulations, is a costly undertaking. As highlighted, high fidelity models require substantial computational power as well as taking a long time to run. Therefore it is imperative from industrial point of view that these simulations are only run when they are really needed. This means that reliable capability should be in place to recognise the presence of nonlinearities and strength with which their presence is affecting overall dynamic behaviour. Naturally for this to work, guidelines for defining weak and strong nonlinearities will have to be identified. This may very well be case specific and probably not straightforward. Even though at this stage no quantification is provided, it is still immensely beneficial in its own right as expensive simulations will not have to be run for cases in which nonlinearities are deemed not strong enough.

For cases in which handling of nonlinearities is found to be critical to total system behaviour, the character of nonlinearities at play will have to be identified. This is not a trivial problem as simple measures such as the way in which symmetry of frequency response curves is distorted about a resonance frequency are not always effective. In addition to character of nonlinearity, locations on the structure where they are activated also need identifying so that simulation models can be informed intelligently as to what needs to be modelled and where. Applications of some recent physics based localisation methods appear promising [6], but they need maturing for large scale industrial applications.

The ultimate aim, once nonlinearities are identified, characterised and localised, is to quantify its defining parameters. It is important that these parameters are physical such that they can be readily transferred to simulation models. The biggest challenge is from the operational data where forcing is not known and the responses are ultimately a combination of many factors at play. This can be very complex in an environment like the aero engine. Given the diverse operational boundaries and build variations any quantification effort will also have to come up with realistic bounds for nonlinear parameters.

Most of the established assessment tools are based on stress distributions obtained from linear dynamics analysis. Bearing in mind that nonlinearity changes stress distribution, the impact of this on assessment of high cycle fatigue for calculation of endurances will have to be investigated and new methods will have to be defined.

It is now possible to put together detailed explicit models for analysis of various nonlinear effects. However it takes a considerable specialist effort to generate these models and even more computational resource to run them. In some cases they end up being too complex that, generating operational boundaries according to expected variations in the input parameters for probabilistic solutions becomes impracticable in a development cycle. What is urgently needed is to focus collective research effort on development of models that are low fidelity in terms of model discretisation but yet adequate in terms of retaining key driving features. It is only through such low-fidelity, high-performance models that responsive design tools can be generated. Can ways in which test and simulations are fused be developed to close the gaps?

Clearly advances in modelling capability will have to be matched by similar improvements to experimental methods. As mentioned earlier in the paper, adequate testing for characterisation of nonlinear parameters currently takes too long and is not always effective. The main objective in current capability is to linearize the system so that existing analysis tools can be applied. Development of fit for purpose characterisation tools will allow handling of nonlinear responses directly. For them to be used in industrial applications routinely no less than conventional modal analysis equivalent of nonlinear dynamics needs to be developed.

Optimised designs of complex structures are resulting in intricately thin geometries. Some of the challenges with such structures begin at the manufacturing stage, well before they are installed in their operating environment. High speed machining of such structures is a particular area of concern where chatter, high nonlinearities and zones of instability etc. are real concerns. Optimal speeds of machining, effect of tip rubs and overall impact on eventual HCF life are areas where mature capabilities are an urgent need.

23.6 Conclusions

Need to develop ever so efficient aero engines means that so much effort is devoted to optimise individual components at earl design phases. This is resulting in new and complex geometries which are in turn presenting more challenging dynamic behaviours. One result of this is increased nonlinearities in dynamic response which are difficult to adequately simulate or analyse from measurements. The lack of understanding in dealing with these behaviours is often compensated by overdesigns, in the process undoing optimisation efforts made in the early stages.

In this paper evidence from various stages of engine development, from component to full assembly, were given where nonlinearities could be observed. Some of these are shown to be very strong that unless they are incorporated in modelling and analysis activities appropriately, their true impact cannot be accounted for. However the tools needed to satisfactorily do this are lacking both in terms of simulation capabilities and characterisation of measurement results.

Industry urgently needs easily accessible tools for recognition, localisation, characterisation and quantification of nonlinearities that are present in their designs. Ability to classify strength of nonlinearties in terms of effect they have on overall system dynamics is very important in making sure that available resource are used where they are needed. It is highly desirable to initiate serious engagement towards generation of low-fidelity, high-performance models such that design spaces can be evaluated in a cost effective manner. Equally, fast testing techniques together with efficient methods to characterise measurements acquired from these tests are also needed.

The word “nonlinearity” to an average engineer signals a very difficult task that is best avoided. This is so, despite so much academic activity in the subject which does not appear to be unified. It is necessary to focus this effort in an organised way with a purpose of developing tools that are effective in operational environment and therefore directly relevant to real industrial applications. Only then can confident steps towards deliberate use of nonlinearity be taken to leverage full advantages of such behaviour, as well as understanding their consequences. This way nonlinearity may finally be liberated from being a taboo and scary subject to one that is an enabler for better designs.

Acknowledgements The author is grateful to Rolls-Royce plc for allowing the publication of this work.

References

1. Ewins, D.J.: Modal Testing: Theory, Practice and Application, 2nd edn. Research Studies Press, Baldock (2000)
2. Peng, C., Miyakozawa, T., Schroeter, T., Schnitzler, J., Lyndon, I.: Nonlinear vibration behaviour of an axial compressor rotor blade. In: Proceedings of ASME Turbo Expo 2015, Montreal, 15–19 June 2015
3. Di Maio, D., Schwingshackl, C., Sever, I.A.: Development of a test planning methodology for performing experimental model validation of bolted flanges. J. Nonlinear Dyn. **12**, 1–20 (2015). doi:10.1007/s11071-015-2382-9
4. Schwingshackl, C., Di Maio, D., Sever, I.A., Green, J.S.: Modeling and validation of the nonlinear dynamic behavior of bolted flange joints. J. Eng. Gas Turbines Power **135**(12) (2013)
5. Gondhalekar, A. C.: Strategies for non-linear system identification. PhD Thesis, Imperial College (2009)
6. Delli Carri, A., Di Maio, D., Lucchetti, A., Sever, I.A.: Experimental model validation of a non-linear structure with lap-joint using the physical space approach. In: Proceedings of ISMA 2014 - International Conference on Noise and Vibration Engineering, Leuven, pp. 1185–1198, 15–17 Sep 2014

Chapter 24
Instantaneous Frequency and Damping from Transient Ring-Down Data

Robert J. Kuether and Matthew R. W. Brake

Abstract Broadband impact excitation in structural dynamics is a common technique used to detect and characterize nonlinearities in mechanical systems since it excites many frequencies of a structure at once. Non-stationary time signals from transient ring-down measurements require time-frequency analysis tools to observe variations in frequency and energy dissipation as the response evolves. This work uses the short-time Fourier transform to estimate the instantaneous parameters from measured or simulated data. By combining the discrete Fourier transform with an expanding or contracting window function that moves along the time axis, the resulting spectra are used to estimate the instantaneous frequencies, damping ratios and complex Fourier coefficients. This method is demonstrated on a multi-degree-of-freedom beam with a cubic spring attachment. The amplitude-frequency dependence in the damped response is compared to the undamped nonlinear normal modes. A second example shows the results from experimental ring-down measurements taken on a beam with a lap joint, revealing how the mechanical interface introduces nonlinear frequency and damping parameters.

Keywords Time-frequency analysis • Nonlinear vibrations • Instantaneous frequency • Instantaneous damping • Nonlinear normal modes

24.1 Introduction

Analyzing vibration responses in the frequency domain have long provided insight into the dynamics of linear structures, such as the identification of invariant modal frequencies and damping ratios from transient ring-down data. The most widespread tool for frequency domain analysis is the Fourier transform, partly due to the efficiency of the Fast Fourier Transform (FFT) algorithm [1]. One of the limitations to this method is that it only provides meaningful information to linear systems and responses that are stationary and periodic (albeit windowing a time signal lightens the latter requirement). Nonlinear systems and non-stationary time signals require a new set of tools for frequency domain analysis of transient responses. The review by Neild et al. [2] provides a thorough discussion of various time-frequency distribution tools such as moving window discrete Fourier transform, moving window auto-regressive model, and harmonic wavelet transform. These signal processing tools can be used to identify how the instantaneous frequency and damping of a measurement changes as a function of time, or response amplitude, providing system parameters conceptually similar those obtained from linear systems.

A number of techniques have been developed to estimate the time-varying frequency and damping from transient ring-down data. Feldman developed the 'FREEVIB' method in [3] by processing the free vibration response with the Hilbert transform and determining a single-degree-of-freedom (SDOF) modal model based on the analytic signal and its time derivatives. Later Sumali and Kellogg [4] improved on this method by fitting the analytic signal to a polynomial function in order to better estimate the phase and decaying envelope. The curve fitting procedure was developed to smooth the effects of noise during experimentation [4–6]. The method developed by Londoño et al. in [7] uses zero-crossing detection of the time signal to estimate the instantaneous frequency and decaying envelope of a nonlinear system.

The zero-crossing detection algorithm and Hilbert transform are somewhat limited when applied with broadband excitation because these methods assume the response behaves as a monophase, SDOF oscillator. These approaches require additional data processing (e.g. band-pass filtering) for signals with multiple harmonic components. One approach to process non-stationary signals with multiple harmonics uses empirical mode decomposition (EMD) to create a set of intrinsic mode functions that are then processed using a Hilbert transformation [8]. Vakakis et al. developed a nonlinear system identification and model reduction strategy [9–11] using EMD, wavelet transforms and slow flow constructions. Recently

R.J. Kuether (✉) • M.R.W. Brake
Sandia National Laboratories, P.O. Box 5800 MS 0346, Albuquerque, NM 87185, USA
e-mail: rjkueth@sandia.gov

© The Society for Experimental Mechanics, Inc. 2016

M. Allen et al. (eds.), *Dynamics of Coupled Structures, Volume 4*, Conference Proceedings of the Society for Experimental Mechanics Series, DOI 10.1007/978-3-319-29763-7_24

Kurt et al. [12] developed a model updating strategy for mechanical systems with local nonlinearities by comparing the instantaneous frequencies and energies from simulated broadband excitation using the wavelet transform. The "empirical" instantaneous frequencies and amplitudes are compared with the undamped nonlinear normal modes (NNMs) [13, 14] of the underlying Hamiltonian system as a metric to update the model.

In this paper, the short-time Fourier transform (STFT) is used to estimate the instantaneous frequencies and damping ratios from measurements under broadband excitation. The STFT takes a discrete Fourier transform of small windowed sections of the response to estimate the frequency content at a given time-point. In this work, the frequency-domain tool is modified to allow the short-time period of the window function to expand or contract as it slides down the time axis, allowing for better averaging of the frequencies and amplitudes. This approach is essentially that of the wavelet transform. From the processed time-frequency distribution, a peak picking method identifies the instantaneous "natural frequency" and complex amplitude of the Fourier coefficient from which the instantaneous damping ratio is estimated. These amplitude dependent properties of the system have a wide range of application including nonlinear detection, characterization, and potentially quantification.

One of the research questions posed by this work is this: what is the connection between the structures damped response to a broadband excitation and its nonlinear normal modes? The work of Kurt et al. [12] suggests that in the presence of light damping, these freely decaying responses should follow the same frequency/energy path as the NNM. Other researchers have successfully demonstrated how the damped response from initial conditions near the NNM initial conditions closely follow the damped invariant manifold [15–18], which is well approximated by the undamped NNM for light damping. This paper uses a nonlinear finite element beam model to investigate whether the NNMs agree with the instantaneous frequency and amplitude of the transient response. One could hypothesize that if the instantaneous frequencies and amplitudes agree with the invariant NNM, then these measurements could be thought of as invariant properties of the nonlinear system that are independent of excitation amplitude and location. The lack of superposition for nonlinear systems makes it unlikely that such a simple connection exists for strongly nonlinear systems, and is demonstrated in this work.

The paper is outlined as follows: Sect. 24.2 presents the theoretical developments of the modified short-time Fourier transform algorithm along with the approach to extract the instantaneous frequency and damping as a function of response amplitude. Section 24.3 demonstrates the methodology on a nonlinear beam with a cubic spring attachment at the tip. The frequency versus amplitude at a pseudo-measurement location is compared with the underlying NNM. Section 24.4 processes measured time data from two beams assembled with a lap joint excited with three different impact amplitudes. The conclusions and future work are discussed lastly in Sect. 24.5.

24.2 Theoretical Development

24.2.1 Short Time Fourier Transform with Time Varying Window

The short-time Fourier transform operates on the freely decaying time signal of a nonlinear mechanical system, denoted as $x(t)$, measured over a period T. The signal is sampled at N evenly spaced points in time such that the increment is defined as $\Delta = T/N$, resulting in N discrete measurement $x_0, x_1, \ldots, x_{N-1}$ where $x_n = x(n\Delta)$. A window function, $w(t-\tau)$, moves along the time axis at discrete time shifts $\tau = m\Delta$, and has a much shorter time period than the measurement period, $T_w << T$. The discretized window is sampled at the same N points in time, denoted as $w_{0-m}, w_{1-m}, \ldots, w_{N-1-m}$ where $w_{n-m} = w((n-m)\Delta)$ and is applied to the signal prior to taking the Fourier transform. The time point m controls the center time of the window, allowing a Fourier transform to be taken from different sections of the signal and approximate the instantaneous frequency content. Mathematically, the discrete Fourier transform of the windowed signal is taken as

$$X(k,m) = \sum_{n=0}^{N-1} x_n w_{n-m} e^{-\mathrm{i}2\pi kn/N} \tag{24.1}$$

defined at discrete frequencies

$$\omega_k = \frac{2\pi k}{T} \tag{24.2}$$

One of the issues with the STFT is that the period of the window function, T_w, dictates the accuracy and resolution of the spectrum. For example, if the window period is too large, then the frequency of the signal will be poorly averaged. Conversely, if the window is too small, then the poor frequency resolution makes it difficult to approximate the instantaneous

frequency. In an effort to improve this, the STFT is modified to allow for the time period of the window to change as it moves down the time axis, making the period, $T_w(m)$, explicitly dependent on the time instant, m. This ability to either expand or contract the window size helps produce a STFT with better averaging and resolution. The modified STFT simply becomes

$$X(k,m) = \sum_{n=0}^{N-1} x_n w_{n-m}(m) e^{-i2\pi kn/N} \tag{24.3}$$

and from this is an approximation to the Fourier series coefficients

$$\widehat{X}(k,m) = \frac{2X(k,m)}{\sum_{n=0}^{N-1} w_{n-m}(m)} \tag{24.4}$$

Each windowed Fourier transform is related to the time-point at the center of the window

$$t_{cw}(m) = \frac{mT}{N} + \frac{T_w(m)}{2} \tag{24.5}$$

Unlike the discrete Fourier transform, the STFT is a two-dimensional spectrum that changes as the window moves on the time axis. The moving window is zero-padded to improve the frequency resolution, but this does not actually improve on the estimation of the Fourier coefficients in Eq. (24.4). A variety of window functions can be used (e.g. Rectangle, Hamming, etc.) depending on the application of interest. The authors found that the Hanning window offered the best results for transient ring-down data, and this is the one used throughout this work. The discretized function for the time varying Hanning window is given as

$$w_{n-m}(m) = \begin{cases} \frac{1}{2}\left(1 - \cos\left(\frac{2\pi(n-m)T}{T_w(m)N}\right)\right) & \text{if } 0 \le (n-m)\frac{T}{N} < T_w(m) \\ 0 & \text{if } (n-m)\frac{T}{N} \ge T_w(m) \text{ or } (n-m)\frac{T}{N} < 0 \end{cases} \tag{24.6}$$

The period of the Hanning window explicitly depends on the time instant, m, allowing for the period to expand or contract as the window moves position. An example of this is shown in Fig. 24.1, where the period of three Hanning windows expands linearly, exponentially, or remains constant (the constant window length is what is used in the original STFT). These linearly and exponentially expanding windows cover a 1.0 s signal, with initial and final periods of 0.2 s and 0.4 s, respectively. They are discretized over six evenly spaced intervals between the initial and final window center times in Eq. (24.5). The constant

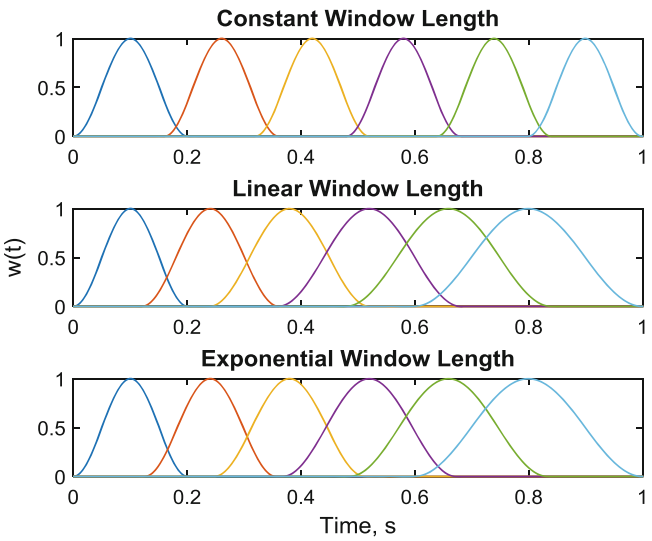

Fig. 24.1 Three different varying window length functions for the modified STFT algorithm

window has six windows with a period length of 0.2 s defined over a 1.0 s period. These linear and exponentially varying windows parameters would be used for signals that decrease in frequency as time (energy) increases (decreases). The variable window gives more flexibility when analyzing non-stationary signals, and results in a better estimate of the instantaneous frequency content.

24.2.2 Parameter Estimation from Ring-Down

The transient ring-down response, $x(t)$, can be generally represented as a summation of decaying harmonic functions of the form

$$x(t) = \sum_{r=1}^{p} \text{Re}\left\{A_{r,0} e^{-\beta_r(t)t} e^{i\varphi_r(t)}\right\} \tag{24.7}$$

The assumed form of the signal has a total of p decaying harmonic functions each having an initial complex amplitude, $A_{r,0}$, time dependent decay rate, $\beta_r(t)$, and time dependent phase, $\varphi_r(t)$. Time-frequency analyses such as the modified STFT described above are needed to identify the time dependency of the phase and decay rate. Following the approach in [4], the decay rate and phase are rewritten as

$$\beta_r(t) = \zeta_r(t)\omega_r(t) \tag{24.8}$$

$$\varphi_r(t) = \omega_{r,D}(t) \cdot t \tag{24.9}$$

In keeping notation with the free response of an underdamped, linear oscillator, the decaying harmonic functions are described by a time dependent damping ratio, $\zeta_r(t)$, and damped and undamped natural frequencies $\omega_{r,D}(t)$ and $\omega_r(t)$, respectively. Substituting Eqs. (24.8) and (24.9) into Eq. (24.7) would produce a form similar to the linear solution. The time dependent frequencies and damping ratios are estimated from the STFT data by simply using peak picking methods. The damped frequency occurs where there is a maximum absolute value of the Fourier coefficient, within a user defined frequency range of the spectrum for each windowed response.

This subsection describes how to fit the frequency, $\omega_r(t)$, damping, $\zeta_r(t)$, and initial complex amplitude, $A_{r,0}$, for the r^{th} decaying harmonic function in Eq. (24.7). The same process is repeated to extract the coefficients of other harmonic functions from the same STFT data by looking for peaks in a different frequency range. Starting with the collection of Fourier coefficients in Eq. (24.4) with a center time, $t_{cw}(m_j)$, the maximum amplitude of $\widehat{X}\left(k, m_j\right)$ is found within a subset of frequencies defined by the set $\left\{k_l \; k_u\right\}$, as given by Eq. (24.2). The maximum amplitude of the Fourier coefficient is determined mathematically as

$$A_r\left(t_{cw}\left(m_j\right)\right) = \max_{k \in \left\{k_l \; k_u\right\}} \left(\left|\widehat{X}\left(k, m_j\right)\right|\right) \tag{24.10}$$

and the damped frequency at the peak is

$$\omega_{r,D}\left(t_{cw}\left(m_j\right)\right) = \frac{2\pi k_{\max}}{T} \tag{24.11}$$

Taking the magnitude of the r^{th} decaying harmonic function, this is related to the peak Fourier coefficient at window time $t_{cw}(m_j)$ as

$$A_r\left(t_{cw}\left(m_j\right)\right) = \left|A_{r,0}\right| e^{-\beta_r\left(t_{cw}(m_j)\right) \cdot t_{cw}(m_j)} \tag{24.12}$$

This equation alone does not uniquely solve for all unknown values of $A_{r,0}$ and $\beta_r(t_{cw}(m_j))$, so it is assumed that the decay rate at the end of the windowed response has decayed to a linear response amplitude such that $\beta_r\left(t_{cw}\left(m_{end-1}\right)\right) = \beta_r\left(t_{cw}\left(m_{end}\right)\right)$. Combing this relationship with Eq. (24.12) offers the unique solution to $A_{r,0}$ and $\beta_r(t_{cw}(m_j))$.

Assuming the damped natural frequency relates to the undamped frequency as

$$\omega_{r,D}\left(t_{cw}\left(m_j\right)\right) = \omega_r\left(t_{cw}\left(m_j\right)\right)\sqrt{1-\zeta_r^2\left(t_{cw}\left(m_j\right)\right)} \tag{24.13}$$

the instantaneous (undamped) frequency is estimated by combining Eqs. (24.8) and (24.13) to get

$$\omega_r\left(t_{cw}\left(m_j\right)\right) = \sqrt{\omega_{r,D}^2\left(t_{cw}\left(m_j\right)\right)+\beta_r^2\left(t_{cw}\left(m_j\right)\right)} \tag{24.14}$$

As a final step, the instantaneous damping ratio becomes

$$\zeta_r\left(t_{cw}\left(m_j\right)\right) = \frac{\beta_r\left(t_{cw}\left(m_j\right)\right)}{\omega_r\left(t_{cw}\left(m_j\right)\right)} \tag{24.15}$$

The next two sections show the proposed methodology for transient ring-down data obtained from a simulated model and experimental data on real life hardware.

24.3 Numerical Results: Multi-DOF Nonlinear Beam

The proposed technique is now demonstrated on a cantilever beam model with a cubic spring attachment at the beam tip. The model was originally investigated in [19], and has the following dimensions: 0.7 m long, cross sectional width and height of 0.014 m. The linear portion of the finite element model has a total of 20 Euler-Bernoulli beam elements with the material properties: Young's modulus of 205 GPa, and density of 7800 kg/m^3. The cubic spring stiffness at the tip has a strength of $6 \cdot 10^9$ N/m^3, and a 0.5 % linear modal damping model accounts for dissipation. A schematic of the structure is shown in Fig. 24.2. The 0.5 kg lumped mass at a distance $a = 0.31$ m from the fixed end results in the linear natural frequencies of the first and second mode to be at 22.0 Hz and 108 Hz, respectively. In the subsections that follow, the undamped nonlinear normal modes of the beam are computed using the algorithm in [20]. Section 24.3.1 starts the freely decaying response with initial conditions that initiate the solution of the first and second NNM, and compares the frequency-amplitude dependence of the two solutions. Section 24.3.2 makes a similar comparison but instead for a broadband excitation applied at the beam tip, as shown in Fig. 24.2.

24.3.1 Initial Conditions of NNM

First, the freely decaying response of the beam is simulated with an initial condition that also initiates the solution of either the first or second nonlinear normal mode. The spectrograms of these responses are plotted in Fig. 24.3 for the following cases: free response initiated on a low energy (top row) and high energy (bottom row) solution of the NNM 1 backbone (left column), and responses that start on a low energy (top row) and high energy (bottom row) backbone solution of NNM 2 (right column). In all four cases, a linearly time varying Hanning window was used with a total of 75 windowed frames

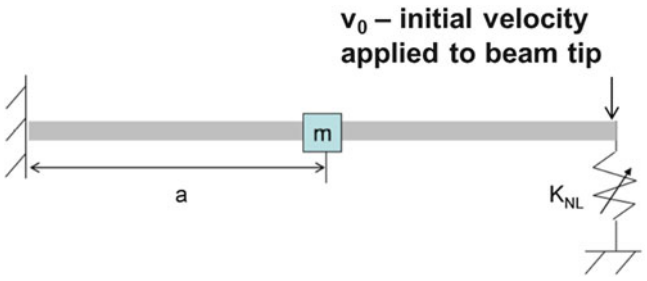

Fig. 24.2 Schematic of the cantilever beam with a cubic spring at the beam tip

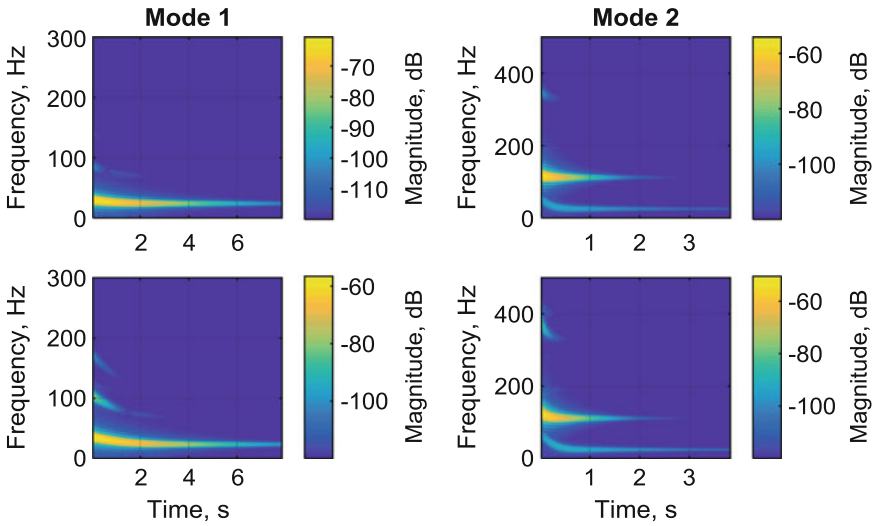

Fig. 24.3 Spectrogram of the STFT of freely decaying response along (*left column*) NNM 1 and (*right column*) NNM 2. The *top row* is initiated at low energy and *bottom row* at high energy

along the time axis. For the decay along NNM 1, the window had an initial period of 0.2 s and an ending period of 0.4 s, while the shorter time scales of NNM 2 required an initial and final period length of 0.1 and 0.2 s, respectively.

The spectra of the modified STFT algorithm can be used for the detection of nonlinear behavior in transient responses such as these. For example, the higher energy response near NNM 1 shows that the fundamental frequency starts at 35 Hz when $t = 0.0$ s, but as time marches forward the frequency shifts down to 22 Hz, converging to the first natural frequency of the *linear* cantilever beam (i.e. with no cubic spring attachment). Nonlinear behavior is further evidenced by the presence of higher order harmonics of the most dominant frequencies. It is interesting to note that for the decay along NNM 2 (right column Fig. 24.3) some of the vibration energy leaks into the first mode and appears as a super harmonic frequency, and completely dominates the response after about 2.5 s for both cases. This transfer of energy could be attributed to the numerical sensitivity of the initial conditions used to initiate the free decay, or the fact that a separate numerical integration scheme was used to compute the transient response. The spectrograms qualitatively revealed that the instantaneous frequency of the free response decreased as energy decreased, characteristic of hardening type nonlinearities. By further processing the STFT spectra, quantitative values for the instantaneous frequency and damping ratio are estimated following the approach in Sect. 24.2.2. Figure 24.4 shows the frequency and damping ratio versus the magnitude of the Fourier coefficient of the beam tip displacement. The (blue triangles) represent a lower energy solution on the backbone, and (red pluses) are higher energy ones.

As expected, the instantaneous frequency-amplitude of the transient response and that of the NNM are in excellent agreement with one another thanks to the fact that the damped invariant manifold is well approximated by the undamped NNM in the presence of light damping. Furthermore, the invariance property of NNMs (i.e. a solution that starts out on the damped NNM manifold will remain on that manifold for all time [21]) makes it possible for the free response to follow such path. These useful properties have been used to develop phase resonance techniques to experimentally excite the NNMs of real life structures [7, 16, 17, 22]. It is interesting to note that the damping ratio for each simulated response decreased for large response amplitudes, even though the beam had only linear modal damping. A displacement-dependent nonlinearity (i.e. cubic spring) can produce a seemingly nonlinear instantaneous damping ratio even without the presence of a nonlinear damping model.

24.3.2 Broadband Excitation

Next an initial transverse velocity was applied to the beam tip to simulate a broadband excitation at three different amplitudes: 1, 2 and 3 m/s. The transverse tip displacement was used to process the STFT using a linearly time varying Hanning window. The window had an initial period of 0.2 s and an ending period of 0.4 s, and a total of 75 windowed frames to estimate the frequencies and damping ratios. The spectrogram and windowed FFTs of the transient ring-down are shown in Fig. 24.5. The first row corresponds to the 1 m/s excitation, while the second and third rows are from the 2 and 3 m/s initial velocities,

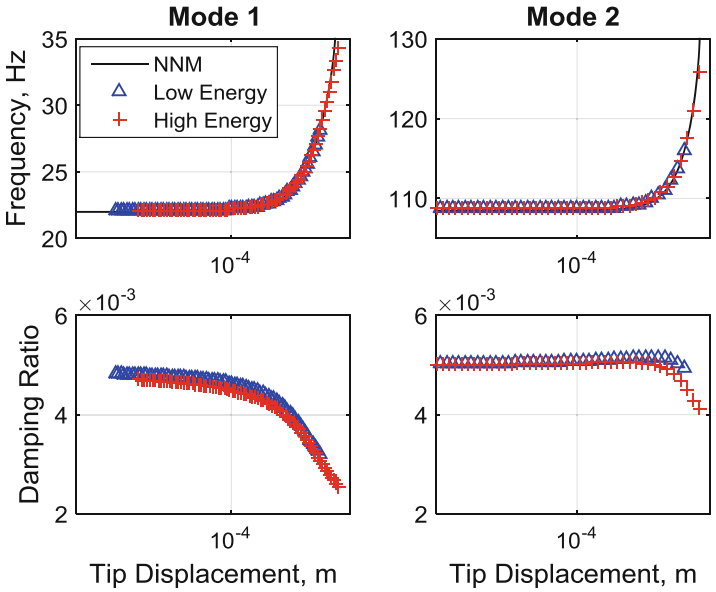

Fig. 24.4 Instantaneous frequency and damping ratio versus tip displacement amplitude of (*left column*) mode 1 and (*right column*) mode 2 for damped response with initial conditions on NNM backbone

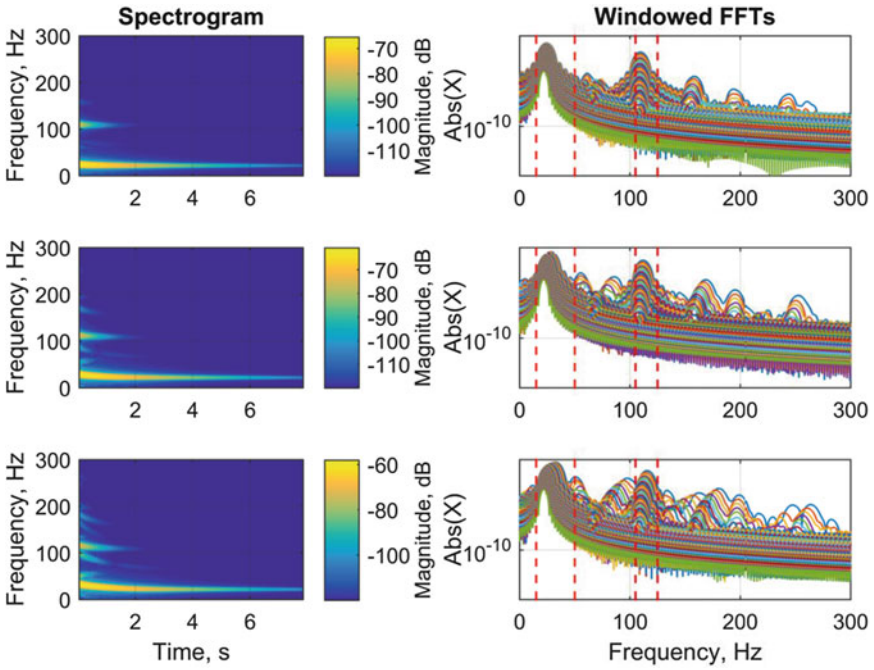

Fig. 24.5 (*Left column*) spectrogram of the STFT and (*right column*) corresponding windowed FFTs. The *top row* is the 1 m/s initial velocity response, (*middle*) 2 m/s and (*bottom*) 3 m/s

respectively. The vertical, red dashed lines in the windowed FFTs show the frequency bandwidth from which the peak Fourier coefficients are used to estimate the amplitude dependent frequencies and damping ratios.

The spectrogram again qualitatively detects the presence of nonlinearity due to the change in frequency content as the overall response amplitude decreases. Broadband excitation is much more complicated than the NNM decay simulations shown previously since all frequencies are excited in the response at once and the nonlinear modes cannot be easily decoupled. If the beam were a linear structure, the underlying modal frequencies and damping ratios extracted from the signal would be unchanged as the response evolves due to linear superposition (not shown here for brevity). In a nonlinear system, it is expected that the frequency and damping change as energy dissipates, however the lack of superposition makes

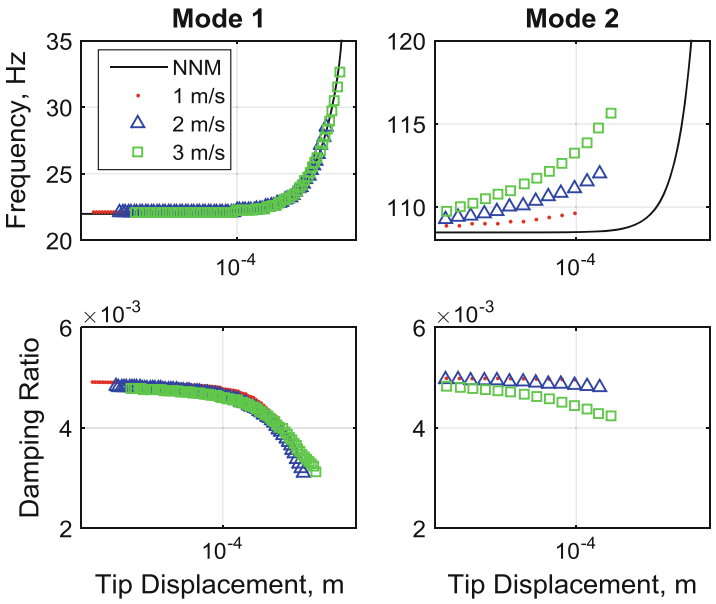

Fig. 24.6 Instantaneous frequency and damping ratio versus tip displacement amplitude of (*left column*) mode 1 and (*right column*) mode 2 for simulated broadband excitation

it unlikely that these parameters are, in general, independent of the type, amplitude, and location of the excitation due to the nonlinear modal coupling. The estimated frequency and damping ratios are shown below in Fig. 24.6 for the first and second modes. The (red dots) are estimated from the 1 m/s initial velocity response, the (blue triangles) are from the initial 2 m/s response and the (green squares) represent the 3 m/s data. The undamped NNM is also overlaid in the frequency versus amplitude plots.

The frequency-amplitude dependence of the broadband excitation appears to be in excellent agreement with the first NNM of the undamped beam. The frequency content appears to follow the same path for each of the three initial velocities. The damping ratio versus amplitude for the first mode also looks to follow a similar path, and plateaus to a value of 0.005 at low energy. In each case, the first NNM would be accurately identified from the broadband excitation data. Unfortunately, the same cannot be said for the second mode since it does not agree well with the underlying NNM. The simulated data has a different frequency-amplitude path for each of the levels of excitation, none of which are in agreement with the NNM. This result is not surprising due to the complicated modal coupling in such nonlinear response regimes and the lack of a superposition theory for nonlinear structures.

In some cases, for example jointed structures with strong damping nonlinearities [6], very good results are obtained assuming that the modes are uncoupled, allowing for the amplitude dependent properties to be identified with an approach similar to this. In the example presented here, the stiffness nonlinearity is quite strong and damping is weak, increasing the likelihood that modal interactions play a more important role and therefore makes it more difficult to validate such an assumption. Recent developments by Ardeh have shown that the undamped NNMs can be used to reconstruct the undamped transient response to an arbitrary initial condition using a local, nonlinear connecting function [23]. This nonlinear function describes the modal coupling between each NNM, and could potentially be used to decouple the response from a broadband excitation. While this was not explored here in this paper, it remains an objective for future work.

24.4 Experimental Results: Beam with Bolted Lap Joint

Next the STFT algorithm is applied to experimental data measured on a two beam structure assembled with three bolted connections, creating a lap joint interface between the two. This structure, referred as the Brake-Reuß (BR) beam, was originally tested in [24] and has since been examined both experimentally [25–27] and numerically [28, 29] due to its rich nonlinear behavior and simple construction. The two individual beams are machined from Type AISI 304 Stainless Steel bar stock. The bolt holes have a diameter of 0.84 cm and are located along the center line of the beam. The two beams are assembled by three 5 cm long M8 bolts, giving it an effective overall length of 72 cm with a square width and height

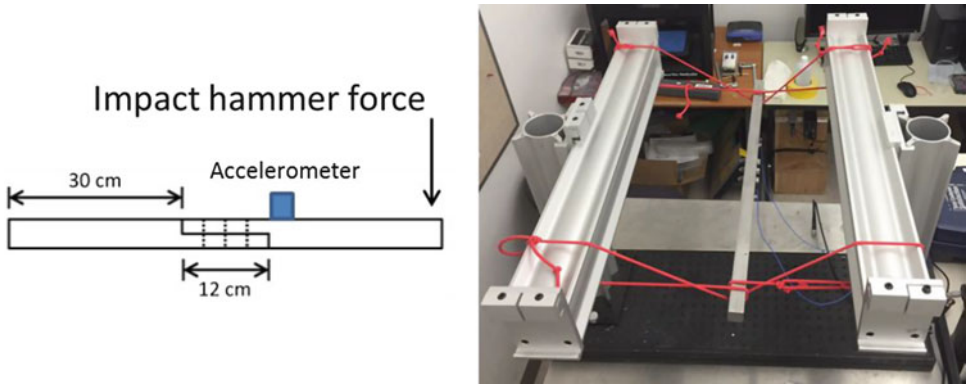

Fig. 24.7 (*Left*) schematic of the BR beam input/output locations; (*right*) photograph of the free-free experimental setup

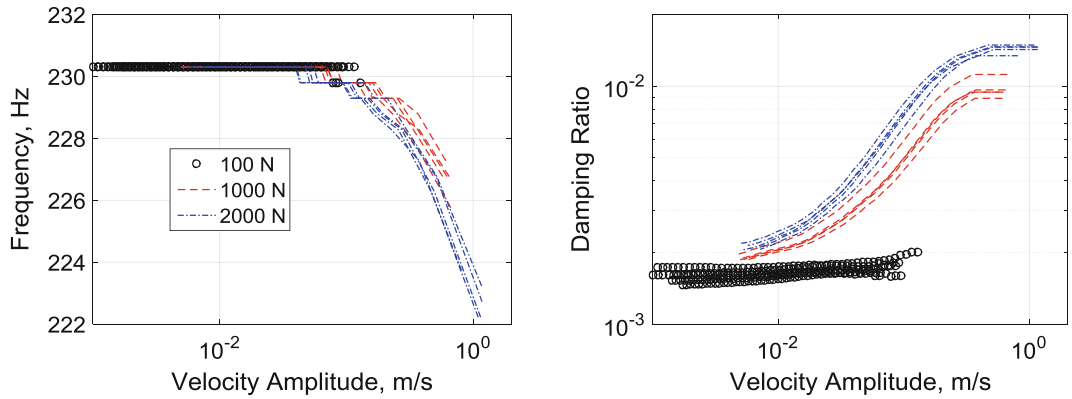

Fig. 24.8 Instantaneous frequency (*left*) and damping ratio (*right*) versus velocity amplitude

of 2.5 cm. The bolts were torqued to 15 N-m and the interface surfaces were not ground after machining, leaving the surfaces relatively rough. Note that a range of experimental data with various bolt torques and surface finishes were collected in [26], however the data presented here is only a small subset of that. A schematic of the beam and the actual hardware in its free-free boundary condition are shown in Fig. 24.7.

The experimental hardware was exposed to broadband excitation using an impact hammer applied to the beam tip. The tests were carried out as follows: after assembling the beams to the specified torque levels, five tests were run with an impact force of 100 N, followed by five with a 1000 N impact, and ending with five tests at 2000 N. For each test, the transient ring-down data was collected using an accelerometer attached near the lap joint (see left schematic in Fig. 24.7). From this measured data, the STFT was processed using a linearly varying Hanning window with starting and ending window lengths of 0.02 s and 0.14 s, respectively. A total of 50 windowed sections were computed, and used to estimate the velocity dependent frequency and damping values during the decay. The instantaneous frequency and damping ratio of the beam from each test are shown in the Fig. 24.8 where the (black circles) are computed from the 100 N data, (red dashed) from the 1000 N data and the (blue dash-dotted) are from the 2000 N impulse.

The processed data from the 100 N impact show that the beam vibrates predominantly in the linear regime since there is minimal shift in the instantaneous frequency and damping estimates. The larger impact forces assaulting the beam caused it to behave nonlinearly due to microslip at the bolted lap joint. The effective damping of the beam appears to change by an order of magnitude due to the frictional rubbing and impacts along the interface. The softening in the frequency-amplitude dependency can be explained by the loss of stiffness in the interface during microslip, as seen in the left plot of Fig. 24.8. It is interesting to note here that the path of the instantaneous damping ratio depends on the impact force level, however the frequency versus amplitude plot shows that the curves match quite well regardless of load level. Perhaps one could assume that the modes of this system are uncoupled and its frequency and damping are amplitude dependent, as proposed in [6].

24.5 Conclusion

A modification to the short-time Fourier transform was presented and used to extract the instantaneous frequency and damping ratio from measured transient ring-down responses. The short-time period of the window function can expand or contract as it moves down the time axis, allowing for better estimates of the frequency content at a given time instant. The time-frequency distribution is then used to find the peak Fourier coefficients in the spectra and estimate the instantaneous natural frequency and damping ratio. One advantage to this approach is that it can be applied to any time signal with multi-harmonic components without the need to do any pre-processing such as band-pass or modal filtering.

The methodology is demonstrated on a cantilever beam with a cubic spring attachment at the tip. The freely decaying response initiated with initial conditions of the undamped nonlinear normal modes show that the frequency-amplitude dependence of the ring-down response agrees well with that of the NNM due to the invariance property of the damped manifold. However, in the presence of broadband excitation, the extracted harmonic content of the signal does not follow the same frequency-amplitude path for all the NNMs in the excitation bandwidth. This is due to the fact that these modes are somehow coupled and no global theory of superposition exists for strongly nonlinear systems. The modified STFT algorithm is further demonstrated on experimental measurements taken from a beam with a lap joint. The instantaneous frequency and damping ratio show how nonlinearities in jointed structures can be detected for various amplitudes of excitation. The lap joint has a softening effect on the overall stiffness, and introduces amplitude dependent damping that increases with response amplitude.

In future work, we will further explore the connection between the decaying harmonic functions estimated from transient ring-down response and the nonlinear normal modes. A nonlinear connecting function describing the modal coupling would allow for the modes to be separated from the response, however at this time it's not fully understood how this will be done. The ability to extract invariant modal properties, independent of load amplitude, location and type, would offer a truly nonlinear extension to nonlinear modal analysis with a solid theoretical framework. These parameters could one day be used as a basis for many applications including model reduction, test-analysis correlation, or system identification.

Acknowledgements This work was funded by Sandia National Laboratories. Sandia National Laboratories is a multi-program laboratory managed and operated by Sandia Corporation, a wholly owned subsidiary of Lockheed Martin Corporation, for the U.S. Department of Energy's National Nuclear Security Administration under contract DE-AC04-94AL85000. The authors would also like to thank Matt Bonney, Brett Robertson and Fabian Schempp for sharing the experimental data they collected on the lap joint presented in Sect. 24.4. Finally, the authors would like to thank Scott Smith and Caroline Nielsen for their help developing the algorithm in Matlab and working on a graphical user interface.

References

1. Cooley, J.W., Tukey, J.W.: An algorithm for the machine calculation of complex Fourier series. Math. Comput. **19**, 297–301 (1965)
2. Neild, S.A., McFadden, P.D., Williams, M.S.: A review of time-frequency methods for structural vibration analysis. Eng. Struct. **25**, 713–728 (2003)
3. Feldman, M.: Non-linear system vibration analysis using Hilbert transform–I. Free vibration analysis method 'Freevib'. Mech. Syst. Signal Process. **8**, 119–127 (1994)
4. Sumali, H., Kellogg, R.A.: Calculating damping from ring-down using Hilbert transform and curve fitting. Presented at the 4th International Operational Modal Analysis Conference (IOMAC), Istanbul, Turkey, May 2011
5. Sracic, M.W., Allen, M.S., Sumali, H.: Identifying the modal properties of nonlinear structures using measured free response time histories from a scanning laser Doppler vibrometer. In: Topics in Nonlinear Dynamics, Conference Proceedings of the Society for Experimental Mechanics Series, vol. 3, pp. 269–286. Springer (2012)
6. Deaner, B.J., Allen, M.S., Starr, M.J., Segalman, D.J., Sumali, H.: Application of viscous and Iwan modal damping models to experimental measurements from bolted structures. J. Vib. Acoust. **137**, 021012 (2015)
7. Londoño, J.M., Neild, S.A., Cooper, J.E.: Identification of backbone curves of nonlinear systems from resonance decay responses. J. Sound Vib. **348**, 224–238 (2015)
8. Huang, N.E., Shen, Z., Long, S.R., Wu, M.C., Shih, H.H., Zheng, Q., et al.: The empirical mode decomposition and the Hilbert spectrum for nonlinear and non-stationary time series analysis. In: Proceedings of the Royal Society of London A: Mathematical, Physical and Engineering Sciences, pp. 903–995. (1998)
9. Eriten, M., Kurt, M., Luo, G., McFarland, D.M., Bergman, L.A., Vakakis, A.F.: Nonlinear system identification of frictional effects in a beam with a bolted joint connection. Mech. Syst. Signal Process. **39**, 245–264 (2013)
10. Lee, Y., Vakakis, A., McFarland, D., Bergman, L.: A global–local approach to nonlinear system identification: a review. Struct. Control Health Monit. **17**, 742–760 (2010)
11. Vakakis, A., Bergman, L., McFarland, D., Lee, Y., Kurt, M.: Current efforts towards a non-linear system identification methodology of broad applicability. In: Proceedings of the Institution of Mechanical Engineers, Part C: Journal of Mechanical Engineering Science, 2011

12. Kurt, M., Eriten, M., McFarland, D.M., Bergman, L.A., Vakakis, A.F.: Methodology for model updating of mechanical components with local nonlinearities. J. Sound Vib. **357**, 331–348 (2015)
13. Kerschen, G., Peeters, M., Golinval, J.C., Vakakis, A.F.: Nonlinear normal modes. Part I. A useful framework for the structural dynamicist. Mech. Syst. Signal Process. **23**, 170–194 (2009)
14. Vakakis, A.F.: Non-linear normal modes (NNMs) and their applications in vibration theory: an overview. Mech. Syst. Signal Process. **11**, 3–22 (1997)
15. Panagopoulos, P., Georgiades, F., Tsakirtzis, S., Vakakis, A.F., Bergman, L.A.: Multi-scaled analysis of the damped dynamics of an elastic rod with an essentially nonlinear end attachment. Int. J. Solids Struct. **44**, 6256–6278 (2007)
16. Peeters, M., Kerschen, G., Golinval, J.C.: Dynamic testing of nonlinear vibrating structures using nonlinear normal modes. J. Sound Vib. **330**, 486–509 (2011)
17. Peeters, M., Kerschen, G., Golinval, J.C.: Modal testing of nonlinear vibrating structures based on nonlinear normal modes: experimental demonstration. Mech. Syst. Signal Process. **25**, 1227–1247 (2011)
18. Ardeh, H., Allen, M.: Investigating cases of jump phenomenon in a nonlinear oscillatory system. In: Topics in Nonlinear Dynamics, Conference Proceedings of the Society for Experimental Mechanics Series, vol. 1, pp. 299–318. Springer, New York, 2013
19. Kuether, R.J., Renson, L., Detroux, T., Grappasonni, C., Kerschen, G., Allen, M.S.: Nonlinear normal modes, modal interactions and isolated resonance curves. J. Sound Vib. **351**, 299–310 (2015)
20. Peeters, M., Viguié, R., Sérandour, G., Kerschen, G., Golinval, J.C.: Nonlinear normal modes, Part II: toward a practical computation using numerical continuation techniques. Mech. Syst. Signal Process. **23**, 195–216 (2009)
21. Shaw, S.W., Pierre, C.: Normal modes for non-linear vibratory systems. J. Sound Vib. **164**, 85–124 (1993)
22. Ehrhardt, D., Harris, R., Allen, M.: Numerical and experimental determination of nonlinear normal modes of a circular perforated plate. In: Topics in Modal Analysis I, Conference Proceedings of the Society for Experimental Mechanics, vol. 7, pp. 239–251. Series Springer International Publishing, 2014
23. Ardeh, H.A.: Geometrical theory of nonlinear modal analysis. Ph.D Dissertation, University of Wisconsin-Madison (2014)
24. Brake, M., Reuss, P., Segalman, D., Gaul, L.: Variability and repeatability of jointed structures with frictional interfaces. In: Dynamics of Coupled Structures, Conference Proceedings of the Society for Experimental Mechanics Series, vol. 1, pp. 245–252. Springer International Publishing (2014)
25. Smith, S., Bilbao-Ludena, J.C., Catalfamo, S., Brake, M.R.W., Reuß, P., Schwingshackl, C.W.: The effects of boundary conditions, measurement techniques, and excitation type on measurements of the properties of mechanical joints. In: Nonlinear Dynamics, Conference Proceedings of the Society for Experimental Mechanics Series, vol. 1, pp. 415–431. Springer International Publishing (2016)
26. Bonney, M., Robertson, B., Schempp, F., Brake, M.R.W., Mignolet, M.: experimental determination of frictional interface models. Presented at the 34th International Modal Analysis Conference (IMAC XXXIV), Orlando, 2016
27. Catalfamo, S., Smith, S.A., Morlock, F., Brake, M.R.W., Reuß, P., Schwingshackl, C.W., et al.: Effects of experimental methods on the measurements of a nonlinear structure. Presented at the 34th International Modal Analysis Conference (IMAC XXXIV), Orlando, 2016
28. Salles, L., Swacek, C., Lacayo, R.M., Reuss, P., Brake, M.R.W., Schwingshackl, C.W.: Numerical round robin for prediction of dissipation in lap joints. In: Nonlinear Dynamics, Conference Proceedings of the Society for Experimental Mechanics Series, vol. 1, pp. 53–64. Springer International Publishing (2016)
29. Gross, J., Armand, J., Lacayo, R.M., Reuß, P., Salles, L., Schwingshackl, C.W., et al.: A numerical round robin for the prediction of the dynamics of jointed structures. Presented at the 34th International Modal Analysis Conference (IMAC XXXIV), Orlando, 2016

Chapter 25
Explicit Modelling of Microslip Behaviour in Dry Friction Contact

C. W. Schwingshackl and A. Natoli

Abstract In many engineering applications the influence of a slipping contact interface has a major impact on the experienced damping in the structure. Predicting the generated damping is of uttermost importance to ensure an accurate analysis of the dynamic response of the system. Microslip, during which part of the contact is still stuck, and part is already slipping, plays a significant role in this damping, since many applications experience only this from of energy dissipation during operation. This paper investigates the possibility to capture microslip accurately with an explicit, quasi static modelling approach, where a large amount of traditional friction elements are distributed over a small contact area and a realistic pressure field is applied to reproduce the contact conditions. The resulting predicted hysteresis loops show microslip like behaviour, and the detailed contact mesh allows identifying the underlying nonlinear mechanism.

Keywords Microslip • Quasi static analysis • Friction • Nonlinear analysis • Tangential stiffness

25.1 Introduction

Linear dynamic analysis can predicted the response of a single component very accurately today, but once several components are combined to an assembly, the accuracy of the prediction significantly reduces, due to the presence of nonlinearity in the joints. Commonly these connections are dry friction joints, with two metal surfaces in direct contact under load (eg. bolted joints) leading to a nonlinear dynamic system that can show amplitude dependant stiffness and damping behaviour due to slip in the contact area during a vibration cycle.

The modelling of the nonlinear behaviour in the contact interface has attracted much attention in the past leading to a range of analysis approaches [1–5]. These methods attempt to model the different contact conditions during a vibration cycle at the interface to investigate their impact on the global response of the assembled structure. During a vibration cycle, a friction joint can experience up to four different conditions: (1) the contact interface can be fully stuck, (2) it can come to a transition from a stuck interface to a sliding interface, (3) out of plane motion can lead to a separation of the contact interface at one stage in the vibration cycle, and/or (4) the interface can be permanently separated due to large initial gaps. The presence of these different conditions introduces hysteresis behaviour, where at small excitation levels the displacement of the stuck contact is purely driven by the tangential contact stiffness, k_t. Once the contact forces get too large, parts of the contact area begin to slide leading to microslip. It is initially dominated by the contact stiffness of the stuck areas, but as more and more of the contact interface starts to slide, it becomes dominated by the friction coefficient, μ. Once slip has developed everywhere in the contact zone, macroslip is present, which is dominated by the friction coefficient and the applied normal load, N_0. Modelling the first and the last stage of the hysteresis loop is reasonably well understood and it can be achieved by a combination of springs and Coulomb sliders, but the microslip transition stage is much harder to capture due to the underlying nonlinear mechanism. Unfortunately many engineering applications such as under platform dampers [6–8], blade roots [9, 10], and bolted joints [1–4] may operate mainly in the microslip regime requiring an accurate prediction technique.

Two different approaches can be generally pursuit to capture the microslip behaviour in a contact interface. A dedicated microslip element can be used to capture the transition from stick to slip based on a set of parameters that are usually extracted from a specific measurement for a particular joint [2, 11] and which then allow to replicate the dynamic behaviour of that particular joint accurately.

A slightly different approach is the modelling of the microslip behaviour with the help of a large number of explicit macroslip elements that are used to capture the local slip/stick transition at the contact interface without the need of additional

C.W. Schwingshackl (✉) • A. Natoli
Imperial College London, Exhibition Road, SW7 2AZ London, UK
e-mail: c.schwingshackl@imperial.ac.uk

© The Society for Experimental Mechanics, Inc. 2016

M. Allen et al. (eds.), *Dynamics of Coupled Structures, Volume 4*, Conference Proceedings of the Society for Experimental Mechanics Series, DOI 10.1007/978-3-319-29763-7_25

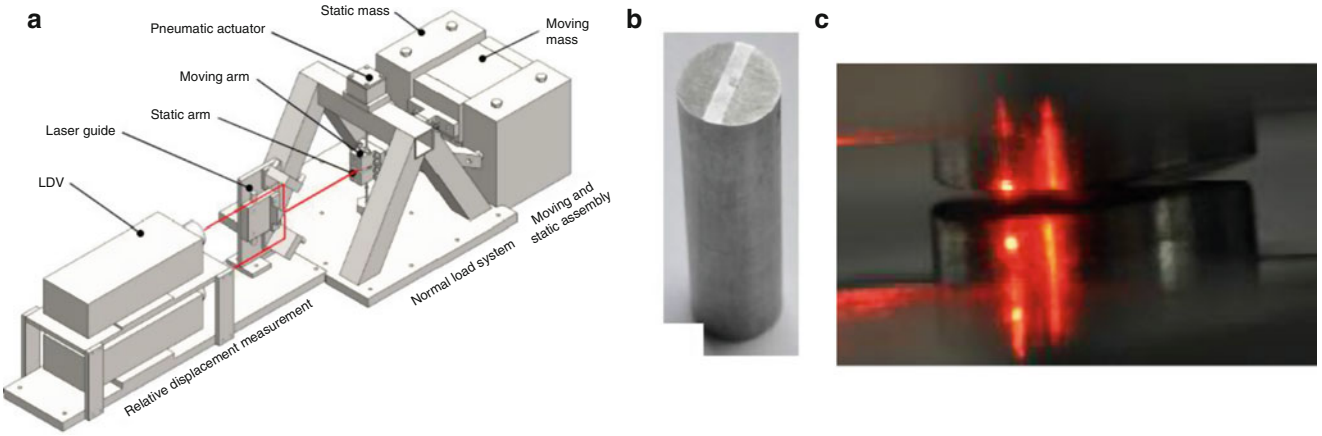

Fig. 25.1 (**a**) Friction test rig setup and (**b**) test specimen

input parameters. The general validity of the idea has been demonstrated in [12], and this paper will focus on a detailed quasi static analysis to investigate the accuracy of such an approach and gain an understanding of the underlying mechanism at the contact surface during a microslip event.

25.2 Friction Test Rig

The friction test rig at Imperial College London (see Fig. 25.1a) allows the extraction of a hysteresis loop over a wide range of frequencies (20–150 Hz) and normal loads (50–500 N), that can be used to extract the tangential contact stiffness, k_t, and friction coefficient, μ, for a given material combination. A detailed description of the test rig can be found in [13], and only the specimen design will be discussed at this point due to its relevance for the analysis.

The round specimen for the 1D friction rig from Fig. 25.1b has been designed with a 1 mm flat top leading to a flat contact area of 1 mm^2 when rotating the two specimens by 90°. The flat contact interface has been chosen over a spherical one to provide more realistic contact geometry for industrial applications. Each specimen is held in place via a rigid specimen arm to minimise rig compliance. To further minimise the effect of potential elastic deformation in the rig or specimen, the relative displacement of the specimens is being measured as close as possible to the contact interface via two laser Doppler Vibrometers (see Fig. 25.1c) and the transmitted force is measured with three force transducers at the static side of the rig. A controlled normal load, N_0, can be applied to the contact interface via a pneumatic loading system, and the excitation is provided to the upper specimen via a large inertia mass driven by an electromagnetic shaker. The resulting hysteresis loops (see Fig. 25.2) can be used to extract the tangential contact stiffness, k_t, from the elastic section of the loop after the reversal of the vibration direction, and the friction coefficient, μ, from the distance between the two macroslip lines and the known normal load, N_0.

The hysteresis loop in Fig. 25.2 shows that the test rig with its flat contact interface leads to a well-established microslip transition between the elastic contact deformation and the full macroslip zone, making it an ideal test case for the attempted modelling of microslip with a quasi-static FE approach.

25.3 Finite Element Modelling

The main aim of the finite element model is to attempt to capture the microslip transition at the contact interface during small relative displacements of the test specimens. For this purpose a very detailed model (Fig. 25.3a) of the two specimens was created in Abaqus, consisting of 140 k elements, where a particularly fine mesh of tetrahedral elements was used to cover the 1 mm^2 contact interface (5000 elements, see Fig. 25.3b) between the two specimens. Great care was taken to ensure that the linear contact interface mesh of the two rotated specimens was matching to ensure an accurate nonlinear interface mesh. Material properties for 304 stainless steel were used for the specimen to capture the real specimen behaviour (E = 193 GPa).

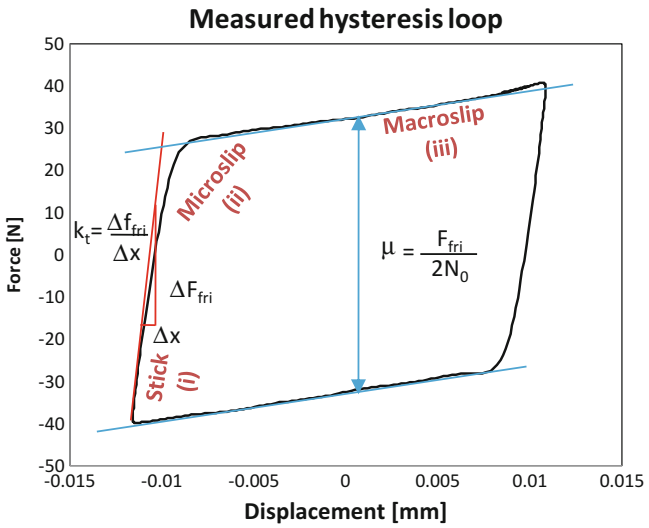

Fig. 25.2 Measured hysteresis loop

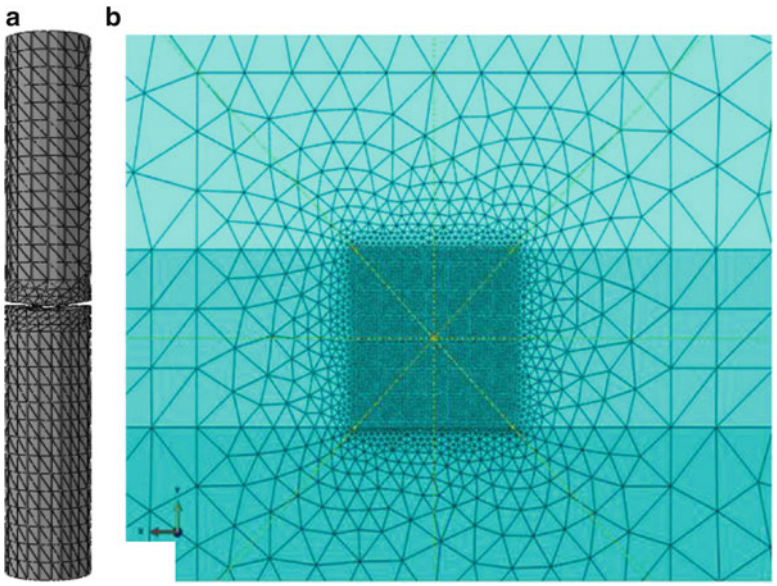

Fig. 25.3 Finite element model of the specimen, (**a**) the full model and (**b**) detailed mesh at contact interface

One of the main challenges of this investigation was the application of the boundary conditions to the mesh. In order to simplify the finite element model, only the specimens were considered, requiring the boundary conditions to replicate the rig behaviour. For this purpose the lower specimen was grounded along four vertical lines around its circumference, replicating the specimen contact zones in the clamp. The boundary conditions of the upper, moving specimen allowed only vertical motion during the application of the normal load, N_0, and only horizontal motion during the application of the shear forces, to ensure convergence of the results and avoid separation of the contact interface during the computation. A static normal load of 95 N was applied via a pressure to the upper surface of the top specimen, simulating the loading of the specimen in the rig.

The main aim of this research work was to investigate if a quasi-static analysis in Abaqus would be able to capture the microslip transition correctly. For this purpose 5000 nonlinear C3D10 elements were spread over the 1 mm^2 contact interface, leading to a discretisation of less than 0.2 μm^2. It was assumed that such a detailed mesh would be able to represent the normal load distribution accurately and capture the transition from stick to slip correctly. The penalty method was used to compute the contact interaction between the two surfaces, requiring the input of the friction coefficient, μ, and the penalty stiffness in the vertical and horizontal direction. The critical shear stress in a node at the contact interface is thereby calculated

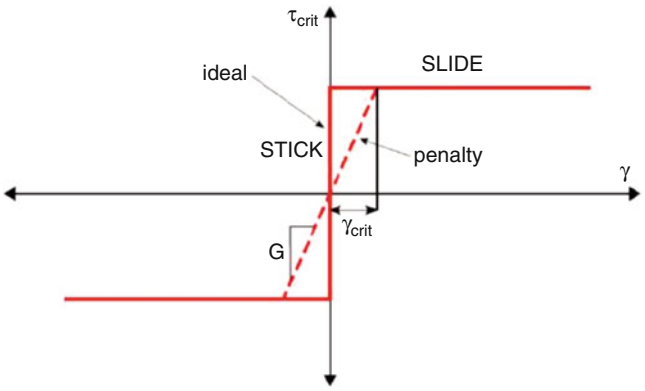

Fig. 25.4 The used contact model with the critical elastic slip definition

via $\tau_{cr} = \mu p$, where p is the contact pressure, obtained during the initial loading stage in the normal direction. A measured friction coefficient, $\mu = 0.55$, for the stainless steel specimens was used for the analysis. The implementation of the correct penalty stiffness in the tangential direction represented a bigger challenge, since it is defined via the critical elastic slip, γ_{crit}, from Fig. 25.4, which describes the maximum displacement between two linked nodes before the element starts to slip. It can be related to the measured tangential contact stiffness, k_t, via

$$k_t = \frac{\Delta F_{fric}}{\Delta x} = \frac{\tau_{\mathrm{cr}}}{\gamma_{\mathrm{cr}}} \tag{25.1}$$

where ΔF_{fric} is the variation in the friction force of an element and Δx is the relative displacement between two contact nodes.

During the analysis, an initial load step was used to apply the normal contact load to the specimen, leading to a contact pressure, p, for each node. For this analysis the standard Abaqus settings with an automatic correction were use, since a quick parameter study did not reveal any major sensitivity of the results towards the settings. The pressure distribution for three different contact conditions were computed to investigate their influence on the results, where (1) the two contact surfaces were fully glued and no relative motion was possible, (2) no out of plane motion was allowed, but friction-less sliding was possible in the horizontal plane, and (3) friction at the interface was taken into account.

Once the contact pressure was available, the boundary conditions of the upper specimen were changed to a pure horizontal sliding motion, and a gradually increasing horizontal force was applied to the upper specimen in the sliding direction at six discrete evenly spaced locations. The gradual increase of the force ensured convergence of the results up to the point where full macro slip occurred, where the unrestraint nature of the problem in the sliding direction prevented convergence.

The contact conditions of each node at the contact surface was obtained for each increment of the tangential loading, and the resulting relative displacement between the specimens was calculated at the measurement location (see Fig. 25.1c). Plotting the applied force over the resulting displacement for different load levels led to the computed hysteresis loop.

25.4 Results

25.4.1 Experimental Results

Tests were conducted with the 1D friction rig to obtain the reference hysteresis loops for this investigation, and to extract the input parameters for the analysis. Figure 25.5a shows a set of ten typical loops for a normal load of 95 N, from which an average tangential contact stiffness, $k_t = 6.58\text{e}7$ N/m/mm^2, and a friction coefficient, $\mu = 0.55$, can be extracted.

Figure 25.5b shows the resulting microslip transition in more detail. A continuous microslip transition from the fully stuck contact condition defined by the linear elastic behaviour to a fully slipping contact can be observed. The accurate capture of this transition with a quasi-static analysis will be the main focus of the investigation in the next section.

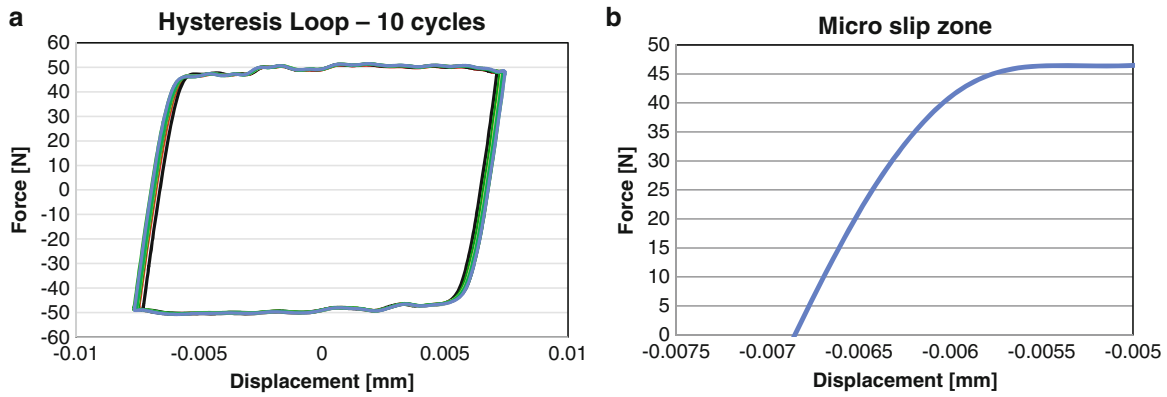

Fig. 25.5 (**a**) Ten measured hysteresis loops and (**b**) a corresponding microslip zone

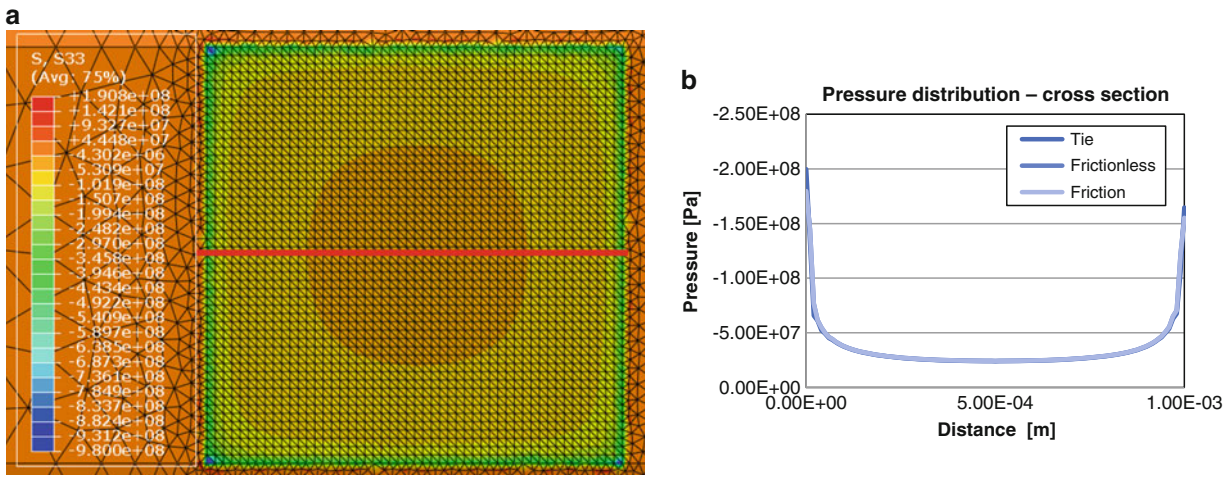

Fig. 25.6 (**a**) The pressure distribution in the contact and (**b**) a comparison between tied, frictionless and friction contact pressure distribution along the centre of the contact in the sliding direction

25.4.2 Finite Element Results

25.4.2.1 Pressure Distribution

The resulting pressure distribution for the 95 N normal load case at the contact interface with friction can be seen in Fig. 25.6a. It indicates relatively low pressure in the centre of the contact zone, and a significant concentration around the edges. The values right at the edges must be considered with some care, since they are most likely inaccurate due to singularities at the sharp corners, but the overall pressure distribution is considered to be a good representation of the flat on flat contact surface between the two specimens. The pressure profile along the sliding direction in Fig. 25.6b highlights this sharp pressure rise at the edges. A comparison of the fully tied, frictionless and friction included interfaces shows up to 15 % different pressure at the corners but the central pressure distribution is very similar for all three models.

25.4.2.2 Tangential Contact Stiffness

The computation of the resulting contact stiffness during the elastic deformation of the contact interface led to different stiffness values for the exterior nodes of the specimen close to the actual measurement locations and an interior node set at the contact surface (see Fig. 25.7). This could be attributed to the elastic compliance of the specimen bulk material which was active between the contact interface and the actual measurement location. Using a much high Young's modulus to minimise the specimen compliance led to a much better agreement between the two measurement locations, highlighting the importance of the compliance of the specimen.

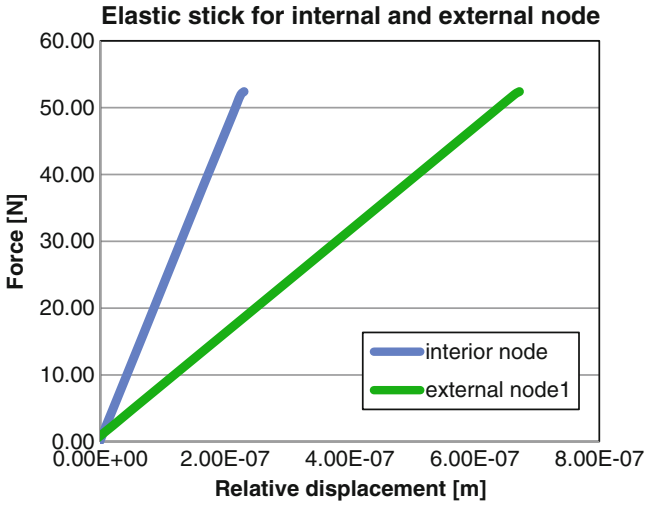

Fig. 25.7 Compliance in the specimen for an internal and external node

A comparison between the computed and measured contact stiffness, k_t, showed an order of magnitude stiffer model when compared to the measured data from Fig. 25.5. With the previously obtained understanding of the influence of compliance on the stiffness behaviour, the observed additional flexibility of the model was attributed to the compliance of the clamping mechanism and the other components in the test rig, which were not present in the FE model with its rigid boundary conditions. This implies, that the measured contact stiffness, k_t, actually includes the flexibility of the contact surface itself but also the flexibility of the rig whereas the simplified FE model lacks some of this information. To address this issue it will be assumed that the analytic stiffness for each element, k_2, in series with the stiffness of the FE model, k_1, must show the same stiffness as the measured contact stiffness, k_t.

$$\frac{1}{k_t} = \frac{1}{k_1} + \frac{1}{k_2} \tag{25.2}$$

where the model stiffness, $k_1 = 9e7$ N/m/mm^2, can be obtained from the computation of the relative displacement between the two measurement points for a fully tied contact and the measured tangential stiffness, k_t, was 6.58e7 N/m/mm^2. Based on this assumption a modified critical elastic slip, γ_{crit}, can be computed that will take the additional flexibility of the experimental rig into account

$$\gamma_{crit} = \frac{\mu N_0}{k_2} \tag{25.3}$$

Applying this value to the nonlinear analysis leads to a significantly better representation of the stiffness behaviour (see Fig. 25.8b), highlighting the deficiencies of the simplified FE model and the need to implement its flexibility somehow into the analysis.

25.4.2.3 Microslip

The computation of the microslip behaviour was based on the assumption that enough nonlinear elements in the contact zone will initially introduce partial slip in areas with lower pressure while areas with higher normal loads will remain stuck for longer. The resulting predicted microslip transition in Fig. 25.8a indicates that this is indeed the case, with a small transition region between the elastic deformation of the contact and the full slip. Figure 25.8b shows a comparison between the simulated and the measured hysteresis loop. The predicted tangential contact stiffness is still somewhat stiffer than expected, indicating that additional, currently unknown, features are not being captured correctly by the model. The microslip transition of the FE analysis seems to be starting slightly later and is also somewhat shorter than the measured one, but it can be shown that a detailed FE model can capture the underlying mechanism of the microslip transition. The observed differences are most likely due to the difference between the real pressure distribution at the worn contact surface and the predicted one in Fig. 25.6.

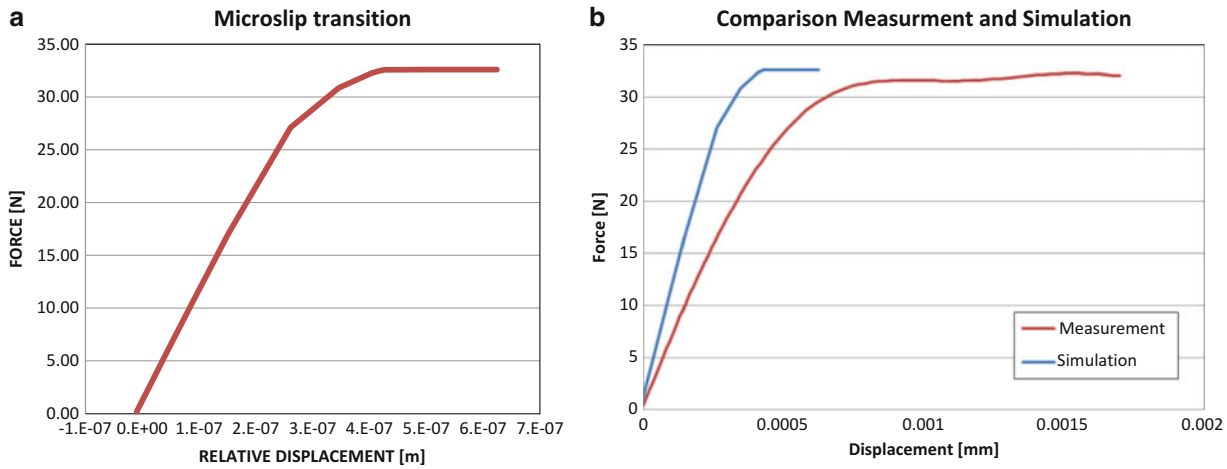

Fig. 25.8 Mircroslip behaviour (**a**) predicted transition and (**b**) comparison with measurement

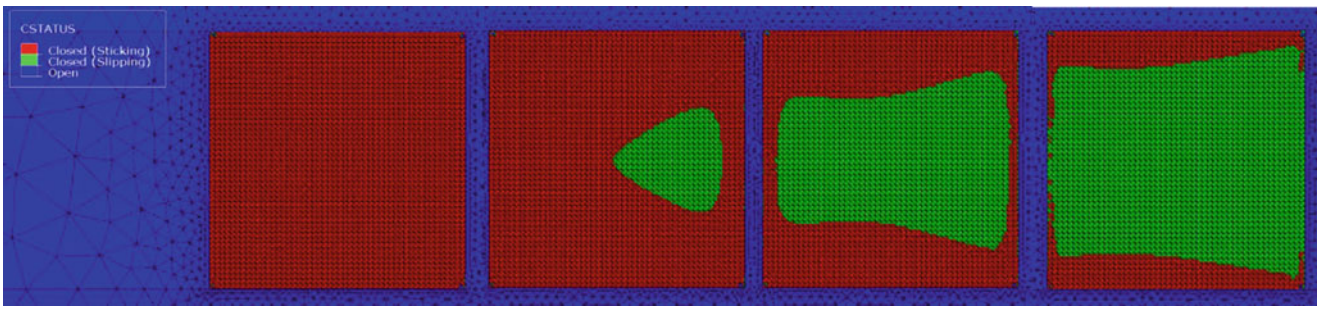

Fig. 25.9 Predicted microslip transition at the contact interface

Figure 25.9 shows the local transition from stuck to nearly full slip at the contact interface which is leading to the microslip behaviour from Fig. 25.8. It can be seen that the initially stuck contact zone starts to slip in the central area where a low contact load is present. It is interesting to notice that the initial slip does not occur right at the centre of the contact, as could be expected from the applied symmetric pressure distribution, but closer to the edge where the horizontal force is being applied. This indicates that even with a distributed tangential loading and a horizontal constraint to the upper specimen a small amount of elastic deformation in the specimen is present, which causes a slight unloading of one side of the contact surface, triggering the micro slip in this zone. As the tangential loading is increased the micro slip zone gradually becomes more symmetric until it covers nearly all of the contact area. Only the edges with their high contact pressure remain stuck until the end. Due to convergence issues the final stage of full slip could not be computed, but it can be assumed that eventually only the four corners will be stuck before all of the contact is slipping.

25.5 Conclusion

The aim of this work was to investigate if the experimentally observed stick-microslip-macroslip transition of a flat contact interface can be modelled explicitly with a quasi-static analysis in Abaqus.

It could be shown that the elastic deformation at the contact surface is strongly influenced by the compliance of the test setup, and adjustments to the computational tangential stiffness value are required to achieve a reasonable representation with the Abaqus elements.

The large number of nonlinear elements in the contact zone allowed modelling the microslip behaviour, with a gradual transition from stick to slip. The resulting transition started later and occurred somewhat faster than in the experimental observation, which was attributed to a difference between the computed normal load distribution and the real contact pressure at the interface. The microslip transition started in the centre of the contact patch, where the lowest normal loads were present and gradually extended over the full contact surface.

In summary it can be said, that the micro-slip behaviour in a contact interface can be captured with a large number of discrete elements in a quasi-static analysis, but further understanding is required for an accurate and reliable analysis.

References

1. Boeswald, M., Link, M.: Experimental and analytical investigations of non-linear cylindrical casing joints using base excitation testing. In: Proceedings of International Modal Analysis Conference 2003, IMAC XXI, Kissimmee, 2003
2. Gaul, L., Lenz, J.: Nonlinear dynamics of structures assembled by bolted joints. Acta Mech. **125**(1–4), 169–181 (1997)
3. Ibrahim, R.A., Pettit, C.L.: Uncertainties and dynamic problems of bolted joints and other fasteners. J. Sound Vib. **279**(3–5), 857–936 (2003)
4. Schwingshackl, C.W., Petrov, E.P.: Modelling of flange joints for the nonlinear dynamic analysis of gas turbine engine casings. J. Eng. Gas Turbines Power **134**(12), 122504 (2012)
5. Petrov, E.P., Ewins, D.J.: Analytical formulation of friction interface elements for analysis of nonlinear multiharmonic vibrations of bladed discs. ASME J. Turbomach. **125**(2), 364–371 (2003)
6. Firrone, C.M., Zucca, S., Gola, M.: Effect of static/dynamic coupling on the forced response of turbine bladed disks with underplatform dampers. In: Proceedings of ASME Turbo Expo, Orlando, GT2009-59905, 8–12 June 2009
7. Cigeroglu, E., An, N., Menq, C.H.: Wedge damper modeling and forced response prediction of frictionally constrained blades. In: Proceedings of ASME Turbo Expo, Montreal, GT2007-27963, 14–17 May 2007
8. Petrov, E.P.: Explicit finite element models of friction dampers in forced response analysis of bladed disks. J. Eng. Gas Turbines Power **130**(2), 022502 (2008)
9. Charleux, D., Gibert, C., Thouverez, F., Dupeux, J.: Numerical and experimental study of friction damping in blade attachments of rotating bladed disks. Int. J. Rotating Mach. **71302**, 1–13 (2006)
10. Petrov, E.P., Ewins, D.J.: Effects of damping and varying contact area at blade-disc joints in forced response analysis of bladed disc assemblies. ASME J. Turbomach. **128**, 403–410 (2006)
11. Segalman, D.: A four parameter model for lap type joints. Sandia Report 2002-3828, November, 2002
12. Schwingshackl, C.W., Petrov, E.P., Ewins, D.J.: Validation of test rig measurements and predicting tools for friction interface modelling. In: Proceedings of the ASME Turbo Exop 2010, Glasgow 2010
13. Schwingshackl, C.W.: Measurement of friction contact parameters for nonlinear dynamic analysis. In: Proceedings of the SEM IMAC XXX Conference, Jacksonville, 2012

Chapter 26
Modal Testing Through Forced Sine Vibrations of a Timber Footbridge

Giacomo Bernagozzi, Luca Landi, and Pier Paolo Diotallevi

Abstract The work aims at performing the dynamic modal identification of the long-span laminated timber footbridge built on the Marecchia River near Rimini, Italy. A first sine vibration test has been performed adopting a mechanical shaker just after the footbridge construction in 2000 in order to check the structural behavior that has been assumed in the project. A second test has been replicated in 2005 using the same excitation and almost the same test set-up adopted in the first one. The dynamic modal extraction is performed on the FRFs through both the peak picking method, applied together with the half power bandwidth technique, and the circle-fit method. The orthogonal properties of the identified mode shapes are verified through the Modal Assurance Criterion (autoMAC). Finally, the results obtained for the two tests and through the two techniques are mutually compared. It is worth noting that the FRFs, evaluated for different intensity levels of the exciting force, reveal an inherent non-linear behavior of the footbridge. The analyses also show that the first natural frequencies of the structure are included in the frequency range of the human step and this could lead to unpleasant feelings for the pedestrians.

Keywords Long-span laminated timber footbridge • Forced sine vibration test • Frequency response function • Frequency-domain identification • SDOF modal extraction

26.1 Introduction

The paper deals with the dynamic modal identification of a long-span footbridge that has been constructed across the Marecchia River in the city of Rimini, Emilia Romagna, Italy. An upper arch and a lower deck, which are connected by vertical ties, mainly constitute the structure of the bridge, which is entirely build in laminated timber except for the connections and the bracing systems.

Due to an evident flexibility of the structure, the local municipal administration requested the execution of a dynamic test just after the construction of the bridge in 2000. The Laboratory of Structural Engineering and the department DISTART (now part of the department DICAM) of the University of Bologna have performed the dynamic test: the structure has been excited through forced sine vibrations generated by a mechanical shaker, both in the horizontal and in the vertical directions. The structural responses have been measured by ten piezoelectric accelerometers, placed both on the deck and on the arch. This kind of testing is commonly adopted both for bridges and for buildings [1–9].

The bridge has been tested again in 2005 through the same dynamic test and with the same instrumentations in order to evaluate possible modifications of the structure 5 years apart. In this second case, all the accelerometers have been positioned on the deck and some improvements in the test set-up have been adopted with respect to the 2000 test.

The objective of the work is to perform the identification of the dynamic properties of the footbridge starting from the data of both the 2000 dynamic test and the 2005 one, in order to deepen some previous analyses that have been conducted on the structure [7–9]. The identification is performed through some SDOF modal extraction methods, such as the peak picking technique (applied together with the half power bandwidth method) and the circle-fit method [10–12]. The mode shapes are extracted from the imaginary part of the FRFs and their orthogonal properties are verified through the Modal Assurance Criterion (autoMAC) [10]. At the end, the results obtained with the different methods and for the two dynamic tests are mutually compared.

G. Bernagozzi (✉) • L. Landi • P.P. Diotallevi
Department DICAM, University of Bologna, Viale Risorgimento 2, 40136 Bologna, Italy
e-mail: giacomo.bernagozzi2@unibo.it

© The Society for Experimental Mechanics, Inc. 2016

M. Allen et al. (eds.), *Dynamics of Coupled Structures, Volume 4*, Conference Proceedings of the Society for Experimental Mechanics Series, DOI 10.1007/978-3-319-29763-7_26

Fig. 26.1 Overview of the Marecchia River bridge

26.2 Marecchia River Footbridge

The analyzed structure is a long-span laminated timber footbridge that crosses the Marecchia River in Rimini, Italy (Fig. 26.1). It is an arch bridge constituted by a twin arch timber section of 22 × 182 cm and two beams with a timber section of 22 × 200 cm; these last support the vertical loads of the deck and absorb the horizontal forces produced by the arch. The arch and the deck are connected through vertical ties that have rectangular timber sections of 12 × 20 cm.

Referring to the geometrical dimensions, the bridge is characterized by a 92 m span and a 5 m width of the deck; the height of the structure at the mid-span is 12 m and the curvature radius of the arch is about 95 m. All the elements of the arch are made in timber except for the connections and the bracing systems: the plates and the bolts are made of zinc-coated steel; diagonal steel elements, constituted by a circular section diameter of 5 cm, are placed as bracings both inside the upper twin arch section and under the trampling level, connecting the horizontal beams.

The bridge has been designed in order to carry the pedestrian loads and the weight of the electrical and the water transportation systems; it is worth noting that this last represents a considerable amount of the total loads acting on the deck.

26.3 Forced Vibration Tests

The bridge has been tested through two forced vibration tests, both conducted by the Laboratory of Structural Engineering and the department DISTART (now part of the department DICAM) at the University of Bologna. In both tests, the structure has been excited by a mechanical shaker, which generates sinusoidal forces at different frequencies, and the responses have been measured by uniaxial piezoelectric accelerometers.

The dynamic actuator (Fig. 26.2) is constituted by two disks that rotate at the same rotation speed but in opposite direction; each disk has two eccentrically positioned masses whose relative angle may be varied in order to generate forces of different magnitude. The maximum force that can be applied by the mechanical shaker is equal to 20 kN and a phasameter is mounted in order to measure the phase angle of the applied input force. According to the constructor, the expression of the sinusoidal force generated by the machine is

$$\mathrm{F}(t) = C f_v^2 \cos\left({}^{\alpha}\!/_{2}\right) \sin\left(2\pi f_v t + \varphi\right) \tag{26.1}$$

$$\varphi = {}^{\alpha}\!/_{2} - \beta + \gamma \tag{26.2}$$

where:

$C = 1.026\ kN/Hz^2$ is the characteristic constant of the machine;
f_v is the frequency in the range 0–25 Hz;
α is the angle between the masses of the vibrodyne, which can vary from 46° to 180°;

Fig. 26.2 Mechanical shaker in position 1 (horizontal forces)

Table 26.1 Description of the 2000 dynamic test

Set-up	Vidrodyne position	Angle between masses (α)	Frequency range f_v (Hz)	Maximum force (kN)
aa	1	46°	0.6 ÷ 4.0	0.34 ÷ 15.11
bb	1	146°	2.5 ÷ 7.0	1.87 ÷ 14.70
cc	2	172°	0.7 ÷ 7.0	0.04 ÷ 3.51

Table 26.2 Description of the 2005 dynamic test

Set-up	Vidrodyne position	Angle between masses (α)	Frequency range f_v (Hz)	Maximum force (kN)
aa	1	46°	0.8 ÷ 4.0	0.60 ÷ 15.11
bb	1	146°	3.0 ÷ 6.9	2.69 ÷ 14.28
dd	1	166°	4.5 ÷ 7.8	2.53 ÷ 7.60
cc	2	172°	0.8 ÷ 8.0	0.04 ÷ 4.58

$\beta = 86.9°$ is the angle between the phasameter and the fixed mass;
γ is the phase measured by the phasameter.

Ten piezoelectric accelerometers have been used for measuring the structural responses and they have been connected, through a wired system, to a signal-conditioning unit and a computer for the data processing and the data storage. Seven sensors PCB/393B12 and three sensors PCB/393A03 have been adopted in the two dynamic tests.

In both tests, the mechanical shaker was placed in the mid-span and different experimental set-ups have been adopted in order to fully characterize the dynamics of the structure: they differ in the investigated frequency range, in the direction and the maximum value of the applied force (Table 26.1—2000 test; Table 26.2—2005 test). The shaker placed in position 1 has generated horizontal forces that have induced transversal oscillations in the bridge; referring to position 2, the vibrodyne has created forces in the vertical direction. The position and the direction of the accelerometers has been thus chosen according to the exciting direction of the set-up. It is worth noting that there are some differences in the position of the accelerometers between the two tests, as reported in Fig. 26.3: in the 2000 test, some accelerometers are placed on the arch while in the 2005 one all the sensors are only positioned on the deck.

In the 2000 dynamic test a frequency step of 0.1 Hz has been adopted in order to scan the selected range and at each frequency four cycles of the force ($n = 4$), corresponding to $N = 256$ samples, have been applied. In the 2005 test the scanning frequency step was 0.1 Hz, reduced to 0.05 Hz around the resonance frequencies, and the force was constituted by 16 cycles ($n = 16$, $N = 1024$ samples).

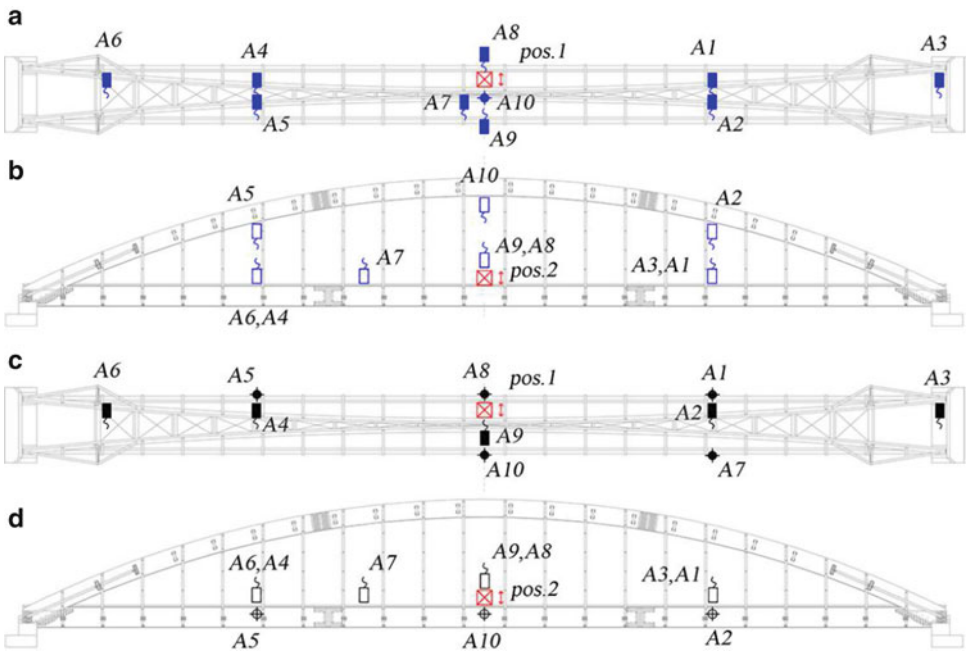

Fig. 26.3 Positions of the accelerometers and the vibrodyne: (**a**) 2000 test—pos. 1; (**b**) 2000 test—pos. 2; (**c**) 2005 test—pos. 1; (**d**) 2005 test—pos. 2

The total time t_{TOT} of each measured signal and the sampling time step Δt are expressed as

$$t_{TOT} = n\,T_v = {}^{n}\!/_{f_v} \tag{26.3}$$

$$\Delta t = {}^{t_{TOT}}\!/_{N} = {}^{n}\!/_{N f_v} \tag{26.4}$$

26.4 Frequency Response Functions (FRFs)

After having reconstructed the input force starting from the signal measured by the phasameter, a Fast Fourier transform (FFT) [13] is applied to both the excitation and the response. The frequency step and the bandwidth in the FFT result as

$$\Delta f = {}^{1}\!/_{t_{TOT}} = {}^{1}\!/_{N\,\Delta t} = {}^{f_v}\!/_{n} \tag{26.5}$$

$$f_s = {}^{1}\!/_{\Delta t} \tag{26.6}$$

The maximum values of the FFTs are used for the computation of the inertance FRFs [10–12], which are defined as the ratio between the FFT of the response acceleration and the FFT of the force. The receptance FRF are subsequently obtained in order to operate the modal extraction. The receptance FRF related to the A9 accelerometer for the shaker placed in position 1 is reported in Fig. 26.4 (modulus and phase) and in Fig. 26.5 (real part and imaginary part).

The first part of the FRFs (i.e., at the low frequencies, below 1 Hz) is characterized by a low accuracy because the applied force does not excite the structure with sufficient energy. The different scanning frequency steps adopted in the two tests affect the determination of the peaks in the FRFs and thus the identification of the natural frequencies. This effect is evident in the modulus plot of the FRF in Fig. 26.4a at the frequency around 1.7 Hz: using a 0.1 Hz step (2000 test) is not possible to correctly individuate the peak, which is, by contrast, well defined using the 0.05 Hz step (2005 test).

It is worth noting that there are some translational shifts of the FRFs in the overlapping part between test set-ups that are characterized by different amplitudes of the exciting force: the natural frequencies increase if the shaker amplitude decreases (e.g., this fact occurs for the FRF reported in Fig. 26.4 at the frequency around 5.5 Hz). This translation is related to a spring softening effect, as also mentioned in [7], and reveals an inherent non-linear behavior of the structure.

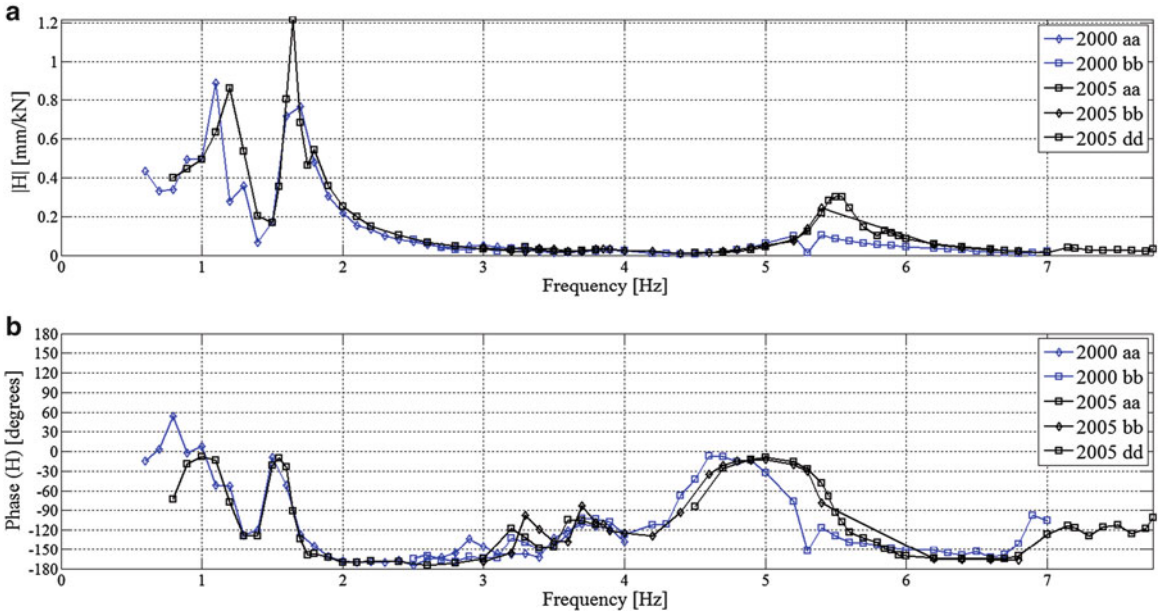

Fig. 26.4 Receptance FRF—A9 sensor—vibrodyne in position 1: (**a**) modulus, (**b**) phase

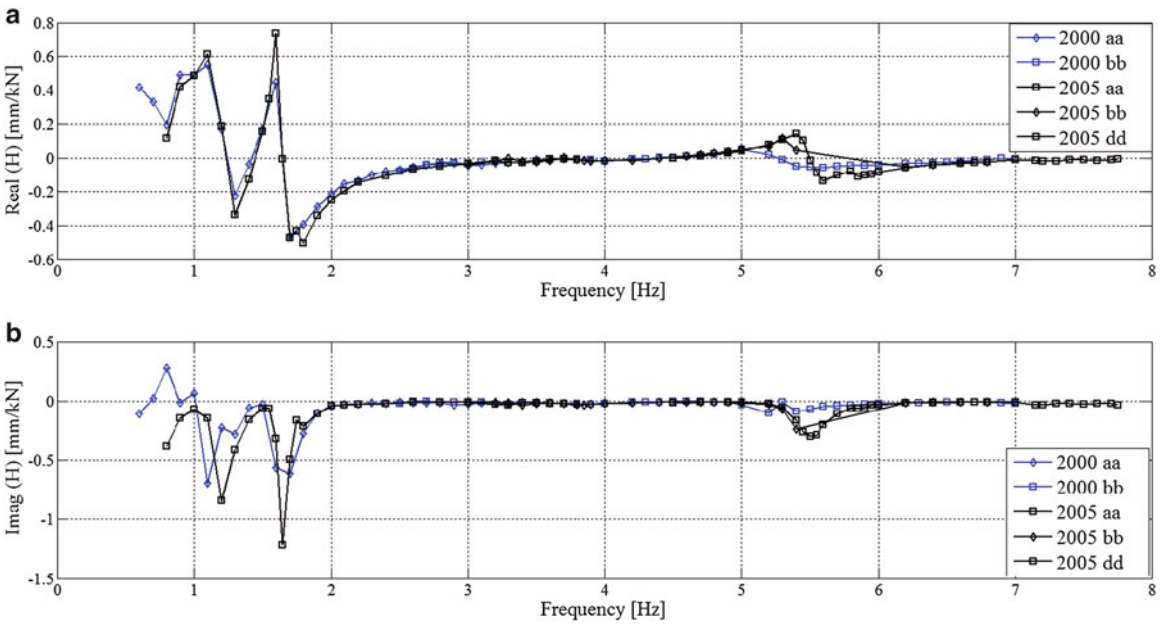

Fig. 26.5 Receptance FRF—A9 sensor—vibrodyne in position 1: (**a**) real part, (**b**) imaginary part

26.5 Modal Identification

Starting from the FRFs of the structure, the modal parameter estimation is performed through SDOF extraction methods [10–12] that are valid for lightly damped structures, which exhibit well-separated modes. The natural frequencies are determined with both the peak picking method and the circle-fit technique; assuming a viscous damping model for the characterization of the bridge, the modal damping ratios are identified with both the half power method and the circle-fit technique. An example of the application of the circle-fit method is reported in Fig. 26.6, which shows the points, for a selected frequency range, of the mobility FRF in the Nyquist plane.

The modal extraction provides information about the first seven modes of the structure (Table 26.3—2000 test; Table 26.4—2005 test). Referring to the identification of the natural frequencies, very similar results are obtained using

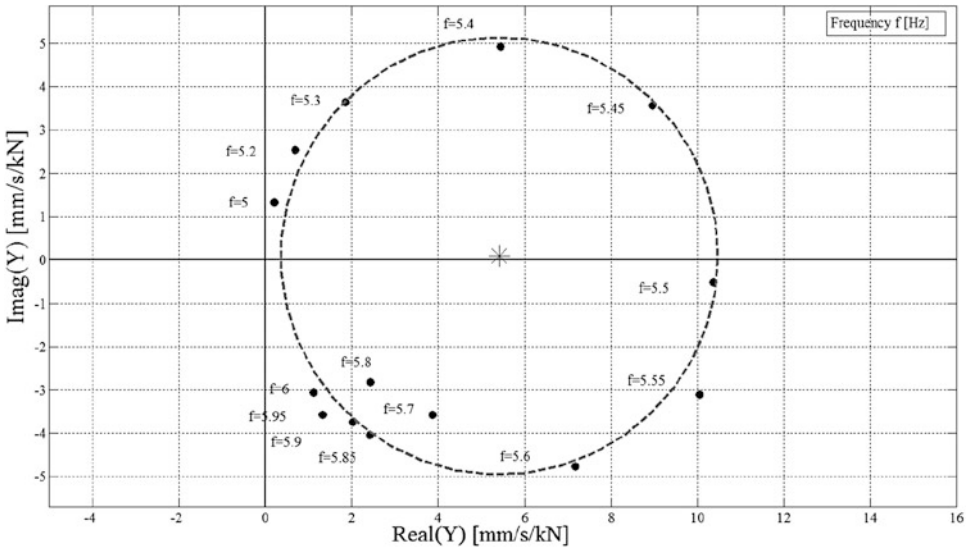

Fig. 26.6 Circle fit of the mobility FRF points in the Nyquist plane—A9 sensor, vibrodyne in pos. 1, around f = 5.5 Hz

Table 26.3 Identified parameters of the 2000 dynamic test

			Natural frequency f_i [Hz]		Modal damping ratio ζ_i [/]	
Mode *i*	Set-up	Sensor	Peak picking	Circle-fit	Half power	Circle-fit
1—horiz.	aa	A9	1.1	1.1	0.046	0.024
2—vert.	cc	A4	1.4	–	0.041	–
3—horiz.	aa	A9	1.7	1.65	0.064	0.039
4—vert.	cc	A4	2.2	–	0.025	–
5—horiz.	bb	A2	3.2	–	0.044	–
6—vert.	cc	A4	3.7	–	0.051	–
7—horiz.	bb	A9	5.1	5.25	0.055	0.050

Table 26.4 Identified parameters of the 2005 dynamic test

			Natural frequency f_i [Hz]		Modal damping ratio ζ_i [/]	
Mode *i*	Set-up	Sensor	Peak picking	Circle-fit	Half power	Circle-fit
1—horiz.	aa	A9	1.2	1.2	0.076	0.035
2—vert.	cc	A4	1.4	–	0.047	–
3—horiz.	aa	A9	1.65	1.65	0.023	0.019
4—vert.	cc	A4	2.2	–	0.032	–
5—horiz.	aa	A7	3.3	–	0.023	–
6—vert.	cc	A4	3.8	–	0.018	–
7—horiz.	dd	A9	5.55	5.55	0.021	0.026

the peak picking technique in comparison to the circle-fit method, when this last is applicable; it requires, indeed, a sufficient number of FRF points around each natural frequency. The determination of the peaks is, sometimes, strongly dependent on the quality of the measurements and on the adopted frequency step for the testing; with respect to this specific issues the circle-fit, if applicable, guarantees more precision and reliability.

Much more uncertainties occur in the identification of the modal damping ratios; especially for the modes at the lower frequencies, the values of the damping obtained through the peak picking method are higher than the one identified by the circle-fit method, when applicable. Furthermore, there is a clear decreasing trend of the damping in the results of the 2005 test passing from the lower frequencies to the higher ones; this trend is not evident in the values of the damping related to the 2000 test.

The mode shapes are obtained by evaluating the peaks of the imaginary part of the receptance FRFs and subsequently performing a maximum-value normalization. Seven mode shapes are clearly individuated and the results for the two tests are graphically compared in Fig. 26.7 referring to the modes with a prevalent horizontal-torsional trend and in Fig. 26.8 for the

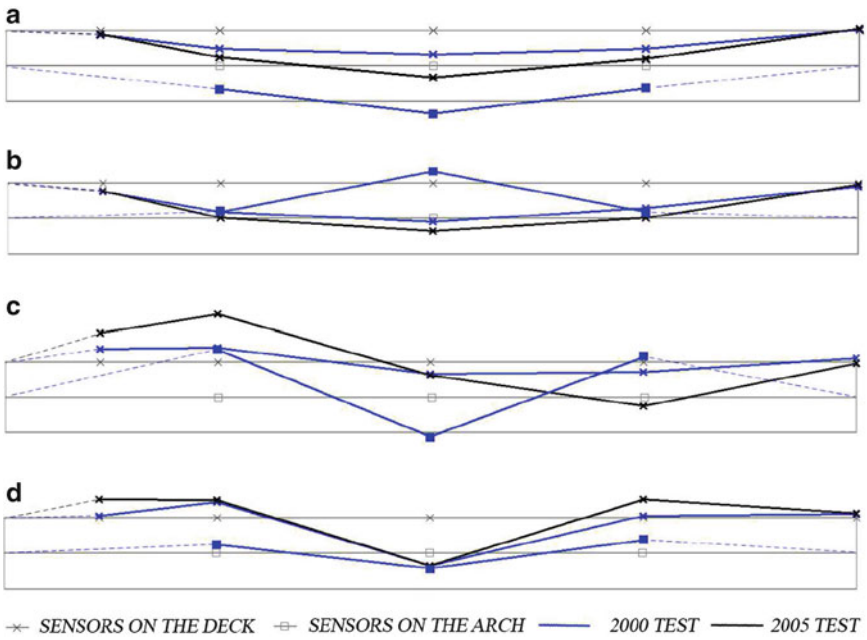

Fig. 26.7 Maximum-value normalized mode shapes (*blue line*: 2000 test; *black line*: 2005 test): (**a**) 1° mode; (**b**) 3° mode; (**c**) 5° mode; (**d**) 7° mode

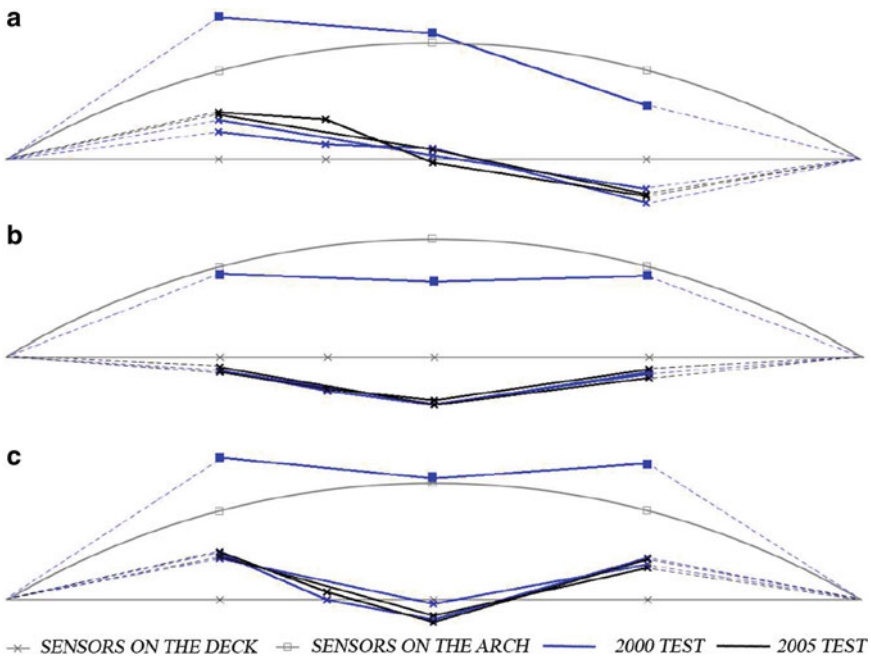

Fig. 26.8 Maximum-value normalized mode shapes (*blue line*: 2000 test; *black line*: 2005 test): (**a**) 2° mode; (**b**) 4° mode; (**c**) 6° mode

modes with prevalent vertical components. The identification of higher modes is inevitably affected by the so-called "spatial aliasing" effect [10], which is generated by the limited number of the adopted sensors.

Referring to the mode shapes, quite similar results are obtained for the two dynamic tests even if they are characterized by different set-ups and slightly different positions of the accelerometers. The mutual orthogonality between the identified mode shapes is demonstrated though the computation of the Modal Assurance Criterion or autoMAC [10]. The autoMAC matrices are graphically reported in Fig. 26.9 for the modes with prevalent horizontal components, which are identified through the 2000 test (Fig. 26.9a) and the 2005 test (Fig. 26.9b). It is worth noting a slight correlation between the first two horizontal

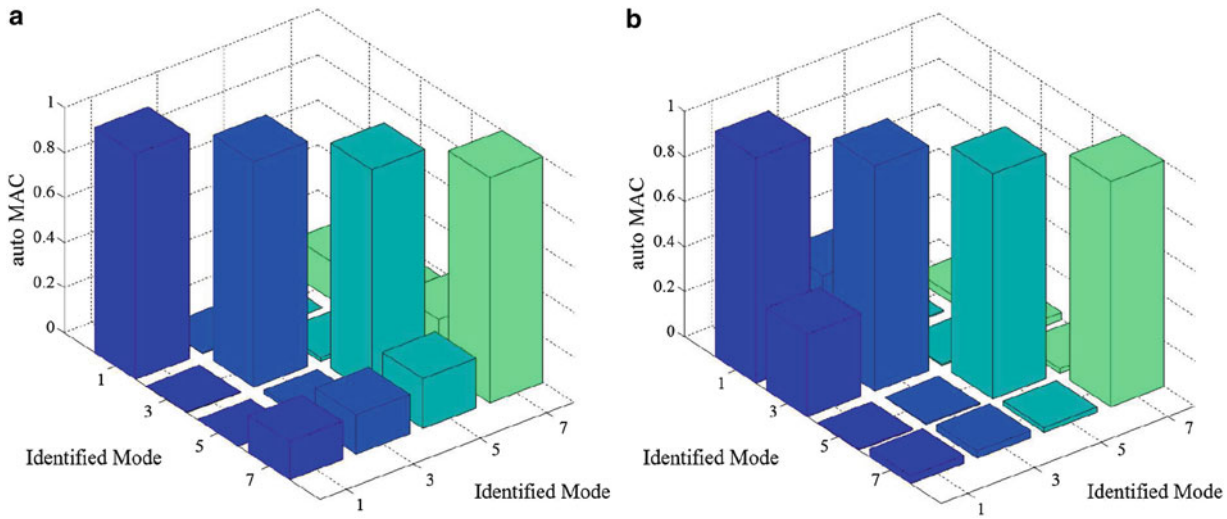

Fig. 26.9 AutoMAC matrices for the identified modes with prevalent horizontal components: (**a**) 2000 test; (**b**) 2005 test

modes in the 2005 test autoMAC matrix; this is due to the set-up choice of not instrumenting the arch and this effect is, indeed, not present in the 2000 test matrix. The orthogonality also holds for the identified modes with prevalent vertical components.

26.6 Conclusions

A laminated timber footbridge has been tested through sinusoidal forced vibrations in 2000 and in 2005; seven modes have been identified through SDOF extraction methods starting from the FRFs of the structure. Adopting the two tests data and comparing two different methods, the natural frequencies have been determined with adequate confidence while more uncertainties affect the identification of the modal damping ratios especially for the 2000 test, which is characterized by shorter time-recordings and a higher scanning frequency step with respect to the 2005 test. The different test set-ups and the different positions of the accelerometers, in the two tests, slightly affect the comparison of the identified results. In the 2000 test, a global torsional characterization has been achieved by the sensors also placed on the arch while in the 2005 test the more sensors placed on the deck reveal some local torsional behaviors in the first mode shapes of the bridge. Notwithstanding these limitations, the mutual orthogonality of the identified mode shapes has been verified through the autoMAC matrices.

An inherent non-linear behavior of the structure is shown by the FRFs due to the different amplitudes of the applied forces; furthermore, the first three modes of the structure are characterized by low natural frequencies in the range of 1–2 Hz and this could entail possible amplifications of the responses due to pedestrian or wind loads.

It is difficult to associate the changes of the identified modal parameters with some structural damages of the footbridge: the natural frequencies are almost constant comparing the two dynamic tests while the modifications of the damping ratios and the mode shapes do not show any clear trends. Further investigations through more complex fitting methods in the frequency domain and, eventually, the execution of another dynamic test on the footbridge may be useful in order to have a better comprehension of the health condition of the structure.

References

1. Salawu, O.S., Williams, C.: Review of full-scale dynamic testing of bridge structures. Eng. Struct. **17**(2), 113–121 (2015)
2. Zivanovic, S., Pavic, A., Reynolds, P.: Modal testing and FE model tuning of a lively footbridge structure. Eng. Struct. **28**, 857–868 (2006)
3. Diotallevi, P.P., Paladin, A., Tralli, A., Tullini, N.: Identificazione strutturale di un edificio di muratura sottoposto a prove di vibrazione forzata. In: IX National conference "L'ingegneria sismica in Italia", Torino, 1999
4. Diotallevi, P.P., Poluzzi, R.: Sperimentazione in situ: contributo alla evoluzione tecnologica ed alla affidabilità delle opere di c.a. e di c.a.p., "L'industria italiana del cemento", November, 1995

5. Ceccoli, C., Diotallevi, P.P., Tullini, N.: Identificazione strutturale di un fabbricato a pareti portanti realizzate con blocchi cassero in legno-cemento. In: X National conference "L'ingegneria sismica in Italia", Potenza-Matera, 9–13 September 2001
6. Diotallevi, P.P., Tullini, N.: Prove di vibrazione armonica forzata su costruzioni pubbliche di tipo strategico ubicate in diverse località della Romagna. In: X National conference "L'ingegneria sismica in Italia", Potenza-Matera, 9–13 September 2001
7. Diotallevi, P.P., Manfroni, O., Tullini, N.: On site dynamic test of a long span timber footbridge. Footbridge 2000 Conference, Paris, 2000
8. Diotallevi, P.P., Manfroni, O., Belmonte, C.: Forced vibration tests carried out on a laminated timber footbridge: comparisons five years apart. Footbridge 2008 Conference, Porto, 2008
9. Diotallevi, P.P., Manfroni, O., Belmonte, C.: Dynamic identification of a timber footbridge subjected to vibration tests. In: 14th World Conference on Earthquake Engineering, Beijing, 12–17 October , 2008
10. Ewins, D.J.: Modal Testing: Theory, Practice and Application. Research Studies Press, Baldock (2000)
11. Inman, D.J.: Engineering Vibration, 3rd edn. Prentice Hall, Upper Saddle River (2007)
12. Maia, N.M.M., Silva, J.M.M.: Theoretical and Experimental Modal Analysis. John Wiley & Sons Inc, Chichester (2007)
13. Papoulis, A.: Signal Analysis. McGraw-Hill, New York (1977)

Chapter 27
Damping Characteristics of a Footbridge: Mysteries and Truths

Reto Cantieni, Anela Bajrić, and Rune Brincker

Abstract As a consequence of a paper presented by Michael Mistler at the VDI-Baudynamik-Tagung in Kassel, Germany, in April 2015, the authors checked the damping coefficients having been estimated for a footbridge in autumn 2014. Mistler stated that the critical damping ratio estimated from a halfpower bandwidth procedure to be dependent on frequency resolution for low frequency modes. Based on the data presented here this statement can be confirmed. The dependency on frequency resolution was found to be due to the leakage phenomenon on the spectral density. This fact may have been known in the academic world but not in the world of engineers applying OMA in practice. In this paper it is presented how the leakage on the spectral density estimate is affecting the damping estimation through OMA based frequency domain identification. Finally the paper compares the damping estimated in the time and frequency domain from ambient tests, with the damping estimated from the free decays. Unfortunately, bias error on damping values determined from analyses in the frequency domain is worst on low frequency modes usually being the most important ones when dealing with a resonance problem in practice.

Keywords Structural damping ratio • Ambient vibration testing • Enhanced frequency domain decomposition • Ibrahim time domain identification • Free decay process • Half power bandwidth procedure

27.1 Introduction

The dynamic behavior of a new footbridge consisting of a 52 m single-span span steel space truss structure (Fig. 27.1) is discussed here. An experimental ambient modal test as well as dynamic loading tests were performed on this bridge in October 2014. The dynamic loading tests performed subsequently to the ambient tests aimed at a controlled excitation of three of the fundamental bridge modes. These resulted in a satisfactory harmonic free decay process for the first three bridge modes. The respective tests are described in detail in Rohner et al. [1].

To determine the structural damping ratio for a number of natural modes as estimated from ambient tests, Enhanced Frequency Domain Decomposition (EFDD) was applied as offered through the ARTeMIS software [2], as formulated by Brincker et al. [3].

It is well known that the spectral density estimate used for the estimation in the frequency domain, is contaminated with spectral leakage which affects the estimation of damping [4]. It was therefore thought to be necessary to estimate the damping using time domain OMA techniques, such as the classical Ibrahim Time Domain (ITD) technique and the Eigensystem Realization Algorithm (ERA) formulated by Ibrahim (1977), Juang and Pappa (1985) respectively [5, 6].

R. Cantieni (✉)
RCI Dynamics, Structural Dynamics Consultants, CH-8600 Duebendorf, Switzerland
e-mail: reto.cantieni@rcidynamics.ch

A. Bajrić
Department of Mechanical Engineering, Technical University of Denmark, Kongens Lyngby, Denmark

R. Brincker
Center for Oil and Gas, Technical University of Denmark, DK-2800 Kongens Lyngby, Denmark

© The Society for Experimental Mechanics, Inc. 2016

M. Allen et al. (eds.), *Dynamics of Coupled Structures, Volume 4*, Conference Proceedings of the Society for Experimental Mechanics Series, DOI 10.1007/978-3-319-29763-7_27

Fig. 27.1 Footbridge on the Sarine River at Broc, Switzerland

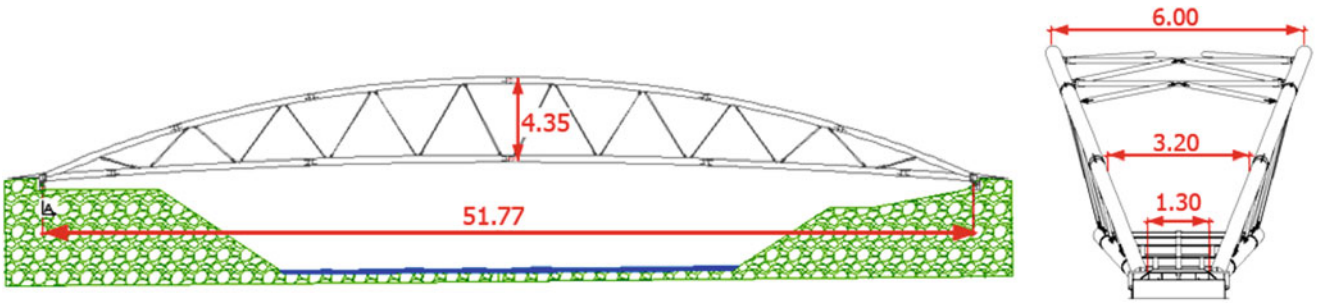

Fig. 27.2 Sarine River Footbridge geometry. Dimensions in meters

27.2 The Bridge

The Sarine River Footbridge is composed of steel tubes and, at the bridge deck level, of rolled section steel beams. The main dimensions can be taken from Fig. 27.2. The abutments are fixed in the vertical and lateral directions and are free in the longitudinal direction.

27.3 Experimental Modal Analysis of the Structure Under Ambient Excitation

27.3.1 Test Strategy

With seven cross sections and four structural points per section a complete 3D-grid would consist of 72 DOF's (Degrees of Freedom). Since the tests should have been performed in one day some strategic planning was necessary. First of all the number of DOF's to be measured was reduced from 72 to 45. DOF's where a reasonable solution using slave node equations existed were omitted only.

As moving of the rovers was time critical (Fig. 27.3) the number of references was chosen to an unusually high but still reasonable 15 DOF's. The number of rovers was chosen to six. The references were located close to the measurement center thus limiting the number of long cables needed to those connecting the rovers with the measurement center. It was therefore possible to handle the problem using five setups with a time window length of 20 min each. The full instrumentation is shown in Fig. 27.4. Using a 24-channel LMS SCM05 frontend, the signals were sampled at sR = 200 Hz and stored in a laptop.

Fig. 27.3 Attaching sensors to the top chord

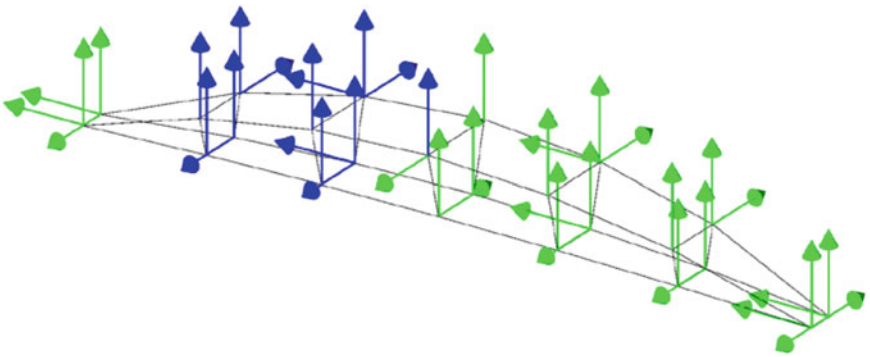

Fig. 27.4 Instrumentation for the modal test. *Blue*: References: *Green*: Rovers

27.3.2 Results from Signal Processing of the Data

Figure 27.5 shows the SVD diagrams as derived using the ARTeMIS EFDD routine. To end up with a reasonable frequency resolution as used for the manual optimization of the EFDD procedure the data were decimated by a factor of 4, the Nyquist frequency thus becoming $f_v = 25$ Hz, and the number of frequency lines was chosen to 2 K. It can be seen from Fig. 27.5b that visual inspection of the SVD diagram and adaptation of decimation and frequency resolution to the (visual) requirements is a reasonable approach to get optimum results for frequency, mode shape and damping coefficient for each mode. This approach has successfully been applied to many civil engineering structures by the first author in the last 15 years. Using this procedure here, 29 natural bridge modes could be successfully identified (frequency, mode shape and damping) (Fig. 27.5a, [1]). Being interested in human-structure interaction we will concentrate on the first three bridge modes.

The shape of the first mode is dominated by a horizontal lateral and torsional bridge "roof" motion (Fig. 27.6a). Its frequency is in the range of the step frequency as produced in the horizontal lateral direction through a walking pedestrian. The shape of the second mode is dominated by a horizontal lateral and torsional bridge deck motion (Fig. 27.6b). Its frequency is in the range of the step frequency as produced in the vertical direction through a walking pedestrian. The shape of the third mode is dominated by an almost pure vertical motion (Fig. 27.6c). Its frequency is in the range of the step frequency as produced in the vertical direction through a high-speed jogger.

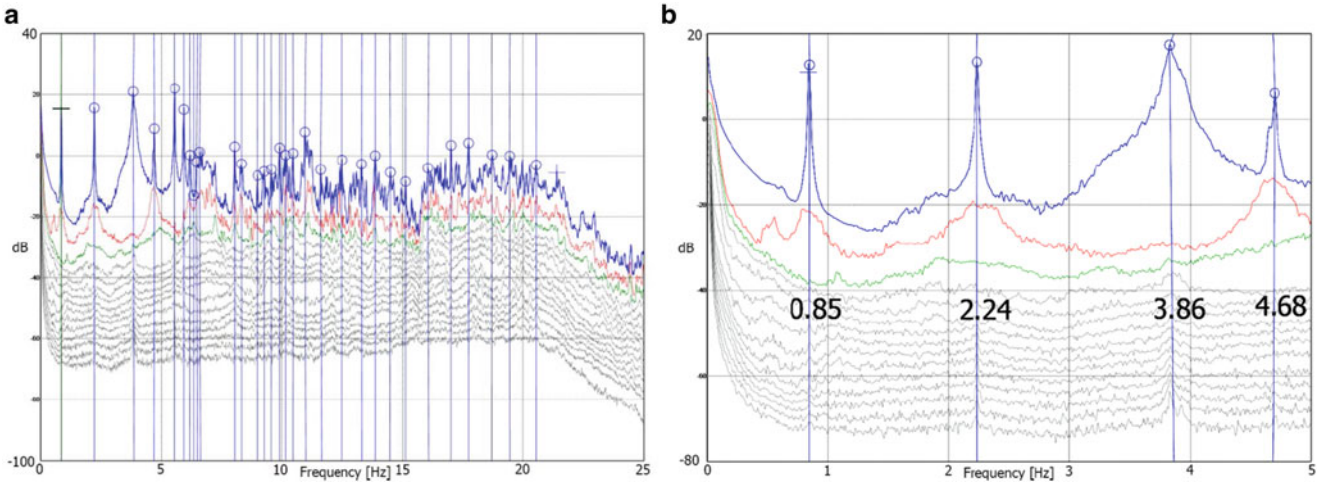

Fig. 27.5 (**a**) EFDD-SVD diagram; f = 0 . . . 25 Hz. (**b**) EFDD-SVD diagram, simply zoomed-in in the graph given in (**a**), down to f = 5 Hz

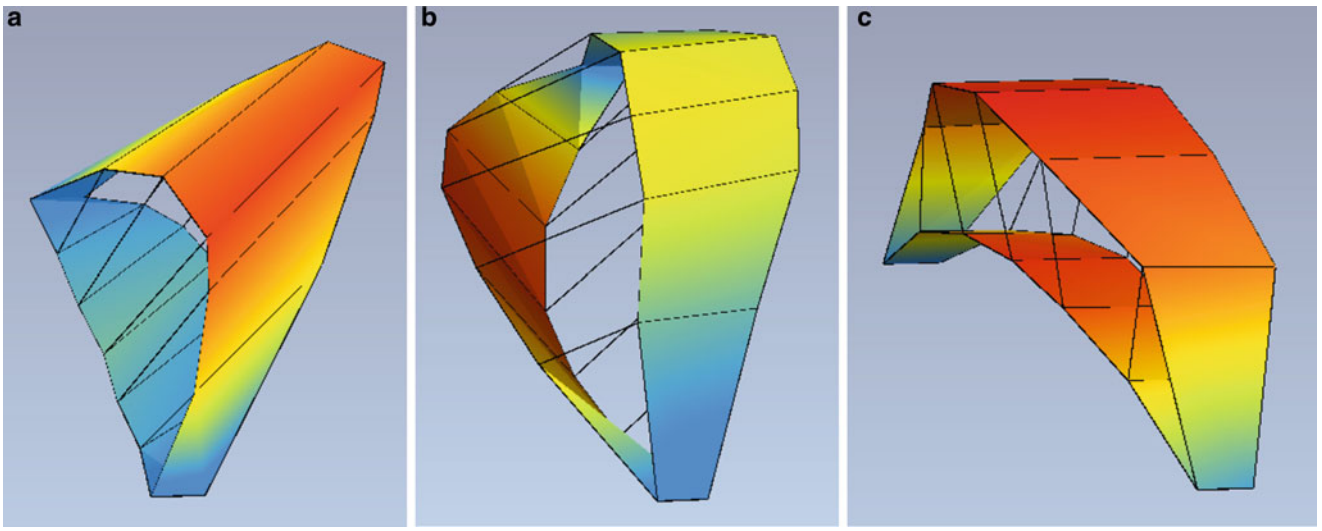

Fig. 27.6 (**a**) Mode 1, f = 0.85 Hz, ζ = 0.83 %. (**b**) Mode 2, f = 2.24 Hz, ζ = 0.34 %. (**c**) Mode 3, f = 3.86 Hz, ζ = 0.77 %

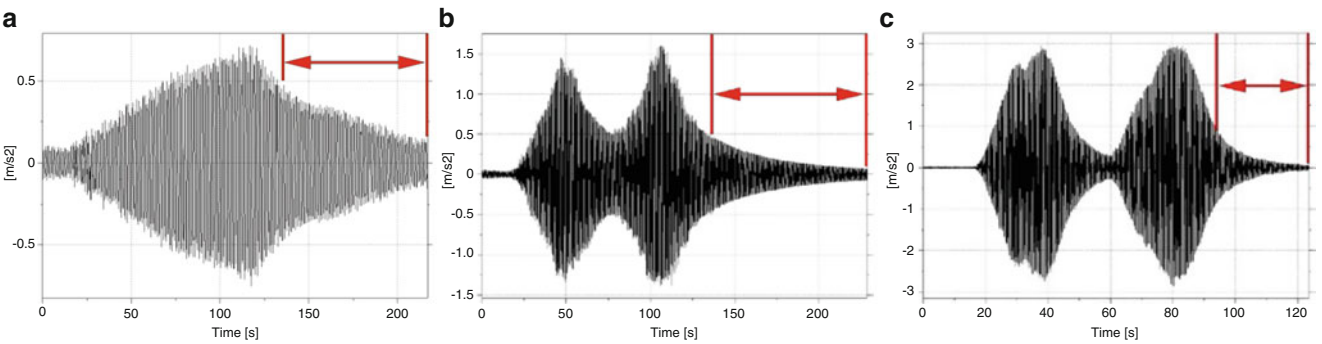

Fig. 27.7 (**a**) Mode 1, f = 0.85 Hz, ζ = 0.29 %. (**b**) Mode 2, f = 2.24 Hz, ζ = 0.15 %. (**c**) Mode 3, f = 3.85 Hz, ζ = 0.40 %

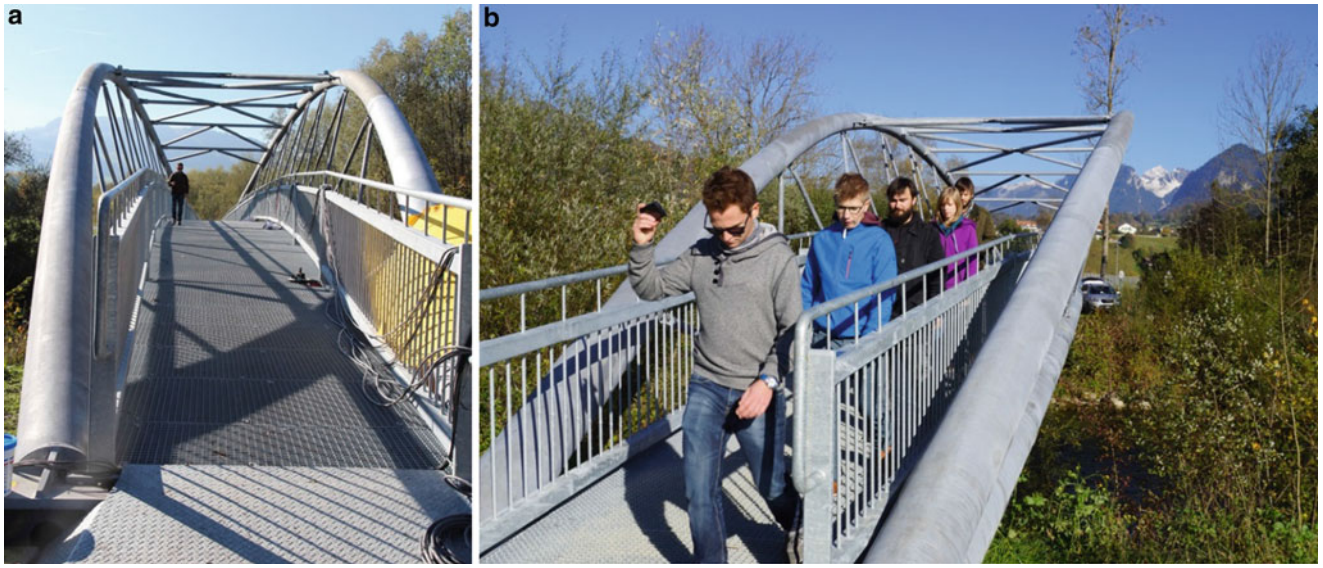

Fig. 27.8 (**a**) One person, walking eccentrically. The instruments can be seen on the right hand side on the bridge deck. (**b**) Five people, walking eccentrically. The pace-giving metronome can be seen in the right hand of the leading person

27.3.3 Dynamic Loading Tests

Investigating the dynamic behaviour of a footbridge is centred towards the question whether or not we are confronted with a resonance problem. And the most important parameter in a resonance case is damping. Based on the results of the modal tests discussed above, the loading tests were designed considering frequency and mode shape of the modes with a strong relation to the dynamic loads possibly being exerted by human beings:

Mode 1: Four people acting manually on the guard rail in the horizontal lateral direction with $f = 0.85$ Hz.
Mode 2: Several people walking in line close to a guard rail, i.e. eccentrically, with $f = 2.24$ Hz.
Mode 3: Several people jogging in line in the bridge center line with $f = 3.86$ Hz.

In most cases, one, two or five persons were walking or jogging over the bridge and back at different step paces (Fig. 27.8a). The step pace was controlled using an electronic metronome (Fig. 27.8b). A total of 32 loading tests were performed. Two points on the bridge were 3D-instrumented: at mid-span and in a quarter point (Fig. 27.8a). The maximum acceleration values reached with this kind of dynamic loading tests are discussed in detail in [1]. We are concentrating here on the three cases where a nice purely harmonic free decay process could be registered after the loading group had left the bridge (Figs. 27.7a–c).

The damping values determined from this were about half of the values determined with the EFDD procedure (Fig. 27.6). Considering the well-known uncertainty in damping estimation this was however accepted in October 2014 [1].

27.4 The Michael Mistler Paper

Michael Mistler presented data acquired from dynamic tests on a tall building under ambient excitation, in 2015 [7]. He found that the damping values for the first mode are significantly influenced by the frequency resolution used for the analysis. This can somehow be understood for the halfpower bandwidth method (“Halbwertsbreite”, Figs. 27.9a and 27.10), as the frequency spectrum is dependent on the number of sampling points. It is however not understood how the damping estimation through EFDD is affected, and therefore this Mistler information had to be cross-checked based on the data acquired for the Sarine River Footbridge.

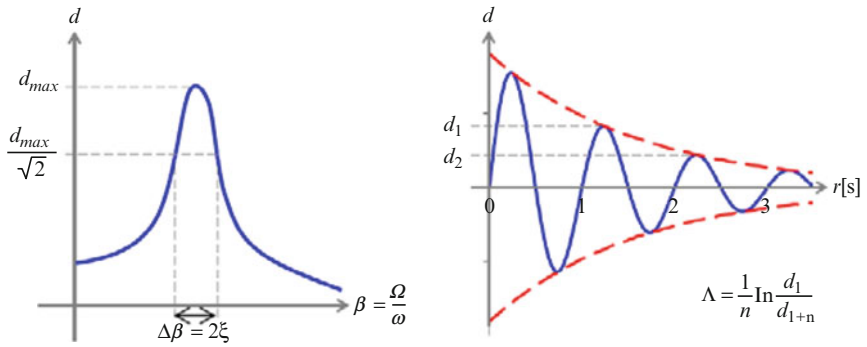

Fig. 27.9 (**a**) Damping derived using the halfpower bandwidth method (Figure taken from [7]). (**b**) Estimating the log. decrement Λ from a free decay process. $\zeta = \Lambda/2\pi$ ([7])

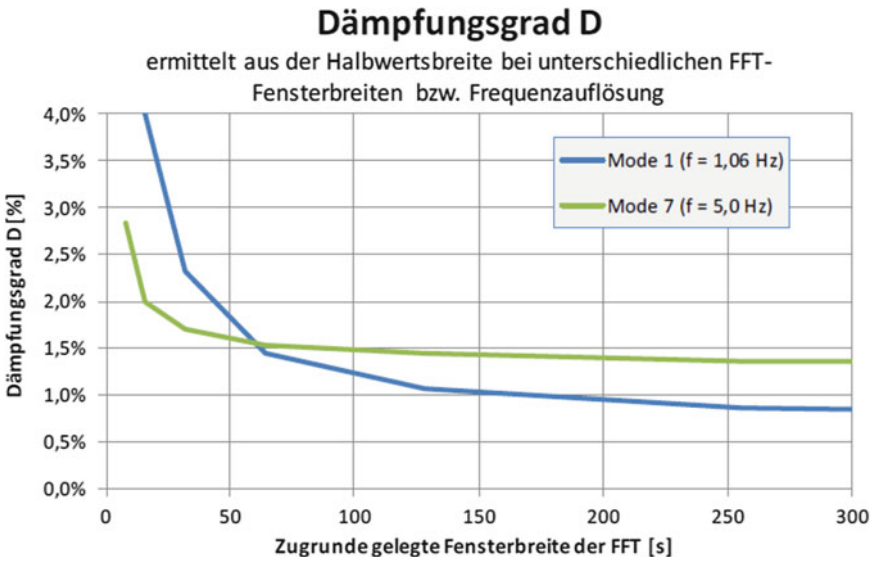

Fig. 27.10 Halfpower damping coefficient D (equal to ζ, percent of critical) versus time window length T [s] used for FFT calculation. The frequency resolution is 1/T, T given in seconds for the X-axis labelling (Figure taken from [7])

27.5 Damping as a Function of Frequency Resolution: EFDD

To investigate the influence of the frequency resolution on the damping coefficients estimated, ten different EFDD identifications of modal parameters with varying frequency resolution were performed on the same raw data collected for the Sarine River Footbridge. To begin with, the decimation factor was chosen to dec = 4, and a Nyquist frequency $f_v = 25$ Hz, as was used for the initial analysis (Fig. 27.5a). Furthermore, the number of frequency lines was chosen to 1 K, 2 K, 4 K, 8 K, 16 K and 32 K. In a next step, decimation was increased to dec = 10, such that the Nyquist frequency was f_v =10 Hz, and the number of frequency lines was chosen to 0.5 K, 1 K, 2 K and 4 K.

Here, the number of frequency lines N is the number of data points in the positive and negative part of the spectral density, which is equivalent to the total number of data points in the data segment. The standard expression for the frequency resolution is given by,

$$\Delta f = \frac{f_v}{N/2} = \frac{1}{2\,\Delta t} = \frac{1}{T} \tag{27.1}$$

which is herein used for the computation of the frequency resolution.

The resulting damping estimated through EFDD is given in Table 27.1 and illustrated in Fig. 27.11 (left). This result implies that the damping estimation is linearly dependent on the frequency resolution, and the varying gradients for each mode imply that the damping estimates furthermore depend on the frequency of the respective mode.

Table 27.1 The critical damping ratio ζ for the first four modes using EFDD for variations of frequency resolution Δf

Decimation [−]	N [−]	Δf [Hz]	ζ_1 [%]	ζ_2 [%]	ζ_3 [%]	ζ_4 [%]
4	32 K	0.0015	0.184	0.100	0.746	0.126
4	16 K	0.0031	0.256	0.130	0.774	0.172
10	4 K	0.0049	0.359	0.162	0.778	0.174
4	8 K	0.0061	0.442	0.191	0.761	0.192
10	2 K	0.0098	0.672	0.273	0.753	0.209
4	4 K	0.0122	0.833	0.334	0.774	0.235
10	1 K	0.0195	1.338	0.512	0.808	0.320
4	2 K	0.0244	1.687	0.636	0.841	0.384
10	0.5 K	0.0391	2.660	1.000	0.965	0.529
4	1 K	0.0488	3.224	1.184	1.077	0.640
ζ_{max}/ζ_{min}			*17.5*	*11.8*	*1.44*	*5.08*

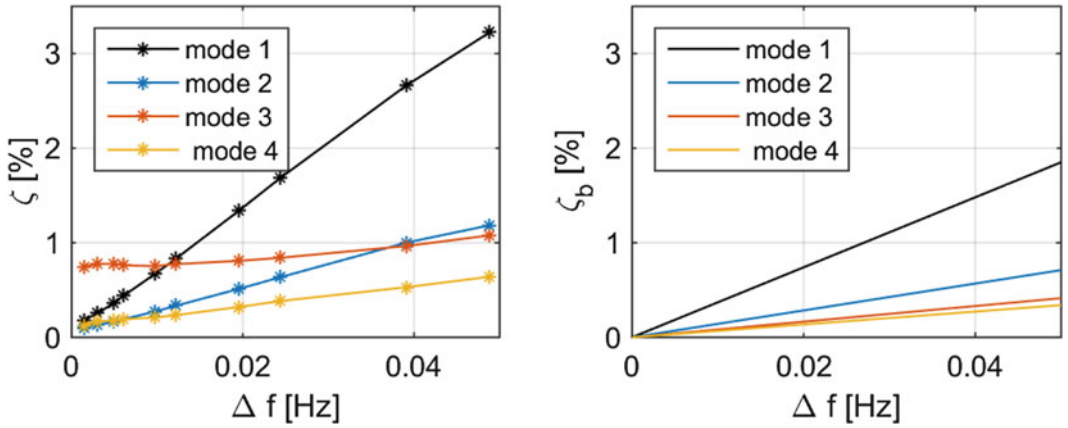

Fig. 27.11 The damping estimates from the footbridge ambient vibration test through EFDD (*left*) and the bias error on damping (*right*) as a function of the frequency resolution Δf

The increase in damping with frequency resolution is directly related to the spectral leakage phenomenon which introduces bias on the damping estimate. The spectral density estimate is computed using a correlation function estimate and the Welch averaging method. The basic assumption of the correlation function estimate is periodicity, which is not the case for real data, hence bias errors propagates through the computation and introduces bias error on the damping estimate. The bias error on damping can be expressed as (Brandt et al. [3]),

$$\zeta_b = \frac{2 f_v}{\pi f_n N} \tag{27.2}$$

where f_n is the natural frequency of mode n, f_v is the Nyquist frequency and N is the total number of data points in the data segment. The damping bias ζ_b in Eq. (27.2) is illustrated in Figs. 27.11 and 27.12, which shows that the bias error on damping converges to Zero with a sufficiently high frequency resolution.

The dimensionless parameter $f/\Delta f$, is proportional to the period T, which explains that the tendency observed by Michael Mistler is due to the bias error on the damping estimate introduced by the leakage phenomenon.

Finally, Fig. 27.12 (left) shows that depending on the parameters chosen for an EFDD analysis, the damping estimated can vary to a great extent. The frequency resolution must therefore be chosen with caution to minimize the influence introduced by spectral leakage. The simplest way to reduce the bias on the damping estimate is to increase the number of points in the data segment. For this particular case, a reliable damping value for mode 1 requires a frequency resolution of $\Delta f < 0.0007$ Hz.

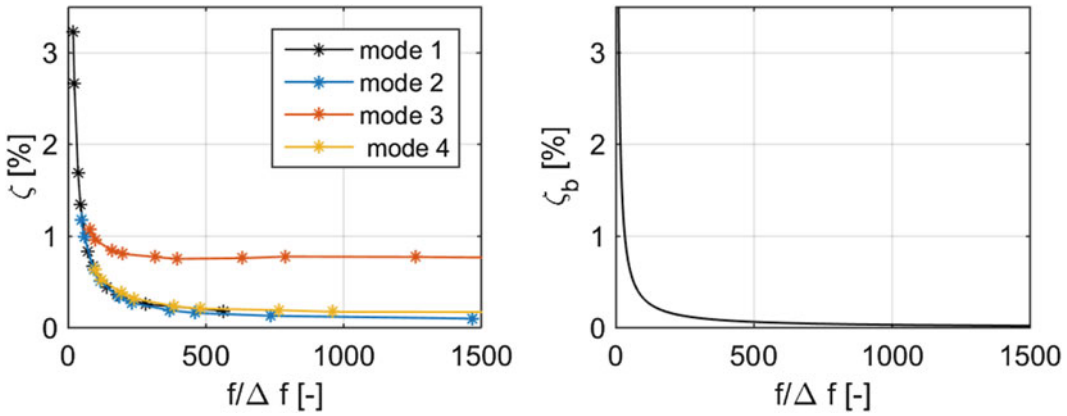

Fig. 27.12 The damping estimates from the footbridge ambient vibration test through EFDD (*left*) and the bias error on damping (*right*) as a function of the dimensionless parameter $f/\Delta f$

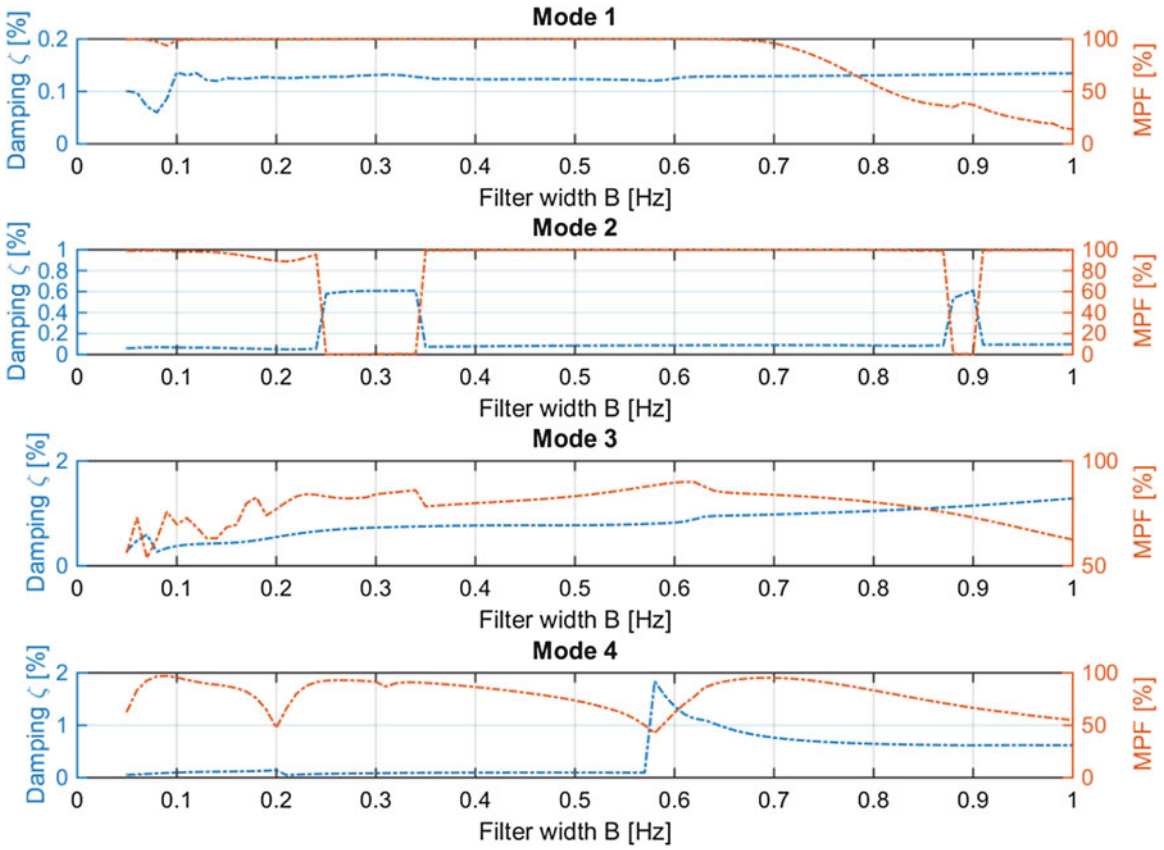

Fig. 27.13 The critical damping ratio estimated for the first four modes and the modal participation factor (MPF) as a function of the filter width B, representing the width of the bandpass filter

27.6 Damping Estimation in the Time Domain

Five of the measurement channels are included in the time domain analysis, due to over-fitting. The channels are selected based on the level of response exhibited by the structure in the given location and direction. Additionally, it is also considered which measurements enable the estimation of the mode shapes. For more information on condensation and the over fitting problem the reader is referred to Brincker and Camargo [8].

The data is pre-processed with a band-pass filter to isolate the modes of interest. The center frequency f_0 of the filter is the natural frequency of the respective mode. The bandwidth of the band-pass filter is assumed to have an effect on the damping estimation. Therefore a convergence analysis is performed, and the stable bandwidth is thereby selected for each mode. Figure 27.13 (see Appendix), shows the convergence analysis, where the bandwidth B is the difference between the upper

Table 27.2 Critical damping ratio ζ estimated using the ambient vibration test and OMA techniques, and the free decays with the logarithmic decrement procedure

Method		Decimation	N	Δf [Hz]	ζ_1 [%]	ζ_2 [%]	ζ_3 [%]	ζ_4 [%]
Frequency domain	EFDD	4	32 K	0.0015	0.184	0.100	0.746	0.126
	FDD/ITD	4	32 K	0.0015	0.156	0.092	0.464	0.154
Time domain	ITD	8	–	–	0.122	0.098	0.462	0.164
	ERA	8	–	–	0.124	0.104	0.562	0.158
Free decay	Log.dec.	–	–	–	0.29	0.15	0.40	–

and lower cutoff frequencies. The filter is flat in the interval $[f_0 - B/2; f_0 + B/2]$ and zero outside $[f_0 - B/2 + B; f_0 + B/2 + B]$. Based on the convergence analysis a bandwidth of 0.5 Hz was selected.

The correlation function estimate used as input in the time domain identification was adjusted to limit the effect of signal noise in the measured data. This is controlled by disregarding the first cycle in the correlation function and excluding the so called noise tail, which is the correlation function at higher time lags. The exact cut of the noise tail is based on the decay of the correlation function of white noise filtered with a band-pass filter of width 0.5 Hz, referred to as B above.

27.7 Comparison of Identification Techniques for Damping Estimation

Table 27.2 shows the mean damping coefficients estimated using the frequency domain techniques, EFDD/FDD, and the time domain techniques, ITD and ERA, respectively as well as the combined technique FDD/ITD [9, 10]. The results from the EFDD show a higher damping for the first three modes, compared to the classical time domain methods. There is no leakage introduced in the time domain, and the estimated damping by OMA time domain identification are close to the damping estimated by the logarithmic decrement procedure on the free decay process.

27.8 Summary

Estimating the critical damping ratio using ambient response data from a footbridge through the EFDD techniques is a challenge, especially for low frequency modes. There is a risk of estimating values which are decades away from the physically present damping due to spectral leakage. However leakage bias can be estimated and an appropriate frequency resolution can be chosen, such that the influence from leakage is minimized. For classical time domain techniques, where no leakage is introduced, OMA based damping estimates are close to damping estimated when exciting the structure harmonically in a given natural mode to initiate a free decay process.

References

1. Rohner, N., Devaux, M., Cantieni, R.: Analytical and experimental investigation of the dynamic behavior of a footbridge. In: Proceedings of 6th IOMAC, International Operational Modal Analysis Conference, Gijón, Spain, 2015
2. ARTeMIS Modal 4.0 (Computer software), Issued by Structural Vibration Solutions A/S, NOVI Science Park, Niels Jernes Vej 10, DK 9220 Aalborg East, Denmark (2015)
3. Brincker R., Zhang L., Andersen P.: Modal identification from ambient responses using frequency domain decomposition. In: Proceedings of IMAC 18, the International Modal Analysis Conference, pp. 625–630. San Antonio, TX, February 2000
4. Brandt, A., Brincker, R., Ahlin, K.: Welchs method for PSD estimation - Revisited, Presentation at Inter-national Operational Modal Analysis Conference Workshop, Copenhagen, Denmark, 2006
5. Ibrahim, S.R., Milkulcik, E.C.: A method for direct identification of vibration parameters from the free response. Shock Vib. Bull. **47**, 183–196 (1977)
6. Juang, J.N., Pappa, R.S.: An eigen system realization algorithm for modal parameter identification and modal reduction. J. Guid. Control Dyn. **8**(5), 620–627 (1985)

7. Mistler, M., Heiland, D., Experimentelle modale Dämpfungsermittlung an bestehenden Bauwerken. In: Proceedings of 5. VDI-Fachtagung Baudynamik 2015. VDI-Berichte 2244, pp. 197–208. VDI-Verlag, Düsseldorf (2015)
8. Brincker, R., Camargo, E., Skafte, A.: An example of correlation matrix based mode shape expansion. International Modal Analysis Conference (IMAC-XXXIII), Orlando, 2015
9. Brincker, R., Ventura, C.: Introduction to Operational Modal Analysis. Wiley (2015)
10. OMA toolbox (Matlab), included in [9], can be downloaded from http://www.brinckerdynamics.com/

Chapter 28
A Critical Analysis of Simplified Procedures for Footbridges' Serviceability Assessment

Federica Tubino and Giuseppe Piccardo

Abstract This paper provides a critical analysis of the procedures available in the literature for the serviceability assessment of footbridges in unrestricted pedestrian traffic condition. Based on a full probabilistic model of walking-induced forces, Monte Carlo simulations are carried out and the numerically obtained dynamic response is compared with the one provided by simplified procedures. Furthermore, a new technical procedure is proposed which permits a direct and simple evaluation of footbridge maximum acceleration as a function of the expected average pedestrian flow and the modal properties of the footbridge.

Keywords Footbridges • Human-induced vibrations • Monte Carlo simulations • Serviceability • Equivalent spectral model

28.1 Introduction

For modern footbridges, vibration serviceability often constitutes a critical design requirement (see, e.g., [1–4]). One of the most frequent loading scenarios is unrestricted pedestrian traffic, which should be modeled probabilistically, considering several sources of randomness among which pedestrian arrivals, step frequencies and velocities, force amplitudes and pedestrian weights [5]. Recent Guidelines ([6–9]) introduce simplified procedures for serviceability analysis, providing equivalent uniformly-distributed resonant load distributions ([6–8]), response spectrum techniques [7], equivalent resonant moving harmonic load ([8, 9]) or simple formula for the estimate of the maximum acceleration [10]. The equivalent loading models proposed by SETRA [6], HIVOSS [7] and BSI [8] are based on Monte Carlo simulations of pedestrian streams that were carried out on different bridge geometries, always characterized by a mean step frequency coincident with the considered dominant natural frequency of the bridge, and assuming a fixed value for the variation coefficient of the pedestrian step frequency.

An interesting alternative to simplified loading distributions are spectral models of pedestrian excitation [11–13], that allow to deal with serviceability assessment in the frequency domain through the methods of linear random dynamics. The Equivalent Spectral Model (ESM) introduced by the authors has been derived analytically, based on suitable probabilistic models of all the parameters involved under some simplifying assumptions [12, 13]. Simple closed-form expressions for the evaluation of the mean value of the maximum dynamic response have been provided, which can be applied at the design stage to assess the footbridge vibrations sensitivity in the spirit of recent guidelines (e.g. SETRA, HIVOSS). Differently from those, which are based on specific values of the random parameters involved as previously specified, ESM allows to take into account the intrinsic randomness of the walking parameters.

The main objective of the present paper is to provide a critical comparison of the simplified procedures for the serviceability assessment of footbridges in unrestricted traffic conditions. Based on a full probabilistic model of walking-induced forces, Monte Carlo simulations are carried out. The influence of the statistical distribution of walking speed, dynamic load factor, pedestrian weight and step frequency on the maximum dynamic response is analyzed. Furthermore, the numerically obtained dynamic response are compared with those provided by simplified procedures. Finally, a direct and simple graphical evaluation of footbridge maximum acceleration is proposed which allows to assess at the early design stage if the structure is potentially sensitive to vibrations induced by unrestricted pedestrian traffic.

F. Tubino (✉) • G. Piccardo
Department of Civil, Chemical and Environmental Engineering, University of Genova, Via Montallegro 1, 16145 Genoa, Italy
e-mail: federica.tubino@unige.it; giuseppe.piccardo@unige.it

© The Society for Experimental Mechanics, Inc. 2016

M. Allen et al. (eds.), *Dynamics of Coupled Structures, Volume 4*, Conference Proceedings of the Society for Experimental Mechanics Series, DOI 10.1007/978-3-319-29763-7_28

28.2 Unrestricted Pedestrian Traffic: Approximate Evaluation of the Maximum Dynamic Response

Unrestricted pedestrian traffic occurs for pedestrian density lower than 0.3−0.6 Ped/m^2 [10] and it is characterized by pedestrians arriving in a random way and able to move undisturbed, each of them with his own characteristics in terms of loading amplitude, frequency, velocity and phase. Taking into account only the first walking harmonic for each pedestrian, the force induced by N_p pedestrians can be expressed as the sum of harmonic moving loads with random amplitude, frequency, phase angle, speed, arrival times. Focusing the attention on the j-th principal coordinate of the structure, its equation of motion can be written in non-dimensional form as follows (e.g., [14]):

$$\begin{aligned} &\ddot{\tilde{p}}_j(\tilde{t}) + 2\xi_j \dot{\tilde{p}}_j(\tilde{t}) + \tilde{p}_j(\tilde{t}) = \tilde{F}_j(\tilde{t}) \\ &\tilde{F}_j(\tilde{t}) = \sum_{i=1}^{N_p} \tilde{\alpha}_i \tilde{G}_i \sin\left(\tilde{\Omega}_i(\tilde{t}-\tilde{\tau}_i) + \Psi_i\right) \varphi_j\left(\tilde{\Omega}_{ci}(\tilde{t}-\tilde{\tau}_i)\right) \left[H(\tilde{t}-\tilde{\tau}_i) - H\left(\tilde{t}-\tilde{\tau}_i - \tfrac{1}{\tilde{\Omega}_{ci}}\right)\right] \end{aligned} \tag{28.1}$$

where ξ_j is the j-th damping ratio and the non-dimensional quantities read:

$$\tilde{t} = \omega_j t \quad \tilde{p}_j = \frac{p_j}{p_{j\,s}} = \frac{p_j\ M_j \omega_j^2}{\alpha_m G_m} \quad \tilde{F}_j(\tilde{t}) = \frac{F_j(t)}{\alpha_m G_m} \quad \tilde{x} = \frac{x}{L} \quad \tilde{\alpha}_i = \frac{\alpha_i}{\alpha_m} \quad \tilde{G}_i = \frac{G_i}{G_m} \quad \tilde{\Omega}_i = \frac{\Omega_i}{\omega_j} \quad \tilde{\Omega}_{ci} = \frac{c_i}{\omega_j L} \quad \tilde{\tau}_i = \omega_j \tau_i \tag{28.2}$$

In Eq. (28.2), t is the time, p_j is the j-th principal coordinate, F_j is the j-th modal force, x is the abscissa along the structure, L is the footbridge span length, ω_j is the j-th natural circular frequency, M_j is the j-th modal mass, α_i, G_i Ω_i, Ψ_i, c_i and τ_i are, respectively, the Dynamic Loading Factor (DLF), the weight, the step circular frequency, the phase-angle, the walking speed and the arrival time of the i-th pedestrian, α_m is the mean DLF, G_m is the mean pedestrian weight, and $p_{j\,s}$ is the static response induced by the mean force. Starting from the probabilistic characterization of all the parameters involved in the force model, the footbridge random dynamic response to unrestricted pedestrian traffic can be numerically determined through Monte Carlo simulations (e.g. [14]).

A normalized acceleration can be defined as follows [15]:

$$\ddot{\tilde{p}}_{j_{\text{norm}}} = \ddot{\tilde{p}}_j \sqrt{\xi_j \Big/ N_p} \tag{28.3}$$

Assuming a unitary value for the maximum mode shape, the structural acceleration in dimensional form can be expressed as a function of the normalized acceleration:

$$\ddot{q} = \frac{\alpha_m G_m}{M_j} \sqrt{\frac{N_p}{\xi_j}}\, \ddot{\tilde{p}}_{j_{\text{norm}}} \tag{28.4}$$

In order to avoid burdensome Monte Carlo simulations and to have predictive formulas, simplified equivalent loading models have been proposed, which can be classified into three categories: Equivalent Uniformly distributed Resonant Load (EURL), Equivalent Moving Resonant Load (EMRL) and Equivalent Spectral Model (ESM).

EURL is provided by various guidelines (e.g., [6–8]); based on this approach, the normalized maximum acceleration $\ddot{\tilde{p}}_{j_{\text{norm}}}$ becomes:

$$\ddot{\tilde{p}}_{j_{\text{norm,max}}} = \frac{\tilde{F}_u}{2\sqrt{N_p \xi_j}} \tag{28.5}$$

where the non-dimensional loading amplitude $\tilde{F}_u$ is given by:

$$\tilde{F}_u = \frac{2F_u L}{\pi \alpha_m G_m} \qquad \begin{aligned} F_u &= \frac{10.8 \alpha_m G_m \psi(n_j)}{L} \sqrt{N_p \xi_j} \ \text{Setra [6]} \quad \text{Hivoss [7] (a)} \\ F_u &= \frac{1.8 \alpha_m G_m k(n_j)}{L} \sqrt{\frac{\gamma N_p}{\lambda}} \ \text{BSI crowd scenario [8] (b)} \end{aligned} \tag{28.6}$$

EMRL is provided by ISO [9] for a group of N_p uncoordinated pedestrians. An approximate procedure for the estimate of the maximum acceleration based on an equivalent resonant moving load is also proposed by FIB [10]. Adopting EMRL and based on the results in [16], the normalized maximum acceleration becomes:

$$\begin{aligned} \ddot{\tilde{p}}_{j_{\text{norm, max}}} &= \frac{\sqrt{\xi_j}}{2\left(\pi^2\tilde{\Omega}_{cm}^2+\xi_j^2\right)}\left[-\pi\tilde{\Omega}_{cm}\exp\left(-\xi_j\tilde{t}_{\max}\right)+\pi\tilde{\Omega}_{cm}\cos\left(\pi\tilde{\Omega}_{cm}\tilde{t}_{\max}\right)-\xi_j\sin\left(\pi\tilde{\Omega}_{cm}\tilde{t}_{\max}\right)\right] \\ \tilde{t}_{\max} &= \frac{1}{\pi\tilde{\Omega}_{cm}}\left[\operatorname{atan}\left(-\frac{\xi_j}{\pi\tilde{\Omega}_{cm}}\right)+\pi\right] \quad \tilde{\Omega}_{cm}=\frac{c_m}{\omega_j L} \end{aligned} \tag{28.7}$$

Based on ESM [13], the standard deviation and the maximum value of the normalized acceleration are given by:

$$\begin{aligned} \sigma_{\ddot{\tilde{p}}_{j_{\text{norm}}}} &= \frac{\sqrt{\pi}}{4}\sqrt{p_{\tilde{\Omega}}(1)} \\ \ddot{\tilde{p}}_{j_{\text{norm,max}}} &= g_{\ddot{\tilde{p}}_j}\frac{\sqrt{\pi}}{4}\sqrt{p_{\tilde{\Omega}}(1)} \end{aligned} \tag{28.8}$$

where $g_{\ddot{\tilde{p}}_j}$ is the so-called peak factor of $\ddot{\tilde{p}}_j$. It can be expressed as:

$$g_{\ddot{\tilde{p}}_j} = \sqrt{2\ln\left(2\nu_{\ddot{\tilde{p}}_j}^{e}\tilde{T}\right)}+\frac{0.5772}{\sqrt{2\ln\left(2\nu_{\ddot{\tilde{p}}_j}^{e}\tilde{T}\right)}} \tag{28.9}$$

In Eq. (28.9), the following non-dimensional parameters appear [15]:

$$\tilde{T}=\omega_j\frac{NL}{c_m}=\frac{N}{\tilde{\Omega}_{cm}} \quad \nu_{\ddot{\tilde{p}}_j}^{e}=\begin{cases}\left(1.63q_{\ddot{\tilde{p}}_j}^{0.45}-0.38\right)\nu_{\ddot{\tilde{p}}_j} & \text{Vanmarcke formulation (a)} \\ \nu_{\ddot{\tilde{p}}_j}\simeq\tilde{n}_j=\frac{1}{2\pi} & \text{Davenport formulation (b)}\end{cases} \quad q_{\ddot{\tilde{p}}_j}\simeq 2\sqrt{\frac{\xi_j}{\pi}} \tag{28.10}$$

In Eq. (28.10), the first expression is based on the theory developed by Vanmarcke and Der Kiureghian for the analysis of the extreme distribution of narrow-band random processes (threshold up-crossings in clumps). The second expression corresponds to the classic formulation proposed by Davenport, and it is commonly applied for broad band random processes (independent threshold up-crossings).

28.3 Numerical Validation of the Approximate Procedures

Monte Carlo simulations are carried out for different values of the non-dimensional mean step frequency $\tilde{\Omega}_m$ and coefficient of variation of the pedestrian weight V_G, of the walking velocity V_c and of the step frequency V_Ω . The simulations have two different aims: to check the sensitivity of the maximum dynamic response to stochastic walking parameters, and to assess the reliability of the simplified loading models in the estimate of the normalized maximum acceleration. For every case analyzed, the mean value among 10^4 simulations is estimated.

Monte Carlo simulations carried out varying the coefficient of variation of the walking speed and of the pedestrian weight have confirmed the negligible influence of the statistical distribution of these random variables on the maximum dynamic response. For this reason, in the following, only the effects of variation of the non-dimensional mean step frequency and its coefficient of variation are shown. According to the literature (see, e.g., [14] for a brief summary), the coefficient of variation of the step frequency is assumed in the interval 0.06–0.1.

Figure 28.1 plots the mean value of the normalized maximum acceleration derived from Monte Carlo simulations, as a function of the coefficient of variation of the step frequency V_Ω; the different gray scales correspond to different values of the non-dimensional mean step frequency $\tilde{\Omega}_m$. The results of numerical simulations (symbols) are compared with the ESM closed-form expression (thin lines) based on the Vanmarcke (Fig. 28.1a) and Davenport (Fig. 28.1b) formulations. Furthermore, Fig. 28.1c compares the results of numerical simulations with the predictions by the EURL provided by Setra ($\Psi = 1$) and BS ($k = 1$), and by the EMRL provided by ISO, for different values of the non-dimensional mean step frequency $\tilde{\Omega}_m$.

Figure 28.1a, b point out the delicacy of the choice of the peak factor. In particular, the Davenport expression of the peak factor provides a large overestimation of the numerical results when the non-dimensional mean step frequency is

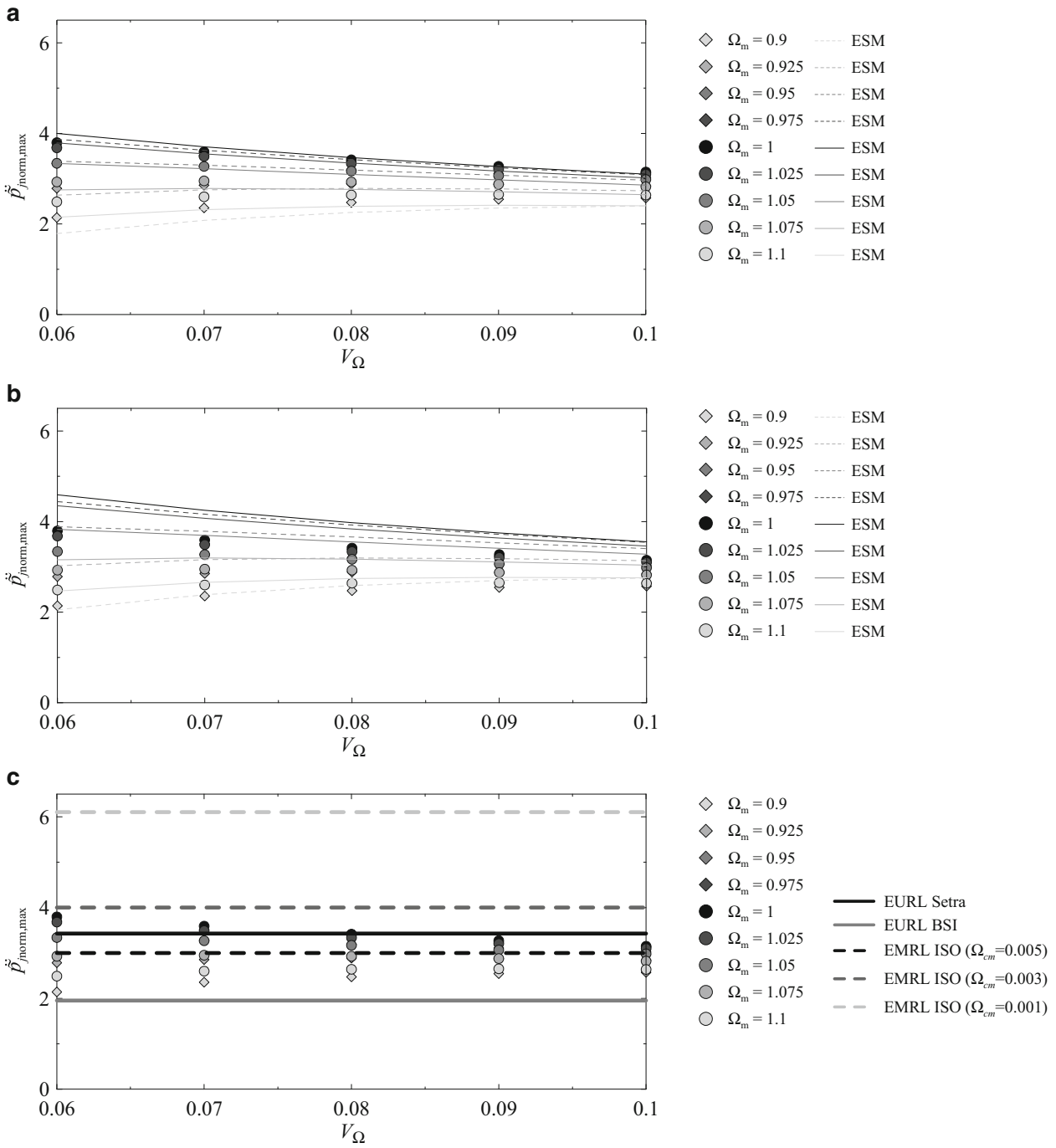

Fig. 28.1 Mean value of the normalized maximum non-dimensional acceleration: comparison among Monte Carlo simulations (symbols) and ESM with peak factor by Vanmarcke (**a**) and by Davenport (**b**), EURL and EMRL (**c**)

approximately one and the coefficient of variation V_Ω is small: in this case, the dynamic response is a narrow band random process and Vanmarcke theory provides very good results. On the other hand, the Davenport formulation provides a better approximation of the numerical results when the non-dimensional mean step frequency is lower than 0.95 or higher than 1.05, especially for large values of V_Ω, when the dynamic response is not really a narrow band random process. In any case, ESM based on Davenport formulation provides conservative estimates of the maximum dynamic response.

Figure 28.1c clearly shows that EURL and EMRL do not allow to take into account the probability distribution of the step frequency and they provide a maximum values of the structural response independent of V_Ω and $\tilde{\Omega}_m$. However, SETRA model provides a normalized maximum non-dimensional acceleration that is in perfect accordance with numerical

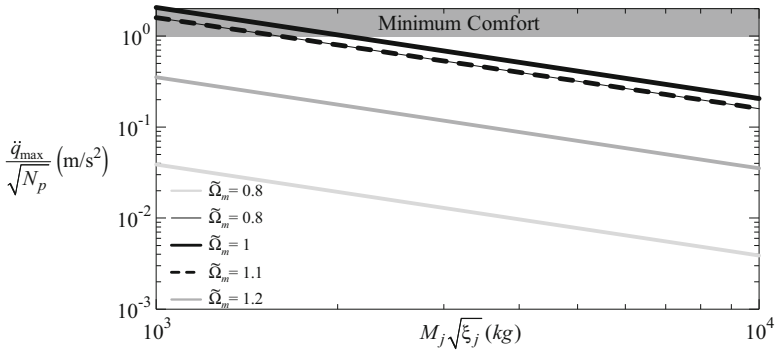

Fig. 28.2 Conservative a priori estimate of maximum structural acceleration

simulations carried out for $V_\Omega = 0.08$ and $\tilde{\Omega}_m = 1$. BSI provides an estimate which is not conservative, being smaller than the results of Monte Carlo simulations for any value of $\tilde{\Omega}_m$ and V_Ω. EMRL by ISO provides very conservative estimates for $\tilde{\Omega}_{cm} = 0.001$ and $\tilde{\Omega}_{cm} = 0.003$, while the estimate is closer to numerical results (even if often non-conservative) if $\tilde{\Omega}_{cm}$ is larger (e.g., $\tilde{\Omega}_{cm} = 0.005$).

28.4 Technical Considerations

The results of Monte Carlo simulations have confirmed that, as predicted by the ESM, the distribution of the step frequency has a strong influence on the footbridge dynamic response. Thus, concerning pedestrian walking parameters, footbridge serviceability is essentially governed by the non-dimensional mean step frequency and its coefficient of variation. A parametric analysis has been performed, in order to assess the effective role of the statistical distribution of the step frequency on footbridge serviceability [15].

Figure 28.2 plots the ratio $\ddot{q}_{max}/\sqrt{N_p}$ as a function of the product $M_j\sqrt{\xi_j}$, setting a classic value for the average weight and DLF of pedestrians, $\alpha_m G_m = 280$ N (e.g., [10]). The different curves correspond to different values of the non-dimensional mean step frequency $\tilde{\Omega}_m$, which is assumed in the range 0.8–1.2; in each case the more conservative coefficient of variation is selected according to results presented in [15] ($V_\Omega = 0.06$ for $\tilde{\Omega}_m = 0.93-1.09$, $V_\Omega = 0.1$ for $\tilde{\Omega}_m$ outside this interval). The response curves appear almost linear in a bi-logarithmic scale. As expected, both the non-dimensional mean step frequency $\tilde{\Omega}_m$ and the product $M_j\sqrt{\xi_j}$ strongly affect the maximum structural acceleration, and, thus, footbridge serviceability. The graph quantifies the well-known beneficial effect on the dynamical behavior due to the increase of the modal mass and of the damping ratio. Moreover, the maximum structural acceleration greatly increases as the non-dimensional mean step frequency $\tilde{\Omega}_m$ moves closer to 1. Bridges characterized by $\tilde{\Omega}_m$ in the neighborhood of unity (0.93−1.09), associated with low values of the product $M_j\sqrt{\xi_j}$, appear to be very prone to pedestrian-induced vibrations; on the contrary, very small accelerations are expected for reduced $\tilde{\Omega}_m$ (especially if associated with high values of $M_j\sqrt{\xi_j}$), such as $\tilde{\Omega}_m = 0.8$ (i.e., when the dominant frequency of the bridge is sufficiently different from the mean step frequency). Finally, it should be noted that values of 1 m/s^2 on the ordinate of Fig. 28.2 are clearly out-of-comfort as regards any possible criteria, since the maximum acceleration caused by N_p pedestrians is obtained by multiplying the ordinate value by $\sqrt{N_p}$ (N_p being in general a number greater than 5). Bridges that exceed this limit are certainly poorly designed from a dynamic viewpoint.

28.5 Concluding Remarks

In this paper, a critical analysis of the simplified procedures available in the literature for the serviceability assessment of footbridges has been provided.

Monte Carlo simulations have shown that the non-dimensional mean step frequency and the coefficient of variation of the step frequency have significant influence on the maximum value of the footbridge dynamic response. The results of numerical simulations are in good accordance with the predictions based on the Equivalent Spectral Model. Equivalent loading models

suggested by recent guidelines do not take into account the explicit dependence on the probability distribution of the step frequency and, therefore, may not always be conservative.

Finally, the maximum footbridge acceleration is expressed in a very synthetic way, useful for design analysis, through a simple graphical procedure which permits a direct and simple evaluation of footbridge maximum acceleration. Starting from the values of modal mass, damping ratio and expected average pedestrian flow, it is possible to assess at the early design stage if the structure is really sensitive to vibrations and, then, to modify the structure or to design possible systems for vibration control, avoiding expensive repairs after construction. These results seem of interest also from a technical point of view, and might apply to codes and guidelines for a safe evaluation of footbridge serviceability.

Acknowledgements This work was partially supported by the Italian Ministry of Education, Universities and Research (MIUR) through the PRIN co-financed program "Dynamics, Stability and Control of Flexible Structures" (grant number 2010MBJK5B) and by University of Genoa (Progetto di Ateneo 2014 "Modelli semplificati per l'analisi dinamica delle strutture").

References

1. Zivanovic, S., Pavic, A., Ingolfsson, E.T.: Modeling spatially unrestricted pedestrian traffic on footbridges. J. Struct. Eng. ASCE **136**, 1296–1308 (2010)
2. Van Nimmen, K., Lombaert, G., De Roeck, G., Van den Broeck, P.: Vibration serviceability of footbridges: evaluation of the current codes of practice. Eng. Struct. **59**, 448–461 (2014)
3. Zivanovic, S.: Benchmark footbridge for vibration serviceability assessment under the vertical component of pedestrian load. J. Struct. Eng. ASCE **138**(10), 1193–1202 (2010)
4. Tubino, F., Carassale, L., Piccardo, G.: Human-induced vibrations on two lively footbridges in Milan. J. Bridge Eng. ASCE (2016). doi:10.1061/(ASCE)BE.1943-5592.0000816
5. Racic, V., Pavic, A., Brownjohn, J.M.W.: Experimental identification and analytical modeling of human walking forces: literature review. J. Sound Vib. **326**, 1–49 (2009)
6. SETRA: Footbridges - assessment of vibrational behaviour of footbridges under pedestrian loading. Paris: Technical Department for Transport, Roads and Bridges Engineering and Road Safety, Ministry of Transport and Infrastructure (2006)
7. HIVOSS: Design of footbridges guideline. Human induced vibrations of steel structures, http://www.stb.rwth-aachen.de/projekte/2007/HIVOSS/download.php RFS2-CT-2007-00033 (2009)
8. BSI. British Standards Institution: UK National Annex to Eurocode 1: actions on structures—Part 2: traffic loads on bridges. NA to BS EN 1991-2:2003. British Standards Institution (2008)
9. ISO10137, Bases for design of structures – serviceability of buildings and walkways against vibration. International Organization for Standardization, Geneva (2007)
10. FIB, Bulletin 32 – guidelines for the design of footbridges, International Federation for Structural Concrete. Sprint-Digital-Druck, Stuttgart (2005)
11. Brownjohn, J.M.W., Pavic, A., Omentzetter, P.A.: Spectral density approach for modelling continuous vertical forces on pedestrian structures due to walking. Can. J. Civil Eng. **31**(1), 65–77 (2004)
12. Tubino, F., Piccardo, G.: A spectral model for pedestrian loading of footbridges. In: Proceedings of the VIII European Conference on Structural Dynamics, EURODYN 2011, Leuven, Belgium, 2011
13. Piccardo, G., Tubino, F.: Equivalent spectral model and maximum dynamic response for the serviceability analysis of footbridges. Eng. Struct. **40**, 445–456 (2012)
14. Piccardo, G., Tubino, F.: Simplified procedures for the vibration serviceability analysis of footbridges subjected to realistic walking loads. Comput. Struct. **87**, 890–903 (2009)
15. Tubino, F., Piccardo, G.: Serviceability assessment of footbridges in unrestricted pedestrian traffic condition. Structure and Infrastucture Engineering. (2016). 10.1080/15732479.2016.1157610
16. Piccardo, G., Tubino, F.: Dynamic response of Euler- Bernoulli beams to resonant harmonic moving loads. Struct. Eng. Mech. **44**(5), 681–704 (2012)

Chapter 29
Human-Induced Vibrations of Footbridges: The Effect of Vertical Human-Structure Interaction

Katrien Van Nimmen, Geert Lombaert, Guido De Roeck, and Peter Van den Broeck

Abstract Slender and lightweight structures are often unduly responsive to human excitation. The concerns of vibration comfort and safety are strengthened by unexplored human-structure interaction (HSI) phenomena. The present contribution proposes a numerical model for pedestrian excitation including HSI. In addition to the well-known forces induced by a pedestrian on a rigid floor, the pedestrian is represented by a linear mechanical model to simulate the interaction with the supporting structure. Inspired by the body postures assumed during the walking cycle, the mechanical properties are chosen to represent the dynamic behaviour of the human body with one or two legs slightly bent. The effect of HSI on the structural response is evaluated for various footbridge parameters and pedestrian densities. It is shown that by taking into account HSI, the structural response is reduced. Furthermore, it is demonstrated that the unrealistic high acceleration levels as predicted by simplified force models are not reached as the result of HSI. It is concluded that the mechanical interaction with the crowd is relevant for the vertical low-frequency dynamic behaviour of footbridges.

Keywords Human-induced vibrations • Footbridge • Human-structure interaction • Vibration serviceability

29.1 Introduction

Driven by the economic demand of efficiency and the increasing strength of (new) materials, architects and engineers are pushing the limits to build ever longer, taller and lighter. In the particular case where the structure is designed for human occupants (i.e. grandstands, footbridges, gymnasia, staircases, open plan offices), this trend is further stimulated by the relatively small service loads. Typically, light and slender structures have one or more natural frequencies that lie within the dominant spectrum of common human activities such as walking, running or jumping. Likely to be subject to (near-)resonant excitation, they are often unduly responsive to human motion, resulting in disturbing or even harmful vibrations [1].

The loading induced by a person walking on a rigid floor has been studied comprehensively in biomechanical laboratories, yielding large datasets of measured ground reaction forces (GRFs) [2]. Based on these experimentally identified GRFs, numerous mathematical load models have been developed to describe the human-induced loading as a function of some principal influence parameters such as the weight and the pacing rate [3–6]. However, when applying these force models to simulate the structural response, significant differences are sometimes observed in comparison to the measured response [7–9]. The nature and possible causes of these differences are many including, inter alia, neglecting intra-subject variability and HSI.

Whereas pedestrian are generally represented by simplified (moving) loads, they are in fact mechanical systems on their own, interacting with the structure that is supporting them [10]. In some cases, the characteristics of the coupled crowd-structure system display significant changes in comparison to those of the empty footbridge [11–13]. The degree to which the dynamic behaviour is modified, is expected to increase with an increasing ratio of the crowd's mass to the structural mass. Hence, for lightweight footbridges these effects are expected to be non-negligible [14, 15].

K. Van Nimmen (✉) • P. Van den Broeck
KU Leuven, Department of Civil Engineering, Structural Mechanics, B-3001 Leuven, Belgium

KU Leuven, Department of Civil Engineering, Technology Cluster Construction, Structural Mechanics and Building Materials Section, Technology Campus Ghent, Ghent, Belgium
e-mail: katrien.vannimmen@kuleuven.be

G. Lombaert • G. De Roeck
KU Leuven, Department of Civil Engineering, Structural Mechanics, B-3001 Leuven, Belgium

© The Society for Experimental Mechanics, Inc. 2016

M. Allen et al. (eds.), *Dynamics of Coupled Structures, Volume 4*, Conference Proceedings of the Society for Experimental Mechanics Series, DOI 10.1007/978-3-319-29763-7_29

This paper proposes a crowd-structure model that accounts for pedestrian excitation and HSI. To this end, the pedestrian is viewed as an internally driven mechanical system which interacts with the supporting structure. Focus is on the analysis of the predicted structural response to pedestrian excitation. In addition, the impact of HSI is evaluated by comparison with the structural response predicted by a moving force model.

The outline of this paper is as follows. First, the moving crowd model is presented (Sect. 29.2). Second, the generation of random pedestrian flows is discussed (Sect. 29.3). Finally, the structural response is predicted for various footbridge parameters and pedestrian densities and the impact of HSI is evaluated (Sect. 29.4).

29.2 The Moving Crowd Model

Pedestrians in a crowd are active systems for which the walking behaviour is defined by an internal driving term. In the *moving crowd model* developed in this section, the pedestrian and the footbridge are considered as two linear sub-systems, coupled at a single point (Fig. 29.1). The contact force not only depends on the internal excitation of the pedestrian but also on the dynamic properties of both components [16]. The approach proposed in this section is similar to the source-structure system as discussed in engineering acoustics [17, 18].

29.2.1 The Supporting Structure

The governing equations of motion in modal coordinates for the linear system representing the footbridge read:

$$\ddot{\mathbf{z}}(t) + \Gamma\dot{\mathbf{z}}(t) + \Omega^2\mathbf{z}(t) = \Phi^\top\mathbf{p}(t) \tag{29.1}$$

with $\mathbf{z}(t) \in \mathbb{R}^{n_m}$ the modal coordinate vector, n_m the number of modes retained in the modally reduced system, $\Omega^2 \in \mathbb{R}^{n_m \times n_m}$ a diagonal matrix containing the square of the natural frequencies $\omega_{\mathrm{B}j} = 2\pi f_{\mathrm{B}j}$ in rad/s, $\Gamma \in \mathbb{R}^{n_m \times n_m}$ a diagonal matrix containing the terms $2\xi_{\mathrm{B}j}\omega_{\mathrm{B}j}$ with $\xi_{\mathrm{B}j}$ [−] the modal damping ratios, $\Phi \in \mathbb{R}^{n_{\mathrm{DOF}} \times n_m}$ a matrix which has the mass-normalised mode shapes $\boldsymbol{\phi}_j$ as columns, $\Phi^\top\mathbf{p}(t)$ the modal projection of the external forces $\mathbf{p}(t) \in \mathbb{R}^{n_{\mathrm{DOF}}}$ with n_{DOF} the number of degrees of freedom of the FE model of the footbridge.

29.2.2 The Pedestrians

As a pedestrian is walking along the bridge deck, he generates time varying forces at the contact points between his feet and the supporting structure. In the present study, this contact is reduced to a single point, an assumption which is justified given the small stride to span length ratios.

In the following, the time history of the contact force(s) with n_{H} pedestrians are collected in the force vector $\mathbf{p}_{\mathbf{p}}(t)$. The corresponding time-variant location(s) on the bridge deck are indicated by the matrix $\mathbf{S}_{\mathbf{p}}(t) \in \mathbb{R}^{n\mathrm{DOF} \times n\mathrm{H}}$. The vector of forces applied to the bridge deck $\mathbf{p}(t)$ in Eq. (29.1) now reads:

$$\mathbf{p}(t) = \mathbf{S}_{\mathbf{p}}(t)\mathbf{p}_{\mathbf{p}}(t) \tag{29.2}$$

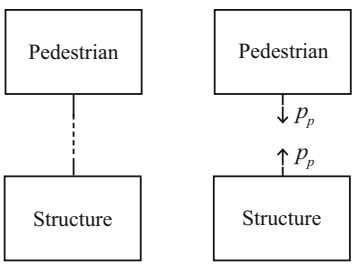

Fig. 29.1 Representation of a general pedestrian-structure system with a single contact point and contact force ($\mathrm{p_p}$)

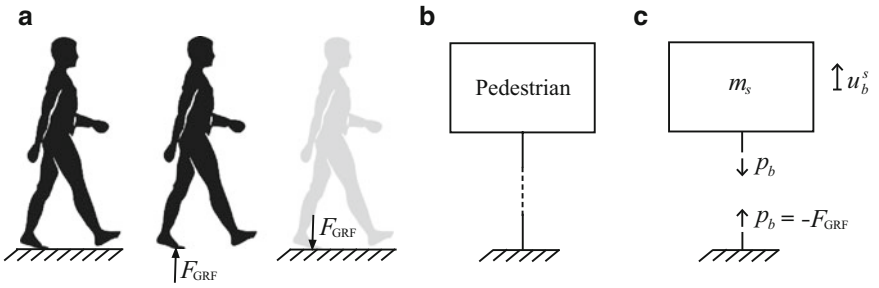

Fig. 29.2 Schematic representation of the blocked force p_b in relation to vertical GRFs: (**a**) the convention of the GRFs, (**b**) general representation of the pedestrian on a fixed support and (**c**) the corresponding contact forces

29.2.3 Stiff Supporting System

The force exerted by the pedestrian on a perfectly rigid floor is denoted as the *blocked force* $p_{b,k}(t)$ [18]:

$$p_{p,k}(t) = p_{b,k}(t) \tag{29.3}$$

These forces correspond to the GRFs as registered by the force plates or an instrumented treadmill fixed to a rigid laboratory floor [2] (Fig. 29.2). When the human body is modelled as a system consisting of n_s rigid segments, the vertical blocked force $p_{b,k}(t)$ can be computed from the corresponding vertical accelerations:

$$p_{b,k}(t) = -F_{GRF,k}(t) = -\sum_{s=1}^{n_s} m_{s,k}\left(\ddot{u}_{b,k}^s(t) + g\right) \tag{29.4}$$

with $F_{GRF,k}(t)$ the GRFs, $m_{s,k}$ the mass attributed to segment s, $u_{b,k}^s$ the vertical displacements of the CoM of the sth body segment relative to the rigid floor and g representing gravity. Note that by choice of convention, a minus sign was introduced in Eq. (29.4).

29.2.4 Flexible Supporting System

When the supporting structure is flexible, the contact force in addition depends on the interaction between the two subsystems [16]. To account for this interaction, each pedestrian is represented by a linear mechanical system. To describe the low-frequency (0–10 Hz) dynamic behaviour of the human body [19–22], a SDOF model is adopted here (a sprung mass m_{H1}, an unsprung mass m_{H0} and a spring k_{H1} and damping element c_{H1}). Inspired by the postures assumed during the walking cycle, the mechanical properties are set to approximate the dynamic behaviour of a body posture with one or two legs slightly bent: $f_{H1} \approx 3.25$ Hz, $\xi_{H1} \approx 0.30$ [–] with $m_H = m_{H1} + m_{H0} = 70$ kg and $\mu_{H1} = m_{H1}/m_H = 0.95$ [20, 23]. Inter-subject variability is accounted for by sampling the characteristics for the different individuals in the crowd from the following distributions: $f_{H1} = \mathcal{N}(\mu_{f_{H1}}, \sigma_{f_{H1}}) = \mathcal{N}(3.25, 0.32)$ [Hz], $\xi_{H1} = \mathcal{N}(\mu_{\xi_{H1}}, \sigma_{\xi_{H1}}) = \mathcal{N}(0.30, 0.05)$ [–] [20, 24].

In this study, the key assumption is made that the driving term of the pedestrian is not affected by the vibrating surface, i.e. the driving term is identical to the one in case of a stiff supporting system. This assumption is probably justified in case the displacements of the bridge deck are (sufficiently) small. For *lock-in* phenomena, where the perceived motion causes the pedestrians to adapt their walking behaviour [25, 26], this condition is not met. However, the latter has never been observed due to vertical bridge motion.

Assuming a *fixed driving term* allows the motion of the body segments to be decomposed in a term resulting from the driving term $u_{b,k}^s(t)$ and a term resulting from the interaction with the supporting structure $u_{r,k}^s(t)$:

$$u_k^s(t) = u_{b,k}^s(t) + u_{r,k}^s(t) \tag{29.5}$$

Introducing Eq. (29.5) in Eq. (29.4):

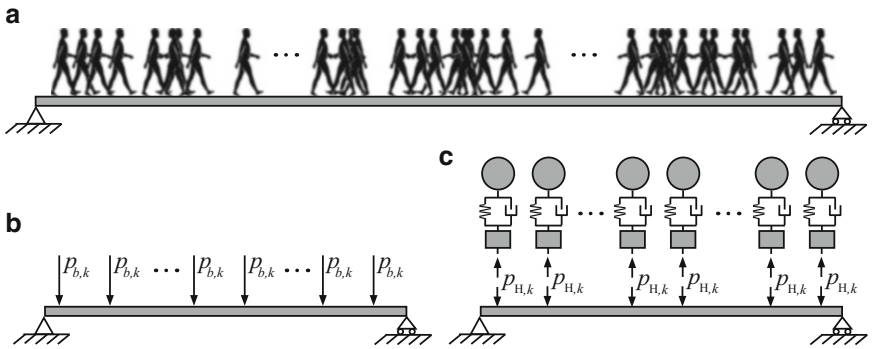

Fig. 29.3 (**a**) Schematic representation of a footbridge subjected to pedestrian excitation and the proposed decomposition of the contact force into (**b**) the blocked force ($\mathbf{p_b}$) and (**c**) the interaction term ($\mathbf{p_H}$)

$$p_{b,k}(t) = -\sum_{s=1}^{n_s} m_{s,k}\left(\ddot{u}^s_{b,k}(t) + g\right) - \sum_{s=1}^{n_s} m_{s,k}\left(\ddot{u}^s_{r,k}(t)\right) \tag{29.6}$$

By definition, the first term on the right hand side of Eq. (29.6) equals the blocked force $p_b(t)$ [see Eq. (29.4)]. The last term in Eq. (29.6), i.e. the interaction term, is further elaborated by adopting the SDOF model for the human body:

$$p_{p,k}(t) = p_{b,k}(t) - m_{\mathrm{H0},k}\ddot{u}_{r0,k}(t) - m_{\mathrm{H1},k}\ddot{u}_{r1,k}(t) \tag{29.7}$$

Through the equilibrium of $m_{\mathrm{H1},k}$, Eq. (29.7) can be written as:

$$p_{p,k}(t) = p_{b,k}(t) - m_{\mathrm{H0},k}\ddot{u}_{r0,k}(t) + k_{\mathrm{H1},k}u_{r1,k}(t) + c_{\mathrm{H1},k}\dot{u}_{r1,k}(t) \tag{29.8}$$

where:

$$\begin{aligned} u_{r1,k}(t) &= u_{\mathrm{H1},k}(t) - u_{\mathrm{B},k}(t) \\ u_{r0,k}(t) &= u_{\mathrm{B},k}(t) \end{aligned} \tag{29.9}$$

with $u_{\mathrm{H1},k}(t)$ and $u_{\mathrm{B},k}(t)$ denoting the displacements of the mass $m_{\mathrm{H1},k}$ and the bridge at the contact point, respectively. Equation (29.7) is therefore equivalent to:

$$p_{p,k}(t) = p_{b,k}(t) + p_{\mathrm{H},k}(t) \tag{29.10}$$

where $p_{\mathrm{H},k}(t)$ corresponds to the interaction force between the two linear subsystems.

The advantage of the proposed approach is the decomposition of the contact force in the blocked force and the interaction term (see Fig. 29.3). Where the blocked force corresponds to the GRFs as discussed in section 29.2.3 and depends solely on the pedestrian's characteristics (e.g. weight, step frequency, etc.), the interaction between the pedestrian and the supporting structure depends on the mechanical properties of the two sub-systems [16, 17]. The blocked force term is in this study determined by the load model defined by Li et al. [6].

29.2.5 Response Calculation

The continuous-time state-space model is given by the following system of equations:

$$\dot{\mathbf{x}}(t) = \mathbf{A_c}(t)\mathbf{x}(t) + \mathbf{B_c}(t)\mathbf{S_p}(t)\mathbf{p_b}(t) \tag{29.11}$$

where $\mathbf{x}(t) \in \mathbb{R}^{n_s}$ represents the modal state vector:

$$\mathbf{x}(t) = \begin{bmatrix} \mathbf{z}(t) \\ \mathbf{u}_{\mathrm{H}}(t) \\ \dot{\mathbf{z}}(t) \\ \dot{\mathbf{u}}_{\mathrm{H}}(t) \end{bmatrix} \tag{29.12}$$

with $n_s = 2(n_m + n_{\mathrm{H}})$. The time-variant system matrix $\mathbf{A_c}(t) \in \mathbb{R}^{n_s \times n_s}$ and the time-invariant matrix $\mathbf{B_c}(t) \in \mathbb{R}^{n_s \times n_m}$ are defined as:

$$\mathbf{A_c}(t) = \begin{bmatrix} \mathbf{0} & \mathbf{I} \\ -\bar{\mathbf{M}}_{\mathrm{HB}}^{-1}(t)\bar{\mathbf{K}}_{\mathrm{HB}}(t) & -\bar{\mathbf{M}}_{\mathrm{HB}}^{-1}(t)\bar{\mathbf{C}}_{\mathrm{HB}}(t) \end{bmatrix} \tag{29.13}$$

$$\mathbf{B_c} = \begin{bmatrix} \mathbf{0} \\ \Phi^{\top} \\ \mathbf{0} \end{bmatrix} \tag{29.14}$$

where the matrices $\bar{\mathbf{M}}_{\mathrm{HB}}(t)$, $\bar{\mathbf{K}}_{\mathrm{HB}}(t)$ and $\bar{\mathbf{C}}_{\mathrm{HB}}(t)$ refer to the generalised mass-, stiffness and damping matrices of the coupled human-structure system as derived [27].

Using a sampling rate of $1/\Delta t$, the state-space model of Eq. (29.11) is discretised to yield its discrete-time equivalent:

$$\mathbf{x}_{\kappa+1} = \mathbf{A}_{\kappa}\mathbf{x}_{\kappa} + \mathbf{B}_{\kappa}\mathbf{p}_{\mathbf{b}\kappa} \tag{29.15}$$

where $\mathbf{x}_{\kappa} = \mathbf{x}(\kappa\Delta t)$, $\mathbf{p}_{\mathbf{b}\kappa} = \mathbf{p}_{\mathbf{b}}(\kappa\Delta t)$ for $\kappa = 1, \ldots, N$ and

$$\mathbf{A}_{\kappa} = e^{\mathbf{A_c}(\kappa\Delta t)\Delta t} \tag{29.16}$$

$$\mathbf{B}_{\kappa} = [\mathbf{A}_{\kappa} - \mathbf{I}]\,\mathbf{A_c}(\kappa\Delta t)^{-1}\mathbf{B_c} \tag{29.17}$$

29.3 Crowd Flow Model

Given the inter- and intra-subject variabilities inherent to pedestrian excitation [28, 29], a statistical analysis is required for the evaluation of the associated structural response. To this end, the present study applies a Monte Carlo procedure. As in the present study focus is on the resulting structural response, a number of reasonable simplifying assumptions are made. Although the simulation model accounts for inter-subject variability, intra-subject variability and human-structure synchronisation phenomena are disregarded.

The walking trajectories assumed in the analysis are straight lines parallel to the longitudinal axis (x) of the bridge deck. The offsets in the lateral direction are chosen randomly along the bridge deck width. All pedestrians are assumed to move at the same walking speed ($v_s = 1.5$ m/s). The step length (l_s) for a given pacing rate (f_s) follows from:

$$l_s = \frac{v_s}{f_s} \tag{29.18}$$

The time taken by a pedestrian to cross the bridge is calculated as:

$$T = \frac{L}{v_s} \tag{29.19}$$

where L [m] is the length of the bridge. The arrival rate λ [persons/s] is computed from the pedestrian density d:

$$\lambda = \frac{n_{\mathrm{H}}}{T} = \frac{A_{\mathrm{eff}}\, d}{T} \tag{29.20}$$

The arrival times are assumed to follow a Poisson distribution [30–32]. Low pedestrian densities (d $<$ 1 persons/m^2) are simulated assuming unrestricted traffic, represented here by a Gaussian distribution of the step frequencies centred

around one of the natural frequencies of the footbridge f_l with a standard deviation of 0.175 Hz ($f_{s,k} \sim \mathcal{N}(\mu_{f_{s,k}}, \sigma_{f_{s,k}}) = \mathcal{N}(f_l, 0.175)$ [Hz]). To account for the higher synchronisation rate that is expected for high pedestrian densities ($1 \geq d \geq 1.5\ \mathrm{persons/m^2}$), all pedestrians are given the same step frequency. Note that the above stated properties for sparse and dense crowd conditions are chosen in agreement with the stochastic load model applied by the design guides [33, 34] in deriving their equivalent load model. A more comprehensive discussion of the pedestrian flow model applied here, can be found in [35]. Following this crowd flow model, an increasing number of pedestrian flows is simulated until the desired convergence of the observed output parameter is reached.

29.4 Impact HSI

In this section, the moving crowd model is applied to predict the structural response for a number of footbridge parameters and pedestrian densities. The pedestrian flows are generated according to the crowd flow model defined in Sect. 29.3. By comparison of the response predicted by a moving force model, it is in addition evaluated in which cases HSI is significant.

In the following, the input parameters and the output quantities of interest are discussed. Lastly, the predicted structural response and the interaction effect are evaluated.

29.4.1 Input Parameters

The following footbridge and crowd parameters are considered:

- *Footbridge parameters*: A reference structure representative for over 150 recently constructed footbridges is used [13]. The footbridge has a span of 50 m, a bridge deck of 3 m wide and a total mass m_{BRIDGE} of 50×10^3 kg [13]. Only the fundamental vertical bending mode is considered. As for a simply supported beam, this mode has a sinusoidal mode shape and a modal mass equal to half of the total mass of the bridge. As footbridges are generally lowly-damped, a modal damping ratio of 0.5 % is selected. The natural frequency f_{B} is varied between 1 and 6 Hz, which is in line with the vibration serviceability issues of footbridges [33, 34, 36].
- *Crowd parameters*: Two pedestrian densities are considered: $d = \{0.2, 1.0\}\ \mathrm{persons/m^2}$, corresponding to 30 and 150 pedestrians, respectively. The pedestrian flows are simulated according to the crowd flow defined in Sect. 29.3. Aiming at resonance, (the centre frequency of the Gaussian distribution of) the step frequencies is set to match the natural frequency of the structure. Up to 2.5 Hz, resonance occurs with the fundamental harmonic of the walking load, while between 2.5 and 5.0 Hz and 5.0 and 7.5 Hz, resonance is considered with the second and the third harmonic of the walking load, respectively.

29.4.2 Output Quantities of Interest

The 95 percentile value of the maximum predicted acceleration is evaluated. To quantify the reduction of the structural acceleration due to HSI, the reduction factor R_{HSI} [-] is defined:

$$R_{\mathrm{HSI}} = \frac{\ddot{u}_{b,\mathrm{max95}}}{\ddot{u}_{\mathrm{HSI,max95}}} \tag{29.21}$$

where $\ddot{u}_{b,\mathrm{max95}}$ and $\ddot{u}_{\mathrm{HSI,max95}}$ represent the 95 percentile value of the maximum acceleration predicted when the interaction term defined in Sect. 29.2 is disregarded and accounted for, respectively.

29.4.3 Results

Figure 29.4 presents the 95 percentile value of the maximum acceleration levels in terms of the natural frequency and the modal mass of the footbridge, predicted when HSI is disregarded. The largest values of $\ddot{u}_{b,\mathrm{max95}}$ are found for natural

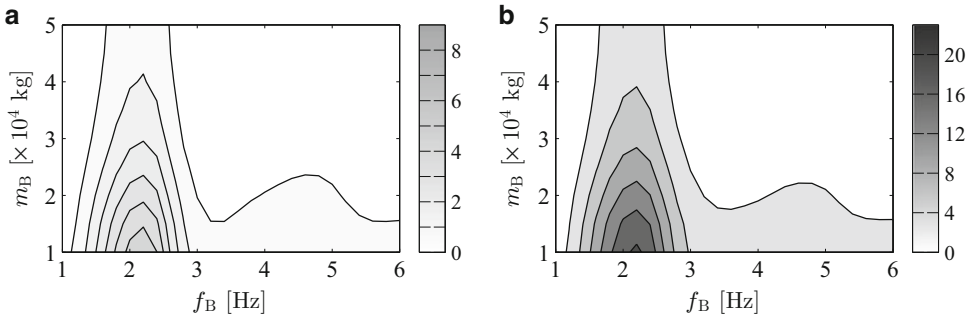

Fig. 29.4 The 95 percentile value of the maximum acceleration predicted for the moving force model ($\ddot{u}_{b,\max 95}$ [$\mathrm{m/s^2}$]) in terms of the natural frequency (f_B) and modal mass (m_B) of the footbridge with $\xi_B = 0.5\,\%$ for: (**a**) a low (0.2 $\mathrm{persons/m^2}$) and (**b**) a high (1.0 $\mathrm{persons/m^2}$) pedestrian density

frequencies between 1.5 and 2.5 Hz, thus, where resonance occurs with the fundamental harmonic of the walking load. Resonance with the second harmonic of the walking load, i.e. for natural frequencies between 2.5 and 5.0 Hz, leads to a lower structural response. Acceleration levels as high as 6 and 20 $\mathrm{m/s^2}$ are observed for a pedestrian density of 0.2 $\mathrm{persons/m^2}$ and 1.0 $\mathrm{persons/m^2}$, respectively. It is, however, highly unlikely that these extremely high levels will occur in reality because of (1) the expected increase in structural damping for larger vibration amplitudes and (2) the large structural motion that will hinder the pedestrians in walking, i.e. the self-limiting nature of pedestrian-induced vibrations [37–39].

29.4.3.1 Evaluation of the Structural Response

Figure 29.5 presents the 95 percentile value of the maximum acceleration ($\ddot{u}_{\mathrm{HSI},\max 95}$) predicted by the moving crowd model, in terms of the natural frequency and the modal mass of the footbridge. Again, the largest acceleration levels are observed for natural frequencies between 1.5 and 3.0 Hz, i.e. when resonance occurs with the fundamental harmonic of the walking load. A second peak is found when resonance occurs with the second harmonic of the walking load, thus, for natural frequencies of the footbridge between 4.0 and 5.0 Hz. Analogous to the case where HSI was disregarded (Fig. 29.4), it is observed that for a decreasing modal damping ratio and a decreasing modal mass of the footbridge, the structural response increases. However, the rate of this increase is much smaller when HSI is accounted for (Fig. 29.5). The latter is due to the fact that a decreasing modal damping ratio and a decreasing modal mass of the footbridge are associated with an increasing impact of HSI, thus, leading to a larger effective damping ratio of the coupled crowd-structure system [13].

As the modal mass of the footbridge decreases, the natural frequencies at which the highest accelerations are found, slightly increase, in particular for the higher pedestrian density. The latter is due to the fact that the effective natural frequency of the coupled crowd-structure system decreases [13]. In some cases, the reduced effective natural frequency is then situated in the range where resonance occurs with the fundamental harmonic of the walking load.

In addition, it is noted that for the predicted maximum acceleration levels do not exceed 5.0 $\mathrm{m/s^2}$. As a result of taking into account HSI, the unrealistically high acceleration levels predicted by simplified force models are no longer reached.

29.4.3.2 Impact of HSI

Finally, focus is at the reduction factor R_{HSI}, presented in Fig. 29.6. As apparent from this figure, the reduction factor is always equal to or larger than unity. Hence, taking into account HSI results into a reduction of the predicted structural response. Furthermore it is observed that the reduction factor and thus, the impact of HSI, increases with the pedestrian density.

The highest reduction factors are found for natural frequencies of the footbridge between 2.5 and 5 Hz, which are close to the natural frequency of the human body models. This was expected as the increase in effective damping ratio was found to be most significant for frequency ratios (f_{H1}/f_B) close to unity [13]. Finally, it is observed that for natural frequencies of the empty footbridge above 1.5 Hz, the predicted response reduces by a minimum of 30 %, hence, HSI can be considered sufficiently important to be considered in practical design.

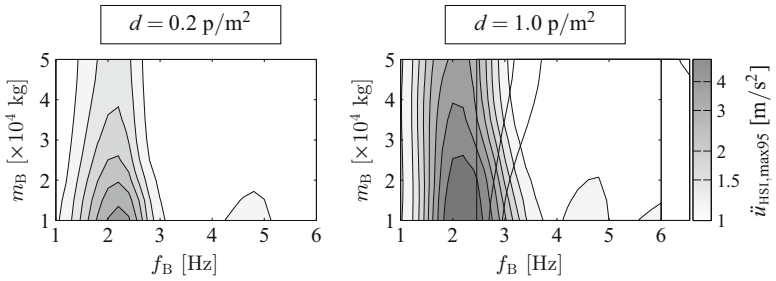

Fig. 29.5 The 95 percentile values of the maximum acceleration levels at midspan of the bridge ($\ddot{u}_{\mathrm{HSI,max95}}$ [m/s^2]) predicted by the pseudo moving crowd model for a low ($d = 0.2\,\mathrm{persons/m^2}$) and a high ($d = 1\,\mathrm{persons/m^2}$) pedestrian density, for a structural inherent damping ratio of $\xi_B = 0.5\,\%$, in terms of the natural frequency (f_B) and modal mass (m_B) of the footbridge

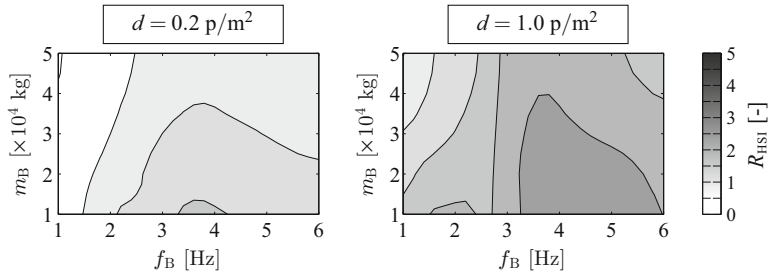

Fig. 29.6 The reduction factor R_{HSI} [-] derived a low ($d = 0.2\,\mathrm{persons/m^2}$) and a high ($d = 1\,\mathrm{persons/m^2}$) pedestrian density, for a structural inherent damping ratio of $\xi_B = 0.5\,\%$, in terms of the natural frequency (f_B) and modal mass (m_B) of the footbridge

29.5 Conclusions

This contribution proposes a moving crowd model for pedestrian excitation including vertical HSI. To this end, the pedestrian excitation is modelled as a superposition of the well-known forces induced by a pedestrian on a rigid floor and a component due to the interaction with a SDOF system. Inspired by the body postures assumed during the walking cycle, the mechanical properties of the SDOF system are chosen to represent the low-frequency dynamic behaviour of the human body with one or two legs slightly bent.

To account for the inherent variabilities of pedestrian excitation, the predicted structural response is evaluated by Monte Carlo simulations. In this way, the structural response is predicted for various footbridge parameters and pedestrian densities. By comparison with the response predicted by a moving force model, it is investigated in which cases HSI is significant.

The results show that taking into account HSI leads to a reduction in the structural response. In addition, it is observed that the unrealistically high acceleration levels predicted by simplified force models are no longer reached as the result of HSI. Finally, it is observed that for the considered range of footbridge parameters, the predicted response reduces by a minimum of 30 % when the natural frequency of the empty footbridge is situated between 1.5 and 6.0 Hz. In those cases, HSI is sufficiently important to be considered in practical design.

Acknowledgements The first author is a post-doctoral fellow of the Research Foundation Flanders (FWO). The financial support is gratefully acknowledged.

References

1. Bachmann, H., Ammann, W.: Vibrations in structures induced by man and machines. IABSE-AIPC-IVBH, 1987
2. Racić, V., Pavić, A., Reynolds, P.: Experimental identification and analytical modelling of walking forces: a literature review. J. Sound Vib. **326**, 1–49 (2009)
3. Kerr, S.: Human induced loading of staircases. Ph.D. thesis, University College London, Mechanical Engineering Department, 1998
4. Willford, M., Field, C., Young, P.: Improved methodologies for the prediction of footfall-induced vibration. In: ASCE - Building Integration Solutions, pp. 1–15, 2004
5. Butz, C.: Beutrag zur Berechnung fussgängerinduzierter Brückenschwingungen - Shaker Verlag. Ph.D. thesis, RWTH Aachen, 2006

6. Li, Q., Fan, J., Nie, J., Li, Q., Chen, Y.: Crowd-induced random vibration of footbridge and vibration control using multiple tuned mass dampers. J. Sound Vib. **329**, 4068–4092 (2010)
7. Pavić, A., Reynolds, P.: Experimental verification of novel 3DOF model for grandstand crowd-structure dynamic interaction. In: Proceedings of IMAC 26, the International Modal Analysis Conference, Orlando, FL, Feb 2008
8. Živanović, S., Pavić, A., Reynolds, P.: Human-structure dynamic interaction in footbridges. Bridg. Eng. **158**(4), 165–177 (2005)
9. Zuo, D., Hua, J., Van Landuyt, D.: A model of pedestrian-induced bridge vibration based on full-scale measurement. Eng. Struct. **45**, 117–126 (2012)
10. Sachse, R., Pavić, A., Reynolds, P.: Parametric study of modal properties of damped two-degree-of-freedom crowd-structure dynamic systems. J. Sound Vib. **274**, 461–480 (2004)
11. Bocian, M., Macdonald, J., Burn, J.: Biomechanically-inspired modelling of pedestrian-induced vertical self-excited forces. J. Bridg. Eng. **18**, 1336–1346 (2013)
12. Brownjohn, J., Fok, P., Roche, M., Omenzetter, P.: Long span steel pedestrian bridge at Singapore Changi Airport - part 2: crowd loading tests and vibration mitigation measures. Struct. Eng. **82**(16), 28–34 (2004)
13. Van Nimmen, K., Maes, K., Lombaert, G., De Roeck, G., Van den Broeck, P.: The impact of vertical human-structure interaction for footbridges. In: COMPDYN – ECCOMAS: Proceedings of the Thematic Conference on Computational Methods in Structural Dynamics and Earthquake Engineering, Crete Island, May 2015
14. Dougil, J., Wright, J., Parkhouse, J., Harrison, R.: Human structure interaction during rhythmic bobbing. Struct. Eng. **84** 32–39, (2006)
15. Jones, C., Reynolds, P., Pavić, A.: Vibration serviceability of stadia structures subjected to dynamic crowd loads: a literature review. J. Sound Vib. **330**, 1531–1566 (2011)
16. Fahy, F., Gardonio, P.: Sound and structural vibration: radiation, transmission and response, 2nd edn. Academic, New York (2007)
17. Cremer, L., Heckl, M., Petersson, B.: Structure-Borne Sound. Springer, Berlin (2010)
18. Dijckmans, A.: Wave based calculation methods for sound-structure interaction: application to sound insulation and sound radiation of composite walls and floors. Ph.D. thesis, KU Leuven, 2011
19. International Organisation for Standardization, ISO 5982:1981 Vibration and shock - Mechanical driving point impedance of the human body, 1981
20. Matsumoto, Y., Griffin, M.: Mathematical models for the apparent masses of standing subjects exposed to vertical whole-body vibration. J. Sound Vib. **260**, 431–451 (2003)
21. Brownjohn, J.: Energy dissipation from vibration floor slabs due to human-structure interaction. J. Shock Vib. **8**, 315–323 (2001)
22. Zheng, X., Brownjohn, J.: Modelling and simulation of human-floor system under vertical vibration. In: Davis, L. (ed.) Proceedings of SPIE: Smart Structures and Material, vol. 4327, pp. 513–520, 2001
23. Matsumoto, Y., Griffin, M.: Dynamic response of the standing human body exposed to vertical vibration: influence of posture and vibration magnitude. J. Sound Vib. **212**(1), 85–107 (1998)
24. Van Nimmen, K., Maes, K., Živanović, S., Lombaert, G., De Roeck, G., Van den Broeck, P.: Identification and modelling of vertical human-structure interaction. In: Proceedings of IMAC 33, the International Modal Analysis Conference, 2015
25. Bocian, M., Macdonald, J., Burn, J.: Biomechanically inspired modelling of pedestrian-induced forces on laterally oscillating structures. J. Sound Vib. **331**, 3914–3929 (2012)
26. Ingólfsson, E., Georgakis, C., Jönsson, J.: Pedestrian-induced lateral vibrations of footbridges: a literature review. Eng. Struct. **45**, 21–52 (2012)
27. Van Nimmen, K., Verbeke, P., Lombaert, G., De Roeck, G., Van den Broeck, P.: Numerical and experimental evaluation of the dynamic performance of a footbridge with tuned mass dampers. J. Bridge Eng. (2016). 10.1061/(ASCE)BE.1943-5592.0000815, C4016001. doi:http://dx.doi.org/10.1061/(ASCE)BE.1943-5592.0000815
28. Caprani, C., Keogh, J., Archbold, P., Fanning, P.: Enhancement for the vertical response of footbridges subjected to stochastic crowd loading. Comput. Struct. **102–103**, 87–96 (2012)
29. Sahnaci, C., Kasperski, M.: Simulation of random pedestrian flow. In: Proceedings of the 8th International Conference on Structural Dynamics of EURODYN, Leuven July 2011
30. Helbing, D.: Modeling and optimization of production processes: Lessons from traffic dynamics, SFI Working Paper, no. 10–057, 2003
31. Matsumoto, Y., Nishioka, T., Shiojiri, H., Matsuzaki, K.: Dynamic design of footbridges. In: IABSE Proceedings, No.P 17–78, pp. 1–15, 1978
32. Živanović, S.: Benchmark footbridge for vibration serviceability assessment under vertical component of pedestrian load. J. Struct. Eng. **138**, 1193–1202 (2012)
33. Association Française de Génie Civil, Sétra/AFGC, Sétra: Evaluation du comportement vibratoire des passerelles piétonnes sous l'action des piétons, 2006
34. Heinemeyer, C., Butz, C., Keil, A., Schlaich, M., Goldack, A., Lukić, M., Chabrolin, B., Lemaire, A., Martin, P., Cunha, A., Caetano, E.: Design of Lightweight Footbridges for Human Induced Vibrations - Background document in support to the implementation, harmonization and further development of the Eurocodes. JRC-ECCS 2009, 2009
35. Van Nimmen, K., Verbeke, P., Lombaert, G., De Roeck, G., Van den Broeck, P.: Numerical and experimental evaluation of the dynamic performance of a footbridge with tuned mass dampers. J. Bridg. Eng. 2015 doi:http://dx.doi.org/10.1061/(ASCE)BE.1943-5592.0000815
36. Butz, C., Feldmann, M., Heinemeyer, C., Sedlacek, G.: SYNPEX: advanced load models for synchronous pedestrian excitation and optimised design guidelines for steel footbridges. Technical Report, Research Fund for Coal and Steel, 2008
37. Ingólfsson, E.: Pedestrian-induced lateral vibrations of footbridges: experimental studies and probabilistic modelling. Ph.D. thesis, Technical University of Denmark, 2011
38. Nakamura, S.: Model for lateral excitation of footbridges by synchronous walking. ASCE J. Struct. Eng. **130**(1), 32–37, (2011)
39. Scheller, J., Starossek, U.: Design and experimental verification of a new active mass damper for control of pedestrian-induced bridge vibrations. In: Proceedings of the 4th International Footbridge Conference, Wroclaw, July 2011

Chapter 30
Nonlinear Time-Varying Dynamic Analysis of a Multi-Mesh Spur Gear Train

Siar Deniz Yavuz, Zihni Burcay Saribay, and Ender Cigeroglu

Abstract The nonlinear dynamics of a multi-mesh spur gear train is considered in this study. The gear train consists of three spur gears, with one of the gears in mesh with the other two. Dynamic model includes gear backlash in the form of clearance-type displacement functions and time variation of gear mesh stiffness. The system is reduced to a two-degree-of-freedom definite model by using the relative gear mesh displacements as the coordinates. The equations of motion are solved for periodic steady-state response by using Harmonic Balance Method (HBM). The accuracy of the HBM solutions is demonstrated by comparing them to direct numerical integration solutions. Floquet theory is applied to determine the stability of the steady-state solutions. Two different loading conditions, where the system is driven by the middle gear and driven by one of the end gears, are considered. Phase difference between the two gear meshes is determined under each loading condition and natural modes are predicted for each loading condition. The forced response due to the combination of parametric excitation and static transmission error excitation is obtained and effects of loading conditions and asymmetric positioning on the response are explored.

Keywords Nonlinear gear dynamics • Multi-mesh spur gear train • Mesh phasing • Time-varying mesh stiffness • Multi-term harmonic balance method

Nomenclature

b	Half of gear backlash
c	Damping coefficient
e	Static transmission error
g	Nonlinear displacement functions
F	External force
G	Periodic state matrix
I	Polar mass moment of inertia
J	Jacobian matrix
k	Mesh stiffness
M	Monodromy matrix
m	Equivalent mass
p	Relative gear mesh displacement
Δp	Perturbation of relative gear mesh displacement
r	Gear base radius
S	Nonlinear algebraic equations in matrix form

S.D. Yavuz
Department of Mechanical Engineering, Middle East Technical University, Universiteler Mahallesi, Dumlupinar Bulvari No:1, 06800 Cankaya, Ankara, Turkey

Turkish Aerospace Industries, Inc. (TAI), Fethiye Mahallesi Havacilik Bulvari No:17, 06980 Kazan, Ankara, Turkey

Z.B.Saribay
Turkish Aerospace Industries, Inc. (TAI), Fethiye Mahallesi Havacilik Bulvari No:17, 06980 Kazan, Ankara, Turkey

E. Cigeroglu (✉)
Department of Mechanical Engineering, Middle East Technical University, Universiteler Mahallesi, Dumlupinar Bulvari No:1, 06800 Cankaya, Ankara, Turkey
e-mail: ender@metu.edu.tr

© The Society for Experimental Mechanics, Inc. 2016

M. Allen et al. (eds.), *Dynamics of Coupled Structures, Volume 4*, Conference Proceedings of the Society for Experimental Mechanics Series, DOI 10.1007/978-3-319-29763-7_30

T	Torque
t	Time
$\mathbf{U}$	Solution vector
u	Gear mesh displacement harmonic amplitude
Z	Number of teeth
$\mathbf{z}$	Perturbation state vector
α	Phase of static transmission error harmonic
ρ	Discrete time interval
ϕ	Discontinuous separation function
θ	Rotational displacement
Π	Phase difference between meshes
Ω	Dimensionless frequency
ω	Characteristic frequency
ζ	Damping ratio
ψ	Angle between the lines connecting the centers of the gears
γ	Constant angle in mesh phasing calculation

Subscripts

a	Alternating component
i	Mesh index
m	Mean component

Superscripts

i	Mesh index
rms	Root-mean-square value
T	Matrix transpose
$\cdot$	Derivative with respect to time
’	Derivative with respect to dimensionless time
–	Dimensional quantities

30.1 Introduction

Gear vibration is an important consideration in drive-train systems due to noise and durability problems. Under dynamic conditions, gear systems produce much higher gear mesh forces than static forces transmitted. These high frequency dynamic forces must be supported by the bearings and are eventually transmitted to the housing to act as the main excitations for gear related noise. Furthermore, alternating forces induced by the vibration reduce fatigue life of the driveline components. Therefore, a better understanding of the gear system dynamics is vital in order to design more silent and durable transmission.

There are a large number of gear dynamics related studies in the literature and in the vast majority of these studies, a single gear pair is considered. Numerous mathematical models are constructed and analytical and numerical solution methods are developed in those studies. The models including a spur gear pair are mostly nonlinear (piecewise-linear) due to backlash but differ in incorporating time variation of mesh stiffness. Some of these models are nonlinear time-invariant (NTI) [1], whereas the others are nonlinear time-varying (NTV) [2–6]. However, published experimental data [3, 4, 7] show that the dynamic behavior of a spur gear pair can only be described by a NTV model. These single-degree-of-freedom (DOF) models are extended to multiple DOFs nonlinear models of geared rotor-bearing systems [8–11]. Moreover, linear and time-invariant characteristics of helical gears are studied in [12–14].

The studies on multi-mesh gear systems are fewer than the ones on single gear pair systems even though most practical systems use multi-mesh, multi-stage gear trains. Nonlinear time-varying dynamic models of multi-mesh spur gear trains are

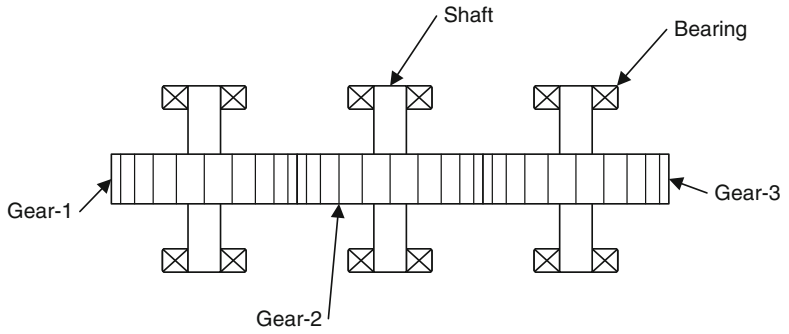

Fig. 30.1 Multi-mesh spur gear train considered in this study

developed in [15–17]. In those studies, a multi-term Harmonic Balance Method (HBM) is used in conjunction with discrete Fourier Transform (DFT) to obtain period-1 and subharmonic responses. Authors examined the nonlinear, parametrically excited dynamics of idler and two-stage counter-shaft configurations of spur gears in [18, 19]. NTV [20] and LTI [21] dynamic models are also proposed for planetary gear sets composed of spur and helical gears, respectively.

In this study, considering both backlash nonlinearity and time-varying mesh stiffness, a nonlinear dynamic model of a multi-mesh gear train is considered. The model consists of three spur gears with one of the gears in mesh with the other two as shown in Fig. 30.1. Both static transmission error excitation and parametric excitation due to time variation of mesh stiffness are considered. The multi-term HBM coupled with DFT and arc-length numerical continuation method are applied to solve the equation of motions for periodic steady-state response. The results of HBM are validated by comparing them to direct numerical integration solutions, which are computationally more intensive. Furthermore, the stability of the steady-state solutions is determined by the use of Floquet theory. Dynamics of both split-torque and idler arrangements are studied. In the split-torque arrangement, the system is driven by the middle gear, whereas one of the end gears is the input and the other one is the output in the idler arrangement. The interaction between meshes such as phasing is investigated for each loading condition and the influence of mesh phasing on the dynamic response is discussed. The effects of asymmetric positioning of the gears around the middle gear on the dynamic response are also studied.

30.2 Dynamic Model Formulation

30.2.1 Physical System and Dynamic Model

The geared system considered in this study, Fig. 30.1, consists of three spur gears with rigid gear blanks mounted on rigid bearings and shafts. The gear in the middle, gear-2, meshes with the other two gears, gear-1 and gear-3. The mesh coupling between the gears includes gear backlash, time-varying mesh stiffness, which acts as parametric excitation, and time-invariant mesh damping. The system is also excited by the static transmission errors, $\overline{e}_1(\bar{t})$ and, $\overline{e}_2(\bar{t})$ which are connected in series to the stiffness and damping elements as shown in Fig. 30.2. Gear mesh damping elements are also assumed not to be subjected to gear backlash nonlinearity.

In Fig. 30.2, torsional vibrations of each gear are considered where I_i is the polar mass moment of inertia and r_i is the base radius of the i^{th} gear. Therefore, the system can be represented by a three-degrees-of-freedom semi-definite dynamic model with coordinates $\overline{\theta}_i$, $(i = 1-3)$. The equations of motion of this system can be obtained as follows

$$I_1\ddot{\overline{\theta}}_1(\bar{t}) + r_1\bar{c}_1\left[r_1\dot{\overline{\theta}}_1(\bar{t}) + r_2\dot{\overline{\theta}}_2(\bar{t}) + \dot{\overline{e}}_1(\bar{t})\right] + r_1\bar{k}_1(\bar{t})\,\overline{g}_1(\bar{t}) = \overline{T}_1, \tag{30.1a}$$

$$I_2\ddot{\overline{\theta}}_2(\bar{t}) + r_2\bar{c}_1\left[r_1\dot{\overline{\theta}}_1(\bar{t}) + r_2\dot{\overline{\theta}}_2(\bar{t}) + \dot{\overline{e}}_1(\bar{t})\right] + r_2\bar{k}_1(\bar{t})\,\overline{g}_1(\bar{t}) + r_2\bar{c}_2\left[r_2\dot{\overline{\theta}}_2(\bar{t}) + r_3\dot{\overline{\theta}}_3(\bar{t}) + \dot{\overline{e}}_2(\bar{t})\right] + r_2\bar{k}_2(\bar{t})\,\overline{g}_2(\bar{t}) = \overline{T}_2, \tag{30.1b}$$

$$I_3\ddot{\overline{\theta}}_3(\bar{t}) + r_3\bar{c}_2\left[r_2\dot{\overline{\theta}}_2(\bar{t}) + r_3\dot{\overline{\theta}}_3(\bar{t}) + \dot{\overline{e}}_2(\bar{t})\right] + r_3\bar{k}_2(\bar{t})\,\overline{g}_2(\bar{t}) = \overline{T}_3, \tag{30.1c}$$

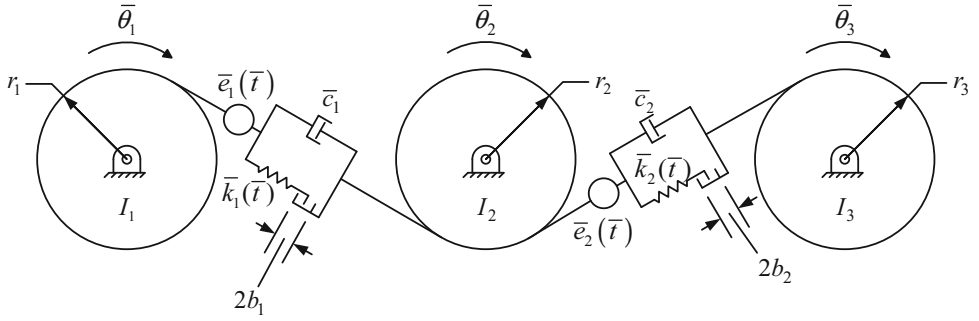

Fig. 30.2 Dynamic model of the system

where $\overline{g}_1$ and $\overline{g}_2$ are nonlinear displacement functions defined mathematically as

$$\overline{g}_1 = \begin{cases} \left[r_1\overline{\theta}_1(\overline{t}) + r_2\overline{\theta}_2(\overline{t}) + \overline{e}_1(\overline{t})\right] - \overline{b}_1, & \left[r_1\overline{\theta}_1(\overline{t}) + r_2\overline{\theta}_2(\overline{t}) + \overline{e}_1(\overline{t})\right] > \overline{b}_1 \\ 0, & \left|r_1\overline{\theta}_1(\overline{t}) + r_2\overline{\theta}_2(\overline{t}) + \overline{e}_1(\overline{t})\right| \le \overline{b}_1 \\ \left[r_1\overline{\theta}_1(\overline{t}) + r_2\overline{\theta}_2(\overline{t}) + \overline{e}_1(\overline{t})\right] + \overline{b}_1, & \left[r_1\overline{\theta}_1(\overline{t}) + r_2\overline{\theta}_2(\overline{t}) + \overline{e}_1(\overline{t})\right] < -\overline{b}_1 \end{cases}, \tag{30.2a}$$

$$\overline{g}_2 = \begin{cases} \left[r_2\overline{\theta}_2(\overline{t}) + r_3\overline{\theta}_3(\overline{t}) + \overline{e}_2(\overline{t})\right] - \overline{b}_2, & \left[r_2\overline{\theta}_2(\overline{t}) + r_3\overline{\theta}_3(\overline{t}) + \overline{e}_2(\overline{t})\right] > \overline{b}_2 \\ 0, & \left|r_2\overline{\theta}_2(\overline{t}) + r_3\overline{\theta}_3(\overline{t}) + \overline{e}_2(\overline{t})\right| \le \overline{b}_2 \\ \left[r_2\overline{\theta}_2(\overline{t}) + r_3\overline{\theta}_3(\overline{t}) + \overline{e}_2(\overline{t})\right] + \overline{b}_2, & \left[r_2\overline{\theta}_2(\overline{t}) + r_3\overline{\theta}_3(\overline{t}) + \overline{e}_2(\overline{t})\right] < -\overline{b}_2 \end{cases}. \tag{30.2b}$$

The above three-degrees-of-freedom semi-definite system can be reduced to a two-degrees-of-freedom definite system by defining the following two new coordinates:

$$\overline{p}_1(\overline{t}) = r_1\overline{\theta}_1(\overline{t}) + r_2\overline{\theta}_2(\overline{t}) + \overline{e}_1(\overline{t}), \tag{30.3a}$$

$$\overline{p}_2(\overline{t}) = r_2\overline{\theta}_2(\overline{t}) + r_3\overline{\theta}_3(\overline{t}) + \overline{e}_2(\overline{t}). \tag{30.3b}$$

These new coordinates represent the relative gear mesh displacements, which are the combinations of the dynamic and static transmission errors. Using Eqs. (30.1)–(30.3), the following new system of equations is obtained

$$\ddot{\overline{p}}_1(\overline{t}) + \overline{c}_1\left[\frac{r_1^2}{I_1} + \frac{r_2^2}{I_2}\right]\dot{\overline{p}}_1(\overline{t}) + \overline{c}_2\frac{r_2^2}{I_2}\dot{\overline{p}}_2(\overline{t}) + \overline{k}_1(\overline{t})\left[\frac{r_1^2}{I_1} + \frac{r_2^2}{I_2}\right]\overline{g}_1(\overline{t}) + \overline{k}_2(\overline{t})\frac{r_2^2}{I_2}\overline{g}_2(\overline{t}) = \frac{r_1}{I_1}\overline{T}_1 + \frac{r_2}{I_2}\overline{T}_2 + \ddot{\overline{e}}_1(\overline{t}), \tag{30.4a}$$

$$\ddot{\overline{p}}_2(\overline{t}) + \overline{c}_1\frac{r_2^2}{I_2}\dot{\overline{p}}_1(\overline{t}) + \overline{c}_2\left[\frac{r_2^2}{I_2} + \frac{r_3^2}{I_3}\right]\dot{\overline{p}}_2(\overline{t}) + \overline{k}_1(\overline{t})\frac{r_2^2}{I_2}\overline{g}_1(\overline{t}) + \overline{k}_2(\overline{t})\left[\frac{r_2^2}{I_2} + \frac{r_3^2}{I_3}\right]\overline{g}_2(\overline{t}) = \frac{r_2}{I_2}\overline{T}_2 + \frac{r_3}{I_3}\overline{T}_3 + \ddot{\overline{e}}_2(\overline{t}). \tag{30.4b}$$

In order to obtain the dimensionless equations of motion, the following transformations are applied:

$$m_1 = \frac{I_1I_2}{r_1^2I_2 + r_2^2I_1}, \quad m_2 = \frac{I_2}{r_2^2}, \quad m_3 = \frac{I_2I_3}{r_3^2I_2 + r_2^2I_3}, \tag{30.5a-c}$$

$$k_1(\overline{t}) = \frac{\overline{k}_1(\overline{t})}{k_{1m}}, \quad k_2(\overline{t}) = \frac{\overline{k}_2(\overline{t})}{k_{2m}}, \tag{30.5d,e}$$

$$\overline{\omega}_{11}^2 = \frac{k_{1m}}{m_1}, \quad \overline{\omega}_{12}^2 = \frac{k_{2m}}{m_2}, \quad \overline{\omega}_{21}^2 = \frac{k_{1m}}{m_2}, \quad \overline{\omega}_{22}^2 = \frac{k_{2m}}{m_3}, \tag{30.5f-i}$$

$$\zeta_{11} = \frac{\overline{c}_1}{2m_1\overline{\omega}_{11}}, \quad \zeta_{12} = \frac{\overline{c}_2}{2m_2\overline{\omega}_{12}}, \quad \zeta_{21} = \frac{\overline{c}_1}{2m_2\overline{\omega}_{21}}, \quad \zeta_{22} = \frac{\overline{c}_2}{2m_3\overline{\omega}_{22}}, \tag{30.5j-m}$$

where k_{1m} and k_{2m} are the mean components of $\overline{k}_1(\overline{t})$ and $\overline{k}_2(\overline{t})$, respectively, $\overline{\omega}_{ij}$ $(i,j=1,2)$ is the characteristic frequency, and ζ_{ij} $(i,j=1,2)$ defines the damping of the system. Moreover, a dimensionless time parameter is obtained by setting $t=\overline{t}\omega_c$, where ω_c is one of the characteristic frequencies. Also, dimensionless displacements are defined as $p_i(\overline{t})=\overline{p}_i(\overline{t})/b_c$, $e_i(\overline{t})=\overline{e}_i(\overline{t})/b_c$, and $b_i=\overline{b}_i/b_c$ $(i=1,2)$ by employing a characteristic length b_c. Using these dimensionless parameters and letting $\omega_{ij}=\overline{\omega}_{ij}/\omega_c$ $(i,j=1,2)$, the following dimensionless equations of motion are obtained:

$$\begin{Bmatrix} p_1''(t) \\ p_2''(t) \end{Bmatrix} + 2\begin{bmatrix} \zeta_{11}\omega_{11} & \zeta_{12}\omega_{12} \\ \zeta_{21}\omega_{21} & \zeta_{22}\omega_{22} \end{bmatrix}\begin{Bmatrix} p_1'(t) \\ p_2'(t) \end{Bmatrix} + \begin{bmatrix} \omega_{11}^2 k_1(t) & \omega_{12}^2 k_2(t) \\ \omega_{21}^2 k_1(t) & \omega_{22}^2 k_2(t) \end{bmatrix}\begin{Bmatrix} g_1(t) \\ g_2(t) \end{Bmatrix} = \begin{Bmatrix} F_m^{(1)} + e_1''(t) \\ F_m^{(2)} + e_2''(t) \end{Bmatrix}, \tag{30.6a}$$

where

$$g_i(t) = \begin{cases} p_i(t) - b_i, & p_i(t) > b_i \\ 0, & |p_i(t)| \le b_i \\ p_i(t) + b_i, & p_i(t) < -b_i \end{cases}, \quad i = 1,2, \tag{30.6b}$$

$$F_m^{(1)}(t) = \frac{1}{\omega_c^2 b_c}\left(\frac{r_1}{I_1}\overline{T}_1 + \frac{r_2}{I_2}\overline{T}_2\right), \quad F_m^{(2)}(t) = \frac{1}{\omega_c^2 b_c}\left(\frac{r_2}{I_2}\overline{T}_2 + \frac{r_3}{I_3}\overline{T}_3\right). \tag{30.6c}$$

30.2.2 Period-One Dynamics

The multi-term harmonic balance method coupled with discrete Fourier Transform process and the numerical continuation method, which has been successfully applied in [3, 4, 15, 16], is used in this study to solve the dimensionless equations of motion for p_i $(i=1,2)$. The solution is periodic based on the assumption that both excitations and time-varying parameters are periodic [15]. This also implies that the nonlinear displacement functions $g_i(t)$ $(i=1,2)$ can also be described periodically. The harmonic expression for mesh stiffness and static transmission error can be written as

$$k_i(t) = 1 + \sum_{a=1}^{A}\left[\kappa_{2a}^{(i)}\cos(a\Omega t) + \kappa_{2a+1}^{(i)}\sin(a\Omega t)\right], \quad (i=1,2), \tag{30.7a}$$

$$e_i(t) = \sum_{j=1}^{J}\left[\varepsilon_{2j}^{(i)}\cos(j\Omega t) + \varepsilon_{2j+1}^{(i)}\sin(j\Omega t)\right], \quad (i=1,2). \tag{30.7b}$$

The mean values of the static transmission errors are set to zero since only the second order derivatives of them are included in the equations of motion (30.6a) as parts of the excitation terms on the right hand side of the equation.

Given the periodic excitations of Eqs. (30.7a, 30.7b), the steady-state solution is assumed to be of the form

$$p_i(t) = u_1^{(i)} + \sum_{r=1}^{R}\left[u_{2r}^{(i)}\cos(r\Omega t) + u_{2r+1}^{(i)}\sin(r\Omega t)\right], \quad (i=1,2), \tag{30.8}$$

which can be differentiated to yield

$$p_i'(t) = \sum_{r=1}^{R}\left[-(r\Omega)u_{2r}^{(i)}\sin(r\Omega t) + (r\Omega)u_{2r+1}^{(i)}\cos(r\Omega t)\right], \quad (i=1,2), \tag{30.9a}$$

$$p_i''(t) = -\sum_{r=1}^{R}\left[(r\Omega)^2 u_{2r}^{(i)}\cos(r\Omega t) + (r\Omega)^2 u_{2r+1}^{(i)}\sin(r\Omega t)\right], \quad (i=1,2). \tag{30.9b}$$

Then, the time series of nonlinear restoring forces can be obtained by sampling N points within one fundamental mesh period. Here, N must be larger than $2R$ where R is the highest harmonics of the solution in order to avoid aliasing errors. Hence, the time series of the nonlinear restoring forces are

$$F_k^{(i)}(t_n) = \omega_{i1}^2 k_1(t_n) g_1(t_n) + \omega_{i2}^2 k_2(t_n) g_2(t_n), \quad (i = 1, 2), \tag{30.10}$$

where $t_n = n\rho$ $(n = 0, 1, 2, \ldots N-1)$. Here, $\rho = 2\pi/(N\Omega)$.

In order to use multi-term HBM, the nonlinear restoring forces must be represented by Fourier series as

$$F_k^{(i)}(t) = F_{k1}^{(i)} + \sum_{r=1}^{R} \left[F_{k(2r)}^{(i)} \cos(r\Omega t) + F_{k(2r+1)}^{(i)} \sin(r\Omega t) \right], \quad (i = 1, 2), \tag{30.11}$$

where the coefficients can be calculated using the discrete Fourier Transform as $(r = 1, 2, \ldots R)$

$$F_{k1}^{(i)} = \frac{1}{N} \sum_{n=0}^{N-1} F_k^{(i)}, \quad (i = 1, 2), \tag{30.12a}$$

$$F_{k(2r)}^{(i)} = \frac{2}{N} \sum_{n=0}^{N-1} F_k^{(i)} \cos\left(\frac{2\pi rn}{N}\right), \quad (i = 1, 2), \tag{30.12b}$$

$$F_{k(2r+1)}^{(i)} = \frac{2}{N} \sum_{n=0}^{N-1} F_k^{(i)} \sin\left(\frac{2\pi rn}{N}\right), \quad (i = 1, 2). \tag{30.12c}$$

Substituting Eqs. (30.7b), (30.9a, 30.9b), and (30.11) into Eq. (30.6a) and equating the coefficients of the like harmonic terms, a set of $(4R + 2)$ nonlinear algebraic equations are obtained with $(i = 1, 2)$ and $(r = 1, 2, \ldots R)$

$$S_1^{(i)} = F_{k1}^{(i)} - F_m^{(i)}, \tag{30.13a}$$

$$S_{2r}^{(i)} = -(r\Omega)^2 u_{2r}^{(i)} + 2\zeta_{i1}\omega_{i1}(r\Omega) u_{2r+1}^{(1)} + 2\zeta_{i2}\omega_{i2}(r\Omega) u_{2r+1}^{(2)} + F_{k(2r)}^{(i)} + (r\Omega)^2 \varepsilon_{2r}^{(i)}, \tag{30.13b}$$

$$S_{2r+1}^{(i)} = -(r\Omega)^2 u_{2r+1}^{(i)} - 2\zeta_{i1}\omega_{i1}(r\Omega) u_{2r}^{(1)} - 2\zeta_{i2}\omega_{i2}(r\Omega) u_{2r}^{(2)} + F_{k(2r+1)}^{(i)} + (r\Omega)^2 \varepsilon_{2r+1}^{(i)}. \tag{30.13c}$$

Finally, the solution vector $\mathbf{U} = \left[u_1^{(1)}, u_2^{(1)}, \ldots u_{2R}^{(1)}, u_{2R+1}^{(1)}, u_1^{(2)}, u_2^{(2)}, \ldots u_{2R}^{(2)}, u_{2R+1}^{(2)} \right]^T$ is determined by using Newton's Method with arc length continuation. Newton's method can be applied as follows

$$\mathbf{U}^{(m)} = \mathbf{U}^{(m-1)} - \left(\mathbf{J}^{-1}\right)^{(m-1)} \mathbf{S}^{(m-1)}, \tag{30.14}$$

where $\mathbf{U}^{(m)}$ is the m^{th} iterative solution based on the $(m-1)^{th}$ solution and $\left(\mathbf{J}^{-1}\right)^{(m-1)}$ is the inverse of the Jacobian matrix of the vector function $\mathbf{S}$ estimated at the previous point $(m-1)$. The iteration procedure described by Eq. (30.14) is repeated until the vector norm of $\mathbf{S}^{(m)}$ is below a predefined error limit for that excitation frequency. Furthermore, arc-length continuation method is used in the solution and a new parameter, arc-length, which is the radius of a hypothetical sphere in which the next solution point will be searched, is chosen as the continuation parameter instead of the frequency in order to follow the solution path even at the turning points. Details of Newton's method with arc-length continuation can be found in [22–24].

The Floquet theory is used to determine the stability of the steady state solutions p_i, $(i = 1, 2)$ obtained above. This is done by examining the stability of the perturbed solution $p_i + \Delta p_i$, $(i = 1, 2)$. The variational equation for the perturbation Δp_i, $(i = 1, 2)$ is

$$\begin{Bmatrix} \Delta p_1''(t) \\ \Delta p_2''(t) \end{Bmatrix} + 2 \begin{bmatrix} \zeta_{11}\omega_{11} & \zeta_{12}\omega_{12} \\ \zeta_{21}\omega_{21} & \zeta_{22}\omega_{22} \end{bmatrix} \begin{Bmatrix} \Delta p_1'(t) \\ \Delta p_2'(t) \end{Bmatrix} + \begin{bmatrix} \omega_{11}^2 k_1(t)\phi_1(t) & \omega_{12}^2 k_2(t)\phi_2(t) \\ \omega_{21}^2 k_1(t)\phi_1(t) & \omega_{22}^2 k_2(t)\phi_2(t) \end{bmatrix} \begin{Bmatrix} \Delta p_1(t) \\ \Delta p_2(t) \end{Bmatrix} = \{0\}, \tag{30.15}$$

where $\phi_i(t)$ is a discontinuous separation function

$$\phi_i(t) = \begin{cases} 1, & |p_i(t)| > 1 \\ 0, & |p_i(t)| \leq 1 \end{cases}, \quad (i = 1, 2). \tag{30.16}$$

Equation (30.15) can be written in state-space form $\mathbf{z}'(t) = \mathbf{G}(t)\mathbf{z}(t)$ where $\mathbf{z}(t) = \left[\, \Delta p_1 \;\; \Delta p_2 \;\; \Delta p_1' \;\; \Delta p_2' \,\right]^T$ is the state vector and $\mathbf{G}(t) = \mathbf{G}\,(t+T)$ is the periodic state matrix given by

$$\mathbf{G}(t) = \begin{bmatrix} 0 & 0 & 1 & 0 \\ 0 & 0 & 0 & 1 \\ -\omega_{11}^2 k_1(t)\phi_1(t) & -\omega_{12}^2 k_2(t)\phi_2(t) & -2\zeta_{11}\omega_{11} & -2\zeta_{12}\omega_{12} \\ -\omega_{21}^2 k_1(t)\phi_1(t) & -\omega_{22}^2 k_2(t)\phi_2(t) & -2\zeta_{21}\omega_{21} & -2\zeta_{22}\omega_{22} \end{bmatrix}. \tag{30.17}$$

Then, the monodromy matrix, $\mathbf{M} = \mathbf{z}(T)$ is defined as the state transition matrix at the end of one analysis period, which is obtained by solving the homogenous matrix equation $\mathbf{z}'(t) = \mathbf{G}(t)\mathbf{z}(t)$ given initial condition $\mathbf{z}(0) = \mathbf{I}_4$, and the stability of the perturbed solution and consequently the stability of the corresponding solution are determined by examining the eigenvalues of this matrix. Here $\mathbf{I}_4$ is $4x4$ identity matrix [3].

$\mathbf{M}$ can be computed with a method that is based on an assumed stepwise variation of the state transition matrix. The state matrix $\mathbf{G}(t)$ is approximated as a series of step functions $\mathbf{G}_n$ at N discrete time intervals $\tau = nh$ as follows

$$\mathbf{G}_n = \frac{1}{h}\int_{(n-1)h}^{nh} \mathbf{G}\,(\tau)\,d\tau, \quad (n = 1, 2, \ldots N)\,. \tag{30.18}$$

If large number of time steps, N, is used, $\mathbf{G}(t)$ can be considered constant between two consecutive time steps and the integration is not needed. Between these two time instants, the following relation, where the exponential term is the state transition matrix, can be written

$$\mathbf{z}_{n+1} = e^{h\mathbf{G}_n}\mathbf{z}_n. \tag{30.19}$$

Then, the monodromy matrix is computed as the product of the individual transition matrices [25]:

$$\mathbf{z}_N = \prod_{n=0}^{N-1} e^{h\mathbf{G}_n}\mathbf{z}_0, \tag{30.20a}$$

$$\mathbf{M} = \prod_{n=0}^{N-1} e^{h\mathbf{G}_n}. \tag{30.20b}$$

Using Pade approximation or L^{th} order truncated Taylor series approximation as in [3] to calculate the matrix exponentiation above, monodromy matrix $\mathbf{M}$ is calculated. The solution is considered unstable when the modulus of any of the four eigenvalues λ_i of $\mathbf{M}$ is greater than unity; otherwise the solution is stable [3, 25].

30.2.3 Loading Conditions and Mesh Phases

Two different loading conditions as shown in Fig. 30.3 are considered here. In case-I, the system is driven by the middle gear (gear-2) and gears at the ends, gear-1 and gear-3, are outputs. This is known as split-torque arrangement. On the other hand, in case-II, gear-3 (output) is driven by gear-1 (input) through gear-2 (idler), which is idler arrangement. Therefore, the dynamic model shown in Fig. 30.2 is actually for idler arrangement but the same equations of motion can be obtained for split-torque arrangement by defining the same coordinates $\overline{p}_1\,(\overline{t})$ and $\overline{p}_2\,(\overline{t})$ as given in Eqs. (30.3a) and (30.3b).

The static transmission errors for the two meshes in the system are defined as

$$e_1(t) = \sum_{j=1}^{J} E_j^{(1)} \sin\left(j\Omega t + \alpha_{1j}\right), \tag{30.21a}$$

$$e_2(t) = \sum_{j=1}^{J} E_j^{(2)} \sin\left[j\Omega t + \alpha_{2j} + j\Pi\right], \tag{30.21b}$$

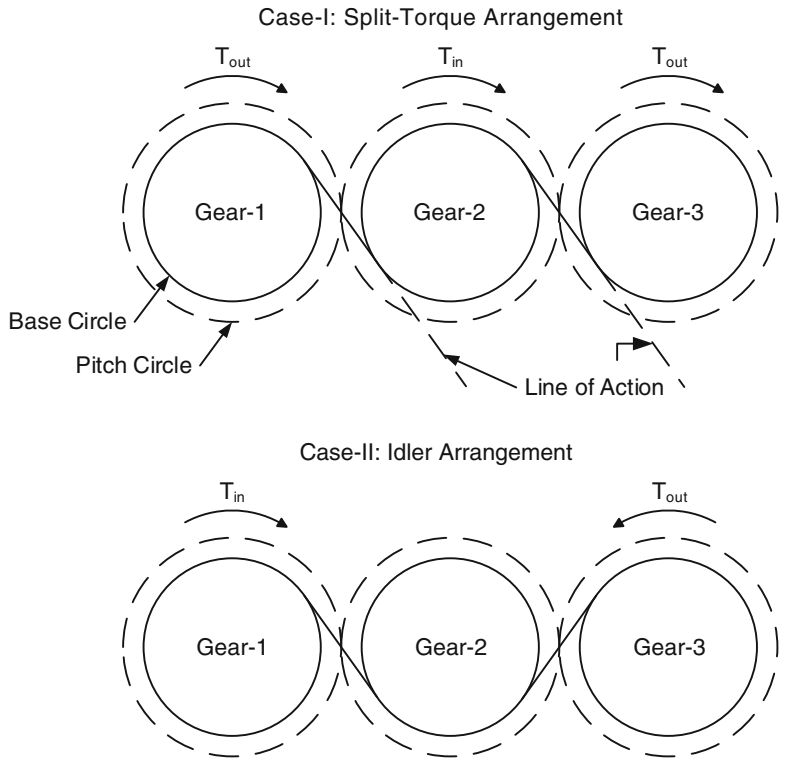

Fig. 30.3 Different loading conditions such as split-torque and idler arrangements

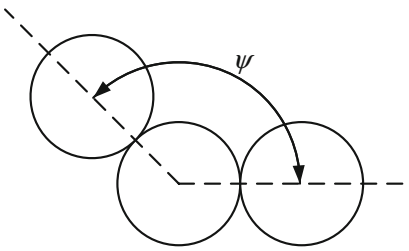

Fig. 30.4 Definition of the angle ψ

where $E_j^{(i)}$ and α_{ij} are the j^{th} harmonic amplitude and phase angle of the i^{th} gear mesh, respectively. Assuming that the both gear meshes are subject to same flank modifications yields $\alpha_{1j} = \alpha_{2j}$ [13]. Therefore, the only phase difference between the meshes is Π, which is defined as

$$\Pi = Z_2 (\psi + \gamma), \tag{30.22}$$

where Z_2 is the number of teeth of gear-2, ψ is the angle between the lines connecting the centers of the gears forming the meshes, which is shown in Fig. 30.4. γ is given as

$$\gamma = \begin{cases} 0, & \text{split-torque arrangement} \\ \pi/Z_2, & \text{idler arrangement} \end{cases}. \tag{30.23}$$

The same phase relationship is also valid for the mesh stiffness. In addition, tooth deflection is maximum when the mesh stiffness is minimum. Similarly, the minimum tooth deflection corresponds to the maximum mesh stiffness. Thus, there is an out-of-phase relationship between the static transmission error and mesh stiffness of a gear mesh:

$$k_1(t) = \sum_{a=1}^{A} K_a^{(1)} \sin\left(a\Omega t + \alpha_{1j} + \pi\right), \tag{30.24a}$$

$$k_2(t) = \sum_{a=1}^{A} K_a^{(2)} \sin\left(a\Omega t + \alpha_{1j} + \pi + a\Pi\right). \tag{30.24b}$$

Definition of static transmission error e_i and mesh stiffness k_i can be converted to expressions that contain sine and cosine functions as in Eqs. (30.7a) and (30.7b).

30.3 Results and Discussion

A multi-mesh gear train composed of three identical spur gears with the parameters listed in Table 30.1 is considered as the example case. In order to simplify the study, only the first harmonics of the mesh stiffness functions $k_i(t)$ $(i = 1, 2)$ and static transmission errors $e_i(t)$ $(i = 1, 2)$ are considered. Furthermore, external torque values are taken as constant with no disturbances in the form of pulsations.

Firstly, the period-1 motion solutions found by HBM are compared to the results of the direct numerical integration. Figure 30.5 shows the comparison of the root-mean-square (rms) values of the displacement response in the idler arrangement, whereas the corresponding mean components are plotted in Fig. 30.6. Here, the HBM solution is obtained by assuming three harmonics ($R = 3$ in Eq. (30.8)). The number of teeth of the middle gear Z_2 is taken as even, which results in a phase difference of π between the two meshes.

A characteristic length of $b_c = 20\ \mu\mathrm{m}$ is used, which means that each gear has $40\,\mu\mathrm{m}$ total backlash. The characteristic frequency $\omega_c = 39667\ \mathrm{rad/s}$ corresponds to the $\overline{\omega}_{11}$ given in Eq. (30.5f-i). With this characteristic frequency, the dimensionless undamped natural frequencies of the corresponding linear system are $\omega_{n1} = 0.71$ and $\omega_{n2} = 1.25$. The rms values are calculated as

Table 30.1 Parameters of the example system

Parameter ($i = 1,\ 2,\ 3$)	Numerical value
r_i, [m]	0.0423
Mass, [kg]	1.029
I_i, [kg m^2]	0.00136
$k_{1m},\ k_{2m}$ [N/m]	6 (10^8)
$c_1,\ c_2$ [Ns/m]	3000
$T_1,\ T_2,\ T_3$ in idler arrangement [Nm]	100, 0, −100
$T_1,\ T_2,\ T_3$ in split-torque arrangement [Nm]	100, 200, 100
$K_1^{(1)},\ K_1^{(2)}$	0.3
$E_1^{(1)},\ E_1^{(2)}$	0.15
ψ	180 °

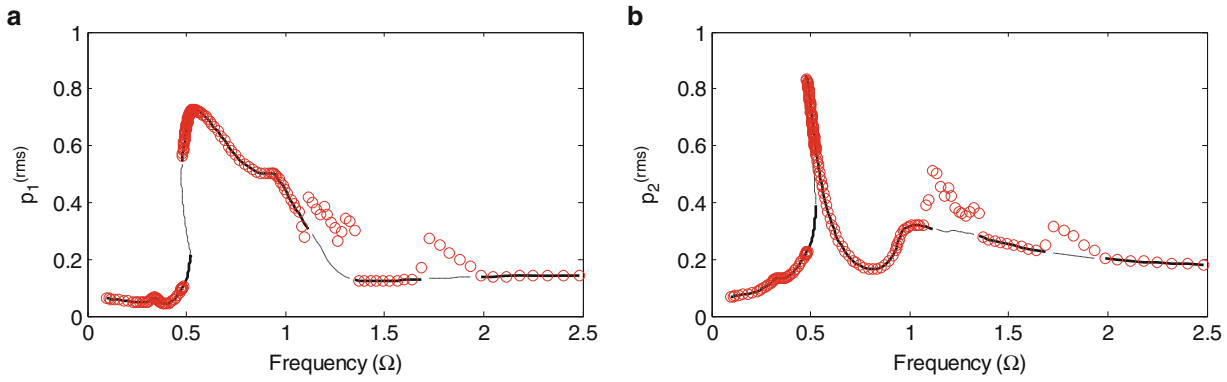

Fig. 30.5 Comparison of rms values of the responses, $p_1(t)$ and $p_2(t)$ predicted by HBM and NI in the idler arrangement with even Z_2. (*straight line*) Stable and (*dashed line*) unstable HBM solution, (*circle*) NI solutions, (**a**) $p_1^{(rms)}$ (**b**) $p_2^{(rms)}$

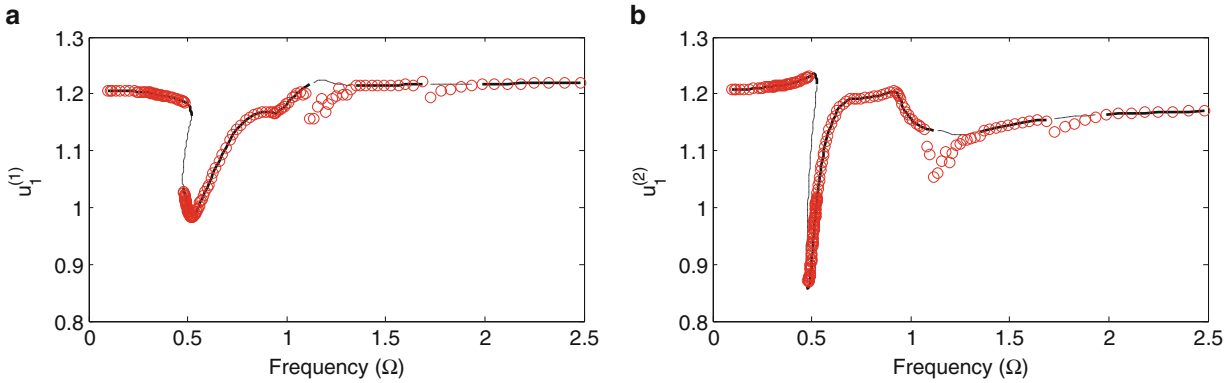

Fig. 30.6 Comparison of the mean components of the responses, $p_1(t)$ and $p_2(t)$ predicted by HBM and NI in the idler arrangement with even Z_2. (*straight line*) Stable and (*dashed line*) unstable HBM solution, (*circle*) NI solutions, (**a**) $u_1^{(1)}$ (**b**) $u_1^{(2)}$

$$p_i^{(\mathrm{rms})} = \left\{ \sum_{r=1}^{R} \left[A_r^{(i)} \right]^2 \right\}^{1/2}, \tag{30.25}$$

where $A_r^{(i)}$ is the amplitude of the r^{th} harmonic of $p_i(t)$ that can be defined as

$$A_r^{(i)} = \left\{ \left[u_{2r}^{(i)} \right]^2 + \left[u_{2r+1}^{(i)} \right]^2 \right\}. \tag{30.26}$$

In Figs. 30.5 and 30.6, thick solid lines are the stable HBM solutions, while thin dashed lines represent the unstable HBM solutions. It is seen that the solutions of the two methods are in very good agreement except around the unstable frequency ranges observed at $\Omega = [1.13 - 1.33]$ and $\Omega = [1.73 - 1.93]$. This shows the existence of subharmonic motions dictating these ranges, which correspond to the parametric resonances due to the time variation of the mesh stiffness. While the NI solution can converge to these motions depending on the initial condition used, HBM cannot find these motions since the subharmonics are not included in the solutions assumed.

From past studies [1, 3, 4], it is known that spur gears can exhibit both single-sided and double-sided tooth impacts depending on the system parameters. Similar behaviors are also seen here in the results of both HBM and NI. Focusing on Fig. 30.5, gear pairs behave quite linearly with no tooth impact in the low frequency range. As the frequency increases, $p_1^{(\mathrm{rms})}$ and $p_2^{(\mathrm{rms})}$ forced response curves exhibit single-sided tooth impact, which is a softening-type nonlinear behavior due to tooth separation occurring near the primary resonance frequency, $\Omega = \omega_{n1}$. However, the double-sided impact, which is a hardening-type nonlinear behavior due to the additional impact with the preceding tooth, is not observed in the responses, since the vibration amplitudes are small compared to the backlash amount.

Another observation from Fig. 30.5 is that there is a super-harmonic resonance peak at $\Omega \approx 0.5\ \omega_{n1} = 0.35$ due to the parametric excitation. This peak can only be observed if sufficient number of harmonics is used in HBM. The nonlinear behavior is also obvious in Fig. 30.6. Mean amplitudes of $p_1(t)$ and $p_2(t)$ remain nearly constant in the case of no tooth separation. However, the values of $u_1^{(1)}$ and $u_1^{(2)}$ vary significantly in the case of tooth separation.

In Fig. 30.7, the response $p_1(t)$ of the split-torque arrangement obtained by HBM and NI is compared. Again, the number of teeth of gear-2 is even; hence, the two meshes are in phase. Due to the symmetry, the responses $p_1(t)$ and $p_2(t)$ are exactly the same; therefore, only $p_1(t)$ is shown here. The gear train in the split-torque arrangement exhibits nonlinear behavior as single-sided impact near the primary resonance frequency at $\Omega = \omega_{n2}$. Contrary to the idler arrangement, anti-resonance occurs near the primary resonance frequency at $\Omega = \omega_{n1}$ in the split-torque case. It is also clear in Fig. 30.7 that HBM and NI solutions are again in very good agreement. In this case, there are no frequency ranges which are dictated by subharmonic motions.

The influence of the out-of-phase relationship between the static transmission error and mesh stiffness in the gear train with even Z_2 is shown in Fig. 30.8. Here, the combined response due to the static transmission error and parametric excitations is compared with the responses of the system, where only one of the excitation sources exists. Split-torque arrangement is considered in Fig. 30.8a while Fig. 30.8b demonstrates the effect in idler case. Focusing on Fig. 30.8a, each excitation alone forms a response peak at the same resonance frequency $\Omega = \omega_{n2}$. However, the out-of-phase relationship results in a decrease

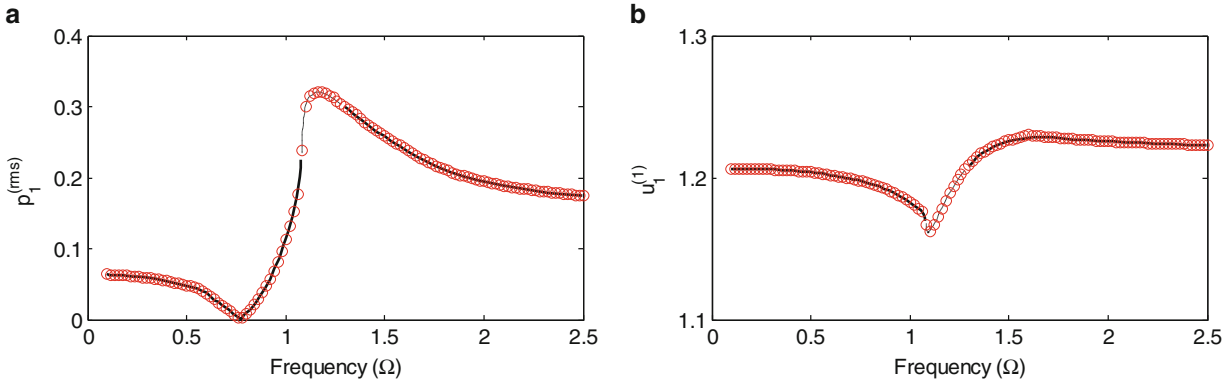

Fig. 30.7 Comparison of rms value and mean component of the response $p_1(t)$ predicted by HBM and NI in the split-torque arrangement with even Z_2. (*straight line*) Stable and (*dashed line*) unstable HBM solution, (*circle*) NI solutions, (**a**) $p_1^{(\mathrm{rms})}$ (**b**) $u_1^{(1)}$

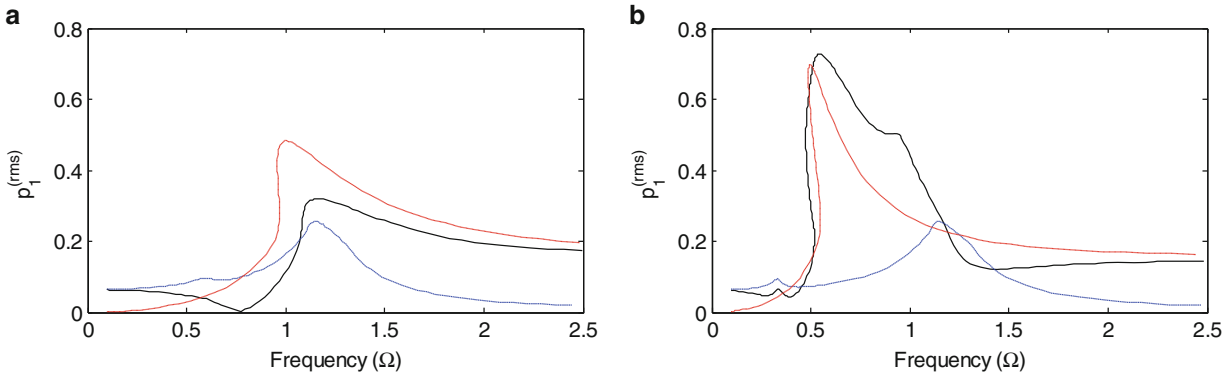

Fig. 30.8 Effect of the out-of-phase relationship between the static transmission error and mesh stiffness. Z_2 is even. (*long-short-dashed blue line*) Response of the only parametric excitation (*dashed red line*) Response of the only static transmission error excitation (*straight line*) Combined response (**a**) $p_1^{(\mathrm{rms})}$ in split-torque arrangement (**b**) $p_1^{(\mathrm{rms})}$ in idler arrangement

in the combined response at the resonance frequencies. It is also noted in Fig. 30.8a that the super-harmonic resonance peak at $\Omega \approx 0.5\ \omega_{n2} = 0.62$ observed in the response curve of the only parametric excitation vanishes in the combined response. On the other hand, in the idler arrangement, the peak due to each excitation alone appears at different resonance frequency; hence, they do not affect each other significantly.

Figure 30.9 compares the dynamic responses of four different loading conditions: (1) idler arrangement, $Z_2 = even$, (2) idler arrangement, $Z_2 = odd$, (3) split-torque arrangement, $Z_2 = even$, (4) split-torque arrangement, $Z_2 = odd$. As seen from Fig. 30.9, the split-torque arrangement excites the second mode shape at $\Omega = \omega_{n2}$ when $Z_2 = even$ and the first mode shape at $\Omega = \omega_{n1}$ when $Z_2 = odd$. Therefore, a shift in the frequency range occurs due to the change of the excited mode shape. On the other hand, the idler arrangement has always two peaks at both resonance frequencies independent from the number of teeth of gear-2. The amplitudes of the peaks are affected significantly depending on the interaction between the mesh stiffness and static transmission errors in terms of phasing.

Influence of the orientation angles of the end gears around the middle gear is illustrated in Fig. 30.10 for the split-torque arrangement with $Z_2 = 30$. The phase difference between the meshes are found as 0°, 90° and 180° by using Eq. (30.22) corresponding to the orientation angles of 180°, 135° and 90°, respectively. In the configuration with $\psi = 180°$, the peaks in the response curves of both meshes occur at the resonance frequency $\Omega = \omega_{n2}$, while configuration with $\psi = 90°$ triggers the first mode shape at $\Omega = \omega_{n1}$. For $\psi = 135°$, two distinct peaks exist in both $p_1^{(\mathrm{rms})}$ and $p_2^{(\mathrm{rms})}$. This agrees with the results of the linear time-invariant model of multi-mesh helical gear train studied in [13].

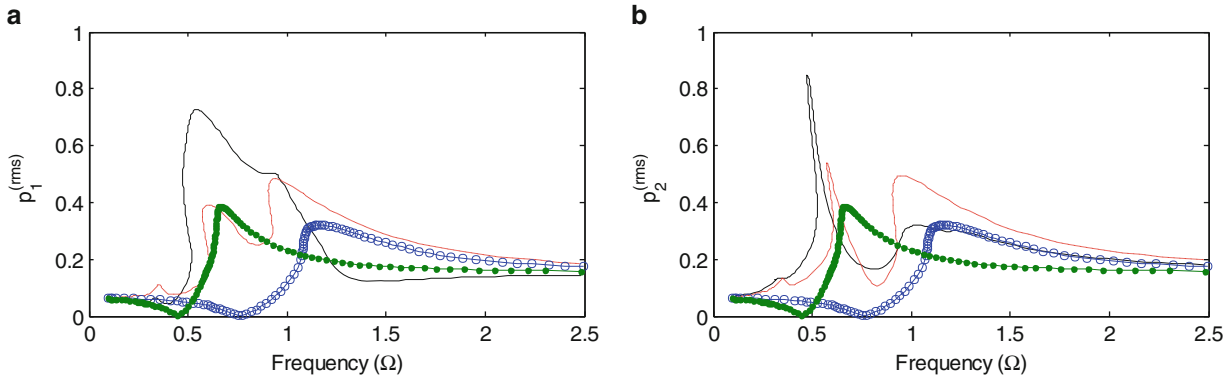

Fig. 30.9 Effect of loading conditions on dynamic response. (*straight line*) idler arrangement with even Z_2 (*dashed red line*) idler arrangement with odd Z_2 (*blue line with circle*) split-torque arrangement with even Z_2 (*green line with circle*) split-torque arrangement with odd Z_2 (**a**) $p_1^{(rms)}$ (**b**) $p_2^{(rms)}$

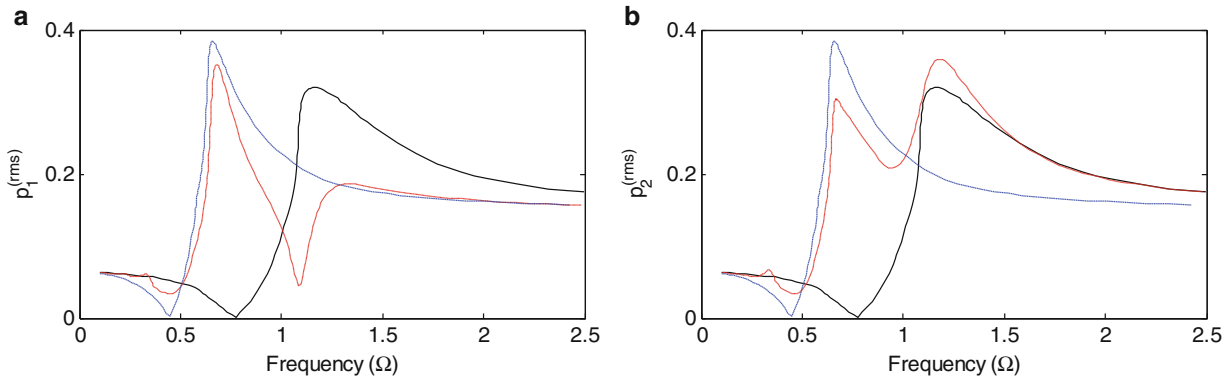

Fig. 30.10 Effect of orientation angle on dynamic response of the split-torque arrangement with $Z_2 = 30$. (*straight line*) $\psi = 180°$ (*dashed red line*) $\psi = 135°$ (*long-short-dashed blue line*) $\psi = 90°$ (**a**) $p_1^{(rms)}$ (**b**) $p_2^{(rms)}$

30.4 Conclusion

A nonlinear time-varying dynamic model for a multi-mesh spur gear train consisting of three gears and three shafts is formulated in this study. The resultant dimensionless equations of motion are solved for steady-state period-1 response by using a multi-term Harmonic Balance Method in conjunction with discrete Fourier Transform. The solutions obtained by HBM are compared to ones obtained by direct numerical integration. Floquet theory is applied to determine the stability of the steady state solutions. It is seen from the results that the multi-mesh gear train exhibits nonlinear behavior as single-sided impact with the given system parameters. No back collisions (double-sided impacts) are observed. Solutions obtained by numerical integration also show the existence of the subharmonic motions near the frequencies corresponding to the parametric resonances.

The interaction between the static transmission error and parametric excitations is analyzed by considering the phasing between them. It is shown that the number of teeth of gear-2 has a significant effect on the dynamic response since it directly determines the phase angle between the meshes. Dynamic response is also influenced greatly by the positions of the end gears. Therefore, optimization of these parameters in the design may reduce vibration and noise.

References

1. Kahraman, A., Singh, R.: Non-linear dynamics of a spur gear pair. J. Sound Vib. **142**(1), 49–75 (1990)
2. Kahraman, A., Singh, R.: Interactions between time-varying mesh stiffness and clearance non-linearities in a geared system. J. Sound Vib. **146**(1), 135–156 (1991)

3. Kahraman, A., Blankenship, G.W.: Steady state forced response of a mechanical oscillator with combined parametric excitation and clearance type non-linearity. J. Sound Vib. **185**(5), 743–765 (1995)
4. Kahraman, A., Blankenship, G.W.: Interactions between commensurate parametric and forcing excitations in a system with clearance. J. Sound Vib. **194**(3), 317–336 (1996)
5. Kahraman, A., Lim, J., Ding, H.: A dynamic model of a spur gear pair with friction. In: Proceesdings of 12th IFToMM World Congress, Besançon (2007)
6. Shen, Y., Yang, S., Liu, X.: Nonlinear dynamics of a spur gear pair with time-varying stiffness and backlash based on incremental harmonic balance method. Int. J. Mech. Sci. **48**, 1256–1263 (2006)
7. Kahraman, A., Blankenship, G.W.: Experiments on nonlinear dynamic behavior of an oscillator with clearance and periodically time-varying parameters. J. Appl. Mech. **64**, 217–226 (1997)
8. Kahraman, A., Singh, R.: Non-linear dynamics of a geared rotor-bearing system with multiple clearances. J. Sound Vib. **144**(3), 469–506 (1991)
9. Özgüven, H.N.: A non-linear mathematical model for dynamic analysis of spur gears including shaft and bearing dynamics. J. Sound Vib. **145**(2), 239–260 (1991)
10. Maliha, R., Doruer, C.U., Ozguven, H.N.: Nonlinear dynamic modeling of gear-shaft-disk-bearing systems using finite elements and describing functions. J. Mech. Des. **126**, 534–541 (2004)
11. Gürkan, N.E., Ozguven, H.N.: Interactions Between backlash and bearing clearance nonlinearity in geared flexible rotors. In: Proceedings of IDETC/PTG 2007 ASME 2007 International Design Engineering Technical Conferences and ASME International Power Transmission and Gearing Conference, Las Vegas, pp. 1–10 (2007)
12. Kahraman, A.: Effect of axial vibrations on the dynamics of a helical gear pair. J. Vib. Acoust. **115**, 33–39 (1993)
13. Kahraman, A.: Dynamic analysis of a multi-mesh helical gear train. J. Mech. Des. **116**, 706–712 (1994)
14. Kubur, M., Kahraman, A., Zini, D.M., Kienzle, K.: Dynamic analysis of a multi-shaft helical gear transmission by finite elements: model and experiment. J. Vib. Acoust. **126**(3), 398–406 (2004)
15. Al-shyyab, A., Kahraman, A.: Non-linear dynamic analysis of a multi-mesh gear train using multi-term harmonic balance method: period-one motions. J. Sound Vib. **284**, 151–172 (2005)
16. Al-shyyab, A., Kahraman, A.: Non-linear dynamic analysis of a multi-mesh gear train using multi-term harmonic balance method: sub-harmonic motions. J. Sound Vib. **279**, 417–451 (2005)
17. Al-shyyab, A., Kahraman, A.: A nonlinear torsional dynamic model of multi-mesh gear trains having flexible shafts. Jordan J. Mech. Ind. Eng. **1**(1), 31–41 (2007)
18. Liu, G., Parker, R.G.: Nonlinear dynamics of idler gear systems. Nonlinear Dyn. **53**(4), 345–367 (2008)
19. Liu, G., Parker, R.G.: Nonlinear, parametrically excited dynamics of two-stage spur gear trains with mesh stiffness fluctuation. Proc. Inst. Mech. Eng. C J. Mech. Eng. Sci. **226**(8), 1939–1957 (2012)
20. Al-shyyab, A., Kahraman, A.: A non-linear dynamic model for planetary gear sets. Proc. Inst. Mech. Eng. Part K J. Multi-body Dyn. **221**(4), 567–576 (2007)
21. Sondkar, P., Kahraman, A.: A dynamic model of a double-helical planetary gear set. Mech. Mach. Theory **70**, 157–174 (2013)
22. Cigeroglu, E., Samandari, H.: Nonlinear free vibration of double walled carbon nanotubes by using describing function method with multiple trial functions. Phys. E Low-dimensional Syst. Nanostructures **46**, 160–173 (2012)
23. Yümer, M.E., Ciğeroglu, E., Özgüven, H.N.: Non-linear forced response analysis of mistuned bladed disk assemblies. In: Proceedings of ASME Turbo Expo 2010: Power for Land, Sea and Air, Glascow (2010)
24. Von Groll, G., Ewins, D.J.: The harmonic balance method with arc-length continuation in rotor/stator contact problems. J. Sound Vib. **241**(2), 223–233 (2001)
25. Cardona, A., Lerusse, A., and Geradin, M.: Fast Fourier nonlinear vibration analysis. Comput. Mech. **22**, 128–142 (1998)

Chapter 31
Energy Dissipation of a System with Foam to Metal Interfaces

Laura D. Jacobs, Robert J. Kuether, and John H. Hofer

Abstract The physical mechanisms of energy dissipation in foam to metal interfaces must be understood in order to develop predictive models of systems with foam packaging common to many aerospace and aeronautical applications. Experimental data was obtained from hardware termed "Ministack", which has large, unbonded interfaces held under compressive preload. This setup has a solid aluminum mass placed into two foam cups which are then inserted into an aluminum can and fastened with a known preload. Ministack was tested on a shaker using upward sine sweep base acceleration excitations to estimate the linearized natural frequency and energy dissipation of the first axial mode. The experimental system was disassembled and reassembled before each series of tests in order to observe the effects of the assembly to assembly variability on the dynamics. There are some important findings in the measured data: there is significant assembly to assembly variability, the order in which the sine sweeps are performed influence the dynamic response, and the system exhibits nontrivial damping and stiffness nonlinearities that must be accounted for in modeling efforts. A Craig-Bampton model connected with a four-parameter Iwan element and piecewise linear springs is developed and calibrated using test data with the intention of capturing the nonlinear energy dissipation and loss of stiffness observed in experiment.

Keywords Energy dissipation • Harmonic loading • Contact friction • Craig-Bampton model • Model validation

31.1 Introduction

Electronic and electromechanical components are packaged in foam to prevent excessive vibration amplitudes during transportation and operation. Solid foams are used to package defense components per MIL-STD 2073 [1]. This packaging leads to foam/metal interfaces, which have long been recognized as significant contributors to energy dissipation. The mechanisms for energy dissipation in these systems include friction, impacts and the large material damping common in most foams. Standards, such as MIL-STD 810G [2], require qualification of military components under vibration environments in their packaging. To be able to model and understand how systems containing foam to metal interfaces will respond to various vibration environments, it is important to understand the energy dissipation mechanisms and their effect on the dynamics. Currently, modeling capabilities to capture the dissipative behavior of metal parts in foam are being developed. Physical experiments are crucial to validate models and gain an understanding of the physical phenomena required for modeling.

A simple system, called "Ministack", consisting of a solid aluminum mass placed in two foam cups that are then inserted into an aluminum can, is developed to represent a metal part packaged in foam. Ministack contains a small number of interfaces and is a relatively simple geometry to model. The simplicity of the design enables the study and explanation of the physics through experimentation and computational modeling. Details of Ministack are described in Sect. 31.2.

Experiments with Ministack, utilizing sinusoidal excitation to measure the energy loss per cycle in a manner similar to that reported by other investigators [3–12] are performed. The experiments performed on Ministack investigate the influence of several different parameters, including: amplitude of excitation, snugness of fit, load path, and sequence of testing. For each configuration, a series of upward sine sweep base accelerations at different amplitudes are performed, exciting the first axial mode of the system. Acceleration data is collected at the top of Ministack and analyzed to determine the natural frequency and energy dissipation of the system. Section 31.3 presents the resulting data from the experiments.

Sandia is a multiprogram laboratory operated by Sandia Corporation, a Lockheed Martin Company, for the United States Department of Energy under contract DE-AC04-94AL85000.

L.D. Jacobs (✉) • R.J. Kuether • J.H. Hofer
Sandia National Laboratories, P.O. Box 5800 MS 0557, Albuquerque, NM 87185, USA
e-mail: ldjacob@sandia.gov

© The Society for Experimental Mechanics, Inc. 2016

M. Allen et al. (eds.), *Dynamics of Coupled Structures, Volume 4*, Conference Proceedings of the Society for Experimental Mechanics Series, DOI 10.1007/978-3-319-29763-7_31

A Craig-Bampton reduced order model [13] of Ministack is developed in Sect. 31.4 with the intention of capturing the loss of stiffness in the interface as well as the nonlinear energy dissipation as the amplitude of excitation increases. The interface between the solid mass and foam cups is modeled with two gap elements, otherwise known as piecewise linear springs, and a four-parameter Iwan element [14]. The parameters of these constitutive models are calibrated based on the measured transfer functions in order to see whether a simplified model can capture the salient nonlinear behavior.

31.2 Experimental Setup

To create a system with a dominant axial mode that exercises the large foam to metal interfaces, a solid aluminum mass is placed in foam cups and then inserted into an aluminum can, as illustrated in Fig. 31.1. A preload is then applied to the steel disk on the top of the foam cups using a press, and then a threaded steel ring is tightened to secure the preload. The aluminum can has an inner diameter of 10 cm, an outer diameter of 12.7 cm and a depth of 15.2 cm. The can is welded to a square plate that has nine bolt holes (Fig. 31.1) to allow the specimen to be attached to a shaker. The plate has a recess in the bottom of it (not shown) to accommodate a uniaxial accelerometer to control the input acceleration. A triaxial accelerometer is placed on top of the solid mass to measure the response of the system. The steel disk has a hole in the middle to allow for the accelerometer cable to exit the specimen.

31.2.1 Foam Specimen Details

The foam specimens are made from 320 kg/m^3 closed cell PMDI foam. The foam specimens are in two parts, a top half which has an access hole for attaching an accelerometer and a bottom half which has a solid bottom. The two halves are cup-like in nature with an outer diameter of 10 cm and an inner diameter of 7.62 cm. The bottoms and sides of the cups are 12.7 mm thick. The surface of the foam specimens is friable.

Two different depths of cups are used in the experiment. One set of foam specimens has an interior depth of 5 cm. Nominally, the solid mass would fit exactly in the specimens yielding parallel load paths of through the solid mass and through the foam. However, with machining tolerances, there are cases where the load path is either through the foam alone or through the mass alone in addition to the cases of parallel load paths. The second set of foam specimens were manufactured to have a smaller interior depth of 4.68 cm. Nominally, there would be a 6.35 mm gap between the two pieces of foam, thus ensuring a load path through the solid mass even with variations due to machining tolerances.

Fig. 31.1 Test specimen

31.2.2 Solid Mass Details

Three solid masses of different diameters are used in the experiments to determine the effects of snugness of fit on the frequency and energy dissipation characteristics of the system. The nominal, or no gap, specimen has a diameter of 7.62 cm, so that it fits snugly in the foam specimens. The 1.5875 mm gap specimen has a diameter of 7.46 cm so that there is a gap between the solid mass and the foam. The 3.175 mm gap specimen has a diameter of 7.30 cm. All three solid masses are 10 cm in length and are made from 6061-T6 Aluminum. They have a recessed area in the top that can accommodate a triaxial accelerometer.

31.2.3 Specimen Assembly

The solid mass is placed in both halves of the foam cups, with markings on the cups being lined up to help limit the variability in alignment from assembly to assembly. Then, the cups are placed in the can, with markings on the cups and the can being aligned to help with the repeatability of assembly. The steel plate is placed on top of the foam and solid mass assembly in the can, after which a load cell is placed on top of the assembly. A preload is applied using a press until the reading on the load cell is approximately the nominal preload. The retaining ring is tightened to maintain the preload, the press is released, and Ministack is ready for testing.

31.2.4 Test Specifications and Data Collection

During testing, Ministack is oriented so that the plate on the bottom is flat on the shaker. In this orientation the specimen is being excited in the direction of the load path. The energy dissipation comes from the foam rubbing against the metal interface as well as the interface between the two sets of foam for the cases when there is contact.

A constant acceleration sine sweep base excitation is run from 500 to 3000 Hz at a rate of 3 octaves per minute (an octave represents a doubling of frequency). The sweep rate allows for the test article to experience several cycles at each frequency, allowing for sufficient data at each frequency to estimate the natural frequency and energy dissipation. Four different amplitudes, 1 g, 2 g, 5 g and 10 g, are used to determine the effects of excitation amplitude on the response of the test article.

A triaxial accelerometer measures data in the three mutually perpendicular directions at the top of the solid mass. A uniaxial accelerometer attached to the baseplate is used to control the input to the structure. The data measured at the triaxial accelerometer at the top of the solid mass and the control accelerometer are used to calculate transfer functions between the responses of the three different axes at the top of the solid mass and the input accelerations. The maximum amplitude of the transfer function gives Q, the amplification factor of the input at the natural frequency. The amplification factor, Q, can then be used to calculate the energy dissipation of Ministack using Eq. 31.1 derived in [15].

$$\frac{\pi * Q * A_b^2}{f_n^2} \tag{31.1}$$

Where f_n is the natural frequency of the first axial mode in Hz, A_b is the amplitude of the excitation in g's and Q is the amplification factor of the response.

A configuration is comprised of one set of the two lengths of foam cups and one of the three solid masses. A test series was run for all possible combinations. Between series of tests on each configuration, the setup was disassembled and then reassembled. This reassembly allows for determination of the assembly to assembly variation of the response of the test article. The test sequences are enumerated in Table 31.1. In all assemblies in Table 31.1, the sequence of tests was always repeated to determine if vibrating the specimen changed the dynamic characteristics. The final test assembly 3 was run to see if the order in which the amplitudes were applied affected the dynamics.

Table 31.1 Test sequence

Assembly number	Sweep series amplitudes
1	1 g, 2 g, 5 g, 10 g, 1 g, 2 g, 5 g, 10 g
2	1 g, 2 g, 5 g, 10 g, 1 g, 2 g, 5 g, 10 g
3	10 g, 2 g, 5 g, 1 g, 10 g, 5 g, 2 g, 1 g

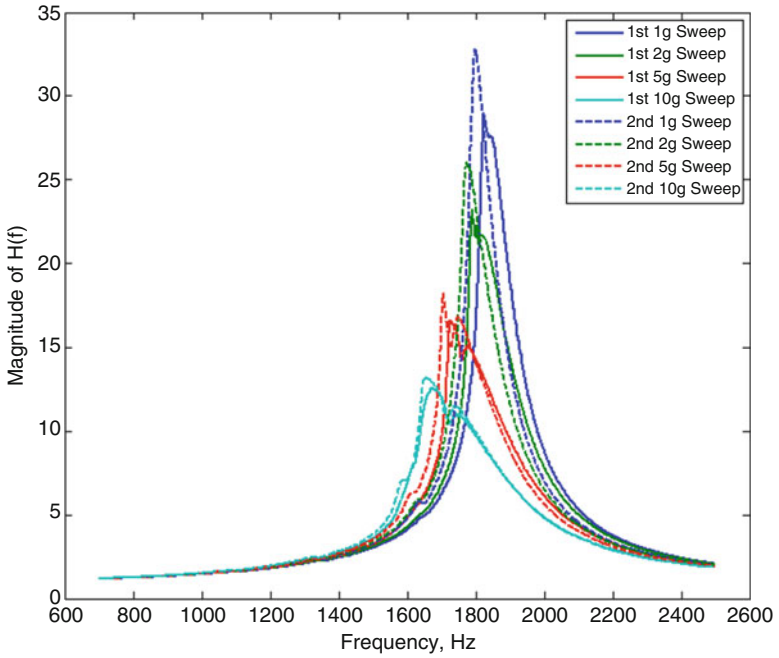

Fig. 31.2 Transfer functions for a specimen preloaded to 3110 N through foam and cylinder, assembly 1

31.3 Experimental Results

31.3.1 Effects of Amplitude of Excitation

This subsection shows the resulting transfer functions for the three test sequences in Table 31.1 on the configuration with the foam cup depth of 5 cm and the solid mass diameter of 7.62 cm (i.e. no gap). In this configuration, the load path goes through both the foam and the solid mass and the solid mass fits snugly into the foam cups. The results for the test sequences shown in Figs. 31.2, 31.3 and 31.4 show that the natural frequency decreases and the amount of energy dissipation increases as the excitation amplitude increases. The frequency shifts suggest that the foam to metal interface loses stiffness at high excitation levels, likely due to micro- or possibly macroslip. The impacts and the friction between the frictional interfaces introduces nonlinear energy dissipation observed at higher excitation levels.

When starting the test series at 1 g and increasing the amplitude to 10 g, the natural frequency from the second run is lower than the first; and the amount of energy dissipation is lower. These phenomena are seen in the data in Figs. 31.2 and 31.3. When starting the test series at 10 g and decreasing the amplitude down to 1 g, there is no appreciable difference in the natural frequency and energy dissipation as seen in Fig. 31.4. One hypothesis for this behavior could be attributed to the higher amplitude sine sweeps causing wear or loss of preload in Ministack. Going from the 1 g to 10 g sweeps and repeating, the settling position of the solid mass after the 10 g run may be different than the initial 1 g run. This could explain why the stiffness and the damping in the transfer functions during the second runs shifted a noticeable amount.

31.3.2 Effects of Snugness of Fit

In this section, the estimated natural frequencies and normalized energy dissipation values are evaluated for different diameters of the solid mass; in other words, how snugly the mass fits into the foam cups. These parameters are plotted

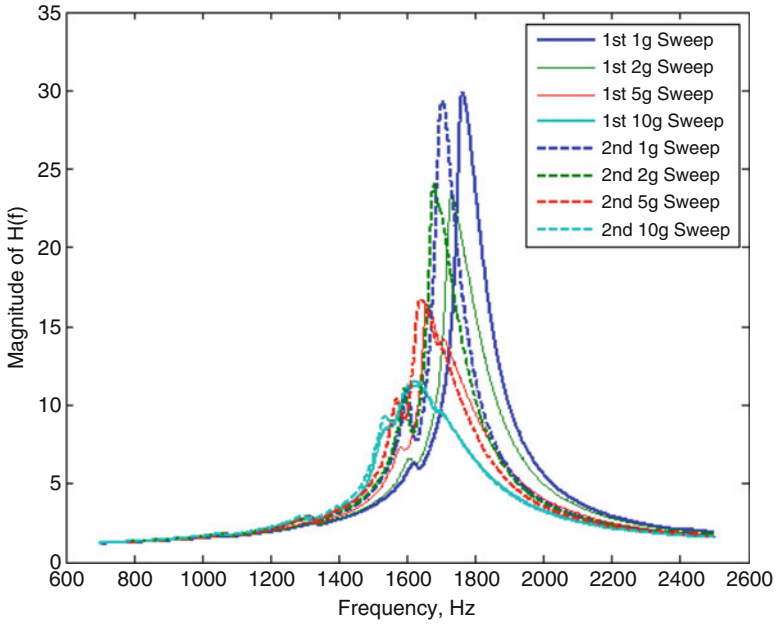

Fig. 31.3 Transfer functions for a specimen preloaded to 3110 N through foam and cylinder, assembly 2

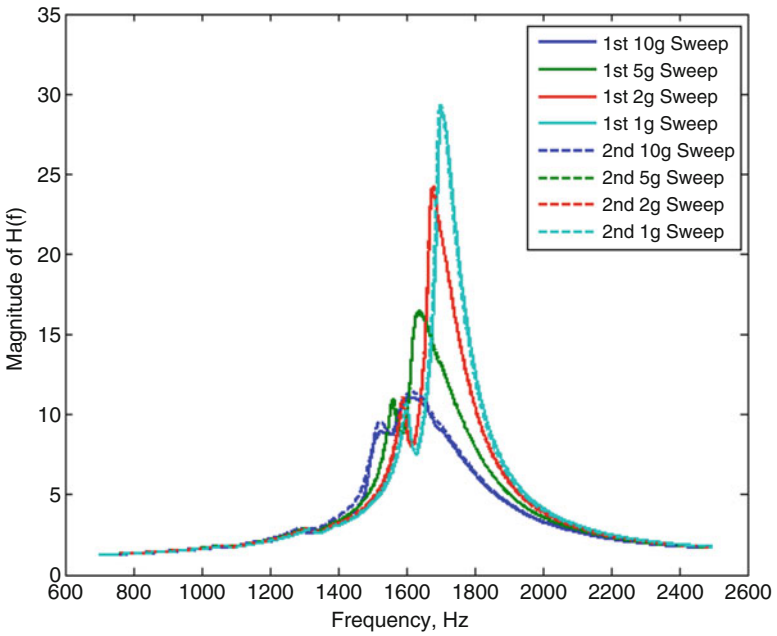

Fig. 31.4 Transfer functions for a specimen preloaded to 3110 N through foam and cylinder, assembly 3

versus the excitation amplitude, because these parameters were shown to be amplitude dependent in the previous subsection. The plot in Fig. 31.5 shows the distribution of the natural frequency for all three gap sizes with the 5 cm depth foam cups, for which the 3110 N preload goes through both the foam and cylinder. The results in Fig. 31.6 show the distribution of the natural frequency with the preload path through the cylinder only (cup depth of 4.68 cm).

Regardless of the load path, the snugness of fit has no statistically significant effect on the variance of the natural frequency, indicating gap size does not affect the repeatability of the assembly process. When the load path goes through both the mass and the foam, the snugness of fit has an impact on the natural frequency. When the gap size is 1.5875 mm, the natural frequency is higher than when there is no gap. The natural frequencies are lower when the gap size is 3.175 mm than either of the other two gap sizes. When the load path goes through the mass only, the snugness of fit has no appreciable effect on the variance of the natural frequency. Additionally, the natural frequency is higher in the case where there is no

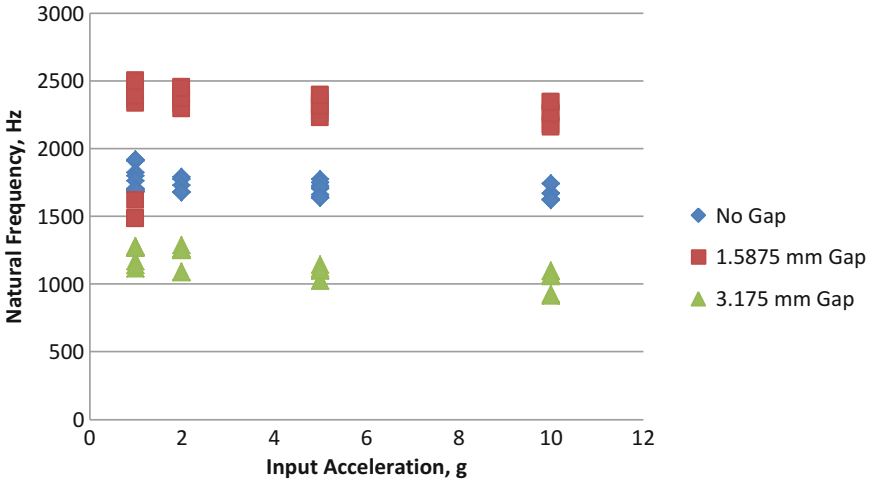

Fig. 31.5 Distribution of natural frequency per gap size with a 3110 N preload through the foam and cylinder

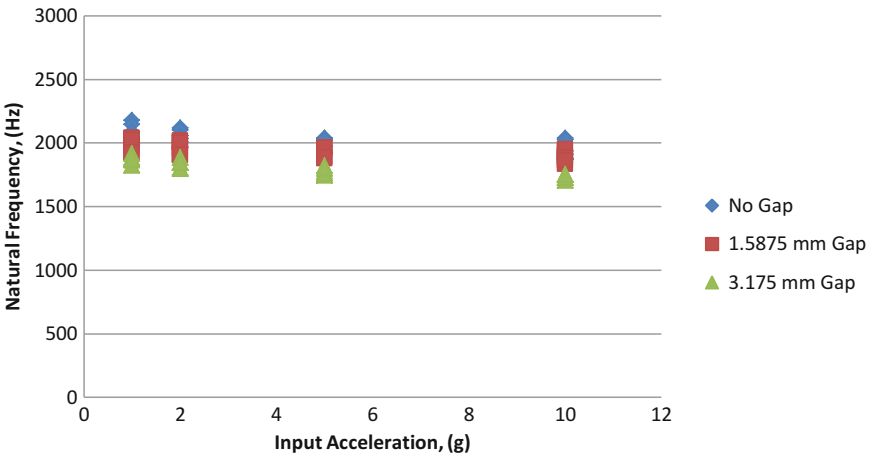

Fig. 31.6 Distribution of natural frequency per gap size with a 3110 N preload through the cylinder only

gap than in the cases where there are gaps. These results suggest that the snugness of fit has a larger effect on the stiffness of the system when the load path goes through the mass and the foam than when the load path goes through the mass only. Additionally, the uncertainty of the natural frequency is larger in the case of the preload going through the mass and the foam, For modeling implications, if the item does not fit snugly in the foam, it is not critical to know how loose it is to determine the natural frequency of the foam/item system when the load path is through the part alone.

The second parameter studied is the energy dissipation. Figure 31.7 shows the distribution of the energy dissipation when the preload for specimens has a load path through the cylinder and foam (5 cm cup depth). Figure 31.8 shows the data for a load path through the cylinder only. A power line is fit to the data to determine the slope of the relationship between energy loss per cycle and the input acceleration. The amount of energy dissipation when the specimens that are preloaded through the foam and cylinder is greater for the specimens that include a radial gap than the specimens that contained no radial gap. The amount of energy dissipation when the specimens are preloaded through the mass only is larger for the case of the specimen with the 3.175 mm radial gap.

These results show that the snugness of fit has an effect on the energy dissipation. The amount of energy dissipated when the specimens are preloaded through the foam and cylinder is greatest when there is a radial gap. One hypothesis for this could be that when there is no gap between the foam and solid mass, the large amount of sliding friction prevents the mass from moving within the container. However, when this large frictional interface is removed with a radial gap, the mass has less resistance to motion and is more likely to impact with the top and bottom surfaces of the foam; these impacts likely dissipate energy differently than sliding friction alone. There will still be some friction along the length of the mass, due to contact along the sides. Additionally, the mass is able to slide laterally with the cross-axis motion of the shaker, introducing a different frictional interface. Finally, the mass and foam are no longer confined as they are when the mass snugly fits in

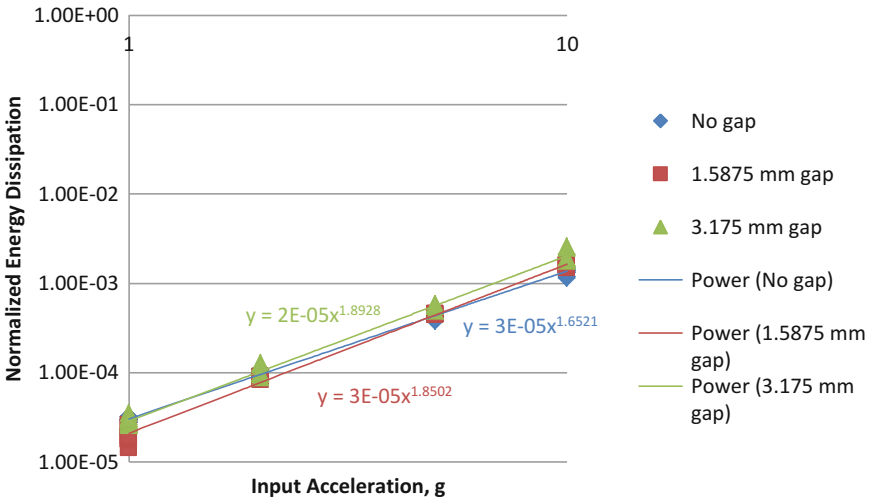

Fig. 31.7 Distribution of normalized energy dissipation per gap size with a 3110 N preload through the foam and cylinder

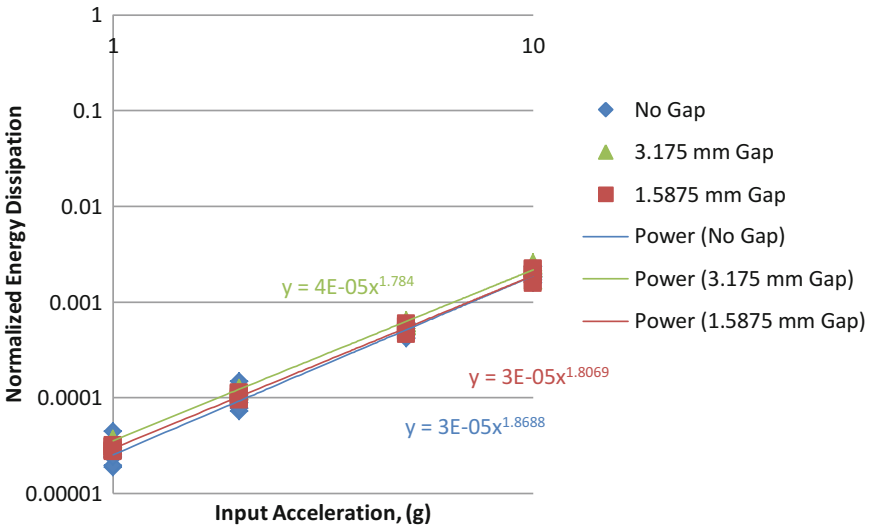

Fig. 31.8 Distribution of normalized energy dissipation per gap size with a 3110 N preload through the cylinder only

the foam, allowing for additional motion and deformation of the foam and mass due to the lack of confinement. In summary, there are additional mechanisms of energy dissipation that occur when there is a radial gap, so it is not surprising that there is more energy dissipation in those cases. The results for the preload going through the cylinder only indicate that again the largest amount of dissipation occurs when the specimen has a 3.175 mm radial gap. For modeling implications, these results suggest that it is important to understand the amount of friction that occurs between the contacting surfaces but also the coefficient of restitution for impacts.

As done in previous studies [3–12], the normalized energy dissipation is plotted vs. the input acceleration on a log–log plot. The data show the anticipated straight line, indicating a power law relationship between energy loss per cycle and the input acceleration. In the fitted results, the slope ranges from 1.65 to 1.89, where 2 is the theoretical value for a linear system with contact friction [3].

31.4 Numerical Results

31.4.1 Computational Model

A high fidelity finite element model was created in Sierra/SD to predict some of the nonlinear behavior observed during the experiments. A mesh of Ministack is shown in Fig. 31.9a; the geometry has the same dimensions as the experimental hardware. There are a total of 198,856 8-noded hexahedral elements, and 15,888 beam elements resulting in a total of 214,744 elements. The hexahedral elements model all the component materials (i.e. ring nut, cover plate, outer can, foam cups, solid mass) with linear elastic properties, as given in Table 31.2. The model assumes that the foam cups behave as a linear elastic material, and a modal damping model accounts for the material damping. We assume that a majority of the nonlinear energy dissipation occurs at the interface between the inner solid mass and the inner surface of the foam cups as shown in Fig. 31.9b. All the beam elements in the model are abnormally stiff beams that rigidly tie the interfacing surfaces of either the solid mass or foam cups to a single node. From this model, two Craig-Bampton reduced order models (ROMs) [13] are created; one of the solid mass and one of the rest of the foam/can assembly. The solid mass has three boundary nodes (top and bottom gap interface, one Iwan interface), resulting in a total of 18 constraint modes. The high stiffness of the solid mass required only a single fixed-interface mode. The foam/can assembly has 4 boundary nodes with the additional one being an excitation node at the base plate of the can. Keeping 20 fixed-interface modes gives this subcomponent ROM a total of 39 degrees-of-freedom. The modal damping values were set to 0.5 % for the solid mass and 2.0 % for the can/foam assembly.

The three boundary nodes of the ROMs are connected to the respective nodes using a single joint element having six different constitutive models for each of the nodal DOF (3 transverse and 3 rotational). The top and bottom interfaces between the solid mass and the corresponding inner surfaces of the foam cups are modeled with a gap element (i.e. piecewise linear spring) in only the y-direction. The parameters for the unloaded and loaded stiffness K_u and K_l, respectively, and the initial gap opening U_0 are given in Table 31.3. No other constitutive models are applied to the top and bottom interfaces. The outer radial surface of the solid mass is tied to a joint element with a four-parameter Iwan model [14] in the y-direction, and stiff elastic springs in all the other directions. The stiffness parameters K_T and K_l were adjusted to best match the 1 g test data in Fig. 31.4 as this was nearest to a linear response. The rest of the parameters were manually adjusted to in order to best align with the repeatable transfer functions at the various excitation levels in Fig. 31.4.

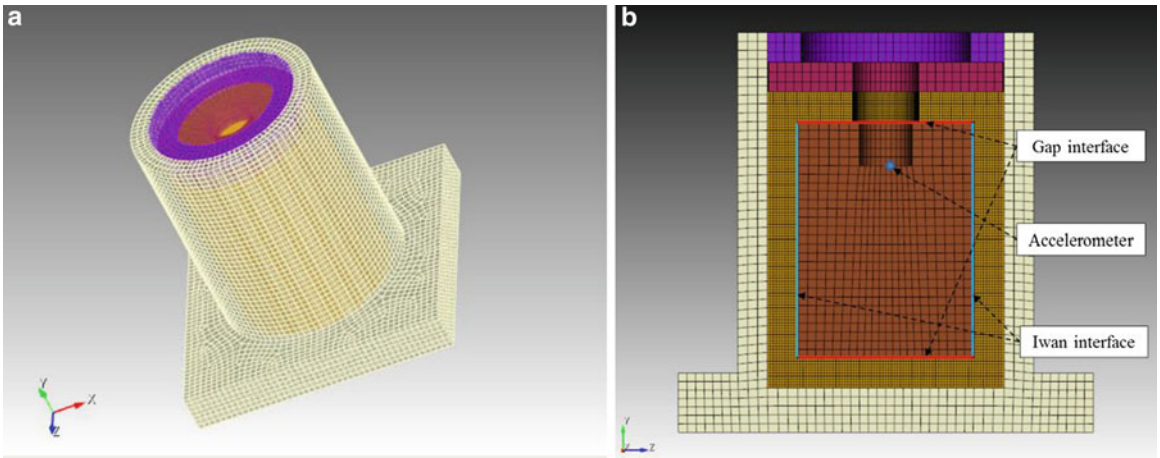

Fig. 31.9 (**a**) Finite element model of Ministack, (**b**) solid mass to foam interface

Table 31.2 Linear elastic material properties

Material	Component(s)	Young's modulus	Density	Poisson's ratio
Aluminum 6061-T6	Slug, outer can	68.9 GPa	2640 kg/m^3	0.33
Structural steel	Ring nut, cover plate	207 GPa	7705 kg/m^3	0.33
PMDI	Foam cups	162 MPa	289 kg/m^3	0.30

Table 31.3 Parameters in nonlinear joint elements

	Parameters			
Element	K_u	K_l	U_0	–
Top & bottom gap	0.0 lbf/in	1.0 E + 06 lbf/in	0.0 in.	–
	Parameters			
	K_T	F_s	B	χ
Iwan	2.0 E + 06 lbf/in	100.0 lbf	0.0	−0.5

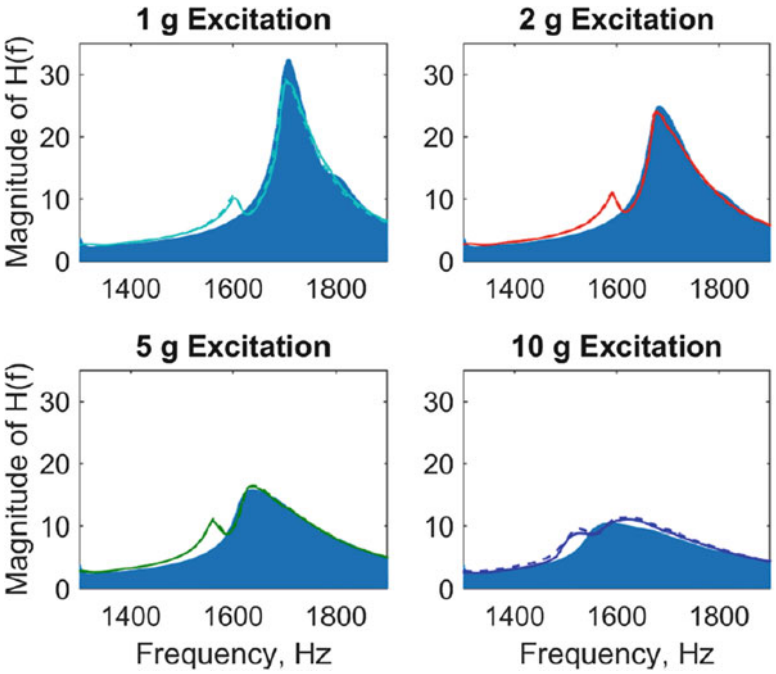

Fig. 31.10 Comparison of experimental transfer functions and simulated sine sweeps from 10 g to 1 g

31.4.2 Comparison Between Model and Experiments

The assembled ROMs with nonlinear connections were subject to an upward sine sweep excitation from 1300 to 1900 Hz at a sweep rate of 750 Hz/s. Each sweep applied a base acceleration in the y-direction at various amplitudes (1 g, 2 g, 5 g, and 10 g) in order to excite the first axial mode of Ministack. The objective of the simulation was to identify the appropriate constitutive parameters in Table 31.3 that correlate with the measured transfer functions shown in Fig. 31.4. This experimental data was chosen since it was repeatable and did not depend on prior test runs. The simulated sweeps are overlaid onto the experimental data in Fig. 31.10. The solid mass exercises the Iwan interface since the excitation sweeps through the frequency of the first axial mode. The model captures a loss of stiffness of 1708 Hz at a 1 g load down to 1585 Hz at 10 g's. The peak of the transfer function also decreases as the load amplitude increases, suggesting that the amount of energy dissipation in the Ministack is reasonably captured with the Iwan element. In future efforts, the model will be updated to capture the bi-modal hump seen in the test data as this phenomenon is likely due to the loss of contact between the solid mass and the foam.

31.5 Conclusions

A series of upward sine sweeps are run on Ministack, which is a simple system representing a metal component packaged in foam. The measured results give insight into the influence of input amplitude, snugness of fit, load path and sequence of testing on the energy dissipation and natural frequency in the system. As the amplitude of excitation increases, the natural frequency decreases and the amount of energy dissipated each cycle increases. The foam to metal interface seems to be

responsible for this behavior due to friction, impact, loss of preload, and material damping. The nonlinear nature of these physics presents itself in the measured transfer functions and estimated parameters.

The first set of results show the effect of the order of the amplitudes of the sine sweeps. When the sine sweeps start at a low amplitude and increase, the natural frequency from the second run shifts to a lower frequency in comparison to the first run. Similarly, the amount of energy dissipation is lower on the second run. When starting the test series at a high amplitude and decreasing the amplitude there was no appreciable difference in the parameters. Starting the run with a 10 g load case may cause the mass to initially settle and lose some of its preload, which could explain why the order of sweep amplitude influence the behavior.

Three different size solid masses were tested along with sets of foam cups with two different depths, which changes the load path of the preload. Regardless of the load path, the snugness of fit has no statistically significant effect on the variance of the natural frequency, indicating gap size does not affect the repeatability of the assembly process. When the load path goes through both the mass and the foam, the snugness of fit has an impact on the natural frequency. The smaller gap case has higher natural frequencies than the no gap case and the larger gap case has lower natural frequencies than the no gap case. When the load path goes through the mass alone, the natural frequency is higher in the case where there is no gap than in the cases where there are gaps. These results suggest that the snugness of fit has a larger effect on the stiffness of the system when the load path goes through the mass and the foam than when the load path goes through the mass only. Additionally, the uncertainty of the natural frequency is larger in the case of the preload going through the mass and the foam, likely due to the variation in the foam.

The results of this study show that the snugness of fit has an effect on the energy dissipation. Regardless of load path, the amount of energy dissipated is greatest when there is a radial gap. It is likely that the increased energy dissipation in the presence of a radial gap is due to mechanisms of energy dissipation that occur when there is a radial gap in addition to the contact friction that is present when there is no radial gap. For modeling implications, these results suggest that it is important to understand the amount of friction that occurs between the contacting surfaces but also the coefficient of restitution for impacts.

A first attempt at modeling Ministack was done using a Craig-Bampton model connected with various nonlinear elements. The simulated sine sweeps with an Iwan element and two gap elements matched the test data quite well. In future work, other interfaces models will be explored along with a more systematic way of identifying the model parameters from test data.

References

1. U.S. Department of Defense Standard Practice for Military Packaging, MIL-STD-2073-1E w/Change 1, January 2011
2. U.S. Department of Defense Environmental Engineering Considerations and Laboratory Tests, MIL-STD-810G, Oct. 2008
3. Goodman, L.E.: A review of progress in analysis of interfacial slip damping. In: Jerome E Ruzincka (ed.) Structural Dumping, papers presented at a colloquium on structural damping held at the ASME annual meeting in Atlantic City, pp 35–48. NJ (1959)
4. Goodman, L.E., Brown, C.B.: Energy dissipation in contact friction: constant normal and cyclic tangential loading. J. Appl. Mech. **29**, 17–22 (1962)
5. Ungar, E.E.: The status of engineering knowledge concerning the damping of built-up structures. J. Sound Vib. **26**, 141–154 (1977)
6. Metherell, A.F., Diller, S.V.: Instantaneous energy dissipation rate in a lap joint - uniform clamping pressure. J. Appl. Mech. **35**, 333–340 (1968)
7. Groper, M.: Microslip and macroslip in bolted joints. Exp. Mech. **25**, 171–174 (1985)
8. Menq, C.H., Bielak, J., Griffin, J.H.: The influence of microslip on vibratory response, Part 1, a new microslip model. J. Sound Vib. **107**, 279–293 (1986)
9. Gaul, L., Lenz, J.: Nonlinear dynamics of structures assembled by bolted joints. Acta Mech. **125**, 169–181 (1997)
10. Sanliturk, K.Y., Stanbridge, A.B., Ewins, D.J.: Friction dampers: measurement, modelling and application to blade vibration control. ASME Design Engineering Technical Conferences vol. 3, Part B, 1995
11. Rogers, P.F., Boothroyd, G.: Damping at metallic interfaces subjected to oscillating tangential loads. J. Eng. Ind. **97**, 1087–1093 (1975)
12. Padmanabhan, K.K., Murty, A.S.R.: Damping in structural joints subjected to tangential loads. Proc. Inst. Mech. Eng. **205**, 121–129 (1991)
13. Craig, R.R.J., Kurdila, A.J.: Fundamentals of Structural Dynamics, 2nd edn, pp. 531–570. Wiley, New York (2006)
14. Segalman, D.J.: A four-parameter Iwan model for lap-type joints. ASME. J. Appl. Mech **72**(5), 752–760 (2005). doi:10.1115/1.1989354
15. Chopra, A.K.: Dynamics of Structures, 2nd edn, pp. 65–118. Prentice Hall, New Jersey (2001)

Chapter 32
Nonlinear System Identification of Mechanical Interfaces Based on Wave Scattering

Keegan J. Moore, Mehmet Kurt, Melih Eriten, D. Michael McFarland, Lawrence A. Bergman, and Alexander F. Vakakis

Abstract We study stress wave propagation in two impulsively forced split Hopkinson bar systems: one with a prestressed interface and one with a frictional interface. We first consider only primary wave transmission and reflection, allowing for reduction of the problem to a first-order, strongly, nonlinear ordinary differential equation. A high-order finite element model is then developed and used to validate the results of the primary-pulse model. A spring that hardens with increasing preload is used to model the prestressed interface while an Iwan element is used to model the frictional interface. Using the primary-wave propagation model, we perform nonlinear system identification by matching simulation and experiment results and identify the nonlinear hardening characteristics for the prestressed interface and Iwan parameters for the frictional interface. These parameters are then used in the finite element model to compare the experimentally measured secondary effects with the simulated effects. Our results demonstrate that the primary-wave propagation model can be used as a reduced order model for nonlinear system identification at a fraction of the computational cost of higher-order models.

Keywords Wave propagation • Iwan elements • Mechanical joints • Nonlinear system identification • Interface dynamics

32.1 Introduction

Computational models are of primary use for analyzing and predicting the complex behavior observed in mechanical structures. High-order finite element (FE) models are often employed to accurately identify the appropriate system parameters, leading to high computational cost. As such, it is often desirable to develop a reduced order model that can be used to accurately identify system parameters at a fraction of the cost of high-order models. One area where this proves to be difficult is in the prediction of mechanical waves due to an impulsive load propagating across a nonlinear interface in a waveguide. A common waveguide used in experiments is the split Hopkinson pressure bar (SHPB), which traditionally has been used to study the mechanical properties of materials [1–3]. More recently, [4, 5] have used the SHPB system to study the strongly nonlinear effects of dynamic friction. Additionally, the SHPB system has been extended to study the effects of static preloads in clearance interfaces [6, 7] and threaded interfaces [8]. These works relied on a combination of linear and torsional springs as well as high-order FE models to model the interface dynamics.

By considering only the primary transmitted and reflected pulses across an interface, the difficulty of simulating these systems can be greatly reduced. Specifically, a reduced order model based on the study of primary transmitted and reflected pulses was proposed in [9] and then further applied to granular interfaces in [10, 11]. This work proposes a new nonlinear system identification method using the primary-pulse (PP) model proposed in [9] to identify the system parameters of the nonlinear interfaces studied in [7, 8]. We show that the proposed methodology is able to identify the system parameters at a fraction of the computational cost of high-order FE models without sacrificing accuracy.

K.J. Moore (✉) • A.F. Vakakis
Department of Mechanical Science and Engineering, University of Illinois, Urbana, IL 61801, USA
e-mail: kmoore14@illinois.edu

M. Kurt
Department of Bioengineering, Stanford University, Stanford, CA 94305, USA

M. Eriten
Department of Mechanical Engineering, University of Wisconsin at Madison, Madison, WI 53706, USA

D.M. McFarland • L.A. Bergman
Department of Aerospace Engineering, University of Illinois, Urbana, IL 61801, USA

© The Society for Experimental Mechanics, Inc. 2016

M. Allen et al. (eds.), *Dynamics of Coupled Structures, Volume 4*, Conference Proceedings of the Society for Experimental Mechanics Series, DOI 10.1007/978-3-319-29763-7_32

32.2 Problem Formulation

We consider the system depicted in Fig. 32.1, composed of two linear elastic layers coupled by a nonlinear interface. The equation of motion governing the longitudinal waves in each layer is

$$\frac{\partial^2 u_i}{\partial t^2} - \frac{\partial^2 u_i}{\partial x^2} = 0, \quad i = 1, 2, \tag{32.1}$$

where $u_i = u_i(t, x)$ is the longitudinal displacement and all variables are normalized such that $0 \leq x \leq 1$. The layers are assumed to start with zero initial conditions, with $t = 0$ defined as the time when the primary-pulse reaches the left boundary $x = 0$ of the layer, that is

$$u_i = 0, \quad \frac{\partial u_i}{\partial t} = 0, \quad \text{for} \quad t = 0, \quad i = 1, 2. \tag{32.2}$$

The boundary conditions for the first layer are

$$\left.\frac{\partial u_1}{\partial x}\right|_{x=\ 0} = F_{in}(t), \quad \left.\frac{\partial u_1}{\partial x}\right|_{x=\ 1} = K\left(z, \dot{z}\right), \tag{32.3}$$

where the relative displacement is

$$z(t) = u_2(t, 0) - u_1(t, 1). \tag{32.4}$$

The left boundary condition for the second layer is

$$\left.\frac{\partial u_2}{\partial t}\right|_{x=0} = K\left(z, \dot{z}\right) = F_2, \tag{32.5}$$

and the right boundary condition is not specified at this time. With the system defined appropriately, we seek to use only the primary transmission and reflection in order to identify the parameters for the nonlinear stiffness coupling. To this end, we turn to method developed by Pilipchuk in [9], which reduces the problem from two second-order partial differential equations (PDE) to a single first-order, nonlinear ordinary differential equation (ODE). A full derivation is provided in [9]; here we present only the resulting equations:

$$\frac{1}{2}\dot{z} + K\left(z, \dot{z}\right) = F_{in}(t); \quad z|_{t=\ 0} = 0. \tag{32.6}$$

$$F_2(t) = F_{in}(t) - \frac{1}{2}\dot{z}. \tag{32.7}$$

where F_2 is the force acting on the second layer due to the interface. Additionally, the reflection into the first layer is

$$\Phi_1(t) = -F_{in}(t-2) + K(t-1), \tag{32.8}$$

where Φ_1 is the reflection in the first layer based on the D'Alembert representation of the solution. Thus, by solving for $\dot{z}$ in (32.6) we can determine the force transmitted through the interface to the second layer as well as the reflection in

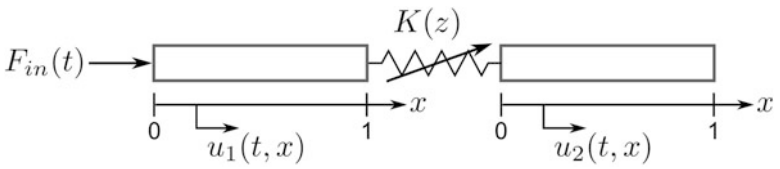

Fig. 32.1 Impulsively forced dual layer system with nonlinear interface

the first layer, and the system parameters can be identified by matching the PP model predictions with data taken from experimentally measured strains. In the next section, we apply the PP model to identification of the nonlinear interfaces of two SHBP experiments: one with a prestressed clearance interface and one with a prestressed frictional interface.

32.3 Nonlinear System Identification

32.3.1 Preloaded Clearance Interface

The first system we study is a SHPB system composed of two hardened AISI 1566 steel bars ($\rho = 7.8\ \mathrm{g/cm^3}$, $E = 210$ GPa, $\nu = 0.29$) with a prestressed clearance interface and is depicted in Fig. 32.2. The incident bar had length of 96 in. (244 cm) and a step up in diameter from 1.25 in. (3.2 cm) to 1.5 in. (3.8 cm) at the midpoint, and was supported by a backstop placed at the midpoint. The backstop also served to support the static axial preload that was applied to the system. The transmission bar had a length of 48 in. (122 cm) and a diameter of 1.5 in. (3.8 cm), and was supported by two bushing supports. Additionally, the right end was attached to a hydraulic press, which provided the static axial preload on the system. The bars were not match finished, thus the contact area is relatively small with low preload and fully closed with high preload. Uniaxial semiconductor strain gages were placed diametrically opposed at four locations, two before and two after the interface. The strains were measured for 10 ms at a sampling rate of 2.5 MHz. A standard modal impact hammer was used to apply the impulsive force at the left boundary of the incident bar. All experiments were conducted by the Air Force Research Laboratory at Eglin Air Force Base, FL and are fully documented in [6, 7].

For the system identification discussed herein, a 100 lb preload case (minimal contact) and a 4000 lb preload case (maximum contact) are chosen. A qualitative analysis revealed that an additional tensile wave followed the compressive wave to the interface. This additional tensile wave is either due to the externally applied load or is a result of the compression between the step up in diameter and the backstop. As the purpose of this research is to identify the nonlinear interface and not the interaction at the backstop, the superposition of the compressive wave and the tensile wave is used as the input force to the PP model. Since some contact exists at low preload, the interface is modeled as two springs in series: one depending on the preload and one independent of the preload

$$K(z,P) = \left(\frac{1}{k_1(P)} + \frac{1}{k_2}\right)^{-1} z, \tag{32.9}$$

where P is the preload on the system, k_1 is the stiffness that depends on the preload, and k_2 is the stiffness independent of the preload. The system parameters are identified using MATLAB's patternsearch optimization algorithm with the objective of maximizing the R-squared value between the experimentally measured waves and the predicted PP model waves for the first three measurement locations. The optimization was run simultaneously for both preload cases in order to accurately identify the constant stiffness term, but was only run up to a dimensionless time of 2.5 as secondary effects are dominant after this time. The optimized dimensionless stiffness values are found to be

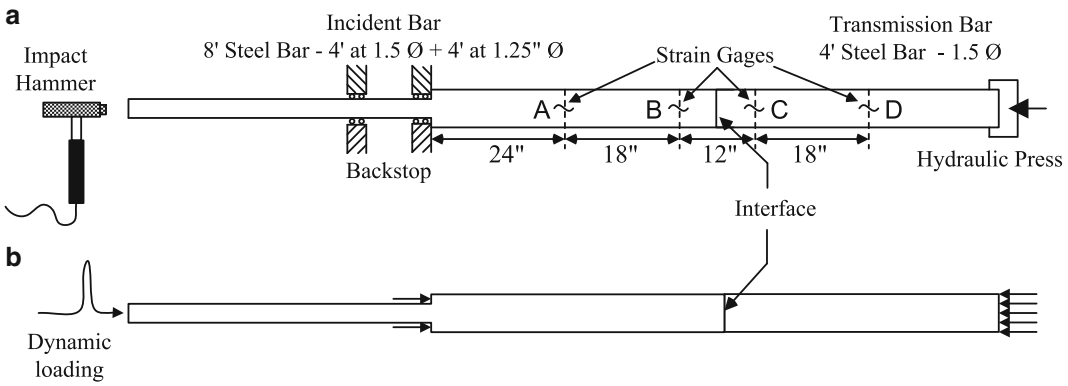

Fig. 32.2 The preload interface bar: (**a**) experimental setup and (**b**) static dynamic loading. Reprinted with permission from [7]

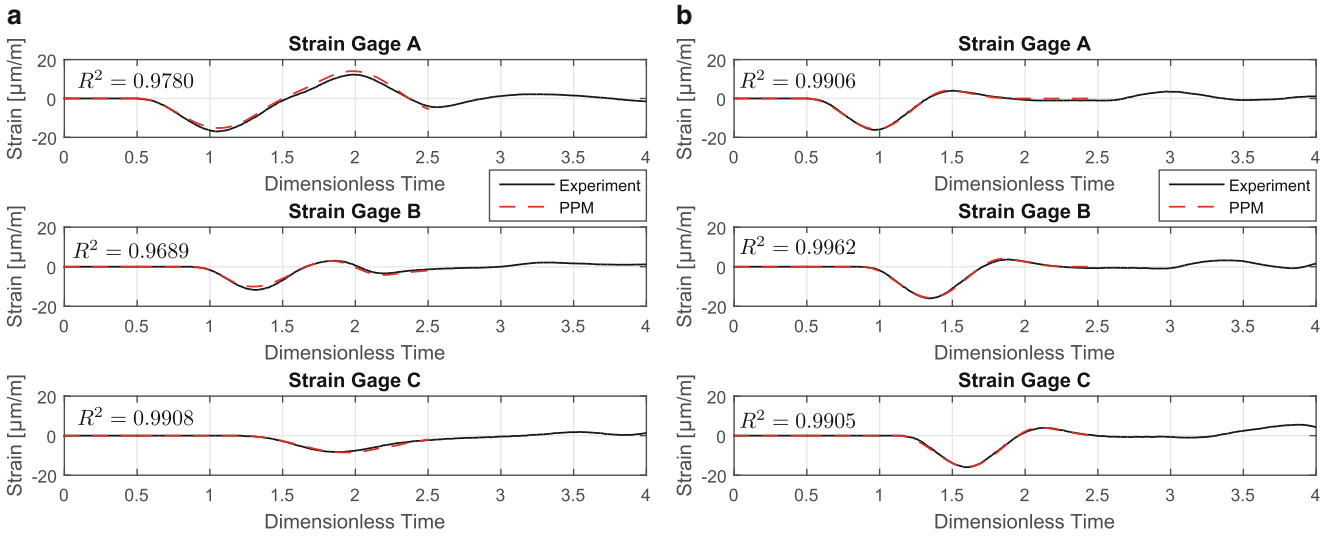

Fig. 32.3 The resulting waves from the PP model using the optimized parameters with a preload of (**a**) 100 lb and (**b**) 4000 lb

$$k_1 = \begin{cases} 0.953 & \text{for } P = 100 \text{ lb} \\ 68.76 & \text{for } P = 4000 \text{ lb} \end{cases} \qquad (32.10)$$
$$k_2 = 98.61,$$

resulting in an overall stiffness of

$$K(z) = \begin{cases} 0.944 & \text{for } P = 100 \text{ lb} \\ 40.51 & \text{for } P = 4000 \text{ lb}. \end{cases} \qquad (32.11)$$

The lowest R-squared values were 0.9689 for the 100 lb preload case and 0.9905 for the 4000 lb preload case. The resulting waves predicted by the PP model using the optimized parameters are depicted in Fig. 32.3.

32.3.2 Frictional Interface

The second system we study is a SHPB system composed of two hardened AISI 1566 steel bars ($\rho = 7.8$ g/cm^3, $E = 210$ GPa, $\nu = 0.29$) with a threaded interface and is depicted in Fig. 32.4. Both the incident and transmission bar had a length of 48 in (122 cm) and a diameter of 1.5 in (3.8 cm). The incident bar is machined with male 1″-8 UNC threads and the transmission bar is machined with the corresponding female threads. An initial static torque preload, applied by hand (near zero torque) or by using a handle-less strap wrench, ranged from 25 ft-lbf to 40 ft-lbf. A 6 in. long striker propelled by an air gun with velocities ranging from 7 to 14 m/s was used to dynamically excite the incident bar. Uniaxial semiconductor strain gages were placed diametrically opposed at two locations before and two locations after the interface. The strains were measured for 10 ms at a sampling rate of 2.5 MHz. All experiments were conducted by the Air Force Research Laboratory at Eglin Air Force Base, FL and are fully documented in [8].

The frictional interface in this system is modeled using an Iwan element [12, 13], which contains an infinite distribution of Jenkins elements in parallel, where a single Jenkins element is made up of a dry-friction slider in series with a linear spring. The stiffness in each Jenkins element is chosen to be the equal, whereas the slip force for each slider varies in the form of a distribution function. Thus, the Iwan element is able to reproduce the hysteresis effects due to micro-slip at low loads, and the macro-slip effects at large loads, and accounts for the sticking of sliders when the slip direction changes. The resulting Iwan force is defined for three different slip motions:

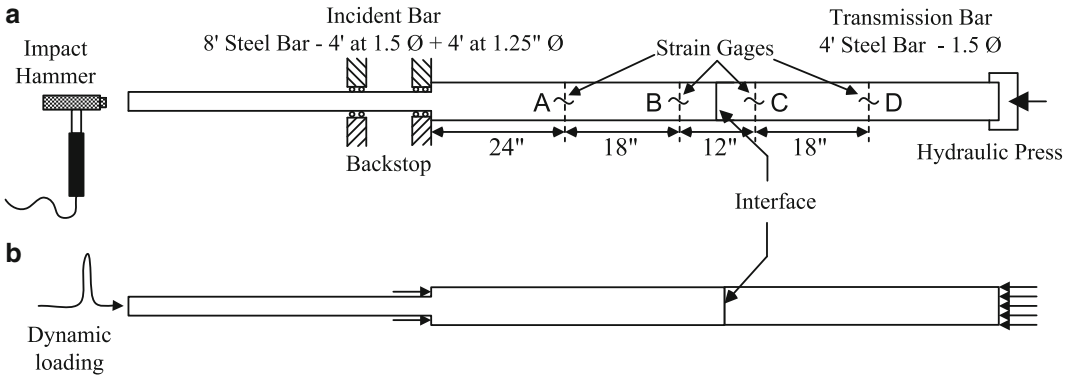

Fig. 32.4 Schematic of the threaded-bar interface experiments showing the layout of the sensors and the details of the threaded interface. The system is supported by low-friction linear bearings. Reprinted with permission from [8]

$$
\begin{aligned}
K(z,z_0) &= \int_0^{kz} \phi\rho(\phi)\,d\phi + kz\int_{kz}^{\infty} \rho(\phi)\,d\phi \quad \text{for initial slip,}\\
K(z,z_0) &= \int_0^{k(z+z_0)/2} \phi\rho(\phi)\,d\phi + \int_{k(z+z_0)/2}^{kz_0} (kz+kz_0-\phi)\,\rho(\phi)\,d\phi + kz\int_{kz_0}^{\infty} \rho(\phi)\,d\phi \quad \text{for positive slip,}\\
K(z,z_0) &= -\int_0^{k(z_0-z)/2} \phi\rho(\phi)\,d\phi + \int_{k(z_0-z)/2}^{kz_0} (kz-kz_0+\phi)\,\rho(\phi)\,d\phi + kz\int_{kz_0}^{\infty} \rho(\phi)\,d\phi \quad \text{for negative slip,}
\end{aligned}
\tag{32.12}
$$

where K is the Iwan force, z is the interface displacement, z_0 is the last value of interface displacement at the instant the slip direction reverses, k is the linear stiffness coefficient common to all Jenkins elements, ϕ is the macro-slip force, and $\rho(\phi)$ is the distribution of slip forces of the dry sliders. For the distribution, a band-limited function centered about ϕ with width $\Delta\phi$ and an area equal to unity is chosen as Iwan used in [12]. The advantage of choosing this distribution is that the relations in (32.12) can be evaluated in closed form so that the system parameters are reduced to only ϕ and k.

Because the system properties (stiffness and macro-slip force) change based on the amount of static torque applied to the bars, we chose to identify the Iwan parameters for each torque case separately. Since the input forces were not measured in the experiments, the input force is chosen to be a half-sine impulse with parameters that are identified in the optimization scheme. The system and forcing parameters are identified using MATLAB's patternsearch optimization algorithm with the objective of maximizing the R-squared value between the experimentally measured waves and the predicted PP model waves for all four measurement locations. Again the optimization was only run up to a dimensionless time of 2.5 as the secondary effects dominate after this time. For the 25 ft-lb static torque preload case, the lowest R-squared value is 0.9454 and the optimized dimensionless parameters are $k = 43.42$ and $\phi = 2224$. The resulting waves using these parameters in the PP model are depicted in Fig. 32.5a for strain gages A and D. The optimized Iwan parameters are then passed to a high-order FE model (100 elements in each bar), which is used to predict the secondary reflections and transmissions. The results of using the FE model with the Iwan parameters optimized using the PP model for strain gages A and D are depicted in Fig. 32.5b. The lowest R-squared value between the experimental data and the FE model predicted data is 0.8915. On average the FE model takes 52 s to complete the simulation whereas the PP model takes an average of 1.95 s resulting in a signification reduction in the computational time. Thus, if the FE model was used in the optimization process the total time to completion would be on the order of days whereas the PP model is able complete the optimization task within a matter of hours.

32.4 Concluding Remarks

In this work, a new nonlinear system identification method for identifying nonlinear interfaces in waveguides was proposed. The method is based on the reduction of the second order wave equation, which captures all propagating waves, to a first-order nonlinear ODE that models only the incident, primary transmitted, and primary reflected waves. This reduction results in a computationally cheap method for performing system identification of nonlinear interfaces in waveguides, in that, only the primary-pulses need to be considered. The proposed methodology was then applied to two experimentally measured SHPB experiments: one with a preloaded clearance interface and one with a thread frictional interface. Models were selected for

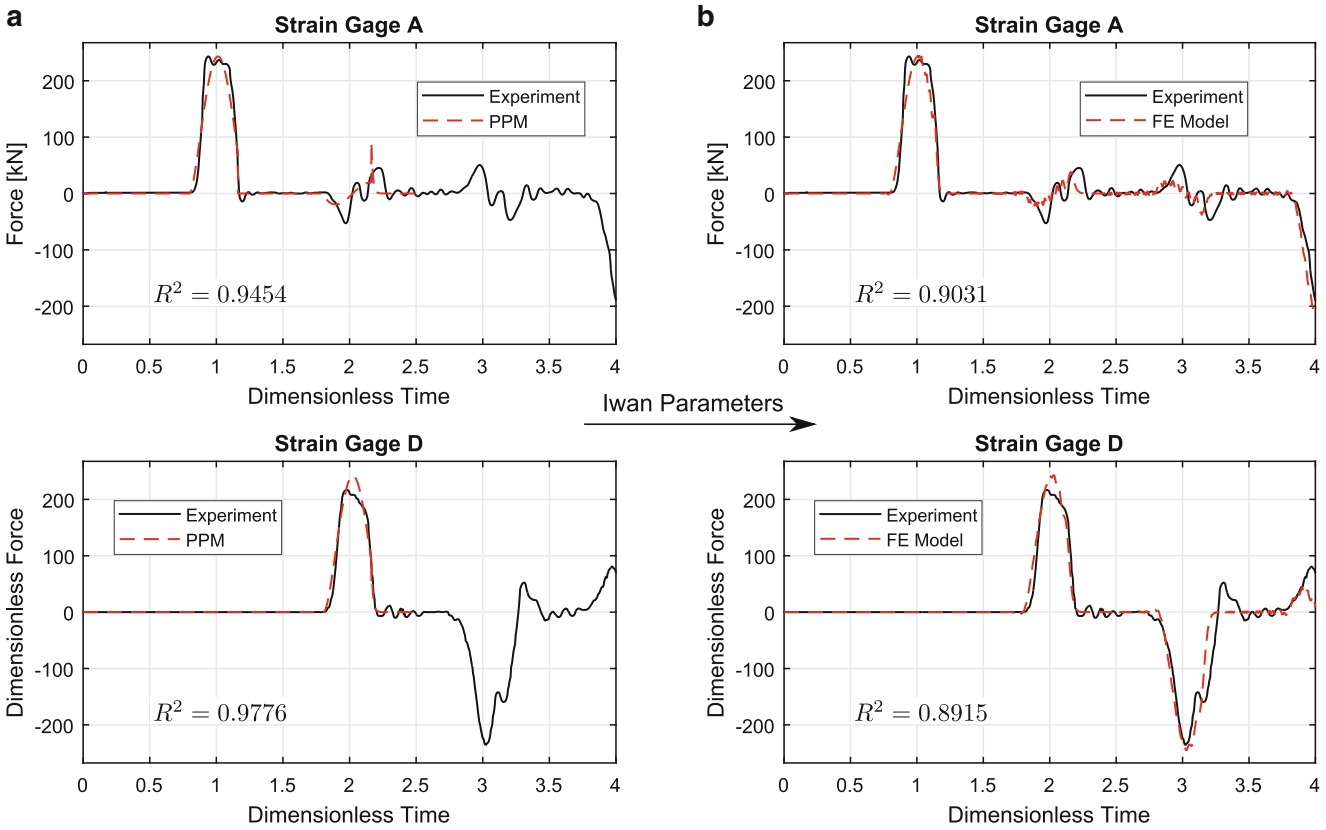

Fig. 32.5 Resulting waves for a static torque preload of 25 ft-lbf and a striker velocity of 13.5 m/s predicted using (**a**) PP model and (**b**) FE model where the Iwan parameters are optimized using the PP model and then passed to the FE model

both interfaces and the PP model was used to optimize and identify the system parameters. In both cases, the PP model was shown to accurately model the primary transmission and reflection across the interfaces. Additionally, a high-order FE model using the PP model optimized parameters for the second split Hopkinson bar system was used to show that the secondary effects could also be accurately reproduced. Thus, we conclude that the proposed methodology is able to accurately identify the system using only the primary-pulses and at a fraction of the computational cost of traditional methods.

References

1. Hopkinson, B.: A method of measuring the pressure produced in the detonation of high explosives or by the impact of bullets. Philos. Trans. R. Soc. A **213**, 437–456 (1914)
2. Kolsky, H.: An Investigation of the mechanical properties of materials at very high rates of loading. Proc. Phys. Soc. **B62**, 676–700 (1949)
3. Gray, G.T.: Classical Split Hopkinson pressure bar technique. In: Kuhn, H., Medlin, D. (eds.) ASM Handbook, Vol. 8, Mechanical Testing and Evaluation, pp. 462–476. ASM International, Materials Park (2000)
4. Rajagopalan, S., Prakash, V.: A modified torsional Kolsky bar for investigating dynamic friction. Exp. Mech. **39**(4), 295–303 (1999)
5. Espinosa, H.D., Patanella, A., Fischer, M.: A novel dynamic friction experiment using a modified Kolsky bar apparatus. Exp. Mech. **40**(2), 138–153 (2000)
6. Foley, J. R., Dodson, J. C., McKinnon, C. M., Luk, V. K., and Falbo, G. L.: Split Hopkinson bar experiments of preloaded interfaces. In: Proceedings of the IMPLAST 2010 conference, Society for Experimental Mechanics, 2010
7. Dodson, J.C., Wolfson, J., Foley, J.R., Inman, D.J.: Transmission of guided waves across prestressed interfaces. In: Adams D. (ed.) Topics in Nonlinear Dynamics, Conference Proceedings of the Society of Experimental Mechanics Series 28, vol. 3, pp. 83–94. Springer, New York (2012)
8. Dodson, J.C., Lowe, R.D., Foley, J.R., Mougeotte, C., Geissler, D., Cordes, J.: Dynamics of interfaces with static initial loading. In: Song B. (ed.) Dynamic Behavior of Materials, Conference Proceedings of the Society for Experimental Mechanics Series, vol. 1, pp. 37–50. Springer, New York (2014)
9. Pilipchuck, V.N., Azeez, M.A.F., Vakakis, A.F.: Primary-pulse transmission in strongly nonlinear periodic system. Nonlinear Dyn. **11**, 61–81 (1996)

10. Starosvetsky, Y., Vakakis, A.F.: Primary wave transmission in systems of elastic rods with granular interfaces. Wave Motion **48**, 568–585 (2011)
11. Starosvetsky, Y., Jayaprakash, K.R., Vakakis, A.F., Kerschen, G., Manevitch, L.I.: Effective particles and classification of the dynamics of homogeneous granular chains with no precompression. Phys. Rev. E **85**, 036606 (2012)
12. Iwan, W.D.: A distributed-element model for hysteresis and its steady-state dynamic response. ASME J. Appl. Mech. **33**, 839–900 (1996)
13. Iwan, W.B.: On a class of models for the yielding behavior of continuous and composite systems. ASME J. Appl. Mech. **34**, 612–617 (1967)

Chapter 33
Studies of a Geometrical Nonlinear Friction Damped System Using NNMs

Martin Jerschl, Dominik Süß, and Kai Willner

Abstract In the 1960s Rosenberg extended the definition of linear normal modes (LNM) for conservative systems to nonlinear systems: On a Nonlinear Normal Mode (NNM) every degree-of-freedom (DOF) vibrates in unison. Later Shaw and Pierre provided a definition for nonconservative systems and defined NNMs as invariant manifolds in phase space. If the system vibrates on such a manifold all other modes shall remain quiescent for all time.

Nowadays there are many publications using the concept of NNMs to investigate systems with polynomial nonlinearities. But until now the upper mentioned definition is mostly used to investigate viscously damped systems. In this paper an oscillator containing a geometrically nonlinear (cubic) spring and a dry friction damper is considered. The system is driven into resonance and decay processes are evaluated. Wavelet analysis is used to identify which frequencies and harmonics remain during the decay process.

Keywords Nonlinear dynamics • Nonlinear coupling • Nonlinear normal modes (NNMs) • Friction • Optimal system design

33.1 Introduction

Within the design process it is often sufficient for the structural dynamic analysis to treat real-life applications as linear systems because only small strains and displacements are considered. Since structures have to provide higher performances in speed and often linked to that in lightweight constructions the system automatically undergoes larger displacements while the strains remain small. This fact leads to geometrical nonlinearities and loss of some comfortable properties of linear systems like the invariance of the resonance frequency of the energy. In this paper a geometrically nonlinear system is investigated numerically concerning its possibility to restrict this frequency-energy dependence. Therefore a dry friction damper is added to the system. During the experiments with different parameter sets the system is driven near or into resonance to isolate a single NNM and decay processes are evaluated. This is motivated by the invariance property of a nonlinear mode and is further explained in Sect. 33.2. An identified *modal* system shall be used as an equivalent one.

The paper is organised as follows: After this introduction a short overview of the concept of nonlinear normal modes is given in Sect. 33.2 which shall serve as motivation of the authors' intention. This is followed in Sect. 33.3 by the numerical modelling of the friction modified geometrically nonlinear system and the proposed methodology to design this system frequency-energy independent. Finally the numerical results are presented in Sect. 33.4.

33.2 The Concept of Nonlinear Normal Modes

As described in literature nonlinear normal modes are a concept to extend modal analysis to nonlinear systems. For the sake of completeness a few properties and definitions of NNMs are repeated for understanding the motivation behind the procedure of this work. For more details the reader is referred to [1–3].

In contrast to linear systems a property of nonlinear oscillations is the frequency-energy dependence which can be described with the tool of NNMs. The frequency shift with rising system energy can be identified for conservative systems in a frequency-energy plot (FEP) by path-following techniques [4–6]. Thereby periodic motions of the nonlinear system are

M. Jerschl (✉) • D. Süß • K. Willner
Friedrich-Alexander Universitaet Erlangen-Nuernberg Chair of Applied Mechanics, Egerlandstr. 591058 Erlangen, Germany
e-mail: martin.jerschl@ltm.uni-erlangen.de

© The Society for Experimental Mechanics, Inc. 2016

M. Allen et al. (eds.), *Dynamics of Coupled Structures, Volume 4*, Conference Proceedings of the Society for Experimental Mechanics Series, DOI 10.1007/978-3-319-29763-7_33

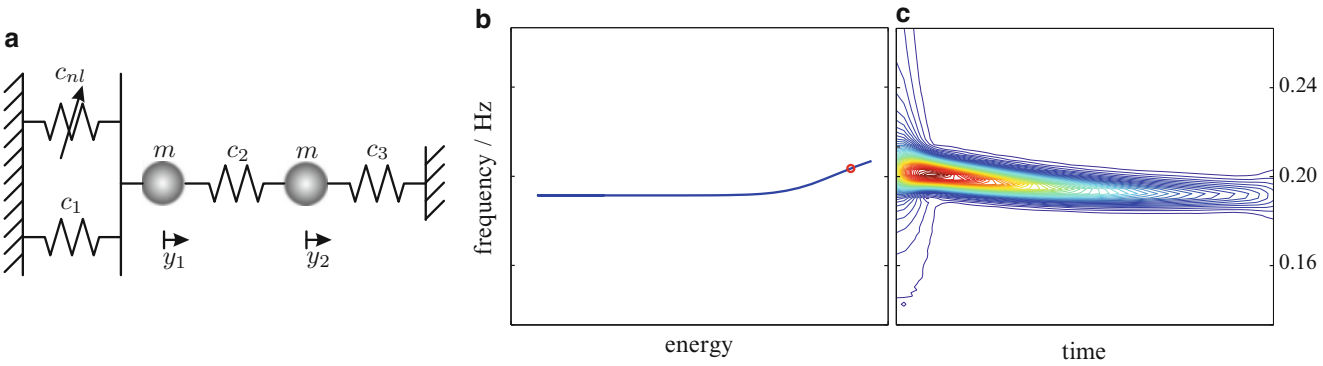

Fig. 33.1 Frequency-energy dependence of two-DOF duffing oscillator with $c_1 = 2$, $c_2 = c_3 = 1$, $c_{nl} = 0.01$ and $m_1 = m_2 = 1$: (**a**) two-DOF duffing model, (**b**) frequency-energy plot of first NNM, (**c**) wavelet analysis of decay process, initiated on first NNM

forced according to Rosenberg's definition of a NNM [7]. In Fig. 33.1b a FEP (fundamental frequency of the periodic motion over sum of potential and kinetic energy) is shown of a two-DOF Duffing oscillator (see Fig. 33.1a), calculated with this technique.

Krack gives a new definition of a nonlinear mode (he doesn't use the word *normal* in his work because of the lack of orthogonality of the modes) for non-conservative systems and defines a nonlinear mode also as a family of periodic orbits but enforced by mass-proportional damping in the case of non-conservative systems [1]. Therefore the energy dissipation is compensated by additional negative damping.

From the mathematical point of view not all properties of linear normal modes (LNMs) can be transferred to nonlinear regimes. For example the modal superposition principle is no longer valid and the orthogonality relations between the mode shapes are missing what complicates model order reduction techniques (as far as there exist techniques). So only some basic facts can be adjusted to nonlinear systems. For example the *invariance property* holds. It includes the fact that all other modes won't be excited as long a vibration of an autonomous system starts on a nonlinear mode. To get such a state the only dynamic regime of interest in this paper is an isolated resonance. According to Krack's definition of an isolated resonance the dynamic flow of the autonomous system may be dominated by this resonance, if the motion was started there [1]. This can be seen in Fig. 33.1c, were an wavelet analysis of the first DOF of a two-DOF Duffing oscillation during an autonomous decay process is shown (with this kind of analysis the variation of the spectral contents of the oscillation can be investigated over time. Further information about the wavelet analysis can be read e.g. in [8].) For this frequency-time analysis the motion is initiated on the first NNM (red bullet Fig. 33.1b) and very weak damping is added to the system for dissipating energy. Like shown in [2] this is admissible: The damped dynamics often closely follow the NNM of the underlying undamped system. It can be seen that no other spectral contents arise and therefore only the NNM vibrates with the frequency-energy dependence of Fig. 33.1b.

33.3 Investigation of a Frequency-Energy-Independent Geometrically Nonlinear System

With the given properties and definitions of Sect. 33.2 a two degree-of-freedom duffing oscillator with an additional dry friction damper is investigated.

33.3.1 Definition of the Numerical Model

The differential equations of the model investigated in this paper are given by

$$\ddot{y}_1 + (2y_1 - y_2) + c_{nl}y_1^3 + k_{fr}(y_1, \dot{y}_1) = 0 \tag{33.1}$$

$$\ddot{y}_2 + (2y_2 - y_1) = 0 \tag{33.2}$$

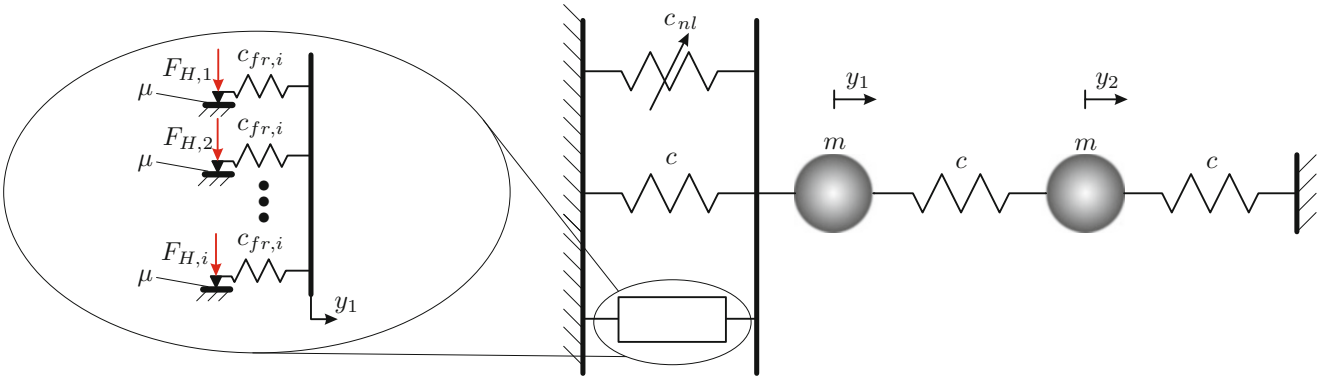

Fig. 33.2 Geometrically nonlinear two-DOF system with dry friction damper

Table 33.1 Basic parameter configuration of the geometrically two-DOF system with dry friction damper

m	c	c_{nl}	μ
1	1	0.01	1

with the cubic stiffness c_{nl} and the nonlinear friction force $k_{fr}(y_1, \dot{y}_1)$. The system is depicted in Fig. 33.2 where also the friction damper is shown in detail. An amount of i Jenkin elements are put in parallel with a constant friction element stiffness $c_{fr,i}$ and different sticking forces $\mu F_{H,i}$. The i normal forces $F_{H,i}$ are distributed logarithmically and the sum of all single sticking forces gives the total sticking force

$$\mu F_{H,tot} = \mu \sum_i F_{H,i} \,. \tag{33.3}$$

The stiffness of a single friction element is constant and the sum of all i springs is equal to the linear stiffness

$$c_{fr} = \sum_i c_{fr,i} = i c_{fr,i} = c. \tag{33.4}$$

Therefore no Jenkin element starts to slip at the same time and micro slip can be represented by this so called Masing element. The reason for the linear spring between the boundary and the first mass is to restrict the oscillation around the equilibrium point of the linear system to avoid vibrations around new equilibrium points in the case when macro slip has occurred. The basic parameter configuration is given in Table 33.1. With this system setup different dynamic performances can be generated with variable parameter sets. The frequency-response-functions (FRF's) are shown in Fig. 33.3 comparing three configurations with the multi-harmonic-balance method (MHBM, for details the reader is refereed to [9]) at the same excitation amplitude (1 N at second DOF). The blue curve shows a pure geometrically nonlinear/cubic (progressive) behaviour because the total sticking force is set to infinity that no slip occurs. Very rich dynamics are present at this energy level. The red curve describes pure friction (declining) behaviour with setting the cubic stiffness to zero and the total normal force to one. The green curve demonstrates the hybrid system setup where regulation of the total normal force $F_{h,tot}$ causes elimination of both opposite behaviours. The aim of this work is to find system configurations for different energy levels where no frequency-energy dependence occurs.

33.3.2 Proposed Methodology

In this paper an attempt is made to design a geometrically nonlinear system whose fundamental frequencies are independent in a certain range of energy. Therefore a dry friction damper is added to the system.

The present section introduces a three step approach that proofs its possibility in realizing the requested behaviour.

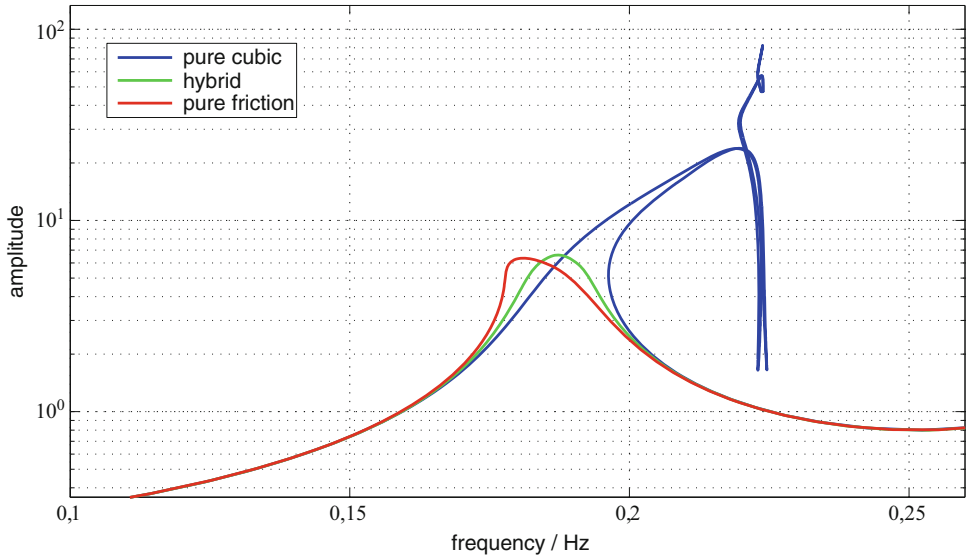

Fig. 33.3 Dynamic performance of the two-DOF system with different parameters c_{nl} and $f_{H,tot}$ and 1 N excitation amplitude

33.3.2.1 Finding an Isolated Resonance

First j system responses for harmonic excitation in the frequency range of the first mode of the underlying linear system (0.1–0.25 Hz) are calculated for a chosen amplitude level and varying the total normal force $F^j_{H,tot}$. For harmonic excitation $\boldsymbol{f}_e(t)$ the solution $\boldsymbol{y}(t)$ of Eqs. (33.1) and (33.2) has to be harmonic as well or at least periodic. Therefore the following ansatz of a truncated Fourier series is used within the MHBM

$$\boldsymbol{f}_e(t) \approxeq \boldsymbol{F}_{e,(0)} + \sum_{k=1}^{n_h} (\tilde{\boldsymbol{F}}_{e,(k)} \mathrm{e}^{ik\omega t} + \tilde{\boldsymbol{F}}^*_{e,(k)} \mathrm{e}^{-ik\omega t}) \tag{33.5}$$

and

$$\boldsymbol{y}(t) \approxeq \boldsymbol{Y}_{(0)} + \sum_{k=1}^{n_h} (\tilde{\boldsymbol{Y}}_{(k)} \mathrm{e}^{ik\omega t} + \tilde{\boldsymbol{Y}}^*_{(k)} \mathrm{e}^{-ik\omega t}) \tag{33.6}$$

with n_h harmonic parts which is used for calculation the responses in the frequency domain. For further information the reader is referred to [9]. For the solution of the nonlinear system equations, path following techniques are used to overcome turning points. It is the aim to get an isolated resonance on the path of solutions. As criterion the 90° phase lag of the response with respect to the excitation is used [10]. It has to be mentioned that due to nonconservative system this phase criterion is not fulfilled for both degrees of freedom at the same frequency. It exists a small phase shift between both DOFs dependent on the equivalent damping of the friction hysteresis. In this case the middle frequency between both frequencies, nearby the phase criterion is fulfilled, is chosen as fundamental frequency ω_R of the isolated resonance.

33.3.2.2 Autonomous Decay Process with Damping Identification

Secondly the initial conditions in the time domain are calculated using the solution for an isolated resonance in the frequency domain with

$$\boldsymbol{y}_0 = \sum_{k=1}^{n_h} \Re(\boldsymbol{Y}_{(k)}(\omega_R)), \tag{33.7}$$

$$\dot{\boldsymbol{y}}_0 = -\sum_{k=1}^{n_h} [\Im(\boldsymbol{Y}_{(k)}(\omega_R)) k\omega_R]. \tag{33.8}$$

The autonomous decay process is calculated as reference solutions $\boldsymbol{y}(t)$ and $\dot{\boldsymbol{y}}(t)$ using NEWMARK-method with $\Delta t = 0.01$ s. Initiated on the isolated NNM an equivalent modal damping δ_N is identified by the logarithmic decrement [11] for every oscillation period $T = \frac{2\pi}{\omega_R}$ of the reference solution during the decay process

$$\delta_N = \frac{1}{T} \ln \left| \frac{y(NT)}{y(NT+T)} \right| \tag{33.9}$$

assuming that the modal damping is constant at least over one period. Due to the fact of an isolated resonance the calculation of the modal damping must be done for one DOF only. Because of the energy dissipation introduced by the friction damper the damping value is not constant in the whole decay process but only valid during the period it is identified. For decreasing energy level less and less Jenkin elements (see Fig. 33.2) are slipping, dependent on the sticking force distribution, and therefore the damping varies with energy and time.

With the identified modal damping and the requested constant vibration frequency ω_R the general solution for a weak damped system can be written as

$$q_i(t) = \mathrm{e}^{-\delta_N[t-NT]} \left[q_{i,0(N)} \cos(\omega_R[t-NT]) + \frac{\dot{q}_{i,0(N)} + \delta_N q_{i,0(N)}}{\omega_R} \sin(\omega_R[t-NT]) \right] \tag{33.10}$$

and

$$\dot{q}_i(t) = \mathrm{e}^{-\delta_N[t-NT]} \left[\dot{q}_{i,0(N)} \cos(\omega_R[t-NT]) - \frac{\delta_N \dot{q}_{i,0(N)} + [\delta_N^2 + \omega_R^2] q_{i,0(N)}}{\omega_R} \sin(\omega_R[t-NT]) \right] \tag{33.11}$$

with

$$NT \le t \le [N+1]T\,, \quad N = 0 \ldots \frac{t_{end}}{T}\,, \quad q_{i,0(N)} = \begin{cases} y_{i,0} & \Rightarrow N = 0 \\ q_i(NT) & \Rightarrow N > 0 \end{cases}\,, \quad \dot{q}_{i,0(N)} = \begin{cases} \dot{y}_{i,0} & \Rightarrow N = 0 \\ \dot{q}_i(NT) & \Rightarrow N > 0 \end{cases} \tag{33.12}$$

for every period N. This is called the *modal* solution in this work.

33.3.2.3 Identification of Frequency-Independent System Configuration

Thirdly, all modal decay processes $\boldsymbol{q}_j(t)$ and $\dot{\boldsymbol{q}}_j(t)$, calculated with Eqs. (33.10) and (33.11), are compared to the j reference solutions of the decay processes $\boldsymbol{y}_j(t)$ and $\dot{\boldsymbol{y}}_j(t)$. An optimal j and connected to that an optimal sticking force is identified by an error estimation between the reference and the modal solution. Therefore this comparison gives an indicator if the requested assumption of a constant oscillation frequency persists during the decay process.

33.4 Numerical Results

In this section the described procedure is applied for different excitation amplitudes and linked to that for different energy levels. The system parameters of Table 33.1 are used.

For every excitation amplitude (0.05, 0.1, 0.25 0,5 and 1 N) $j = 30$ FRFs (number of harmonics in the MHBM $n_h = 5$) are calculated with varying normal force $F^j_{H,tot}$. An normal force is found for $F^j_{H,tot} = 4.16$ N where the error between the reference solution and the model solution is minimal.

The decay process initiated on the isolated resonance with an excitation amplitude of 1 N is shown in Fig. 33.4. For both degrees of freedom the displacement and velocity, calculated with NEWMARK integration (y_i and $\dot{y}_i$) and the modal ansatz of Eqs. (33.10) and (33.11) (q_i and $\dot{q}_i$) respectively, is shown. In two time zooms the congruence between the reference and the modal solution can be seen at different decay sectors (see Fig. 33.4b and c), including amplitude and time period. The modal damping identified during this process is shown in Fig. 33.5 where the δ_N over the logarithm of the kinetic energy is diagrammed. With decreasing energy in the system the damping sinks as well due to the fact that less Jenkin elements

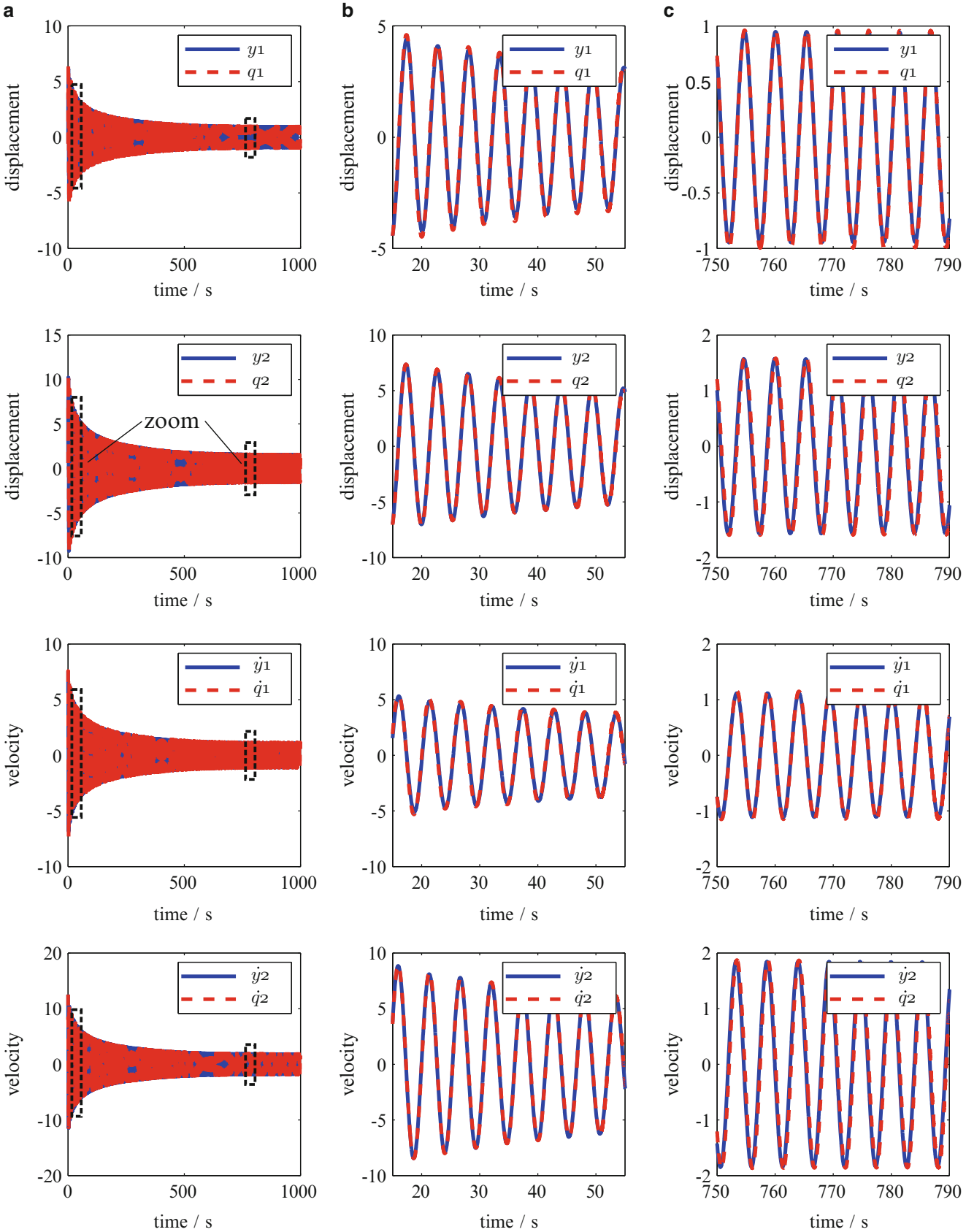

Fig. 33.4 Decay process initiated on isolated resonance with $F_{H,tot} = 4.16\,\mathrm{N}$ and excitation amplitude 1 N. Comparison between the numerically integrated solution and the modal solution. (**a**) whole decay process, (**b**) first zoom, (**c**) second zoom

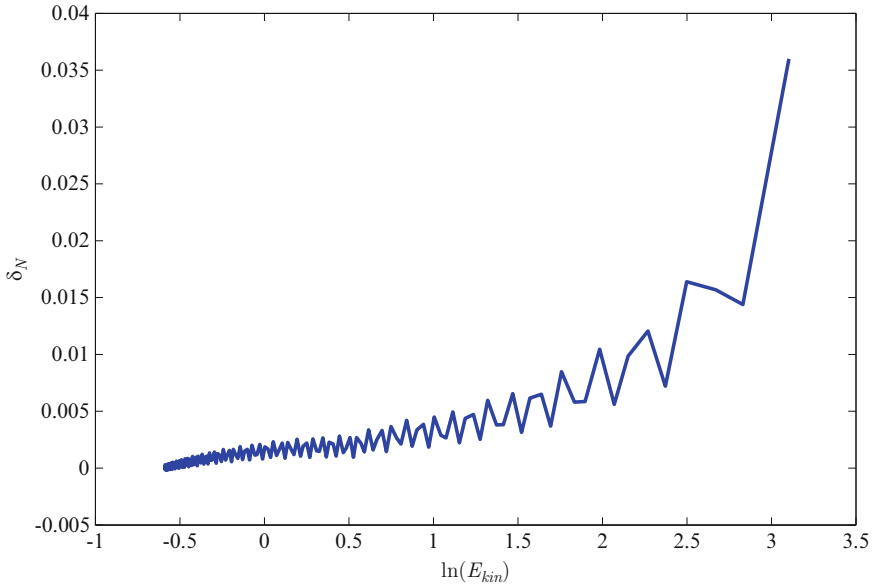

Fig. 33.5 Relationship between kinetic energy of the oscillation and the damping coefficient

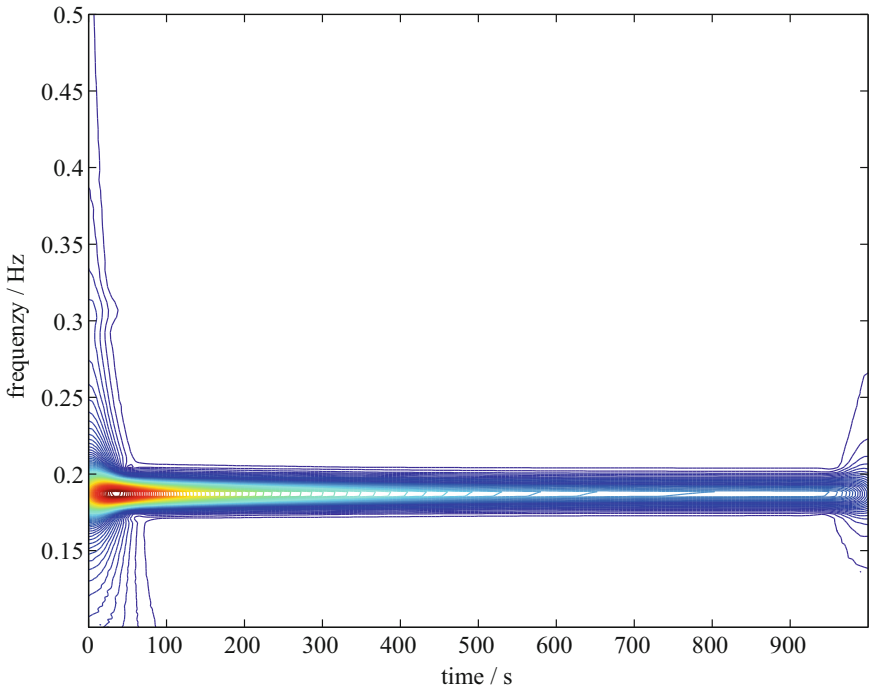

Fig. 33.6 Wavelet analysis of the decay process with the identified sticking force $f_{H,tot} = 4.16\,\text{N}$, initiated on isolated resonance forced by excitation amplitude of 1 N

are sliding. The wavelet analysis is used in Fig. 33.6 to show that no frequency-energy dependence and no other spectral components are showing up. With the identified normal force FRFs are calculated with the MHBM at different excitation levels in Fig. 33.7. It can be seen that the damping arises with increasing amplitude but no declining or progressive bending of the resonance peak can be realized. This also shows the possibility to make the fundamental system frequency independent of the excitation amplitude or the energy.

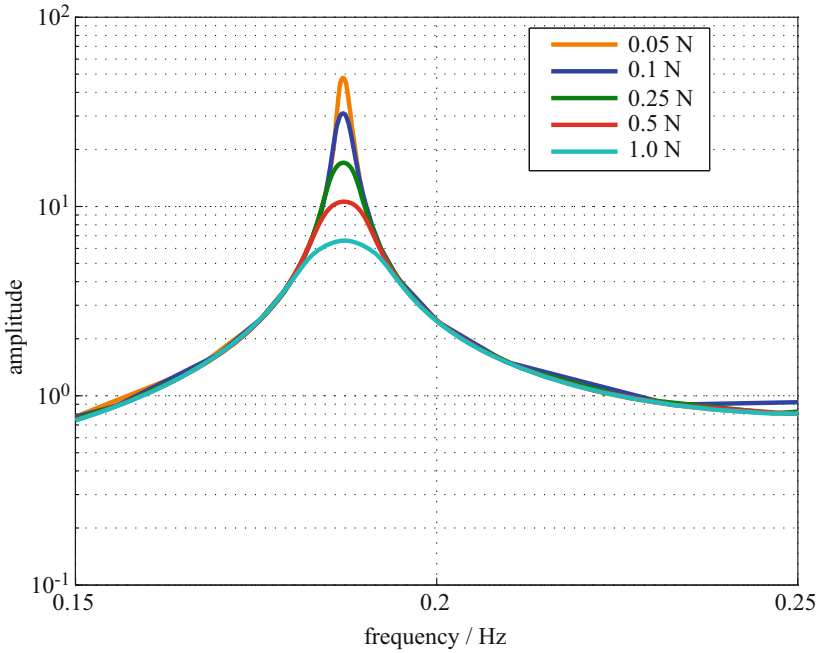

Fig. 33.7 Variation of the excitation amplitude in the identified system. No frequency-energy dependence is recognizable

33.5 Conclusion

It was the aim in this paper to design a frequency-energy independent geometrically nonlinear system by adding a dry friction damper. This was fulfilled for an identified normal force of the friction damper for different excitation amplitudes and energy levels. Several decay processes initiated on an isolated resonance were investigated with a modal approach and the wavelet analysis. This showed congruence with the numerically integrated solutions.

Further investigations can be made for broader parameter variations of the friction damper to reach even higher energy levels. Systems with more complexity and degrees of freedom shall be investigated as well.

References

1. Krack, M.: The Concept of Nonlinear Modes Applied to Friction-Damped Systems, vol. 2014,5 of Berichte aus dem IDS. PZH Verl., TEWISS - Technik und Wissen GmbH, Garbsen, 2014
2. Kerschen, G., Peeters, M., Golinval, J.-C., Vakakis, A.F.: Nonlinear normal modes, part i: a useful framework for the structural dynamicist. Mech. Syst. Signal Process. **23**, 170–194 (2009)
3. Renson, L. Nonlinear modal analysis of conservative and nonconservative aerospace structures. Ph.D. thesis, Université de Liège, Liège, 2014
4. Peeters, M., Viguié, R., Sérandour, G., Kerschen, G., Golinval, J.-C.: Nonlinear normal modes, part ii: toward a practical computation using numerical continuation techniques. Mech. Syst. Signal Process. **23**(1), 195–216 (2009)
5. Jerschl, M., Süß, D., Willner, K.: Numerical continuation methods for the concept of non-linear normal modes. In: Catbas, F.N. (ed.) Dynamics of Civil Structures Conference Proceedings of the Society for Experimental Mechanics Series, vol. 4, pp. 19–26. Springer International Publishing, Berlin. Cham (2014)
6. Jerschl, M., Willner, K.: Arclength continuation methods for the investigation of non-linear oscillating systems with the concept of non-linear normal modes. PAMM **14**(1), 287–288 (2014)
7. Rosenberg, R.M.: Normal modes of nonlinear dual-mode systems. J. Appl. Mech. **27**, 263–268 (1960)
8. Mallat, S.G.: A Wavelet Tour of Signal Processing, 2 edn. Academic, San Diego (1999)
9. Süß, D., Willner, K.: Investigation of a jointed friction oscillator using the multiharmonic balance method. Mech. Syst. Signal Process. **52–53**, 73–87 (2015)
10. Peeters, M., Kerschen, G., Golinval, J.-C.: Dynamic testing of nonlinear vibrating structures using nonlinear normal modes. J. Sound Vib. **330**(3), 486–509 (2011)
11. Lamarque, C.-H., Pernot, S., Cuer, A.: Damping identification in multi-degree-of-freedom systems via a wavelet-logarithmic decrement—part 1: theory. J. Sound Vib. **235**(3), 361–374 (2000)

Chapter 34
Scale-Dependent Modeling of Joint Behavior

Kai Willner

Abstract An investigation of the influence of constitutive friction laws on the damping behavior of dry friction joints is presented. The modeling starts at the micro- scale of the surface roughness leading to constitutive laws with regard to both the normal and tangential contact. These laws are used in a 3D finite element simulation of a simplified model joint. Numerical simulations show the influence of various levels of sophistication of the used contact laws. Here, the influence of high level contact laws proves to be limited in a spatially resolved joint model.

Keywords Joint • Friction • Dissipation • Rough surface • Simulation

34.1 Introduction

Over the last years several attempts have been made to improve the finite element modeling of joints by introducing elaborate constitutive contact laws to improve friction modeling beyond simple Coulomb models, see for example [1–5]. In the following we will present such an elaborate contact law and use it in a finite element model of a simple lap joint. The calculated hysteresis loops and the corresponding dissipated work of this model will then served as a reference model for the identification of simpler models both in terms of complexity of the contact model as well as level of discretization. The maybe not so surprising result is that the elaborate reference model can be fitted quite well using much simpler contact laws, typically by a simple linear penalty formulation in normal and tangential direction.

34.2 Constitutive Contact Laws

The constitutive contact laws derived in this section are obtained by an elasto-plastic halfspace simulation [6–9] of the contact of two rough surfaces. We will present first the rough surface data followed by the results of the halfspace simulations.

34.2.1 Rough Surface

As an example we use a polished steel surface, which has been measured using a laser scanning microscope Keyence VK-X200K. The lateral resolution is $3.3\ \mu\mathrm{m}$, the theoretical vertical resolution is $0.1\ \mathrm{nm}$. To get rid of measurement outliers and other artefacts the raw surface data is smoothed by a moving average filter using $N_{\mathrm{Smooth}} \times N_{\mathrm{Smooth}}$ points with equal weights. The contact of two rough surfaces is then simulated by adding two shifted and rotated cutouts of 512×512 points from the measured surface data.

Since the surface roughness is isotropic, it is sufficient to use a charcterization along a profile. Here, we use a fractal surface characterisation based on the structure function [9]

$$S(x_k) = 2[R_q^2 - \mathrm{ACF}(x_k)]\ , \tag{34.1}$$

K. Willner (✉)
Friedrich-Alexander Universitaet Erlangen-Nuernberg Chair of Applied Mechanics Egerlandstr. 5 91058 Erlangen, Germany
e-mail: kai.willner@fau.de

© The Society for Experimental Mechanics, Inc. 2016

M. Allen et al. (eds.), *Dynamics of Coupled Structures, Volume 4*, Conference Proceedings of the Society for Experimental Mechanics Series, DOI 10.1007/978-3-319-29763-7_34

Table 34.1 Roughness parameters

N_{Smooth}	R_q	x_T	D
1	0.0044	0.0284	1.491
2	0.0042	0.0298	1.253
5	0.0039	0.0307	1.088
10	0.0033	0.0374	1.041
20	0.0024	0.0526	1.024
50	0.0012	0.0911	1.019

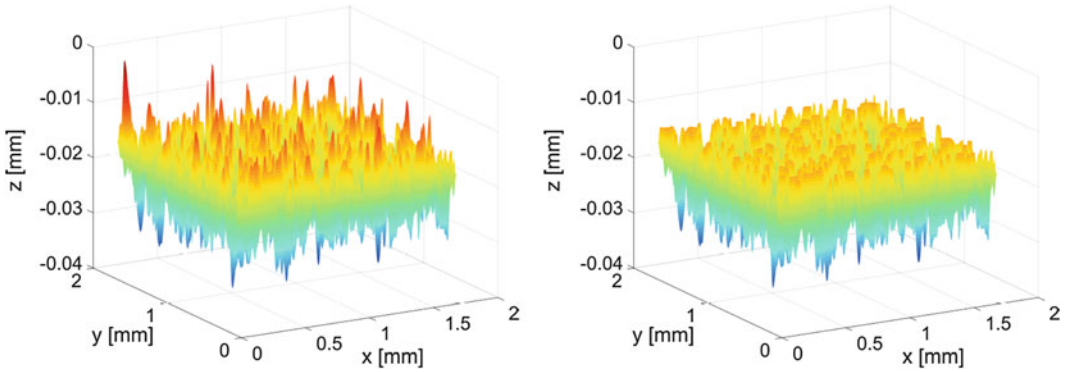

Fig. 34.1 Equivalent rough surface for $N_{\mathrm{Smooth}} = 5$. (*Left*) Undeformed. (*Right*) Deformed after normal loading with $p_0 = 30\ \mathrm{N/mm^2}$

Table 34.2 Material parameters

E	ν	H	$\tau_{\max}$
$2.1\ 10^5\ \mathrm{N/mm^2}$	0.3	$800\ \mathrm{N/mm^2}$	$200\ \mathrm{N/mm^2}$

where $\mathrm{ACF}(x_k)$ is the autocorrelation function given by

$$\mathrm{ACF}(x_k) = \frac{1}{N-k}\sum_{i=1}^{N-k} z_{i+k} z_k \qquad k = 1, \ldots, N-1\ . \tag{34.2}$$

A typical structure function can fitted by the Berry-Blackwell approximation [10]

$$S(x_k) = 2R_q \left\{ 1 - \exp\left[-\left(\frac{x_k}{x_T} \right)^{4-2D} \right] \right\} \tag{34.3}$$

using three resolution independent parameters: rms-roughness R_q, fractal dimension D, and transition length x_T.

The identified roughness parameters are shown in Table 34.1 for increasing filter size. As can be expected, the rms roughness and the fractal dimension decreases with stronger smoothing, while the transition length increases. A value of $N_{\mathrm{Smooth}} = 5$ is chosen in the following as a compromise between sufficient smoothing and preservation of the original roughness features (Fig. 34.1).

34.2.2 Constitutive Contact Laws

The contact is simulated by a numerical halfspace model [11] using a simplified elasto-plastic material law, which limits the local pressure to a maximum hardness value H. For the tangential direction a fully decoupled approach using the Cattaneo-Mindlin assumptions is taken, employing a local Tresca friction law, which limits the local friction stress to a fixed maximum value $\tau_{\max}$. The material parameters are given in Table 34.2.

Typical results for normal and tangential behavior are presented in Figs. 34.2 and 34.3, respectively.

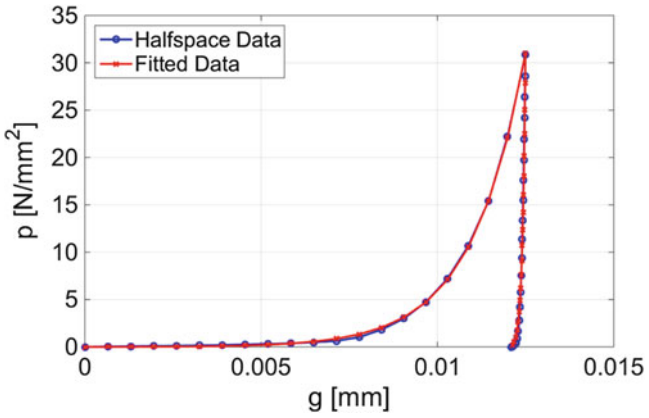

Fig. 34.2 Constitutive contact law in normal direction

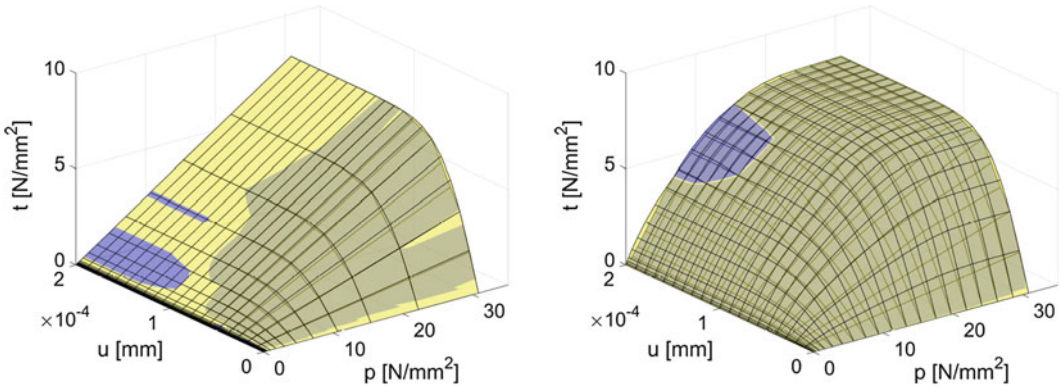

Fig. 34.3 (*Left*) Tangential traction at loading (*Right*) Tangential traction at unloading and reloading (*Blue*: Halfspace simulation, *Yellow*: Fit using five Masing elements)

34.2.2.1 Normal Behavior

Figure 34.2 shows the nominal pressure p_0 as a function of the gap distance g exhibiting the usual progressive behavior.

The results can be fitted quite well using an exponential law for the normal contact

$$p(g) = \begin{cases} C_1 \left[\exp\left(C_2 \frac{g}{R_q} \right) - 1 \right] & \text{if} \quad g > g_{\max} \\ D_1 \left[\exp\left(D_2 \frac{g - g_{pl}}{R_q} \right) - 1 \right] & \text{if} \quad g < g_{\max} \end{cases} \tag{34.4}$$

using the RMS roughness R_q as a normalization and the plastic deformation given by the maximum pressure and gap values as

$$g_{pl} = g_{\max} - \frac{R_q}{D_2} \ln\left(\frac{p_{\max}}{D_1} + 1 \right). \tag{34.5}$$

34.2.2.2 Tangential behavior

Figure 34.3 shows the nominal tangential stress τ_0 as a function of pressure p_0 and relative displacement u for the loading and the unloading case. For the loading case, Fig. 34.3 (Left), one finds a Coulomb-like behavior with a linear increase of the limit macro shear stress with nominal pressure and a small transition zone from stick to full slip with increasing relative displacement. However, for the unloading and reloading case, Fig. 34.3 (Right), one finds a nonlinear traction-pressure relation. This behavior can be fitted quite well by an Iwan-type model employing five parallel Jenkin elements,

$$t = \sum_{j=1}^{n=5} t_j \tag{34.6}$$

Table 34.3 Contact parameters

C_1	C_2	D_1	D_2		
7.5 10^{-3} N/mm^2	2.56	0.31 N/mm^2	43.89		
μ_1	μ_2	μ_3	μ_4	μ_5	α
0.058	0.123	0.057	0.012	0.002	5.20
ξ_1	ξ_2	ξ_3	ξ_4	ξ_5	β
0.3 µm	0.4 µm	1.4 µm	9.1 µm	70.4 µm	1.33

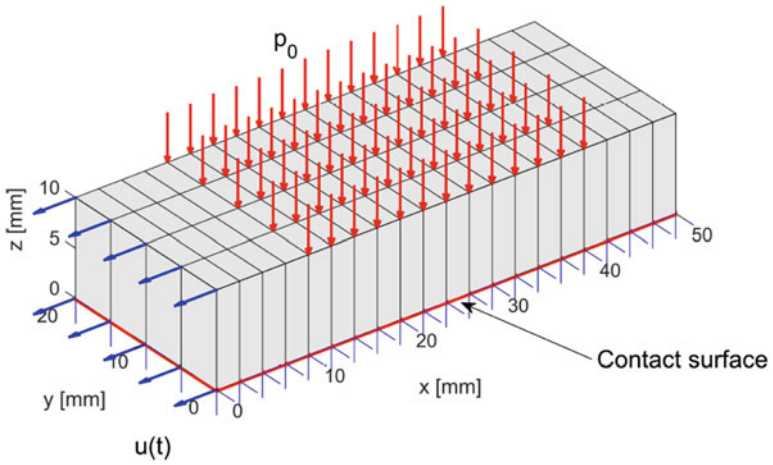

Fig. 34.4 Simple joint model

with

$$t_j = \begin{cases} \frac{p}{\xi_j} u & \text{if} \quad \frac{p}{\xi_j} u \le t_{\max,j} \\ \mu_j p & \text{if} \quad \frac{p}{\xi_j} u > t_{\max,j} \end{cases}, \tag{34.7}$$

where

$$\frac{p}{\xi_j} = C_{t,j} \tag{34.8}$$

resembles a pressure dependent tangential stiffness. The slip limit is given for the loading case $g > g_{\max}$ by

$$t_{\max,j} = \mu_j p \tag{34.9}$$

and for the unloading case $g > g_{\max}$ by

$$t_{\max,j} = \mu_j p \left[1 - \exp\left(-\alpha \left[\frac{p}{p_{\max}} \right]^{\beta} \right) \right], \tag{34.10}$$

where the bracketed term for the unloading case models the nonlinear elastic recovery of the rough surface upon unloading. The parameters of the model are given in Table 34.3.

34.3 Simple Joint Model

A Menq-type set-up [12] as shown in Fig. 34.4 is used as a simple joint model representing one half of a symmetric lap joint. This very simplicistic model and the relatively coarse discretization is chosen to minimize the computational effort during the many evaluations of this model during the following parameter optimizations. For the same reason only quasi-static calculations are performed.

The normal load p_0 is applied over the middle part of the top surface representing a bolt force. The tangential load is then applied by given displacements $u(t)$ at the left side to avoid problems in the macro-slip range.

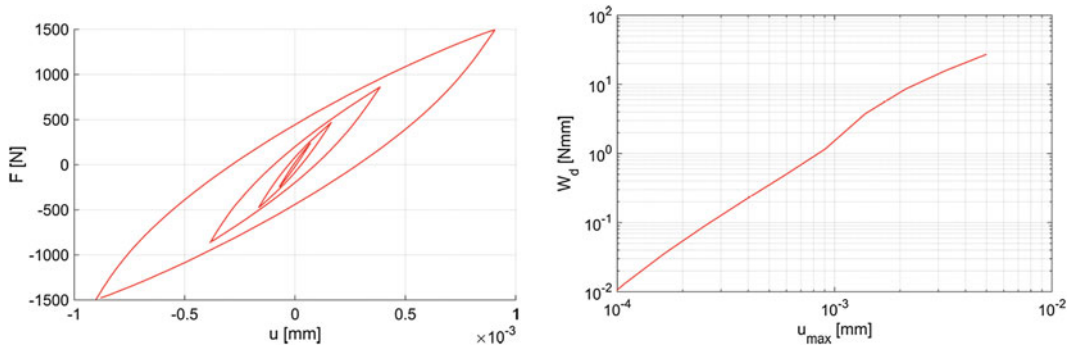

Fig. 34.5 Fine discretization using the constitutive contact law. (*Left*) Typical hysteresis loops (*Right*) Dissipated work

The constitutive contact laws developed in the last section have been implemented in a zero-thickness element formulation and are used in the following as the reference solution. Figure 34.5 shows on the left typical hysteresis loops and on the right the dissipated work calculated at $p_0 = 10\ \mathrm{N/mm^2}$ and various tangential displacement amplitudes.

34.4 Parameter Identification

Using the results of the elaborate constitutive contact laws as a reference, we will try to identify parameters of a much simpler contact model, namely a linear penalty formulation in normal and a simple linear elastic-slip model in tangential direction While the constant friction coefficient is easily identified from the hysteresis loops at macro-slip as $\mu = 0.26$, the normal and tangential penalty parameters C_n and C_t, respectively, are identified using a numerical optimization routine (i.e. Matlab's `fminsearch`) by a least squares fit to the single reference hysteresis loop at $p_0 = 10\ \mathrm{N/mm^2}$ and $A = 0.6\ \mu\mathrm{m}$. This hysteresis loop shows significant dissipation but is still well below the macro slip limit and is thus considered as typical. The identified parameters are $C_n = 8.75\ 10^3\ \mathrm{N/mm^3}$ and $C_t = 6.08\ 10^5\ \mathrm{N/mm^3}$.

Figure 34.6 shows typical hysteresis loops obtained with these linear parameters in comparison with the reference solution obtained with the full nonlinear constitutive contact laws. Obviously the fit is not perfect, but is reasonably good over a considerable range of pressure and amplitudes and thus seems sufficient for most practical purposes. The prediction of dissipation is correct except for very low amplitudes, where the linear model overestimates the dissipation. This corresponds to the hysteresis loops wich are wider for the linear model at small amplitudes. However, for larger amplitudes the difference becomes negligible. The reason for this surprisingly good approximation is the slip behavior. The dissipation is dominated by *partial slip* of the interface, where macroscopic parts of the interface are slipping while others are sticking. This can be resolved by a sufficiently fine discretization of the interface, but using a simple linear contact law. However, micro slip effects as included in the elaborate nonlinear constitutive contact law of Sect. 34.2 do not contribute significantly to the dissipation.

34.5 Reduced Model

Using the coarse mesh shown in Fig. 34.7, the identification of a linear contact model as described above leads to $C_n = 1.44\ 10^4\ \mathrm{N/mm^3}$ and $C_t = 9.67\ 10^4\ \mathrm{N/mm^3}$. The identified contact stiffness values are reasonably close to the ones identified above for the fine discretisation and actually could be interchanged without making any visible difference in the hysteresis or dissipation plots, which are given in Fig. 34.8. The results are still comparable to the fine discretization, even if the influence of the discretization begins to show especially at low amplitudes.

A slight improvement of the approximation at low amplitudes can be obtained by using a pressure dependent tangential stiffness, such that

$$C_t = \frac{p}{\xi} \tag{34.11}$$

where now ξ has to be identified instead of C_t. Numerical optimization using again the single reference hysteresis loop at $p_0 = 10\ \mathrm{N/mm^2}$ and $A = 0.6\ \mu\mathrm{m}$ of the fine model leads to $C_n = 7.33\ 10^3\ \mathrm{N/mm^3}$ and $\xi = 0.16\ \mu\mathrm{m}$. The corresponding results are shown in Fig. 34.9. In comparison to the linear penalty law with fixed tangential stiffness a better approximation

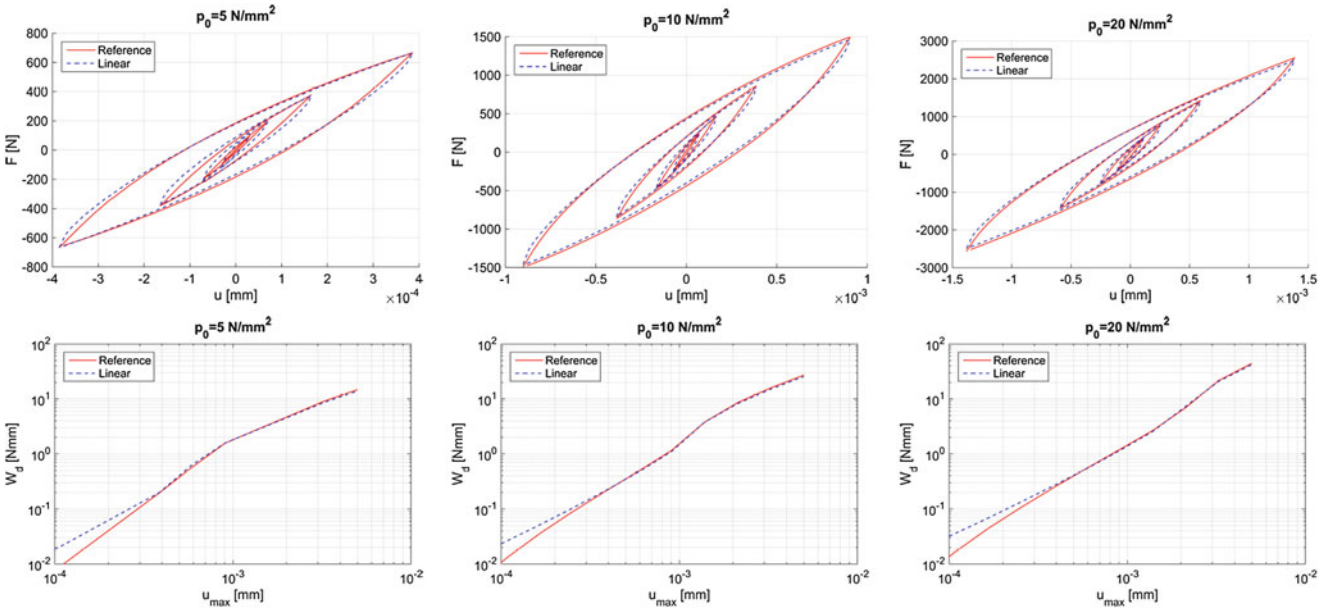

Fig. 34.6 Fine discretization using a linear contact law. (*Top*) Typical hysteresis loops at $p_0 = 5/10/20\ \mathrm{N/mm^2}$ (*Bottom*) Dissipated work at $p_0 = 5/10/20\ \mathrm{N/mm^2}$

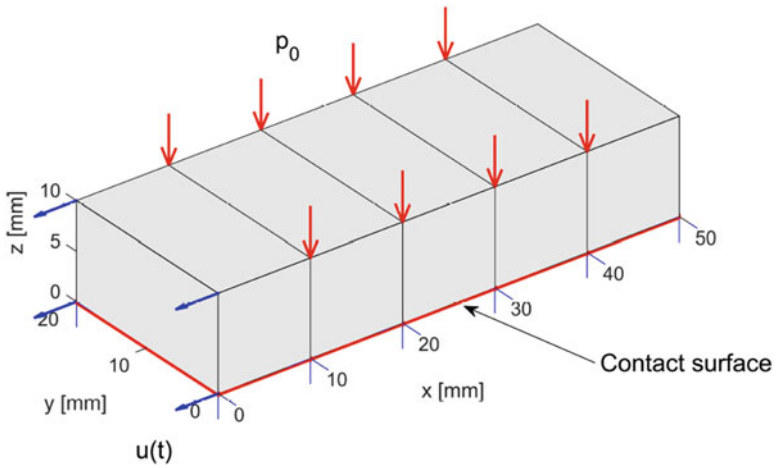

Fig. 34.7 Coarse discretization of joint model

of the hysteresis loops and thus of the dissipated work can be observed for low amplitudes. The improvement is significant at the nominal pressure p_0 used for the identification and lower pressures. However, no improvement can be observed for higher pressures.

34.6 Conclusion

Three major conclusions can be drawn from the presented results:

1. The use of elaborate constitutive contact laws for joint modelling seems unnecessary if the spatial discretization of the contact interface is sufficiently fine to resolve partial slip effects.
2. The use of a pressure dependent tangential stiffness is advisable.
3. The normal stiffness has no pronounced influence.

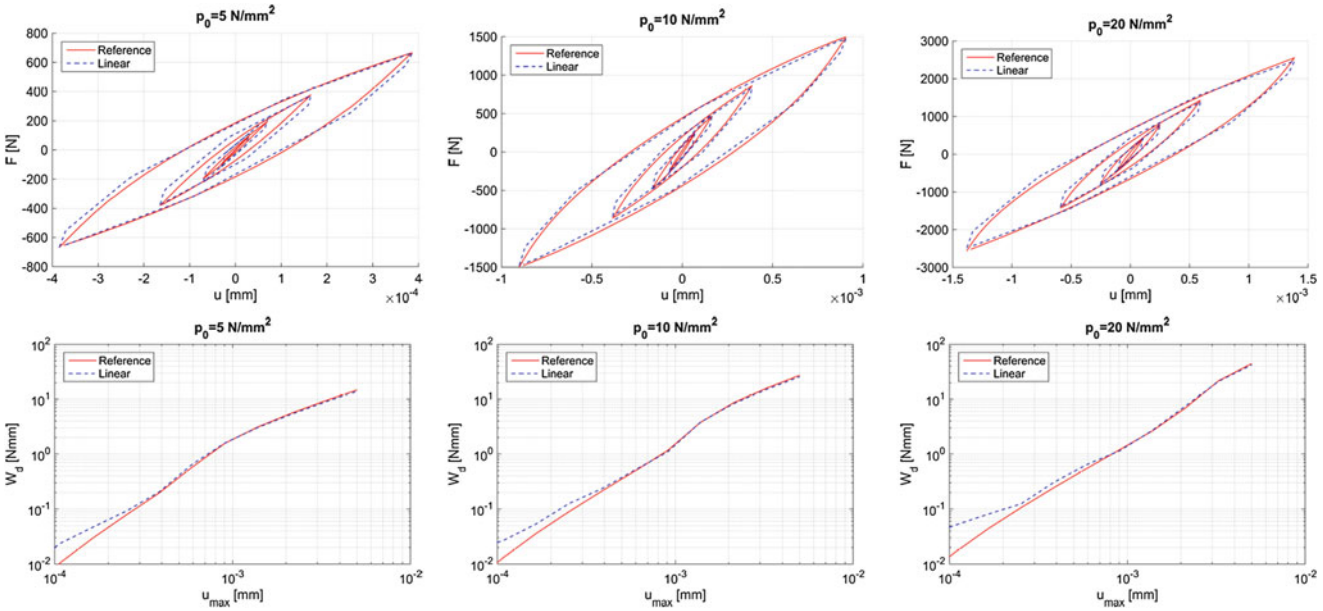

Fig. 34.8 Coarse discretization using a linear contact law. (*Top*) Typical hysteresis loops of coarse model at $p_0 = 5/10/20\ \mathrm{N/mm^2}$ (*Bottom*) Dissipated work at $p_0 = 5/10/20\ \mathrm{N/mm^2}$

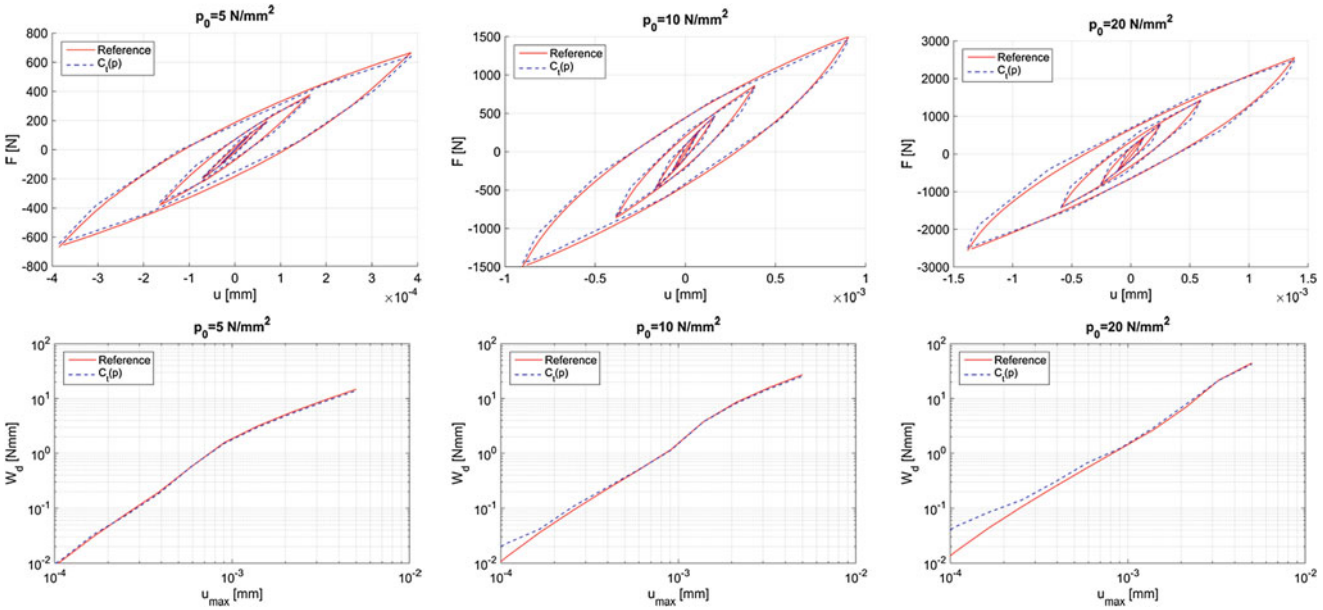

Fig. 34.9 Coarse discretization using a pressure dependent tangential stiffness. (*Top*) Typical hysteresis loops of coarse model at $p_0 = 5/10/20\ \mathrm{N/mm^2}$ (*Bottom*) Dissipated work at $p_0 = 5/10/20\ \mathrm{N/mm^2}$

References

1. Lobitz, D.W., Gregory, D.L., Smallwood, D.O.: Comparison of finite element predictions to measurements from the Sandia microslip experiment. In: Proceedings of the International Modal Analysis Conference IMAC XX, Los Angeles, pp. 1388–1394 (2001)
2. Koh, K.-H., Griffin, J.H., Filippi, S., Akay, A.: Characterization of turbine blade friction dampers. In: Proceedings of ASME Turbo Expo 2004 (2004). CD-ROM
3. Mayer, M., Gaul, L.: Segment-to-segment contact elements for modelling joint interfaces in finite element analysis. Mech. Syst. Signal Process. **21**, 724–734 (2007)
4. Bograd, S., Reuss, R., Schmidt, A., Gaul, L., Mayer, M.: Modeling the dynamics of mechanical joints. Mech. Syst. Signal Process. **25**, 2801–2826 (2011)

5. Sitzmann, S., Willner, K., Wohlmuth, B.I.: A dual lagrange method for contact problems with regularized frictional contact conditions: modelling microslip. Comput. Methods Appl. Mech. Eng. **285**, 468–487 (2015)
6. Kalker, J.J., van Randen, Y.: A minimum principle for frictionless elastic contact with application to non-Hertzian half-space contact problems. J. Eng. Math. **6**, 193–206 (1972)
7. Tian, X., Bhushan, B.: A numerical three-dimensional model for the contact of rough surfaces by variational principle. J. Tribol. **118**, 33–42 (1996)
8. Willner, K.: Elasto-plastic normal contact of three-dimensional fractal surfaces using halfspace theory. J. Tribol. **126**, 28–33 (2004)
9. Willner, K.: Influence of surface parameters on the elastoplastic contact behavior of fractal-regular surfaces. J. Tribol. **130**, 024502–1–024502–6 (2008)
10. Berry, M.V., Blackwell, T.M.: Diffractal echoes. J. Phys. A **14**, 3101–3110 (1981)
11. Willner, K.: Fully coupled frictional contact using elastic halfspace theory. J. Tribol. **130**, 031405–1–031405–8 (2008)
12. Menq, C.H., Bielak, J., Griffin, J.H.: The influence of microslip on vibratory response. J. Sound Vib. **107**(2), 279–307 (1986)

Chapter 35
Robust Occupant Detection Through Step-Induced Floor Vibration by Incorporating Structural Characteristics

Mike Lam, Mostafa Mirshekari, Shijia Pan, Pei Zhang, and Hae Young Noh

Abstract The objective of this paper is to present an occupant detection method through step-induced structural vibration. Occupant detection enables various smart building applications such as space/energy management. Ambient structural vibration monitoring provides a non-intrusive sensing approach to achieve that. The main challenges for structural vibration based occupant footstep detection include that (1) the ambient structural vibration noise may overwhelm the step-induced vibration and (2) there are various other impulse-like excitations that look similar to footstep excitations in the sensing environment (e.g., door closing, chair dragging, etc.), which increase the false alarm rate for occupant detection. To overcome these challenges, a two-stage step-induced signal detection algorithm is developed to (1) incorporate the structural characteristics by selecting the dominant frequencies of the structure to increase the signal-to-noise ratio in the vibration data and thus improve the detection performance and (2) perform footstep classification on detected events to distinguish step-induced floor vibrations from other impulse excitations. The method is validated experimentally in two different buildings with distinct structural properties and noise characteristics, Carnegie Mellon University (CMU) campus building and Vincentian Nursing Home deployments in Pittsburgh, PA. The occupant footstep detection F1 score shows up to 4X reduction in detection error compared to traditional thresholding method.

Keywords Occupant detection • Structural vibration • Wavelet analysis • One-class classification • Natural frequency

35.1 Introduction

Accurately detecting occupants is an important starting point for successful analysis of occupant information. Occupant detection has extensive applications in smart infrastructures. For example, detecting occupants can help understand infrastructure utilization and thus improve maintenance schedule and management. Furthermore, the presence and number of occupants can aid HVAC control for energy management purpose.

Current indoor occupant detection makes use of several types of sensors, and each has its own benefits and limitations. The main sensor types include cameras, infrared (IR) sensors, radio frequency (RF) sensors, acoustic sensors, and vibration sensors [1–8]. Cameras, IR sensors, and RF sensors require line-of-sights to capture occupants, which introduces difficulty in installation. RF sensors also face the multipath problem, which makes the sensing sensitive to the ambient environment. Acoustic sensors detect occupant presence by their talk or footstep sounds, however such methods are often sensitive to high ambient noise in the sensing environment. In addition, under some scenarios users do not want their images being captured in cameras and their conversations being recorded by microphones due to privacy reasons. The vibration sensors are used for pedestrian spatio-temporal information sensing [9–11], however the application's performance depends on the footsteps detection performance.

We use vibration sensors in this paper to detect occupants due to its non-intrusive deployment nature, which makes the system easy to install and maintain. The main idea of our method is to detect individual occupants through their footstep-induced vibration in the building structure. Challenges for occupant detection through ambient structural vibration sensing are mainly two folds: (1) the ambient structural vibration noise may overwhelm the step-induced vibration signals; and (2) various other impulse excitations in the environment generate vibration signals similar to step-induced signals, thus introduce false alarms (low precision) on footstep-induced vibration detection.

M. Lam (✉) • M. Mirshekari • H.Y. Noh
Department of Civil and Environmental Engineering, Carnegie Mellon University, 5000 Forbes Avenue, Pittsburgh, PA 15213, USA
e-mail: yanpuil@andrew.cmu.edu

S. Pan • P. Zhang
Department of Electrical and Computer Engineering, Carnegie Mellon University, Building 23, Moffett Field, CA 94035, USA

© The Society for Experimental Mechanics, Inc. 2016

M. Allen et al. (eds.), *Dynamics of Coupled Structures, Volume 4*, Conference Proceedings of the Society for Experimental Mechanics Series, DOI 10.1007/978-3-319-29763-7_35

In this paper, we present an algorithm to detect occupants through step-induced floor vibration that takes those challenges into account. To address the first challenge, the signal is decomposed into specific components, which correspond to the natural frequencies of the structure. Vibration responses of a structure amplify near natural frequencies of the structure, which results in a higher signal-to-noise ratio (SNR) at these frequencies. Thus, focusing on the vibration signal components at natural frequencies allows higher recall rate for detection comparing to using the original signal. Wavelet analysis is used for decomposing the signal. To exclude non-step impulse excitations detected, the system runs a classification algorithm to determine whether the detected signals are induced by occupant footsteps.

The algorithm consists of two modules: structure characterization and occupant footstep detection. The structure characterization module is an offline component of the algorithm, which identifies the floor structure characteristics needed for subsequent modules. The occupant footstep detection module is an online component of the algorithm, which includes event detection and event classification. In the event detection module, various impulse-like events (footsteps or other excitations, such as ball dropping, door closing, crutches, etc.) are detected from the incoming signal. In the event classification module, the detected events are classified into step events or non-step events. The algorithm is validated in one of the Carnegie Mellon University (CMU) campus buildings and a nursing home in Pittsburgh, Vincentian Home, to show the detection algorithm performance in different structures with different usages. The CMU campus building is a 3-story reinforced concrete commercial building with offices, classrooms and lecture theatres. The Vincentian Home is a 3-story steel residential building with 60 elderly resident rooms. The results show up to 4X reduction in detection error compared to traditional thresholding method.

The main contributions of the paper are:

- We proposed a two-stage footstep detection algorithm that incorporates structural characteristics to increase detection performance.
- We present an algorithm that distinguishes footstep-induced signals from other detected impulse excitations signal to achieve occupant detection.
- We evaluated the algorithm with implementations at different buildings, including a commercial school building at CMU and a residential building at Vincentian Nursing Home.

The rest of the paper is structured as follows. Section 35.2 covers literature survey on techniques and background information related to the project. Sections 35.3 and 35.4 explain the developed algorithm and its evaluation, respectively. Finally, Sect. 35.5 describes future works, and Sect. 35.6 concludes the paper.

35.2 Literature Survey

Many footstep detection algorithms consist of feature extraction using signal processing and detection using machine learning. Proposed features for detecting human footstep excitations, based on which domain of the signal they are analyzing, can be classified into three categories: time, frequency, and time-frequency domain analysis. Some of the features defined using a time domain approach include auto-regressive models [12, 13], auto-correlation functions [14], and kurtosis [15, 16]. However, underlying structure, surrounding noise, and the non-stationary property of footstep signal bring inconsistency to the waveform in time domain and makes robust footstep signal detection difficult. Features defined using a frequency domain approach mainly include spectrum of the signals [17]. The main shortcoming of frequency domain based features is their unsuitability for dealing with non-stationary transient excitations such as footstep-induced vibration signals. Finally, some of the features defined using a time-frequency domain approach include the wavelet energy [18], PWV distribution assisted Renyi entropy (PWVD-RE) [19], and wavelet packet node energy (WPNE) [20]. The advantage of using time-frequency based features is their ability to deal with non-stationary signals (e.g., footsteps, seismic waves, impact loads) [18, 21–24]. Thus, we use wavelet analysis for floor characterization and event detection, as discussed in Sect. 35.3.

For classification, we investigate the cases in which there are only one class samples (positive class) available for training. Outlier detection with one-class classification (OCC) has been developed in machine learning community for this purpose [25]. OCC aims to build classifier when negative class is not available, is poorly sampled or not well defined [26]. Our objective of classification is to separate the excitations induced by steps from other excitations. However, we do not know all the possible non-step excitations. There could be unexpected excitations which are not collected in the signal library for training the classifier in database-based approaches. In our case, OCC allows us to train the classifier just by footstep signals. Major OCC algorithms are based on one-class ensembles, neural networks, decision trees, nearest neighbors, and Bayesian classifiers [26]. Among them, One-class SVM (OSVM) has been extensively studied and widely applied with various parameter estimation methods [26–30]. Researchers have used it for fall detection [31], intrusion detection [32],

machine fault detection [33], document classification [34], sound classification [35] and extraction of brain tumor from MR images [36]. We use the OSVM algorithm in this paper to map the data into the feature space using the radial basis function kernel and then to classify with maximum margin [37].

35.3 Occupant Detection Algorithm Using Structural Characteristics

The proposed algorithm detects occupants through detecting general events and then classifying footsteps from other excitations. To do this it has an *offline* component which characterizes the structure and an *online* component which performs footstep detection incorporating the structure characteristics.

Figure 35.1 shows the components of the system. Ambient floor vibration signal captured contains both events that we like to measure (e.g., footsteps, door closing, objects dropping, etc.), as well as noise that we do not want to measure (i.e., all signals other than events). These signals are propagated through the unique building structure and is absorbed at different rates. Therefore, in the offline component, ambient vibration noise is analyzed to characterize this process in order to improve signal to noise ratio for subsequent modules. This structure characterization procedure is described in Sect. 35.3.1.

Then, with that characterization, the online component detects occupants through two modules, (1) event detection and (2) event classification. Event detection is performed to distinguish event signals from the noise signals by thresholding on

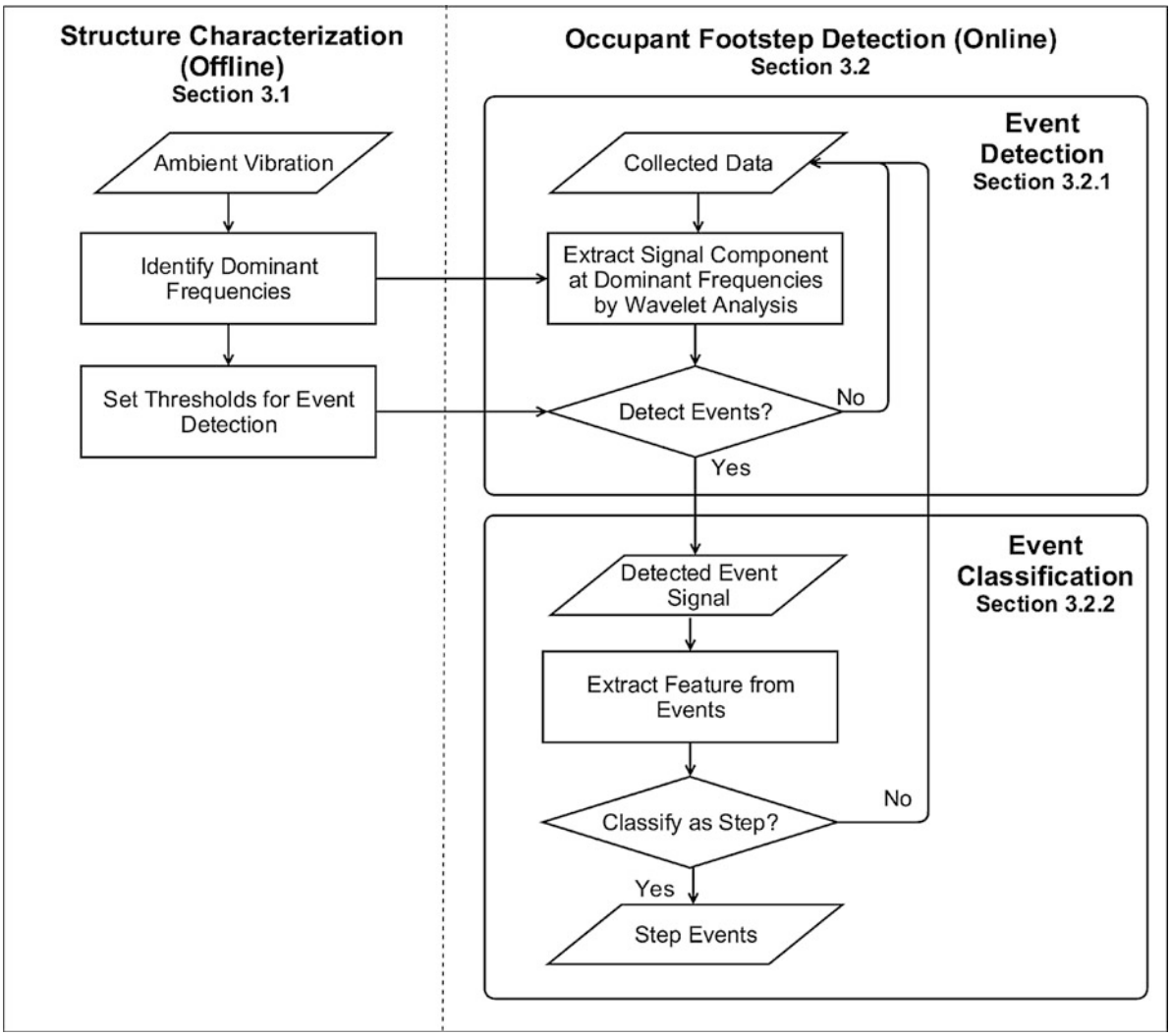

Fig. 35.1 Algorithm flowchart

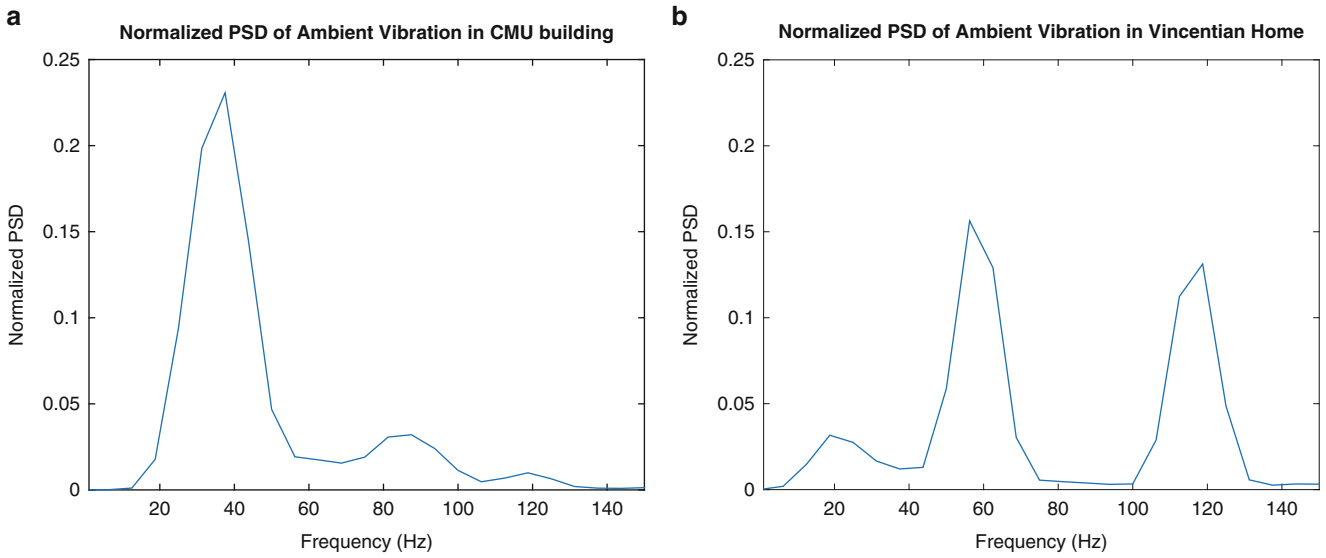

Fig. 35.2 Normalized PSD of ambient vibration in two different buildings. (**a**) CMU campus testing location. (**b**) Vincentian home testing location

the signal component at dominant structural frequencies base on the offline module. We detail this approach in Sect. 35.3.2.1. If an event is detected, event classification then classifies the resulting event as a step event (an occupant is detected) or a non-step event. We describe this approach in Sect. 35.3.2.2.

35.3.1 Structure Characterization

Structure characterization is necessary to improve the signal quality thus increasing the signal to noise ratio of the events. Using the fact that the vibration is amplified near natural frequencies, this module identifies the dominant vibration frequencies from collected floor ambient vibration data and then set threshold for Event Detection.

The algorithm first *identifies dominant frequencies* of the unique building structure that can potentially be used to better identify events. It does this by first finding the percentage of energy contribution at each frequency of the ambient vibration signal captured when minimal footsteps or other excitations are present. This is accomplished by computing the normalized power spectrum density (PSD). Then the algorithm applies peak picking [38] on the normalized PSD to obtain the dominant frequencies of the structural vibration. These dominant frequencies are important to the analysis because these frequencies include the natural frequencies of the structure. Vibration at natural frequencies is amplified and footsteps far away from sensor will have a higher chance to be detected if they have frequency components at the natural frequencies. Fourier transform, instead of time-frequency domain analysis, is used here because the background signal is relatively stationary, thus inspecting the Fourier transform is sufficient to provide insights on structural characteristics while being computationally more efficient than time-frequency analysis. Figure 35.2 shows normalized PSDs in two different buildings which show different values of dominant frequencies, confirming the need of structure characterization.

With the analysis on the normalized PSD, the algorithm *sets thresholds to be used for online event detection* module by applying the wavelet analysis on the signals. Wavelet analysis is commonly used for analyzing non-stationary signals (such as step-induced vibration signal). we used continuous wavelet transform (CWT) to measure the similarity between target signal and wavelet filter stretched to different extent (scale) at different time (shift). The choice of the wavelet filter is determined to be Mexican hat wavelet because of the resemblance between the footstep induced signal shape and a combination of the Mexican hat wavelet filters at different scales [39]. Figure 35.3 shows a sample footstep signal and its CWT output. The following equation explains the wavelet transform of function f, with wavelet filter ψ at different scales s, shift u and time t.

$$Wf(s,u) = \int_{-\infty}^{\infty} f(t) \frac{1}{\sqrt{s}} \psi^*\left(\frac{t-u}{s}\right) dt \tag{35.1}$$

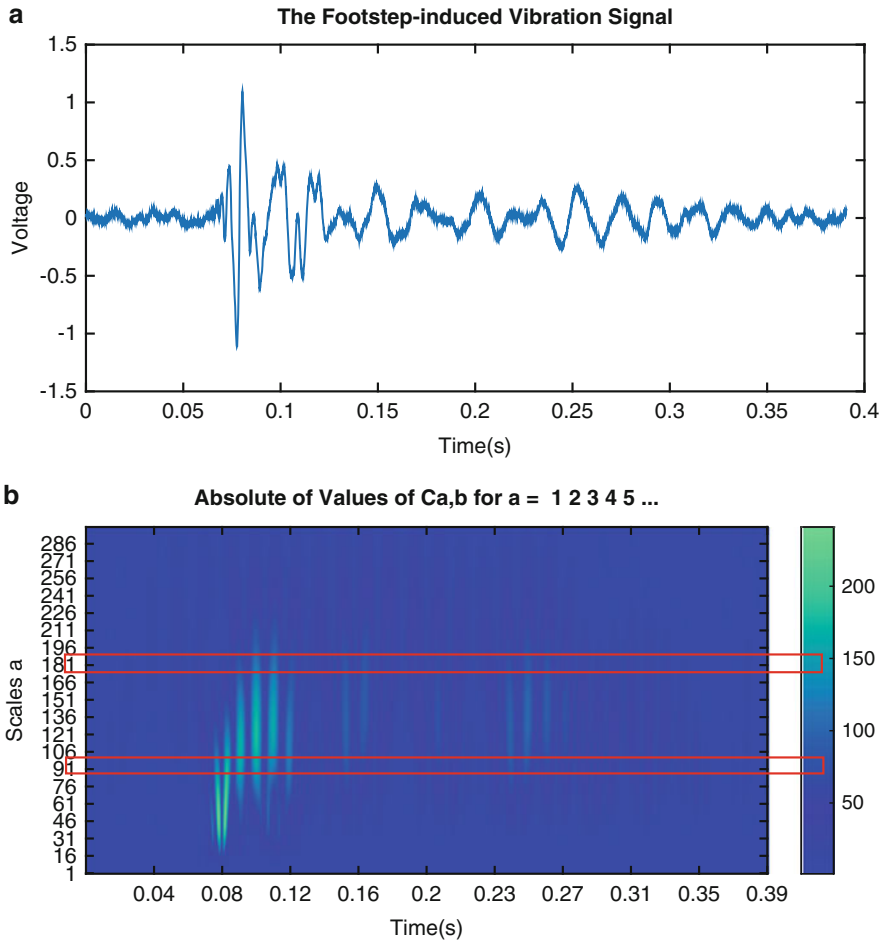

Fig. 35.3 Wavelet analysis of a signal induced by a sequence of footsteps. (**a**) shows the step-induced signal, and (**b**) shows the CWT of the signal. The *red boxes* indicate the scales that correspond to dominant frequencies of floor vibration

ψ^* represents complex conjugate of ψ. To determine the threshold value for the signal component at dominant frequencies, the corresponding wavelet scales are computed, and CWT is performed at these scales. The output wavelet coefficient matrix is used to compute the thresholds for each scale. Assuming the ambient vibration noise is a Gaussian noise, at each scale, one standard deviation above the mean ($\mu + \sigma$) of the squared wavelet coefficients is set to be the threshold for that scale. The reason for using one standard deviation is that we only exclude noise with high certainty so that more possible events can be discovered and analyzed. More footsteps and noise will be detected and false alarm rate will increase at this stage because of the low threshold. However the false alarms will be filtered as non-step events in the event classification module.

The dominant frequencies and the thresholds are passed to occupant footstep detection module described in Sect. 35.3.2. Structural characterization module needs to be performed offline when the system is first deployed in a new structure.

35.3.2 Occupant Footstep Detection

The online component of the algorithm is responsible for detecting footsteps. It is a two-stage footstep detection algorithm which includes an event detection sub-module (that identifies all possible events) and an event classification sub-module (that determines if an event is a footstep). The online component continuously analyzes incoming vibration signals, detects possible events, and classifies footstep events from other excitations.

35.3.2.1 Event Detection

The goal of event detection module is to capture all possible events that can be footsteps as well as other excitations such as door closing. It obtains information such as dominant frequencies and thresholds for each corresponding frequency from structural characteristic module (Sect. 35.3.1). Since footstep signals are non-stationary, CWT is applied in this module to detect events. A lenient threshold value, $\mu+\sigma$, from offline component is adopted in order to detect more steps, as mentioned in Sect. 35.3.1. Therefore, some noise may be detected as an event and then classified as non-step event in event classification sub-module.

After converting dominant frequencies into wavelet scales of Mexican hat wavelet filter, CWT at these scales is performed on collected signal to obtain a matrix of wavelet coefficients. At each scale, the algorithm searches for possible events that have squared wavelet coefficients exceeding the threshold. If several dominant frequencies are found, event detection is performed at these frequencies (scales) simultaneously. The combination of scales allows more events to be detected, since the events may have different frequency contents and different events may exceed threshold in different dominant frequencies. If wavelet coefficients exceed thresholds at one or more frequencies, an event is said to be occurred.

35.3.2.2 Event Classification on Detected Events

In event classification module, detected events described earlier are classified into step events and non-step events.

The first step is to extract features from the detected events. PSD under 150 Hz is used as the main feature for classification in this paper because human footstep frequency range mostly lies in this range [2, 17, 40]. The frequency components contributing less than 1 % of total signal energy are set to be 0 to reduce the noise effects in classification.

In the proposed algorithm, one-class SVM (OSVM) is adopted as the classification method since in real settings, the sources of excitations and noise are unknown a priori. Collection of training samples for all possible excitation sources is both time-consuming and inefficient. One-class classification using OSVM allows us to classify footsteps with only positive training samples (footstep signals).

According to the OSVM proposed by Schölkopf, the objective is to separate all data points from the origin in feature space and maximize the distance from the separating hyperplane to the origin [29, 37]. An important parameter for this method is the regularization parameter ν. It is the upper bound on the fraction of margin errors (outliers) and the lower bound of the fraction of support vectors relative to the total number of training examples. Trade-off between the power to identify other excitations and detecting footsteps is controlled by the ν parameter. A small value of ν will lead to a small number of outliers in training samples, while a large value of ν will lead to more outliers. Therefore, a smaller ν fits the training data well and classifies test samples closer to training samples as steps. It should have lower true positive rate and a high true negative rate. As ν increases, the true positive rate should increase and true negative rate should decrease. In this paper, ν is selected by searching through 0 to 1 at an interval of 0.01. The ν value achieving the best cross-validation result is adopted for the building. The dual expression to be minimized is shown in Eq. (35.2).

$$0.5 \sum_{jk} \alpha_j \alpha_k G(x_j, x_k) \tag{35.2}$$

with respect to $\alpha_1, \ldots \alpha_n$, subject to $\sum \alpha_j = n\nu$ and $0 \leq \alpha_j \leq 1$ for all $j = 1, \ldots n$. G is the Gram matrix of which each element is defined by the inner product of the transformed predictors using a kernel function.

35.4 Evaluation

In order to evaluate the performance of the proposed algorithm on detecting and classifying footsteps from other impulse excitations, experiments were carried out in two buildings: CMU campus building and Vincentian Nursing Home. The CMU campus building is a 4-story concrete building with offices, classrooms, and lecture theatres. The Vincentian Home is a 3-story steel frame residential building housing 60 elderly residents. The event detection and classifier are trained and cross-validated for each building. Evaluation metrics adopted here are precision, recall rate, and F1 score. Section 35.4.1 covers the experiment details, and Sect. 35.4.2 covers the results and discussion.

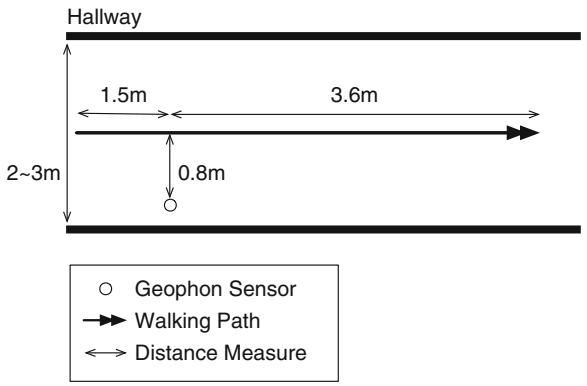

Fig. 35.4 Experimental setup

35.4.1 Description of Experiments

Two sets of experiments are conducted for testing the algorithm under various excitation scenarios. The first dataset (dataset 1) is occupant step-induced structural vibration signals, collected with multiple people walking in one direction for about 5 m under the scenario shown in Fig. 35.4. The second dataset (dataset 2) is structural vibration signals induced by impulse-like excitations other than footsteps, within a 3.5 m radius around the sensor. The impulses investigated here include objects dropping, chair dragging, and door closing from the CMU campus building, and walker hitting ground and wheelchair pushing from Vincentian Nursing Home. This dataset is combined with the first dataset to evaluate the event classification algorithm.

The structural characteristics of the floors in two test sites are different, which allows us to evaluate the robustness of algorithm for different structures. The test location in the CMU campus building is a concrete floor area on ground floor (referred to as CMU Testing Location). Testing in Vincentian Home includes carpeted concrete hallway on a metal deck (referred to as Vincentian Home Testing Location). These locations are hallways with the widths between 2–3 m. The setup is shown in Fig. 35.4. One geophone (SM-24) is used with a DAQ assistant to collect vibration signal at 25.6 kHz to explore wide frequency band [41]. Twenty traces (seven steps each) of walking are collected at each testing location and five sets of each excitation mentioned above are collected.

35.4.2 Results and Discussion

The metrics used to evaluate the footstep detection rate include precision, recall rate, and the resulting F1 score. Traditional threshold method using time domain signal energy is compared as a baseline with the proposed algorithm [10]. The performance of the event detection module alone and the full two-stage footstep detection algorithm is evaluated. The recall rate [Eq. (35.3)] represents the ratio of the number of detected true footsteps to that of all true footsteps and is adopted here to validate the improvement of event detection rate of our algorithm compared to the baseline. The precision rate [Eq. (35.4)] represents the ratio of detected true footstep to that of all detected footsteps and is used to evaluate the event classification's false alarm elimination effects. The F1 score [Eq. (35.5)] is the overall performance metric on the algorithm's ability to detect step-induced signals. The results are presented in Fig. 35.5 and each result will be discussed in the following subsections.

$$Recall = \frac{True\ Positives}{True\ Positives + False\ Negatives} \tag{35.3}$$

$$Precision = \frac{True\ Positives}{True\ Positives + False\ Positives} \tag{35.4}$$

$$F_1 = 2 \cdot \frac{precision \cdot recall}{precision + recall} \tag{35.5}$$

Where True Positives mean the number of detected footstep events, False Positives mean the number of detected non-footstep events, and False Negatives mean the number of missed footstep events.

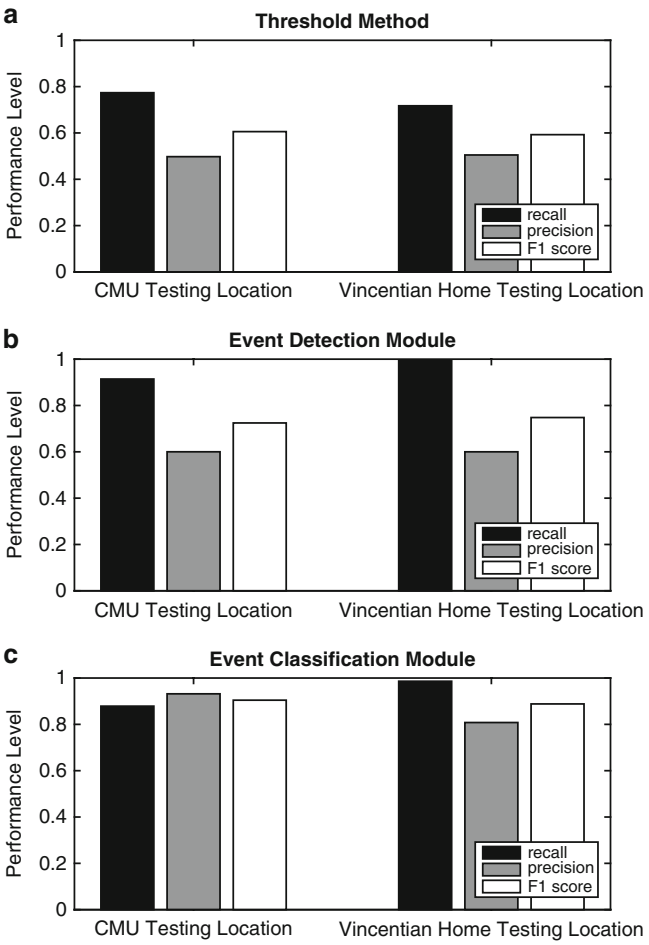

Fig. 35.5 Recall, Precision Rates and F1 score for Proposed Algorithm and Traditional Energy Threshold Based Method. The event detection module alone shows an up to 20 % improvement on recall rate comparing to the baseline. The event classification module shows an additional 20 % improvement on precision rate comparing to event detection module only case. (**a**) Performance of threshold method at testing locations. (**b**) Performance of event detection module at testing locations. (**c**) Performance of event classification method at testing locations

35.4.2.1 Baseline Method

Traditional threshold method is adopted as the baseline method to compare the performance with our detection algorithm [10, 42, 43]. The threshold method performs outlier detection by keeping track of surrounding ambient noise level. Events are detected whenever the measured signal has a energy level falling out of the $\mu + 3\sigma$ range, assuming the noise is modeled as Gaussian distribution with average of μ and standard deviation of σ. The algorithm keeps updating the Gaussian noise model when there is no event detected.

The results of applying the baseline method on all the data show the average of 0.75 recall rate, 0.50 precision, and 0.60 F1 score at the two test locations. Detailed breakdown of results for the two buildings are given in Table 35.1. The baseline method demonstrates low precision rate, i.e., high false alarm rate, because the events detected from dataset 2 cannot be distinguished as non-step events and therefore are false alarms. The recall rate of the baseline method is also relatively low. That is because when a footstep impulse is far away from the sensor or has a low amplitude, the step-induced vibration signal is then overwhelmed by the ambient noise and cannot be detected, therefore causing miss count. The baseline method fails to detect events under such condition due to the following factors: (1) noise amplitude varies in different locations, and when the signal-to-noise ratio is low, the detection may fail, and (2) the ambient vibration noise fail to meet the assumption of Gaussian noise model may lead to detection failure.

Table 35.1 Recall, precision, and F1 score for CMU and Vincentian Home testing locations using baseline method

	CMU testing location	Vincentian home testing location	Average
Recall	0.77	0.72	0.75
Precision	0.50	0.50	0.50
F1 Score	0.61	0.60	0.60

Table 35.2 Recall, precision, and F1 score for CMU and Vincentian Home testing locations using event detection module

	CMU testing location	Vincentian home testing location	Average
Recall	0.91	0.99	0.95
Precision	0.60	0.60	0.60
F1 Score	0.72	0.75	0.74

Table 35.3 Recall, precision, and F1 score for CMU and Vincentian Home testing locations using event detection and classification modules

	CMU testing location	Vincentian home testing location	Average
Recall	0.88	0.99	0.93
Precision	0.93	0.81	0.87
F1 Score	0.90	0.89	0.90

35.4.2.2 Event Detection Module

The event detection module aims to detect footsteps in time-frequency domain by incorporating structural characteristics. Analyzing signal component at dominant frequencies instead of the entire spectrum reduces the effect of surrounding ambient noise level on detection rate. The results of the event detection module show a higher recall rate and an improved precision rate, compared to the baseline method, as shown in Table 35.2. It shows approximately 10 and 20 % improvement in precision and recall rates, respectively. The 20 % improvement on recall rate suggests that our approach to investigate the signal component at dominant frequencies is able to discover more events and less sensitive to noise. The increase in precision rate in this case could be caused by the increase of the true positive cases. The average precision of applying the event detection module is at 0.60, due to the false alarms caused by the lack of the ability to classify between step events and non-step events. Therefore, such results indicate the need for classification module to classify detected excitations correctly.

35.4.2.3 Event Classification Module

Given that the event detection module alone cannot distinguish footstep events from other impulse-like excitation events, the event classification module aims to separate the footstep events using the normalized PSD.

The average of precision rate has reached 0.87 and the average recall rate is 0.93. More detailed results are shown in Table 35.3. There is a slight decrease in recall rate as compared to the event detection module, which is caused by mis-classification on the True Positive cases. The precision rate is improve by over 20 %, due to the elimination of the non-step events through classification. Comparing with the baseline method, the detection algorithm shows an improvement of over 30 % in precision and approximately 20 % in recall rate, which translates to up to 4X reduction in detection error. This indicates that our footstep detection algorithm can detect events surrounded by ambient vibration noise and eliminate other impulse-like excitations as non-step events.

35.5 Future Work

The future work related to footstep sensing can be vast. Particular to the topic covered in this paper we see two main directions for future work: improve robustness to noise and to structure variation. To improve the robustness to noise under different situations, we will explore more features in both time and frequency domains. We will also investigate the effects

of different walking patterns and more factors affecting the wave propagation. Structural variation is another remaining challenge. Footstep-induced signals propagate through the floor structure to reach the sensor. Thus, structural characteristics affect the collected signal forms, which influences the detection algorithm performance. This leads to the need for separate calibration and training for each location. We plan to overcome this challenge through developing a structure independent features for footstep signal detection.

35.6 Conclusions

Detecting occupants can provide essential information for smart infrastructure applications. In this paper, we utilized human footstep induced floor vibration to detect occupants in buildings. The advantages of this approach includes non-intrusive nature, ease of setup and maintenance. The main challenges regarding the footstep detection using vibration sensors are: (1) the signal-to-noise ratio is often low, which result in high rate of missed detection. (2) it is possible to detect other impulse-like excitations instead of footsteps as the shape of the signals received is similar, especially in time domain. To overcome these challenges, we proposed a two-stage footstep detection algorithm, which by incorporating structural characteristics, is able to increase detection performance. The proposed algorithm involves structure characterization module and occupant footstep detection module. In structure characterization module, the dominant frequencies of the floor structure is obtained from ambient vibration. Occupant footstep detection module consists of two sub-modules: event detection and event classification. Event detection sub-module is carried out to detect events, which can potentially be footsteps or other impulse excitations, using the vibration signal components at floor dominant frequencies. The signal at the dominant frequencies is amplified higher than other frequencies, which leads to higher signal-to-noise ratio, and hence improves step detection accuracy. Then, event classification sub-module classifies the detected events into step events or non-step events. Two-stage footstep detection algorithm is used for footstep detection in two buildings with different structure and usage pattern. We validated our two-stage detection algorithm in both a Carnegie Mellon University building and Vincentian Nursing Home. The results show up to 50 % improvement over the traditional threshold method, which also translates to up to 4X reduction in detection error.

Acknowledgements This work is partially supported by National Science Foundation (NSF) under awards CNS-1149611, Pennsylvania Infrastructure Technology Alliance (PITA), CMU-SYSU Collaborative Innovation Research Center (CIRC), Intel, Nokia, and Renault. The authors would also like to acknowledge Vincentian Nursing Home for providing deployment sites to conduct experiments and collect data.

References

1. Teixeira, T., Dublon, G., Savvides, A.: A survey of human-sensing: methods for detecting presence, count, location, track, and identity. ACM Comput. Surv. **5**, 1–77 (2010)
2. Ekimov, A., Sabatier, J.M.: Vibration and sound signatures of human footsteps in buildings. J. Acoust. Soc. Am. **120**(2), 762–768 (2006)
3. Jin, X., Sarkar, S., Ray, A., Gupta, S., Damarla, T.: Target detection and classification using seismic and PIR sensors. IEEE Sensors J. **12**(6), 1709–1718 (2012)
4. Sun, Z., Pan, S., Su, Y.-C., Zhang, P.: Headio: zero-configured heading acquisition for indoor mobile devices through multimodal context sensing. In: Proceedings of the 2013 ACM International Joint Conference on Pervasive and Ubiquitous Computing, pp. 33–42. ACM, New York (2013)
5. Sun, Z., Purohit, A., Chen, K., Pan, S., Pering, T., Zhang, P.: PANDAA: physical arrangement detection of networked devices through ambient-sound awareness. In: Proceedings of the 13th International Conference on Ubiquitous Computing, pp. 425–434. ACM, New York (2011)
6. Sun, Z., Purohit, A., Bose, R., Zhang, P.: Spartacus: spatially-aware interaction for mobile devices through energy-efficient audio sensing. In: Proceeding of the 11th Annual International Conference on Mobile Systems, Applications, and Services, pp. 263–276. ACM, New York (2013)
7. Nunes, D.S, Zhang, P., Silva, J.S.: A survey on human-in-the-loop applications towards an internet of all. IEEE Commun. Surv. Tutorials **17**(2), 944–965 Secondquarter (2015)
8. Purohit, A., Sun, Z., Pan, S., Zhang, P.: Sugartrail: indoor navigation in retail environments without surveys and maps. In: 10th Annual IEEE Communications Society Conference on Sensor, Mesh and Ad Hoc Communications and Networks (SECON), 2013, pp. 300–308. IEEE, New York (2013)
9. Mirshekari, M., Pan, S., Bannis, A., Pui, Y., Lam, M., Zhang, P., Noh, H.Y.: Step-level person localization through sparse sensing of structural vibration. In: Proceedings of the 14th International Conference on Information Processing in Sensor Networks, pp. 376–377. ACM, New York (2015)

10. Pan, S., Bonde, A., Jing, J., Zhang, L., Zhang, P., Noh, H.Y.: Boes: building occupancy estimation system using sparse ambient vibration monitoring. In SPIE Smart Structures and Materials+ Nondestructive Evaluation and Health Monitoring, pp. 90611O–90611O. International Society for Optics and Photonics (2014)
11. Pan, S., Wang, N., Qian, Y., Velibeyoglu, I., Noh, H.Y., Zhang, P.: Indoor person identification through footstep induced structural vibration. In: Proceedings of the 16th International Workshop on Mobile Computing Systems and Applications, pp. 81–86. ACM, New York (2015)
12. Subramanian, A., Mehrotra, K.G., Mohan, C.K., Varshney, P.K., Damarla T.: Feature selection and occupancy classification using seismic sensors. In: Trends in Applied Intelligent Systems, pp. 605–614. Springer, Berlin (2010)
13. Bland, R.E.: Acoustic and seismic signal processing for footstep detection. Ph.D. thesis, Massachusetts Institute of Technology (2006)
14. Alyamkin, S.A., Eremenko, S.I.: Pedestrian detection algorithms based on an analysis of the autocorrelation function of a seismic signal. Optoelectronics Instrum. Data Process. **47**(2), 124–129 (2011)
15. Succi, G.P., Clapp, D., Gampert, R., Prado, G.: Footstep detection and tracking. In: Aerospace/Defense Sensing, Simulation, and Controls, pp. 22–29. International Society for Optics and Photonics (2001)
16. Koç, G., Yegin, K.: Footstep and vehicle detection using slow and quick adaptive thresholds algorithm. Int. J. Distrib. Sens. Netw. **2013**, 9 (2013). doi:10.1155/2013/783604
17. Houston, K.M., McGaffigan, D.P.: Spectrum analysis techniques for personnel detection using seismic sensors. In: AeroSense 2003, pp. 162–173. International Society for Optics and Photonics (2003)
18. Xing, H.-F., Li, F., Liu, Y.-L.: Wavelet denoising and feature extraction of seismic signal for footstep detection. In: ICWAPR'07. International Conference on Wavelet Analysis and Pattern Recognition, 2007, vol. 1, pp. 218–223. IEEE, New York (2007)
19. Ripul Ghosh, Aparna Akula, Satish Kumar, and HK Sardana. Time-frequency analysis based robust vehicle detection using seismic sensor. J. Sound Vib. **346**, 424–434 (2015)
20. Huang, J., Zhou, Q., Zhang, X., Song, E., Li, B., Yuan, X.: Seismic target classification using a wavelet packet manifold in unattended ground sensors systems. Sensors **13**(7), 8534–8550 (2013)
21. Noh, H.Y., Nair, K.K., Lignos, D.G., Kiremidjian, A.S.: Use of wavelet-based damage-sensitive features for structural damage diagnosis using strong motion data. J. Struct. Eng. **137**(10), 1215–1228 (2011)
22. Noh, H., Kiremidjian, A.S.: On the use of wavelet coefficient energy for structural damage diagnosis. In: Proceedings of the10th International Conference on Structural Safety and Reliability, Osaka (2009)
23. Noh, H.Y., Lignos, D., Nair, K.K., Kiremidjian, A.S.: Application of wavelet based damage sensitive features for structural damage diagnosis. In: Proceedings of the 7th International Workshop on Structural Health Monitoring (2009)
24. Ling, T.-H., Li, X.-B.: Analysis of energy distributions of millisecond blast vibration signals using the wavelet packet method. Chin. J. Rock Mech. Eng. **24**(7), 1117–1122 (2005)
25. David, M.J.: Tax. one-class classification; concept-learning in the absence of counter-examples. ASCI Dissertation Series, 65 (2001)
26. Khan, S.S., Madden, M.G.: One-class classification: taxonomy of study and review of techniques. Knowl. Eng. Rev. **29**(03), 345–374 (2014)
27. Khan, S.S., Madden, M.G.: A survey of recent trends in one class classification. In Artificial Intelligence and Cognitive Science, pp. 188–197. Springer, Berlin (2010)
28. Chang, C.-C., Lin, C.-J.: Training v-support vector classifiers: theory and algorithms. Neural Comput. **13**(9), 2119–2147 (2001)
29. Schölkopf, B., et al.: Support vector method for novelty detection. NIPS. **12** (1999)
30. Tax, D.M.J., Duin, R.P.W.: Support vector data description. Mach. Learn. **54**(1), 45–66 (2004)
31. Preece, S.J., Goulermas, J.Y., Kenney, L.P.J., Howard, D., Meijer, K., Crompton, R.: Activity identification using body-mounted sensors a review of classification techniques. Physiol. Meas. **30**(4), R1(2009)
32. Li, K.-L., Huang, H.-K., Tian, S.-F., Xu, W.: Improving one-class SVM for anomaly detection. In: 2003 International Conference on Machine Learning and Cybernetics, vol. 5, pp. 3077–3081. IEEE, New York (2003)
33. Shin, H.J., Eom, D.-H., Kim, S.-S.: One-class support vector machines an application in machine fault detection and classification. Comput. Ind. Eng. **48**(2), 395–408 (2005)
34. Manevitz, L.M., Yousef, M.: One-class SVMs for document classification. J. Mach. Learn. Res. **2**, 139–154 (2002)
35. Rabaoui, A., Davy, M., Rossignol, S., Lachiri, Z., Ellouze, N.: Improved one-class SVM classifier for sounds classification. In: IEEE Conference on Advanced Video and Signal Based Surveillance, 2007. AVSS 2007, pp. 117–122. IEEE, New York (2007)
36. Zhou, J, Chan, K.L., Chong, V.F.H., Krishnan, S.M.: Extraction of brain tumor from mr images using one-class support vector machine. In: 27th Annual International Conference of the Engineering in Medicine and Biology Society, 2005. IEEE-EMBS 2005, pp. 6411–6414. IEEE, New York (2006)
37. Schölkopf, B., Platt, J.C., Shawe-Taylor, J., Smola, A.J., Williamson, R.C.: Estimating the support of a high-dimensional distribution. Neural Comput. **13**(7), 1443–1471 (2001)
38. Ren, W.-X., Zong, Z.-H.: Output-only modal parameter identification of civil engineering structures. Struct. Eng. Mech. **17**(3–4), 429–444 (2004)
39. Edwards, M., Xie, X.: Footstep pressure signal analysis for human identification. In: 2014 7th International Conference on Biomedical Engineering and Informatics (BMEI), pp. 307–312. IEEE, New York (2014)
40. Sabatier, J.M., Ekimov, A.E.: A review of human signatures in urban environments using seismic and acoustic methods. In: 2008 IEEE Conference on Technologies for Homeland Security, pp. 215–220. IEEE, New York (2008)
41. I/O Sensor Nederland bv. SM-24 Geophone Element, 2006. P/N 1004117
42. Aggarwal, C.C.: Outlier Analysis. Springer Science & Business Media, Berlin (2013)
43. Hodge, V.J., Austin, J.: A survey of outlier detection methodologies. Artif. Intell. Rev. **22**(2), 85–126 (2004)

Chapter 36
Assessment of Large Error Time-Differences for Localization in a Plate Simulation

Americo G. Woolard, Austin A. Phoenix, and Pablo A. Tarazaga

Abstract The advent of structural building instrumentation invites research into novel applications of such systems. Previous research has shown that the propagative nature of ground impacts on the floor of a building can be assimilated to a thin plate. This research presents results for time-difference of arrival (TDOA) and cross-correlation methods used for source localization in a sparsely instrumented plate Finite Element Model (FEM), where acceleration data is used. The overall accuracy is evaluated for various wave speeds with two different configurations of sensor positions, and the consistency of the perceived wave speeds are assessed by the coefficient of variance. The accuracy of localization is considered, with emphasis on the sign of arrival (SOA), as a method to provide directional inference. Peak-difference and cross-correlation techniques are found to be significantly erroneous, while the SOAs are consistently accurate, with less than 10 % of 126 SOAs being reported incorrectly for all cases. Repositioning the sensors closer to the boundary increased the errors for all methods.

Keywords Plate localization • Time difference of arrival • Hyperbolic localization • Structural health monitoring • Finite element analysis (FEA)

36.1 Introduction

The recent prevalence of structurally instrumenting buildings brings an inherent desire to investigate novel applications of such systems. While the typical purpose of structural instrumentation is for Structural Health Monitoring (SHM), there are alternative applications that may be considered. One particular area of interest is the localization of vibration events within a building, which includes events such as human footsteps, the starting and stopping of machinery, machinery malfunction, occupant building ingress and egress, dropped objects, etc. The ability to track personnel invites numerous possibilities in areas such as security, efficient occupant driven HVAC systems, and emergency response, to name a few. With this in mind the work herein investigates the ability to extract differences in time of arrival for impact localization in a plate, using acceleration data, where dispersion and reflections play a significant role.

The use of structural sensors to locate ground impacts has been implemented in previous studies [1, 2], where attempts to localize footsteps are made. It has been experimentally verified that a concrete slab as the floor of a building exhibits flexural wave mode dominance when subject to impacts, and can be assimilated to a thin plate [3]. The flexural wave mode of thin plates is highly dispersive; meaning the speed of wave propagation is frequency dependent. This dispersion makes traditional localization techniques that rely on the time difference of arrival between sensors and a constant wave speed more difficult. With the addition of reflections from the boundaries, time-difference based localization techniques become difficult to implement accurately [3, 4].

There are several methods presented in the literature that address the location of impacts in dispersive plates [5–9]. These methods take the dispersive nature of the plate into consideration, and typically rely on either high time resolution or accurate dispersion models of the medium. An exception to this is presented in [8], where a data driven model is used with matched field processing to localize the source. In a building environment, there are numerous factors that contribute to accuracy limitations: dispersion, boundary reflections, the inhomogeneous nature of concrete, building noise, and the various nonlinear effects (joints, cracks, etc.) that occur on the path from the source to the sensors. It is the purpose of this research to demonstrate the localization errors for TDOA techniques when large wave reflections are considered. The accuracy

A.G. Woolard (✉) • A.A. Phoenix • P.A. Tarazaga
Department of Mechanical Engineering Virginia Tech, Virginia Tech Smart Infrastructure Laboratory (VTSIL), Virginia Polytechnic Institute and State University, Blacksburg, VA 24061, USA
e-mail: awool012@vt.edu

© The Society for Experimental Mechanics, Inc. 2016

M. Allen et al. (eds.), *Dynamics of Coupled Structures, Volume 4*, Conference Proceedings of the Society for Experimental Mechanics Series, DOI 10.1007/978-3-319-29763-7_36

limitations of localization based on time difference of arrival (TDOA) and hyperbolic localization is investigated in a noiseless, simulation environment for an isotropic, homogenous plate, where significantly large boundary reflections are considered in a dispersive media. In the next section, the FEM and simulation of a plate is described, followed by the techniques used for localization and simulation. Finally, results are presented and discussed.

36.2 Modeling and Simulation of Source Localization

A finite element model (FEM) is used to simulate the plate dynamics due to an applied load. The square plate dimensions are 48.75 in. and thickness 0.25 in. The material properties used are intended to represent that of medium-density-fiberboard (MDF) with Young's modulus $E = 580\,\text{kpsi}$, density $\rho = 0.0266\,\text{lbm/in}^3$, Poisson's ratio $\nu = 0.25$. The FEM contains 10,000 linear CQUAD4 elements that contain 4-nodes with three translational and two rotational degrees of freedom each. This results in 10,201 nodes and a total 51,005 degrees of freedom. To model this transient excitation MSC Nastran solution 109, Direct Transient Response, is used with a time step of 1×10^{-4} for 0.6 s resulting in 6001 time steps. The simulation response is shown for several time intervals in Fig. 36.1. To provide an impulse response, an out of plane force with duration of one time step and amplitude of 1 lbf is used to excite all frequencies of the system up to 500 Hz, and band-limited to ensure a minimum of 4 elements/wavelength. Direct transient response analysis does not permit the use of complex coefficients. Therefore, structural damping cannot be used and has to be evaluated by means of equivalent viscous damping. A relation between structural damping and equivalent viscous damping was defined using the first mode of the system and 1 % structural damping. The configuration of sensors and impact locations is shown in Fig. 36.2 for two sensor configurations. For the first configuration, sensors are placed more inwards toward the board, while the second configuration has all sensors closer to the boundaries. The simulation measures acceleration. By using acceleration as opposed to displacement, high frequency wave reflections are more significant due to their greater propagation velocity.

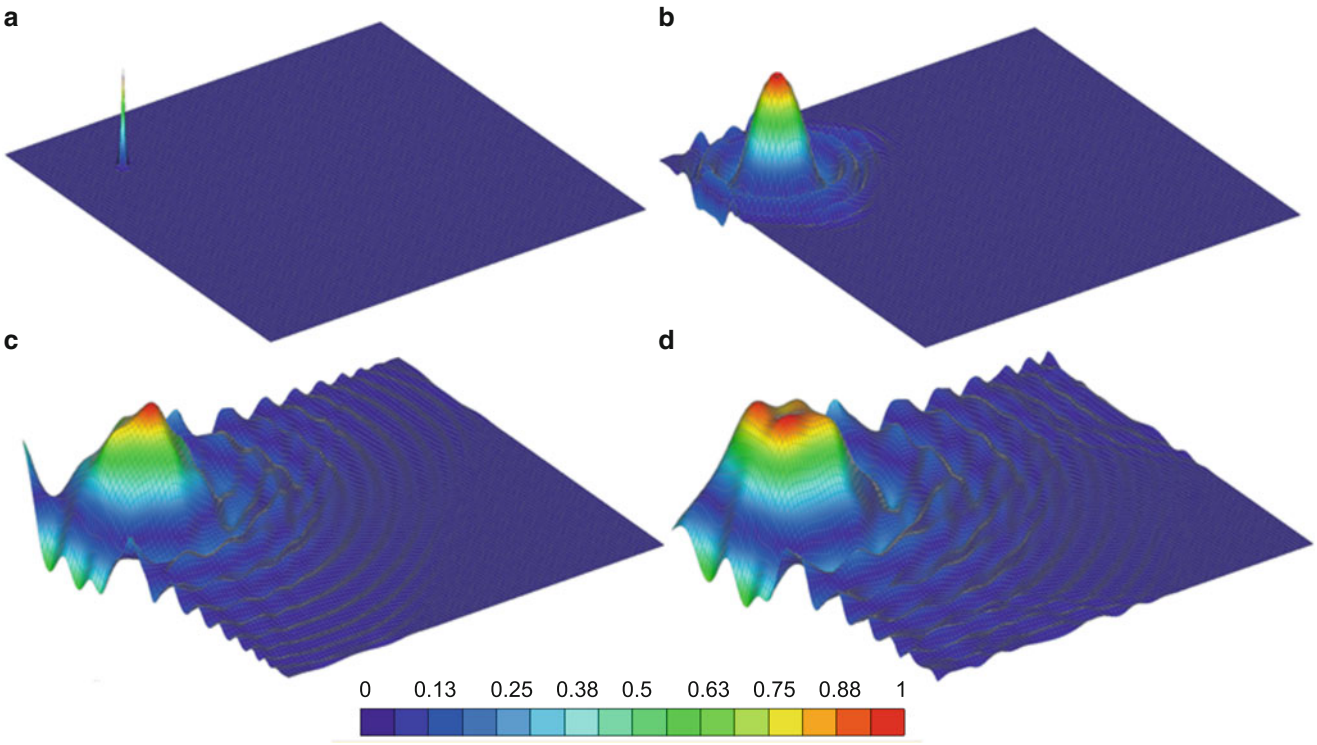

Fig. 36.1 Simulation response of a plate under an impact load: (**a**) Impact simulation at $t = 0$ (**b**) response at $t = 7.2$ ms (**c**) response at $t = 24.1$ ms and (**d**) response at $t = 30.6$ ms

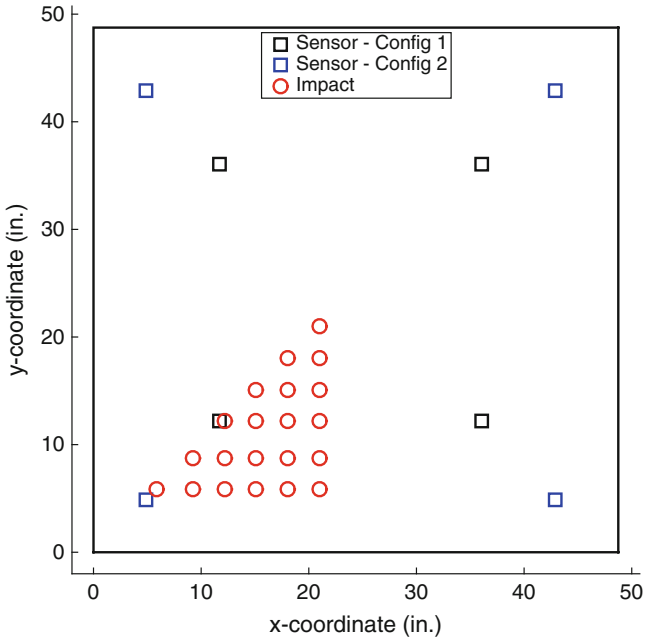

Fig. 36.2 Impact and sensor locations for two different sensor configurations. All 21 impact locations are simulated for each sensor configuration case

The accuracy of a localization algorithm may be assessed by the overall root-mean-square error (RMSE), which is calculated:

$$RMSE = \sqrt{RMSE(X)^2 + RMSE(Y)^2} \tag{36.1}$$

Where $RMSE(X)$ and $RMSE(Y)$ are the root-mean-square error of the x and y coordinates respectively. An alternative method can be used to assess the consistency of the perceived wave speed based on the known true distance-difference values referred to as the coefficient of variance (COV). It is not necessarily the case that the COV corresponds directly to accuracy, but provides insight into the consistency of the perceived wave speed, which is highly correlated to the accuracy of the calculated time-differences. The perceived wave speed is calculated as the true distance-difference over the measured time-difference. The COV is determined by σ/μ, where σ and μ are the standard deviation and mean of the perceived wave velocity, respectively. In addition to the RMSE and COV, the signs of arrival (SOAs) are considered. The SOA between any two sensors is either 1, -1 or 0, dictated by which sensor received the signal first, or at the same time for the case of 0. This can be used to create a spatial grid of separation lines between each sensor pair and reduce the solution to some area defined by the grid [3].

Attempts to locate impacts are made by estimating the TDOA between sensors using either cross-correlation or a peak-difference method (subtracting the peak response time between two sensors). Hyperbolic localization is used over a span of wave speeds with the algorithm described in [10], using the lower left sensor in both cases as the reference. This localization process is repeated for both sensor configurations, with those closer to the boundaries expected to experience more variation due to higher reflection intensities. The spatial relationship recovered from scaling the time-differences with a wave speed will be referred to as the "distance-difference."

Next, an example is presented and discussed for a constructed case with small TDOA errors. The RMSE from hyperbolic localization is examined, along with the COV and SOAs from the time-difference. Consider a case of the impact originating from (18.0, 12.2) with the first sensor configuration. The true distance-differences are calculated using the bottom-left sensor as the reference, and are 11.7, 18.4 and 23.6 in. between the bottom-right, top-left, and top-right sensors respectively. That is to say, the bottom-left sensor is 11.7 in. closer to the impact location than the bottom-right sensor, 18.4 in. closer than the top-left sensor, and 23.6 in. closer than the top-right sensor. Assuming a wave speed of 1500 in./s, the corresponding time differences are 7.80, 12.3 and 15.7 ms. Applying a small TDOA error of ± 1 ms, new TDOAs are calculated as 8.9, 11.3 and 16.7 ms. The perceived propagation velocities determined by dividing the true distance-differences over the new time-differences are then found to be 1330, 1633 and 1410, yielding a COV of 0.108. Without any errors in the TDOAs, all velocities are 1500 in./s (the assumed value), and so the COV is 0. The SOAs are retained as all positive since the magnitude

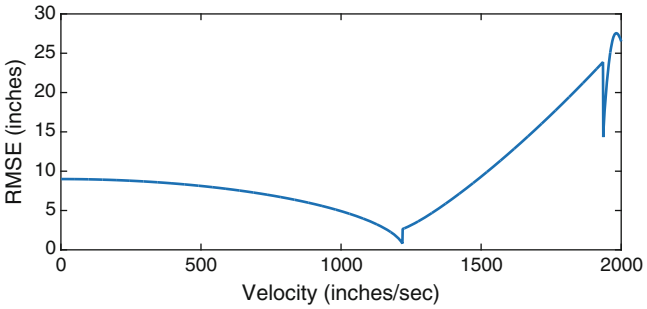

Fig. 36.3 RMSE over velocity range for the example case of an impact originating at (18.0, 12.2) and TDOA errors of ±1 ms

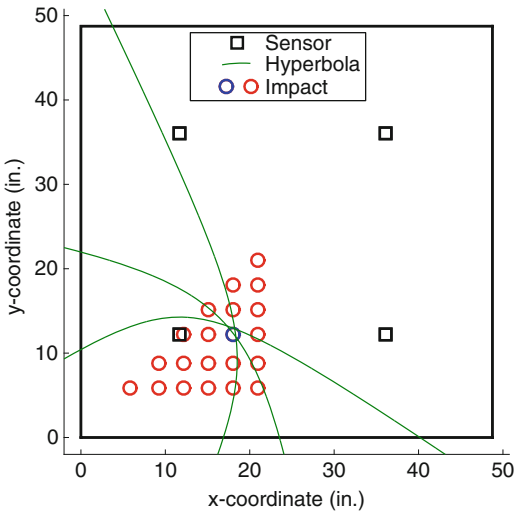

Fig. 36.4 Hyperbolae resulting from TDOAs with ±1 ms error and a wave speed of 1200 in./s for an impact at (18.0, 12.2) (*blue*)

of the TDOA errors (±1 ms) is not greater than any of the TDOAs (and therefore will not affect the sign). Due to the errors introduced to the TDOAs, the assumed wave speed of 1500 in./s may not provide the most accurate result. This is shown in Fig. 36.3, where the RMSE is calculated over a range of 1000–2000 in./s. The speed range used here is arbitrarily selected based on the perceived propagation velocities. The minimum RMSE of 0.8 in. is found at a velocity of 1219 in./s. The hyperbolic results for this small TDOA error case is shown in Fig. 36.4, with the true impact location highlighted in blue. Each hyperbola corresponds to a sensor pair, where the solution is at the intersection.

36.3 Results and Discussion

A sample response of the first 40 ms as seen from location (11.7, 12.2) and (36, 36), is shown in Fig. 36.5 for an impact at the location in (15, 15). The first "sensor" is significantly closer to the impact, and the initial waveform and its reflection can be seen. The second sensor is much further, where the waveform has significantly dispersed and the reflection is not observably separate. The time-difference of arrival calculations for both methods and sensor configurations are found to be significantly erroneous, resulting in poor localization results. In order to calculate an RMSE for time-difference methods, an assumed propagation velocity must first scale the time delays. In non-dispersive media (e.g. air), there is only a single propagation velocity for all frequency content of the input signal. This is not the case for dispersive media, where the dispersion relation governs the phase velocity, and so a single velocity must be selected with the desired trait of having a minimum RMSE. Because of this, the application of TDOA method to dispersive media requires the wave speed assumption be tuned to a specific velocity. This presents an issue for large TDOA errors, since the results are inaccurate for all wave speeds, and thus at very low speed scales, a small distance-difference is observed, and the solution approaches the point with the smallest distance-difference that minimizes the error function of the hyperbolic estimator. Depending on the geometry of the sensors, it is possible for this low wave speed solution to result in the minimum RMSE, regardless of the impact location. For the plate used in this simulation, the center of the plate is resolved as the best solution for very low wave speeds, and so produces

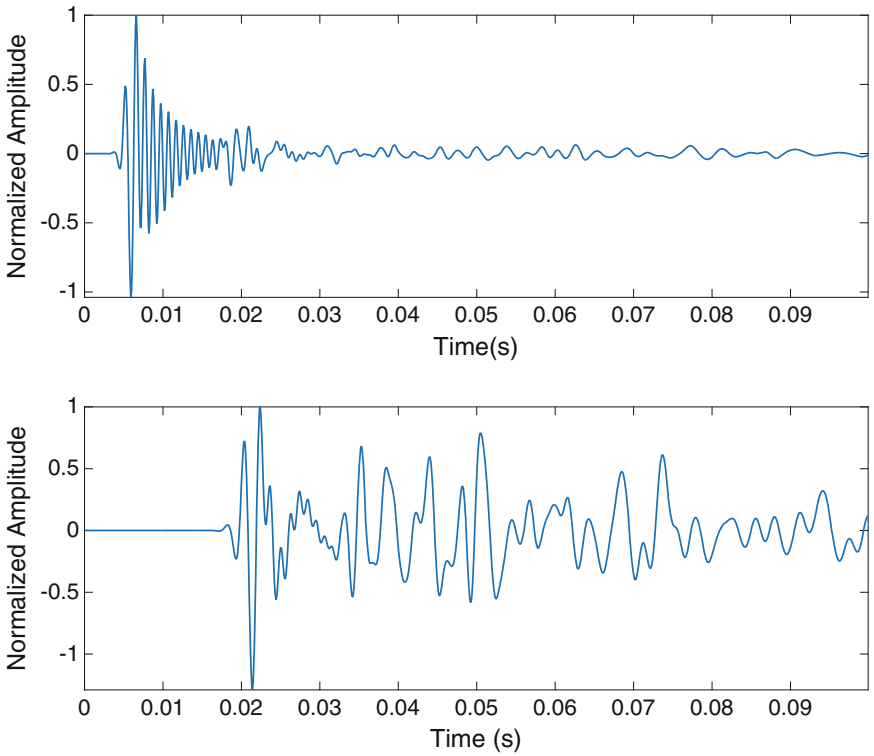

Fig. 36.5 Time trace of acceleration response as seen at the point located at (11.7, 12.2) above and as seen at the point located at (36, 36) below for impact at location (15, 15)

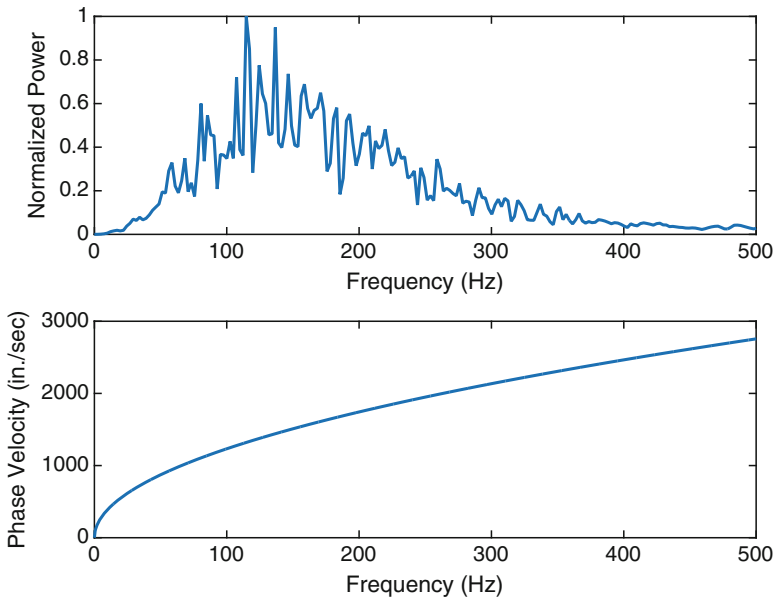

Fig. 36.6 Averaged power spectrum over all impacts and sensors; dispersion curve for the flexural wave mode

the smallest RMSE. Conceptually, this issue is more likely to arise when the source is near the sensors, as the solution to the smallest difference-distance is not likely the minimum RMSE when the source is far from the sensors. The average accuracy for all impact locations is assessed over the entire velocity range 1–3000 in./s, which corresponds to the phase velocities derived in [11] for a thin plate of these properties. This is done to verify that no particular velocity assumption results in low RMSE results for all impacts. The dispersion curve of the flexural wave mode in the 500 Hz bandwidth of interest is shown in Fig. 36.6 along with the averaged power spectrum over all impacts for all sensors.

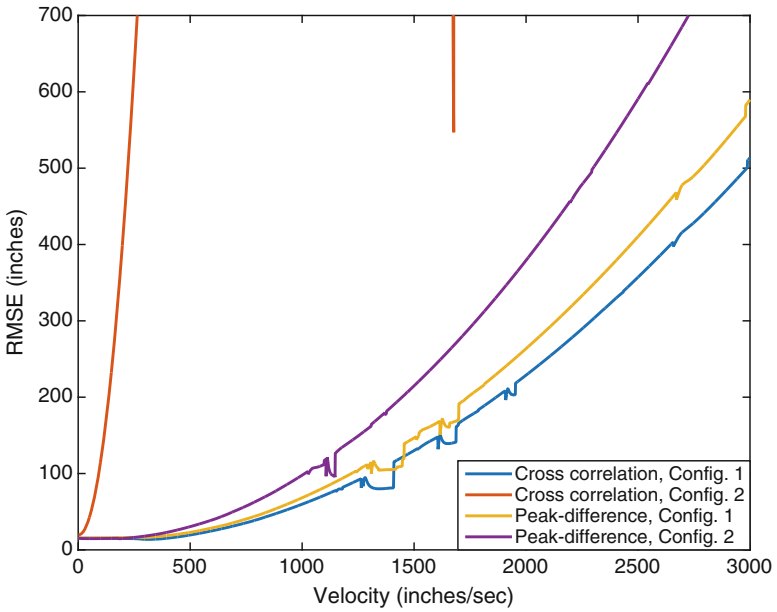

Fig. 36.7 RMSE over a 3000 in./s velocity range for two TDOA methods and two sensor configurations

The RMSE results are shown in Fig. 36.7; however, they are not a good measure of the accuracy of the TDOAs due to indiscriminate outliers. For example: the RMSEs for cross-correlation in the second configuration are orders of magnitude above the first configuration because of one particular impact case. Since the reliance of any localization method is of considerable importance, all outliers are retained. Instead of assessing accuracy based on RMSE, the coefficient of variation (COV) is considered for the perceived propagation velocity, along with the number of SOA errors. The COV represents the consistency of the perceived propagation velocity, i.e.: the ability to scale the time-differences by a single wave speed and get accurate results, while the number of SOA errors represents the ability to accurately discern a wave source as originating from one side or another for any sensor pair.

Considering the RMSE over the entire velocity range, there are several drops in the error as the velocity increases. These drops are either associated with wave speeds that dominate that particular response, or sporadic events that occur due to the nonlinear nature of hyperbolic localization. An example of this is shown in Fig. 36.8 for a particularly good localization case (COV 0.081), where we see RMSE values below 2 in. for a wave speed of 807 in./s. The low COV accurately suggests the existence of a particular wave speed that provides accurate results. The drops in RMSE above the ideal wave speed are inconsistent, and can be recognized by the gradient leading up to a particular drop off. Several other cases are included for comparison, showing inconsistency in which wave speed produces the minimum RMSE. Examining the two impacts at (9.26, 5.85) and (12.2, 8.78), the error of the calculated TDOAs are so large that no wave speed solution is better than assuming the middle of the plate as the source.

The percent error for SOAs represents the percent of SOAs that are reported incorrectly out of 126 (6 sensor pairs, 21 impacts), and is a good measure of the ability to isolate the source to an area by constructing a grid of sensor pairs. For the cross-correlation method in the first configuration, there is a COV of 0.79, with 7.1 % error of SOAs. In the second configuration, the COV increases to 2.81 (highly variable wave speed), and the SOAs error also increases to 8.7 %. This suggests that the increase in reflections from the boundaries in the second configuration increases the variance in the perceived wave speed and reduces the ability to isolate the source to an area from the SOAs.

For the peak-difference method in the first configuration, there is a COV of 0.74, and SOAs error of 4.0 %, while the second configuration has a COV of 4.68 with 9.5 % SOAs error. This shows a similar trend as the cross-correlation method between the first and second configurations: that the increase in reflections increases the COV and SOAs error. A noticeable difference in the peak-difference method, however, is the magnitude that the COV and SOAs increase between the first and second configurations, suggesting that the accuracy of the peak-difference method may be more negatively affected when reflections are significantly large.

For both cases, moving the sensors closer to the boundaries decreases the overall accuracy. When the sensors are very near to the boundaries and reflections are large, it appears that the cross-correlation method may perform better than peak-difference. This could be the result of the symmetry of the structure since all sensors are symmetric at the boundaries, the

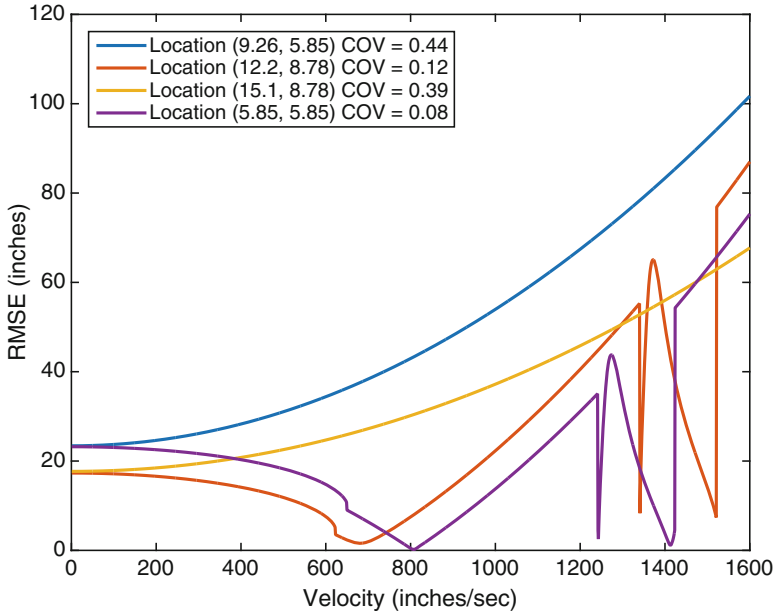

Fig. 36.8 RMSE over a portion of the velocity range for several select impacts. The most accurate velocity changes based on impact location: 807 in./s and 681 in./s for impacts at (12.2, 8.78) and (15.1, 8.78) respectively

convolution of the reflections could yield an approximation of the time-difference. The SOAs are relatively accurate in all cases, with only a small percentage of signs being interpreted incorrectly, suggesting that when heavy reflections are present in the signal, the SO-TDOA algorithm would still perform well, and could be used to locate the source to a specific area.

36.4 Conclusion

This research presents results for time-difference of arrival (TDOA) and cross-correlation methods for a sparsely instrumented plate in a simulation environment where acceleration data is used and reflections are significant. Wave reflections play an important role in the accuracy of localization algorithms in dispersive media. When reflections are significantly large, neither cross-correlation nor peak-difference methods produce accurate localization results. The peak-difference is found to perform better when the sensors are further from the boundaries, while cross-correlation results appear slightly better when the sensors are near the edge. This suggests that cross-correlation may be better tool if reflections are sufficiently large. The SOAs have less than 10 % error for all cases, suggesting good accuracy when despite large TDOA errors.

Acknowledgements The authors are thankful for the support and collaborative efforts provided by our sponsors VTI Instruments, PCB Piezotronics, Inc.; Dytran Instruments, Inc.; and Oregano Systems. The authors are particularly thankful for the support provided by the College of Engineering at Virginia Tech through Ed Nelson and Dean Richard Benson as well as Capital Project Manager Todd Shelton. The authors would also like to acknowledge the collaboration with Gilbane, Inc. in particular members David Childress and Eric Hotek. We are especially thankful to the Student Engineering Council at Virginia Tech and their financial support for this project. The work was conducted under the patronage of the Virginia Tech Smart Infrastructure Laboratory and its members.

References

1. Schloemann, J., et al.: Vibration event localization in an instrumented building. In: Experimental Techniques, Rotating Machinery, and Acoustics, Volume 8, pp. 265–271. Springer, Cham (2015)
2. Poston, J.D., et al.: Towards indoor localization of pedestrians via smart building vibration sensing. In: Proceedings of the 2015 International Conference on Localization and GNSS (ICL-GNSS). IEEE, Gothenburg, 22–24 June 2015, (2015)
3. Bahroun, R., et al.: New algorithm for footstep localization using seismic sensors in an indoor environment. J. Sound Vib. **333**(3), 1046–1066 (2014)

4. Ziola, S.M., Gorman, M.R.: Source location in thin plates using cross-correlation. J. Acoust. Soc. Am. **90**(5), 2551–2556 (1991)
5. De Marchi, L., et al.: A passive monitoring technique based on dispersion compensation to locate impacts in plate-like structures. Smart Mater. Struct. **20**(3), 035021 (2011)
6. Perelli, A., et al.: Acoustic emission localization in plates with dispersion and reverberations using sparse PZT sensors in passive mode. Smart Mater. Struct. **21**(2), 025010 (2012)
7. Park, J.-H., Kim, Y.-H.: Impact source localization on an elastic plate in a noisy environment. Meas. Sci. Technol. **17**(10), 2757 (2006)
8. Harley, J.B., Moura J.M.: Broadband localization in a dispersive medium through sparse wavenumber analysis. In: 2013 IEEE International Conference on Acoustics, Speech and Signal Processing (ICASSP). IEEE, Vancouver, 26–31 May 2013 (2013)
9. Gaul, L., Hurlebaus, S.: Identification of the impact location on a plate using wavelets. Mech. Syst. Signal Process. **12**(6), 783–795 (1998)
10. Chan, Y., Ho, K.: A simple and efficient estimator for hyperbolic location. IEEE Trans. Signal Process. **42**(8), 1905–1915 (1994)
11. Graff, K.F.: Wave Motion in Elastic Solids. Courier Corporation, Mineola, New York (2012)

Chapter 37
Gender Classification Using Under Floor Vibration Measurements

Dustin Bales, Pablo Tarazaga, Mary Kasarda, and Dhruv Batra

Abstract The ability to automatically classify the gender of occupants in a building has far-reaching applications in multiple areas spanning security and threat detection, retail sales, and possibly biometric identification in smart buildings. While other classification techniques provide potential for gender classification, they face varied limitations such as invasion of privacy, occupant compliance, line of sight, and high sensor density. High-sensitivity accelerometers mounted under the floors provide a robust alternative for occupant classification. The authors take advantage of the highly-instrumented Goodwin Hall on the Virginia Tech campus to measure vibrations of the walking surface caused by individual walkers. A machine learning technique known as Support Vector Machines (SVMs) is used to classify gender. In this study, the gait (i.e. walking) of 15 individual walkers (eight male and seven female) was recorded as they, alone, walked down the instrumented hallway, in multiple trials. The trials were recorded via 14 accelerometers which were mounted underneath the walking surface with the placement of the sensors unknown to the walker. A tenfold-cross-validation method is used to comment on the validity of the algorithm's ability to generalize to new walkers. This work demonstrates that a gender classification accuracy of 88 % is achievable using the underfloor vibration data from the Virginia Tech Goodwin Hall applying an SVM approach.

Keywords Machine learning • Gait measurement • Gender classification • Goodwin Hall • Vibrations

37.1 Introduction

Building occupant classification from non-invasive gait measurement has the potential to be of prime importance in numerous applications such as improving sales in a retail space, advancing security and threat detection, and improving emergency response. There are various methods of gait measurement (e.g. computer vision, wearable accelerometry, etc.), and many have been used to classify a variety of characteristics of building occupants [1–8]. The novelty of this work includes the use of non-invasive underfloor mounted accelerometers as a method of measuring gait and the application of machine learning techniques to classify the gender of the walkers.

Gait, the manner in which humans walk, consists of the interaction between hundreds of muscles and joints in the body [9]. The patterns associated with this movement are similar in humans, but not identical [9]. These differences in gait lead to the assumption that gender can be inferred from their analysis. This idea is supported by Nixon and Carter [10], who have determined that gender classification is achievable by observation with cameras in conjunction with computer vision techniques due to differences in gender behavior such as larger hip swing for women and shoulder swing for men.

One approach on organizing existing gait measurement methods in the literature is to broadly label an approach as either visual based or non-visual based. Visual based methods involve some form of computer vision to measure the movement of a walker. These measurements are broken down further into active and passive methods. The active method, known as Structure from Motion, tracks specific points on the body to characterize its motion [11]. Passive methods are less interested in the underlying physical structure of the motion and treat each frame of the video as a unique pose made by a walker [12]. Visual based methods have limitations associated with video recording and computer vision processing (e.g. line of sight requirement, large data, ability to mask identity, privacy concerns, etc.). Non-visual methods of gait measurement are achieved with a variety of techniques including: step loggers, accelerometer instrumented vests, mobile force plate, instrumented shoes, walker mounted accelerometers, sound wave measurement, and pressure and load sensitive floors [5, 8, 13–21]. These technologies have various limitations that restrict wide adoption. For example, they may require active participation of a walker (i.e. wearing a sensor), may have significant potential for the violation of privacy (i.e. recording of

D. Bales (✉) • P. Tarazaga • M. Kasarda • D. Batra
Virginia Tech Smart Infrastructure Laboratory, Virginia Tech, 635 Prices Fork Road, Blacksburg, VA 204060, USA
e-mail: dbbales@vt.edu

© The Society for Experimental Mechanics, Inc. 2016

M. Allen et al. (eds.), *Dynamics of Coupled Structures, Volume 4*, Conference Proceedings of the Society for Experimental Mechanics Series, DOI 10.1007/978-3-319-29763-7_37

conversations), and/or pre-installation of the system is very expensive and difficult (i.e. no current way to retrofit a building). Another subcategory under non-visual methods is one where ground movements are utilized for gait measurement. Pan et al. [1, 22] and Sabatier and Ekimov [23, 24] measure vertical velocity (using geophones) or the vertical acceleration (using accelerometers) of the ground caused by footsteps. These works require sensors to be mounted on the walking surface where they could be destroyed or evaded in a security application. In this work, the authors use data from novel underfloor mounted accelerometers that have the potential to allow for easy installation in existing buildings with locations that are unknown to building occupants.

There are many gait measurement techniques and much of the data produced in these previous works have been used for the purpose of classification. These algorithms range from simple thresholding of a single term to complex non-linear learning strategies. Numerous studies have classified various attributes using only gait measurements. These classifications range from walker identification to diagnosing neurodegenerative diseases [4, 7]. Yun [8] contains a list of gait classification examples for further reading. The most similar effort in gender classification as proposed in this work is by DeLoney [18] and Li et al. [19], where both use acoustic measurements of walkers with gender classification accuracies that were not reported (NR) and 75 %, respectively. Our work uses machine learning techniques to interpret the vibrational data measured by the novel underfloor accelerometers to classify the gender of a walker.

37.2 Experimental Setup

The 5-story, 155,000 sq. ft Goodwin Hall, as shown in Fig. 37.1, on the Virginia Tech campus has been instrumented with 212 accelerometers, with more in various stages of installation and commissioning. All accelerometers are mounted to structural members of the building via steel mounting beams as shown in Fig. 37.2. The instrumentation of an operational building allows Goodwin Hall to be the ideal "real-world" test bed for walker classification since measurements will encounter complications not present in a simplified and carefully controlled laboratory system. The varied nature of the building (i.e. classrooms, laboratories, auditoriums, and staff offices) allow for developed technologies to translate directly into many other types of buildings.

For this study data was collected in a single hallway with each participant walking alone. Fifteen individuals (eight males and seven females) walked in this study. Walkers were asked to state whether they considered their shoes hard or soft soled. Three females and two males were asked to walk in both hard and soft soled shoes, while the rest walked in either hard or soft soled shoes. This strategy was used to reduce bias in walker characteristics while accounting for differences in footwear. Although, footwear has been shown to have small effect on gait measurements [19, 25]. In summary, 13 soft sole and 7 hard sole walkers were tested. Each of the 20 walkers completed six trials, totaling 120 walking trials. Participants walked in both directions of the hallway: Eastward (East to West) and Westward (West to East) for three trails each.

The hallway where the study was completed, shown in Fig. 37.3, used only 14 of the 212 PCB393B04 accelerometers with nominal 1000 mV/g sensitivity, sampling at 51,200 Hz. The time taken to complete a trial was dependent on the

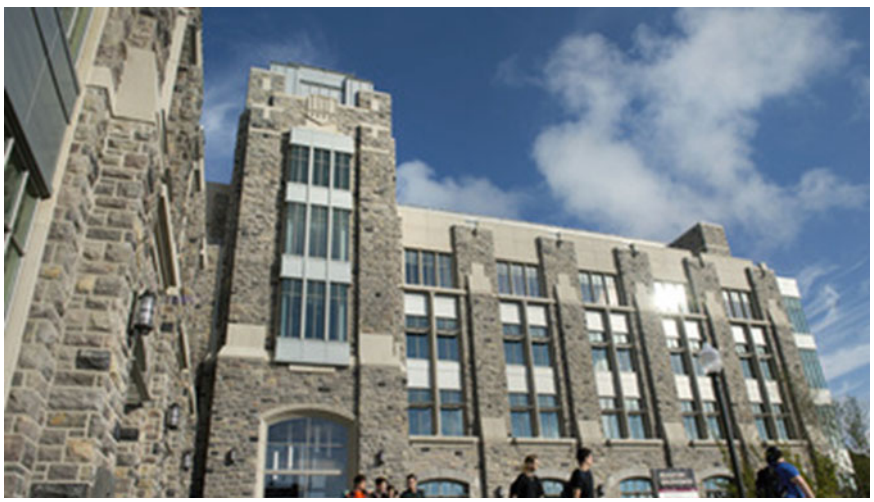

Fig. 37.1 Goodwin Hall on the Virginia Tech campus

Fig. 37.2 Accelerometer mount. Vertical, single-axis sensor shown. The mount is welded to a structural member with the fire retardant stripped to expose steel

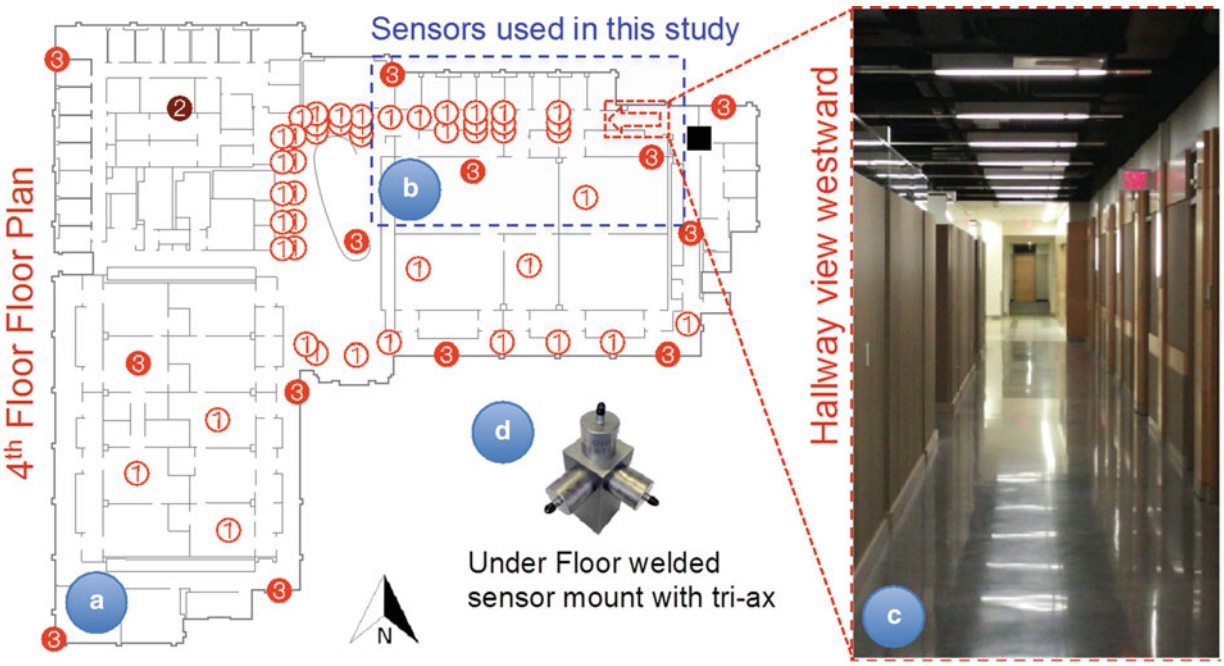

Fig. 37.3 The hallway used for testing: (**a**) shows a floor plan of the 4th floor depicting the location of the sensors mounted under the floor, (**b**) the *blue shaded area* shows the section used in this study, (**c**) show the view from the east side of the building facing westward, and (**d**) a picture of a three sensors on a mount is shown *bottom center*. Building north is labeled

walking speed of the individual as no instructions were given about appropriate walking speed. These times ranged from approximately 30–45 s for individuals to traverse the hallway. The recorded data was processed by removing the DC offset of each accelerometer, giving a zero initial value for each signal, and applying a low pass filter. A Butterworth filter of order three with a 500 Hz cutoff frequency was used in order to capture all the expected frequency content of the normal force for measurement in the vertical direction [17].

37.3 Data Representation

The dimensionality of the raw data for a single footstep is $\mathbb{R}^D$ where $D =\sim 800,000 \times 14$. The 800,000 dimension is nominally the number of samples required to complete a walking trial and 14 is the number of sensors used in the study. A typical walking signal is found in Fig. 37.4 for reference. Due to the large dimensionality the raw data is not an ideal set of features (i.e. inputs) for a machine learning algorithm, as these lead to large computation time and low accuracies in classification due to overfitting [26]. To reduce the dimensionality, a Sensor Averaged Step (SAS) feature set was developed.

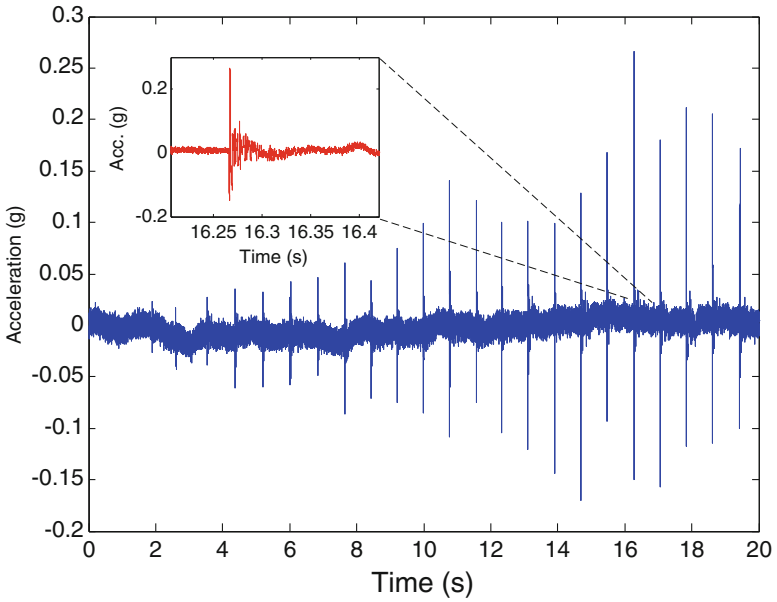

Fig. 37.4 A typical walking signal. This particular signal is the first trial of Female A (the name of a study participant). A wearing hard soled shoes. The peaks of the signal represent footsteps. In inlaid plot shows a portion of the same signal

The SAS feature set is constructed by selecting the n most prevalent steps (based on amplitude) recorded by a single sensor during the entirety of a single walking trial. In this study approximately 30 steps were required to walk the length of the hallway. These n steps were maximum value aligned and averaged. The most appropriate number of steps to average is unknown a priori and as such $n = 10$, 5, and 3 are used to construct three SAS datasets (denoted SAS-10, SAS-5, and SAS-3 while collectively referred to as SAS). The SAS data sets were then transformed to the frequency domain, using an FFT, to study the influence on data representation. Meaning that there are six total data sets investigated in this work: SAS-10 time, SAS-5 time, SAS-3 time, SAS-10 frequency, SAS-5 frequency, and SAS-3 frequency.

A single footstep in all time data sets was defined as the 61.0 ms before a footstep peak and 152.6 ms after the peak, as shown in the inlaid figure of Fig. 37.4. Further studies could be dedicated to ascertain the validity or optimal length of this sample. Here the length was chosen arbitrarily to encompass the entirety of a step.

37.4 Machine Learning Technique

The approach in this work to classify gender is via a supervised machine learning approach. Machine learning is the study of algorithms that 'learn' from training data. The training data in this work is the SAS feature sets as well as the gender labels noted during experimentation. The algorithms develop models that make predictions on new or test data. The algorithms used in this work require three steps: training, validation, and testing. The training step develops a generalized predictive model, the validation step sets or updates 'hyper-parameters' or model design choices, and the test step determines the ability of the algorithm to classify new or unseen walker data. The error (i.e. percentage of gender misclassifications) of each step is tracked, and only test errors are reported throughout this work.

To reduce the effect of data initialization (i.e. which trials of walking data are sorted into each of the three required steps) this work uses a tenfold-cross-validation method. This method randomly partitions the vectors of the SAS data set into ten, nearly equal parts, known as folds (for 120 trials each fold holds 12 trials). A single fold is held out, and the remaining nine folds are used in the training and validation steps to develop a model. The developed model is used to classify the held out tenth fold and the test error is recorded. Then, a different fold is held out, repeating this process until all folds of the feature vectors have been held out a single time. Each of the test errors are then averaged together. This averaged test error serves as a good representation of the error that can be expected on a never before seen feature set (i.e. walker) [27].

The machine learning algorithm explored in this work is a support vector machine (SVM). These algorithms 'learn' a hyperplane between the classes (i.e. female and male), in particular, the hyperplane that maximizes the margin between the two classes. A representative illustration for SVMs is shown in Fig. 37.5. Often associated with SVMs is the use of what

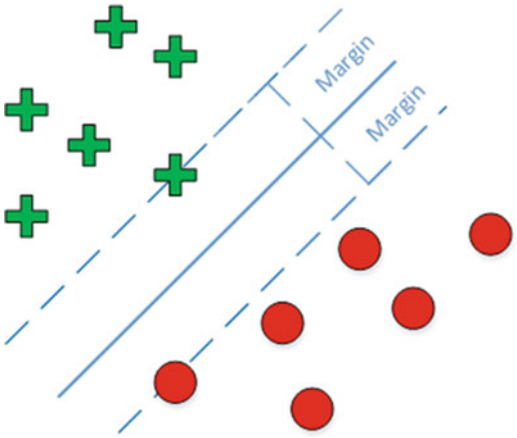

Fig. 37.5 Support vector machines illustration. There are many lines that can separate the two classes, but the SVM solve for the line that gives the maximum margin between them

is called the kernel trick. The kernel trick allows for the replacement of inner products (i.e. measures of similarity) with kernel functions [28]. Kernels map the feature vectors (in this case the SAS data) into a higher dimensional space, via a chosen non-linear mapping. The non-linear mapping (i.e. polynomial) is chosen a priori to develop an optimal hyperplane that separates the classes [29, 30]. Specifically, our work studied the Radial Basis Function (RBF) and polynomials of order 1–25 SVMs to understand how the type of SVM affects classification rate.

37.5 Results

This work intends to answer the following using the combinations of the type of SVM and SAS data type: (1) the best domain representation (i.e. time or frequency), (2) the best type of SVM independent of the type of SAS data type, and (3) the best SAS data representation independent of which SVM model is used. The best in each are defined as those producing minimum classification error.

The classification errors for all SVM and SAS data type combinations are found in Table 37.1. The table is divided into the time and frequency domains by the slashes dividing two error rates in a table entry. The first rate is that for time and the second is frequency. The columns representing the types of SAS data and the rows represent the error of the lowest error reporting SVM (24th order polynomial). Figure 37.6 details the determination of the 24th order polynomial, as the model that produces the lowest classification error within the parameters of this study (i.e. order 1–25 and RBF).

When comparing the SAS domain types, the frequency data sets yielded less accurate classification rates of 32.3 % error over all SAS frequency data types than the SAS time at 18.6 % error. The larger errors for the frequency domain may be explained by the sensitivity of SVMs to the input features. More specifically, a possible explanation of the differentiation between domains is that the time domain has more numerous interesting (non-noise adding) features than the frequency domain. Based on Ekimov and Sabatier's [17] findings the energy in the frequency domain is bounded by 500 Hz for normal force interaction between the foot and the ground. The frequency domain in this work is un-truncated (i.e. contains frequencies over 500 Hz) and may contribute near zero values to the system.

The 24th order polynomial SVM produced the least average error across all six types of SAS data at 25 %. There is relatively low change in accuracy of classification as the degree of polynomial associated with the SVM increased suggesting robustness to overfitting (which is defined as classifying well on training data but performing poorly on test data).

The most accurate data set is the SAS-5 time data set which produced an average of 21 % error averaging across all 26 SVM models (25 polynomials and RBF).

As is shown in Table 37.1, the best performing SVM, 24th order polynomial, and the best performing data type, SAS-5 time, had a misclassified rate of 14.2 % therefore, an 85.8 % accurate classification. It is interesting to note that the best performing SAS data type (SAS-5 time) and the best performing SVM (polynomial order 24) combine to produce the single best combination.

After answering the questions previously posed in the results section, there are other interesting results to be discussed. Namely the difference in Eastward and Westward trials and the effect on the number of steps averaged together on classification error. The misclassification rate for Westward trials and Eastward trials is 15 % and 13.3 % respectively, for the SAS-5 time data set with 24th order SVM. There is no statistical significance between Westward and Eastward trials with a

Table 37.1 Error summary

Time/**Frequency** domain						
Data type	SAS-10		SAS-5		SAS-3	
Trial direction	Westward	Eastward	Westward	Eastward	Westward	Eastward
SVM (24th order)	23/**32 %**	20/**32 %**	15/**33 %**	13/**32 %**	17/**28 %**	23/**35 %**
Average error of data type	22/**32 %**		14/**33 %**		20/**32 %**	

The time and frequency domain errors for a 24th order polynomial SVM is detailed. The data types (columns) are broken into Westward and Eastward trials

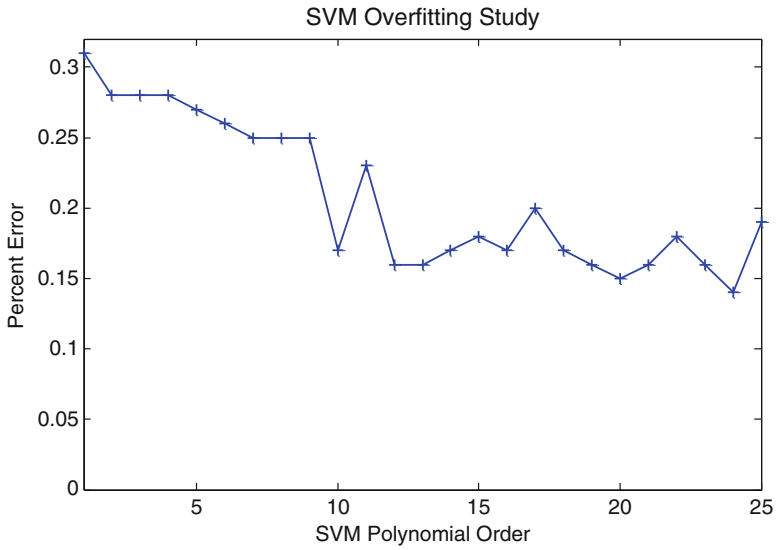

Fig. 37.6 Support vector machine dimensionality study. The error of an SVM model on the SAS-5 time data set. The minimum error selected was 14 % at 24th order. The plateau of the trend suggests robustness to overfitting. RBF error, not shown, for the SAS-5 data set is 29.2 %

p-value of 0.68. Where the p-value is the representative probability associated with a two sample t-test. When examining the time SAS data only, there is an interesting trend associated with the number of steps that are averaged together. Five steps averaged produce the most accurate gender classification with ten and three steps producing higher error rates. This trend implies that there is an optimum number of steps for use in an averaging scheme. Further study into the most appropriate number of averaged steps will be investigated in future work.

37.6 Conclusions

Using underfloor mounted accelerometers in conjunction with machine learning techniques show promising results to classify gender. The novel mountings of accelerometers overcomes some of the limitations of current gait measurement techniques using cameras and microphones (i.e. privacy concerns). The primary results of this work were found to be: (1) the time domain produces lower classification error than the frequency domain, (2) a 24th order polynomial SVM produced the lowest classification error regardless of the SAS data type used (at 25 %) and (3) the SAS-5 time, constructed by averaging 5 peak aligned steps, data set produced the lowest classification error independent of the SVM model used (at 21 %). Secondary results were also noted. There is no statistical difference in error rates between walking direction, and there is an optimum number of steps to average for low classification error (five steps were the most accurate in this work). The single best classifier developed in this study was SAS-5 data type with a 24th order polynomial providing a classification accuracy of 85 %. This pilot work shows the potential of walker classification when using underfloor accelerometers for gait measurement and machine learning techniques for classification purposes.

Future work includes expanding the types of machine learning algorithms investigated and constructing other data types to understand the effectiveness of different methodologies on gender classification. The most appropriate methods to reduce the large amounts of data taken will also be investigated. Work will also focus on understanding the fundamental physics that result in a specific data type and/or machine learning algorithm to classify gender better than another.

Acknowledgements The authors wish to acknowledge the support as well as the collaborative efforts provided by our sponsors, VTI Instruments, PCB Piezotronics, Inc.; Dytran Instruments, Inc.; and Oregano Systems. The authors are particularly appreciative for the support provided by the College of Engineering at Virginia Tech through Dean Richard Benson and Associate Dean Ed Nelson as well as VT Capital Project Manager, Todd Shelton, and VT University Building Official, William Hinson. The authors would also like to acknowledge Gilbane, Inc. and in particular, David Childress and Eric Hotek. We are especially thankful to the Student Engineering Council (SEC) at Virginia Tech and their financial commitment to this project. The work was conducted through the support of the Virginia Tech Smart Infrastructure Laboratory and its members. Special thanks to collaborators Dr. Bryan Joyce, Sriram Malladi, Mico Woolard, and Jeff Poston.

References

1. Pan, S., Bonde, A., Jing, J., Zhang, L., Zhang, P., Noh, H.Y.: BOES: building occupancy estimation system using sparse ambient vibration monitoring. pp. 90611O-90611O-90616 (2014)
2. Middleton, L., Buss, A.A., Bazin, A., Nixon, M.S.: A floor sensor system for gait recognition. In: Proceedings of the Fourth IEEE Workshop on Automatic Identification Advanced Technologies, 2005, pp. 171–176 (2005)
3. BenAbdelkader, C., Cutler, R., Nanda, H., Davis, L.: EigenGait: motion-based recognition of people using image self-similarity. In: Bigun, J., Smeraldi, F. (eds.) Audio- and Video-Based Biometric Person Authentication, pp. 284–294. Springer, Berlin/Heidelberg (2001)
4. Hayfron-Acquah, J.B., Nixon, M.S., Carter, J.N.: Recognising human and animal movement by symmetry. In: Proceedings of 2001 International Conference on Image Processing, vol. 293, pp. 290–293 (2001)
5. Nyan, M.N., Tay, F.E.H., Seah, K.H.W., Sitoh, Y.Y.: Classification of gait patterns in the time–frequency domain. J. Biomech. **39**, 2647–2656 (2006)
6. Lin, Y.-C., Yang, B.-S., Lin, Y.-T., Yang, Y.-T.: Human recognition based on kinematics and kinetics of gait. J. Med. Biol. Eng. **31**, 225–263 (2010)
7. Yang, M., Zheng, H., Wang, H., McClean, S.: Feature selection and construction for the discrimination of neurodegenerative diseases based on gait analysis. In: 3rd International Conference on Pervasive Computing Technologies for Healthcare, PervasiveHealth 2009, pp. 1–7 (2009)
8. Yun, J.: User identification using gait patterns on UbiFloorII. Sensors (Basel) **11**, 2611–2639 (2011)
9. BenAbdelkader, C., Cutler, R., Davis, L.: Stride and cadence as a biometric in automatic person identification and verification. In: Proceedings of the Fifth IEEE International Conference on Automatic Face and Gesture Recognition, pp. 372–377 (2002)
10. Nixon, M.S., Carter, J.N.: Automatic recognition by gait. Proc. IEEE **94**, 2013–2024 (2006)
11. Hoffman, D.D., Flinchbaugh, B.E.: The interpretation of biological motion. Biol. Cybern. **42**, 195–204 (1982)
12. Cedras, C., Shah, M.: A survey of motion analysis from moving light displays. In: Proceedings CVPR '94, 1994 IEEE Computer Society Conference on Computer Vision and Pattern Recognition, pp. 214–221 (1994)
13. Liu, T., Inoue, Y., Shibata, K., Shiojima, K.: A mobile force plate and three-dimensional motion analysis system for three-dimensional gait assessment. IEEE Sensors J. **12**, 1461–1467 (2012)
14. Sousa, M., Techmer, A., Steinhage, A., Lauterbach, C., Lukowicz, P.: Human tracking and identification using a sensitive floor and wearable accelerometers. In: 2013 IEEE International Conference on Pervasive Computing and Communications (PerCom), pp. 166–171 (2013)
15. Sinclair, J., Hobbs, S.J., Protheroe, L., Edmundson, C.J., Greenhalgh, A.: Determination of gait events using an externally mounted shank accelerometer. J. Appl. Biomech. **29**, 118–122 (2013)
16. Godfrey, A., Conway, R., Meagher, D., ÓLaighin, G.: Direct measurement of human movement by accelerometry. Med. Eng. Phys. **30**, 1364–1386 (2008)
17. Ekimov, A., Sabatier, J.M.: Vibration and sound signatures of human footsteps in buildings. J. Acoust. Soc. Am. **120**, 762–768 (2006)
18. DeLoney, C.: Person identification and gender recognition from footstep sound using modulation analysis (2008)
19. Li, X., Logan, R.J., Pastore, R.E.: Perception of acoustic source characteristics: walking sounds. J. Acoust. Soc. Am. **90**, 3036–3049 (1991)
20. Qian, G., Zhang, J., Kidané, A.: People identification using floor pressure sensing and analysis. IEEE Sensors J. **10**, 1447–1460 (2010)
21. Kohle, M., Merkl, D.: Identification of gait patterns with self-organizing maps based on ground reaction force. In: ESANN, pp. 24–26 (1996)
22. Pan, S., Wang, N., Qian, Y., Velibeyoglu, I., Noh, H.Y., Zhang, P.: Indoor person identification through footstep induced structural vibration. In: Proceedings of the 16th International Workshop on Mobile Computing Systems and Applications, pp. 81–86. ACM, New York (2015)
23. Sabatier, J.M., Ekimov, A.E.: A review of human signatures in urban environments using seismic and acoustic methods. In: Proceedings of the 2008 IEEE Conference on Technologies for Homeland Security, pp. 215–220 (2008)
24. Sabatier, J.M., Ekimov, A.E.: Range limitation for seismic footstep detection, pp. 69630V-69630V-69612 (2008)
25. Orr, R.J., Abowd, G.D.: The smart floor: a mechanism for natural user identification and tracking. InCHI'00 extended abstracts on Human factors in computing systems 2000 Apr 1 (pp. 275–276). ACM
26. Czarnowski, I., Jdrzejowicz, P.: Data reduction algorithm for machine learning and data mining. In: Nguyen, N.T., Borzemski, L., Grzech, A., Ali, M. (eds.) New Frontiers in Applied Artificial Intelligence, pp. 276–285. Springer, Berlin/Heidelberg (2008)
27. Parmanto, B., Munro, P.W., Doyle, H.R.: Reducing variance of committee prediction with resampling techniques. Connect. Sci. **8**, 405–426 (1996)
28. Murphy, K.P.: Machine Learning: A Probabilistic Perspective. MIT, Cambridge, MA (2012)
29. Boser, B.E., Guyon, I.M., Vapnik, V.N.: A training algorithm for optimal margin classifiers. In Proceedings of the fifth annual workshop on Computational learning theory, pp. 144–152. ACM, 1992.
30. Vapnik, V.N.: The Nature of Statistical Learning Theory. Springer, New York (2000)

Chapter 38
Human-Structure Interaction and Implications

Lars Pedersen

Abstract On civil engineering structures human occupancy is often modeled as a static load. Modeling humans as a static load is a simplification of matters, as will be demonstrated in the paper. The paper addresses the complexity of having both passive humans (sitting or standing) as well as active humans on a structure when evaluating the serviceability limit state of a structure carrying humans. The subject is addressed with offset in numerical modelling and experimental findings and is discussed in relation to existing design codes.

Keywords Human-structure interaction • Floor vibrations • Experimental testing • Numerical prediction • Serviceability limit state

Nomenclature

a	Floor acceleration
f_s	Walking frequency
M_H	Human mass
q	Load
ζ_F	Floor damping ratio
f_F	Floor natural frequency
G	Mass of walking person
n	Integer
α	Dynamic load factor
ζ_H	Human damping ratio
f_H	Human natural frequency
M_F	Floor modal mass
r	Ratio
ζ	Damping ratio
θ	Phase

38.1 Introduction

In ultimate limit state calculations of floors, passive humans occupying floors are normally modelled as a static weight. This is useful, but on flexible structures occupied by passive humans (sitting or standing) and excited dynamically by humans in motion (active persons), this modelling approach might be insufficient. Often in this case it is the serviceability limit state that is of concern rather than the ultimate limit state, and this paper addresses some of complexities involved when evaluating structural performance in the serviceability limit state.

The fact that passive persons influence floor damping characteristics has previously been demonstrated in [1–3]. The referenced investigations involved field measurements on a structure that carried a massive crowd of people. Investigations

L. Pedersen (✉)
Department of Civil Engineering, Aalborg University, Sofiendalsvej 9-11, 9200 Aalborg SV, Denmark
e-mail: lp@civil.aau.dk

© The Society for Experimental Mechanics, Inc. 2016

M. Allen et al. (eds.), *Dynamics of Coupled Structures, Volume 4*, Conference Proceedings of the Society for Experimental Mechanics Series, DOI 10.1007/978-3-319-29763-7_38

in laboratories have also revealed that passive humans can add damping [4, 5]. This paper addresses how passive humans occupying a structure can influence its damping characteristics but also how it can influence vibration levels.

Having established that passive humans on a structure can provide damping it is considered relevant also to establish some sort of reference. Therefore the investigations reported in this paper considers scenarios where humans are seated directly on the surface of a vibrating floor, and scenarios where humans are sitting in a chair, in order to study possible differences in dynamic behaviour of the floor.

Also it is considered useful to conduct and report results of experiments in which a sandbag (with a mass equal to that of a passive person) is employed in tests, yet again in order to establish an overview of interaction mechanisms.

Section 38.2 describes the experiments and the results (which are discussed), and Sect. 38.3 provides results of a numerical study focusing on implications of dynamic human-structure interaction.

38.2 Experiments

38.2.1 The Test Floor

A one-way spanning hollow-core prestressed concrete element is applied in tests. The length of the floor is about 11 m and it weighs more than 5 tons. The floor is pin-supported at both ends.

38.2.2 Tests on the Empty Floor

At floor midspan a displacement sensor is installed. By impacting the floor at the position of the displacement sensor, vibrations occur and a free decay is picked up by the displacement sensor.

Analysing the measured decay provides an estimate of the damping ratio of the empty floor which is denoted $\zeta(0)$.

A logarithmic decrement approach is applied for deriving damping characteristics.

38.2.3 Further Tests on the Floor

Following the tests made on the empty floor, damping characteristics of the floor are also derived under the following conditions that involved the presence of humans occupying the floor strip:

H1. Humans sitting on the floor strips (no chair used)
H2. Humans sitting in seats of swivel chairs (no use of chair backrest)

The number of humans atop the floor is denoted n and numbers of n of 1, 2 and 3 are tested.

In test H1 test persons are sitting relaxed with legs hanging over the side of the 1.2 m wide floor strip. The hands of a test person rested on his knees.

In test H2 test persons are sitting relaxed in the swivel chair with no use of its backrest.

Reference tests are also made involving sandbags instead of humans:

S1. Sandbags placed on the floor strips (no chair used)
S2. Sandbags placed in seat of swivel chairs

The number of sandbags atop the floor is denoted n and numbers of n of 1, 2 and 3 are tested.

In all tests, test persons or sandbags are placed close to floor midspan. The weight of a sandbag equals 80 kg and the weight of the test persons is measured to be within 5 kg of the sandbag weight.

The swivel chairs used in tests are standard swivel chairs used at the university.

Free decays of the floor are enforced by impacting the floor strip at midspan. The damping of the floor under these conditions is determined and is denoted $\zeta_{H1}(n)$, $\zeta_{H2}(n)$, $\zeta_{S1}(n)$, and $\zeta_{S2}(n)$, respectively.

Table 38.1 Ratio r_ζ determined in tests with sandbags on test floor

Ratio	Test	n, Number of sandbags present on floor			
		0	1	2	3
r_ζ	S1	1	1	1	1
r_ζ	S2	1	8	12	13

Table 38.2 Ratio r_ζ determined in tests with humans on test floor

Ratio	Test	n, Number of test persons present on floor			
		0	1	2	3
r_ζ	H1	1	8	13	17
r_ζ	H2	1	10	13	17

Table 38.3 Ratio r_ζ determined in tests with humans on test floor

Ratio	Test	n, Number of test persons present on floor			
		0	1	2	3
r_ζ	H2	1	10	13	17
r_ζ	H3	1	8	19	28

38.2.4 Results

For the presentation of results it is useful to relate the damping ratio determined for the occupied floor (carrying either n test persons or n sandbags) to the damping ratio determined for the empty floor.

Therefore the ratio defined in Eq. (38.1) is introduced.

$$r_\zeta(n) = \frac{\zeta(n)}{\zeta\,(n=0)} \tag{38.1}$$

In the equation, the nominator represents empty floor damping, so if the ratio attains a value higher than unity, damping is added to the floor. For $\zeta(n)$ either $\zeta_{H1}(n)$, $\zeta_{H2}(n)$, $\zeta_{S1}(n)$, or $\zeta_{S2}(n)$ is entered.

Table 38.1 lists the response ratio, r_ζ, calculated for tests with sandbags on the test floor.

One item to notice is that adding sandbags on the surface of the test floor (as done in test S1) does not result in a change of floor damping. However, if a swivel chair carries the sandbag (as the case in test S2) a different dynamic behaviour of the floor prevails.

It can be seen that with one sandbag on a swivel chair, the damping of the floor increases by a factor 8 compared to the damping of the empty floor. This is a quite considerable increase in floor damping especially when considering that the mass of the sandbag is very small compared to the test floor mass.

Somehow the system "rigid mass on a swivel chair" tends to behave as a passive damper (and actually a quite effective passive damper). As can also be seen in Table 38.1, the amount of damping added to the test floor increases as more swivel chairs carrying a sandbag are placed on the test floor.

Turning to the tests with humans sitting on the test floor, Table 38.2 presents the calculated ratios.

It can be seen that when humans are sitting on the test floor, they also act as passive dampers in that the ratio r_ζ increases with increases in values of n. In test H1 the test persons sad directly on the test floor (no use of a swivel chair) and in test H2 the test persons sad in seats of swivel chairs.

Comparing the ratios obtained in the two tests it is seen that there is no significant difference suggesting that the presence of the chair does not have a bearing on the damping characteristics of the floor. This is opposite to what was observed in tests with sandbags.

Comparing the results in terms of the ratio r_ζ obtained in test H1 with those obtained in test S2, it is found that the test persons adds just as must damping to the floor as does the swivel chair carrying a sandbag.

A supplementary set of tests were made namely test H3, and test conditions are outlined below.

H3. Humans sitting in seats of swivel chairs with (this time use of chair backrest)

The test procedures were similar and results in terms of the ratio r_ζ are listed in Table 38.3 along with ratios obtained for test H2.

It can be seen that the use of backrest also have some bearing on the vibration behaviour of the floor.

38.2.5 Discussion

It is apparent that humans act as passive dampers when placed on a vibrating structure. They cannot with reasoning be modelled as a simple static weight (as a sandbag) placed on the structure although this is the approach adapted in ultimate limit state calculations of structures.

When focus is on the serviceability limit state it is accelerations that that determine the feasibility of a structure. Here the presence of passive humans (such as those sitting in the present tests) plays a role. They are able to alter the damping characteristics of the combined human-floor system as shown.

Nevertheless, it is not common in serviceability limit state evaluations to account for the human-structure interaction mechanism. At least in some cases it is the passive person for which there is concern in the serviceability limit state evaluation, as he may feel vibration levels annoying. Nevertheless it is not common to model his presence in the vibrating system when judging serviceability performance of a structure. However, he needs to be present for him to feel annoying vibrations.

There are indications that it may be useful to model passive humans as a mass dynamically interacting with the floor mass. This is in agreement with the modelling approach applied in biomechanics [6].

The following numerical study shows how the presence of a passive person might be integrated into a serviceability evaluation of a structure.

38.3 Numerical Case Study

38.3.1 The Interaction Model

The case study assumes a 2DOF human-structure interaction model. The floor is represented by a SDOF system with the dynamic characteristics (natural frequency of the first bending mode (f_F), the modal mass of this mode of vibration (M_F) and the damping ratio (ζ_F)) given in Table 38.4.

This system is attached to ground and it is assumed to carry a SDOF model representing the presence of a passive person atop the floor. The dynamic characteristics assumed for the person are given in Table 38.5.

The value assumed for the characteristics are considered to be fairly realistic.

All connections of the 2DOF model are assumed to behave linearly.

38.3.2 The Load Model

A walking load model is applied for an active person on the floor.

The force that the pedestrian applies to the floor is given in Eq. (38.2).

$$q(t) = G + G\sum_{i=1}^{3} \alpha_i \sin\left(2\pi\, i f_S t + \theta_i\right) \tag{38.2}$$

G represents the static weight of the pedestrian and α_i is the dynamic load factor for harmonic i. In Eq. (38.2) f_S is the walking frequency.

The values for the dynamic load factors are modelled as suggested in [7] which for instance reflects that the first dynamic load factor ($i = 1$) depends on walking frequency.

Table 38.4 Dynamic characteristics of floor

f_F	M_F	ζ_F
6 Hz	2.5×10^3 kg	0.4 %

Table 38.5 Dynamic characteristics of person

f_H	M_H	ζ_H
7.5 Hz	60 kg	0.30

For simplicity, the floor is assumed to be one-way spanning, and the pedestrian is assumed to walk across the floor with a constant walking speed, v, and the model for v suggested in [8] is assumed.

On these conditions the modal load on the floor can be modelled by Eq. (38.3).

$$p(t) = q(t) \sin(\pi v t / L) \tag{38.3}$$

The length of the one-way spanning floor, L, is assumed be 11 m.

38.3.3 Calculated Floor Response and Results

A Newmark approach was employed for modelling the load action. Floor accelerations, a, at midspan were calculated for walking frequencies ranging from 1.7 to 2.3 Hz with increments of 0.05 Hz.

From the time series derived for each assumption of walking frequency, the peak value of floor acceleration was identified.

This was done assuming an empty floor and assuming the presence of passive person at floor midspan. The maximum peak acceleration in each case was identified.

It was found that peak acceleration response under the assumption of the presence of passive person on the floor was about half of that calculated for the empty floor.

Hence the bare presence of the passive person on the floor has reduced the vibration level of the floor considerably.

38.4 Conclusion and Discussion

The paper has investigated mechanisms of interaction between a vibrating floor strip and different items placed on it.

In tests, a sandbag placed directly on the surface of the floor did not add any damping to the floor. However, when a swivel chair carried the sandbag considerable damping was added to the floor.

A high degree of added damping was also found when passive humans occupied the floor, and results suggests that it might be more appropriate to model the human mass as SDOF system attached to the floor mass rather than as a static load simply clamped to the floor.

A procedure as to how such model might be implemented for computing floor vibration levels was shown in a case study.

Acknowledgements The author acknowledges test persons for their participation in tests.

References

1. Ellis, B.R., Ji, T.: Human-structure interaction in vertical vibrations. In: Proceedings of the ICE: Structures and Buildings, London, UK vol. 122, pp. 1–9, (1997)
2. Brownjohn, J.M.W.: Energy dissipation from vibrating floor slabs due to human-structure interaction. Shock. Vib. **8**(6), 315–323 (2001)
3. Reynolds, P., Pavic, A., Ibrahim, Z.: Changes of modal properties of a stadium structure occupied by a crowd. In: Proceedings of the 22nd International Modal Analysis Conference, Dearborn, Michigan (2004)
4. Pedersen, L.: Updating of the dynamic model of floors carrying stationary humans. In: Proceedings of the 1st International Operational Modal Analysis Conference, Copenhagen, Denmark pp. 421–428, (2005)
5. Sachse, R., Pavic, A., Prichard, S.: The influence of a group of humans on modal properties of a structure. In: Proceedings of the Fifth International Conference on Structural Dynamics, Munich, Germany pp. 1241–1246, (2002)
6. Griffin, M.J.: Handbook of Human Vibration. Academic, London (1990)
7. Kerr, S.C., Bishop, N.W.N.: Human induced loading on flexible staircases. Eng. Struct. **23**, 37–45 (2001)
8. Bachmann, H., Ammann, W.: Vibrations in structures – induced by man and machines, In: IABSE Structural Engineering Documents 3e, Zürich (1987)

Chapter 39
Study of Human-Structure Dynamic Interactions

Mehdi Setareh and Shiqi Gan

Abstract Structural engineers usually consider the building occupants as added weight (or mass). Even though this may be a reasonable assumption for the static analysis and design of structures, it can result in discrepancies between the predicted and measured dynamic responses of a structure. This paper presents the results of a research effort conducted to evaluate the effects of human bodies on the dynamic properties and responses of civil engineering structures. A laboratory test structure and a footbridge were used, and the Component Mode Synthesis technique was applied to compute the structural response. Using a parameter search technique, the dynamic properties of an equivalent single-degree-of-freedom lumped mass model to represent groups of people in different postures on a test structure, were found. The model was used to compute the dynamic properties and response of a footbridge when occupied by people. Comparison of the results with the measured properties and responses of the footbridge demonstrated the validity of the human dynamic model.

Keywords Human-structure interaction • Vibration serviceability • Human vibrations • Human dynamic parameters • Civil engineering structures

39.1 Introduction

There have been numerous studies on the dynamic properties of human bodies. Most these studies have been conducted by researchers in bio-mechanics. Various lumped-mass models of human body with various degrees of freedom have been proposed and studied. Allen [1] used a 2-DOF system with masses in series connected to each other by springs and dampers. Wei and Griffin [2] used single-degree-of-freedom (SDOF) and 2-DOF models to represent dynamic characteristics of seated humans. They considered rigid support mass to represent the effects of other modes that are above the frequency range of interest, and as a result, they contribute to the mass only. Coermann [3] found a natural frequency of 5.9 Hz for individuals when standing straight and 2 Hz in bent-knees posture. Randall et al. [4] found the resonant frequencies of 113 individual standing subjects on a vibrating beam while applying very low accelerations at their feet. They found mean values of 12.2 ± 0.1 Hz for males, 12.8 ± 0.2 Hz for females with an overall mean for the population of 12.3 ± 0.1 Hz.

Matsumoto and Griffin [5] studied the effects of vibration magnitude and posture on 12 individual male subjects in standing position. They found that the human resonance frequency reduced from 6.75 Hz to 5.25 Hz with acceleration increase from 0.125 m/s^2 to 2.0 m/s^2 root-mean-squared (r.m.s.). The main resonance frequencies of subjects at 1.0 m/s^2 r.m.s. changed with postures: 5.5 Hz in the normal standing posture, 2.75 Hz in the bent-legs posture, and 3.75 Hz in the one-leg posture. Matsumoto and Griffin [6] compared the human dynamic responses in sitting and standing positions using eight individual male subjects subjected to vertical whole-body vibrations. They found that for both positions subjects had resonances in the apparent mass in the 5–6 Hz range (slightly higher for standing than for sitting).

Matsumoto and Griffin [7] introduced SDOF models (with and without rigid support mass) and 2-DOF models with parallel and serial masses (with and without rigid mass) to approximate the dynamic behavior of individual human bodies. They studied the responses of 12 individual male subjects in standing, bent-leg, and one-leg postures. They found that the 2-DOF models better represented the measured apparent masses of the human subjects. They estimated the human resonance frequencies at approximately 5 Hz (for the first mode) and 10–15 Hz (for the second mode). The individuals' damping ratio ranged between 30 % and 50 %. Matsumoto and Griffin studied the effects of vibration magnitudes from 0.25 m/s^2 to 2.0 m/s^2 r.m.s. They found that the human stiffness and damping ratio reduced with an increase in the vibration magnitude.

M. Setareh (✉) • S. Gan
Virginia Tech, Blacksburg, VA 24061, USA
e-mail: setareh@vt.edu

© The Society for Experimental Mechanics, Inc. 2016

M. Allen et al. (eds.), *Dynamics of Coupled Structures, Volume 4*, Conference Proceedings of the Society for Experimental Mechanics Series, DOI 10.1007/978-3-319-29763-7_39

Different lumped mass systems have been used to represent the dynamic behavior of human bodies on civil engineering structures. Foschi and Gupta [8] used SDOF dynamic models of humans on wood joist floors. Folz and Foschi [9] used different 2-DOF models and proposed an 11-DOF model to substitute the 15-DOF model of Nigam and Malik [10] for analyzing the vibration of a joist floor system. Foschi et al. [11] used the 2-DOF model of human body proposed by ISO7962 [12] on a wood joist floor system. The natural frequencies and damping ratios for the model were $f_1 = 5.0$ Hz and $\xi_1 = 37\%$, and $f_2 = 12.49$ Hz and $\xi_2 = 46\%$. They concluded that the effects of the second mode on the floor response was not significant. Therefore, they proposed an equivalent SDOF model to represent the dynamic characteristic of human body as a substitute for the 2-DOF model of ISO7962. This model had a natural frequency of 3.34 Hz and damping ratio of 33 %.

Ji [13] proposed a continuous bar with two different mass and stiffness segments to represent a standing human. Brownjohn [14] performed a series of experiments to estimate the parameter of a SDOF human model as a substitute to the ISO7962 [12], 2-DOF human model. He conducted a series of experiments using a subject in standing erect, with knees bent, and sitting postures. He estimated the human natural frequency and damping ratio to be 4.88 Hz and 37 %, respectively.

Zheng and Brownjohn [15] studied the interaction of a reinforced concrete slab model with a human body subjected to the vibrations generated by a shaker. Using the known parameters of the structure, they computed the natural frequency and damping ratio of the human body as a SDOF model. From this study they found the average human parameters of $f_H = 5.24 \pm 0.40$ Hz, and $\xi_H = 39\% \pm 5\%$.

Falati [16] used a pre-stressed concrete test floor and performed a number of experiments to evaluate the interactions between the test structure and one human subject. From the measured response, he estimated the dynamic properties of an SDOF human model to be: $f_H = 10.43$ Hz and $\xi_H = 45\%–55\%$.

Using an experimental test setup consisting of a simply-supported pre-stressed concrete slab, Sachse [17] studied the effects of up to five stationary human subjects on the floor. From this study, she found that in all cases, presence of humans resulted in a reduction in the floor natural frequency and an increase in damping. She concluded that the natural frequency of human body, f_H, and the damping ratio, ξ_H, increase with increasing f_S (natural frequency of the structure). For $f_S < 16.95$ Hz, the approximate bands for the human dynamic parameters are $m_H > 0.6\, m_T$ (total human mass), $f_H < 9$ Hz, and $\xi_H < 40\%$, approximately.

Pedersen and Hansen [18] considered the effects of the human-structure interaction (HSI) on floors using SDOF models to represent the humans and a specific mode of a floor to form a 2-DOF dynamic model. The human parameters were assumed to be $f_H = 6$ Hz and $\xi_H = 20\%$. The results of study showed that the presence of humans have different effects on the low and high frequency floors.

Sim et al. [19] developed a 2-DOF crowd model using the individual human dynamic properties recommended by [2] and [7] for the seated and standing individuals. They conducted an analytical study, which showed that passive crowd add mass and damping to the structure, resulting in a reduction in natural frequency and response compared to the empty structure.

Agu and Kasperski [20] conducted a probabilistic study to check how random scatter of individual human dynamic properties in a group can affect the dynamic properties (f and ξ) of the structure with a crowd. They concluded that due to the randomness of dynamic properties of human body, the mean values for individual human dynamic properties cannot be used for all cases to represent the human-structure dynamic interactions.

Zheng [21] developed a continuous model of a standing human body from the available natural frequency measurements of standing subjects by [7]. By incorporating the available information in biomechanics and his interaction human body model [21], he identified parameters for the 2-DOF human model to be $f_1 = 5.78$ Hz and $\xi_1 = 36.9\%$, and $f_2 = 13.2$ Hz and $\xi_2 = 44.5\%$. From the results of experimental studies on four individual subjects, he found that their identified natural frequencies varied from 3.17 to 5.81 Hz with their mean natural frequencies ranging from 4.16 to 4.57 Hz. The identified damping ratio of the human body varied from 2.5 % to 38.8 %, and the mean damping ratio of the four individuals were from 8.6 % to 22.5 %.

This paper presents an experimental and analytical study to identify the dynamic properties of a group of people using a laboratory test structure. Several rounds of modal and vibration tests were conducted for this purpose. The identified human properties were then used to predict the response of a footbridge structure when occupied by people, which showed close match with the measurements.

39.2 Description of the Test Structure

The test structure is comprised of a two-story steel structure located at the Virginia Tech Vibration Testing Laboratory. The structure has a single square bay with center to center column dimensions of 9.15 m by 9.15 m (30 ft by 30 ft) as shown in Fig. 39.1. The floor is made of a 50.8 mm (2 in.) steel deck with 50.8 mm (2 in.) of concrete topping, supported by 20LH06 steel joists as shown in Fig. 39.2. The joists are supported by W18x40 girders. The test floor does not include any non-structural elements

Fig. 39.1 Test structure at the Virginia Tech Vibration Testing Laboratory

39.3 Modal Testing

A full modal test of the floor was conducted using an APS-400 electrodynamic shaker. The shaker was placed at the quarter point from a corner column to excite several lower modes of the floor. A burst chirp excitation with 30 s on and 15 s off and a frequency bandwidth of 3–20 Hz was used. The measured records were used in MEscope VES [22] to estimate the natural frequencies, damping ratios and mode shapes of the structure. The measured natural frequencies and damping ratios for the first three lower modes are as follows: $f_1 = 4.28$ Hz, $\xi_1 = 0.264\%$; $f_2 = 7.72$ Hz, $\xi_2 = 0.205\%$; and $f_3 = 8.91$ Hz, $\xi_3 = 0.227\%$. Higher modes were not identified since their contributions towards the floor vibrations were limited. Figure 39.3 shows the shaker and accelerometers during one of the stages of the modal test.

39.4 Vibration Tests with Human Subjects

To study the effects of a group of people on the dynamic properties of the test floor and estimate the crowd dynamic properties, six groups of human subjects with different sizes from 4 to 41 individuals were placed on the floor in three postures: sitting on chairs, standing erect, and standing with the bent knees. Each individual was weighed before conducting the tests.

PCB 393C accelerometers were placed at different locations on the floor and the shaker was placed at the same location as for the floor modal test. A burst chirp excitation with 30 s on and 15 s off and a frequency band of 3–15 Hz was used. Low levels of vibration within the range typically resulted from human movements were applied. The vibration magnitudes were at the lower limits of those used in the biomechanics research.

To directly evaluate the effects of humans on the test structure as compared to rigid masses, concrete blocks with equivalent weights to each individual were placed at the subjects' specific locations on the test structure and the floor response was measured. The same excitation setting and location of the accelerometers were used for consistency. Figure 39.4 shows one of the stages of the vibration tests with 24 human subjects in sitting, standing, and bent-knees postures along with the tests with concrete blocks (weights).

Figure 39.5 shows the comparison of the drive point frequency response function (FRF) without people, with 24 people in sitting, standing, and bent-knees positions, and concrete blocks in place of people. This clearly shows that the humans interact dynamically with the floor and they cannot be considered as rigid masses (concrete blocks).

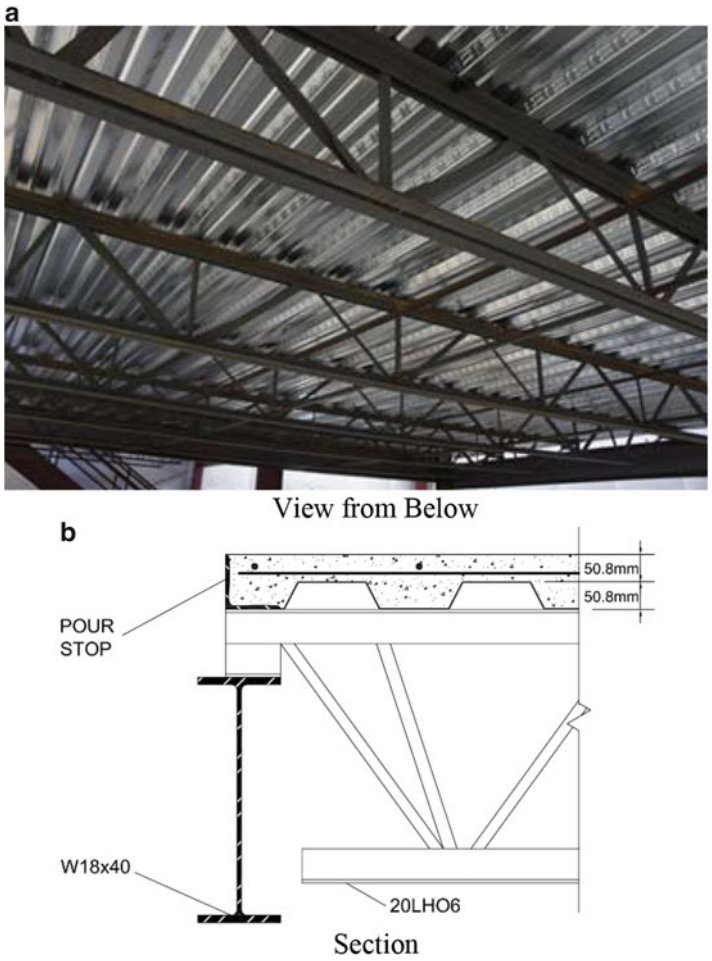

Fig. 39.2 Test structure floor

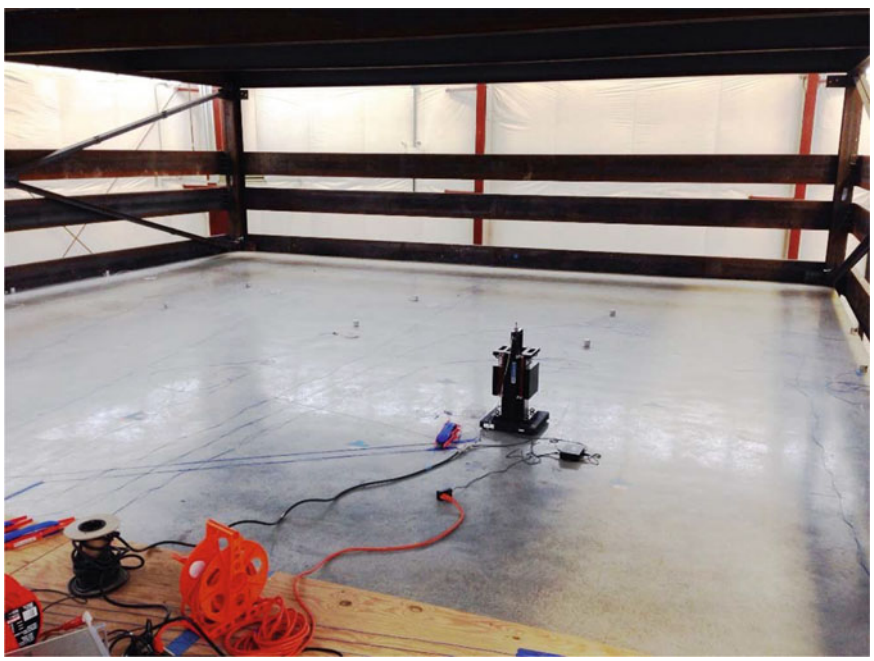

Fig. 39.3 Modal testing of floor

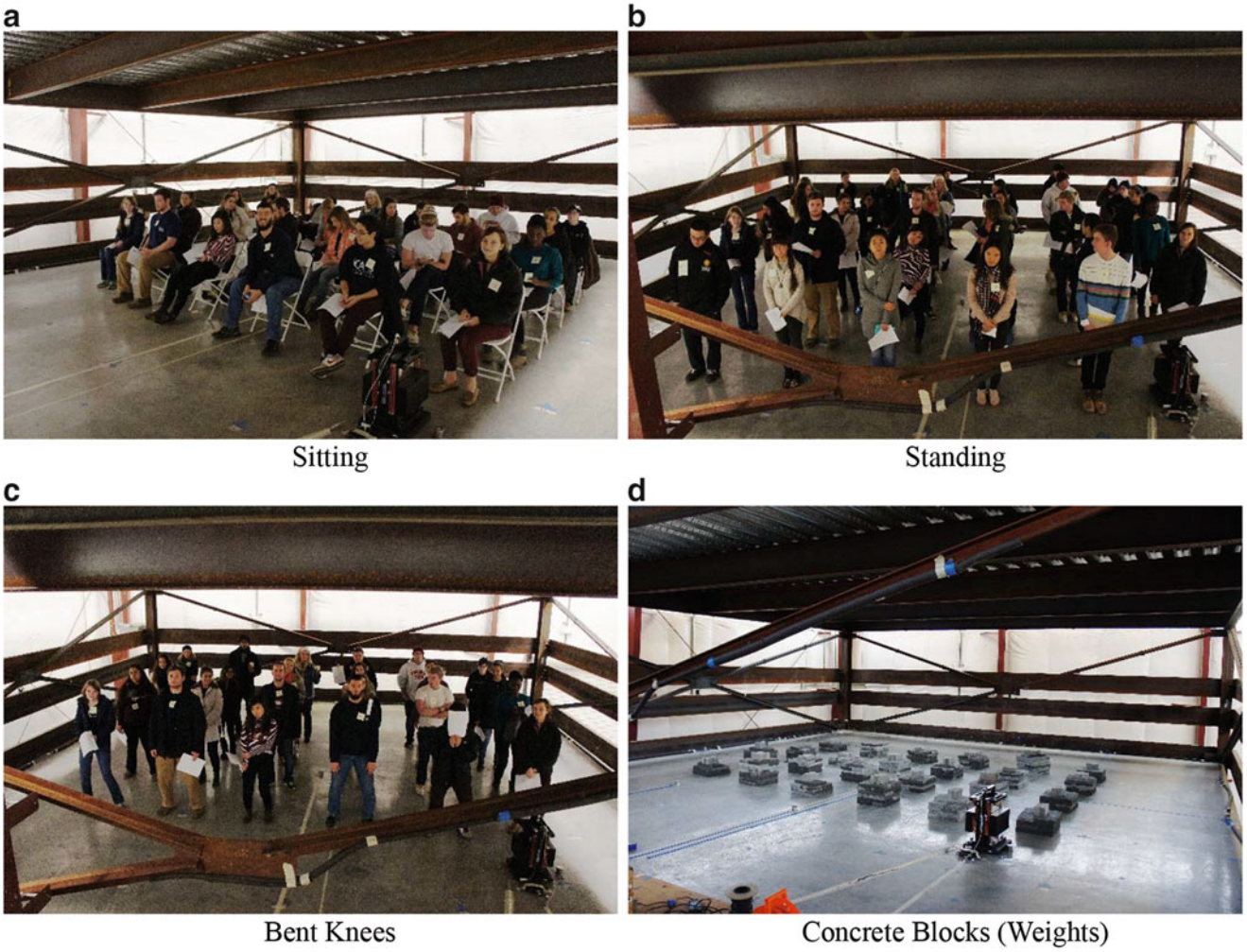

Fig. 39.4 Vibration tests with human subjects and concrete blocks

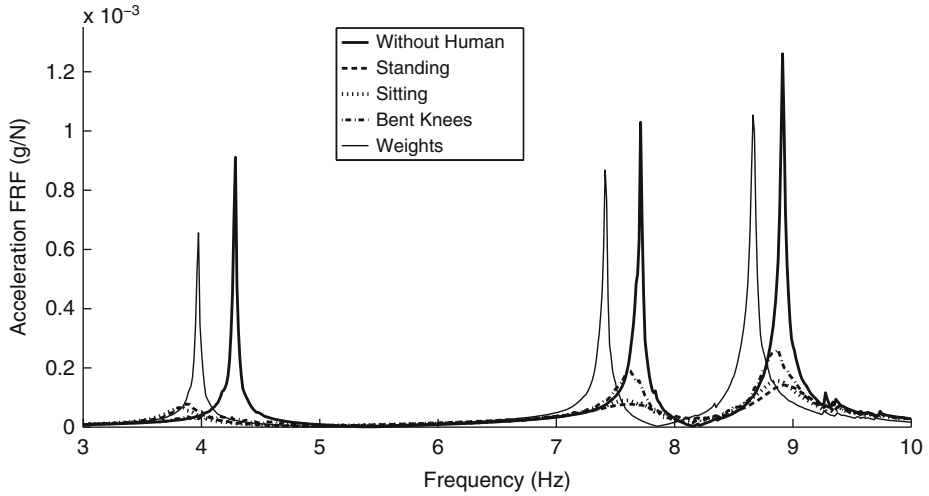

Fig. 39.5 Comparison of the floor drive point FRF without people and with 24 people in different postures and the equivalent concrete blocks

39.5 Estimation of the Human Dynamic Properties

In the introduction section, different dynamic models to represent the human body were discussed. An absolute majority of these models were SDOF or 2-DOF models representing individual human bodies. In this study SDOF models as shown in Fig. 39.6 will be used to represent the dynamic properties of groups of people.

To estimate the dynamic properties of the human model shown in Fig. 39.6, the dynamic properties of the test structure without people were measured as indicated above. The Component Mode Synthesis (CMS) technique [23] was then used to compute the floor FRF considering the addition of humans based on the SDOF model shown in Fig. 39.6. The peak resonance FRF values and resonance frequencies were compared to those from the measurements. The human dynamic parameters were then varied to minimize the differences between the computed and measured resonance frequencies and peak resonance FRF amplitudes. The importance of the CMS is in computation of the coupled human-structure system response using the measured properties of the empty floor and assumed properties of the groups of people.

The error function, e, used to estimate the human dynamic properties is shown in Eq. (39.1):

$$e = \sum_{i=1}^{p} \left[\left(\frac{f_i^c - f_i^m}{f_i^m} \right)^2 + \left(\frac{A_i^c - A_i^m}{A_i^m} \right)^2 \right] \tag{39.1}$$

where f_i^c and A_i^c are the computed resonance frequency and peak FRF amplitude of the floor with human subjects using the CMS technique, respectively, f_i^m and A_i^m are their measured counterparts, and p is the total number of component modes used. Using the above procedure, the human crowd model natural frequency, f_H, and damping ratio, ξ_H, were computed for each posture and number of people present on the floor.

As mentioned before, six groups of people were present on the floor for this study. The total number of people in each group is as follows: A (41 people), B (35 people), C (24 people), D (16 people), E (8 people), and F (4 people). Table 39.1 shows f_H and ξ_H estimated for each group in different postures.

The results shown in Table 39.1 are relatively consistent with the exception of damping in group B. Generally, a larger number of people in each group provides more consistent group effects; however, it results in a larger level of measurement noise due to the interaction of people with the floor. This can be observed in Fig. 39.7 which shows the comparison between the predicted FRF using the CMS technique and those from the measurement for the people in the standing posture. Comparison for the other postures can be found in Shiqi and Setareh [24].

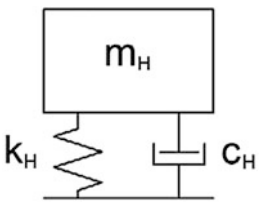

Fig. 39.6 SDOF model representing a group of people

Table 39.1 Estimated human parameters for each group in different postures

	Postures					
	Standing		Sitting		Bent knees	
Group	f_H (Hz)	ξ_H	f_H (Hz)	ξ_H	f_H (Hz)	ξ_H
A	5.7	25 %	5.4	26 %	2.9	40 %
B	5.9	60 %	4.6	87 %	–	–
C	5.7	26 %	5.4	24 %	3	39 %
D	5.8	26 %	5.5	23 %	3.1	46 %
E	5.6	32 %	5.3	32 %	4.9	24 %
F	5.7	33 %	5	40 %	4.7	35 %

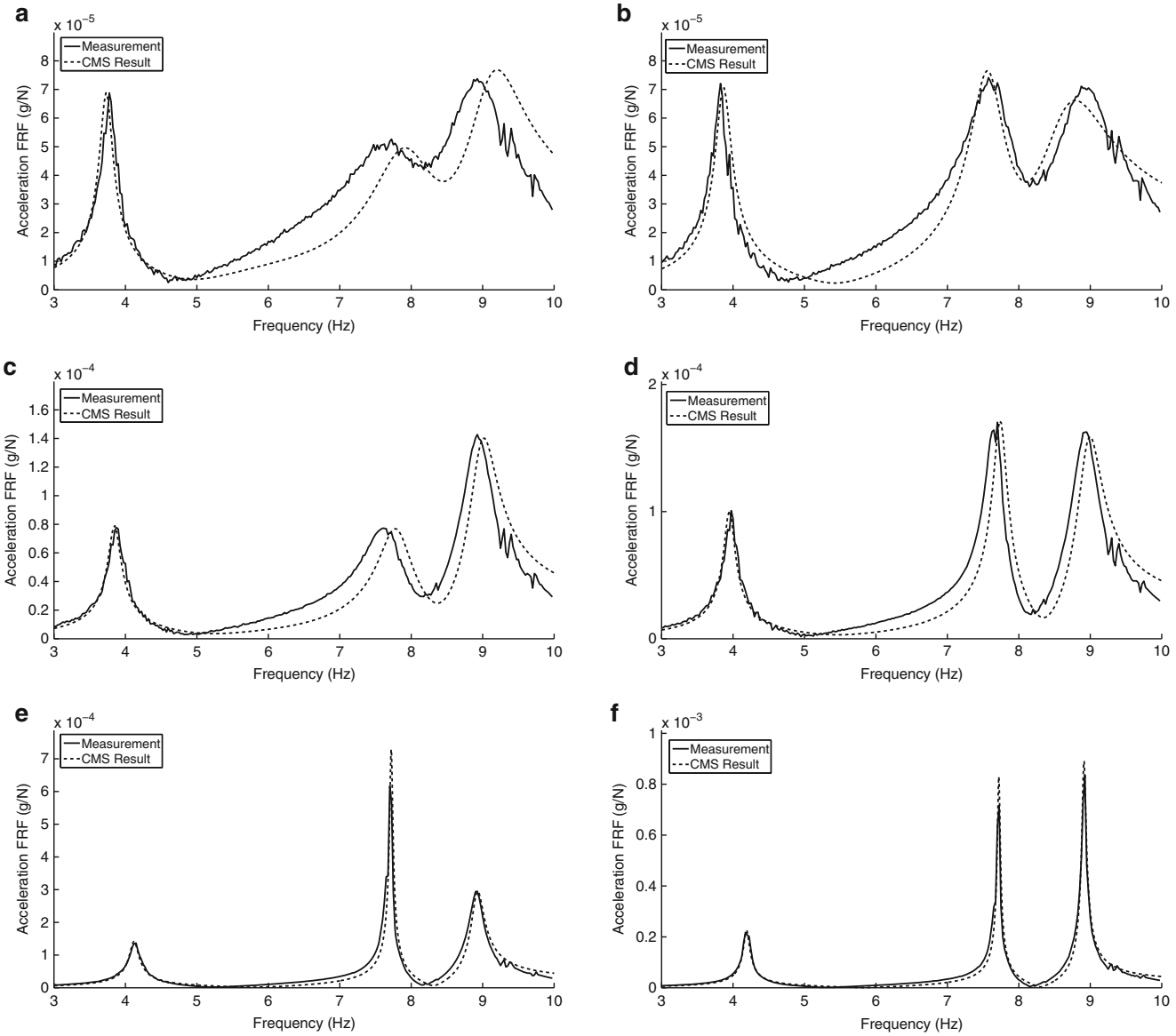

Fig. 39.7 Comparison of the acceleration FRF (accelerance) between the measurements and the Results from CMS for different groups in standing posture: (**a**) group A; (**b**) group B; (**c**) group C; (**d**) group D; (**e**) group E; (**f**) group F

39.6 Verification of the Identified Human Dynamic Parameters

To verify the consistency of the results obtained in this study, the human parameters shown in Table 39.1 were used to predict the response of an outdoor footbridge with sixteen people standing in two different configurations. Details of the footbridge along with the modal tests and human presence on the structure can be found in Setareh et al. [25].

The structure is susceptible to excessive vibrations due to human movements. The footbridge is also used at times by people to watch musical performances at an adjacent amphitheater while standing on the structure. In addition, due to its relatively small mass it results in large human-structure interaction effects. Two configurations of the people on the footbridge were considered: (1) HSI-1 represents human subjects spread over the footbridge span, and (2) HSI-2 with people gathered close to the mid-span.

Since group A parameters in Table 39.1 had the largest HSI effects and the parameters were generally consistent, $f_H = 5.7$ Hz and $\xi_H = 25\%$ were used to represent the groups of standing people. Figure 39.8 shows the comparison of the maximum vertical FRF of the footbridge without people, predicted using the CMS method based on the assumed human model and the measurements. The results show good match between the measurements and the predicted response.

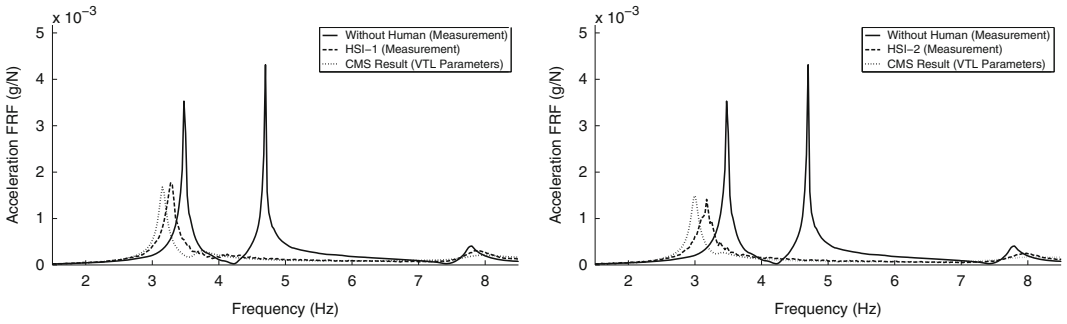

Fig. 39.8 Comparison of the footbridge acceleration FRF for (1) without people; (2) with people from the measurements, and (3) with people (HSI-1/HSI-2) using the CMS technique

Therefore, it was concluded that the identified SDOF human parameters for groups of humans can be a simple acceptable representation to estimate the effects of HSI on the dynamic properties of floors.

39.7 Summary and Conclusions

This paper presented a study of the human-structure interactions (HSI) using a laboratory test structure. The measured modal parameters of the structure and the Component Mode Synthesis technique were used to estimate dynamic parameters of groups of people in different standing, sitting, and standing with bent-knees postures as follows: (1) for standing ($f_H = 5.7$ Hz, $\xi_H = 25\%$), (2) for sitting ($f_H = 5.4$ Hz, $\xi_H = 26\%$), (3) for bent-knees ($f_H = 2.9$ Hz, $\xi_H = 40\%$). The parameters for the standing posture were verified using the measurement on an outdoor footbridge.

Acknowledgements This study was supported by the National Science Foundation under Grant No. CMMI-1335004. This support is gratefully acknowledged. Any opinions, findings, and conclusions expressed in this paper are those of the writers and do not necessarily reflect the views of the National Science Foundation. The authors would like to acknowledge the support of Vibrant Technology, Inc., in particular Dr. Mark Richardson.

References

1. Allen, G.: A critical look at biodynamic modeling in relation to specifications for human tolerance of vibration and shock. In: AGARD Conference Proceedings, pp. A25-5–A25-15, Paris, France (1978)
2. Wei, L., Griffin, M.J.: Mathematical Models for the apparent mass of the seated human body exposed to vertical vibration. J. Sound Vib. **212**(5), 855–874 (1998)
3. Coermann, R.R.: The mechanical impedance of the human body in sitting and standing position at low frequencies. Hum. Factors **4**, 227–253 (1962)
4. Randall, J.M., Matthews, R.T., Stiles, M.A.: Resonant frequencies of standing humans. Ergonomics **40**(9), 879–886 (1997)
5. Matsumoto, Y., Griffin, M.J.: Dynamic response of the standing human body exposed to vertical vibration: influence of posture and vibration magnitude. J. Sound Vib. **212**(1), 85–107 (1998)
6. Matsumoto, Y., Griffin, M.J.: Comparison of biodynamic response in standing and seated human bodies. J. Sound Vib. **238**(4), 691–704 (2000)
7. Matsumoto, Y., Griffin, M.J.: Mathematical models for the apparent masses of standing subjects exposed to vertical whole-body vibration. J. Sound Vib. **260**(3), 431–451 (2003)
8. Foschi, R.O., Gupta, A.: Reliability of floors under impact vibration. Can. J. Civ. Eng. **14**(5), 683–689 (1987)
9. Folz, B., Foschi, R.O.: Coupled vibrational response of floor systems with occupants. J. Eng. Mech. ASCE **117**(4), 872–892 (1991)
10. Nigam, S.P., Malik, M.: A study on a vibratory model of a human body. J. Biomech. Eng. **109**(2), 148–153 (1987)
11. Foschi, R.O., Neumann, G.A., Yao, F., Folz, B.: Floor vibration due to occupants and reliability-based design guidelines. Can. J. Civ. Eng. **22**(3), 471–479 (1995)
12. ISO 7962: Mechanical vibration and shock-mechanical transmissibility of the human body in the z-direction. In: ISO 7962, International Standards Organization, Geneva (1987)
13. Ji, T.: A continuous model for the vertical vibration of the human body in a standing position. In: UK Informal Group Meeting on Human Response to Vibration, Silsoe, 18–20 September 1995
14. Brownjohn, J.M.W.: Energy dissipation in one-way slabs with human participation. In: Proceedings of the Asia-Pacific Vibration Conference'99, Nanyang Technological University, Singapore, 11–13 December, pp. 155–160 (1999)

15. Zheng, X., Brownjohn, J.M.W.: Modeling and simulation of human-floor system under vertical vibration. In: Smart Structures and Materials 2001: Smart Structures and Integrated Systems, Proceedings of SPIE, vol. 4327, pp. 513–520, Newport Beach, California, USA (2001)
16. Falati, S.: The Contribution of Non-Structural Components to the Overall Dynamic Behaviour of Concrete Floor Slabs. University of Oxford, Oxford (1999)
17. Sachse, R.: The influence of human occupants on the dynamic properties of slender structures. Ph.D. thesis, Department of Civil and Structural Engineering, University of Sheffield, Sheffield (2002)
18. Pedersen, L., Hansen, L.: Human damping and its capacity to control floor vibrations. In: Smart Structures and Materials 2004: Damping and Isolation. Proceedings of SPIE, vol. 5386. SPIE, Bellingham (2004)
19. Sim, J., Blakeborough, A., Williams, M.: Modelling effects of passive crowds on grandstand vibration. In: Structures and Buildings, Proceedings of the Institution of Civil Engineers, vol. **159**(585), pp. 261–272, London, UK (2006)
20. Agu, E., Kasperski, M.: Influence of the random dynamic parameters of the human body on the dynamic characteristics of the coupled system of structure-crowd. J. Sound Vib. **330**, 431–444 (2011)
21. Zheng, Q.: Models of a standing human body in structural vibration. Ph.D. thesis, School of Mechanical, Aerospace and Civil Engineering, University of Manchester (2013)
22. ME'scope VES: ME'scope VES 6.0. Vibrant Technology, Inc., Scotts Valley (2013)
23. Hurty, W.C.: Dynamic analysis of structural systems using component modes. AIAA J. **3**(4), 678–685 (1965)
24. Gan, S., Setareh, M.: Human-structure interaction study. School of Architecture and Design, Virginia Tech, Blacksburg (2015)
25. Setareh, M., Woolard, M., Schlichting, A.: A study of vibrations of a slender footbridge due to human movements. In: Footbridge 2014 - The Fifth International Conference, Footbridges: Past, Present and Future, London (2014)

Chapter 40
Characterisation of Transient Actions Induced by Spectators on Sport Stadia

A. Quattrone, M. Bocian, V. Racic, J.M.W. Brownjohn, E.J. Hudson, D. Hester, and J. Davies

Abstract In a wake of Hillsborough disaster of 1989, all stadia hosting major sport championships in the UK were converted from terraced to all-seated. Driven by spectators' demands for improving the quality of their experience and organisers' interest in increasing the capacity of their venues, a debate has arisen recently about the possible introduction of safe standing areas. Some issues have been already highlighted, mainly related to security aspects and comfort. This study investigates how the introduction of safe standing areas and the expected increase of the density of a crowd could impact the dynamic loading induced by the spectators and the resulting structural response. To this end an experimental campaign has been conducted in a laboratory delving into the effects of common actions performed by seated and standing cheering spectators. The data on dynamic behaviour of a lively test structure in both conditions have been collected, simultaneously with data on behaviour of the spectators. The forces applied by the spectators have been inferred using inverse dynamics, by analysing the structural response. The results are presented in the context of human-to-structure interaction and human-to-human coordination.

Keywords Force identification • Human dynamic loading • Vibration serviceability • Dynamic testing grandstand

40.1 Introduction

As a result of recommendations made in the Taylor Report [1], an inquiry into the Hillsborough disaster of 1989, all stadia hosting major sport championships in the UK were converted from terraced to all-seated. In recent years, a debate has arisen about the reintroduction of standing areas, driven by football supporters, which demand for improving the quality of their experience, and by professional clubs, attracted by the possibility of increasing the capacity of their structures with relatively low costs. Nevertheless, standing at football matches within seating areas is a common occurrence, leading to safety concerns. Hence there is a need to consider seriously solutions to enable standing amongst football supporters [2].

The Guide To Safety At Sports Grounds, also known as Green Guide [3], specifies the allocated space needed for seated and standing spectators respectively. A ratio of 18 standing people for every 10 spectators in seats has been deduced [4], with an increase of capacity of 80 %. While it could easily appear financially advantageous for the clubs, some issues mainly related to security and comfort should be carefully considered in the decision making process. Real case studies demonstrate that sports stadia are susceptible to human-induced vibration issues as they play host to large, lively crowds [5, 6]. The introduction of safe standing in the place of seats, and the ensued increased capacity, could negatively couple its effects with changes in the dynamic interaction between spectators and structure, resulting in serviceability or even structural safety problems. Consequently, these aspects should be conveniently considered by stadia operators in the decision making process.

This work is a first step in investigating how the installation of safe standing areas could affect the dynamic response of grandstands. In particular, the effects of transient actions, e.g. those commonly performed in occasion of scoring, have been

A. Quattrone (✉) • J.M.W. Brownjohn • E.J. Hudson • J. Davies
University of Exeter, North Park Road, Exeter, UK
e-mail: a.quattrone@exeter.ac.uk

M. Bocian
University of Leicester, University Road, Leicester, UK

V. Racic
Politecnico di Milano, Piazza Leonardo da Vinci 32, Milan, Italy

D. Hester
Queen's University Belfast, University Rd, Belfast, Northern Ireland, UK

© The Society for Experimental Mechanics, Inc. 2016

M. Allen et al. (eds.), *Dynamics of Coupled Structures, Volume 4*, Conference Proceedings of the Society for Experimental Mechanics Series, DOI 10.1007/978-3-319-29763-7_40

investigated. The chosen actions have been reproduced on a laboratory test structure, and results were compared in terms of exerted forces and structural responses. The collected data have been then used to validate a testing methodology, based on inverse dynamics, aimed at reconstructing the human dynamic loading on real grandstands from structural responses.

40.2 Human-Induced Vibrations on Stadia

Sport stadia grandstands are structures particularly susceptible to vibrations induced by human activity [6–9]. Due to the large number of people involved, and the design trend of adopting slender structural solutions, the amplitude of vibrations could result in uncomfortable feeling of spectators, up to causing panic in the occupants, or even structural failures [5]. Consequently, the dynamic behaviour of grandstands is a public safety concern faced by stadia operators. Several examples of excessive vibrations on football stadia have been reported in literature in presence of external rhythmic stimuli [10–12]. These studies indicate the main cause in the synchronization of spectators reacting at a same rate near the natural frequencies of the grandstands or their multiples, resulting in the amplification of dynamic responses. Similar concerns have been observed during sport matches, in absence of such rhythmic external stimuli being present [13–15]. Published results indicate that the higher dynamic response arises when significant events such as goals occur. During these events, spectators induce a sort of impulsive loading raising from their seats, jumping and bouncing for a limited period. In these cases, structural response is characterised by a broader energy content compared with concerts, where synchronised rhythmic loading can be easily observed. These cases studies, in addition to reported failures [4, 16], demonstrated that vibrations can be an issue within stadia even when synchronisation such as rhythmic bouncing and jumping does not occur, and therefore need to be researched.

A majority of published research is focused towards rhythmic loading as opposed to the impulse like response that occurs when these events happen. Mathematical models for a singular person and crowd bouncing have been deduced from experimental tests conducted on grandstand simulator in Oxford [17] and from the experiments in Manchester by Harrison et al. [18]. During a sport match, the presence of spectators occupying the structure can be classified as either active or passive [19]. Active occupants are those that perform motions that exert dynamic forces upon the structure, whereas passive ones are those that are stationary, either sitting or standing, and only exert load on the structure due to mass and damping properties arising from their induced motion. Harrison et al. [18] studied also the influence of movement of the structure on the human jumping and bouncing. Another highlighted aspect concerns how the presence of spectators affect the structural dynamic properties compared with the unoccupied structure. In the presence of passive occupants, the increase of damping [20] and the variation of natural frequency, with different rates between seated and standing conditions, have been observed [21]. These results seem to indicate that the introduction of safe standing areas could also affect the dynamic characteristics of the grandstand, potentially causing vibration issues in structures previously not prone to these.

Since the complexity of the factors involved and their strong interconnection, evaluating how the reintroduction of safe standings could affect the behaviour of grandstands requires deepening the knowledge of all the aforementioned aspects. In particular, the assessment of the structural performance based on numerical simulation needs to define loading models that realistically describe the forces induced by seated and standing spectators. At this purpose, a series of tests have been performed on a laboratory test structure to characterise the actions commonly performed by seated and standing spectators during a match. Measurements of both forces and structural responses have been collected and compared. Measuring forces induced by a large crowd in real conditions presents different challenges and, even if it is possible in theory, it is hardly feasible practically at this moment. Hence, the laboratory trials have been used to calibrate a methodology of testing based on inverse dynamics and aimed at indirectly estimate the human dynamic forces from structural measurements on real grandstands.

40.3 Inverse Force Reconstruction from Structural Responses

The reconstruction of the force induced by a human acting on a structure, usually called Ground Reaction Force (GRF), is a complex problem. Forces can be measured directly by using instrumented treadmills or force plates, or indirectly from measurements of human body motion. Indirect methods essentially rely on building a dynamic model of the body and recovering the forces from the acceleration measured on representative points and the corresponding estimated masses. Two main technologies are usually applied: image capture systems and inertial sensors units. The former technology provides records of displacements of markers placed on extremities of body segments (or rotation axes of joints) which allow the

locations of the centres of mass of body segments to be established based on anthropometric data. These records need to be double-differentiated in order to obtain acceleration for force reconstruction. The latter technology allows acceleration records to be obtained directly by the so-called Inertial Measurements Units (IMUs), which combine accelerometers, gyroscopes and magnetometers to get accelerations along a reference coordinate system.

Both of these technologies have been shown to give good estimation of human-induced forces in several laboratory or/and field tests, but they also have some limitations. For example, the accuracy of optical image capture systems can be highly influenced by lighting conditions or by the density of the crowd when the body markers are likely to become occluded. On the other hand, the accuracy of force reconstruction using inertial units is not totally investigated and the measurements actually require the use of purposely designed sensors. This implies that both of them do not easily lend themselves to be employed in in-situ testing. A way to overcome this could be by adopting the inverse reconstruction of the forces from the measured structural responses. These methods require a reliable dynamic model of the investigated structure in both empty and full-crowded conditions, in order to take into account the aforementioned influence of spectators on the structural behaviour.

The reconstruction of the excitation force from observed responses can be seen simply as the inverse application of the equation of motion, where the response of a system is measurable but not the forces acting on the system. Although it could appear intuitive and straightforward, several issues exist, mainly related to ill-conditioning in inverting algorithm, noise in measurements and inaccuracies in the structural model adopted. Inverse force identification is a classic problem in dynamics and different methodologies have been proposed over the years [22]. Despite the multiplicity of proposed approaches, a solution to overcome numerical issues related to input identification is currently lacking.

The frequency domain approach discussed herein is probably the most intuitive way to address the problem. For a linear system, the relationship between q forcing functions $\{F(\omega)\}$ and p structural responses $\{X(\omega)\}$ is fully described in frequency domain by the frequency response function matrix $[H(\omega)]$ (Eq. (40.1)):

$$\underset{(p\ x\ 1)}{\{X(\omega)\}} = \underset{(p\ x\ q)}{[H(\omega)]}\underset{(q\ x\ 1)}{\{F(\omega)\}} \tag{40.1}$$

The element of FRF matrix $H_{kj}(\omega)$ maps the input $F_k(\omega)$, applied at the k-th degree of freedom (DOF), and the output X_j measured at the j-th DOF. If the responses are accelerations, as usually measured during in-situ testing, the FRF matrix can be expressed in the accelerance form. The generic element of the accelerance matrix, expressed in terms of modal properties, is given by:

$$A_{j,k}(\omega) = \frac{\ddot{X}_j(\omega)}{F_k(\omega)} = -\omega^2 \sum_{r=1}^{N} \frac{1}{m_r} \frac{{}^r\psi_j\, {}^r\psi_k}{\omega_r^2 - \omega^2 + 2i\omega\omega_r} \tag{40.2}$$

For the r-th mode, ${}^r\psi_j$ is the modal shape element corresponding to the j-th degree of freedom (DOF), m_r is the modal mass, ω_r is the angular frequency and N is the number of modal modes. The spectral components of forces are then reconstructed inverting Eq. (40.1):

$$\underset{(q\ x\ 1)}{\{F(\omega)\}} = \underset{(q\ x\ p)}{[A(\omega)]^{-1}}\underset{(p\ x\ 1)}{\{\ddot{X}(\omega)\}} \tag{40.3}$$

Next, the time histories of the p forces are calculated by deconvolution of $F_k(\omega)$. In theory, it is possible to estimate the inputs from measurements if the number of forces q and their locations are known a priori or they can be estimated, and the number of measurements points p are equal to the number of the applied forces [23] and collected from sensors collocated with the points of application of the forces. The main concern in this procedure is related with the numerical instability in the inversion of FRF matrix, which easily occur when the number of forces q and measures p differs, and the evaluation of the pseudo-inverse is required. These difficulties in the inversion can be mitigated by 'over defining' the problem, adopting more responses than forces applied ($p > q$) [24]. A crucial role is played by the accuracy of the dynamic model adopted. It can be calculated by numerical simulation, but for a structure that has been already completed or retrofitted the most reliable estimation is given by in-situ testing. The elements of the FRF matrices can be calculated from identified modal parameters (Eq. (40.2)). Even if it is difficult generalising a rule valid in all the cases, the modal model can be built using a reduced subset of parameters, as shown in previous works [25].

40.4 Laboratory Testing

The purpose of the experimental campaign was to identify and compare the effects of main transient actions of a group of cheering spectators in seated and standing conditions. The laboratory floor structure used in this study is hosted at the Structural Dynamics Laboratory at the University of Exeter. Design specifically to serve as a flexible platform for investigation of vibration serviceability on structures due to human occupancy, the structure is highly reconfigurable thus allowing a range of spatial arrangements to be achieved of varying modal properties. The structural arrangement chosen for this study is a 5 m by 7.5 m configuration (Fig. 40.1a). Detailed description of the test structure and its dynamic characterisation can be found in [26]. In order to build a reliable model of the floor, essential in the inverse force reconstruction procedure, an extensive dynamic test campaign was performed. Electromechanical shakers were used as force input to the structure and its response was measured with Honeycomb QA accelerometers to obtain modal parameters, summarised in Fig. 40.1b.

40.4.1 Experimental Testing Methodology

Preliminary observations made during real football matches allowed the different actions of spectators performed in response to a goal being scored to be recognised and organised into three categories:

- Cheering, whereby the arms are raised, while feet remain planted on the structure;
- Bouncing, where the heels are raised and then strike the structure, which is accompanied by a cheer;
- Juming, where both feet leave the structure momentarily, which is accompanied by a cheer.

From these categorised actions, six specific motions were identified as those that should be tested in order to make comparisons between seated and standing response to such events. These actions are shown in Fig. 40.2. In order to best recreate the stadium feeling, the actions were performed in response to visual and auditory stimuli from HD video footage of goals being scored during football matches. The audio of the videos consisted only of background crowd noise as would be the case during an actual match (i.e. no commentary available). The videos were displayed on a large screen in front of the subjects. Six different videos were used to ensure enough variation to keep subjects' interest. They were presented in a randomised order to avoid subjects' predictive behaviour. In order to represent the proposed increase in capacity that is facilitated by the installation of safe standing areas, the standing tests used a larger number of subject than the seated ones (five instead of three), placed in the same area (1400×800 mm^2). For the seated tests (Fig. 40.3a), a test rig consisting of a row of three plastic tip-up seats was fixed to the structure. The test rig was placed in the centre of the structure in order to achieve the most severe dynamic response possible in the lowest vibration mode (see Fig. 40.1b). The response of the structure was measured using two wired Honeywell QA 750 accelerometers of which one was placed in the centre of the

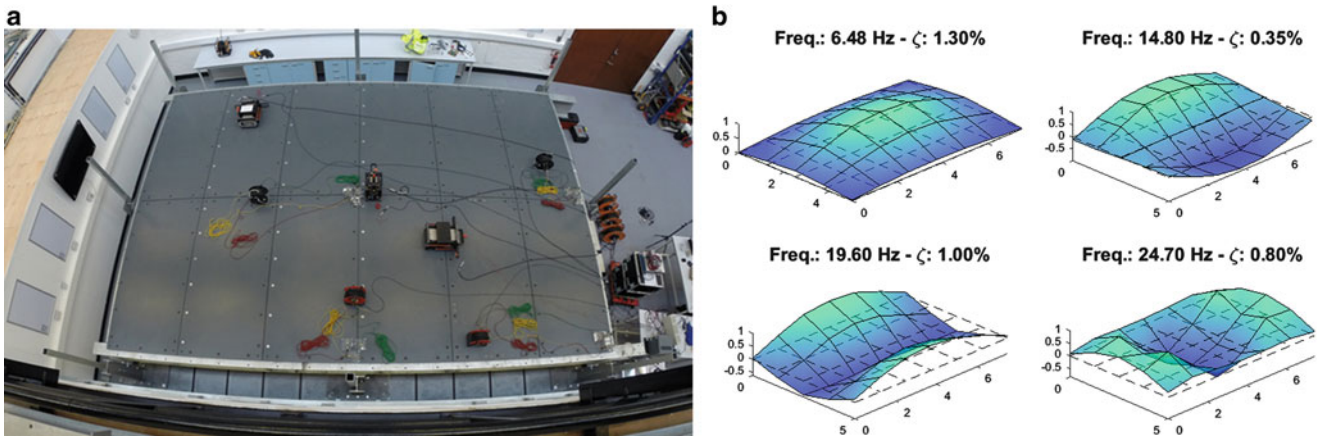

Fig. 40.1 (**a**) The laboratory floor structure during the dynamic characterization tests; (**b**) The first four identified vibration modes

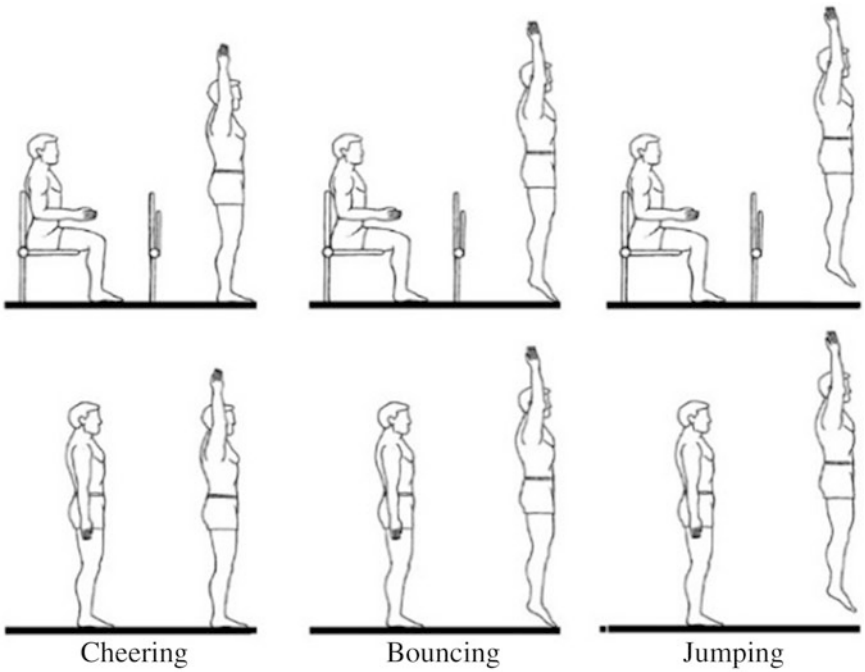

Fig. 40.2 The investigated actions in seated (*up*) and standing (*bottom*) tests

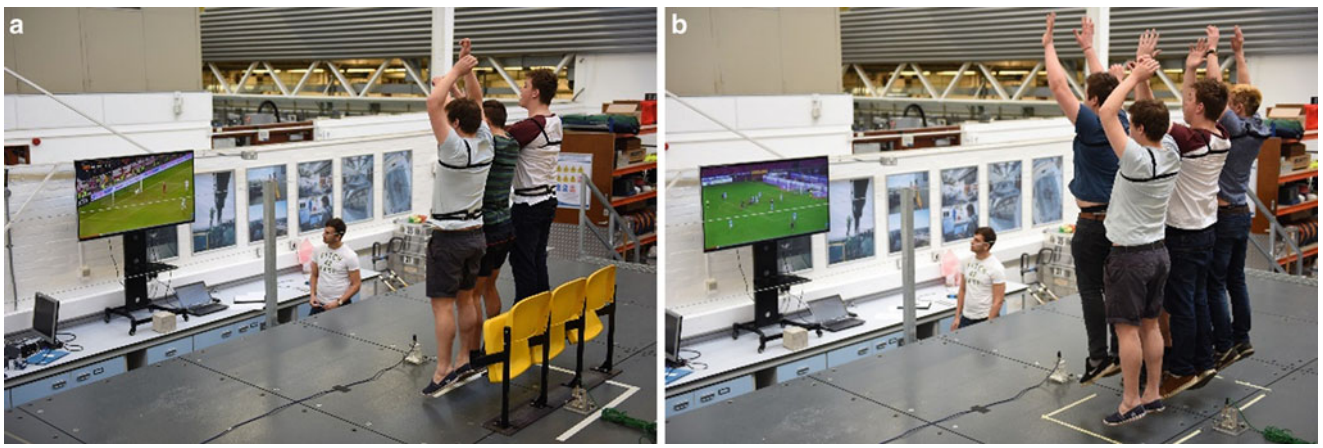

Fig. 40.3 Laboratory tests (**a**) subjects performing seating-to-jump action and (**b**) standing-to-jump action

floor and the other directly in front of the test area. The standing tests (Fig. 40.3b) were carried out in the same way as the seated tests, with the test rig containing the seats removed. The test area was marked out upon the structure and all of the subjects stood and performed the actions within that allocated area.

While performing the actions, the subjects wore APDM OpalTM monitors, which are inertial measurement units (IMUs) with on-board data-processing capability, developed specifically for applications in human movement research. During standing tests, each subject wore a sensor attached tightly at the sternum level (S) with helps of an elastic harness. During sited tests, each subject also wore a monitor attached tightly at the lower back (LB) level. The data from IMUs were used to understand the levels of synchronisation between subjects and provide means of estimation of the GRFs exerted by the subjects upon the structure. It was hypothesised that acceleration signals collected by a single monitor can represented the vertical motion of the centre of mass of the subject hence, after multiplying by the subject mass, could be used to obtain the vertical force exerted on the structure. This assumption was assessed by an independent experimental campaign, shows IMU data generally overestimate GRFs. For jumping tests at beat from 1.4 to 2.1 Hz, forces estimated by IMU on S, used as reference in this work, lead to an averaged error of around 25 %.

40.5 Results and Discussion

The inverse reconstruction algorithm previously described was applied to recover the total force exerted by the subjects in both seated and standing tests for each type of action performed. The total subjects' force was calculated summing the individual forces based on data from IMUs attached at the sternum. The point of application of the resultant force was taken as the centre of the testing area. The frequency response function matrix was defined via the identified modal parameters (Eq. (40.2)), using the first four modes in Fig. 40.1b. The number of modes was chosen such to include modal frequencies in the bandwidth of the maximum energy content of floor response up to 25 Hz. The force in frequency domain was calculated by multiplying the FRF matrix by Fourier transform of the floor responses, and finally the time-history of the reconstructed force was obtained from the inverse Fourier transform and filtered in order to eliminate low frequency disturbance.

The comparison between forces recovered based on data from IMUs and reconstructed by inversion in time and frequency domain is shown in Figs. 40.4 and 40.5.

The reliability of the procedure is summarized in Table 40.1, where the coefficient of correlation R^2 and the difference in maximum force amplitude are reported for each of the five tests (T1–T5). In all cases, the maximum amplitude of forces obtained with the inverse dynamics underestimate those based on data from IMUs, with an average error of −22.7 %. This discrepancy is consistent with the overestimation of the force model based on vertical acceleration data recorded at sternum, as previously discussed.

It is worth noting that in standing condition, cheering forces Fig. 40.4a are poorly reconstructed by inertial measurement. During cheering, there is just a minimal movement of the body mass in vertical direction and consequently, GRF can't be correctly estimated by a single measurement point. On the contrary, a good agreement has been obtained for the same action but performed starting from a seated position (Fig. 40.5a). In this case, in fact, the subjects rise from the chairs, moving their centres of mass predominantly in vertical direction, pushing the feet against the floor. Therefore, the inertial effect became prominent and IMUs can correctly catch the whole bodies' movements. A better agreement between the two methods for force reconstruction can be seen for bounce and jump in Figures 40.4 and 40.5b, c, respectively. The effect of standing up from chairs is also reflected in the maximum amplitude of GRFs and of structural responses. In Fig. 40.6, static (red) and dynamic peak loads (blue) are compared. In all the tests from seated, the estimated dynamic loads had magnitude comparable with the total body weight of participants, resulting in an average ratio between dynamic and static peaks components of 0.93, 1.28 and 1.49 for cheering, bouncing and jumping, respectively. On the contrary, in standing tests, the effects of cheering and bouncing are 0.27 and 0.42 of the static load respectively, whereas for jumping tests the average ratio is 1.48, close to the results obtained from the seated tests.

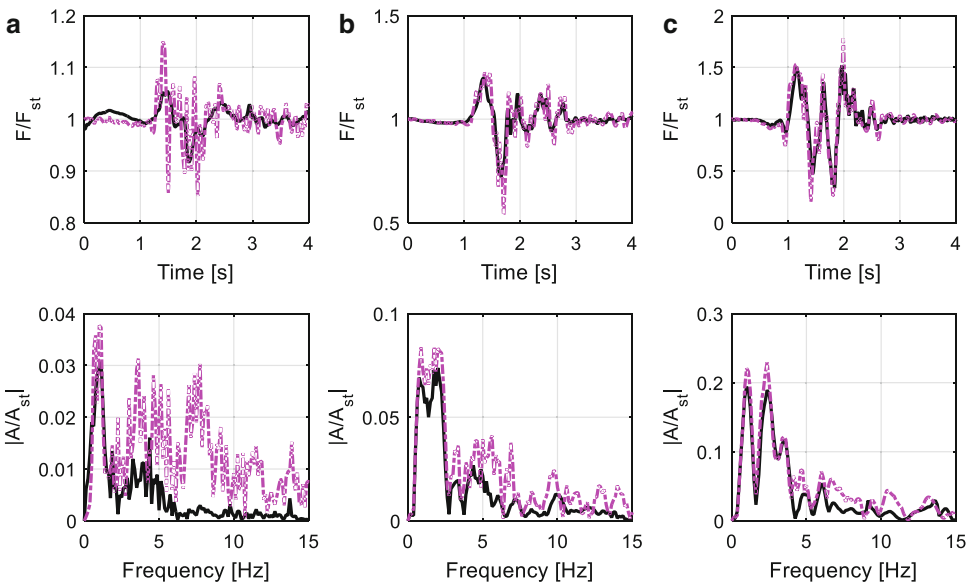

Fig. 40.4 Standing tests (five subject, total mass 449 kg), forces from IMUs and reconstructed based on inverse dynamics procedure are denoted by *dotted purple* and *black curves*, respectively. Comparison of forces, normalized by the body weight of subjects, in time domain (*top row*) and frequency domain (*bottom row*) for (**a**) cheering, (**b**) bouncing, (**c**) jumping tests

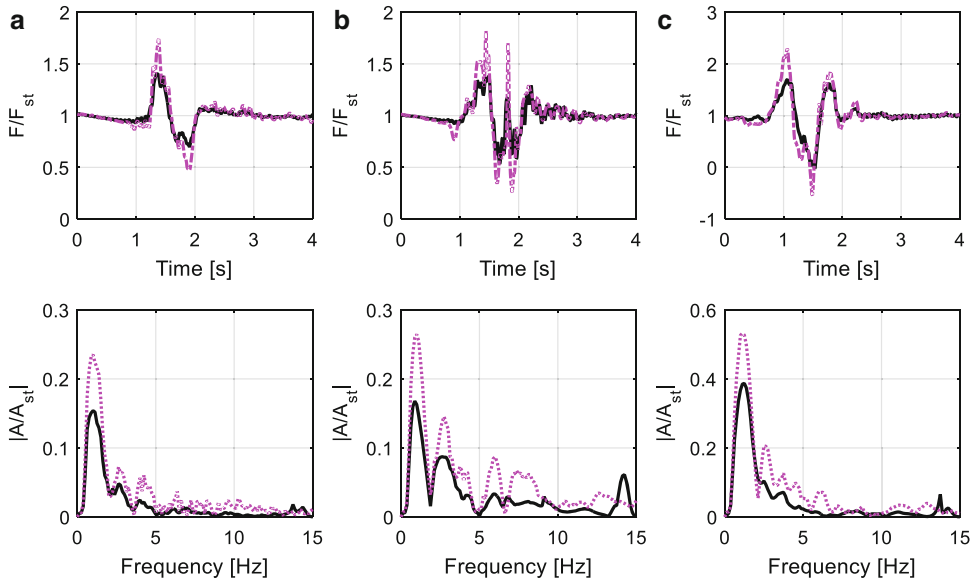

Fig. 40.5 Seated tests (three subject, total mass 274 kg), forces from IMUs and reconstructed based on inverse dynamics procedure are denoted by *dotted purple* and *black curves*, respectively. Comparison of forces, normalized by the body weight of subjects, in time domain (*top row*) and frequency domain (*bottom row*) for (**a**) cheering, (**b**) bouncing, (**c**) jumping tests

Table 40.1 Goodness of reconstructed forces compared with the IMUs measures

			T1	T2	T3	T4	T5
Cheering	Difference in maximum force amplitude	Seated	−20 %	−28 %	−21 %	−24 %	−20 %
		Standing	−23 %	−17 %	−18 %	−9 %	−17 %
	Coefficient of correlation R^2	Seated	0.81	0.79	0.76	0.78	0.76
		Standing	0.11	0.29	0.36	0.17	0.62
Bouncing	Difference in maximum force amplitude	Seated	−39 %	−31 %	−23 %	−25 %	−28 %
		Standing	−30 %	−3 %	−18 %	−19 %	−21 %
	Coefficient of correlation R^2	Seated	0.82	0.75	0.77	0.71	0.71
		Standing	0.76	0.66	0.64	0.65	0.76
Jumping	Difference in maximum force amplitude	Seated	−26 %	−29 %	−26 %	−24 %	−38 %
		Standing	−30 %	−15 %	−12 %	−21 %	−28 %
	Coefficient of correlation R^2	Seated	0.84	0.85	0.81	0.75	0.77
		Standing	0.74	0.90	0.87	0.93	0.79

It can also be seen in previous figures that the force amplitudes for five tests associated with each action for subjects starting either from seated or standing position can differ significantly. For example it worth pointing out that, despite the increased number of people involved, at least in one case the bounce from seated position induced higher total force than jump from standing. The primary reason for this is the varying degree of synchronisation between the subjects during the tests. Perfect synchronisation is of course impossible, but the transient actions prompted by a goal of other similar event are highly likely to be well aligned in time. This is an important issue which needs to be considered when making recommendations for the design loads. Further tests are necessary to gain better statistical significance of the results and assess this issue in detail. These results suggest that for cheering and bouncing the transient effects might not change significantly by reintroducing standing areas. On the other hand, standing crowd, usually more prone to lively move, might generate higher vibration amplitudes potentially causing vibration serviceability issues. However, further tests should be conducted to assess the reliability of the inverse dynamics procedure for the assessment of crowd loads from larger groups of people and in real life conditions.

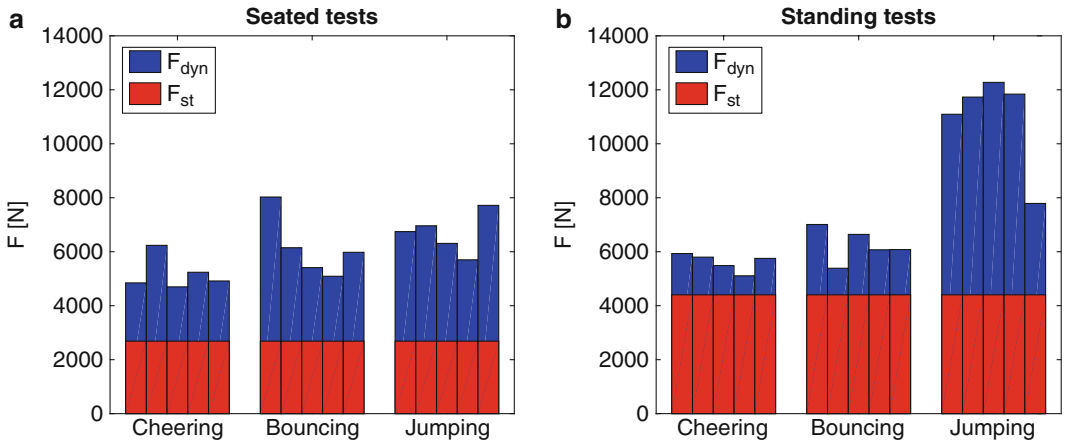

Fig. 40.6 The total force exerted by all subjects obtained with data from APDM Opal® monitors placed on sternum, for each of five test conducted with cheering, bouncing and jumping. *Blue bars* represent the dynamic component of forces, *red bars* the total body weight of subjects

40.6 Conclusions

This work presents the results of an experimental test campaign aimed at investigating how the introduction of safe standing areas can affect the dynamic performance of stadia grandstands, particularly focusing on transient effects. The most common actions executed by spectators in seated and standing conditions have been reproduced in a laboratory. The analysis of the data collected on the structure suggest that, for a less-lively crowd (cheering and bouncing actions), the introduction of safe standing areas could allow an increase in capacity without increasing the dynamic response of the structure. On the contrary, it is also suggested that for more lively crowds, with prevalent jumping actions, could cause an increase in the dynamic response of the structure of the same magnitude of the increase of static loading. Experimental campaigns on real cases could help understanding how a crowd act in both the conditions, due to the belief that standing areas are more likely to be occupied by the more lively spectators. At this purpose, a methodology to identify the dynamic loading from vibration data collected on real grandstands has been illustrated and successfully applied to the data collected in laboratory.

Acknowledgements The research presented in this study was funded by EPSRC (grant reference EP/I029567/2).

References

1. Taylor, J.: The Hillsborough stadium disaster - Final Report of the Inquiry (1990)
2. Sports Grounds Safety Authority: Standing in seated areas at football grounds. http://www.safetyatsportsgrounds.org.uk/publications/standing-in-seated-areas (2013)
3. Department for Culture Media and Sport: Guide to safety at sports grounds (2008)
4. CED Environmental, Norwich City Football Stadium (2010)
5. Kasperski, M.: Actual problems with stand structures due to spectator-induced vibrations. In: Augusti, G., Borri, C., Spinelli, P. (eds.) EURODYN 1996, Florence, pp. 455–461. Balkema, Rotterdam (1996)
6. Jones, C.A., Reynolds, P., Pavic, A.: Vibration serviceability of stadia structures subjected to dynamic crowd loads: a literature review. J. Sound Vib. **330**, 1531–1566 (2011). doi:10.1016/j.jsv.2010.10.032
7. Saul, W.E., Tuan, C.Y.: Review of live loads due to human movements. ASCE J. Struct. Eng. **112**, 995–1004 (1986)
8. Ellis, B.R., Ji, T., Littler, J.D.: The response of grandstands to dynamic crowd loads. Proc. ICE Struct. Build. **140**, 355–365 (2000)
9. Catbas, F.N., Celik, O.: Serviceability and human comfort in a stadium, 2 (2007)
10. Pernica, G.: Dynamic live loads at a rock concert. Can. J. Civ. Eng. **10**, 185–191 (1983)
11. Reynolds P., Pavic A.: The dynamic performance of sports stadia under crowd dynamic loading at concert events. In: Structural Dynamics - EURODYN 2005, vols. 1–3, pp. 473–478. Mill Press, Rotterdam (2005)
12. Cigada, A., Caprioli, A., Redaelli, M., Vanali, M.: Vibration testing at Meazza stadium: reliability of operational modal analysis to health monitoring purposes. ASCE J. Perform. Constr. Facil. **22**, 228–237 (2008)
13. Batista, R.C., Magluta, C.: Spectator-induced vibration of Maracana football stadium, pp. 985–992 (1993)
14. Reynolds, P., Pavic, A.: Vibration performance of a large cantilever grandstand during an international football match. ASCE J. Perform. Constr. Facil. **20**, 202–212 (2006)
15. Catbas, F.N., Gul, M.: Dynamic response monitoring and correlation to crowd movement at a football stadium (2009)

16. Rogers, D., Thompson, R.: Liverpool stand gets a red card. Construction News (2000)
17. Comer, A.J., Blakeborough, A., Williams, M.S.: Rhythmic crowd bobbing on a grandstand simulator. J. Sound Vib. **332**, 442–454 (2013). doi:10.1016/j.jsv.2012.08.012
18. Harrison, R.E., Yao, S., Wright, J.R., Pavic, A., Reynolds, P.: Human jumping and bobbing forces on flexible structures: effect of structural properties. J. Eng. Mech. **134**(8), 663–675 (2008)
19. Institution of Structural Engineers: Dynamic performance requirements for permanent grandstands subject to crowd action: recommendations for management, design and assessment. The Institution of Structural Engineers, The Department for Communities and Local Government, The Department for Culture Media and Sport, London (2008)
20. Brownjohn, J.M.W.: Energy dissipation in one-way slabs with human participation, vol. 1, pp. 155–160 (1999)
21. Reynolds, P., Pavic, A.: Changes of modal properties of a stadium structure occupied by a crowd. In: Proceedings of IMAC 2004, 1–10 (2004)
22. Sanchez, J., Benaroya, H.: Review of force reconstruction techniques. J. Sound Vib. **333**, 2999–3018 (2014)
23. Bernal, D., Ussia, A.: Sequential deconvolution input reconstruction. Mech. Syst. Signal Process. **50–51**, 41–55 (2015)
24. Dobson, B.J., Rider, E.: A review of the indirect calculation of excitation forces from measured structural response data. Proc. Inst. Mech. Eng. C J. Mech. Eng. Sci. **204**, 69–75 (1990) (vols 203–210)
25. Sim, J., Blakeborough, A., Williams, M.: Modelling effects of passive crowds on grandstand vibration. Struct. Build. **159**, 261–272 (2006)
26. Hester, D., Brownjohn, J.M.W., Bocian, M., Hudson E.J.: Wireless sensor network for structural monitoring: a laboratory trial. In: Structural Health Monitoring of Intelligent Infrastructure, SHMII-7, 1–10. Turin (2015)

Chapter 41
Recent Issues on Stadium Monitoring and Serviceability: A Review

Ozan Celik, Ngoan Tien Do, Osama Abdeljaber, Mustafa Gul, Onur Avci, and F. Necati Catbas

Abstract Unlike most of civil engineering structures whose static and dynamic responses are estimated accurately through several codes and guidance, stadiums reserve a distinctive place especially when it comes to their dynamic behavior. This difference takes its source from several factors such as influence of crowd size, motion and slenderness of the structure. The most noticeable form of this difference shows itself as excessive vibration levels which is actually a threat to the serviceability of these structures. Eventually, it becomes essential to carefully evaluate several steps of this particular problem starting from correct representation of crowd activity through accurate loadings and human-structure interaction models to arranging acceptable vibration serviceability limits. This publication intends to point out the newly developed techniques and discovered issues on several stages of the problem during the last decade.

Keywords Stadium • Serviceability • Vibration • Crowd loading • Human structure interaction

41.1 Introduction

Stadiums are prominent structures when compared with other structural engineering counterparts as to hosting large crowds and having slender structural members in return for their unique architectures (Fig. 41.1). These characteristics in conjunction with the effects such as occupant-mass ratio, actions of the occupants during events and the inherent abilities of the human body make the loadings described in current design approaches either over conservative or away from predicting true nature of crowd motion [1–3].

Serviceability problem for stadiums are handled in three steps namely input/excitation/source, system/path/structure and output/response/receiver [1, 2]. The input represents the estimation and recreation of loading functions utilizing either direct mathematical and statistical representations or recreation of real-life force time histories. In the last decade, there has been valuable research on this part of the problem by proposing stochastic modelling and computer vision methods. These are explained along this study.

Research topics regarding the system (stadium) hovers around alterations in dynamic parameters caused by the density of the crowd, active or passive occupants and their activities. More detailed insight on this issues is earned in light of the recent research. The issues related to output are serviceability and human comfort. The methods related to the assessment of risky perception levels in codes and standards need a better investigation for several reasons such as the insufficient explanations on the calculation of these values, disparity of perception from person to person, the inability of running controlled experiments to create serious discomfort levels, etc. This current study is intended to convey a brief information on the new approaches to the solution of those problems surveying the literature picking up from the year 2008 [2].

O. Celik • F.N. Catbas (✉)
Department of Civil, Environmental and Construction Engineering, University of Central Florida, Central Florida Blvd, Orlando, FL 32816-2450, USA
e-mail: catbas@ucf.edu

N.T. Do • M. Gul
Department of Civil and Environmental Engineering, University of Alberta, 7-257 Donadeo Innovation Centre for Engineering, 9211-116th Street NW, Edmonton, AB, Canada

O. Abdeljaber • O. Avci
Department of Civil and Architectural Engineering, Qatar University, College of Engineering, P.O. Box 2713, Doha, Qatar

© The Society for Experimental Mechanics, Inc. 2016

M. Allen et al. (eds.), *Dynamics of Coupled Structures, Volume 4*, Conference Proceedings of the Society for Experimental Mechanics Series, DOI 10.1007/978-3-319-29763-7_41

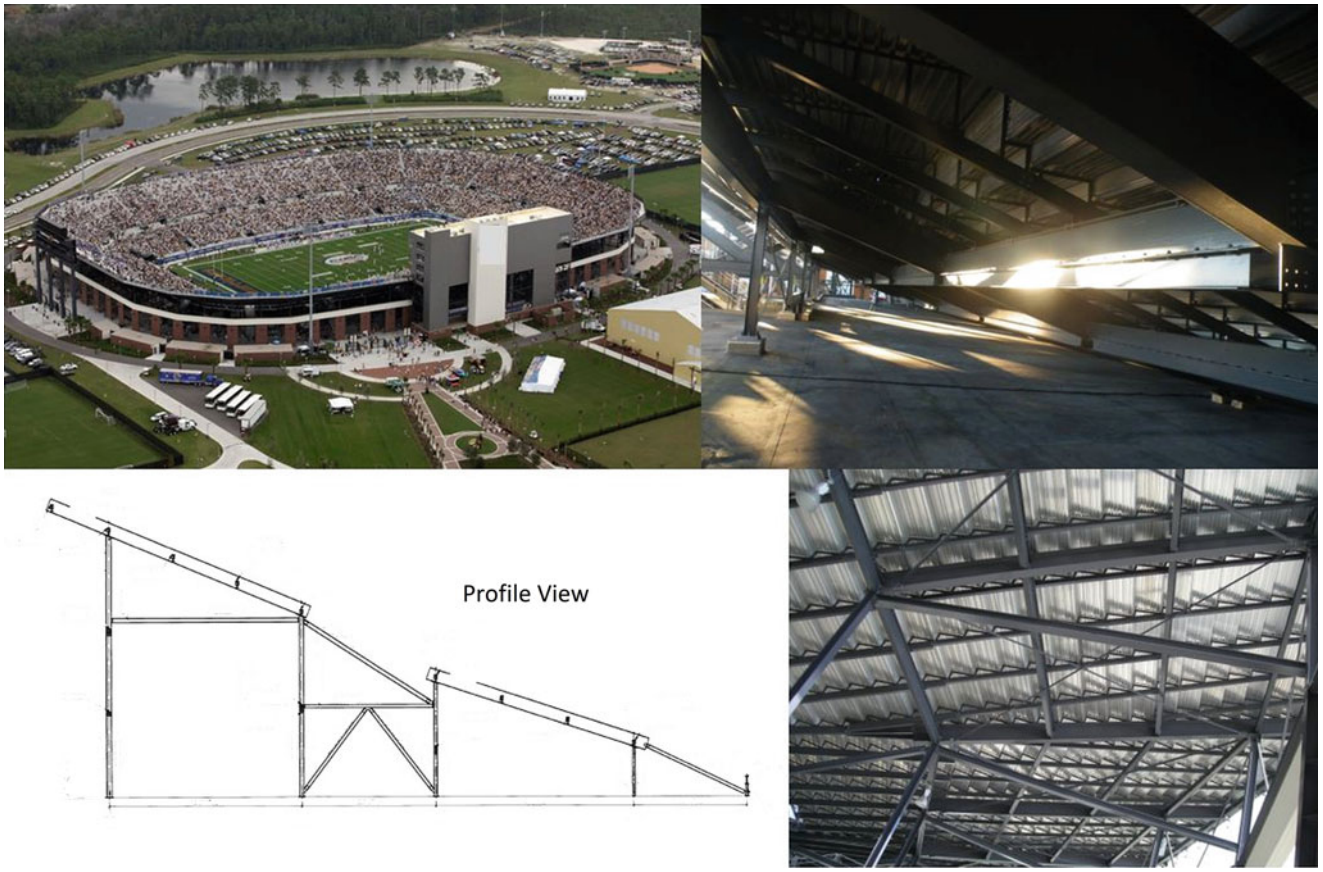

Fig. 41.1 Architectural and structural details of a stadium as a demonstration of their slender nature

41.2 Load Modeling

Recent research is condensed mainly on the rehabilitation of conventional recreated force-time history measurements and relatively new image-based techniques. It has been shown by various researchers [3–7] that walking and jumping loads are not perfectly periodic and are narrow-band phenomenon (intra-subject variation) by evincing the leakage around higher harmonics and frequently varying phase lags Fig. 41.2.

These first approaches considering the altered morphology, variability of both peak to peak intervals and amplitudes of real jumping records are made through an autoregression model [8]. However, due to cosine-squared functions being inadequate to fit into imperfectly shaped pulses and representing full frequency band, the problem is resolved with a novel approach [9–11] using stochastic processes in which combination of different Gaussian functions are used. Synthetic force time histories are generated utilizing a closed-loop trajectory in three dimensional space laying on a unit circle in the plane. This method seems to be the most realistic method by far.

Problems measuring the jumping and bobbing forces using force plates such as distorted patterns and additional inertial forces [12–14] are tried to be resolved using motion tracking technologies in which several data markers are attached to the subject's body and each body part is evaluated separately [15]. The data markers are tracked down by a high frequency optoelectronic device and GRFs are estimated accordingly.

There has also been novel studies on load estimation by making use of image processing and computer vision techniques as well as a comparison of these methods with previously mentioned data marker tracking [16]. The first works carried out in this area are based on the fundamental family of algorithms such as correlation in consecutive images [17], contour detection [18, 19] and Bayesian clustering methods for crowd tracking [20]. Subsequently, calculation of forcing functions, motion measurement of people and the patterns of their behavior in terms velocity amplitude and frequency [21, 22] or utilization of off the shelf regular or thermal imaging cameras on a portion of a real grandstand [23, 24] become viable. Some studies [25, 26] among these come forward with their ability to be performed in both laboratory and real life stadiums. Despite the idea of expanding an individual forcing to crowd, the proposed method uses the motion of the crowd directly for generating forcing functions.

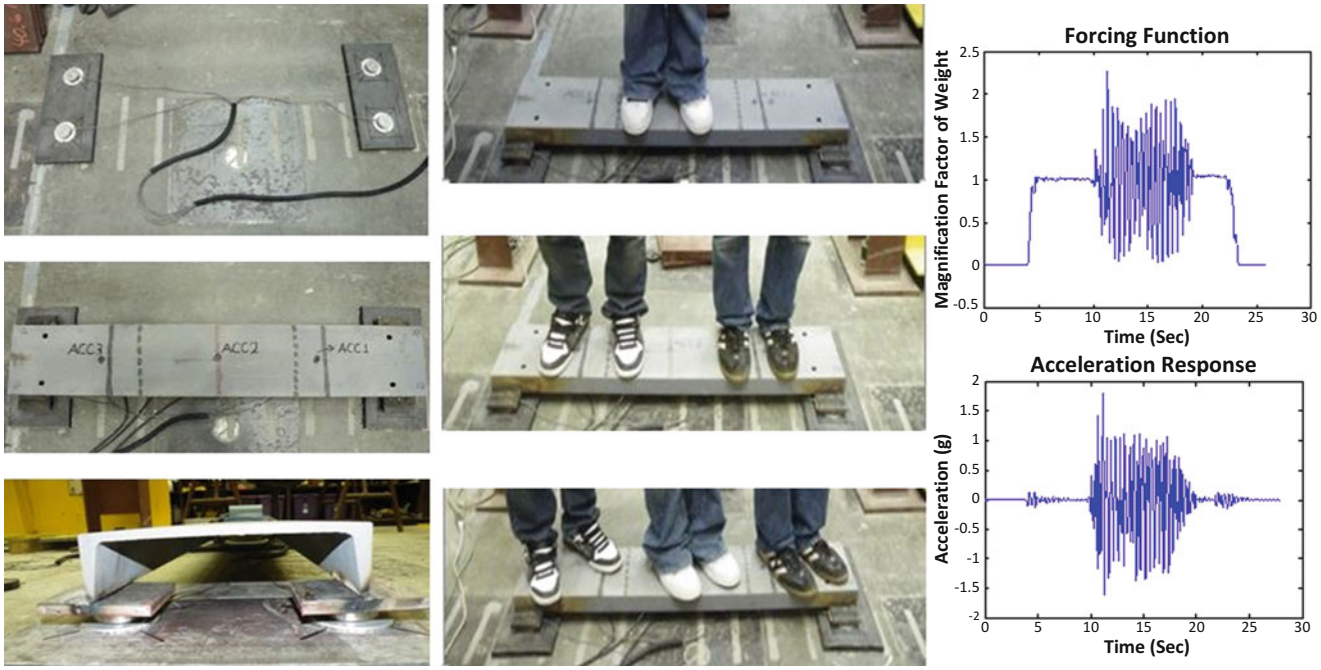

Fig. 41.2 Forcing function measurements showing non-periodic nature

41.3 Human Structure Interaction

Recent research dwells on the effects of as mass ratio of occupants to structure, distribution of the crowd, portion of the crowd being active or passive, and the posture of the occupants. One study provides results from an experimental study by narrowing this investigation down to passive crowds by looking at their distribution, mass ratios and different postures [27]. Results from three different postures (standing-straight knees, standing-bent knees and seated) on a composite slab which is excited by an electromechanical shaker states that the sparse or dense distribution of the crowd does not seem to have an effect on the dynamic properties for the same number of people. Alterations of frequencies and damping ratios in relation with the size and posture of the crowd are also given. This work, in a continuous sense, is further detailed into the investigation of only standing with straight knees and standing with bent knees postures of completely passive crowds by interacting with the slab structure which is specially designed to simulate adjustable first dominant frequencies and cantilever effect [28, 29]. These studies indicate that the natural frequency is also effective on damping ratio as well as the posture by making comparisons to British Joint Working Group (JWG) models. Under and over estimations are stated based on the experimental results and JWG recommendations. Subsequently, a new SDOF passive implementation is proposed.

A new factor called "drop out- p" which is defined as the minimum force at resonance divided by the value away from resonance where the force reaches its typical jumping level and which is an insight about the significance level of human-structure interaction, is shown as a result of the tests that are conducted under six different scenarios involving change of mass and damping [30]. Further suggestions are made on the reduction of dynamic load factors (DLFs) [2] and might serve to creation of adaptable and useful curve to better fit in performance design. Two more possibilities being group absorbing and supplying energy from and to the system regarding DLF reduction are also realized in another study [31] on a specially built laboratory grandstand [32, 33] simulator that has adjustable rigid and flexible support conditions.

Some additional studies propose a revision to mass-spring-damper models by advising the addition of the effect of the seat type pointing out the outcomes of experiments which are done using different seat types (a grandstand seat, a work desk chair, a swivel chair and a rigid seat) occupied by subjects having different postures along with changing occupant-structure mass ratios [34, 35].

Determination of the correct OMA method to be applied on stadium data is investigated in a comparative manner by implementing different operational modal analysis methods, namely singular value decomposition (SVD), stochastic subspace identification (SSI), Natural Excitation Technique (NExT) are put to test in a comparative manner [36, 37]. Every technique is applied on six different sets of data namely: empty structure, crowd filling, crowd seating, half-time, crowd leaving and goal followed by weak and strong aspects of each method one over another. The same cases and the structure

are used in another study for the comparison of two well-known methods: PolyMAX and SSI [38]. It can be clearly stated that the parameter estimation is highly affected when there is crowd excitation and different methods must be applied on the same data to assure a robust identification.

Another point to be considered is the reliability of the current OMA methods to be applied on stadium identification since some of the assumptions such as excitation of the whole frequency band, a linear and time invariant structural system and most importantly, excitation being Gaussian random white noise need to be satisfied. However, Gaussian white noise assumption, time dependent variation of dynamic parameters and the possibility of having nonlinear systems [39] are to be questioned.

All the techniques mentioned here have their benefits yet constrained with their limitations. Since the reliability of the identification procedure is put to question due to crowd excitation, these techniques might be implemented and optimum solutions might be sought.

41.4 Perception and Human Comfort

The assessment methodology is generally carried out by following the well-known and widely used guidance [40–42]. Assessment measures given in these standards such as root mean square (RMS), running RMS, maximum transient vibration value (MTVV), fourth power vibration dose value (VDV) or root mean quad (RMQ) have slight differences regarding their calculations as to measurement directions, subject's posture, application of frequency weightings, etc.

The research in the last decade mainly focus on the application of health, perception, motion sickness and comfort classification measures by emphasizing on sport events [5, 6, 43], concerts [44, 45] or hybrid type involving both of them and for a long term [46–49].

A psychophysical experimental method called subjective scaling was used to distinguish the two concepts as perception and comfort from each other in both sitting and standing positions [50]. The subjects are required to scale their responses via text descriptors provided and their choices were compared with frequency weighted acceleration of two particular standards [40, 51]. Extreme perception levels are seemed to be occurring before the feeling of discomfort making it more important for serviceability assessment.

Following the same scaling method [50], a possible new vibration assessment method is proposed depending upon the root mean square (RMS) of the normalized ground reaction forces (GRF) (when standing) time history or the normalized foot point acceleration time history [52] since the GRFs obtained with stationary measurements are different when on a moving grandstand [53]. GRF oscillations show the same characteristics as the grandstand oscillations for frequencies of excitation lower than 2 Hz whereas GRF wave forms are found to be randomly inconsistent and almost in nonlinear trend in higher frequencies.

In most cases, perception or human discomfort levels assessed looking at the measurement scale do not match with the observed behavior of the occupants in reality which again is a sign of questioning the appropriateness of the application on grandstands.

41.5 Conclusions

- Stochastic load modeling approach brings about quite reliable and realistic insight for the recreation of force-time histories by incorporating several variations from one pulse to another and having the ability of having arbitrary length recordings. Besides, each harmonic as in the real recordings are acquired.
- As well as stochastic load modeling approach, motion tracking, image processing and computer vision methods seem promising as to being alternative to force plate measurements, having field free characteristics, contactless measurement of loads and being able to track large number of people. The weak points such as difficulty of data markers being tracked in a crowd, placement of cameras, large amount of data and illumination conditions are yet to be developed.
- Although many of the findings fall in line with the previous literature stating that frequencies are to be decreased and damping ratios to be increased with the increasing mass, some studies bring new questions by showing otherwise or claiming that these changes also depend on both posture and frequency. Additionally, the interaction of the passive and active crowds as well as their effects on the structure are still in question.
- Structural identification methods that have been used so far in different studies show distinctive results on the same data outperforming one another on certain estimation steps. However, the convenience of these methods for stadium

problems are to be explored for the reasons such as Gaussian white noise assumption, time dependent variation of dynamic parameters and the possibility of having nonlinear systems.

- As to vibration serviceability assessment measures, of all the preceding research, the main point of discussion is actually the applicability and compatibility of these operating machinery based standards on grandstand serviceability problem as the excitation type have different inherence compared to machinery based vibrations. The idea of forming new type vibration serviceability limits or rehabilitation of existing ones taking human induced excitation and building characteristics into account is widely agreed upon since the ones currently in use are not capable of reflecting a true state.

Acknowledgement The financial support for this research was provided by Qatar National Research Fund [QNRF (a member of Qatar Foundation)] via the National Priorities Research Program (NPRP), Project Number: NPRP 6-526-2-218. The statements made herein are solely the responsibility of the authors.

References

1. ISO 10137:2007: Bases for Design of Structures - Serviceability of Buildings and Walkways Against Vibrations. International Organization for Standardization (2007)
2. Jones, C.A., Reynolds, P., Pavic, A.: Vibration serviceability of stadia structures subjected to dynamic crowd loads: a literature review. J. Sound Vib. **330**(8), 1531–1566 (2011)
3. Brownjohn, J.M., Pavic, A., Omenzetter, P.: A spectral density approach for modelling continuous vertical forces on pedestrian structures due to walking. Can. J. Civ. Eng. **31**(1), 65–77 (2004)
4. Newland, D.E.: An Introduction to Random Vibrations, Spectral and Wavelet Analysis. Wiley, New York (1993)
5. Catbas, F.N., Gul, M.: Dynamic response monitoring and correlation to crowd movement at a football stadium. In: Proceedings of the 27th International Modal Analysis Conference, Orlando (2009)
6. Catbas, F.N., Gul, M., Sazak, H.O.: Dynamic testing and analysis of a football stadium. In: Dynamics of Civil Structures, vol. 4, pp. 195–203. Springer, New York (2011)
7. Sazak, H.O., Catbas, F.N., Gul, M.: Structural health monitoring and evaluating structural performance of a stadium. In: Proulx, T. (ed.) Civil Engineering Topics, vol. 4, pp. 365–372. Springer, New York (2011)
8. Sim, J., Blakeborough, A., Williams, M.S., Parkhouse, G.: Statistical model of crowd jumping loads. J. Struct. Eng. **134**(12), 1852–1861 (2008)
9. Racic, V., Pavic, A., Brownjohn, J.M.W.: Mathematical modelling of near-periodic jumping force signals. In: Proceedings of the 28th International Modal Analysis Conference, Jacksonville (2010)
10. Racic, V., Pavic, A.: Mathematical model to generate asymmetric pulses due to human jumping. J. Eng. Mech. **135**(10), 1206–1211 (2009)
11. Racic, V., Pavic, A.: Mathematical model to generate near-periodic human jumping force signals. Mech. Syst. Signal Process. **24**(1), 138–152 (2010)
12. AMTI User Manuals. AMTI User Man (2008)
13. Perry, J.: Gait Analysis: Normal and Pathological Function. SLACK Incorporated, Thorofare (1992)
14. Racic, V., Brownjohn, J.M.W., Pavic, A.: Measurement and application of bouncing and jumping loads using motion tracking technology. In: Proulx, T. (ed.) Civil Engineering Topics, vol. 4, pp. 201–210. Springer, New York (2011)
15. Racic, V., Brownjohn, J.M.W., Pavic, A.: Novel experimental characterisation of human-induced loading. In: Proceedings of the 27th International Modal Analysis Conference, Orlando (2009)
16. Feng, Z., Racic, V., Brownjohn, J.M.W., Elliot, M.T., Wing, A.: Vision-based tracking of human body motion. In: Proceedings of the 32nd IMAC, pp. 171–174. Springer, New York (2014)
17. Hoath, R.M., Blakeborough, A., Williams, M.S.: Using video tracking to estimate the loads applied to grandstands by large crowds. In: Proceedings of the 25th International Modal Analysis Conference (2007)
18. Beucher, S., Lantuejoul, C.: Use of watersheds in contour detection. In: International Workshop on Image Processing: Real-time Edge and Motion Detection/Estimation, Rennes (1979)
19. Blake, A., Isard, M.: Active Contours. Springer, New York (1998)
20. Brostow, G., Cipolla, R.: Unsupervised Bayesian detection of independent motion in crowds. In: IEEE Conference on Computer Vision and Pattern Recognition, New York, pp. 594–601 (2006)
21. Caprioli, A., Manzoni, S., Zappa, E.: Crowd motion measurement based on image processing. In: Proceedings of the 26th International Modal Analysis Conference (2008)
22. Caprioli, A., Manzoni, S., Zappa, E.: People-induced vibrations of civil structures: image-based measurement of crowd motion. Exp. Tech. 173 **35**(3), 71–79 (2011)
23. Caprioli, A., Cigada, A., Sala, R., Zappa, E.: Image based measurement of a stadium excitation due to jumping people. In: Proceedings of the 24th International Modal Analysis Conference (2006)
24. Cigada, A., Zappa, E.: Analysis of jumping crowd on stadium stands through image processing to security purposes. In: Proceedings of the 2006 IEEE International Workshop on Measurement Systems, pp. 56–61. IEEE, Alexandria (2006)
25. Jones, C.A., Reynolds, P., Zappa, E., Manzoni, S., Cigada, A.: Verification of crowd dynamic excitation estimated from image processing techniques. In: Proulx, T. (ed.) Dynamics of Civil Structures, vol. 4, pp. 205–216. Springer, New York (2011)

26. Mazzoleni, P., Zappa, E.: Vision-based estimation of vertical dynamic loading induced by jumping and bobbing crowds on civil structures. Mech. Syst. Signal Process. **33**, 1–12 (2012)
27. Salyards, K.A., Firman, R.J.: Human-structure interaction: effects of crowd characteristics. In: Proulx, T. (ed.) Civil Engineering Topics, vol. 4, pp. 247–254. Springer, New York (2011)
28. Noss, N. C., Salyards, K. A.: Development of a laboratory test program to examine human-structure interaction. In: Society for Experimental Mechanics Series, pp. 7–16. Springer, Jacksonville (2012)
29. Salyards, K.A., Noss, N.C.: Experimental evaluation of the influence of human-structure interaction for vibration serviceability. J. Perform. Constr. Facil. **28**(3), 458–465 (2014)
30. Harrison, R.E., Yao, S., Wright, J.R., Pavic, A., Reynolds, P.: Human jumping and bobbing forces on flexible structures: effect of structural properties. J. Eng. Mech. **134**(8), 663–675 (2008)
31. Comer, A.J., Blakeborough, A., Williams, M.S.: Rhythmic crowd bobbing on a grandstand simulator. J. Sound Vib. **332**(2), 442–454 (2013)
32. Comer, A., Blakeborough, A., Williams, M.S.: Grandstand simulator for dynamic human-structure interaction experiments. Exp. Mech. **50**(6), 825–834 (2010)
33. Comer, A.J., Blakeborough, A., Williams, M.S.: Human-structure interaction in cantilever grandstands-design of a section of a full scale raked grandstand. In: 25th International Modal Analysis Conference (2007)
34. Pedersen, L.: Aspects of prediction accuracy in human-structure interaction. In: Proceedings of the 27th International Modal Analysis Conference, Orlando (2009)
35. Pedersen, L.: An aspect dynamic human-structure interaction. In: Proceedings of the 26th International Modal Analysis Conference (2008)
36. Prasenjit, M., Reynolds, P., Pavic, A.: Statistical analysis of online response data of a stadium structure. In: Proceedings of the 23rd International Modal Analysis Conference (2005)
37. Reynolds, P., Prasenjit, M., Pavic, A.: Use of operational modal analysis on empty and occupied stadia structures. In: Proceedings of the 1st International Operational Modal Analysis Conference (IOMAC), Copenhagen (2005)
38. Peeters, B., Van der Auweraer, H., Vanhollebeke, F., Guillaume, P.: Operational modal analysis for estimating the dynamic properties of a stadium structure during a football game. Shock. Vib. **14**(4), 283–303 (2007)
39. Jones, C.A., Reynolds, P.: Finite element modelling and updating of a stadium structure using in-service data. In: Proceedings of the 27th International Modal Analysis Conference, Orlando (2009)
40. BS 6841: Guide to Measurement and Evaluation of Human Exposure to Whole-Body Mechanical Vibration and Repeated Shock. British Standards Institution (1987)
41. ISO 2631-1: Mechanical Vibration and Shock-Evaluation of Human Exposure to Whole-Body Vibration. Part 1: General Requirements. International Organization for Standardization (1997)
42. ISO2631-2: Mechanical Vibration and Shock-Evaluation of Human Exposure to Whole-Body Vibration. Part 2: Vibration in Buildings (1Hz to 80 Hz). International Organization for Standardization (2003)
43. Salyards, K. A., Hanagan, L.M.: Analysis of coordinated crowd vibration levels in a stadium structure. In: Proceedings of the 25th International Modal Analysis Conference (2007)
44. Caprioli, A., Reynolds, P.: Evaluation of serviceability assessment measures for different stadia structures and different live concert events. In: Proceedings of the 25th International Modal Analysis Conference (2007)
45. Salyards, K.A., Hanagan, L.M., Trethewey, M.: Comparing vibration serviceability assessment measures for stadium rock concert data. In: Proceedings of the 24th International Modal Analysis Conference (2006)
46. Cappellini, A., Fagiani, R., Vanali, M.: Serviceability assessment of two different stadium grandstand during different events. In: Dynamics of Civil Structures, vol. 2, pp. 299–310. Springer, New York (2015)
47. Caprioli, A., Vanali, M., Cigada, A.: One year of structural health monitoring of the Meazza stadium in Milan: analysis of the collected data. In: Proceedings of the 27th International Modal Analysis Conference, Orlando (2009)
48. Caprioli, A., and Vanali, M.: Comparison of different serviceability assessment measures for different events held in the G. Meazza Stadium in Milano. In: Proceedings of the 27th International Modal Analysis Conference, Orlando (2009)
49. Salyards, K.A., Hanagan, L.M.: Evaluation of vibration assessment criteria and their application to stadium serviceability. J. Perform. Constr. Facil. **24**(2), 100–107 (2010)
50. Nhleko, S.P., Williams, M.S., Blakeborough, A.: Vibration perception and comfort levels for an audience occupying a grandstand with perceivable motion, Orlando (2009)
51. BS6472: Guide to Evaluation of Human Exposure to Vibration in Buildings (1 Hz to 80 Hz). British Standards Institution (1992)
52. Nhleko, S.P., Blakeborough, A., Williams, M.S.: Ground reaction forces on vibrating structures. In: Proceedings of the 27th International Modal Analysis Conference, Orlando (2009)
53. Yao, S., Wright, J.R., Pavic, A., Reynolds, P.: Experimental study of human-induced dynamic forces due to jumping on a perceptibly moving structure. J. Sound Vib. **296**(1-2), 150–165 (2006)

Chapter 42
Characterising Randomness in Human Actions on Civil Engineering Structures

S. Živanović, M.G. McDonald, and H.V. Dang

Abstract Developing reliable stochastic models of people walking and jumping is of crucial importance for accurate vibration serviceability assessment of structures such as footbridges, building floors and grandstands. To inform stochastic modelling, experiments which observe the kinetic and kinematic features of human actions should be conducted. The objective of this paper is to present a laboratory-based experimental programme designed to characterise walking and jumping actions performed on rigid surfaces by a population of 8–10 test subjects. A detailed characterisation of intra-subject variability was conducted in order to quantify randomness of parameters, such as pacing frequency, step length and step width in case of walking and the frequency, impulse area and contact ratio in case of jumping. The walking locomotion parameters on a lively surface were also monitored and compared against the benchmark data collected on a rigid surface. It was observed that an increase in the liveliness (in the vertical direction) of the supporting surface tends to lead to an increase in the intra-subject variability. In addition, it was shown that neglecting intra-subject randomness in the human-induced force could lead to significant error in calculation of the vibration response.

Keywords Walking • Jumping • Force • Variability • Vibration

42.1 Introduction

Low-frequency structures, such as footbridges, long span floors and grandstands, frequently exhibit strong vibration responses to human-generated dynamic forces, such as walking and jumping. The vibration serviceability state of these structures is often the governing design criterion. To successfully estimate the vibration response the development of reliable, high fidelity models of human-induced forces is required. These models are expected to represent the force waveform adequately, i.e. to replicate the narrow-band nature of the excitation typical of human activities [1] which is a consequence of inherent randomness (also called intra-subject variability) in the parameters describing the dynamic force.

Significant developments in force modelling of both walking and jumping excitations have been made over the last decade. In particular, understanding of the inter-subject variability in key parameters (such as the activity frequency) in the population of structural users has been improved. Some of these developments have already been included in design guidance [2]. Significant advances in modelling intra-subject variations have also been made [3–6], often resulting in complex models that might be difficult to implement in design practice. Quantifying randomness in key force parameters can contribute towards better understanding of human actions and development of the effective modelling strategies. This paper intends to provide some insight into the randomness of human walking and jumping and examine the significance of capturing this type of information in force modelling.

The outline of the paper is as follows. The experiments involving the walking and jumping on a rigid surface are described in Sect. 42.2, followed by a brief overview of acquired data and basic processing in Sect. 42.3. Randomness in the key parameters is presented in Sect. 42.4. A subset of walking experiments on lively structures is analysed in Sect. 42.5 and compared with the data recorded on the rigid surface. This is followed by an insight into the sensitivity of the vibration response to randomness in the force in Sect. 42.6. Finally, conclusions are presented in Sect. 42.7.

S. Živanović (✉) • M.G. McDonald
School of Engineering, University of Warwick, Coventry CV4 7AL, UK
e-mail: s.zivanovic@warwick.ac.uk

H.V. Dang
TSP, Alpha Tower, Birmingham B1 1TT, UK

© The Society for Experimental Mechanics, Inc. 2016

M. Allen et al. (eds.), *Dynamics of Coupled Structures, Volume 4*, Conference Proceedings of the Society for Experimental Mechanics Series, DOI 10.1007/978-3-319-29763-7_42

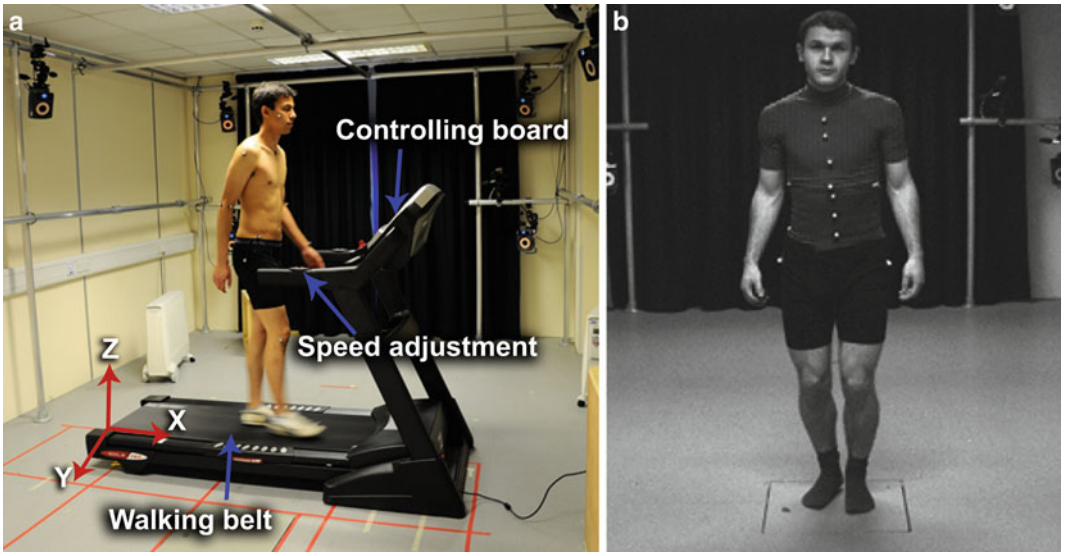

Fig. 42.1 Test setup in the Gait Laboratory for experiments involving human (**a**) walking and (**b**) jumping

42.2 Experiments on Rigid Surface

Experiments were conducted in the Gait Laboratory at the University of Warwick. Ten test subjects volunteered to perform walking trials [7], while eight test subjects took part in tests involving jumping [8]. In both cases, each test subject performed the actions on their own, i.e. without involvement and interaction with other test participants. Both sets of experiments were approved by the Biomedical and Scientific Research Ethics Committee at the University of Warwick.

To study the walking activity, test subjects were instrumented with 18 reflective markers and monitored using a Vicon motion capture system (equipped with 12 infra-red cameras) while walking on a treadmill (Fig. 42.1a). Utilising recorded marker trajectories and well-known model for mass distribution and geometry of body segments [9], the ground reaction force (GRF) was calculated as the sum of inertial forces of individual body parts [7]. Every test subject was asked to walk at a series of treadmill speeds, which followed this pseudo-random order: 1.15, 1.56, 1.36, 1.88, 1.67, 2.08, 1.76, 1.04, 1.24, 0.84, 0.93, 1.97 and 1.45 m/s. Overall, 130 tests were performed, each with about 450 steps.

In the jumping tests, subjects were instrumented with 17 markers (Fig. 42.1b) to track the trunk displacements, and asked to jump on a force plate (also shown in Fig. 42.1b) at frequencies of 1, 2 and 3 Hz. Each test lasted 20 s [8].

In both sets of experiments the test subjects were offered short breaks during which the test setup and data acquired were checked. The data were sampled at frequency of 200 Hz.

42.3 Data Processing

In the walking tests, marker trajectories were low-pass filtered using a fourth-order zero-phase-shift Butterworth filter with a cut-off frequency of 10 Hz. An example of a derived GRF is shown in Fig. 42.2a. The period of each force cycle was determined as shown in the same figure, and all the periods were extracted for each time history. The reciprocal value of the period was then calculated to find the pacing frequency. The imposed treadmill speed was divided by the pacing rate to get the step length in each walking cycle. All parameters (pacing frequency, step length and step width) were extracted on a cycle-by-cycle basis and the average value and the coefficient of variation (CoV) were obtained. A more detailed description of the extraction of these parameters is provided elsewhere [7, 10].

The time-domain GRF signals acquired using the force plate whilst jumping were filtered using a low-pass fifth order Butterworth filter, with the cut-off frequency having value of either 1 Hz above the frequency of the 3rd harmonic or 7 Hz, whichever was larger [8]. A filtered GRF is shown in Fig. 42.2b. The parameters extracted on a jump-by-jump basis were the period, contact ratio (i.e. contact time CT divided by period T) and impulse (i.e. the area enclosed by the force signal), all of which are shown in the figure.

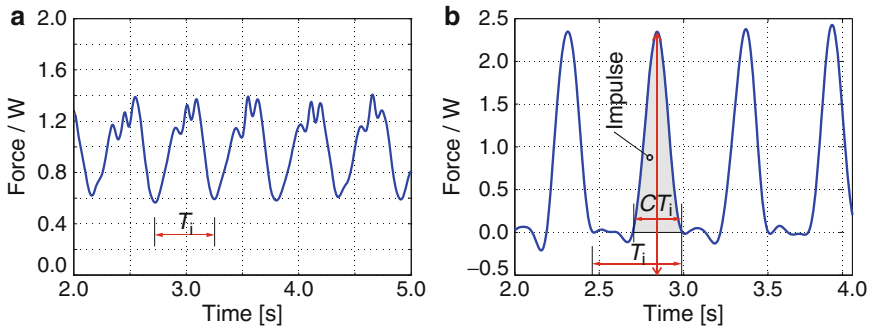

Fig. 42.2 Ground reaction force waveforms measured whilst (**a**) walking and (**b**) jumping

All data analysed in this paper are related to the vertical component of the force. The CoV is used as a key measure of the parameter randomness in each time history.

42.4 Randomness of Key Parameters

42.4.1 Walking

Figure 42.3 shows the average and CoV parameters for step length as functions of treadmill (i.e. walking) speed. The figure demonstrates that the average step length increases with increase in walking speed (Fig. 42.3a). The mean and mean ± one standard deviation (STD) lines are also shown in the figure, indicating that the STD does not change significantly across the studied population of test subjects. Figure 42.3b demonstrates that the CoV ranges between 1 and 5 %, with minimum variation achieved at the boundary between the normal (solid circles) and fast (crosses) walking speeds (1.6–1.8 m/s). While the probability distribution of the average step length (and averages of other parameters of interest) within a population of structural users is often available in literature [11–13], the detailed information regarding the intra-subject variability (i.e. CoV) is not frequently available. This is the reason that the CoV of different parameters is the main focus of this paper.

The CoV of pacing frequency is shown in Fig. 42.4a. This is very similar to the CoV for step length, due to mutual dependence of the two parameters (the product between the pacing rate and the step length represents the walking speed). A much larger value of CoV (up to 40 %) is seen for the step width (Fig. 42.4b). Variation in this parameter is relatively independent from the walking speed.

The CoV of three angular parameters (angle of attack, end-of-step angle and trunk angle) were also monitored during the experiments and they exhibited low variation (up to 2.3 %) [10].

42.4.2 Jumping

Figure 42.5a shows that the randomness in the frequency whilst jumping is larger than when walking (Fig. 42.4a), and therefore maintaining the cycle consistency is more difficult for the activity of jumping. The CoV values for the contact ratios (Fig. 42.5b) and the normalised impulse values (Fig. 42.5c) are in a similar range (up to 8 %). More detailed characterisation of the jumping action is available elsewhere [8].

All the data presented in this section could be used to develop and calibrate the models for humans walking and jumping, as well as develop an understanding of the level of variability in the parameters of interest frequently used to describe human actions.

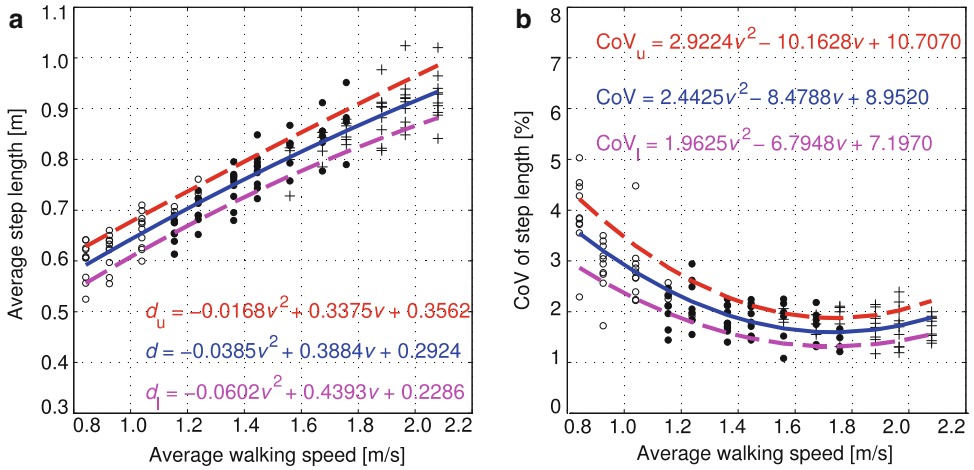

Fig. 42.3 (**a**) Average and (**b**) CoV values for the step length parameter as functions of the walking speed

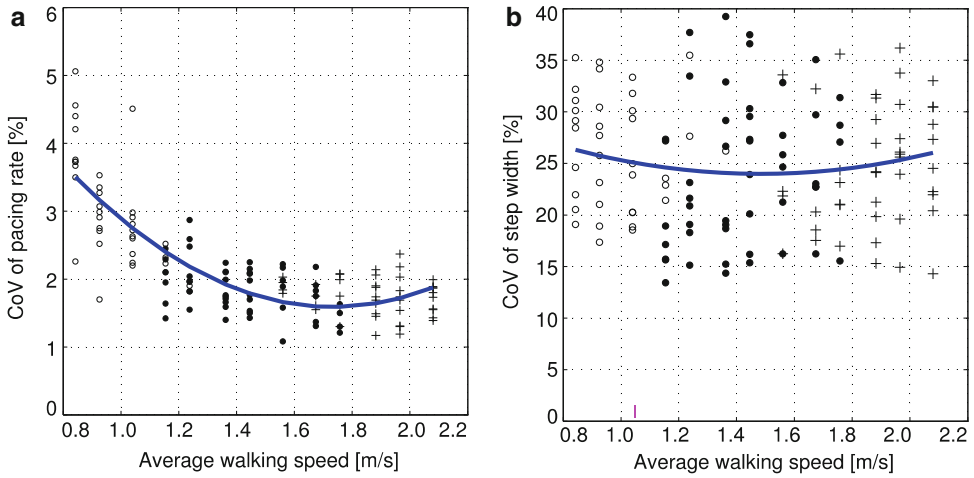

Fig. 42.4 CoV for (**a**) pacing rate and (**b**) step width as functions of the walking speed

42.5 Experiments on Lively Surface

Three test subjects who took part in the walking sessions in the Gait Laboratory, also participated in nominally the same set of experiments on the Warwick Bridge (WB). Two configurations of the bridge were utilised: WB1 having span of 16.2 m and WB2 spanning 17.4 m. The bridge and the experimental setup are explained in this section, followed by a comparison of the data with those collected in the Gait Laboratory.

42.5.1 WB Description and Test Setup

The WB is a steel-concrete composite structure with total deck length of 19.9 m and deck width of 2.0 m [14]. The bridge is situated in the Structures Laboratory at the University of Warwick. The fundamental mode of vibration is 2.44 Hz for WB1 and 2.18 Hz for WB2, with damping in both cases being between 0.30 and 0.55 %, depending on the vibration amplitude. The natural frequency is also mildly dependent on the vibration amplitude [7].

The plan view of the bridge in the WB2 configuration is shown in Fig. 42.6a. The figure also shows the position of the treadmill on the deck, as well as the shaker used in some tests. In addition, close up side views of the treadmill and the shaker are shown in Fig. 42.6b, c. The motion capture cameras were attached to the steel frames built around the bridge (Fig. 42.6a). The test subjects were instrumented with reflective markers in the same way as in the previous tests in the Gait Laboratory.

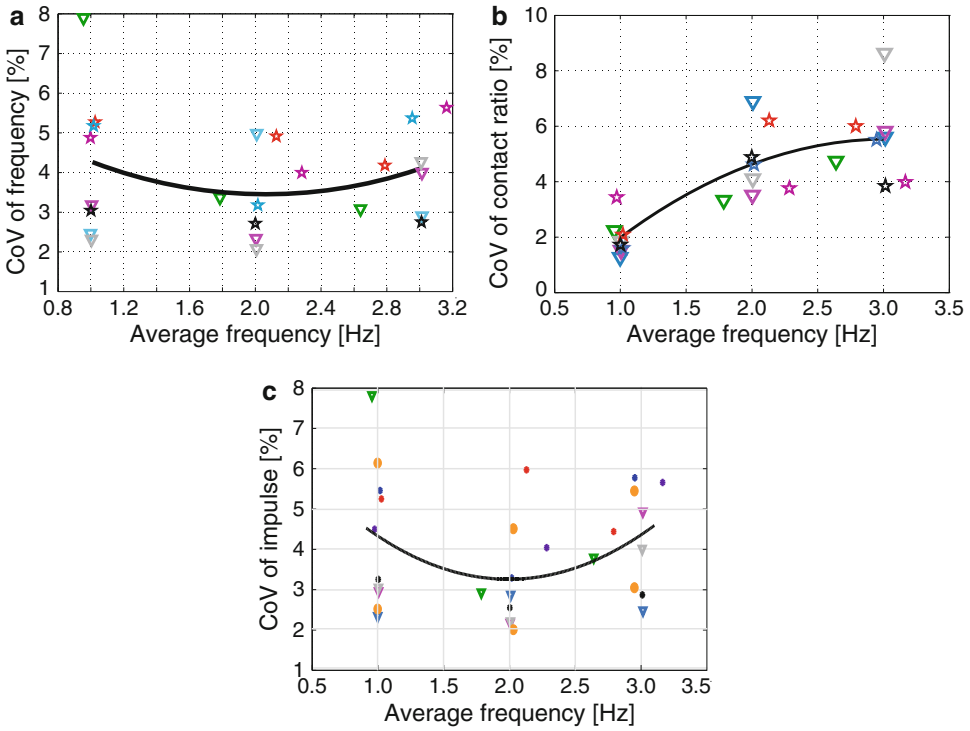

Fig. 42.5 CoV for (**a**) frequency, (**b**) contact ratio and (**c**) normalised impulse whilst jumping

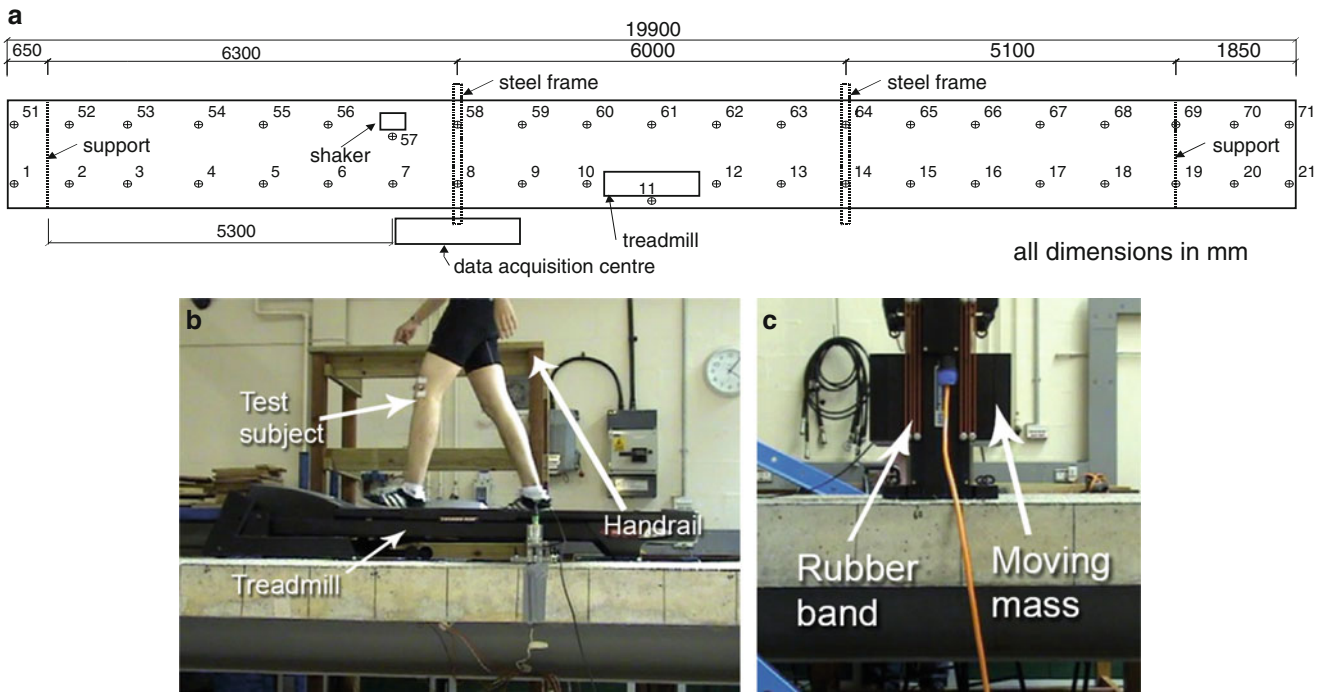

Fig. 42.6 (**a**) Plan view of the Warwick Bridge. Photos of (**b**) walking on treadmill and (**c**) electrodynamic shaker

In addition to conducting tests on the bridge with the shaker switched off, where the bridge vibrations were exclusively caused by the test subject walking, the tests were also repeated whilst the bridge was exposed to a steady-state vibration amplitude of 1.2 m/s^2 induced by the shaker before (and during) the walking trial. The force induced by the shaker was a harmonic force matching the fundamental frequency of the bridge.

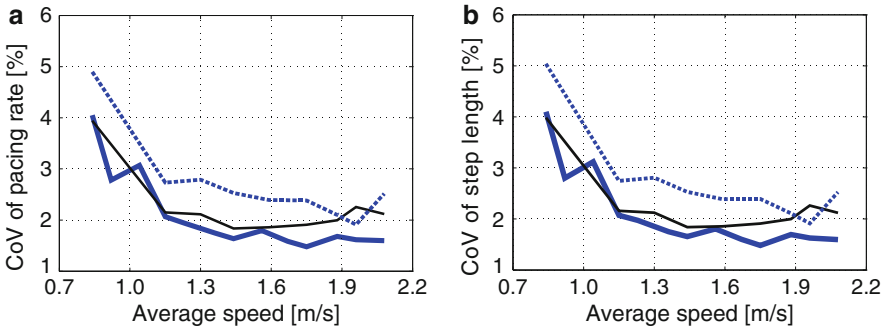

Fig. 42.7 CoV for (**a**) pacing rate and (**b**) step length. *Thick solid line*: walking on rigid surface; *thin solid line*: walking on bridge; *dotted line*: walking on bridge pre-excited by the shaker

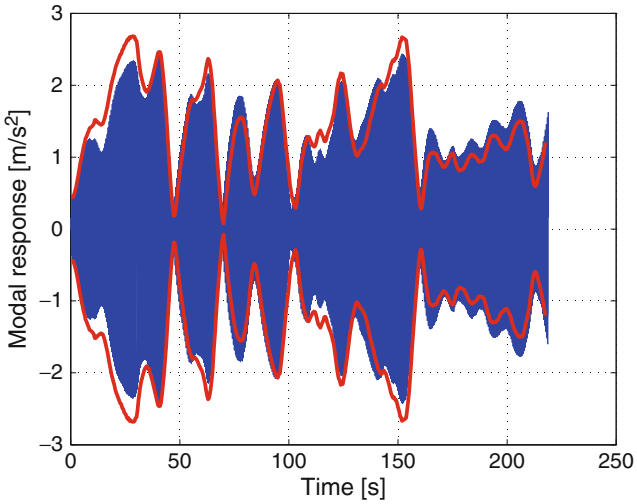

Fig. 42.8 A measured vibration response time history and the envelope of the simulated response on WB2

42.5.2 Randomness on Lively Bridge

Figure 42.7a shows the CoV of the pacing rate as a function of the walking speed. It can be seen that the CoV for walking over bridge exposed to low-level vibrations (i.e. when excited by the pedestrian only, see thin solid line in the figure) is relatively similar to that recorded on the rigid surface in the Gait Laboratory (thick solid line). When walking on the bridge strongly pre-excited by the shaker, the CoV increased (dotted line). The same conclusions can be drawn for the step length parameter (Fig. 42.7b). While the CoV increase is not too large, it still could be important for modelling human-induced excitation, especially in relation to the pacing frequency parameter, to which the vibration response is most sensitive.

Interestingly, in these tests involving the vertical vibration, the dependence of the CoV of the step width, a parameter important for controlling walking locomotion in the frontal plane [15], on the vibration level could not be established [7]. This supports the hypothesis that the walking locomotion control strategies are direction-dependent [16].

An example of a response time history measured at test point 11 (Fig. 42.6a) on WB2 is shown in Fig. 42.8. Using the measured force, the response was also simulated and its envelope presented in Fig. 42.8. It can be seen that the agreement between the two responses is very good. The bridge response, therefore, can be predicted sufficiently accurately provided the key features of the force are known and the amplitude dependent modal properties of the empty structure are utilised in the simulations.

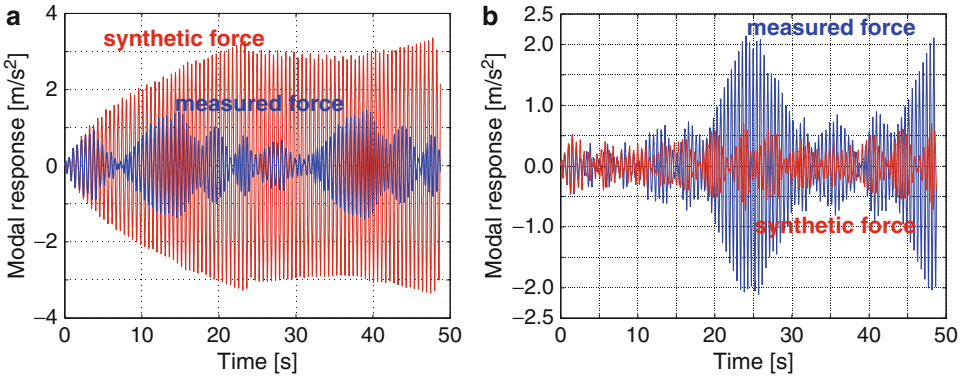

Fig. 42.9 Vibration response time histories under measured and synthetic forces representing test subject 2 jumping at 0.94 Hz for structure with a natural frequency of (**a**) 1.88 Hz and (**b**) 2.12 Hz

42.6 Sensitivity of Vibration Response

The CoV of the force parameters shown previously varies between different parameters; of note are the relatively low CoV values for frequency. However, given the known sensitivity of the slender structures to excitation frequency, the sensitivity of the simulated vibration response to the randomness in the frequency will be investigated in this section. For this purpose, a structure is modelled as a single-degree-of-freedom system, with a damping ratio of 1 % and a modal mass of 10,000 kg. The response to the force measured while test subject 2 was jumping at nominal frequency of 1 Hz was calculated. This was done using the measured force and then the simulation was repeated using a synthetic force signal generated in such a way to enforce the same frequency in each jumping cycle (at the same time preserving the measured shape and the amplitude of the force signal). The enforced frequency was set to 0.94 Hz, which is the average pacing frequency achieved in the actual test.

The vibration response was calculated for two structures having natural frequency of 1.88 and 2.12 Hz. For the 1.88 Hz case, the resonance response due to the second harmonic of the force was expected. Figure 42.9a shows that the response to the synthetic force does resemble the resonance shape, while the response to the measured force differs significantly. It is the randomness in the frequency parameter of the measured force which causes such a deviation from the expected response. An out-of-resonance response was also simulated on the 2.12 Hz structure. This time neglecting the randomness in the actual force caused an under-estimation of the response to the actual force (Fig. 42.9b).

These simple examples show that neglecting the randomness in the jumping frequency (CoV = 8 % in the test analysed), can result in both over-estimations and under-estimations of the vibration response. The former is typical of vibration responses in or near the (expected) "resonance" while the latter is usually relevant for responses away from resonance. In the examples analysed, the over-estimation of the peak response is by factor 2.3 while the under-estimation is by factor of 3.0. These findings suggest that the randomness in the frequency of the activity should be accounted for in the force modelling. There is also a need to investigate the sensitivity of the response to randomness in other parameters of interest.

42.7 Conclusions

In this study, randomness in parameters typical of walking and jumping has been investigated. The main conclusions are:

- Data on randomness of key parameters characterising walking and jumping were collected successfully. The test population consisted of ten test subjects in walking tests and eight test subjects in jumping tests.
- It is more difficult to preserve consistency whilst jumping than while walking.
- The coefficient of variation of the cycle-by-cycle frequency could be up to 8 % and 5 % for jumping and walking, respectively.
- Exposure to vertical vibration increases randomness in the pacing frequency and step length whilst walking.
- Vibration response is sensitive to the randomness in the frequency of the activity, and it can lead to both over- and under-estimation of the actual vibration response, depending on the relative ratio between the frequency of the relevant forcing harmonic and the natural frequency of the structure.

Acknowledgements This research was supported by the UK Engineering and Physical Sciences Research Council (Ref no. EP/I03839X/1: *Pedestrian Interaction with Lively Low-Frequency Structures*).

References

1. Brownjohn, J.M.W., Pavic, A., Omenzetter, P.: A spectral density approach for modelling continuous vertical forces on pedestrian structures due to walking. Can. J. Civ. Eng. **31**, 65–77 (2004)
2. Sétra: Footbridges, Assessment of Vibrational Behaviour of Footbridges under Pedestrian Loading, Technical Guide. Service d'Etudes Techniques des Routes et Autoroutes, Paris (2006)
3. Sim, J.H., Blakeborough, A., Williams, M.S., Parkhouse, J.G.: Statistical model of crowd jumping loads. J. Struct. Eng. **134**, 1852–1861 (2008)
4. Racic, V., Pavic, A.: Stochastic approach to modelling of near-periodic jumping loads. Mech. Syst. Signal Process. **24**, 3037–3059 (2010)
5. Racic, V., Brownjohn, J.M.W.: Stochastic model of near-periodic vertical loads due to humans walking. Adv. Eng. Inform. **25**(2), 259–275 (2011)
6. Caprani, C.C.: Application of the pseudo-excitation method to assessment of walking variability on footbridge vibration. Comput. Struct. **132**, 43–54 (2014)
7. Dang, H.V.: Experimental and numerical modelling of walking locomotion on vertically vibrating low-frequency structures. Ph.D. thesis, School of Engineering, University of Warwick (2014)
8. McDonald, M.G.: Experimental characterisation of jumping and bobbing actions for individuals and small groups. Ph.D. thesis, School of Engineering, University of Warwick (2015)
9. de Leva, P.: Adjustments to Zatsiorsky-Seluyanov's segment inertia parameters. J. Biomech. **29**(9), 1223–1230 (1996)
10. Dang, H.V., Živanović, S.: Experimental characterisation of walking locomotion on rigid level surfaces using motion capture system. Eng. Struct. **91**, 141–154 (2015)
11. Rainer, J.H., Pernica, G., Allen, D.E.: Dynamic loading and response of footbridges. Can. J. Civ. Eng. **15**, 66–71 (1988)
12. Pachi, A., Ji, T.: Frequency and velocity of people walking. Struct. Eng. **83**(3), 36–40 (2005)
13. Živanović, S.: Benchmark footbridge for vibration serviceability assessment under vertical component of pedestrian load. J. Struct. Eng. **138**(10), 1193–1202 (2012)
14. Živanović, S., Johnson, R.P., Dang, H.V. Dobric, J.: Design and construction of a very lively bridge. In: Proceedings of IMAC-XXXI, Orange County, California, 11–14 February (2013)
15. Carroll, S.P., Owen, J.S., Hussein, M.F.M.: Reproduction of lateral ground reaction forces from visual marker data and analysis of balance response while walking on a laterally oscillating deck. Eng. Struct. **49**, 1034–1047 (2013)
16. Bocian, M., Macdonald, J.H.G., Burn, J.F.: Biomechanically-inspired modeling of pedestrian-induced vertical self-excited forces. J. Bridg. Eng. **18**(12), 1336–1346 (2013)

Chapter 43
Optimal Restraint Conditions for the SID-IIs Dummy with Different Objective Functions

Yibing Shi, Jianping Wu, and Guy S. Nusholtz

Abstract This study formulates and numerically solves the optimal restraint condition problem for the SID-IIs side impact crash dummy under given impact conditions. It extends a previous study (Shi, Y., Wu, J., Nusholtz, G.S.: ASME J. Dyn. Syst. Meas. Control 135, 031007-1–031007-8, 2013) on the optimal restraint for this dummy which has the peak of the thoracic compression as the objective function. This extension allows for the peak of the different responses of the dummy, or their weighted average to be used as the objective function to reflect different strategies for reducing the impact load on the dummy. The requirements of the FMVSS 214 regulation are considered with these formulations. At the center of these formulations is a spring-mass model of the SID-IIs dummy established previously. The loading on the dummy, i.e., the restraint condition, is optimized through a discretization scheme which reduces the problem to a linear programming problem. Numerical examples are presented which illustrate the numerical effectiveness of the formulation. The results from these identify the optimal restraint action under different objectives and different impact conditions. They also combine to provide insight on some fundamental response characteristics of this dummy, such as the relationship between thoracic loading and pelvic loading. Additional optimization results are presented which identify the minimum restraint space requirement under given impact conditions. Such information can be referenced in practical engineering of side impact protection.

Keywords Optimal control • Impact response • SID-IIs crash dummy • FMVSS • Side impact

43.1 Introduction

The SID-IIs [2] is a side impact crash test dummy used in vehicle side crash tests to represent small-stature occupants. It is currently used in the Federal Motor Vehicle Safety Standard 214 (FMVSS 214) [3] and the Insurance Institute of Highway Safety (IIHS) side crash tests. These applications lead to an interest in understanding the characteristics required of the restraints to reduce force/acceleration and/or rib compressions as measured by this dummy in a crash. At the theoretical limit of this is the question: What is the optimal restraint that will produce the lowest dummy response under a given impactor motion history? The answer to this question promises to provide direction for restraint design, and the bound of the possible performance. This question is the topic of the study reported in [1]. The peak thoracic compression during the transient impact loading, which is an injury assessment measure in the existing IIHS side impact test that often requires particular engineering efforts to ensure a satisfactory level of performance, was used as the objective function—the optimal restraint condition in that case therefore is the one that provides the lowest peak thoracic compression. In the formulation and numerical solution in [1], the peak thoracic acceleration and the pelvic force were subjected to given limits which are realized in the optimization formulation as constraints.

Thoracic compression, however, is not included as one of the performance measures in the FMVSS214 regulation; instead, included are the peak thoracic acceleration and peak pelvic force. This regulation requires each of these two measures not to exceed their respective "injury assessment reference value" (IARV, which is crash performance limit), which are 82 g and 5.525 kN. With this background, the work reported in [1] is modified in this study to provide information specifically pertinent to this regulation.

A modification in this case could follow several possible approaches. If the single-objective scheme is kept, the objective function would need to be changed from the peak thoracic compression in [1] to the peak thoracic acceleration, or the peak pelvic force. With such a scheme, with either of the two requirements as the objective function, the other would need to be brought into the picture in the form of a constraint condition. Therefore, conceivably, two alternative optimization problems

Y. Shi (✉) • J. Wu • G.S. Nusholtz
FCA US LLC, CIMS 483-05-10, 800 Chrysler Drive, Auburn Hills, MI 48375, USA
e-mail: yibing.shi@fcagroup.com

© The Society for Experimental Mechanics, Inc. 2016

M. Allen et al. (eds.), *Dynamics of Coupled Structures, Volume 4*, Conference Proceedings of the Society for Experimental Mechanics Series, DOI 10.1007/978-3-319-29763-7_43

are solved separately, with each highlighting the characteristics of the restraint specifically optimal to the performance measure chosen as the objective function. A different approach to this problem would be to concurrently consider both requirements in the FMVSS214 through a weighted average of the peaks of the two responses, and perhaps with the thoracic compression included as well. Finally, a third approach would be to minimizes the larger of the two responses normalized to their respective IARV (i.e., maximum the "compliance margin"). Each of these three schemes reflects a different strategy and the confluence of the information from these could provide a more complete understanding of the response characteristics of the dummy and restraint strategy. These are explored in this study.

43.2 Formulation of the Optimal Problem

43.2.1 A Spring-Mass Model for the SID-IIs

The basis for the optimization study in [1] and the current work is a spring-mass model of the SID-IIs dummy as shown in Fig. 43.1. The key equations for this model are summarized here. Details for the construction of the model and the choice of the values of the spring and mass parameters can be found in [1].

This model consists of two lumped masses and three springs. The first lumped mass represents the thoracic mass, and the second the pelvic mass of the dummy. The first spring (S_1 in Fig. 43.1) connects the thoracic mass with the thoracic "interface point" (whose motion is denoted y_1 in Fig. 43.1), and the second spring S_2 connects the pelvic mass with the pelvic "interface point" (motion denoted by y_2 in Fig. 43.1). The "interface points" are mass-less points which represent the outmost surface of the thorax and the pelvis of the actual dummy. They are made mass-less since relatively little effective mass is present in the actual dummy at these locations. The third spring S3 represents the lumbar spine of the dummy, and it forms a load path between the thoracic and pelvic masses. The entire model is one-dimensional in the lateral direction.

z_1 and z_2 in Fig. 43.1 denote the motion of the impactor at the thoracic and pelvic locations respectively. They correspond to the vehicle side structures which directly impact the dummy. At each of these locations, an initial gap (g_1, or g_2) exists in which the restraint, for example, side impact airbag, operates. The initial gap is referred to as the "(available) restraint space" here.

The springs are assumed to be linear in stiffness and viscous damping, motivated by ease in solution and supported by impact tests on thoracic compression and pelvic impact tests on this dummy (the dummy is certainly *elastic*, being a device designed for repeat use). Therefore, the equation of motion of the above impactor-restraint-dummy system, which relates the response of the dummy to the motion of the interface points ($\boldsymbol{y}$), can be written in a linear state-space format as:

$$\dot{\boldsymbol{x}} = \boldsymbol{P}\boldsymbol{x} + \boldsymbol{Q}\boldsymbol{y}, \tag{43.1}$$

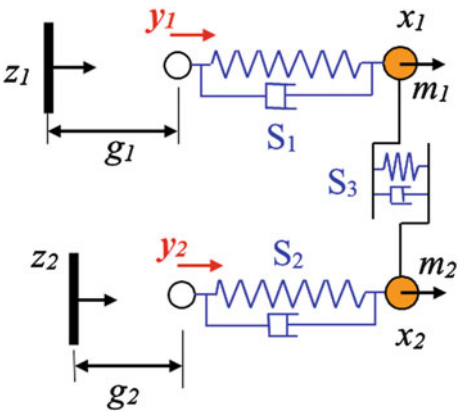

Fig. 43.1 Spring-mass model of the SID-IIs dummy. Also shown schematically are the impactor and the "restraint space" (g_1 and g_2)

where

$$\boldsymbol{x} = \left[x_1 \ \dot{x}_1 \ x_2 \ \dot{x}_2 \right]^T, \text{ and } \boldsymbol{y} = \left[y_1 \ \dot{y}_1 \ y_2 \ \dot{y}_2 \right]^T, \text{ and}$$
$$\boldsymbol{P} = \begin{bmatrix} 0 & 1 & 0 & 0 \\ -\frac{k_1+k_3}{m_1} & -\frac{c_1+c_3}{m_1} & \frac{k_3}{m_1} & \frac{c_3}{m_1} \\ 0 & 0 & 0 & 1 \\ \frac{k_3}{m_2} & \frac{c_3}{m_2} & -\frac{k_2+k_3}{m_2} & -\frac{c_2+c_3}{m_2} \end{bmatrix}, \boldsymbol{Q} = \begin{bmatrix} 0 & 0 & 0 & 0 \\ \frac{k_1}{m_1} & \frac{c_1}{m_1} & 0 & 0 \\ 0 & 0 & 0 & 0 \\ 0 & 0 & \frac{k_2}{m_2} & \frac{c_2}{m_2} \end{bmatrix}. \tag{43.2}$$

43.2.2 Formulation of the Multi-Objective Optimal Restraint Problem

The first two approaches towards the FMVSS214 SID-IIs optimization problem mentioned in the Introduction are special cases of the following weighted sum form:

$$o = \boldsymbol{w}^T \boldsymbol{q}./\boldsymbol{L}, \tag{43.3}$$

where $\boldsymbol{w}$ is a vector of weighting factors as an input to the problem, and $\boldsymbol{q}$ a vector consisting of the peaks of the thoracic compression, thoracic acceleration, and pelvic force:

$$\boldsymbol{q} = \left[\max_t (y_1 - x_1) \ \max_t (\ddot{x}_1) \ \max_t (f_2) \right]^T. \tag{43.4}$$

$\boldsymbol{L}$ in Eq. (43.3) contains the IARVs, and the values of *44* mm, *82* g, and *5.5* kN are used in this study. The peak thoracic compression is formally included in Eq. (43.4) for generality although it is not specified in the FMVSS 214. $\boldsymbol{q}./\boldsymbol{L}$gives the normalized peak responses.

The weighting factors for the three responses can be individually specified, and their relative magnitude provides a means to reflect desired emphasis. For example, a setting of $[0\ 0.5\ 0.5]^{\mathrm{T}}$ would correspond to the FMVSS214 requirement with an equal emphasis on the two required measures; a setting of $[1\ 0\ 0]^{\mathrm{T}}$ degenerates this general form to the special case studies in [1].

With the above choice of combining the multiple objectives, the subject problem can be expressed as:

$$\min_{y_1;y_2} o\left(y_1, y_2 \middle| \boldsymbol{w}, \boldsymbol{L}; z_1, z_2, g_1, g_2\right) \tag{43.5}$$

The above is subject to the restraint space constraints that reflect the contact between the impactor and the dummy:

$$z_i(t) - y_i(t) \le g_i, \ i = 1, \ 2\,. \tag{43.6}$$

In the context of the FMVSS214, each of the individual objectives in Eq. (43.4) will need to be lower than their individual IARV. In addition, it may also be desirable to limit the thoracic compression to a certain level. These lead to the following constraints:

$$\frac{q_i}{\beta_i L_i} \le 1, \ i = 1, \ 2, \ or \ 3. \tag{43.7}$$

β_ι in Eq. (43.7) are constant scale factor of the IARV limits (L_i), and when β_ι<*1* a safety margin is effectively implemented. The value of 0.8 is used for β_ι is used in the numerical examples presented here, unless explicitly indicated otherwise.

The optimization problem is now completely defined by Eq. (43.5) and the constraints of Eqs. (43.6) and (43.7), with Eq. (43.1) associating the input and response of the dynamic system. It basically asks the question: what time histories (y_1, y_2) the restraint between the impactor and the dummy needs to have while driving the interface points of the dummy, so that the composite objective o in Eq. (43.3) is minimized; and the conditions for this are that g_1, g_2 are the only available space for the restraint to operate in, and that each of the peak responses involved in o has to stay below its given limit (Eq. 43.7). Mathematically, this is a functional optimization problem. The solution of the similar problem in [1] was through two treatments which approximated and reduced the problem into a linear programming problem solvable with established numerical algorithms. One of these treatments is the discretization of the variable functions (y_1 and y_2) in time domain and approximation of their acceleration time histories to be constant in each time step; the other simplifying treatment is the

introduction of an auxiliary variable which is the peak value of the thoracic compression (the objective function in that case) to transform the peak value selection through time into a linear constraint. The first treatment and a variant of the second treatment are used here to solve the current problem. The formulation for numerical solution is outlined below.

The first treatment discretizes solution time duration into n equal time steps:

$$t_k = t_{k-1} + \Delta t,\ k = 1, .., n. \tag{43.8}$$

As a result, an explicit solution can be obtained for Eq. (43.1). The solution steps are given in detail in [1] and they are omitted here. The end result of this is the following linear solution:

$$\boldsymbol{X} = \boldsymbol{N}\boldsymbol{u}, \tag{43.9}$$

where $\boldsymbol{X} = \left[\boldsymbol{x}(1)\ \boldsymbol{x}(2)\ \boldsymbol{x}(3)\ \ldots\ \boldsymbol{x}(n)\right]$, in which $\boldsymbol{x}(i)$ is the state x (defined in Eq. 43.1) at time t_i, and of dimension 4-by-1. $\boldsymbol{u} = [u_{11} \ldots u_{1n}\ \ u_{21} \ldots u_{2n}]^T$ is the discretized acceleration of the thoracic and pelvic interface points (i.e., discretized acceleration corresponding to the position variables y_1 and y_2), and it is the variable of the optimization. Since $\boldsymbol{u}$ determines the response of the dummy, it is also called the *control acceleration* here. Physically, it is to be interpreted as the action of the restraint.$\boldsymbol{N} = \left[\boldsymbol{N}_1\ \boldsymbol{N}_2\ \boldsymbol{N}_3\ \ldots\ \boldsymbol{N}_n\right]$, where $\boldsymbol{N}_i$, is a response matrix at time t_i, involving the linear parameters of the dummy and the time step size. The N_i matrix is a result of the integration of Equation (43.1), and its evaluation is given in [1].

The motion of the control points themselves, under the control acceleration $\boldsymbol{u}$, with zero initial position and velocity conditions, can be written as:

$$\boldsymbol{Y} = \boldsymbol{R}\boldsymbol{u}, \tag{43.10}$$

where $\boldsymbol{R}$ is a transformation matrix derived from the integration of the step-wise constant control point acceleration time history $\boldsymbol{u}$. $\boldsymbol{R}$ can be evaluated explicitly with k and the time step size.

Similarly, the motion of the impactor can be written as:

$$\boldsymbol{Z} = \boldsymbol{S}\boldsymbol{v_0} + \boldsymbol{R}\boldsymbol{a}, \tag{43.11}$$

where v_0 is the initial velocity of the impactor, and $\boldsymbol{a}$ its acceleration time history. v_0 and $\boldsymbol{a}$ are known inputs to the problem. The matrix $\boldsymbol{S}$ is a result of the explicit integration, similar to $\boldsymbol{R}$.

Equations (43.9)–(43.11) constitute a linear solution to the response of the system under consideration, i.e., given the initial velocity and acceleration time history of the impactor (v_0 and $\boldsymbol{a}$), and the control point acceleration ($\boldsymbol{u}$), the motion of the dummy ($\boldsymbol{X}$), the control points ($\boldsymbol{Y}$) and the impactor ($\boldsymbol{Z}$) can be obtained with linear transformations.

Equations (43.9)–(43.11) are now used to rewrite the optimization problem of Eqs. (43.5)–(43.7) into an explicit parameter optimization in terms of $\boldsymbol{u}$.

To achieve this, another treatment which is an extension of that given in [4] and applied in [1] is needed. This involves combining $\boldsymbol{q}$ in Eq. (43.4) with the unknown variable $\boldsymbol{u}$ to form a new variable for the optimization:

$$\boldsymbol{U} = \begin{bmatrix} \boldsymbol{q} \\ \boldsymbol{u} \end{bmatrix} \tag{43.12}$$

Equations (43.5) can now be equivalently written as:

$$\min_{\mathbf{U}} \mathbf{f}^T\mathbf{U}, \tag{43.13a}$$

subject to:

$$\begin{bmatrix} \left[-\mathbf{I_1}\ \mathbf{0}\ \mathbf{0}\right] & \mathbf{R}_{\mathbf{y_1}} - \mathbf{N}_{\mathbf{x_1}} \\ \left[\mathbf{0}\ -\mathbf{I_1}\ \mathbf{0}\right] & \mathbf{V}_{\ddot{x}_1} \\ \left[\mathbf{0}\ \mathbf{0}\ -\mathbf{I_1}\right] & k_2\left(\mathbf{R}_{\mathbf{y_2}} - \mathbf{N}_{\mathbf{x_2}}\right) + c_2\left(\mathbf{R}_{\dot{\mathbf{y}}_2} - \mathbf{N}_{\dot{\mathbf{x}}_2}\right) \end{bmatrix} \mathbf{U} \le \mathbf{0}, \tag{43.13b}$$

where $\boldsymbol{f} = \left[\boldsymbol{w}./\boldsymbol{L}\left[0 \ldots 0\right]^T\right]$.

Equation (43.13b) is simply the discrete version of the definition of the 3-element vector $\boldsymbol{q}$ defined in Eq. (43.4). The discretization turns the selection of the peaks in continuous time into a set of linear constraints (that, for example in the case

of the first equation in (43.13b), the compression y_1-x_1 at all time-steps be no larger than an auxiliary variable $\boldsymbol{q}(1)$, which when minimized, will be the peak compression through time by definition). The three equations in (43.13b) are for the peak thoracic compression, peak thoracic acceleration, and peak pelvic force, respectively. The matrices on the left hand side with subscripts (e.g., $\boldsymbol{R_{y1}}$) in Eq. (43.13b) are defined in [1]. They are simply sub-matrices of $\boldsymbol{R}$ and $\boldsymbol{N}$ in Eqs. (43.9) and (43.10), and when acting on the variable $\boldsymbol{u}$, they produce a column vector of the responses indicated by their subscript (e.g., $\boldsymbol{y_1}$ in the case of $\boldsymbol{R_{y1}}$). $\boldsymbol{I}_1$ in Eq. (43.13b) is a unit column vector of length $2n$ (n being the number of time steps). Further details on this method and formulation are given in [1, 4].

The original constraint of Eq. (43.6) is transformed into:

$$\begin{bmatrix} \mathbf{0} & -\boldsymbol{R}_{y_1} \\ \mathbf{0} & -\boldsymbol{R}_{y_2} \end{bmatrix} \boldsymbol{U} \leq \begin{bmatrix} g_1 \boldsymbol{I}_1 - (\boldsymbol{S}_{z_1} v_0 + \boldsymbol{R}_{z_1} \boldsymbol{a}) \\ g_2 \boldsymbol{I}_2 - (\boldsymbol{S}_{z_2} v_0 + \boldsymbol{R}_{z_2} \mathbf{a}) \end{bmatrix}. \tag{43.13c}$$

The remaining original constraint, Eq. (43.7), is transformed into:

$$\left[diag^{-1}(\boldsymbol{L}) ./ \boldsymbol{\beta} \ \mathbf{0} \right] \boldsymbol{U} \leq \left[1 \ 1 \ 1 \right]^T, \tag{43.13d}$$

where *diag(**L**)* is a diagonal matrix with elements of the vector $\boldsymbol{L}$ in the diagonal locations, and $\boldsymbol{L}$ is the row vector containing the limits on the three responses, defined in Eq. (43.7).

Equations (43.13a)–(43.13d) amount to a standard linear programming problem. Therefore, with the manipulation so far, our original functional optimal problem has been turned into a simpler problem with known numerical solution algorithms. It is noted that more constraints can easily be appended, so long as they can be written linearly in the variable $\boldsymbol{U}$. Examples of these are "non-stretching" requirement between the impactor and the control point, and "non-negative" force at the pelvic location, etc. Bounds can also be imposed on the control point acceleration themselves, as discussed in [1] and later in this paper.

The third approach mentioned in the Introduction, the "maximum compliance margin (MCM)" approach, can be formulated with further application of the idea of auxiliary variable. Specifically, we introduce an additional auxiliary variable p, and formulate a new optimization problem:

$$\min_{p,\mathbf{q},\mathbf{u}} \left(p = \left[1 \ \mathbf{0}^T \ \mathbf{0}^T \right] \left[p \ \mathbf{q} \ \mathbf{u} \right]^T \right) \tag{43.14a}$$

$$\text{subject to}: \frac{q_i}{L_i} \leq p \ \ (i = 1, \ 2 \text{ and } 3). \tag{43.14b}$$

Equation (43.14a), with the constraints of Eq. (43.14b) and Eqs. (43.13b)–(43.13d) constitute a new linear programming problem, reflecting the MCM strategy for complying with the FMVSS 214, which seeks to minimize the highest of the normalized peak responses.

The above formulations are used to perform a series of numerical case studies. The solution is carried out in the environment of the software Matlab (http://www.mathworks.com). In contrast to [1] where the linprog.m function in Matlab was used, the linear programming optimization here is carried out utilizing the optimization package TOMLAB [5] (through a trial license) which invokes the CPLEX optimizer [6]. The TOMLAB-CPLEX search is found to be consistently faster and superior in solution convergence. It is used to obtain all the numerical results reported in this paper.

43.3 Numerical Results

Numerical computations are carried out for cases with different setting of the weighting vector.

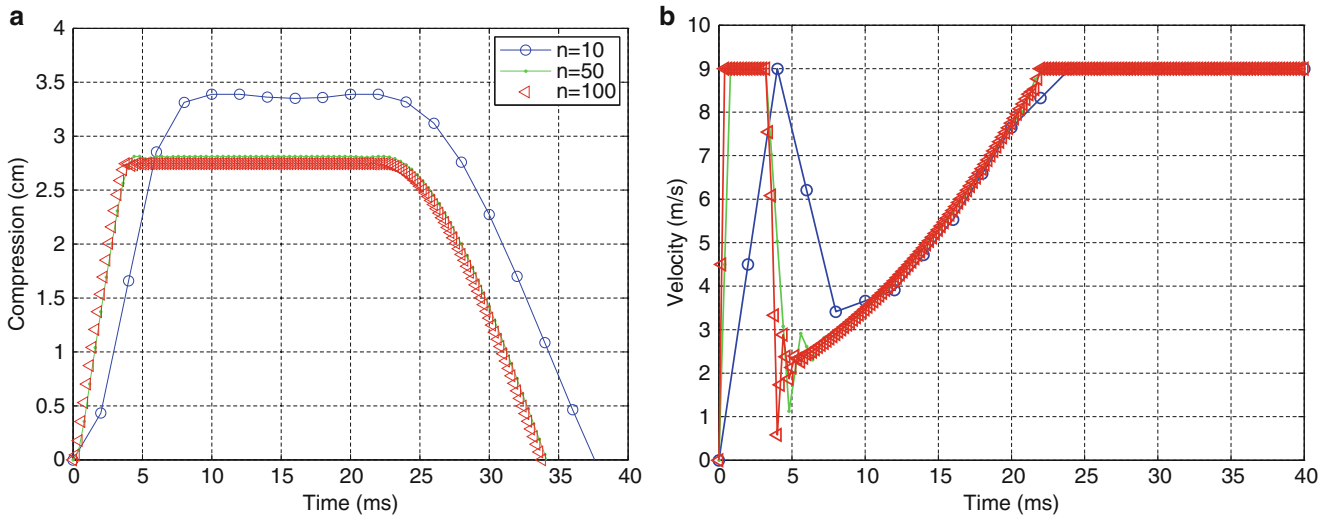

Fig. 43.2 (**a**) Thoracic compression response with 10, 50, and 100 discretization divisions in 40 ms solution domain. Impactor has constant velocity of 9 m/s; allowable space between the impactor and the control points is 8 cm. (**b**) Thoracic control point velocity time history under 10, 50, and 100 divisions in 40 ms solution domain. Same runs as shown in (**a**)

43.3.1 Weighting Vector w = [1 0 0]

In this first numerical study, the weighting vector is set to [1 0 0], i.e., the peak thoracic compression is the objective function, which basically corresponds to the cases in [1]. Figure 43.2a, b show the results of the optimization with discretization divisions (n) of 10, 50, and 100. As with a similar convergence study in [1], the thoracic compression response converges quickly. Figure 43.2a, b show that between $n = 50$ and 100, both the thoracic compression response and the velocity of the control point converge. Based on such results, all computations reported in this paper have n set to 100.

Two differences should be noted between this series of runs and the convergence study result in [1]. The first is that this series has imposed a constraint between the impactor and the control point so that throughout the event, the velocity of the control point will not exceed that of the impactor. This effectively means that the gap between the impactor and the control point will become increasingly smaller (or at least stay constant) throughout time. In other words, the restraint will not *expand* at any time during the event. This condition provides a better representation of a *"passive"* restraint after full deployment. The velocity time history in Fig. 43.2b shows the effect of this constraint (with the velocity bound by the 9 m/s velocity of the impactor).

The second difference between the runs shown in Fig. 43.2 and all the runs reported in [1] is a numerical remedy to a numerical oscillation issue which becomes obvious in this study when the objective function becomes more complex. A close examination identified an idiosyncrasy of the discretization scheme as the cause to this, as explained in Fig. 43.3.

Figure 43.3 shows that with the constant-step acceleration discretization scheme, two different acceleration inputs differing by an oscillation produce the same displacement at the time steps, although the velocity results are different. Therefore, if the objective function of an optimization involves only the displacement, the search result for the acceleration will be non-unique, and the search may end up with a solution containing step-to-step oscillation. (This behavior in a sense is analogous to the hourglass, or zero-energy, mode in displacement-based finite element method for solid continuum mechanics problems with integration only carried out at the center of the element). This numerical issue can be overcome if we also compute the velocity and displacement results in the middle of the time step. As shown in Fig. 43.3d, the two different accelerations produce different displacement results at the mid-points. This remedy is readily incorporated into the existing formulation, by using a time step size half of that for the acceleration in calculating with the existing formulations in Eqs. (43.9)–(43.11). Therefore, in all results reported in this paper, the responses are computed at $2n$ locations for forming the constraints (Eqs. (43.13b) and (43.13c), etc.), as may be detected in Fig. 43.2.

Figure 43.4 shows the result of an optimization run with $n = 100$. The constant impactor velocity is 9 m/s, and the restraint space is set to 10 cm. The "flat-top" shaped optimal thoracic compression time history is very close to that given in [1], even with the extra constraint on the velocity of the loading points. Note that the pelvic force, not a factor in the objective function in this case, reaches the ceiling of 80 % of its IARV.

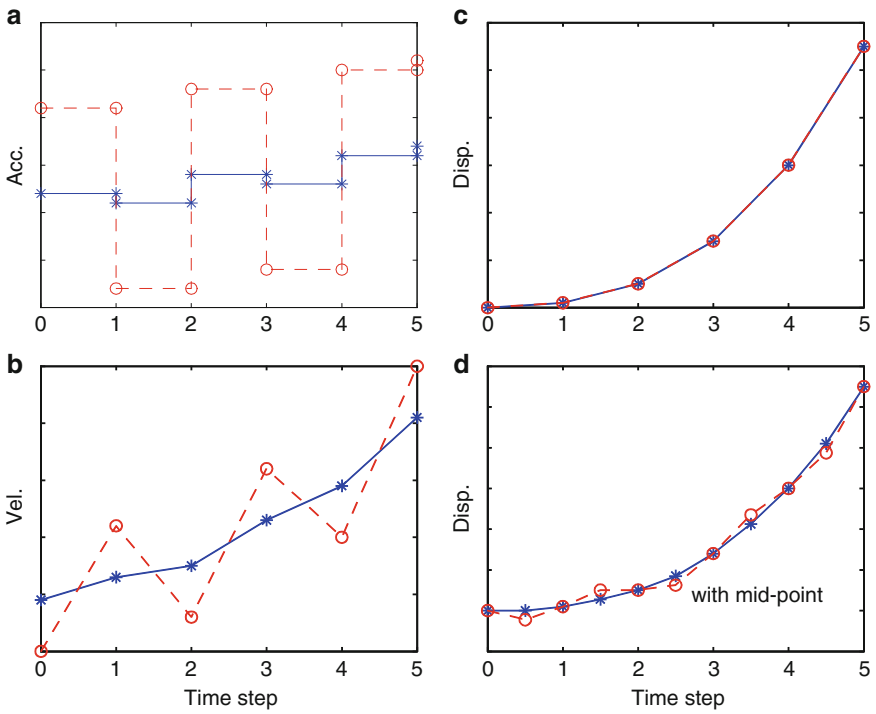

Fig. 43.3 Illustration of effect of oscillation on velocity and displacement with constant-step acceleration discretization. (**a**) Two different acceleration profiles, a base, and another with superimposed oscillation; (**b**) Velocities from the accelerations in (**a**); (**c**) Displacements calculated at time steps giving identical results; (**d**) Displacements calculated at half-steps giving two different results, distinguishing the two acceleration profiles

In Fig. 43.4a–c disturbances are noticed in the system near and after 25 ms (e.g., in f_2 in Fig. 43.4a, and y_{2v} in Fig. 43.4b). Since these appear after the loading phase (thoracic and pelvic masses reaching the impactor speed), they do not have an influence in the objective function (the peak value of the thoracic compression). In fact, the solution in this region is non-unique without further constraint. The disturbances, which are seen in some other runs in this paper, are ignored in the current study.

43.3.2 Weighting Vector w = [0 0 1]

The second numerical study has the weighting vector set to [0 0 1], i.e., the peak pelvic force is the only response to be minimized. Figure 43.5a–c highlight the optimal result. The external parameters, i.e., the impactor velocity and restraint space are the same as the preceding case. The optimal pelvic force now takes the "flat-top" shape (Fig. 43.5a) and its normalized peak is the lowest among the three responses being tracked. Note that the thoracic compression, not a contributor to the objective function in this case, reached the 80 % IARV ceiling.

43.3.3 Weighting Vector w = [0 0.5 0.5]

This setting of the weighting vector effectively means that the average of the peaks of the thoracic acceleration and pelvic force will be minimized (the thoracic compression is still subjected to the constraint of 80 % of its IARV). Aside from the difference in $\boldsymbol{w}$, the value of the restraint space is set to 10 cm at the thorax and 7 cm at the pelvis (as an example of $g_1 \neq g_2$ cases). The impactor velocity remains constant at 9 m/s. Figure 43.6a shows the responses from the solution. The normalized compression and force in this case both take the "flat-top" shape, and their peak values are close but not identical. The control point velocities and the restraint force from the optimal solution are shown in Fig. 43.6b, c.

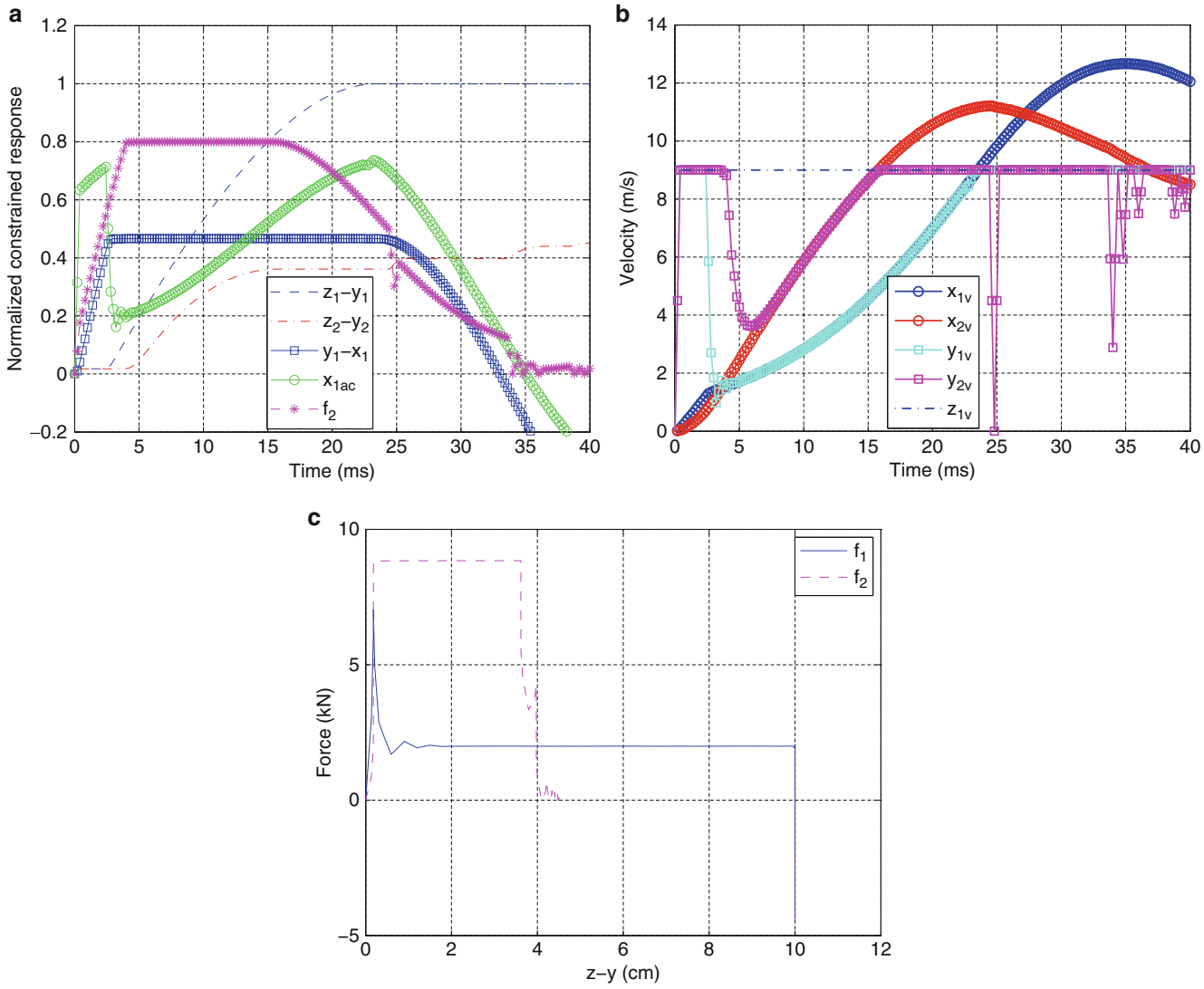

Fig. 43.4 (**a**) Normalized thoracic compression (y_1-x_1), thoracic acceleration (x_{1acc}), and pelvic force (f_2). Also shown are the relative motions between the impactor and the control points (i.e., restraint compression), z_1-y_1 and z_2-y_2, which are normalized by the initial restraint space (10 cm in this run). (**b**) Velocity time history from the optimal solution case shown in (**a**). x_{1v}: thoracic mass, x_{2v}: pelvic mass; y_{1v}: thoracic control point, y_{2v}: pelvic control point; z_{1v} the impactor. (**c**) The force-compression relationship for the restraints from the case in (**a**) and (**b**). f_1: thoracic restraint force; f_2: pelvic restraint force

Mapped to engineering practice in the context of FMVSS214, this optimal solution would be the answer if the strategy for compliance is to have an equal emphasis on both of the requirements.

43.3.4 Maximum Compliance Margin Numerical Example

A solution scheme for the MCM strategy has been given in Eqs. (43.14a) and (43.14b). The aforementioned weighting vector no longer enters into the formulation. The margin factor in Eq. (43.7), however, is still relevant. Consistent with the premise of passing the FMVSS 214 with the highest margin, the margin factor in Eq. (43.7) is set to $\beta = [140\ \%\ 80\ \%\ 80\ \%]$. The reason for the 140 % is to only limit the thoracic compression to about 62 mm (140 % of the 44 mm value used so far), which is taken as the maximum physically possible thoracic compression by the dummy. Figure 43.7 shows the solution with the MCM formulation of the same problem that is presented in Fig. 43.6. The responses shown here are similar to the solution shown in Fig. 43.6a in the relevant time frame before unloading (before 30 ms), but a difference exists that in the

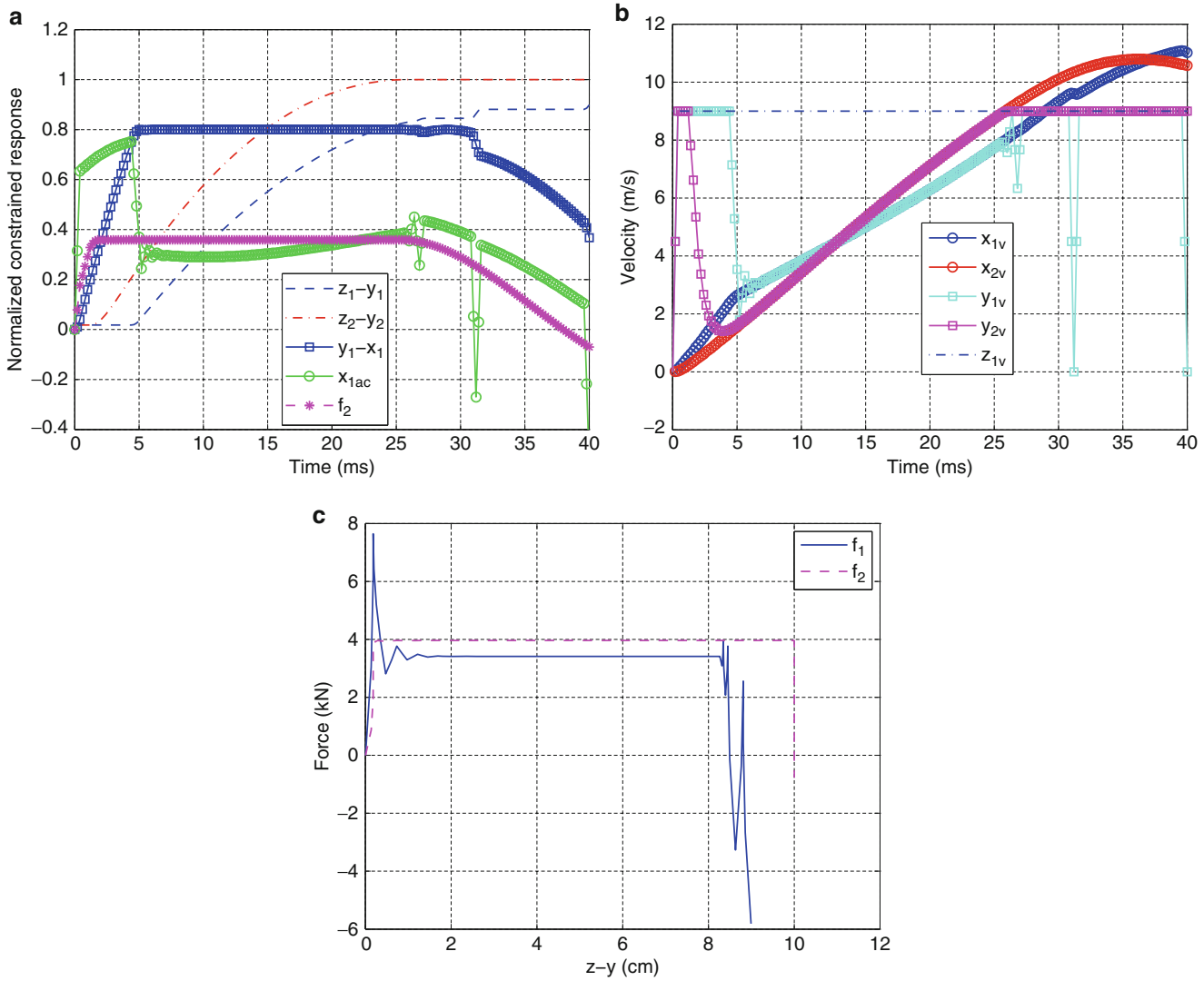

Fig. 43.5 (**a**) Normalized thoracic compression (y_1-x_1), thoracic acceleration (x_{1acc}), and pelvic force (f_2). Also shown are the relative motions between the impactor and the control points (i.e., restraint compression), z_1-y_1 and z_2-y_2, which are normalized by the initial restraint space. (**b**) Velocity time history from the optimal solution case shown in (**a**). x_{1v}: thoracic mass, x_{2v}: pelvic mass; y_{1v}: thoracic control point, y_{2v}: pelvic control point; z_{1v} the impactor. (**c**) The force-compression relationship for the restraints from the case in (**a**) and (**b**). f_1: thoracic restraint force; f_2: pelvic restraint force

MCM case, the normalized peaks of the two objective-related responses are identical. In the case in Fig. 43.6, the higher of the normalized peaks of the two responses involved in the objective function is from the pelvic force at 0.5451, while the normalized peak of these is 0.5165 in Fig. 43.7, consistent with the MCM requirement. At the same time, the objective function value for the case in Fig. 43.6 is a lower 0.4842, reflective of the goal there which is to minimize the average of the normalized peaks.

43.4 Discussion

The numerical results given in the last section show that the formulation and the computational methods can successfully identify an optimal solution once the objective function is chosen, under given external parameters. The results themselves also serve to help understand the response behavior of the dummy, and provide direction for designing the restraint.

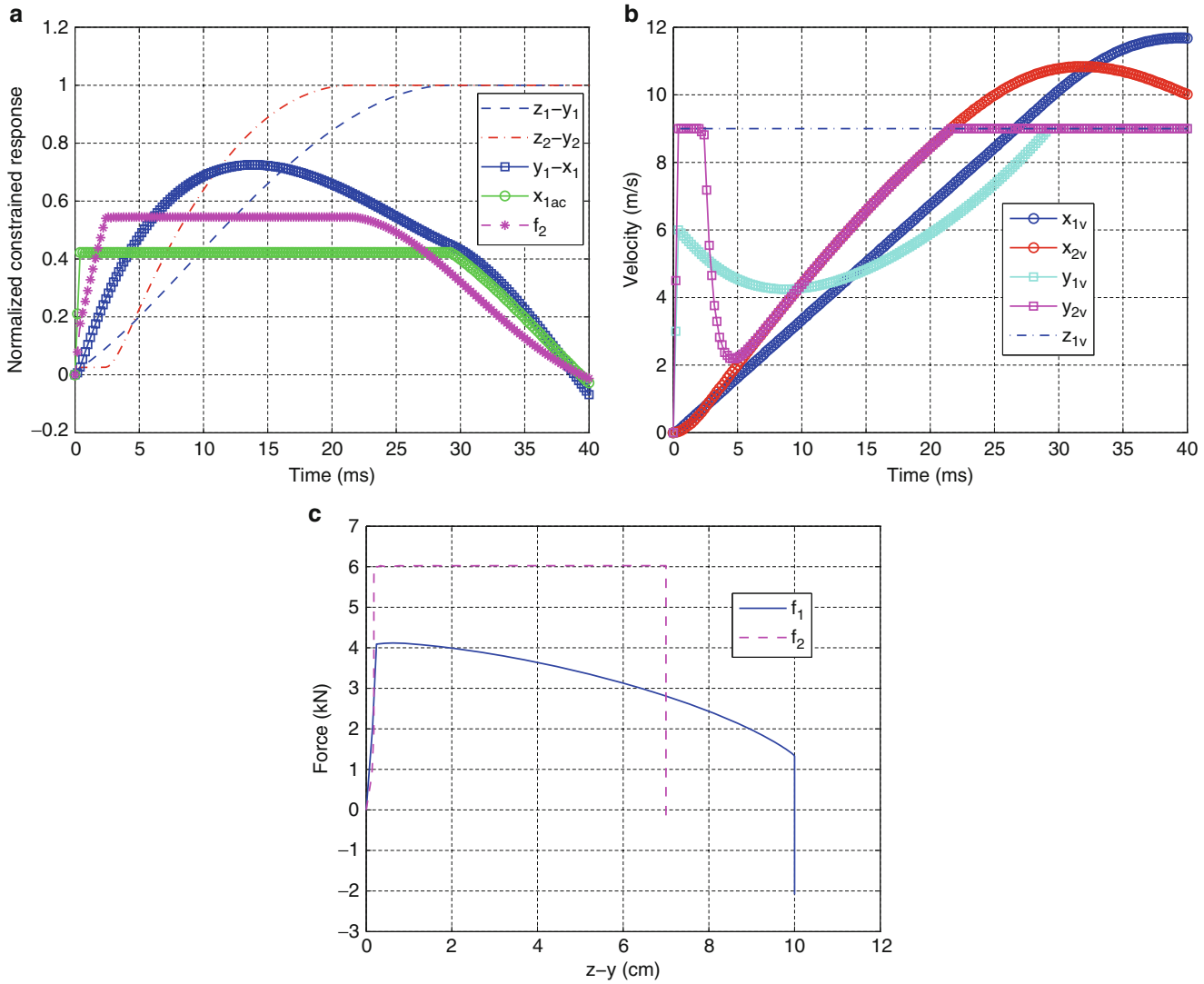

Fig. 43.6 (**a**) Normalized thoracic compression (y_1-x_1), thoracic acceleration (x_{1acc}), and pelvic force (f_2). Also shown are the relative motions between the impactor and the control points (i.e., restraint compression), z_1-y_1 and z_2-y_2, which are normalized by the initial restraint space. (**b**) Velocity time history from the optimal solution case shown in (**a**). x_{1v}: thoracic mass, x_{2v}: pelvic mass; y_{1v}: thoracic control point, y_{2v}: pelvic control point; z_{1v} the impactor. (**c**) The force-compression relationship for the restraints from the case in (**a**) and (**b**). f_1: thoracic restraint force; f_2: pelvic restraint force

For example, results in Figs. 43.4 and 43.5 (for $\boldsymbol{w} = [1\ 0\ 0]$ and $[0\ 0\ 1]$) show a substantial difference in the restraint force profiles (Figs. 43.4c and 43.5c). A corresponding difference is seen in the control point velocity time history plots shown in Figs. 43.4b and 43.5b. In the initial loading stage, the pelvic control point moves more than that at the thoracic in the first case; whereas it is the reverse for the peak pelvic force minimization case. An examination of Fig. 43.4a shows that the pelvic force, which does not enter the objective function, reached its constraint of 0.8; whereas in the case of Fig. 43.5a, the thoracic compression saturated at its constraint of 0.8. This is more clearly seen in Fig. 43.8 where the weighting factor $\boldsymbol{w}$ is set to $[\alpha\ 0\ 1\text{-}\alpha]$ with α varying from 0 to 1. The case shown in Fig. 43.4 is the case of $\alpha = 1$ and that in Fig. 43.5 is $\alpha = 0$. The plot indicates that the requirements of thoracic compression and pelvic force are competing. The restraint strategy for a thoracic-compression only requirement is different from that for a pelvic-force only requirement.

Another example of the information that can be derived from the optimization exercises is to define the minimum restraint space necessary to achieve a certain level of response. A large restraint space in practice is not easy to achieve due to packaging limitation. For a given impactor motion history, it is of interest to determine the minimum space necessary as a guide to design. Towards this, a series of optimizations are carried out using the MCM type of objective function by setting the restraint space from 3 to 12 cm at a 0.5 cm interval. In these runs, the margin factor in Eq. (43.7) is again set to

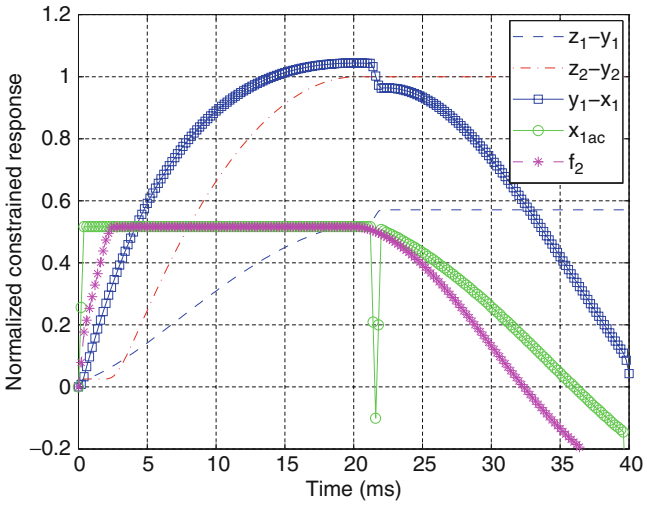

Fig. 43.7 Normalized thoracic compression (y_1-x_1), thoracic acceleration (x_{1acc}), and pelvic force (f_2). Also shown are the relative motions between the impactor and the control points (i.e., restraint compression), z_1-y_1 and z_2-y_2, which are normalized by the initial restraint space (10 cm and 7 cm respectively). Impactor constant velocity is 9 m/s

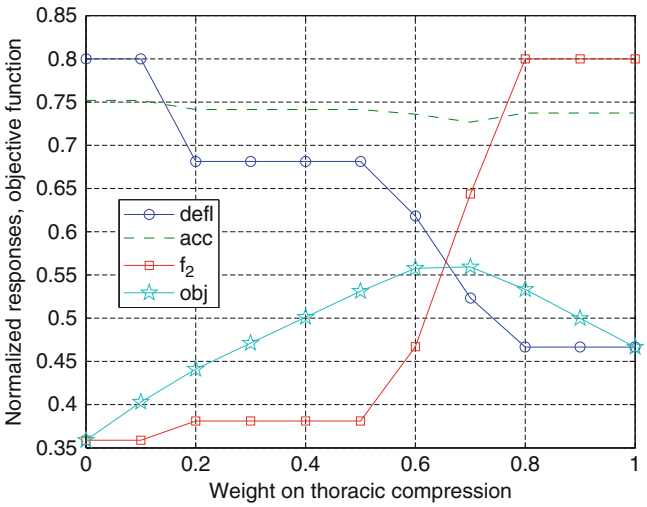

Fig. 43.8 Optimal solution under different weight split between thoracic compression and pelvic force. Constant 9 m/s impactor velocity, 10 cm restraint space

$\beta = [140\ \%\ 80\ \%\ 80\ \%]$. The initial impactor velocity is set to 9 m/s, and with either no change through time, or a constant deceleration of −14 g (as explained in [1], the −14 g deceleration is related to the moving barrier impact test). Figure 43.8 summarizes the results showing both the objective function, and the peak value of the thoracic compression resulting from the optimal solution. In the constant velocity case, the optimization problem is found to be infeasible at 3 cm, therefore, results are only plotted starting from 3.5 cm. At this value and at 4 cm, the thoracic compression already "bottoms out" at 140 % of the 44 mm IARV. With increasing restraint space, the best that can be achieved monotonically improves, and at 12 cm, the objective function is less than 40 %, and the thoracic compression is less than 80 % of 44 mm. Compared to this set of results, the optimal result for the −14 g case, due to the lowering impact, is always better, as shown in the figure.

The optimal control point motion histories shown in this paper so far, including those solutions of the runs in Fig. 43.8, all characteristically rise at very high accelerations at the very beginning of the event to optimally utilize the restraint space. This also is a documented characteristic of the optimal pulse based on single degree of freedom spring-mass models for frontal impact [7, 8], and other "mini-max" problems. In practice, due to limitations such as that on the deploying power of side air bags or even the mechanical response time of the restraint device, such high accelerations may not be permissible or attainable. In this sense, the results provided so far in this paper are all "theoretical" limits. However, as reasoned in [1], additional constraints may be imposed on the acceleration time history of the control points to factor in such limitations,

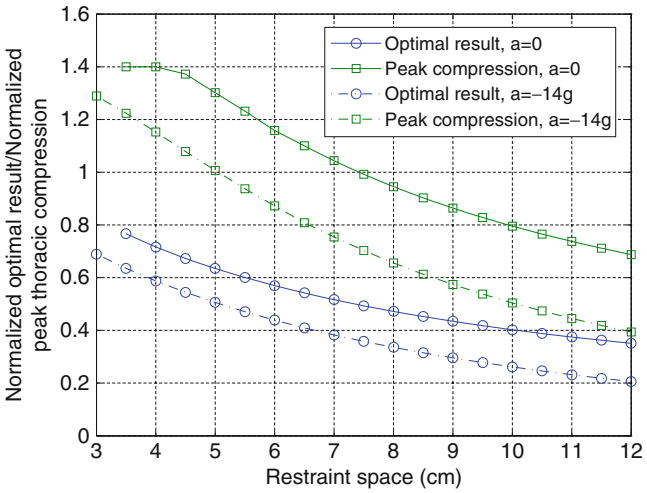

Fig. 43.9 Dependence of optimal solution on the restraint space with the MCM scheme

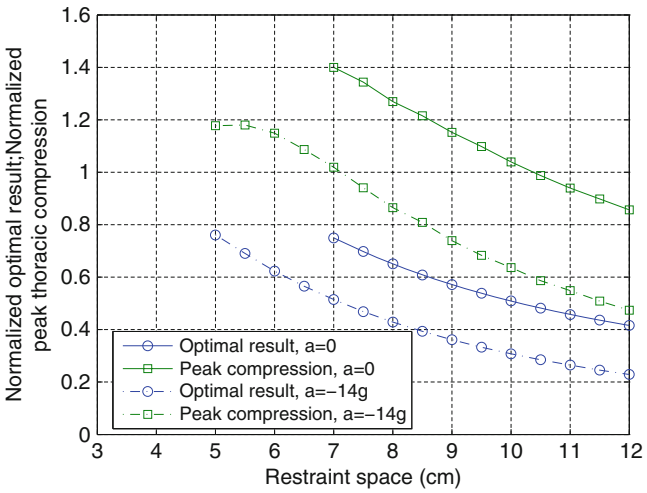

Fig. 43.10 Dependence of optimal solution on the restraint space with the M-CM scheme. An upper bound of 100 g is imposed on the control accelerations

and render a more "realistic" or "practicable" solution. With this in mind, the runs shown in Fig. 43.9 are repeated, but with 100 g specified as the upper and lower bound of the thoracic and pelvic control point accelerations (The 100 g magnitude is generally the level of the peak acceleration seen on the rib acceleration of the SID-IIs in side impact tests). The results from the new runs are shown in Fig. 43.10. The minimum restraint space now is 7 cm for the constant velocity case (with the thoracic compression bottomed out), and 5 cm for the decelerating case.

The information provided in Fig. 43.10, given the bound on the acceleration, could be used as a reference in determining the restraint space in actual engineering design. It is worthy of noting that in this paper, the word "restraint" is used to generically refer to all the energy absorbing elements between the dummy and the impactor. In terms of practical engineering, this would include passive energy absorbing elements such as the deformable part of the door metal structure and interior trim, as well as the active energy absorbing elements such as the side impact airbag.

43.5 Conclusion

A previously established formulation for the optimization of the thoracic compression of the SID-IIs dummy has been extended in this study to address the performance requirements in the FMVSS 214 on the SID-IIs dummy. This extended formulation provides a generalized weighted average of the peak responses of the thoracic acceleration and the peak pelvic

force, which are given performance requirements in the regulation. The generalized formulation also allows the inclusion of the thoracic compression into the objective function. Different definitions of optimality, i.e., different strategies in engineering practice can be achieved by setting the weighting factor in the objective function appropriately. An alternative formulation is also given to reflect a strategy of maximizing the compliance margin towards the FMVSS 214 requirements.

Numerical examples using the formulations are carried out and results presented. Good numerical convergence is observed with a linear programming optimization algorithm. The examples demonstrate that given the impactor motion, and a feasible available restraint space, the formulations are capable of identifying the optimal solution. Comparison of the numerical results also shows that a lower thoracic compression can be achieved with an elevated pelvic force, and vice versa.

Numerical runs are also performed to identify the minimum restraint space necessary to achieve compliance to the FMVSS 214 requirements. In particular, these include runs where the restraint acceleration is bounded at 100 g, which should be of reference value to practical design.

References

1. Shi, Y., Wu, J., Nusholtz, G.S.: Optimal restraint for the thoracic compression of the SID-IIs crash dummy using a linear spring-mass model. ASME J. Dyn. Syst. Meas. Control **135**, 031007-1–031007-8 (2013)
2. SID-IIs Small Side Impact Dummy. http://www.humaneticsatd.com/crash-test-dummies/side-impact/sid-iis. Accessed 23 Sept 2014
3. Federal motor vehicle safety standards; occupant protection in interior impact; side impact protection; .... Fed. Regist. **72**(175), 51908–51973 (2007)
4. Balandin, D.V., Bolotnik, N.N., Pilkey, W.D.: Optimal Protection from Impact, Shock, and Vibration. Taylor and Francis, Philadelphia (2001)
5. http://tomopt.com/tomlab/. Accessed 23 Sept 2014
6. http://www.ilog.com/products/cplex/. Accessed 23 Sept 2014
7. Wu, J., Nusholtz, G.S., Bilkhu, S.: Optimization of vehicle crash pulses in relative displacement domain. Int. J. Crashworthiness **7**(4), 397–414 (2002)
8. Shi, Y., Wu, J., Nusholtz, G.S.: Optimal frontal vehicle crash pulses – a numerical method for design. In: Proceedings of 18th International Technical Conference on the Enhanced Safety of Vehicles, Paper #514 (2003)

Chapter 44
A Comparison of Common Model Updating Approaches

D. Xu, M. Karamooz Mahdiabadi, A. Bartl, and D.J. Rixen

Abstract In this paper, three common model updating approaches are considered to evaluate their efficiencies for model calibration on a component of an Ampair 600W wind turbine. This turbine is a test bed for the Substructuring Focus Group of the Society of Experimental Mechanics. The fin of the wind turbine is chosen to be investigated in updating procedures. Firstly, model updating method has been developed using an objective function based on extracted eigenfrequencies. The objective function is chosen as a sum of weighted eigenfrequencies with respect to their importance. In the second procedure, weighted Modal Assurance Criteria (MAC) are used to define the objective function. Finally, measured and simulated Frequency Response Functions (FRFs) are directly used to find the best correlated Finite Element (FE) model. The results of three updating procedures are then compared to measured eigenfrequencies, mode shapes and FRFs, and the evaluation of the performance of these three different model updating methods is discussed.

Keywords Model updating • Modal analysis • FRF • MAC • FRAC

44.1 Introduction

Nowadays reliable dynamic mathematical models are essential for dynamic design and analysis, since the complexity of engineering assembly is growing fast. Model updating is often performed in order to obtain a model that can precisely represent the dynamic behavior of a real structure. To do so, a large variety of model updating methods have been defined, many of which are described in [1]. In general, model updating approaches are divided into two categories, namely methods based on modal data and the ones based on FRFs.

Since the FE model is expected to match the reference data, in many updating methods a good correlation between the measured and numerical modal data is pursued as the objective of updating. In other words, after model updating the Finite Element Analysis (FEA) results of a FE model should better reflect the measured dynamic data of a real structure. However the accuracy of these methods depends on the accuracy of FE model and is highly affected by the errors of modal extraction [2].

In 1990s the use of frequency response function (FRF) instead of modal parameters for model updating was first investigated by Lin et al. [3], which leads to another category of model updating methods. Model updating using FRFs provides some advantages [4]. First, a large amount of data is available, including the effect of eigenfrequencies out of measured range and anti-resonances, which can increase the accuracy of model updating. Furthermore, the errors from modal parameter extraction in the model updating methods using modal data can be avoided in this way. However, the noise in the measured FRF can cause new errors.

Although these two categories of model updating methods are properly defined, they have still not been compared for efficient implementation on different structures. In this work, model updating methods based on eigenfrequencies, eigenmodes and FRFs are performed and compared by different criteria, with a perspective to identify the efficiency of algorithms. The fin of an Ampair 600W wind turbine is investigated as example. The Ampair 600W wind turbine is the benchmark of the Dynamic Substructuring Focus Group within the Society for Experimental Mechanics. Experimental measurement was performed to collect the dynamic data of the fin. Furthermore, the fin was modeled, then the material properties were updated. Matlab and ANSYS software were used for optimization and modal analysis repectively. Finally, the efficiency of different model updating methods were compared directly. It is shown that the updating method based on FRF is most efficient.

D. Xu • M.K. Mahdiabadi (✉) • A. Bartl • D. Rixen
Technical University of Munich, Institute of Applied Mechanics, Boltzmannstr. 15, 85748 Garching, Germany
e-mail: m.karamooz@tum.de; andreas.bartl@tum.de

© The Society for Experimental Mechanics, Inc. 2016

M. Allen et al. (eds.), *Dynamics of Coupled Structures, Volume 4*, Conference Proceedings of the Society for Experimental Mechanics Series, DOI 10.1007/978-3-319-29763-7_44

The remainder of this paper is structured in the following way: Sect. 44.2 describes the common model updating techniques. Section 44.3 introduces the measurement of dynamic data of the fin. In Sect. 44.4 detailed modeling is given. Adjacently, the model updating process is shown in Sect. 44.5 whereas Sect. 44.6 shows model updating results. Finally, Sect. 44.7 holds concluding remarks.

44.2 Common Model Updating Techniques

44.2.1 Model Updating Methods Using Modal Data

These methods are based on the correlation of numerical and measured modal data (including eigenfrequencies and eigenmodes). They rely on an objective function, which is to be minimized during the model updating procedure.

The most common and straightforward approach is to introduce weighted deviation between the measured and simulated eigenfrequencies into the objective function J defined as [5]:

$$J = \sum_{i=1}^{n} k_i \left(\omega_{r,i}^{a} - \omega_{r,i}^{m}\right)^2 \tag{44.1}$$

where $\omega_{r,i}^{a}$ and $\omega_{r,i}^{m}$ are the i-th numerical and measured eigenfrequencies, k_i the weighting factors of the i-th deviation of the measured and simulated eigenfrequencies. Since the model was good enough and only the first several modes are investigated, it is assumed that the i-th modes from model and the measurement come in the same order in the present case.

Another commonly used method introduces MAC [6] in objective function. MAC relates the numerical mode shapes to the measured ones and indicates the deviation between two mode shapes. MAC is defined as

$$MAC_{ii} = \frac{\left(\{\varphi_a\}_i^T \{\varphi_m\}_i\right)^2}{\{\varphi_a\}_i^T \{\varphi_a\}_i \{\varphi_m\}_i^T \{\varphi_m\}_i} \tag{44.2}$$

where φ_a and φ_m are the i-th numerical and measured mode shapes. MAC always has a value between 0 and 1. A MAC value of 1 indicates that the numerical model has the same mode shapes as the real structure.

Objective function of method using MAC can be defined with the weighted deviation of MACs, so that a minimized objective function corresponds to maximized MAC values and therefore a satisfying correlation between measured and numerical mode shapes. Objective function J can be written as

$$J = \sum_{i=1}^{n} k_i \left(1 - MAC_{ii}\right) \tag{44.3}$$

where MAC_{ii} is the MAC value of the i-th corresponding measured and numerical mode shapes. k_i indicates the weighting factor.

44.2.2 Model Updating Methods Using Frequency Response Data

The use of FRFs in the objective function instead of modal data leads to another group of methods. Frequency Response Assurance Criterion (FRAC) [7, 8] is introduced to indicate the deviation between two FRFs, which is defined as

$$FRAC\,(i,j) = \frac{\left|\left(H_{ij}^{m}(\omega)\right)^H H_{ij}^{a}(\omega)\right|^2}{\left(\left(H_{ij}^{m}(\omega)\right)^H H_{ij}^{m}(\omega)\right)\left(\left(H_{ij}^{a}(\omega)\right)^H H_{ij}^{a}(\omega)\right)} \tag{44.4}$$

Where $H_{ij}^{a}(\omega_{r,k})$ and $H_{ij}^{m}(\omega_{r,k})$ indicate the numerical and experimental measured FRFs at point i and excited at point j. FRAC always has a value between 0 and 1, where a FRAC of 1 indicates that two compared FRFs have a good correlation.

The objective function J for the model updating method using FRFs can be defined as

$$J = \sum_{i=0}^{n} k_i \left(1 - FRAC_{ij}\right) \tag{44.5}$$

Where k_i indicates the weighting coefficient of the FRAC at the i-th point and j the specified point of excitation.

In the following two sections the efficiency of these three model updating methods will be investigated on the Ampair 600W wind turbine's fin as an example of simple homogeneous structure.

44.3 Measurement

An impact test was performed with a standard modal analysis software under free-free condition to identify the dynamic data of the fin as the reference for the model updating. For sake of simplicity, the fin was considered being a plane surface. A measurement grid of 7 points was defined as shown in Fig. 44.1. By measurement the fin was excited in the direction perpendicular to the plane surface at point 4. The FRF of measurement points respect to the excitation point in the frequency range from 300 to 700 Hz with 1 Hz increment and the first 5 eigenmodes were extracted and used to calculate MAC and FRAC values. The measured eigenfrequencies are listed in Table 44.3.

44.4 Modeling

The CAD model of the fin was provided by University of Stuttgart [9]. The geometry of this model is assumed to be properly defined. A FE model was generated in ANSYS Workbench 15.0. In order to get the best compromise between the accuracy and computing time of FEA, a mesh study was performed to find the best mesh size. The convergence of numerical eigenfrequencies is shown in Fig. 44.2. Finally a mesh with 34,584 nodes and 29,061 solid tetra elements was adapted (see Fig. 44.3). The nodes with the same location as measurement points were defined to extract mode shapes in FEA. The fin is made of steel and is considered to be homogeneous. Therefore the model of fin provides three parameters to update, namely density ρ, Young's modulus E and Poisson's ratio γ.

44.5 Model Updating

Model updating is considered as a process of minimization of the deviation of the dynamic response of FE model with respect to the truth data. In other words, the objective functions introduced in Sect. 2 must be optimized iteratively. To do so, Matlab Optimization Toolbox and ANSYS were applied to perform Optimization and FEA and text files were used as media of the

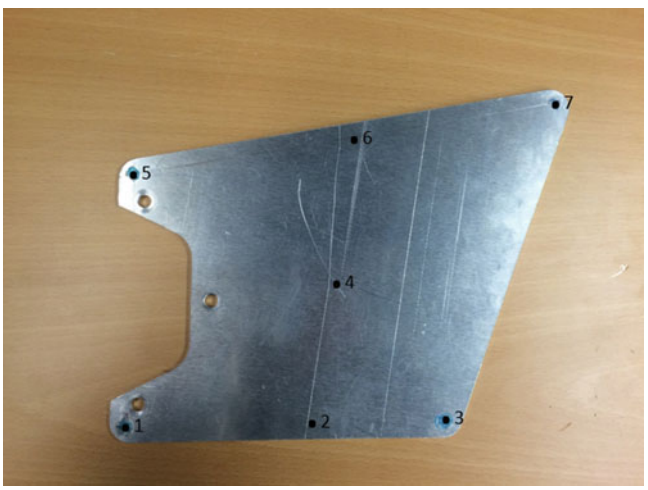

Fig. 44.1 Measurement grid for fin

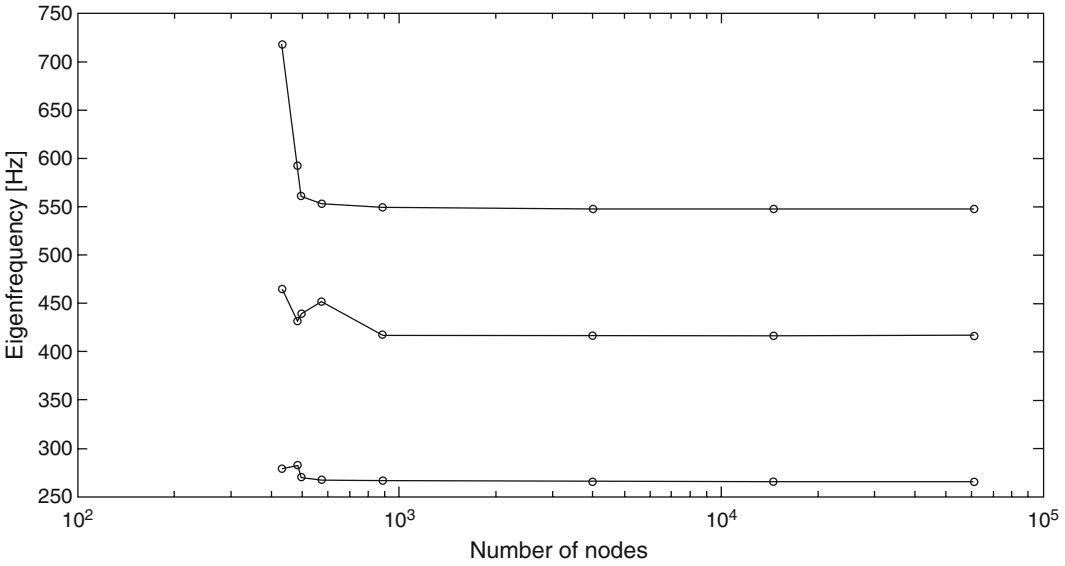

Fig. 44.2 Convergence of the first three numerical eigenfrequencies. Note that the eigenfrequencies in this figure don't correspond to the final result

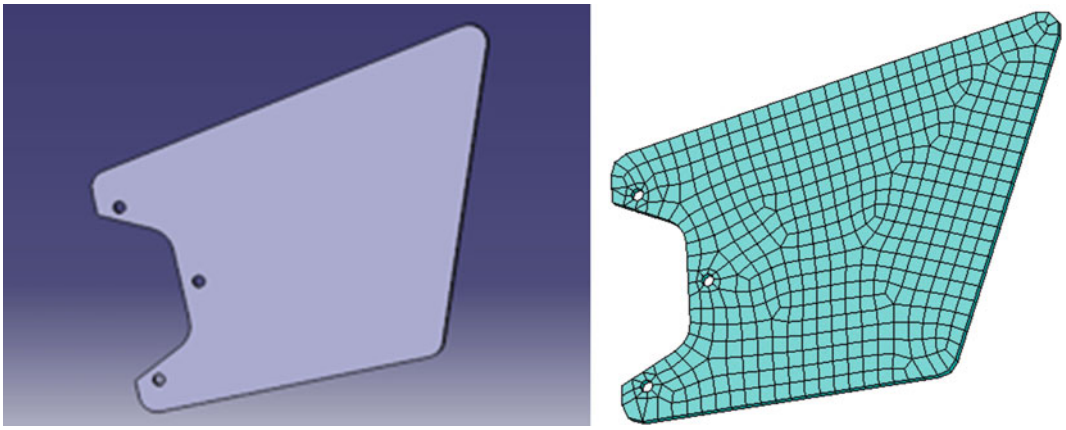

Fig. 44.3 *Left*: CAD model of fin. *Right*: FE model of fin

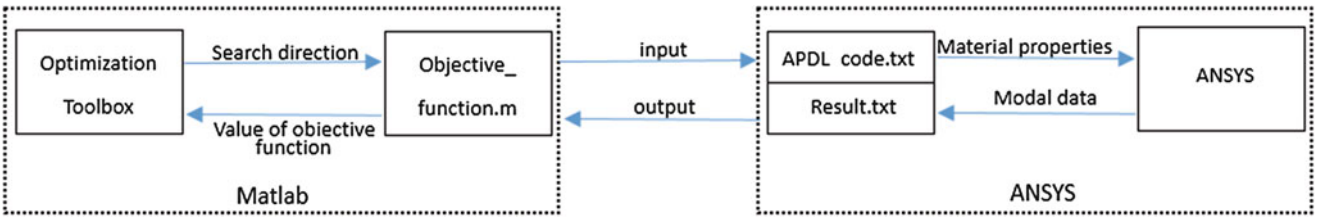

Fig. 44.4 Model updating procedure with Matlab and ANSYS

communication between these two programs, as shown in Fig. 44.4. For each iteration step Matlab Optimization defines a search direction for proper material properties and writes corresponding APDL code into APDL.txt and calls for ANSYS to execute it in background. After the modal analysis is performed in ANSYS, the results including modal data are written into Result.txt, which will be read by MATLAB, so that the value of objective function defined in Sect. 44.2 can be calculated. In order to update the FE model of the fin an Active Set algorithm in Matlab Optimization Toolbox [10] was used to optimize

the objective functions with the default material properties of steel in ANSYS as start point. The first 5 eigenfrequencies and eigenmodes and the FRFs of 7 measurement points in the frequency range from 300 to 700 Hz with 1 Hz increment were used to update the model.

44.6 Results

The proposed methods with different objective functions were applied to the FE model of the fin. After convergence of the objective functions the material properties listed in Table 44.1 were obtained and the corresponding eigenparameters are shown in Tables 44.2 and 44.3 and Figs. 44.5, 44.6, 44.7 and 44.8. In Fig. 44.7 the FRFs of point 3 and 6 are shown as examples.

Table 44.1 Material properties of fin before and after model updating with different methods

Parameter	Before updating	Eigenfrequencies[a]	Mode shapes[a]	FRFs[a]	Unit
E	220	137.5	137.5	134.0	GP
ν	0.3	0.232	0.263	0.248	–
ρ	7850	5657	5657	5406	kg/m^3

[a]Eigenfrequencies, mode shapes and FRFs indicate the results of updating methods using eigenfrequencies, mode shapes and FRFs respectively

Table 44.2 Eigenfrequencies of fin before and after model updating with different methods

Frequency comparison [Hz]						Relative deviation with respect to measured data [%]				
Mode	Measured	Before updating	Eigenfrequencies	Mode shapes	FRFs	Meas.	Before updating	Eigenfrequencies	Mode shapes	FRFs
1	263.4	266.0	263.9	262.0	265.5	–	0.99	0.19	0.53	0.80
2	412.6	416.7	410.9	409.1	414.0	–	0.99	0.41	0.85	0.34
3	542.3	547.7	537.8	536.4	542.3	–	1.00	0.83	1.09	0
4	655.9	671.5	648.5	651.5	656.4	–	2.38	1.13	0.67	0.08
5	920.0	947.9	929.8	928.1	938.1	–	3.03	1.07	0.88	1.97

Table 44.3 FRAC before and after model updating with different methods

	1	2	3	4	5	6	7
Before updating	0.061	0.082	0.059	0.058	0.075	0.0660	0.065
Eigenfrequency	0.120	0.059	0.117	0.120	0.089	0.109	0.091
Mode shape	0.207	0.050	0.199	0.200	0.074	0.138	0.117
FRF	0.691	0.592	0.698	0.709	0.760	0.739	0.651

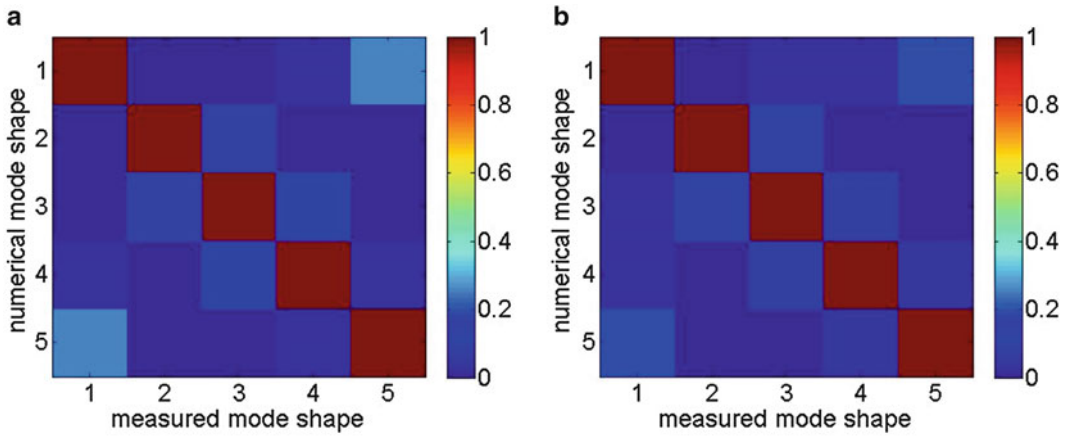

Fig. 44.5 AutoMAC of fin. (**a**) Numerical. (**b**) Measured

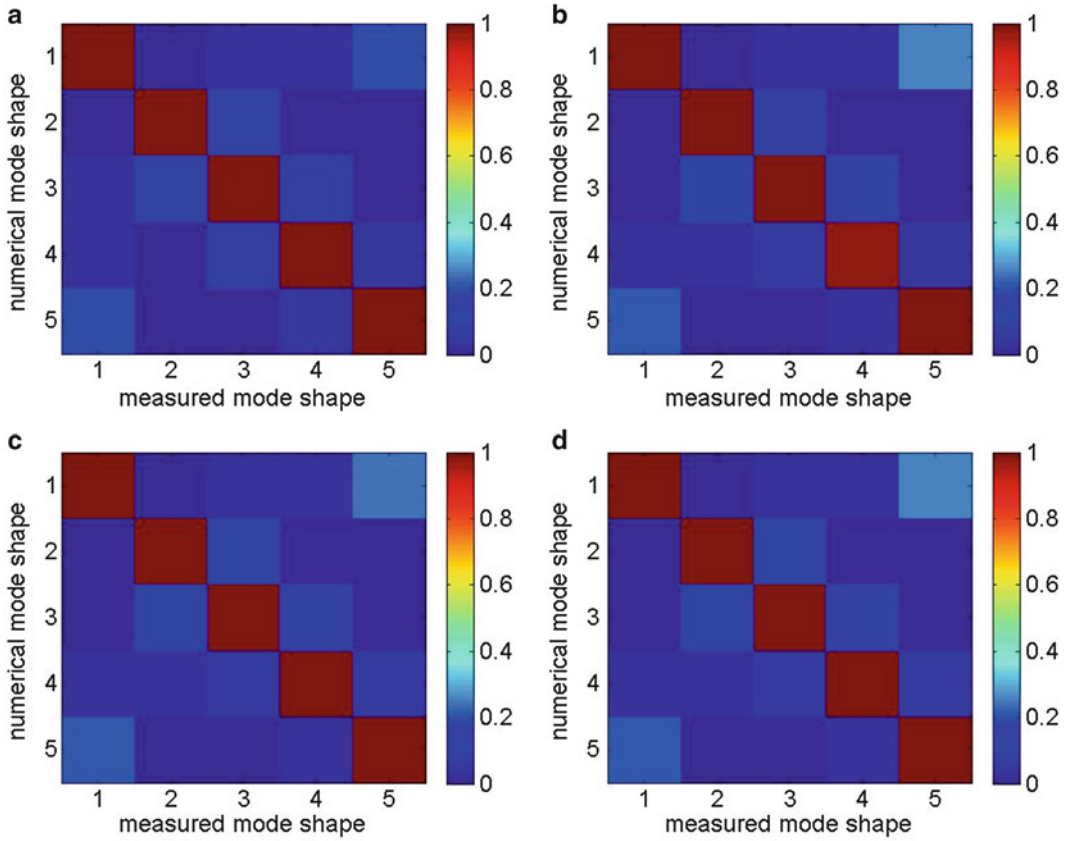

Fig. 44.6 MAC relating the numerical mode shape of first 6 eigenmodes of fin model to the measured ones after updating with different methods. (**a**) Before model updating. (**b**) Eigenfrequencies. (**c**) Mode shapes. (**d**) FRFs

The average deviation of eigenfrequencies after updating with the method based on eigenfrequencies is below 1.5 % (see Fig. 44.2). It can be seen in Fig. 44.5 that the AutoMAC is satisfying. Therefore the model of the fin is successfully updated. However, the numerical FRFs don't fit the measured ones very well. After updating with eigenmodes close results are obtained compared to the result updated with eigenfrequences, as shown in Tables 44.1, 44.2 and 44.3. The MAC and FRAC values are only slightly improved after model updating with the method using mode shapes (see Table 44.3 and Figs. 44.6 and 44.7). After model updating with FRFs the correlation between numerical and measured FRFs is largely improved (see Table 44.3 and Fig. 44.8). More accurate eigenfrequencies within the frequency range used to update the model are obtained, jet this method leads to bigger deviation of the eigenfrequencies outside the frequency range.

44.7 Conclusion

This paper compares three common model updating methods through applying them on a simple homogeneous structure. The aim was to examine the efficiency of model updating approaches. To do so, the measured dynamic data of the Ampair 600W wind turbine fin, including modal information and FRFs, were extracted. Then, based on the measured data model updating methods using eigenfrequencies, mode shapes and FRFs were applied on the model of the fin and evaluated with obtained numerical dynamic data after updating.

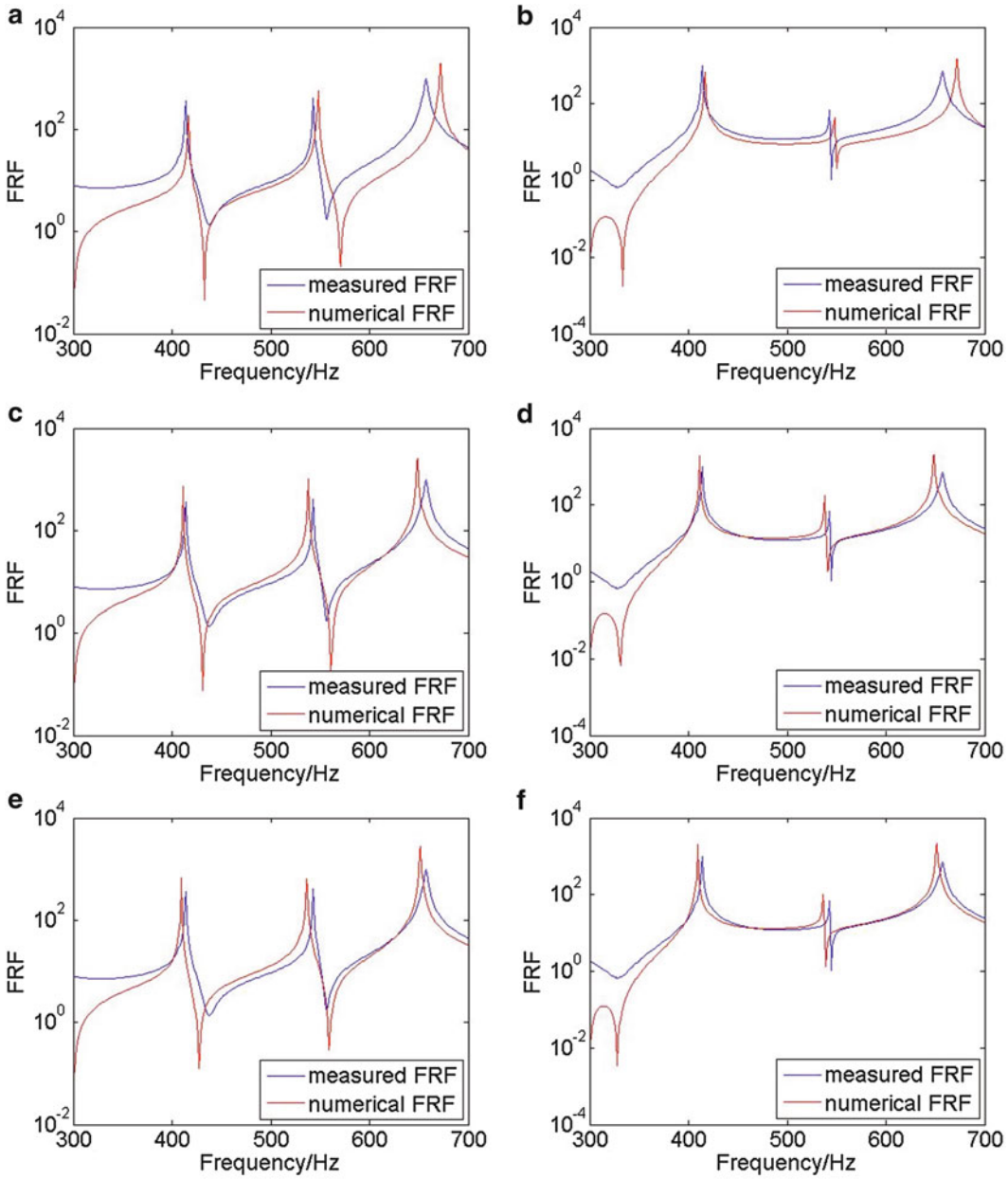

Fig. 44.7 FRFs of point 3 and 6 obtained before and after model updating with different methods. (**a**) FRFs of point 3 before model updating. (**b**) FRFs of point 6 before model updating. (**c**) Updated FRFs of point 3 with eigenfrequencies. (**d**) Updated FRFs of point 6 with eigenfrequencies. (**e**) Updated FRFs of point 3 with mode shapes. **(f)** Updated FRFs of point 6 with mode shapes

The results show that none of these methods has absolute advantage over others. The method based on FRFs performs the best in terms of the correlation between numerical and measured FRFs and also obtains the best compromise between the accuracy of eigenfrequencies, mode shapes and FRFs. After updating using eigenfrequencies the most accurate eigenfrequencies were obtained when one considers all modes. Although the MAC and FRAC values can be improved slightly with the method based on mode shapes, bigger deviation of eigenfrequencies was caused as a result. Therefore unless one is very interested in the accuracy of eigenfrequencies, the model updating method using FRFs should be given priority. Further work is needed to investigate the performance of these three model updating methods on more complex und non-homogeneous structures and the physical phenomena that affects the efficiency of different model updating methods on different structures.

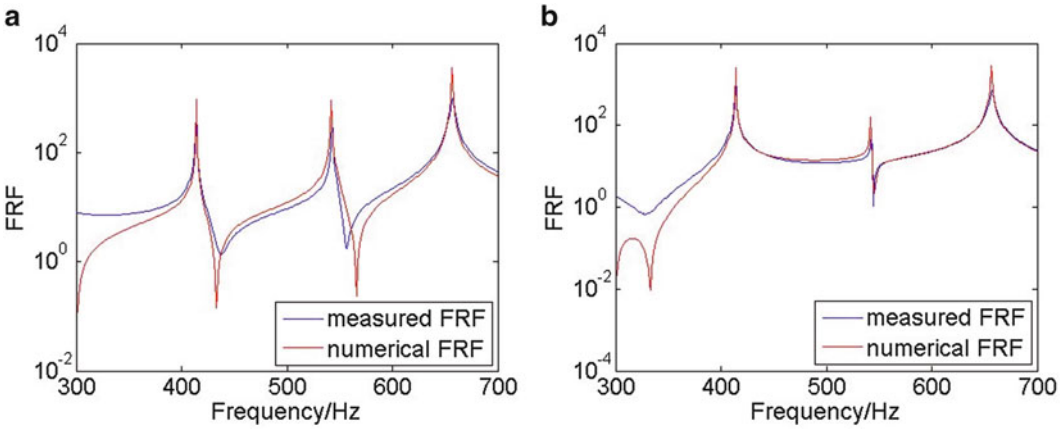

Fig. 44.8 FRFs of point 3 and 6 after updating using FRFs. (**a**) Updated FRFs of point 3 with FRFs. (**b**) Updated FRFs of point 6 with FRFs

References

1. Friswell, M.I., Mottershead, J.E.: Finite Element Model Updating in Structural Dynamics. Springer Science & Business Media (1995)
2. Visser, W.J.: Updating structural dynamics models using frequency response data. University of London (1992)
3. Lin, R.M., Ewins, D.J.: Model updating using FRF data. In: Proceedings of the 15th International Seminar on Modal Analysis, Society for Experimental Mechanics (1990)
4. Rad, S.Z.: Methods for updating numerical models in structural dynamics. University of London (1997)
5. Gross, J., Oberhardt T.: Model updating of the Ampair wind turbine substructures. In: Proceedings of IMAC XXXII Conference, Orlando (2014)
6. Allemang, R.J.: The modal assurance criterion (MAC): twenty years of use and abuse. Sound and Vibration Magazine. **37**(8), 14–23 (2003)
7. Silva, T.A.N., Maia, N.M.M., Barbosa, J.I.: A model updating technique based on FRFs for damped structures. In: Proceedings of International Conference on Noise and Vibration Engineering (ISMA2012)/International Conference on Uncertainty in Structural Dynamics (USD2012), pp. 2213–2226, Leuven (2012)
8. Heylen, W., Lammens, S.: FRAC: a consistent way of comparing frequency response functions. In: Friswell, M.I., Mottershead, J.E. (eds.) Proceedings of the International Conference on Identification in Engineering Systems, pp. 48–57, Swansea, UK (1996)
9. Gill, P.E., et al.: Procedures for optimization problems with a mixture of bounds and general linear constraints. ACM Trans. Math. Softw. **10**, 282–298 (1984)
10. Substructure.engr.wisc.edu.: Dynamic Substructuring Wiki - Dynamic Substructuring Focus Group Wiki. Retrieved from http://substructure.engr.wisc.edu/substwiki/index.php/Main_Page (2015)

Chapter 45
Experimental Coupling and Decoupling of Engineering Structures Using Frequency-Based Substructuring

S. Manzato, C. Napoli,, G. Coppotelli, A. Fregolent, W. D'Ambrogio, and B. Peeters

Abstract In many engineering application there are many instances in which it is convenient to be able to consider a complex engineering structure as an assembly of simpler components or substructures. Similarly, there exist applications in which, for model validation purposes, it might be important to identify the dynamic behavior of the structural subsystem starting from the known dynamic behavior of the coupled system and from information about the remaining part of the structural system. However, if the theoretical framework for Frequency Based Substructuring (FBS) has been widely studied and demonstrated, measurement errors, ill-conditioning and difficulties in measuring all required degrees of freedom—in particular at the connections—lead to poor results when trying to apply these techniques to real structures. This paper will focus on the analysis of the results obtained by applying Experimental Frequency-Based Substructuring on a test structure, both for coupling and decoupling applications and under different boundary conditions. The paper will particularly discuss the effects of typical measurement errors on the final results and potential techniques that could be used to improve the robustness and applicability of this methodology.

Keywords Substructuring • FBS • Coupling • Decoupling • Experimental validation

45.1 Introduction

Dynamic Substructuring (DS) is a topic deeply developed from the theoretical point of view in the last 40 years. It is based on the componentwise analysis of a structural system, and in particular:

- too large or complex systems can be partitioned, in order to avoid a high computational time or a big effort from the numerical/experimental point of view;
- DS allows the identification of local dynamic behaviors and the representation of a simplified dynamics;
- parts modeled in a different way (discretized or analytical) can be combined, performing an hybrid analysis; components can be developed by different project teams, with the possibility to combine them as final step.

Dynamic Substructuring can be divided in two branches: coupling and decoupling. Coupling is applied when one wants to know the characteristics of a structure formed by simpler components (called substructures or subsystems), while decoupling has to deal with the inverse problem: to know more about a substructure, starting from the investigation of the assembled structure and of the "residual" part.

Whilst analytical substructuring forms the basis of the Finite Element Method and related techniques (i.e. the Craig-Bampton method), Experimental/Analytical Substructuring is less widely applied, as it requires that at least one of the substructures is experimentally identified. As the method generally requires the inversion of a matrix, ill-conditioning,

S. Manzato (✉) • B. Peeters
Siemens Industry Software NV, Interleuvenlaan 68, 3001 Leuven, Belgium
e-mail: simone.manzato@lmsintl.com

C. Napoli
Siemens Industry Software NV, Interleuvenlaan 68, 3001 Leuven, Belgium

Dipartimento di Ingegneria Meccanica e Aerospaziale, Università degli Studi di Roma "La Sapienza", Via Eudossiana 18, 00184 Rome, Italy

G. Coppotelli • A. Fregolent
Dipartimento di Ingegneria Meccanica e Aerospaziale, Università degli Studi di Roma "La Sapienza", Via Eudossiana 18, 00184 Rome, Italy

W. D'Ambrogio
Università degli Studi dell'Aquila, DIIE, Via G. Gronchi 18, I 67100 L'Aquila, Italy

© The Society for Experimental Mechanics, Inc. 2016

M. Allen et al. (eds.), *Dynamics of Coupled Structures, Volume 4*, Conference Proceedings of the Society for Experimental Mechanics Series, DOI 10.1007/978-3-319-29763-7_45

measurement errors and difficulties in measuring all required degrees of freedom have limited the application of the method to real industrial cases. These applications range from the possibility of combining experimental and numerical models of substructures to predict the coupled dynamic response [1] to the possibility of subtracting the dynamic behavior of a fixture when a component is connected to it to facilitate its testing [2]. Moreover, wind turbine manufactures can be interested of predicting the effect of installing a new gearbox on a wind turbine. As gearboxes are usually tested by manufacturers on dedicated test-rig, if they can be first decoupled from the rig and then coupled on the turbine (either numerically or experimentally modeled), possible coupling problems could be identified before the turbines are installed [3].

This list is not at all comprehensive of all possible practical applications of analytical/experimental dynamic substructuring, but gives only an idea of the range of possible applications and problems that could be solved. Recently, de Klerk et al. [4] have summarized 50 years of dynamic substructuring and classified the different methods, providing a general framework and outlining the relations between them. In [3–6], current bottlenecks in the application of dynamic substructuring to experimental data are discussed and possible solutions that could improve the quality of the results proposed.

This paper will focus on Frequency-Based Substructuring (FBS) methods, aiming at a validation of substructuring procedures from the experimental point of view, carrying out a test activity and suggesting the field of applicability of the aforementioned procedures. In Sect. 45.2, some of these methods are summarized, both for coupling and decoupling of substructures. Some numerical techniques to improve the quality of the matrix inversion will also be presented. In Sect. 45.3, these techniques will be applied on real FRFs acquired on an experimental structure. The results will be reviewed and analyzed with the use of some mathematical tools. Some practical guidelines and lessons learned will be then summarized to design future experimental campaigns.

45.2 Theoretical Background

The theoretical foundations of Frequency Based Substructuring are widely presented in literature and the methods implemented and used in this paper can be found in [7] for the substructure coupling problem and in [3, 4, 8] for the decoupling. Only the most important equations will be here reported for clarity.

45.2.1 Frequency-Based Substructuring Using the Dual Formulation

As shown in Fig. 45.1, let's consider three different models: models A and B, which represent two substructures or components, and model AB, which is the assembled structures obtained by connecting A and B at some degrees of freedom. The equation of motion of a general substructure is expressed in the physical domain as:

$$M^{(s)}\ddot{u} + C^{(s)}\dot{u} + K^{(s)}u = f^{(s)} + g^{(s)} \tag{45.1}$$

Where M, C and K are respectively the mass, damping and stiffness matrix, u are the degrees of freedom and f and g the external and internal forces applied at each degree of freedom. Similarly, the assembled behavior of n substructures that are to be coupled can be rewritten in a block-diagonal format as:

$$M\ddot{u} + C\dot{u} + Ku = f + g \tag{45.2}$$

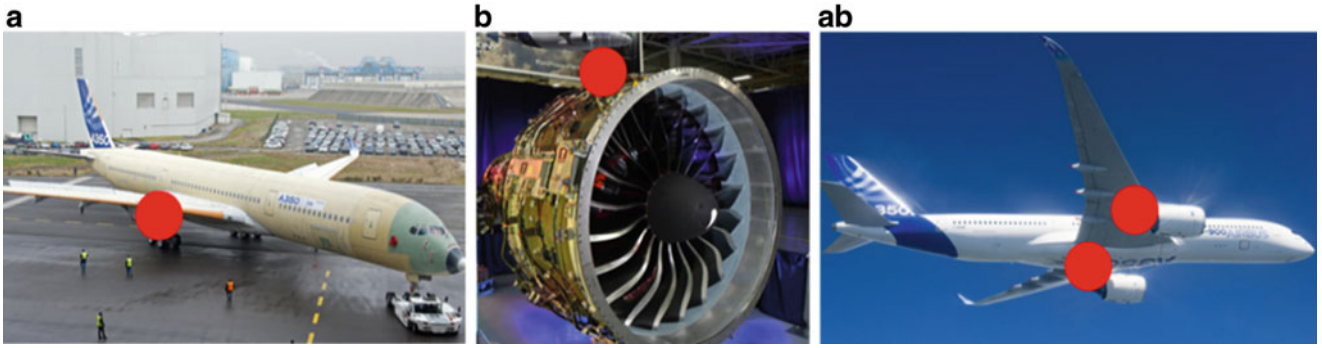

Fig. 45.1 Example of subsystem A and B combined into the coupled structure AB. The *red dots* indicate the connection points

Moreover, the degrees of freedom (dof) u of the two substructures A and B to be assembled can be conveniently order as:

- ua: internal dofs to substructure A;
- uc: dofs connecting the two substructures;
- ub: internal dofs to substructure B.

The compatibility condition can be expressed as:

$$Bu = 0 \tag{45.3}$$

where the B matrix operates on the interface dofs and is a signed Boolean matrix if the interface dofs are matching. Similarly, the equilibrium condition is expressed as:

$$L^T g = 0 \tag{45.4}$$

where the matrix L is the Boolean matrix localizing the interface dofs of the substructures in the global dual set of dofs. By using a dual assembly formulation, the full set of global dofs is retained, so that all interface dofs uc are present as many times as there are subdomains connected on the corresponding node. The dual assembled system is thus obtained by satisfied a priori the interface equilibrium by choosing the interface forces in the form:

$$g = -B^T \lambda \tag{45.5}$$

where λ are Lagrange multipliers corresponding physically to the interface forces intensities. Including the condition in Eq. (45.5), the system of equations built using Eqs. (45.2), (45.3) and (45.4) and expressing the coupled behavior of two or more substructures can be expressed in the dual formulation as:

$$\begin{cases} M\ddot{u} + C\dot{u} + Ku + B^T\lambda = f \\ Bu = 0 \end{cases} \tag{45.6}$$

The dual formulation for the behavior of coupled substructures expressed in Eq. (45.6) in the physical domain can be written in the frequency domain as:

$$\begin{bmatrix} Z & B^T \\ B & 0 \end{bmatrix} \begin{bmatrix} u \\ \lambda \end{bmatrix} = \begin{bmatrix} f \\ 0 \end{bmatrix} \tag{45.7}$$

where Z is now the block-diagonal matrix containing the dynamic stiffness matrices of the substructures. In experimental structural dynamics, one usually computes Frequency Response Functions H by applying a force and measuring accelerations at specific points of the structures and dynamic stiffness information (which is the inverse of the receptance FRFs) is not readily available. Thus, eliminating the Lagrange multipliers in the system of equation (45.7), one finds the so-called dual interface problem in the frequency domain, suitable for the coupling of accelerance matrices H(ω) obtained with experimental data:

$$u = Hf - HB^T\left(BHB^T\right)^{-1}BHf = \overline{H}f \tag{45.8}$$

By taking advantage of the distinction between internal and connecting dofs, Eq. (45.8) can be rewritten in a more extended and clear form to directly compute the accelerance matrix of the coupled structure AB from the measured accelerance matrices of the two substructures A and B as:

$$\overline{H} = H^{AB} = \begin{bmatrix} H^{AB}_{aa} & H^{AB}_{ac} & H^{AB}_{ab} \\ H^{AB}_{ca} & H^{AB}_{cc} & H^{AB}_{cb} \\ H^{AB}_{ba} & H^{AB}_{bc} & H^{AB}_{bb} \end{bmatrix} = \begin{bmatrix} H^{A}_{aa} & H^{A}_{ac} & 0 \\ H^{A}_{ca} & H^{A}_{cc} & 0 \\ 0 & 0 & H^{B}_{bb} \end{bmatrix} - \begin{bmatrix} H^{A}_{ac} \\ H^{A}_{cc} \\ -H^{B}_{bc} \end{bmatrix} \left[H^{A}_{cc} + H^{B}_{cc}\right]^{-1} \begin{bmatrix} H^{A}_{ac} \\ H^{A}_{cc} \\ -H^{B}_{bc} \end{bmatrix}^T \tag{45.9}$$

With reference to Fig. 45.1, Eq. (45.9) allows to calculate the dynamic response of the coupled system AB from the known dynamic response of structure A and B. Substructure decoupling (that is deriving the response of subsystem B from the known AB and A systems) is derived as a particular case of Eq. (45.9), where now substructure A is subtracted from the

coupled system AB. The standard interface decoupling method, where equilibrium and compatibility conditions are solely applied to the connecting dofs, can be written as:

$$H^B_{CC} = \begin{bmatrix} H^B_{aa} & H^B_{ac} & H^B_{ab} \\ H^B_{ca} & H^B_{cc} & H^B_{cb} \\ H^B_{ba} & H^B_{bc} & H^B_{bb} \end{bmatrix} = \begin{bmatrix} H^{AB}_{aa} & H^{AB}_{ac} & H^{AB}_{ab} \\ H^{AB}_{ca} & H^{AB}_{cc} & H^{AB}_{cb} \\ H^{AB}_{ba} & H^{AB}_{bc} & H^{AB}_{bb} \end{bmatrix} - \begin{bmatrix} H^{AB}_{ac} \\ H^{AB}_{cc} \\ H^{AB}_{bc} \end{bmatrix} \left[H^{AB}_{cc} - H^{A}_{cc} \right]^{-1} \begin{bmatrix} H^{AB}_{ac} \\ H^{AB}_{cc} \\ H^{AB}_{bc} \end{bmatrix}^T \tag{45.10}$$

Note in particular that by explicitly writing down Eq. (45.10), the first column and row of the resulting dynamic matrix of substructure B correspond to the internal dofs of subsystem A when additional interface forces are applied and can be neglected for simplicity as they are usually not of interest.

45.2.2 Numerical Improvements of the General Methods

The solution of Eqs. (45.9) and (45.10) requires that all connection dofs FRFs are accessible and measurable and that the matrix inversion problem required to solve the method is well conditioned. Whilst these problems can be neglected when dealing with analytical or numerical FRFs, they can create serious error or even completely hamper the dynamic substructuring results when one deals with experimentally measured FRFs. An overview of these problems and possible solutions proposed by different research groups can be found in [3–6, 9]. One of the most important problems in experimental substructuring is that the rotational dofs at the connection point are seldom measurable in an accurate fashion, thus not all the required information can be measured. Typically, two solutions were identified in literature to solve this problem: estimating these rotational FRFs by modal expansion techniques [5] or by applying the so-called Equivalent Multi-Point connection method [10]. These solutions are not applied here and will be the objective of future investigations. A further solution, only valid for decoupling problems, is to substitute unmeasured rotational dofs at connection points with internal dofs of the residual substructure A [11], as in the subsequent Eqs. (45.11) and (45.12). The second problem is purely numerical and is related to the inversion of the matrix. This is related to the ill-conditioning of the problem and the generally high condition number of the FRF matrix, in particular in correspondence of resonance, causes the inverse solution to be very sensitive even to small perturbations. As measured FRFs will always contain some amount of noise, the Moore-Penrose pseudoinverse based on the singular value decomposition is commonly used instead of the standard inverse.

Over the years, several methods have been proposed to improve the quality of experimental substructuring by imposing the equilibrium and compatibility conditions (Eqs. (45.3) and (45.4)) not only to the connection dofs but also to additional internal dofs of the residual substructure A. Using the standard interface approach for decoupling, the connection forces between the substructures are determined only using the minimum information needed, that is the responses on the interface dofs. In [3, 8, 9] it is shown that by using this relaxed interface approach is possible to exploit information coming from other points of the structure, thus solving an overdetermined problem when inverting the matrix. This will then require the use of the Moore-Penrose pseudoinverse (as the matrix is not square anymore) with a tolerance on the lower singular value to be included in the inversion. The smaller singular values in fact usually correspond to large term in the inverse and can lead to numerical errors in the solution. Of course the selection of the lower singular value to be included is based on a compromise choice between condition number and accuracy of the estimation and depends on the specific application. Some more details on the methods, as well as on an alternative regularization, are given in [12].

A first example of these relaxed interfaces is the so-called Extended Interface, where additional internal dofs of the residual structure A are considered in the compatibility and equilibrium conditions:

$$H^B_{AC,AC} = \begin{bmatrix} H^{AB}_{aa} & H^{AB}_{ac} & H^{AB}_{ab} \\ H^{AB}_{ca} & H^{AB}_{cc} & H^{AB}_{cb} \\ H^{AB}_{ba} & H^{AB}_{bc} & H^{AB}_{bb} \end{bmatrix} - \begin{bmatrix} H^{AB}_{aa} & H^{AB}_{ac} \\ H^{AB}_{ca} & H^{AB}_{cc} \\ H^{AB}_{ba} & H^{AB}_{bc} \end{bmatrix} \left[\begin{bmatrix} H^{AB}_{aa} & H^{AB}_{ac} \\ H^{AB}_{ca} & H^{AB}_{cc} \end{bmatrix} - \begin{bmatrix} H^{A}_{aa} & H^{A}_{ac} \\ H^{A}_{ca} & H^{A}_{cc} \end{bmatrix} \right]^{+} \begin{bmatrix} H^{AB}_{aa} & H^{AB}_{ac} \\ H^{AB}_{ca} & H^{AB}_{cc} \\ H^{AB}_{ba} & H^{AB}_{bc} \end{bmatrix}^T \tag{45.11}$$

where the symbol + denotes the pseudo-inverse. Both the Standard and Extended interface method are collocated, as compatibility and equilibrium conditions are enforced on the same points. This condition is however not strictly required and compatibility and equilibrium can be enforced on different dofs in a so-called non-collocated approach.

A method can also be derived by enforcing the equilibrium and compatibility only on internal dofs of subsystem A:

$$H^B_{A,A} = \begin{bmatrix} H^{AB}_{aa} & H^{AB}_{ac} & H^{AB}_{ab} \\ H^{AB}_{ca} & H^{AB}_{cc} & H^{AB}_{cb} \\ H^{AB}_{ba} & H^{AB}_{bc} & H^{AB}_{bb} \end{bmatrix} - \begin{bmatrix} H^{AB}_{aa} \\ H^{AB}_{cc} \\ H^{AB}_{ba} \end{bmatrix} \left[H^{AB}_{aa} - H^{A}_{aa} \right]^{+} \begin{bmatrix} H^{AB}_{aa} \\ H^{AB}_{cc} \\ H^{AB}_{ba} \end{bmatrix}^{T} \tag{45.12}$$

The advantage of this method is that it neglects the connection FRFs in the inversion problem, thus improving the robustness of the inversion. These FRFs, as can be observed, will still need to be measured to allow the decoupling.

45.3 Experimental Data Analysis

In literature [5], the sensitivity of frequency based substructuring to small errors (e.g. noise, spykes, etc.) on the measured FRFs is widely reported. In a previous publication from the authors [13] this trend was also confirmed both by analyzing numerical and experimental results and the requirement for extremely high quality measurements was stressed. In this paper, these findings were applied on the structure shown in Fig. 45.2 with the objective of demonstrating that, with enough care in the acquisition of FRFs, FBS can be applied and acceptable results can be obtained. Some numerical and experimental previous works on the same structure are discussed in [11, 14]; with this paper, the objective is to expand the results using different methods and boundaries conditions.

The analyzed aluminum structure is composed of:

- A beam, considered as substructure B (the long horizontal beam on top of Fig. 45.2);
- A beam with two short horizontal arms near the connection point (45.11), considered as substructure A;
- Screws and washers at the connection area to simulate a rigid interface.

The geometrical dimensions are reported in Table 45.1. The applied technique is impact testing: to this end, roving hammer is used, and both clamped and free-free boundary conditions will be assumed for the assembled structure AB and for substructure A, while substructure B will be always tested in free-free conditions to have reference values after decoupling. FRFs are measured in the frequency range 0–2048 Hz with a spectral resolution of 0.5 Hz. The beam B is suspended to a metal frame in the horizontal position, using some soft rubber bands to approximate free-free boundary conditions (Fig. 45.3). Four mono-directional accelerometers are placed at the connection point #11 (Z direction) and at points #13, #16 and #20 (Z direction), as in Fig. 45.2. As regards the assembled structure AB, points #3, #6, #9, #10, #11,

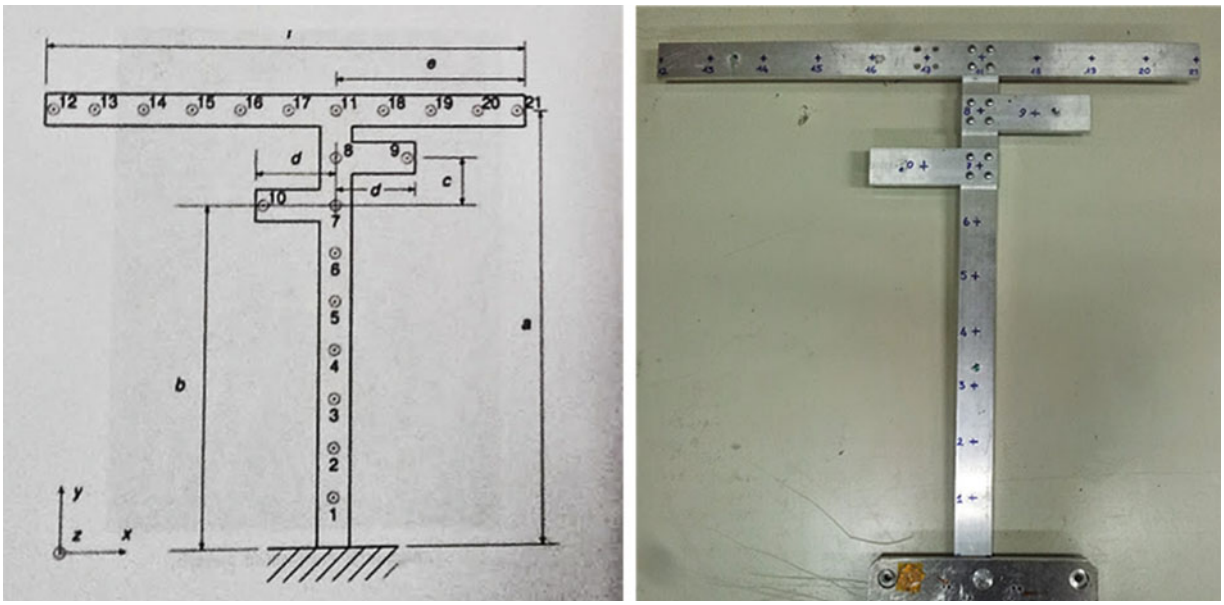

Fig. 45.2 The selected test structure (*left*) with its dimensions (*right*)

Table 45.1 Geometrical dimension of the tested structure

Dimensions	[mm]
a	540
b	420
c	60
d	100
e	240
l	600

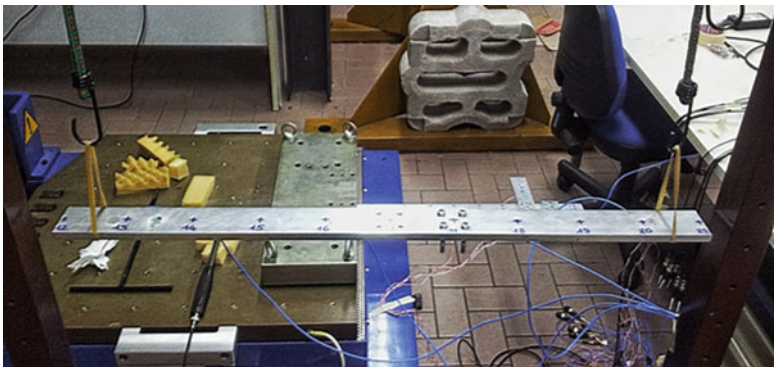

Fig. 45.3 Substructure B suspended on soft bungees

#13, #16 and #20 are chosen, hence points #3, #6, #9, #10 and #11 are considered for substructure A. It can also be noticed that:

- it is possible to hit on the upper part of the item and to measure exactly on the same location on the lower part, also at the connection;
- the material has no discontinuities or superficial defects;
- the surface to hit is flat.

45.3.1 Measured FRFs Analysis

During the acquisition of the FRFs, particular attention was put in:

- quality of the driving point FRF at each impact location (impact direction and location, similar input spectrum).
- Reciprocity.

Both these properties are at the basis of each experimental analysis with FRFs, but, as clearly discussed in literature [5], they become extremely critical in Frequency-Based Substructuring applications and have a very high sensitivity on the results. Figure 45.4 compare the reciprocal FRFs for the assembled structure between a point on substructure A and a point on substructure B for both boundary conditions. The displayed FRFs cover the 0–1300 Hz band, as at higher frequencies the reciprocity is relatively poor. In this range, the FRFs nicely overlap at resonances, but they differ at the anti-resonances and in particular in the band from 400 to 600 Hz. Also, the differences above 600 Hz are mostly related to noise in the measurements. Figure 45.5 on the other hand tries to quantify the quality of the driving points FRFs: beside any consideration on noise, for a driving point FRF the phase is limited between 0° and 180° or, equivalently, the imaginary part should be either always positive or negative. In this case, this assumption generally holds for the majority of the measured driving points FRFs below 1 kHz. It can however be observed that also at lower frequencies some phase values are negative and they will negatively influence the quality of the measured model.

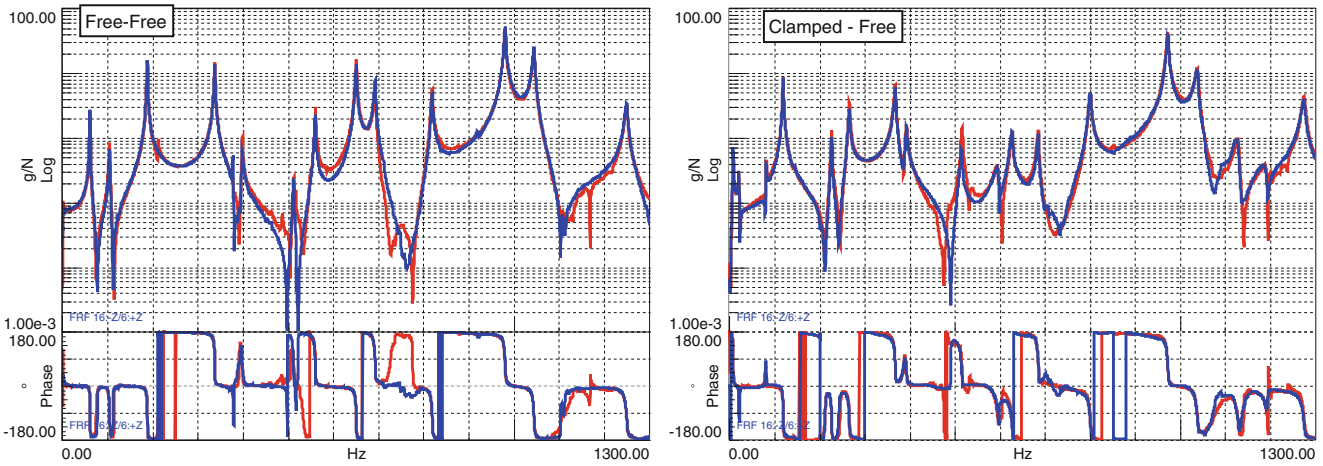

Fig. 45.4 Reciprocity check for both tested boundary conditions

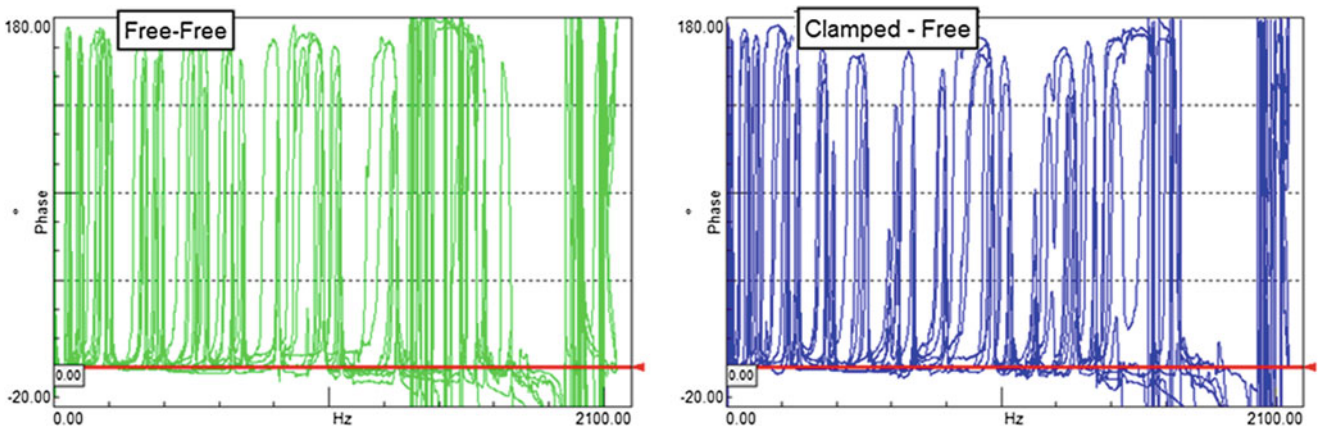

Fig. 45.5 FRF quality analysis for all driving point FRFs

45.3.2 Decoupling Results

In general, when performing "standard" FBS according to Eq. (45.10), all connection DOFs should be measured. There are however many and clear difficulties in measuring these FRFs and, as already discussed in Sect. 45.2.2, several decoupling methods have been proposed to compensate for the lack of information. Moreover, only the vertical dynamics of the structure is considered.

As the rotational DOFs at the connection are not measured, all method relying only on connection information (CC, Eq. (45.10) or AC-C will not be discussed here). The analysis will then focus on the results obtained using a combination of connection and internal DOFs for both equilibrium and compatibility (AC-AC, Eq. (45.11)) or only internal (45.12). Figure 45.6 shows the results obtained using the measured FRFs, with the assembled and residual substructures in clamped-free as well as free-free boundary condition. In general, it is observed that free-free boundary conditions give better and less noisy results. In both conditions and for both analyzed decoupling techniques, the first peaks are correctly captured. At the third peak around 620 Hz, the FRF becomes noisier and the peak is slightly shifted at higher frequencies. The estimated FRFs start to significantly diverge from the reference one at frequencies above 1000 Hz (corresponding to the dominant peak at the center of the plots). Above, the results have almost no correlation with the behavior of the residual structure. This is also in line with the analysis in Sect. 45.3.1 where poor reciprocity and low quality driving point FRFs were discussed at the higher frequencies.

A way to actually assess the results of decoupling is to verify the usability of the calculated FRFs. To do so, a possibility is to use these FRFs for modal identification and then compare the identified modal model with the one obtained by processing the measured FRFs on the beam. To fit a modal model on FRFs, some strict assumptions need to be satisfied which are related to the nature of the model. The noise in the decoupled FRFs is mainly related to the high condition number in the inversion process, which then propagate into the results. As the inversion is performed per frequency line, the objective here

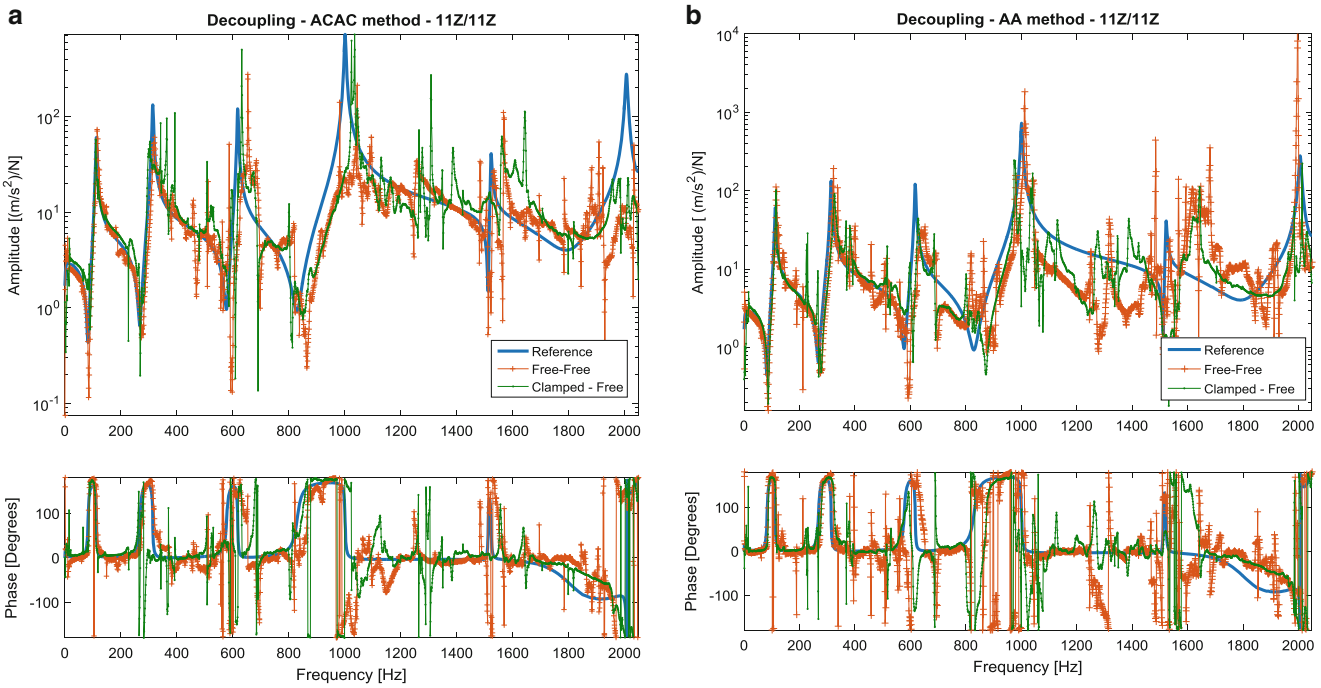

Fig. 45.6 Decoupling results at the connection DOF using the measured FRFs directly for both Free-Free and Clamped-Free boundary conditions. (**a**) ACAC method (**b**) AA method

Table 45.2 Modal Parameter of Substructure B: reference model vs. decoupled FRFs

Reference		Free free ACAC		Clamp-free ACAC		Free free AA		Clamp-free AA	
Freq.	Damp.	Freq.	Damp.	Freq.	Damp.	Freq.	Damp.	Freq.	Damp.
112.2	0.27	115.8	0.1	110.1	0.11	116.5	0.05	114.7	0.09
313.7	0.06	319.4	0.1	300.3	0.03	321.9	0.02	326.1	0.08
617.2	0.02	648.8	0.02	631.7	0	639.5	0.05	517	0.04
942.4	0.35	–	–	–	–	–	–	–	–
1000.8	0.08	1047	0.04	1042.5	0	1012.2	0	997.6	0.04

is to show that still some consistent and useful information can be derived from decoupling by means of modal analysis. In this process, the PolyMAX identification algorithm will be applied to the whole $[4 \times 4]$ FRF matrix of the residual structure. The identified modal parameters are shown in Table 45.2. In general, there is a frequency shift in the decoupled FRFs, which can be related to some measurement error or mass loading (e.g. different suspension or cabling in the different setups). However, despite the noise in the estimated FRFs, the dominant modes can still be identified and the damping is comparable to the original one. The mode at 942.4 Hz which is only identified using the reference FRFs is the beam torsion, that is lowly excited in the implemented setup.

Figure 45.7 shows the results of applying MAC analysis to the modes obtained from decoupling FRFs using the ACAC method for both considered boundary conditions. In general, the first three bending modes are captured correctly. The 5th mode, corresponding to the 4th bending, is also generally identified with a MAC above 70 %. The significant off-diagonal high correlation is related to the limited number of sensors used (only 4) to characterize each mode, and could also be observed in the reference data set autoMAC. The MAC analysis on the AA decoupled FRFs slightly less good, identifying the same modes but with less correlation to the original data.

A possible improvement of the proposed method is to use the AC-AC decoupling method and optimize the number and locations of internal points of A used. Assuming this is a planar problem, the connection DOFs that need to be considered is 3, thus, as me measure only the acceleration in the Z direction, a minimum of 2 additional points should be used in the problem. However, in such application over-determination is generally used to improve the accuracy of the matrix inversion. The FRFs from free-free boundary conditions are here analyzed and, as internal dofs on substructure A, the following combinations are analyzed:

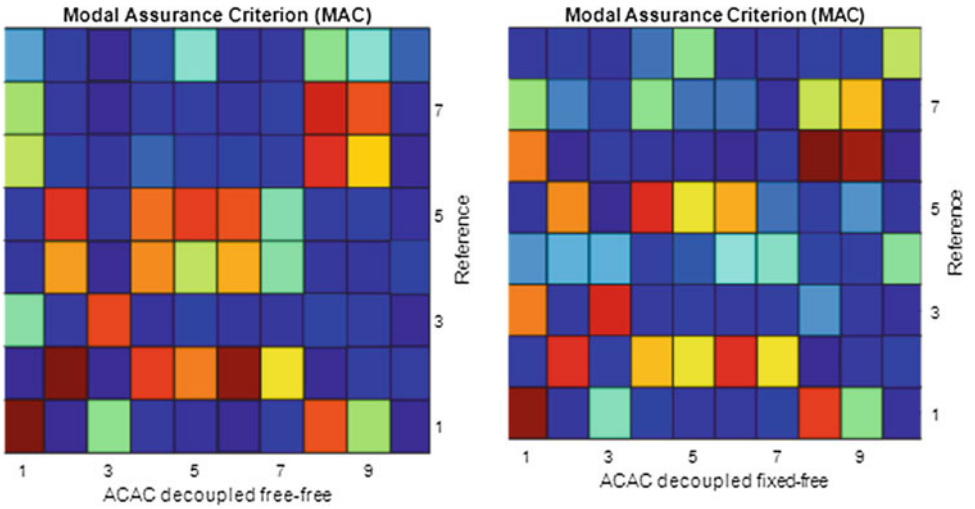

Fig. 45.7 MAC analysis between reference modes and those obtained by applying experimental modal analysis on decoupled FRFs

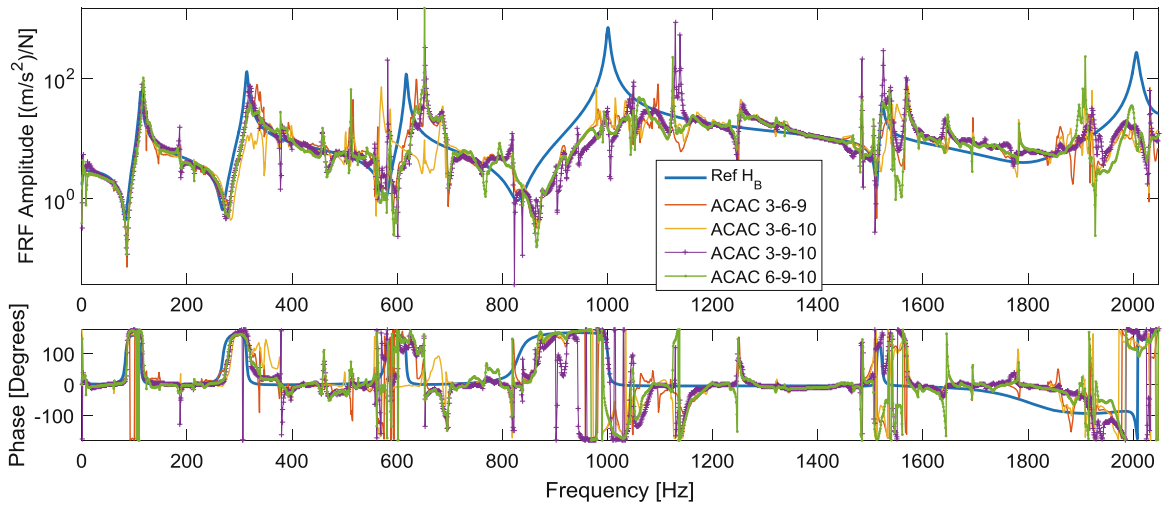

Fig. 45.8 AC-AC Decoupling results when using only a subset of internal points on substructure A

- Points 3, 6, 9;
- Points 3,6,10;
- Points 3,9,10;
- Points 6,9,10.

As can be observed in Fig. 45.8, the best results for the connection FRF on point B are obtained with the subsets 6-9-10, while for the others the results are comparable if the whole frequency range is taken into account. These results are also confirmed when applying Polymax on the decoupled FRFs. While the case 3-6-10 is not considered as it gives the worst FRFs, the others give generally comparable results Table 45.3, but the best correlation for the mode shapes is obtained with subset 6-9-10 (Fig. 45.9). In general, the 3rd mode is the most difficult to identify. Using the whole set of points or just a limited one doesn't significantly improve the quality of the results, but it shows how the measurement points can be optimally chosen without influencing the quality of the decoupling. On the other hand, by defining adequate pre-test procedures based on numerical models, it is expected that not only the effort can be minimized but also the quality of the results increased.

Table 45.3 Natural frequencies and damping for different combination of internal points on A for ACAC method

6-9-10		3-6-9		3-9-10	
Freq.	Damp.	Freq.	Damp.	Freq.	Damp.
117.4	0.07	116.1	0.13	115.4	0.1
322.5	0.15	327.1	0.07	322.5	0.1
652.0	0	637.0	0.03	649.3	0
–	–	–	–	–	–
1047.1	0	1047.3	0	1017.4	0.09

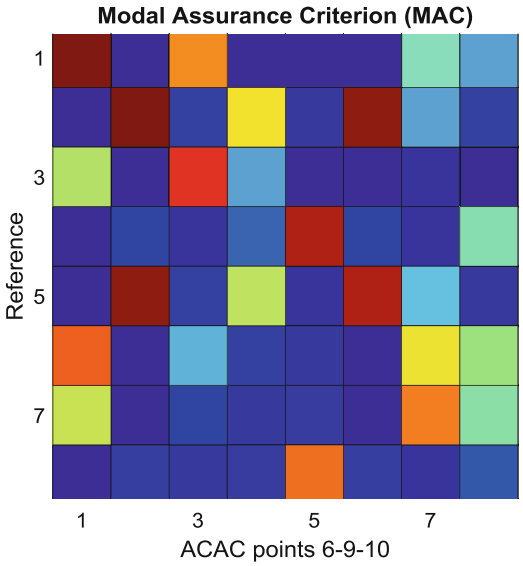

Fig. 45.9 MAC matrix between references modes and identified modes from ACAC decoupling using internal points of A 6-9-10

45.3.3 Improved FRFs for Decoupling

As two of the main causes that negatively affect the result of decoupling are noise in the measured data and limited reciprocity in the measured FRFs, some methods to improve these FRFs will be here discussed. In particular, three solutions will be here investigated:

- Reduce noise in the FRFs by using a synthesized model obtained from modal fitting with standard Polymax;
- Impose reciprocity by copying the FRFs on the lower diagonal on the upper diagonal and viceversa;
- Use the new modal analysis algorithm proposed in [15, 16] imposing FRF reciprocity as an additional constraint on the sought modal model.

45.3.3.1 Decoupling Using Synthesized Input FRFs

The first method to improve the results of decoupling is based on the use of synthesized FRFs to reduce noise and condition number in the inversion. Only the case with free-free boundary conditions is here considered. First, Polymax was applied on the full measured FRF matrices of the assembly and residual structure A. Since the roving hammer approach was used to measure the FRFs, small inconsistencies may appear, resulting is a not very clear stabilization diagram. However, by processing the full FRF matrix, these inconsistencies can be removed imposing the same pole on all curves. The synthesized model will not be the best achievable and mode shapes may also be affected, but on the other hand, for substructuring purpose, noise reduction and consistency may play a much stronger role. The synthesized FRFs were then used for decoupling and the ACAC method was applied.

The results are shown in Fig. 45.10. The decoupled FRFs are now less noisier and with less numerical spikes, but on the other hand they start diverging from the true behavior already at 600 Hz (3rd bending). However, in terms of MAC between the two mode sets, except the torsion mode, relatively good correlation can be found up to the 6th mode (5th bending). On the other hand, the frequency difference is now higher than the results listed in Table 45.2.

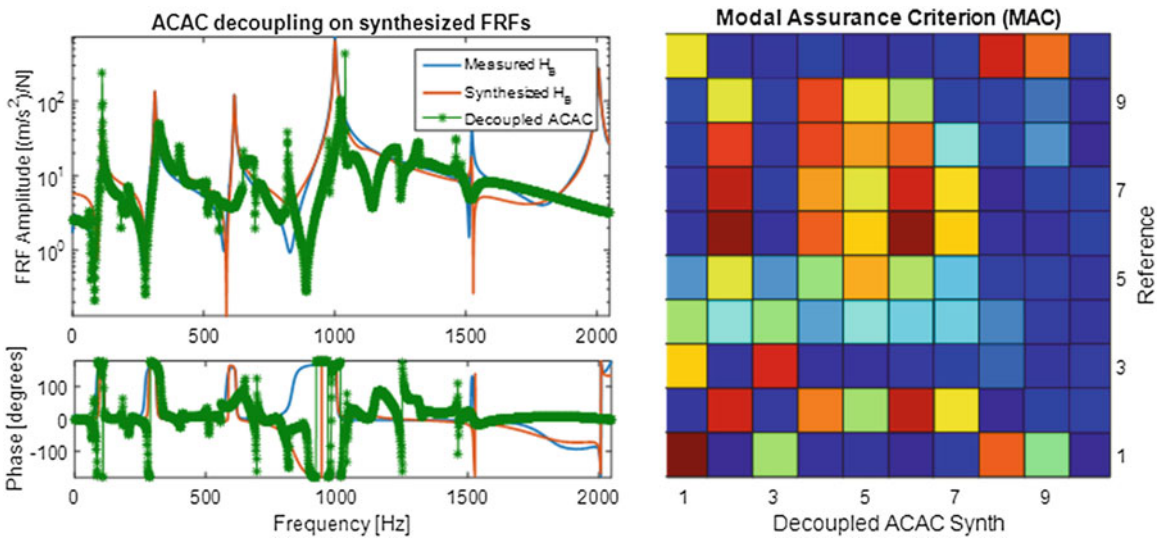

Fig. 45.10 Decoupling results using synthesized input FRFs. *Left*: Decoupled FRF. *Right*: MAC reference and decoupled modal models

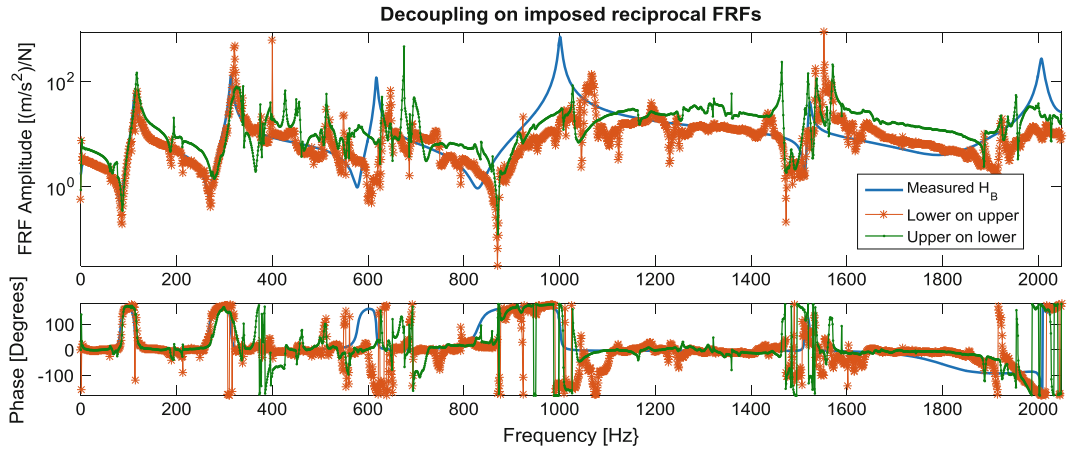

Fig. 45.11 Decoupling results making the input FRF matrix reciprocal

45.3.3.2 Decoupling Imposing Reciprocity on Input FRFs

Reciprocity of the FRFs matrix is a fundamental assumption in all structural dynamics applications. Although Polymax was applied in the previous paragraph to the complete FRFs matrix, the synthesized model doesn't lead to reciprocal synthesized FRFs. Although there is the possibility to make the synthesized FRFs matrix symmetric after the modal model has been calculated, this process will ignore the lower and upper residuals, that have also a strong effect on decoupling. As a first solution, to impose reciprocity, we will impose the element of the lower diagonal of the measured FRF matrix on the upper diagonal and viceversa. This will not solve all inconsistencies (the elements on the main diagonal are unchanged) but should lead to a more consistent model.

The results are shown in Fig. 45.11. The quality of the substructured FRFs are similar to those shown in Fig. 45.6 obtained by processing the raw FRFs. Imposing reciprocity by just changing the elements in the matrix is not improving the results and, moreover, applying modal analysis on these FRFs only gives good results for the first two modes. Fitting the FRFs with Polymax after imposing reciprocity doesn't help but on the contrary make the results worse.

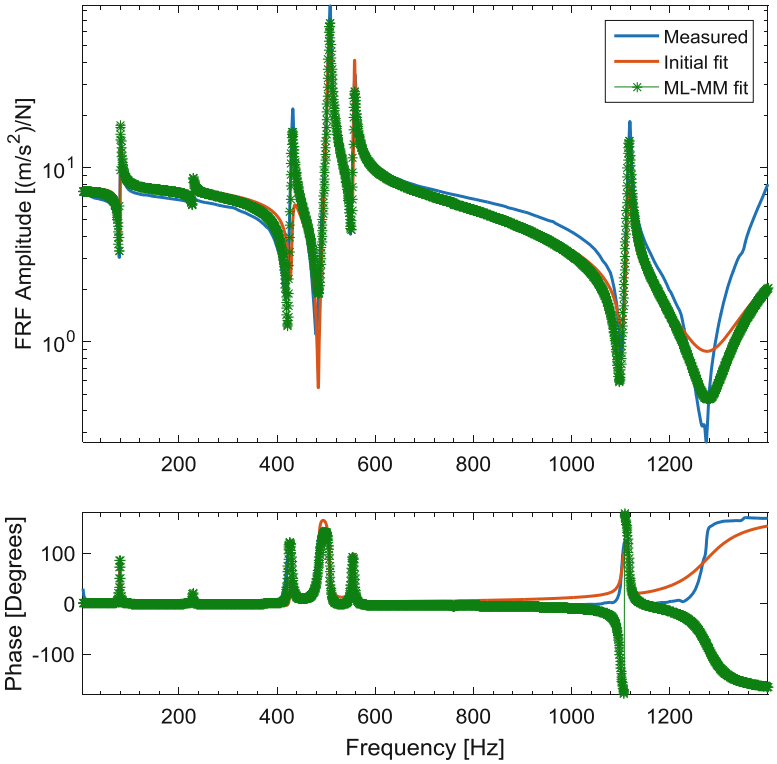

Fig. 45.12 Example of using ML-MM method with reciprocity constraint on one FRF of substructure A

45.3.3.3 Decoupling Imposing Synthesized FRFs with the ML-MM Method

The final method investigated in this paper to improve the quality of the decoupled FRFs is to combine the two previous methods (imposing reciprocity and using synthesized FRFs to reduce noise) by using the recently developed multivariable frequency-domain maximum likelihood estimator based on a modal model presented in [15] and further improved and validated in [16]. This method estimates the parameters of a modal model directly instead of identifying a rational fraction polynomial model. Polymax or other standard modal parameter estimation techniques are still used to derive an initial modal model, which the ML-MM method will then optimize to better fit the data. The method is particularly suited for noisy datasets, when the input data are inconsistent, modes are highly damped or the number of input is high. Particularly useful for this application is also the possibility to impose that the resulting modal model is reciprocal as a constraint in the optimization process.

First, the measured FRFs on the assembled structure AB and substructure A are processed using the ML-MM method imposing reciprocity constraints. Figure 45.12 shows the results of the method for one FRF on substructure A, comparing the measured FRF with the initial fit and with the ML-MM fit after the iterations on the modal model are performed. Although with standard Polymax the fit was sometimes better, it should be remembered that here the reciprocity of the modal model was imposed as a constraint and, for inconsistent data, this can results in a lower correlation with the measured data. Also, the analysis focused only on frequencies below 1400 Hz, as it was already observed that above decoupling didn't give satisfactory results.

The decoupling results are shown in Fig. 45.13. The FRFs are now much smoother in the whole frequency band, but significant deviations can be observed already as of 400 Hz. Polymax is then applied to the decoupled FRFs and the results are again compared with the reference one from the measured FRFs. The obtained results are shown in Fig. 45.14 and Table 45.4. In general, higher differences in the identified modal frequencies are observed, also compared with the results discussed in the previous sections. In terms of modes, except the first one, the other 4 correlate quite well with the original one. In conclusion, although the FRFs are cleaner and reciprocity is enforced in the model, the results are not improving as one might have expected.

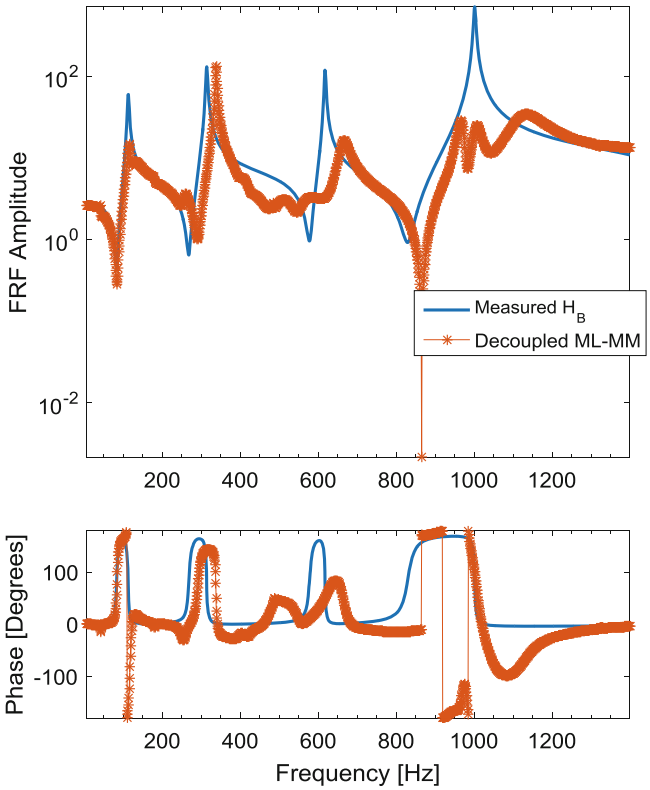

Fig. 45.13 Decoupling results using ML-MM processed FRFs

Fig. 45.14 MAC between reference modes and those from decoupling FRFs process with ML-MM

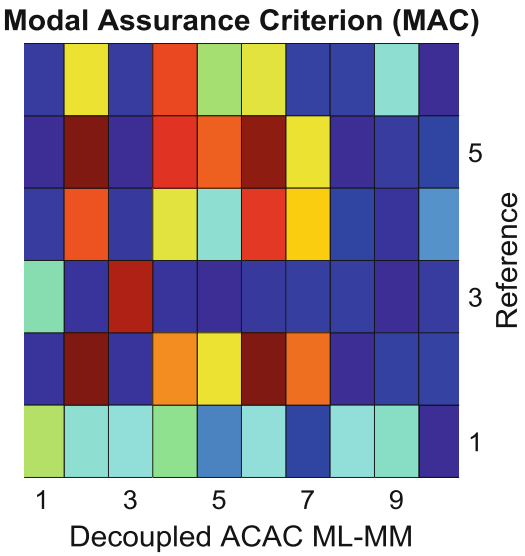

Table 45.4 Comparison between reference modal parameters and those from decoupling FRFs process with ML-MM

Reference		ACAC ML-MM	
Freq.	Damp.	Freq.	Damp.
112.2	0.27	122.8	1.1
313.7	0.06	337.1	0.06
617.2	0.02	663.5	0.19
942.4	0.35	952.9	0.17
1000.8	0.08	1006	0.11

45.4 Conclusions

The general rules described in literature to apply frequency based dynamic substructuring to experimental data always stress that the quality of the measured FRFs must be significantly higher than those typically used in the context of experimental modal analysis. In this paper, experimental data have been collected, keeping in mind these rules, on a relatively simple aluminum structure to verify the applicability of Frequency Based Substructuring and to test different techniques to try to improve the quality of the results. The analysis focused also on using different boundary conditions to see their influence on the results. First, the results of using standard extended interface methods were presented. Then, a sensitivity study on the internal DOFs of substructure A used to overdetermine the problem was performed, showing that an optimal point selection can improve the quality of the results by reducing the number redundant information. In this perspective, future activities will further investigate this topic to try to develop rules to optimally choose the measurement point to improve the quality of the results, possibly by making use of validated numerical models in a pre-test approach. In the last section of the paper, different methods were tested to improve the quality of decoupling by enforcing reciprocity on the measured FRFs and reducing noise. In all cases, a slight improvement compared to the original results is observed, but these methods are very sensitive to the processing parameters. Also, it should be stressed that FBS generally relies on the fact that by measuring FRFs all information on the structure are present at all frequencies lines; by applying these techniques, however, some of these information might be lost and the relation between the assembled structure and the substructures partially lost. In general, it can be concluded that for this application the quality of the measured data needs to be extremely higher than in other structural dynamic applications and that a-posteriori method have only limited effects on improving the quality of the results. However, despite the decoupled FRFs are often very noisy, modal analysis can still be applied to obtain a model of the decoupled target structure. Beside the investigation of a procedure for the selection of an optimal set of measurement points, future research will aim at investigating statistical method to exploit the sensitivity of frequency based substructuring to errors in the input data and thus deriving a “more probable” set of decoupled FRFs.

Acknowledgements This research was conducted in the frame of the project IWT 130936 ADVENT (Advanced Vibration Environmental Testing). The financial support of the IWT (Flemish Agency for Innovation by Science and Technology) is gratefully acknowledged.

References

1. Rohe, D.P., Allen, M.S.: Investigation of the effectiveness of using an experiment to validate experimental substructure models. Mech. Syst. Signal Process. **43**, 192–216 (2014)
2. Allen, M.S., Gindlin, H.M., Mayes, R.L.: Experimental modal substructuring to estimate fixed-base modes from a tests on a flexible fixture. J Sound Vib **330**, 4413–4428 (2011)
3. Peeters, P., Tamarozzi, T., Vanhollebeke, F., Desmet, W.: In: A robust approach for substructure decoupling. In: Proceedings of the International Seminar on Modal Analysis (ISMA), Leuven (2014)
4. De Klerk, D., Rixen, D., Voormeeren, S.N.: General framework for dynamic substructuring: history, review and classification of techniques. AIAA J. **46**(5), 1169–1181 (2008)
5. Nicgorski, D., Avitabile, P.: Experimental issues related to frequency response function measurements for frequency-based substructuring. Mech. Syst. Signal Process. **24**, 1324–1337 (2010)
6. Rixen, D.J.: How measurement inaccuracies induce spurious peaks in frequency based substructuring. In: Proceedings of the International Modal Analysis Conference (IMAC), Jacksonville (2010)
7. Jetmundsen, B., Biewala, R., Flannelly, W.: Generalized frequency domain substructure synthesis. J. Am. Helicopter Soc. **33**(1), 55–65 (1988)
8. Voormeeren, S.N., Rixen, D.J.: A dual approach to substructure decoupling techniques. In: Proceedings of the International Modal Analysis Conference (IMAC), Jacksonville (2010)
9. D’Ambrogio, W., Fregolent, A.: The role of interface DoFs in decoupling of substructures based on the dual domain decomposition. Mech. Syst. Signal Process. **24**(7), 2035–2048 (2010)
10. De Klerk, D., Rixen, D., Voormeeren, S.N., Pasteuning, F.: Solving the RDoF problem in experimental dynamic substructuring. In: Proceedings of the International Modal Analysis Conference (IMAC), Orlando (2008)
11. D’Ambrogio, W., Fregolent, A.: Ignoring rotational dofs in decoupling structures connected through flexotorsional joints. In: Dynamics of Coupled Structures. Conference Proceedings of the Society for Experimental Mechanics Series, vol. 4, pp. 57–69. Springer, Berlin (2015)
12. Choi, H.G., Thite, A.N., Thompson, D.J.: A threshold for the use of Tikhonov regularization in inverse force determination. Appl Acoust **67**, 700–719 (2006)
13. Manzato, S., Risaliti, E., Napoli, C., Tamarozzi, T., Peeters, B.: A review of frequency-based substructuring methods and their applicability to engineering structures. In: Proceedings of the International Conference on Structural Engineering Dynamics (ICEDyn) 2015, Lagos (2015)

14. Milana, S., Fregolent, A., Culla, A.: Observation dofs optimization for structural forces identification. In: Model Validation and Uncertainty Quantification. Conference Proceedings of the Society for Experimental Mechanics Series, vol. 3, pp. 27–34. Springer, Berlin (2015)
15. El-Kafafy, M., De Troyer, T., Peeters, B., Guillaume, P.: Fast maximum-likelihood identification of modal parameters with uncertainty intervals: a modal model-based formulation. Mech. Syst. Signal Process. **37**, 422–439 (2013)
16. El-Kafafy, M.E., Accardo, G., Peeters, B., Janssens, K., De Troyer, T., Guillaume P.: A fast maximum likelihood-based estimation of a modal model. In: Proceedings of the International Modal Analysis Conference (IMAC), Orlando (2015)

Chapter 46
New FRF Based Methods for Substructure Decoupling

Taner Kalaycıoğlu and H. Nevzat Özgüven

Abstract Substructuring methods are well known and are widely used in predicting dynamics of coupled structures. In theory, there is no reason why the same techniques could not be used in a reverse problem of predicting the dynamic behavior of a particular substructure from the knowledge of the dynamics of the coupled structure and of all the other substructures. However, the reverse problem, known as decoupling, usually requires matrix inversions, and therefore even small measurement errors may easily affect the accuracy of such methods. In this study two new FRF based approaches are presented for decoupling. The methods proposed require coupled system FRFs at coordinates that belong to the known subsystem as well as the measured or calculated FRFs of the known subsystem alone. Formulations are based on the reverse application of the structural coupling method proposed in a previous publication co-authored by one of the authors of this paper. The performances of the proposed methods are demonstrated and then compared with those of some well-known recent methods in the literature through a case study.

Keywords Decoupling • Uncoupling • Inverse substructuring • Subsystem identification • Subsystem subtraction

46.1 Introduction

The modal analysis and testing is widely used to analyze the dynamic characteristics of a whole machine or its components [1]. Since engineering structures are generally designed as an assembly of several components, a lot of effort has been devoted to structural coupling methods that predict the total dynamic behavior of a complex machine from those of its components in recent decades. Conversely, in some cases, the dynamic characteristics of a whole system may be known but that of its component may be hard to measure because of the difficulty of performing measurements or excitation on a subsystem individually under its normal operating conditions.

In this study, the decoupling problem, the identification of the dynamic behavior of a structural subsystem that is part of a larger system is addressed. One of the earliest studies on the substructure decoupling is performed by Okubo and Miyazaki [2] in 1986. In their solution, FRFs of the complete system and the known subsystem is used to obtain FRF of the unknown subsystem. After a long break, Gontier and Bensaibi [3] presented a decoupling technique based on time domain approach which still remains as the only technique in time domain. Silva et al. [4] presented a study regarding joint identification. They used decoupling methodology in order to eliminate difficulties in measurement and experimenting for joint identification. Later, they proposed a different technique for joint identification [5]. In this technique, they used coupling formulation of Jetmundsen et al. [6] and obtained a better formulation in terms of the number of matrix inversions. In this formulation, joint (i.e. connection) degrees of freedom (DoFs) are not taken into account. Ind and Ewins [7] presented an approach similar to that of Silva et al. [5]. Kalling et al. [8] studied the decoupling problem by performing state-space model identification. D'Ambrogio and Fregolent [9] presented a modal based approach for decoupling analyses which suffers from modal truncation problems.

D'Ambrogio and Fregolent [10] presented an FRF based decoupling technique similar to that of Okubo and Miyazaki [2]. In this work, they pointed out the problems due to unmeasured rotational DoFs as well. Afterwards, D'Ambrogio and

T. Kalaycıoğlu (✉)
Department of Mechanical Engineering, Middle East Technical University, 06800 Ankara, Turkey

MGEO Sector, ASELSAN Inc., 06011 Ankara, Turkey
e-mail: tkalayci@aselsan.com.tr

H.N. Özgüven
Department of Mechanical Engineering, Middle East Technical University, 06800 Ankara, Turkey
e-mail: ozguven@metu.edu.tr

© The Society for Experimental Mechanics, Inc. 2016

M. Allen et al. (eds.), *Dynamics of Coupled Structures, Volume 4*, Conference Proceedings of the Society for Experimental Mechanics Series, DOI 10.1007/978-3-319-29763-7_46

Fregolent [11] proposed two decoupling procedures; namely, impedance based and mobility based approaches, which calculate the FRFs of the connection DoF on an unknown subsystem by using the FRFs of the coupled system and the residual subsystem at residual subsystem DoFs. The latter is equivalent to the approach presented by Sjövall and Abrahamsson [12]. A general framework for dynamic substructuring is provided in [13] and [14] in which the so called dual domain decomposition technique that allows retaining the full set of global DoFs by ensuring equilibrium at the interface between substructures is introduced. When performing substructuring by using the dual domain decomposition, the coupling problem can be directly formulated from [14], whereas a similar formulation for the decoupling problem is developed and discussed in [15] for collocated approach where DoFs used to enforce equilibrium are the same as DoFs used to enforce compatibility, and in [16] and [17] for non-collocated approach where DoFs used to enforce equilibrium are not the same as DoFs used to enforce compatibility.

Batista and Maia [18] proposed three different decoupling formulations based on the classical decoupling procedure of Jetmundsen et al. [6]. They consider the effects of including different sets of DoF of the coupled system: (1) exclusion of connection DoFs, (2) inclusion of connection DoFs only and (3) inclusion of connection DoFs and internal DoFs of the residual subsystem. Cloutier and Avitabile [19] presented inverse frequency based substructuring approach that requires measurements on the unknown substructure. Later, D'Ambrogio and Fregolent [20] proposed the so called hybrid assembly approach. They compared dual [15] and hybrid assembly approaches through an experimental case study and ended up with very similar results in terms of predicted FRFs of the unknown subsystem.

In this paper, two new FRF based decoupling approaches are developed which are based on the structural modification method suggested by Tahtalı and Özgüven [21] two decades ago. The approaches developed can predict the FRFs of an unknown subsystem from the measured FRFs of the coupled system and the measured or calculated FRFs of the other subsystem. The methods are tested on a simple lumped parameter system by using simulated experimental data. Results are compared with those obtained through some well-known decoupling methods.

46.2 Theory

In this section, the theory of the decoupling approaches proposed is given. In this approach, the structural modification method suggested by Tahtalı and Özgüven [21] is revisited and modified to be used for substructure decoupling. The notation used throughout the paper for all systems/subsystems and the coordinate sets are given in Fig. 46.1.

Here, first, the basic equations of the Coupling Force Method suggested by Tahtalı and Özgüven [21] will be given. The displacement vectors for the unknown and the residual subsystems can be written, respectively, as:

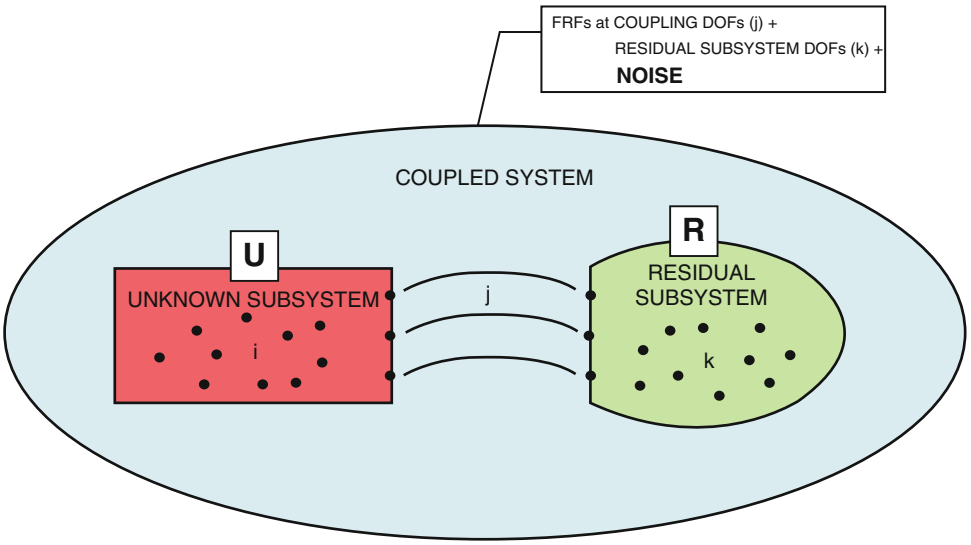

Fig. 46.1 Notation used for systems and sets of coordinates

$$\begin{Bmatrix} \mathbf{X}_i^U \\ \mathbf{X}_j^U \end{Bmatrix} = \begin{pmatrix} \mathbf{H}_{ii}^U & \mathbf{H}_{ij}^U \\ \mathbf{H}_{ji}^U & \mathbf{H}_{jj}^U \end{pmatrix} \begin{Bmatrix} \mathbf{F}_i^U \\ \mathbf{F}_j^U + \mathbf{f} \end{Bmatrix} \tag{46.1}$$

$$\begin{Bmatrix} \mathbf{X}_j^R \\ \mathbf{X}_k^R \end{Bmatrix} = \begin{pmatrix} \mathbf{H}_{jj}^R & \mathbf{H}_{jk}^R \\ \mathbf{H}_{kj}^R & \mathbf{H}_{kk}^R \end{pmatrix} \begin{Bmatrix} -\mathbf{f} \\ \mathbf{F}_k^R \end{Bmatrix} \tag{46.2}$$

where superscripts U and R refer to the vectors related to the unknown and the residual subsystems, respectively. Subscript i refers to the coordinates of the unknown subsystem only, subscript j refers to the coordinates that are common to the unknown and residual subsystem, and finally subscript k refers to the coordinates of the residual subsystem only (Fig. 46.1). Here, **f**, **F** and **H** represent coupling reaction force vector, external force vector and the FRF matrix, respectively. Expanding Eqs. (46.1) and (46.2) leads to following equations:

$$\mathbf{X}_i^U = \mathbf{H}_{ii}^U \mathbf{F}_i^U + \mathbf{H}_{ij}^U \left(\mathbf{F}_j^U + \mathbf{f}\right) \tag{46.3}$$

$$\mathbf{X}_j^U = \mathbf{H}_{ji}^U \mathbf{F}_i^U + \mathbf{H}_{jj}^U \left(\mathbf{F}_j^U + \mathbf{f}\right) \tag{46.4}$$

$$\mathbf{X}_j^R = -\mathbf{H}_{jj}^R \mathbf{f} + \mathbf{H}_{jk}^R \mathbf{F}_k^R \tag{46.5}$$

$$\mathbf{X}_k^R = -\mathbf{H}_{kj}^R \mathbf{f} + \mathbf{H}_{kk}^R \mathbf{F}_k^R \tag{46.6}$$

Note that, when two subsystems are rigidly coupled, $\mathbf{X}_j^U = \mathbf{X}_j^R$, which represents the displacement vector at the coupling coordinates. Therefore Eqs. (46.4) and (46.5) are equal to each other. Thus, by equating the right hand sides of these equations coupling reaction force can be written as follows:

$$\mathbf{f} = \left[\mathbf{H}_{jj}^U + \mathbf{H}_{jj}^R\right]^{-1} \left[\mathbf{H}_{jk}^R \mathbf{F}_k^R - \mathbf{H}_{ji}^U \mathbf{F}_i^U - \mathbf{H}_{jj}^U \mathbf{F}_j^U\right] \tag{46.7}$$

After having obtained the coupling reaction force **f**, the response of the coupled system can be obtained by substituting **f** in Eqs. (46.3), (46.5) and (46.6) as follows:

$$\mathbf{X}_i^U = \mathbf{H}_{ii}^U \mathbf{F}_i^U + \mathbf{H}_{ij}^U \left(\mathbf{F}_j^U + \left[\mathbf{H}_{jj}^U + \mathbf{H}_{jj}^R\right]^{-1} \left[\mathbf{H}_{jk}^R \mathbf{F}_k^R - \mathbf{H}_{ji}^U \mathbf{F}_i^U - \mathbf{H}_{jj}^U \mathbf{F}_j^U\right]\right) \tag{46.8}$$

$$\mathbf{X}_j^R = -\mathbf{H}_{jj}^R \left[\mathbf{H}_{jj}^U + \mathbf{H}_{jj}^R\right]^{-1} \left[\mathbf{H}_{jk}^R \mathbf{F}_k^R - \mathbf{H}_{ji}^U \mathbf{F}_i^U - \mathbf{H}_{jj}^U \mathbf{F}_j^U\right] + \mathbf{H}_{jk}^R \mathbf{F}_k^R \tag{46.9}$$

$$\mathbf{X}_k^R = -\mathbf{H}_{kj}^R \left[\mathbf{H}_{jj}^U + \mathbf{H}_{jj}^R\right]^{-1} \left[\mathbf{H}_{jk}^R \mathbf{F}_k^R - \mathbf{H}_{ji}^U \mathbf{F}_i^U - \mathbf{H}_{jj}^U \mathbf{F}_j^U\right] + \mathbf{H}_{kk}^R \mathbf{F}_k^R \tag{46.10}$$

Note that the response of the coupled system can also be written as follows:

$$\begin{pmatrix} \mathbf{X}_i^U \\ \mathbf{X}_j^R \\ \mathbf{X}_k^R \end{pmatrix} = \begin{pmatrix} \mathbf{H}_{ii} & \mathbf{H}_{ij} & \mathbf{H}_{ik} \\ \mathbf{H}_{ji} & \mathbf{H}_{jj} & \mathbf{H}_{jk} \\ \mathbf{H}_{ki} & \mathbf{H}_{kj} & \mathbf{H}_{kk} \end{pmatrix} \begin{pmatrix} \mathbf{F}_i^U \\ \mathbf{F}_j^U \\ \mathbf{F}_k^R \end{pmatrix} \tag{46.11}$$

The above formulation gives the basic equations of the Coupling Force Method proposed by Tahtalı and Özgüven [21]. From now on, formulation to be given will be about the derivation of decoupling formulations. In the following section the use of these equations for decoupling will be given.

46.2.1 Formulation Using Equation (46.9)

Let us assume that external forcing is applied only to the kth coordinates of the coupled system and the rest of the external forcing is equal to zero;

$$\begin{pmatrix} \mathbf{F}_{\mathrm{i}}^{\mathrm{U}} \\ \mathbf{F}_{\mathrm{j}}^{\mathrm{U}} \\ \mathbf{F}_{\mathrm{k}}^{\mathrm{R}} \end{pmatrix} = \begin{pmatrix} \mathbf{0}_{i\times 1} \\ \mathbf{0}_{j\times 1} \\ \mathbf{F}_{k\times 1} \end{pmatrix} \tag{46.12}$$

By using Eqs. (46.11) and (46.12), Eq. (46.9) can be rewritten as follows:

$$\mathbf{H}_{\mathrm{jk}}\mathbf{F}_{k\times 1} = -\mathbf{H}_{\mathrm{jj}}^{\mathrm{R}}\left(\mathbf{H}_{\mathrm{jj}}^{\mathrm{U}} + \mathbf{H}_{\mathrm{jj}}^{\mathrm{R}}\right)^{-1}\mathbf{H}_{\mathrm{jk}}^{\mathrm{R}}\mathbf{F}_{k\times 1} + \mathbf{H}_{\mathrm{jk}}^{\mathrm{R}}\mathbf{F}_{k\times 1} \tag{46.13}$$

By multiplying both sides of Eq. (46.13) with $(\mathbf{F}_{k\times 1})^{-1}$ from right hand side, one can obtain

$$\mathbf{H}_{\mathrm{jk}}^{\mathrm{R}} - \mathbf{H}_{\mathrm{jk}} = \mathbf{H}_{\mathrm{jj}}^{\mathrm{R}}\left(\mathbf{H}_{\mathrm{jj}}^{\mathrm{U}} + \mathbf{H}_{\mathrm{jj}}^{\mathrm{R}}\right)^{-1}\mathbf{H}_{\mathrm{jk}}^{\mathrm{R}} \tag{46.14}$$

Premultiplying all terms of Eq. (46.14) by $\left(\mathbf{H}_{\mathrm{jj}}^{\mathrm{R}}\right)^{-1}$ and post multiplying them by $\left(\mathbf{H}_{\mathrm{jk}}^{\mathrm{R}}\right)^{-1}$ yields

$$\left(\mathbf{H}_{\mathrm{jj}}^{\mathrm{R}}\right)^{-1}\left(\mathbf{H}_{\mathrm{jk}}^{\mathrm{R}} - \mathbf{H}_{\mathrm{jk}}\right)\left(\mathbf{H}_{\mathrm{jk}}^{\mathrm{R}}\right)^{-1} = \left(\mathbf{H}_{\mathrm{jj}}^{\mathrm{U}} + \mathbf{H}_{\mathrm{jj}}^{\mathrm{R}}\right)^{-1} \tag{46.15}$$

Taking inverse of the both sides of Eq. (46.15), the following equation can be written:

$$\mathbf{H}_{\mathrm{jk}}^{\mathrm{R}}\left(\mathbf{H}_{\mathrm{jk}}^{\mathrm{R}} - \mathbf{H}_{\mathrm{jk}}\right)^{-1}\mathbf{H}_{\mathrm{jj}}^{\mathrm{R}} = \mathbf{H}_{\mathrm{jj}}^{\mathrm{U}} + \mathbf{H}_{\mathrm{jj}}^{\mathrm{R}} \tag{46.16}$$

Rearranging Eq. (46.16) yields the final equation which gives the FRF matrix of the unknown subsystems in terms of those of coupled system and residual subsystem:

$$\mathbf{H}_{\mathrm{jj}}^{\mathrm{U}} = \mathbf{H}_{\mathrm{jk}}^{\mathrm{R}}\left(\mathbf{H}_{\mathrm{jk}}^{\mathrm{R}} - \mathbf{H}_{\mathrm{jk}}\right)^{-1}\mathbf{H}_{\mathrm{jj}}^{\mathrm{R}} - \mathbf{H}_{\mathrm{jj}}^{\mathrm{R}} \tag{46.17}$$

It is interesting to note that if it is assumed that external forcing is applied only to the jth coordinates of the coupled system while the rest of the external forces are zero, that is

$$\begin{pmatrix} \mathbf{F}_{\mathrm{i}}^{\mathrm{U}} \\ \mathbf{F}_{\mathrm{j}}^{\mathrm{U}} \\ \mathbf{F}_{\mathrm{k}}^{\mathrm{R}} \end{pmatrix} = \begin{pmatrix} \mathbf{0}_{i\times 1} \\ \mathbf{F}_{j\times 1} \\ \mathbf{0}_{k\times 1} \end{pmatrix} \tag{46.18}$$

one will end up with the decoupling formulation given by Batista and Maia [18]:

$$\mathbf{H}_{\mathrm{jj}}^{\mathrm{U}} = \mathbf{H}_{\mathrm{jj}}^{\mathrm{R}}\left(\left(\mathbf{H}_{\mathrm{jj}}\right)^{-1}\mathbf{H}_{\mathrm{jj}}^{\mathrm{R}} - \mathbf{I}_{j\times j}\right)^{-1} \tag{46.19}$$

46.2.2 Formulation Using Equation (46.10)

Let us assume again that external forcing is applied only to the jth coordinates of the coupled system and the rest of the external forces are zero as given in Eq. (46.18), and let us use Eq. (46.10) rather than Eq. (46.9). Then by using Eqs. (46.11) and (46.18), one can rewrite Eq. (46.10) as follows:

$$\mathbf{H}_{\mathrm{kj}}\,\mathbf{F}_{j\times 1} = \mathbf{H}_{\mathrm{kj}}^{\mathrm{R}}\left(\mathbf{H}_{\mathrm{jj}}^{\mathrm{U}} + \mathbf{H}_{\mathrm{jj}}^{\mathrm{R}}\right)^{-1}\mathbf{H}_{\mathrm{jj}}^{\mathrm{U}}\,\mathbf{F}_{j\times 1} \tag{46.20}$$

By multiplying both sides of Eq. (46.20) with $\left(\mathbf{F}_{j\times 1}\right)^{-1}$ from right hand side, one can obtain:

$$\mathbf{H}_{\mathrm{kj}} = \mathbf{H}_{\mathrm{kj}}^{\mathrm{R}}\left(\mathbf{H}_{\mathrm{jj}}^{\mathrm{U}} + \mathbf{H}_{\mathrm{jj}}^{\mathrm{R}}\right)^{-1}\mathbf{H}_{\mathrm{jj}}^{\mathrm{U}} \tag{46.21}$$

Premultiplying all terms of Eq. (46.21) by $\left(\mathbf{H}_{jj}^{R}\right)^{-1}$ and post multiplying them by $\left(\mathbf{H}_{jj}^{U}\right)^{-1}$ gives

$$\left(\mathbf{H}_{kj}^{R}\right)^{-1}\mathbf{H}_{kj}\left(\mathbf{H}_{jj}^{U}\right)^{-1} = \left(\mathbf{H}_{jj}^{U} + \mathbf{H}_{jj}^{R}\right)^{-1} \tag{46.22}$$

Taking inverse of both sides of Eq. (46.22), the following equation can be obtained

$$\mathbf{H}_{jj}^{U}\left(\mathbf{H}_{kj}\right)^{-1}\mathbf{H}_{kj}^{R} = \mathbf{H}_{jj}^{U} + \mathbf{H}_{jj}^{R} \tag{46.23}$$

Then, the final equation which gives the FRF matrix of the unknown subsystems in terms of those of coupled system and residual subsystem can be obtained as follows:

$$\mathbf{H}_{jj}^{U} = \mathbf{H}_{jj}^{R}\left(\left(\mathbf{H}_{kj}\right)^{-1}\mathbf{H}_{kj}^{R} - \mathbf{I}_{j\times j}\right)^{-1} \tag{46.24}$$

Again it is interesting to note that if it is assumed that external forcing is applied only to the k^{th} coordinates of the coupled system as shown in Eq. (46.12), the formulation given by Maia et al. [5] can be easily obtained:

$$\mathbf{H}_{jj}^{U} = \mathbf{H}_{jk}^{R}\left(\mathbf{H}_{kk}^{R} - \mathbf{H}_{kk}\right)^{-1}\mathbf{H}_{kj}^{R} - \mathbf{H}_{jj}^{R} \tag{46.25}$$

46.3 Case Studies

In this section, application of the proposed decoupling formulations to a lumped parameter system is presented. Furthermore, performances of the proposed formulations are compared with those of some well-known techniques by using the same case study.

46.3.1 Application of the Approaches to a Lumped Parameter System

The coupled system considered in this application is composed of two subsystems rigidly connected to each other as shown in Fig. 46.2. Physical parameters of the residual and the unknown subsystem are given in Table 46.1. Note that k, m and c represent stiffness, mass and viscous damping parameters, respectively.

Here, it is assumed that the FRFs of the coupled system are experimentally measured and the physical model of the residual subsystem is available. It is aimed to determine the FRF of the unknown subsystem at its connection coordinate.

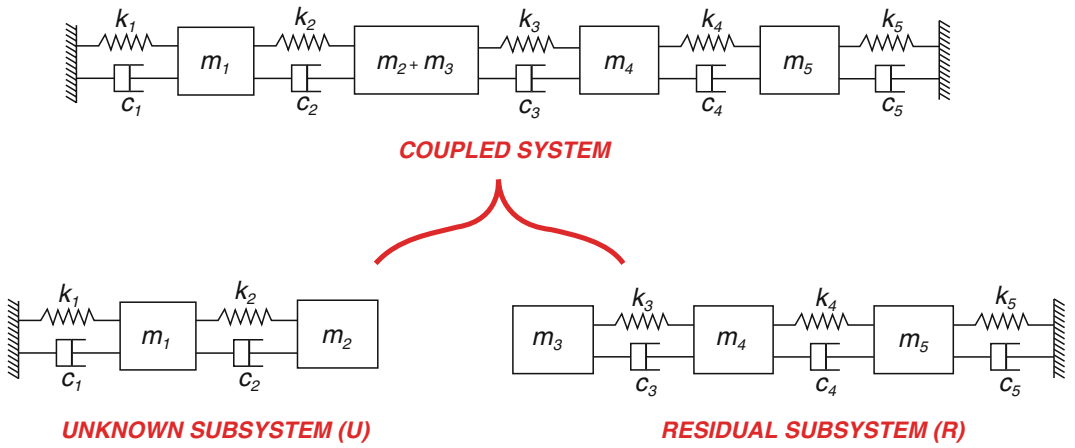

Fig. 46.2 Lumped parameter system model

Table 46.1 Physical parameters

Element Number (i)	m_i [kg]	k_i [N/m]	c_i [Ns/m]
1	2.5	1500	0.15
2	3	2000	0.20
3	2	2100	0.21
4	3	1900	0.19
5	2.5	2200	0.22

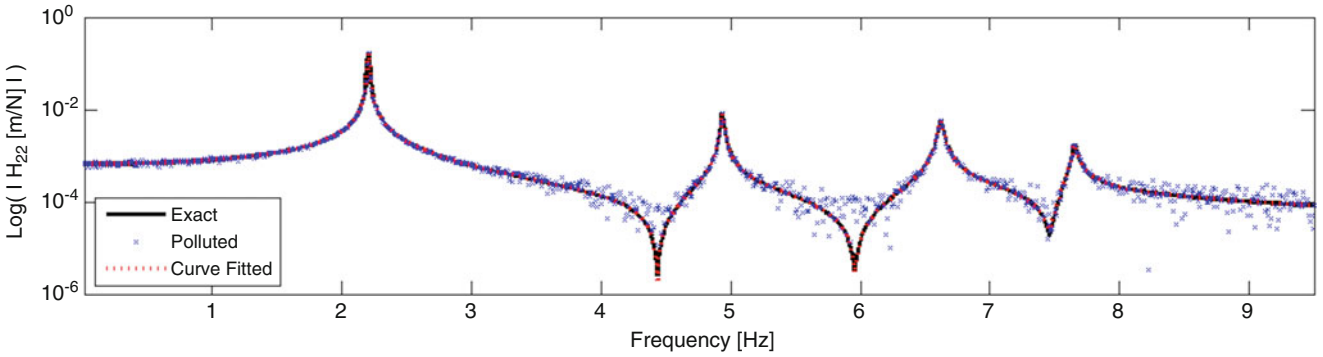

Fig. 46.3 Driving point FRF of the coupled system at the 2nd DoF: true (*solid black line*), polluted (*blue asterisks*) and curve fitted (*red dashed lines*)

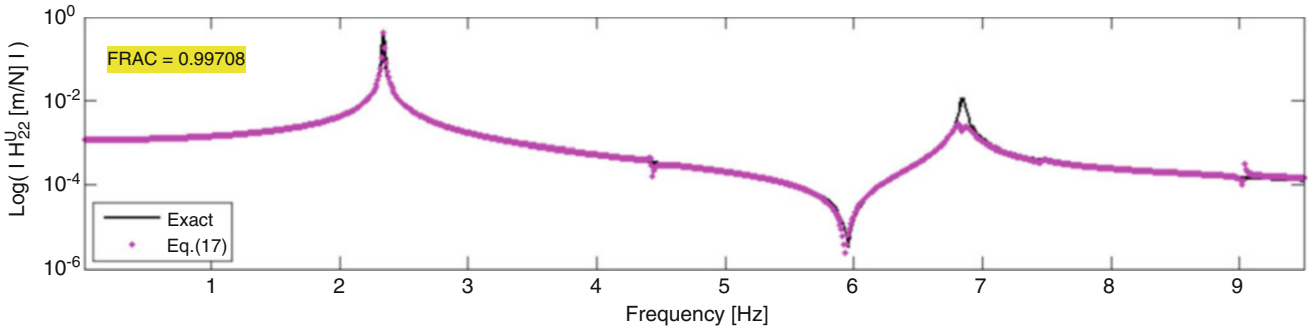

Fig. 46.4 Driving point FRF at the 2nd DoF of the unknown subsystem: true (*solid black line*), predicted using Eq. (46.17) (*magenta asterisks*)

In order to simulate the measured FRFs of the coupled system, first the exact FRFs of the coupled system ($\hat{\mathbf{H}}$) are calculated by using the physical parameters given in Table 46.1 and then they are polluted by simply adding complex random variables as shown below:

$$\mathbf{H}_{\mathrm{ij}}(\omega_{\mathrm{k}}) = \widehat{\mathbf{H}}_{\mathrm{ij}}(\omega_{\mathrm{k}}) + p_{\mathrm{ij,k}} + i\, q_{\mathrm{ij,k}} \tag{46.26}$$

Here, $p_{\mathrm{ij,k}}$ and $q_{\mathrm{ij,k}}$ are independent random variables with Gaussian distribution, zero mean and a standard deviation of 5×10^{-5} m/N. The effect of such a pollution on the driving point FRF at the 2nd DoF (the coupling DoF) of the coupled system is shown in Fig. 46.3 together with the FRF obtained after curve fitting.

Then, by using the curves fitted to the polluted FRFs of the coupled structure, driving point FRF at the coupling DoF of the unknown subsystem is calculated using the proposed formulations, and the results are given in Figs. 46.4 and 46.5.

Figures 46.4 and 46.5 show that both approaches predict the unknown subsystem FRF satisfactorily. If the performances of both approaches are compared with each other around resonances, the predicted FRF via Eq. (46.24) seem to fit better to the true FRF by visual inspection.

However, in order to make a reliable and sound comparison, it is required to use a metric rather than making visual inspection. For that purpose, the Frequency Response Assurance Criterion (FRAC) [22] is used. The FRAC values calculated for FRFs calculated by using Eqs. (46.17) and (46.24) are 0.99708 and 0.99791, respectively. So, it can be said again that, at least for the example case given here, both equations can successfully be used for decoupling, and Eq. (46.24) gives slightly better results compared to Eq. (46.17).

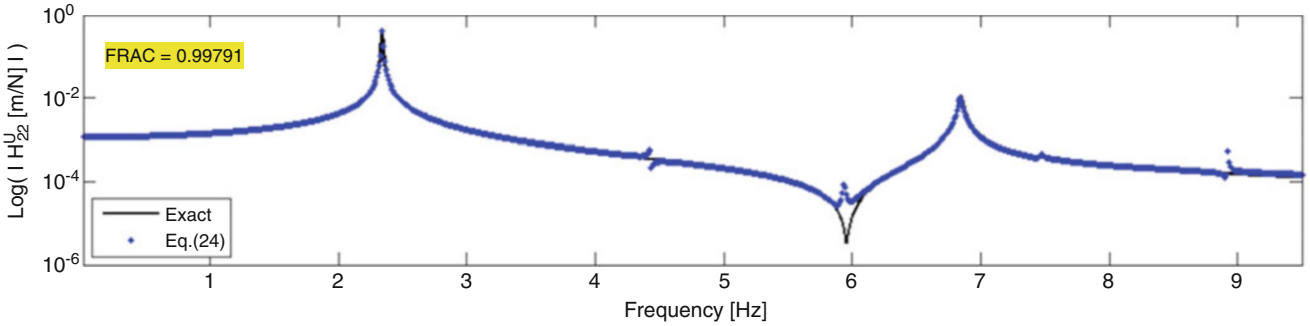

Fig. 46.5 Driving point FRF at the 2nd DoF of the unknown subsystem: true (*solid black line*), predicted using Eq. (46.24) (*blue asterisks*)

Table 46.2 List of most recent decoupling methods

Ref.	Final equation	Needs (residual)	Needs (coupled)	Equation
[18]	$\mathbf{H}^{\mathrm{U}}_{\mathrm{jj}} = \mathbf{H}^{\mathrm{R}}_{\mathrm{jk}}\mathbf{H}^{\mathrm{R}}_{\mathrm{kj}}\left(\mathbf{H}^{\mathrm{R}}_{\mathrm{jk}}\left(\mathbf{H}^{\mathrm{R}}_{\mathrm{kk}}\text{-}\mathbf{H}_{\mathrm{kk}}\right)\mathbf{H}^{\mathrm{R}}_{\mathrm{kj}}\right)^{-1}\mathbf{H}^{\mathrm{R}}_{\mathrm{jk}}\mathbf{H}^{\mathrm{R}}_{\mathrm{kj}}\text{-}\mathbf{H}^{\mathrm{R}}_{\mathrm{jj}}$	$\begin{pmatrix}\mathbf{H}^{\mathrm{R}}_{\mathrm{jj}} & \mathbf{H}^{\mathrm{R}}_{\mathrm{jk}}\\ \mathbf{H}^{\mathrm{R}}_{\mathrm{kj}} & \mathbf{H}^{\mathrm{R}}_{\mathrm{kk}}\end{pmatrix}$	$\mathbf{H}_{\mathrm{kk}}$	(46.27)
[18]	$\mathbf{H}^{\mathrm{U}}_{\mathrm{jj}} = \left(\mathbf{H}^{\mathrm{R}}_{\mathrm{jj}}\left(\mathbf{H}^{\mathrm{R}}_{\mathrm{jj}}\text{-}\mathbf{H}_{\mathrm{jj}}\right)^{-1} - \mathbf{I}_{\mathrm{jj}}\right)\mathbf{H}^{\mathrm{R}}_{\mathrm{jj}}$	$\mathbf{H}^{\mathrm{R}}_{\mathrm{jj}}$	$\mathbf{H}_{\mathrm{jj}}$	(46.28)
[18]	$\mathbf{H}^{\mathrm{U}}_{\mathrm{jj}} = \mathbf{H}^{\mathrm{R}}_{\mathrm{jj}}\mathbf{H}^{\mathrm{R}}_{\mathrm{jj}}\left(\mathbf{H}^{\mathrm{R}}_{\mathrm{jk}}\left(\mathbf{H}^{\mathrm{R}}_{\mathrm{kj}}\text{-}\mathbf{H}_{\mathrm{kj}}\right)\mathbf{H}^{\mathrm{R}}_{\mathrm{jj}}\right)^{-1}\mathbf{H}^{\mathrm{R}}_{\mathrm{jk}}\mathbf{H}^{\mathrm{R}}_{\mathrm{kj}}\text{-}\mathbf{H}^{\mathrm{R}}_{\mathrm{jj}}$	$\begin{pmatrix}\mathbf{H}^{\mathrm{R}}_{\mathrm{jj}} & \mathbf{H}^{\mathrm{R}}_{\mathrm{jk}}\\ \mathbf{H}^{\mathrm{R}}_{\mathrm{kj}} & \mathbf{H}^{\mathrm{R}}_{\mathrm{kk}}\end{pmatrix}$	$\mathbf{H}_{\mathrm{kj}}$	(46.29)
[5]	$\mathbf{H}^{\mathrm{U}}_{\mathrm{jj}} = \mathbf{H}^{\mathrm{R}}_{\mathrm{jk}}\left(\mathbf{H}^{\mathrm{R}}_{\mathrm{kk}}\text{-}\mathbf{H}_{\mathrm{kk}}\right)^{-1}\mathbf{H}^{\mathrm{R}}_{\mathrm{kj}}\text{-}\mathbf{H}^{\mathrm{R}}_{\mathrm{jj}}$	$\begin{pmatrix}\mathbf{H}^{\mathrm{R}}_{\mathrm{jj}} & \mathbf{H}^{\mathrm{R}}_{\mathrm{jk}}\\ \mathbf{H}^{\mathrm{R}}_{\mathrm{kj}} & \mathbf{H}^{\mathrm{R}}_{\mathrm{kk}}\end{pmatrix}$	$\mathbf{H}_{\mathrm{kk}}$	(46.30)
[2]	$\mathbf{H}^{\mathrm{U}}_{\mathrm{jj}} = \left(\mathbf{I}\text{-}\mathbf{H}_{\mathrm{jj}}\left[\mathbf{H}^{\mathrm{R}}_{\mathrm{jj}}\right]^{-1}\right)^{-1}\mathbf{H}_{\mathrm{jj}}$	$\mathbf{H}^{\mathrm{R}}_{\mathrm{jj}}$	$\mathbf{H}_{\mathrm{jj}}$	(46.31)
[11]	$\mathbf{H}^{\mathrm{U}}_{\mathrm{jj}} = \begin{pmatrix}\mathbf{I}\text{-}\mathbf{H}_{\mathrm{jj}}\,\mathbf{Z}^{\mathrm{R}}_{\mathrm{jj}} - \mathbf{H}_{\mathrm{jk}}\,\mathbf{Z}^{\mathrm{R}}_{\mathrm{kj}}\\ -\mathbf{H}_{\mathrm{kj}}\,\mathbf{Z}^{\mathrm{R}}_{\mathrm{jj}} - \mathbf{H}_{\mathrm{kk}}\,\mathbf{Z}^{\mathrm{R}}_{\mathrm{kj}}\end{pmatrix}^{+}\begin{pmatrix}\mathbf{H}_{\mathrm{jj}}\\ \mathbf{H}_{\mathrm{kj}}\end{pmatrix}$	$\begin{pmatrix}\mathbf{Z}^{\mathrm{R}}_{\mathrm{jj}} & -\\ \mathbf{Z}^{\mathrm{R}}_{\mathrm{kj}} & -\end{pmatrix}$	$\begin{pmatrix}\mathbf{H}_{\mathrm{jj}} & \mathbf{H}_{\mathrm{jk}}\\ \mathbf{H}_{\mathrm{kj}} & \mathbf{H}_{\mathrm{kk}}\end{pmatrix}$	(46.32)
[11]	$\mathbf{H}^{\mathrm{U}}_{\mathrm{jj}} = \begin{pmatrix}\mathbf{H}_{\mathrm{jj}}\\ \mathbf{H}_{\mathrm{jk}}\end{pmatrix}^{\mathrm{T}}\left(\begin{pmatrix}\mathbf{I}_{\mathrm{jj}} & \mathbf{0}_{\mathrm{jk}}\end{pmatrix} - \begin{pmatrix}\mathbf{H}^{\mathrm{R}}_{\mathrm{jj}}\\ \mathbf{H}^{\mathrm{R}}_{\mathrm{kj}}\end{pmatrix}^{+}\begin{pmatrix}\mathbf{H}_{\mathrm{jj}} & \mathbf{H}_{\mathrm{jk}} - \mathbf{H}^{\mathrm{R}}_{\mathrm{jk}}\\ \mathbf{H}_{\mathrm{kj}} & \mathbf{H}_{\mathrm{kk}} - \mathbf{H}^{\mathrm{R}}_{\mathrm{kk}}\end{pmatrix}\right)^{+}$	$\begin{pmatrix}\mathbf{H}^{\mathrm{R}}_{\mathrm{jj}} & \mathbf{H}^{\mathrm{R}}_{\mathrm{jk}}\\ \mathbf{H}^{\mathrm{R}}_{\mathrm{kj}} & \mathbf{H}^{\mathrm{R}}_{\mathrm{kk}}\end{pmatrix}$	$\begin{pmatrix}\mathbf{H}_{\mathrm{jj}} & \mathbf{H}_{\mathrm{jk}}\\ \mathbf{H}_{\mathrm{kj}} & \mathbf{H}_{\mathrm{kk}}\end{pmatrix}$	(46.33)
[15]	$\mathbf{H}^{\mathrm{U}} = \begin{pmatrix}\mathbf{H} & \mathbf{0}\\ \mathbf{0} & -\mathbf{H}^{\mathrm{R}}\end{pmatrix} - \begin{pmatrix}\mathbf{H} & \mathbf{0}\\ \mathbf{0} & -\mathbf{H}^{\mathrm{R}}\end{pmatrix}\begin{pmatrix}\mathbf{B}^{\mathrm{T}}\\ \left(\mathbf{B}^{\mathrm{R}}\right)^{\mathrm{T}}\end{pmatrix}\cdots$ $\left(\begin{pmatrix}\mathbf{B} & \mathbf{B}^{\mathrm{R}}\end{pmatrix}\begin{pmatrix}\mathbf{H} & \mathbf{0}\\ \mathbf{0} & -\mathbf{H}^{\mathrm{R}}\end{pmatrix}\begin{pmatrix}\mathbf{B}^{\mathrm{T}}\\ \left(\mathbf{B}^{\mathrm{R}}\right)^{\mathrm{T}}\end{pmatrix}\right)^{-1}\begin{pmatrix}\mathbf{B} & \mathbf{B}^{\mathrm{R}}\end{pmatrix}\begin{pmatrix}\mathbf{H} & \mathbf{0}\\ \mathbf{0} & -\mathbf{H}^{\mathrm{R}}\end{pmatrix}$	$\begin{pmatrix}\mathbf{H}^{\mathrm{R}}_{\mathrm{jj}} & \mathbf{H}^{\mathrm{R}}_{\mathrm{jk}}\\ \mathbf{H}^{\mathrm{R}}_{\mathrm{kj}} & \mathbf{H}^{\mathrm{R}}_{\mathrm{kk}}\end{pmatrix}$	$\begin{pmatrix}\mathbf{H}_{\mathrm{jj}} & \mathbf{H}_{\mathrm{jk}}\\ \mathbf{H}_{\mathrm{kj}} & \mathbf{H}_{\mathrm{kk}}\end{pmatrix}$	(46.34)

46.3.2 A Comparison of the Approaches with Well-Known Existing Methods

In this section, the performances of proposed methods are compared with those of well-known recent methods. The final equations for these methods, their references and the input data required for each of them are summarized in Table 46.2.

Among the first three formulations given in the table, Eq. (46.28) was shown to be the one that produces the smallest error throughout the frequency range [18]. Moreover, among the last three formulations given in the table, Eq. (46.34) was shown to give better results [15]. Note also that Eq. (46.31) is a special case of the Eq. (46.32) as also mentioned in reference [11]. Consequently, it will be more to the point to compare the proposed formulations with Eqs. (46.28), (46.30) and (46.34) in Table 46.2.

So, the problem given in Sect. 46.3.1 is also solved by using Eqs. (46.28), (46.30) and (46.34) in addition to employing the proposed formulations, i.e., Eqs. (46.23) and (46.24). Moreover in order to see the effect of increasing noise level in measured FRFs on the performances of different methods, coupled system FRFs are polluted by five different sets of random variables, $p_{\mathrm{ij,k}}$ and $q_{\mathrm{ij,k}}$ in Eq. (46.26), with Gaussian distribution, zero mean and standard deviations ranging from 5×10^{-5} to 25×10^{-5} m/N. Results obtained for the standard deviation of 15×10^{-5} m/N are given in Fig. 46.6.

It is observed that using different pollution sets with the same standard deviation may give slightly different results. Therefore, in order to compare the performances of different formulations and to study the effect of increasing measurement errors (increasing standard deviation of pollution), calculations with each method are repeated 100 times for each standard deviation of pollution, and the averages of the FRAC values are compared in Table 46.3.

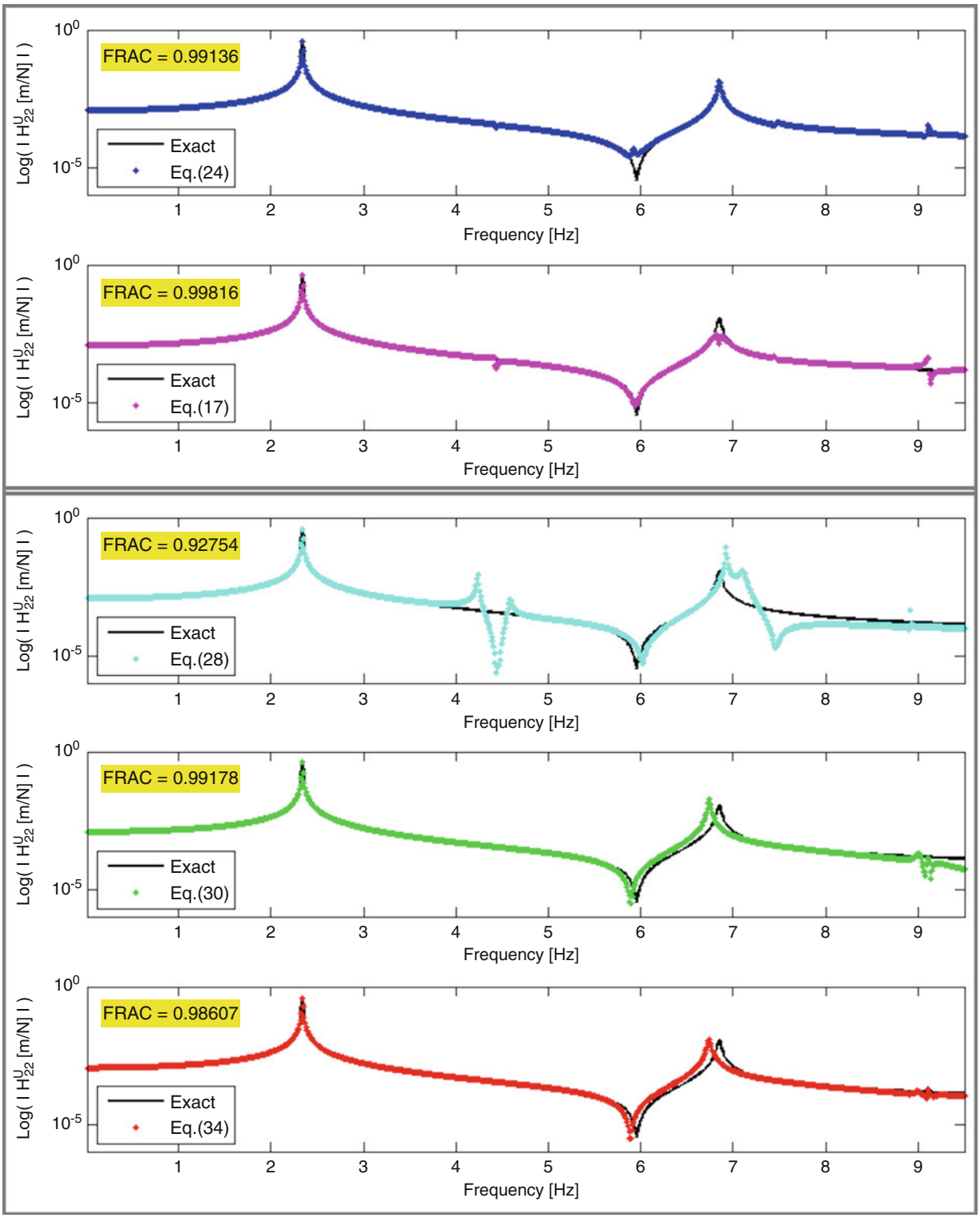

Fig. 46.6 Driving point FRF at the 2nd DoF of the unknown subsystem: true (*solid black line*), predicted using standard deviation of 15×10^{-5} m/N via proposed formulations: Eq. (46.24) (*blue asterisks*), Eq. (46.17) (*magenta asterisks*) and via formulations given in literature: Eq. (46.28) (*cyan asterisks*), Eq. (46.30) (*green asterisks*), Eq. (46.34) (*red asterisks*)

When mean FRAC values given in the Table 46.3 are compared to each other, the overall performances of the proposed formulations (i.e., Eqs. (46.24) and (46.17)) are found to be better. Especially, Eq. (46.24) proved to be statistically the best performer among all formulations.

Table 46.3 Mean (M) and Standard deviation (SD) of FRAC values obtained for each method

	FRAC values (M ± SD values calculated for 100 runs)				
Method	SD of 5×10^{-5} m/N	SD of 1×10^{-4} m/N	SD of 15×10^{-5} m/N	SD of 2×10^{-4} m/N	SD of 25×10^{-5} m/N
Eq. (46.24)	0.9979 ± 0.0019	0.9970 ± 0.0024	0.9900 ± 0.0234	0.9869 ± 0.0107	0.9792 ± 0.0184
Eq. (46.17)	0.9948 ± 0.0218	0.9947 ± 0.0077	0.9912 ± 0.0096	0.9796 ± 0.0189	0.9744 ± 0.0238
Eq. (46.28)	0.9971 ± 0.0215	0.9759 ± 0.0274	0.9701 ± 0.0307	0.9601 ± 0.0404	0.9522 ± 0.0639
Eq. (46.34)	0.9928 ± 0.0192	0.9794 ± 0.0358	0.9767 ± 0.0529	0.9615 ± 0.1067	0.9778 ± 0.0340
Eq. (46.30)	0.9921 ± 0.0050	0.9859 ± 0.0183	0.9822 ± 0.0211	0.9736 ± 0.0435	0.9696 ± 0.0562

46.4 Discussion and Conclusions

In this paper the decoupling problem, i.e. the prediction of the dynamic behavior of a structural subsystem, starting from information about the remaining subsystems (residual subsystems) and from the known dynamic behavior of the complete system, is considered. The dynamic behavior of the whole structure is assumed to be known from experiments, together with the experimentally measured or theoretically calculated dynamics of the residual substructure.

In this work, two different decoupling formulations derived from the work of Tahtalı and Özgüven [21] are presented and thus two new methods are proposed. Both methods give exact results, as it is the case in most of the decoupling methods, when exact FRFs are used in all equations. However, the problem in all of such methods is the sensitivity of the formulations to even very slight errors which are inevitable due to the use of measured data. All formulations usually include matrix inversions, and depending on the nature of the equations, some methods are more sensitive to measurement errors and therefore do not perform well. Hence, it is important to test the performance of any new decoupling technique, and compare its performance with existing best ones. Application of the proposed decoupling formulations is presented on a lumped parameter system. In this case study simulated experimental results are used, and in order to simulate experimentally measured FRFs of the coupled system, theoretically calculated exact FRFs are polluted. In studying the performances of the proposed methods, Frequency Response Assurance Criteria, which shows the correlation between the predicted FRFs and the true FRFs of the unknown subsystem, are used.

Furthermore, performances of the proposed formulations together with some of those available in the literature are investigated through the same case study. Also, effect of noise on the performance of the decoupling methods is examined by polluting the true FRFs of the coupled system using different sets of independent random variables with same mean but gradually increased standard deviations. However, decoupling methods in question do not yield FRAC values in regular trend to the increasing level of noise. Thus, an appropriate statistical comparison becomes essential to establish comparability between the decoupling methods investigated. It is observed from the results of the statistical comparison that proposed methods come up with the most correlated results for each of five standard deviation of pollution.

Consequently, it can be said that proposed methods can be used as alternative approaches results of which should be taken into consideration during decoupling studies. The applicability and accuracy of the methods proposed are demonstrated only on a simple lumped parameter system and additionally they need to be tested on real structures.

References

1. Ewins, D.J.: Modal Testing: Theory Practice and Application. Research Studies Press Ltd., Baldock (2000)
2. Okubo, N., Miyazaki, M.: Development of uncoupling technique and its application. In: Proceedings of 4th International Modal Analysis Conference, Los Angeles, California, USA (1986)
3. Gontier, C., Bensaibi, M.: Time domain identification of a substructure from in situ analysis of the whole structure. Mech. Syst. Signal Process. **9**(4), 379–396 (1995)
4. Silva, J.M.M., Maia, N.M.M., Ribeiro, P.M.L.: Dynamic modeling: application of uncoupling techniques. In: Proceedings of the 14th International Modal Analysis Conference, Dearborn, Michigan, USA (1996)
5. Maia, N.M.M., Silva, J.M.M., Ribeiro, A.M.R., Silva, P.L.C.: On the dynamic characterization of joints using uncoupling techniques. In: Proceedings of the 16th International Modal Analysis Conference, Santa Barbara, California, USA (1998)
6. Jetmundsen, B., Bielawa, R.L., Flannely, W.G.: Generalized frequency domain substructuring synthesis. J. Am. Helicopter Soc. **33**(1), 55–64 (1988)
7. Ind, P.R., Ewins, D.J.: Impedance based decoupling and its application to indirect modal testing and component measurement: a numerical investigation. In: Proceedings of the 21st International Modal Analysis Conference, Kissimmee, Florida, USA (2003)

8. Kalling, P., Abrahamsson, T., McKelvey, T.: Subsystem state-space model identification and its sensitivity to test variability. In: Sas, P., De Munck, M. (eds.) Proceedings of ISMA 2004 - International Conference on Noise and Vibration Engineering, Leuven, pp. 2729–2744, September 2004
9. D'Ambrogio, W., Fregolent, A.: Decoupling of a substructure from modal data of the complete structure. In: Sas, P., De Munck, M. (eds.) Proceedings of ISMA 2004 - International Conference on Noise and Vibration Engineering, Leuven, pp. 2693–2706, September 2004
10. D'Ambrogio, W., Fregolent, A.: Prediction of substructure properties using decoupling procedures, structural dynamics. In: Soize, C., Schüeller, G. (eds.) Proceedings of Eurodyn 2005 - International Conference on Structural Dynamics, Paris, pp. 1893–1898, September 2005
11. D'Ambrogio, W., Fregolent, A.: Promises and pitfalls of decoupling techniques. In: Proceedings of the 26th International Modal Analysis Conference, Orlando, Florida, USA (2008)
12. Sjövall, P., Abrahamsson, T.: Substructure system identification from coupled system test data. Mech. Syst. Signal Process. **22**(1), 15–33 (2008)
13. De Klerk, D., Rixen, D.J., de Jong, J.: Frequency based substructuring (FBS) method reformulated according to the dual domain decomposition method. In: Proceedings of the 24th International Modal Analysis Conference, St. Louis, Missouri, USA (2006)
14. De Klerk, D., Rixen, D.J., Voormeeren, S.: General framework for dynamic substructuring: history, review, and classification of techniques. AIAA J. **46**(5), 1169–1181 (2008)
15. D'Ambrogio, W., Fregolent, A.: The role of interface DoFs in decoupling of substructures based on the dual domain decomposition. Mech. Syst. Signal Process. **24**(7), 2035–2048 (2010)
16. Voormeeren, S.N., Rixen, D.J.: A dual approach to substructure decoupling techniques. In: Proceedings of the 28th International Modal Analysis Conference, Jacksonville, Florida, USA (2010)
17. D'Ambrogio, W., Fregolent, A.: Direct decoupling of substructures using primal and dual formulation. In: Proceedings of the 29th International Modal Analysis Conference, Jacksonville, Florida, USA (2011)
18. Batista, F.C., Maia, N.M.M.: Uncoupling techniques for the dynamic characterization of sub-structures. In: Proceedings of the 29th International Modal Analysis Conference, Jacksonville, Florida, USA (2011)
19. Cloutier, D., Avitabile, P.: Dynamic uncoupling of a system model for component identification. In: Proceedings of the 29th International Modal Analysis Conference, Jacksonville, Florida, USA (2011)
20. D'Ambrogio, W., Fregolent, A.: Inverse dynamic substructuring using direct hybrid assembly in the frequency domain. Mech. Syst. Signal Process. **45**(2), 360–377 (2014)
21. Tahtalı, M., Özgüven, H.N.: Vibration analysis of dynamic structures using a new structural modification method. In: Proceedings of the 6th International Machine Design and Production Conference, METU, Ankara, pp. 511–520, 21–23 September 1994
22. Heylen, W., Lammens, S.: FRAC: a consistent way of comparing frequency response functions. In: Proceedings of the International Conference on Identification in Engineering, Swansea, pp. 48–57 (1996)

Chapter 47
Experimental Determination of Frictional Interface Models

Matthew S. Bonney, Brett A. Robertson, Marc Mignolet, Fabian Schempp, and Matthew R. Brake

Abstract The focus of this paper is on continuing the experimental/modeling investigation of the Brake-Reuß beam which was initiated a year ago as part of the NOMAD program at Sandia National Labs. The ultimate goal of the overall effort is to (1) determine the parameters of joint models, in particular the Iwan model in its modal form, from well delineated tests and (2) extend this approach to identify statistical distributions of the model parameters to account for joint uncertainty. The present effort focused on free response of the beam resulting from an impact test. The use of this data in conjunction with the Hilbert transform is shown to provide a straightforward framework for the identification of the joint model parameters at the contrary of the forced response data used earlier. The resulting frequency and damping vs. amplitude curves are particularly conducive to a Iwan-type modeling which is demonstrated. The curves also show the effect of the bolt torque on the joint behavior, i.e., increase in natural frequency, linear limit, and macroslip threshold. Macroslip is shown to have occurred in some of the tests and it is concluded from ensuing testing that this event changed the nature of the jointed beams. Specifically, the linear natural frequency (observed under very low level impact test) shifted permanently by 20 Hz and, in one case, the linear natural frequency was observed to decrease with increasing bolt torque level in opposition to other beams and physical expectations. An analysis of the joint surface strongly suggest that a significant plastic zone developed during the macroslip phase which induced the above unusual behaviors.

Keywords Brake-Reuß beam • Uncertainty quantification • Iwan model • Plasticity • Tribology

47.1 Introduction and Background

The prediction of the dynamic response of assembled structures is of particular importance in many different areas such as the automotive, aerospace, and nuclear weapons areas. The characterization of joints, most notably their complex nonlinear behavior and variability, represents one of the most significant challenges in achieving the desired accuracy of predictions [7]. Accordingly, the dynamics of joints has been an important research topic for many years with many significant results obtained. Yet, there is still need for additional work, in particular for the gathering and analysis of experimental data on simple configuration(s)to support the modeling effort of both deterministic and stochastic joint models. Such an effort was initiated last year under the framework of the NOMAD program at Sandia National Labs [6]. The present investigation is the continuation of these efforts.

The reported work focuses on the Brake-Reuß beam which is a squared cross-section long beam exhibiting a 3-bolt lap joint at its middle. It is desired first to define a clear and comprehensive test protocol for this beam addressing the questions of free response or forced excitation, excitation level, bolt torque control, surface condition, etc. Next, the potential

M.S. Bonney (✉)
University of Wisconsin-Madison, Madison, WI, USA
e-mail: msbonney@wisc.edu

B.A. Robertson • Marc Mignolet
Arizona State University, Tempe, AZ, USA
e-mail: barober@sandia.gov; marc.mignolet@asu.edu

F. Schempp
University of Stuttgart, Stuttgart, Germany
e-mail: fabian_schempp@gmx.de

M.R. Brake
Sandia National Labs, Albuquerque, NM, USA
e-mail: mrbrake@sandia.gov

© The Society for Experimental Mechanics, Inc. 2016

M. Allen et al. (eds.), *Dynamics of Coupled Structures, Volume 4*, Conference Proceedings of the Society for Experimental Mechanics Series, DOI 10.1007/978-3-319-29763-7_47

determination of the parameters of proposed joint models is investigated using such techniques as the Hilbert transform. The variability of the parameters of these joint models is a third component of this global effort.

The contributions of this paper within the multi-year effort described above focused more specifically on assessing the potential use of free response data and proposing a corresponding preliminary test protocol. The use of the Hilbert transform of this free response data to support the identification of the parameters of an Iwan model is also assessed.

47.2 Proposed Joint Models

Several different models have been created to represent joints in structures [3]. A few that are commonly used are the Coulomb friction model, the Jenkins element, and the Iwan element. Each of these has a different way of simulating the friction and dissipation across a joint. Coulomb friction and the Jenkins element are discrete models while the Iwan element [8] is a more distributive one. Although they all are based on friction between two surfaces, the parameters that characterize each model are different and therefore must be obtained separately. The coefficient of friction can be found using a Coulomb friction and wear experiment while other parameters must be found using response data from say modal impact hammer tests. More details of each model and their parameters are described in the following sections.

47.2.1 Coulomb Friction

The Coulomb friction model takes into account basic sliding contact friction and is depicted as in Fig. 47.1. The only parameter present in this model is the coefficient of friction, which for a given surface can be measured experimentally as discussed in more detail in the Experimentation section.

Modeling a joint using Coulomb friction leads to energy dissipation when the two surfaces slide on each other. However, unlike the more complex joint models, it does not allow microslip at the interface to occur; it only accounts for the entire surface sliding, i.e., macroslip. Note that the capability to slip provides new deformation possibilities and thus lowers the natural frequencies. A physical interpretation of a Coulomb friction slider and its forces is shown in Fig. 47.1.

47.2.2 Jenkins Element

The Jenkins element [4], see Fig. 47.2, is a spring-slider combination that can be in one of two states: stick or slip. If the slider is stuck, there is no friction or energy dissipation and only the linear spring is active. Once the force in the spring reaches the static friction threshold, the slider will then slip causing friction to become active and the spring force to stay constant. The Jenkins model allows for linear and nonlinear deformations in the joint at the contrary of the Coulomb friction which does not exhibit linear deformations. However, the Jenkins element only allows for the entire joint to slip, so the joint can exhibit macroslip but not microslip. The model parameters for a Jenkins element are the coefficient of friction and the spring coefficient.

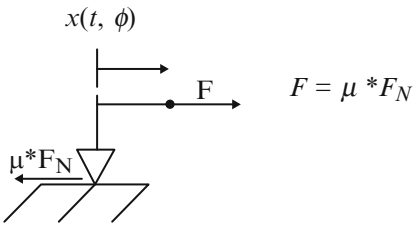

Fig. 47.1 Coulomb friction model

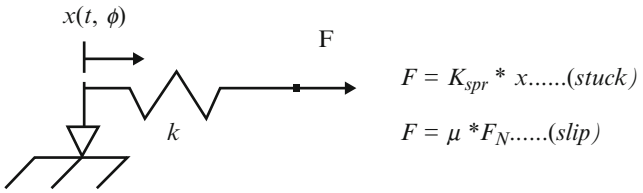

Fig. 47.2 Jenkins model

Fig. 47.3 Iwan model

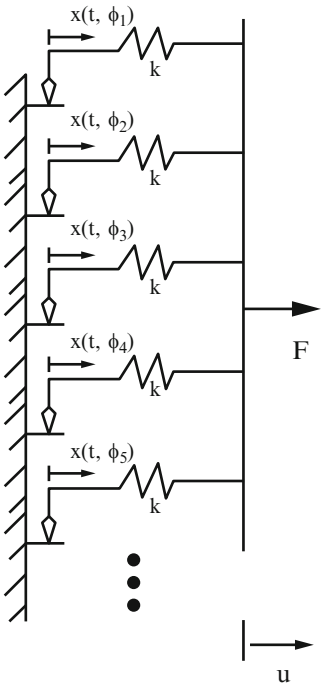

47.2.3 Iwan Element

The Iwan element is a more complex joint model involving multiple Jenkins elements connected in parallel, see Fig. 47.3 [8]. Specifically, assuming a continuous distribution of them, the total force in the element corresponding to a displacement x is

$$F(t) = \int_0^\infty \rho(\phi)(u(t) - x(t,\phi))d\phi, \tag{47.1}$$

where the distribution of sliders, ρ, is given by

$$\rho(\phi) = R\phi^\chi[H(\phi) - H(\phi - \phi_{max})] + S\delta(\phi - \phi_{max}) \tag{47.2}$$

for the particular case of the 4-parameter model [8]. In the above equation, H is the Heavyside (step) function and $\delta()$ is the Dirac-delta function while R, χ, ϕ_{max}, and S are the parameters of the model. The latter two specify the macroslip limit $\phi = \phi_{max}$ with S denoting the number of sliders slipping at that level. The parameters R, ϕ_{max}, and S are usually converted to another set of more physical parameters that can be determined experimentally. They are F_s, K_T, and β (see [8] for relations). Specifically, F_s is the force at which macroslip occurs and K_T is the interface stiffness of the joint. Note that χ characterizes the change in energy dissipation vs. amplitude.

Unlike the single Jenkins element, a microslip region is possible for the Iwan model as each of the sliders has a different threshold at which it transitions from stick to slip. From that standpoint, it is a more desirable phenomenological representation of a joint because microslip is a important phenomenon of jointed interfaces.

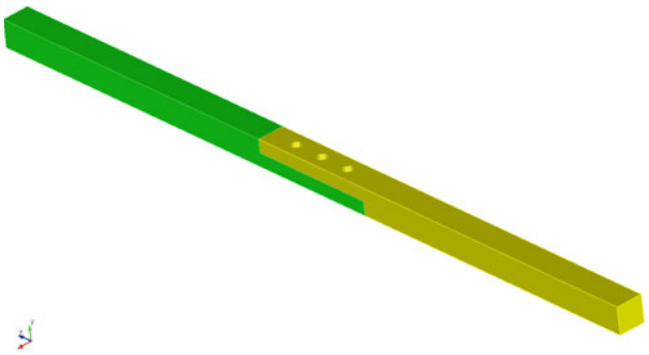

Fig. 47.4 The Brake-Reuß beam

47.3 Experimentation

The main objective of the present effort was to collect a large data set that can be used by other researchers for the development of uncertainty quantification techniques. This data is available to anyone by request to the authors. During the course of this research, three different experimental set-ups were used to (1) determine the Iwan model properties, (2) determine the friction coefficients, and (3) measure the interface profile. Each of these tests is explained separately below.

The test article is the Brake-Reuß beam, a computer rendering of which is shown in Fig. 47.4. The beam consists of two half beams that are cut from a solid beam. These two half beams are connected by three bolts in a lap joint. The model below shows the bolt holes but does not show the holes that are drilled to be attached to a mechanical shaker.

During the testing, a total of six different beams with three different interface surface conditions were used. The first surface condition is the one resulting from the wire cutting procedure, i.e., without any polishing, beams 1 and 2. The other surfaces have prescribed surface conditions with mean asperity heights of 0.8 μm for beams 5 and 6, and 1.6–3.2 μm for beams 3 and 4. These heights are measured as described in the profiling testing section to verify the manufacturing process.

47.3.1 Impact Hammer Testing

The first experiment on this system consists in dynamic impact tests. The impulsive impact force from a hammer is recorded by its load cell and records of acceleration time histories are obtained from the accelerometers mounted on the beam. These time histories are first used to compute the corresponding frequency response function (FRF) for each accelerometer direction and then post-processed to determine the non-linear characteristics of the system, see Sect. 47.4.

47.3.1.1 Experimental Setup

The experimental setup for this test can be seen in Fig. 47.5. The beam is supported near its ends by bungee cords connected to a fixture to emulate a free-free condition [9]. The bolts were torqued to several different values, 3, 5, 7, 10, and 15 Nm, to assess the effect of this preload on the joint behavior. As will be seen, these values lead to a broad range of the first linear natural frequency of the beam which becomes saturated at the higher torque levels.

The magnitude of the impact was also varied leading to maximum input force approximately equal to 100, 800 to 1000, 2000, 4000, and 8000 N. Note that the impact duration was around 1 ms. For impacts with maximum force larger or equal to 2000 N, the beam was thereafter retested at 100 N to assess whether any permanent deformation occurred during the high impact. Note that beams 1 and 5 were the only two impacted at levels corresponding to 4000 and 8000 N maximum forces.

The beams were tested in its two transverse directions denoted as the Z for direction aligned with the axis of the bolt and Y as the direction along the width of the beam. Two accelerometers were used to capture the response of the beam, they were placed equidistantly from the center of the beam, outside of the joint zone.

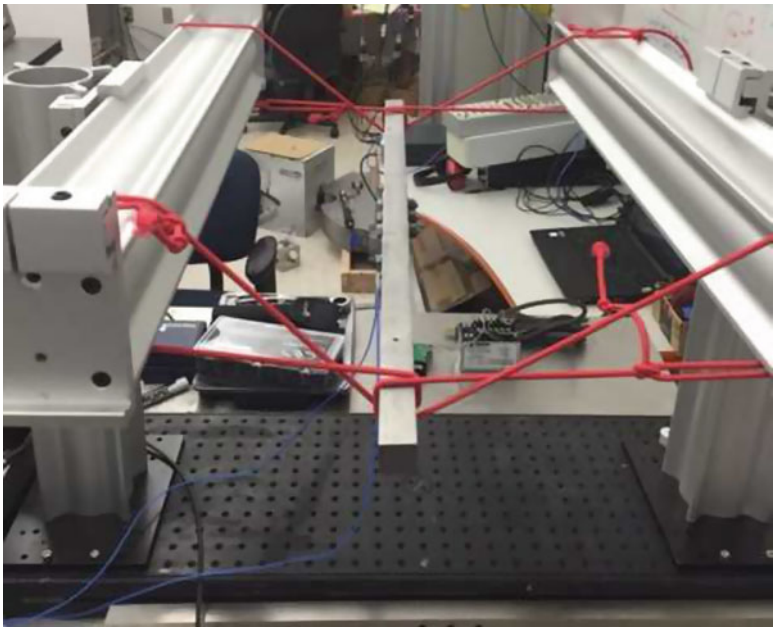

Fig. 47.5 Experimental setup

47.3.1.2 Test Data and Preliminary Analysis

Two types of data are collected during the testing: time history and frequency response. The time history is primarily used to identify the joint model parameters as explained in Sect. 47.4. The frequency response is used to diagnose any problems in the testing. For reference in the ensuing discussion, it was first desired to assess the effects of (1) surface finish, (2) torque level, and (3) impact level on the linear natural frequencies of the beams.

The effects of surface finish were first considered. It was expected that the linear natural frequency would increase as the surface becomes more smooth because there is more surface area in contact which allows for more stiffness in the interface and increases the natural frequency. The linear natural frequencies obtained with an impact level of 100 N and torque level of 3 Nm can be seen in Fig. 47.6. The above expectation is seen to hold overall with beams 1 and 2 of lower frequency than 3, itself of lower frequency than beams 5 and 6. Note the anomalous behavior of beam 4 which has the lowest natural frequency by a substantial amount, around 15 Hz lower. The reasons for this shift are not known but it is surmised that high impact (12, 000 N peak force) pre-testing experimentation generated large residual stresses. The occurrence of such stresses as a result of high impacts is discussed in Sect. 47.5.

Consider next the changes in natural frequency with varying torque level. As it increases, it is expected that the natural frequency would increase as well as the resulting higher pressure at the interface increases the surface contact area. In turn, an increase in surface contact area increases the stiffness of the interface and consequently the natural frequency. This increase can be seen in Fig. 47.7.

Finally, the change in identified natural frequency resulting from an increase in impact force level is assessed. Prior testing of the Brake-Reuß beam [1] showed this beam to have a softening non-linearity. Thus, an increase with impact force level should result in a decrease in natural frequency. This was indeed the observed behavior, see Fig. 47.8.

47.3.2 Profile Testing

A wide variety of factors can influence the dynamic behavior of a joint and have consequently an effect on the parameters deduced for a numerical joint model. Such a factor could be the condition of the beam surface at the interface. Hence, to detect a possible correlation between the surface condition and the joint model parameters, profilometer data is collected and compared for all the different joint interfaces.

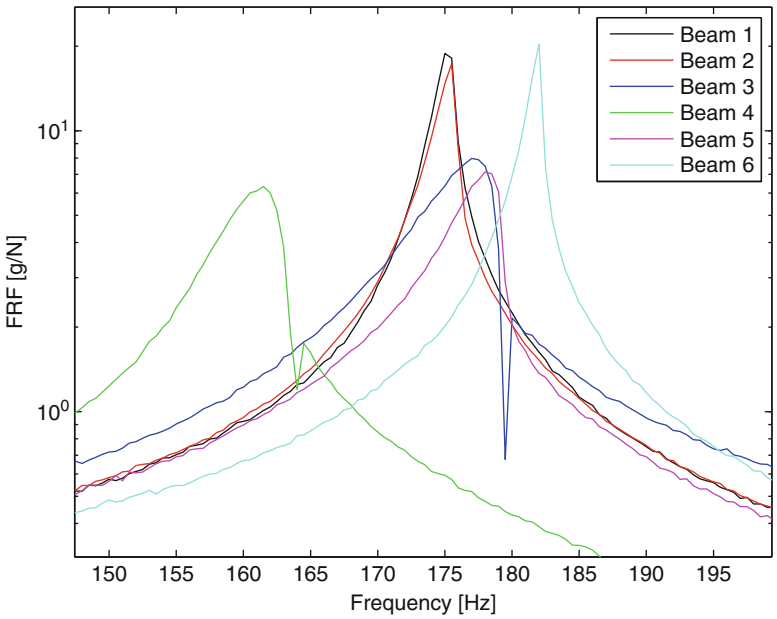

Fig. 47.6 Linear fundamental frequencies of the 6 different beams

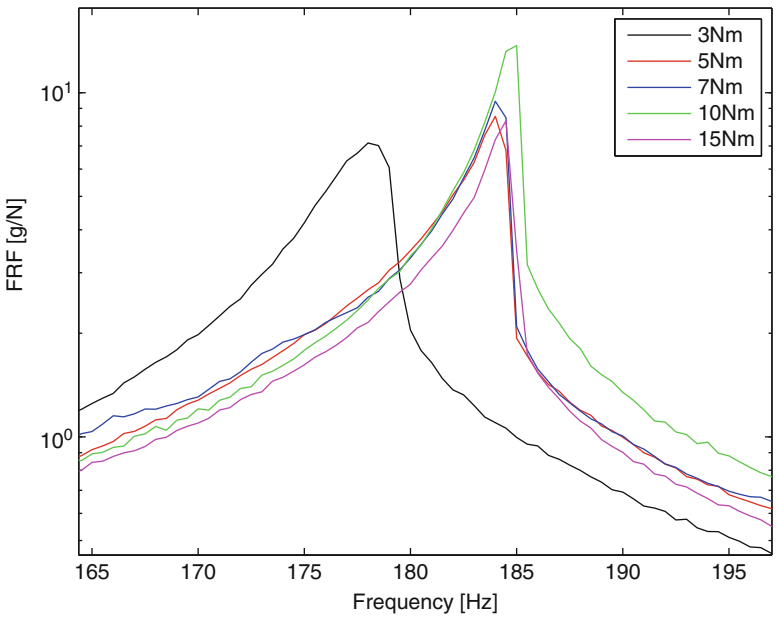

Fig. 47.7 Fundamental frequency of beam 5 as a function of bolt torque

47.3.2.1 Experimental Setup

A Veeco Dektak 150 profilometer is used to carry out the tests. The data is collected by a stationary stylus that has a radius of 12.5 μm and senses the surface with a resolution of 2 μm. To measure the surface condition on the lines depicted in Fig. 47.9, the beam is clamped on a movable disk.

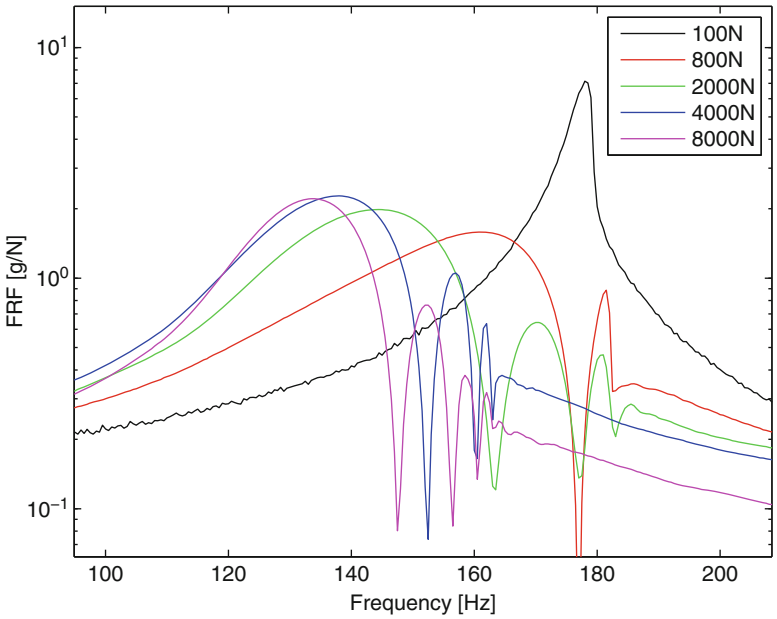

Fig. 47.8 Beam 5 fundamental frequency as a function of maximum input force

Fig. 47.9 Positions of the measurements on the surface

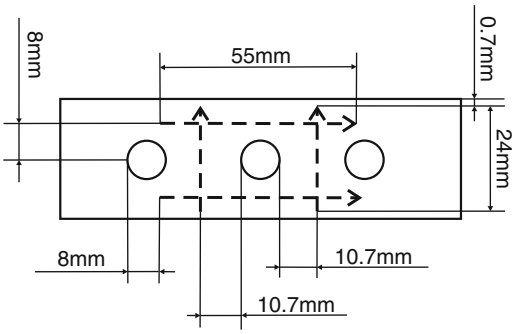

47.3.2.2 Reasoning

The six tested beams can be subdivided into three groups by the treatment of their interface surface. An untreated surface and two increments of polishing. For each of the three groups there are four half beams. The data from all beams are evaluated for roughness and waviness. For beams with different surface treatments, a substantial difference in roughness is expected, whereas the waviness should be fairly similar over all samples.

47.3.2.3 Test Data

Due to the mechanics of the disk and the clamping procedure, the surface is not exactly level when clamped on the disk of the profilometer during the measurement. The data is corrected for this in the first post-processing step. From this raw data the roughness and waviness of the surfaces of each beam are then deduced. The roughness and waviness of all beams can be seen in Figs. 47.10, 47.11, 47.12, 47.13, 47.14, and 47.15.

It can be seen that the waviness is similar for all surfaces within a few micrometers. In the surface of beam 3*a* is a small crack, which leads to the distorted result and the big drop in the waviness of the surface, as seen in Fig. 47.12. The roughness measurements provide some interesting results. Not only is the roughness different between beams with different surface treatments but there are also differences in the roughness values for measurements on the same surface. Beams 1 and 2 are not treated and have therefore the roughest surfaces. The roughness is consistent in longitudinal and perpendicular direction. The polishing of beams 3 and 4 reduces the roughness, however, inconsistencies in the polishing process are causing different roughness values for the longitudinal and perpendicular direction. Beams 5 and 6 are polished even finer. This results in a

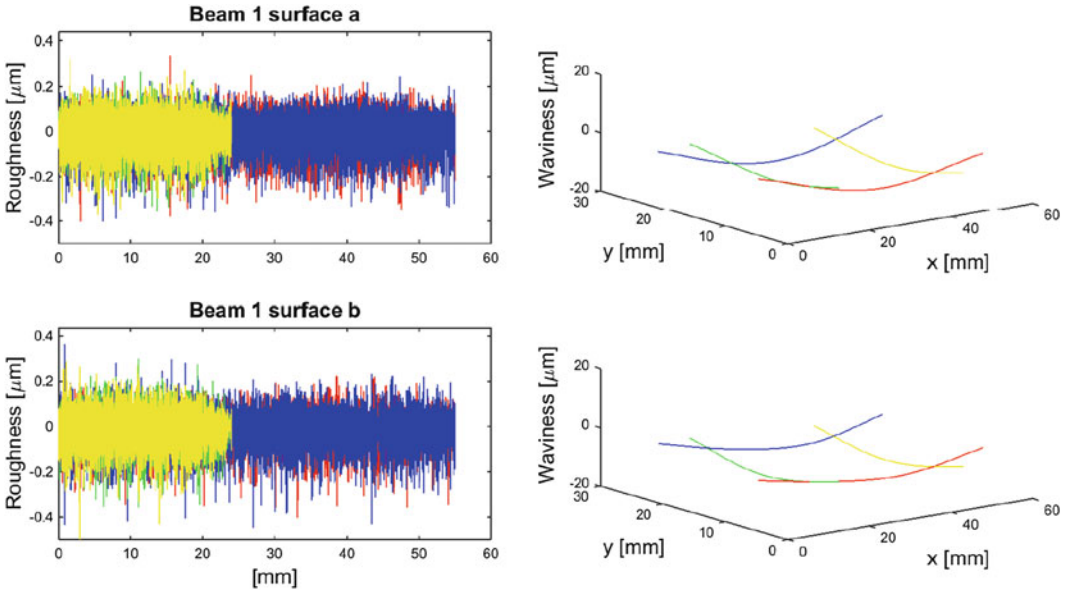

Fig. 47.10 Roughness and waviness of the two surfaces of beam 1

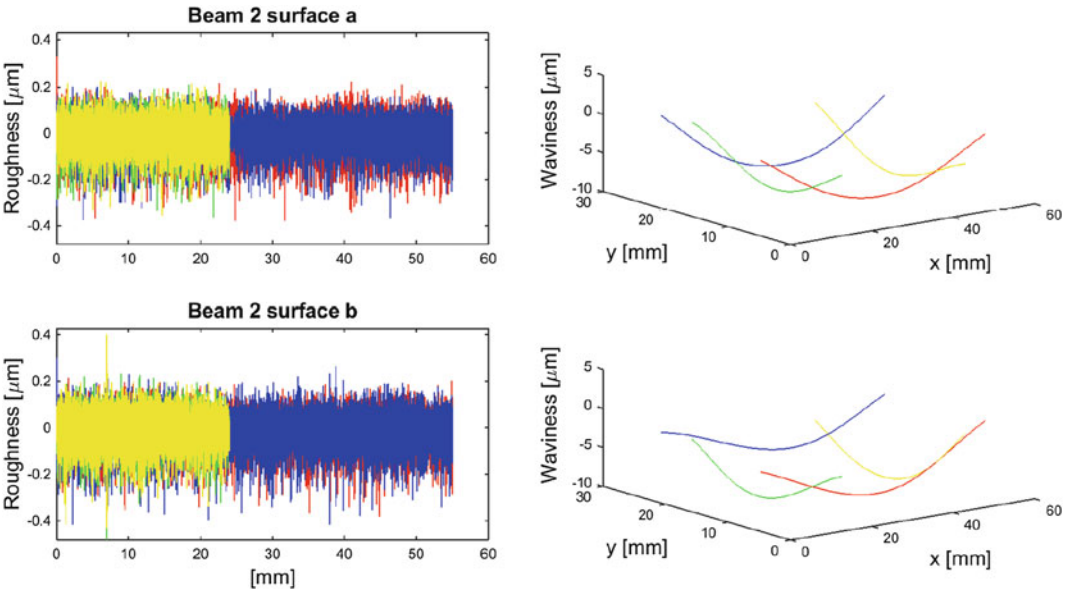

Fig. 47.11 Roughness and waviness of the two surfaces of beam 2

further decrease of roughness. A similar effect to the one observed for the roughness of beam 3 and 4 can be seen on beam 5*a*. The roughness is different in longitudinal and perpendicular direction. In contrary to beam 3 and 4, for beam 5*a* the roughness in longitudinal direction is higher.

This data shows just how important manufacturing techniques are, and how sensitive a system can be due to small changes. Just by having a slightly smoother surface, the entire dynamics of a jointed structure are subject to change and can behave differently. Therefore, it is always important to understand the entire system and be able to account for all sources of uncertainty.

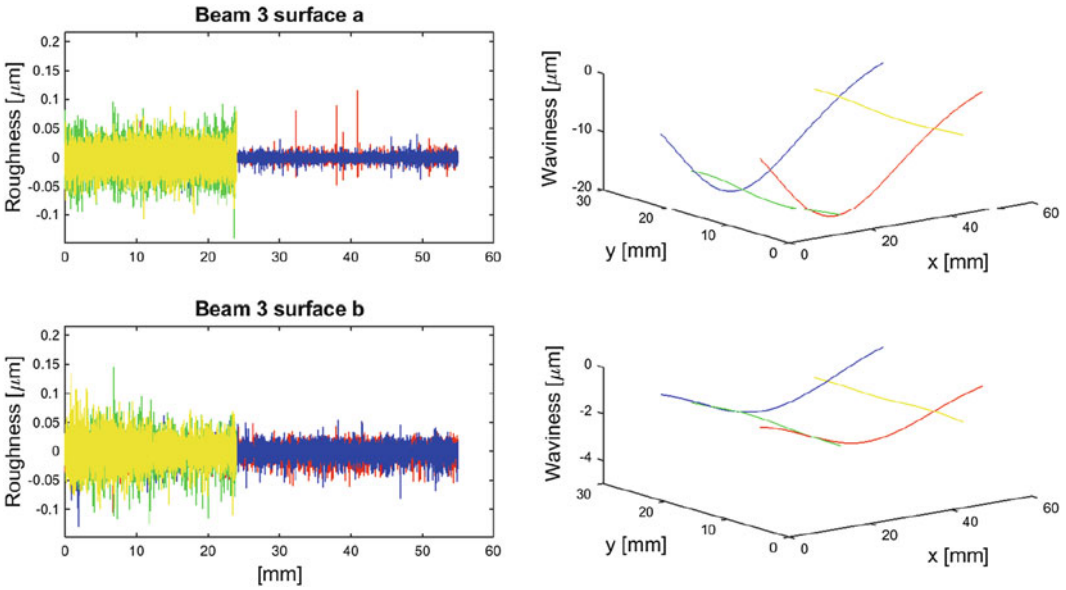

Fig. 47.12 Roughness and waviness of the two surfaces of beam 3

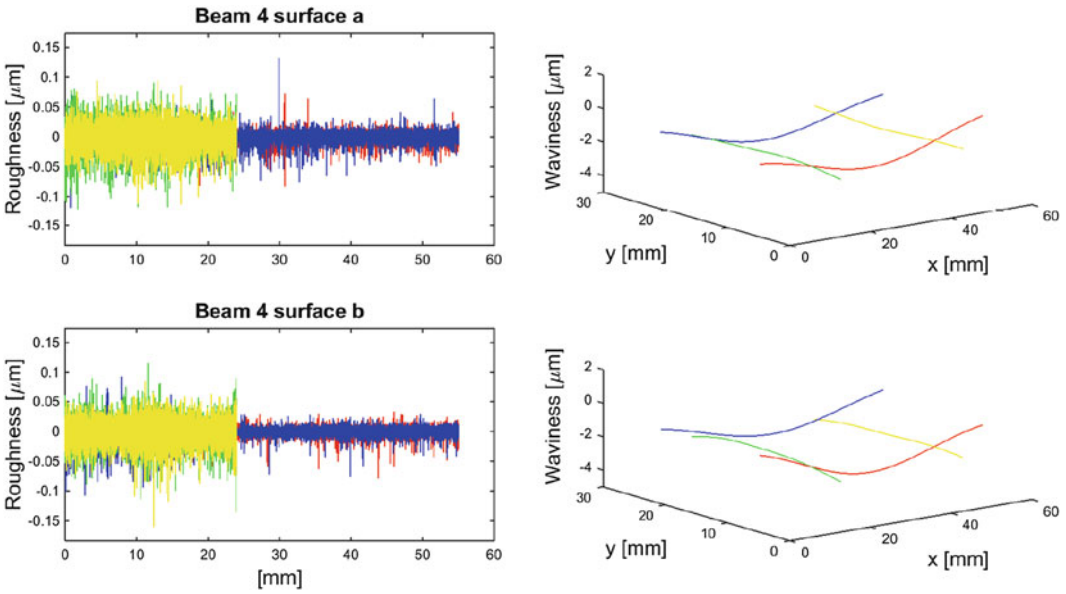

Fig. 47.13 Roughness and waviness of the two surfaces of beam 4

47.4 Joint Model Parameter Estimation

As stated in the Introduction, the objective of the present investigation was to collect joint response data appropriate to carry an ensuing identification yielding non-linear joint model parameters. This last effort is demonstrated here on the impact response data of Sect. 3.1 and the parameters of the modal formulation of the Iwan model [2] are obtained.

In carrying out this identification, it is important to recognize the physical bounds on the parameters. In particular, note that K_t, F_s, β, all belong to $(0, inf)$ while χ is in the domain $[-1, 0]$ with -1 corresponding to a purely linear system.

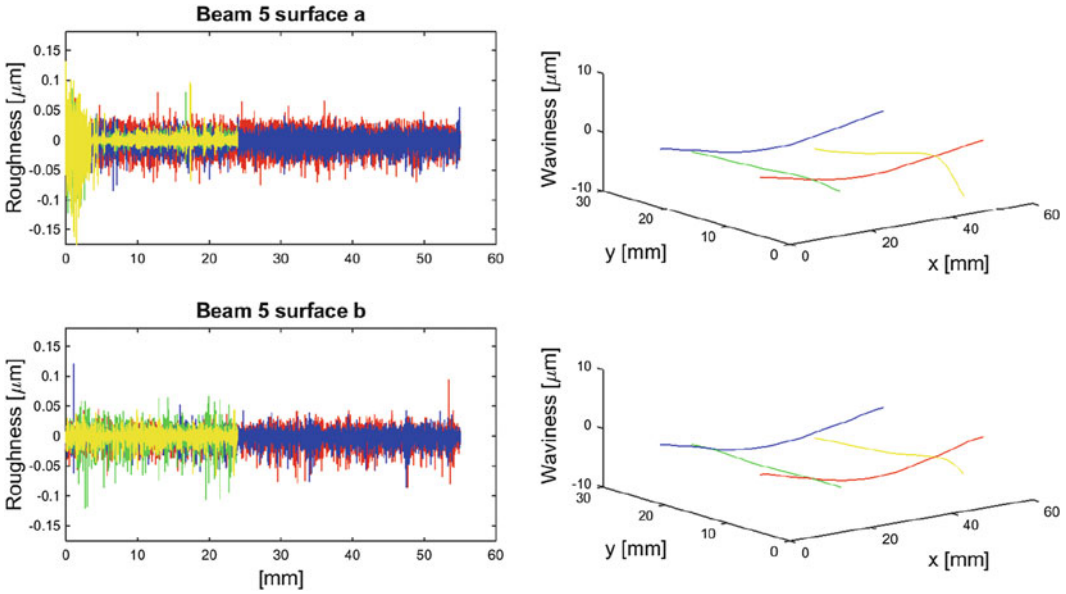

Fig. 47.14 Roughness and waviness of the two surfaces of beam 5

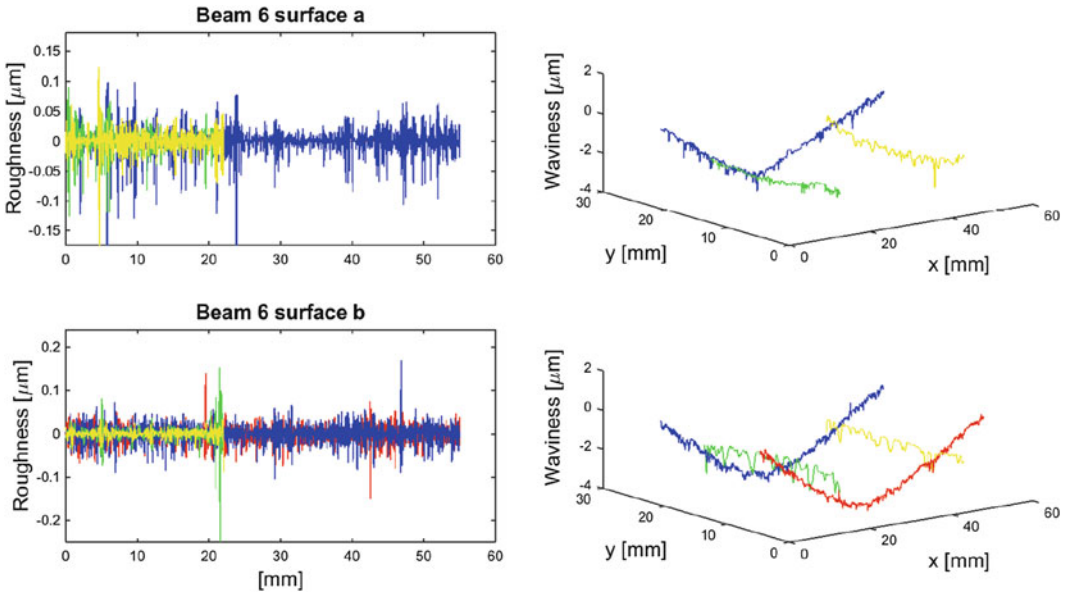

Fig. 47.15 Roughness and waviness of the two surfaces of beam 6

47.4.1 Theory and Background

The four parameter Iwan [8], see Sect. 2.3, was originally proposed to characterize a physical joint in terms of the force it carries and physical slip displacements it exhibits. However, it has recently been proposed as a modal representation of the joint(s) relating the modal force and corresponding generalized coordinate [2]. The same four parameters are used in both physical and modal representation but have different units.

The measurements used here are the time histories of the beam response (accelerations) to the impact at the accelerometer locations. These time histories exhibit non-linear effects at low time, when the system is in macro or microslip, and becomes the response of a linear system as the time increases. The proposed analysis method of the acceleration data uses a combination of techniques [2]. The first step in the analysis is to decimate the time history to reduce the measurement error when the signal is close to zero and the system is not moving. After the signal is decimated, a band pass filter is applied to it to isolate the desired system resonance. This is an important step in the modal Iwan formulation to effectively reduce

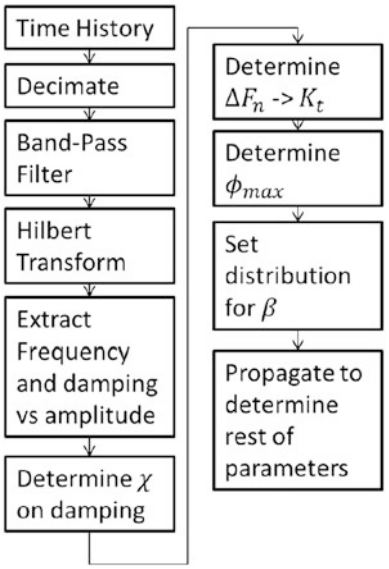

Fig. 47.16 Non-linear parameter estimation process

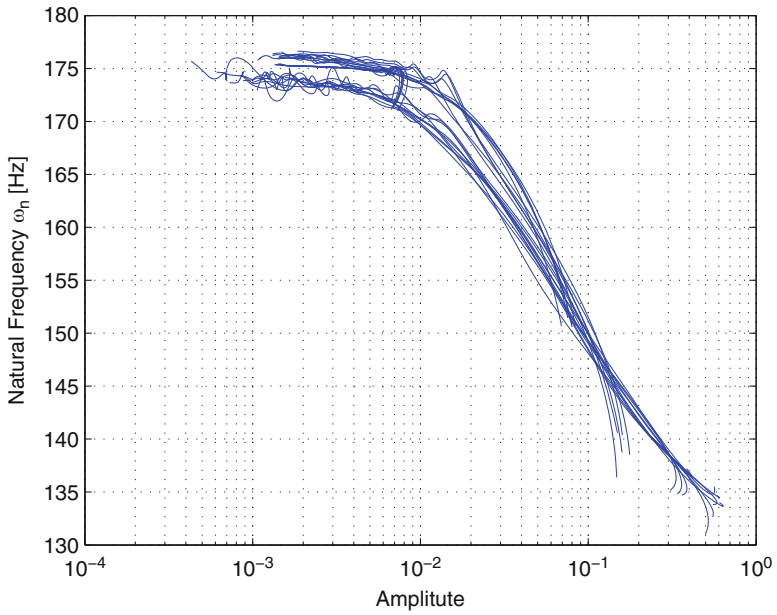

Fig. 47.17 3 NM torque natural frequency vs. amplitude

the system to a single degree of freedom model. Once the band pass filter is applied, the Hilbert transform is performed on the treated time history. This transform is utilized to get the frequency and damping of the signal as a function of amplitude which is the primary data used to determine the model Iwan joint parameters. The steps of the process are highlighted in the flowchart of Fig. 47.16.

The results of this process are shown in Figs. 47.17, 47.18 for beam 1 with a bolt torque of 3 Nm. It is seen that the frequency of the response decreases with increasing modal amplitude consistently with the previously observed softening behavior. In fact, these results match those obtained in the previous experiments reported in [1]. The damping plot, Fig. 47.18, exhibit three different regions: linear damping, microslip, and macroslip zones. In the linear range, i.e., for amplitudes below 10^{-2}, the damping is constant and small, which is highly affected by the Hilbert transform noise. The microslip region extends from an amplitude of 10^{-2} till 7×10^{-2} and is characterized by a linear increase of the damping in a log-log plot. The slope of this line is related to χ as will be seen below. Finally, in the macroslip region, for amplitudes higher than 7×10^{-2}, the damping is a quadratic function of amplitude. From Fig. 47.18, it is concluded that the joint experienced macroslip during the testing.

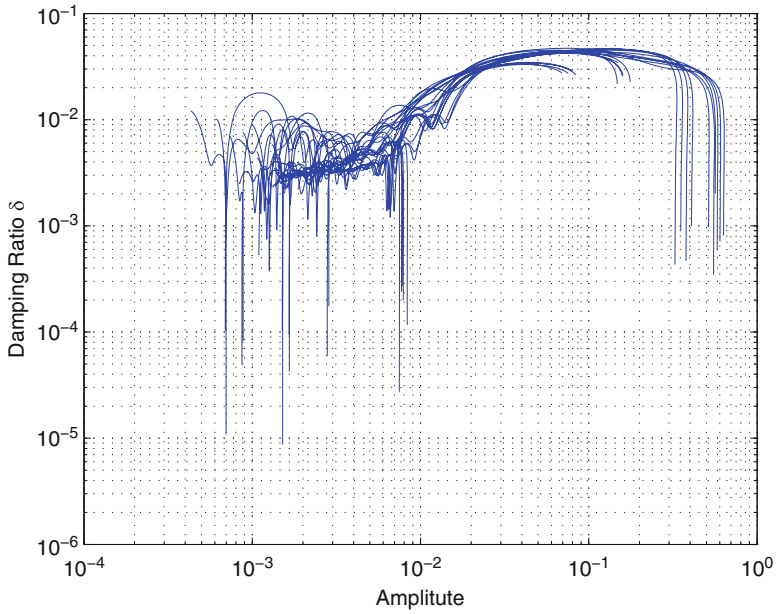

Fig. 47.18 3 NM torque damping ratio vs. amplitude

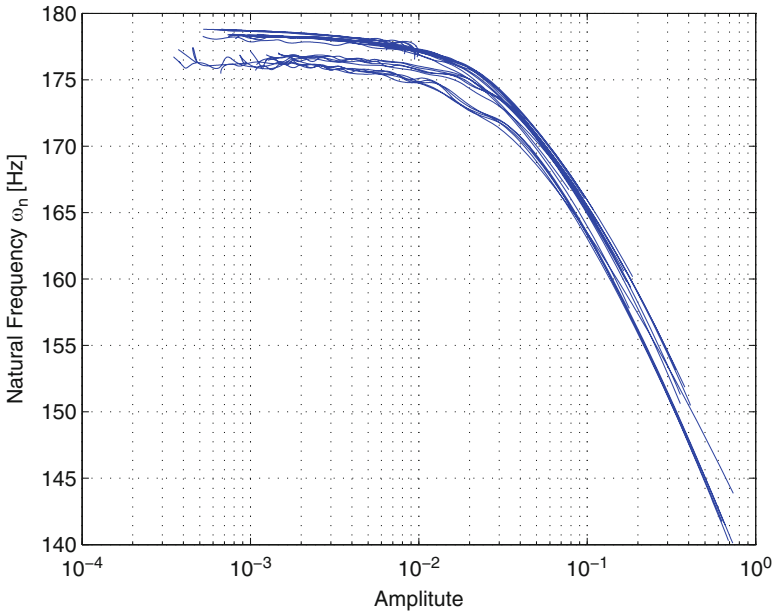

Fig. 47.19 15 NM torque natural frequency vs. amplitude

Consider next Figs. 47.19, 47.20 which present frequency and damping vs. amplitude from the Hilbert transform for beam 1 with a bolt torque of 15 Nm. Comparing these figures with Figs. 47.17, 47.18, 47.19, and 47.18, it is first confirmed that the increase in torque renders the joint stiffer but also more linear, i.e., the linear range of the damping extends further and macroslip does not appear to have occurred. Finally, note from Fig. 47.19 that the decrease in the natural frequency is linear with respect to the amplitude.

Note in Figs. 47.17, 47.18, 47.19, and 47.20 that the multiple curves shown correspond to different repeats of the same condition. Their clustering shows the repeatability of the experimental techniques. Note as well the consistency of the frequency and damping vs. amplitudes curves obtained from high and low torque levels results suggesting the applicability of the Hilbert transform in a broad set of conditions.

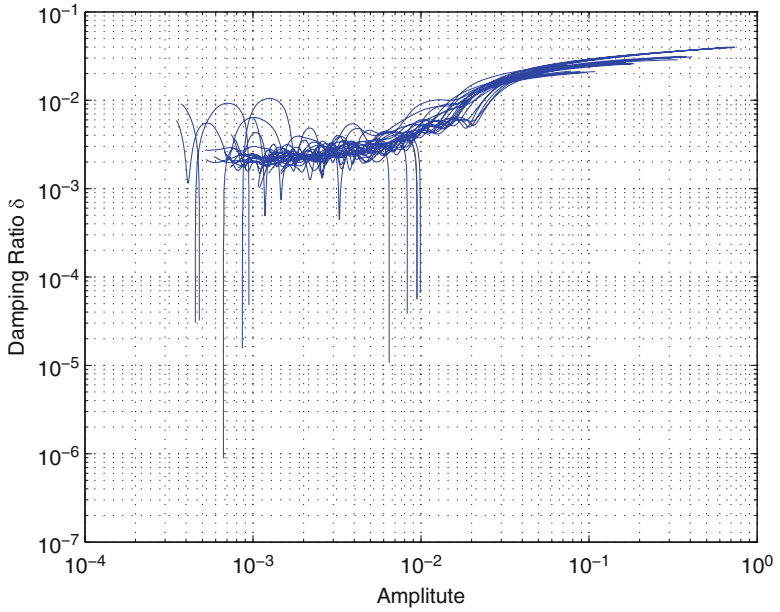

Fig. 47.20 15 NM torque damping ratio vs. amplitude

47.4.2 Parameter Distributions

Three of the modal Iwan parameters can be determined from the frequency and damping vs. amplitudes curves shown above. The first such parameter is χ. Specifically, it can be obtained from the slope of the damping vs. amplitude curve in the microslip regime [8] as

$$\chi = slope - 1. \tag{47.3}$$

The slope was determined by a simple linear least squares fit. The many repeats that were recorded can be used to obtain not only a typical value for χ but also to estimate the variability (or uncertainty) of this parameter. With 25 data points, it is not possible to construct a probability density function using standard nonparametric methods (i.e., histograms) but given the range of χ, i.e., $[-1, 0]$, it is suggested here that it may be modeled by a Beta distribution. In order to chose a distribution for this value, a parametric approach is used since there is 25 data points that is unable to determine a full probability density function. The distribution chosen for this parameter is a beta distribution yielding the model

$$\chi \sim \beta(a, b) - 1, \tag{47.4}$$

where $\beta(a, b)$ denotes a standard Beta distributed random variables with parameters a and b (referred to as hyper-parameters).

The remaining two parameters of the modal Iwan model are determined from the frequency vs. amplitude curves. Specifically, ϕ_{max} is the modal amplitude at which macroslip is expected to occur. This event triggers a rapid change of frequency and thus ϕ_{max} would be determined from such a change. Figures 47.17 and 47.19 shows a fast but gradual change and thus the above condition to determine ϕ_{max} must be accordingly amended. The zone of frequencies in which it varies rapidly is first identified as follows. Its upper limit is the frequency equal to 99 % of the maximum frequency observed while the lower limit is 101 % of the minimum frequency observed. The average of these frequencies is assumed to give the frequency at macroslip and thus ϕ_{max} is read as the corresponding amplitude. Again, the multiple repeats allow the possibility for a probabilistic modeling of this parameter. As it is positive, a Gamma distribution was assumed as in [5] and fitted to the data.

The last experimentally determined parameter is the joint tangential stiffness K_T, it can be estimated similar to [2] as

$$K_T = \omega_{max}^2 - (\omega_{max} - \Delta\omega)^2, \tag{47.5}$$

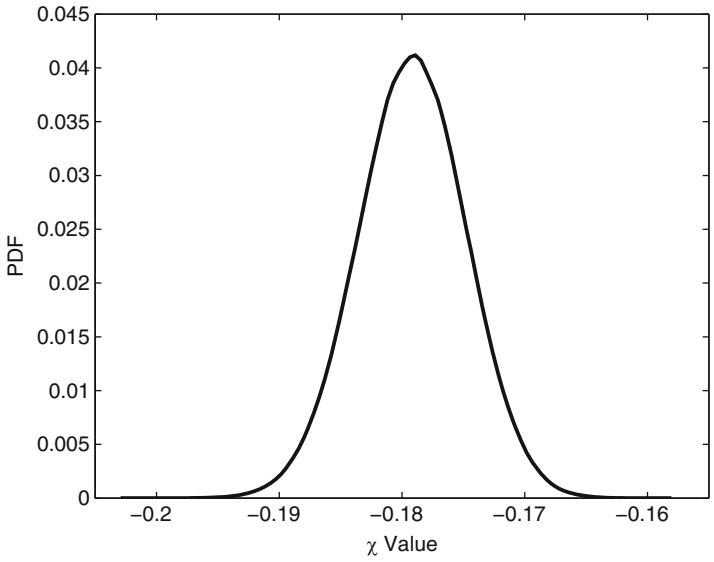

Fig. 47.21 χ distribution

where ω_{max} is the maximum frequency in *radians*/*sec*, and $\Delta\omega$ is the total frequency shift is the difference between the upper and lower limits of the zone of frequency change defined above. Since $\Delta\omega$ uses the data from all impacts, only a single value of it can be determined. Thus, only a nominal value of K_T can be obtained in this manner, otherwise an exponential distribution would be selected as in [5] and fitted to the data. The selection of an exponential distribution utilizes that the stiffness can go to zero that corresponds to complete separation inside the lap joint. While this separation was not realized experimentally, a very small value of stiffness can be realized if the bolt torque is small and the impact is large enough. This outcome would result in complete separation of the beam, which is unable to happen due to the bolts in the joint. A small stiffness would correspond to the response of a test where pinning occurs but before the physical pinning happens.

With the experimental parameters determined, one parameter remains undetermined, β. The β parameter is bounded to be positive but is typically small. To fit the bounds and an expected value, a gamma distribution is given to the β parameter. The hyper-parameters of the β parameter distribution are chosen based on expert knowledge. The four parameters determined are in both the physical and the mathematical formulations of the Iwan model. Three of the parameters are in physical formulation with one in the mathematical formulation. The fourth physical parameter is the force at macroslip F_s. The macroslip force can be determined via

$$F_s = \frac{\phi_{max} K_T (\beta + \frac{\chi+1}{\chi+2})}{1+\beta}. \tag{47.6}$$

Performing a Monte-Carlo analysis yields the distribution of the macroslip force. This method is done for the beam one with a bolt torque of 3 Nm. The distributions of this Monte-Carlo analysis are shown in Figs. 47.21, 47.22, 47.23, and 47.24. The output distribution fits a gamma distribution in both shape and bounds and is shown in Fig. 47.24.

The distribution of the parameters look similar to the distribution at different torque values. The analysis is also run on beam one with a bolt torque of 5 Nm, which is similar to the previous analysis but still show the changes due to a change in bolt torque. The values for the mean and standard deviation of each parameter is shown in Table 47.1. An important relationships that is expected is with the increase in torque, the joint becomes stiffer and more linear. This is denoted by the increase in tangential stiffness and slip force. The linear relation is seen in χ, which is closer to -1 that corresponds to a linear system.

47.5 Plasticity Effects

The impact testing effort began by completing a series of low level impact tests on the beams which behave almost entirely in the linear range, resulting in a first natural frequency around 180 Hz. Once the low level impact tests were completed, higher level ones were performed that showed not only microslip but with definite macroslip as well. In those tests, the natural frequency dropped to around 130 Hz.

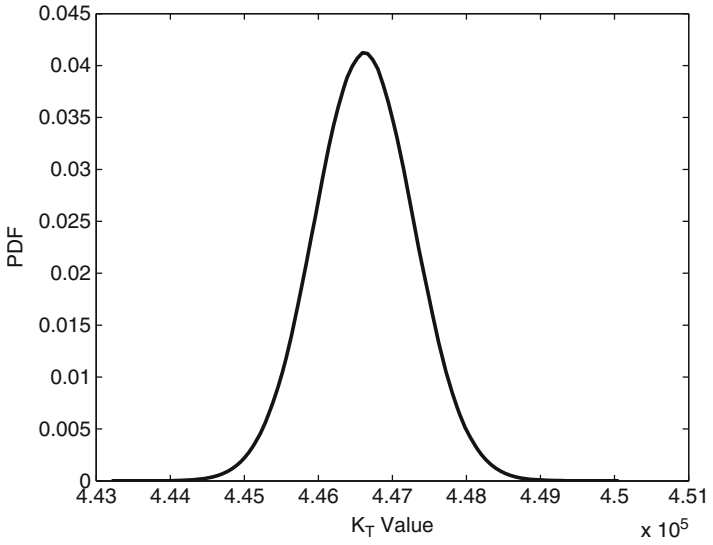

Fig. 47.22 K_T distribution

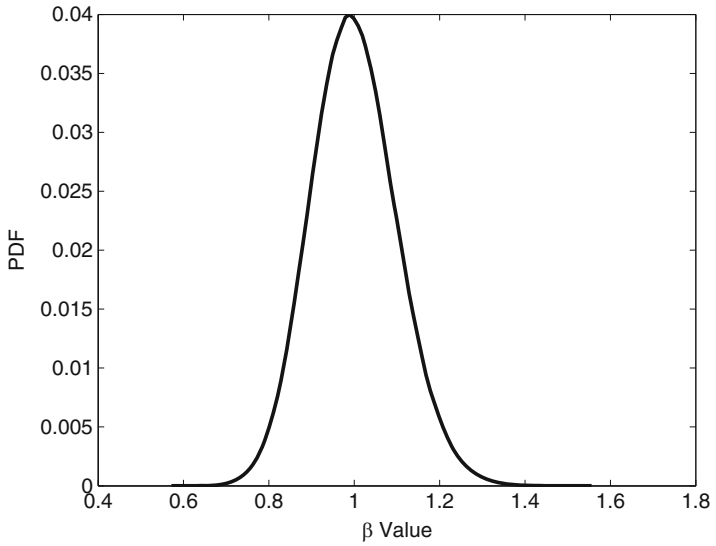

Fig. 47.23 β distribution

Given the magnitude of the drop in frequency, it was decided to repeat low impact level tests to confirm that the large loads had not modified the joint. These tests however did not recover the 180 Hz frequency but rather around 160 Hz. There was thus a permanent loss of stiffness leading to a 20 Hz frequency drop. Figure 47.25 shows frequency response functions before and after the high level impacts and the frequency shift.

To understand the reasons for the change in joint behavior, disassembly and reassembly was first performed to check for loose connections but the natural frequency remained in the neighborhood of 160 Hz. Next, a close inspection of the surfaces was undertaken to check for defects and this effort revealed the pair of markings seen on Fig. 47.26. It is construed that plastic deformations have occurred in that zone thus irreversibly changing the joint.

Likely related to the damage of Fig. 47.26, an unusual behavior of beams 3 and 4 was observed after the high level impacts were completed. Specifically, it was found that their natural frequencies decrease with increasing torque level at the contrary of both physical expectations (see above for discussion) and findings on other beams, compare Figs. 47.27 and 47.28. The mechanics of this observation is not clear that it appears to be an interaction between the stress induced by the bolts and the residual stress distribution resulting from the macroslip event.

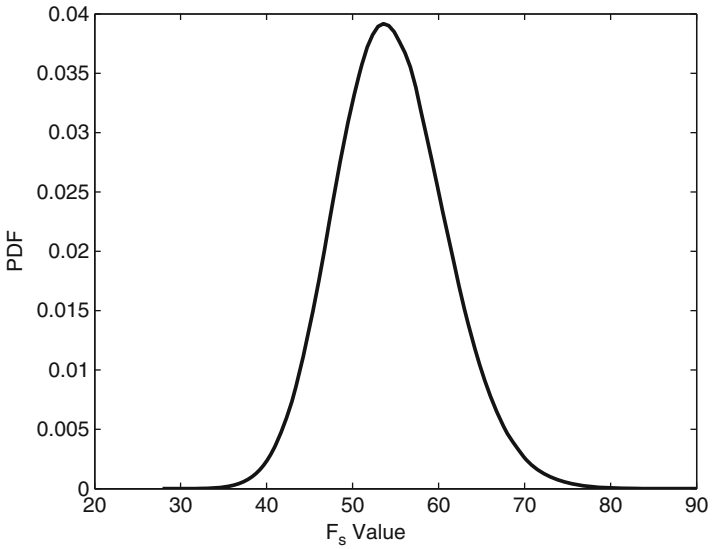

Fig. 47.24 F_s distribution

Table 47.1 Parameters for Beam 1 with 3 and 5 Nm torque

	3 Nm torque		5 Nm torque	
Parameter	Mean	Standard deviation	Mean	Standard deviation
ϕ_{max}	1.68×10^{-4}	1.955×10^{-5}	1.62×10^{-4}	1.01×10^{-5}
K_T	4.47×10^{5}	$\sim$	6.048×10^{5}	$\sim$
χ	-0.179	0.0044	-0.480	0.062
F_s	54.5	6.42	65.8	4.60

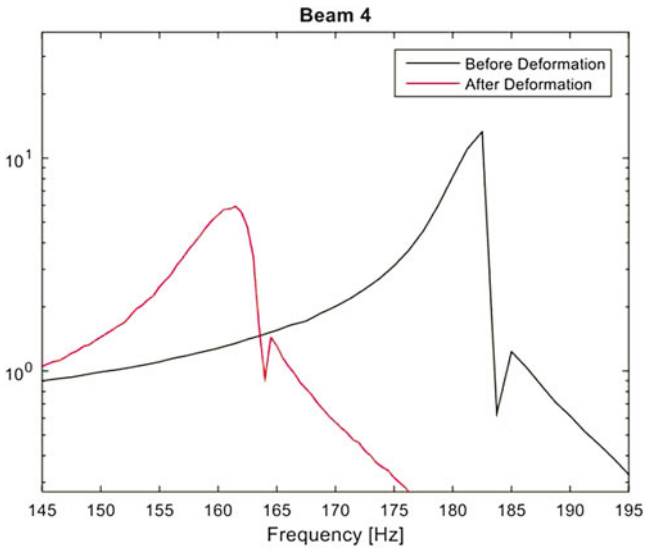

Fig. 47.25 Permanent frequency shift—beam 4

47.6 Conclusions

The present investigation focused on generating, analyzing, and processing free responses, acceleration data more specifically, of the Brake-Reuß beam to assess its potential to determine the parameters of a modal Iwan model of the lap joint. Consideration was also given to developing uncertain models of these parameters.

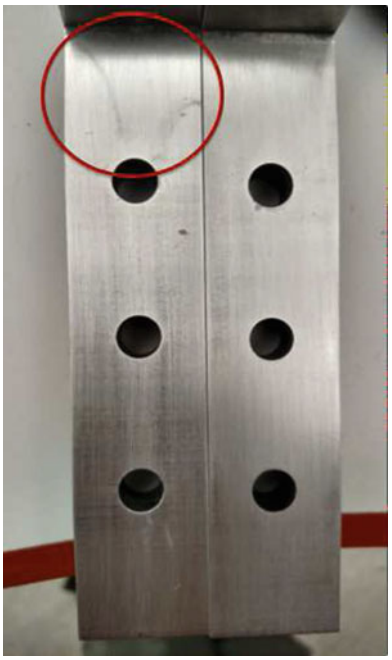

Fig. 47.26 Visible damage in beam 4

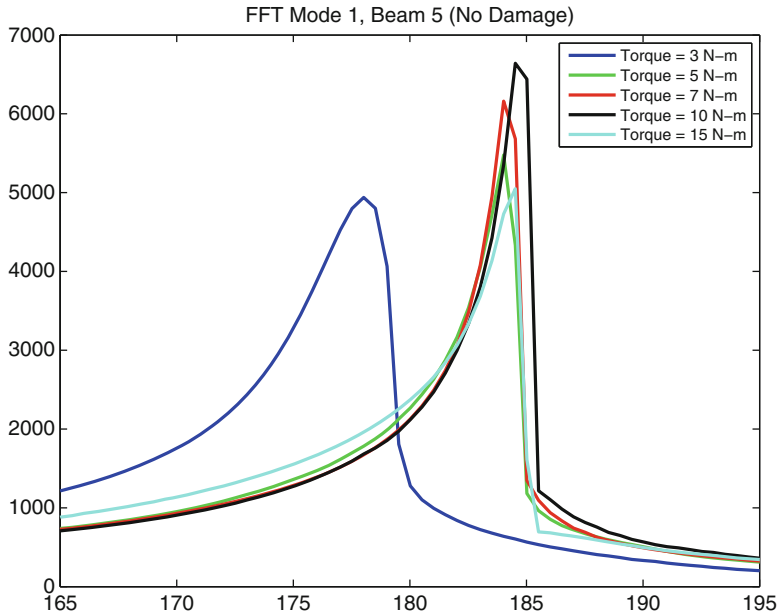

Fig. 47.27 Frequency shift increase due to increased torque—beam 5 (no abnormality)

This effort has demonstrated the application of the Hilbert transform applied as follows on the acceleration data. The time history is first decimated to reduce the measurement error, a bandpass filter is then applied to the signal to isolate a signal resonance, and finally the Hilbert transform is performed on the treated time history. The result of this process are frequency and damping vs. amplitude curves which permit the identification of the parameters of a modal Iwan model as demonstrated. There curves also show the effect of the bolt torque on the joint behavior, i.e., increase in natural frequency, linear limit, and macroslip threshold.

Macroslip is shown to have occurred in some of the tests and it is concluded from ensuing testing that this event changed the nature of the jointed beams. Specifically, the linear natural frequency (observed under very low level impact test) shifted permanently by 20 Hz and, in one case, the linear natural frequency was observed to decrease with increasing bolt torque level in opposition to other beams and physical expectations. An analysis of the joint surface strongly suggest that a significant

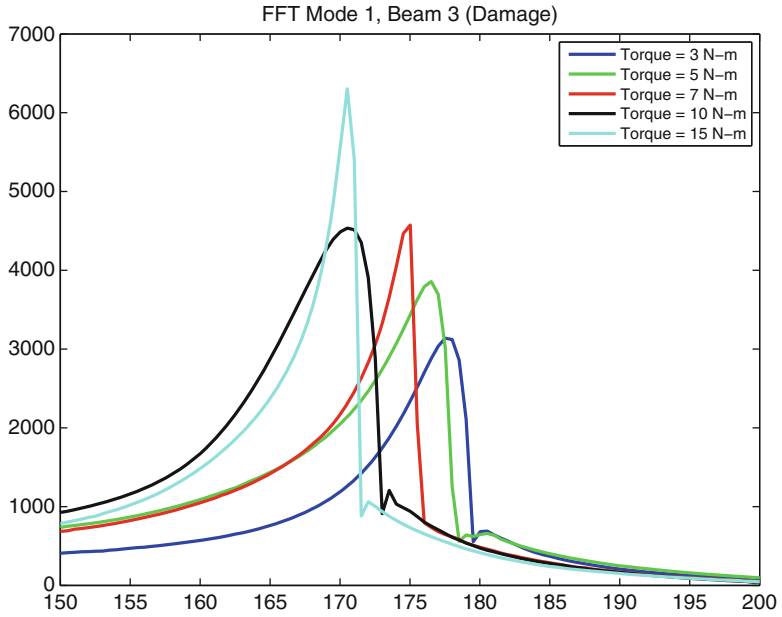

Fig. 47.28 Frequency shift decrease due to increased torque—beam 3 (abnormality)

plastic zone developed during the macroslip phase which induced the above unusual behaviors. This finding suggests that the testing process should be done in increasing impact magnitude to capture the linear zone, then microslip, and finally macroslip with the testing stopped when the linear natural frequency is no longer recovered after a test.

Detailed measurements of the profile of the joint surface was also carried out for the beams tested. This data will be used in the near future with the impact test analyses to develop correlations between state of surface, torque levels, impact levels, and the corresponding modal Iwan parameters to better understand the effects of these conditions on the joint behavior.

References

1. Brake, M.R.W., Reuss, P., Schwingshackl, C.W., Salles, L., Negus, M.E., Peebles, D.E., Mayes, R.L., Bilbao-Ludena, M.S., Bonney, J.C., Catalfamo, S., Gastaldi, C., Gross, J., Lacayo, R.M., Robertson, B.A., Smith, S., Swacek, C., Tiedemann, M.: The 2014 Sandia nonlinear mechanics and dynamics summer research institute. Technical Report SAND2015-1876, Sandia National Laboratories Livermore, CA; Sandia National Laboratories (SNL-NM), Albuquerque, NM, 2015
2. Deaner, B., Allen, M.S., Starr, M.J., Segalman, D.J., Sumali, H.: Application of viscous and Iwan modal damping models to experimental measurements from bolted structures. ASME J. Vib. Accoust. **137** (2015)
3. Gaul, L., Nitsche, R.: The role of friction in mechanical joints. Appl. Mech. Rev. **54**(2), 93–109 (2001)
4. Jenkins, G.M.: Analysis of the stress-strain relationships in reactor grade graphite. Brit. J. Appl. Phys. **13**, 30–32 (1962)
5. Mignolet, M.P., Song, P., Wang, X.Q.: A stochastic Iwan-type model for joint behavior variability modeling. J. Sound Vib. **349**, 189–298 (2015)
6. Robertson, B.A., Bonney, M.S., Gastaldi, C., Brake, M.R.W.: Quantifying epistemic and aleatoric uncertainty in the Ampair 600 wind turbine. In: Proceedings of the 33rd International Modal Analysis Conference (IMAC XXXIII), 2015
7. Segalman, D.J., Gregory, D.L., Starr, M.J., Resor, B.R., Jew, M.D., Lauffer, J.P., Ames, N.M.: Handbook on dynamics of jointed structures. Technical Report SAND2009-4164, Sandia National Laboratories, Albuquerque, NM, 2009
8. Segalman, D.J., Star, M.J.: A four-parameter Iwan model for lap-type joints. ASME J. Appl. Mech. **72**, 752–760 (2005)
9. Smith, S., Bilbao-Ludena, J.C., Catalfamo, S., Brake, M.R.W., Reuss, P., Schwingshackl, C.W.: The effects of boundary conditions, measurement techniques, and excitation type on measurements of the properties of mechanical joints. In: Proceedings of the 33rd International Modal Analysis Conference (IMAC XXXIII), 2015

Chapter 48
Effects of Experimental Methods on the Measurements of a Nonlinear Structure

S. Catalfamo, S.A. Smith, F. Morlock, M.R.W. Brake, P. Reuß, C.W. Schwingshackl, and W.D. Zhu

Abstract This paper continues the investigation from a paper presented at IMAC XXXIII that looked into the influence of various experimental setups on the nonlinear measurements of structures with mechanical joints. The previous study reported how the system stiffness and damping was affected by the force input method, boundary conditions and measurement techniques. However, during the stepped sine excitation experiments the parameters for the control schemes were neglected. In this paper, different control strategies, namely force and acceleration control, are used to observe how the parameters affect the measurements at different levels of excitation. The experiments are conducted on bolted beams containing a lap joint with different boundary conditions. The beams are excited by a shaker using a stepped sine signal using narrow bandwidths around three of the natural frequencies. The results show that acceleration amplitude control can produce cleaner transfer functions compared to the force amplitude control method.

Keywords Bolted joints • Nonlinear vibration • Experimental setup • Measurement effects • Testing guidelines

48.1 Introduction

Measuring the steady state response of nonlinear mechanical systems is a challenging venture since these systems tend to have multiple stable and unstable equilibria in the measured response. These difficulties originate from the fact that the measurements can be sensitive to excitation and initial conditions, and require advanced techniques not typically available in commercial software. Furthermore, recent developments have shown that small differences in the constitutive models can result in a large change in a system's response [1, 2]. In the study of mechanical joints, the lack of understanding of interfacial physics complicates the issue further [3]. In light of these known issues, the question arises: "Can the response of a nonlinear system be measured using linear measurement algorithms, and can the stiffness and damping parameters be extracted when excitation or initial condition parameters change?"

To answer this question, a candidate lap joint system termed the Brake-Reuß beam (BR beam), is proposed [4]. The beam, shown in Fig. 48.1, is designed to contain the nonlinear effects of a lap-joint in a mechanical system using a simple geometry. The joint has a strong effect on the system's transfer function (TF) [4], which is not always discernable [5], making this an ideal system to study.

Sandia National Laboratories is a multi-program laboratory managed and operated by Sandia Corporation, a wholly owned subsidiary of Lockheed Martin Company, for the U.S. Department of Energy's National Nuclear Security Administration under Contract DE-AC04-94AL85000

S. Catalfamo • F. Morlock • P. Reuß
Universität Stuttgart, Keplerstraße 7, 70174 Stuttgart, Germany

S.A. Smith (✉)
Sandia National Laboratories, 1000 Hilltop Circle, Baltimore, MD 21250, USA

Sandia National Laboratories, PO Box 5800, Albuquerque, NM 87185, USA
e-mail: ssmith11@umbc.edu

M.R.W. Brake • W.D. Zhu
Sandia National Laboratories

C.W. Schwingshackl
Imperial College London, London SW7 2AZ, UK

© The Society for Experimental Mechanics, Inc. 2016

M. Allen et al. (eds.), *Dynamics of Coupled Structures, Volume 4*, Conference Proceedings of the Society for Experimental Mechanics Series, DOI 10.1007/978-3-319-29763-7_48

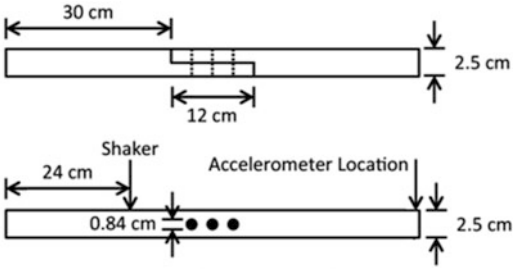

Fig. 48.1 The geometry of the Brake-Reuß beam

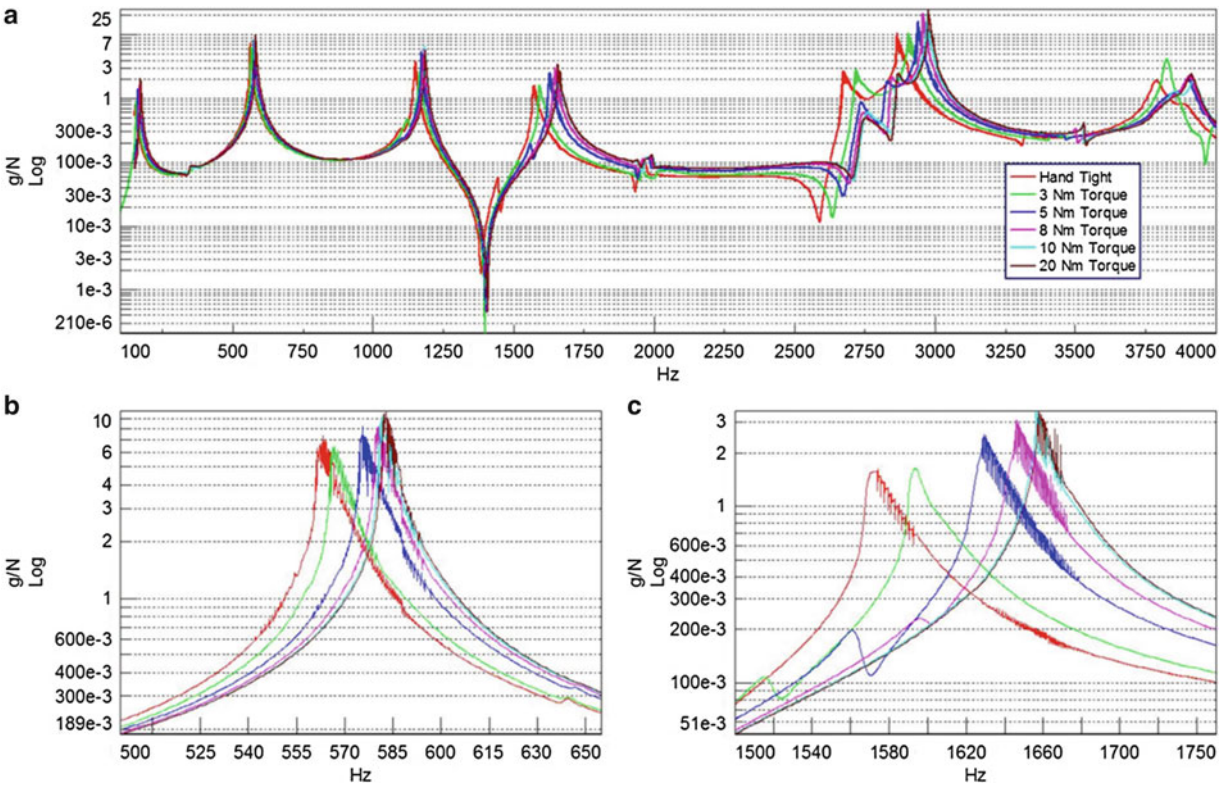

Fig. 48.2 Sample TF of the response measured using force control for (**a**) the entire frequency range, (**b**) the second natural frequency, and (**c**) the fourth natural frequency [6]

In the previous work, a "free-free" boundary condition was extensively studied [6]. A number of variables were found to have little effect on the measured frequency and damping under impact excitation, including stiffness of bungees, length of the bungees, location of the bungees, accelerometer attachment technique, mass of an impact hammer, and sensor cable orientation. A noticeable effect was seen on the torsional modes, likely due to the location or attachment technique of the bungees. Changing the size and number of accelerometers had a large effect on the frequency and damping of the system. To minimize the effects of accelerometer size and number on the response of the system, they should be eliminated or kept small and few. A shaker was then suspended to test the effects of different types of stingers: a Wire, M2 and 10-32 UNF stingers. The tests showed that the 10-32 UNF stinger had the smallest influence on the response of the system. The Wire and M2 stingers had greater influence because the torsional modes where excited. The torsional modes should not have been excited since the stringer was attached along the center of the beam's face in the vertical direction. Once boundary conditions and experimental setup was determined, the TF of the beam was measured using a shaker with a stepped sine signal and a force amplitude control algorithm. The TF of a "free-free" beam using a 1.75 N input force was not smooth, as would be expected for a control test. The issue arose from the control algorithm over correcting the divergence from the control level and not updating the TF to which it was controlling. A sample TF of the response previously measured is shown in Fig. 48.2 [6].

A continuation of the work in [6] is presented here. The only difference between the beam studied in [6] and the current system is the additional holes added for a stinger so that the torsional modes could be excited. Different control strategies for both force and acceleration amplitude control are studied. The experiments are conducted on a BR beam with either a

"free-free" or "fixed-free" boundary conditions, each excited by a shaker. The results of the experimentation are the basis for the recommendations of control parameters for more reliable and repeatable measurements of a mechanical joint.

48.2 Experimental Setups

The work presented is on a "free-free" or "fixed-free" boundary condition. Regardless of the boundary condition, the beam has many common features: the interface of the joint has the same finish level, there are two accelerometers (PCB 356A01 Triaxial accelerometer) attached at the end of the beam opposite the shaker or the "fixed" boundary. Both beams are excited by a Brüel & Kjær Measurement Exciter Type 4809 which is attached to the table via bolts; the shaker is attached using the off-center holes closest to the interface via a short 10-32 UNF barrel stinger. The input force and acceleration are measured by a PCB 208C02 ICP® Force Sensor and a PCB 356A01 Triaxial Accelerometer, respectively. The accelerometer is attached to the beam on the surface opposite the force sensor.

The "free-free" boundary condition is implemented by hanging the beams using 1.2 m of 50 lb fishing line at the ends of the beam approximately 5 cm from the ends of the beam, as shown in Fig. 48.3a. The accelerometers are attached to the end of the beam furthest from the shaker. The "fixed-free" boundary is implemented by epoxying one end of the beam to a $0.127 \times 0.127 \times 0.1524$ m, 20 kg steel block. The steel block is then clamped to the table and the free end of the beam left is unsupported. The shaker is attached using the off-center hole closest to the interface, opposite the steel block, shown in Fig. 48.3b.

The rigidness of the "fixed" boundary is tested by sending a stepped-sine signal ranging from 584.5 to 585.5 Hz through the half-beam with accelerometers (PCB 356A01) attached on the beam near the block and one on the block near the other accelerometer, as shown in Fig. 48.4. The acceleration of the beam compared to the acceleration of the block at 15 and 25 g acceleration input is shown in Fig. 48.5. The results suggest that the boundary is not a true fixed boundary as there is high acceleration on the beam near the block. This high acceleration tells us that the connection to the block behaves more like a pinned joint with translational and rotational springs, and any comparison to a model must take this into account.

The "free-free" boundary condition is used in Sect. 48.3 for the determination of the control parameters. The "fixed-free" is used in Sect. 48.4 to determine if repeatable results can be received using the parameters from Sect. 48.3.

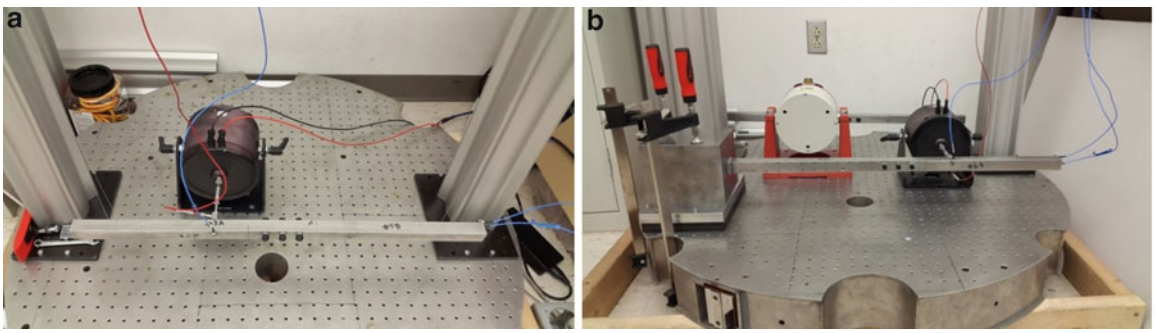

Fig. 48.3 (**a**) "Free-Free" and (**b**) "Fixed-Free" boundary conditions for the BR beam

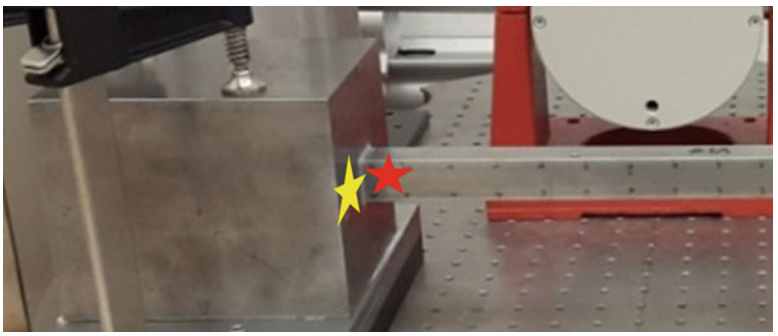

Fig. 48.4 Locations of the accelerometers for testing the rigidness of the "fixed" boundary, the *yellow star* is the location on block, and *red* the location on the beam

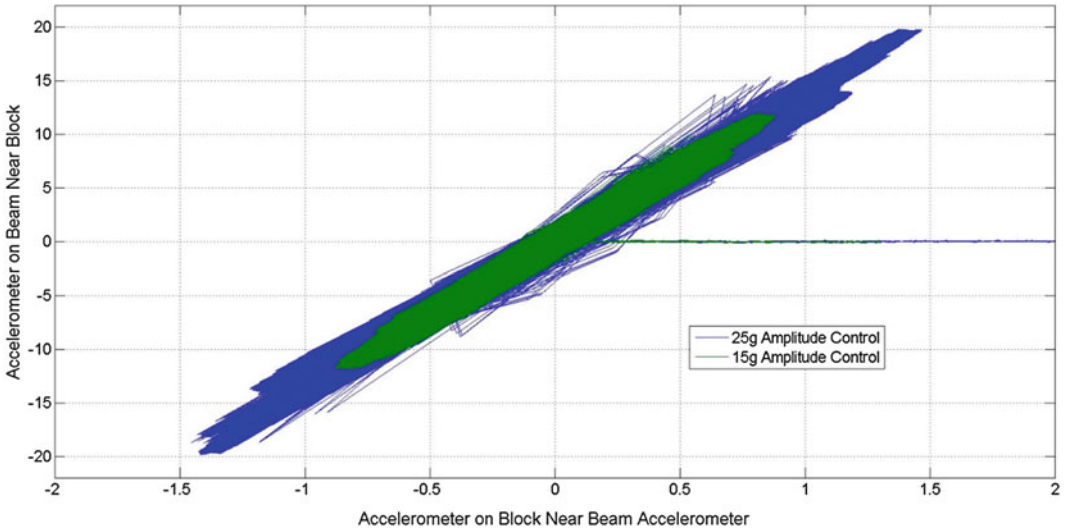

Fig. 48.5 Acceleration on the beam vs. acceleration on the block to test the rigidness of the "fixed" boundary

48.3 Control Parameter

In this section the control parameters used in LMS Test.Lab are studied to reduce/remove the saw tooth effect seen in the previous study [6]. LMS Test.Lab 15A MIMO Sweep & Stepped Sine Testing has five main parameters that affect the measured data. The first parameter is the Confidence in Measured System Frequency Response Function (FRF). Before each test a white noise signal is passed to the system and a FRF of the sensors and voltage output is created. This is what the control algorithm uses to control the output voltage. When the confidence is set to high, the algorithm assumes that the system FRF is correct for all frequencies and output amplitudes; when set to low, the algorithm does a quasi-closed loop control in which it uses the previous measurement as the starting point for controlling. In the results that follow, the low confidence parameter is always used since the nonlinear behavior in the measurements strongly influence the FRF used to control the excitation. Another parameter is the Error Correction Factor (ECF). This factor determines how much the algorithm corrects the divergence from the control band in one frequency step. When this factor is set high, a saw tooth effect may be seen in the input spectrum, resulting in a non-smooth TF. When the factor is set to low, the algorithm may not correct the divergence from the control level enough in a step, resulting in responses that may be outside the control bands and responses not controlled at the desired level.

The third parameter studied is the number of delay cycles. This is the number of cycles that the system will hold at a frequency before it starts taking a measurement; a high number would ensure that the results reach steady state, but this increases the amount of time needed to run the test. Setting this value too low could result in poor estimation of the TF since the response may not be at steady state. The fourth parameter is the number of hold cycles, which is the number of cycles that the algorithm controls at a given frequency before taking a measurement. A high number of cycles would ensure that the steady state response has less aliasing due to more averaging, but this increases the amount of time needed to run the test. Setting this value to low could result in poor estimation of the TF due to aliasing caused by the acquisition system's sampling frequency. The last parameter is the step size which determines the resolution of the TF. A large step-size may result in a large change in amplitude which is hard for the control algorithm to correctly predict, and a small step gives better frequency resolution but requires an increased amount of time needed to run an experiment.

Each of these parameters are listed below in Table 48.1. The parameters used for the stepped sine testing in the previous 2014 study [6] are given in the first column. These parameters were the default in LMS and no attempt was made to find the optimal settings. The second column is the combination of parameters that were used at the onset of this testing. The only two parameters varied during these tests are the ECF and number of hold cycles. All of the tests were run with the confidence parameter set to low, the number of delay cycles at 30, and a 0.05 Hz step size. The third column shows the recommended settings based on the results presented later in this Section.

The measurements were taken from the "free-free" boundary conditions with a 10 Nm torque applied to the bolts. Utilizing a 5 N force amplitude control, different values of the ECF is compared using a stepped-sine test from 570–580 to 1176–1184 Hz with 40 hold cycles. The results shown in Fig. 48.6 compare the measurements either stepping the signal up

Table 48.1 Control parameters used in control study

Control parameters	2014	2015	Optimal
Confidence in measured system FRF	High	Low	Low
Error correction factor	100 %	Vary	60 %
Number of delay cycles	1	30	30
Number of hold cycles	15	Vary	40
Step size	0.1 Hz	0.05 Hz	0.05 Hz

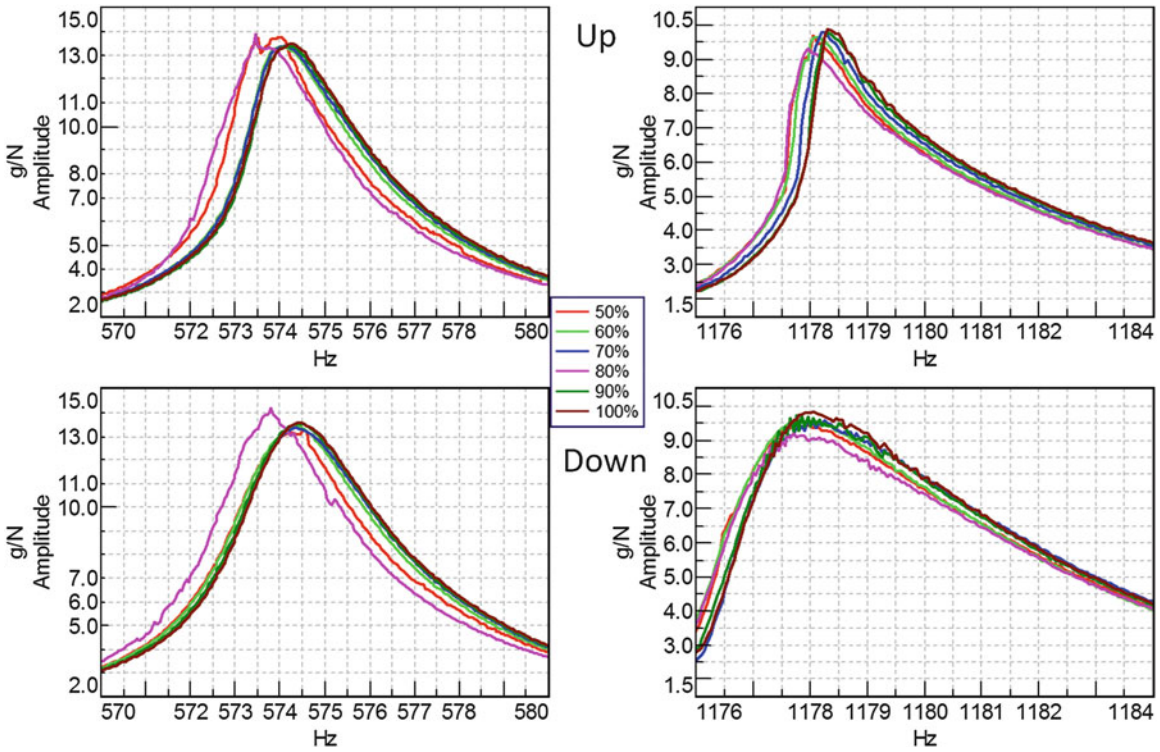

Fig. 48.6 FRFs of 5 N force control to locate optimal ECF; (*top row*) sweep up, (*bottom row*) sweep down

(top row) or down (bottom row) through the frequency ranges defined. An ECF of 60 % is the best balance of speed and accuracy for the control algorithm (these test took approximately 5 min). When the value is higher than 60 % the TF starts to get a saw tooth look; while below 60 % resulted in the algorithm not correcting the error in the amplitude towards the desired level.

Once the optimal ECF was determined the number of hold cycles using the same parameters was tested, shown in Fig. 48.7. The test was run with 5, 10, 20, 40, and 60 hold cycles. From Fig. 48.7 it is seen that the 40 and 60 hold cycles produced the smoothest TFs. Forty hold cycles though is better for testing because increasing to 60 cycles nearly doubled the amount of time a test took.

The same tests were run using 10 g acceleration amplitude control; the results are shown in Figs. 48.8 and 48.9. The parameter tests for both force amplitude and acceleration amplitude control show that an ECF of 60 % and 40 hold cycles are the optimal settings, and are listed in Table 48.1. Figures 48.6, 48.7, 48.8, and 48.9 show that the force control has more of a saw tooth response than the acceleration control. The effect could be from how fast the force amplitude drops at resonance, which requires the control to quickly put out more voltage to keep the same force level. While in acceleration control the amplitude increases quickly, however the control can more easily decrease the voltage which reduces the amount of saw tooth like effects in the signals.

The TF and time signals of the system using the parameters from the previous and the optimal parameters are compared under a 10 g acceleration amplitude control in Fig. 48.10. The comparison of the TFs (top row) shows that the optimal parameters removed the saw tooth effect seen in the previous study. As a result of using the optimal parameters the amount of time (bottom row) required to run a test increases; however, the acceleration was controlled to the level specified very well.

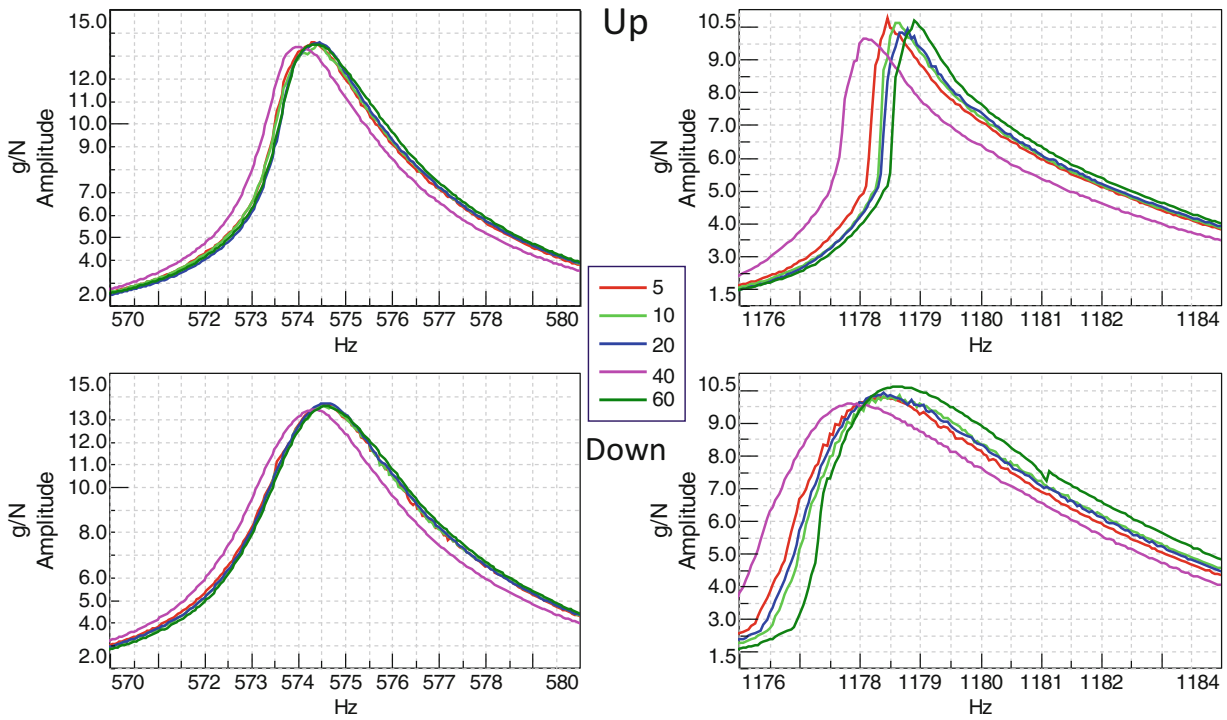

Fig. 48.7 FRFs of 5 N force control to locate optimal number of hold cycles; (*top row*) sweep up, (*bottom row*) sweep down

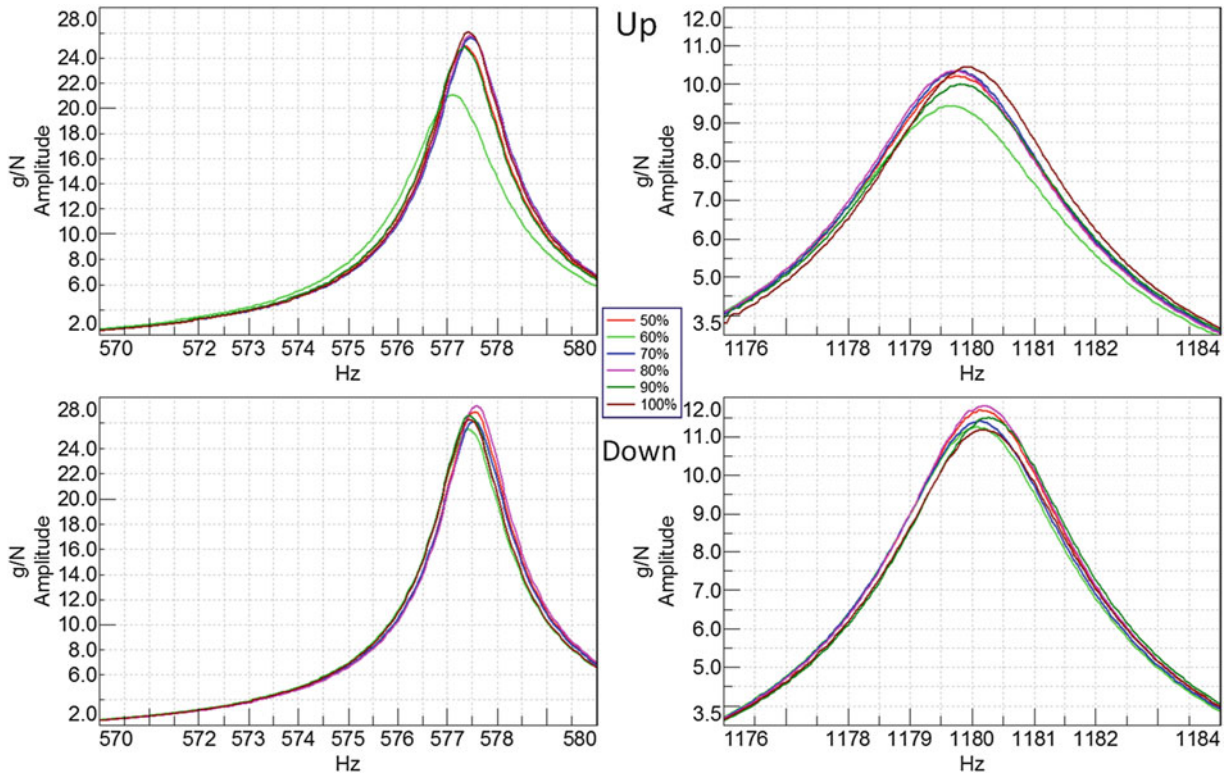

Fig. 48.8 FRFs of 10 g acceleration control to locate optimal ECF; (*top row*) sweep up, (*bottom row*) sweep down

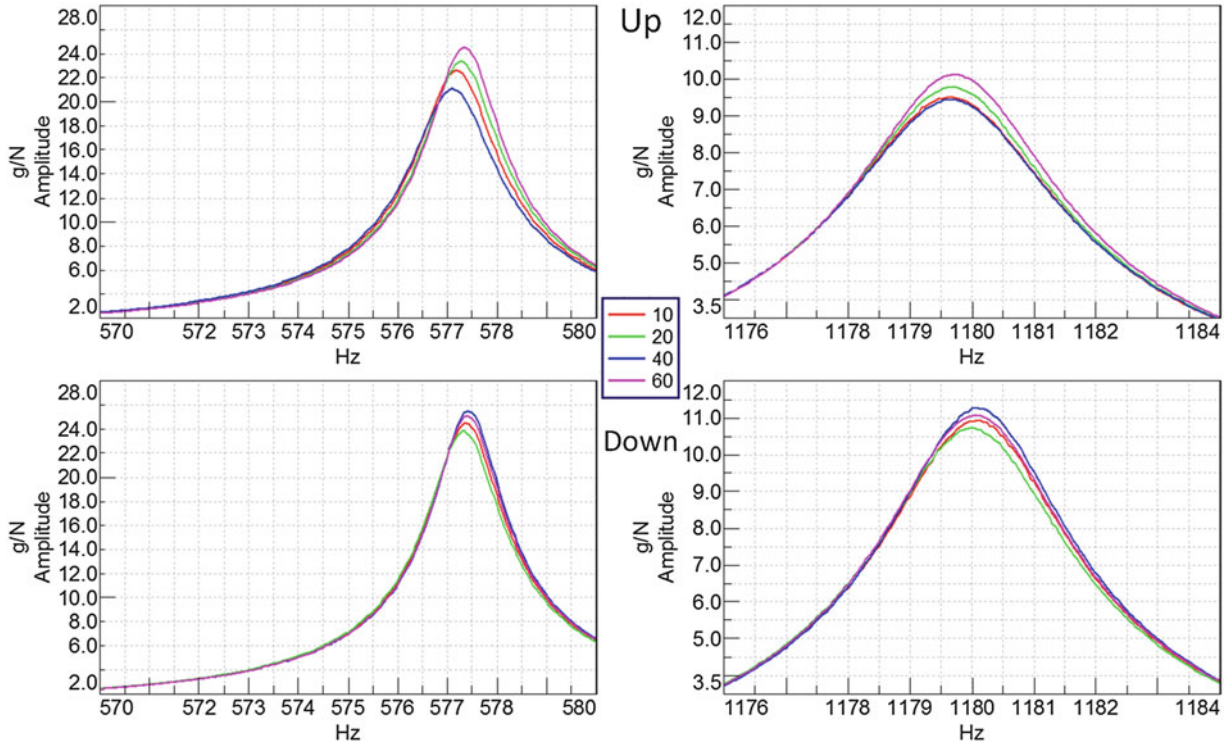

Fig. 48.9 FRFs of 10 g acceleration control to locate optimal number of hold cycles; (*top row*) sweep up, (*bottom row*) sweep down

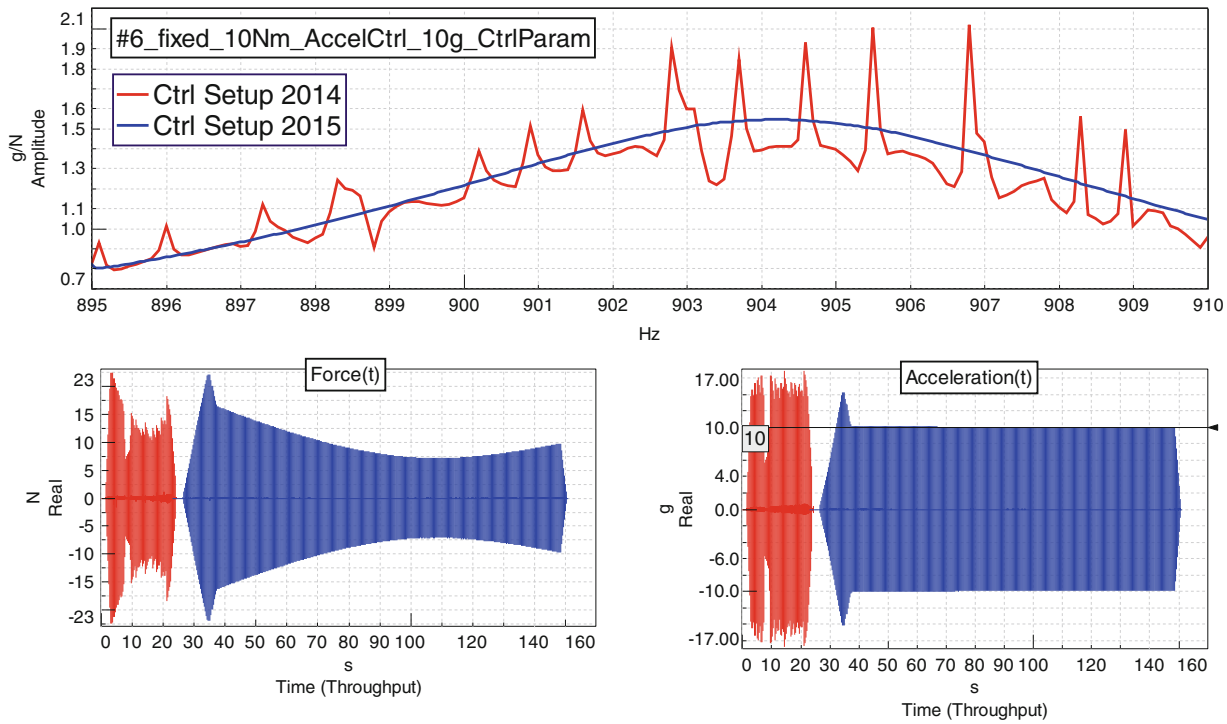

Fig. 48.10 Comparison of the (*top*) FRF and (*bottom*) time signals using (*red*) the parameters from the previous study and (*blue*) optimal parameters

It is not recommended to use force control, unless one has a large shaker that can handle high current. At resonance the force level needed to drive the structure drops drastically. This drop in force requires the amperage going to the shake to increase; the increase may be larger than the shaker can handle. To use force control, low force amplitude would need to be selected; if the force level is set too low a linear analysis maybe tested. Acceleration control gives the best response curve at resonance because the amperage decreases as the amplitude of acceleration at resonance increases, but has the same issue as the force control in off-resonant regions.

48.4 Repeatability Experiments

Once the optimal parameters are identified, the next step is to determine if repeatable results can be achieved. Micro-scale interface differences in roughness cause there to be little repeatability in the response of jointed structures, even from experiment to experiment of the same specimen [4]. To determine repeatability of BR beam results, the system with the "fixed-free" boundary condition is excited using acceleration stepped-sine control. The bolts of the beam are torqued to 5, 10 and 20 Nm. The system is excited around its second bending (174–195 Hz), first torsional (890–930 Hz), and fifth bending (1195–1255 Hz) modes. The ranges are reduced in some of the experiments due to the off-resonance issues with acceleration control; however, all of the experiment ranges fall within those listed. Due to the amplitude variation of each peak's response the acceleration amplitude is controlled at different values, listed in Table 48.2.

To determine the repeatability, the following procedure is used:

1. The beam is torqued to half the desired level, then the desired level
2. A uncontrolled sweep signal near the shakers maximum amperage is run, sweeping up then down
3. The stepped-sine acceleration control is then ran for each peak at all three amplitudes in Table 48.2, starting with the highest amplitude and ending with the lowest
4. After all peaks and amplitudes are ran the beam is disassembled then reassembled using the procedure in step 1
5. Steps 2 through 4 are repeated 3 times for each torque level

An example of the results for the first peak at 10 Nm torque is shown in Fig. 48.11. To better see the shifts in damping and frequency of all the experiments, the values at the peaks are plotted versus the amplitude in Fig. 48.12.

As can be seen in Fig. 48.12 the frequency of first run for each torque level is shifted from the other two runs. This could be that the interface for this first run at each torque level is not settled even with the interfaces being reseated. To produce a smaller range for the frequency locations a fourth run should be performed and the first run should be treated as an additional settling run like the sweeps.

48.5 Conclusions

This research sought to expand the work previous presented in [6] by studying the optimal parameters for controlling the input of a nonlinear system and a process to receive more repeatable results. The optimal parameters and recommendation for this work are:

- The optimal parameters for the LMS Test.Lab Stepped-Sine control are:
  - Low Confidence in Measured System FRF
  - 60 % Error Correction Factor
  - 30 Delay Cycles
  - 40 Hold Cycles

Table 48.2 Control amplitudes for the excitation peaks

Peak	Amplitude 1 (g)	Amplitude 2 (g)	Amplitude 3 (g)
1	0.5	1	2
2	5	10	25
3	1	3	5

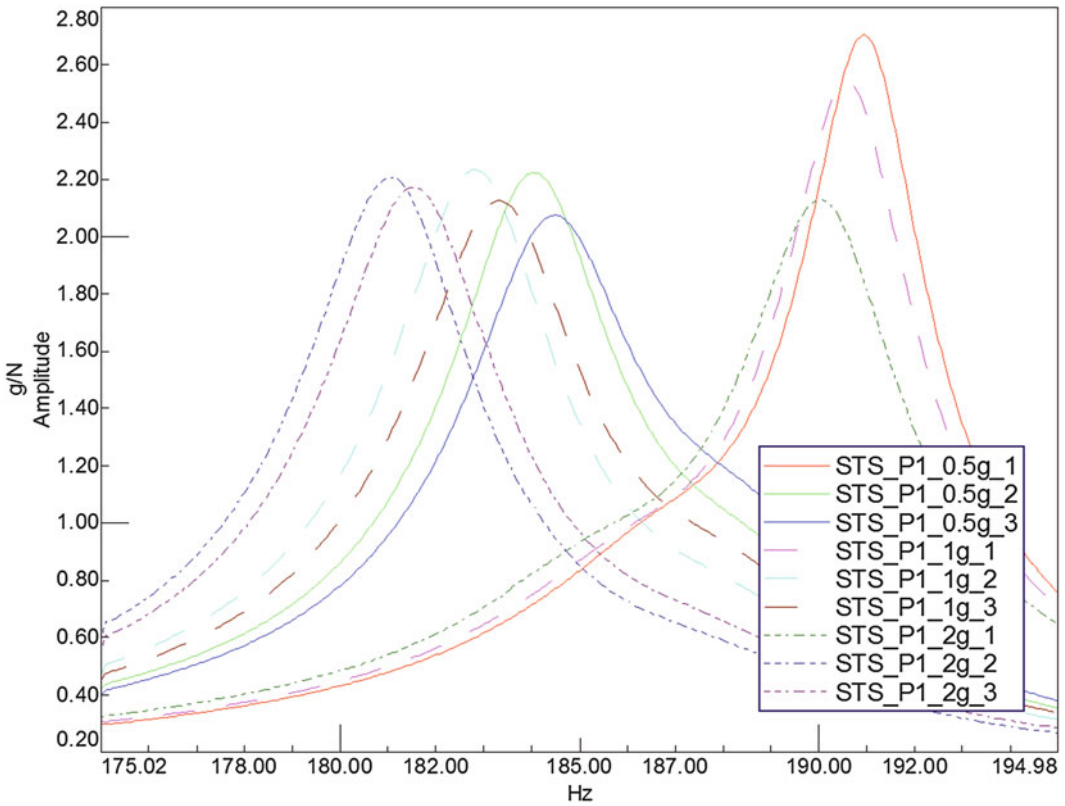

Fig. 48.11 Example repeatability experiment of the first peak at 10 Nm torque

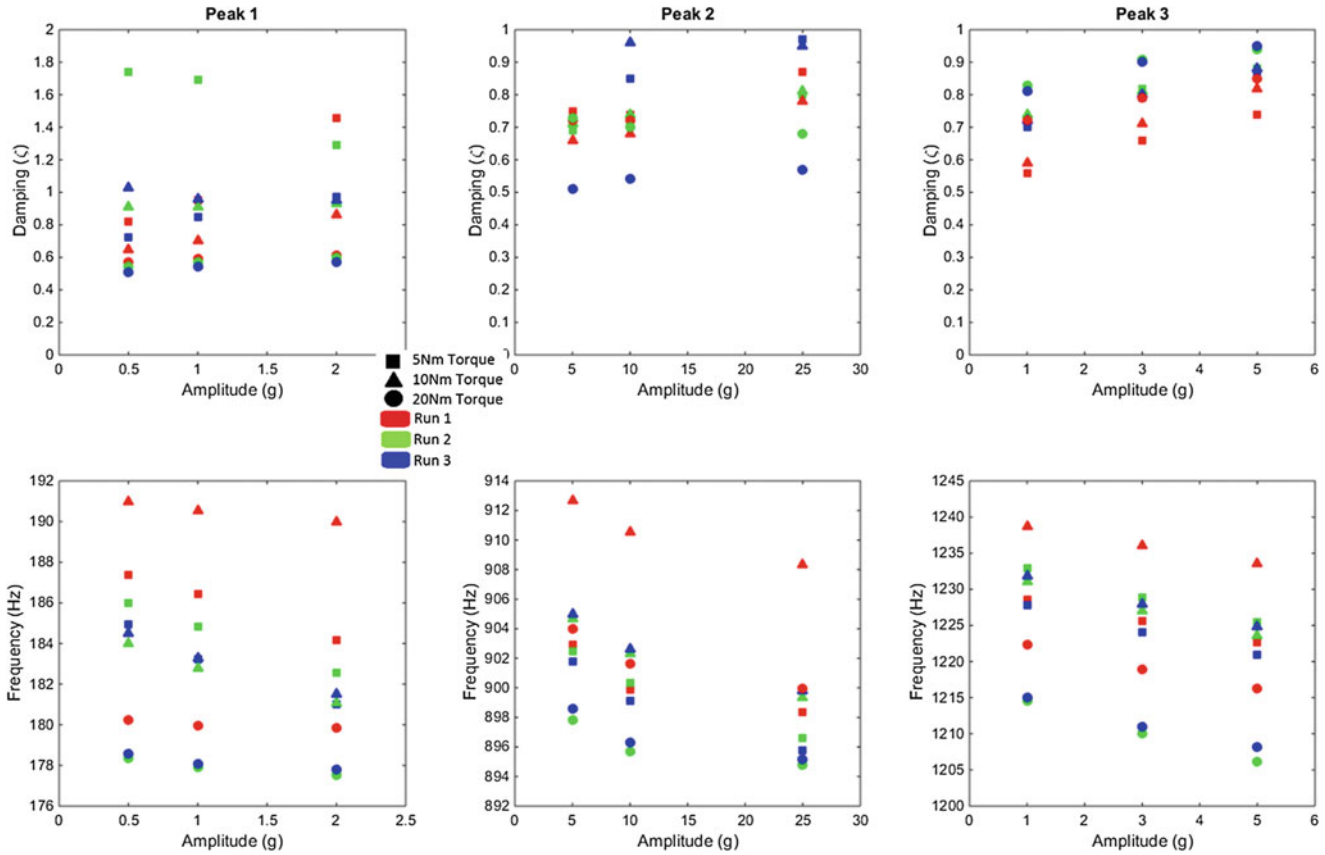

Fig. 48.12 Peak values of damping and frequency versus amplitude of excitation

- Acceleration amplitude control is recommended as the force control has to increase the amperage to the shaker drastically on the resonant peaks
- For fairly repeatable results, the interface should be settled using a sweep signal at the maximum amperage the shaker can handle
- The first stepped-sine signal should be used as a settling signal as well

Future work should aim at the use and development of force control that does not have issues at the resonance of the system, as well as mapping the changes in repeatability of the interface with a large number of tests.

Acknowledgements This work was funded by Sandia National Laboratories. Sandia National Laboratories is a multi-program laboratory managed and operated by Sandia Corporation, a wholly owned subsidiary of Lockheed Martin Corporation, for the U.S. Department of Energy's National Nuclear Security Administration under contract DE-AC04-94AL85000. The authors would like to thank Dr. Matthew Allen from the University of Wisconsin- Madison for his input during the tests

References

1. Brake, M.R.W: The role of epistemic uncertainty of contact models in the design and optimization of mechanical systems with aleatoric uncertainty. Nonlinear Dyn. **77**, 899–922 (2014)
2. Brake, M.R.W: The effect of the contact model on the impact-vibration response of continuous and discrete systems. J. Sound Vib. **332**, 3849–3878 (2013)
3. Segalman, D.J., Gregory, D.L., Starr, M.J., Resor, B.R., Jew, M.D., Lauffer, J.P., Ames, N.M.: Handbook on Dynamics of Jointed Structures, SAND2009-4164. Sandia National Laboratories, Albuquerque (2009)
4. Brake, M.R.W., Reuß, P., Segalman, D.J., Gaul, L.: Variability and Repeatability of jointed structures with frictional interfaces. In: Proceedings of the IMAC XXXII A Conference and Exposition on Structural Dynamics, Orlando (2014)
5. Sracic, M.W., Allen, M.S., Sumali, H.: Identifying the modal properties of nonlinear structures using measured free response time histories from a scanning laser Doppler vibrometer. In: Proceedings of the IMAC XXX A Conference and Expositions on Structural Dynamics, JacksonVille (2012)
6. Smith, S.A., Bilbao-Ludena, J.C., Catalfamo, S., Brake, M.R.W., Reuß, P., Schwingshackl, C.W.: The effects of boundary conditions, measurement techniques, and excitation type on measurements of the properties of mechanical joints. In: Kerschen G. (ed.) Nonlinear Dynamics, Proceedings of the 33rd IMAC, A Conference and Exposition on Structural Dynamics, vol. 1, pp. 415–431. Springer, New York (2015)

Chapter 49
Stress Waves Propagating Through Bolted Joints

R.C. Flicek, K.J. Moore, G.M. Castelluccio, M.R.W. Brake, T. Truster, and C.I. Hammetter

Abstract This paper examines the mechanical response of a simple bolted joint, the Brake–Reuß beam, under shock loading. This is done by creating a high-fidelity finite element model of the beam and subjecting it to a quasi-static bolt load followed by a dynamic shock load. The influence of several parameters on the beam's response is studied, which include impact force, impact duration, impact location, and residual stress. The results indicate that when the energy input into the beam is held constant, the most influential parameter is the shock's frequency and that increasing its frequency significantly increases dissipation. The next most influential parameter is the impact location, though its effect is frequency dependent and becomes stronger for higher frequencies. Finally, the results show that while residual stresses can significantly modify the contact-pressure distribution, they have minimal influence on the energy dissipated due to friction resulting from shock loading.

Keywords Bolted joints • Interfacial mechanics • Frictional dissipation • Wave propagation • Dynamic contact

49.1 Introduction

Lack of repeatability is a major concern in the field of joint testing and modeling. In some cases, this effect can be so pronounced that an individual jointed component can exhibit significantly different behavior simply as a result of being disassembled and re-assembled between tests [1]. It is generally assumed that this variability is due to very minor changes in the test conditions from one test to the next and that the joint's behavior is extraordinarily sensitive to some number of these conditions. In addition, recent investigations by [1, 2] have found that test repeatability can be highly sensitive to the type of loading that is applied to the joint. For instance, Smith et al. [2] found that for a particular design of lap joint, the Brake–Reuß beam, which is shown in Fig. 49.1, highly repeatable results could be obtained when exciting bending modes but not when exciting torsional modes.

This paper studies how stress waves propagate through bolted joints. To do this, a high-fidelity finite element model of the Brake–Reuß beam [1] is created and its response to shock loading is examined. The Brake–Reuß beam has been chosen for this investigation because its geometry is quite simple and thus easy to manufacture, but the frictional interface still produces the same types of analytical challenges that are observed in much more geometrically complex systems. In addition, experimental data is available for this system subjected to dynamic excitation using both shakers and impact hammers [1, 2].

The structure of this paper is as follows. In Sect. 49.2, the finite element model of the Brake–Reuß beam is described along with the loading regime that is used. In Sect. 49.3, the contact behavior resulting from quasi-statically applying the bolt loads

Sandia National Laboratories is a multi-program laboratory managed and operated by Sandia Corporation, a wholly owned subsidiary of Lockheed Martin Corporation, for the U.S. Department of Energy's National Nuclear Security Administration under contract DE-AC04-94AL85000.

R.C. Flicek
Akima Infrastructure Services, under contract to Sandia National Laboratories, PO Box 5800, Albuquerque, NM 87175-1070, USA

K.J. Moore (✉)
Department of Mechanical Science and Engineering, University of Illinois Urbana-Champaign, 1206 W. Green St., Urbana, IL 61801, USA
e-mail: kmoore14@illinois.edu

G.M. Castelluccio • M.R.W. Brake • C.I. Hammetter
Sandia National Laboratories†, PO Box 5800, Albuquerque, NM 87175, USA

T. Truster
Department of Civil and Environmental Engineering, University of Tennessee, 318 John D. Tickle Engineering Building, 851 Neyland Drive, Knoxville, TN 37996, USA

© The Society for Experimental Mechanics, Inc. 2016

M. Allen et al. (eds.), *Dynamics of Coupled Structures, Volume 4*, Conference Proceedings of the Society for Experimental Mechanics Series, DOI 10.1007/978-3-319-29763-7_49

Fig. 49.1 The Brake–Reuß beam

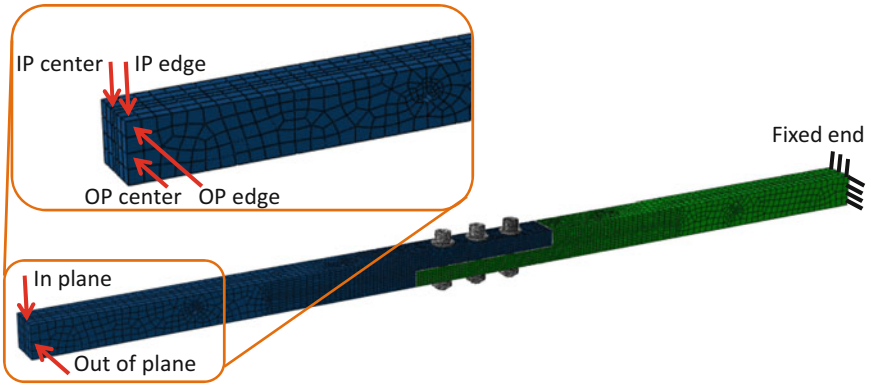

Fig. 49.2 Finite element model of the Brake–Reuß beam, which shows the boundary conditions and impact locations

with different residual stresses is examined. In Sect. 49.4, a parameter study is performed to determine the influence of impact force, impact duration, impact location, and residual stress state on the beam's response under shock loading. A discussion of the results is presented in Sect. 49.5, and a brief summary of the paper is given in Sect. 49.6.

49.2 Approach

The high-fidelity finite element model of the Brake–Reuß beam was created using the commercial software package ABAQUS/CAE version 6.14, and an image of this model is shown in Fig. 49.2. Free-fixed boundary conditions were used for all of the simulations considered in this paper, and these are also shown in Fig. 49.2. More specifically, the left beam was free, whereas a zero-displacement condition was applied (in all three directions) to the rightmost face of the right beam. Bending loads were then applied to the free end of the beam in both the in-plane and out-of-plane directions, which are shown in Fig. 49.2. Note that the load is referred to as 'in-plane' when it is applied parallel to the axis of the bolts and as 'out-of-plane' when it is applied perpendicular to the axis of the bolts.

The finite element model was comprised entirely of `C3D8R` elements, which are three-dimensional, linear, hexahedral, reduced-integration elements. The mesh controls were set to `Sweep` for all regions of the model except for a cylindrical region surrounding the three bolt holes where the `Structured` meshing scheme was used. Each half of the Brake–Reuß beam was modeled as a separate part, which incorporated 15,630 nodes and 12,503 elements.

This model also included separate parts to model the three nuts, three bolts, and six washers that were used to fasten the beam together. However, node-tie (i.e. continuity of displacement) constraints were applied to all potential regions of contact between the nuts, washers, and bolts. The only region of the model in which frictional contact was allowed to occur was the interface between the two surfaces of the beam that are perpendicular to the axes of the bolts. A surface-to-surface contact pair was defined in this region using the finite-sliding formulation, and a standard Coulomb dry friction model was used to model the frictional interaction. Unless otherwise stated, the friction coefficient was taken to be 0.3. The pressure-overclosure relationship was set to `Hard Contact`, and the penalty contact algorithm was used in both the normal and tangential directions.

This finite element model was then used to study the Brake–Reuß beam subjected to a quasi-static pre-load followed by a shock load. All the simulations consisted of three phases: (1) apply a pre-stress, (2) apply the bolt loads, and (3) apply the shock load. In the first phase, a static residual stress was installed in the right beam under displacement controlled conditions.

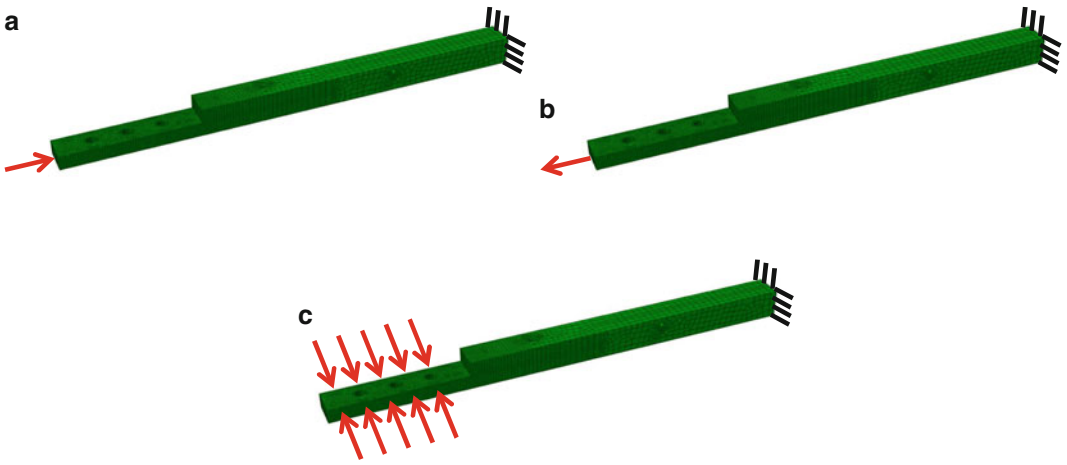

Fig. 49.3 Types of residual stresses that were applied: (**a**) axial compression, (**b**) axial tension, and (**c**) transverse compression

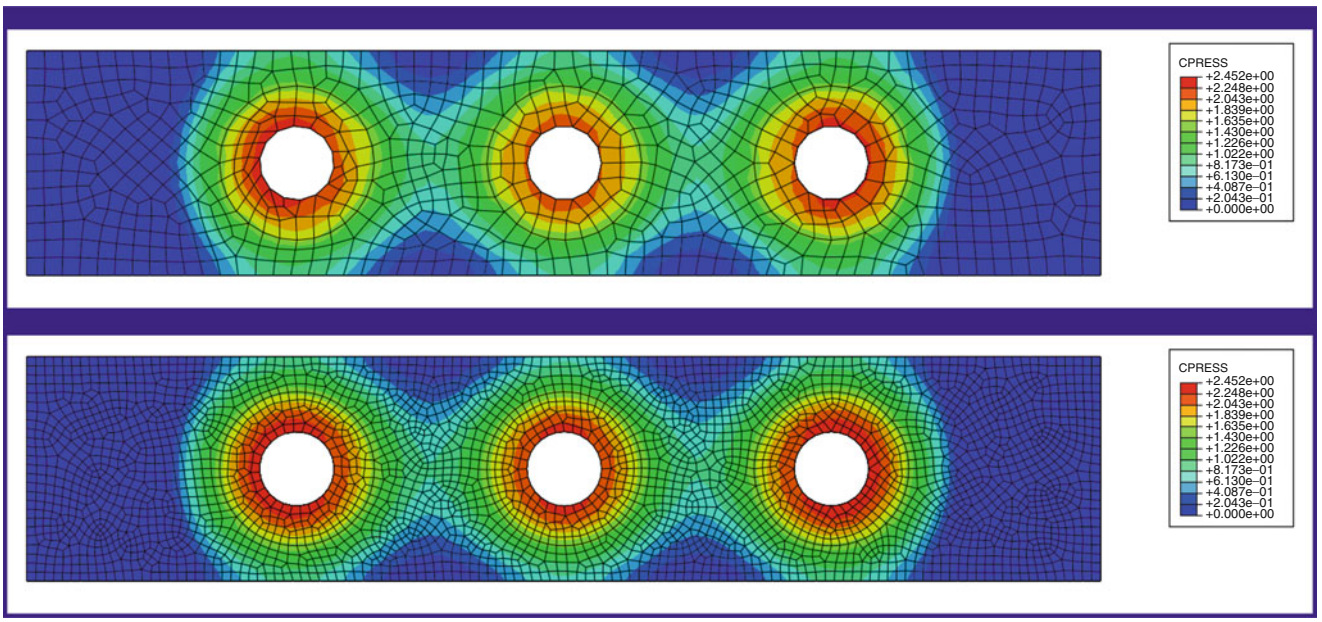

Fig. 49.4 Contact pressure (units in *MPa*) when $f = 0.3, B = 4\,\text{kN}$, and no residual stress is applied

The three types of residual stresses that were used are shown in Fig. 49.3, which are: (a) axial compression, (b) axial tension, and (c) transverse compression. Note that for many simulations, no residual stress was applied, and this is referred to as the stress-free initial condition. Following the pre-stressing phase of the loading, the static bolt loads were then applied using the `Bolt Load` command in ABAQUS/CAE, and the pre-stress was removed. Finally, a shock load was applied to the end of the left beam at one of the locations shown in Fig. 49.2. Note that all the quasi-static steps in the simulation were performed using the ABAQUS/Standard Implicit Statics solver, whereas the dynamic steps in the simulation used the ABAQUS/Standard Implicit Dynamics solver.

49.3 Bolt Load

An example plot of the contact pressure when no residual stress is applied prior to the bolt load is shown in Fig. 49.4 for a friction coefficient of $f = 0.3$ and a bolt force of $B = 4\,\text{kN}$. In this figure, results are shown both for a coarse mesh and for a fine mesh. Since both models provide a sufficiently converged result, all subsequent results in this paper were obtained

using the coarser mesh. Figure 49.4 illustrates that the contact pressure is symmetrical about both the horizontal and vertical centerlines of the interface, as expected. In addition, the contact pressure is localized around the edges of the bolt holes. This figure also shows that contact is maintained throughout the region between the bolts, but separation occurs over about 10 % of the interface at its left and right edges.

Although the results shown in Fig. 49.4 were obtained for the specific friction coefficient and bolt force mentioned above, varying these parameters does not change the pattern of stick, slip, and separation that forms. In fact, changing the coefficient of friction has virtually no effect on the contact pressure. This is because this problem is dominated by the normal load, so virtually no shear tractions are present. Of course, changing the bolt load does change the magnitude of the contact stresses that arise; however, the sizes of the zones of stick, slip, and separation still remain virtually identical. This result might also be expected since this problem has some parallels to the more idealized *receding contacts* studied for example by Ahn and Barber [3], which exhibit similar behavior.[2]

49.3.1 Residual Stress

In contrast to the friction coefficient and the bolt force, the initial residual stress state can have a significant influence on the contact pressure and the pattern of stick, slip, and separation that arises along the interface. To investigate these effects, three types of residual stresses were applied to the fixed (right) beam, which are shown in Fig. 49.3: namely, axial tension, axial compression, and transverse compression. These residual stresses were installed by first applying a pre-load to the right beam, next applying the bolt load, and then releasing the pre-load.

The effect of these pre-loads on the contact pressure is shown in Fig. 49.5 when a displacement-controlled pre-load of 0.05 % strain is applied. This figure clearly illustrates that the pre-load significantly modifies the contact's behavior. In fact, the peak contact pressure, the total contact area, the shape of the contact zone, and even the number of contact patches can be altered by the type of pre-load that is applied. However, different types of pre-loads have quite different effects. For instance, the axial pre-loads significantly modify the shape of the contact zone, whereas the transverse compression pre-load has much less of an influence. Conversely, the transverse compression pre-load promotes separation along the top and bottom edges of the contact, which reduces the contact area and thus slightly increases the contact pressure. However, this increase is quite uniform, so the contact pressure remains qualitatively similar to the case when no pre-load is applied.

As might be expected, tensile and compressive axial pre-loads have opposite effects: the compressive pre-load reduces the contact area, whereas the tensile pre-load increases the contact area. In fact, for this level of pre-load, the compressive pre-load actually reduces the contact pressure between the bolts to such an extent that separation occurs in these regions, such that a separate contact patch forms under each bolt. It can also be seen that the contact pressure for the compressive

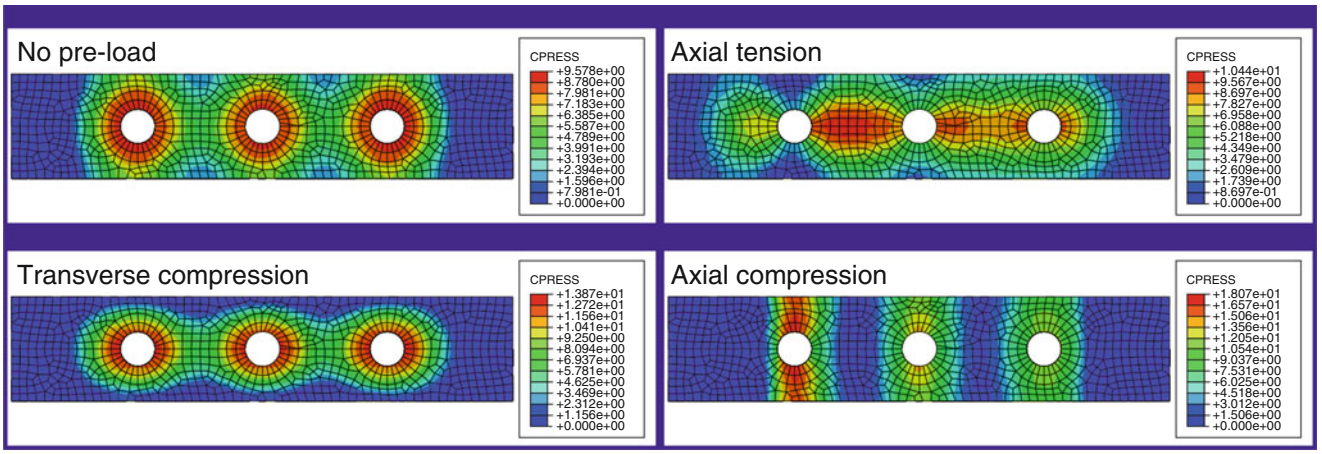

Fig. 49.5 Influence of three types of pre-loads on the contact pressure (units in *MPa*) when a pre-load strain of 0.05 % is applied

[2]Dundurs and Stippes [4] have shown that on the application of an infinitesimal normal load, receding contacts 'snap' to a particular pattern of stick, slip, and separation, and as the normal load is monotonically raised, the sizes of these zones remains fixed, while the stresses and displacements scale linearly with the applied load.

axial pre-load is highest along a vertical band at the left bolt hole. The lack of symmetry in this result (and that of the axial tensile pre-load) can be explained by the unsymmetrical way in which the pre-load is applied only to the right beam.

Conversely, for the tensile axial pre-load, the peak contact pressure does not occur under any of the bolts but rather between the left and center bolts. It is somewhat surprising that a pre-load could cause the peak contact pressure to occur away from the bolt loads and in a region where no load is applied. Moreover, the contact pressure is so low near the left bolt that some separation actually occurs in this region (where the peak pressure occurs for the compressive case). Thus, it is clear that pre-loads of a sufficiently large magnitude can have quite dramatic effects on contact behavior. However, if the pre-load's amplitude is sufficiently small (e.g. less than 5 % of the yield strength), such dramatic effects will not occur. Thus, the influence of pre-loads may be able to be ignored if only small pre-loads are expected to be present.

49.4 Shock Loading

This section investigates the influence of some of the model's parameters on frictional dissipation under shock loading. Of course, the parameter space comprising the possible simulations that could be performed is vast; important parameters that should be studied include: bolt force, input force, shock duration, input energy, simulation duration, impact location, residual stress type and amplitude, and friction coefficient. However, here a limited set of simulations were performed to examine subset of these parameters for a practical range of values. Note that all the results in this section were obtained for a bolt force of 4 kN and a friction coefficient of 0.3. Also note that the shock load was applied using the `Smooth Step` amplitude command in ABAQUS/CAE.

49.4.1 Types of Dissipative Responses

The qualitative behavior of a bolted joint can be divided into three categories based on how much dissipation the interface produces: namely, fully stuck, micro-slip, and macro-slip. The fully stuck regime results when the applied load is too low to produce any slip at the interface. In this case, the friction at the interface is not 'activated' since no slip occurs, so the problem behaves linearly and acts as though the interface were not present. Micro-slip results when the applied load is large enough to cause some particles along the interface to slip, while other particles remain stuck. Finally, macro-slip occurs when the load is so large that it causes every particle along the interface to slip

Macro-slip is not generally of interest in joints research because bolted connections are typically designed to remain in persistent contact under the service loads. Similarly, the fully stuck regime is not the focus of this study, because the system will behave linearly in this regime, so standard linear dynamics techniques can be used. Conversely, micro-slip is often excited by the service loads of real engineering assemblies, which means linear dynamics techniques may not be appropriate. In addition, micro-slip can result in fretting fatigue damage, which significantly reduces the fatigue life of many engineering assemblies.

Thus, the object of this study is to perform an initial exploratory analysis of the Brake–Reuß beam's parameters and to determine the conditions that result in micro-slip. The parameters that will be studied here are: impact location, input force, shock duration, and residual stress. To study impact location, shock loads were applied to four different points at the end of the left beam, which are shown in Fig. 49.2. Specifically, shocks were applied in the in-plane and out-of-plane directions at the edge and center of the beam.

49.4.2 Results

The first group of simulations that are examined in this section investigate the influence of impact location, impact force, and impact duration. Note that for these simulations, the impact force and impact duration were varied simultaneously so as to maintain the same input energy for all the simulations. The results are shown in Fig. 49.7, which displays plots of frictional dissipation vs. time for four load cases: namely, (a) a 1 kN impact applied for 2 ms, (b) a 2 kN impact applied for 1 ms, (c) an 8 kN impact applied for 0.25 ms, and (d) a 20 kN impact applied for 0.1 ms.

These results show that the interface's behavior is highly sensitive to the loading frequency. In addition, the amount of frictional dissipation is seen to vary by an order of magnitude from the longest impact pulse (2 ms) to the shortest impact

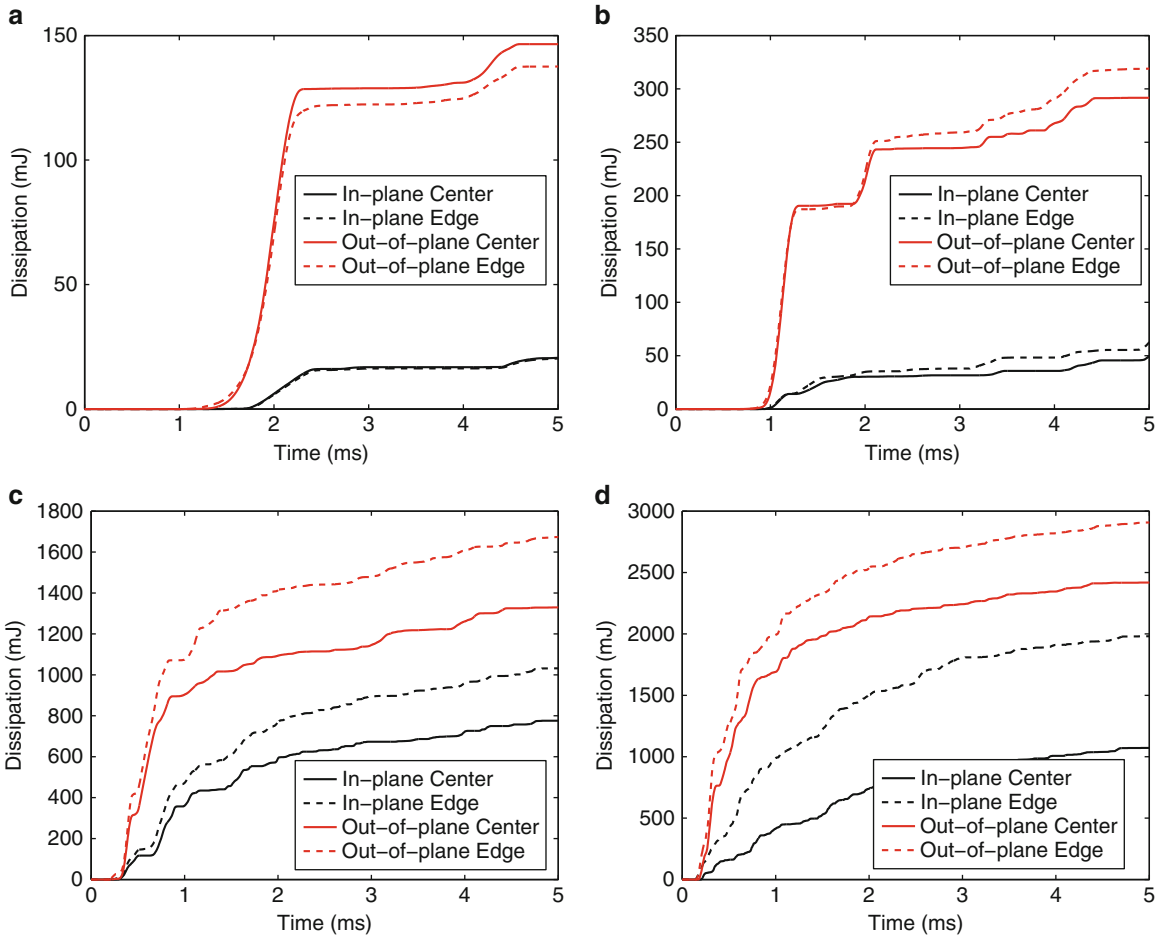

Fig. 49.6 Frictional dissipation vs. time for different impact locations, impact forces, and impact durations, while holding the input energy constant. (**a**) 1 kN impact, 2 ms pulse. (**b**) 2 kN impact, 1 ms pulse. (**c**) 8 kN Impact, 0.25 ms pulse. (**d**) 20 kN impact, 0.1 ms pulse

pulse (0.1 ms) that was used. Figure 49.7 also shows that out-of-plane loading resulted in significantly more dissipation than in-plane loading, though this effect is highly frequency dependent. For example, for the 1 ms pulse width case, out-of-plane loading resulted in about 6 times more dissipation than in-plane loading, whereas for the 0.1 ms pulse, out-of-plane loading resulted in a little less than twice as much dissipation as in-plane loading.

Similarly, these results demonstrate that impacting the beam on-center vs. at a corner (i.e. an edge) only makes a difference above a certain frequency of loading. This is not surprising because for quasi-static loading the only difference between loading at the edge vs. at the center is a small additional moment associated with applying the load off-center. Since the beam is quite narrow, this moment will be small and will have a minimal effect on the solution. Conversely, for high-frequency loading, the edge impacts excite both torsional and bending modes of vibration, whereas the on-center impacts only excite bending modes. Thus, it is not surprising that the addition of torsional modes results in more frictional dissipation.

The second set of simulations that were performed only consider in-plane loading and examine the influence of the residual stresses shown in Figs. 49.3 and 49.5. The results are displayed in Fig. 49.6, which again shows frictional dissipation vs. time for four load cases: namely, (a) a 1 kN impact applied for 2 ms, (b) a 4 kN impact applied for 0.5 ms, (c) an 8 kN impact applied for 0.25 ms, and (d) a 20 kN impact applied for 0.1 ms. Note that the input energy for all these simulations was held constant and is the same as that for the results shown in Fig. 49.7. Interestingly, Fig. 49.6 suggests that residual stresses have only a small influence on frictional dissipation. Moreover, unlike all the other parameters examined thus far, their effect appears to be unaffected by the loading frequency.

Figure 49.6 also displays many of the trends seen in Fig. 49.7: namely, dissipation increases sharply with loading frequency, and a difference between edge and center impacts only appears for high enough loading frequencies. Since the influence of residual stresses does not vary much with loading frequency, residual stresses have a larger influence than impact location (edge vs. center) for the low-frequency simulations but a much smaller influence for the higher-frequency simulations.

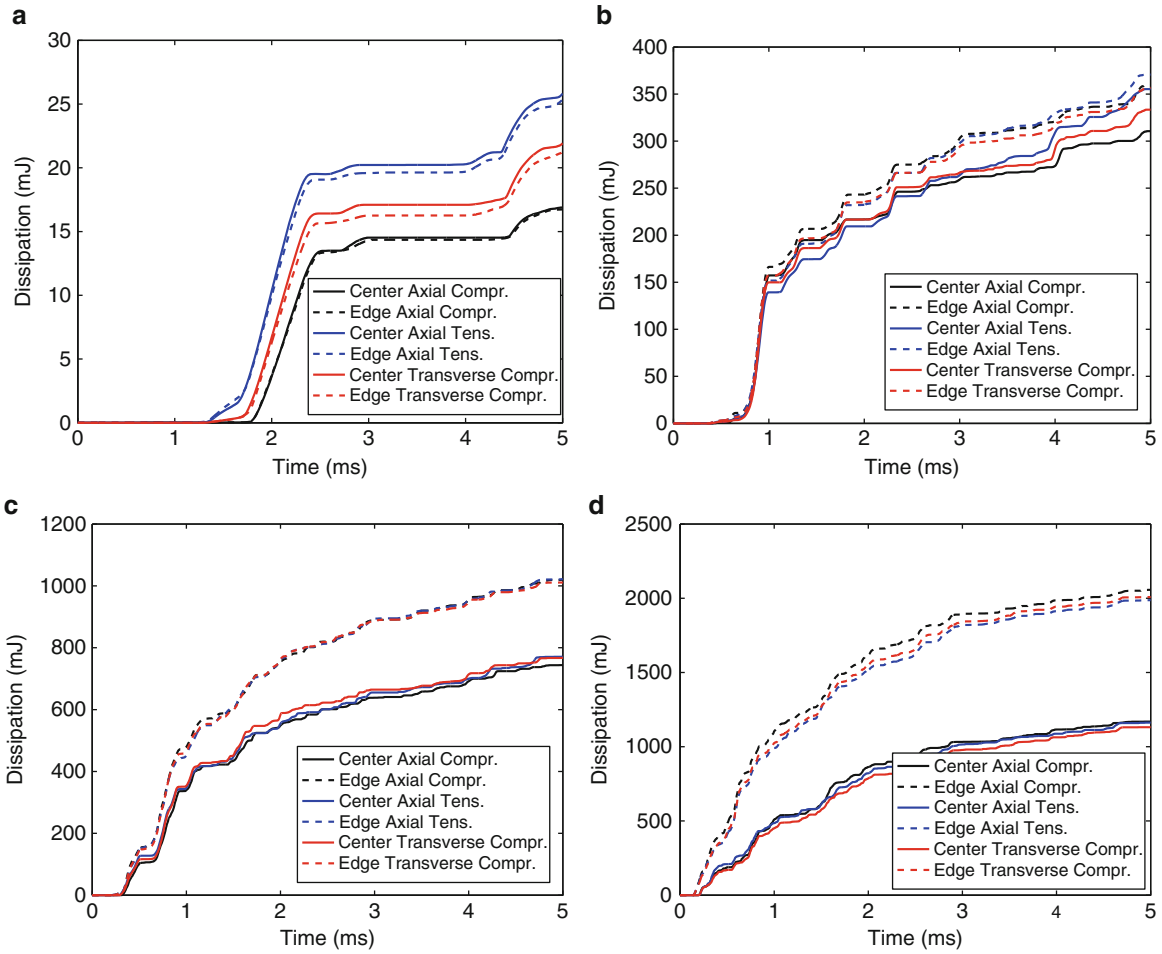

Fig. 49.7 Frictional dissipation vs. time for different residual stresses, impact locations, impact forces, and impact durations, while holding the input energy constant. (**a**) In-plane 1 kN impact, 2 ms pulse. (**b**) In-plane 8 kN Impact, 0.25 ms pulse. (**c**) In-plane 20 kN impact, 0.1 ms pulse. (**d**) In-plane 4 kN impact, 0.5 ms pulse

The results presented in this section suggest that the most important parameter influencing frictional dissipation is the loading frequency, where higher-frequency impacts result in more dissipation (for the same input energy). Impact direction (i.e. in-plane vs. out-of-plane) is the second most influential parameter, where out-of-plane loading results in significantly more dissipation than in-plane loading. Impact location (i.e. edge vs. center) can also be important, but to a lesser extent and only when loading at a sufficiently high frequency. Finally, residual stresses appear only to have a minor effect on frictional dissipation resulting from shock loading.

49.5 Discussion

At the present time, predicting the behavior of the frictional interfaces in jointed structures is notoriously difficult and highly computationally expensive. As a result, joints tend to be a liability for engineering design that significant resources must be used to mitigate. The reason for this is simply that the physics of how jointed interfaces behave is complex and is not sufficiently well understood. However, if predictive models of joints were available, joints' properties could be optimized for their intended application and could actually become an asset in the designer's toolkit. At a minimum, better models should enable the effect of using different types joints to be predicted accurately during the design phase, and this information could be used to select the best design.

The purpose of this work has been to develop a better understanding of how stress waves propagate through frictional interfaces with the expectation that such understanding will lead to better predictive models of frictional interfaces. A first step towards developing a predictive model is determining which parameters have the largest impact on the system's behavior, and the results presented here provide useful data on this topic. One interesting result is that residual stresses can have a major influence on the contact pressure resulting from applying the (quasi-static) bolt load, but they have almost no influence on frictional dissipation resulting from shock loading. This result is quite surprising because it is clear that the contact pressure is significantly modified by the residual stresses, yet the total energy dissipated by the interface due to a shock ends up being largely unchanged. The practical implication of this result is that variations in the residual stress state prior to shock loading cannot be used to explain the lack of repeatability that is often observed in the experimental data.

In light of these results, it would be very interesting to investigate the influence of other interfacial parameters such as friction coefficient and bolt force on frictional dissipation. Recall from Sect. 49.3 that variations in the friction coefficient and bolt force had virtually no influence on the distribution of contact pressure resulting from applying the bolt load (aside from the contact pressure's magnitude scaling with the bolt force). However, experimental results [1] clearly indicate that the bolt force has a major impact on the beam's behavior. Thus, the influence of these parameters should be examined in future work.

Perhaps the most prominent feature of the results in Sect. 49.4 is the very strong dependence of frictional dissipation on loading frequency. This result emphasizes that frictional dissipation is not simply a function of the energy input into the system; it also depends strongly on the frequency of the loading. Thus, any model that aims to predict a joint's response for more than a very narrow band of frequencies must be able to model this effect.

The results also indicate that the Brake–Reuß beam is significantly stiffer for in-plane loading than for out-of-plane loading. This is evidenced by there being much more dissipation for out-of-plane loading across all frequencies, though this effect decreases as loading frequency is increased. This result is not at all surprising because this beam is clearly designed to be stiffer in the in-plane direction than in the out-of-plane direction. Thus, a hypothesis that follows from this result is that making the beam stiffer in the out-of-plane direction would reduce the dissipation for out-of-plane loading, and this will be examined in future work.

Finally, one feature of the data that may help explain the lack of repeatability of joints experiments is the influence of impacting the beam at an edge vs. at the center. Both Figs. 49.6 and 49.7 show that this effect is quite sensitive to the frequency of loading. However, for sufficiently high-frequency loading (e.g. the 0.25 and 0.1 ms duration pulses), changing the impact location from the center to the edge can increase dissipation by 25–100 %. Conversely, for the low frequency loading (i.e. 2 ms pulse width), the edge and center impacts produce effectively identical responses. This result provides a possible explanation for some of the lack of repeatability in tests conducted with an impact hammer: namely, small variations in the precise point of impact may have a non-negligible effect on the results. Thus, controlling the impact location with greater precision may result in more repeatable tests.

49.6 Conclusion

In this paper, a high-fidelity finite element model of the Brake–Reuß beam is created and subjected to shock loading. A parameter study is performed to study the influence of impact force, impact duration, impact location, and residual stress on the beam's response. The results show that loading frequency is the most important parameter influencing frictional dissipation and that higher-frequency impacts result in more dissipation (for the same input energy). Impact location is second most influential parameter, and this parameter is studied in two ways: (1) the shock is applied in the in-plane vs. the out-of-plane direction, and (2) the shock is applied at the center vs. at the edge of the beam. In addition, the beam's sensitivity to in-plane vs. out-of-plane loading is highest for low loading frequencies. However, out-of-plane loading always results in significantly more dissipation than in-plane loading because the beam is stiffer in the in-plane direction than in the out-of-plane direction. Conversely, the beam's sensitivity to edge vs. center impacts is greatest for high loading frequencies. Finally, while residual stresses can significantly modify the contact-pressure distribution, they have minimal influence on the frictional dissipation resulting from shock loading.

References

1. Brake, M.R., Reuß, P., Segalman, D.J., Gaul, L.: Variability and repeatability of jointed structures with frictional interfaces. In: Dynamics of Coupled Structures, Volume 1: Proceedings of the 32nd IMAC, a Conference and Exposition on Structural Dynamics, pp. 245–252, 2014. doi:10.1007/978-3-319-04501-6_23
2. Smith, S., Bilbao-Ludena, J.C., Catalfamo, S., Brake, M.R.W., Reuß, P., Schwingshackl, C.W.: The effects of boundary conditions, measurement techniques, and excitation type on measurements of the properties of mechanical joints. In: Nonlinear Dynamics, Volume 1: Proceedings of the 33rd IMAC, a Conference and Exposition on Structural Dynamics, pp. 415–431, 2016. doi:10.1007/978-3-319-15221-9_36
3. Ahn, Y.J., Barber, J.R.: Response of frictional receding contact problems to cyclic loading. Int. J. Mech. Sci. **50**(10–11), 1519–1525 (2008). doi:10.1016/j.ijmecsci.2008.08.003
4. Dundurs, J., Stippes, M.: Role of elastic constants in certain contact problems. J. Appl. Mech. **37**(4), 965–970 (1970). doi:10.1115/1.3408725

Chapter 50
A Comparison of Reduced Order Modeling Techniques Used in Dynamic Substructuring

Daniel Roettgen, Benjamin Seeger, Wei Che Tai, Seunghun Baek, Tilán Dossogne, Matthew Allen, Robert Kuether, Matthew R.W. Brake, and Randall Mayes

Abstract Experimental dynamic substructuring is a means whereby a mathematical model for a substructure can be obtained experimentally and then coupled to a model for the rest of the assembly to predict the response. Recently, various methods have been proposed that use a transmission simulator to overcome sensitivity to measurement errors and to exercise the interface between the substructures; including the Craig-Bampton, Dual Craig-Bampton, and Craig-Mayes methods. This work compares the advantages and disadvantages of these reduced order modeling strategies for two dynamic substructuring problems. The methods are first used on an analytical beam model to validate the methodologies. Then they are used to obtain an experimental model for structure consisting of a cylinder with several components inside connected to the outside case by foam with uncertain properties. This represents an exceedingly difficult structure to model and so experimental substructuring could be an attractive way to obtain a model of the system.

Keywords Reduced order modelling • Dynamic substructuring • Craig-Bampton • Craig-Mayes • Craig-Chang

50.1 Introduction and Motivation

Experimental-analytical substructuring allows one to predict the dynamic response of an assembly by coupling substructures derived from experiments hardware with a finite element model representing the rest of the assembly. There are numerous applications of experimental analytical substructuring, but in particular this is useful when one has a subcomponent of a system that is difficult to model. This work looks at dynamic substructuring and the effects of using different reduced order models when completing the substructuring process by looking at two problems. First, a simple system is investigated using

*Sandia National Laboratories is a multi-program laboratory managed and operated by Sandia Corporation, a wholly owned subsidiary of Lockheed Martin Corporation, for the U.S. Department of Energy's National Nuclear Security Administration under contract DE-AC04-94AL85000.

D. Roettgen (✉) • M. Allen
University of Wisconsin, Madison, WI 53706, USA
e-mail: droettgen@wisc.edu; matt.allen@wisc.edu

B. Seeger
Universität Stuttgart, Keplerstraße 7, 70174 Stuttgart, Germany
e-mail: b_seeger@arcor.de

W.C. Tai
University of Washington, Seattle, WA, USA
e-mail: wchtai@uw.edu

S. Baek
University of Michigan, Ann Arbor, Michigan, MI, USA
e-mail: baeksh@umich.edu

T. Dossogne
University of Liége, Place du 20 Août 7, 4000 Liège, Belgium
e-mail: tdossogne@ulg.ac.be

R. Kuether • M.R.W. Brake • R. Mayes
Sandia National Labs, Albuquerque, NM, USA
e-mail: rjkueth@sandia.gov; mrbrake@sandia.gov; rlmayes@sandia.gov

© The Society for Experimental Mechanics, Inc. 2016

M. Allen et al. (eds.), *Dynamics of Coupled Structures, Volume 4*, Conference Proceedings of the Society for Experimental Mechanics Series, DOI 10.1007/978-3-319-29763-7_50

two beams connected by means of a transmission simulator. With this simple system, multiple dynamic substructuring and model reduction techniques are considered including the traditional transmission simulator [1–3], Craig-Bampton [4], Craig-Chang [4], and Craig-Mayes [5] methods. The second system consists of a beam attached to a plate on one end of a cylinder that encases a pressed foam and metal assembly. This second example uses actual experimental measurements while the beam example is purely a numerical demonstration. By using a finite element model of the beam-plate-can assembly, an experimental model of the dynamics for the internal foam system can be described using dynamic substructuring. This is investigated using the traditional transmission simulator and Craig-Mayes techniques.

The paper is organized as follows; Sect. 50.2 provides a high level look at a few of the model reduction and dynamic substructuring forms used in this work. In Sects. 50.3 and 50.4 this theory is put to use with a simple beam substructuring system and the beam-plate-can system, respectively.

50.2 Theory

50.2.1 Transmission Simulator

The transmission simulator is a useful tool in experimental analytical substructuring as described in [1–3] and is briefly described in this section. A key advantage of this method is that the transmission simulator works to mass-load the interface and improve the modal basis of the subsystem. To complete the transmission simulator method, one takes experimental data on the substructure of interest, denoted subsystem C. Then a negative form of the subsystem A, the transmission simulator, is coupled to the system. Finally, the actual substructure of interest which can be modeled with a finite element program, denoted subsystem D, is coupled into the system. See Fig. 50.1.

Mathematically, to complete this substructuring the equations of motion of the experimental and analytical component are first converted into modal coordinates.

$$\begin{bmatrix} \mathbf{I}_C & 0 & 0 \\ 0 & \mathbf{I}_D & 0 \\ 0 & 0 & -\mathbf{I}_A \end{bmatrix} \begin{Bmatrix} \ddot{q}_C \\ \ddot{q}_D \\ \ddot{q}_A \end{Bmatrix} + \begin{bmatrix} \omega_C^2 & 0 & 0 \\ 0 & \omega_D^2 & 0 \\ 0 & 0 & -\omega_A^2 \end{bmatrix} \begin{Bmatrix} q_C \\ q_D \\ q_A \end{Bmatrix} = \begin{Bmatrix} \mathbf{\Phi}_C^T F_C \\ \mathbf{\Phi}_D^T F_D \\ \mathbf{\Phi}_A^T F_A \end{Bmatrix} \tag{50.1}$$

The physical constraints can be defined by equating the motion of each subsystem with that of the transmission simulator and then transformed into modal coordinates. This equation only applies to the subset of degrees of freedom which act to connect the transmission simulator between substructures.

$$\begin{bmatrix} \mathbf{I} & 0 & -\mathbf{I} \\ 0 & \mathbf{I} & -\mathbf{I} \end{bmatrix} \begin{Bmatrix} x_C \\ x_D \\ x_A \end{Bmatrix} = \begin{Bmatrix} 0 \\ 0 \\ 0 \end{Bmatrix} \tag{50.2}$$

$$\begin{bmatrix} \mathbf{\Phi}_C & 0 & -\mathbf{\Phi}_A \\ 0 & \mathbf{\Phi}_D & -\mathbf{\Phi}_A \end{bmatrix} \begin{Bmatrix} q_C \\ q_D \\ q_A \end{Bmatrix} = \begin{Bmatrix} 0 \\ 0 \\ 0 \end{Bmatrix} \tag{50.3}$$

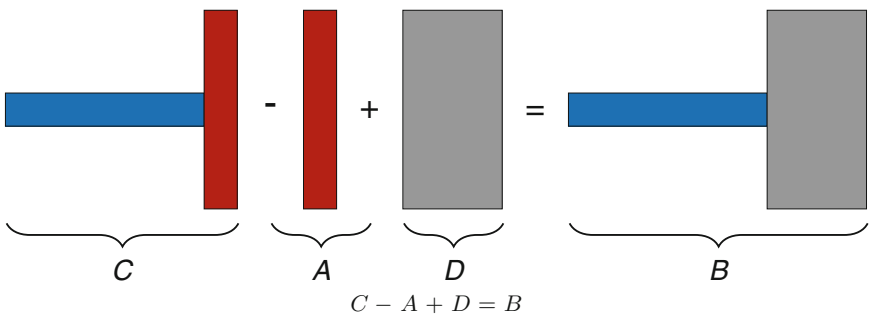

Fig. 50.1 Transmission simulator diagram

In order to take advantage of the transmission simulator method, the constraints are now pre-multiplied by the pseudo-inverse of the transmission simulator mode shapes partitioned to the constraint degrees of freedom. This forces the projection of modal degrees of freedom q_A onto q_C.

$$\begin{bmatrix} \boldsymbol{\Phi}_A^{\dagger} & 0 \\ 0 & \boldsymbol{\Phi}_A^{\dagger} \end{bmatrix} \begin{bmatrix} \boldsymbol{\Phi}_C & 0 & -\boldsymbol{\Phi}_A \\ 0 & \boldsymbol{\Phi}_D & -\boldsymbol{\Phi}_A \end{bmatrix} \begin{Bmatrix} q_C \\ q_D \\ q_A \end{Bmatrix} = \begin{Bmatrix} 0 \\ 0 \\ 0 \end{Bmatrix} \tag{50.4}$$

The two leading matrices can now be collected to form a single matrix, $\mathbf{B}$, that contains the constraints for the modal degrees of freedom.

$$\mathbf{B} \begin{Bmatrix} q_C \\ q_D \\ q_A \end{Bmatrix} = \begin{Bmatrix} 0 \\ 0 \\ 0 \end{Bmatrix} \tag{50.5}$$

These constrained modal degrees of freedom can be transformed by some matrix, $\mathbf{L}$, into a set of unconstrained generalized coordinates. In order to avoid a trivial solution, $\mathbf{L}$ must reside in the null space of $\mathbf{B}$.

$$\{q\} = \mathbf{L} \{q_g\} \tag{50.6}$$

$$\mathbf{BL} \{q_g\} = \mathbf{0} \tag{50.7}$$

This transformation matrix, $\mathbf{L}$, is then used in Eq. (50.1), which is also pre-multiplied by $\mathbf{L}^T$ resulting in the coupled equations of motion for the system. The modal properties for this system can then be found as the modal properties for the new analytically assembled system. A final transform can then used to bring the solution for the modal degrees of freedom back into the physical domain.

$$\mathbf{x} = \begin{bmatrix} \boldsymbol{\Phi}_C & 0 & 0 \\ 0 & \boldsymbol{\Phi}_D & 0 \\ 0 & 0 & \boldsymbol{\Phi}_A \end{bmatrix} \mathbf{L} \{q_g\} \tag{50.8}$$

This is the basis of the transmission simulator method. In this work we will look at two main types of model reduction techniques. First, those involving fixed interface modes such as the Craig-Bampton formulation, and then those involving the free-interface modes such as the Craig-Chang formulation.

50.2.2 Craig-Bampton

In order to take a system of equations from the physical domain into a Craig-Bampton form, a few steps are involved. First, the degrees of freedom are partitioned into two sets; the boundary set (the *b*-set), where this substructure will eventually be interfaced with another piece, and the interior set (the *i*-set) which are the remaining degrees of freedom.

$$\mathbf{x} = \begin{Bmatrix} \mathbf{x}_i \\ \mathbf{x}_b \end{Bmatrix} \tag{50.9}$$

$$\mathbf{M} = \begin{bmatrix} \mathbf{M}_{ii} & \mathbf{M}_{ib} \\ \mathbf{M}_{bi} & \mathbf{M}_{bb} \end{bmatrix} \tag{50.10}$$

$$\mathbf{K} = \begin{bmatrix} \mathbf{K}_{ii} & \mathbf{K}_{ib} \\ \mathbf{K}_{bi} & \mathbf{K}_{bb} \end{bmatrix} \tag{50.11}$$

The physical coordinates can then be transformed into Craig-Bampton coordinates using the transformation.

$$\mathbf{x} = \begin{Bmatrix} \mathbf{x}_i \\ \mathbf{x}_b \end{Bmatrix} = \begin{bmatrix} \mathbf{\Phi}_{ik} & \mathbf{\Psi}_{ib} \\ 0 & \mathbf{I}_{bb} \end{bmatrix} \begin{Bmatrix} \mathbf{q}_k \\ \mathbf{x}_b \end{Bmatrix} = \mathbf{T_{CB}} \begin{Bmatrix} \mathbf{q}_k \\ \mathbf{x}_b \end{Bmatrix} \tag{50.12}$$

In the transformation matrix the first column partition are the fixed-interface modes. These can be described as the interior degree of freedom motion when the interface is fixed (or constrained in all interface degrees of freedom). The number of kept fixed-interface modes can be reduced to k in order to decrease the total number of degrees of freedom. The second column partition represents the constraint modes. These describe the motion of the system when each boundary degree of freedom is given a unit displacement while holding the other boundary degrees of freedom fixed. $\mathbf{q}_k$ is a set of displacements corresponding to the fixed-interface motion and $\mathbf{u}_b$ is preserved from the original equation of motion as the boundary physical degrees of freedom.

This transformation matrix can be used to transform the subcomponent mass and stiffness matrices into their Craig-Bampton formulations.

$$\mathbf{M_{CB}} = \mathbf{T_{CB}^T M T_{CB}} = \begin{bmatrix} \mathbf{I} & \mathbf{M}_{kb} \\ \mathbf{M}_{bk} & \hat{\boldsymbol{M}}_{bb} \end{bmatrix} \tag{50.13}$$

$$\mathbf{K_{CB}} = \mathbf{T_{CB}^T K T_{CB}} = \begin{bmatrix} \omega_k^2 & 0 \\ 0 & \hat{\boldsymbol{K}}_{bb} \end{bmatrix} \tag{50.14}$$

Assembly of two Craig-Bampton matrices can then be completed by simply writing the constraints equation coupling the boundary degrees of freedom between the two subsystems [4]. With this constraint equation, a transformation matrix can be defined in order to couple the systems. When in the Craig-Bampton form, the interface degrees of freedom are preserved and the number of fixed-interface modes can be reduced. It is not possible to measure the fixed interface modes experimentally but this reduction can be used in an analytically model. The Craig-Mayes method proposes a way to estimate these fixed interface modes from the free modes of $\mathbf{C}$.

50.2.3 Craig-Mayes

The Craig-Mayes formulation [5] is a method to generate a Craig-Bampton representation for the experimental side of the substructure. The resulting form resembles the dynamics of subsystem C (the experiment) minus subsystem A (the transmission simulator). The Craig-Mayes method is a proposed method to create a Craig-Bampton like structure with experimentally measured results using the free modes of the transmission simulator. To begin the experimental data from subsystem C can be written in modal coordinates.

$$\left[\omega_n^2 - \omega^2 \mathbf{I}\right] \bar{\boldsymbol{q}} = 0 \tag{50.15}$$

One must assume that a transformation matrix, $\mathbf{T}$, exists that would bring the experimental modal results of C into a Craig-Bampton like form

$$\bar{\boldsymbol{q}} = \mathbf{T} \begin{Bmatrix} \bar{\boldsymbol{p}} \\ \bar{\boldsymbol{s}} \end{Bmatrix} \tag{50.16}$$

where $\bar{\boldsymbol{q}}$ represents the experimentally derived modal degrees of freedom, $\bar{\boldsymbol{p}}$ represents the fixed-interface modal coordinates, or motion when the boundary is fixed, and $\bar{\boldsymbol{s}}$ are coordinates that describe the motion of the TS. For this Craig-Bampton like formulation the transmission simulator degrees of freedom are considered the boundary.

The fixed-interface modal coordinates are found by fixing the boundary degrees of freedom, where $\mathbf{\Psi}_b$ represents the free modes of the transmission simulator and $\mathbf{\Phi}_b$ represents the experimental derived modes both partitioned to the boundary (TS) degrees of freedom.

$$\mathbf{\Psi}_b^{\dagger} \mathbf{\Phi}_b \bar{\boldsymbol{q}} = 0 \tag{50.17}$$

The modal degrees of freedom can now be replaced by a new set of coordinates, $\bar{\eta}$, which satisfy the constraints by using,

$$\boldsymbol{\Psi}_b^{\dagger}\boldsymbol{\Phi}_b\mathbf{L}_{fix}\bar{\boldsymbol{\eta}} = 0 \tag{50.18}$$

where, $\mathbf{L}_{fix}$ must reside in the null space of $\boldsymbol{\Psi}_b^{\dagger}\boldsymbol{\Phi}_b$. $\mathbf{L}_{fix}$ can then be used to transform the modal representation from Eq. (50.15). This transformed equation can be solved for the eigen vectors $\boldsymbol{\Gamma}$ which uncouple the fixed interface modal degrees of freedom, $\bar{\boldsymbol{p}}$.

$$\bar{\boldsymbol{q}} = \mathbf{L}_{fix}\boldsymbol{\Gamma}\bar{\boldsymbol{p}} \tag{50.19}$$

This solves the partition of the transformation matrix related to the fixed interface modal amplitude, $\bar{\boldsymbol{p}}$, from Eq. (50.16). The partition associated with the boundary degrees of freedom, $\bar{\boldsymbol{s}}$, is found by setting the motion of the TS in the experimental system equal to the free modal motion of the TS.

$$\boldsymbol{\Phi}_b\bar{\boldsymbol{q}} = \boldsymbol{\Psi}_b\bar{\boldsymbol{s}} \tag{50.20}$$

The transformation matrix can now be defined as shown in the equation below.

$$\mathbf{T} = \left[\begin{array}{cc} \mathbf{L}_{fix}\boldsymbol{\Gamma} & \boldsymbol{\Phi}_b^{\dagger}\boldsymbol{\Psi}_b \end{array}\right] \tag{50.21}$$

Pre and post multiplying by $\mathbf{T}^T$ and $\mathbf{T}$ respectively results in a new set of equations of motion in terms of $\bar{\boldsymbol{p}}$ and $\bar{\boldsymbol{s}}$ coordinates.

$$\left[\left[\begin{array}{cc} \omega_{fix}^2 & \mathbf{K}_{ps} \\ \mathbf{K}_{sp} & \mathbf{K}_{ss} \end{array}\right] - \omega^2\left[\begin{array}{cc} \mathbf{I} & \mathbf{M}_{ps} \\ \mathbf{M}_{sp} & \mathbf{M}_{ss} \end{array}\right]\right]\left\{\begin{array}{c} \bar{\boldsymbol{p}} \\ \bar{\boldsymbol{s}} \end{array}\right\} = 0 \tag{50.22}$$

To remove the mass and stiffness of the transmission simulator, the terms are simply subtracted from the lower right partitions of the new equations of motion which pertains to the transmission simulator motion. This is done using the free modes of the transmission simulator as shown in Eq. (50.23).

$$\left[\left[\begin{array}{cc} \omega_{fix}^2 & \mathbf{K}_{ps} \\ \mathbf{K}_{sp} & \mathbf{K}_{ss} - \omega_{\mathbf{TS}}^2 \end{array}\right] - \omega^2\left[\begin{array}{cc} \mathbf{I} & \mathbf{M}_{ps} \\ \mathbf{M}_{sp} & \mathbf{M}_{ss} - \mathbf{I} \end{array}\right]\right]\left\{\begin{array}{c} \bar{\boldsymbol{p}} \\ \bar{\boldsymbol{s}} \end{array}\right\} = 0 \tag{50.23}$$

The coordinates, $\bar{\boldsymbol{s}}$, which are the amplitudes of a set of shapes that span the motion of the interface degrees of freedom, can be readily related to the interface motion $\mathbf{x}_b$ and thus when the substructuring model is written in this Craig-Mayes it is easily coupled with a finite element model of subsystem D.

50.2.4 Craig-Chang Reduction Method

While the Craig-Bampton method utilizes fixed-interface modes, there exists a family of model reduction techniques relying on a basis of free-interface modes. This basis must also include interface attachment modes in order to meet static completeness and rigid-body modes if the system possesses rigid-body degrees of freedom.

One of those techniques is the so-called Craig-Chang reduction method [4]. Physical coordinates are transformed into Craig-Chang coordinates by means of a transformation matrix combining rigid-body modes $\boldsymbol{\Psi}_r$, a set of kept free-interface normal modes $\boldsymbol{\Phi}_k$ and inertia-relief residual-flexibility attachment modes $\boldsymbol{\Psi}_d$. Using the same partition between internal (i) and boundary (b) degrees of freedom as before, the transformation can be written as follows.

$$\mathbf{x} = \left\{\begin{array}{c} \mathbf{x}_i \\ \mathbf{x}_b \end{array}\right\} = \left[\begin{array}{ccc} \boldsymbol{\Psi}_{ir} & \boldsymbol{\Phi}_{ik} & \boldsymbol{\Psi}_{id} \\ \boldsymbol{\Psi}_{br} & \boldsymbol{\Phi}_{bk} & \boldsymbol{\Psi}_{bd} \end{array}\right]\left\{\begin{array}{c} \mathbf{q}_r \\ \mathbf{q}_k \\ \mathbf{q}_d \end{array}\right\} = \mathbf{T}_{\mathbf{CC}}\left\{\begin{array}{c} \mathbf{q}_r \\ \mathbf{q}_k \\ \mathbf{q}_d \end{array}\right\} \tag{50.24}$$

The transformation matrix $\mathbf{T}_{\mathbf{CC}}$ is thus applied to mass and stiffness matrices of the component to reduce them into their Craig-Chang formulations as described in Eqs. (50.25) and (50.26).

$$\mathbf{M_{CC}} = \mathbf{T_{CC}^T M T_{CC}} = \begin{bmatrix} \mathbf{I}_r & 0 & 0 \\ 0 & \mathbf{I}_k & 0 \\ 0 & 0 & \hat{\boldsymbol{M}}_{dd} \end{bmatrix} \tag{50.25}$$

$$\mathbf{K_{CC}} = \mathbf{T_{CC}^T K T_{CC}} = \begin{bmatrix} 0 & 0 & 0 \\ 0 & \boldsymbol{\omega}_k^2 & 0 \\ 0 & 0 & \hat{\boldsymbol{K}}_{dd} \end{bmatrix} \tag{50.26}$$

Where $\hat{\mathbf{M}}_{dd} = \boldsymbol{\Psi}_d \mathbf{M} \boldsymbol{\Psi}_d$ and $\hat{\boldsymbol{K}}_{dd} = \boldsymbol{\Psi}_d \mathbf{K} \boldsymbol{\Psi}_d = \boldsymbol{\Psi}_{bd}$. Contrary to Craig-Bampton method, the interface degrees of freedom are not preserved. Therefore, the assembly process of two components, one reduced using Craig-Bampton and the other by Craig-Chang, requires a constraint matrix $\mathbf{S}$ that is not simply boolean. Its expression is given by Eq. (50.28).

$$\begin{Bmatrix} \mathbf{q}_d^{(\mathbf{CC})} \\ \mathbf{q}_r^{(\mathbf{CC})} \\ \mathbf{q}_{k_1}^{(\mathbf{CC})} \\ \hline \mathbf{q}_{k_2}^{(\mathbf{CB})} \\ \mathbf{u}_b^{(\mathbf{CB})} \end{Bmatrix} = \mathbf{S} \begin{Bmatrix} \mathbf{q}_r^{(\mathbf{CC})} \\ \mathbf{q}_{k_1}^{(\mathbf{CC})} \\ \hline \mathbf{q}_{k_2}^{(\mathbf{CB})} \\ \mathbf{u}_b^{(\mathbf{CB})} \end{Bmatrix} \tag{50.27}$$

$$\mathbf{S} = \begin{bmatrix} -\left(\boldsymbol{\Psi}_{bd}^{(\mathbf{CC})}\right)^{\dagger} \boldsymbol{\Psi}_{br}^{(\mathbf{CC})} & -\left(\boldsymbol{\Psi}_{bd}^{(\mathbf{CC})}\right)^{\dagger} \boldsymbol{\Phi}_{bk_1}^{(\mathbf{CC})} & \mathbf{0}_{bk_2}^{(\mathbf{CB})} & -\left(\boldsymbol{\Psi}_{bd}^{(\mathbf{CC})}\right)^{\dagger} \\ \multicolumn{4}{c}{\mathbf{I}_{(r+k_1+k_2+b)}} \end{bmatrix} \tag{50.28}$$

Mass and stiffness matrices of the assembled system are then calculated by pre- and post-multiplying the associated matrices of the two components by the constraint matrix.

$$\mathbf{M_{CC+CB}} = \mathbf{S}^T \begin{bmatrix} \mathbf{M_{CC}} & 0 \\ 0 & \mathbf{M_{CB}} \end{bmatrix} \mathbf{S} \tag{50.29}$$

$$\mathbf{K_{CC+CB}} = \mathbf{S}^T \begin{bmatrix} \mathbf{K_{CC}} & 0 \\ 0 & \mathbf{K_{CB}} \end{bmatrix} \mathbf{S} \tag{50.30}$$

As the constraint matrix is obtained by enforcing the compatibility condition between boundary displacements of the two components, the assembly process is hence considered as a *primal* assembly. Another method based on free-interface normal modes but using a *dual* assembly is the so-called dual Craig-Bampton method [4], which is described below.

A few complications arise when using the Craig-Chang formulation with experimental measurements for substructure **C**. It requires the measurement of the free interface modes which is simple. It also requires the rigid body modes to be measured or obtained from a finite element model. In addition, all of these modes would need to be measured at the interface degrees of freedom. These can be obtained from an input that excites all of the modes of interest. Finally one must determine a method to measure the residual flexibility at the interface. This requires an input and output at each interface degree of freedom which is not very feasible in an experimental set-up.

50.2.5 Dual Craig-Bampton Method

Dual assembly of components uses interface forces and consequently, compatibility at boundaries is weakly enforced in comparison with primal assembly. Equations of motion of each subcomponent can be expressed with the explicit formulation of those interface forces by means of Lagrange multipliers λ and constraint matrix **C**.

$$\begin{bmatrix} \mathbf{M} & 0 \\ 0 & 0 \end{bmatrix} \begin{Bmatrix} \ddot{\boldsymbol{x}} \\ \boldsymbol{\lambda} \end{Bmatrix} + \begin{bmatrix} \mathbf{K} & -\mathbf{C}^T \\ -\mathbf{C} & 0 \end{bmatrix} \begin{Bmatrix} \mathbf{x} \\ \boldsymbol{\lambda} \end{Bmatrix} = \begin{Bmatrix} F \\ 0 \end{Bmatrix} \tag{50.31}$$

Similarly to Craig-Chang techniques, the dual Craig-Bampton is based on free-interface normal modes and residual-flexibility attachment modes. Therefore, the displacement of each subsystem can be expressed as follows.

$$\mathbf{x} = \boldsymbol{\Psi}_r \mathbf{q}_r + \boldsymbol{\Phi}_k \mathbf{q}_k + \mathbf{G}_d \mathbf{C}^T \boldsymbol{\lambda} \tag{50.32}$$

Where $\mathbf{G}_d$ is the residual-flexibility matrix. If rigid-body modes exist, the first term of the sum is non-zero and the residual-flexibility matrix must also be inertia-relief.

Subcomponents (1) and (2) can then be both reduced and assembled using the transformation matrix $\mathbf{T_{DCB}}$ defined in Eq. (50.33).

$$\left\{\begin{array}{c}\mathbf{x}^{(1)}\\ \hline \mathbf{x}^{(2)}\\ \hline \boldsymbol{\lambda}\end{array}\right\} = \left[\begin{array}{cc|cc|c} \boldsymbol{\Psi}_r^{(1)} & \boldsymbol{\Phi}_k^{(1)} & 0 & 0 & \mathbf{G}_d^{(1)}\mathbf{C}^{(1)T} \\ 0 & 0 & \boldsymbol{\Psi}_r^{(2)} & \boldsymbol{\Phi}_k^{(2)} & \mathbf{G}_d^{(2)}\mathbf{C}^{(2)T} \\ 0 & 0 & 0 & 0 & \mathbf{I} \end{array}\right] \left\{\begin{array}{c}\mathbf{q}_r^{(1)}\\ \mathbf{q}_k^{(1)}\\ \hline \mathbf{q}_r^{(2)}\\ \mathbf{q}_k^{(2)}\\ \hline \boldsymbol{\lambda}\end{array}\right\} = \mathbf{T_{DCB}} \left\{\begin{array}{c}\mathbf{q}_r^{(1)}\\ \mathbf{q}_k^{(1)}\\ \mathbf{q}_r^{(2)}\\ \mathbf{q}_k^{(2)}\\ \hline \boldsymbol{\lambda}\end{array}\right\} \tag{50.33}$$

$$\tilde{M}_{DCB} = \mathbf{T}_{\mathbf{DCB}}^T \begin{bmatrix} \mathbf{M}^{(1)} & 0 & 0 \\ 0 & \mathbf{M}^{(2)} & 0 \\ 0 & 0 & 0 \end{bmatrix} \mathbf{T_{DCB}} \tag{50.34}$$

$$\tilde{K}_{DCB} = \mathbf{T}_{\mathbf{DCB}}^T \begin{bmatrix} \mathbf{K}^{(1)} & 0 & -\mathbf{C}^{(1)T} \\ 0 & \mathbf{K}^{(2)} & -\mathbf{C}^{(2)T} \\ -\mathbf{C}^{(1)} & -\mathbf{C}^{(2)} & 0 \end{bmatrix} \mathbf{T_{DCB}} \tag{50.35}$$

The obtained mass and stiffness matrices using the dual Craig-Bampton method have the advantage of keeping mostly their sparsity unlike the Craig-Chang reduction. Degrees of freedom corresponding to interconnecting forces are added to the final reduced system.

50.3 Simple Beam System

50.3.1 Substructuring Example

To demonstrate this theory, the simple beam system from [6] will be used. The schematic of the system is shown in Fig. 50.2. The red beam is the substructure that we do not want to model analytically. The thick dark red beam, denoted as the TS beam, is the transmission simulator, which was designed so that when it is assembled to the red beam, the stiffness increases in a similar manner as when the blue beam is attached. The red beam with the transmission simulator attached, denoted as the experimental beam, is the substructure of interest, on which we take experimental data. Specifically, the red beam is 15 elements long and the transmission simulator is four elements long which overlaps the left most four elements of the red beam. The blue beam is the finite element model which is 20 elements long, denoted as the FE beam. The plus/cross on the FE beam and the experimental beam are where the two beams overlap and are connected after coupled.

During the substructuring process, the red beam will be coupled to the FE beam to produce the response of two beams attached one the other, denoted as the final system beam. The substructured beam will be compared to the finite element model of the final system beam which acts as the truth model.

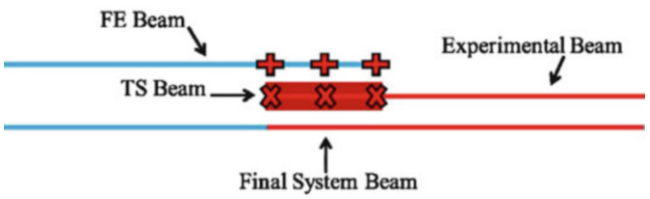

Fig. 50.2 Beam substructures and final assembled beam

In order to be coupled to the FE beam, the experimental-analytical model of the red beam will be obtained by five substructuring methods which are, in turn, the traditional Transmission Simulator method (TS), the Craig-Mayes method (CM), the Craig-Chang method (CC), the dual Craig-Bampton method (DCB), and finally the Craig-Bampton method (CB).

In the transmission simulator method, the TS serves both to mass load the interface, improving the modal basis by changing the shapes of the modes and bringing additional modes into the testable bandwidth. The CM method also makes use of a TS, but the other methods use different means to enrich the modal basis.

The other important reason for using a transmission simulator is to avoid having to measure the interface rotations and to average out errors in the measurements near the critical interface DOF. The CC and CB methods do not have any means of doing this, but for this beam structure the displacement DOF are close together and so the rotations can be neglected. Furthermore, the effect of noise and measurement errors will not be considered here. However, it is important to note that, in an experimental context, these methods would require very different measurements. The CC and DCB methods require a test on the component (red beam in this case) with free boundary conditions. The residual flexibilities are also needed, which can be measured if an input-output pair of measurements is available at each of the connection DOF (six in this case). These residual terms are more challenging to measure than traditional modes, but they have been used with success in several works. The CB method requires a test on the component of interest with its interface fixed, which is rarely practical. It also requires the fixed interface modes, which are practically impossible to measure. The results of the CB method are included here simply for reference and not because this is a viable experimental technique.

The substructuring process is summarized in below. First of all, the experimental-analytical model of the red beam was obtained by the aforementioned five methods, respectively. Based on the theory, these five methods obtained the model in different ways. The TS and CM method utilized the transmission simulator to obtain the model and thus were applied to the experimental beam which subtracted the thick dark red beam during the substructuring process. On the other hand, the traditional substructuring methods, including the CC, DCB, and CB method, were directly applied to the red beam and thus did not remove the transmission simulator. Therefore, the modes retained were not identical in each method. For the TS and CM method, all the rigid body modes and the first bending modes of the transmission simulator, and the three rigid body modes and the first seven bending modes (up to 22,185.9 Hz) of the *experimental beam* were retained in the formulation. The transmission simulator had six measured degrees of freedom, three vertical translations and three horizontal translations at the three nodes located at the transmission simulator left end, center, and right end, marked by the cross symbols in Fig. 50.2. For the other methods, all the rigid body modes and the first seven bending modes of the *red beam* (up to 22,366.0 Hz) were instead retained. Furthermore, the interface degrees of freedom of the red beam are considered to be those same six DOF that were the measurement points for the transmission simulator method. Second of all, The experimental-analytical models were individually coupled to the full finite element model of the FE beam via the connection points marked by the plus symbols in Fig. 50.2. Typically, inclusion of finite element modes is not as limited as experimental modes, and therefore the finite element model of the FE beam was not reduced, retaining all the degrees of freedoms.

To evaluate the methods, the natural frequencies predicted by substructuring are compared for the first ten bending modes (up to 10,137.6 Hz) of the truth model. The results of this comparison are listed in Table 50.1 and the relative errors in frequency are listed in Table 50.2. As shown in Tables 50.1 and 50.2, the TS and CM method yielded almost identical natural frequencies and relative errors. On the other hand, the CC and DCB method had almost identical results. Finally, all the experimentally-based methods show satisfactorily converge to the truth frequency within 2 % error and to the frequencies predicted by the CB method.

As a final remark, these five methods generated different numbers of spurious modes within the frequency range of interest (the spurious modes were previously filtered out and are not shown in Tables 50.1 and 50.2 to save space). The TS and CM method each generated two spurious modes whereas the CC and DCB and CB method each had three spurious modes.

50.3.2 Condition of Substructuring

As far as the TS and CM method are concerned, the convergence of substructuring depends on how accurately the connection point motion can be estimated from the motion at the measurement points. Based on the theory, the TS method uses the transmission simulator mode shape matrix $\boldsymbol{\Phi}_A$ in Eq. (50.3) to estimate the connection point motion whereas the CM method uses $\boldsymbol{\Phi}_b^{\dagger}\boldsymbol{\Psi}_b$ in Eq. (50.21). The connection point motion is expanded in the modal spaces spanned by these matrices which have to be full rank. Therefore, the condition numbers of these matrices indicate the condition of substructuring as pointed out in [1, 5].

To demonstrate this idea, the influence of the condition numbers of $\boldsymbol{\Phi}_A$ and $\boldsymbol{\Phi}_b^{\dagger}\boldsymbol{\Psi}_b$ on the simple beam system was examined. Table 50.3 shows the condition number of $\boldsymbol{\Phi}_A$ with respect to the number of the transmission simulator modes

Table 50.1 Comparison of beam truth frequency and TS, CM, CC, DCB, and CB substructured frequency (bending modes only)

Truth frequency (Hz)	Frequency TS (Hz)	Frequency CM (Hz)	Frequency CC (Hz)	Frequency DCB (Hz)	Frequency CB (Hz)
211.9	211.2	211.3	208.7	208.7	208.7
574.6	578.6	578.6	571.2	571.2	571.2
1121.0	1114.8	1114.7	1114.1	1114.1	1114.1
1867.3	1869.1	1869.3	1853.4	1853.4	1853.5
2750.2	2741.6	2741.4	2732.1	2731.0	2731.0
3949.6	3949.8	3949.8	3938.5	3938.5	3939.0
5115.9	5104.5	5104.3	5072.9	5073.0	5079.4
6703.0	6710.3	6710.1	6685.4	6685.5	6700.6
8338.9	8311.0	8311.0	8305.6	8305.7	8309.9
10,137.6	10,150.6	10,150.4	10,078.6	10,080.0	10,177.7

Table 50.2 Relative errors between the truth frequency and TS, CM, CC, DCB, and CB substructured frequency of the beam system (bending modes only)

Relative error TS (Hz)	Relative error CM (Hz)	Relative error CC (Hz)	Relative error DCB (Hz)	Relative error CB (Hz)
−0.35	−0.30	−1.51	−1.51	−1.51
0.70	0.71	−0.60	−0.60	−0.60
−0.56	−0.56	−0.62	−0.62	−0.62
0.10	0.11	−0.74	−0.74	−0.74
−0.31	−0.32	−0.70	−0.70	−0.66
0.01	0.01	−0.28	−0.28	−0.27
−0.22	−0.23	−0.84	−0.84	−0.71
0.11	0.11	−0.26	−0.26	−0.04
−0.33	−0.33	−0.40	−0.40	−0.35
0.13	0.13	−0.58	−0.57	0.40

Table 50.3 Condition number of $\mathbf{\Phi}_A$ with respect to transmission simulator modes

Number of TS modes retained	Condition number of Φ_A
1	1.00
2	1.17
3	1.41
4	2.31
5	2.31
6	1.14×10^{15}

from the simple beam system. Typically, there are at least as many measurement points as there are transmission simulator modes retained. Therefore, Table 50.3 only shows the condition numbers up to the sixth of the transmission simulator modes. As shown in Table 50.3, the condition numbers were less than 2.4 when the number of transmission simulator modes was kept less than five. When the number of transmission simulator modes was equal to six the condition number sky-rocketed to 1.14×10^{15}. It was also found that the former yielded the satisfactory convergence of frequency within 0.7 % absolute error compared with the truth frequency in Table 50.1 while the latter yielded one negative frequency and huge errors within the frequency range of interest and the substructuring failed.

On the other hand, the condition number of $\mathbf{\Phi}_b^{\dagger}\mathbf{\Psi}_b$ indicates the condition of substructuring using the CM method. Contrary to the TS method, the condition number of $\mathbf{\Phi}_b^{\dagger}\mathbf{\Psi}_b$ not only depends on transmission simulator modes but also on the modes of the experimental structure. As a result, a contour plot of the condition number of $\mathbf{\Phi}_b^{\dagger}\mathbf{\Psi}_b$ with respect to various combination of modes between the transmission simulator and the experimental beam from the simple beam system is plotted in Fig. 50.3. Totally, 13 modes of the experimental beam were considered which have their highest frequency equal to that in Sect. 50.3, and again the same six transmission simulator modes were considered. As shown in Fig. 50.3, when the number of the transmission simulator modes was kept less than four, all the combinations of modes gave relatively small condition numbers, shown as the cold region. It was also confirmed that the combinations of modes made in the cold region

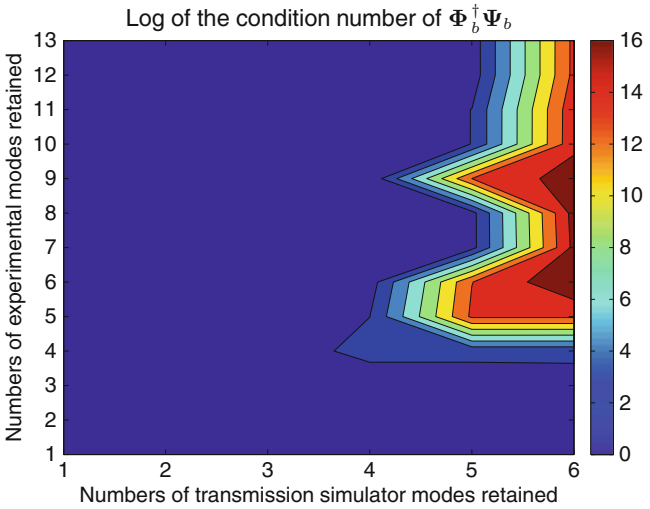

Fig. 50.3 Condition number of $\mathbf{\Phi}_b^\dagger \mathbf{\Psi}_b$ in contour plot

all led to accurate substructuring predictions without any spurious modes. When number of the transmission simulator modes was five or six, however, there were some combinations that forbid successful convergence due to large condition numbers (minimum magnitude of 10^{13}), shown as the hot region. Based on the formulation of the CM method, the number of modes of the experimental structure has be to greater than that of the transmission simulator. As such, when the transmission simulator modes were kept six, all combination of modes were in the hot region. When there were five of the transmission simulator modes, the combination with six or nine of the experimental beam modes were within the hot region. It was found that combinations made in the hot region yielded negative frequencies and led to failure of substructuring.

If both $\mathbf{\Phi}_A$ and $\mathbf{\Phi}_b^\dagger \mathbf{\Psi}_b$ are well-conditioned, the TS and CM method show no significant difference. Furthermore, the converge rates were observed to improve if the connection point motion were more accurately estimated. Figure 50.4 shows a convergence study done by using the TS and CM method on the simple beam system with increasing numbers of the experimental beam modes and two different choices of the transmission simulator modes to retain. Consequently, two groups of data sets are presented in Fig. 50.4. The first group of data concerns the convergence rates of the TS and CM method with retaining only the rigid body modes of the transmission simulator. The second group, on the other hand, considers the convergence rates with additional inclusion of the first bending mode of the transmission simulator. As shown in Fig. 50.4, after including sufficient (e.g., > 6 for the fist group or > 8 for the second group) experimental beam modes convergence rates had no significant improvement. Further improvement was observed when the first bending mode of the transmission simulator was included. This could be an important point. Including that mode not only gives a better model for the TS, it allows us to more accurately estimate the motion of the connection point, to which the analytical structure will eventually be coupled.

50.4 Cylinder-Plate-Beam System

50.4.1 Introduce System

To test this theory with experimental data, a sample experimental system was chosen from [6]. The cylinder-plate-beam (CPB) system consists of a cylinder packed with pressed foam that houses an internal mass. At one end of the cylinder a plate and beam are attached to the system to simulate the rest of the structure of interest. The cross section of a solid model is shown in Fig. 50.5. The cylinder and plate-beam are 6061 T6 aluminum. The goal of this example is to estimate a model for the dynamics of the foam and the internal mass. These internals are extremely challenging to model because the foam's properties are poorly defined and depend non-linearly on the preload in the foam. In addition the contact conditions between the foam and the rest of the structure are not known.

For this, the full CPB system is considered subsystem **C** and will be tested to deduce a model for the internals. The transmission simulator and Craig-Mayes methods can easily be applied using a finite element model of the transmission

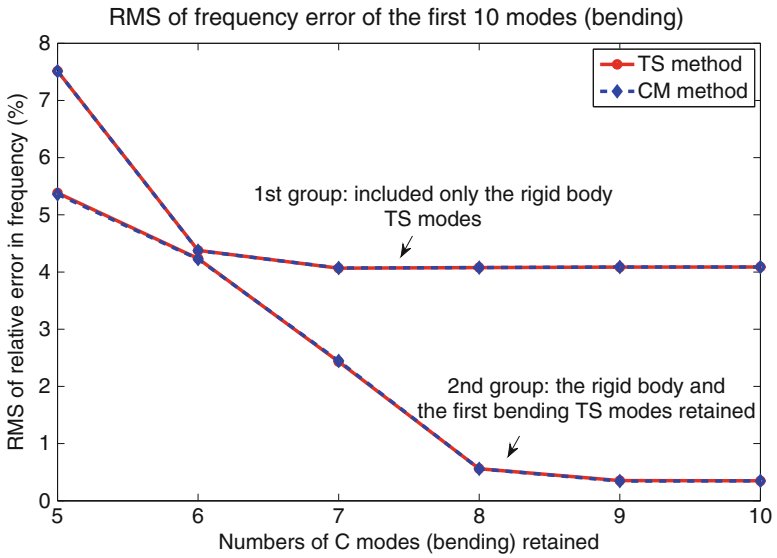

Fig. 50.4 Root mean square (RMS) of relative error in frequency. Comparison with the first ten modes (*bending*) of the truth model

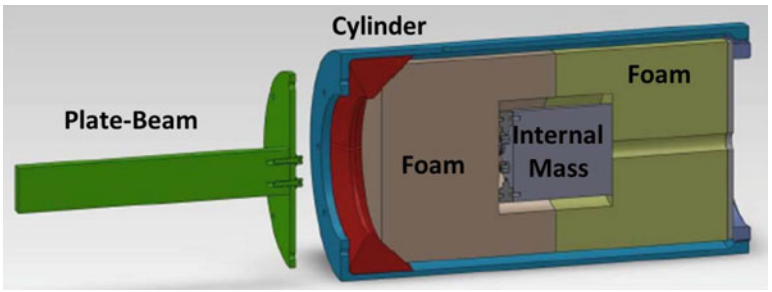

Fig. 50.5 Experimental system solid model

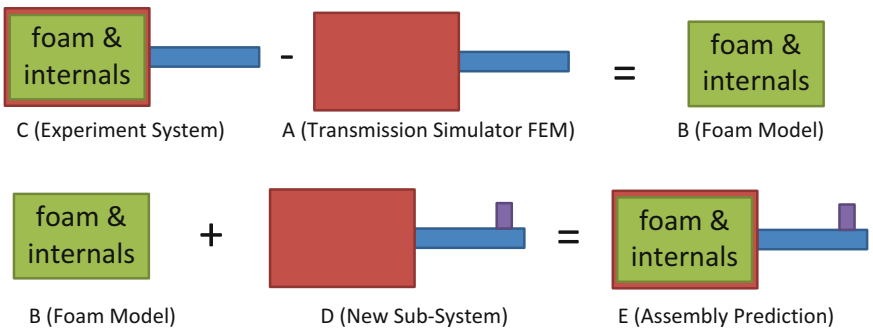

Fig. 50.6 Transmission simulator subsystem designation

simulator **A** (consisting of the beam, plate and cylinder) leaving an experimental model for the foam and internal mass. To validate the model for the internals, the authors have added a new beam, plate, and cylinder external system but with a mass loading the end of the beam. This simulates a situation in which the substructure model would be used to predict the response after the other substructures have been modified. A validation test was completed to check the accuracy of the substructuring predictions. Figure 50.6 shows the different subsystems being used in this substructuring example.

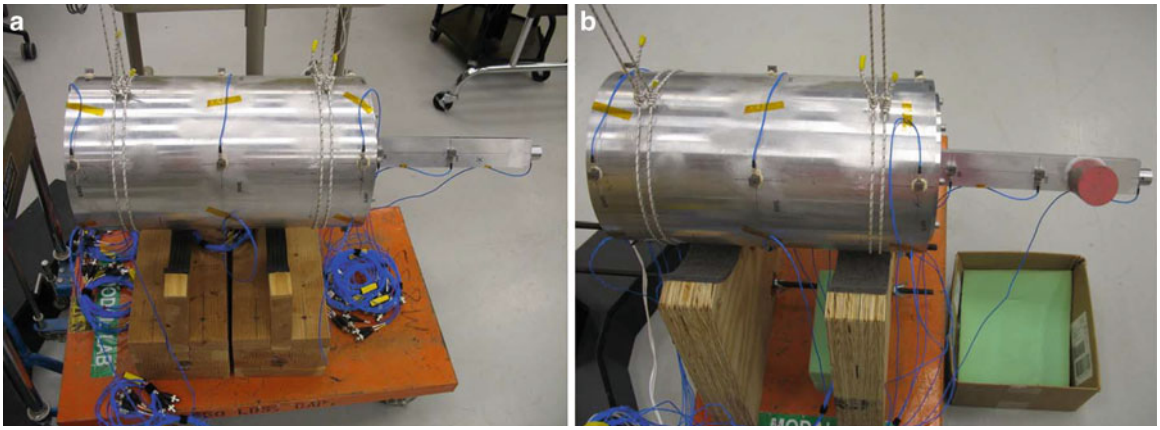

Fig. 50.7 Experimental setup for system C (*left*) validation test on system E with added mass (*right*)

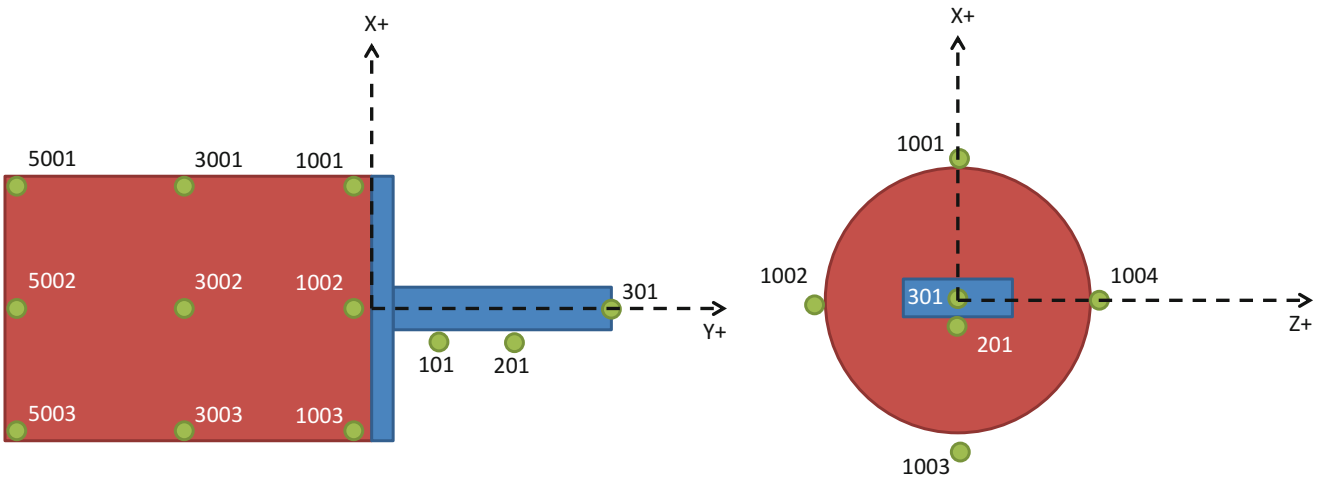

Fig. 50.8 External instrumentation

50.4.1.1 Experiment

A modal test was completed for both the CPB system and the mass-loaded truth test. The system was instrumented with 18 triaxial accelerometers with sensitivities of 100 mV/g. Fifteen of these accelerometers were placed on the external side of the hardware (12 on the can at three axial stations with four equally spaced around the circumference at each station and 3 on the beam). The remaining three triaxial accelerometers were placed on the internal mass, which is packed between the foam blocks. Figure 50.7 shows the experimental set up for the CPB system with and without the added mass.

The external accelerometers were configured as shown in Fig. 50.8. These were placed to capture the motion of the CPB system up to 1000 Hz based on previous experience [7].

A series of low-level forcing tests were completed at several driving point locations in order to avoid any non-linearities in the system. For each mode, the location at which it responded most strongly was used to extract the modal parameters using the SMAC algorithm [7]. These driving points are listed in Table 50.4 in the column labeled "Reference". The information from the linear test on the baseline CPB system is shown in Table 50.4. Note, the rigid body modes were generated analytically but were checked and compared to the mass lines of the measured frequency response functions.

50.4.1.2 Model

A finite element model (FEM) of the cylinder-plate-beam (CPB) was constructed and is detailed in Fig. 50.9. The three-dimensional solid structure was modeled by brick type higher order 20-node solid elements with quadratic displacement behavior. The CPB FE model comprises beam, plate, washer, cylinder and ring Fig. 50.9. The FE model was constructed as a

Table 50.4 Cylinder-plate-beam test results

Mode	Frequency (Hz)	Damping ratio (%)	Reference	Description
1	1	1	NA	Rigid translation in X
2	1	1	NA	Rigid translation in Y
3	1	1	NA	Rigid translation in Z
4	1	1	NA	Rigid rotation about X
5	1	1	NA	Rigid rotation about Y
6	1	1	NA	Rigid rotation about Z
7	116	0.27	5003X+	First bending in the X-Direction
8	153	0.15	5002Z+	First bending in the Z-Direction
9	276	2.37	5002Z+	Internals rotation about Y plus translation in Z
10	282	2.08	5003X+	Internals translation in X and Z
11	300	2.26	5002Z+	Off-axis rotation of internals about Y plus translation in X
12	455	0.32	301Y−	Axial mode, internals and nose out of phase
13	589	2.09	301Y−	Internals rotation about Z
14	634	1.96	5002Z+	Internals rotation about X
15	691	1.28	301Y−	Axial mode, internals and nose in phase
16	742	1.19	3003X+	Suspected foam mode mostly in X
17	761	1.13	3002Z+	Suspected foam mode mostly in Z
18	831	1.00	5002X+	First axial torsion
19	914	0.79	3002Z+	(2,0) ovaling on-axis
20	964	0.22	1301X+	2nd bending in the X-Direction

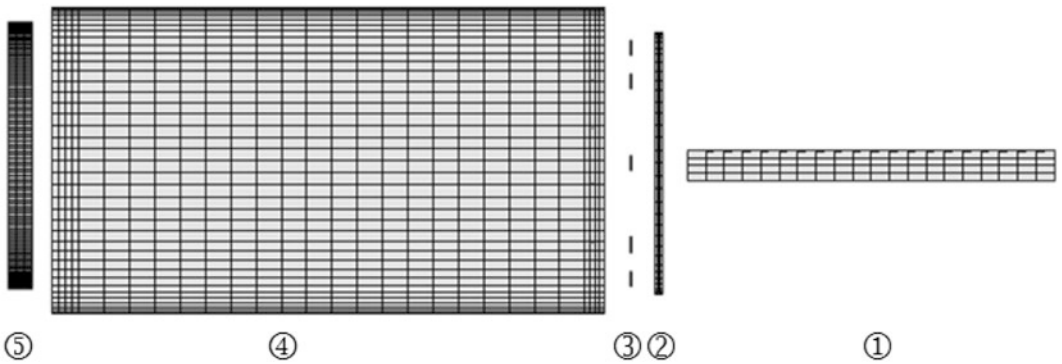

Fig. 50.9 Configuration of CBP FE model: *1*—Beam, *2*—Plate, *3*—Washer, *4*—Cylinder, *5*—Ring

Table 50.5 Element properties of each component

	Component	Material	Material properties
①	Beam	6061 T6 Aluminum	$E = 1.0 \times 10^7$ psi, $\nu = 0.33$, $\rho = 0.0975\,\mathrm{lb/in^3}$
②	Plate	6061 T6 Aluminum	$E = 1.0 \times 10^7$ psi, $\nu = 0.33$, $\rho = 0.0975\,\mathrm{lb/in^3}$
③	Washer	Steel	$E = 3.0 \times 10^7$ psi, $\nu = 0.29$, $\rho = 0.2800\,\mathrm{lb/in^3}$
④	Cylinder	6061 T6 Aluminum	$E = 1.0 \times 10^7$ psi, $\nu = 0.33$, $\rho = 0.0975\,\mathrm{lb/in^3}$
⑤	Ring	6061 T6 Aluminum	$E = 1.0 \times 10^7$ psi, $\nu = 0.33$, $\rho = 0.0975\,\mathrm{lb/in^3}$

single linear structure by merging the adjacent nodes at the contact points between each component. The element properties of all of the components except the washers are set as 6061 T6 Aluminum, with the material properties listed in Table 50.5. The detailed component name and properties are shown in Table 50.5. Fifteen nodes were selected as the sensor positions and the mesh was constructed such that these corresponded precisely to the actual accelerometer locations.

To validate the FE model, the natural frequencies of the cylinder-plate-beam system were examined. Table 50.6 shows the first eleven elastic frequencies of CPB model with the retaining ring on the far left removed. These are compared to the measured natural frequencies of the actual hardware, from a test that was performed before the foam and retaining ring had been installed [6] (Fig. 50.10).

Table 50.6 Elastic modal frequencies of CPB

Mode	Test frequency (Hz)	FEM frequency (Hz)	Error (%)
1	134.2	133.83	−0.28
2	171.2	171.30	0.06
3	430	435.15	1.20
4	511.2	497.42	−2.70
5	975.7	954.60	−2.16
6	1027	1038.14	1.08
7	1312	1301.33	−0.81
8	1528	1535.62	0.5
9	1637	1589.17	−2.92
10	1801	1846.45	2.52
11	1833	1859.75	1.46

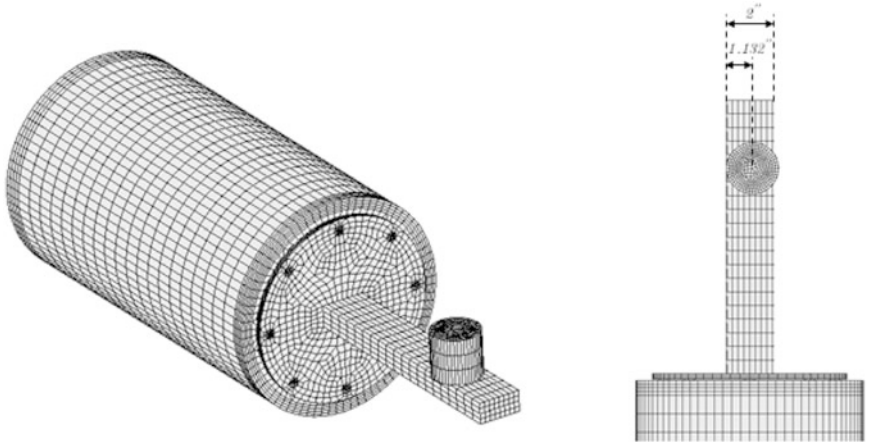

Fig. 50.10 CPB model with additional mass

The additional mass attached at the end of the beam is modeled with 20 node hex elements (Fig. 50.10). The nodes in this mesh did not naturally align with those in the beam mesh, so the two substructures were connected using the multi-point constraint method.

50.4.2 Predictions and Comparison with Experimental Truth Data

Here we shall consider a substructuring problem in which the first 20 free normal modes (6 rigid body modes and 14 elastic modes) up to 970 Hz were extracted from the experimental system *C* in Fig. 50.6, consisting of the CBP structure with the foam inside. These 20 free normal modes also included the experimental damping ratio. A FE model of the transmission simulator, i.e. the CBP structure (*A* in Fig. 50.6), was used to remove the effects of the transmission simulator. From the FE model of the transmission simulator, ten free normal modes (six rigid body modes and the first four elastic modes) up to 805 Hz were retained with an arbitrarily assigned damping ratio of 0.5 %. Subsequently, the dynamics of the modified CBP structure (i.e. with the mass attached, system *D* in Fig. 50.6) were added to predict the dynamical behavior of the truth hardware (system *E* in Fig. 50.6) and shown on the right in Fig. 50.7. The predictions will then be compared to the results of the test on the truth hardware to evaluate the substructuring methods.

Two different substructuring approaches were applied, the traditional transmission simulator method (TS) and the Craig-Mayes method (CM).

Table 50.7 Frequencies, damping ratios and MAC values, traditional transmission simulator method

Traditional transmission simulator method							
Mode No.	$f_{experiment}$	$f_{prediction}$	f error	$\zeta_{experiment}$	$\zeta_{prediction}$	ζ error	MAC
(-)	(Hz)	(Hz)	(%)	(-)	(-)	(%)	(-)
7	88.33	86.59	−1.96	0.00196	0.00215	9.38	0.9803
8	115.80	115.06	−0.64	0.00163	0.00207	26.83	0.9929
9	275.97	276.11	0.05	0.02468	0.02466	−0.10	0.9006
10	283.32	283.24	−0.03	0.02151	0.02168	0.80	0.9995
11	301.40	301.77	0.12	0.02327	0.02290	−1.61	0.9957
12	346.25	349.76	1.01	0.00291	0.00359	23.47	0.9867
13	584.71	583.20	−0.26	0.02119	0.02135	−0.77	0.9963
14	635.16	634.89	−0.04	0.02037	0.01897	−6.87	0.9948
–	NA	670.72	NA	NA	0.00504	NA	NA
15	688.92	690.36	0.21	0.01515	0.01363	−10.03	0.9320
–	NA	717.45	NA	NA	0.00537	NA	NA
16	758.36	NA	NA	0.01131	NA	NA	NA
17	769.71	770.99	0.17	0.01191	0.01201	0.84	0.8827

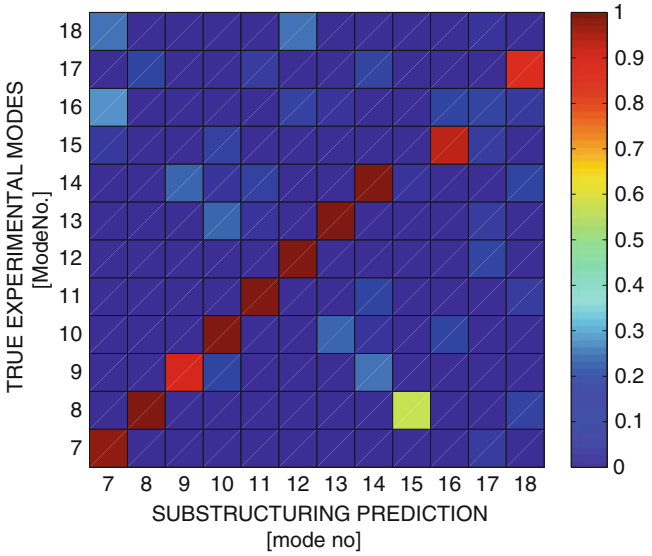

Fig. 50.11 MAC traditional TS method vs. Truth

50.4.2.1 Traditional TS Method

From the FE model of the modified CBP structure *D*, 13 free normal modes (six rigid body modes and the first seven elastic modes) up to 858 Hz were retained and an arbitrary damping ratio of 0.5 percent was assigned. All three structures (experimental system *C*, transmission simulator *A* and modified CBP structure *D*) were connected using modal constraints at the 45 exterior measurement degrees of freedom (i.e. $\Phi_A^{\dagger}$ in Eq. (4) contained 45 rows corresponding to all of the exterior measurement degrees of freedom).

Table 50.7 shows the prediction obtained by the traditional TS method compared to the truth experiment *E*.

The modes are well predicted up to the 14th mode at 635 Hz, with relative frequency errors between −1.96 % and 1.01 %, relative damping errors between −6.87 % and 26.83 % and MAC values between 0.9006 and 0.9995.

By visualizing the predicted mode shapes with a wireframe model built of the sensor nodes, the modes predicted at 670.72 Hz and at 717.45 Hz could be identified as non-physical, so-called spurious modes. In this case, the traditional TS Method is not able to predict the 16th mode of the truth experiment at 758.36 Hz with the number of modes retained from the transmission simulator and from the modified CBP structure. The MAC between the predicted and true experimental modes are shown in Fig. 50.11, and was used to do the pairing in Table 50.7.

Table 50.8 Frequencies, damping ratios and MAC values, Craig-Mayes method

Craig-Mayes transmission simulator method							
Mode No.	$f_{experiment}$	$f_{prediction}$	f error	$\zeta_{experiment}$	$\zeta_{prediction}$	ζ error	MAC
(-)	(Hz)	(Hz)	(%)	(-)	(-)	(%)	(-)
7	88.33	89.58	1.42	0.00196	0.00208	5.84	0.9861
8	115.80	115.25	−0.47	0.00163	0.00204	25.14	0.9975
9	275.97	275.83	−0.05	0.02468	0.02459	−0.36	0.8886
10	283.32	282.61	−0.25	0.02151	0.02156	0.23	0.9986
11	301.40	301.48	0.03	0.02327	0.02284	−1.84	0.9966
12	346.25	350.61	1.26	0.00291	0.00343	17.96	0.9897
13	584.71	583.64	−0.18	0.02119	0.02141	1.05	0.9971
14	635.16	634.85	−0.05	0.02037	0.01900	−6.69	0.9961
–	NA	679.99	NA	NA	0.00491	NA	NA
15	688.92	691.85	0.43	0.01515	0.01351	10.83	0.9075
–	NA	707.57	NA	NA	0.00574	NA	NA
16	758.36	NA	NA	0.01131	NA	NA	NA
17	769.71	760.69	−1.17	0.01191	0.01125	−5.54	0.8308

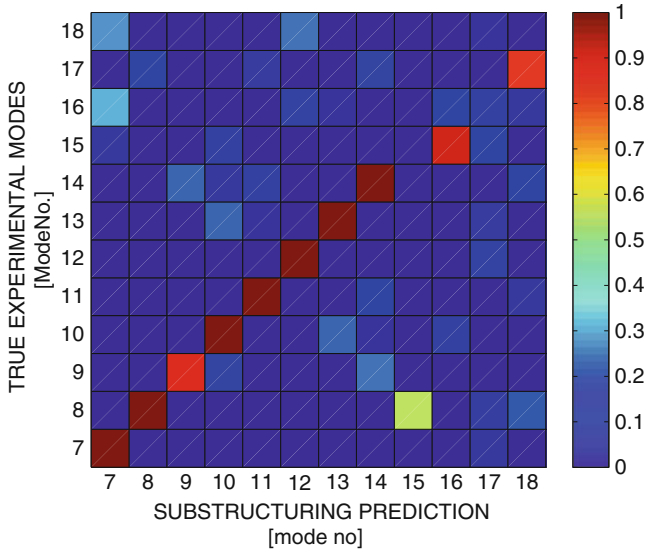

Fig. 50.12 MAC Craig-Mayes method vs. Truth

50.4.2.2 Craig-Mayes Method

The FE model of the modified CBP structure D was transformed to Craig-Bampton coordinates after arbitrarily assigning a damping ratio of 0.5 %. Eight fixed-interface normal modes up to 1898 Hz were retained during the transformation. Here, the 45 exterior measurement degrees of freedom were considered as the interface and held fixed. The Craig-Mayes representation resulting from the experimental system C and the transmission simulator A was connected to the Craig-Bampton representation of the modified CBP structure D by primal assembly at the 45 exterior measurement degrees of freedom.

Table 50.8 shows the prediction obtained by the Craig-Mayes method compared to the truth experiment E.

The modes are well predicted up to the 14th mode at 635 Hz, with the relative frequency errors ranging from −0.47 % to 1.42 %, relative damping errors between −6.69 % and 25.14 % and the MAC values ranging from 0.8886 to 0.9986.

The modes predicted at 679.99 Hz and at 707.57 Hz could be identified as spurious modes. Here, the Craig-Mayes method is not able to predict the 16th mode of the truth experiment at 758.36 Hz with the number of modes retained from the transmission simulator and from the modified CBP structure. In Fig. 50.12, the MAC values for the mode shapes predicted by the Craig-Mayes method and the true experimental mode shapes are shown.

50.4.2.3 Observations and Comparison of Traditional TS Method and Craig-Mayes Method

The traditional TS method and the Craig-Mayes method show the same characteristics concerning the number of modes used for the respective substructuring steps and the frequency and damping predictions for system *E*.

The number of modes used for the subtraction of the transmission simulator (CBP structure *A*) was varied. With both methods, at least the six rigid body modes plus two elastic modes up to 178 Hz were needed to get results with a relative frequency error smaller than 10 % and a relative damping error smaller than 100 %. As soon as the number of modes used for the subtraction exceeded the frequency range of the experimental system *C*, the relative frequency errors were bigger than 40 % and no meaningful results could be obtained for the damping using either of the methods.

The number of modes used to add the dynamics of the modified CBP structure *D* was varied, too. Enough modes to cover the same frequency range as at the subtraction of the TS had to be used in order to get frequency errors smaller than 10 % after the addition of the modified CBP structure (free normal modes for the traditional TS method and fixed-interface normal modes for the Craig-Mayes method). Once that number of modes was reached, using more modes of the modified CBP structure only affected the second decimal place of the frequency predictions and also no significant change in the damping predictions could be observed for either of the methods.

Both methods predict the modes of the truth experiment *E* up to 635 Hz (mode no 14) quite well, which is more than half of the frequency range considered (970 Hz system *C*). The relative frequency errors range from −1.96 % to 1.01 % (traditional Transmission Simulator method) and −1.17 to 1.42 % (Craig-Mayes method), respectively. The relative damping errors range from −6.87 % to 26.83 % (traditional Transmission Simulator method) and −6.69 to 25.14 % (Craig-Mayes method), respectively. Regarding those relative frequency and damping errors, the two methods are almost equivalent in their predictions.

The traditional TS method and the Craig-Mayes method both predict a spurious mode between the 14th mode and the 15th mode and between the 15th mode and the 16th mode of the truth system. As applied here, neither of both methods is able to predict the 16th mode of the truth system at 758.36 Hz. In Fig. 50.13, the MAC values for the mode shapes predicted by the Craig-Mayes method and the mode shapes predicted by the traditional TS method are shown. The lowest MAC value on the diagonal is 0.9483 at mode no 17, showing that both methods predict almost the same mode shapes for the truth system (including the two spurious modes).

The traditional TS method and the Craig-Mayes method both seem to be well suited to predict the frequencies, damping and mode shapes of the modified CBP structure with the foam inside up to half of the frequency range considered.

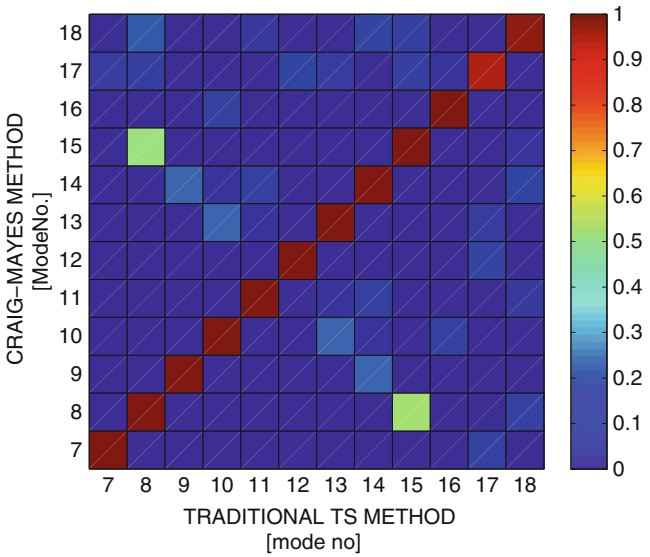

Fig. 50.13 MAC Traditional TS method vs. Craig-Mayes method

50.5 Conclusions

This paper presented multiple examples of both the Transmission Simulator method and the Craig-Mayes method. The first example was of a simple beam model where the TS and CM methods were compared. Additional comparisons were made to the Craig-Chang, Craig-Bampton, and dual Craig-Bampton methods. In these comparisons the TS and CM methods were found to have similar results with a maximum frequency error of 0.70 %. This paper also looks at a few parameters to be checked when completing the TS and CM methods. Of particular note the TS method requires the mode shapes to be well conditioned such that the pseudo-inverse does not amplify any experimental error. In contrast, the CM method also requires that the modes of the experimental structure be well condition when partitioned to just the connection degrees of freedom.

The second example is comprised of a more complicated Cylinder-Plate-Beam system. In this example, both the TS and CM methods were employed to remove the cylinder-plate-beam from experimental results generating an experimental model of just the internal foam and mass. A finite element model of the cylinder-plate-beam was used as a transmission simulator for both of these methods. Another FEM model with an additional mass added to the beam was then substructured with the experimental foam model. This process was completed with both the traditional transmission simulator and the Craig-Mayes formulation. After comparing these results to an experimental truth test the maximum frequency error was less than 2 % while the maximum damping error was near 25 % for both methods.

References

1. Allen, M., Mayes, R., Bergman, E.: Experimental modal substructuring to couple and uncouple substructures with flexible fitures and multi-point connections. J. Sound Vib. **329**, 4891–4906 (2010)
2. Mayes, R., Allen, M., Kammer, D.: Correcting indefinite mass matrices due to substructure uncoupling. J. Sound Vib. **332**, 5856–5866 (2013)
3. Allen, M., Kammer, D., Mayes, R.: Metrics for diagnosing negative mass and stiffness when uncoupling experimental and analytical substructures. J. Sound Vib. **331**, 5435–5448 (2012)
4. Craig, R., Kurdila, A.: Fundamentals of Structural Dynamics, 2nd edn. Wiley, Hoboken, NJ (2006)
5. Mayes, R.: A craig-bampton experimental dynamics substructure using the transmission simulator method. In Proceedings of the 33rd International Modal Analysis Conference (2015)
6. Mayes, R., Rohe, D.: Coupling experimental and analytical substructures with a continuous connection using the transmission simulator method. In: 31st International Modal Analysis Conference (2013)
7. Hensley, D.P., Mayes, R.L.: Extending smac to multiple references. In: Proceedings of the 24th International Modal Analysis Conference, pp. 220–230 (2006)